ALL SCIENCES ACADEMY

8th International Conference on Engineering, Natural and Social Sciences ICENSOS 2026



September 06-07, 2026 | **Proceeding Book** | Konya, Turkey

All Sciences Academy

PEOCEEDING BOOK OF 8TH INTERNATIONAL CONFERENCE ON ENGINEERING, NATURAL AND SOCIAL SCIENCES ICENSOS 2026

PROCEEDING BOOK OF 8TH ICENSOS 2026:

06-07 September 2026

Konya, Turkey

Publication date: 15.09.2026

Publisher: All Sciences Academy

Proceeding Book of 8th International Conference on Engineering, Natural and Social Sciences ICENSOS 2026

https://www.icensos.com/

8th International Conference on Engineering, Natural and Social Sciences ICENSOS 2026: edited by All Sciences Academy.

ISBN: 978-625-8839-87-6

As this is a serial book published, it has ISBN. All abstracts were peer reviewed.

ISBN: 978-625-8839-87-6

Printed in the Turkey with ISBN 978-625-8839-87-6

International Conference Website

https://www.icensos.com/

INTRODUCTION

We had the great honor of 8th International Conference on Engineering, Natural and Social Sciences ICENSOS 2026. It was truly a great pleasure for us to greet a lot of participants from many different countries to attend ICENSOS 2026! We firmly believe that the conference will become an important international event in the field of cross-industry discussion about innovations in Academic Studies.

Three cooperating organizations supported the two-day conference. There were 163 papers accepted for presentation at ICENSOS 2026, contributed from different countries. We had plenary speeches and several well-known scientists and experts, to give invited talks at differentsessions.

The purpose of ICENSOS 2026 was to provide a forum for the participants to report and review innovative ideas, with up-to-date progress and developments, and discuss novel approaches to the application in the field of their own research areas and discuss challenges of doing science.

We sincerely hope that the exchange of ideas on doing research, science and improving education will help the participants, and international cooperation sharing the common interest will be enhanced.

On behalf the Organization Committee of ICENSOS 2026, we would like to heartily thank our cooperating organizations for all they have done for the conference. We would also like to thank the authors for theircontribution to the proceedings; the participants and friends of ICENSOS 2026, for their interest and efforts in helping us to make the conference possible; and the Editorial boards for their effective work and valuable advice, especially the ICENSOS 2026 secretariat and the ICENSOD 2026 staff, for their tireless efforts and outstanding services in preparing the conference and publishing the Proceedings.

Publisher: All Sciences Academy

TABLE OF CONTENTS

Introduction II
Table of Contents III
Conference Chairs XI
Scientific Committees XII
Document of Academic Incentive XIII
Document of International Conference XIV

Table List of Content

Content of Abstract Papers

Page No	Title	Authors	Country	Submission ID
1	Bridging Accuracy and Access: Deep Learning-Driven Simultaneous Translation in Libyan Public Institutions Reliability, Challenges, and Implications for Medium-Size Organizations	Rima Subhi Husain Taher, Llahm Ben Dalla, Ayyah Mustafa Salih, Mohamed Khaleel, Ebtisam Fakroun, Asma Agaal	Libya, Turkey, Libya,Libya,Libya,Libya	Mail Submission 1
2	Synthesis, characterization and evaluation of new N-vinylpyrrolidons derivatives as corrosion inhibitor for carbon steel in in 1M HCl medium: Combination of experimental, surface morphological and computational insights	Youssef Youssefi, Lahcen Oucheikh, Omar Ou-ani, Ahmad Oubair, Mohamed Znini	Morocco, Morocco, Morocco, Morocco, Morocco	Mail Submission 4
3	Hybrid Statistical–Deep Learning Inference for Parameter Estimation of Rayleigh–Generalized Gamma Mixture Distributions	BENTOUMI AHMED, BENTOUMI MILOUD, BENDIB AHMED3, ARIOUA ISSLEM, AZIZ ROUEBHI	Algeria, Algeria, Algeria, Algeria, Algeria	Submission 664
4	Halide Perovskite Solar Cells: Interface Engineering for Enhanced Stability, Efficiency and Sustainable Energy Conversion.	Muhammad Abbas, Muhammad Haseeb-u-Rehman, Ghulam Hasnain Tariq	Pakistan, Pakistan, Pakistan	Submission 666
5	Orientalists' Criticism On Isra' wal-Mi'raj and their Responses: An Analytical Study	Fariha Fatima	Pakistan	Submission 667
6	From Choice to Necessity: How Artificial Intelligence (AI) Has Become a Need for Everything	Abdul Waheed, Umer Ayub, Syed Ahmad Ali	Pakistan, Pakistan, Pakistan	Submission 669
7	A Specific Case of a Flat Translation Surface of Type 5 in the Lorentz-Heisenberg Space Group H_3	Rafik Medjati, Hanifi Zoubir	Algeria, Algeria	Submission 671
8	Biocontrol Potential of Trichoderma afroharzianum Against Botrytis cinerea Causing Chocolate Spot of Faba Bean in Algeria	BOUANAKA, Hamza, HARRAT, Wahiba, SADRATI, Nouari, BOUSSAHA, Saoussene	Algeria, Algeria, Algeria, Algeria	Submission 672
9	The Era of Smart Thinking: Role of Human-Intelligence in Implementing Artificial-Intelligence	Mehwish Asghar Ali, Mehnaz, Abdul Waheed, Humera Imtiaz, Ayesha Qayyum	Pakistan, Pakistan, Pakistan, Pakistan, Pakistan	Submission 673
10	Evaluation of a Low-Cost Rotary Drum Composter for Rapid Date Palm Waste Stabilization under Arid Conditions	Abdelouahad Ouali, Abderrazak Mabrouki, Youssouf Ouzani, Fatima Hiouani, Djamila Madani	Algeria, Algeria, Algeria, Algeria, Algeria	Submission 674
11	Controllability Analysis of Irregular Descriptor Systems via Matrix Decomposition and Normal Equivalent Forms	MAKRELOUFI Abed	Algeria	Submission 675
12	Distributed Hierarchical Optimization for Coordinated Control of Interconnected Wind Farms	Ali Abderrazak Tadjeddine, Soumia Djelaila, Latifa Smail, Lachache Salih, Abdelyamine Boukhobza	Algeria, Algeria, Algeria, Algeria, Algeria	Submission 676
13	Flexible Power Point Tracking with Frequency Support for Grid-Connected PV Systems	Ali Abderrazak Tadjeddine, Hassane Dahbi, Iliace Arbaoui, Touhami Ghaitaoui	Algeria, Algeria, Algeria, Algeria	Submission 677
14	Resilience, Opportunity Recognition, and Entrepreneurial Intentions in Aviation	Shahid Mahmood	Pakistan	Submission 680
15	The Potential of Artificial Intelligence in Biology Education	Parvin Gafarova, Sanubar Aslanova	Azerbaijan, Azerbaijan	Submission 681
16	Digital Technologies and Virtual Laboratories in Biology Education	Parvin Gafarova, Sanubar Aslanova	Azerbaijan, Azerbaijan	Submission 682
17	Finite element simulation of the deformation of concrete incorporating thermal effect using ANSYS	Farid Bouziadi, Nefissa Belkacem, Bensaid Boulekbache, Mostefa Hamrat, Mohamed Ladjel	Algeria, Algeria, Algeria, Algeria, Algeria	Submission 688
18	Seasonal variability in the diet	TABECHE Ali, BOUHADIBA	Algeria, Algeria, Algeria, Algeria,	Submission 692

	composition of Solea solea in Oran Bay	Sultana, AOUADJ Sid Ahmed, BELHOUCINE Fatma, ALIOUA BERREBBAH Amel	Algeria	
19	Ontogenetic changes in diet and trophic niche in Solea solea in Oran Bay	TABECHE Ali, BOUHADIBA Sultana, AOUADJ Sid Ahmed, BELHOUCINE Fatma, ALIOUA BERREBBAH Amel	Algeria, Algeria, Algeria, Algeria, Algeria	Submission 693
20	RE-AWAKENING HUMAN CONSCIOUSNESS ON CULTURE AND LANGUAGE THROUGH A SOCIALIZED EPISTEMOLOGICAL MODEL	Abiodun Moses Jinadu	Nigeria	Submission 694
21	Numerical Investigation and Performance Optimization of $CsSnI_3$-Based Solar Cells Using SCAPS-1D	Mourad BELLA	Algeria	Submission 697
22	Numerical Modeling and Optimization of CZTSSe Thin-Film Solar Cells Using SCAPS-1D	Mourad BELLA	Algeria	Submission 698
23	Propagating Modes in the Quark-Gluon Plasma	Embarka Boutalbi, Leila Ait-Gougam -Tribeche, Abdennour Bouchebak	Algeria, Algeria, Algeria	Submission 699
24	First-Principles Investigation of the Structural, Electronic, Optical, and Elastic Properties of YN1-xAsx Alloys	Nour El Imen Zeghoum, Said Lakel	Algeria, Algeria	Submission 700
25	Ab Initio Study of Structural Properties and Charge Transfer Mechanisms in ZrV_2O_7/Graphene and $ZrTi_2O_6$/Graphene Heterojunctions	Laghari Aqsa, Mansha Asim	Pakistan, Pakistan	Submission 704
26	PVP-Stabilized Metal Nanoparticles Supported on MOF for Enhanced Hydrogen Generation from Sodium Borohydride	Tuğçe Emine Çakal, Mehmet Yurderi, Mehmet Zahmakıran	Turkey, Turkey, Turkey	Submission 706
27	Spectrophotometric Evaluation of the UV Photoprotective Potential of Plant Extracts	Hamit Ismaili, Imer Haziri, Arben Haziri, Ilirjana Osmani	Kosovo, Kosovo, Kosovo, Kosovo	Submission 707
28	Predicting Football Fandom in Turkey: A Machine Learning and Statistical Approach Based on Demographic and Socioeconomic Factors	Abdulkadir Gürbüz	Turkey	Submission 709
29	IMPACT OF AI-POWERED LEARNING APPLICATIONS ON SECONDARY SCHOOL STUDENTS' ACADEMIC ACHIEVEMENT IN ECONOMICS IN SOUTH WEST NIGERIA	MICHAEL BAMIDELE OJO	Nigeria	Submission 711
30	Önemli Bir Doğa Alanı Olan Bahşayiş Seddesi	Arif Cemal Özsemir	Turkey	Submission 712
31	Waste Valorization for Sustainable Building Materials: A Review	BOUSLAH Mahmoud, MAZA Mekki, RAHMOUNI Zine EL Abidine, TEBBAL Nadia	Algeria, Algeria, Algeria, Algeria	Submission 713
32	Blockchain-Based Requirement Prioritization in Agile Global Software Development	Asif Ahmad, Zain Ul Iman, Muhammad Saad Asif, Fahad Rizwan	Pakistan, Pakistan, Pakistan	Submission 714
33	Neutron Anti - Neutron Oscillations via Mirror Sector	Tinatin Tsiskaridze, Zourab Berezhiani	Georgia, Italy	Submission 715
34	Isolation and Biochemical Characterization of Bacterial Isolates from Fermented Dairy Products	Noou ul ain Naseem, Iftikhar Ali, Imran Tipu, Muhammad Irfan Fareed, Muhammad Akram	Pakistan, Pakistan, Pakistan, Pakistan, Pakistan	Submission 718
35	Detoxification of Aflatoxins using Plant Extracts	Abdullah Ghulam Nabi, Imran Tipu, Iftikhar Ali, Muhammad Irfan Fareed, Muhammad Akram	Pakistan, Pakistan, Pakistan, Pakistan, Pakistan	Submission 720
36	Innovation in Contemporary Economic Thought: A Theoretical and Analytical Approach	Benreghida Mohamed Mahdi, Zanat Said	Algeria, Algeria	Submission 722
37	Psychological Flexibility, Joint Family Interference, and Relational Turbulence In married Individuals	Iman Fatima, Fatima Latif, Amarah Qureshi	Pakistan, Pakistan, Pakistan	Submission 723
38	Dynamics of Saturation Fronts in Heterogeneous Porous Media Under Pulse Injection with Non-Equilibrium Capillarity	Amel SELMANE, Mohamed Lamine MOSTEFAI	Algeria, Algeria	Submission 724
39	Yapı Kalıntılarının Kronolojik Olarak Yerinin Saptanmasında Harçların Karakteristik Özelliklerinin Kullanılabilirliği	Tülay Uğur	Turkey	Submission 725
40	Performance Trade-Offs in Polypropylene Fiber-Reinforced Self-Compacting	Iqbal Ahmad, Muhammad Usman Farooqi	Pakistan, Pakistan	Submission 729

	Concrete: A Normalized Response and Tensile-Flexural Performance Index Approach			
41	The first inventory and record of the rare, endemic, and threatened flora of the mounts of Relizane region (Algeria)	Aouadj Sid Ahmed, Houari Hadj Habib, Nouar Belgacem, Benkaddour Benyekhlef, Bekhedda Hadjer, Hanis Fawzia, Hamad Hanane, Tabeche Ali, Bouhadiba Sultana, Hasnaoui Okkacha, Nasrallah Yahia, Khatir Hadj	Algeria, Algeria, Algeria, Algeria, Algeria, Algeria, Algeria, Algeria, Algeria, Canada	Submission 730
42	Use of machine learning (maxent algorithm) for species distribution model (SDM) of orchids flora in the Relizane region (Algeria)	Aouadj Sid Ahmed, Houari Hadj Habib, Nouar Belgacem, Benkaddour Benyekhlef, Bekhedda Hadjer, Hanis Fawzia, Hamad Hanane, Tabeche Ali, Bouhadiba Sultana, Hasnaoui Okkacha, Nasrallah Yahia, Khatir Hadj	Algeria, Algeria, Algeria, Algeria, Algeria, Algeria, Algeria, Algeria, Algeria, Canada	Submission 731
43	The Construct of “Standard English”	Blagica Upcheva, Sashka Jovanovska	Republic of North Macedonia, Republic of North Macedonia	Submission 732
44	Dynamic of a natural Portuguese oak ecosystem (endemic and protected) in Algeria : using machine learning approach	Aouadj Sid Ahmed, Houari Hadj Habib, Nouar Belgacem, Benkaddour Benyekhlef, Bekhedda Hadjer, Hanis Fawzia, Hamad Hanane, Tabeche Ali, Bouhadiba Sultana, Hasnaoui Okkacha, Nasrallah Yahia, Khatir Hadj	Algeria, Algeria, Algeria, Algeria, Algeria, Algeria, Algeria, Algeria, Algeria, Canada	Submission 733
45	The Effect of Organic & Mineral amendments and biofertilizers on Soil Fertility and the Content and Uptake of N.P.K by Stipa tenacissima L.	Aouadj Sid Ahmed, Houari Hadj Habib, Nouar Belgacem, Benkaddour Benyekhlef, Bekhedda Hadjer, Hanis Fawzia, Hamad Hanane, Tabeche Ali, Bouhadiba Sultana, Hasnaoui Okkacha, Nasrallah Yahia, Khatir Hadj	Algeria, Algeria, Algeria, Algeria, Algeria, Algeria, Algeria, Algeria, Algeria, Canada	Submission 734
46	Influence of Anodization Voltage on the Formation and Morphology of ZnO Nanoflowers on Textured Si Substrates	Neslihan Sakar, Metin Yurddaskal, Kutsal Camdalı, Yagmur Catkın, Alper Akalın, Mustafa Erol, Yavuz Ozturk	Turkey, Turkey, Turkey, Turkey, Turkey, Turkey, Turkey	Submission 741
47	Sustainable Congo Red Removal from Tannery Effluents Using Sugarcane Bagasse-Derived Cellulose/Bentonite Composite: Experimental, DFT, and Molecular Dynamics Investigation	Soukaina El Abbadi, Hajar El Moustansiri, Malika Khnifira, Mounia Baidou, El Mokhtar Lemdek, Abdelmjid Bouazizi, Mohamed Douma	Morocco, Morocco, Morocco, Morocco, Morocco, Morocco, Morocco	Submission 745
48	Toward Locally-Sourced Seawater Pretreatment: Algerian Saharan Sand and Agro-Food Biochar as Sustainable Alternatives to Imported Dual-Media Filters-The “Myah-Tipaza” Desalination Plant Case	Rafik El Arslene DRA, Mounya ZENASNI, Malika MEDJAHDI	Algeria, Algeria, Algeria	Submission 747
49	The Construction of Collective Consciousness: Power, Knowledge, and Epistemic Rigidity in Organizations	Amal Algouti	Morocco	Submission 749
50	Digitalization of Public Services and Its Impact on the Quality of Public Administration in Kosovo	Arnesa Sahiti, Abdulla Azizi	Kosovo, Kosovo	Submission 751
51	VACUUM DRYING AND QUALITY RETENTION	Sara ZIDANI, Fayçal BAIRA	Algeria, Algeria	Submission 755
52	Sustainable and Resilient Rehabilitation of Agriculture and Food Systems through AI-Driven and Emerging Technologies	Mahwash Aziz	Pakistan	Submission 757
53	AI-Driven Urban Traffic Management: Real-Time Congestion Prediction and Adaptive Control	Omar Mahmood Al Aani	Iraq	Submission 758
54	Abies nordmanniana subsp. equi-trojani as a Biological Sentinel of Atmospheric Palladium Accumulation	Mehmet Cetin	Turkey	Submission 767
55	Atmospheric Palladium Biomonitoring Using Pinus nigra subsp. Pallasiana	Mehmet Cetin	Turkey	Submission 768
56	Spatial and Temporal Patterns of Chromium Retention in Fagus orientalis Lipsky: Implications for Atmospheric Biomonitoring	Mehmet Cetin	Turkey	Submission 769
57	Optimization of Gamma-Aminobutyric Acid Production by a Lactic Acid Bacterium Isolated from Fermented Anchovy Sauce	Sangkaran Pannerchelvan, Fadzlie Wong Faizal Wong, Helmi Wasoh, Mohd Shamzi Mohamed, Rosfarizan Mohamad, Murni Halim	Malaysia, Malaysia, Malaysia, Malaysia, Malaysia, Malaysia, Malaysia	Submission 772
58	Hybrid Digital Twin for Real-Time	Khadidja El-Bahdja DJEBBAR	Algeria	Submission 776

	Energy Optimization in Smart Buildings			
59	Experimental-Numerical Correlation of Drilling-Induced Residual Stresses in IMI-834 Titanium Alloy Using DEFORM and Linear Regression	Zaki Abdelfetah ABED	Algeria	Submission 778
60	Correlation of Drilling-Induced Residual Stresses in IMI-834 Titanium Alloy Using DEFORM and Linear Regression	Zaki Abdelfetah ABED	Algeria	Submission 779
61	A Hybrid FE-ANN Approach for Predicting Drilling-Induced Residual Stresses in IMI-834 Titanium Alloy	Zaki Abdelfetah ABED	Algeria	Submission 780
62	Predicting Residual Stresses in Drilled IMI-834 Near-Alpha Titanium Alloy Using Linear Support Vector Regression	Zaki Abdelfetah ABED	Algeria	Submission 781
63	A Hybrid DEFORM-Cubic SVM Approach for Predicting Drilling-Induced Residual Stresses in IMI-834 Titanium Alloy	Zaki Abdelfetah ABED	Algeria	Submission 782
64	Integrative FEA and Quadratic Support Vector Regression for Evaluating Machining Residual Stresses in Drilled IMI-834 Alloy	Zaki Abdelfetah ABED	Algeria	Submission 783
65	A Hybrid DEFORM 3D and Nonlinear Regression Modeling Framework for Predicting Drilling-Induced Residual Stresses in IMI-834 Titanium Alloy	Zaki Abdelfetah ABED	Algeria	Submission 784
66	Towards Predictive DEFORM-Medium Gaussian Support Vector Regression Framework for Evaluating Surface Integrity in Drilled IMI-834 Alloy	Zaki Abdelfetah ABED	Algeria	Submission 785
67	High-Resolution Surface Integrity Modeling in Drilled IMI-834 Alloy via Fine Gaussian Support Vector Regression	Zaki Abdelfetah ABED	Algeria	Submission 786
68	A Probabilistic DEFORM-Rational Quadratic GPR Framework for Residual Stress Prediction in Drilled IMI-834 Alloy	Zaki Abdelfetah ABED	Algeria	Submission 795
69	A Non-Parametric DEFORM-Squared Exponential GPR Framework for Predicting Residual Stresses in Drilled IMI-834 Alloy	Zaki Abdelfetah ABED	Algeria	Submission 796
70	A DEFORM-Matérn 5/2 Gaussian Process Regression Model Based on Physics for Predicting Residual Stress in Drilled IMI-834 Titanium Alloy	Zaki Abdelfetah ABED	Algeria	Submission 797
71	A Non-Smooth DEFORM-Exponential Gaussian Process Regression Framework for Residual Stress Prediction in Drilled IMI-834 Ti-Alloy	Zaki Abdelfetah ABED	Algeria	Submission 798
72	An Adaptive Neuro-Fuzzy Inference System (ANFIS)-DEFORM 3D Framework for Residual Stress Prediction in Drilled IMI-834 Titanium Alloy	Zaki Abdelfetah ABED	Algeria	Submission 799
73	Surface Integrity Optimization in IMI-834 Titanium Drilling: A Comparative Soft-Computing and DEFORM 3D Study	Zaki Abdelfetah ABED	Algeria	Submission 800
74	Comparative Analysis of ANN and Linear SVM Machine Learning Models Integrated with DEFORM 3D for Residual Stress Prediction in Drilled IMI-834 Alloy	Zaki Abdelfetah ABED	Algeria	Submission 801
75	Data-Driven Modeling of Drilling-Induced Residual Stresses in IMI-834 Titanium Alloy: A Comparative Study of DEFORM 3D, ANN, and Quadratic SVM	Zaki Abdelfetah ABED	Algeria	Submission 802
76	A Comparative Hybrid DEFORM-ANN and Cubic SVM Framework for Residual Stress Prediction in Drilled IMI-834 Titanium Alloy	Zaki Abdelfetah ABED	Algeria	Submission 803
77	Addressing Finite Element Numerical Deviations in Titanium Drilling Using Matérn 5/2 and Exponential Gaussian Process Regression Frameworks	Zaki Abdelfetah ABED	Algeria	Submission 804
78	Correcting Finite Element Numerical Deviations in Titanium Drilling Using Parametric Linear and Non-Parametric Squared Exponential GPR Models	Zaki Abdelfetah ABED	Algeria	Submission 805

79	An investigation into the in vitro antibacterial activity of various 1,3,4-thiadiazole derivatives	Sanmati Kumar Jain	India	Submission 806
80	Domateste Hıyar Mozaik Hastalığı	Serkan YEŞİL	Turkey	Submission 811
81	Properties of certain classes of fractional differential equations	MENAD Bendehiba, DERKAOUI Rafik, MOUSLIM Noureddine	Algeria, Algeria, Algeria	Submission 815
82	The Effect of Flux Used in Aluminum Ingot Casting from Scrap Cans on Impurity Removal	Elif ARANCI ÖZTÜRK, Emrah ÇELİK, Gizem KİŞMAN, Mustafa BOYRAZLI	Turkey, Turkey, Turkey, Turkey	Submission 819
83	Dijital Kamusal Alanda Kadın Hakları Karşıtı Söylem: Ekşi Sözlük Örneği	Dilek Keleş	Turkey	Submission 821
84	DFT Study of the Composition Dependent Mechanical Properties of FeCrAl Alloys	R. Masrour	Morocco	Submission 823
85	DFT Investigation of the Structural, Electronic, Magnetic, and Thermal Properties of Monolayer Fe3GaTe2	R. Masrour	Morocco	Submission 824
86	DFT Study of the Electronic and Photovoltaic Properties of ZnSnN2 Homojunctions	R. Masrour	Morocco	Submission 825
87	MHD Mixed Convection and Entropy Generation in a Triangular Enclosure Filled with Ferrofluid-Saturated Porous Media	Kamel Zitouni	Algeria	Submission 834
88	From Theory to Experiment: Laboratory Access, Practical Science Learning, and PISA Performance in Albania, Kosovo, and North Macedonia	Rudina Osmanaj (Zeqirllari), Edlira Habilaj, Dafina Xhako	Albania, Albania, Albania	Submission 836
89	A Mass-Properties-Based Approach to the Dynamic Simulation of Optical Rotary Encoders Under Mechanical Vibrations	Violeta Krcheva, Stojance Nusev, Miša Tomić	North Macedonia, North Macedonia, Serbia	Submission 842
90	Transient Power Overshoot and Control Challenges During Black-Start Restoration	Charaf Abdelkarim Mosbah, El Mouatez Billah Messini	Algeria, Saudi Arabia	Submission 843
91	Numerical Analysis of Water Film Evaporation through Porous Layers for Energy-Efficient Cooling Applications	Karima SELLAMI, Nabila LABSI, Youb Khaled BENKAHLA, BOUARNOUNA Kaoutar, BAKHTA Soumia	Algeria, Algeria, Algeria, Algeria, Algeria	Submission 850
92	Modeling Swelling Pressure Response of Fly Ash-Lime Treated Clayey Soils	Youssouf Toualbia, Tahir Saiah, Ali Benzaamia, Billal Sari-Ahme, Mohamed Ghrici	Algeria, Algeria, Algeria, Algeria, Algeria	Submission 855
93	Inclusion in Higher Education through Sign Language Interpreters: Challenges and Opportunities	Irfan Bashir, Afshan Naseem, Aisha Sami, Abdul Malik	Pakistan, Pakistan, Pakistan, Pakistan	Submission 665
94	Citizen's Satisfaction in Public Institutions in Bangladesh: Quality, Social Capital, and Performance	Ruhul Amin	Bangladesh	Submission 685
95	Crying the Burning Landscape: Fire, Forest Destruction, and Ecological Crisis in African Literature	Mounira ADJAL, Ibtissam BENTALEB	Algeria, Algeria	Submission 770

Table List of Content

Content of Full Papers

Page No	Title	Authors	Country	Submission ID
1-12	ÜLKELERİN EĞİTİM ETKİNLİKLERİNİN VERİ ZARFLAMA ANALİZİYLE İNCELENMESİ	Yeşim Camcı, Hasan Bulut	Turkey, Turkey	Mail Submission 2
13-18	Seasonal Changes in Drinking-Water Chemistry: A Comparative Study of Two Albanian Water-Supply Systems	Shkelqıme Poga, Erjon Mamoçi, Drıte Mema	Albania, Albania, Albania	Mail Submission 3
19-33	Risk-Based Maintenance Prioritization for Marine Main Engine Shutdown Prevention: A Reassessment of Lubrication and Jacket Cooling Failures	Bulut Ozan Ceylan, Oğuzhan Der, Arif Savaş	Turkey, Turkey, Turkey	Submission 668
34-44	Fuzzy Risk Prioritization to On-board Controls: A Mitigation Framework for Biodiesel Use in Marine Diesel Engines	Bulut Ozan Ceylan, Oğuzhan Der, Arif Savaş	Turkey, Turkey, Turkey	Submission 670
45-49	Characterizations for N-Pedal Strip in Euclidean Space E^3	Filiz ERTEM KAYA	Turkey	Submission 678
50-57	Ekmeklik Buğdayda (Triticum aestivum L.) CBDP Primerlerinin Optimum Bağlanma Sıcaklıklarının Belirlenmesi	Muhammet İslam IŞIK, Aras TÜRKOĞLU	Turkey, Turkey	Submission 679
58-61	RLC TİPİ DİNAMİK SİSTEMLERİN NÜMERİK ANALİZİ	Muzaffer ATEŞ, Esra YILMAZ	Turkey, Turkey	Submission 686
62-67	Sony Hisse Senedi Kapanış Fiyatı Tahmini için Makine Öğrenmesi ve Derin Öğrenme Modellerinin Karşılaştırmalı Analizi	Anıl Utku	Turkey	Submission 687
68-72	Bir Yerel Politika Alanı Olarak Biyoçeşitlilik: Seçilmiş Büyükşehir Belediyelerinin Stratejik Planları Üzerine Karşılaştırmalı Bir İnceleme	Miray Özden, Seray Özden Keleş	Turkey, Turkey	Submission 690
73-78	İklim Değişikliğine Uyumda Yerel Yönetimler: Aşırı Sıcaklarla Mücadele Politikaları Üzerine Bir Değerlendirme	Miray Özden, Seray Özden Keleş	Turkey, Turkey	Submission 691
79-87	Evaluation of the Nurse Plant Potential of Certain Species in the Yeşilırmak Basin Vegetation Based on Leaf and Soil Functional Characteristics	Dudu Duygu KILIÇ	Turkey	Submission 695
88-96	Facilitation in Ecological Communities Mechanisms, Functions, and Applications Across Environmental Contexts	Dudu Duygu KILIÇ	Turkey	Submission 696
97-108	ESG Integration in Table Olive Production, Processing and Packaging: A Sustainable Farm-to-Market Framework for Mediterranean Table Olives	Bekir Erol AK, Georgios J. ZAKYNTHINOS	Turkey, Greece	Submission 702
109-120	ESG Integration in Almond Production, Processing and Packaging: A Climate-Resilient Farm-to-Market Framework for Mediterranean Almond Products	Bekir Erol AK, Georgios J. ZAKYNTHINOS	Turkey, Greece	Submission 703
121-128	Numerical Analysis of the Effect of Different Wind Speeds on PVT Collector Performance	Murat ÖZTÜRK, Erdem ÇİFTÇİ	Turkey, Turkey	Submission 705
129-134	Parkinson Hastalığının Sınıflandırılmasında Çift Akışlı Swin Transformer ve Mrmr	Abidin Çalışkan	Turkey	Submission 708
135-141	Campus Trees for a Changing Climate: Lessons from Tekirdağ, Türkiye	Seray ÖZDEN KELEŞ, Miray ÖZDEN	Turkey, Turkey	Submission 710
142-148	A Bibliometric Analysis of Studies on Extracurricular Activities	Hasan Yücel Ertem	Turkey	Submission 716
149-155	How Should We Interpret Research on Teacher Motivation in the 21st Century?: A Bibliometric Analysis	Hasan Yücel Ertem	Turkey	Submission 717
156-164	Investigating the Anticancer Potential of Broccoli Phytochemicals as VEGFR2 Inhibitors: Molecular Docking and 100 ns Atomistic Molecular Dynamics Simulation	Tahir Tilki, Ömer Dilek, Tolga Acar Yeşil	Turkey, Turkey, Turkey	Submission 719
165-171	Tersane İşletmelerinin WEB Sitelerinin İçerik Analizi ile Değerlendirmesi: Yalova Altınova Örneği	Kutluhan DOĞAN, Ömer ŞENGÜL, Murat YORULMAZ	Turkey, Turkey, Turkey	Submission 721
172-183	Spatiotemporal Dynamics of Atmospheric Pollutants along the Urban–Rural Gradient: A Remote Sensing-Based Analysis of Bolu, Türkiye	İlknur Zeren Cetin	Turkey	Submission 726
184-195	Spatiotemporal Characterization of Multi-Pollutant Dynamics along the Urban–Rural Gradient of Sakarya, Türkiye	İlknur Zeren Cetin	Turkey	Submission 727

196-207	Urban–Rural Gradients and Multi-Pollutant Variability in Kayseri, Türkiye: An Integrated Parametric Remote-Sensing and Machine-Learning Framework	İlknur Zeren Cetin	Turkey	Submission 728
208-215	Kısmi Gölgelenme Altındaki Fotovoltaik Sistemlerde Küresel Maksimum Güç Noktasının Harris Şahinleri Optimizasyonu ile Takibi	Yasin BEKTAŞ, Necibe Füsun OYMAN SERTELLER	Turkey, Turkey	Submission 735
216-224	Electrified Vehicle Adoption in Türkiye: Operational CO_2 Emissions, Economic Payback, and Consumer Perception	Aybüke Sena Ünal, Ömer Önder Erat, Bülent Yeşilata	Turkey, Turkey, Turkey	Submission 736
225-232	Integration of Vertical-Axis Tracking Floating Photovoltaics Into Hydroelectric Power Plants: A Case Study for Sarıyar Dam	Umut Mete Hakverir, Cengizhan Özaltın, Ömer Önder Erat, Bülent Yeşilata	Turkey, Turkey, Turkey, Turkey	Submission 737
233-238	Energy-Shading Optimization of Greenhouse-Integrated Agrivoltaic Systems in Türkiye Using PVGIS-TMY Data and Geometric Shadow Modelling	Umut Ege Karacakale, Ömer Önder Erat, Bülent Yeşilata	Turkey, Turkey, Turkey	Submission 738
239-246	Two-Dimensional Cutting Stock Algorithm for Sequencing Cart Layout Optimization	Caner Türker, Sevgi Karaca Bellofatto, Sema Alcan, Zehra Kamışlı Öztürk	Turkey, Germany, Turkey, Turkey	Submission 740
247-251	Yaşam Tarzı, Telomerler ve Kardiyovasküler Sağlık	Mesude AÇIKBAŞ	Turkey	Submission 742
252-257	Design and Functional Optimization of 3D-Printed Polymer Molds for PET Bottle Blow Molding	Dorian Osmanaj, Erald Piperi	Albania, Albania	Submission 743
258-266	Machine Learning-Based Surrogate Prediction of Peak Crush Energy in Vehicle-to-Barrier Collisions	Vedat Yeğin	Turkey	Submission 744
267-272	Fractional Order PID Position Control Application for DC Motor with Jetson Nano Platform	Erdem Ilten	Turkey	Submission 746
273-279	Hyperparameter Tuning in Gradient Boosting Models: A Comparative Study on Residential Property Price Prediction	Halit Çetiner	Turkey	Submission 748
280-289	Effect of Heat Treatment Temperature on Microhardness and Microstructural Evolution of DIN St28 Low-Carbon Steel	Muhammet Gökhan Albayrak	Turkey	Submission 750
290-296	Farklı Rotor Geometrilerine Sahip Anahtarlamalı Relüktans Motorun Moment Dalgalanması ve Moment Değişimlerinin Analizi	Murat İmre, Mehmet Murat Tezcan, Asım Gökhan Yetgin	Turkey, Turkey, Turkey	Submission 754
297-303	Gyroid TPMS Kafes Yapılarda Laminer Hava Akışının Hesaplamalı Akışkanlar Dinamiği Yöntemiyle İncelenmesi	İsmail Tur, Erkan Bahçe, Mustafa Ercan GÜNDÜZ, Özgün Ceren AKBAY	Turkey, Turkey, Turkey, Turkey	Submission 759
304-314	Comparative Evaluation of Deep Learning Models for Pediatric Pneumonia Classification from Chest X-ray Images	Hüseyin FIRAT	Turkey	Submission 760
315-321	Material Balance Analysis for Reservoir Performance Evaluation and Estimation of Orginal Oil in Place	Armida Brakaj, Zhifka Muka, Fizeleni Lekli	Albania, Albania, Albania	Submission 761
322-327	Indicator Bacteria and Biofilm Dynamics in Sarıçay Stream, Türkiye	Mehmet Doğukan Maraş, Nil Atalay, Nurcihan Hacıoğlu Doğru	Turkey, Turkey, Turkey	Submission 762
328-330	Current Developments in Memristor Technology	İshak PARLAR, Onur SİLAHTAR	Turkey, Turkey	Submission 764
331-338	Closed-Loop State Regulation of Memristive Neuromorphic Circuits Using a Filtered PI-Type Intuitionistic Fuzzy Logic Controller	Onur SİLAHTAR, İshak PARLAR	Turkey, Turkey	Submission 765
339-346	Investigation of the Effects of Drilling Parameters on the Surface Roughness of EN AW-5083 Aluminum Alloy	Ömer ÇERLEK	Turkey	Submission 766
347-355	Packaging Design, Psychological Response, and Sustainability: An Empirical Model of Consumer Purchase Decisions	Irma Shyle	Albania	Submission 773
356-363	Evaluation of Multi-Model Consensus in Unmanned Aerial Vehicle Mapping Missions with Respect to In-Flight Decision Reliability	Fadiş Rabia YILDIRIM, Fatma YILDIRIM DALKIRAN, Mehmet KONAR	Turkey, Turkey, Turkey	Submission 774
364-370	The Role of the Relief Parameter in Landslide Susceptibility Studies	Seda Çellek	Turkey	Submission 777
371-381	Public Diplomacy as a Compensatory Mechanism of Traditional Diplomacy in Contexts of Contested Statehood- Case study Kosovo	Armend KRASNIQI, Jonuz ABDULLAI	Kosovo, Kosovo	Submission 808
382-384	Depolanan Ham Balık Yağında Mikrobiyal Popülasyon ve Hidrolitik Bozulma Parametreleri	Leyla Buse Sağır, Nurcihan Hacıoğlu Doğru	Turkey, Turkey	Submission 810

385-391	AA1060 Esaslı Al-Nb Alaşımlarında İletkenlik ve Mekanik Dayanımın Eşzamanlı Geliştirilmesi	Ramazan YETİM	Turkey	Submission 814
392-401	Dynamic Response Assessment of a ZrO2-Retrofitted Parallel Strand Lumber Pedestrian Bridge by FEA	Sertaç Tuhta	Turkey	Submission 816
402-411	Numerical Characterization of Dynamic Behavior in Fe2O3-Strengthened Laminated Strand Lumber Timber Pathway	Sertaç Tuhta	Turkey	Submission 817
412-414	From Vaborbactam to Taniborbactam: Evolution and Therapeutic Potential of Boronate Beta-Lactamase Inhibitors	Murat Şentürk	Turkey	Submission 826
415-419	Preliminary Rationale for Uracil-Based Modulators of KDM5B in Cancer Therapy Resistance	Murat Şentürk	Turkey	Submission 827
420-424	Comparative Structural Feasibility of FTO and KDM5B for Structure-Guided Drug Repurposing	Murat Şentürk	Turkey	Submission 828
425-432	Comparative Analysis of YOLOv8s, YOLO11s and YOLO26s Architectures for Medical Pill Detection	Muslume Beyza YILDIZ, Murat KOKLU	Turkey, Turkey	Submission 829
433-440	AI-Assisted Quality Control in Textile Manufacturing: A Conceptual Evaluation of Fabric Defect Detection and Color Consistency	Beyza Buzol Mülayim, Selma Bulut	Turkey, Turkey	Submission 831
441-450	Copyright, Originality, and Ethical Use in Generative AI Textile Pattern Design	Selma Bulut, Beyza Buzol Mülayim	Turkey, Turkey	Submission 832
451-456	Density functional theory investigation of the structural, electronic and noncovalent interaction properties of a benzoxadiazocine derivative	Mustafa Kemal GÜMÜŞ, Sevgi KANSIZ	Turkey, Turkey	Submission 837
457-463	DFT, ADME, and boiled egg analysis of Schiff base derived from nitrobenzaldehyde	Sevgi KANSIZ, Mustafa Kemal GÜMÜŞ	Turkey, Turkey	Submission 838
464-467	Radyofarmasötiklerin Nükleer Tıpta Tanı ve Tedavideki Güncel Uygulamaları	Hatice DEMİR BECEREKLİ, Yalçın ALTUNKAYNAK	Turkey, Turkey	Submission 839
468-473	Optimization Approaches in Sustainable Structural Design: Current Methodologies and Research Gaps in the Literature	Ali Mortazavi	Turkey	Submission 840
474-479	Environmental Performance Criteria and Greenhouse Gas Mitigation Policies for Climate Change Adaptation in the Construction Sector	Ali Mortazavi	Turkey	Submission 841
480-484	Taklit Öğrenme Kullanılarak Bir PID Kontrolcünün Taklit Edilmesi: Motor Pozisyon Kontrolü Üzerine Simulink Tabanlı Bir Çalışma	Halit HÜLAKO, Mehmet Latif LEVENT, Sertaç YAMAN	Turkey, Turkey, Turkey	Submission 845
485-491	Comprehensive Multi Biomarker Profiling for Accurate Diagnosis of Pheochromocytoma	Brunilda Mezani, Anila Mitre	Albania, Albania	Submission 846
492-497	Clinical Use of Metanephrines and Catecholamines in Combination with Chromogranin A for the Biochemical Diagnosis of Pheochromocytoma	Brunilda Mezani, Anila Mitre	Albania, Albania	Submission 847
498-508	Investigation of the Effect of Masonry Piers on the Modal Behavior of Hollow Concrete Block Walls	Furkan Günday	Turkey	Submission 851
509-519	Smart Face Recognition for Attendance in Education	Viola Bakiasi (Shtino)	Albania	Submission 852
520-529	Fault Detection and Load Prediction in a Push-Pull Converter Using Machine Learning	Serhat Küçükdermenci	Turkey	Submission 853

COMMITTEE

ORGANIZING COMMITTEES

Assoc. Prof. Admir Jance, European University of Tirana
Assoc. Prof. Elif Küçük Durur, Atatürk University
Assoc. Prof. Nermin Kişi, Zonguldak Bülent Ecevit University
Assoc. Prof. Ülhak Çimen, Atatürk University
Dr. Krisztina Czakoova, J. Selye University
Dr. Ondrej Takac, J. Selye University
Dr. Ladislav Vegh, J. Selye University

SCIENTIFIC COMMITTES

Prof. Dr. Abdurazzag Ali Aburas, University of Kwazulu-Natal
Prof. Dr. Adnan Sözen, Gazi University
Prof. Dr. Amit Soni, Manıpal University
Prof. Dr. Anis Koubaa, Prince Sultan University
Prof. Dr. Carlos A. Coelho, Universidade Nova de Lisboa
Prof. Dr. Josep Guerrero, Aalborg University
Prof. Dr. Juan Vasquez, Aalborg University
Prof. Dr. Laszlo T. Koczy, Budapest University of Technology and Economics
Prof. Dr. Mohammad Ashraf Gondal, King Fahd University
Prof. Dr. Murat Yakar, Mersin University, Turkey
Prof. Dr. Muhammad Rashid, University of West Florida
Prof. Dr. Saad Mekhilef, Malaya University
Prof. Dr. Salim Ibrir, King Fahd University
Prof. Dr. Subarna Shakya, Tribhuvan University
Prof. Dr. Suzuki Hisashi, Chuo University
Prof. Dr. Usha Mehta, Institute of Technology, Nirma University
Prof. Dr. Vagif Gasimov, Azerbaijan Technical University
Prof. Dr. Weidong Zhu, University of Maryland
Assoc. Prof. Ali Hakan Işık, Burdur Mehmet Akif Ersoy University
Assoc. Prof. Amita Nandal, Manıpal University
Assoc. Prof. Aslan İnan, Yıldız Teknik University
Assoc. Prof. Atif Iqbal, Qatar University
Assoc. Prof. Elif Küçük Durur, Atatürk University
Assoc. Prof. Francesco Cottone, University of Perugia
Assoc. Prof. Farid Melgani, University of Trento
Assoc. Prof. Halit Öztekin, Sakarya Applied Science University
Assoc. Prof. Hamdy Ziedan, Assiut University
Assoc. Prof. Harun Kemal Öztürk, Pamukkale University
Assoc. Prof. Jiri Pela, Brno University of Technology
Assoc. Prof. Merih Palandöken, İzmir Katip Çelebi University
Assoc. Prof. Nermin Kişi, Zonguldak Bülent Ecevit University
Assoc. Prof. Rita Ismailova, Kyrgyz Turkish Manas University
Assoc. Prof. Sadia Samar Ali, King Abdul-Aziz University
Assoc. Prof. Ülhak Çimen, Atatürk University
Assoc. Prof. Tanmay De, National Institute of Technology Durgapur
Assoc. Prof. Zeashan Khan, Air University
Dr. Ali Almisreb, International University of Sarajevo
Dr. Amina Othmani, University of Monastir-Tunisia
Dr. Arti Jain, Jaypee Institute of Information Technology
Dr. Arun Kumar Verma, Malaviya National Institute of Technology Jaipur
Dr. Aziz Shah, University of Glaskow
Dr. Bal Chand Nagar, ECE National Institute of Technology Patna
Dr. Baoze Wei, Aalborg University
Dr. Bohumil Brtník, University of Pardubice
Dr. Diptiranjan Behera, The University of the West Indies at Mona
Dr. Fayçal BENSAALI, Qatar University
Dr. Fugui Qi, Fourth Military Medical University
Dr. Magdi S. Mahmoud, King Fahd University
Dr. Mariya Ouaissa, Moulay Ismail University
Dr. Merdaci Slimane, University of -Sidi Bel Abbés, Algeria
Dr. Moharram Challenger, Antwerp University
Dr. Muhammad Sultan, Zakariya University
Dr. Lesya Anishchenko, Bauman Moscow State Technical University
Dr. R.A. Ilyas, Universiti Teknologi Malaysia
Dr. Sadina Gagula Palalić, International University of Sarajevo
Dr. Stefania Tomasiello, University of Tartu
Dr. Syed Omer Gilani, National University of Sciences and Technology (NUST)
Dr. Tarık Namas, International University of Sarajevo
Dr. Uduak A. Umoh, University of Uyo
Dr. Yajuan Guan, Aalborg University

15.09.2026

06-07 Eylül 2026 tarihlerinde MEET üzerinden çevrimiçi olarak gerçekleştirilen 8th International Conference on Engineering, Natural and Social Sciences ICENSOS 2026 konferansı akademik teşvik yönetmeliğinin 9. Maddesine istinaden "Tebliğlerin sunulduğu yurt içinde veya yurt dışındaki etkinliğin uluslararası olarak nitelendirilebilmesi için Türkiye dışında en az beş farklı ülkeden sözlü tebliğ sunan konuşmacının katılım sağlaması ve tebliğlerin yarıdan fazlasının Türkiye dışından katılımcılar tarafından sunulması esastır." kriterlerini sağlamaktadır. Toplam 163 adet bildirinin yer aldığı kongre iki gün boyunca çevrimiçi olarak gerçekleştirilmiştir.

Türkiye dışından toplam 19 farklı ülkeden (Fas, Cezayir, Pakistan, Arnavutluk, Malezya, Hindistan, Kosova, Suudi Arabistan, Azerbaycan, Libya, Nijerya, Irak, Gürcistan, İtalya, Kuzey Makedonya, Kanada, Bangladeş, Yunanistan, Almanya) katılım sağlanmış olup, 163 adet bildirinin 91 (%55,82) tanesi yabancı katılımcı tarafından sunulmuştur.

Kongremize ilginiz için teşekkür ederiz.

Saygılarımızla,



All Sciences Academy

15.09.2026

06-07 Eylül 2026 tarihlerinde MEET üzerinden çevrimiçi olarak gerçekleştirilen 8th International Conference on Engineering, Natural and Social Sciences ICENSOS 2026 Konferansı, 2025 MART DÖNEMİ DOÇENTLİK BAŞVURU ŞARTLARI yönetmeliğinin 2. bölümde yer alan Uluslararası Bilimsel Toplantı tanımlaması "Farklı ülkelerden bilim insanlarının bilim kurulunda bulunduğu ve sunumların bilimsel ön incelemeden geçirilerek kabul edildiği toplantı." şeklindedir.

8TH ICENSOS 2026 konferansı bilimsel komitesinin çoğunluğu yabancı bilim insanlarından oluşmaktadır. Aşağıdaki link ile bilimsel komite incelenebilir:

https://www.icensos.com/com

Ayrıca konferansımızda hakem değerlendirmesi olup hakem değerlendirmesi olumlu sonuçlanmadan ücret talebinde bulunulmamaktadır.

2024 MART DÖNEMİ DOÇENTLİK BAŞVURU ŞARTLARI yönetmeliğinin 8. bölümde yer alan Bilimsel Toplantı tanımlamasının b bendindeki "Diğer Uluslararası/Ulusal bilimsel toplantının düzenlenme komitesinde, kurum/tüzel kişilik/karar organı tarafından resmi olarak görevlendirilmiş üniversite/enstitü/bilimsel kurum/branş derneği akademisyen temsilcisi bulunması zorunludur." şeklindedir.

8TH ICENSOS 2026 konferansı düzenleme komitesinde farklı kurumlar tarafından görevlendirilmiş birden fazla üniversiteden akademik temsilciler bulunmaktadır. Aşağıdaki link ile düzenleme komitesindeki akademik temsilcilerin görevlendirme yazıları incelenebilir:

https://drive.google.com/file/d/1eZalxRl8q6-eXATZzwUraH9KOhtQzFho/view

Ayrıca görevlendirme yazıları ilgili konferansın özet ve tam metin kitapçıklarında yer almaktadır.

Kongremize ilginiz için teşekkür ederiz.

Saygılarımızla,



All Sciences Academy

04.09.2023

LETTER OF ASSIGNMENT

We confirm that Ing. Ondrej Takáč, PhD. working at J. Selye University takes part in the organization committee of the conferences organized by of All Sciences Academy.

Confirmation of the Vice Dean of the Faculty of Economics and Informatics

Name of Responsible Person and Signature:

Name and Surname Sign:

PhDr. Imrich Antalík, PhD. _____

Date: 04.09.2023

UNIVERZITA J. SELYEHO
SELYE JÁNOS EGYETEM
FAKULTA EKONÓMIE A INFORMATIKY
DEKANÁT
Bratislavská 167/21, 945 01 Komárno

04.09.2023

LETTER OF ASSIGNMENT

We confirm that PaedDr. Ladislav Végh, PhD. working at J. Selye University takes part in the organization committee of the conferences organized by of All Sciences Academy.

Confirmation of the Vice Dean of the Faculty of Economics and Informatics

Name of Responsible Person and Signature:

Name and Surname Sign:

PhDr. Imrich Antalík, PhD. _____

Date: 04.09.2023

Universiteti Europian i Tiranës

16.08.2023

LETTER OF ASSIGNMENT

We confirm that Prof. Assoc. Dr. Admir Jançe, who is employed full-time as a lecturer, as well as holding the position of Head of the Imaging Department and Vice Dean of the Faculty of Technical Medical Sciences, takes part in the organization committee of the conferences organized by of All Sciences Academy.

Confirmation of the Rector/Dean/Vice Dean/Head of Department

Name of Responsible Person and Signature:



Rector: Prof. Dr. Tonin GJURAJ

_ _

Date: 16.08.2023

15.09.2023

İlgili Makama

Atatürk Üniversitesi İletişim Fakültesinde görev yapan Doçent Doktor Ülhak Çimen'in All Sciences Academy yayınevi ile beraber düzenlenmesi planlanan konferanslarda ve organizasyonlarda düzenleme veya bilim kurullarında yer alması uygun görülmüştür.

Gereğini rica ederim.

Ad ve Soyad Prof. Dr. Adem YILMAZ Dekan Tarih 15.09.2023	İmza: Prof.Dr. Adem YILMAZ DEKAN

15.09.2023

İlgili Makama

Atatürk Üniversitesi İletişim Fakültesinde görev yapan Doçent Doktor Elif Küçük DURUR'un All Sciences Academy yayınevi ile beraber düzenlenmesi planlanan konferanslarda ve organizasyonlarda düzenleme veya bilim kurullarında yer alması uygun görülmüştür.

Gereğini rica ederim.

Ad ve Soyad Prof. Dr. Adem YILMAZ Dekan Tarih 15.09.2023	İmza: Prof.Dr. Adem YILMAZ DEKAN

04.09.2023

LETTER OF ASSIGNMENT

We confirm that PaedDr. Krisztina Czakóová, PhD. working at J. Selye University takes part in the organization committee of the conferences organized by of All Sciences Academy.

Confirmation of the Vice Dean of the Faculty of Economics and Informatics

Name of Responsible Person and Signature:

Name and Surname Sign: _____

PhDr. Imrich Antalík, PhD.

Date: 04.09.2023

T.C.
ZONGULDAK BÜLENT ECEVİT ÜNİVERSİTESİ REKTÖRLÜĞÜ
Çaycuma Meslek Yüksekokulu Müdürlüğü

Sayı : E-84604848-903.07.04-371012 01.11.2023
Konu : Bilimsel Toplantı Görevlendirme

İLGİLİ MAKAMA

İlgi : Öğretim Üyesi Doç. Dr. Nermin KİŞİ'nin 30.10.2023 tarihli dilekçesi.

Yüksekokulumuz Yönetim ve Organizasyon Bölümü Öğretim Üyesi Doç. Dr. Nermin KİŞİ'nin "All Sciences Academy Yayınevi"nin düzenleyeceği bilimsel toplantıların düzenleme ve bilim kurullarında görev almasında Yüksekokulumuzca bir sakınca bulunmamaktadır. İş bu belge ilgilinin isteği üzerine tanzim edilmiştir.

Bilgilerinizi ve gereğini rica/arz ederim.

Doç. Dr. Hikmet YAZICI
Meslek Yüksekokulu Müdürü

Bu belge, güvenli elektronik imza ile imzalanmıştır.

Adres : BEÜ Çaycuma Meslek Yüksekokulu, 67900, Çaycuma, Zonguldak
Telefon : (0372) 643 66 01 Faks:(0372) 643 66 04
e-Posta : caycumamyo@beun.edu.tr Web : https://cmyo.beun.edu.tr/
Kep Adresi : beun@hs03.kep.tr
Bilgi için : Tülay KEÇECİ
Unvanı : İşçi

8th International Conference on Engineering, Natural and Social Sciences

September 06-07, 2026: Konya, Turkey

© 2026 Published by All Sciences Academy

https://www.icensos.com/

ÜLKELERİN EĞİTİM ETKİNLİKLERİNİN VERİ ZARFLAMA ANALİZİYLE İNCELENMESİ

Yeşim Camcı[1]*, Hasan Bulut [2]

[1]*İstatistik / Fen Bilimleri Enstitüsü, Ondokuz Mayıs Üniversitesi, Türkiye*

[*]*yesimcamci08@gmail.com*

Özet **–** Eğitim sistemlerinin performansı, küresel rekabet gücü ve sürdürülebilir kalkınmanın temel göstergelerinden biridir. Bu bağlamda, Ekonomik İşbirliği ve Kalkınma Örgütü (OECD) tarafından üçer yıllık dönemlerle uygulanan Uluslararası Öğrenci Değerlendirme Programı (PISA), üye ve ortak ülkelerin eğitim başarılarını uluslararası düzeyde kıyaslamada merkezi bir rol üstlenmektedir. PISA, ülkelerin sadece mutlak başarı puanlarını değil, aynı zamanda eğitimde etkililik ve verimliliğin değerlendirilmesini sağlamaktadır. Zira, yüksek başarı puanları çoğu zaman yüksek kaynak harcamalarıyla birlikte gelmektedir, kısıtlı kaynakla optimum çıktıyı elde edebilmek önemlidir. Bu çalışma ile literatür taraması gerçekleştirilerek eğitimin tanımı, Ekonomik İşbirliği ve Kalkınma Örgütü (OECD) tarafından yapılan Uluslararası Öğrenci Değerlendirme Programı (PISA) ve Veri Zarflama Analizi hakkında genel bilgi verilip araştırma hakkında genel bir çerçeve oluşturulmuştur. OECD ülkelerinin 2022 PISA sonuçlarına göre ülkelerin etkinlikleri VZA programı ile yorumlanarak ülkelerin araştırma sonuçları paylaşılmıştır. Analizin girdi ve çıktı değişkenleri, ilgili literatür taraması sonucunda PISA başarısı üzerinde etkisi olduğu kabul edilen faktörlerden seçilmiştir. Çıktı olarak ülkelerin PISA sınav sonuçları kullanılmıştır. VZA sonuçlarına göre tamamen etkin (Skor=1.00) kabul edilen bulgular, bu ülkelerin mevcut beşeri ve fiziksel kaynaklarını, PISA başarı ortalaması çıktısını maksimize edecek şekilde en verimli kullanan sistemler olduğunu göstermektedir. Bu çalışma ile etkin olmayan diğer ülkeler için birer "En İyi Uygulama Modeli" (Benchmark) teşkil etmekte olan ülkeler belirlenmektedir.

Anahtar Kelimeler – eğitim, etkinlik, OECD, PİSA, VZA, verimlilik, DEA, KVB, Karar Verme Birimi

I. GİRİŞ

Eğitim; toplumsal ve kültürel mirasın gelecek nesillere aktarılmasında köprü işlevi gören, beşerî sermaye birikimini artırarak sürdürülebilir ekonomik büyümeyi ve toplumsal refahı destekleyen dinamik bir süreçtir. Eğitimin temelinde kişiyi bir bütün olarak geliştirme; kişinin yaratıcılığını artırıp, kendini gerçekleştirme; toplumda sosyal uyum sağlamak ve bireyleri yönetime hazırlamak vardır.

Küreselleşen dünyada ülkeler, eğitim müfredatlarını günün şartlarına uyarlama gereksinimi duymaktadır. Bu süreçte mevcut eğitim sistemlerinin niteliğini ve eksik yönlerini görebilmek adına uluslararası değerlendirme ve ölçekler referans alınabilmektedir. Öğrenci Değerlendirme Programı (PISA), Ekonomik İşbirliği ve Kalkınma Teşkilatı (OECD) tarafından gerçekleştirilen etkinlik bunlardan biridir. PISA; 15 yaşındaki öğrencilerin modern toplumda yerlerini alabilmeleri için gereken bilgi ve becerileri ölçmeyi amaçlamaktadır. Bu araştırma, öğrencilerin matematik okuryazarlığı, fen okuryazarlığı ve okuma becerileri değerlendirmektedir.[1]

Bu araştırmanın amacı ülkelerin eğitim için harcadıkları kaynaklarla 2022 yılında elde ettikleri sonuçlarının etkinliklerini değerlendirmektir. OECD ülkelerinin PISA 2022 sonuçlarına göre belirlenen teknik etkinlik skorları ve sıralamaları nedir? Etkin olmayan ülkelerin tam etkinliğe ulaşması için hangi girdi değişkenlerinde (harcama, oran vb.) oransal iyileştirme yapması gerekmektedir? Etkin olmayan ülkelerin, hangi etkin sistemleri kendilerine model almaları önerilmektedir? Sorularına yanıt aramaktadır.

Çalışmada, çoklu girdi ve çoklu çıktı değişkenlerini aynı anda değerlendirebilen, parametrik olmayan bir teknik olan Veri Zarflama Analizi (VZA) kullanılmıştır. Analizin girdi ve çıktı değişkenleri, ilgili literatür taraması sonucunda PISA başarısı üzerinde etkisi olduğu kabul edilen faktörlerden seçilmiştir.

II. MATERYAL VE YÖNTEM

Çalışmada, ölçeğe göre sabit getiri varsayımına dayanan çıktı odaklı (Output-Oriented) CRS VZA modeli kullanılmıştır. Bu yaklaşım; analize konu olan ülkelerin mevcut girdi seviyelerini (eğitim ve finansal harcamalar, demografik ve toplumsal refah göstergeleri) korurken, elde edebilecekleri PISA akademik çıktılarını (Matematik, Fen ve Okuma puanları) maksimum düzeye çıkarma potansiyellerini ve yönetsel verimlilik sınırlarını ölçmeyi hedeflemektedir. VZA yöntemi, Karar Verme Birimlerinin (KVB) görece etkinlik sınırlarını belirlemede esnek bir yapı sunduğu için tercih edilmiştir. Modelde kullanılan girdi ve çıktı seti, PISA performansını etkileyen temel belirleyicileri kapsayacak şekilde geniş bir literatür taraması doğrultusunda titizlikle oluşturulmuştur. VZA modelinde verimlilik yönünü doğru temsil etmek amacıyla, öğretmen başına öğrenci sayısı değişkeni tersine çevrilerek (1/X) olarak kullanılmıştır. Analiz kapsamında VZA modellerinin çalıştırılması ve etkinlik skorlarının elde edilmesinde MaxDEA yazılımı [2]; verilerin ön işleme tabi tutulması, istatistiksel analizleri ve grafiksel görselleştirme süreçlerinde ise R istatistiksel programlama dili (v4.5.2) [3] kullanılmıştır.

ETKİNLİK KAVRAMI VE VERİ ZARFLAMA ANALİZİ

A Veri Zarflama Analizi

Veri Zarflama Analizi (VZA), etkinlik ölçümünde en sık başvurulan yöntemlerden biridir. Parametrik olmayan bir teknik olan VZA, önsel bir üretim fonksiyonu varsayımında bulunmak yerine, en etkin birimlerin girdi ve çıktı bileşimlerinden yararlanarak göreli etkinlik sınırını belirlemek amacıyla doğrusal programlama yaklaşımını kullanmaktadır [4]. VZA'nın temel felsefesi, benzer nitelikteki Karar Verme Birimleri (KVB) arasından en iyi performans gösterenleri tespit ederek referans bir sınır oluşturmaktır. Bunun yanı sıra yöntem, etkin sınırın altında kalan birimlerin derecesini ölçmeye ve bu birimlerin iyileştirilmesinde esas alınacak referans kümelerini belirlemeye imkân tanımaktadır [5]. Girdilerin hedefler doğrultusunda verimli kullanılıp kullanılmadığı değerlendirilirken, atıl kaynakların saptanması birimlerin performansının artırılması açısından kritik önem taşımaktadır.

VZA yöntemiyle yapılacak bir etkinlik çalışması, başlıca aşağıdaki beş aşamada gerçekleştirilir [6]:

1. Karar Verme Birimlerinin (KVB) seçimi
2. Girdi ve çıktıların seçimi
3. Verilerin elde edilmesi
4. Göreli etkinliğin ölçülmesi
5. Sonuçların değerlendirilmesi ve yönetsel yorumların yapılması

A.1 Veri Zarflama Analizi Sonuçlarının Yorumlanması

Veri Zarflandırma Analizi (VZA) çıktılarının değerlendirilmesinde temel performans göstergesi Etkinlik Skoru (Efficiency Score) değeridir. Bu değer, analize dahil edilen her bir Karar Verme Biriminin (KVB / DMU) bu çalışma özelinde ülkelerin mevcut girdilerini ne derece verimli kullanarak hedeflenen çıktıları elde ettiğini bağıl olarak ortaya koyar. Analiz sonucunda etkinlik skor değeri 1 olan ülkeler göreli olarak tam etkin (verimli) kabul edilir. Bu ülkeler, ellerindeki mevcut kaynakları (eğitim harcamaları, öğretmen/öğrenci oranları vb. girdileri) en ideal biçimde optimize ederek en yüksek PISA başarı ortalamalarını (çıktıları) elde etmiş birimlerdir. Söz konusu ülkeler, etkin sınır üzerinde yer aldıklarından dolayı analizde tam etkinlik sağlayamayan diğer ülkeler için "En İyi Uygulama" (Benchmark) olarak tanımlanır.

Etkinlik Skoru 1.00'in Altında Olan Ülkeler (Etkin Olmayan Birimler):Skor değeri 1'den küçük olan ülkeler ise göreli olarak etkin olmayan birimleri temsil eder. Bu ülkeler, aynı girdi seviyesiyle daha yüksek PISA başarısı yakalama veya mevcut PISA başarı düzeylerini daha az girdi kullanarak elde edebilme potansiyeline sahiptir.

B OECD Ülkelerinin Girdi Olarak Kullanılan Bazı Kaynakları

Bu çalışmada kullanılan eğitime ilişkin harcamalar, makroekonomik göstergeler ve uluslararası başarı skorlarına ait tüm veriler, Ekonomik İşbirliği ve Kalkınma Örgütü (OECD) tarafından yayımlanan *Education at a Glance* raporlarından [7] PISA 2022 sonuç raporlarından[8] ve Dünya Bankası (World Bank Open Data) resmî veri tabanından[9] derlenmiştir. Çalışmada modelin çıktı değişkenlerini oluşturan PISA 2022 Matematik, Fen ve Okuma puanları OECD'nin yayımladığı PISA sonuç raporlarından [8] alınmıştır. İnceleme kapsamına alınan 37 ülkeye ait veriler, kurumların yayımladığı en güncel resmî istatistikler esas alınarak oluşturulmuş ve analiz edilmiştir.

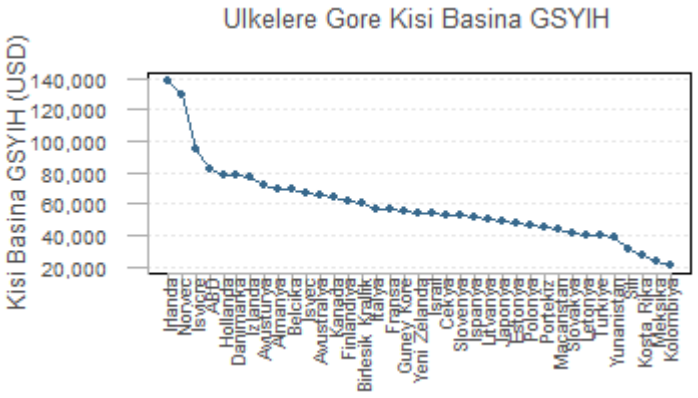

Şekil 1. Kişi Başına GSYIH (USD)

Veri setinde yer alan 37 ülkeye ait Satın Alma Gücü Paritesine (PPP) göre hesaplanmış kişi başına Gayri Safi Yurtiçi Hasıla değişkenine ilişkin betimsel istatistiksel analiz sonuçları Tablo 1'de verilmiştir. Örneklem dâhilindeki uç değerler incelendiğinde; İrlanda (138.464,80 USD), Norveç (129.914,00 USD) ve İsviçre (94.629,70 USD) kişi başına GSYİH seviyesi en yüksek olan ülkeler olarak öne çıkmaktadır. Buna karşılık Kolombiya (20.854,00 USD), Meksika (23.135,50 USD) ve Kosta Rika (26.892,00 USD) değişkenin en düşük gözlemlendiği ülkelerdir. Türkiye ise 39.919,20 USD'lik kişi başına GSYİH değeri ile 37 ülke arasında 32. sırada konumlanmakta ve ortalamasının gerisinde yer almaktadır.

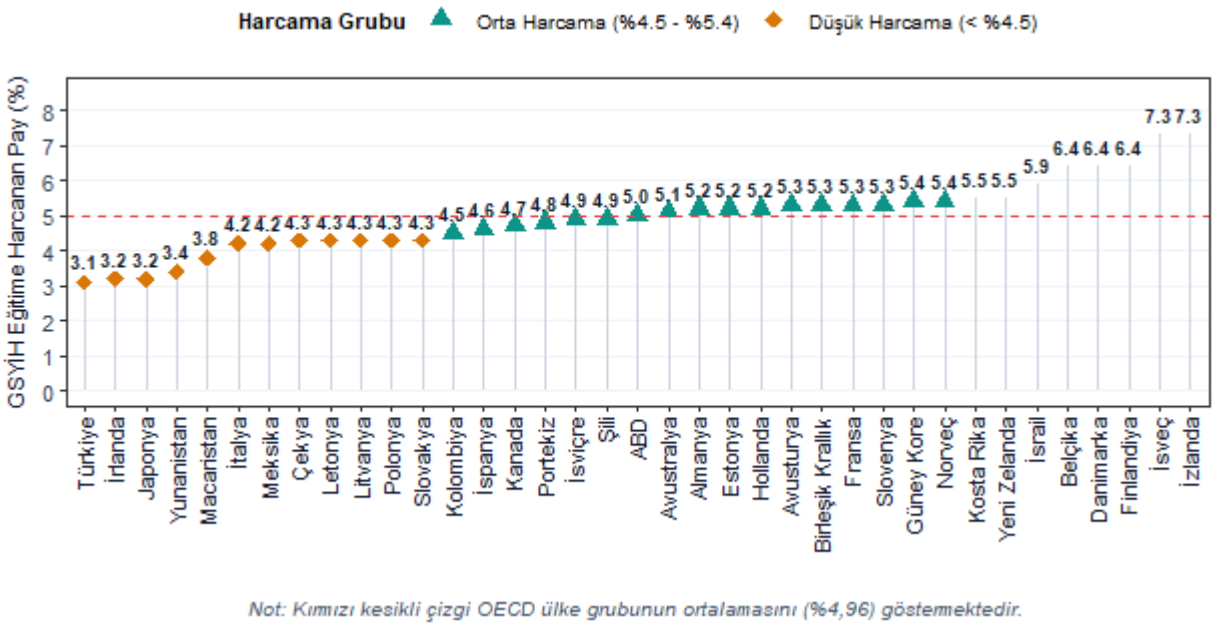

Şekil 2. Ülkelerin Eğitime Yönelik Devlet Harcamaları (% GSYIH)

Ülkelerin 2022 yılı GSYİH'lerinden eğitime ayırdıkları paylar incelendiğinde; İsveç (%7,30) ve İzlanda (%7,30) bütçelerinden eğitime en yüksek oranı tahsis eden ülkelerdir. Bu ülkeleri sırasıyla Belçika (%6,40), Danimarka (%6,40) ve Finlandiya (%6,40) takip etmektedir.Öte yandan bütçesinden eğitime en düşük oranı ayıran ülkeler Türkiye (%3,10), İrlanda (%3,20) ve Japonya (%3,20)'dır. Türkiye, %3,10'luk oranıyla veri setinde yer alan ülkeler arasında son sırada (37. sıra) bulunmakta ve OECD ortalamasının gerisinde kalmaktadır.

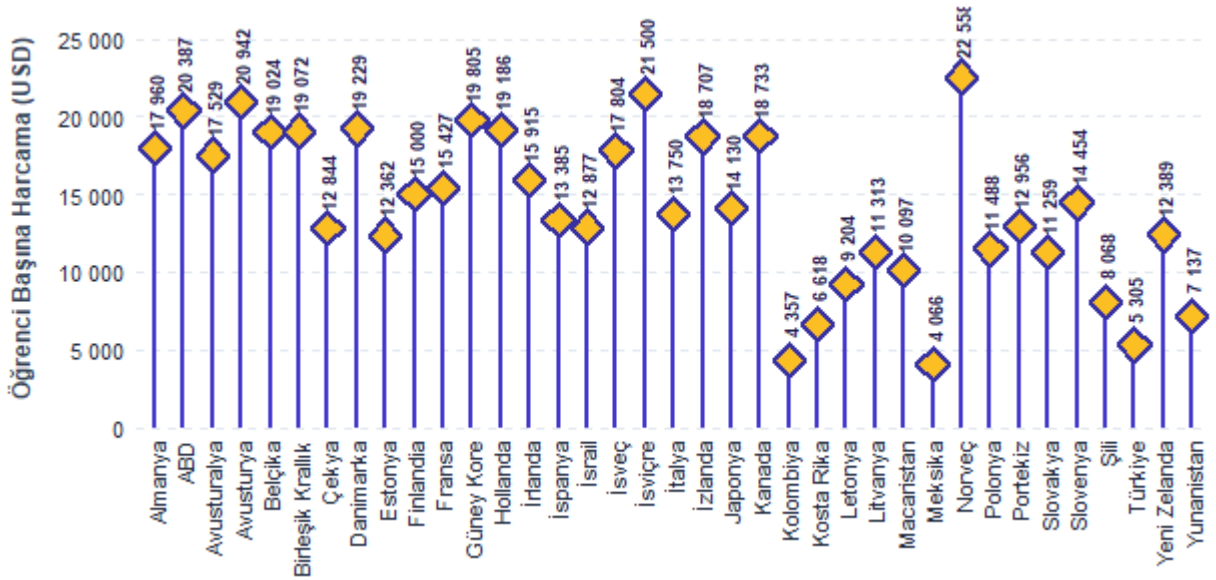

Şekil 3. Ülkelere Göre Öğrenci Başına Yıllık Eğitim Harcaması

İncelenen ülkelerin öğrenci başına yaptıkları eğitim harcamaları (USD) dikkate alındığında, ülkeler arasında belirgin bir finansal kapasite ve kamusal kaynak tahsisi farkı göze çarpmaktadır. Veri tablosunda öğrenci başına en yüksek harcamayı yapan ülkelerin başında 22.558 USD ile Norveç, 21.500 USD ile İsviçre ve 20.387 USD ile ABD gelmektedir. Bu ülkeleri, Fransa (15.427 USD) ve Finlandiya (15.000 USD) gibi harcamaların 15.000 USD bandında dengelendiği orta-yüksek gruptaki gelişmiş ekonomiler ile

10.000–12.000 USD bandında yer alan Çekya (12.844 USD) ve Polonya (11.488 USD) gibi ülkeler izlemektedir. Listenin alt sıralarında ise öğrenci başına yapılan harcama miktarlarının belirgin biçimde düştüğü görülmektedir; nitekim Türkiye (5.305 USD), Kolombiya (4.357 USD) ve Meksika (4.066 USD) en düşük finansal kaynağı ayıran ülkeler olarak öne çıkmaktadır. Tablodaki bu odak noktaları, ülkelerin ulusal gelir düzeyleri ile eğitim bütçeleri arasındaki doğrudan ilişkiyi doğrulamakta; yüksek harcama yapan ülkelerin altyapı ve nitelik hususunda avantaj sağladığını, en alt gruptaki ülkelerin ise bütçe kısıtları nedeniyle eğitimde fırsat eşitliği ve niteliksel dönüşüm süreçlerinde zorlandığını göstermektedir.

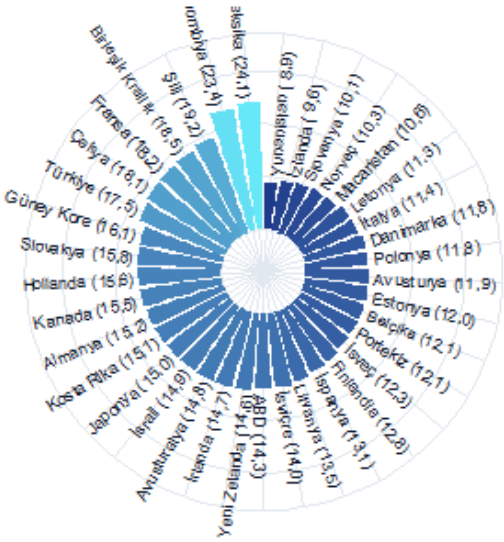

Şekil 4. Öğretmen Başına Düşen Öğrenci Sayısı

Eğitim sistemlerinin niteliğini ve öğrenme süreçlerindeki bireysel etkileşim kapasitesini gösteren temel göstergelerden biri olan öğretmen başına düşen öğrenci sayısı verileri incelendiğinde, ülkeler arasında belirgin yapısal farklılıkların bulunduğu görülmektedir. Veri tablosuna göre öğrenci-öğretmen oranının en düşük (yani öğretmen başına düşen öğrenci sayısının en az) olduğu ülkelerin başında 8,9 ile Yunanistan, 9,6 ile İzlanda ve 10,3 ile Norveç gelmektedir. Bu ülkeleri; Avusturya (11,9), Estonya (12,0), İsveç (12,3) ve Finlandiya (12,8) gibi oranların 10–13 bandında seyrettiği İskandinav ve Kıta Avrupası ülkeleri takip etmektedir. Tabloda orta-yüksek grupta yer alan ABD (14,3), Almanya (15,2), Kanada (15,5) ve Güney Kore (16,1) gibi gelişmiş ekonomilerde öğretmen başına düşen öğrenci sayısının 14–16 aralığında dengelendiği görülmektedir. Listenin son sıralarında ise oranların belirgin biçimde yükseldiği; Türkiye (17,5), Fransa (18,2), Birleşik Krallık (18,5), Kolombiya (23,4) ve Meksika'nın (24,1) öğretmen başına en yüksek öğrenci sayısına sahip ülkeler olarak ayrıştığı gözlemlenmektedir.

Söz konusu sayısal göstergeler, pedagojik açıdan öğretmen-öğrenci etkileşiminin yoğunluğu ve sınıf yönetimi dinamikleriyle doğrudan ilişkilidir. Öğretmen başına düşen öğrenci sayısının düşük olduğu ülkelerde öğretmenlerin bireyselleştirilmiş öğretim yöntemlerini uygulama, öğrenci takibini güçlendirme ve ders içi katılımı artırma imkânlarının daha yüksek olduğu değerlendirilmektedir. Buna karşın, kalabalık sınıf yapısını veya öğretmen kaynağının sınırlılığını temsil eden yüksek oranlı ülkelerde, öğretim süreçlerinde niteliksel sürdürülebilirliği sağlama ve bütçesel/beşeri altyapı kısıtlarını aşma gereksinimi ön plana çıkmaktadır.

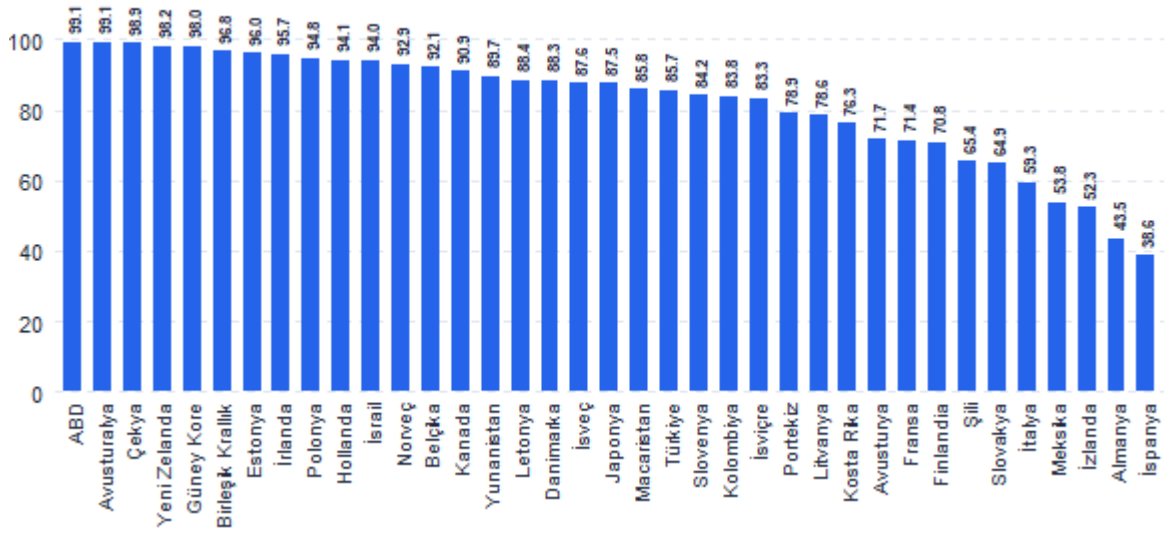

Şekil 5. Ülkelerin Öğretmen Danışmanlığı Oranı (%)

PISA 2022 araştırması kapsamında okul müdürlüklerine uygulanan anketler aracılığıyla elde edilen veriler, okullarda öğrencilere sunulan öğretmen danışmanlığı imkânlarının ülkeler arasındaki dağılımını ortaya koymaktadır. Söz konusu gösterge; öğrencilerin öğrenme eksikliklerini gidermek, akademik başarılarını desteklemek ve okul ortamındaki duyuşsal ihtiyaçlarına yanıt vermek amacıyla sağlanan ek rehberlik, bireysel takviye ve danışmanlık hizmetlerinin erişilebilirliğini temsil etmesi bakımından büyük önem taşımaktadır. Birebir veya küçük gruplar halinde yürütülen bu danışmanlık süreçleri, öğrencilerin okulla olan bağlarını güçlendirerek öğrenme kayıplarının önlenmesinde ve fırsat eşitliğinin sağlanmasında kritik bir işlev üstlenmektedir.

Okul yönetimlerinin bildirimlerine dayanan veri tablosu incelendiğinde, öğrencilerine öğretmen danışmanlığı sağlama oranının en yüksek olduğu ülkelerin başında %99,1 ile ABD ve Avustralya, %98,9 ile Çekya, %98,0 ile Güney Kore ve %96,8 ile Birleşik Krallık gelmektedir. Türkiye ise %85,7'lik danışmanlık oranıyla uluslararası alanda orta-yüksek destek sunan ülkeler arasında yer almaktadır. Buna karşın, okul müdürlüklerinin bildirdiği danışmanlık oranlarının belirgin bir şekilde düştüğü ülkelerde durum farklılaşmakta, Fransa'da %71,4, Almanya'da %43,5 ve İspanya'da %38,6 seviyelerine gerilediği gözlemlenmektedir.

Elde edilen sayısal değerler, ülkelerin eğitim sistemlerinde danışmanlık mekanizmalarının kurumsallaşma düzeyini yansıtmaktadır. Danışmanlık oranının yüksek olduğu sistemlerde öğrencilerin akademik ve duyuşsal bir engelle karşılaştıklarında doğrudan öğretmen desteğine erişim yetenekleri artmakta, bu durum okul iklimini olumlu etkilemektedir. Danışmanlık oranlarının düşük kaldığı sistemlerde ise eğitim süreçlerinin daha çok standart sınıf içi öğretimle yürütüldüğü ve bireyselleştirilmiş akademik rehberlik imkânlarının sınırlandırıldığı değerlendirilmektedir.

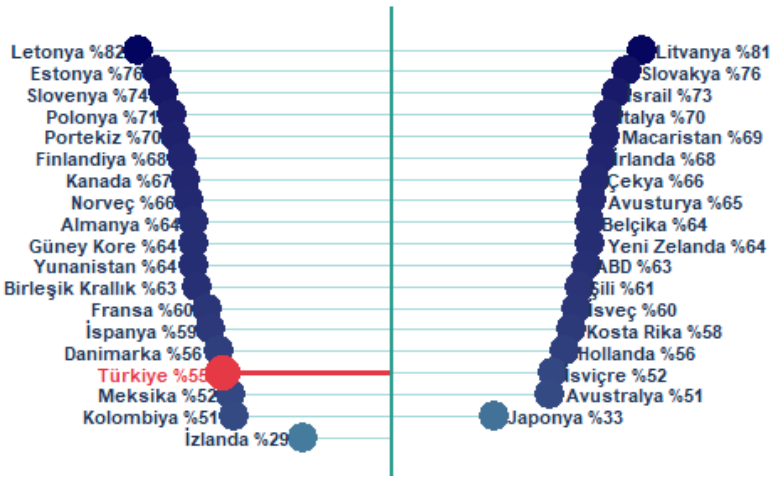

Şekil 6. Ortaöğretim Düzeyinde Kadın Öğretmen Oranı (%)

Eğitim sistemlerinin verimliliği Veri Zarflama Analizi (VZA) ile incelenirken, finansal harcamaların yanı sıra beşeri sermayenin demografik yapısı ve sosyal boyutu da temel bir unsur olarak öne çıkmaktadır. Bu doğrultuda modele dahil edilen "Ortaöğretim Kadın Öğretmen Oranı (%)" değişkeni, eğitim sistemlerinin sosyal sermaye kapasitesini, kurumsal iklimini ve toplumsal yapısını temsil eden stratejik bir çevresel girdi değişkenidir. Literatürde öğretim kadrosunun cinsiyet dağılımı; ders içi iletişim dinamikleri, duyuşsal rehberlik ve rol model etkisi üzerinden okul ortamının niteliğini güçlendiren önemli bir unsur olarak kabul edilmektedir. İncelenen veri tablosunda ülkelerin ortaöğretim düzeyindeki kadın öğretmen oranları %29,0 ile %82,0 arasında geniş bir yelpazede dağılmakta; kadın öğretmen temsilinin en yüksek olduğu ülkeler Letonya (%82,0), Litvanya (%81,0) ve Estonya (%76,0) şeklinde sıralanırken; Finlandiya (%68,0), Almanya (%64,0), Birleşik Krallık (%63,0) ve ABD (%63,0) gibi gelişmiş ekonomiler %60–70 bandında yer almakta, Türkiye %55,0'lik oranla daha dengeli bir cinsiyet dağılımı sergilemekte, Japonya (%33,0) ve İzlanda (%29,0) ise en düşük oranlara sahip ülkeler olarak öne çıkmaktadır. Sonuç olarak, ülkeler arasındaki bu belirgin demografik farklar VZA modelinde kontrol altına alınarak finansal kaynakların çıktıya dönüşme etkinliğinin metodolojik açıdan çok daha doğru değerlendirilmesi sağlanmaktadır.

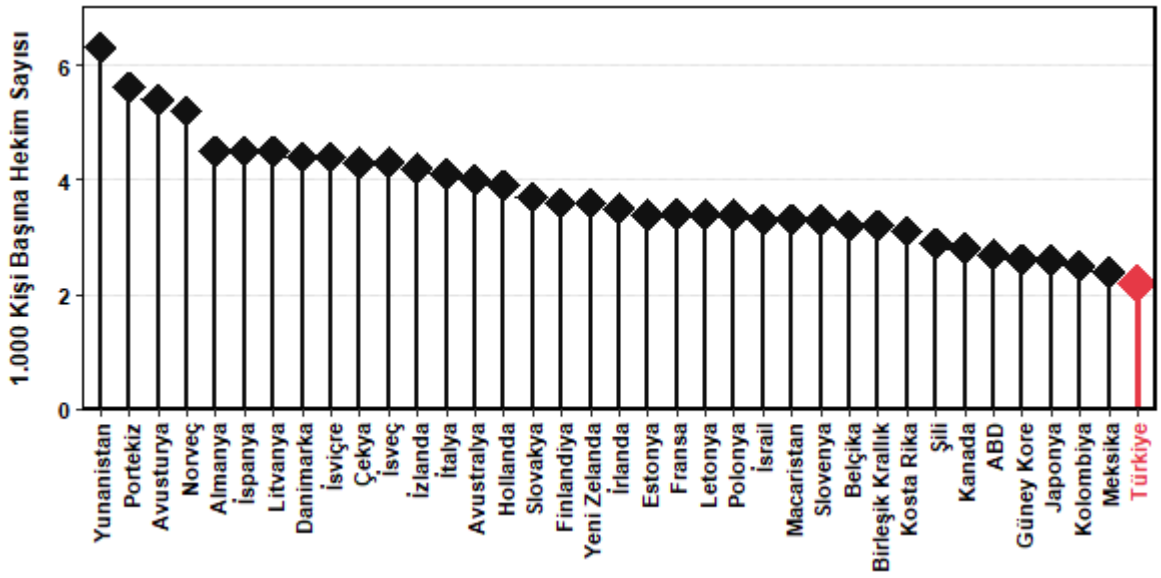

Şekil 7. 1000 Kişi Başına Düşen Hekim Sayısı

Toplumsal gelişim süreçleri değerlendirilirken doğrudan eğitim harcamalarının yanı sıra, beşeri kaynağın genel niteliği ve yaşam kalitesi de belirleyici bir unsur olarak öne çıkmaktadır. Bu doğrultuda modele eklenen "1000 Kişiye Düşen Hekim Sayısı" değişkeni, öğrenim süreçlerinin arka planındaki toplumsal refah düzeyini ve kamu hizmet kapasitesini temsil eden bir çevresel göstergedir. Literatürde çocukluk dönemi sağlık durumunun; okula devamlılık, zihinsel gelişim ve öğrenme kapasitesi üzerinde doğrudan etkili olduğu kabul edilmektedir. İncelenen veri setinde hekim yoğunluğu en yüksek ülkeler Yunanistan (6,6) ve Portekiz (5,9) şeklinde sıralanırken; Avusturya (5,4), Almanya (4,5) ve İsveç (4,4) gibi gelişmiş ekonomiler üst grupta yer almaktadır. Listenin son sıralarında ise Kolombiya (2,5), Meksika (2,6) ve Japonya (2,6) gibi hekim kapasitesi sınırlı ülkeler bulunmakta, Türkiye ise 2,2'lik oranla bu göstergede düşük değere sahip ülke olarak öne çıkmaktadır.

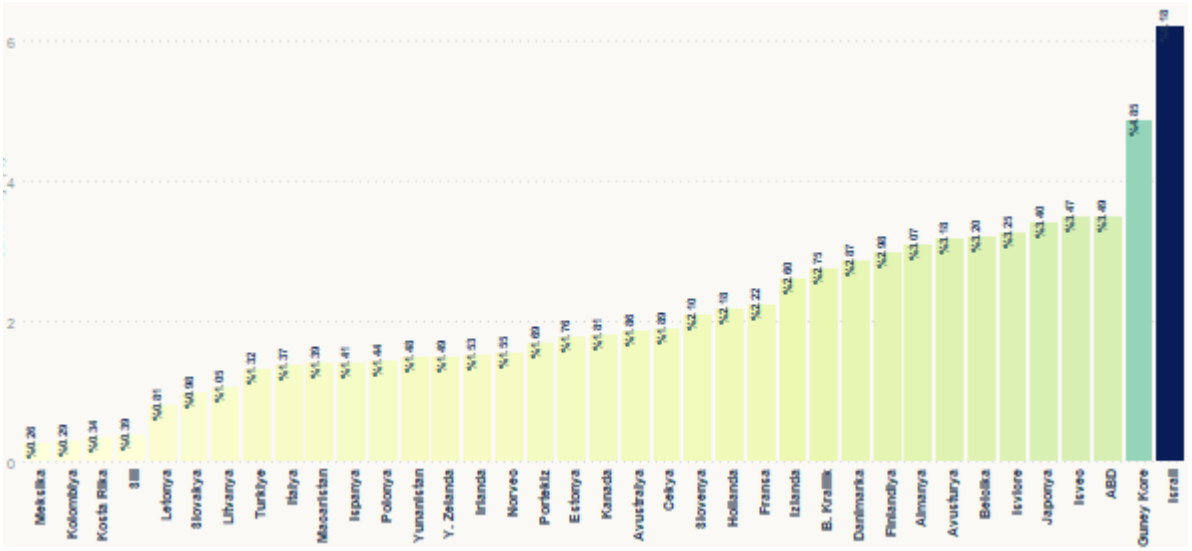

Şekil 8.Ülkelerin Ar-Ge Harcamalarının GSYİH İçindeki Payı (%)

Ulusal düzeydeki kalkınma stratejilerinin içinde yer alan Ar-Ge yatırımları, ülkelerin Gayrisafi Yurtiçi Hasıla (GSYİH) içindeki payları üzerinden değerlendirildiğinde farklı performans seviyelerini net biçimde yansıtmaktadır. Veriler incelendiğinde %6.18 ile İsrail ve %4.85 ile Güney Kore Ar-Ge'ye en yüksek payı ayıran ülkeler olarak öne çıkmaktadır. Bu ülkeleri ABD (%3.49), İsveç (%3.47) ve Japonya (%3.40) gibi güçlü yatırım oranlarına sahip yapılar izlemektedir. Tablonun devamında Almanya (%3.07) %3 seviyesini aşan yapısıyla dikkat çekerken; Fransa (%2.22) ve Hollanda (%2.18) gibi ülkelerin ardından gelen Türkiye (%1.32), İtalya (%1.37) ve İspanya (%1.41) %1.30–1.40 bandında konumlanarak orta grupta dengelenmektedir. Listenin alt sıralarında yer alan Latin Amerika ekonomilerinde ise Ar-Ge yatırımlarının GSYİH içindeki oranının genel olarak %0.5'in altında kaldığı görülmektedir.

III. BULGULAR

Çalışmanın bulgular kısmında iki aşamalı bir analiz süreci izlenmiştir; ilk olarak klasik Veri Zarflandırma Analizi (VZA) ile 10 ülke tam etkin (1) ve 27 ülke etkinsiz (<1) olarak tespit edilmiş,genel etkinlik düzeyleri belirlenerek tam etkin olan ve olmayan ülkeler ayrıştırılmış, ardından tam etkin bulunan ülkeler kendi aralarında derecelendirilebilmek amacıyla Süper Etkinlik Analizi yapılmıştır.

Tablo 1.

Ulke (DMU)	Skor	Ulke (DMU)	Skor	Ulke (DMU)	Skor
Almanya	1.0000	Irlanda	1.0000	Macaristan	0.9396
ABD	0.8248	Ispanya	1.0000	Meksika	1.0000
Avusturalya	0.9324	Israil	0.7571	Norvec	0.7749
Avusturya	0.8003	Isvec	0.7686	Polonya	0.8802
Belcika	0.7799	Isvicre	0.8771	Portekiz	0.8464
Birlesik Krallik	0.9794	Italya	0.9905	Slovakya	0.9843
Cekya	0.9938	Izlanda	1.0000	Slovenya	0.8426
Danimarka	0.7794	Japonya	1.0000	Sili	0.9114
Estonya	0.8283	Kanada	0.9453	Turkiye	1.0000
Finlandiya	0.9156	Kolombiya	1.0000	Yeni Zelanda	0.8316
Fransa	0.9373	Kosta Rika	0.9406	Yunanistan	0.9285
Guney Kore	1.0000	Letonya	1.0000		
Hollanda	0.8761	Litvanya	0.9477		

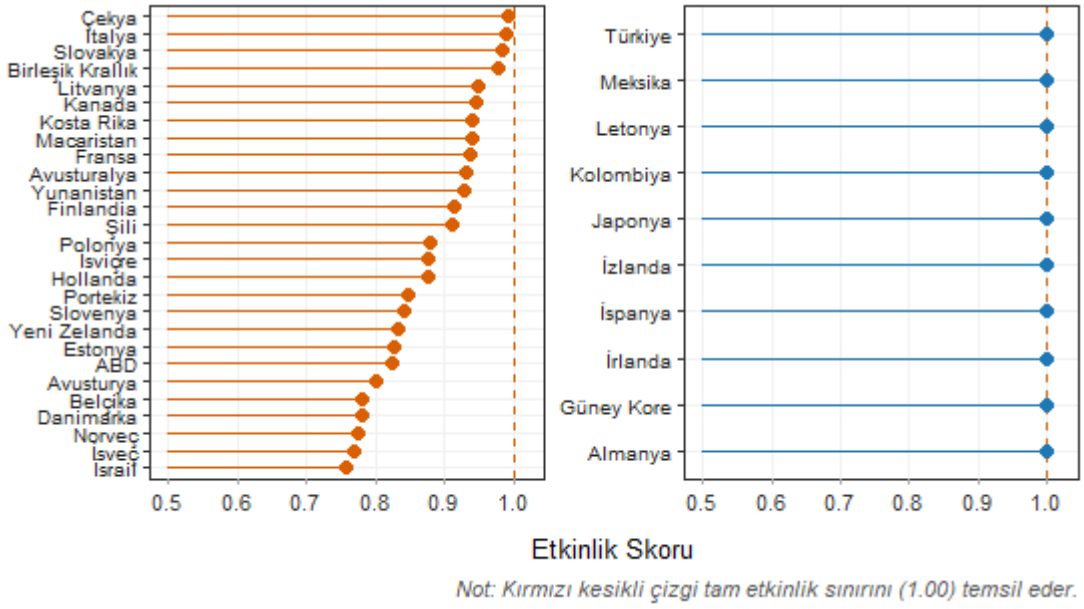

Şekil 9.

Tablo 1 ve Şekil 9 incelendiğinde, 10 ülkenin 1,0000 skoru ile tam etkinlik sınırında yer aldığı, etkinsiz gruptaki 27 ülkenin skorlarının ise 0,7571 ile 0,9938 arasında değiştiği görülmektedir. Etkinsiz ülkeler arasında tam etkinliğe en yakın ülke Çekya (0,9938) iken, en düşük skor İsrail'e (0,7571) aittir.

Tablo 2.

Sira	Ulke (DMU)	Super Etkinlik Skoru
1.	Japonya	1.6550
2.	Meksika	1.5017
3.	Turkiye	1.3537
4.	Ispanya	1.3515
5.	Izlanda	1.2414
6.	Kolombiya	1.1121
7.	Irlanda	1.0876
8.	Almanya	1.0612
9.	Guney Kore	1.0329
10.	Letonya	1.0015

Tablo 2.de etkin çıkan 10 ülkenin süper etkinlik analizine göre elde edilen sayısal değerleri verilmektedir.



Şekil10. Süper Etkinlik Analiz Sonuçları

Tam etkin çıkan 10 ülkenin performans düzeylerini derecelendirmek amacıyla yapılan Süper Etkinlik Analizi sonuçları Tablo 2 ve Şekil 10 da sunulmuştur. Daire alanlarının süper etkinlik skorlarının büyüklüğünü temsil ettiği grafiğe göre; Japonya ve Meksika en büyük daire alanlarına sahip olarak süper etkinlik sıralamasında ilk iki sırada yer almıştır. Türkiye ve Almanya ise bu iki ülkeyi takip eden en yüksek süper etkinlik değerlerine sahip diğer ülkeler olmuştur. Süper etkinlik grubu içerisinde daire alanı

en küçük olan ve dolayısıyla göreli olarak en düşük skoru elde eden ülke ise Kolombiya olarak gerçekleşmiştir.

IV. TARTIŞMA

Analizden üstlerde yer alan Japonya ve Güney Kore, yüksek girdi seviyelerini küresel ölçekte lider PISA skorlarına dönüştürerek sınırın tepe noktasını oluşturmuştur. Japonya; 14.130 USD öğrenci başı harcama girdisiyle Matematik (536), Okuma (516) ve Fen (547) alanlarında analizin en yüksek çıktısını elde etmiştir. Benzer şekilde Güney Kore, 19.805 USD tutarındaki harcamasını yüksek PISA çıktılarıyla (Matematik: 527, Fen: 528) yüksek verimlilik düzeyinde temellendirmiştir.

Buna karşılık Meksika ve Kolombiya 37 ülke arasındaki en düşük finansal girdilerle eğitim sistemlerini yönetmelerine rağmen verimlilik sınırında yer almıştır. Türkiye (5.305 USD harcama, 17,5 öğretmen başına öğrenci oranı) ve Letonya (9.204 USD harcama), harcama bazında alt sıralarda kalmalarına rağmen elde ettikleri ortalama üstü akademik performansla göreli verimlilik sınırını yakalamıştır. Bu durum, eğitim sistemlerinde verimliliğin yalnızca yüksek bütçelere değil, kaynakların yönetimine bağlı olduğunu göstermektedir.

Çalışmanın en dikkat çekici bulgusu; kişi başı geliri ve eğitim bütçesi en yüksek olan ülkelerin verimlilik sırasında alt bölümlere gerilemesidir. Norveç, öğrenci başına yapılan 22.558 USD tutarındaki harcamaya ve öğretmen başına sadece 10,3 öğrenci düşmesine rağmen elde ettiği PISA skorları (Matematik: 468, Fen: 478) ile girdilerinin gerisinde kalmıştır. İsveç (öğrenci başı 17.804 USD harcama), Danimarka (19.229 USD harcama), Belçika (19.024 USD harcama) ve ABD (öğrenci başına 20.387 USD harcama ve 82.587 USD kişi başı GSYİH) yüksek finansal girdilerine karşın etkinsiz grupta yer almıştır. Bu durum, eğitimde yüksek harcama yapmanın otomatik olarak yüksek performans getirmediğini ve asıl belirleyici unsurun bütçenin büyüklüğü değil, bu kaynakların çıktılara dönüştürülme sürecindeki yönetsel etkinlik olduğunu kanıtlamaktadır.

V. SONUÇLAR

Bu çalışmada, 37 ülkenin eğitim sistemlerine aktardıkları finansal ve beşeri girdiler ile elde ettikleri PISA akademik çıktıları arasındaki verimlilik ilişkisi Veri Zarflandırma Analizi (VZA) ve Süper Etkinlik modelleriyle incelenmiştir. Analizden elde edilen ana bulgular, eğitimde verimliliğin tek başına bütçe büyüklüğüyle sınırlı olmadığını; aksine performansın ülkelerin kaynak kullanım niteliğine göre şekillendiğini ortaya koymaktadır. Maksimum verimlilik gösteren lider ülkeler grubunda yer alan Japonya ve Güney Kore, yüksek düzeydeki öğrenci başı harcama ve beşeri kaynak girdilerini küresel ölçekte üst sıradaki PISA çıktılarına dönüştürerek Süper Etkinlik sıralamasının zirvesini oluşturmuştur.

Buna karşın Meksika, Kolombiya, Türkiye ve Letonya; bütçe büyüklüğü ve harcama bazında alt sıralarda yer almalarına rağmen ellerindeki kısıtlı kaynakları optimal biçimde yöneterek göreli verimlilik sınırını yakalamayı başarmıştır.

Çalışmanın en dikkat çekici ana sonucu ise kişi başı geliri ve eğitim bütçesi en yüksek olan Norveç, ABD, İsveç, Danimarka ve Belçika gibi gelişmiş ülkelerin etkinsiz grupta konumlanmasıdır. Bu durum, eldeki yüksek finansal ve beşeri imkânların nitelikli akademik performans çıktısına dönüştürülmesinde sistemsel tıkanıklıklar yaşandığına işaret etmektedir.

Özetle araştırma; eğitim sistemlerinde başarının ana belirleyicisinin bütçelerin mutlak büyüklüğü değil, bu kaynakların eğitsel çıktılara dönüştürülme sürecindeki yönetsel etkinlik olduğunu ortaya koymaktadır.

Gelecekte yapılacak araştırmalarda, COVID-19 küresel salgını (pandemi) sürecinin ve sonrasının veriler dâhil edilerek benzer analizlerin tekrarlanması önerilmektedir. Uzaktan eğitim modeli, dijital altyapı yatırımları ve salgın döneminde değişen bütçe önceliklerinin ülkelerin eğitimdeki verimlilik sınırlarını nasıl etkilediğinin incelenmesi, kriz dönemlerindeki kaynak yönetiminin dinamiklerini anlamak açısından literatüre önemli katkılar sağlayacaktır.

TEŞEKKÜR

Bu çalışmanın hazırlık ve uygulama süreçlerinde değerli katkı ve yönlendirmeleriyle çalışmaya rehberlik eden Sayın Doç. Dr. Hasan Bulut 'a ve akademik gelişimime katkı sağlayan tüm bölüm hocalarıma teşekkür ederim.

KAYNAKLAR

[1] MEB, PISA 2018 TÜRKIYE ÖN RAPORU, T.C. MILLÎ EĞITIM BAKANLIĞI ÖLÇME, DEĞERLENDIRME VE SINAV HIZMETLERI GENEL MÜDÜRLÜĞÜ, ANKARA, 2019.

[2] G. Cheng, Data Envelopment Analysis: Methods and MaxDEA Software, Beijing: Intellectual Property Publishing House, 2014.S

[3] R Core Team, R: A Language and Environment for Statistical Computing, R Foundation for Statistical Computing, Vienna, Austria, 2025. https://www.R-project.org/

[4] A. Charnes, W. W. Cooper, and E. Rhodes, "Measuring the efficiency of decision making units," European Journal of Operational Research, vol. 2, no. 6, pp. 429–444, 1978.

[5] W. D. Cook and L. M. Seiford, "Data envelopment analysis (DEA) – Thirty years on," European Journal of Operational Research, vol. 192, no. 1, pp. 1–17, 2009.

[6] A. V. Yavuz, "Veri zarflandırma analizi ve bankacılık sektöründe bir uygulama," Gazi Üniversitesi İktisadi ve İdari Bilimler Fakültesi Dergisi, cilt 3, sayı 3, ss. 177–189, 2001.

[7] OECD, Education at a Glance: OECD Indicators, OECD Publishing, Paris. 2023

[8] OECD, PISA 2022 Results (Volume I and Volume II), PISA, OECD Publishing, Paris, 2023. [Çevrim içi]. Erişilebilir: https://doi.org/10.1787/53f23881-en

[9] World Bank, "World Bank Open Data," World Bank Group. [Çevrim içi]. Erişilebilir: https://data.worldbank.org

8th International Conference on Engineering, Natural and Social Sciences

September 06-07, 2026: Konya, Turkey

© 2026 Published by All Sciences Academy

https://www.icensos.com/

Seasonal Changes in Drinking-Water Chemistry: A Comparative Study of Two Albanian Water-Supply Systems

Shkelqıme Poga[1]*, Erjon Mamoçi[2] and Drıte Mema[3]

[1]*Department of Assessment and Treatment of Risks in Public Health, Institute of Public Health Tirana, Albania*
[2]*Department of Food Science and Biotechnology, Faculty of Biotechnology and Food, Agricultural University Tirana, Albania*
[3]*Department of National Reference Laboratories, Institute of Public Health Tirana, Albania*

** Corresponding author: shkelqimetobli@gmail.com*

Abstract - This study investigated seasonal changes in drinking-water chemistry in Tirana and Shkodra using the permanganate index as an indicator of oxidizable organic substances. Monthly sampling was conducted at 16 monitoring points in each water-supply system from September 2024 to April 2025. Tirana is supplied predominantly by surface water, supplemented by groundwater, whereas Shkodra relies mainly on groundwater. The permanganate index was determined according to ISO 8467 by potassium permanganate titration using oxalic acid, and the results were expressed as mg/L O_2. In Tirana, values ranged from 0.420 to 9.880 mg/L O_2, with a median of 1.551 mg/L O_2. The highest value was recorded at M8 in December 2024. In Shkodra, values ranged from 0.329 to 4.942 mg/L O_2, with a median of 0.923 mg/L O_2, and the maximum was recorded at M16 in February 2025. Seasonal mean values increased from 1.24 mg/L O_2 in autumn to 1.87 mg/L O_2 in winter in Tirana and from 0.67 to 1.44 mg/L O_2, respectively, in Shkodra. Tirana exhibited greater overall variability and a higher extreme value, whereas Shkodra generally showed lower and more stable values. The winter increases observed in both systems indicate seasonal changes in oxidizable organic load and highlight the importance of continuous chemical monitoring and appropriate treatment control, particularly because oxidizable organic substances may increase disinfectant demand and contribute to the formation of disinfection by-products.

Keywords - drinking-water chemistry; permanganate index; oxidizable organic substances; seasonal variability; surface water; groundwater

I. INTRODUCTION

Safe drinking water depends on the effective control of chemical, physical and microbiological hazards from the source to the consumer. Oxidizable substances in water originate from natural organic inputs, biological activity, anthropogenic contamination and processes occurring within treatment and distribution systems. Their amount and composition vary with source type, catchment conditions, hydrology and treatment performance [1]-[3]. Surface waters generally respond rapidly to rainfall and runoff, whereas groundwater systems tend to show greater short-term stability because of subsurface storage and attenuation [2], [3].

The permanganate index is a conventional measure of the oxygen equivalent of substances oxidized by permanganate under defined conditions. It reflects oxidizable organic matter and may also include some oxidizable inorganic constituents; therefore, it should not be interpreted as a direct or comprehensive measurement of natural organic matter [4]. Nevertheless, it remains a useful operational indicator for comparing temporal and spatial changes in drinking-water systems.

Oxidizable organic substances can influence coagulation and filtration, increase disinfectant demand and contribute to the formation of disinfection by-products when chlorine is used [5]-[8]. They may also affect biological stability and microbial regrowth within distribution networks [9]-[11]. Risk-based drinking-

water management therefore requires monitoring that is adapted to source characteristics and seasonal changes [12], [13].

Evidence on seasonal changes in this chemical indicator remains limited in Albania. The present study compared two major urban water-supply systems with different predominant source types: Tirana, supplied mainly by surface water from the Bovilla reservoir with additional groundwater sources, and Shkodra, supplied mainly by groundwater. The objective was to characterize spatial and seasonal variability in the permanganate index and consider its operational implications for drinking-water treatment and monitoring.

II. MATERIALS AND METHOD

Study areas

Tirana operates a mixed supply dominated by surface water from the Bovilla reservoir and supplemented by groundwater wells. Shkodra is supplied mainly by groundwater. These systems provide a useful comparison of chemical variability under different predominant source conditions.

Sampling design

Monthly sampling campaigns were conducted from September 2024 to April 2025. Sixteen monitoring points were included in each city. In Tirana, the network comprised two pre-treatment points (M1-M2) and 14 post-treatment or distribution points (M3-M16). In Shkodra, M1 represented the raw-water source and M2-M16 represented post-treatment or distribution locations. In total, 256 site-month observations were evaluated. Samples were collected in pre-cleaned amber glass bottles of at least 500 mL, kept at 4 °C in the dark and transported to the laboratory within 24 h.

Analytical method

The permanganate index was determined according to ISO 8467 [4]. Under the specified acidic and heated conditions, oxidizable substances consume a known amount of potassium permanganate. The remaining permanganate is reduced with oxalate, and the excess is determined by titration with permanganate. Results were expressed as mg/L O_2. Each analytical batch included a blank and a standard control sample.

Data analysis

Results were summarized by city using the median, range and mean ± standard deviation where appropriate. Seasons were defined as autumn (September-November), winter (December-February) and early spring (March-April). Values were also examined by month and monitoring point to identify spatial and temporal patterns. The analysis was descriptive; no causal effect of source type or season was inferred.

III. RESULTS

Overall distribution

Across the 128 site-month observations in Tirana, the permanganate index ranged from 0.420 to 9.880 mg/L O_2, with a median of 1.551 mg/L O_2. The maximum was recorded at M8 in December 2024. In Shkodra, the 128 observations ranged from 0.329 to 4.942 mg/L O_2, with a median of 0.923 mg/L O_2; the maximum occurred at M16 in February 2025. The highest pre-treatment values were 3.107 mg/L O_2 at M1 in Tirana in September 2024 and 2.573 mg/L O_2 at M1 in Shkodra in February 2025.

Seasonal and monthly patterns

Mean values increased from autumn to winter in both systems. In Tirana, the seasonal mean increased from 1.24 mg/L O_2 in autumn to 1.87 mg/L O_2 in winter and was 1.71 mg/L O_2 in early spring. In Shkodra, the corresponding means were 0.67, 1.44 and 1.38 mg/L O_2. Tirana reached its highest monthly mean in December 2024 (2.14 mg/L O_2), whereas Shkodra reached its highest monthly mean in February 2025 (2.04 mg/L O_2). Values converged in April 2025 (1.75 mg/L O_2 in Tirana and 1.67 mg/L O_2 in Shkodra).

Spatial patterns

Tirana showed a higher central tendency and a more pronounced single-site maximum than Shkodra. Although Shkodra generally had lower values, the February peak at M16 demonstrated that localized increases also occurred in the groundwater-dominated system. Because source type was not assigned separately to every distribution point and no hydraulic variables were measured, the observed differences should be interpreted as system-level patterns rather than direct causal effects of surface water or groundwater.

Table 1. Permanganate index at monitoring points in Tirana (mg/L O_2)

Point	Sep-24	Oct-24	Nov-24	Dec-24	Jan-25	Feb-25	Mar-25	Apr-25
M1	3.107	1.071	1.860	1.837	1.643	2.800	1.330	1.527
M2	1.734	0.884	1.334	1.699	1.398	1.580	1.242	1.177
M3	1.463	0.926	1.406	2.100	1.640	2.233	1.313	1.319
M4	1.938	1.420	0.573	1.399	2.323	1.232	1.518	1.759
M5	1.929	0.420	1.242	1.760	1.680	1.429	1.699	1.707
M6	1.244	0.947	2.050	1.486	1.106	2.800	1.684	2.758
M7	1.552	0.948	0.934	1.213	1.879	1.106	1.879	1.704
M8	1.164	0.797	0.830	9.880	1.787	1.681	1.677	1.876
M9	1.274	0.897	0.850	1.609	1.478	1.716	1.904	1.795
M10	1.351	1.006	2.025	1.660	1.459	1.756	1.287	1.426
M11	1.384	0.923	1.681	0.950	1.659	1.814	1.605	2.406
M12	1.328	0.828	0.909	1.200	1.590	1.787	1.590	2.451
M13	1.324	0.983	0.798	2.005	1.598	1.720	1.793	1.346
M14	1.451	0.848	1.900	2.000	1.408	1.740	2.263	1.555
M15	1.057	0.799	0.909	1.200	1.550	1.205	1.991	1.568
M16	1.315	0.938	0.798	2.239	1.740	2.783	2.009	1.581

Table 2. Permanganate index at monitoring points in Shkodra (mg/L O_2)

Point	Sep-24	Oct-24	Nov-24	Dec-24	Jan-25	Feb-25	Mar-25	Apr-25
M1	0.518	0.685	0.817	1.035	1.998	2.573	1.110	1.795
M2	0.414	0.799	0.923	0.562	2.396	3.460	1.064	1.325
M3	0.729	0.762	0.718	0.997	0.849	2.152	0.715	1.116
M4	0.466	0.698	0.706	0.923	0.804	1.602	1.224	1.633
M5	0.792	0.664	0.852	1.127	1.424	1.708	1.219	1.462
M6	0.556	0.675	0.852	1.087	0.984	2.370	0.848	1.533
M7	0.552	0.870	0.852	0.896	1.360	2.374	0.966	1.750

Point	Sep-24	Oct-24	Nov-24	Dec-24	Jan-25	Feb-25	Mar-25	Apr-25
M8	0.495	0.716	0.782	0.850	1.260	0.420	1.064	1.289
M9	0.394	0.736	0.853	0.771	1.266	1.172	1.183	1.483
M10	0.393	0.570	0.772	0.810	1.236	1.680	1.354	2.139
M11	0.428	0.830	0.695	0.793	1.222	2.060	1.155	1.292
M12	0.369	0.793	0.727	0.893	1.778	1.727	1.224	1.279
M13	0.366	0.764	0.658	0.859	1.545	0.921	1.068	1.605
M14	0.432	0.704	0.759	0.993	1.540	2.828	1.228	1.967
M15	0.329	0.996	0.914	0.905	1.246	0.700	1.178	2.629
M16	0.405	0.797	0.695	0.906	1.298	4.942	0.922	2.481

Table 3. Summary statistics by water-supply system

Metric	Tirana	Shkodra
Median (mg/L O_2)	1.551	0.923
Range (mg/L O_2)	0.420-9.880	0.329-4.942
Overall maximum	9.880 (M8, Dec 2024)	4.942 (M16, Feb 2025)
Pre-treatment maximum	3.107 (M1, Sep 2024)	2.573 (M1, Feb 2025)

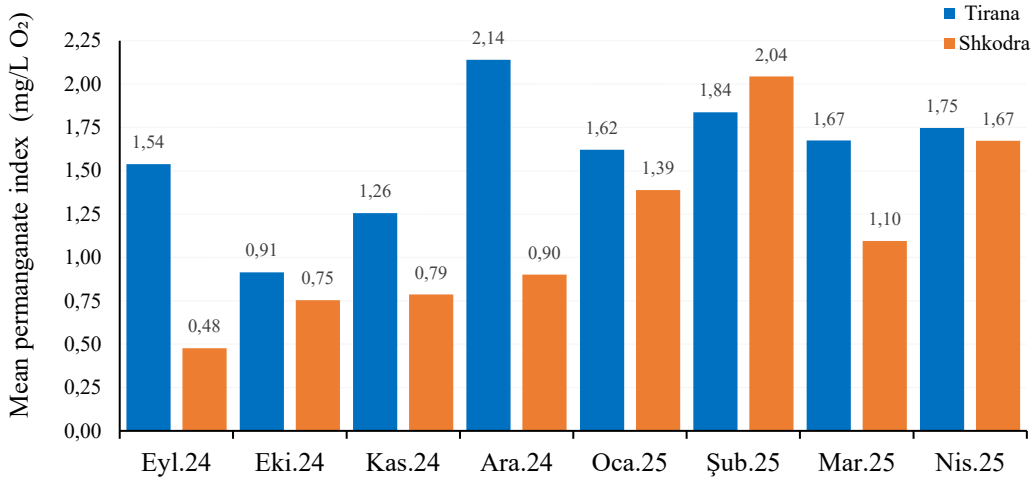

Fig. 1. Monthly mean permanganate index in Tirana and Shkodra, September 2024-April 2025.

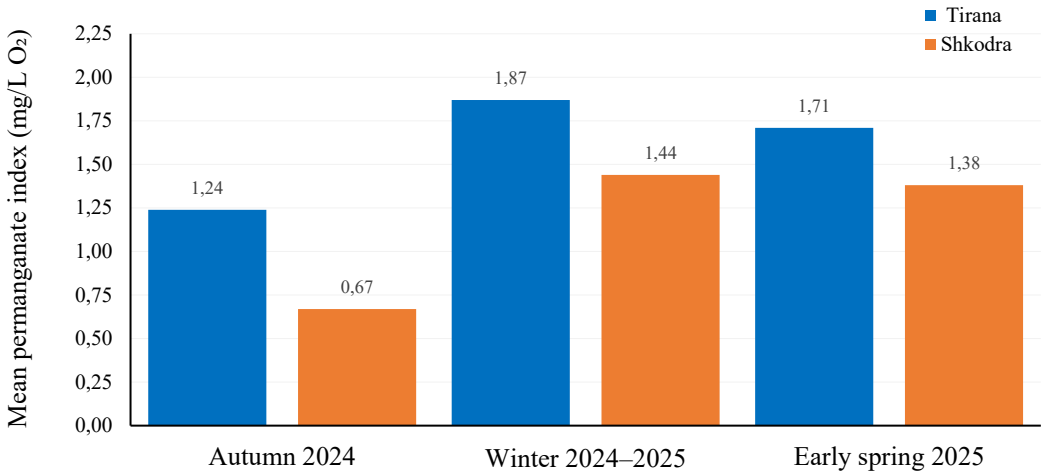

Fig. 2. Seasonal mean permanganate index in Tirana and Shkodra.

IV. DISCUSSION

The two systems displayed distinct distributions and seasonal patterns. Tirana had a higher median and a higher maximum, while Shkodra generally showed lower values. Winter increases in both cities are consistent with seasonal changes in source-water conditions, treatment demand and distribution-system behavior. In surface-water catchments, rainfall and runoff can mobilize oxidizable material; groundwater storage can dampen short-term variability, although local peaks may still occur [2], [3]. Because rainfall, flow, water age and treatment-process data were not analyzed, these mechanisms remain plausible explanations rather than demonstrated causes.

The permanganate index is operationally relevant because increases in oxidizable load may raise oxidant and coagulant demand. Where chlorine is applied, organic precursors can contribute to disinfection by-product formation [5]-[8]. However, this study did not measure dissolved organic carbon, specific ultraviolet absorbance, trihalomethanes, haloacetic acids or chlorine demand. Consequently, the observed index values cannot be used to quantify disinfection by-product concentrations or direct health risk.

For the Tirana system, the December maximum supports closer review of source conditions, treatment records and local hydraulic conditions at M8. The Shkodra maximum at M16 similarly warrants examination of water age, intermittent flow, storage and local inputs. Appropriate responses may include event-based resampling and verification of coagulation, filtration and disinfectant-residual control, selected according to plant and network conditions [14], [15]. Any change in chlorine dosing should be supported by site-specific microbial and disinfection-by-product monitoring rather than by the permanganate index alone.

The main strengths of the study are repeated monthly monitoring at 32 points and comparison of two systems with different predominant source types. Limitations include the eight-month observation period, the absence of a complete annual cycle, reliance on a single aggregate chemical indicator, lack of inferential testing and the absence of meteorological, hydraulic, treatment-process and disinfection-by-product measurements. Future work should extend monitoring across multiple years and integrate rainfall, raw-water characteristics, treatment operations, chlorine residuals, dissolved organic carbon and regulated disinfection by-products.

V. CONCLUSION

The permanganate index showed clear spatial and seasonal variability in the two Albanian water-supply systems. Tirana had a higher median and a larger maximum, with the highest value recorded at M8 in December 2024, while Shkodra generally showed lower values but recorded a localized maximum at M16 in February 2025. Mean values increased during winter in both systems. These findings support continuous chemical monitoring and targeted investigation of locations and periods with elevated values. Because the

permanganate index is an aggregate indicator rather than a direct measure of natural organic matter or disinfection by-products, it should be interpreted together with source-water, treatment, hydraulic, chlorine-residual and disinfection-by-product data.

ACKNOWLEDGMENT

The authors gratefully acknowledge the Institute of Public Health, Tirana, for laboratory facilities and technical support. The authors also thank the Tirana and Shkodra water utilities for their collaboration during field sampling and logistical support.

REFERENCES

[1] A. Matilainen, E. T. Gjessing, T. Lahtinen, L. Hed, A. Bhatnagar, and M. Sillanpaa, 'An overview of the methods used in the characterisation of natural organic matter in relation to drinking water treatment,' Chemosphere, vol. 83, no. 11, pp. 1431-1442, 2011, doi: 10.1016/j.chemosphere.2011.01.018.

[2] Health Canada, Guidance on Natural Organic Matter in Drinking Water. Ottawa, Canada: Government of Canada, 2020.

[3] L. K. McDonough et al., 'Changes in global groundwater organic carbon driven by climate change and urbanization,' Nature Communications, vol. 11, art. 5126, 2020, doi: 10.1038/s41467-020-14946-1.

[4] International Organization for Standardization, Water quality - Determination of permanganate index, ISO 8467:1993, Geneva, Switzerland, 1993.

[5] A. L. Srivastav, N. Patel, and M. Chaudhary, 'Disinfection by-products in drinking water: Occurrence, toxicology and control,' Environment International, vol. 143, art. 105924, 2020, doi: 10.1016/j.envint.2020.105924.

[6] S. D. Richardson, M. J. Plewa, E. D. Wagner, R. Schoeny, and D. M. DeMarini, 'Occurrence, genotoxicity, and carcinogenicity of regulated and emerging disinfection by-products in drinking water,' Mutation Research, vol. 636, nos. 1-3, pp. 178-242, 2007, doi: 10.1016/j.mrrev.2007.09.001.

[7] S. D. Richardson, 'Tackling unknown disinfection by-products in drinking water,' Current Opinion in Chemical Engineering, vol. 31, 2021, doi: 10.1016/j.coche.2020.11.001.

[8] European Parliament and Council, 'Directive (EU) 2020/2184 of 16 December 2020 on the quality of water intended for human consumption,' Official Journal of the European Union, L 435, pp. 1-62, 2020.

[9] D. van der Kooij, 'Assimilable organic carbon as an indicator of bacterial regrowth in drinking-water distribution systems,' Journal AWWA, vol. 84, no. 2, pp. 57-65, 1992.

[10] F. Hammes and T. Egli, 'New method for assimilable organic carbon determination using flow cytometry and a natural microbial consortium as inoculum,' Environmental Science & Technology, vol. 39, no. 9, pp. 3289-3294, 2005, doi: 10.1021/es048277c.

[11] F. C. Pick et al., 'Cycling of assimilable organic carbon within drinking water distribution systems,' Water Research, vol. 202, art. 117437, 2021, doi: 10.1016/j.watres.2021.117437.

[12] World Health Organization, Guidelines for Drinking-water Quality, 4th ed., incorporating the first and second addenda. Geneva, Switzerland: WHO, 2022.

[13] World Health Organization and International Water Association, Water Safety Plan Manual: Step-by-step Risk Management for Drinking-water Suppliers, 2nd ed. Geneva, Switzerland: WHO, 2023.

[14] U.S. Environmental Protection Agency, Enhanced Coagulation and Enhanced Precipitative Softening Guidance Manual, EPA 815-R-99-012. Washington, DC, USA: Office of Water, 1999.

[15] U.S. Environmental Protection Agency, Alternative Disinfectants and Oxidants Guidance Manual, EPA 815-R-99-014. Washington, DC, USA: Office of Water, 1999.

8th International Conference on Engineering, Natural and Social Sciences

September 06-07, 2026: Konya, Turkey

© 2026 Published by All Sciences Academy

https://www.icensos.com/

Risk-Based Maintenance Prioritization for Marine Main Engine Shutdown Prevention: A Reassessment of Lubrication and Jacket Cooling Failures

Bulut Ozan Ceylan[1*], Oğuzhan Der[2], Arif Savaş[3]

[1]*Department of Marine Engineering, Maritime Faculty, Bandirma Onyedi Eylul University, Balikesir 10200, Türkiye (ORCID: https://orcid.org/0000-0003-1182-3566)*

[2]*Department of Marine Engineering, Maritime Faculty, Bandirma Onyedi Eylul University, Balikesir 10200, Türkiye (ORCID: https://orcid.org/0000-0001-5679-2594)*

[3]*Department of Marine Engineering, Maritime Faculty, Bandirma Onyedi Eylul University, Balikesir 10200, Türkiye (ORCID: https://orcid.org/0000-0002-1509-5183)*

[*]*(bceylan@bandirma.edu.tr) Email of the corresponding author*

Abstract – Automatic shutdown functions protect the engine against severe damage, but their activation also produces an immediate loss of propulsion and may create operational, navigational, and economic consequences. This paper presents a focused maintenance-oriented secondary analysis of a Fuzzy Fault Tree Analysis (FFTA) model for the shutdown mechanism of a two-stroke low-speed marine diesel engine. The original model included five shutdown branches and 34 basic events. The present study narrows the scope to the 15 basic events belonging to the two dominant branches: low lubricating oil pressure and abnormal jacket cooling water inlet condition. Converted failure probability, Fussell-Vesely importance, and one-at-a-time sensitivity were normalised and combined through an equal-weight Maintenance Priority Index (MPI). Lubricating oil filter blockage (X3) and clogging or fouling in the cooling water flow path (X27) achieved the maximum MPI value of 1.000 and formed the critical-priority group. Jacket cooling water leakage (X24) and an incorrectly positioned or closed cooling water valve (X26) followed with an MPI of 0.554 and formed the high-priority group. Alternative weighting scenarios did not change the identity of the four leading events. The results were translated into a four-level maintenance framework covering critical, high, medium, and routine actions. The proposed framework provides a transparent way to convert existing reliability results into practical inspection, preventive-maintenance, and condition-monitoring priorities without reconstructing the complete fault tree.

Keywords – Marine diesel engine; main engine shutdown; risk-based maintenance; lubricating oil system; jacket cooling water system.

I. INTRODUCTION

The main propulsion engine is one of the most safety-critical technical systems on board a ship. Its operation affects propulsion availability, manoeuvrability, voyage continuity, and the ability of the vessel to respond to external hazards. A loss of propulsion may be particularly serious during port manoeuvres, in narrow waterways, in traffic-dense areas, or under adverse environmental conditions. In addition to the immediate navigational risk, main-engine unavailability may lead to schedule disruption, off-hire, emergency repair, additional fuel consumption, and increased maintenance expenditure [1]. For these reasons, the prevention of propulsion failures remains a central objective of ship machinery reliability management [2], [3]. Modern marine diesel engines are equipped with alarm, monitoring, slowdown, and shutdown functions that prevent abnormal operating conditions from escalating into severe mechanical damage. The automatic shutdown function is activated when one or more monitored variables exceed predefined protection limits. Typical shutdown-related variables include lubricating oil pressure, rotational speed, thrust-bearing temperature, jacket cooling water condition, and crankcase oil-mist concentration [1]. A correctly functioning shutdown system may prevent bearing seizure, piston or cylinder damage, crankcase explosion, or complete engine failure. Transient engine behaviour during emergency shutdown also demonstrates that protective stopping is a dynamic machinery event rather than a simple binary command [4]. However, a shutdown command simultaneously removes propulsion power. The function must therefore be understood as both a protective barrier and an event with significant operational consequences [5]–[7]. Maintenance planning is the principal organisational mechanism used to reduce the probability of machinery failure and to maintain the availability of safety-critical functions. Corrective maintenance restores equipment after failure, whereas preventive maintenance intervenes according to predetermined intervals [1]. Reliability-centred maintenance and risk-based maintenance extend this approach by focusing resources on the components and failure mechanisms whose loss has the greatest safety, operational, or economic significance. In maritime operations, implementation is complicated by limited component-level failure data, variable operating conditions, restricted crew and spare-part resources, and the need to complete many tasks while the vessel remains in service. Mokashi et al. [8] noted that reliability-centred maintenance can become resource intensive when applied indiscriminately and argued for beginning with critical systems. This logic is relevant to the propulsion plant, where the number of potential maintenance tasks is large but their contribution to shutdown risk is not uniform.

Condition-based and predictive maintenance methods have further expanded the available decision-support tools. Real-time and historical measurements can be used to identify abnormal trends in pressure, temperature, vibration, speed, oil condition, and equipment performance. Jimenez et al. [9] demonstrated the potential of machinery data for predictive maintenance while also showing that incomplete maintenance records and the interpretation of abnormal parameters remain major obstacles. Lazakis et al. [10] combined analytical reliability tools with artificial neural networks to estimate the future condition of critical ship machinery. Karatuğ et al. [11] developed a hybrid reliability-centred and condition-based approach for main-engine bearings, while Xiao et al. [12] proposed a dynamic Bayesian framework for the reliability of ship lubricating oil systems. These studies show that data-driven maintenance can improve anticipation of deterioration, but they also imply a prior question: which components and failure mechanisms deserve the greatest monitoring and maintenance attention?

Risk analysis offers a structured answer to this question. Fault Tree Analysis (FTA) decomposes an undesired top event into intermediate and basic events through Boolean logic. The method can identify minimal cut sets and quantify how individual failure paths contribute to system-level risk. FTA has been widely reviewed as a dependability-analysis technique and remains particularly useful when the analyst needs a transparent causal representation of complex technical systems [13], [14]. In the maritime field, FTA and fuzzy extensions have been applied to mooring operations, steering loss, blackout, hydrogen-powered ships, and other safety-critical events [15]–[18]. Fuzzy Fault Tree Analysis is especially useful when reliable statistical failure data are unavailable because expert linguistic assessments can be transformed into quantitative probability inputs.

Marine-engine research has also increasingly applied risk-based and probabilistic approaches to specific machinery problems. Ünver et al. [19] ranked 46 maintenance activities for a two-stroke marine diesel

engine using fuzzy AHP, demonstrating that maintenance tasks differ substantially in risk significance. Başhan et al. [20] analysed causes of slow-down processes in two-stroke main engines using a fuzzy Bayesian network. Sánchez-Herguedas et al. [21] developed a preventive-maintenance interval model using a semi-Markov process and z-transform. Domeh et al. [22] proposed a risk-based maintenance methodology for fishing-vessel propulsion systems. Together, these studies support the transition from uniform schedule-based maintenance toward maintenance strategies informed by relative failure contribution and system consequences.

The present work is based on the published FFTA study of Ceylan et al. [23], which modelled the protective shutdown mechanism of a MAN B&W S50MC6 two-stroke low-speed marine diesel engine. The original model included five main shutdown branches and 34 basic events. The total top-event probability was calculated as 0.2764. Abnormal jacket cooling water inlet condition was the dominant branch with a probability of 0.1763, followed by low lubricating oil pressure with 0.1169. The most important individual events were lubricating oil filter blockage (X3) and clogging or fouling in the cooling water flow path (X27), each with a Fussell-Vesely value of 0.3543. Jacket cooling water leakage (X24) and an incorrectly positioned or closed cooling water valve (X26) followed with values of 0.1285. The original sensitivity analysis confirmed that changes in these events produced the largest changes in the total shutdown probability [23].

Although the published FFTA study identified the dominant contributors, a full fault-tree analysis does not automatically define how shipboard maintenance resources should be allocated. The present study addresses this practical gap by converting three existing reliability indicators into an integrated maintenance-priority score. The scope is deliberately narrower than the original article. Only the low-lubricating-oil-pressure and abnormal-jacket-cooling-water-inlet branches are retained, and no new expert judgement or failure probability is introduced. The study asks the following research question: “Which lubricating oil and jacket cooling water failure sources should receive priority in maintenance planning to reduce the probability of marine main-engine shutdown”. The contribution of the paper is threefold. First, it provides a transparent secondary-analysis procedure for translating published FFTA results into maintenance priorities. Second, it develops an equal-weight Maintenance Priority Index based on failure probability, Fussell-Vesely importance, and score sensitivity. Third, it links the resulting priority classes to practical inspection, functional-testing, preventive-maintenance, and condition-monitoring actions.

II. Technical Background and Scope

A. *Main-engine shutdown function*

The reference system is a two-stroke low-speed marine diesel engine directly connected to the propeller shaft. Safe operation depends on the coordinated performance of the lubricating oil, jacket cooling water, fuel-control, speed-control, thrust-bearing, and crankcase-monitoring systems. The protective shutdown system continuously receives signals from sensors and control elements. When a monitored condition reaches a shutdown limit, the system generates a command that stops fuel admission and brings the engine to a safe condition. The shutdown event modelled by Ceylan et al. [23] represents the demand or activation of the protective function caused by critical monitored conditions. It does not represent every possible cause of complete propulsion loss. The model excludes the reliability of the shutdown actuator after the command is produced, purely spurious trips caused only by sensor malfunction, bridge manoeuvring consequences, restart and recovery actions, and wider accident sequences following shutdown. This boundary is important because the numerical results should be interpreted as the relative contribution of shutdown-demand mechanisms within the defined protection logic.

The original model contained five main branches: low lubricating oil pressure, engine overspeed, high thrust-bearing segment temperature, abnormal jacket cooling water inlet condition, and oil mist in the crankcase or cylinder area. The present reassessment retains only the first and fourth branches because their probabilities were substantially higher than those of overspeed, thrust-bearing temperature, and oil-mist branches. Figure 1 presents the focused system scope.

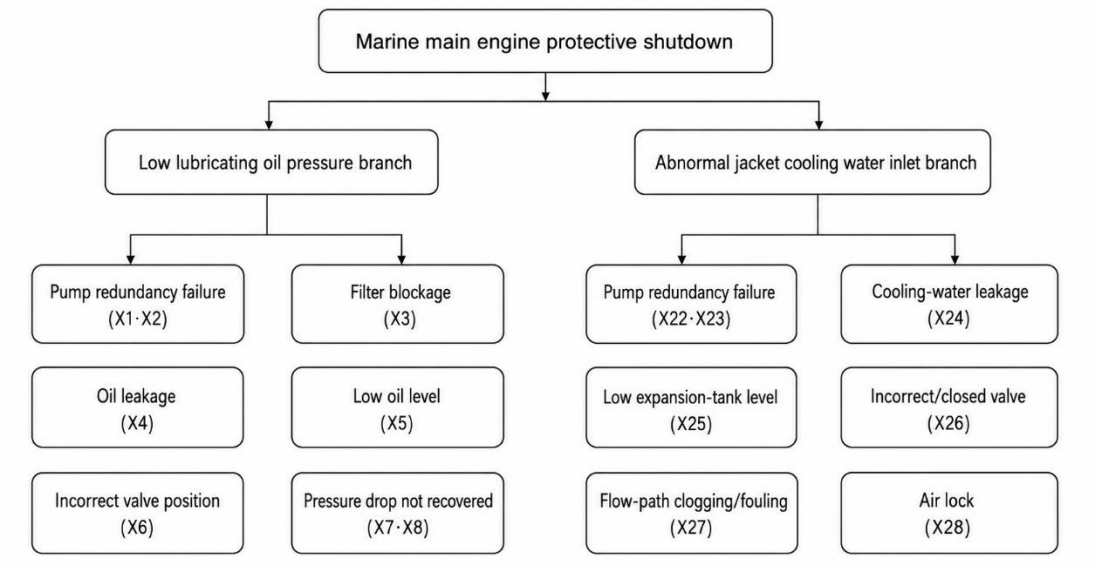

Fig. 1 Focused scope of the maintenance-oriented reassessment

B. *Lubricating oil system*

The lubricating oil system supplies filtered and temperature-controlled oil to bearings and frictional surfaces. It supports hydrodynamic film formation, removes heat, limits wear, and transports contaminants away from critical components. A loss of adequate oil pressure may reduce film thickness and increase friction, temperature, and surface damage [1]. The condition may therefore trigger protective action before irreversible mechanical damage develops. The importance of lubrication condition is also reflected in predictive-maintenance studies focused on main-engine bearings and ship lubricating oil systems [11], [12].

In the fault tree, low lubricating oil pressure was decomposed into three intermediate mechanisms. The first was lubricating oil supply failure, represented by the simultaneous failure of the main lubricating oil pump and failure of the standby pump to start. The AND-gate structure reflects redundancy: failure of the operating pump should not independently create the final supply-loss condition when the standby pump starts correctly. The second mechanism was local pressure loss. Filter blockage, oil leakage, low tank or sump level, and incorrect valve position were connected by an OR gate because each can independently reduce local pressure. The third mechanism was failure to recover pressure after a pressure-drop signal, represented by the simultaneous occurrence of the signal and unsuccessful restoration of adequate pressure. The logical structure has direct maintenance implications. Redundant pump combinations require functional testing of both the operating and standby paths, including automatic changeover. By contrast, filter blockage, leakage, low level, and valve-position errors are single-event failure paths and can independently produce a shutdown-relevant condition. Maintenance planning should therefore include differential-pressure monitoring across filters, leakage inspection, inventory control, valve-alignment verification, pump testing, and confirmation that alarm-response procedures successfully restore pressure.

C. *Jacket water system*

The jacket cooling water system removes combustion heat from the engine structure and maintains acceptable metal temperatures. Its performance depends on sufficient water inventory, continuous circulation, effective heat transfer, correct valve alignment, and the absence of restrictive deposits or trapped air. Cooling-system behaviour is affected by engine load, ambient and seawater conditions, and the condition of pumps, heat exchangers, valves, piping, and treatment chemistry. Seasonal and operational effects on two-stroke engine parameters further demonstrate the need to interpret cooling conditions within their operating context [24].

The original abnormal-jacket-cooling-water-inlet branch contained three intermediate mechanisms. Cooling-water supply failure was represented by the simultaneous failure of the main pump and failure of

the standby pump to start. Cooling-water inventory loss included leakage and low expansion or deaerating tank level. Cooling-water flow-path restriction included an incorrectly positioned or closed valve, clogging or fouling, and an air lock. The inventory and restriction mechanisms were modelled with OR gates because each basic event can independently disturb the inlet condition. These mechanisms require different maintenance responses. Pump failures call for running-condition checks, standby testing, and verification of automatic start logic. Leakage and low level require inspection of piping, connections, seals, expansion-tank trends, and recurring make-up requirements. Valve-position errors require positive line-up verification, particularly after maintenance or changeover. Fouling and blockage require water-quality control, differential-temperature and differential-pressure trending, heat-exchanger inspection, and cleaning. Air locks require effective venting, confirmation of deaeration, and attention after draining, filling, or maintenance interventions.

D. Maintenance-oriented scope

Table 1 summarises the 15 basic events retained from the two dominant branches. The study does not add new failure mechanisms or change the original logic. Its purpose is to reorganise existing results according to maintenance significance.

Table 1. Basic events included in the focused reassessment

Code	Subsystem	Basic event	Original logical context
X1	Lubricating oil	Main lubricating oil pump failure	AND with X2
X2	Lubricating oil	Standby lubricating oil pump fails to start	AND with X1
X3	Lubricating oil	Lubricating oil filter blockage	Single-event cut set
X4	Lubricating oil	Lubricating oil leakage	Single-event cut set
X5	Lubricating oil	Low lubricating oil tank or sump level	Single-event cut set
X6	Lubricating oil	Incorrect valve position in lubricating oil line	Single-event cut set
X7	Lubricating oil	Lubricating oil pressure-drop signal or alarm	AND with X8
X8	Lubricating oil	Failure to restore adequate lubricating oil pressure	AND with X7
X22	Jacket cooling	Main jacket cooling water pump failure	AND with X23
X23	Jacket cooling	Standby jacket cooling water pump fails to start	AND with X22
X24	Jacket cooling	Jacket cooling water leakage	Single-event cut set
X25	Jacket cooling	Low expansion or deaerating tank level	Single-event cut set
X26	Jacket cooling	Incorrectly positioned or closed cooling water valve	Single-event cut set
X27	Jacket cooling	Clogging or fouling in cooling water flow path	Single-event cut set
X28	Jacket cooling	Air lock in jacket cooling water line	Single-event cut set

III. METHODOLOGY

A. *Main-engine shutdown function*

This study is a focused secondary analysis of the numerical dataset reported by Ceylan et al. [23]. No new expert elicitation, shipboard measurement, failure database, or fault-tree reconstruction was performed. The source data consisted of the expert scores, converted failure probabilities, minimal cut-set probabilities, Fussell-Vesely importance values, and one-at-a-time sensitivity procedure of the published article. The analytical steps are shown in Figure 2.

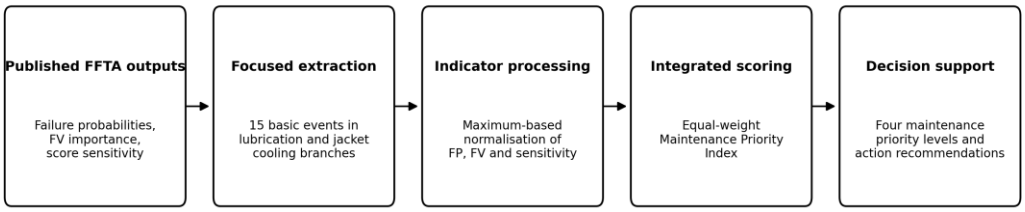

Fig. 2 Methodological workflow.

The original study converted seven-level expert scores to trapezoidal fuzzy numbers, defuzzified them, transformed failure possibilities into probabilities, and propagated the results through the Boolean fault tree. The present study uses the resulting probability values directly. Repeating the fuzzy-number aggregation and probability transformation would not add information because no new expert judgement was collected.

The baseline top-event probability was P0(T) = 0.276375, equivalent to the reported rounded value of 0.2764. The selected basic events were analysed using three complementary indicators: basic-event failure probability, Fussell-Vesely importance, and maximum absolute change in top-event probability under a one-level score variation.

B. *Fussell-Vesely importance*

Fussell-Vesely importance describes the relative contribution of a minimal cut set to the top-event probability. It is expressed as:

$$\mathrm{FV}_i = \frac{P(MCS_i)}{P(T)}$$

where FV_i is the importance of the i_{th} minimal cut set, $P(MCS_i)$ is the cut-set probability, and P(T) is the top-event probability. For single-event cut sets, the value represents the event's contribution. For an AND-gate pair, the cut-set importance was assigned to both constituent events only for maintenance screening. This does not imply that either event independently produces the top event; it indicates that both components belong to the same relevant failure path.

C. *One-at-a-time sensitivity indicator*

The published sensitivity analysis varied each expert score by one linguistic level while all other scores remained fixed. Events at the lower or upper boundary were changed in only one direction. The percentage change in the shutdown probability was calculated as:

$$\Delta P_i(T) = \left(\frac{P_i(T) - P_0(T)}{P_0(T)}\right) \times 100$$

where Pi(T) is the recalculated top-event probability after changing the score of event i. For the focused reassessment, the sensitivity indicator was defined as the maximum absolute percentage change obtained from the available upward and downward variations:

$$S_i = \max(A_i, B_i)$$

Here, A_i and B_i denote the positive magnitudes of the downward and upward percentage changes, respectively. For an event at score 1 or 7, only the feasible one-sided variation was used. All calculations followed the score-to-probability mapping and Boolean structure reported by Ceylan et al. [23]. Recalculation reproduced the published dominant scenarios: reducing X3 or X27 from score 7 to 6 decreased the top-event probability by 18.11%, while increasing X24 or X26 from score 6 to 7 increased it by 16.94%.

D. Normalisation

The three indicators have different numerical scales. Each was therefore normalised by the maximum value among the 15 selected events:

$$\mathrm{NFP}_i = \frac{FP_i}{\max(FP)}$$

$$\mathrm{NFV}_i = \frac{FV_i}{\max(FV)}$$

$$\mathrm{NS}_i = \frac{S_i}{\max(S)}$$

where FP_i, FV_i, and S_i are the event failure probability, Fussell-Vesely importance, and sensitivity indicator. Maximum-based normalisation was preferred because it preserves the proportional relationship with the dominant event and produces values between 0 and 1.

E. Maintenance Priority Index

An equal-weight Maintenance Priority Index was calculated as:

$$\mathrm{MPI}_i = \frac{\mathrm{NFP}_i + \mathrm{NFV}_i + \mathrm{NS}_i}{3}$$

Equal weighting avoids introducing a second subjective weighting exercise into a study whose probability inputs already originate from expert judgement. The index combines three distinct interpretations: occurrence tendency, contribution to shutdown risk, and responsiveness of the system-level result to a reasonable input change. The MPI is a comparative screening index, not a universal criticality measure. It does not directly include repair cost, downtime, detectability, spare-part availability, task duration, or consequence severity after shutdown. These factors may be incorporated in a more extensive maintenance-optimisation study.

F. Priority classes

Four case-specific classes were used:

i. Critical: MPI >= 0.75
ii. High: 0.30 <= MPI < 0.75
iii. Medium: 0.05 <= MPI < 0.30
iv. Routine: MPI < 0.05

The thresholds were selected to separate the clear numerical groups observed in the case results. They are not proposed as universal limits for all ships or engine types. Critical items require intensive monitoring and prompt intervention. High-priority items require frequent verification and preventive action. Medium items remain within enhanced planned maintenance and trend monitoring. Routine items remain in the planned maintenance system with periodic functional testing.

G. *Weighting robustness*

To test whether the leading ranking depended on equal weighting, three alternative scenarios were evaluated:

i. probability-emphasis: (0.50, 0.25, 0.25);
ii. Fussell-Vesely-emphasis: (0.25, 0.50, 0.25);
iii. sensitivity-emphasis: (0.25, 0.25, 0.50).

The general weighted formulation was:

$$\mathrm{MPI}_i^{(w)} = w_1\mathrm{NFP}_i + w_2\mathrm{NFV}_i + w_3\mathrm{NS}_i, \qquad w_1 + w_2 + w_3 = 1$$

This supplementary analysis was used only to check rank stability; the equal-weight result remained the principal classification.

IV. RESULTS

A. *Comparison of the two shutdown branches*

The baseline probability of abnormal jacket cooling water inlet condition was 0.1763, while the low lubricating oil pressure branch had a probability of 0.1169. The cooling branch was therefore approximately 1.51 times the lubrication branch. Together, these branches dominated the top-event structure, whereas overspeed, high thrust-bearing temperature, and oil-mist branches contributed much smaller probabilities in the original model. This result does not mean that cooling failures are universally more severe than lubrication failures. The branch probabilities reflect the combination of the source expert scores and the Boolean model. In particular, the cooling branch contained several single-event OR paths with relatively high probability inputs. Severity was not used as a separate indicator in the present reassessment; the ranking concerns contribution to shutdown demand and maintenance priority within the defined model.

B. *Integrated maintenance-priority ranking*

Table 2 presents the calculated results. The maximum absolute sensitivity values were derived by recalculating all feasible one-level variations for the selected events. Figure 3 visualises the MPI ranking.

Table 2. Maintenance Priority Index results for the selected basic events.

Code	Basic event	FP	FV	Sensitivity (%)	MPI	Priority
X3	Lubricating oil filter blockage	0.09793	0.3543	18.115	1.000	Critical
X27	Clogging/fouling in cooling water flow path	0.09793	0.3543	18.115	1.000	Critical
X24	Jacket cooling water leakage	0.03552	0.1285	16.942	0.554	High
X26	Incorrectly positioned/closed cooling water valve	0.03552	0.1285	16.942	0.554	High
X28	Air lock in jacket cooling water line	0.01343	0.0486	5.862	0.199	Medium
X4	Lubricating oil leakage	0.01343	0.0486	5.862	0.199	Medium
X7	Lubricating oil pressure-drop signal/alarm	0.03552	0.0046	0.581	0.136	Medium
X8	Failure to restore adequate lubricating oil pressure	0.03552	0.0046	0.581	0.136	Medium
X22	Main jacket cooling water pump failure	0.03552	0.0002	0.024	0.122	Medium
X25	Low expansion/deaerating tank level	0.005000	0.0181	2.218	0.075	Medium
X6	Incorrect valve position in lubricating oil line	0.005000	0.0181	2.218	0.075	Medium
X5	Low lubricating oil tank/sump level	0.001485	0.0054	0.922	0.027	Routine

X23	Standby jacket cooling water pump fails to start	0.001485	0.0002	0.033	0.006	Routine
X1	Main lubricating oil pump failure	0.001485	0.000001	0.0002	0.005	Routine
X2	Standby lubricating oil pump fails to start	0.0002225	0.000001	0.0005	0.001	Routine

Note: FP = converted failure probability; FV = Fussell-Vesely importance; Max. |ΔP(T)| = maximum absolute percentage change in the top-event probability under a one-level score variation. Values are rounded for presentation.

X3 and X27 achieved the maximum value for all three normalised indicators and therefore obtained an MPI of 1.000. Both events were classified as critical. X24 and X26 received an MPI of 0.554 and were classified as high priority. The numerical gap between the high-priority group and the next events is substantial: X4 and X28 each obtained 0.199.

The medium group included X4, X28, X7, X8, X22, X25, and X6. These events reached medium priority for different reasons. X4 and X28 combined moderate failure probability, moderate FV importance, and noticeable sensitivity. X7 and X8 had relatively high individual failure-probability inputs, but their shutdown contribution was reduced because the two events formed an AND-gate cut set. X22 similarly had a high basic-event probability input, but the corresponding cooling-supply failure required simultaneous failure of the standby path, which reduced its FV contribution. X25 and X6 had lower probability and importance values but remained relevant single-event paths.

The routine group included X5, X23, X1, and X2. Their lower MPI values do not mean that maintenance can be omitted. X1 and X2 are essential elements of a redundant lubricating oil supply arrangement, while X23 is essential to the redundant cooling-water pump arrangement. Their low integrated scores are a consequence of the low probability of simultaneous failure in the fault-tree structure. They should therefore remain subject to periodic testing and planned maintenance, even though they do not require the same concentration of resources as the leading events.

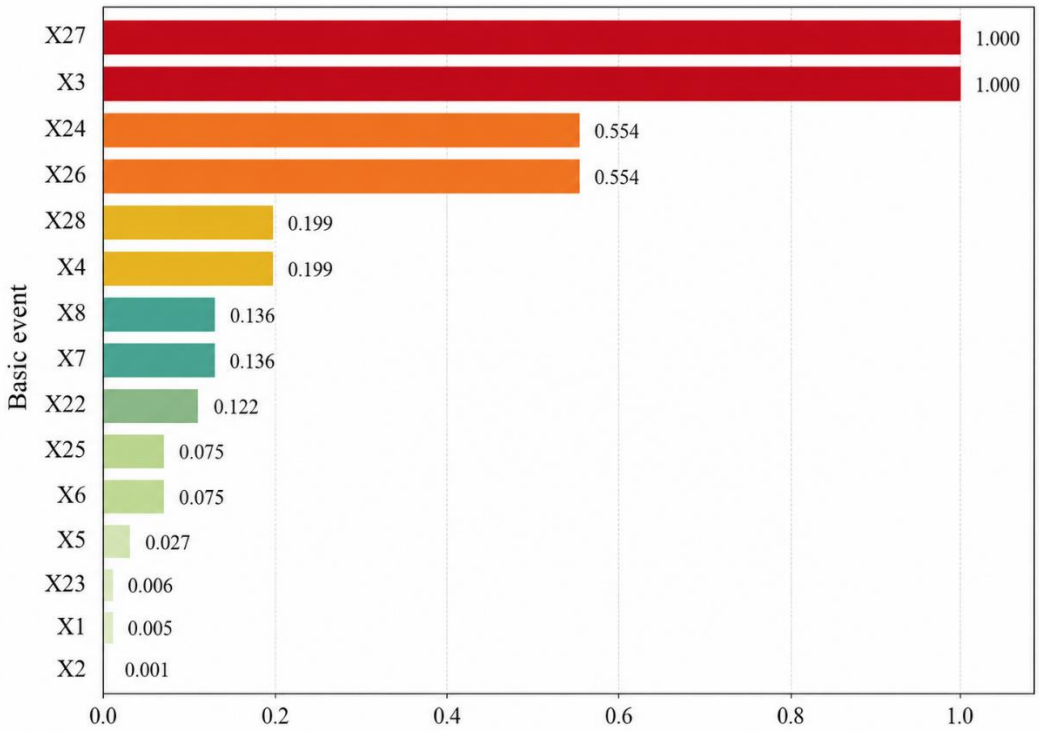

Fig. 3. Maintenance Priority Index ranking

C. *Maintenance actions by priority level*

The numerical ranking was translated into an action-oriented framework in Table 3. The proposed actions are intentionally generic because exact intervals depend on the manufacturer's instructions, classification requirements, vessel planned-maintenance system, operating history, and company procedures.

Table 3. Proposed maintenance actions for the ranked failure sources

Priority	Events	Maintenance objective	Suggested shipboard actions	Useful indicators
Critical	X3 - lubricating oil filter blockage	Prevent progressive restriction and pressure loss	Trend differential pressure; inspect and clean/replace filters before limit; verify bypass condition; investigate abnormal contamination; review oil-analysis results	Filter differential pressure, oil cleanliness, pressure trend, filter service history
Critical	X27 - cooling-water flow-path clogging/fouling	Maintain unrestricted circulation and heat transfer	Control water treatment; trend temperatures and pressure differences; inspect heat exchangers and lines; clean deposits; investigate recurrent restriction	Inlet/outlet temperature, differential temperature, flow/pressure trend, water quality
High	X24 - jacket cooling water leakage	Prevent inventory loss and air ingress	Inspect piping, connections, seals, coolers, and drain points; trend make-up water; repair persistent leaks; verify expansion-tank stability	Make-up rate, tank level, visible leakage, pressure decay
High	X26 - incorrectly positioned or closed valve	Prevent configuration-induced loss of flow	Use valve line-up checklists; verify position after maintenance/changeover; apply clear labelling; confirm local and remote indications	Valve-position confirmation, post-maintenance checklist, flow/temperature response
Medium	X4 - lubricating oil leakage	Maintain pressure and inventory	Routine leak rounds; inspect flanges, seals, pumps, and piping; trend sump level; repair recurring leakage	Sump level, make-up rate, local leakage, pressure stability
Medium	X28 - air lock in cooling line	Maintain continuous circulation	Vent high points; confirm deaeration after draining/filling; inspect expansion tank and vents; monitor unstable temperatures	Temperature fluctuation, vent discharge, pump noise, tank behaviour
Medium	X7 and X8 - pressure drop and unsuccessful recovery	Strengthen detection and response effectiveness	Test alarm and response procedures; verify standby-pump start and valve line-up; train engineers in rapid recovery actions	Alarm test, recovery time, standby start, post-event review
Medium	X22 - main cooling-water pump failure	Preserve cooling availability	Monitor pump condition; check vibration, seal condition, motor current, and discharge pressure; test standby availability	Vibration, current, discharge pressure, bearing temperature
Medium	X25 - low expansion/deaerating tank level	Prevent inventory and deaeration problems	Verify level instrumentation; inspect recurring level loss; maintain correct filling and venting	Level trend, alarm test, make-up frequency
Medium	X6 - incorrect lubricating-oil valve position	Prevent configuration-induced pressure loss	Apply line-up verification; use lock/tag or position controls where appropriate; confirm pressure response after work	Valve position, checklist compliance, pressure trend

Routine	X1, X2, X23, X5	Maintain redundancy and basic inventory control	Periodic functional testing, planned overhaul, automatic-start test, level-alarm test, routine inspections	Test records, start reliability, alarm status, maintenance history

D. *Robustness under alternative weights*

Table 4 compares the leading ranks under the equal-weight and three emphasis scenarios. X3 and X27 remained tied for first place in all scenarios. X24 and X26 remained tied for the next position. The identity of the first four events was therefore fully stable. Weighting mainly affected the ordering of medium-priority events.

Table 4. Leading event groups under alternative weighting scenarios

Weighting scenario (FP, FV, S)	**Rank group 1**	**Rank group 2**	**Rank group 3**	**Rank group 4**
Equal (0.333, 0.333, 0.333)	X3, X27	X24, X26	X4, X28	X7, X8
Probability emphasis (0.50, 0.25, 0.25)	X3, X27	X24, X26	X7, X8	X4, X28
FV emphasis (0.25, 0.50, 0.25)	X3, X27	X24, X26	X4, X28	X7, X8
Sensitivity emphasis (0.25, 0.25, 0.50)	X3, X27	X24, X26	X4, X28	X7, X8

V. DISCUSSION

A. *Critical maintenance priorities*

The first major finding is the equal critical ranking of lubricating oil filter blockage and cooling-water flow-path clogging or fouling. Both events were assigned the highest source expert score, had the largest converted probability, formed single-event minimal cut sets, and produced the strongest sensitivity effect. Their maintenance significance is therefore supported by all three indicators. Lubricating oil filter blockage can create a local pressure loss even when both pumps remain mechanically available. This explains why a filter-related event can outrank pump-failure combinations. The fault-tree logic differentiates between equipment availability and the ability of the system to deliver oil through an unrestricted path. A maintenance programme that focuses heavily on pump overhaul but inadequately monitors filter differential pressure and contamination may therefore leave a dominant shutdown path insufficiently controlled.

The critical position of X3 supports a combination of planned and condition-based maintenance. Planned actions include filter inspection, element cleaning or replacement, and examination of the bypass arrangement. Condition-based actions include differential-pressure trending, oil cleanliness monitoring, and investigation of accelerated contamination. Jimenez et al. [9] showed that lubrication-related data can support predictive maintenance but also highlighted the importance of reliable records and interpretation. Karatuğ et al. [11] similarly linked main-engine bearing protection to lubrication-condition monitoring. The present ranking adds a risk-based reason for assigning high attention to filter condition. Cooling-water flow-path clogging or fouling was equally critical. Deposits, contamination, restricted passages, and heat-exchanger fouling can reduce circulation or heat transfer without an immediate pump failure. The result indicates that cooling-system reliability depends not only on rotating equipment but also on internal cleanliness and water-treatment effectiveness. Monitoring should therefore combine temperature and pressure trends with water-quality records, inspection findings, and cleaning history. A stable pump discharge pressure alone may not prove that adequate heat transfer is available throughout the circuit.

The sensitivity result is operationally meaningful. Reducing the score of either X3 or X27 by one linguistic level lowered the modelled top-event probability by approximately 18.11%. This is not a direct

prediction that one maintenance action will physically reduce real-world shutdown frequency by exactly that percentage. Rather, it shows that the system-level result is highly responsive to the assumed occurrence tendency of these events. It strengthens the case for maintenance measures capable of keeping their likelihood at the lowest practicable level.

B. *High-priority events*

Jacket cooling water leakage and an incorrectly positioned or closed cooling-water valve formed the high-priority group. Both are single-event paths with substantial probability, FV importance, and sensitivity. Their ranking shows that shutdown risk is strongly influenced by two fundamentally different mechanisms: physical degradation and configuration error. Cooling-water leakage may develop gradually and become normalised if small make-up requirements are not trended. Persistent leakage can reduce system inventory, introduce air, affect pump suction conditions, and reduce thermal stability. The maintenance response should not be limited to visible leak repair. Trend-based review of make-up water and expansion-tank level can identify deterioration before a shutdown threshold is reached. Recurrent leakage should trigger investigation of seals, piping supports, thermal expansion, cooler integrity, and connection quality.

Valve-position error differs because it may be introduced during operation, maintenance, changeover, or system restoration. It is therefore partly a hardware and partly a human/organisational problem. The result supports positive valve identification, clear labelling, post-maintenance line-up checks, and independent verification for critical configurations. Ahn et al. [5] demonstrated the importance of human interaction in emergency shutdown reliability, while Ceylan et al. [2] showed that complex main-engine failures may require system-theoretic interpretation rather than purely component-based analysis. Although the present model does not explicitly quantify human reliability, the high rank of X26 indicates that procedural controls are integral to technical reliability.

C. *Interpretation of priorities*

The medium-priority group illustrates why multiple indicators are useful. Lubricating oil leakage and cooling-line air lock had similar probability, FV, and sensitivity values, resulting in identical MPI scores. Both can independently affect system condition and deserve enhanced monitoring. Pressure-drop signal and unsuccessful recovery also entered the medium group, although their joint cut-set contribution was smaller. Their maintenance relevance concerns not only equipment condition but also barrier performance: alarms, standby response, line-up, and recovery procedures must function together. Main cooling-water pump failure had a relatively high basic-event probability but a low FV contribution because shutdown-related supply failure required simultaneous standby failure. This demonstrates the protective value of redundancy. However, redundancy is only effective when standby equipment is available, correctly configured, and tested. A low integrated risk contribution should therefore not be interpreted as permission to extend testing indefinitely. Dragffy [6] and Kumar et al. [7] emphasised the importance of reliability design and analysis for shutdown systems; the same principle applies to auxiliary-system redundancy.

Routine-priority events should remain in the planned-maintenance system. X1, X2, and X23 are parts of redundant pump arrangements, while X5 represents low oil inventory. Their lower ranking reflects the model structure and source probabilities, not the absence of operational importance. Scheduled overhauls, automatic-start tests, alarm tests, and routine rounds remain necessary. Risk-based prioritisation reallocates attention; it does not remove baseline maintenance obligations.

D. *Integration with shipboard maintenance management*

The proposed framework can be implemented without replacing the vessel's planned-maintenance system. It can be used as a screening layer that modifies inspection intensity, data-review frequency, and escalation rules. A practical sequence is as follows:

i. retain manufacturer and statutory tasks as the minimum maintenance baseline;
ii. mark critical and high-priority items in the planned-maintenance system;
iii. identify measurable indicators for each leading event;

iv. define trend-review and intervention criteria;
v. record defects, near misses, and shutdown demands using consistent event codes;
vi. periodically update the ranking when ship-specific evidence becomes available.

The approach is consistent with reliability-centred maintenance, which begins with critical functions and failure consequences [8], and with risk-based maintenance, which directs resources to the dominant contributors [22]. It also creates a bridge toward predictive maintenance. Data-driven methods are most useful when the monitored variables correspond to failure mechanisms that matter at system level. The MPI ranking can therefore guide sensor selection and data-review priorities. For X3, the most relevant data may include filter differential pressure, oil cleanliness, oil pressure, and filter replacement history. For X27, useful indicators include temperature differences, flow or pressure behaviour, water-treatment records, and heat-exchanger cleaning history. For X24, make-up water and tank-level trends are important. For X26, the key evidence may be procedural: line-up checklists, position indication, and post-maintenance verification. Not every critical event is best controlled by advanced sensors; some require robust basic engineering practice.

E. Relationship with previous research

The results are consistent with earlier research showing that propulsion reliability is influenced by interactions between equipment condition, control functions, human response, and maintenance practice. Stoumpos et al. [3] combined safety assessment and simulation for marine dual-fuel engines, showing the value of integrating component-level failures with system behaviour. Göksu et al. [15] used FTA and Bayesian networks for ship blackout assessment, illustrating the importance of causal and probabilistic modelling. Gürgen et al. [16] and Kuzu et al. [18] demonstrated the usefulness of fuzzy fault trees when precise maritime failure data are limited. The present study differs from those applications because it does not propose another complete risk model. Its contribution lies in post-processing an existing model for maintenance use. This is relevant because extensive risk assessments often produce rankings but stop before defining operational actions. The MPI provides a simple structure for integrating probability, importance, and sensitivity. The findings also complement maintenance-ranking studies. Ünver et al. [19] prioritised individual two-stroke engine maintenance activities using fuzzy AHP, whereas the present study begins with shutdown-related failure sources and derives maintenance priorities from fault-tree outputs. Sánchez-Herguedas et al. [21] optimised preventive intervals using maintenance economics, while this paper does not determine intervals. The methods are therefore complementary: the present model identifies where attention should be concentrated, and interval or optimisation models can subsequently determine when and how often intervention should occur.

F. Limitations

The study has several limitations. First, all quantitative inputs originate from a previously published single-expert FFTA model. The competence of a specialised expert may provide technically coherent judgements, but it does not eliminate epistemic uncertainty. Multi-expert elicitation and experience-based weighting would improve robustness. Second, the source model represents one engine type and a defined shutdown boundary. The ranking should not be transferred to engines with different protection logic, redundancy, cooling configuration, operating profile, or maintenance history. Ship-specific data may change both the probability inputs and the causal structure. Third, the MPI uses equal weights and case-specific thresholds. Alternative weighting confirmed the stability of the leading four events, but the medium-priority order changed slightly. The classes are therefore best used as screening categories, not regulatory limits. Fourth, the index does not include consequence severity, repair cost, downtime, detectability, task feasibility, or spare-part availability. It also does not estimate the quantitative risk reduction achieved by a specific maintenance action. The sensitivity values describe model response to score changes rather than observed intervention effectiveness. Fifth, the study is a secondary analysis of published results and does not provide new shipboard failure observations. Its novelty is methodological and application oriented: it translates an existing reliability assessment into a maintenance framework.

Future work should validate the ranking against planned-maintenance records, alarm histories, shutdown events, oil-analysis data, and cooling-system measurements from multiple vessels.

VI. CONCLUSION

This study converted the published FFTA results of a marine main-engine shutdown mechanism into a focused risk-based maintenance-priority framework. The analysis retained 15 events from the low-lubricating-oil-pressure and abnormal-jacket-cooling-water-inlet branches because these branches dominated the original shutdown probability. Failure probability, Fussell-Vesely importance, and one-at-a-time sensitivity were normalised and combined through an equal-weight Maintenance Priority Index. The following principal conclusions were obtained:

i. Lubricating oil filter blockage (X3) and cooling-water flow-path clogging or fouling (X27) were the dominant maintenance items. Both obtained an MPI of 1.000 and remained first under all alternative weighting scenarios.

ii. Jacket cooling water leakage (X24) and incorrectly positioned or closed cooling-water valve (X26) formed a stable high-priority group with an MPI of 0.554.

iii. The leading events are mainly single-event OR paths. Redundant pump failures produced lower integrated contributions because shutdown-related supply loss required simultaneous failure of the operating and standby paths.

iv. Maintenance priorities should focus on filter differential-pressure control, oil cleanliness, cooling-water treatment and line cleanliness, leakage elimination, and valve line-up verification.

v. Routine-priority equipment must remain within planned maintenance because low model contribution does not eliminate the need to preserve redundancy and basic protection functions.

The proposed method can be applied as a screening layer within an existing planned-maintenance system and can guide the selection of variables for condition monitoring. Its main value is that it converts risk-analysis outputs into clear maintenance decisions without repeating the complete fault-tree analysis. Future studies should incorporate multiple experts, ship-specific operating data, cost and downtime consequences, detectability, and observed maintenance effectiveness. Validation across different engine types would also support the development of more general maintenance-priority thresholds.

REFERENCES

[1] B. O. Ceylan, *Gemi makineleri işletme mühendisliği el kitabı: Temel teknik terminoloji*. Nobel Akademik Yayıncılık, 2025.

[2] B. O. Ceylan, M. S. Celik, and D. A. Akyar, "ANP extended STAMP model for complex system accident analysis: A real case of ship main engine failure," *Journal of Marine Engineering & Technology*, pp. 1–13, 2025, doi: 10.1080/20464177.2025.2502198.

[3] S. Stoumpos, V. Bolbot, G. Theotokatos, and E. Boulougouris, "Safety performance assessment of a marine dual fuel engine by integrating Failure Mode, Effects and Criticality Analysis with simulation tools," *Proceedings of the Institution of Mechanical Engineers, Part M: Journal of Engineering for the Maritime Environment*, vol. 236, pp. 376–393, 2022, doi: 10.1177/14750902211043423.

[4] G. Theotokatos and N. P. Kyrtatos, "Investigation of a large high-speed diesel engine transient behavior including compressor surging and emergency shutdown," *Journal of Engineering for Gas Turbines and Power*, vol. 125, pp. 580–589, 2003, doi: 10.1115/1.1559903.

[5] S. I. Ahn, R. E. Kurt, and O. Turan, "The hybrid method combined STPA and SLIM to assess the reliability of the human interaction system to the emergency shutdown system of LNG ship-to-ship bunkering," *Ocean Engineering*, vol. 265, Art. no. 112643, 2022, doi: 10.1016/j.oceaneng.2022.112643.

[6] G. Dragffy, "The design of a highly reliable safety critical emergency shutdown system," *Reliability Engineering & System Safety*, vol. 61, pp. 215–227, 1998, doi: 10.1016/S0951-8320(98)00012-X.

[7] C. S. Kumar, A. John Arul, O. Pal Singh, and K. Suryaprakasa Rao, "Reliability analysis of shutdown system," *Annals of Nuclear Energy*, vol. 32, pp. 63–87, 2005, doi: 10.1016/j.anucene.2004.08.002.

[8] A. J. Mokashi, J. Wang, and A. K. Vermar, "A study of reliability-centred maintenance in maritime operations," *Marine Policy*, vol. 26, no. 5, pp. 325–335, 2002, doi: 10.1016/S0308-597X(02)00014-3.

[9] V. J. Jimenez, N. Bouhmala, and A. H. Gausdal, "Developing a predictive maintenance model for vessel machinery," *Journal of Ocean Engineering and Science*, vol. 5, no. 4, pp. 358–386, 2020, doi: 10.1016/j.joes.2020.03.003.

[10] I. Lazakis, Y. Raptodimos, and T. Varelas, "Predicting ship machinery system condition through analytical reliability tools and artificial neural networks," *Ocean Engineering*, vol. 152, pp. 404–415, 2018, doi: 10.1016/j.oceaneng.2017.11.017.
[11] Ç. Karatuğ, B. O. Ceylan, and Y. Arslanoğlu, "A hybrid predictive maintenance approach for ship machinery systems: A case of main engine bearings," *Journal of Marine Engineering & Technology*, vol. 24, no. 1, pp. 12–21, 2025, doi: 10.1080/20464177.2024.2393484.
[12] H. Xiao, L. Qi, J. Shi, S. Li, R. Tang, D. Zuo, and B. Da, "Reliability assessment of ship lubricating oil systems through improved dynamic Bayesian networks and multi-source data fusion," *Applied Sciences*, vol. 15, no. 10, Art. no. 5310, 2025, doi: 10.3390/app15105310.
[13] S. Kabir, "An overview of fault tree analysis and its application in model-based dependability analysis," *Expert Systems with Applications*, vol. 77, pp. 114–135, 2017, doi: 10.1016/j.eswa.2017.01.058.
[14] E. Ruijters and M. Stoelinga, "Fault tree analysis: A survey of the state-of-the-art in modeling, analysis and tools," *Computer Science Review*, vols. 15–16, pp. 29–62, 2015, doi: 10.1016/j.cosrev.2015.03.001.
[15] B. Göksu, C. Şakar, and O. Yüksel, "A probabilistic assessment of ship blackout incident with Fault Tree Analysis into Bayesian Network," *Journal of Marine Engineering & Technology*, vol. 24, pp. 54–69, 2025, doi: 10.1080/20464177.2024.2423425.
[16] S. Gürgen, D. Yazır, and O. Konur, "Fuzzy fault tree analysis for loss of ship steering ability," *Ocean Engineering*, vol. 279, Art. no. 114419, 2023, doi: 10.1016/j.oceaneng.2023.114419.
[17] O. B. Inal and Y. E. Senol, "Hydrogen powered ships: Risk analysis by using intuitionistic fuzzy fault tree analysis," *International Journal of Hydrogen Energy*, vol. 198, Art. no. 152781, 2026, doi: 10.1016/j.ijhydene.2025.152781.
[18] A. C. Kuzu, E. Akyuz, and O. Arslan, "Application of Fuzzy Fault Tree Analysis (FFTA) to maritime industry: A risk analysing of ship mooring operation," *Ocean Engineering*, vol. 179, pp. 128–134, 2019, doi: 10.1016/j.oceaneng.2019.03.029.
[19] B. Ünver, İ. Altın, and S. Gürgen, "Risk ranking of maintenance activities in a two-stroke marine diesel engine via fuzzy AHP method," *Applied Ocean Research*, vol. 111, Art. no. 102648, 2021, doi: 10.1016/j.apor.2021.102648.
[20] V. Başhan, M. Yücesan, M. Gül, and H. Demirel, "A fuzzy Bayesian network risk assessment model for analyzing the causes of slow-down processes in two-stroke ship main engines," *Ships and Offshore Structures*, vol. 19, pp. 670–686, 2024, doi: 10.1080/17445302.2024.2323889.
[21] A. Sánchez-Herguedas, A. Mena-Nieto, and F. Rodrigo-Muñoz, "A new analytical method to optimise the preventive maintenance interval by using a semi-Markov process and z-transform with an application to marine diesel engines," *Reliability Engineering & System Safety*, vol. 207, Art. no. 107394, 2021, doi: 10.1016/j.ress.2020.107394.
[22] V. Domeh, F. Obeng, F. Khan, N. Bose, and E. Sanli, "A novel methodology to develop risk-based maintenance strategies for fishing vessels," *Ocean Engineering*, vol. 253, Art. no. 111281, 2022, doi: 10.1016/j.oceaneng.2022.111281.
[23] B. O. Ceylan, O. Der, and A. Savaş, "Fuzzy-fault-tree-based reliability assessment of a marine diesel engine's shutdown mechanism: A case study of a ship's main engine," *Future Transportation*, vol. 6, no. 4, Art. no. 138, 2026, doi: 10.3390/futuretransp6040138.
[24] B. O. Ceylan, "Investigation of seasonal effects on two-stroke marine diesel engine performance parameters and emissions," *Journal of Marine Science and Application*, vol. 22, pp. 795–808, 2023, doi: 10.1007/s11804-023-00383-1.

8th International Conference on Engineering, Natural and Social Sciences

September 06-07, 2026: Konya, Turkey

© 2026 Published by All Sciences Academy

https://www.icensos.com/

Fuzzy Risk Prioritization to On-board Controls: A Mitigation Framework for Biodiesel Use in Marine Diesel Engines

Bulut Ozan Ceylan[1*], Oğuzhan Der[2], Arif Savaş[3]

[1]*Department of Marine Engineering, Maritime Faculty, Bandirma Onyedi Eylul University, Balikesir 10200, Türkiye (ORCID: https://orcid.org/0000-0003-1182-3566)*

[2]*Department of Marine Engineering, Maritime Faculty, Bandirma Onyedi Eylul University, Balikesir 10200, Türkiye (ORCID: https://orcid.org/0000-0001-5679-2594)*

[3]*Department of Marine Engineering, Maritime Faculty, Bandirma Onyedi Eylul University, Balikesir 10200, Türkiye (ORCID: https://orcid.org/0000-0002-1509-5183)*

[*]*(bceylan@bandirma.edu.tr) Email of the corresponding author*

Abstract **–** The use of biodiesel in marine diesel engines offers a near-term decarbonization option because fatty-acid-methyl-ester fuels can be blended with conventional diesel and handled through largely existing liquid-fuel infrastructure. Nevertheless, the transition introduces risks extending from feedstock sustainability and fuel procurement to storage stability, combustion performance, and nitrogen-oxide emissions. This paper presents a mitigation-oriented secondary analysis of an experimental and fuzzy Failure Mode and Effects Analysis study. The source study quantified 34 biodiesel-related failure modes and identified sustainability, NOx emissions, hygroscopicity, low energy content, oxidative degradation, high viscosity, supply-chain dependency, increased fuel consumption, low-temperature instability, and poor atomization as the ten highest-ranked risks. The priorities are translated into an integrated shipboard and shore-side control framework structured around prevention, monitoring, corrective response, and implementation responsibility. The proposed controls include lifecycle and supplier verification, representative bunker sampling, tank segregation, water drainage, storage-time limitation, oxidation and microbial surveillance, cold-flow management, viscosity and fuel-temperature control, injector and filter monitoring, voyage-level fuel-consumption adjustment, and NOx control through engine optimization and compliant exhaust after-treatment. A risk-control matrix links each critical risk to measurable indicators, intervention triggers, and responsible actors. The results show that safe biodiesel adoption requires coordinated management across the entire fuel chain rather than isolated engine adjustments. The framework provides a practical bridge between fuzzy risk rankings and operational procedures that can be incorporated into a vessel's Safety Management System and Planned Maintenance System.

Keywords – biodiesel; marine diesel engine; risk mitigation; shipboard fuel management; fuzzy FMEA; alternative marine fuels

I. INTRODUCTION

International shipping is under sustained pressure to reduce greenhouse-gas and air-pollutant emissions while preserving the reliability, range, and high power density required by marine propulsion. The 2023 IMO Strategy calls for a reduction in carbon intensity of at least 40% by 2030 and for zero- or near-zero-GHG fuels and energy sources to account for at least 5%, striving for 10%, of energy used by international shipping by 2030 [1]. The IMO lifecycle framework further requires marine-fuel choices to be considered on a well-to-wake basis rather than only through exhaust emissions, which is particularly important for biofuels whose environmental performance depends on feedstock, cultivation, processing, and transport pathways [2], [3]. Among the available liquid alternatives, biodiesel has attracted attention because it is renewable, contains little or no sulphur, is biodegradable, and can generally be introduced as a blend without the extensive cryogenic or high-pressure infrastructure required by several other alternative fuels. Reviews of marine alternative fuels identify biodiesel as a technically accessible transition option, although its suitability depends on fuel quality, feedstock sustainability, engine compatibility, blend ratio, and voyage conditions [4]–[6]. Recent marine-focused studies similarly emphasize that biofuels can support decarbonization while presenting challenges involving stability, cold-flow behaviour, material compatibility, fuel-system deposits, and emissions [7]–[10].

Biodiesel is not chemically equivalent to petroleum diesel. Fatty acid methyl ester (FAME) fuels typically have lower heating value, higher density and viscosity, stronger affinity for water, and greater sensitivity to oxidation. These properties can increase the required fuel volume, influence injection and atomization, accelerate degradation during storage, and encourage microbial growth at fuel-water interfaces. The technical consequences are particularly relevant on ships because fuel may remain on board for long periods, experience changing temperature and humidity, pass through several tanks and treatment stages, and be consumed under highly variable engine loads. Studies of marine diesel-biodiesel blends have shown that biodiesel addition can increase microbial sludge formation and that aged B30 blends can experience higher viscosity, water uptake, and filter-blocking tendency [11], [12].Combustion and emission outcomes also involve trade-offs. Biodiesel's oxygenated structure commonly reduces carbon monoxide, unburned hydrocarbon, smoke, and particulate emissions, but lower energy content can increase specific fuel consumption, while changes in combustion temperature and oxygen availability may increase NOx emissions [13], [14]. These outcomes mean that biodiesel cannot be treated simply as a direct fuel substitution. Safe application requires coordinated decisions concerning procurement, fuel acceptance, storage duration, water control, filtration, temperature management, engine settings, exhaust treatment, and maintenance.

The source study for the present paper addressed these uncertainties through an integrated experimental and fuzzy FMEA framework. Biodiesel was produced from commonly used vegetable oils, its fuel properties were measured, and diesel-engine performance and emissions were tested at six loads. Thirty-four failure modes were then evaluated by five maritime experts using occurrence, severity, and detectability inputs processed through a Mamdani fuzzy inference system [15]. The analysis identified engine-performance risks as the highest average category and storage and fuel quality as the second-highest category. At the individual level, sustainability, NOx emissions, hygroscopic nature, low energy content, oxidative degradation, and high viscosity were among the most critical items.

Risk identification and prioritization are necessary but not sufficient for operational decision-making. Ship managers require explicit answers concerning which barriers should be implemented, which variables should be monitored, what response should follow a deviation, and who should be responsible for each action. The paper therefore asks: How can the highest-ranked biodiesel risks be converted into a practical control framework for marine fuel procurement, storage, conditioning, combustion, and emission compliance? The contribution lies not in re-identifying failure modes or recalculating fuzzy risk values, but in translating priorities into a structured set of shipboard and shore-side controls that can be incorporated into the Safety Management System, Planned Maintenance System, and fuel-quality management procedures.

II. Biodiesel Risk Profile and Study Scope

The source investigation used an air-cooled, single-cylinder, direct-injection diesel engine with a rated power of 3.2 kW, a swept volume of 296 cm3, and a constant speed of 3000 rpm. Diesel and neat biodiesel were evaluated at six loads between 0.5 and 3.0 kW. Although the test engine was smaller than a ship propulsion engine, the experimental platform provided direct evidence concerning fuel-property, performance, and emission changes that could inform the expert risk assessment. The original authors explicitly recognized that short-duration laboratory testing could not reproduce long-term injector wear, lubrication degradation, deposit development, or all operational characteristics of large marine engines [15].

The measured biodiesel had a viscosity 57.6% higher than diesel, an energy content 10.8% lower, and a density 7.4% higher. Its freezing point was -3 °C compared with -15 °C for diesel. During the engine tests, biodiesel reduced CO and HC emissions by 34% and 18%, respectively, but increased NOx by 80% and CO2 by 42%. Brake-specific fuel consumption increased by 20%, while brake thermal efficiency decreased by 2% [15]. These results were not interpreted as universal values for all biodiesels or engines; rather, they provided experimental support for evaluating risks associated with fuel consumption, low energy content, viscosity, atomization, and emissions. The fuzzy FMEA model classified 34 failure modes under production and supply, storage and fuel quality, engine performance, and emission and environmental impact. Average category FRPN values were 5.39, 5.61, 5.70, and 5.31, respectively. Engine performance and storage therefore emerged as the most risk-intensive operational domains. The selection includes four high risks with FRPN values at or above 6.00 and six upper-medium risks between 5.77 and 5.98. This cut does not imply that lower-ranked risks are unimportant. Fuel-system clogging, microbial growth, sediment formation, wear, and material incompatibility remain relevant and are incorporated indirectly into the proposed controls where they form consequences or monitoring indicators of the selected risks. Figure 1 demonstrates FRPN values of the ten biodiesel risks retained for the control framework.

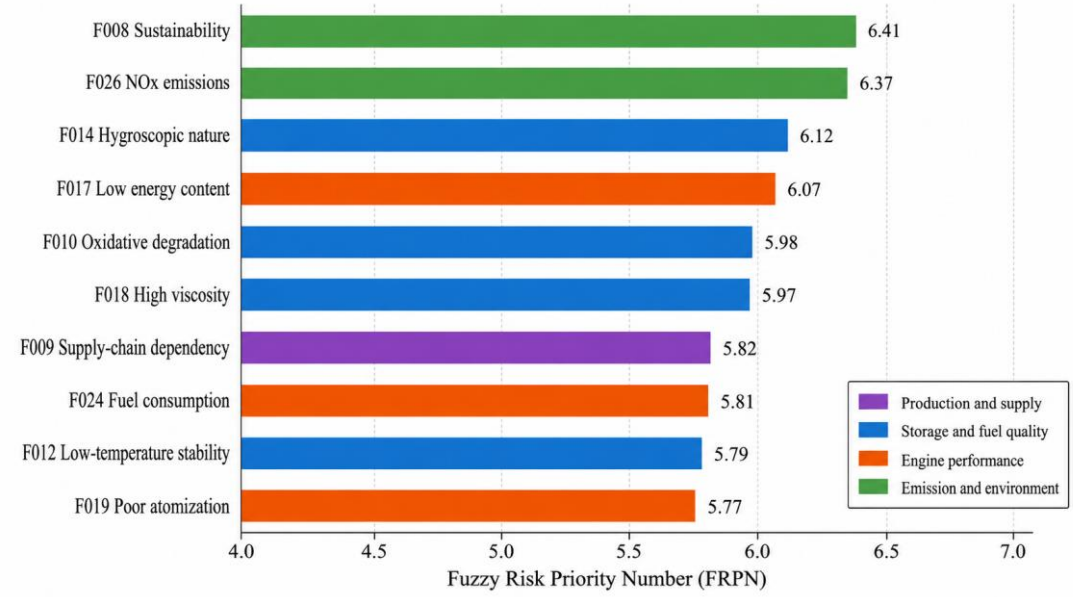

Fig. 1 FRPN values of the ten biodiesel risks retained for the control framework

The selected risks also represent different control locations. Sustainability and supply-chain dependency arise primarily before bunkering and require governance and supplier controls. Hygroscopicity, oxidation, and low-temperature instability are dominated by storage and handling conditions. Low energy content, high viscosity, increased consumption, and poor atomization require fuel-conditioning and engine-management controls. NOx emissions require a combination of in-cylinder optimization, exhaust treatment, and compliance monitoring. The scope therefore extends from shore-side procurement to shipboard storage, combustion, and exhaust management.

Table 1. Experimental findings used to support the mitigation-oriented reassessment

Parameter	Diesel / baseline	Biodiesel result	Operational risk implication
Kinematic viscosity	2.69 mm2/s	4.24 mm2/s (+57.6%)	Injection, atomization, filter and temperature-control sensitivity
Lower heating value	43,199 kJ/kg	38,547 kJ/kg (-10.8%)	Higher fuel volume and consumption for equivalent power
Density	825 kg/m3	886 kg/m3 (+7.4%)	Mass/volume conversion and fuel-delivery calibration
Freezing point	-15 °C	-3 °C	Cold-flow and filter-blocking risk
Brake-specific fuel consumption	Baseline	+20%	Voyage fuel planning and consumption monitoring
Brake thermal efficiency	Baseline	-2%	Need for combustion and injection optimization
CO / HC emissions	Baseline	-34% / -18%	Potential local air-pollutant benefit
NOx / CO2 emissions	Baseline	+80% / +42%	NOx compliance and lifecycle interpretation required

Note: Values are reproduced from the experimental results reported by Ceylan et al. [15].

Table 2. Highest-ranked biodiesel risks retained for control development

Rank	Code and risk	Risk domain	FRPN
1	F008 - Sustainability	Production and supply	6.41
2	F026 - NOx emissions	Emission and environmental impacts	6.37
3	F014 - Hygroscopic nature	Storage and fuel quality	6.12
4	F017 - Low energy content	Engine performance	6.07
5	F010 - Oxidative degradation	Storage and fuel quality	5.98
6	F018 - High viscosity	Engine performance	5.97
7	F009 - Supply-chain dependency	Production and supply	5.82
8	F024 - Fuel consumption	Engine performance	5.81
9	F012 - Low-temperature stability	Storage and fuel quality	5.79
10	F019 - Poor atomization	Engine performance	5.77

III. METHODOLOGY

The research was designed as a mitigation-oriented secondary analysis of the dataset and fuzzy FMEA outputs published by Ceylan et al. [15]. No new engine tests, expert scores, membership functions, fuzzy rules, or FRPN calculations were generated. The original 34 failure modes and their FRPN values were treated as the source dataset. The ten highest-ranked risks were extracted and retained in their original order. This approach avoids presenting previously published risk identification as a new result and makes the analytical contribution explicit: the conversion of risk priorities into operational controls.

Control development combined the source article's experimental and fuzzy-risk results with a targeted review of marine biodiesel, fuel-stability, engine-performance, and emission-control literature. Recent evidence was given particular weight where it directly addressed marine storage or shipboard fuel systems. For example, Bastos et al. [11] reported increased viscosity, water uptake, and filter-blocking tendency in aged B30 marine-gas-oil blends, while Micoli et al. [8] mapped FAME-related challenges across tanks, transfer systems, purifiers, filters, engines, and exhaust equipment. Silva et al. [12] demonstrated greater microbial sludge formation in B20 marine diesel blends than in B0 and B10 under simulated storage. These findings were used to specify preventive controls and monitoring indicators, not to alter the published FRPN values.

Each selected risk was translated through four control layers. The first layer was prevention, defined as measures intended to reduce the likelihood that the risk develops. The second was monitoring and detection, which identified measurable fuel, machinery, emission, or documentary indicators. The third was corrective response, defined as the operational action required when a deviation or unacceptable trend is detected. The fourth was responsibility and governance, which assigned the control to the fuel supplier, shore technical management, master or chief engineer, engine-room personnel, original

equipment manufacturer, or a combination of actors. This structure resembles a barrier-management approach: risks are not controlled by a single recommendation but by linked preventive, detective, and responsive barriers.

The proposed measures were screened against three implementation principles. First, they had to be technically consistent with the physical or organizational mechanism represented by the failure mode. Second, they had to be capable of integration into existing ship systems and procedures, such as bunker planning, fuel acceptance, tank management, purification, planned maintenance, engine monitoring, and emission compliance. Third, they had to avoid universal prescriptive limits where the correct value depends on the fuel specification, blend ratio, climate, engine manufacturer, or vessel design. Accordingly, the framework recommends monitoring margins, trend review, manufacturer-approved settings, and documented intervention criteria rather than arbitrary universal temperature, viscosity, or storage-time thresholds.

Fuel-quality and sustainability controls were aligned with current regulatory and standardization developments. The IMO lifecycle guidelines assess marine fuels from feedstock production to onboard use and identify sustainability aspects that should accompany GHG calculations [2]. Fuel acceptance should also be based on the applicable marine-fuel specification and biodiesel quality documentation, including ISO 8217:2024 [16] and relevant FAME specifications. For NOx mitigation, the framework recognizes both in-cylinder measures and after-treatment; SCR-related recommendations are interpreted consistently with the IMO's 2025 SCR Guidelines [17].

The final output was a risk-control matrix containing the risk code and FRPN, the principal risk pathway, preventive and monitoring controls, and corrective response with responsibility. A second implementation view arranged the controls along the fuel chain: procurement and certification, bunkering and segregation, storage and quality preservation, fuel conditioning and combustion, and exhaust and compliance. The workflow is shown in Fig. 2.

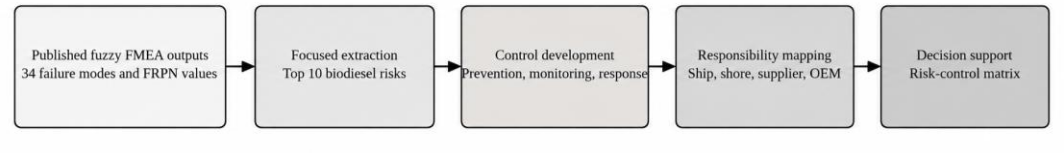

Fig. 2 Methodological workflow of the mitigation-oriented secondary analysis

IV. Results

The control mapping produced a multi-stage framework rather than a single list of precautions. The highest-ranked risk, sustainability (F008, FRPN 6.41), cannot be controlled by machinery adjustment. Its primary barriers are upstream: approved suppliers, traceable feedstocks, lifecycle-GHG documentation, recognized sustainability certification where applicable, and periodic supplier performance review. Fuel quality and sustainability must be treated as separate acceptance dimensions. A biodiesel may meet selected physical-property limits while still having an unacceptable lifecycle or land-use profile. Conversely, a sustainable feedstock does not remove the need for fuel-quality testing. The procurement process should therefore combine documentary verification with representative sampling and laboratory analysis. Supply-chain dependency (F009, FRPN 5.82) requires continuity planning. Operators should avoid assuming that the same blend, feedstock, or specification will be available at every port. The proposed controls include route-based supplier mapping, contractual quality requirements, approved alternative suppliers, minimum contingency stock, and compatibility review before mixing fuels from different sources. The chief engineer should receive the expected blend composition, certificate of quality, safety data, and handling information before bunkering. Where compatibility or stability is uncertain, segregation and controlled onboard trials are preferable to immediate commingling.

The storage-related risks form a closely connected group. Hygroscopic nature (F014, FRPN 6.12) increases the probability of free water, microbial growth, corrosion, and filter blockage. Preventive controls include minimizing water ingress, maintaining closed tank arrangements, draining water from low points, controlling condensation, and avoiding unnecessary tank breathing. Monitoring should

include routine bottom sampling, water-content testing where available, tank-level and drain records, filter differential pressure, and inspection for sludge or microbial contamination. A positive water or microbial trend should trigger fuel segregation, enhanced purification or filtration, tank drainage, microbiological treatment only under an approved procedure, and investigation of the ingress route.

Oxidative degradation (F010, FRPN 5.98) requires storage-time and exposure management. Biodiesel should not be kept indefinitely merely because it remains pumpable. The control framework recommends recording bunker date, blend ratio, tank history, and anticipated consumption date; avoiding contact with catalytic metals where material compatibility is uncertain; limiting heat and air exposure; applying antioxidant treatment only on the basis of supplier or laboratory guidance; and testing oxidation stability, acidity, viscosity, or filterability when fuel has been stored for an extended period or shows deterioration. The 2026 marine ageing study is particularly relevant because B30 exhibited increased water uptake, viscosity, and filter-blocking tendency under both accelerated and onboard ageing conditions [11].

Low-temperature stability (F012, FRPN 5.79) is controlled through route-specific fuel selection and temperature management. Cloud point, pour point, and cold-filter-plugging characteristics should be reviewed against the lowest expected tank, transfer-line, and service-system temperatures. Controls include selecting an appropriate blend for the voyage, maintaining the manufacturer's required temperature margin, using heating or recirculation where the installed system permits, protecting exposed lines, and monitoring filter differential pressure during cold conditions. If wax formation or rapid differential-pressure increase is observed, the response should include reducing exposure to cold zones, restoring temperature within approved limits, changing filters, recirculating or transferring fuel to a suitable tank, and reducing the biodiesel fraction only through an approved compatibility plan. Engine-performance controls address low energy content (F017, FRPN 6.07), high viscosity (F018, FRPN 5.97), increased fuel consumption (F024, FRPN 5.81), and poor atomization (F019, FRPN 5.77). These risks are strongly related but require distinct indicators. Low energy content should be managed by using mass-based fuel properties and actual lower-heating-value information in voyage and endurance calculations. The vessel should expect a higher volume or mass consumption for equivalent shaft output and should preserve adequate reserve margins. Consumption should be normalized against load, speed, weather, and fuel energy content rather than compared with fossil-diesel baselines without correction.

High viscosity and poor atomization require fuel conditioning within manufacturer-approved limits. Recommended controls include verifying the viscosity-temperature relationship of the delivered fuel or blend, confirming heater and viscosity-controller performance where fitted, inspecting filters and injectors, trending fuel pressure and exhaust temperatures, and reviewing combustion balance across cylinders. Abnormal exhaust-temperature spread, smoke, unstable load response, increased filter differential pressure, or injector-correction trends should trigger sampling, filter inspection, fuel-temperature verification, injector testing, and review of the blend ratio. Engine settings should not be altered solely on the basis of a general biodiesel recommendation; injection timing, pressure, and fuel-delivery changes require engine-maker approval and should consider the specific fuel and NOx compliance file.

NOx emissions (F026, FRPN 6.37) require a layered approach. The source experiments showed a substantial increase for the tested biodiesel, supporting the expert assessment that NOx is a high-priority risk. Prevention and control options include selecting an appropriate blend, optimizing injection and combustion within approved limits, maintaining charge-air and cooling conditions, and using compliant exhaust after-treatment. EGR and SCR are established NOx-reduction approaches, but their applicability depends on engine design, operating profile, fuel composition, catalyst condition, reductant quality, and regulatory certification [17]–[19]. Monitoring should combine engine parameters, NOx-related records or measurements where fitted, SCR inlet temperature, reductant consumption, catalyst differential pressure, and alarm history. Exceedance should trigger confirmation of fuel composition and engine condition, inspection of the NOx-control system, and technical consultation before continued operation under the affected configuration.

Table 3 consolidates the proposed controls. The matrix deliberately includes responsible actors because several critical risks cannot be managed by the engine-room team alone. Sustainability and supply continuity are primarily company and supplier responsibilities; water, storage, filters, and conditioning

require shipboard execution; engine calibration requires OEM or authorized technical support; and emission compliance requires coordination among the vessel, company, administration, and equipment supplier.

Table 3. Proposed risk-control matrix for the ten highest-ranked biodiesel risks

Risk and FRPN	Principal pathway	Preventive and monitoring controls	Corrective response and responsibility
F008 Sustainability 6.41	Unsustainable feedstock, weak lifecycle performance, inconsistent production practice	Approved supplier and feedstock traceability; lifecycle-GHG and sustainability documentation; periodic supplier audit; retain certificates and chain-of-custody records	Reject or quarantine unsupported fuel claims; obtain verified documentation or alternative supply. Primary responsibility: company procurement and fuel supplier.
F026 NOx emissions 6.37	Higher oxygen availability and combustion temperature may increase NOx	Approved blend and engine settings; maintain cooling and charge-air systems; monitor NOx-related parameters; verify SCR/EGR readiness, catalyst condition, reductant quality and temperature window	Confirm fuel and engine condition; inspect after-treatment; consult OEM/technical manager; document compliance action. Responsibility: chief engineer, company, OEM and equipment supplier.
F014 Hygroscopic nature 6.12	Water absorption promotes corrosion, microbial growth, sludge and filter blockage	Closed storage; tank drainage; representative bottom sampling; water-content and microbial surveillance; trend filter differential pressure and make-up/drain records	Segregate affected fuel; drain water; enhance purification/filtration; investigate ingress; apply approved biocide only under controlled procedure. Responsibility: chief engineer and fuel-quality support.
F017 Low energy content 6.07	More fuel is required for equivalent power and range	Use verified lower heating value and density; mass-based voyage planning; adjust reserve and tank-capacity calculations; normalize consumption by energy input	Revise fuel plan, speed/load profile or blend strategy; avoid operation below required endurance margin. Responsibility: technical office, master and chief engineer.
F010 Oxidative degradation 5.98	Ageing forms acids, gums, polymers and insoluble deposits	Record storage age and tank history; limit heat/air exposure; verify material compatibility; test oxidation stability, acidity, viscosity or filterability when warranted	Quarantine or segregate deteriorated fuel; laboratory assessment; controlled treatment or disposal; clean tanks/filters if deposits occur. Responsibility: company and chief engineer.
F018 High viscosity 5.97	Poor pumping, injection and spray formation	Verify viscosity-temperature curve; maintain approved fuel temperature; test heater/viscosity-control performance; monitor pressure, filters, injectors and exhaust balance	Restore conditioning; inspect filters and injectors; sample fuel; consult OEM before changing injection settings. Responsibility: engine department and OEM.
F009 Supply-chain dependency 5.82	Limited availability and variable feedstock/blend quality	Route-based supplier mapping; approved alternates; contractual specification; compatibility review; adequate contingency stock; pre-bunkering document review	Use approved alternate supply or segregated contingency fuel; do not commingle uncertain batches. Responsibility: procurement, chartering and vessel management.
F024 Fuel consumption 5.81	Higher mass or volume consumption increases cost and reduces range	Energy-corrected consumption baseline; daily mass balance; meter/tank reconciliation; trend by load, speed, weather and blend ratio	Investigate abnormal deviation; check leaks, meters, filters and combustion; revise voyage/endurance plan. Responsibility: chief engineer and performance team.
F012 Low-temperature stability 5.79	Wax crystallization restricts transfer and blocks filters	Review cloud/pour/CFPP data; voyage-temperature assessment; tank/line heating or recirculation within design; cold-weather differential-pressure monitoring	Restore approved temperature; transfer/recirculate; change filters; implement approved blend correction. Responsibility: chief engineer and supplier.
F019 Poor atomization 5.77	Spray distortion causes incomplete combustion, deposits and thermal imbalance	Maintain viscosity and injection condition; injector inspection; monitor cylinder exhaust spread, smoke, load response and deposit indicators	Verify fuel condition and temperature; test/clean injectors; inspect combustion deposits; OEM-approved adjustment only. Responsibility: engine department and OEM.

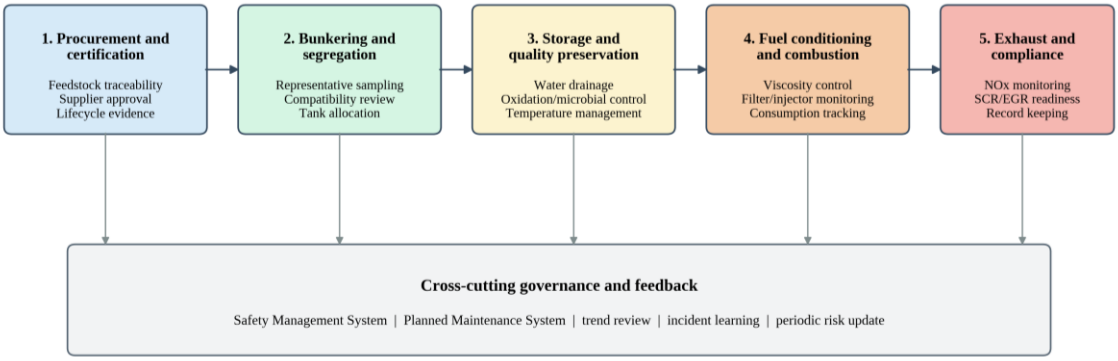

Fig. 3 Integrated control chain for marine biodiesel procurement, storage, use, and compliance

Table 4. Implementation of the control framework within existing ship-management processes

Implementation stage	Primary documents or systems	Key evidence	Review trigger
Procurement and certification	Fuel-purchasing specification; approved-supplier list; lifecycle documentation	Feedstock traceability, certificate of quality, sustainability evidence, blend declaration	New supplier, changed feedstock, inconsistent certificate, lifecycle claim uncertainty
Bunkering and segregation	Bunkering procedure; tank plan; sampling plan	Representative samples, BDN, compatibility review, tank allocation	Off-spec result, unknown blend, incompatible batch, abnormal appearance
Storage and fuel quality	Fuel-management procedure; tank-inspection and drainage routines	Water/sludge findings, oxidation or microbial tests, storage age, filter history	Water increase, sludge, acidity/viscosity change, rapid filter loading
Fuel conditioning and engine operation	PMS; engine-room standing orders; maker instructions	Fuel temperature/viscosity, pressure, consumption, injector and exhaust trends	Combustion imbalance, high consumption, smoke, pressure instability, deposit increase
Exhaust and compliance	NOx Technical File; SCR/EGR procedures; emission records	NOx data, reductant consumption, catalyst temperature and differential pressure	Alarm, emission exceedance, catalyst deterioration, fuel or setting change

V. Discussion

The results demonstrate that biodiesel risk control must begin before the fuel reaches the ship. Sustainability ranked first in the source fuzzy FMEA, and its mitigation depends on feedstock traceability, lifecycle accounting, and supplier governance. This finding is consistent with the direction of IMO lifecycle policy, which seeks to prevent apparent tank-to-wake reductions from being offset by emissions or unsustainable effects elsewhere in the fuel chain [2]. It is also supported by recent lifecycle work showing that the environmental performance of marine biodiesel depends strongly on feedstock and production assumptions [20]. The practical implication is that the certificate of quality and the sustainability evidence must be reviewed together. A low-sulphur, technically usable fuel is not automatically a low-GHG or sustainable fuel. The storage controls are especially important because marine operating patterns can amplify FAME deterioration. Long voyages, warm machinery spaces, humid air, tank breathing, water bottoms, and intermittent consumption create conditions in which water uptake, oxidation, and microbial activity can interact. Pullen and Saeed [21] identified oxidation stability as a central biodiesel limitation, while Sarin et al. [22] showed that metal contaminants can accelerate

oxidation. Broader stability research also emphasizes storage temperature, antioxidant strategy, and fuel composition as key determinants of biodiesel shelf life [23], [24]. The marine-specific evidence is more direct: Silva et al. [12] found greater microbial biomass in B20 than in B0 and B10, and Bastos et al. [11] found that aged B30 showed worsening viscosity, water content, and filterability. These findings justify a control strategy based on storage age, water-bottom management, trend monitoring, and early intervention rather than waiting for engine symptoms.

The proposed framework clarifies the relationship between apparently separate risks. Hygroscopicity may lead to microbial growth; microbial activity and oxidation can create acids and sludge; sludge raises filter differential pressure and promotes injector fouling; restricted flow and poor injection can then increase consumption and thermal imbalance. A control applied at the tank or purification stage can therefore prevent an engine-performance consequence. This systems interpretation is more useful than assigning one maintenance task to each failure mode in isolation. It also explains why fuel sampling, tank drainage, filter history, and injector condition should be reviewed together when abnormal consumption or combustion appears. The engine-related findings confirm that energy and fuel-delivery properties must be managed simultaneously. Lower heating value increases the quantity required for a given output, while higher viscosity can impair injection and atomization if conditioning is inadequate. The source study measured a 20% increase in fuel consumption and a 2% decrease in thermal efficiency for the tested biodiesel. Similar literature generally reports increased specific fuel consumption with biodiesel, although the magnitude varies with blend, feedstock, engine, load, and calibration [13], [14], [25]. The correct operational response is therefore not a universal adjustment factor. Vessels should use actual density and heating-value data, establish an energy-corrected baseline, and compare consumption under comparable operating conditions [26].

Viscosity management requires similar caution. FAME may be described as a drop-in component at lower blends, but higher concentrations can affect seals, pumps, filters, purifiers, and injection systems, particularly in older installations [8]. Excessive heating can itself create problems, whereas inadequate temperature may result in poor atomization or cold-flow restriction. The framework therefore avoids a fixed temperature recommendation and instead requires the viscosity-temperature relationship to be matched with the engine-maker's accepted inlet condition. This is more defensible across different biodiesel grades and machinery arrangements. The NOx result illustrates the environmental trade-off associated with biodiesel. Reductions in CO, HC, smoke, or lifecycle CO2 do not guarantee compliance with every regulated pollutant. The source test produced an 80% NOx increase, and NOx was the second-highest FRPN. Literature reports variable NOx outcomes, but increased NOx remains a recognized concern for some biodiesel-engine combinations [6], [13]. Mitigation may require injection optimization, cooling or charge-air control, EGR, SCR, or a lower blend ratio. However, modifications must remain within the engine's approved technical file and should not compromise efficiency, reliability, or other emissions. The 2025 IMO SCR Guidelines reinforce the need for certified design, testing, monitoring, and documentation of SCR-equipped engines [17].

The control matrix is intentionally broader than a maintenance schedule. Some risks are controlled through procurement, some through operating practice, some through condition monitoring, and some through certified engineering systems. A chief engineer cannot verify the sustainability of a feedstock without reliable shore-side documentation, while a procurement department cannot prevent water accumulation in a settling tank without disciplined onboard routines. Effective biodiesel management therefore requires shared ownership and a clear escalation path between supplier, vessel, technical management, laboratory, and OEM. The framework can be implemented as an additional layer within existing systems rather than as a separate management program. The Safety Management System can define fuel acceptance, segregation, abnormal-quality response, and authority to stop bunkering. The Planned Maintenance System can include tank drainage, filter and purifier monitoring, injector inspection, heater and viscosity-controller tests, and SCR/EGR maintenance. Engine-room standing orders can specify parameters to trend after a fuel change. Near misses, rapid filter loading, abnormal sludge, combustion imbalance, and emission-control alarms should be recorded with consistent failure codes so that company experience can later update the risk ranking [27].

VI. CONCLUSION

This paper translated the ten highest fuzzy-FMEA risks identified for marine biodiesel use into a coordinated mitigation framework extending from fuel procurement to exhaust compliance. The analysis did not repeat the original experiments or risk calculations; it reorganized FRPN results into preventive barriers, monitoring indicators, corrective responses, and assigned responsibilities. The principal conclusions are as follows:

i. Sustainability and supply-chain controls must be applied before bunkering through supplier approval, feedstock traceability, lifecycle documentation, and compatibility planning.

ii. Hygroscopicity, oxidation, and cold-flow instability require active storage management based on water drainage, representative sampling, storage-age control, degradation testing, temperature margin, and filter monitoring.

iii. Low energy content, high viscosity, increased consumption, and poor atomization should be managed using verified fuel properties, energy-corrected voyage planning, manufacturer-approved conditioning, and injector and combustion trending.

iv. NOx is a distinct high-priority risk and should be controlled through approved engine optimization, EGR or SCR where applicable, and documented compliance monitoring.

v. The highest-ranked risks are distributed across suppliers, shore management, ship personnel, and equipment manufacturers; safe adoption therefore depends on shared responsibility rather than a single onboard maintenance action.

vi. The proposed matrix can be incorporated into the Safety Management System and Planned Maintenance System as a practical screening and escalation layer, but ship-specific validation is required before defining universal limits or intervals.

Biodiesel should therefore be managed as an integrated fuel-quality, machinery-reliability, and emission-compliance issue. Its potential contribution to maritime decarbonization can only be realized when lifecycle sustainability, storage stability, engine compatibility, and exhaust performance are controlled together. On the other side, limitations must be acknowledged. The framework uses risk values from a previously published model based on five experts and a laboratory-scale engine. The selected controls are supported by literature and standards but have not been validated through a controlled fleet implementation. FRPN values are static and do not respond to real-time water content, storage age, engine load, ambient conditions, or blend variability. The top-ten threshold was selected for a focused study and should not be interpreted as a boundary below which controls are unnecessary. Material incompatibility, microbial growth, sediment, fuel-system clogging, wear, and exhaust deposits remain important even when their original FRPN values were slightly lower. Finally, the effectiveness and cost of each control were not quantified. Future research should use shipboard fuel analyses, alarm and maintenance records, and intervention outcomes to develop a dynamic and vessel-specific risk-control model.

REFERENCES

[1] International Maritime Organization, *2023 IMO Strategy on Reduction of GHG Emissions from Ships*, Resolution MEPC.377(80), 2023.

[2] International Maritime Organization, *2024 Guidelines on Life Cycle GHG Intensity of Marine Fuels*, Resolution MEPC.391(81), 2024.

[3] L. Bilgili and A. I. Olçer, "IMO 2023 strategy - Where are we and what's next?," *Marine Policy*, vol. 160, Art. no. 105953, 2024, doi: 10.1016/j.marpol.2023.105953.

[4] A. Al-Enazi, E. C. Okonkwo, Y. Bicer, and T. Al-Ansari, "A review of cleaner alternative fuels for maritime transportation," *Energy Reports*, vol. 7, pp. 1962–1985, 2021, doi: 10.1016/j.egyr.2021.03.036.

[5] J. Mohammadpour and F. Salehi, "A review of alternative liquid fuels in marine engines," *Applications in Energy and Combustion Science*, vol. 24, Art. no. 100394, 2025, doi: 10.1016/j.jaecs.2025.100394.

[6] C. W. Mohd Noor, M. M. Noor, and R. Mamat, "Biodiesel as alternative fuel for marine diesel engine applications: A review," *Renewable and Sustainable Energy Reviews*, vol. 94, pp. 127–142, 2018, doi: 10.1016/j.rser.2018.05.031.

[7] D. Christopher Selvam, T. Raja, B. Nagappan, V. J. Upadhye, J. Guntaj, Y. Devarajan, and R. Mishra, “The role of biodiesel in marine decarbonization: Technological innovations and ocean engineering challenges,” *Results in Engineering*, vol. 25, Art. no. 103974, 2025, doi: 10.1016/j.rineng.2025.103974.
[8] L. Micoli, R. Bussi, and A. Macocco, “Technical challenges in the adoption of HVO and FAME as marine fuels,” in *Technology and Science for the Ships of the Future*, 2025, doi: 10.3233/PMST250018.
[9] S. V. Sagin, S. S. Sagin, O. Fomin, O. Gaichenia, Y. Zablotskyi, V. Pištěk, and P. Kučera, “Use of biofuels in marine diesel engines for sustainable and safe maritime transport,” *Renewable Energy*, vol. 224, Art. no. 120221, 2024, doi: 10.1016/j.renene.2024.120221.
[10] S. Sagin, O. Haichenia, S. Karianskyi, O. Kuropyatnyk, R. Razinkin, A. Sagin, and O. Volkov, “Improving green shipping by using alternative fuels in ship diesel engines,” *Journal of Marine Science and Engineering*, vol. 13, no. 3, Art. no. 589, 2025, doi: 10.3390/jmse13030589.
[11] L. L. Bastos, C. G. de Souza, D. F. de Andrade, and L. A. d'Avila, “Study of the oxidation process in marine diesel blended with biodiesel and HVO,” *Proceedings of the Institution of Mechanical Engineers, Part M: Journal of Engineering for the Maritime Environment*, vol. 240, no. 2, 2026, doi: 10.1177/14750902251412462.
[12] T. L. Silva, J. C. Cazarolli, T. M. Pizzolato, A. P. G. Frazzon, M. B. Mann, J. Frazzon, D. K. John, M. F. Ferrão, P. H. Rampelotto, E. B. D'Alessandro, N. R. Antoniosi Filho, and F. M. Bento, “Microbial sludge formation in Brazilian marine diesel oil (B0) and soybean methylic biodiesel blends (B10 and B20) during simulated storage,” *Fuel*, vol. 308, Art. no. 121905, 2022, doi: 10.1016/j.fuel.2021.121905.
[13] N. Yang, X. Deng, B. Liu, L. Li, Y. Li, P. Li, M. Tang, and L. Wu, “Combustion performance and emission characteristics of marine engine burning with different biodiesel,” *Energies*, vol. 15, Art. no. 5177, 2022, doi: 10.3390/en15145177.
[14] Y. Zhang, Y. Zhong, S. Lu, Z. Zhang, and D. Tan, “A comprehensive review of the properties, performance, combustion, and emissions of the diesel engine fueled with different generations of biodiesel,” *Processes*, vol. 10, Art. no. 1178, 2022, doi: 10.3390/pr10061178.
[15] B. O. Ceylan, S. Uslu, and A. Savaş, “Integrated data-driven and fuzzy logic-based failure mode and effects analysis (FMEA) for biodiesel risk quantification in maritime systems,” *Process Safety and Environmental Protection*, vol. 205, Art. no. 108157, 2026, doi: 10.1016/j.psep.2025.108157.
[16] *ISO 8217:2024 Petroleum Products - Fuels (Class F) - Specifications of Marine Fuels*, International Organization for Standardization, Geneva, Switzerland, 2024.
[17] International Maritime Organization, *2025 Guidelines on Selective Catalytic Reduction (SCR) Systems*, Resolution MEPC.399(83), 2025.
[18] K. Bayramoglu and G. Ozmen, “Design and performance evaluation of low-speed marine diesel engine selective catalytic reduction system,” *Process Safety and Environmental Protection*, vol. 155, pp. 184–196, 2021, doi: 10.1016/j.psep.2021.09.010.
[19] V. Praveena and M. L. J. Martin, “A review on various after treatment techniques to reduce NOx emissions in a CI engine,” *Journal of the Energy Institute*, vol. 91, pp. 704–720, 2018, doi: 10.1016/j.joei.2017.05.010.
[20] A. Savaş, L. Bilgili, S. Uslu, and R. Şener, “Life cycle assessment of jojoba (Simmondsia chinensis) biodiesel as a sustainable fuel for maritime decarbonization,” *Biomass and Bioenergy*, vol. 200, Art. no. 108040, 2025, doi: 10.1016/j.biombioe.2025.108040.
[21] J. Pullen and K. Saeed, “An overview of biodiesel oxidation stability,” *Renewable and Sustainable Energy Reviews*, vol. 16, pp. 5924–5950, 2012, doi: 10.1016/j.rser.2012.06.024.
[22] A. Sarin, R. Arora, N. P. Singh, R. Sarin, and R. K. Malhotra, “Oxidation stability of palm methyl ester: Effect of metal contaminants and antioxidants,” *Energy & Fuels*, vol. 24, pp. 2652–2656, 2010, doi: 10.1021/ef901172t.
[23] A. Masudi, O. Muraza, N. W. C. Jusoh, and U. Ubaidillah, “Improvements in the stability of biodiesel fuels: Recent progress and challenges,” *Environmental Science and Pollution Research*, vol. 30, pp. 14104–14125, 2022, doi: 10.1007/s11356-022-25048-4.
[24] M. R. Thompson, B. Mu, C. M. Ewaschuk, Y. Cai, K. J. Oxby, and J. Vlachopoulos, “Long term storage of biodiesel/petrol diesel blends in polyethylene fuel tanks,” *Fuel*, vol. 108, pp. 771–779, 2013, doi: 10.1016/j.fuel.2013.02.040.
[25] H. Aydin and H. Bayindir, “Performance and emission analysis of cottonseed oil methyl ester in a diesel engine,” *Renewable Energy*, vol. 35, pp. 588–592, 2010, doi: 10.1016/j.renene.2009.08.009.
[26] B. O. Ceylan, Gemi makineleri işletme mühendisliği el kitabı: Temel teknik terminoloji. Nobel Akademik Yayıncılık, 2025.
[27] B. O. Ceylan, O. Der, and A. Savaş, “Fuzzy-fault-tree-based reliability assessment of a marine diesel engine’s shutdown mechanism: A case study of a ship’s main engine,” *Future Transportation*, vol. 6, no. 4, Art. no. 138, 2026, doi: 10.3390/futuretransp6040138.

8th International Conference on Engineering, Natural and Social Sciences

September 06-07, 2026: Konya, Turkey

© 2026 Published by All Sciences Academy

https://www.icensos.com/

Characterizations for N-Pedal Strip in Euclidean Space E^3

Filiz ERTEM KAYA*

[1]*Department of Mathematics/Faculty of Science, Niğde Ömer Halisdemir University, Türkiye (ORCID: https://orcid.org/0000-0003-1538-9154)*

**(fertem@ohu.edu.tr) Email of the corresponding author*

Abstract – In this paper, the normal curvature k_n^N, geodesic curvature k_g^N, and geodesic torsion t_r^N of the resulting N-pedal strip were formulated in Euclidean 3-space E^3. By integrating these invariants with cylindrical helix dynamics, we prove the Helix-Strip Intersection Theorem for N-pedal trajectories and establish the geometric conditions under which an N-pedal curve $\beta_{N,M}$ constitutes a helix strip on a smooth surface. Complete analytical proofs and explicitly formatted equations were provided.

Keywords – Include at least 5 keywords or phrases

I. INTRODUCTION

In differential geometry and curve theory, the foundational mathematical framework for investigating the local and global properties of spatial curves and surfaces is provided by moving frames and intrinsic geometric invariants (e.g., [3], [14], [20]). Grounded in the early kinematic and structural principles introduced by Blaschke (1930) (e.g., [2]) and Müller (1959) (e.g., [13]), this field relies heavily on the Frenet-Serret triad along with its modern variations to model vector field behavior and geometric evolutions (e.g., [1]). In present-day mathematics, these traditional methodologies remain essential for geometric modeling, smooth manifold analysis, and visual shape processing (e.g., [15]).

Rooted in classical geometry, the concept of a strip constitutes a fundamental approach in kinematic geometry and surface design. Strip theory has been extensively investigated by various researchers (e.g., [4]–[6], [8]; [10], [16]–[19]). Within classical geometric study, Colin Maclaurin first introduced pedal curves in 1718 (e.g., [12]). Furthermore, the geometric attributes of pedal surfaces (e.g., [11]) as well as vector-field-generated T-pedal curves have been widely analyzed in Euclidean space (e.g., [22]-[38]).

The concept of pedal curves originated in classical geometry with Colin Maclaurin in his seminal 1720 work *Geometria Organica*, where he first investigated loci formed by perpendicular lines dropped from a point to tangents of a given curve. Later, Arthur Cayley remarked on Maclaurin's early contribution in his *Note on the Problem of Pedal Curves*, drawing a parallel between pedal loci and Hamilton's hodograph.

The explicit terminology "pedal" was introduced by the French mathematician Olry Terquem in the 19th century (e.g., [21]). While classical studies primarily focused on T-pedal curves (where perpendiculars are dropped onto tangents), the generalized framework extends to N-pedal curves (perpendiculars onto principal normals) and B-pedal curves (perpendiculars onto binormals) in three-dimensional Euclidean space E^3. In recent years there have been many studies about pedal curves (e.g., [22]-[38]).

In this paper, the normal curvature k_n^N, geodesic curvature k_g^N, and geodesic torsion t_r^N of the resulting N-pedal strip were formulated in Euclidean 3-space E^3. By integrating these invariants with cylindrical helix dynamics, we prove the Helix-Strip Intersection Theorem for N-pedal trajectories and establish the geometric conditions under which an N-pedal strip (β_N, M) constitutes a helix strip on a smooth surface. Complete analytical proofs and explicitly formatted equations are provided in Euclidean 3-space E^3.

II. MATERIALS AND METHOD

2.1. CURVATURE FORMULATIONS OF THE N-PEDAL STRIP

The intrinsic derivatives of the strip frame $\{\xi_N, \eta_N, \zeta_N\}$ with respect to parameter s obey the generalized strip Frenet system:

$$\frac{d}{ds}\begin{pmatrix}\xi_N\\ \eta_N\\ \zeta_N\end{pmatrix} = v_N(s)\begin{pmatrix}0 & k_g^N & k_n^N\\ -k_g^N & 0 & t_r^N\\ -k_n^N & -t_r^N & 0\end{pmatrix}\begin{pmatrix}\xi_N\\ \eta_N\\ \zeta_N\end{pmatrix}$$

Let $\varphi_N(s)$ denote the orientation angle between the strip side-normal η_N and the principal normal N of the base curve. The strip bundle projects onto the base Frenet frame through direction cosines:

$$\xi_N = \cos\psi_1\, T + \cos\psi_2\, N + \cos\psi_3\, B$$
$$\eta_N = \cos\varphi_N\, N - \sin\varphi_N\, B$$
$$\zeta_N = \sin\varphi_N\, N + \cos\varphi_N\, B$$

where $\cos\psi_1 = \frac{P(s)}{v_N}$, $\cos\psi_2 = \frac{Q(s)}{v_N}$, and $\cos\psi_3 = \frac{R(s)}{v_N}$.

2.1.1. Normal Curvature (k_n^N)

Evaluating the projection along the surface normal ζ_N:

$$k_n^N = \frac{1}{v_N}\langle \xi_N{}', \zeta_N\rangle$$
$$k_n^N = \frac{1}{v_N^2}\left[\left(\frac{dQ}{ds} + P\kappa - R\tau\right)\sin\varphi_N + \left(\frac{dR}{ds} + Q\tau\right)\cos\varphi_N\right]$$

2.1.2. Geodesic Curvature (k_g^N)

Evaluating the projection along the side-normal η_N:

$$k_g^N = \frac{1}{v_N}\langle \xi_N{}', \eta_N\rangle$$
$$k_g^N = \frac{1}{v_N^2}\left[\left(\frac{dQ}{ds} + P\kappa - R\tau\right)\cos\varphi_N - \left(\frac{dR}{ds} + Q\tau\right)\sin\varphi_N\right]$$

The intrinsic total curvature κ_N of the N-pedal curve satisfies:

$$\kappa_N^2 = (k_n^N)^2 + \left(k_g^N\right)^2$$

2.1.3. Geodesic Torsion (t_r^N)

Evaluating the variation of the surface normal $\zeta_N{}' = v_N(-k_n^N\xi_N - t_r^N\eta_N)$ yields:

$$t_r^N = \frac{1}{v_N}\left[\frac{d\varphi_N}{ds} + \tau\cos\psi_1 + \frac{k_n^N\frac{d}{ds}(k_g^N) - k_g^N\frac{d}{ds}(k_n^N)}{(k_n^N)^2 + (k_g^N)^2}\right].$$

Definition. An N-pedal strip (β_N, M) is called an N-pedal curvature strip if its geodesic torsion vanishes identically ($t_r^N = 0$) along the entire trajectory.

2.2. HELIX-STRIP INTERSECTION THEOREM FOR N-PEDAL CURVES

Let the base curve $\alpha(s)$ be a cylindrical helix on a cylinder L. A cylindrical helix is characterized by having a constant angle with a fixed axis vector U:

$$\langle T(s), U\rangle = \cos\theta = \text{constant}$$

Theorem 1 (Helix-Strip N-Pedal Theorem)

Let $\alpha(s)$ be a cylindrical helix on a cylinder L sharing a common tangent plane with a surface M along the N-pedal trajectory $\beta_N(s)$. The N-pedal strip (β_N, M) is an N-pedal curvature strip ($t_r^N = 0$) if and only if the N-pedal curve $\beta_N(s)$ constitutes a helix strip, satisfying the constant inclination property:

$$\langle \zeta_N(s), U\rangle = \text{constant}$$

Proof: Let U be the constant unit axis vector of the cylinder L. The derivative of the inner product between the surface normal field $\zeta_N(s)$ and the axis vector U along parameter s is given by:

$$\frac{d}{ds}\langle \zeta_N(s), U\rangle = \left\langle \frac{d\zeta_N}{ds}, U\right\rangle$$

Substituting the strip Frenet relation $\frac{d\zeta_N}{ds} = v_N(s)(-k_n^N \xi_N - t_r^N \eta_N)$ into the inner product yields:

$$\frac{d}{ds}\langle \zeta_N(s), U\rangle = -v_N(s)k_n^N\langle \xi_N, U\rangle - v_N(s)t_r^N\langle \eta_N, U\rangle$$

Substituting the explicit N-pedal unit tangent field $\xi_N = \frac{PT+QN+RB}{v_N}$ into the first term:

$$v_N(s)\langle \xi_N, U\rangle = P(s)\langle T, U\rangle + Q(s)\langle N, U\rangle + R(s)\langle B, U\rangle$$

Since $\alpha(s)$ is a cylindrical helix, $\langle T, U\rangle = \cos\theta$ is constant, which implies $\langle N, U\rangle = 0$. Moreover, $\langle B, U\rangle = \sin\theta$. Thus:

$$v_N(s)\langle \xi_N, U\rangle = P(s)\cos\theta + R(s)\sin\theta$$

Substituting $P(s) = -\kappa\langle \alpha, N\rangle$ and $R(s) = \tau\langle \alpha, N\rangle$ gives:

$$v_N(s)\langle \xi_N, U\rangle = \langle \alpha, N\rangle(-\kappa\cos\theta + \tau\sin\theta)$$

For a cylindrical helix, the ratio of torsion to curvature is constant ($\frac{\tau}{\kappa} = \tan\theta$), which forces $-\kappa\cos\theta + \tau\sin\theta = 0$ identically. Consequently, the inner product term vanishes:

$$\langle \xi_N, U\rangle = 0$$

Substituting this simplification back into the derivative equation yields:

$$\frac{d}{ds}\langle \zeta_N(s), U\rangle = -v_N(s)t_r^N\langle \eta_N, U\rangle$$

Assuming the non-trivial geometric configuration $\langle \eta_N, U\rangle \neq 0$ and $v_N(s) > 0$:

$$\frac{d}{ds}\langle \zeta_N(s), U\rangle = 0 \Leftrightarrow t_r^N = 0$$

This establishes that (β_N, M) is a curvature strip if and only if the surface normal satisfies $\langle \zeta_N(s), U\rangle =$ constant, proving that β_N forms a helix strip.

CONFLICT OF INTEREST

The author declares no conflict of interest.

ACKNOWLEDGMENT

Mathematics Subject Classification: 53A04, 53A05

REFERENCES

[1] L. Auslander, *Differential Geometry*, A Harper International Edition, Harper Roe, New York, 1963.
[2] W. Blaschke, *Vorlesungen Über Differential Geometrie I*. Band I, Verlag Von Julias Springer in Berlin, 1930.
[3] M. P. Do Carmo, *Differential geometry of Curves and Surfaces,* Prentice-Hall, 1976.
[4] F. Ertem Kaya, *Terquem and Joachimsthal Type Theorems in E*^{n}. PhD. Thesis, Ankara University, Graduate School of Natural and Applied Sciences, Ankara, 2010.
[5] F. Ertem Kaya, Y. Yaylı, and H.H. Hacisalihoğlu, A Characterization of Cylindrical Helix Strip, *Communications de la Faculté des Sciences de l'Université d'Ankara Série A1*, 2010, Volume 59, Tome 1.
[6] H. H. Hacisalihoğlu, On the Relations Between The Higher Curvatures of a Curve and A Strip. *Communications de la Faculté des Sciences de l'Université d'Ankara Série A1*, 1982, Tome 31, 71-75.
[7] H. H. Hacisalihoğlu, *Diferensiyel Geometri Cilt I*. Ankara University, Faculty of Science Press, Beşevler, Ankara, 2000.
[8] H. H. Hacisalihoğlu, A New Characterization For Inclined Curves by the Help of Spherical Representations. *International Electronic Journal of Geometry*, 2009, Volume 2, No 2, pages 71-75.
[9] F. Joachimsthal, Demonstrationes theorematum de superficiebus curvis. Journal für die reine und angewandte Mathematik (Crelle's Journal), 1846, 30, 347–350.
[10] S. Keleş, *Manifoldlar için Joachimsthal Teoremleri*. PhD. Thesis, Fırat University, Graduate School of Natural and Applied Sciences, Elazığ, 1982.
[11] N. Kuruoğlu and A. Sarıoğlugil, On the characteristic properties of the a-Pedal surfaces in the Euclidean space, *Commun. Fac. Sci. Univ. Ank. Series A*, 1993, 42, 19-25.
[12] C. Maclaurin, Tractatus de Curvarum Constructione et Mensura, ubi Plurimae Curvarum Proprietates Antehac Incognitae Breviter Explicantur. Philosophical Transactions of the Royal Society of London, 1718, 30(356), 803–814.
[13] H. R. Müller, *Kinematik Dersleri*, Ankara Üniversitesi, Fen Fakültesi Yayınları, Mat. 27, 246-281, 1959.
[14] B. O'Neill, *Elementary Differential Geometry*, Academic Press, New York, 72-74, 1966.
[15] J. Oprea, *Differential Geometry and Its Applications*, The Mathematical Association of America, Pearson Education, U.S.A, 2007.
[16] A. Sabuncuoğlu and H. H. Hacısalihoğlu, Higher Curvatures of A Strip, Communications de la Faculté des Sciences de *l'Université d'Ankara Série A1*, 1975a, Tome 24, 25-33.
[17] A. Sabuncuoğlu and H. H. Hacısalihoğlu, Higher Curvatures of A Curve, Communications de la Faculté des Sciences de *l'Université d'Ankara Série A1*, 1975b, Tome 24, 33-46.
[18] A. Sabuncuoğlu, E^n de (n-1) manifoldlar için Joachimsthal Teoremi, PhD. Thesis, Ankara University, Graduate School of Natural and Applied Sciences, Ankara, 1976.
[19] A. Sabuncuoğlu, *Diferensiyel Geometri Cilt I*. Nobel Yayın Dağıtım, Ankara, 2004.
[20] D. J. Struik, *Lectures on Classical Differential Geometry*, Addison-Wesley Publishing Company, pp:35, Massachusetts, U.S.A, 1957.
[21] O. Terquem, Note sur les lignes pédales. Nouvelles Annales de Mathématiques, 1re série, 1840, tome 1, 321–330.
[22] Y. Li and D. Pei, Pedal curves of fronts in the sphere, *J. Nonlinear Sci. Appl.* 2016, 9, 836-844. http://dx.doi.org/10.22436/jnsa.009.03.12
[23] Y. Li and D. Pei, Pedal curves of frontals in the Euclidean plane, Math. Methods. in the Appl. Sciences, 2018, 41, 1988-1997. https://doi.org/10.1002/mma.4724
[24] A. Y. Ceylan, M. Kara, On pedal and contrapedal curves of Bezier curves, *Konuralp J. Math.*, 2021, 9, 217–221.
[25] Y. Li, and O. O. Tuncer, On (contra)pedals and (anti)orthotomics of frontals in de Sitter 2-space, *Math. Methods. in the Appl. Sciences*, 2023, 46, 11157-11171. https://doi.org/10.1002/mma.9173
[26] Nishimura, T. (2008). Normal forms for singularities of pedal curves produced by non-singular dual curve germs in S^n, Geom. Dedicata, 2008, 133, 59-66. https://doi.org/10.1007/s10711-008-9233-5
[27] Ozdemir, M., (2020). *Diferansiyel Geometri*. Altin Nokta Yayınevi, 2020.

[28] O. O. Tuncer, H. Ceyhan, İ. Gök, and F. N. Ekmekci, Notes on pedal and contrapedal curves of fronts in the Euclidean plane, *Mathematical Methods in the Applied Sciences*, 2018, Volume 41, Issue 13, 5096-5111.
[29] D. Canlı, S. Şenyurt, S. and F. Ertem Kaya, Pedal curves obtained from Frenet vector of a space curve and Smarandache curves belonging to these curves, 2024, *AIMS Mathematics*, 9(8), 20136-20162. doi:10.3934/math.2024981
[30] F. Ertem Kaya, Differential Geometric Aspects of Pedal Curves on Surfaces. *Journal of Mathematics*, 2024, Volume 2024, Article ID: 6237091, 11. doi:10.1155/2024/6237091
[31] S. Şenyurt, S., F. Ertem Kaya, D. Canlı, and L. Grilli, L. (2024). The Pedal Curves Generated by Alternative Frame Vectors and Their Smarandache Curves, 2024, *Symmetry,* 16(8):1012. doi:10.3390/sym16081012
[32] A. Elsharkawy, H.K. Elsayied, M. E. Desouky, and C. Cesarano, T-pedal ruled surface with the Frenet frame of the original curve in E^3, *AIMS Mathematics*, 2025, 10(11), 25606-25623. doi:10.3934/math.20251134
[33] A. Elsharkawy, H.K. Elsayied, M. E. Desouky, and C. Cesarano, C., and Gasymov, A, A Geometric Study of Ruled Surfaces Generated by Frenet Vectors via N-Pedal Curves in E^3, *Azerbaijan Journal of Mathematics*, 2026, 16(1), 3-15, doi:10.59849/2218-6816.2026.1.3
[34] F. Ertem Kaya, Gaussian and Mean Curvatures of the Surface Obtained Along T-Pedal Curve of A Given Curve. Turkish Journal of Science, 2025, 10 (2), 105-120.
[35] S. Şenyurt, and F. Ertem Kaya, Gaussian and Mean Curvatures of The Surface Obtained Along B-Pedal Curve Of A Curve, Proceeding Book of 12th International Conference on Global Practise of Multidisciplinary Scientific Studies, pp. 600-617, Havana, Cuba, January 23-30, 2026.
[36] S. Şenyurt, and F. Ertem Kaya, The Surface Associated With the C-Pedal Curve Of A Curve, Proceeding Book of 8th International Conference on Scientific and Academic Research, pp. 19-28. Konya, Turkey, March 25, 2026.
[37] F. Ertem Kaya, Differential Geometry of Parallel Curves derived from Pedal Curves of a given curve in Euclidean 3-Space. *AIMS Mathematics*, 2026, 11(8), 24397-24418. https://doi.10.3934/math.2026985
[38] F. Ertem Kaya, Helix-Strip for T-Pedal Curves, *Proceeding Book of 8th International Conference on Contemporary Academic Research, ICCAR* 2026, 329-334, 15 August 2026.

8th International Conference on Engineering, Natural and Social Sciences

September 06-07, 2026: Konya, Turkey

© 2026 Published by All Sciences Academy

https://www.icensos.com/

Ekmeklik Buğdayda (*Triticum aestivum* L.) CBDP Primerlerinin Optimum Bağlanma Sıcaklıklarının Belirlenmesi

Muhammet İslam IŞIK[1*], Aras TÜRKOĞLU [1]

[1]*Tarla Bitkileri Bölümü, Ziraat Fakültesi / Necmettin Erbakan Üniversitesi, Konya 42310, Türkiye*

[*]*(muhammetislam.isik@erbakan.edu.tr)*

Özet – Ekmeklik buğday (*Triticum aestivum* L.), küresel gıda güvencesi ve bitkisel protein temininde kritik role sahip stratejik bir tahıl ürünüdür. Artan nüfus ve iklim değişikliği baskısı altında yürütülen ıslah programlarında, genetik çeşitliliğin belirlenmesi ve uygun ebeveyn seçimi büyük önem taşımaktadır. Çevresel koşullardan etkilenmeyen ve gen açısından zengin bölgeleri hedefleyen CBDP (CAAT Box-Derived Polymorphism) moleküler belirteç sistemi, yüksek tekrarlanabilirliği ile öne çıkmaktadır. Ancak PCR tabanlı bu markörlerin güvenilir sonuç vermesi, amplifikasyon koşullarının ve özellikle annealing sıcaklığının optimize edilmesine bağlıdır. Bu çalışmada, Türkiye tescil listesinde yer alan 96 adet ekmeklik buğday çeşidinden CTAB yöntemiyle izole edilen ve eşit oranlarda birleştirilen DNA stoğunda, 15 farklı CBDP primerinin optimum bağlanma sıcaklıkları belirlenmiştir. Gradient PCR protokolü kapsamında her primer için 47.0 °C ile 60.0 °C arasında 8 farklı sıcaklık derecesi (47.0, 47.9, 49.5, 52.0, 55.0, 57.3, 59.0 ve 60.0 °C) test edilmiştir. Amplifikasyon ürünleri %1.5'lik agaroz jel elektroforezinde yürütülerek UV altında görüntülenmiş ve en net, çoklu bant profili veren sıcaklıklar optimum olarak kabul edilmiştir. Elde edilen bulgular doğrultusunda, test edilen primerlerin optimum bağlanma sıcaklıklarının olarak 49.5 °C ile 59.0 °C arasında değiştiği saptanmıştır. Sonuçlar, dominant moleküler belirteçlerle yapılacak genetik çeşitlilik ve popülasyon yapısı analizleri öncesinde primer optimizasyonunun zorunlu olduğunu ortaya koymuş ve ekmeklik buğday ıslahı çalışmalarında CBDP belirteçlerinin etkin kullanımı için teknik bir altyapı oluşturmuştur.

Anahtar Kelimeler – Ekmeklik Buğday (Triticum aestivum L.), CBDP, PCR Optimizasyonu, Annealing Sıcaklığı, Genetik Çeşitlilik.

I. GİRİŞ

Buğday (*Triticum aestivum* L.), bitkisel protein kaynağı ve yaygın olarak tüketilmesi nedeniyle küresel öneme sahip, başlıca tahıl ürünü ve temel gıda maddesidir [1]. Üretimi yıllık yaklaşık 800 milyon tona ulaşmıştır ve dünyada en yaygın olarak yetiştirilen tahıl ürünüdür [2]. Ülkemizde ise 2023 yılı verilerine göre, kuru ve sulu şartlarda toplam 5.6 milyon ha alanda ekmeklik buğday tarımı yapılmıştır ve yaklaşık 17.7 milyon ton üretim gerçekleştirilmiştir [3]. Dünyada ve ülkemizde geniş ölçekte yetiştiriciliği olan ve önemli bir besin kaynağı olması sebebi ile küresel ısınma ve artan dünya nüfusu beraberinde yeni çeşitlerin geliştirilmesine ihtiyaç duyulmakta ve bu süreçte ekmeklik buğdayın ıslahı kritik bir rol oynamaktadır.

Ekmeklik buğday ıslahı programlarında, genellikle yüksek tane fiziksel özellikleri, hastalık direnci, son kullanım kalitesi ve tane verimi ile yeni çeşitler geliştirmeyi sürekli olarak amaçlanmaktadır [4]. Islah amaçları doğrultusunda ebeveyn seçiminde genetik çeşitlilik oldukça önem arz etmektedir. Genetik çeşitlilik daha verimli, dayanıklı ve değişen çevre koşullarına uyum sağlayabilen bitki çeşitlerinin geliştirilmesi için vazgeçilmezdir [5]. Genetik çeşitliliği belirlemede fenotipik ve moleküler belirteçler kullanılabilmektedir. Fakat fenotip tabanlı genetik belirteçlerin sınırlamaları sebebi ile çevresel

koşullardan etkilenmemesi ve güvenilirliğinin yüksek olmasından dolayı DNA tabanlı moleküler belirteçler geliştirilmiştir [6].

Moleküler belirteç tekniklerinden, Kısıtlama Parçası Uzunluğu Polimorfizmi (RFLP), Rastgele Yükseltilmiş Polimorfik DNA (RAPD), Basit Dizi Tekrarları (SSR) ve Yükseltilmiş Parça Uzunluğu Polimorfizmi (AFLP) gibi genetik veya DNA tabanlı belirteç teknikleri, genetik çeşitlilik ve filogenetik çalışmalarında yaygın olarak kullanılmaktadır [7]. Rastgele yükseltilmiş polimorfik DNA (RAPD) ilk PCR tabanlı moleküler belirteç olmuştur ve birçok belirteç tekniği son yirmi yılda geliştirilmiştir [8]. PCR aracılığı ile uygulanan moleküler belirteç tekniklerinden birisi de primerleri 18 nükleotid uzunluğunda olan ve 5' ucuna doğru dolgu dizisi ve 3' ucuna doğru di- veya trinükleotidlerle çevrili merkezi bir CCAAT nükleotid çekirdeğinden oluşan CBDP (CAAT kutusu kaynaklı polimorfizm) tekniğidir [9]. CBDP belirteçleri, bitki genomlarının gen açısından zengin bölgesinde bulunan varyasyonlardan elde edilmesi ve daha yüksek tekrarlanabilirlik göstermesi bakımından avantajlıdırlar.

PCR uygulamalarının eşlik ettiği moleküler belirteç sistemlerinde, uygulanmadan önce bazı optimizasyonların yapılması gerekmektedir. PCR tabanlı belirteç yöntemlerinin başarısı önemli derecede PCR reaksiyon bileşenlerine ve amplifikasyon koşullarına bağlıdır [10]. Optimum koşullar altında amplifikasyonun başarısız olması, istenen ürünün tamamen yok olmasına kadar, birden fazla tanımlanmamış ve istenmeyen ürünün oluşmasına sebep olabilmektedir. Optimizasyon değişkenleri listesinin başında Mg++ konsantrasyonları, tampon pH'ı ve döngü koşulları yer almaktadır ve döngü koşullarından birisi olan annealing sıcaklığı en önemlisidir [11].

Yürütülen bu araştırmada bazı Türkiye tescilli ekmeklik buğday çeşitlerinde genetik çeşitlilik tespiti öncesinde belirli CBDP belirteçlerinin annealing sıcaklıkları tespit edilmeye çalışılmıştır. Genetik çeşitlilik öncesindeki annealing sıcaklıklarının belirlenmesi ileride yürütülecek olan genetik çeşitlilik çalışmalarında kolaylık sağlaması amaçlanmıştır.

II. MATERYAL VE YÖNTEM

II.I. Bitki Materyali

Türkiye tescil listesinde bulunan 96 adet ekmeklik buğday çeşidinin DNA’sı izole edilerek her birinden DNA alınmış ve mix oluşturulmuştur. Elde edilen DNA karışımı CBDP belirteçlerinin annealing sıcaklıkları tespitinde kullanılmıştır.

II.II. Metot

II.II.I. DNA İzolasyonu

DNA izolasyonu için her çeşitten 150 mg yaprak alınarak ve iyice karıştırılarak toz haline gelinceye kadar ezilmiştir. Ezilen örnekler Zeınalzadeh ve Hosseinpour [12] tarafından belirtilen CTAB metoduna göre ekstraksiyon işlemi yapılmış ve DNA’lar elde edilmiştir.

Eş zamanlı toplanan yaprak dokularından izole edilen genomik DNA’ların miktar ve saflık kontrolleri, NanoDrop ND-3300 spektrofotometresinde 1 µl örnek kullanılarak gerçekleştirilmiştir. Olası protein kirliliğini belirlemek amacıyla A260/A280, polifenol ve polisakkarit kontaminasyon düzeylerini saptamak için ise A260/A230 absorbans oranları ölçülmüştür.

Elde edilen DNA’ların yapısal bütünlüğü ve kalitesi, 1X SB tampon çözeltisi içinde hazırlanan %0,8’lik agaroz jel elektroforezi ile test edilmiştir. Bu doğrultuda 5 µl DNA, 5 µl saf su ve 3 µl 6X yükleme tamponu karıştırılarak tarak kuyucuklarına yerleştirilmiştir. 70 V sabit voltaj altında 60 dakika boyunca yürütülen örnekler, işlem sonunda UV görüntüleme sistemi altında incelenerek bant profilleri kaydedilmiştir.

II.II.II. PCR Bileşenleri ve Şartları

Çalışmada primerlerin bağlanma sıcaklıklarını optimize etmek amacıyla 15 farklı CBDP primeri teste tabi tutulmuştur (Tablo 1). Amplifikasyon işlemleri MultiGene Gradient Termal Döngü Cihazı (TC9600-G-230V, Labnet International, Inc.) kullanılarak yürütülmüştür. PCR optimizasyonu kapsamında, 0,2 ml'lik reaksiyon tüplerine 2 µL 10X PCR tamponu, 1 µL MgCl2 (25 mM), 0,5 µL dNTP karışımı (10 mM), her bir primerden 0,5 µL (100 pmol) ve 1 U Taq DNA polimeraz eklenmiş ve ardından karışım ultra saf su ilavesiyle 20 µL nihai hacme ulaştırılmıştır. Termal döngü programında kalıp DNA'nın ilk denatürasyonu 96°C'de 2 dakika (1 döngü) olarak ayarlanmış, döngü içi denatürasyon basamağı ise 96°C'de 30 saniye süreyle uygulanmıştır.

Annealing sıcaklığının tespit edilmesi amacıyla ekmeklik buğdaylardan elde edilen DNA karışımı ile belirtilen CBDP belirteçlerinin gradient PCR uygulaması gerçekleştirilmiştir (Tablo 1.). Primerin bağlanma sıcaklığı, 15 adet her bir primer için 47-60 °C arasında değişecek şekilde 8 farklı (47 °C, 47.9 °C, 49.5 °C, 52 °C, 55 °C, 57.3 °C, 59 °C, 60 °C) sıcaklık uygulanmıştır. Bağlanma sıcaklığının ardından 1 dakika boyunca 72°C'de PCR çalışması üçüncü aşaması 38 döngü olarak gerçekleştirilmiş ve son olarak uzama süresi 15 dakika 72°C olacak şekilde tamamlanmıştır.

Tablo 1. PCR annealing sıcaklığı tespitinde kullanılan CBDP primerlerinin sekans bilgileri [13]

Primer Adı	Sekans 5-3'
CAAT 1	TGAGCACGATCCAAT AGC
CAAT 2	TGAGCACGATCCAATAAT
CAAT 3	TGAGCACGATCCAAT ACC
CAAT 4	TGAGCACGATCCAAT AAG
CAAT 6	TGAGCACGATCCAAT CAG
CAAT 7	TGAGCACGATCCAAT CGA
CAAT 8	TGAGCACGATCCAAT CGG
CAAT 9	TGAGCACGATCCAAT GAT
CAAT 10	TGAGCACGATCCAAT GTT
CAAT 12	TGAGCACGATCCAATATA
CAAT 13	TGAGCACGATCCAATGAG
CAAT 14	TGAGCACGATCCAATGC
CAAT 15	TGAGCACGATCCAATTGA
CAAT 16	TGAGCACGATCCAATTCA
CAAT 17	TGAGCACGATCCAATTTG

Elde edilen PCR ürünleri yatay jel elektroforez cihazında yürütülmüş ve yüklenmeden önce 2 µl brom fenol blue boyası ile boyanmıştır. % 1.5'lik agaroz jeli hazırlanırken jelin boyanması için 100 ml agaroz solüsyonu başına 10µl olacak şekilde SafeView™ Classic (G108, ABM) eklenmiş ve elektroforez kasasına dökülerek örnek sayısına uygun taraklar takılmıştır. Elektroforez yürütme işlemi 70 voltta 3 saat süre ile gerçekleştirilmiştir. Daha sonra ise UV ışığı altında (Vilber Lourmat, France) bantlar görüntülenmiştir.

III. BULGULAR VE TARTIŞMA

Ekmeklik buğday temel besin kaynağı olması sebebi ile dünyada ve ülkemizde oldukça stratejik bir öneme sahiptir. Islah programlarının yürütülmesi de bu nedenle önem kazanmaktadır. Yürütülecek olan ıslah süreçlerinden en önemlisi de popülasyon yapısının bilinmesidir. Popülasyon yapısının sağlıklı ve güvenilir şekilde tespit edilerek ebeveyn seçiminde kullanılması süreçleri oldukça kolaylaştırmaktadır. Ekmeklik buğday da Türkiye tescilli çeşitlerinden elde edilen DNA karışımı ile CBDP belirteçlerinden bazılarının annealing sıcaklıkları tespit edilmesi ve ileriki genetik çeşitlilik çalışmalarına bir taban

oluşturması amaçlanmıştır. Yürütülen araştırmada her bir CBDP belirteci için 47-60 °C arasında 8 farklı uygulanmış ve çoklu bant elde edilen sıcaklık optimum olarak belirlenmiştir.

Şekil 1 incelendiğinde hemen hemen iki primer hariç tamamında her sıcaklıkta çoklu bantların varlığı görülmektedir. En yüksek sayıda bant veren sıcaklık optimum sıcaklık olarak seçilmiştir. Şekil 1f'de optimum sıcaklık 49.5 °C, Şekil 1a,b,c,d,g'de optimum sıcaklık 55 °C, Şekil 1ı,m,n,p'de optimum sıcaklık 57.3 °C, Şekil1j,k,l'de optimum sıcaklık 59 °C olarak tespit edilmiştir. Ayrıca Şekil 1e,h'de hiçbir sıcaklıkta çoklu bantlar elde edilememiş, bu primerlerin bu bitkide 47-60 °C arasında çalışmadığı belirlenmiştir. PCR bağlanma sıcaklıklarının optimizasyonu her bitki ve her primer için değişebilmektedir. Maraş-Vanlıoğlu vd. [14] *Cicer* L. cinsinde iPBS belirteçlerinin bağlanma sıcaklıklarını tespit etmeye çalışmışlar ve 46-58 °C arasında her primerde çoklu bantların elde edilemediğini belirtmişlerdir. Işık vd. [15] yonca bitkisinde annealing optimizasyonu yapmışlar ve 46-61.2 °C sıcaklıklar arasında bazı SRAP belirteçlerinin bağlanma sıcaklıklarını tespit etmişlerdir. Erkol vd. [16] SCoT belirteçlerinin bağlanma sıcaklıklarını *Gundelia* L. genotipleri üzerinde test etmişler ve 45-65 °C arasındaki sıcaklıklarda her primerin farklı sayıda bantlar oluşturduğunu gözlemlemişlerdir. Yürütülen araştırmalarda farklı markör sistemlerinin hem kendi içerisinde hem de markör sistemleri arasında annealing sıcaklığının farklı değerlerde çalıştığı görülmektedir. CBDP markör sisteminde de benzer sonucu elde etmiş olup farklı primerlerin aynı sıcaklıklarda farklı sayıda bant oluşturduğu belirlenmiştir.

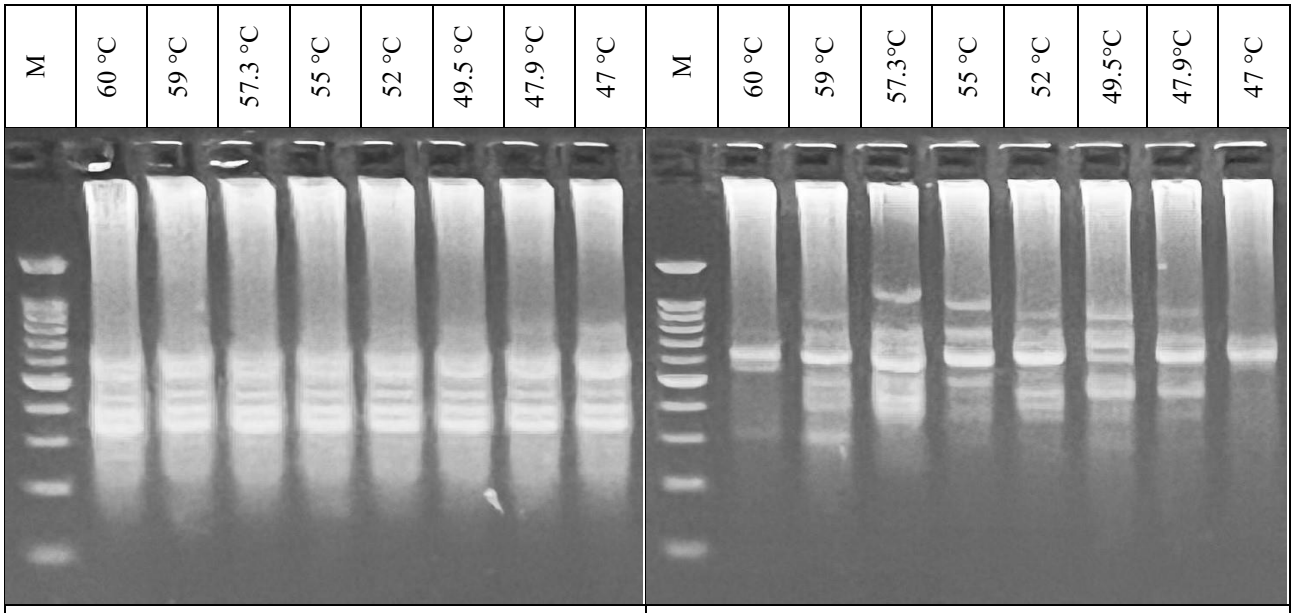

1a 2b

M 60 °C 59 °C 57.3 °C 55 °C 52 °C 49.5 °C 47.9 °C 47 °C M 60 °C 59 °C 57.3 °C 55 °C 52 °C 49.5 °C 47.9 °C 47 °C

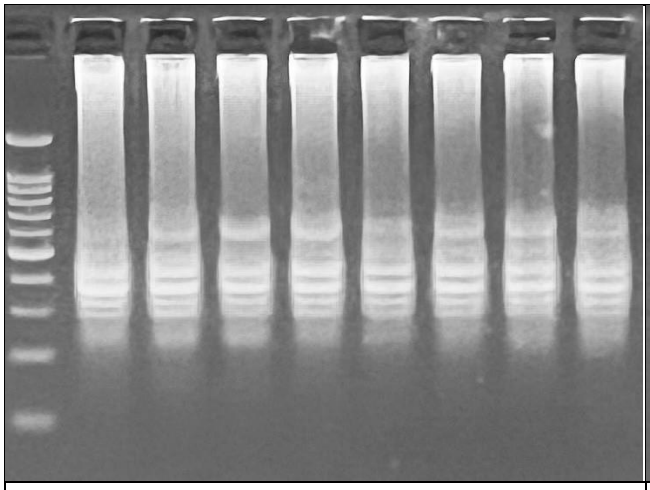

3c

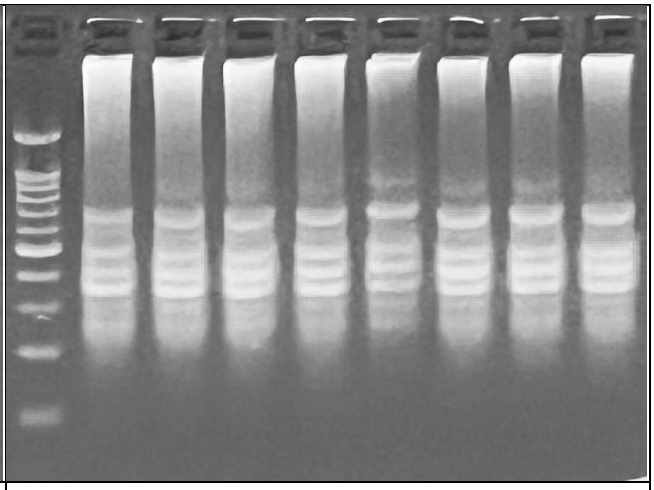

4d

M | 60 °C | 59 °C | 57.3 °C | 55 °C | 52 °C | 49.5 °C | 47.9 °C | 47 °C

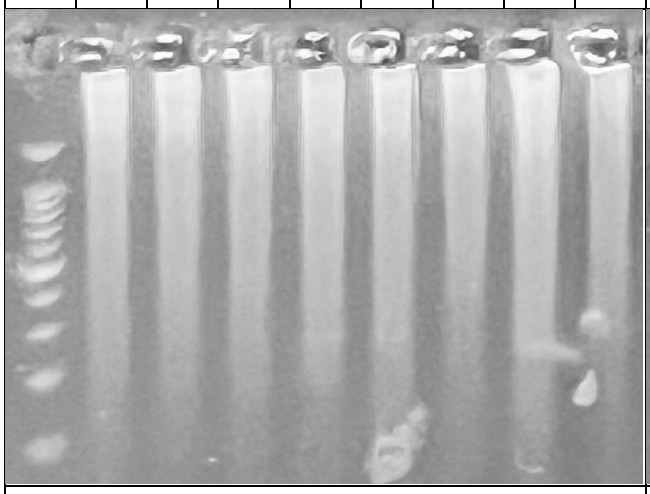

6e

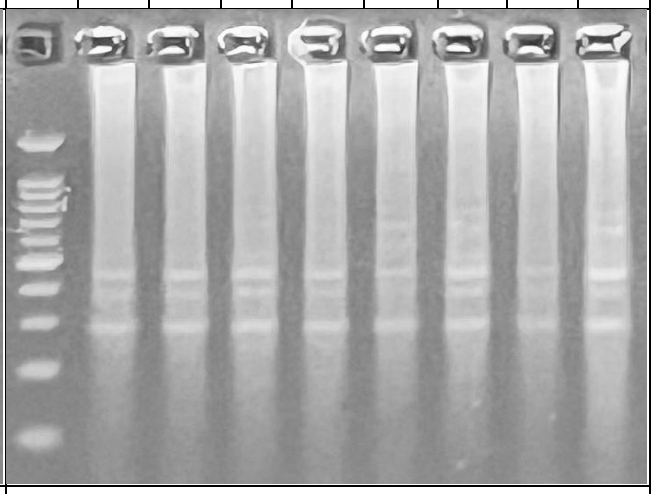

7f

M | 60 °C | 59 °C | 57.3 °C | 55 °C | 52 °C | 49.5 °C | 47.9 °C | 47 °C

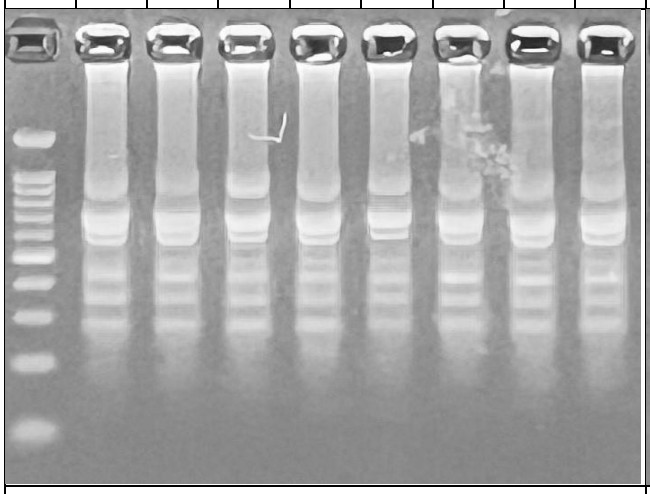

8g

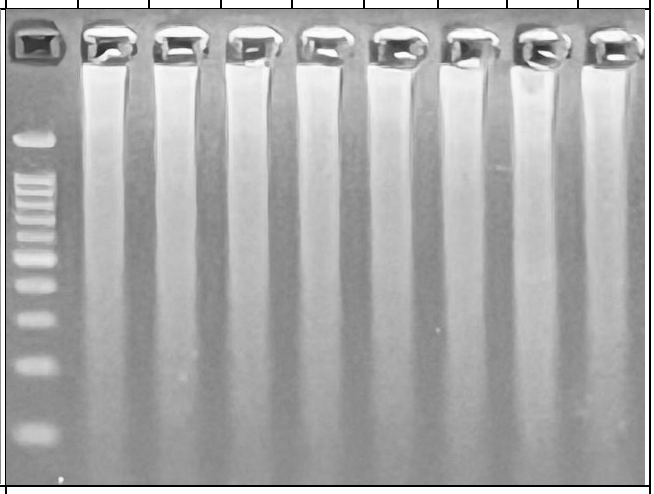

9h

M
60 °C
59 °C
57.3 °C
55 °C
52 °C
49.5 °C
47.9 °C
47 °C
10ı
12j
13k
14l

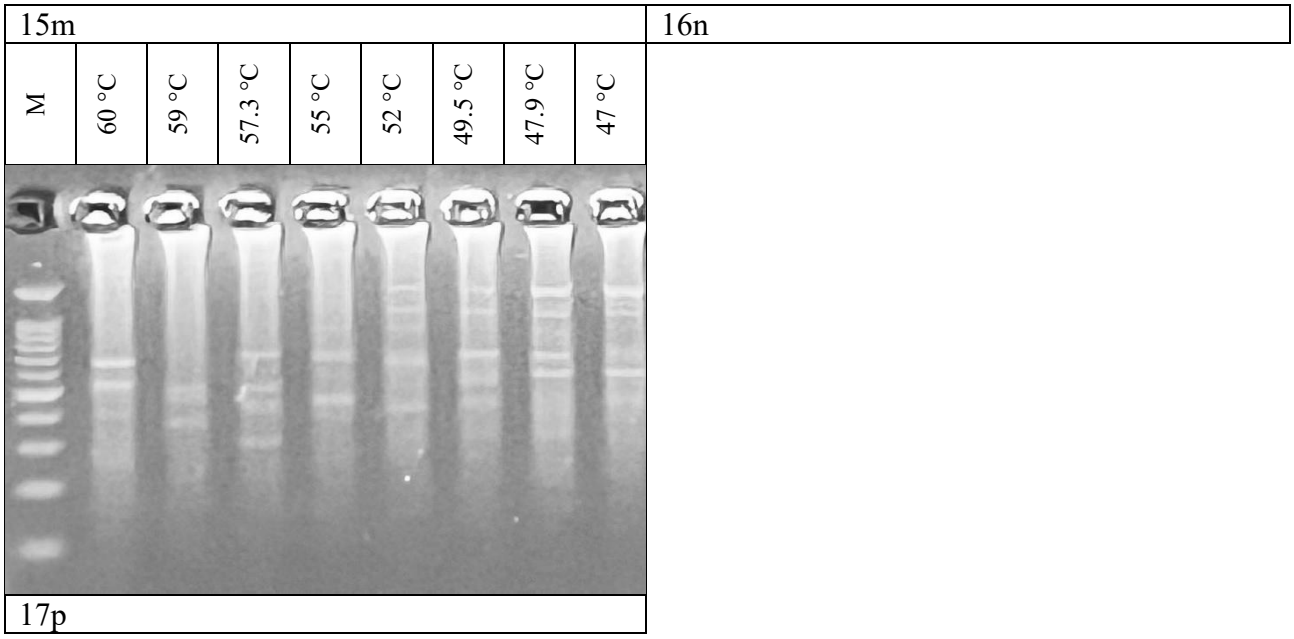

Şekil 1. CBDP belirteçlerinin jel görüntüleri (a: CAAT 1, b: CAAT 2, c: CAAT 3, d: CAAT 4, e: CAAT 6, f: CAAT 7, g: CAAT 8, h: CAAT 9, ı: CAAT 10, j: CAAT 12, k: CAAT 13, l: CAAT 14, m: CAAT 15, n: CAAT 16, p: CAAT 17)

IV. SONUÇLAR

Her dominant markör sistemindeki belirteçler aynı annealing sıcaklıklarında çalışmamaktadır. Bu sebeple PCR aracılığı ile yürütülecek ve dominant markörlerin kullanılması planlanan araştırmalarda, işlemlerin sağlıklı ve daha hızlı yapılabilmesi için optimizasyon gereklidir. PCR optimizasyonu yapılmadığı taktirde istenmeyen, beklenmeyen ve yanlış PCR ürünü ile karşılaşılması kaçınılmazdır. Yürütülen araştırma sonuçlarına göre ekmeklik buğday DNA'ları ile uygulanan CBDP markör sistemindeki her bir belirtecin farklı sıcaklıklarda farklı sayılarda bantların gözlemlendiği belirlenmiştir. Optimum annealing sıcaklıklarının belirlenerek çalışmaya başlanması sürecin daha sağlıklı yürütülmesi açısından önemli olduğu tespit edilmiştir.

KAYNAKLAR

[1] Al Ghafri, S. H., Al-Busaidi, W. M., & Farooq, M. (2025). Enhancing Drought Tolerance in Bread Wheat Through GABA Seed Priming and Optimized Storage Temperatures. *Journal of Plant Growth Regulation*, 1-9.

[2] FAO (2023) World food situation. Available at: https://www.fao.org/worldfoodsituation/csdb/en/ (Accessed June 20 , 2022).

[3] DÜNDAR, M. A., & TOPAK, R. (2025). Konya bölgesinde kısıtlı tamamlayıcı sulamanın ekmeklik buğdayın un verimine etkisi. Ereğli Tarım Bilimleri Dergisi, 5(1), 11-23.

[4] Khan, H. (2019). Genetic improvement for end-use quality in wheat. In Quality breeding in field crops (pp. 239-253). Cham: Springer International Publishing.

[5] Salgotra, R. K., & Chauhan, B. S. (2023). Genetic diversity, conservation, and utilization of plant genetic resources. Genes, 14(1), 174.

[6] Agrawal, P. K., & Shrivastava, R. (2013). Molecular markers. In Advances in Biotechnology (pp. 25-39). New Delhi: Springer India.

[7] Mondini, L., Noorani, A., & Pagnotta, M. A. (2009). Assessing plant genetic diversity by molecular tools. *Diversity*, *1*(1), 19-35.

[8] Williams, J. G., Kubelik, A. R., Livak, K. J., Rafalski, J. A., & Tingey, S. V. (1990). DNA polymorphisms amplified by arbitrary primers are useful as genetic markers. *Nucleic acids research*, *18*(22), 6531-6535.

[9] Singh, A. K., Rana, M. K., Singh, S., Kumar, S., Kumar, R., & Singh, R. (2014). CAAT box-derived polymorphism (CBDP): a novel promoter-targeted molecular marker for plants. Journal of Plant Biochemistry and Biotechnology, 23(2), 175-183.

[10] Lorenz, T. C. (2012). Polymerase chain reaction: basic protocol plus troubleshooting and optimization strategies. Journal of visualized experiments: JoVE, (63), 3998.

[11] Roux, K. H. (2009). Optimization and troubleshooting in PCR. *Cold Spring Harbor Protocols*, *2009*(4), pdb-ip66.

[12] Zeınalzadeh, T. H., & Hosseinpour, A. (2018). Application of a High-throughput Polyacrylamide Electrophoresis Gel System with Ethidium Bromide Staining in Genetic Diversity Estimation of Sunflower Genotypes Using TRAP Markers.

[13] Singh, A. K., Rana, M. K., Singh, S., Kumar, S., Kumar, R., & Singh, R. (2014). CAAT box-derived polymorphism (CBDP): a novel promoter-targeted molecular marker for plants. Journal of Plant Biochemistry and Biotechnology, 23(2), 175-183.

[14] Maraş-Vanlıoğlu, F. G., Yaman, H., Işık, M. İ., Türkoğlu, A. (2025). Cicer L. Cinsinin Genetik Çeşitliliğinin Belirlenmesi için iPBS (Primer Arası Bağlanma Yeri) Markörlerine Dayalı PCR Optimizasyonu. 2nd International Conference on Pioneer and Innovative Studies. 294-298.

[15] Işık, M. İ., Koç, A., İleri, O., Türkoğlu, A., Armağan M., Ulukuş D. (2025). Yonca Genotiplerinde Genetik Çeşitliliğin Dizilimle İlişkili Amplifikasyon Polimorfizmi (SRAP) Belirteçleri ile Belirlenmesinde Primer Bağlanma Sıcaklıklarının Tespiti. 3rd International Conference on Trends in Advanced Research. 14-19.

[16] Erkol, Ş., Işık, M. İ., Armağan M., Türkoğlu, A. (2024). SCoT DNA Markörleri ile Gundelia L.'nin Genetik Çeşitliliğinin Belirlenmesi için PCR Analizinin Optimizasyonu. 3rd International Conference on Engineering, Natural and Social Sciences. 353-357.

8th International Conference on Engineering, Natural and Social Sciences

September 06-07, 2026: Konya, Turkey

© 2026 Published by All Sciences Academy

https://www.icensos.com/

RLC TİPİ DİNAMİK SİSTEMLERİN NÜMERİK ANALİZİ

Muzaffer ATEŞ*, Esra YILMAZ

*Department of Electrical Electronics Engineering University of Van Yüzüncü Yıl University, Van, 65080, Turkey

*(ates.muzaffer65@gmail.com)

Department of Electrical Electronics Engineering University of Van Yüzüncü Yıl University, Van, 65080, Turkey

(esrayyilmaz113@gmail.com)

Özet-RLC tipi sistemler, direnç (R), bobin (L) ve kondansatör (C) elemanlarının birlikte bulunduğu ve elektriksel dinamik davranışların diferansiyel denklemler aracılığıyla modellenebildiği sistemlerdir. Bu çalışmada, seri bağlı bir RLC sisteminin matematiksel modeli oluşturularak nümerik çözüm yöntemleri açısından incelenmesi amaçlanmıştır. Sistem, Kirchhoff'un gerilim yasası kullanılarak ikinci dereceden bir adi diferansiyel denklem biçiminde ifade edilmiş ve nümerik çözüm için birinci dereceden diferansiyel denklem sistemine dönüştürülmüştür. Çözüm yaklaşımında Euler ve dördüncü dereceden Runge-Kutta (RK4) yöntemleri ele alınmıştır. Yöntemlerin performansı; adım büyüklüğü, mutlak hata ve çözümün kararlılığı açısından değerlendirilmiştir. Elde edilen sonuçlar, adım büyüklüğünün küçültülmesinin genel olarak nümerik hatayı azalttığını ve RK4 yönteminin Euler yöntemine göre daha yüksek doğruluk sağladığını göstermektedir. Çalışma, RLC sistemlerinin nümerik analizinde yöntem seçiminin doğruluk ve hesaplama maliyeti açısından önemli olduğunu ortaya koymaktadır.

Anahtar Kelimeler – RLC sistemi, nümerik çözüm, Euler yöntemi, Runge-Kutta yöntemi, hata analizi, diferansiyel denklem.

I. GİRİŞ

RLC devreleri, elektrik ve elektronik mühendisliğinde dinamik sistemlerin modellenmesinde temel örneklerden biridir. Direnç, bobin ve kondansatörün birlikte kullanılması sonucunda sistemde enerji kaybı, manyetik enerji depolanması ve elektriksel enerji depolanması aynı anda gerçekleşmektedir. Bu özellik, RLC sistemlerini hem teorik hem de nümerik analiz açısından önemli hâle getirmektedir. Seri RLC devresinin davranışı Kirchhoff'un gerilim yasası kullanılarak bir diferansiyel denklem ile ifade edilebilir. Devredeki direnç, endüktans ve kapasite değerleri sistemin sönüm ve salınım karakteristiklerini belirlemektedir [1-4].Basit RLC modelleri için analitik çözümler elde edilebilse de mühendislik uygulamalarında doğrusal olmayan elemanlar, zamanla değişen parametreler veya karmaşık giriş fonksiyonları nedeniyle analitik çözüm her zaman mümkün olmayabilir [5-7] . Bu nedenle nümerik yöntemler önemli bir çözüm alternatifi oluşturmaktadır. Bu çalışmada temel amaç, RLC tipi bir sistemin nümerik çözümünü gerçekleştirmek ve kullanılan yöntemlerin hata davranışlarını karşılaştırmalı olarak incelemektir

II. MATERYAL VE YÖNTEM

Çalışmada seri bağlı bir RLC devresi ele alınmıştır. Kirchhoff'un gerilim yasasına göre devrenin matematiksel modeli:

$$\frac{L\, d_q^2}{dt^2} + R\frac{dq}{dt} + \frac{1}{c}q = v(t)$$

şeklinde elde edilmektedir.

Burada q(t) kondansatörde depolanan yükü, R direnç değerini, L endüktansı, C kapasiteyi ve V(t) giriş gerilimini göstermektedir.

Akım:

$$i(t) = \frac{dq}{dt}$$

$$\frac{dq}{dt} = i$$

$$\frac{di}{dt} = \frac{R}{L}i - \frac{1}{LC}q + \frac{1}{L}v(t)$$

Nümerik çözüm amacıyla İleri Euler ve klasik dördüncü dereceden Runge-Kutta (RK4) yöntemleri kullanılmıştır.

Euler yöntemi genel olarak:

$$y_{n+1} = y_n + hf(t_n, y_n)$$

şeklinde ifade edilir.

RK4 yönteminde ise her adımda dört farklı eğim hesaplanarak:

$$y_{n+1} = y_n + \frac{h}{6}(k_1 + 2k_2 + 2k_3 + k_4)$$

bağıntısı kullanılmaktadır.

Yöntemlerin karşılaştırılmasında mutlak hata:

$$E_n = |y(t_n) - y_n|$$

$$Er = \frac{|y(t_n) - y_n|}{|y(t_n)|}$$

ifadeleri kullanılmıştır.

Bu çalışmada yöntemlerin performansının değerlendirilmesi amacıyla farklı zaman adımı değerleri kullanılarak elde edilen nümerik sonuçlar karşılaştırılmıştır.

III. BULGULAR

Yapılan nümerik değerlendirmelerde RLC sisteminin çözüm davranışının kullanılan zaman adımına ve nümerik yönteme bağlı olarak değiştiği görülmüştür. Euler yöntemiyle gerçekleştirilen çözümlerde zaman adımı büyüdükçe analitik çözüme göre sapmanın arttığı gözlenmiştir. Özellikle

sistemin salınımlı karakter gösterdiği durumlarda Euler yönteminin hem genlik hem de faz açısından daha belirgin hata üretebildiği görülmektedir. RK4 yöntemiyle elde edilen sonuçların ise aynı zaman adımlarında analitik çözüme daha yakın olduğu belirlenmiştir. Bunun temel nedeni RK4 yönteminin tek bir zaman adımında birden fazla ara eğim değeri kullanmasıdır.

Genel hata davranışı aşağıdaki şekilde özetlenebilir:

Yöntem	Teorik global hata mertebesi	Genel doğruluk
Euler	O(h)	Düşük
RK4	$O(h^4)$	Yüksek

Zaman adımının azaltılmasıyla her iki yöntemde de hata değerlerinin genel olarak azaldığı belirlenmiştir. Ancak çok küçük adım değerlerinde işlem sayısının artması nedeniyle hesaplama maliyetinin yükseldiği dikkate alınmalıdır.

IV. TARTIŞMA

Elde edilen bulgular, RLC sistemlerinin nümerik çözümünde yöntem seçiminin sonuçların doğruluğu üzerinde belirleyici olduğunu göstermektedir. Euler yönteminin en önemli avantajı algoritmasının basit ve hesaplama maliyetinin düşük olmasıdır. Bununla birlikte birinci dereceden bir yöntem olması nedeniyle yüksek doğruluk gerektiren problemlerde küçük zaman adımlarına ihtiyaç duyulmaktadır. RK4 yöntemi ise daha fazla fonksiyon değerlendirmesi gerektirmesine rağmen daha yüksek doğruluk sağlamaktadır. Özellikle salınımlı RLC sistemlerinde çözümün genlik ve faz özelliklerinin doğru biçimde temsil edilmesi açısından RK4 daha avantajlıdır. Bununla birlikte yalnızca hata büyüklüğünün dikkate alınması yeterli değildir. Nümerik kararlılık da değerlendirilmelidir. Uygun olmayan bir zaman adımı seçildiğinde nümerik çözüm fiziksel sistemin gerçek davranışından uzaklaşabilir. Bu nedenle RLC sistemlerinde doğruluk, kararlılık ve hesaplama maliyeti birlikte değerlendirilmelidir. Ayrıca çok küçük zaman adımlarının her durumda daha iyi sonuç vereceği düşünülmemelidir. Adım büyüklüğünün aşırı küçültülmesi işlem sayısını artırarak yuvarlama hatalarının etkisini belirginleştirebilir. Bu nedenle optimum bir zaman adımı seçimi önem taşımaktadır.

V. SONUÇLAR

Bu çalışmada seri RLC tipi bir sistemin diferansiyel denklem tabanlı matematiksel modeli oluşturulmuş ve nümerik çözüm yaklaşımı incelenmiştir. Euler ve RK4 yöntemleri doğruluk ve hata davranışları bakımından karşılaştırılmıştır. Elde edilen değerlendirmeler sonucunda, Euler yönteminin basitliği ve düşük hesaplama maliyeti nedeniyle ön analizlerde kullanılabileceği, ancak yüksek doğruluk gerektiren RLC sistemlerinde RK4 yönteminin daha uygun olduğu sonucuna ulaşılmıştır. Ayrıca zaman adımının nümerik çözüm kalitesi üzerinde önemli bir etkisi olduğu görülmüştür. Küçük zaman adımları genel olarak hatayı azaltırken hesaplama maliyetini artırmaktadır. Dolayısıyla nümerik analizlerde yalnızca yüksek doğruluk hedeflenmemeli; yöntemin kararlılığı ve hesaplama maliyeti de göz önünde bulundurulmalıdır. Sonuç olarak RLC sistemleri, nümerik diferansiyel denklem çözümlerinin doğruluk, yakınsama ve kararlılık özelliklerinin incelenmesi için uygun bir model oluşturmaktadır. İlerleyen çalışmalarda örtük yöntemler, uyarlamalı zaman adımları ve doğrusal olmayan RLC modellerinin incelenmesi çalışmanın kapsamını genişletebilir.

KAYNAKLAR

[1] Burden, R. L., & Faires, J. D. (2011). *Numerical Analysis*. Brooks/Cole, Cengage Learning.

[2]Chapra, S. C., & Canale, R. P. (2015). *Numerical Methods for Engineers*. McGraw-Hill Education.

[3]Hayt, W. H., Kemmerly, J. E., & Durbin, S. M. (2019). *Engineering Circuit Analysis*. McGraw-Hill Education.

[4]Boyce, W. E., & DiPrima, R. C. (2017). *Elementary Differential Equations and Boundary Value Problems*. Wiley.

[5] Karris, S. T. (2007). *Circuit Analysis I with MATLAB Applications*. Orchard Publications.

[6] Sauer, T. (2018). *Numerical Analysis*. Pearson.

[7] Atkinson, K., & Han, W. (2009). *Theoretical Numerical Analysis: A Functional Analysis Framework*.Springer.

8th International Conference on Engineering, Natural and Social Sciences

September 06-07, 2026: Konya, Turkey

© 2026 Published by All Sciences Academy

https://www.icensos.com/

Sony Hisse Senedi Kapanış Fiyatı Tahmini için Makine Öğrenmesi ve Derin Öğrenme Modellerinin Karşılaştırmalı Analizi

Anıl Utku[1*]

[1]*Bilgisayar Mühendisliği / Munzur Üniversitesi, Türkiye*

[*]*anilutku@munzur.edu.tr*

Özet – Bu çalışmada, Sony Group Corporation'a ait tarihsel hisse senedi verileri kullanılarak bir sonraki işlem gününün kapanış fiyatının tahmin edilmesi ve farklı makine öğrenmesi ile derin öğrenme modellerinin karşılaştırılması amaçlanmıştır. Bu kapsamda LR, RF, SVR, XGBoost, CNN, LSTM ve GRU modelleri değerlendirilmiştir. Modellerin girdileri, geçmiş 20 işlem gününe ait Open, High, Low, Close ve Volume değişkenlerinden oluşturulmuş, veri seti zaman serisi yapısı korunacak şekilde kronolojik olarak eğitim, doğrulama ve test kümelerine ayrılmıştır. Model performansları MAE, RMSE ve R2 metrikleri kullanılarak karşılaştırılmıştır. Deneysel sonuçlar, derin öğrenme modellerinin genel olarak makine öğrenmesi yöntemlerinden daha yüksek tahmin başarısı sağladığını göstermiştir. En başarılı model olan GRU, 0,3578 MAE, 0,4772 RMSE ve 0,9776 R2 değerlerine ulaşmıştır. GRU'yu LSTM ve CNN modelleri takip ederken, geleneksel makine öğrenmesi yöntemleri içerisinde en iyi performans XGBoost tarafından elde edilmiştir. Bulgular, finansal zaman serilerindeki zamansal bağımlılıkların modellenmesinde özellikle GRU ve LSTM gibi tekrarlayan sinir ağı mimarilerinin etkili olduğunu göstermektedir.

Anahtar Kelimeler – Hisse senedi tahmini, makine öğrenmesi, derin öğrenme, GRU, LSTM, XGBoost

I. GİRİŞ

Finansal piyasalar, yatırımcı davranışları, makroekonomik gelişmeler, şirket performansı, küresel riskler ve piyasa beklentileri gibi çok sayıda faktörün eş zamanlı etkisi altında şekillenen dinamik ve doğrusal olmayan yapılardır [1]. Bu nedenle hisse senedi fiyatlarının güvenilir biçimde tahmin edilmesi, hem akademik araştırmalar hem de yatırım kararlarının desteklenmesi açısından önemli bir problem olarak değerlendirilmektedir [2]. Özellikle günlük açılış, en yüksek, en düşük ve kapanış fiyatları ile işlem hacmi gibi tarihsel piyasa değişkenleri, gelecekteki fiyat hareketlerinin modellenmesinde yaygın olarak kullanılmaktadır [3].

Geleneksel istatistiksel ve makine öğrenmesi yöntemleri, finansal zaman serilerindeki ilişkilerin modellenmesinde uzun süredir kullanılmaktadır. Linear Regression (LR), Support Vector Regression (SVR), Random Forest (RF) ve XGBoost gibi yöntemler, farklı doğrusal ve doğrusal olmayan ilişki yapılarını temsil edebilmekte ve tablosal finansal veriler üzerinde başarılı sonuçlar üretebilmektedir. Bununla birlikte, hisse senedi verilerinin zamansal bağımlılık içeren ardışık yapısı, yalnızca statik özellik ilişkilerine dayanan yöntemlerin bazı durumlarda sınırlı kalmasına neden olabilmektedir [4].

Derin öğrenme yaklaşımlarının gelişmesiyle birlikte finansal zaman serisi tahmininde Convolutional Neural Network (CNN), Long Short-Term Memory (LSTM) ve Gated Recurrent Unit (GRU) gibi mimariler yaygın biçimde kullanılmaya başlanmıştır [5]. CNN modelleri, ardışık veriler içerisindeki yerel örüntüleri öğrenme yetenekleriyle öne çıkarken, LSTM ve GRU mimarileri uzun ve kısa dönemli zamansal bağımlılıkların modellenmesi amacıyla geliştirilmiştir [6]. Özellikle tekrarlayan sinir ağı tabanlı LSTM ve GRU yapıları, geçmiş gözlemlerin sonraki fiyat hareketleri üzerindeki etkisini doğrudan dikkate alabildikleri için finansal tahmin problemleri açısından uygun yaklaşımlar sunmaktadır [7].

Bu çalışmada, Sony Group Corporation'a ait 2 Ocak 2014 ile 24 Ağustos 2026 tarihleri arasındaki tarihsel hisse senedi verileri kullanılarak bir sonraki işlem gününün kapanış fiyatının tahmin edilmesi amaçlanmıştır. Veri seti günlük Open, High, Low, Close ve Volume değişkenlerinden oluşmakta ve Sony hisse senedinin uzun dönemli fiyat ve işlem hacmi hareketlerini içermektedir. Çalışmada geçmiş 20 işlem gününe ait piyasa verileri kullanılarak bir sonraki günün kapanış fiyatı tahmin edilmiştir.

Çalışmanın temel amacı, geleneksel makine öğrenmesi ve temel derin öğrenme yöntemlerinin aynı tahmin problemi üzerindeki performanslarını karşılaştırmalı olarak incelemektir. Bu kapsamda makine öğrenmesi tarafında LR, RF, SVR ve XGBoost, derin öğrenme tarafında ise CNN, LSTM ve GRU modelleri değerlendirilmiştir. Modellerin tahmin başarıları Mean Absolute Error (MAE), Root Mean Squared Error (RMSE) ve Coefficient of Determination R2 metrikleri kullanılarak karşılaştırılmıştır. Böylece farklı model ailelerinin Sony hisse senedi kapanış fiyatı tahminindeki güçlü ve zayıf yönlerinin ortaya konulması hedeflenmiştir.

II. MATERYAL VE METOT

Bu çalışmada, Sony Group Corporation'a ait tarihsel hisse senedi verileri kullanılarak bir sonraki işlem gününün kapanış fiyatının tahmin edilmesi amaçlanmıştır. Bu kapsamda veri seti ön işleme adımlarından geçirilmiş, geçmiş 20 işlem gününe ait Open, High, Low, Close ve Volume değişkenleri kullanılarak tahmin örnekleri oluşturulmuştur. Makine öğrenmesi ve derin öğrenme tabanlı yedi farklı model aynı deneysel koşullar altında eğitilmiş ve performansları MAE, RMSE ve R2 metrikleri kullanılarak karşılaştırılmıştır.

A. Veri Seti

Bu çalışmada, Sony Group Corporation'a ait uzun dönemli tarihsel hisse senedi verileri kullanılmıştır. Veri seti, 2 Ocak 2014 ile 24 Ağustos 2026 tarihleri arasındaki günlük işlem kayıtlarını içermektedir. Her gözlem bir işlem gününü temsil etmekte olup veri setinde temel olarak Date, Open, High, Low, Close ve Volume değişkenleri bulunmaktadır. Çalışmada tarih değişkeni zaman sıralamasının korunması amacıyla kullanılmış, tahmin modellerine girdi olarak ise açılış fiyatı, gün içi en yüksek ve en düşük fiyat, kapanış fiyatı ve işlem hacmi değerleri verilmiştir.

Open değişkeni ilgili işlem günündeki açılış fiyatını, High gün içerisinde ulaşılan en yüksek fiyatı, Low en düşük fiyatı ve Close işlem gününün kapanış fiyatını ifade etmektedir. Volume değişkeni ise ilgili işlem gününde gerçekleştirilen toplam işlem hacmini göstermektedir. Bu değişkenler, hisse senedinin hem fiyat dinamiklerini hem de piyasa aktivitesini temsil eden temel finansal göstergeler olarak değerlendirilmiştir.

Veri seti analiz öncesinde tarih sütununa göre kronolojik olarak sıralanmış, veri tipleri kontrol edilmiş ve eksik ya da yinelenen gözlemler açısından incelenmiştir. Zaman serisinin doğal yapısını korumak ve geleceğe ait bilgilerin eğitim sürecine sızmasını önlemek amacıyla rastgele veri bölme yaklaşımı kullanılmamıştır. Bunun yerine veriler kronolojik olarak eğitim, doğrulama ve test kümelerine ayrılmıştır. Bu yaklaşım, finansal zaman serisi tahmininde gerçek kullanım koşullarını daha doğru biçimde yansıtmak amacıyla tercih edilmiştir.

Veri setindeki kapanış fiyatlarının zaman içerisindeki değişimi Şekil 1'de gösterilmiştir.

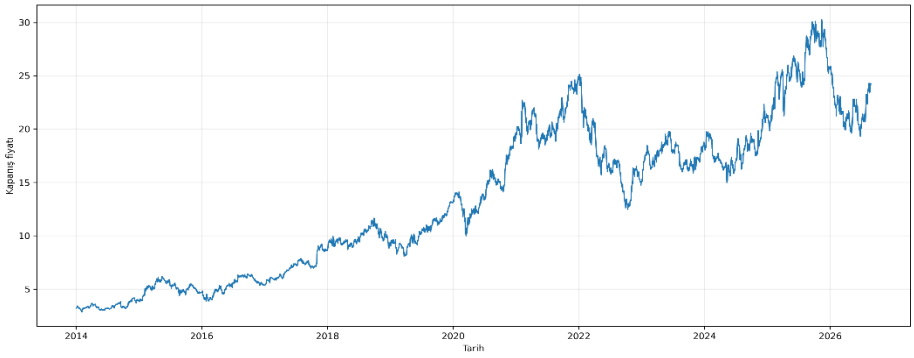

Şekil 1. Veri setindeki kapanış fiyatlarının zaman içerisindeki değişimi

Grafik incelendiğinde Sony hisse senedi fiyatlarının çalışma dönemi boyunca belirgin dalgalanmalar sergilediği, özellikle son yıllarda fiyat seviyelerinin daha yüksek değerlere ulaştığı görülmektedir. İşlem hacminin zamana bağlı değişimi ise Şekil 2'de sunulmuştur. İşlem hacminde dönemsel olarak belirgin sıçramalar bulunması, piyasa aktivitesinin zaman içerisinde sabit olmadığını göstermektedir.

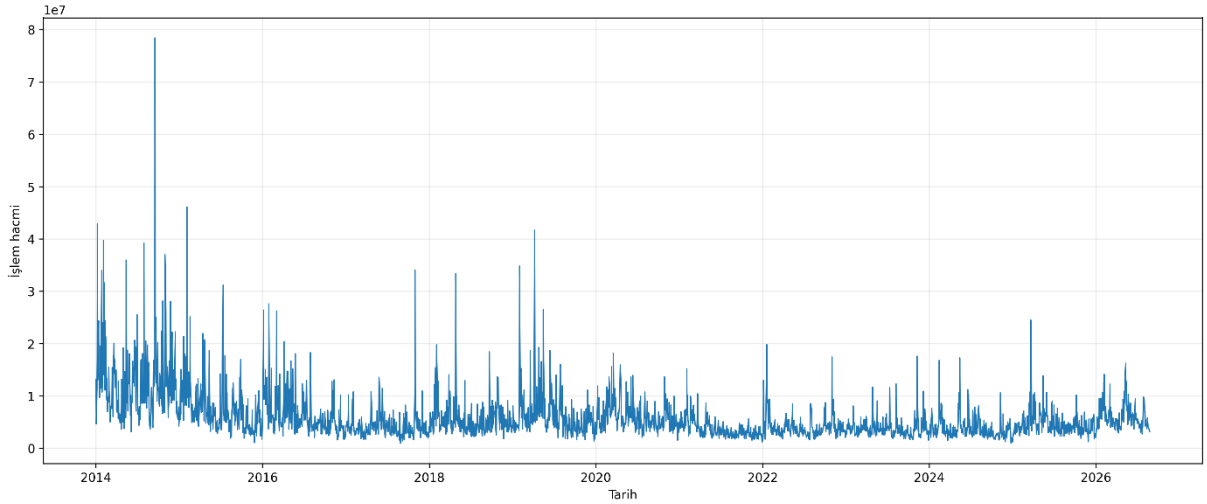

Şekil 2. İşlem hacminin zamana bağlı değişimi

Finansal serinin günlük değişkenliğini incelemek amacıyla kapanış fiyatlarından günlük getiri değerleri de hesaplanmıştır. Günlük getirilerin dağılımı Şekil 3'te verilmiştir.

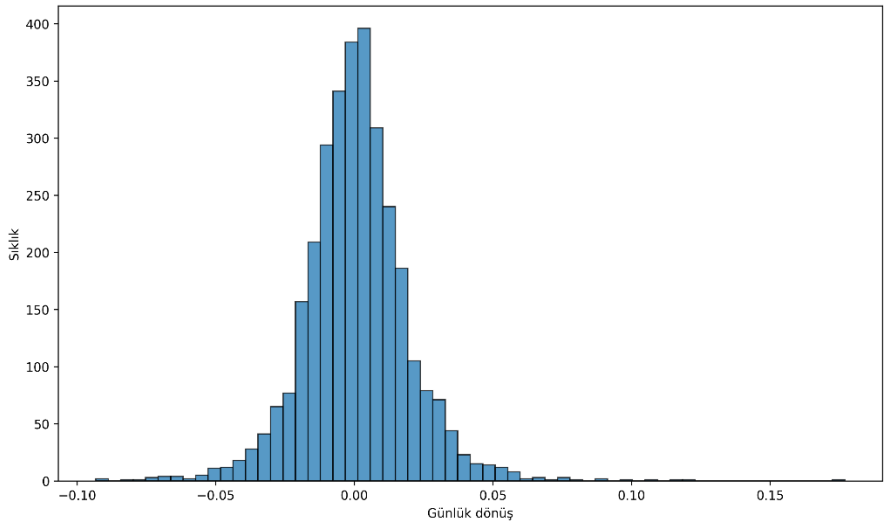

Şekil 3. Günlük getirilerin dağılımı

Dağılımın büyük ölçüde sıfır çevresinde yoğunlaştığı, ancak her iki yönde de uç değerlerin bulunduğu görülmektedir. Bu yapı, hisse senedi fiyat serisinin belirli dönemlerde ani ve yüksek değişimler gösterebildiğine işaret etmektedir.

Tahmin problemi, geçmiş 20 işlem gününe ait Open, High, Low, Close ve Volume bilgilerinin kullanılarak bir sonraki işlem gününün kapanış fiyatının tahmin edilmesi şeklinde tanımlanmıştır. Böylece tüm makine öğrenmesi ve derin öğrenme modelleri aynı tarihsel bilgi penceresi kullanılarak değerlendirilmiş ve modeller arasında karşılaştırılabilir bir deneysel yapı oluşturulmuştur.

B. Tahmin Modelleri

LR, bağımlı ve bağımsız değişkenler arasındaki doğrusal ilişkiyi modelleyen temel regresyon yöntemlerinden biridir [8]. Basit yapısı ve düşük hesaplama maliyeti nedeniyle diğer modeller için temel bir karşılaştırma modeli olarak kullanılmıştır.

RF, çok sayıda karar ağacının birlikte çalışmasına dayanan topluluk öğrenme yöntemidir. Farklı örnekler ve özellik alt kümeleri üzerinde oluşturulan ağaçların sonuçlarını birleştirerek doğrusal olmayan ilişkilerin modellenmesini ve aşırı öğrenme riskinin azaltılmasını amaçlamaktadır [9].

SVR, destek vektör makinelerinin regresyon problemlerine uyarlanmış biçimidir. Özellikle doğrusal olmayan ilişkilerin modellenmesinde çekirdek fonksiyonlarından yararlanabilmesi nedeniyle finansal zaman serisi tahmininde kullanılabilecek güçlü yöntemlerden biridir [10].

XGBoost, ardışık olarak oluşturulan karar ağaçlarına dayanan gradient boosting tabanlı bir algoritmadır. Önceki ağaçların hatalarını azaltacak şekilde yeni ağaçlar oluşturarak yüksek tahmin performansı sağlamayı hedeflemektedir [11]. Düzenlileştirme ve örnekleme gibi mekanizmalar içermesi, modelin genelleme yeteneğini artırmaktadır [12].

Derin öğrenme modellerinden CNN, bir boyutlu evrişim katmanları aracılığıyla zaman serisi içerisindeki kısa dönemli ve yerel örüntüleri öğrenebilmektedir. Bu özellik, ardışık fiyat hareketlerinde tekrar eden yapıların otomatik olarak çıkarılmasına olanak sağlamaktadır [13].

LSTM, klasik tekrarlayan sinir ağlarında görülen uzun dönemli bağımlılıkların öğrenilmesi sorununu azaltmak amacıyla geliştirilmiş bir mimaridir [14]. Hücre durumu ve kapı mekanizmaları sayesinde geçmiş bilgilerden hangilerinin korunacağı veya unutulacağı kontrol edilebilmekte, böylece zaman serilerindeki uzun süreli ilişkiler modellenebilmektedir [15].

GRU ise LSTM'e benzer şekilde ardışık verilerdeki zamansal bağımlılıkları öğrenmek amacıyla kullanılan tekrarlayan bir sinir ağı modelidir. Ancak daha az kapı ve parametre içeren daha sade bir yapıya sahiptir. Bu nedenle bazı problemlerde daha düşük hesaplama maliyetiyle etkili tahmin performansı sağlayabilmektedir.

III. DENEYSEL SONUÇLAR

Önerilen tahmin yaklaşımında LR, RF, XGBoost, CNN, LSTM ve GRU modellerinin performansları MAE, RMSE ve R2 metrikleri kullanılarak karşılaştırılmıştır. Elde edilen sonuçlar Tablo 1'de sunulmuştur. Daha düşük MAE ve RMSE değerleri daha başarılı tahmin performansını ifade ederken, R2 değerinin 1'e yaklaşması modelin gözlenen değişkenliği daha yüksek oranda açıklayabildiğini göstermektedir.

Tablo 1. Makine öğrenmesi ve derin öğrenme modellerinin Sony hisse senedi kapanış fiyatı tahmin performanslarının karşılaştırılması

Model	MAE	RMSE	R^2
GRU	0,3578	0,4772	0,9776
LSTM	0,6013	0,7959	0,9378
CNN	1,0233	1,3030	0,8332
XGBoost	1,2055	1,4232	0,8010
RF	1,2615	1,9448	0,6284
LR	1,4400	2,2367	0,5085

Tablo 1 incelendiğinde, GRU modelinin tüm değerlendirme metriklerinde en yüksek performansı gösterdiği görülmektedir. GRU modeli 0,3578 MAE ve 0,4772 RMSE değerleri ile modeller arasındaki en düşük tahmin hatalarını elde etmiş, ayrıca 0,9776 R2 değeriyle test verisindeki kapanış fiyatı değişiminin yaklaşık %97,8'ini açıklamıştır. Bu sonuç, GRU mimarisinin finansal zaman serilerindeki zamansal bağımlılıkları ve kısa-orta dönemli ardışık örüntüleri başarılı biçimde yakalayabildiğini göstermektedir.

İkinci en başarılı model LSTM olmuştur. LSTM için MAE, RMSE ve R2 değerleri sırasıyla 0,6013, 0,7959 ve 0,9378 olarak hesaplanmıştır. GRU'ya kıyasla hata değerleri daha yüksek olmakla birlikte, LSTM'nin de oldukça yüksek bir açıklayıcılık düzeyine ulaştığı görülmektedir. GRU ve LSTM'nin diğer modellerden belirgin biçimde daha iyi sonuçlar üretmesi, geçmiş fiyat hareketlerinin sıralı yapısını doğrudan işleyebilen tekrarlayan sinir ağı mimarilerinin bu veri seti üzerinde önemli bir avantaj sağladığını göstermektedir.

CNN modeli 1,0233 MAE, 1,3030 RMSE ve 0,8332 R2 ile derin öğrenme modelleri arasında üçüncü sırada yer almıştır. CNN'nin elde ettiği sonuçlar, evrişimsel filtrelerin kısa dönemli yerel örüntüleri yakalamada etkili olduğunu, ancak zaman içerisindeki daha uzun bağımlılıkların modellenmesinde LSTM ve GRU kadar başarılı olmadığını göstermektedir. Buna rağmen CNN, incelenen geleneksel makine öğrenmesi modellerinin büyük bölümünden daha yüksek tahmin başarısı sağlamıştır.

Geleneksel makine öğrenmesi modelleri arasında en başarılı sonuç XGBoost tarafından elde edilmiştir. XGBoost modeli 1,2055 MAE, 1,4232 RMSE ve 0,8010 R2 değerine ulaşmıştır. Bu sonuç, gradient boosting tabanlı yaklaşımın finansal verilerdeki doğrusal olmayan ilişkileri etkili biçimde modelleyebildiğini göstermektedir. Bununla birlikte, XGBoost'un hata değerleri GRU ve LSTM'ye göre belirgin biçimde daha yüksek kalmıştır.

RF modeli 1,2615 MAE, 1,9448 RMSE ve 0,6284 R2 değerleri elde ederken, LR en düşük genel performansı gösteren model olmuştur. LR için MAE 1,4400, RMSE 2,2367 ve R2 0,5085 olarak hesaplanmıştır. Özellikle LR'nin düşük R2 değeri, Sony hisse senedi fiyat hareketlerinin yalnızca doğrusal ilişkilerle yeterince açıklanamadığına işaret etmektedir. RF modeli doğrusal regresyona göre daha başarılı sonuçlar üretmiş olsa da XGBoost ve derin öğrenme modellerinin gerisinde kalmıştır.

Genel olarak Tablo 1'deki sonuçlar, modellerin performans sıralamasının GRU > LSTM > CNN > XGBoost > RF > LR şeklinde olduğunu göstermektedir. Özellikle GRU ve LSTM'nin düşük hata ve yüksek R2 değerleri, zaman serisinin ardışık bağımlılıklarını dikkate alan derin öğrenme yaklaşımlarının Sony hisse senedi kapanış fiyatlarının tahmininde daha etkili olduğunu ortaya koymaktadır. Buna karşılık, geleneksel makine öğrenmesi modelleri içerisinde XGBoost en rekabetçi yaklaşım olarak öne çıkmıştır.

IV. SONUÇLAR

Bu çalışmada, Sony Group Corporation'a ait tarihsel hisse senedi verileri kullanılarak bir sonraki işlem gününün kapanış fiyatının tahmin edilmesi amacıyla dört makine öğrenmesi ve üç derin öğrenme modeli karşılaştırılmıştır. Modellerin performansları MAE, RMSE ve R2 metrikleri kullanılarak değerlendirilmiştir. Elde edilen bulgular, derin öğrenme tabanlı modellerin genel olarak geleneksel makine öğrenmesi yöntemlerinden daha başarılı sonuçlar verdiğini göstermiştir.

Deneysel sonuçlara göre en başarılı model GRU olmuş ve 0,3578 MAE, 0,4772 RMSE ve 0,9776 R2 değerlerine ulaşmıştır. GRU'yu 0,6013 MAE, 0,7959 RMSE ve 0,9378 R2 ile LSTM modeli izlemiştir. CNN modeli de 0,8332 R2 değeriyle başarılı bir performans sergilemiştir. Geleneksel makine öğrenmesi yöntemleri içerisinde ise en iyi sonuç XGBoost modeli tarafından elde edilmiş, buna karşın RF ve özellikle LR modellerinin tahmin performanslarının daha düşük kaldığı görülmüştür.

Bu sonuçlar, Sony hisse senedi fiyat serisinde zamansal bağımlılıkların önemli olduğunu ve bu bağımlılıkları doğrudan modelleyebilen GRU ve LSTM gibi tekrarlayan sinir ağı mimarilerinin tahmin doğruluğu açısından avantaj sağladığını ortaya koymaktadır. Özellikle GRU'nun hem hata metriklerinde en düşük değerlere hem de en yüksek R2 değerine ulaşması, daha sade yapısına rağmen finansal zaman serisi tahmininde etkili bir alternatif olduğunu göstermektedir.

KAYNAKLAR

[1] N. Naifar, "Monetary policy expectations and financial markets: A quantile-on-quantile connectedness approach," The North American Journal of Economics and Finance, vol. 77, Art. no. 102389, 2025.

[2] G. Kumar, S. Jain, and U. P. Singh, "Stock market forecasting using computational intelligence: A survey," Archives of Computational Methods in Engineering, vol. 28, no. 3, pp. 1069–1101, 2021.

[3] J. M. T. Wu, Z. Li, N. Herencsar, B. Vo, and J. C. W. Lin, "A graph-based CNN-LSTM stock price prediction algorithm with leading indicators," Multimedia Systems, vol. 29, no. 3, pp. 1751–1770, 2023.

[4] Y. Li, M. Zhuang, J. Wang, and J. Zhou, "Leveraging multi-time-span sequences and feature correlations for improved stock trend prediction," Neurocomputing, vol. 620, Art. no. 129218, 2025.

[5] P. Lara-Benítez, M. Carranza-García, and J. C. Riquelme, "An experimental review on deep learning architectures for time series forecasting," International Journal of Neural Systems, vol. 31, no. 3, Art. no. 2130001, 2021.

[6] *M. A. A. Afraji, J. Lloret, and L. Peñalver, "An integrated hybrid deep learning framework for intrusion detection in IoT and IIoT networks using CNN-LSTM-GRU architecture," Computation, vol. 13, no. 9, Art. no. 222, 2025.*

[7] J. D. Das, R. K. Thulasiram, C. Henry, and A. Thavaneswaran, “Encoder–decoder based LSTM and GRU architectures for stocks and cryptocurrency prediction,” Journal of Risk and Financial Management, vol. 17, no. 5, Art. no. 200, 2024.
[8] N. Roustaei, “Application and interpretation of linear-regression analysis,” Medical Hypothesis, Discovery and Innovation in Ophthalmology, vol. 13, no. 3, p. 151, 2024.
[9] G. Maselli and A. Nesticò, “Machine learning algorithms and explainable artificial intelligence for property valuation,” Real Estate, vol. 2, no. 3, Art. no. 12, 2025.
[10] S. Karasu, A. Altan, S. Bekiros, and W. Ahmad, “A new forecasting model with wrapper-based feature selection approach using multi-objective optimization technique for chaotic crude oil time series,” Energy, vol. 212, Art. no. 118750, 2020.
[11] Y. Alraba’nah, S. Al-Sharaeh, and G. Al Hindi, “Enhancing intrusion detection using hybrid long short-term memory and XGBoost,” Journal of Soft Computing and Data Mining, vol. 6, no. 1, pp. 247–261, 2025.
[12] P. Zhang, Y. Jia, and Y. Shang, “Research and application of XGBoost in imbalanced data,” International Journal of Distributed Sensor Networks, vol. 18, no. 6, Art. no. 15501329221106935, 2022.
[13] P. Ranjan, R. Itani, and A. Faccia, “An interpretable 1D-CNN framework for stock price forecasting: A comparative study with LSTM and ARIMA,” FinTech, vol. 4, no. 4, Art. no. 63, 2025.
[14] I. D. Mienye, T. G. Swart, and G. Obaido, “Recurrent neural networks: A comprehensive review of architectures, variants, and applications,” Information, vol. 15, no. 9, Art. no. 517, 2024.
[15] M. Krichen and A. Mihoub, “Long short-term memory networks: A comprehensive survey,” AI, vol. 6, no. 9, Art. no. 215, 2025.
[16] Z. Zainuddin, P. A. EA, and M. H. Hasan, “Predicting machine failure using recurrent neural network-gated recurrent unit (RNN-GRU) through time series data,” Bulletin of Electrical Engineering and Informatics, vol. 10, no. 2, pp. 870–878, 2021.

8th International Conference on Engineering, Natural and Social Sciences

September 06-07, 2026: Konya, Turkey

© 2026 Published by All Sciences Academy

https://www.icensos.com/

Bir Yerel Politika Alanı Olarak Biyoçeşitlilik: Seçilmiş Büyükşehir Belediyelerinin Stratejik Planları Üzerine Karşılaştırmalı Bir İnceleme

Miray Özden[1*], Seray Özden Keleş [2]

[1]*Yerel Yönetimler / Sosyal Bilimler MYO, Tekirdağ Namık Kemal Üniversitesi, Türkiye*
[2]*Orman Mühendisliği / Orman Fakültesi, Kastamonu Üniversitesi, Türkiye*

[*](*mirayozden@nku.edu.tr)*

Özet – Biyoçeşitlilik kaybı, iklim değişikliği ve ekosistem bozulmasıyla birlikte günümüzün temel çevresel sorunlarından biridir. Biyoçeşitliliğin korunması uzun süre ulusal ve uluslararası çevre politikalarının konusu olarak ele alınmış olsa da, kentleşmenin doğal alanlar üzerindeki artan baskısı yerel yönetimlerin bu alandaki rolünü güçlendirmiştir. Bu çalışma, biyoçeşitliliğin Türkiye'deki büyükşehir belediyelerinin politika gündeminde ne ölçüde bağımsız bir yerel politika alanına dönüştüğünü incelemeyi amaçlamaktadır.

Araştırmada Tekirdağ, İstanbul ve Diyarbakır Büyükşehir Belediyelerinin 2025-2029 Stratejik Planları, nitel doküman incelemesi ve karşılaştırmalı içerik analizi yoluyla değerlendirilmiştir. Belgeler; biyoçeşitliliğin stratejik hedef düzeyinde görünürlüğü, ekosistem ve habitatların korunması, yerel türlerin korunması, yeşil alanlarla ilişkilendirilmesi, somut faaliyet ve projelerin varlığı ile izleme-performans mekanizmalarının bulunup bulunmadığı boyutlarında incelenmiştir.

Bulgular, her üç belediyede de biyoçeşitliliğin stratejik hedef düzeyinde karşılık bulduğunu, ancak politika araçlarının kapsamı ve ölçülebilirliği açısından belediyeler arasında farklılıklar bulunduğunu ortaya koymaktadır. İstanbul'da biyoçeşitlilik haritalaması ve performans göstergeleri öne çıkarken; Diyarbakır'da ekosistem, yerel bitki türleri ve risk haritalaması çalışmaları, Tekirdağ'da ise biyoçeşitliliğin kırsal ve kentsel kalkınmayla ilişkilendirilmesi dikkat çekmektedir.

Sonuç olarak çalışma, biyoçeşitliliğin belediyelerin geleneksel park ve yeşil alan hizmetlerinin ötesine geçerek gelişmekte olan bağımsız bir yerel politika alanı niteliği kazandığını göstermektedir.

Anahtar Kelimeler – Biyoçeşitlilik, yerel yönetimler, ekosistem, belediyeler, stratejik plan

I. GİRİŞ

Biyolojik çeşitlilik; genetik çeşitlilik, tür çeşitliliği ve ekosistem çeşitliliğini kapsayan, ekolojik sistemlerin devamlılığı ve insan refahı açısından temel öneme sahip bir kavramdır. Sağlıklı ekosistemler; gıda ve su temini, iklimin düzenlenmesi, tozlaşma, hava kalitesi ve doğal afet risklerinin azaltılması gibi çok sayıda ekosistem hizmetinin sürdürülebilirliğine katkı sağlamaktadır. Buna karşılık arazi kullanımındaki değişiklikler, kentleşme, kirlilik, doğal kaynakların aşırı kullanımı ve iklim değişikliği biyoçeşitlilik üzerindeki baskıyı giderek artırmaktadır [1].

Biyoçeşitliliğin korunması geleneksel olarak merkezi yönetimlerin çevre ve doğa koruma politikaları içerisinde değerlendirilmiştir. Bununla birlikte kentleşmenin doğal habitatlar üzerindeki artan etkisi, kentleri biyoçeşitlilik politikalarının önemli uygulama alanlarından biri haline getirmiştir. Arazi kullanımı ve mekânsal planlama, park ve yeşil alanların yönetimi, yerel türlerin korunması, iklim değişikliğine uyum ve kırsal hizmetler gibi pek çok politika alanında belediyelerin aldıkları kararlar kentsel biyoçeşitlilik üzerinde doğrudan veya dolaylı etkiler yaratmaktadır.

Bu dönüşüm uluslararası biyoçeşitlilik politikasında da açık biçimde görülmektedir. Birleşmiş Milletler Biyolojik Çeşitlilik Sözleşmesi kapsamında 2022 yılında kabul edilen Kunming-Montreal Küresel

Biyoçeşitlilik Çerçevesi, 2050 yılına yönelik dört temel amaç ile 2030 yılına kadar gerçekleştirilmesi öngörülen 23 hedef ortaya koymuştur [1]. Çerçevenin özellikle 12. hedefi, kentsel ve yoğun nüfuslu alanlarda yeşil ve mavi alanların miktarının, kalitesinin ve bağlantılılığının artırılması; biyoçeşitliliğin kentsel planlamaya dahil edilmesi; yerel biyoçeşitliliğin geliştirilmesi ve ekolojik bütünlüğün güçlendirilmesi üzerinde durmaktadır [2].

Bu gelişmeler biyoçeşitliliğin korunmasında yerel yönetimlerin konumunu güçlendirirken, biyoçeşitliliğin belediyelerin stratejik politika gündeminde ne ölçüde karşılık bulduğu sorusunu da önemli hale getirmektedir. Bir belediyenin stratejik planında biyoçeşitliliğin yalnızca genel bir çevre koruma söylemi içerisinde anılması ile amaç, hedef, faaliyet ve performans göstergelerine dönüştürülmesi arasında önemli bir farklılık bulunmaktadır.

Kentleşmenin doğal habitatlar üzerindeki artan etkisi, kentleri biyoçeşitliliğin korunması açısından önemli bir yönetişim düzeyi haline getirmiştir. Yerel yönetimlerin arazi kullanımı, mekânsal planlama, yeşil altyapı ve çevre yönetimine ilişkin kararları, biyoçeşitliliğin korunması veya kaybı üzerinde doğrudan ve dolaylı etkiler yaratabilmektedir [7]. Bu nedenle uluslararası biyoçeşitlilik hedeflerinin uygulanmasında kent yönetimlerinin rolü giderek daha fazla önem kazanmaktadır. Nitekim farklı ülkelerdeki 39 kentsel biyoçeşitlilik planını inceleyen Pierce vd. [6], kentlerin biyoçeşitlilik politikalarında eylemlere geniş biçimde yer vermelerine rağmen bu eylemleri ölçülebilir göstergelerle ilişkilendirme düzeylerinin daha sınırlı olduğunu ortaya koymaktadır.

Bu çalışmanın temel araştırma sorusu bu doğrultuda "Biyoçeşitlilik, seçilmiş büyükşehir belediyelerinin stratejik planlarında ne ölçüde özgün bir yerel politika alanı olarak ele alınmaktadır?" şeklinde belirlenmiştir. Bu amaçla Tekirdağ, İstanbul ve Diyarbakır Büyükşehir Belediyelerinin 2025-2029 Stratejik Planları karşılaştırmalı olarak incelenmiştir.

II. MATERYAL VE YÖNTEM

Araştırma nitel araştırma yaklaşımı çerçevesinde tasarlanmış ve veri toplama yöntemi olarak doküman incelemesinden yararlanılmıştır. Araştırmanın temel veri kaynaklarını Tekirdağ Büyükşehir Belediyesi, İstanbul Büyükşehir Belediyesi ve Diyarbakır Büyükşehir Belediyesinin 2025-2029 Stratejik Planları oluşturmaktadır [3], [4], [5].

Araştırmada amaçlı örnekleme yaklaşımı benimsenmiştir. Örneklem seçiminde iki temel ölçüt dikkate alınmıştır. İlk olarak farklı coğrafi, ekolojik ve sosyo-ekonomik özelliklere sahip büyükşehir belediyelerinin karşılaştırılması amaçlanmıştır. İkinci olarak ön inceleme sonucunda biyoçeşitliliğe yalnızca üst politika belgelerine yapılan atıflarda değil, belediyelerin kendi amaç, hedef veya faaliyetleri içerisinde yer veren belediyeler tercih edilmiştir. Böylece kavramın yalnızca belgelerdeki sözcüksel varlığının değil, yerel politika tasarımındaki karşılığının değerlendirilmesi amaçlanmıştır.

Stratejik planlar karşılaştırmalı içerik analizi yoluyla incelenmiştir. Analiz kategorilerinin oluşturulmasında Kunming-Montreal Küresel Biyoçeşitlilik Çerçevesi'nin özellikle kentsel alanlara yönelik 12. hedefi dikkate alınmıştır [1], [2]. Buna göre belgelerde;

- biyoçeşitliliğin stratejik amaç veya hedef düzeyinde görünürlüğü,
- ekosistem ve habitatların korunması,
- yerel türlerin korunması veya geliştirilmesi,
- yeşil/ekolojik alanlarla ilişkilendirilmesi,
- somut faaliyet, proje veya politika araçlarının bulunması,
- izleme ve performans mekanizmalarının bulunması, olmak üzere altı temel boyut aranmıştır.

Analiz sırasında yalnızca "biyoçeşitlilik" sözcüğünün kullanım sıklığı esas alınmamış; ilgili hedefin içeriği, faaliyetler, projeler ve performans göstergeleri birlikte değerlendirilmiştir. Bu nedenle çalışma nicel bir kelime sıklığı analizinden ziyade politika içeriğinin karşılaştırmalı olarak yorumlanmasına dayanmaktadır.

Çalışmanın önemli bir sınırlılığı, stratejik planların belediyelerin politika niyet ve önceliklerini göstermesine karşılık uygulamadaki başarıyı doğrudan ortaya koymamasıdır. Dolayısıyla araştırmada belediyelerin gerçek biyoçeşitlilik performansı değil, biyoçeşitliliğin stratejik politika tasarımındaki görünürlüğü ve kurumsallaşma biçimi değerlendirilmektedir.

III. BULGULAR

İncelenen üç büyükşehir belediyesinin 2025-2029 Stratejik Planları biyoçeşitliliğin belediyelerin politika gündeminde görünür hale geldiğini göstermektedir. Bununla birlikte biyoçeşitliliğin hangi politika alanlarıyla ilişkilendirildiği ve somut politika araçlarına dönüştürülme düzeyi belediyeler arasında farklılaşmaktadır.

Tekirdağ Büyükşehir Belediyesi

Tekirdağ Büyükşehir Belediyesi 2025-2029 Stratejik Planında biyolojik çeşitlilik doğrudan belediyenin stratejik hedeflerinden biriyle ilişkilendirilmiştir. Bu amaç altında yer alan Hedef 6.2, biyolojik çeşitliliğin korunmasını kırsal istihdam ve kentsel kalkınmayla birlikte ele almaktadır Plan kapsamında biyoçeşitliliğin korunması; kırsal istihdamın desteklenmesi, iş birliklerinin geliştirilmesi ve kırsal kalkınmaya katkı sağlanmasıyla birlikte ele alınmaktadır [3].

Tekirdağ örneğinin belirgin özelliği, biyoçeşitliliğin yalnızca kentsel yeşil alan yönetimi içerisinde değil, kentin kırsal yapısı ve tarımsal sürdürülebilirliğiyle ilişkilendirilmesidir. Böylece biyoçeşitlilik ekolojik bir koruma konusu olmanın yanı sıra kırsal kalkınmanın sürdürülebilirliğiyle bağlantılı bir yerel politika unsuru olarak ortaya çıkmaktadır.

İstanbul Büyükşehir Belediyesi

İstanbul Büyükşehir Belediyesi 2025-2029 Stratejik Planında biyoçeşitlilik, "Çevreye Duyarlı İstanbul" tema alanı içerisinde "Kent Ekosistemi ve Biyoçeşitlilik" başlığıyla açık biçimde tanımlanmıştır [4]. Biyoçeşitliliğin ayrı bir politika alt alanı olarak yapılandırılması, kavramın genel çevre veya yeşil alan politikalarından ayrıştırıldığını göstermektedir. Planın A3 amacı "Sürdürülebilir Çevre ve Enerji Yönetimini Güçlendirmek" olarak belirlenmiş ve A3H5 hedefi doğrudan "Kent Ekosistemini ve Biyoçeşitliliği Korumak ve Geliştirmek" biçiminde düzenlenmiştir [4].

İstanbul örneğinde biyoçeşitlilik politikalarının haritalama, izleme, ekolojik temelli yeşil alan uygulamaları ve farkındalık faaliyetleriyle desteklenmesi dikkat çekmektedir. Bu yaklaşım biyoçeşitliliğin yalnızca stratejik söylem düzeyinde kalmadığını, izlenebilir politika araçlarıyla ilişkilendirilmeye çalışıldığını göstermektedir [4].

Diyarbakır Büyükşehir Belediyesi

Diyarbakır Büyükşehir Belediyesi 2025-2029 Stratejik Planında da biyoçeşitlilik doğrudan hedef düzeyinde ele alınmaktadır. Planın H9.3 hedefi "Sürdürülebilir Ekosistemleri Koruyarak Biyoçeşitliliği Artırmak ve Çevre Kirliliğini Azaltmak" şeklinde belirlenmiştir [5]. Plan kapsamında Biyoçeşitlilik ve Dicle Vadisi Risk Haritasının hazırlanması ve akıllı şehircilik uygulamalarıyla bütünleştirilmesi, yerel bitki türlerinin kent peyzajına kazandırılması ve ekolojik yeşil alanların geliştirilmesi öngörülmektedir [5].

Diyarbakır örneğinde özellikle Dicle Vadisi'nin politika içeriğine dahil edilmesi, biyoçeşitliliğin kentin özgün ekolojik değerleri üzerinden yerelleştirilmesi açısından dikkat çekmektedir. Yerel bitki türlerinin kent peyzajında kullanılması da biyoçeşitlilik politikası ile yeşil alan yönetimi arasında doğrudan bir ilişki kurmaktadır.

Araştırmaya konu olan üç büyükşehir belediyesinin biyoçeşitlilik ile ilgili stratejik planlarında yer alan amaç ve hedeflere ilişkin analiz aşağıda Tablo 1'de özetlenmiştir:

Tablo 1. Seçilmiş Büyükşehir Belediyelerinin Biyoçeşitlilik Politikalarının Karşılaştırılması

Analiz Boyutu	**Tekirdağ Büyükşehir Belediyesi**	**İstanbul Büyükşehir Belediyesi**	**Diyarbakır Büyükşehir Belediyesi**
Biyoçeşitliliğin stratejik düzeyde ele alınması	Var	Var	Var
Ekosistem ve habitatların korunmasına yönelik yaklaşım	Kısmen	Var	Var
Yerel türlerin korunması/geliştirilmesi	Kısmen	Var	Var
Yeşil/ekolojik alanlarla ilişkilendirme	Var	Var	Var
Somut politika, faaliyet veya proje	Var	Var	Var
İzleme ve performans mekanizması	Kısmen	Var	Kısmen

Analiz Boyutu	Tekirdağ Büyükşehir Belediyesi	İstanbul Büyükşehir Belediyesi	Diyarbakır Büyükşehir Belediyesi
Öne çıkan politika yaklaşımı	Kırsal kalkınma ve tarımsal sürdürülebilirlik	Kent ekosistemi, biyoçeşitlilik haritalaması ve izleme	Ekosistemlerin korunması, yerel türler ve Dicle Vadisi

*Tablo, belirlenen büyükşehir belediyelerinin stratejik planları incelenerek oluşturulmuştur.

Tablo 1'de görüldüğü üzere üç belediyede de biyoçeşitlilik stratejik politika gündeminde karşılık bulmaktadır. Buna karşın politika içeriğinin ayrıntı düzeyi ve biyoçeşitliliğin ilişkilendirildiği yerel sorun alanları farklılaşmaktadır.

IV. TARTIŞMA

Araştırmanın bulguları biyoçeşitliliğin incelenen büyükşehir belediyelerinde yalnızca geleneksel park ve yeşil alan hizmetleri içerisinde değerlendirilmediğini, giderek daha belirgin bir stratejik politika konusu haline geldiğini göstermektedir. Bu durum küresel biyoçeşitlilik politikasındaki yerelleşme eğilimiyle uyumludur.

Kunming-Montreal Küresel Biyoçeşitlilik Çerçevesi'nin 12. hedefinde kentsel yeşil ve mavi alanların yalnızca miktarının artırılması yeterli görülmemekte; bu alanların niteliği ve ekolojik bağlantılılığı, yerel biyoçeşitliliğin geliştirilmesi ve biyoçeşitliliğin kentsel planlamaya dahil edilmesi de vurgulanmaktadır [1], [2]. İncelenen belediyelerde ekosistem, yerel tür, ekolojik yeşil alan, haritalama ve izleme gibi unsurların görülmesi, yerel stratejik planların en azından politika tasarımı düzeyinde bu daha geniş yaklaşımın bazı unsurlarını yansıttığını göstermektedir.

Bu çalışmada stratejik hedeflerin performans ve izleme araçlarına dönüşme düzeyinin belediyeler arasında farklılaşması, uluslararası literatürdeki bulgularla benzerlik göstermektedir. Pierce vd. [6], inceledikleri 39 kentsel biyoçeşitlilik planının tamamında eylemler bulunmasına karşın planların %67'sinde nicel göstergelere yer verildiğini belirlemiştir. Mahmoud vd. [8] ise on Avrupa kentinin doğa planlarını değerlendirdikleri çalışmalarında izleme ve değerlendirme mekanizmalarının önemli bir gelişme alanı olduğunu göstermektedir. Bu durum, biyoçeşitliliğin stratejik belgelerde görünür hale gelmesinin tek başına politika kurumsallaşmasının yeterli bir göstergesi olmadığını düşündürmektedir.

Varshney vd. [9] tarafından Yeni Zelanda'daki kentsel biyoçeşitlilikle ilişkili politika, strateji ve planlama belgeleri üzerine gerçekleştirilen incelemede de benzer biçimde, biyoçeşitliliğin kentsel gelişme politikalarına açık hedeflerle dahil edilmesinin yanı sıra bu hedeflerin izleme ve yönetim mekanizmalarıyla desteklenmesi gerektiği vurgulanmaktadır. Araştırmacılar, mevcut politika ve planlama belgelerinde biyoçeşitliliğin korunmasına ilişkin unsurlar bulunmasına rağmen, biyoçeşitliliğin geliştirilmesine yönelik açık politika sonuçlarının ve izleme mekanizmalarının yetersiz kalabildiğini ortaya koymaktadır [9]. Bu açıdan çalışmamızda incelenen büyükşehir belediyelerinde biyoçeşitliliğin stratejik hedef düzeyinde görünür hale gelmesi önemli olmakla birlikte, söz konusu hedeflerin ölçülebilir göstergeler ve sistematik izleme araçlarıyla desteklenmesi yerel biyoçeşitlilik politikalarının kurumsallaşması açısından belirleyici görünmektedir.

Biyoçeşitliliğin yerel politikalara entegrasyonu, çevre politikalarının diğer bileşenleriyle kurulan ilişki açısından da önem taşımaktadır. Perera vd. [10], farklı kentlerde uygulanan 12 mavi-yeşil planlama aracını karşılaştırdıkları çalışmalarında bitki örtüsü, yeşil altyapı, su yönetimi ve habitat gibi unsurların bütünleşik biçimde ele alınmasının kentsel çevre politikaları açısından önemli avantajlar sağladığını ortaya koymaktadır. Çalışmada ayrıca politika araçlarının kapsam ve önceliklerinin kentlerin düzenleyici yapıları ve yerel politika önceliklerine bağlı olarak farklılaştığı belirlenmiştir. Bu bulgu, Tekirdağ, İstanbul ve Diyarbakır örneklerinde biyoçeşitliliğin farklı yerel politika alanlarıyla ilişkilendirilmesi yönündeki araştırma bulgularını desteklemektedir.

Bununla birlikte biyoçeşitliliğin yerelleşmesi belediyelerde aynı biçimde gerçekleşmemektedir. Tekirdağ'da kırsal kalkınma ve tarımsal sürdürülebilirlik, İstanbul'da yoğun kentleşme koşullarında kent ekosistemi ve izleme, Diyarbakır'da ise Dicle Vadisi ve yerel bitki türleri ön plana çıkmaktadır. Bu farklılık biyoçeşitlilik politikasının küresel hedeflerin basit biçimde yerel belgelere aktarılmasından ziyade, yerel ekolojik ve sosyo-ekonomik koşullara göre farklılaşan bir politika alanı olarak geliştiğine işaret etmektedir.

Karşılaştırmanın ortaya koyduğu bir diğer nokta stratejik görünürlük ile kurumsallaşma arasındaki ayrımdır. Biyoçeşitliliğin stratejik hedeflerde yer alması önemli olmakla birlikte, politikanın uygulanabilirliği açısından envanter, haritalama, performans göstergeleri ve izleme araçlarıyla desteklenmesi gerekmektedir. Bu nedenle yerel biyoçeşitlilik politikasının gelişmişliği yalnızca kavramın stratejik planda bulunup bulunmadığı üzerinden değerlendirilmemelidir.

V. SONUÇLAR

Bu çalışmada Tekirdağ, İstanbul ve Diyarbakır Büyükşehir Belediyelerinin 2025-2029 Stratejik Planlarından hareketle biyoçeşitliliğin büyükşehir belediyelerinin stratejik politika gündemindeki yeri karşılaştırmalı olarak incelenmiştir.

Araştırma sonucunda biyoçeşitliliğin üç belediyede de stratejik düzeyde karşılık bulduğu, ancak politika yaklaşımının kentsel ve ekolojik özelliklere bağlı olarak farklılaştığı belirlenmiştir. Tekirdağ'da biyoçeşitlilik kırsal kalkınma ve tarımsal sürdürülebilirlik; İstanbul'da kent ekosistemi, haritalama ve izleme; Diyarbakır'da ise ekosistemlerin korunması, Dicle Vadisi ve yerel bitki türleri üzerinden şekillenmektedir.

Bu sonuçlar, biyoçeşitliliğin belediyeler açısından geleneksel park ve yeşil alan hizmetlerinin ötesine geçerek gelişmekte olan özgün bir yerel politika alanı niteliği kazandığına işaret etmektedir. Bununla birlikte stratejik planlarda biyoçeşitlilik hedeflerine yer verilmesi uygulamadaki başarının göstergesi değildir. Yerel biyoçeşitlilik politikalarının daha güçlü biçimde kurumsallaşması için biyoçeşitlilik envanterlerinin hazırlanması, yerel tür ve habitatların izlenmesi, ölçülebilir performans göstergelerinin geliştirilmesi ve biyoçeşitliliğin mekânsal planlama başta olmak üzere farklı belediye politikalarına bütünleştirilmesi önem taşımaktadır.

Gelecek araştırmalarda belediyelerin performans programları ve faaliyet raporlarının stratejik planlarla birlikte incelenmesi, planlanan politikaların uygulamaya ne ölçüde aktarıldığının değerlendirilmesine imkân sağlayacaktır.

KAYNAKLAR

[1] Convention on Biological Diversity, *Kunming-Montreal Global Biodiversity Framework*, Decision 15/4, Montreal, 2022. https://www.cbd.int/doc/decisions/cop-15/cop-15-dec-04-en.

[2] Convention on Biological Diversity, "Target 12: Enhance Green Spaces and Urban Planning for Human Well-Being and Biodiversity," *Kunming-Montreal Global Biodiversity Framework*, 2022. https://www.cbd.int/gbf/targets/12

[3] Tekirdağ Büyükşehir Belediyesi, *2025–2029 Stratejik Planı*, Tekirdağ, 2024. https://www.tekirdag.bel.tr/content/WebSource/file/statejik_plan/stratejik_plan_2025_2029.

[4] İstanbul Büyükşehir Belediyesi, *2025–2029 Stratejik Planı*, İstanbul, 2024. http://www.sp.gov.tr/upload/xSPStratejikPlan/files/Sk2fw+ibb_sp_25-29.

[5] Diyarbakır Büyükşehir Belediyesi, *2025–2029 Stratejik Planı*, Diyarbakır, 2024. http://www.sp.gov.tr/upload/xSPStratejikPlan/files/wjZiK+2025_Stratejik_Plan.

[6] J. R. Pierce, M. A. Barton, M. M. J. Tan, G. Oertel, M. D. Halder, P. A. Lopez-Guijosa and R. Nuttall, "Actions, indicators, and outputs in urban biodiversity plans: A multinational analysis of city practice," *PLOS ONE*, vol. 15, no. 7, e0235773, 2020. DOI: 10.1371/journal.pone.0235773

[7] J. A. Puppim de Oliveira, O. Balaban, C. N. H. Doll, R. Moreno-Peñaranda, A. Gasparatos, D. Iossifova and A. Suwa, "Cities and biodiversity: Perspectives and governance challenges for implementing the Convention on Biological Diversity (CBD) at the city level," *Biological Conservation*, vol. 144, no. 5, pp. 1302–1313, 2011. DOI: 10.1016/j.biocon.2010.12.007

[8] I. Mahmoud, G. Dubois, C. Liquete et al., "Understanding collaborative governance of biodiversity-inclusive urban planning: Methodological approach and benchmarking results for urban nature plans in 10 European cities," *Urban Ecosystems*, vol. 28, article 17, 2025. DOI: 10.1007/s11252-024-01656-5.

[9] K. Varshney, M. MacKinnon, M. Pedersen Zari, D. Shanahan, C. Woolley, C. Freeman and Y. van Heezik, "Biodiverse residential development: A review of New Zealand policies and strategies for urban biodiversity," *Urban Forestry & Urban Greening*, vol. 94, 128276, 2024, doi: 10.1016/j.ufug.2024.128276.

[10] A. C. S. Perera, P. J. Davies and P. L. Graham, "A global review of urban blue-green planning tools," *Land Use Policy*, vol. 140, pp. 1–11, 107093, 2024, doi: 10.1016/j.landusepol.2024.107093.

8th International Conference on Engineering, Natural and Social Sciences

September 06-07, 2026: Konya, Turkey

© 2026 Published by All Sciences Academy

https://www.icensos.com/

İklim Değişikliğine Uyumda Yerel Yönetimler: Aşırı Sıcaklarla Mücadele Politikaları Üzerine Bir Değerlendirme

Miray Özden[1*], Seray Özden Keleş [2]

[1]*Yerel Yönetimler / Sosyal Bilimler MYO, Tekirdağ Namık Kemal Üniversitesi, Türkiye*
[2]*Orman Mühendisliği / Orman Fakültesi, Kastamonu Üniversitesi, Türkiye*

[*](*mirayozden@nku.edu.tr)*

Özet – İklim değişikliğinin kentler üzerindeki en belirgin etkilerinden biri, aşırı sıcaklıkların ve sıcak hava dalgalarının sıklık, süre ve şiddetindeki artıştır. Yoğun yapılaşma, geçirimsiz yüzeyler, yeşil alanların yetersizliği ve kentsel ısı adası etkisi, kentlerde sıcaklık kaynaklı riskleri daha da artırmaktadır. Bu durum, iklim değişikliğine uyum politikalarının yerel yönetimler açısından önemini güçlendirmektedir. Bu çalışmanın amacı, aşırı sıcaklarla mücadele politikalarının büyükşehir belediyelerinin iklim değişikliğine uyum politikalarında nasıl ele alındığını karşılaştırmalı olarak değerlendirmektir. Araştırmada İzmir, Ankara ve Antalya Büyükşehir Belediyeleri örnek olarak seçilmiş; belediyelerin iklim değişikliği eylem planları ve ilgili resmi politika belgeleri nitel doküman incelemesi ve karşılaştırmalı içerik analizi yöntemiyle incelenmiştir. Analiz kapsamında aşırı sıcakların risk olarak tanımlanması, kırılgan grupların dikkate alınması, yeşil-mavi altyapı ve gölgeleme uygulamaları, kentsel ısı adasının azaltılması, erken uyarı ve bilgilendirme mekanizmaları ile izleme ve performans araçları değerlendirilmiştir. Bulgular, üç büyükşehir belediyesinde de aşırı sıcakların iklim değişikliğine uyum kapsamında dikkate alındığını, ancak politika araçlarının kapsam ve ayrıntı düzeylerinin farklılaştığını göstermektedir. Sonuç olarak aşırı sıcaklarla mücadelenin yerel iklim politikalarında giderek görünür hale geldiği; buna karşılık sıcaklık riskinin halk sağlığı, sosyal kırılganlık, erken uyarı ve mekânsal planlama boyutlarını bütünleştiren özel ısı eylem planlarının geliştirilmesine ihtiyaç bulunduğu değerlendirilmektedir.

Anahtar Kelimeler – İklim değişikliği, yerel yönetimler, kentsel ısı adası, iklim uyumu, yerel politika

I. GİRİŞ

İklim değişikliği, kentlerin karşı karşıya bulunduğu çevresel, sosyal ve ekonomik risklerin niteliğini değiştirmekte; özellikle aşırı hava olaylarının sıklığı ve şiddetindeki artış kentsel dirençlilik politikalarını giderek daha önemli hale getirmektedir. Bu riskler içerisinde aşırı sıcaklıklar ve sıcak hava dalgaları, insan sağlığından altyapıya, enerji tüketiminden kamusal alan kullanımına kadar farklı politika alanlarını etkileyen çok boyutlu bir sorun niteliğindedir.

Kentler, yapılı çevrenin yoğunluğu nedeniyle aşırı sıcaklardan özel olarak etkilenmektedir. Beton ve asfalt gibi yüzeylerin ısıyı depolaması, bitki örtüsünün ve geçirgen yüzeylerin azalması, yapı yoğunluğu ve insan faaliyetlerinden kaynaklanan ısı, kent merkezlerinde çevre alanlardan daha yüksek sıcaklıkların oluşmasına neden olabilmektedir. Kentsel ısı adası olarak tanımlanan bu durum, iklim değişikliğinin yol açtığı sıcaklık artışlarıyla birleştiğinde kent nüfusunun aşırı sıcaklara maruz kalma düzeyini yükseltmektedir [1].

Hükümetlerarası İklim Değişikliği Paneli (IPCC), kent ve yerel yönetimlerin iklim değişikliğine uyumun gerçekleştirilmesinde temel aktörlerden biri olduğunu belirtmektedir. Arazi kullanım kararları, yeşil altyapı, yapı standartları, kamusal alanların düzenlenmesi ve sosyal politikalar gibi yerel yönetimlerin

doğrudan veya dolaylı müdahale edebildiği alanlar, sıcaklık kaynaklı risklerin azaltılması açısından önem taşımaktadır [1].

Aşırı sıcaklıkların etkileri toplumun tüm kesimlerinde aynı düzeyde ortaya çıkmamaktadır. Yaşlılar, çocuklar, kronik hastalığı bulunanlar, açık alanda çalışanlar, düşük gelirli gruplar ve uygun soğutma imkânlarına erişimi sınırlı bireyler sıcaklık risklerine karşı daha kırılgan olabilmektedir. Bu nedenle aşırı sıcaklarla mücadele yalnızca fiziksel çevrenin soğutulmasına yönelik teknik bir konu değil; aynı zamanda halk sağlığı ve sosyal kırılganlık boyutları bulunan bir iklim uyum alanıdır [2].

Dünya Sağlık Örgütü, sıcaklık kaynaklı sağlık risklerinin azaltılmasında ısı-sağlık eylem planlarını önemli bir politika aracı olarak değerlendirmektedir. Bu planların yönetişim, sıcaklık-sağlık erken uyarı sistemi, risk altındaki grupların belirlenmesi, risk iletişimi, sağlık sisteminin hazırlığı, ısıya maruziyetin azaltılması, sürveyans ile izleme ve değerlendirme gibi birbirini tamamlayan unsurları içermesi önerilmektedir [2].

Uluslararası literatür de aşırı sıcaklarla mücadelenin tek bir politika aracına indirgenemeyeceğini göstermektedir. Sıcaklık uyarı sistemleri ve bilgilendirme faaliyetleri gibi kısa dönemli müdahalelerin yanı sıra kentsel yeşillendirme, gölgeleme, serin yüzeyler, yapı tasarımı ve mekânsal planlama gibi uzun dönemli önlemlerin birlikte ele alınması gerekmektedir [3].

Bu bağlamda çalışmanın temel araştırma sorusu "Aşırı sıcaklar ve sıcak hava dalgaları, büyükşehir belediyelerinin iklim değişikliğine uyum politikalarında nasıl ele alınmakta ve bu risklere karşı hangi yerel politika araçları geliştirilmektedir?" şeklinde belirlenmiştir. Araştırmada İzmir, Ankara ve Antalya Büyükşehir Belediyelerinin politika belgeleri karşılaştırmalı olarak incelenerek aşırı sıcakların Türkiye'deki yerel iklim politikalarında ne ölçüde somut bir uyum alanına dönüştüğü değerlendirilmektedir.

II. MATERYAL VE YÖNTEM

Araştırma nitel araştırma yaklaşımı çerçevesinde tasarlanmış ve veri toplama yöntemi olarak doküman incelemesinden yararlanılmıştır. Araştırmanın temel veri kaynaklarını İzmir Büyükşehir Belediyesi Sürdürülebilir Enerji ve İklim Eylem Planı, Ankara İli Yerel İklim Değişikliği Eylem Planı ve Antalya Büyükşehir Belediyesi Sürdürülebilir Enerji ve İklim Eylem Planı ile aşırı sıcaklara ilişkin ilgili resmi politika belgeleri oluşturmaktadır [4]-[6].

Araştırmada amaçlı örnekleme yöntemi kullanılmıştır. İzmir, Ankara ve Antalya'nın seçilmesinde farklı iklimsel ve kentsel özelliklere sahip olmalarının yanı sıra belediyelerin iklim değişikliğine uyum konusunda planlama belgelerine sahip olmaları ve bu belgelerde sıcaklık kaynaklı risklere yer vermeleri etkili olmuştur. Böylece farklı yerel koşullarda aşırı sıcak riskinin nasıl tanımlandığının ve hangi politika araçlarıyla ilişkilendirildiğinin karşılaştırılması amaçlanmıştır.

Dokümanlar karşılaştırmalı içerik analizi yoluyla değerlendirilmiştir. Analiz çerçevesinin oluşturulmasında IPCC'nin kentsel iklim uyumuna ilişkin değerlendirmeleri ile Dünya Sağlık Örgütünün ısı-sağlık eylem planlamasına ilişkin yaklaşımından yararlanılmıştır [1], [2]. Buna göre belgelerde;

- aşırı sıcaklık ve sıcak hava dalgasının açık bir iklim riski olarak tanımlanması,
- kırılgan grupların dikkate alınması,
- yeşil-mavi altyapı, gölgeleme ve doğa temelli çözümler,
- kentsel ısı adası etkisinin azaltılmasına yönelik önlemler,
- erken uyarı, bilgilendirme ve toplumsal farkındalık mekanizmaları,
- izleme, haritalama ve performans araçları, olmak üzere altı analiz boyutu belirlenmiştir.

Kodlamada ilgili unsurun belgelerde açık bir risk, hedef, faaliyet veya politika aracıyla desteklenmesi "Var"; dolaylı veya sınırlı biçimde ele alınması "Kısmen"; belirlenebilir bir politika karşılığının bulunmaması ise "Yok" olarak değerlendirilmiştir. Bu sınıflandırma nicel bir performans puanı olarak değil, belediyelerin politika tasarımları arasındaki farklılıkları görünür kılmaya yönelik betimsel bir karşılaştırma aracı olarak kullanılmıştır.

Araştırmanın temel sınırlılığı, incelenen belgelerin politika hedeflerini ve planlanan eylemleri yansıtmasıdır. Dolayısıyla çalışma belediyelerin aşırı sıcaklarla mücadelede uygulamadaki başarısını veya

sıcaklığa bağlı sağlık sonuçlarındaki değişimi ölçmemekte; yerel politika tasarımının kapsamını değerlendirmektedir.

III. BULGULAR

İncelenen belgeler aşırı sıcaklıkların üç büyükşehir belediyesinin de iklim değişikliğine uyum gündeminde karşılık bulduğunu göstermektedir. Bununla birlikte sıcaklık riskinin tanımlanması, mekânsal olarak analiz edilmesi ve somut politika araçlarına dönüştürülmesi açısından belediyeler arasında farklılıklar bulunmaktadır.

İzmir Büyükşehir Belediyesi

İzmir Sürdürülebilir Enerji ve İklim Eylem Planında sıcak hava dalgaları kentin karşı karşıya bulunduğu iklim riskleri arasında ele alınmaktadır [4]. Planda geçmiş sıcak hava dalgalarının kent üzerindeki etkilerine yer verilmesi ve sıcaklık kaynaklı sağlık risklerinin dikkate alınması, aşırı sıcakların yalnızca geleceğe yönelik bir iklim projeksiyonu olarak değil, mevcut bir kentsel risk olarak değerlendirildiğini göstermektedir.

İzmir örneğinde kentsel ısı adası etkisi özellikle ön plana çıkmaktadır. Kent merkezindeki yeşil altyapının sınırlılığı, bitki örtüsünün azlığı ve sert yapay yüzeylerin yaygınlığı kentsel ısı adasını güçlendiren faktörler arasında değerlendirilmektedir [4].

Plan kapsamında kentsel ısı adası modellemesinin yapılması, ısı yönetimi açısından öncelikli bölgelerin belirlenmesi ve uygun kentsel ısı yönetimi çözümlerinin geliştirilmesi öngörülmektedir. Yeşil altyapının artırılması, kentsel malzemelerin özelliklerinin değerlendirilmesi ve doğa temelli çözümler bu yaklaşımın önemli bileşenlerini oluşturmaktadır.

İzmir'in politika yaklaşımının dikkat çekici bir diğer yönü sıcaklık riskinin izlenmesine yönelik göstergelerin bulunmasıdır. Aşırı sıcak veya soğuk gün/gece sayısı, sıcak/soğuk hava dalgası sıklığı ve sıcak hava dalgası riski bulunan alanların değerlendirilmesi gibi göstergeler planın izleme yaklaşımı içerisinde yer almaktadır [4]. Bu durum sıcaklık riskinin yalnızca genel bir iklim uyum söylemi içerisinde değil, ölçülebilir bir risk alanı olarak ele alınmaya çalışıldığını göstermektedir.

Ankara Büyükşehir Belediyesi

Ankara İli Yerel İklim Değişikliği Eylem Planında sıcaklık artışları, sıcak hava dalgaları ve kentsel ısı adası etkisi açık biçimde ele alınmaktadır [5]. Planda iklim projeksiyonları doğrultusunda Ankara'nın gelecekte daha sıcak bir kent haline geleceği ve sıcak hava dalgaları ile kentsel ısı adasının önemli bir iklimsel risk oluşturacağı değerlendirilmektedir.

Ankara örneğinin belirgin özelliklerinden biri, sıcaklık riskinin mekânsal analizlerle ilişkilendirilmesidir. 2019 ve 2020 yıllarına ilişkin yüzey sıcaklığı haritalarından yararlanılarak sıcak hava dalgaları ve kentsel ısı adası açısından riskli olabilecek alt bölgeler değerlendirilmiştir [5].

Plan kapsamında "Kentsel Isı Adası Azaltımı Eylemleri" ayrıca tanımlanmıştır. Bu doğrultuda ısı adası etkisinin konumuna ilişkin bilimsel ölçümlerin yapılması, hassas bölgelerin belirlenmesi ve sıcaklığın halk sağlığı üzerindeki etkilerinin modellenmesi öngörülmektedir. Daha da önemlisi, kentsel ısı adasından kaynaklanan sağlık sorunlarını azaltmak amacıyla bir Isı Dalgası Eylem Planı hazırlanması alt eylem olarak belirlenmiştir [5].

Kentsel ısı adasının azaltılmasında açık ve yeşil alanların artırılması, yeşil sistemlerin planlanması, yeşil koridorların oluşturulması, kentsel dönüşüm ve yeşil çatı uygulamalarından yararlanılması da Ankara'nın politika araçları arasında bulunmaktadır.

Antalya Büyükşehir Belediyesi

Antalya Büyükşehir Belediyesi Sürdürülebilir Enerji ve İklim Eylem Planında sıcak hava dalgaları, kentin iklim değişikliğine bağlı önemli risklerinden biri olarak değerlendirilmektedir [6]. Antalya'nın Akdeniz iklimi özellikleri ve yaz aylarında görülen yüksek sıcaklıklar nedeniyle aşırı sıcaklık riski, kentin iklim uyum politikaları açısından özel önem taşımaktadır.

Antalya SECAP kapsamında ekosistem hizmetleri, biyoçeşitlilik ve yeşil alanlara ilişkin uyum eylemleri arasında kentsel ısı adası bağlamında etkilenebilirlik haritalarının hazırlanması öngörülmektedir [6]. Ulaşım akslarının yeşil koridorlara dönüştürülmesi, yeşil-mavi altyapının geliştirilmesi ve ticari binalarda yeşil çatı uygulamalarının yaygınlaştırılması da sıcaklık etkilerinin azaltılmasıyla ilişkilendirilmektedir.

Bunun yanında açık renkli zemin kaplama malzemelerinin kullanılması ve su geçirimli yüzeylerin artırılması gibi yapılı çevreye yönelik politika araçlarının bulunması Antalya örneğinin dikkat çekici yönlerinden biridir. Açık renkli yüzeylere yönelik pilot alanların belirlenmesi ve sıcaklık takibi yapılarak uygulamanın etkisinin gözlemlenmesi öngörülmektedir [6].

Antalya'nın afet risk azaltma ve iklime uyum yaklaşımında sıcak hava dalgası ayrıca bir risk alanı olarak tanımlanmış; sıcak hava dalgası ve şehir ısı adası etkisinin azaltılması, binalarda enerji verimliliğinin geliştirilmesi ve aşırı sıcak hava olaylarına ilişkin toplumsal farkındalığın artırılması hedeflenmiştir [7].

Araştırmaya konu olan üç büyükşehir belediyesinin sıcaklarla mücadele ile ilgili politika belgelerinde yer alan, analiz aşağıda Tablo 1'de özetlenmiştir:

Tablo 1. Seçilmiş Büyükşehir Belediyelerinin Aşırı Sıcaklıklarla Mücadele Politikalarının Karşılaştırılması

Analiz Boyutu	İzmir Büyükşehir Belediyesi	Ankara Büyükşehir Belediyesi	Antalya Büyükşehir Belediyesi
Aşırı sıcak/sıcak hava dalgasının açık bir risk olarak tanımlanması	Var	Var	Var
Kırılgan grupların dikkate alınması	Var	Var	Var
Yeşil-mavi altyapı ve doğa temelli çözümler	Var	Var	Var
Kentsel ısı adasının azaltılmasına yönelik özel önlemler	Var	Var	Var
Erken uyarı, bilgilendirme ve farkındalık mekanizmaları	Kısmen	Kısmen	Var
Haritalama, izleme ve performans araçları	Var	Var	Var
Öne çıkan politika yaklaşımı	Isı adası modellemesi, yeşil altyapı ve izleme	Riskli alanların belirlenmesi, halk sağlığı ve Isı Dalgası Eylem Planı	Etkilenebilirlik haritalaması, yeşil altyapı, serin yüzeyler ve farkındalık

*Tablo, belirtilen dökümanlar incelenerek yazarlardan tarafından oluşturulmuştur.

Tablo 1'de görüldüğü üzere üç belediyenin de aşırı sıcakları iklim değişikliğine uyum kapsamında değerlendirdiği görülmektedir. En belirgin ortak politika alanı kentsel ısı adasının azaltılması ve yeşil altyapının güçlendirilmesidir. Buna karşılık erken uyarı, sıcaklık-sağlık iletişimi ve doğrudan sıcak hava dalgasına özgü kurumsal müdahale mekanizmaları daha sınırlı görünmektedir..

IV. TARTIŞMA

Araştırmanın bulguları aşırı sıcaklıkların incelenen büyükşehir belediyelerinin iklim uyum gündeminde görünür bir risk alanı haline geldiğini göstermektedir. Bu durum, kent ve yerel yönetimlerin iklim değişikliğine uyumun gerçekleştirilmesindeki rolüne ilişkin uluslararası eğilimlerle uyumludur. IPCC, yerel yönetimlerin kentsel uyumda temel aktörler olduğunu; buna karşılık izleme ve değerlendirme sistemlerindeki eksikliklerin iklim dirençli kentsel gelişmeyi sınırlandırdığını belirtmektedir [1].

İzmir, Ankara ve Antalya örneklerinin ortak yönlerinden biri, sıcaklık riskinin önemli ölçüde kentsel ısı adası ve yeşil altyapı üzerinden ele alınmasıdır. Yeşil alanların artırılması, ağaçlandırma, yeşil koridorlar, yeşil çatılar ve mavi-yeşil altyapı uygulamaları üç kentte farklı düzeylerde politika araçları olarak ortaya çıkmaktadır. Bu yaklaşım uluslararası kent uygulamalarıyla da benzerlik göstermektedir. Kentlerin aşırı ısınmaya karşı geliştirdikleri binlerce yerel eylemi inceleyen çalışmalar, yeşil ve su temelli çözümlerin yerel sıcaklık politikalarında en yaygın araçlar arasında bulunduğunu göstermektedir [8].

Bununla birlikte aşırı sıcaklarla mücadele yalnızca kentlerin fiziksel olarak serinletilmesiyle sınırlı değildir. Dünya Sağlık Örgütünün yaklaşımı, etkili bir ısı-sağlık politikasının risk altındaki nüfusun belirlenmesi, erken uyarı, iletişim, sağlık sistemi hazırlığı, sürveyans ve izleme-değerlendirme mekanizmalarını da içermesi gerektiğini ortaya koymaktadır [2]. Bu açıdan değerlendirildiğinde incelenen belediyelerde mekânsal ve çevresel müdahalelerin görece güçlü; sıcaklık-sağlık erken uyarı sistemleri ve sıcak hava dalgasına özgü operasyonel müdahale mekanizmalarının ise geliştirmeye açık olduğu görülmektedir.

Aşırı sıcaklara uyum konusunda uluslararası deneyimler de benzer bir soruna işaret etmektedir. Sıcaklık-sağlık eylem planlarını sistematik olarak inceleyen çalışmalar, kısa dönemli uyarı ve iletişim önlemlerinin yaygınlaşmasına karşın uzun dönemli kentsel planlama müdahalelerinin daha sınırlı uygulanabildiğini göstermektedir [3]. Diğer taraftan küresel ölçekte gerçekleştirilen aşırı sıcak uyumu incelemeleri, uygulamaların coğrafi ve sosyo-ekonomik koşullara göre önemli ölçüde farklılaştığını ve tek tip bir uyum modelinin bütün kentler açısından yeterli olmadığını ortaya koymaktadır [9].

Bu bağlamda Ankara'nın özel bir Isı Dalgası Eylem Planı hazırlanmasını politika hedefi olarak tanımlaması önemlidir. Benzer biçimde Antalya'da sıcak hava dalgasının afet ve iklim uyum planlamasında özel bir tehlike alanı olarak ele alınması ve İzmir'de sıcak hava dalgası sıklığına ilişkin göstergelerin kullanılması, Türkiye'deki yerel iklim politikalarının genel "iklim değişikliğine uyum" yaklaşımından daha spesifik bir ısı yönetişimi anlayışına doğru gelişebileceğine işaret etmektedir.

Kent iklim eylem planları üzerine gerçekleştirilen geniş ölçekli araştırmalar da uygulama ve izleme boyutlarının önemini göstermektedir. Aboagye ve Sharifi [10] tarafından 257 kentsel iklim eylem planı üzerinde gerçekleştirilen değerlendirmede, planların önemli bölümünün orta düzeyde yeterliliğe sahip olduğu ve özellikle uygulama ile izleme kriterlerinde eksikliklerin bulunduğu belirlenmiştir. Dolayısıyla aşırı sıcakların yerel planlarda risk olarak tanımlanması önemli olmakla birlikte, politika kurumsallaşmasının değerlendirilmesinde eylemlerin sorumlu birim, zamanlama, finansman, gösterge ve izleme mekanizmalarıyla desteklenmesi de dikkate alınmalıdır.

V. SONUÇLAR

Bu çalışmada İzmir, Ankara ve Antalya Büyükşehir Belediyelerinin iklim değişikliğine uyum politikalarında aşırı sıcaklıklar ve sıcak hava dalgalarının nasıl ele alındığı karşılaştırmalı olarak incelenmiştir.

Araştırma sonucunda üç belediyenin de aşırı sıcakları ve/veya kentsel ısı adasını önemli bir iklim riski olarak tanımladığı ve bu riske yönelik çeşitli uyum araçları geliştirdiği belirlenmiştir. Yeşil alanların artırılması, yeşil koridorların oluşturulması, kentsel ısı adası haritalaması ve modellemesi, yeşil çatılar ve yüzey malzemelerine yönelik müdahaleler üç kentte farklı biçimlerde öne çıkmaktadır.

Bununla birlikte karşılaştırma, aşırı sıcaklarla mücadelenin ağırlıklı olarak fiziksel çevre ve mekânsal planlama araçları üzerinden geliştiğini göstermektedir. Aşırı sıcaklığın aynı zamanda bir halk sağlığı ve sosyal kırılganlık sorunu olduğu dikkate alındığında, sıcaklık-sağlık ilişkisini temel alan erken uyarı sistemlerinin, risk iletişiminin, serinleme alanlarının, kırılgan gruplara yönelik müdahalelerin ve sağlık sürveyansının yerel iklim politikalarıyla daha güçlü biçimde bütünleştirilmesi gerekmektedir.

Bu doğrultuda büyükşehir belediyelerinde genel iklim eylem planlarının yanı sıra kentlerin özgün sıcaklık eşikleri ve sosyo-mekânsal kırılganlıkları dikkate alınarak yerel Isı/Sıcak Hava Dalgası Eylem Planlarının hazırlanması önerilebilir. Bu planların sıcaklık risk haritaları, erken uyarı eşikleri, sorumlu kurumlar, kırılgan gruplar, serinleme alanları, iletişim protokolleri ve ölçülebilir performans göstergelerini içermesi, aşırı sıcaklarla mücadelede yerel yönetimlerin müdahale kapasitesini güçlendirebilir.

Sonuç olarak aşırı sıcaklarla mücadele Türkiye'deki yerel iklim uyum politikalarında giderek daha görünür hale gelmekle birlikte, mevcut yaklaşımın "kentsel ısı adasını azaltma" politikasından bütünleşik bir "yerel ısı yönetişimi" politikasına doğru geliştirilmesine ihtiyaç bulunmaktadır. Gelecek araştırmalarda belediyelerin planlanan eylemleri ne ölçüde uygulamaya aktardıkları, sıcak hava dalgaları sırasında yürüttükleri iletişim faaliyetleri ve kırılgan gruplara yönelik uygulamaları ayrıca incelenebilir.

KAYNAKLAR

[1] Intergovernmental Panel on Climate Change (IPCC), "Cities, Settlements and Key Infrastructure," in Climate Change 2022: Impacts, Adaptation and Vulnerability, Cambridge University Press, 2022. https://www.cambridge.org/core/books/climate-change-2022-mitigation-of-climate-change/urban-systems-and-other-settlements/F8AEF956B904563A76D7330DCB1D0D1C

[2] World Health Organization Regional Office for Europe, Heat–Health Action Plans: Guidance, Second Edition, Copenhagen: WHO Regional Office for Europe, 2026. https://iris.who.int/server/api/core/bitstreams/2b297924-2c87-4bd8-b2a0-918a67235bd3/content
[3] R. Kotharkar and A. Ghosh, "Progress in extreme heat management and warning systems: A systematic review of heat-health action plans (1995–2020)," Sustainable Cities and Society, vol. 76, 103487, 2022, doi: 10.1016/j.scs.2021.103487.
[4] İzmir Büyükşehir Belediyesi, İzmir Sürdürülebilir Enerji ve İklim Eylem Planı (SECAP), İzmir. https://skpo.izmir.bel.tr/Upload_Files/FckFiles/file/2020/WEB_SAYFASI_SECAP-Turkce
[5] Ankara Büyükşehir Belediyesi, Ankara İli Yerel İklim Değişikliği Eylem Planı, Ankara.. https://akillisehirekosistem.csb.gov.tr/DataBank/Detail?mId=3300310030003100&source=hp
[6] Antalya Büyükşehir Belediyesi, Sürdürülebilir Enerji ve İklim Eylem Planı (SECAP), Antalya, 2022. https://www.antalya.bel.tr/Content/UserFiles/Files/YarinlardaBizVariz/Dokumanlar/2022/SECAP-SURDURULEBILIR-ENERJI-VE-IKLIM-EYLEM-PLANI-2022.
[7] Antalya Büyükşehir Belediyesi, *Antalya Şehri Afet Riskini Azaltma ve İklime Uyum Eylem Planı*, Antalya, 2024. https://www.antalya.bel.tr/Content/UserFiles/Files/YarinlardaBizVariz/Dokumanlar/2024/Antalya_Afet_Risk_Azaltma_iklim%20Eylem_Plani.
[8] G. Ulpiani, A. Treville, P. Bertoldi, N. Vetters, P. Barbosa, L. Feyen, G. Naumann and M. Santamouris, "Are cities taking action against urban overheating? Insights from over 7,500 local climate actions," One Earth, 2024, doi: 10.1016/j.oneear.2024.04.010.
[9] L. L. Turek-Hankins et al., "Climate change adaptation to extreme heat: A global systematic review of implemented action," Oxford Open Climate Change, vol. 1, no. 1, kgab005, 2021. doi: 10.1093/oxfclm/kgab005.
[10] P. D. Aboagye and A. Sharifi, "Urban climate adaptation and mitigation action plans: A critical review," Renewable and Sustainable Energy Reviews, vol. 189, 113886, 2024. doi: 10.1016/j.rser.2023.113886.

8th International Conference on Engineering, Natural and Social Sciences

September 06-07, 2026: Konya, Turkey

© 2026 Published by All Sciences Academy

https://www.icensos.com/

Evaluation of the Nurse Plant Potential of Certain Species in the Yeşilırmak Basin Vegetation Based on Leaf and Soil Functional Characteristics

Dudu Duygu KILIÇ

Amasya University, Amasya
(drduygukilic@gmail.com)

Abstract – The nurse plant effect refers to positive plant-plant interactions that facilitate the germination, establishment, and development of other species, particularly in degraded and stressed ecosystems. In this study, the nurse plant potential of three naturally occurring species in a disturbed research area within the Yeşilırmak Basin of Amasya, *Crataegus monogyna*, *Juniperus oxycedrus*, and the endemic *Astragalus melanophrurius*, was preliminarily evaluated. For each species, canopy height, leaf area, leaf fresh and dry weights, leaf dry matter content (LDMC), specific leaf area (SLA), and leaf N and C concentrations were determined. Soil samples collected beneath each canopy were analyzed for pH, electrical conductivity, organic matter, C, N, CaCO3, available phosphorus, exchangeable potassium, and texture. Functional trait profiles were compared with international literature within the framework of nurse plant ecology and the stress gradient hypothesis. *Juniperus oxycedrus*, characterized by low SLA and high LDMC, showed high nurse plant potential, consistent with a stress-tolerant strategy, through shading and microclimate buffering. *Crataegus monogyna* also exhibited strong potential through its thorny structure, which provides protection against herbivores, and its moderate canopy height, which promotes shading. *Astragalus melanophrurius*, a nitrogen-fixing Fabaceae species, showed potential to create an "island of fertility" due to its high leaf N concentration and increased soil N and K beneath its canopy. However, no direct nurse plant studies on this species were identified. Overall, *C. monogyna* and *J. oxycedrus* are promising priority nurse species for restoration of degraded areas at the study site, whereas *A. melanophrurius* requires experimental validation as a complementary species for improving soil fertility.

Keywords: Nurse plant, facilitation, functional traits, stress gradient hypothesis, ecological restoration, Amasya

I. INTRODUCTION

In traditional restoration practices, the existing vegetation in the area is generally viewed as a competitor to newly planted seedlings and is often cleared from the site. However, current ecological research demonstrates that when left in place, these plants act as protective facilitators, significantly increasing the survival and growth success of new species (Gómez-Aparicio, 2009; Padilla & Pugnaire, 2006). Nurse plants are species that can positively affect the germination, establishment, survival, or growth performance of neighboring plants by modifying environmental conditions through their canopies or growth forms. These plant-plant interactions provide crucial support, particularly in stressed ecosystems, by ameliorating the microclimate and providing physical refuge from herbivory (Gómez-Aparicio et al., 2004, 2008). In this process, the canopy development of nurse plants and their capacity to mitigate environmental stress factors directly influence the establishment success of late-successional species in degraded lands (Flores-Cano et al., 2023; Löf et al., 2019). Especially in regions with high abiotic stress,

these favorable microhabitats provided by nurse plants offer more suitable conditions for seed germination and seedling development compared to the external environment (Ren et al., 2008). Understanding the impact of the mechanisms by which nurse plants support the development of other species on ecosystem functioning and species diversity is essential for the more effective planning of restoration efforts (Filazzola & Lortie, 2014; Vandenberghe et al., 2009). The success of forest restoration projects largely depends on the environmental interactions during the establishment phase of target species and the facilitative mechanisms among different plant communities (Ibáñez & Rodríguez, 2020). Therefore, the extent to which microsite amelioration around nurse plants support the establishment of new seedlings in the area, and how these protective effects vary across different ecosystems, are among the most fundamental research topics in restoration ecology (Gómez-Aparicio et al., 2005). The advantages provided by nurse plants through canopy formation and the improvement of soil properties stand out as the primary elements determining the survival success of sensitive species under various ecological conditions (Gómez-Aparicio et al., 2005). In many terrestrial ecosystems, ranging from arid and semi-arid ecosystems to mountainous and Mediterranean-type areas, interactions between plant species do not solely consist of competition; in many cases, the presence of one species can facilitate the germination, establishment, and growth of another. Such positive interactions are termed facilitation in the ecological literature, and the adult plants providing this effect are called nurse plants (Callaway, 2007). By providing shade under their canopies, nurse plants reduce extreme temperature and light stress, increase soil moisture and organic matter accumulation, buffer wind effects, provide a physical refuge against herbivores, and, in some cases, enhance soil fertility through deep-rooted nitrogen-fixing species (Padilla & Pugnaire, 2006; Gómez-Aparicio et al., 2004). The intensity and direction of the nurse plant effect vary depending on the level of environmental stress. The stress gradient hypothesis (SGH), proposed by Bertness and Callaway (1994) and later developed by Maestre et al. (2009), predicts that the frequency and importance of positive (facilitative) interactions increase in environments where physical stress or disturbance pressure—such as grazing and cutting—are elevated, whereas competition becomes dominant under more benign and fertile conditions. Within this framework, numerous studies have demonstrated that nurse plants play a significant role in the natural or artificial regeneration of woody species, particularly in Mediterranean and Euro-Siberian transition zone ecosystems where disturbance factors like grazing and logging are intense (Gómez-Aparicio et al., 2004; Smit et al., 2008; Cuesta et al., 2010). The Yeşilırmak basin (Amasya, Turkey), where this research was conducted, has been examined in detail in our previous studies. Kılıç et al. (2018) investigated the plant species in small habitats (microsites) within this area, categorized as grazed/un-grazed and cut/un-cut. The plants were evaluated based on their competitiveness, stress tolerance, and ruderal adaptability (CSR strategies), as well as their environmental indicator values (Ellenberg). The results indicated that the plants developed mixed (secondary) survival strategies rather than a single strategy, which is in full agreement with the intermediate disturbance hypothesis in ecology. In another study conducted by Kılıç et al. (2021), the plant communities in the area were divided into four main groups (grazed, un-grazed, cut, un-cut) based on the type of disturbance. It was determined that elevation and soil moisture were decisive in the spatial distribution of these communities, whereas soil acidity (pH), nitrogen content, and tree canopy cover were the determining factors for species diversity. Both studies revealed that woody plants such as *Juniperus oxycedrus* and *Crataegus monogyna*, as well as spiny, perennial legumes like *Astragalus melanophrurius*, stand out as distinguishing and indicator species at different degradation levels of the site. These two aforementioned studies elucidated how plants in the area respond to various disturbances and their survival strategies. However, they did not directly examine the supportive and facilitative effects of the plants on each other. Since the analyses defining the ecological strategies of plants explain how a species withstands harsh conditions and utilizes resources, they do not directly measure whether that plant can act as a nurse plant protecting other species. Addressing this gap in the literature, the aim of the current study

is to measure the leaf traits and the soil properties beneath the canopies of three species—*Crataegus monogyna*, *Juniperus oxycedrus*, and *Astragalus melanophrurius*—that grow naturally in the same research area and are prominent at various levels of degradation. It is aimed to evaluate these obtained data in comparison with the nurse plant literature and to provide a preliminary assessment of whether these species can be utilized as priority nurse species in ecological restoration efforts in the region.

2. MATERIAL AND METHOD

The research was conducted between the elevations of 400 and 1100 m in the Yeşilırmak Basin of Amasya province, located in the Central Black Sea Region of Turkey (40°39′03.35″N, 35°56′45.23″E). The area is situated in a semi-arid climate zone exhibiting a transition between marine and continental climates, with an average annual temperature of 13.9 °C and precipitation of 397.5 mm. Grazing and irregular wood cutting are common in the area (Kılıç et al., 2018; Kılıç et al., 2021). To evaluate their nurse plant potential, *Crataegus monogyna* subsp. monogyna, *Juniperus oxycedrus*, and the endemic *Astragalus melanophrurius* Boiss. were selected, representing different growth forms and identified as widespread or characteristic within disturbance groups in previous vegetation studies. Three healthy and mature individuals (n = 3) from each species were randomly selected, their canopy heights were measured, and samples were taken from mature leaves exposed to full sunlight. Leaf dry matter content (LDMC) and specific leaf area (SLA) were calculated by determining leaf fresh and dry weights as well as leaf area; in the dried leaves, total nitrogen was determined by the micro-Kjeldahl method (Bradstreet, 1954), and total carbon was determined by elemental analysis to calculate the C/N ratio. In soil samples collected from a depth of 0–35 cm beneath the canopy of each individual, pH, electrical conductivity (EC), organic matter, total N and C, calcium carbonate (CaCO3), available P, exchangeable K, and soil texture were determined. Soil pH was determined in a 1:1 soil-water suspension using a pH meter (Kacar, 2012), organic matter by the Walkley-Black method, total N by the micro-Kjeldahl method (Bradstreet, 1954), lime content by a Scheibler calcimeter, available P by the Olsen method, exchangeable K by ammonium acetate extraction and flame photometry, and soil texture by the hydrometer (Bouyoucos) method (Bayraklı, 1987; Kutbay & Ok, 2003; Kılıç et al., 2018; Kılıç et al., 2021). Leaf and soil properties were evaluated as mean ± standard deviation (n = 3). The obtained functional traits were compared with the literature identified within the scope of Web of Science and Scopus using the keywords "nurse plant", "facilitation", and "stress gradient hypothesis". When species-specific evidence was unavailable, particularly for *A. melanophrurius*, studies on closely related or ecologically similar species belonging to the same genus were utilized as supporting evidence, and this was explicitly stated in the evaluations.

3. RESULTS AND DISCUSSION

According to the findings, all three species adopt entirely different strategies within the leaf economics spectrum. *J. oxycedrus* has the lowest specific leaf area (SLA = 6.97 mm^2 mg^{-1}), the highest leaf dry matter content (LDMC = 58.76%), and the lowest leaf nitrogen concentration (0.65%). These traits indicate that the species follows a conservative strategy regarding resource use. In other words, this plant exhibits a sclerophyllous, long-lived structure with a low metabolic rate that is resistant to environmental stress.In stark contrast, *A. melanophrurius* possesses the highest SLA (11.90 mm^2 mg^{-1}) and the highest leaf nitrogen (4.90%) values. This demonstrates that the species occupies the acquisitive end of the leaf economics spectrum, associated with relatively rapid resource acquisition. These traits are generally associated with relatively rapid resource acquisition and potentially shorter leaf longevity, which is consistent with the acquisitive strategy commonly observed in legumes.*C. monogyna*, on the other hand, has the highest canopy height at 2.56 m and is situated in a balanced position right in the middle of these two opposing strategies in terms of leaf traits (LDMC = 19.18%, SLA = 8.52 mm^2 mg^{-1}). Indeed, the leaf

C:N ratio of this species (19.3) clearly differentiates it from the very high C:N ratio of *J. oxycedrus* (67.6) and the very low C:N ratio of *A. melanophrurius* (9.3) (Table 1).

Table 1. Canopy height and leaf functional traits of the species (mean ± SD, n=3).

Feature	*C. monogyna*	*J. oxycedrus*	*A. melanophrurius*
Canopy height (m)	2,56 ± 0,37	0,89 ± 0,28	0,57 ± 0,12
Fresh leaf mass (mg)	139,53 ± 6,17	34,47 ± 0,76	20,98 ± 1,56
Leaf area (mm²)	227,62 ± 11,80	140,90 ± 0,79	87,81 ± 1,45
Leaf dry mass (mg)	26,70 ± 0,98	20,23 ± 0,92	7,41 ± 0,66
Leaf dry matter content, LDMC (%)	19,18 ± 1,42	58,76 ± 3,83	35,61 ± 5,98
Specific leaf area, SLA (mm² mg⁻¹)	8,52 ± 0,13	6,97 ± 0,31	11,90 ± 0,84
Leaf nitrogen, %N	2,47 ± 0,21	0,65 ± 0,10	4,90 ± 0,27
Leaf carbon, %C	47,63 ± 1,17	43,93 ± 1,00	45,73 ± 1,09
Leaf C:N ratio	19,3	67,6	9,3

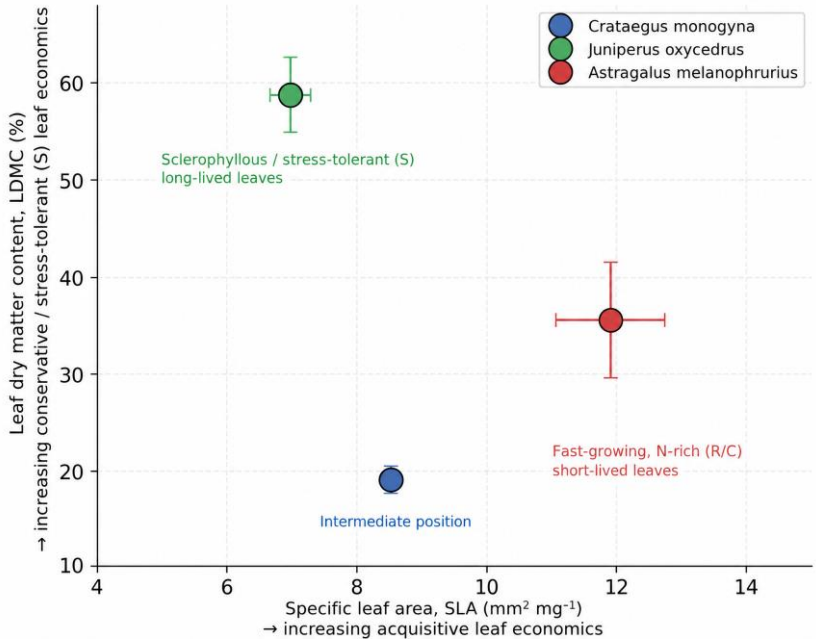

Figure 1. Functional positions of the species on the SLA–LDMC axis.

Figure 1 demonstrates that the investigated species distinctly separate on the leaf economics spectrum. *J. oxycedrus* is positioned towards a resource-conserving and conservative leaf economics strategy with its low SLA (approximately 6.97 mm² mg⁻¹) and high LDMC (approximately 58.76%) values. Low SLA and high dry matter content in leaves are generally associated with a greater structural investment in leaf tissue and prolonged conservation of resources (Wright et al., 2004; Cornelissen et al., 2003). Therefore, the values of *J. oxycedrus* appear to be consistent with a functional strategy that is resistant to stress conditions such as drought and high irradiance. In contrast, *A. melanophrurius*, possessing the highest SLA value (approximately 11.90 mm² mg⁻¹) and a moderate LDMC value (approximately 35.61%), exhibits a position towards faster resource acquisition, moving closer to an acquisitive leaf economics strategy. High SLA values are typically associated with a tendency to produce a larger leaf area per unit of dry mass and to utilize resources more rapidly (Wright et al., 2004; Pérez-Harguindeguy et al., 2013). When evaluated alongside the high leaf nitrogen of *A. melanophrurius*, this points to the species' potential to rapidly utilize nutrients and invest in growth. On the other hand, *C. monogyna* occupies an intermediate position between the two species in terms of its SLA (approximately 8.52 mm² mg⁻¹) and LDMC (approximately 19.18%) values, and is not distinctly linked to a single extreme strategy. Overall, it can be

stated that *J. oxycedrus* has a resource-conserving leaf strategy, *A. melanophrurius* is inclined towards more rapid resource utilization, and *C. monogyna* exhibits intermediate traits. However, although these functional traits are useful indicators for explaining nurse plant potential, they must be supported by measurements of microclimate, soil moisture, and target seedling survival and growth to verify the actual nursing effect (Maestre et al., 2009; Gómez-Aparicio et al., 2004).

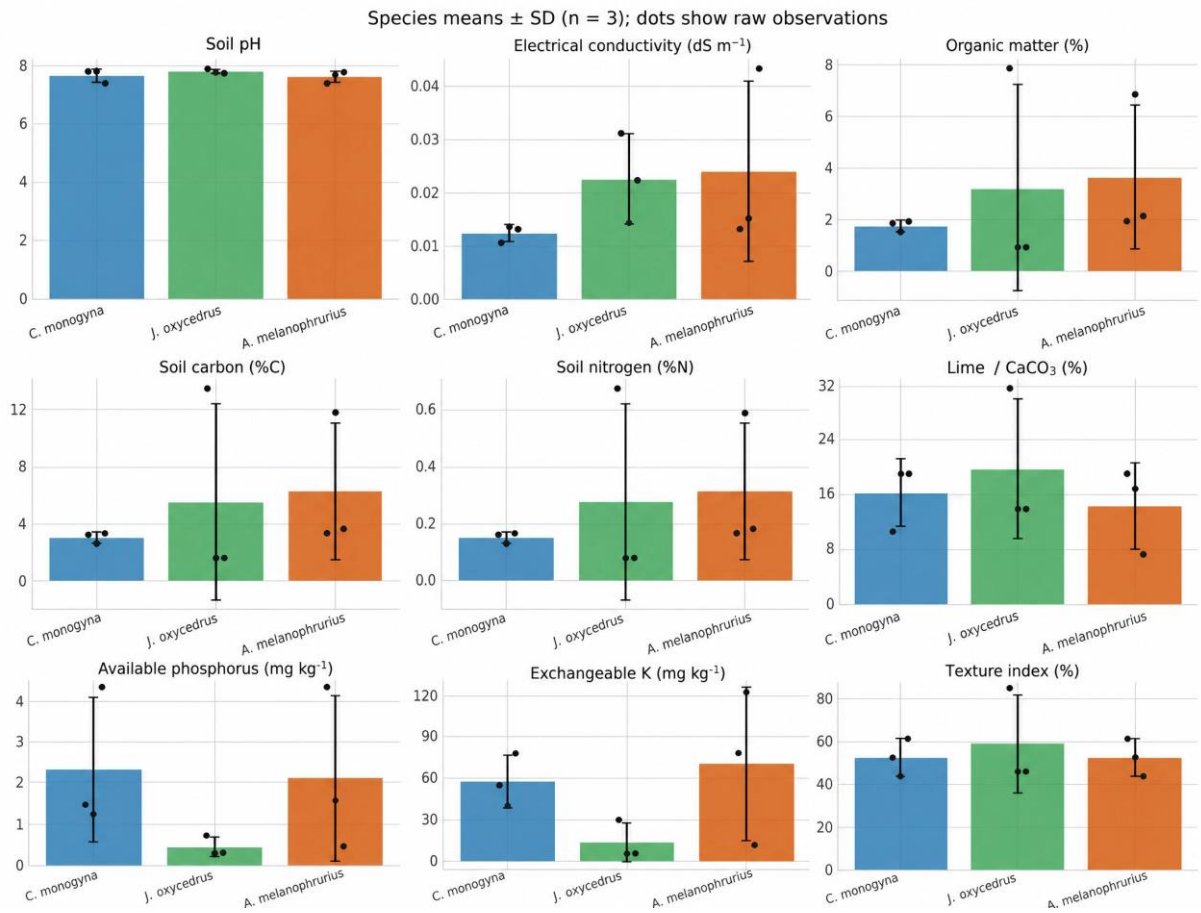

Figure 2. Mean ± SD values of soil properties under the canopies of the species.

Soil analyses conducted in the microhabitats formed by *C. monogyna*, *J. oxycedrus*, and *A. melanophrurius* species indicate that there are differences in specific edaphic parameters among the species (Figure 2). Soil pH values were measured to be similar and slightly alkaline for all three species, ranging approximately between 7.5 and 7.8. While the electrical conductivity parameter was at its lowest level under the *C. monogyna* canopy, it showed an increasing trend for the *J. oxycedrus* and *A. melanophrurius* species. When the amounts of organic matter, soil carbon (%C), and soil nitrogen (%N) were evaluated, a significant accumulation was detected in the soils beneath *J. oxycedrus* and *A. melanophrurius* compared to *C. monogyna*. However, along with this increase, it is observed that the standard deviation values and intra-group variance also exhibit a quite broad distribution. These patterns suggest the potential for an island-of-fertility effect beneath the canopies in the sub-canopy areas of the taxa in question (Pugnaire et al., 1996). Nevertheless, the amounts of available phosphorus and exchangeable potassium, which are critical for plant development, were found to be distinctly lower in the *J. oxycedrus* microhabitat compared to the other two species. The lime (CaCO3) ratio and soil texture

index, on the other hand, were found to be close to each other with high variation among species and within a broad overlapping range (Figure 2). The obtained data suggest that the microhabitat conditions created by nurse plants in their vicinity vary depending on the functional traits of the species. The high levels of essential building block components such as carbon and nitrogen around species like *J. oxycedrus* and *A. melanophrurius* support their potential to create a nutrient-rich and sheltered bed for target species through their litter accumulation and soil-protecting mechanisms (Gómez-Aparicio et al., 2004). The markedly lower concentrations of available phosphorus and exchangeable potassium beneath the *J. oxycedrus* canopy may reflect greater plant demand or uptake of these macronutrients or alterations in microbial activity associated with specific root exudates. The facilitative role of nurse plants in ecosystem restoration is not limited merely to shading or the mitigation of water stress but also directly and bi-directionally modifies the edaphic profile of the area (Callaway, 1995).

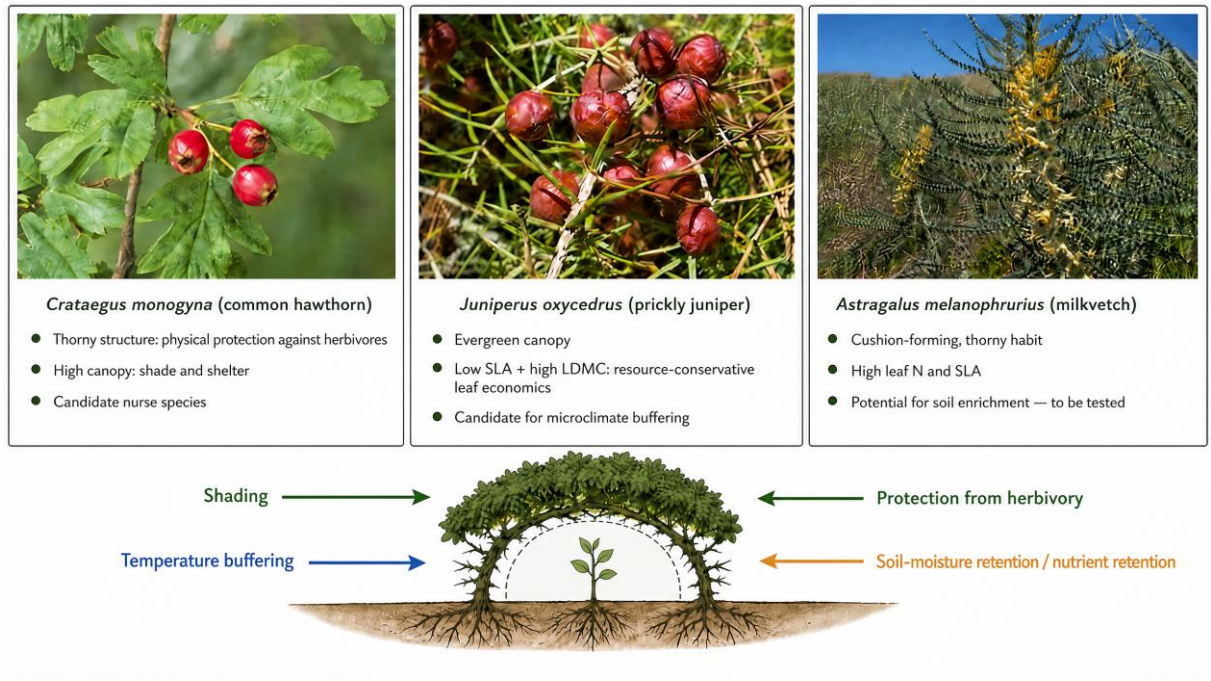

Figure 3. Infographic of Species Traits Indicating Nurse Plant Potential (The image was created with artificial intelligence support based on actual photographs of the species.) (Url1., Url2., Url3)

Figure 3 conceptually illustrates the fundamental traits constituting the nurse plant potential of the three species investigated in the Yeşilırmak Basin. While the thorny branches and broad canopy of *C. monogyna* stand out in terms of providing physical protection against herbivore pressure as well as shade and shelter, the evergreen and dense canopy of *J. oxycedrus* possesses the potential to create a microhabitat capable of buffering irradiance and temperature conditions. *A. melanophrurius*, on the other hand, was evaluated as a candidate species requiring investigation in terms of soil fertility and resource cycling due to its cushion/thorny growth form, high leaf nitrogen, and high specific leaf area. However, the mechanisms shown in the figure are not direct experimental results of the current study, but rather explanations of nursing potential based on the morphological and functional traits of the species and literature knowledge; in particular, the visual used for *A. melanophrurius* is not a field photograph but a verified herbarium specimen. Findings in the literature indicate that different facilitation mechanisms may play a role in the function of the investigated species as nurse plants. For *C. monogyna*, its thorny structure providing physical protection against herbivores, its moderate-to-high canopy creating shading to improve the microclimate, and its facilitation of the establishment of woody species, especially in

successional processes, stand out as the primary mechanisms explaining its nursing effect. These mechanisms for this species have been directly supported by species-specific studies (Gómez-Aparicio et al., 2004; Fichtner et al., 2021). *J. oxycedrus*, thanks to its evergreen and sclerophyllous canopy, can create a more favorable microhabitat by reducing light and temperature stress, particularly in arid and hot conditions. The conservation of soil moisture and the buffering of microclimatic conditions under the canopy are important processes that facilitate the regeneration and survival of Quercus seedlings in particular. Therefore, the nurse plant function of the species is evaluated through mechanisms of microclimatic amelioration and supporting the establishment of young individuals. In addition to species-specific direct evidence for these mechanisms, there are also studies demonstrating nurse plant relationships in Mediterranean ecosystems (Douaihy et al., 2022; Pugnaire et al., 2011; Smit et al., 2008). Regarding *A. melanophrurius*, it is thought that its nursing effect is primarily associated with its growth form and potential soil improvement mechanisms. Its spiny and cushion-like growth form may contribute to the formation of sheltered microhabitats around the plant that reduce temperature, light, and water stress. Furthermore, being a species belonging to the Fabaceae family, it is likely to improve soil nutrient status through symbiotic nitrogen fixation and create a sort of "island of fertility" in its vicinity. However, studies directly testing these mechanisms for *A. melanophrurius* are limited. Thus, the available evidence is more in the nature of indirect evidence based on findings at the level of the genus Astragalus and the Fabaceae family (Bonanomi et al., 2023; Reid et al., 2010; Gencer et al., 2025). Assessed overall, it is evident that species-specific evidence supporting the nursing function is stronger for *C. monogyna* and *J. oxycedrus*, while the mechanisms proposed for *A. melanophrurius* are based more on indirect findings obtained from taxonomically related groups. This situation indicates that the nurse plant role of the species can be explained not only by their morphological traits but also by multiple ecological processes such as the microclimatic conditions they create, the reduction of grazing pressure, and the amelioration of soil resources. The findings obtained largely overlap with the current position of the *C. monogyna* taxon in nurse plant ecology. The thorny structure of the species and its high canopy of 2.56 m confirm the breadth of its shading capacity and its protective effect during the successional process. Studies conducted by Fichtner et al. (2021) and Gómez-Aparicio et al. (2004) support how effective a protector this species is for woody plants and how it positively affects seedling survival rates. Its ability to rapidly resprout under cutting pressure and its grazing tolerance make the species a resilient candidate for regions where human-induced disturbances are intense, such as the Yeşilırmak basin. For *J. oxycedrus*, the determined low specific leaf area, high dry matter content, and low leaf nitrogen clearly explain its S (stress-tolerant) classification in the study by Kılıç et al. (2018). According to the leaf economics spectrum (Wright et al., 2004), these traits indicate slow resource use and a long leaf lifespan. This conservative structure is in complete agreement with the function of protecting stress-sensitive seedlings by buffering the microclimate. Research by Douaihy et al. (2022) and Pugnaire et al. (2011) demonstrates that the species supports the regeneration of woody species in open areas, but this effect weakens as forest canopy closure increases. In the studies by Kılıç et al. (2018, 2021), the determination of this species as a diagnostic species of less degraded areas indicates that its potential role as a nurse plant may be particularly relevant in the late successional stage rather than being a pioneer. Although there is no direct facilitation study focusing on the endemic *A. melanophrurius* species investigated in this study, the measured functional trait profile exhibits parallels with the general ecological functions of the genus Astragalus. The high leaf nitrogen, specific leaf area, and soil nutrient values detected in our study indicate that the species could be a potential soil fertility enhancer. Studies by Bonanomi et al. (2023) and Reid et al. (2010) emphasize that the spiny cushion forms of this genus act as nurse plants by increasing soil organic carbon. The classification of the species with a competitive-ruderal strategy by Kılıç et al. (2018) supports that its potential protective effect might emerge during the initial establishment phase of herbaceous species in the area, rather than for woody seedlings. The three investigated species form a

consistent ecological pattern in the context of the leaf economics spectrum and facilitation mechanisms. While *J. oxycedrus* buffers the microclimate, *A. melanophrurius* enhances soil fertility, and *C. monogyna* acts as a bridge between these two opposing strategies by providing physical protection and shading. This situation is consistent with the interpretation reported by Kılıç et al. (2018) that secondary strategies are dominant, and with ecological theories predicting that the facilitation effect reaches its highest level in moderately degraded environments (Bertness & Callaway, 1994; Maestre et al., 2009).

4. CONCLUSION

In conclusion, when the nurse plant potentials of the three naturally growing species in the Amasya Yeşilırmak basin are evaluated based on their functional traits, it is observed that the species have complementary functions in ecosystem restoration. *C. monogyna*, with its thorny architecture, and *J. oxycedrus*, with its sclerophyllous structure, are priority candidates in regional restoration efforts. The nitrogen-fixing endemic *A. melanophrurius* stands out with its potential to increase soil fertility, and this role needs to be verified through experimental field studies (seedling/seed transplantation experiments, microclimate monitoring). In the reclamation of degraded areas, using species combinations that bring together physical protection, microclimate buffering, and soil fertilization functions, rather than focusing on a single species, may increase restoration success. In ecosystems under grazing and cutting pressure, this multifaceted approach constitutes a strong foundation for future restoration strategies as a low-cost, ecology-based natural tool (Padilla & Pugnaire, 2006).

Acknowledgements: This study is supported by Amasya University Project number (FMB-BAP-14-067). Thank you Amasya University Research Fund for their support. Declaration:Generative artificial intelligence tools were used in this study for language editing, translation, and text formatting

5.REFERENCES

1. Bayraklı F (1987). Toprak ve Bitki Analizleri. OMÜ Ziraat Fakültesi Yayınları, Samsun.
2. Bertness MD, Callaway RM (1994). Positive interactions in communities. Trends in Ecology & Evolution 9(5): 191-193.
3. Bonanomi G, Chiurazzi M, Caporaso S, ve ark. (2023). Nitrogen-fixing cushion Astragalus siculus modulates soil fertility, microclimate, plant facilitation, bacterial and fungal microbiota along an elevation gradient. Journal of Vegetation Science 34(3): e13193.
4. Bradstreet RB (1954). Kjeldahl method for organic nitrogen. Analytical Chemistry 26(1): 185-187.
5. Callaway RM (2007). Positive Interactions and Interdependence in Plant Communities. Springer, Dordrecht.
6. Callaway, R. M. (1995). Positive interactions among plants. The Botanical Review, 61(4), 306-349.
7. Cornelissen, J. H. C., Lavorel, S., Garnier, E., et al. (2003). A handbook of protocols for standardised and easy measurement of plant functional traits worldwide. Australian Journal of Botany, 51, 335–380. https://doi.org/10.1071/BT02124
8. Cuesta B, Villar-Salvador P, Puértolas J, Rey Benayas JM, Michalet R (2010). Facilitation of Quercus ilex in Mediterranean shrubland is explained by both direct and indirect interactions mediated by herbs. Journal of Ecology 98(3): 687-696.
9. Douaihy B, Haber R, Jaoude RA, ve ark. (2022). Forest canopy and mistletoe infestation alter the facilitative effects of *Juniperus oxycedrus* s.l. on woody seedlings on Mount Lebanon (Lebanon). Journal of Vegetation Science 33(6): e13163.
10. Fichtner, A., & Wissemann, V. (2021). Biological flora of the British Isles: *Crataegus monogyna*. Journal of Ecology, 109(1), 541-571.
11. Filazzola, A., & Lortie, C. J. (2014). A systematic review and conceptual framework for the mechanistic pathways of nurse plants. Global Ecology and Biogeography, 23(12), 1335-1345. https://doi.org/10.1111/geb.12202
12. Flores-Cano, J. A., Gelviz-Gelvez, S. M., Douterlungne, D., & Badano, E. I. (2023). Are nurse plants useful for facilitating the reintroduction of mid- and late successional tree species in tropical montane cloud forests?. Botanical Sciences, 101(3), 685-698. https://doi.org/10.17129/botsci.3236
13. Gencer G, Sarikurkcu C, Tepe B (2025). Unveiling the phytochemical diversity and bioactivity of *Astragalus melanophrurius*: a first report integrating experimental and in silico approaches. Pharmaceuticals 18(1): 103.
14. Gómez-Aparicio L, Zamora R, Gómez JM, Hódar JA, Castro J, Baraza E (2004). Applying plant facilitation to forest restoration: a meta-analysis of the use of shrubs as nurse plants. Ecological Applications 14(4): 1128-1138.

15. Gómez-Aparicio, L. (2009). The role of plant interactions in the restoration of degraded ecosystems: a meta-analysis across life-forms and ecosystems. Journal of Ecology, 97(6), 1202-1214.
16. Gómez-Aparicio, L., Valladares, F., Zamora, R., & Quero, J. L. (2005). Response of tree seedlings to the abiotic heterogeneity generated by nurse shrubs: an experimental approach at different scales. Ecography, 28(6), 757-768.
17. Gómez-Aparicio, L., Zamora, R., Castro, J., & Hódar, J. A. (2008). Facilitation of tree saplings by nurse plants: Microhabitat amelioration or protection against herbivores?. Journal of Vegetation Science, 19(2), 161-172.
18. Ibáñez, I., & Rodríguez, A. (2020). Understanding neighborhood effects to increase restoration success of woody plant communities. Ecological Applications, 30(5), e02098. https://doi.org/10.1002/eap.2098
19. Kacar B (2012). Toprak Analizleri (3. baskı). Nobel Yayın, Ankara.
20. Kılıç DD, Kutbay HG, Sürmen B, Hüseyinoğlu R (2018). The classification of some plants subjected to disturbance factors (grazing and cutting) based on ecological strategies in Turkey. Rendiconti Lincei. Scienze Fisiche e Naturali 29(1): 87-102.
21. Kılıç DD, Sürmen B, Kutbay HG (2021). The relationships between environmental and disturbance factors in temperate deciduous forest ecosystem (Amasya/Turkey). Anatolian Journal of Botany 5(1): 44-50.
22. Kutbay HG, Ok T (2003). Foliar N and P resorption and nutrient levels along an elevational gradient in *Juniperus oxycedrus* L. subsp. macrocarpa (Sibth. & Sm.) Ball. Annals of Forest Science 60: 449-454.
23. Löf, M., Madsen, P., Metslaid, M., Witzell, J., & Jacobs, D. F. (2019). Restoring forests: regeneration and ecosystem function for the future. New Forests, 50(2), 139-151. https://doi.org/10.1007/s11056-019-09713-0
24. Maestre FT, Callaway RM, Valladares F, Lortie CJ (2009). Refining the stress-gradient hypothesis for competition and facilitation in plant communities. Journal of Ecology 97(2): 199-205.
25. Padilla FM, Pugnaire FI (2006). The role of nurse plants in the restoration of degraded environments. Frontiers in Ecology and the Environment 4(4): 196-202.
26. Pérez-Harguindeguy, N., Díaz, S., Garnier, E., et al. (2013). New handbook for standardised measurement of plant functional traits worldwide. Australian Journal of Botany, 61, 167–234. https://doi.org/10.1071/BT12225
27. Pugnaire FI, Armas C, Maestre FT (2011). Positive plant interactions in the Iberian Southeast: mechanisms, environmental gradients and ecosystem function. Journal of Arid Environments 75(12): 1310-1320.
28. Pugnaire, F. I., Haase, P., & Puigdefabregas, J. (1996). Facilitation between higher plant species in a semiarid environment. Ecology, 77(5), 1420-1426.
29. Reid AM, Lamarque LJ, Lortie CJ (2010). A systematic review of the recent ecological literature on cushion plants: champions of plant facilitation. Web Ecology 10: 44-49.
30. Ren, H., Yang, L., & Liu, N. (2008). Nurse plant theory and its application in ecological restoration in lower subtropics of China. Progress in Natural Science, 18(2), 137-142. https://doi.org/10.1016/j.pnsc.2007.07.008
31. Smit C, Rietkerk M, Wassen MJ (2008). Facilitation of Quercus ilex recruitment by shrubs in Mediterranean open woodlands. Journal of Vegetation Science 19(2): 193-200.
32. Url1.https://commons.wikimedia.org/wiki/Category:Crataegus_monogyna;
33. Url2: https://www.inaturalist.org/taxa/141764-Juniperus-oxycedrus;
34. Url3: https://yabanicicekler.com/upload/image/flower/5739e7615abb8_1070.jpg
35. Vandenberghe, C., Smit, C., Pohl, M., Buttler, A., & Freléchoux, F. (2009). Does the strength of facilitation by nurse shrubs depend on grazing resistance of tree saplings?. Basic and Applied Ecology, 10(5), 427-436. https://doi.org/10.1016/j.baae.2008.08.009
36. Wright IJ, Reich PB, Westoby M, ve ark. (2004). The worldwide leaf economics spectrum. Nature 428: 821-827.

8th International Conference on Engineering, Natural and Social Sciences

September 06-07, 2026: Konya, Turkey

© 2026 Published by All Sciences Academy

https://www.icensos.com/

Facilitation in Ecological Communities Mechanisms, Functions, and Applications Across Environmental Contexts

Dudu Duygu KILIÇ

Amasya University, Amasya

(drduygukilic@gmail.com)

Abstract **–** Although ecological communities have historically been studied primarily with a focus on competition among species to understand their structure and functioning, positive interactions are now recognized as one of the fundamental mechanisms shaping community dynamics, particularly in areas characterized by harsh environmental conditions. This article reviews the theoretical basis of positive interactions among species, their main mechanisms of action, and their effects at the landscape level in light of the existing literature.

The study discusses the distinctions among concepts such as mutualism, commensalism, and facilitation, as well as the role of the Stress Gradient Hypothesis and habitat engineering approaches in understanding facilitative interactions. In the context of plant–plant interactions, the important roles of nurse plants in regulating microclimatic conditions, improving soil quality, and promoting the establishment and survival of stress-sensitive species are examined. In addition, the contributions of plant–animal and plant–microorganism interactions to key ecosystem functions, including pollination, seed dispersal, nutrient cycling, and soil formation, are addressed.

Although positive interactions can enhance ecosystem resilience, species richness, and functional continuity, these effects may vary depending on the intensity of environmental stress, species traits, spatial scale, and geographic context. Furthermore, the opportunities and constraints associated with positive interactions in ecosystem management are evaluated in the context of climate change, restoration ecology, agricultural systems, and invasive species.

In conclusion, strategies for ecosystem management aimed at conserving biodiversity and restoring the ecological functions of degraded areas should consider not only competitive and negative interactions but also supportive and facilitative interactions.

Keywords: Facilitation; positive species interactions; nurse plants; stress-gradient hypothesis; ecosystem engineering; plant–plant interactions; ecological restoration; climate change

I. INTRODUCTION

Defining interactions among organisms in natural ecosystems solely in terms of competition, predation, and suppression represents an incomplete approach. Various species modify the physical, chemical, or biological characteristics of their environment, thereby facilitating the growth, survival, and establishment of other organisms. These processes are broadly classified as positive interactions. In areas exposed to intense environmental stress, such as extreme cold, drought, high altitude, salinity, nutrient deficiency, or habitat loss, the sheltered microsites created by one species can enable other species to become established within the ecosystem (Brooker et al., 2008; Cavieres & Badano, 2009). One of the most evident examples of these facilitative relationships is the regulation of microclimatic conditions. Shading provided by shrubs and trees reduces soil surface temperature and slows evaporation, thereby contributing to moisture retention. Cushion-forming plants, in turn, reduce wind intensity and buffer abrupt

temperature fluctuations. These sheltered conditions provide a suitable environment for the survival of seedlings at the early stages of development and species that are particularly vulnerable to environmental stress. Facilitation mechanisms extend beyond microclimatic regulation. Processes such as litter decomposition, stimulation and restructuring of rhizosphere microbial communities, modification of soil properties, and enhanced nutrient availability can contribute to facilitative interactions among plants. Root exudates can regulate interactions between plants and soil microorganisms, whereas nurse plants can modify microbial activity, litter decomposition, and nutrient mineralization beneath their canopies (Bais et al., 2006; Rodríguez-Echeverría et al., 2016; Brooker et al., 2008; van der Heijden, Bardgett, & van Straalen, 2008). The ecological consequences of facilitative relationships extend well beyond increased growth at the individual level. Species that act as facilitators can promote species diversity within communities by enabling the establishment of stress-sensitive plants under challenging environmental conditions and can increase the resilience of ecosystems to environmental fluctuations (Cavieres & Badano, 2009). Accordingly, nurse plants, mycorrhizal fungi, symbiotic bacteria, pollinating animals, and organisms that modify the physical structure of habitats constitute fundamental components of ecological integrity at the landscape level. The aim of this review is to examine the theoretical basis of positive interactions and to evaluate plant–plant, plant–microorganism, and animal–plant interactions together with their consequences extending across ecosystems. It also discusses how positive interactions can be incorporated into the management of invasive species, agricultural production systems, ecological restoration practices, and climate change adaptation.

2. Conceptual and Theoretical Framework

2.1. Fundamental Forms of Positive Interactions

Positive interspecific interactions encompass several forms, including mutualism, commensalism, and facilitation, although these concepts differ in their mechanisms, outcomes, and conceptual boundaries. Mutualism refers to a form of association in which all interacting partners derive benefits. The symbiotic relationship between Rhizobium bacteria inhabiting the root nodules of legumes and their host plants is one of the most well-known examples. While the plant provides the bacteria with carbon compounds produced through photosynthesis, the bacteria convert atmospheric nitrogen into forms that can be utilized by the plant (Bronstein, 2009).

Commensalism, in contrast, is an asymmetric interaction in which only one of the interacting partners benefits, while the other experiences neither a significant benefit nor harm. Some epiphytic ferns and mosses that attach to tree trunks obtain physical support and microhabitats from their hosts without substantially affecting their physiological processes. Facilitation, on the other hand, refers to a process in which one organism modifies environmental conditions in a way that supports the establishment, growth, and persistence of other species. The protection of young seedlings by shade-producing shrubs in arid or high-altitude environments clearly illustrates a facilitative mechanism (Callaway, 2007; Brooker et al., 2008).

The boundaries among these concepts cannot always be clearly distinguished. The same pair of species may exhibit facilitative, neutral, or competitive interactions depending on changing environmental conditions. Moreover, the fact that an interaction produces a positive outcome for one of the partners does not necessarily mean that the other partner will benefit to the same extent. Therefore, the assessment of positive interactions should consider not only the direction of the interaction but also the environmental context and the resulting net outcome.

2.2. Nurse and Companion Plants

Species that support the establishment and growth of other plant species by alleviating environmental pressures in their surroundings are referred to as nurse plants. Through the shade they provide, these plants reduce soil temperature, slow evaporation, and allow water to remain in the soil for longer periods. Their ability to reduce wind exposure, contribute to organic matter accumulation through leaf litter, and enhance microbial activity around their roots are among the main characteristics of the microhabitats they create. These functions increase the survival probability of young seedlings while also enabling stress-

sensitive species to become established within the community (Padilla & Pugnaire, 2006; Cavieres & Badano, 2009).

The concept of companion plants is more commonly associated with agricultural systems. Plants grown together in specific combinations can promote each other's growth by suppressing weeds, using nutrients in a complementary manner, attracting pollinators, or limiting harmful organisms. Particularly in cereal–legume mixtures, the ability of legumes to fix atmospheric nitrogen can indirectly contribute to meeting the nitrogen requirements of neighboring species. For this reason, companion planting is considered valuable in agroecological production systems and sustainable agricultural practices (Hauggaard-Nielsen, Ambus, & Jensen, 2001; Lithourgidis et al., 2011).

2.3. Stress Gradient Hypothesis

The Stress Gradient Hypothesis proposes that the intensity of environmental stress influences both the direction and strength of interactions among species. According to the central premise of the hypothesis, competition for access to resources is more pronounced under low-stress conditions, whereas as stress intensity increases, the protective effects provided by one species to another become more evident and facilitation becomes more prominent. The maintenance of soil moisture by shade-producing plants in arid regions and the reduction of wind intensity by cushion-forming species in high-mountain environments are examples of this pattern (Maestre et al., 2009).

Nevertheless, this hypothesis should not be regarded as a universal rule applicable to all ecosystem types and species combinations. The occurrence and strength of facilitation may vary depending on species functional traits, the nature of environmental stress, the spatial distribution of resources, community structure, and the scale of investigation. When environmental stress reaches extreme levels, facilitative interactions may cease because the nurse species itself becomes weakened or competition intensifies over increasingly limited resources. Thus, the relationship between environmental stress and positive interactions does not necessarily follow a linear pattern (He & Bertness, 2014; Maestre et al., 2009).

2.4. Habitat Engineering and Related Concepts

The transformation of the chemical or physical environment by organisms to create new living spaces for themselves or other organisms is defined as habitat engineering (Jones, Lawton, & Shachak, 1994). Examples include corals constructing reefs, beavers building dams and creating wetlands, and plants that stabilize soil through their roots, thereby reducing erosion and creating conditions that facilitate the establishment of new species. This approach demonstrates that facilitation is not limited to direct interactions among individual organisms but also involves the modification of physical conditions at the ecosystem and community levels.

The scientific literature includes several concepts related to the terms companion plants and nurse plants. For example, a broad range of species that promote the development of other organisms by alleviating environmental pressures are referred to as facilitator species (Brooker et al., 2008). Organisms that influence the fundamental structure and functioning of ecosystems through their biomass, spatial distribution, and trophic or mutualistic interactions are classified as foundation species (Ellison, 2019). These organisms can modify the physical conditions of ecosystems, provide mechanical support, influence the metabolic activities of other species, and contribute to the functioning of nutrient and energy cycles (Ellison et al., 2005; Baiser, Whitaker, & Ellison, 2013). Species that ameliorate abiotic factors such as salinity, moisture, and temperature in ways that benefit other organisms are known as habitat ameliorators, whereas structures that provide suitable microsites for seedlings growing on decomposing tree trunks are referred to as nurse logs (Harmon et al., 1986).

3. Fundamental Forms of Positive Interactions at the Landscape Level

3.1. Plant–Plant Interactions

Facilitative interactions among plants are particularly evident in high-altitude, arid, semi-arid, and saline ecosystems. Nurse plants slow evaporation and reduce thermal stress through the shade they provide,

while reducing wind intensity and limiting water loss from seedlings. Enhanced microbial activity around their roots and the accumulation of leaf litter increase soil organic matter and improve the availability of nutrients for plant uptake (Brooker et al., 2008). One of the most prominent examples of plant–plant facilitation is found among the cushion-forming plants of the Andes. The dense, compact structure of species such as those in the genus Azorella reduces the erosive force of wind and buffers abrupt fluctuations in soil temperature, thereby creating a favorable microclimate for surrounding plants. Studies have reported substantially higher survival rates for species establishing around these plants compared with individuals growing alone in exposed areas (Cavieres & Badano, 2009). Comparative studies conducted in alpine ecosystems have also confirmed that facilitative interactions among plants become more pronounced as environmental stress increases (Callaway et al., 2002). In semi-arid Mediterranean communities, facilitation processes often operate through soil-mediated mechanisms. Microbial activity, soil moisture, and organic matter accumulation beneath shrubs are generally greater than in open areas. These favorable conditions promote nutrient uptake and root development in seedlings, thereby increasing their probability of establishment and persistence in the area (Pugnaire, Armas, & Valladares, 2004). Studies in the Mojave Desert have shown that interactions between annual plants and shrubs are not exclusively one-sided. While facilitative mechanisms such as soil improvement and shading may operate, opposing processes, including physical interference and competition for limited resources, may occur simultaneously (Holzapfel & Mahall, 1999). Taken together, these findings indicate that nurse plants should not be regarded as organisms that invariably provide only beneficial effects to their surroundings. The overall ecological outcome of close proximity among plants is determined by the relative balance between facilitative and inhibitory factors. Figure 1 illustrates this balance by comparing the facilitative condition, in which seedling development is enhanced under the shade of a nurse plant, with the interference condition, in which inhibitory factors predominate.

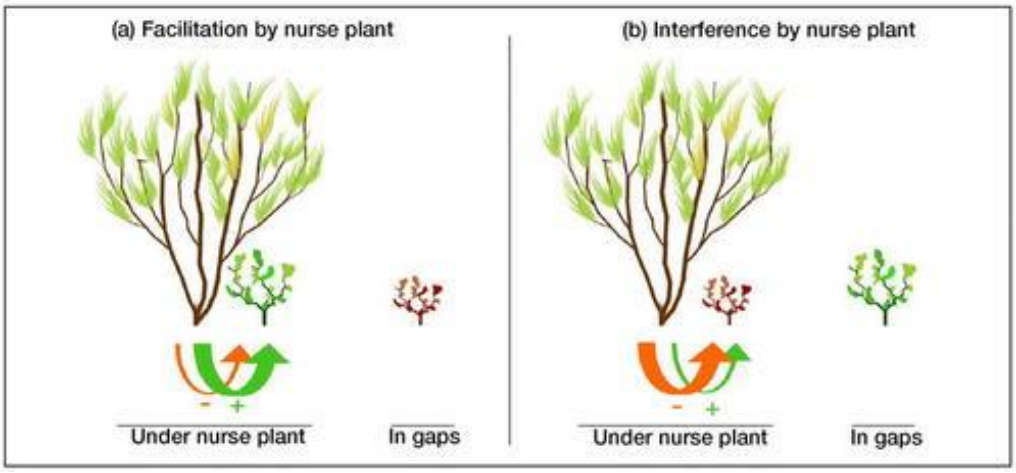

Figure 1. Balance between facilitation and interference beneath nurse plants. When positive effects predominate, the survival or growth rate of seedlings beneath nurse plants increases compared with individuals in open areas; when negative effects predominate, the opposite pattern occurs (Padilla & Pugnaire, 2006).

3.2. Plant–Microorganism Interactions

The success of plants in ecosystems depends not only on their own physiological capacities but also on the relationships they establish with microorganisms inhabiting their root zones. Mycorrhizal fungi that form symbiotic associations with plant roots facilitate the uptake of essential nutrients, particularly phosphorus and nitrogen, as well as water and minerals. In return, plants transfer a portion of the carbon compounds produced through photosynthesis to the fungi. This exchange of resources represents one of the fundamental processes supporting ecosystem productivity and plant growth (Smith & Read, 2008). Nitrogen-fixing symbionts, including rhizobial bacteria associated with legumes and Frankia associated with actinorhizal plants, can increase nitrogen availability to their hosts through biological nitrogen fixation. This biological process is particularly important in nutrient-poor soils, where it contributes to

plant survival and growth. Plant growth-promoting rhizobacteria, commonly referred to as PGPR, inhabit the rhizosphere and support plant development through mechanisms such as the synthesis of auxin- and cytokinin-like hormones, enhanced nutrient solubilization, suppression of pathogenic microorganisms, and increased tolerance to environmental stress. Consequently, these interactions between plants and microorganisms extend beyond effects at the individual level and directly influence plant diversity, ecosystem productivity, and ecological resilience (van der Heijden, Bardgett, & van Straalen, 2008).

3.3. Animal–Plant Interactions

Interactions between animals and plants are not limited to consumption or herbivory. Pollination is commonly regarded as a mutualistic interaction in which animals obtain floral rewards while plants benefit from pollen transfer. Birds, bats, bees, and butterflies collect pollen or nectar from flowers while simultaneously transferring pollen between flowers and thereby contributing to the pollination process. Thus, pollination represents one of the most evident examples of plant–animal mutualism (Bronstein, 2009). Another fundamental process influencing the distribution of plants across the landscape is seed dispersal. Mammals and frugivorous birds detach seeds from parent plants and transport them to different microhabitats; moreover, passage through the digestive tract may sometimes enhance seed germination potential. Ants and rodents also contribute to the spatial distribution of plants by storing seeds or transporting them to different locations (Howe & Smallwood, 1982).

Small mammals and invertebrates inhabiting soil layers facilitate soil aeration and the movement of water into deeper soil profiles through their burrowing activities. By accelerating the decomposition of organic materials and returning nutrients to the cycle, these organisms function as ecosystem engineers that indirectly support plant growth. Consequently, animal–plant interactions extend beyond reproduction and seed dispersal, producing facilitative effects by improving soil processes and contributing to the formation of suitable microhabitats.

4. Ecosystem-Level Implications

4.1. Species Richness, Resilience, and Ecosystem Functions

The cumulative effects of facilitative interactions over time extend beyond the development of individual species and generate broader ecological consequences. The presence of organisms that modify habitats or nurse plants under harsh environmental conditions can facilitate the establishment of stress-sensitive species and contribute to species richness within communities. In this way, organisms that would otherwise be unable to overcome environmental barriers and establish themselves in a given area can find suitable habitats around the sheltered microhabitats created by these organisms (Cavieres & Badano, 2009). Positive interactions also contribute to the stability and resilience of ecosystems. Facilitating the establishment of new individuals can accelerate the reassembly of communities in disturbed or environmentally stressed areas. Increased species diversity can also improve functional integrity within ecological systems. The utilization of resources such as light, water, and nutrients by different species at different times or across different vertical layers can increase the resistance of the community to pressures such as nutrient limitation, drought, and abrupt temperature fluctuations (Brooker et al., 2008).

Interactions between plants and microorganisms, together with habitat engineering processes, also play a key role in maintaining the continuity of ecosystem functioning. Factors such as water cycling, changes in soil physical structure, nutrient availability and transformation, and the accumulation of organic matter influence biomass production and overall ecosystem productivity. By directly shaping carbon cycling and nutrient flows, these mechanisms contribute to the maintenance of ecosystem services associated with positive interactions (van der Heijden, Bardgett, & van Straalen, 2008).

4.2. Positive Interactions in the Context of Invasive Species

The ecological impacts of invasive species are generally examined in terms of competition for resources, habitat degradation, and the suppression of native species. However, some invasive species may facilitate the establishment of additional non-native species and, under specific conditions, may temporarily provide refuge for native species. This situation highlights the need to consider the interaction

networks in which species are embedded rather than focusing solely on the individual success of species when assessing the ecological consequences of biological invasions (Rodríguez, 2006). The process through which an invasive species facilitates the establishment and spread of another non-native species is described by the term invasional meltdown. Non-native plants capable of fixing atmospheric nitrogen can increase site fertility and create favorable conditions for the establishment of other invasive species. Similarly, non-native plants that form extensive colonies along coastlines or in wetlands may alter microhabitat conditions, sediment dynamics, and hydrological regimes, thereby facilitating subsequent invasions (Simberloff & Von Holle, 1999). On the other hand, in areas exposed to severe environmental stress or characterized by habitat degradation, some non-native species may facilitate the establishment and survival of native seedlings through mechanisms such as providing shade, modifying microclimatic conditions, or improving soil properties. Nevertheless, these positive effects are generally temporary, strongly context dependent, and may involve substantial risks for ecosystem management. Consequently, potential facilitative effects provided by non-native species should not be considered as a justification for their persistence in an area. Rather, they should be taken into account to achieve a more realistic understanding of invasion dynamics and to adapt management strategies to prevailing environmental conditions (Rodríguez, 2006).

5. Applications

5.1. Natural Ecosystems and Landscape Management

The most practical application of positive interactions in natural ecosystem management is the conservation of facilitator species in stressful habitats. Shrub species in Mediterranean ecosystems help maintain soil moisture and facilitate the establishment of new seedlings through the shade they provide. Cushion-forming plants in the flora of the Andes reduce wind intensity and provide suitable habitats for stress-sensitive species, while large trees in savannas influence the growth of understory herbaceous plants by providing shade and promoting nutrient accumulation. Studies conducted in alpine ecosystems have also confirmed that facilitative interactions become more pronounced as environmental stress intensifies (Callaway et al., 2002). Therefore, landscape planning should not be limited to planting or conserving target species alone. Species that provide shade conducive to the establishment of desired species, increase soil organic matter, act as windbreaks, and form beneficial microbial associations should also be incorporated into management strategies. Nevertheless, species selection should consider the ecological dynamics of the site, invasion potential, water-use requirements, and temporal variation in facilitative effects as an integrated whole.

5.2. Agricultural Systems

The most common applications of positive interactions in agricultural production involve companion planting and intercropping systems. When plants grown together utilize available resources in a complementary manner, competition with weeds may be reduced and overall system productivity may increase. In cereal–legume combinations such as barley and pea, the performance of agricultural systems is evaluated by considering plant–plant competition, nitrogen use, and weed pressure simultaneously (Hauggaard-Nielsen et al., 2001).Companion species may suppress weed growth through the release of allelopathic compounds, attract pollinators to the field, or contribute to the biological control of pests. The ability of legumes to fix atmospheric nitrogen can indirectly improve the nutritional conditions of neighboring plants. By reducing the need for synthetic fertilizers and pesticides, maintaining soil fertility, and supporting the sustainability of agricultural production, these practices are closely aligned with agroecological principles (Lithourgidis et al., 2011).

5.3. Restoration Ecology

The incorporation of nurse plants into ecological restoration projects is an important approach for restoring the functioning of degraded lands. In erosion-prone or arid areas, shade-producing trees and shrubs can reduce water loss from seedlings and increase their persistence at the site. Microhabitats

formed under stressful conditions such as extreme temperatures, high salinity, and low organic matter content can provide opportunities for native species to re-establish in degraded areas (Padilla & Pugnaire, 2006). For an effective restoration process, pioneer plants should be selected not only according to their tolerance to environmental stress but also according to their net effects on other organisms in their surroundings. Because excessive densities of nurse plant populations may intensify competition for limited resources, planting densities, species combinations, and intervention schedules should be designed according to the ecological characteristics of the site. In coastal and wetland restoration, habitat engineers that control erosion, promote sediment accumulation, and create new microhabitats can be utilized. However, avoiding invasive species that could compromise the ecological integrity of the site is essential.

5.4. Climate Change and Future Landscapes

The increasing intensity of environmental pressures such as habitat fragmentation, salinity, extreme temperature fluctuations, and drought highlights the importance of positive interactions in the capacity of ecosystems to respond to environmental change. Facilitative species can reduce local environmental stress by modifying microclimatic conditions and thereby support the persistence, establishment, and recruitment of other species. In particular, nurse plants can buffer the effects of drought and other climatic stresses by creating more favorable microsites, potentially contributing to the maintenance of biodiversity and ecosystem functioning under changing environmental conditions (Anthelme, Cavieres, & Dangles, 2014; Danet et al., 2024). Climate change may also alter the balance between facilitation and competition. Changes in temperature, precipitation regimes, and the frequency and intensity of drought can modify the strength and direction of plant–plant interactions. For example, warming may reduce the facilitative effects of nurse plants in some alpine ecosystems by alleviating the cold stress that originally generated the need for facilitation. In contrast, increasing drought intensity may strengthen the protective effects of nurse plants in dry environments by increasing the importance of shade, soil moisture retention, and microclimatic buffering (Anthelme et al., 2014; Danet et al., 2024). The loss of facilitator species under climate change may therefore have consequences extending beyond the decline of individual populations. The disappearance or weakening of a nurse plant may reduce the availability of suitable microsites for other species and may restrict their establishment or persistence. Facilitation can also influence the distribution of plant species beyond their optimal environmental ranges, suggesting that nurse plants may contribute to species range shifts and local migration under changing climatic conditions (O'brein et al., 2019). For future landscape planning, reliance on a single key species may therefore be insufficient. Instead, management strategies should incorporate functionally complementary species that differ in their responses to environmental fluctuations. Conserving existing facilitative networks, maintaining structural and functional diversity, and selecting species capable of modifying local environmental conditions may strengthen ecosystem-based approaches to climate adaptation. Recent evidence further indicates that facilitative interactions can contribute to biodiversity conservation and ecosystem restoration, supporting their consideration in ecosystem management under changing environmental conditions

2. DİSCUSSİON AND CONCLUSİON

Positive interactions demonstrate that ecological cycles and community dynamics cannot be understood solely through competitive mechanisms. The ability of one organism to promote the development of another may result from the reduction of environmental stress or from the modification of the physical habitat. However, the ecological outcome of facilitative processes cannot be considered independently of the environmental conditions under which the interaction occurs. A nurse plant may provide moisture and shade under moderate conditions, whereas under conditions of limited resources, it may intensify competition for water or nutrients. Therefore, positive and negative effects should be evaluated simultaneously in the field (Holzapfel & Mahall, 1999; He & Bertness, 2014). Temporal and spatial factors should also be incorporated into the analysis of ecological interactions. Microclimatic improvement observed immediately around a seedling may not fully reflect species composition or patterns of water use across a broader landscape. Similarly, facilitation that is pronounced during the early

stages of the life cycle may be replaced by competitive interactions as plants mature. Field studies should therefore go beyond assessing the presence or absence of species and should monitor different biological stages, including germination, growth, reproduction, establishment, and the capacity of communities to regenerate. The primary objective of applied ecology should not be to turn positive interactions into generalized rules, but rather to determine precisely under which species combinations and environmental conditions these mechanisms operate. When selecting nurse plants for restoration projects, compatibility with the native vegetation, the risk of introducing non-native species, water requirements, economic costs, and long-term community development should all be considered. Similarly, companion planting practices in agricultural systems should be evaluated not only according to crop yield but also in terms of soil biological health, reduced dependence on external inputs, and overall system productivity. Future research should combine manipulative field experiments, broad spatial scales, and long-term monitoring programs to clarify how positive interactions are related to environmental conditions. Because climate change continuously alters the nature, duration, and intensity of environmental stress, the tolerance limits of facilitative plants and their roles within interaction networks require further investigation. New evidence generated through such studies will help determine which organisms should be conserved or reintroduced to achieve the greatest ecological benefits in ecosystem management. Although positive interactions have remained relatively overlooked for a long period in scientific discussions of community structure and dynamics, they represent important driving forces, particularly in disturbed and environmentally stressful habitats. Interactions among animals and plants, plants and microorganisms, and plants themselves, expressed through facilitation, commensalism, and mutualism, directly influence individual performance, community diversity, and ecosystem functioning. Symbiotic bacteria and mycorrhizal fungi enhance nutrient transfer and productivity, while nurse plants protect sensitive individuals and regulate microclimatic conditions. Animal-mediated processes such as soil aeration, seed dispersal, and pollination contribute to the capacity of landscapes to recover and maintain ecological continuity. Habitat engineering and the Stress Gradient Hypothesis provide useful theoretical foundations for understanding the conditions under which positive interactions become more pronounced. Nevertheless, facilitative mechanisms do not represent universal rules that operate under all circumstances. Species characteristics, the type of environmental stress, geographic context, resource availability and distribution, and spatial scale can substantially alter the resulting ecological outcomes. Positive interactions should therefore not be regarded simply as an alternative to competition but as interconnected processes that, together with competition, shape the trajectory of ecological communities. Incorporating positive interactions into conservation, agriculture, ecological restoration, and climate change adaptation projects can contribute to reducing ecosystem vulnerability. Achieving these benefits, however, depends on considering the responses of native species populations, long-term ecological outcomes, and potential negative consequences. Ultimately, landscape management strategies require an integrated perspective that recognizes that ecological continuity is maintained not only through antagonism and competition but also through cooperation, interdependence, and facilitative mechanisms.

Declaration:Generative artificial intelligence tools were used in this study for language editing, translation, and text formatting

REFERENCES

Anthelme, F., Cavieres, L. A., & Dangles, O. (2014). Facilitation among plants in alpine environments in the face of climate change. Frontiers in Plant Science, 5, 387.

Bais, H. P., Weir, T. L., Perry, L. G., Gilroy, S., & Vivanco, J. M. (2006). The role of root exudates in rhizosphere interactions with plants and other organisms. Annual Review of Plant Biology, 57, 233–266

Baiser, B., Whitaker, N., & Ellison, A. M. (2013). Modeling foundation species in food webs. Ecosphere, 4(12), 1–14.

Bronstein, J. L. (2009). The evolution of facilitation and mutualism. Journal of Ecology, 97(6), 1160–1170. https://doi.org/10.1111/j.1365-2745.2009.01566.x

Brooker, R. W., Maestre, F. T., Callaway, R. M., Lortie, C. L., Cavieres, L. A., Kunstler, G., … & Michalet, R. (2008). Facilitation in plant communities: The past, the present, and the future. Journal of Ecology, 96(1), 18–34. https://doi.org/10.1111/j.1365-2745.2007.01295.x

Callaway, R. M. (2007). Positive interactions and interdependence in plant communities. Springer. https://doi.org/10.1007/978-1-4020-6224-7

Callaway, R. M., Brooker, R. W., Choler, P., Kikvidze, Z., Lortie, C. J., Michalet, R., … & Cook, B. J. (2002). Positive interactions among alpine plants increase with stress. Nature, 417(6891), 844–848. https://doi.org/10.1038/nature00812

Cavieres, L. A., & Badano, E. I. (2009). Do facilitative interactions increase species richness at the entire community level? Journal of Ecology, 97(6), 1181–1191. https://doi.org/10.1111/j.1365-2745.2009.01579.x

Danet, A., Bautista, S., Génin, A., Beckerman, A. P., Anthelme, F., & Kéfi, S. (2024). Species diversity promotes facilitation under stressful conditions. Oikos, 2024(9), e10303

Ellison, A. M. (2019). Foundation species, non-trophic interactions, and the value of being common. iScience, 13, 254–268. https://doi.org/10.1016/j.isci.2019.02.020

Ellison, A. M., Bank, M. S., Clinton, B. D., Colburn, E. A., Elliott, K., Ford, C. R., … & Webster, J. R. (2005). Loss of foundation species: Consequences for the structure and dynamics of forested ecosystems. Frontiers in Ecology and the Environment, 3(9), 479–486.

O'Brien, M. J., de Menezes, L. F. T., Bråthen, K. A., Losapio, G., & Pugnaire, F. I. (2019). Facilitation mediates species presence beyond their environmental optimum. Perspectives in plant ecology, evolution and systematics, 38, 24-30.

Harmon, M. E., Franklin, J. F., Swanson, F. J., Sollins, P., Gregory, S. V., Lattin, J. D., … & Cummins, K. W. (1986). Ecology of coarse woody debris in temperate ecosystems. Advances in Ecological Research, 15, 133–302. https://doi.org/10.1016/S0065-2504(08)60121-X

Hauggaard-Nielsen, H., Ambus, P., & Jensen, E. S. (2001). Interspecific competition, N use and interference with weeds in pea–barley intercropping. Field Crops Research, 70(2), 101–109. https://doi.org/10.1016/S0378-4290(01)00126-5

He, Q., & Bertness, M. D. (2014). Extreme stresses, niches, and positive species interactions along stress gradients. Ecology, 95(6), 1437–1443. https://doi.org/10.1890/13-2226.1

Holzapfel, C., & Mahall, B. E. (1999). Bidirectional facilitation and interference between shrubs and annuals in the Mojave Desert. Ecology, 80(5), 1747–1761. https://doi.org/10.1890/0012-9658(1999)080[1747:BFAIBS]2.0.CO;2

Howe, H. F., & Smallwood, J. (1982). Ecology of seed dispersal. Annual Review of Ecology and Systematics, 13(1), 201–228. https://doi.org/10.1146/annurev.es.13.110182.001221

Jones, C. G., Lawton, J. H., & Shachak, M. (1994). Organisms as ecosystem engineers. Oikos, 69(3), 373–386. https://doi.org/10.2307/3545850

Lithourgidis, A. S., Dordas, C. A., Damalas, C. A., & Vlachostergios, D. N. (2011). Annual intercrops: An alternative pathway for sustainable agriculture. Australian Journal of Crop Science, 5(4), 396–410.

Maestre, F. T., Callaway, R. M., Valladares, F., & Lortie, C. J. (2009). Refining the stress-gradient hypothesis for competition and facilitation in plant communities. Journal of Ecology, 97(2), 199–205. https://doi.org/10.1111/j.1365-2745.2008.01476.x

Padilla, F. M., & Pugnaire, F. I. (2006). The role of nurse plants in the restoration of degraded environments. Frontiers in Ecology and the Environment, 4(4), 196–202. https://doi.org/10.1890/1540-9295(2006)004[0196:TRONPI]2.0.CO;2

Pugnaire, F. I., Armas, C., & Valladares, F. (2004). Soil as a mediator in plant–plant interactions in a semi-arid community. Journal of Vegetation Science, 15(1), 85–92. https://doi.org/10.1111/j.1654-1103.2004.tb02240.x

Rodríguez, L. F. (2006). Can invasive species facilitate native species? Biological Invasions, 8(4), 927–939. https://doi.org/10.1007/s10530-005-5103-3

Rodríguez-Echeverría, S., Armas, C., Pugnaire, F. I., & others. (2016). Influence of soil microbiota in nurse plant systems. Functional Ecology.

Simberloff, D., & Von Holle, B. (1999). Positive interactions of nonindigenous species: Invasional meltdown? Biological Invasions, 1(1), 21–32. https://doi.org/10.1023/A:1010086329619

Smith, S. E., & Read, D. J. (2008). Mycorrhizal symbiosis (3rd ed.). Academic Press. ISBN: 978-0123705266

van der Heijden, M. G. A., Bardgett, R. D., & van Straalen, N. M. (2008). The unseen majority: Soil microbes as drivers of plant diversity and productivity in terrestrial ecosystems. Ecology Letters, 11(3), 296–310. https://doi.org/10.1111/j.1461-0248.2007.01139.x

8th International Conference on Engineering, Natural and Social Sciences

September 06-07, 2026: Konya, Turkey

© 2026 Published by All Sciences Academy

https://www.icensos.com/

ESG Integration in Almond Production, Processing and Packaging: A Climate-Resilient Farm-to-Market Framework for Mediterranean Almond Products

Georgios J. ZAKYNTHINOS[1], Bekir Erol AK[2]*

[1]*University of West Attica, School Of Public Health, Department Of Public And Community Health, Athens- GREECE (https://orcid.org/0009-0007-4207-1279)*
[2]*University of Harran, Faculty of Agriculture, Department of Horticulture, Sanliurfa- TURKIYE. (Https://orcid.org/0000-0001-6938-942X)*

**(beak@harran.edu.tr)*

Abstract **–** The transition toward sustainable and climate-resilient agri-food systems requires Environmental, Social and Governance (ESG) principles to evolve from corporate reporting mechanisms into operational tools applicable at farm and value-chain level. Almond (*Prunus dulcis* [Mill.] D.A. Webb) represents a particularly relevant perennial crop for such an approach because its production combines high economic value with substantial exposure to water scarcity, climate variability, pollination dependence, input-related environmental impacts and increasing requirements for traceability and sustainable sourcing. This study proposes an integrated Almond ESG Value Chain Framework covering orchard establishment and management, flowering and pollination, irrigation, harvesting, hulling and shelling, sorting, processing, food-safety management, packaging, by-product valorization, traceability and market positioning. The Environmental dimension incorporates greenhouse-gas emissions, water and energy efficiency, soil health, biodiversity, pollination services, climate adaptation and circularity. The Social dimension addresses occupational safety, training, seasonal employment, producer resilience, rural development, food safety and consumer protection, while Governance incorporates traceability, supplier control, quality assurance, regulatory compliance, data quality and ESG verification.Two crop-specific methodological instruments are proposed: the Almond ESG Performance Index (AESGPI) and the digital Almond ESG Passport. In addition, the framework introduces **Pollination Natural Capital** as a crop-specific sustainability component connecting biodiversity, ecosystem services and productive resilience.

Published life-cycle evidence indicates that irrigation, fertilization and pest management constitute major environmental hotspots in almond production, demonstrating the importance of a hotspot-oriented ESG management approach [1]. The proposed framework connects resource efficiency with climate resilience, natural-capital management, food safety, circular bioeconomy, digital traceability and market differentiation.The framework provides a methodological basis for subsequent field validation in Mediterranean almond-producing systems and for the development of verified sustainability-differentiated almond products.

Keywords – Prunus dulcis; almond; ESG; sustainability; Mediterranean agriculture; climate resilience; water productivity; pollination; natural capital; life cycle assessment; circular economy; food safety; traceability; digital product passport.

I. INTRODUCTION

Environmental, Social and Governance (ESG) principles provide a potentially useful architecture for this transition. Nevertheless, their application in agriculture requires adaptation to the biological, environmental and socio-economic characteristics of primary production. Agricultural sustainability cannot be represented adequately solely through company-level greenhouse-gas emissions or generic sustainability declarations. It requires indicators capable of connecting resource use, biological production, ecosystem services, processing, food safety and governance.

Almond (*Prunus dulcis*) provides an especially relevant case. Almond cultivation is economically important in Mediterranean-type production systems but is strongly dependent on climatic conditions, water availability, nutrient management, plant protection and successful pollination. These factors are increasingly material under conditions of water scarcity, increasing temperature and climatic variability.

Recent life-cycle evidence reinforces the environmental significance of these variables. Asaf et al. [1], in a cradle-to-farm-gate Life Cycle Assessment covering 94 almond plots across Mediterranean, semi-arid and arid environments, reported substantial variation in environmental performance among production systems. Irrigation, fertilizers and pest management collectively accounted for more than 90% of the assessed greenhouse-gas emissions. These findings indicate that meaningful almond ESG assessment should move beyond general sustainability declarations and identify the operational hotspots responsible for environmental performance.

Water is particularly important. Under Mediterranean and semi-arid conditions, sustainability depends not only on the amount of irrigation applied but on the capacity of the production system to convert available water into stable marketable yield. Therefore, water productivity becomes more informative than water use alone. At the same time, almond productivity depends substantially on pollination. This creates a direct connection between biodiversity, ecosystem services and agricultural productivity. Pollination can consequently be considered a form of Natural Capital whose maintenance contributes directly to productive resilience.

Almond sustainability does not terminate at the orchard gate. Harvesting, transportation, hulling, shelling, sorting, processing, storage, packaging and distribution contribute to the environmental and social profile of the final marketed product.

Almond processing also generates hulls, shells, skins, broken kernels and other fractions with considerable potential for valorization. Scientific literature demonstrates opportunities for converting these materials into animal feed, food ingredients, phenolic extracts, bioactive compounds, biomaterials, activated carbon, biochar and energy products [6].

A complete sustainability model therefore requires a transition from: Sustainable Almond Orchard to: Sustainable Almond Value Chain.The objective of the present study is to develop an integrated Almond ESG Value Chain Framework extending from orchard management to the final marketed product. Particular emphasis is placed on four interconnected dimensions: Resource Efficiency → Climate Resilience → Natural Capital → Safe and Circular Processing. The study further introduces two methodological instruments: the Almond ESG Performance Index (AESGPI) and the Almond ESG Passport, providing a conceptual architecture for measuring, comparing and communicating crop-specific ESG performance.

2. METHODOLOGY

2.1. Framework Development

The proposed methodology follows a conceptual value-chain approach integrating ESG principles with almond-specific agronomic, environmental, ecological, processing and food-safety parameters. The framework does not represent a primary experimental or farm-survey study. It provides a methodological architecture requiring subsequent empirical validation before its use for certification or comparative commercial sustainability claims.

The system boundary extends across: Orchard Establishment → Cultivation → Flowering & Pollination → Irrigation & Field Management → Harvest → Hulling/Shelling → Sorting & Processing → Packaging → Distribution → Market.

Life Cycle Assessment principles according to ISO 14040 and ISO 14044 are incorporated into the Environmental component [2,3]. Product carbon-footprint assessment can be aligned with ISO 14067 [4], while formal water-footprint assessment should follow ISO 14046 principles [5].

The proposed functional unit for product-level comparison is: 1 kg marketable almond kernel at the defined system boundary. An additional area-based environmental indicator should be maintained because product- and area-based indicators provide different information.

Thus: **Carbon Intensity = kg CO_2eq/kg marketable almond kernel**

while: **Area-Based Emissions = kg CO_2eq/ha/year.**

The distinction is important because environmental intensity depends on both input use and productivity.

2.2. Environmental Dimension

The Environmental pillar includes:

- greenhouse-gas emissions;
- water use and productivity;
- energy consumption;
- soil health;
- soil organic carbon;
- nutrient management;
- Integrated Pest Management;
- biodiversity;
- pollination services;
- renewable energy;
- circularity;
- packaging performance.

Published LCA evidence supports a hotspot-oriented approach, particularly because irrigation, fertilizer and pest-management practices can account for a major proportion of the environmental burden of almond production [1]. Water performance is assessed through three complementary indicators: **Water Input = m^3 irrigation water/ha/year.**

Product Water Intensity = m³ irrigation water/kg marketable kernel

and: **Water Productivity = kg marketable kernel/m³ irrigation water.**

The three indicators should not be considered interchangeable.

2.3. Pollination Natural Capital

Almond production demonstrates a direct relationship between agricultural productivity and ecosystem services.

The framework therefore introduces the concept:

Pollination Natural Capital: which incorporates: Pollinator Availability + Habitat + Floral Resources + Biodiversity + Safe Plant Protection + Orchard Management.

The objective is not to assign an arbitrary monetary value to pollinators. Rather, it is to recognize pollination capacity as an ecosystem service directly connected with orchard productivity and resilience. Relevant indicators include semi-natural habitat, flowering vegetation, ecological corridors, pollinator-supporting practices, timing of pesticide applications relative to flowering, Integrated Pest Management and managed or wild pollinator availability.

2.4. Social and Governance Dimensions: The Social pillar incorporates occupational health and safety, seasonal employment, producer training, climate-adaptation capacity, local employment, rural value creation, food safety and consumer protection. The Governance pillar includes farm registration, input documentation, supplier control, harvest records, processing records, food-safety management, product traceability, certifications, internal auditing, corrective actions, ESG data integrity and verification of sustainability claims.

A fundamental Governance principle is: **No ESG claim should exceed the quality of the underlying evidence.** Measured, calculated, modelled and qualitative information should therefore be clearly differentiated.

2.5. Almond ESG Performance Index

Overall ESG performance is conceptually represented through the proposed:

Almond ESG Performance Index — AESGPI

AESGPI = wE(E) + wS(S) + wG(G)

where:

E = Environmental Performance
S = Social Performance
G = Governance Performance

and:

wE + wS + wG = 1.

The weighting coefficients should not be assigned arbitrarily. Future validation should establish appropriate weights using expert elicitation, Delphi analysis, Analytic Hierarchy Process, stakeholder consultation and sensitivity analysis. Individual indicators can subsequently be normalized to a common 0–100 scale, where thresholds are based on empirical datasets, legal limits or scientifically justified benchmarks.

II. RESULTS

Application of the Almond ESG Framework: Implementation begins at orchard level through establishment of a digital baseline containing farm identity, parcel, geographical location, cultivar, orchard age, soil characteristics, irrigation system and production history. Environmental monitoring subsequently quantifies irrigation water, fertilizers, plant-protection inputs, electricity, fuels, soil characteristics, biodiversity indicators and production-related greenhouse-gas emissions. Pollination monitoring should include orchard flowering conditions, pollinator-supporting habitat, managed pollinator use where applicable, flowering vegetation and plant-protection practices during flowering.

Post-harvest monitoring extends the ESG boundary to: **Harvest → Transport → Hulling/Shelling → Sorting → Processing → Storage → Packaging.**

Processing facilities should record incoming almond mass, marketable product output, rejected material, broken kernels, electricity, fuel, water, packaging, cleaning materials, food losses and by-product streams. Food safety is simultaneously incorporated into Social and Governance performance through HACCP, Good Hygiene Practices, allergen management, microbiological and chemical controls, pesticide-residue compliance, mycotoxin management, foreign-body control, traceability and recall capability (Table 1-3).

Table 1. Core Almond ESG Indicators

Dimension	**KPI**	**Unit/Indicator**
Carbon	Carbon intensity	kg CO_2eq/kg kernel
Carbon	Area-based emissions	kg CO_2eq/ha/year
Water	Irrigation intensity	m^3/ha
Water	Product water intensity	m^3/kg kernel
Water	Water productivity	kg kernel/m^3
Energy	Energy intensity	kWh/kg
Energy	Renewable energy	%
Soil	Soil organic carbon	% / t C ha^{-1}
Plant protection	IPM adoption	%
Biodiversity	Habitat-supporting area	%
Pollination	Pollinator-supporting practices	index
Circularity	By-product valorization	%
Packaging	Recyclable/reusable packaging	%
Social	Training	h/person/year
Safety	Occupational incidents	rate
Food safety	Compliance	%
Governance	Fully traceable lots	%
Governance	Verified ESG data	%

Table 2. ESG Application Across the Almond Value Chain

Value-chain stage	Environmental	Social	Governance
Orchard	Water, carbon, soil, biodiversity	Worker safety, producer resilience	Farm/input records
Flowering/Pollination	Biodiversity, natural capital	Pollination awareness, knowledge	Pollination/application records
Irrigation & Management	Water, nutrients, IPM, energy	Training, fair labor	Irrigation/fertilizer/IPM records
Harvest	Fuel, losses	Occupational safety	Harvest/lot records
Hulling/Shelling	Energy, residues	Safe equipment use	Processing/by-product records
Processing	Energy, water, losses	Food safety	HACCP, quality control
Packaging	Materials, footprint	Consumer information	Labelling/claims
Distribution	Transport emissions	Market access	Logistics records
Market	ESG communication	Consumer protection	ESG Passport

Table 3. Circular Valorization of Almond By-products

By-product	Valorization pathway	Potential ESG contribution
Hull	Animal feed	Resource recovery
Hull	Bioactive extraction	Higher-value ingredients
Hull	Compost	Nutrient recycling
Shell	Biochar	Carbon/soil applications
Shell	Activated carbon	Industrial valorization
Shell	Bioenergy	Renewable-energy pathway
Shell	Biomaterials	Material substitution
Skin	Phenolic recovery	Functional ingredients
Broken kernels	Flour/paste	Food-chain value recovery
Processing fractions	Integrated biorefinery	Circular value creation

The valorization potential of almond residues is well documented. Almond hulls, shells and skins contain structural and phytochemical components that can support applications in food, feed and industrial systems [6].

A preliminary indicator can therefore be calculated as: By-product Valorization Rate (%) = Beneficially valorized by-product mass / Total by-product mass × 100.

Nevertheless, the percentage of biomass recovered should not alone determine circularity performance. The environmental burden, economic value, safety and regulatory suitability of each valorization pathway should also be considered.



Figure 1. Integrated Almond ESG Value Chain

III. DISCUSSION

The proposed framework extends conventional ESG methodology in several important directions. The first concerns environmental materiality (Fig.1-3).

An agricultural ESG framework can easily become excessively complex by accumulating large numbers of indicators without distinguishing between material and secondary environmental impacts. The findings of Asaf et al. [1] are particularly relevant in this respect. Their LCA demonstrated that irrigation, fertilizer and pest-management activities collectively accounted for more than 90% of assessed greenhouse-gas emissions in the almond systems studied. Therefore, materiality and hotspot analysis should precede target setting.

The appropriate sequence becomes: Measurement → Hotspot Identification → Intervention → Monitoring → Verification.

The second contribution concerns **water stewardship**.

Water use alone cannot adequately characterize almond sustainability. Two orchards can consume similar quantities of irrigation water but produce substantially different quantities of marketable kernels. Water productivity consequently provides a direct link between natural-resource consumption and productive performance.

The management objective should therefore evolve from: **Minimum Water Use** toward:**Maximum Sustainable Water Productivity.**

Formal water-footprint claims should nevertheless follow ISO 14046 principles rather than equating water withdrawal with environmental water footprint [5].

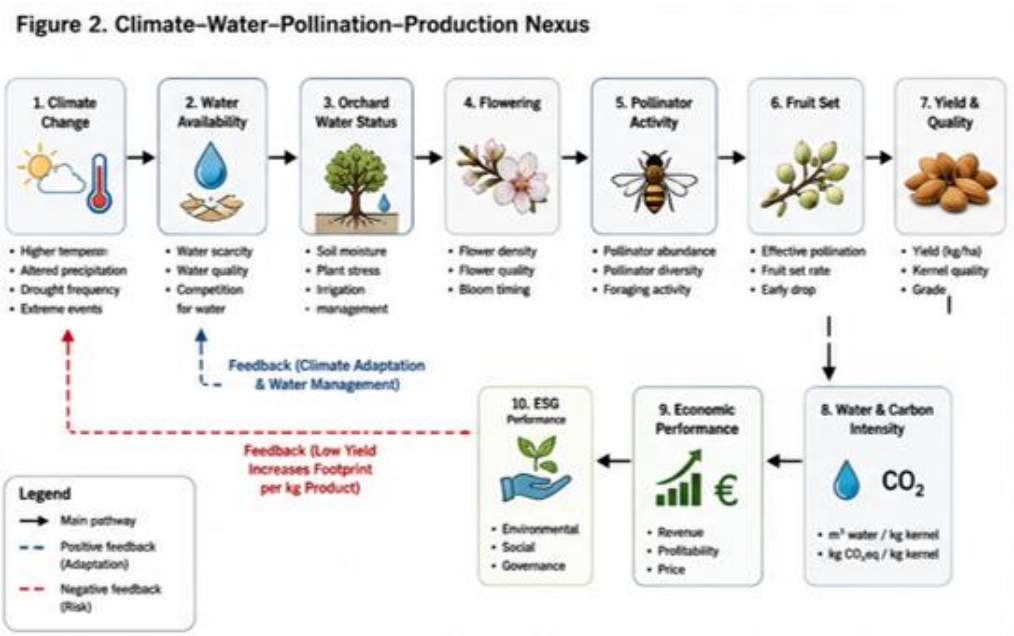

Figure 2. Climate–Water–Pollination–Production Nexus

Two important feedback mechanisms emerge. Climate adaptation and water management influence orchard resilience, while reduced yield can increase environmental intensity per kg marketable kernel. A third contribution is the incorporation of Pollination Natural Capital. Pollination illustrates particularly clearly why agricultural sustainability cannot be separated from ecosystem function.

The relevant relationship can be expressed as: **Biodiversity → Pollinator Habitat → Pollinator Activity → Pollination → Fruit Set → Yield → Economic Resilience.**

Consequently, biodiversity management is not merely an environmental conservation issue. It can also constitute productive risk management. A fourth contribution concerns **safe sustainability**.

Almond products require systematic food-safety management, including allergen management, microbiological and chemical controls, pesticide-residue compliance, mycotoxin risk management and traceability.Food safety therefore occupies two ESG dimensions simultaneously: **Social → Consumer Protection** and: **Governance → HACCP, Documentation, Verification, Traceability and Recall.**

An environmentally efficient food product cannot reasonably be characterized as fully sustainable if consumer safety is inadequately controlled.

A fifth contribution concerns circular bioeconomy. Almond processing generates substantial biomass fractions. Almond hulls, shells and skins have been studied as sources of phytochemicals and functional materials, demonstrating that residues can be transformed into value-added products rather than treated solely as waste [6].

This transformation can be represented as: By-product → Resource → Ingredient/Material/Energy → Economic Value.

Nevertheless, circularity should not reward all pathways equally. High-value food or bioactive applications, material recovery, soil applications and energy recovery have different economic and environmental characteristics. Life-cycle thinking should therefore accompany circularity assessment.

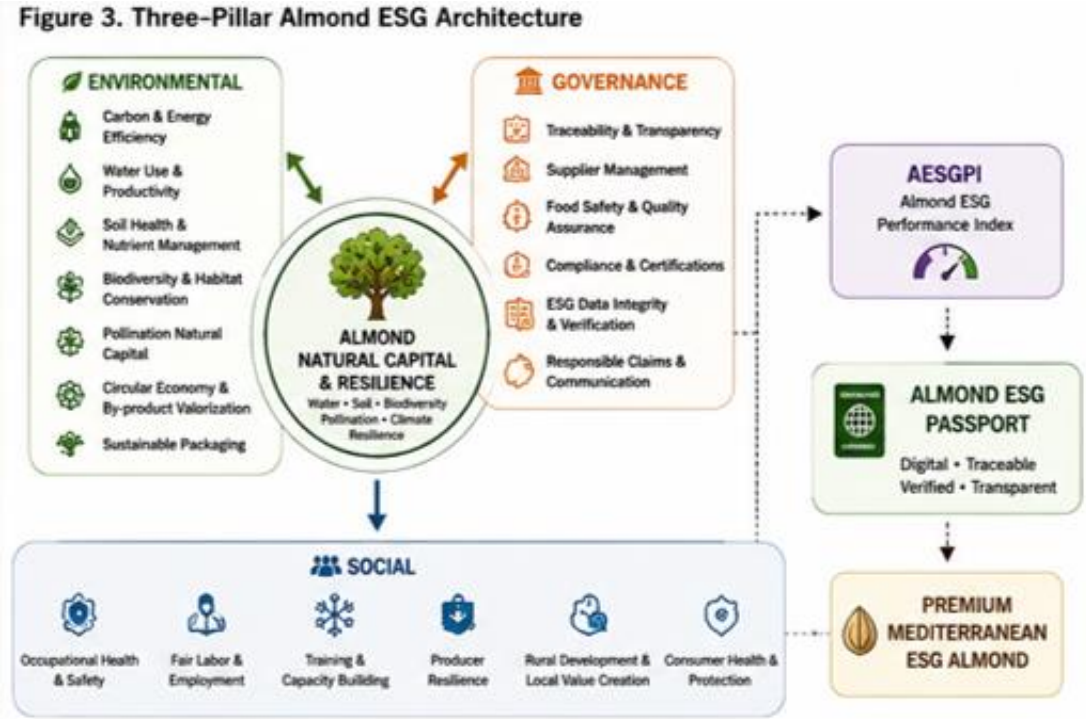

Figure 3. Three-Pillar Almond ESG Architecture

Digital traceability provides the final connection between measured ESG performance and product identity. Conventional traceability primarily answers:

Where did the product come from? The proposed Almond ESG Passport adds: **How was the product produced?**

The traceability chain becomes: Farm → Parcel → Variety → Harvest → Processing Batch → Packaging Lot → Product.

The Almond ESG Passport could incorporate origin, cultivar, harvest year, carbon footprint, water performance, energy indicators, biodiversity and pollination information, worker-safety controls, food-safety status, circularity and data-verification level. The Passport should not initially be interpreted as a certification scheme. It represents a structured data architecture requiring field validation and verification before formal sustainability claims are made.

The commercial transition can consequently evolve from:
Commodity Almond
→ Origin Almond
→ Traceable Almond
→ Sustainability-Measured Almond
→ Verified ESG Almond

→ Almond ESG Passport
→ Premium Mediterranean ESG Almond.
This transition expands differentiation from conventional product attributes toward:
Quality + Origin + Safety + Natural Capital + Sustainability + Transparency.

IV. CONCLUSION

Table olives provide a particularly suitable model for developing product-specific ESG methodology because their sustainability results from interactions among agricultural production, water management, technological processing, fermentation, food safety, circularity and governance.

Almond represents an appropriate model for developing crop-specific ESG methodology because its long-term sustainability results from interactions among climate, water resources, soil, biodiversity, pollination, agricultural inputs, processing, food safety, circularity and governance.

The proposed framework demonstrates that ESG assessment in perennial agriculture should extend beyond conventional corporate environmental reporting.

Carbon footprint, water productivity, energy use, soil health, biodiversity and plant-protection management constitute fundamental Environmental parameters. However, the particular biological characteristics of almond production justify the explicit incorporation of **Pollination Natural Capital**, connecting biodiversity and ecosystem services directly with agricultural productivity and resilience.

The framework additionally demonstrates that the orchard cannot be assessed in isolation. Hulling, shelling, processing, packaging, food losses, transport and by-product management contribute to the sustainability profile of the marketed almond product.

Circular valorization creates an additional pathway for transforming almond hulls, shells, skins and processing fractions from residual biomass into potentially valuable food, feed, bioactive, material and energy resources [6].

Food safety, occupational safety, producer resilience, traceability and data verification simultaneously connect the Environmental performance of the production system with its Social and Governance dimensions.

Two principal methodological instruments are proposed.

The Almond ESG Performance Index (AESGPI) provides a framework for integrated crop-specific ESG benchmarking.

The Almond ESG Passport provides a mechanism for translating farm-to-market environmental, social, food-safety, circularity and governance information into transparent product identity.

The resulting pathway can be summarized as:

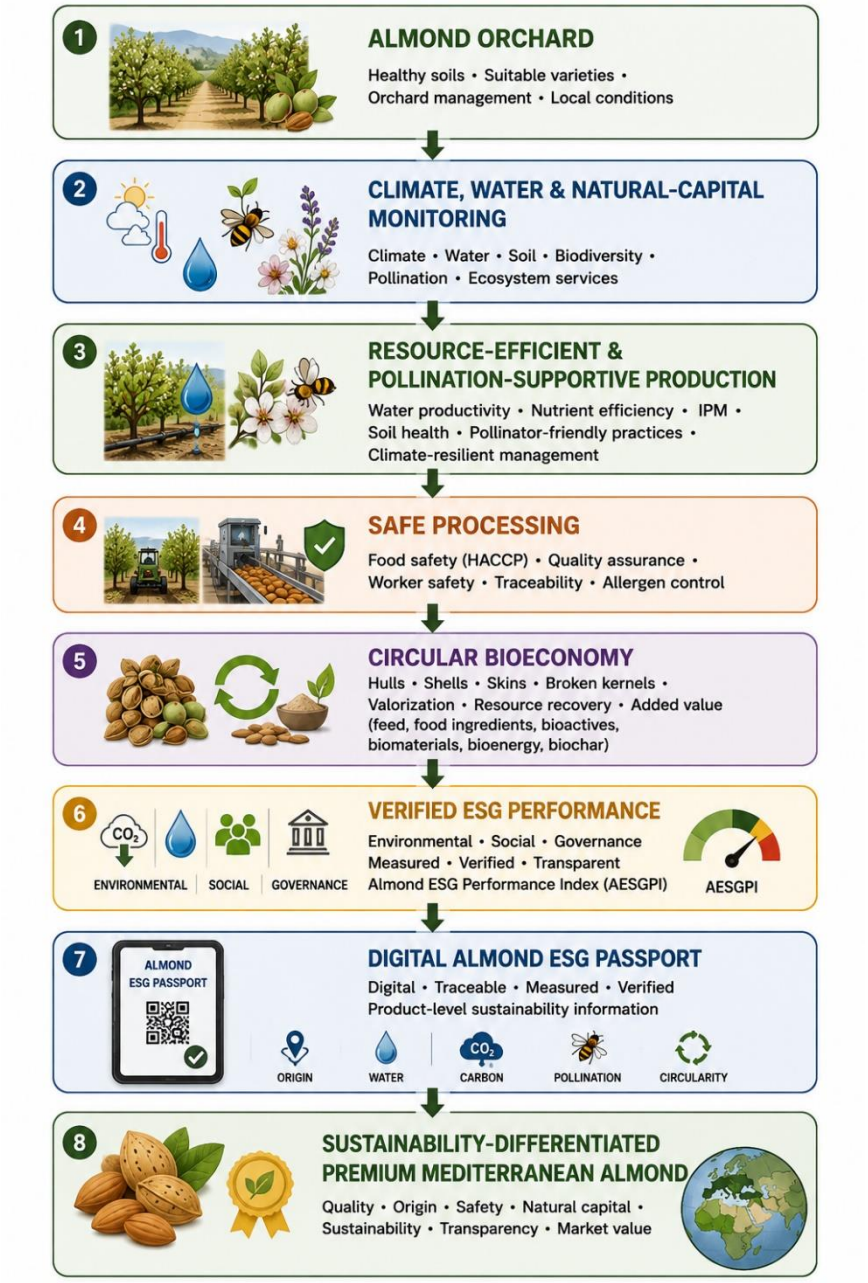

Figure 4. Proposed pathway from Almond Orchard to Sustainability-Differentiated Premium Mediterranean Almond through natural-capital monitoring, resource-efficient production, safe processing, circular bioeconomy, verified ESG performance and the Digital Almond ESG Passport. The AESGPI and Almond ESG Passport remain conceptual instruments. Their thresholds, normalization procedures and weighting systems require empirical validation across cultivars, production systems and Mediterranean climatic regions.

The next scientific step should therefore be a multi-year and multi-region field validation integrating agronomy, irrigation, biodiversity and pollination indicators, Life Cycle Assessment, food safety, processing, circularity and socio-economic performance.

The central conclusion is that ESG in almond production can evolve from an external reporting obligation into an integrated resource-efficiency, climate-resilience, natural-capital, food-safety, circularity, governance and value-creation system.

REFERENCES

[1] S. Asaf, A. Grinstein, S. Lavee, et al., "Embracing a life cycle assessment (LCA) approach to analyze the environmental impacts of almonds grown along a climatic gradient in Israel," Science of the Total Environment, vol. 957, Art. no. 177495, 2024. https://doi.org/10.1016/j.scitotenv.2024.177495

[2] International Organization for Standardization, ISO 14040: Environmental Management—Life Cycle Assessment—Principles and Framework. Geneva, Switzerland: ISO, 2006.

[3] International Organization for Standardization, ISO 14044: Environmental Management—Life Cycle Assessment—Requirements and Guidelines. Geneva, Switzerland: ISO, 2006.

[4] International Organization for Standardization, ISO 14067: Greenhouse Gases—Carbon Footprint of Products—Requirements and Guidelines for Quantification. Geneva, Switzerland: ISO, 2018.

[5] International Organization for Standardization, ISO 14046: Environmental Management—Water Footprint—Principles, Requirements and Guidelines. Geneva, Switzerland: ISO, 2014.

[6] I. Prgomet, B. Gonçalves, R. Domínguez-Perles, N. Pascual-Seva, and A. I. R. N. A. Barros, "Valorization challenges to almond residues: Phytochemical composition and functional application," Molecules, vol. 22, no. 10, Art. no. 1774, 2017.

[7] Food and Agriculture Organization of the United Nations, Developing Sustainable Food Value Chains: Guiding Principles. Rome, Italy: FAO, 2014.

[8] World Resources Institute and World Business Council for Sustainable Development, Product Life Cycle Accounting and Reporting Standard. Washington, DC, USA: WRI/WBCSD, 2011.

[9] "Revalorization of almond by-products for the design of novel functional foods: An updated review," Foods, vol. 10, no. 8, Art. no. 1823, 2021.

[10] "Recent innovations on the reuse of almond and hazelnut by-products: A review," Sustainability, vol. 16, no. 6, Art. no. 2577, 2024.

[11] World Resources Institute and World Business Council for Sustainable Development, Greenhouse Gas Protocol: Standards and Guidance. Washington, DC, USA: WRI/WBCSD.

8th International Conference on Engineering, Natural and Social Sciences

September 06-07, 2026: Konya, Turkey

© 2026 Published by All Sciences Academy

https://www.icensos.com/

ESG Integration in Table Olive Production, Processing and Packaging: A Sustainable Farm-to-Market Framework for Mediterranean Table Olives

Georgios J. ZAKYNTHINOS[1], Bekir Erol AK[2]*

[1]*University of West Attica,* School Of Public Health, Department Of Public And Community Health, Athens- GREECE (https://orcid.org/0009-0007-4207-1279)

[2]*University of Harran, Faculty of Agriculture, Department of Horticulture, Sanliurfa- TURKIYE.* (Https://orcid.org/0000-0001-6938-942X)

**(beak@harran.edu.tr)*

Abstract **–** The transition toward sustainable and climate-resilient agri-food systems requires Environmental, Social and Governance (ESG) principles to evolve from corporate reporting mechanisms into operational management tools applicable throughout agricultural and food value chains. Table olives constitute a particularly relevant Mediterranean product for such an approach because their sustainability depends not only on orchard management but also on harvesting, debittering, fermentation, water and salt use, energy consumption, food safety, wastewater management, packaging, traceability and by-product valorization.

This paper proposes an integrated Table Olive ESG Value Chain Framework extending from orchard production to the final marketed product. The Environmental dimension incorporates greenhouse-gas emissions, water productivity, energy efficiency, soil health, biodiversity, Integrated Pest Management, processing-water consumption, brine and debittering-liquid management, circularity and packaging. The Social dimension addresses occupational health and safety, seasonal employment, producer and processor training, rural value creation, food safety and consumer protection. Governance incorporates farm and batch traceability, fermentation monitoring, HACCP, analytical control, regulatory compliance, supplier management, ESG data integrity and verification of sustainability claims.A crop- and product-specific Table Olive ESG Performance Index (TO-ESGPI) and a digital Table Olive ESG Passport are proposed as methodological instruments for sustainability benchmarking and product-level communication. Particular emphasis is placed on the processing stage. Table olive processing can generate wastewater streams characterized by substantial organic loads, phenolic compounds, salinity and conductivity, making water, fermentation and effluent management material ESG issues. At the same time, these streams may contain valuable compounds, including hydroxytyrosol and tyrosol, creating opportunities for transition from waste treatment toward circular biorefinery and resource recovery.The proposed framework therefore connects sustainable cultivation, controlled fermentation, safe processing, circular management of processing streams and verified traceability into a unified farm-to-market ESG architecture.

Keywords – Table olives; ESG; sustainability; fermentation; debittering; water; brine; food safety; circular bioeconomy; hydroxytyrosol; traceability; Mediterranean agriculture; ESG Passport.

I. INTRODUCTION

Table olives constitute one of the most characteristic fermented and processed plant foods of the Mediterranean region. Their economic, nutritional, cultural and gastronomic importance extends

throughout a production chain connecting olive cultivation, harvesting, processing, fermentation, packaging and trade.

Unlike products consumed directly after harvest, however, fresh olives generally require technological processing to reduce bitterness and develop acceptable sensory, microbiological and physicochemical characteristics. Different commercial preparation systems therefore involve combinations of alkaline treatment, washing, natural or controlled fermentation, brining, oxidation and packaging.

This technological requirement gives table olives a distinctive sustainability profile. The environmental performance of the final product depends not only on agricultural inputs at orchard level but also on the consumption of water, sodium hydroxide where alkaline debittering is applied, sodium chloride, energy, packaging materials and the management of processing effluents.

Recent scientific literature emphasizes that conventional table olive processing can involve substantial chemical use, prolonged processing periods and significant wastewater generation, reinforcing the need for more sustainable processing strategies [1].

Processing wastewater represents a particularly important environmental issue. The principal streams include alkaline debittering liquids, washing waters, fermentation brines and preservation or packaging brines. Their characteristics differ considerably according to processing method. Alkaline streams may present high pH, whereas fermentation brines are generally characterized by high salinity and substantial organic and phenolic loads [2].

Consequently, table olive sustainability cannot be evaluated solely through conventional agricultural indicators such as carbon footprint, irrigation water or fertilizer consumption.

The complete relationship is: Orchard Management → Fruit Quality → Processing → Fermentation → Food Safety → Effluent Management → Packaging → Market and therefore requires a **farm-to-market ESG approach**.

At the same time, the environmental challenge associated with processing liquids creates an important circular-bioeconomy opportunity.

Table olive processing waters contain phenolic compounds and other potentially valuable constituents. Hydroxytyrosol and tyrosol are among the compounds identified as promising targets for recovery, while biological processes have also been investigated for production of biogas, lactic acid and other value-added compounds [3,4].

Thus, an environmental liability can potentially become a biological resource:**Processing Effluent → Separation/Recovery → Bioactive Compounds / Bioproducts → Circular Value**

provided that technical feasibility, safety, environmental performance and regulatory compliance are demonstrated.

The objective of this paper is therefore to develop an integrated Table Olive ESG Value Chain Framework covering orchard production, harvesting, processing, fermentation, food safety, circularity, packaging, traceability and market differentiation.

Two methodological instruments are additionally proposed:

Table Olive ESG Performance Index (TO-ESGPI) and **Table Olive ESG Passport.**

The central hypothesis is that ESG can evolve from a corporate reporting concept into an operational management framework capable of connecting agronomic sustainability, processing sustainability, food safety, circular bioeconomy and verified product identity.

2. METHODOLOGY

2.1. Framework Development

The study follows a conceptual value-chain methodology integrating ESG principles with table-olive-specific agricultural, technological, environmental and food-safety parameters. The system boundary includes:

Orchard Establishment & Management
↓
Fruit Development
↓
Harvest
↓
Transport & Reception
↓
Debittering / Preparation
↓
Fermentation
↓
Sorting & Processing
↓
Packaging & Storage
↓
Distribution
↓
Market

Life Cycle Assessment principles can be applied according to ISO 14040 and ISO 14044 [5,6], while carbon- and water-footprint assessments can be aligned respectively with ISO 14067 [7] and ISO 14046 [8].

The principal product-level functional unit proposed is: **1 kg marketable packaged table olives** at a clearly defined system boundary. Complementary area-based indicators should also be retained at orchard level.

2.2. Environmental Dimension

The Environmental pillar includes: carbon footprint; irrigation water; water productivity; soil health; soil organic carbon; nutrient management; Integrated Pest Management; biodiversity; energy; processing water; NaOH and NaCl use where applicable; wastewater and brine management; by-product valorization; and packaging.

Processing requires particular attention.Table olive production can generate several chemically different wastewater streams. Their environmental burden depends on the preparation method, water use, salt concentration, alkaline treatments and fermentation system [2]. Consequently, separate monitoring of process streams is preferable to a single undifferentiated wastewater indicator.

2.3. Social Dimension

The Social pillar includes: occupational health and safety; seasonal employment; fair labor; worker and producer training; rural employment; local value creation; food safety; sensory quality; and consumer protection. Food safety occupies a particularly important position because table olives are transformed through biological and technological processes before consumption. Fermentation management therefore connects Social responsibility directly with production technology.

2.4. Governance Dimension

Governance includes: farm identification; parcel records; cultivar; harvest-lot identification; processing-batch identification; fermentation records; pH and physicochemical monitoring; HACCP; supplier management; analytical controls; traceability; certification; corrective actions; recall capability; ESG data integrity; and substantiation of sustainability claims.

The traceability chain is: **Farm → Parcel → Cultivar → Harvest Lot → Processing Batch → Fermentation Tank → Packaging Lot → Market.**

2.5. Table Olive ESG Performance Index

The proposed integrated indicator is designated:
TO-ESGPI — Table Olive ESG Performance Index
Conceptually:
TO-ESGPI = wE(E) + wS(S) + wG(G)
where:
E = Environmental Performance
S = Social Performance
G = Governance Performance
and:
wE + wS + wG = 1.

No universal weights are proposed at this stage.

Weighting and normalization should subsequently be validated using empirical datasets, expert consultation, stakeholder analysis and sensitivity testing. The TO-ESGPI should therefore presently be considered a research and benchmarking framework, rather than a certification system.

II. RESULTS

Application of the Table Olive ESG Framework

Implementation begins with establishment of an orchard baseline including farm and parcel identification, cultivar, orchard age, irrigation infrastructure, soil characteristics, production system and historical yield. Annual monitoring should quantify water, fertilizers, plant-protection products, energy, fuels, soil indicators, biodiversity-related practices and marketable production. At harvest, the system should record fruit maturity, fruit condition, mechanical damage, harvest method, transport conditions and lot identification (Table 1).

The processing stage introduces additional ESG variables. These include water consumption, alkaline treatment where applicable, washing, salt consumption, fermentation, temperature, pH, energy, losses, processing liquids, packaging materials and food-safety controls.

Table 1. Core Table Olive ESG Indicators

Dimension	KPI	Unit / Indicator
Carbon	Carbon intensity	kg CO_2eq/kg product
Water	Orchard irrigation	m^3/ha
Water	Agricultural water productivity	kg olives/m^3
Processing	Process-water intensity	L/kg product
Energy	Energy intensity	kWh/kg
Soil	Soil organic carbon	% / t C ha^{-1}
Plant protection	IPM adoption	%
Biodiversity	Habitat-supporting area	%
Processing	NaOH use, where applicable	kg/t olives
Processing	NaCl use	kg/t product
Fermentation	Controlled batches	%
Circularity	Processing-stream valorization	%
Packaging	Recyclable/reusable packaging	%
Social	Training	h/person/year
Safety	Occupational incidents	rate
Food safety	Compliant batches	%
Governance	Fully traceable lots	%
Governance	Verified ESG data	%

3.1. Processing Water and Debiterness liquids

Water constitutes a central material issue in table olive processing. Alkaline-treated preparations can require substantial quantities of water for debittering and subsequent washing. Natural processing avoids some alkaline-treatment streams but still requires brining and extended fermentation. Published reviews report that water consumption and wastewater characteristics vary substantially according to processing technology and that alkaline debittering and washing can generate particularly problematic effluents [2].

For the present ESG framework, **debiterness liquids (debittering liquids)** are treated as a specific material stream rather than being grouped indiscriminately with all processing waste water. This distinction is important because the chemical characteristics and potential valorization pathways of alkaline debittering liquids, washing waters and fermentation brines are not identical.

3.2. Fermentation and Food Safety

Fermentation constitutes a defining technological stage in many table olive preparations. It influences product preservation, acidity, microbial ecology, sensory characteristics and stability. Modern fermentation management can therefore be considered simultaneously: a processing variable, a food-safety variable, and an ESG Governance variable.

The sustainability objective should not be to reduce fermentation to a single nvironmental KPI but to establish controlled fermentation capable of delivering safe, stable and sensory-acceptable products while optimizing water, salt, energy and process management. Scientific literature on table olive fermentation highlights microbial stability, safety, sensory quality and wastewater management as interconnected research and industrial challenges (Table 2).

Table 2. ESG Application Across the Table Olive Value Chain

Stage	Environmental	Social	Governance
Orchard	Water, carbon, soil, biodiversity	Worker/producer resilience	Farm/input records
Harvest	Fuel, losses	Occupational safety	Harvest-lot records
Reception	Water, losses	Worker safety	Lot segregation
Debittering	Water, NaOH, effluents	Chemical safety	Process records
Fermentation	Water, salt, energy	Food safety	pH/fermentation records
Sorting/Processing	Energy, losses	Worker safety	HACCP/quality systems
Packaging	Materials, footprint	Consumer information	Labelling/claims
Distribution	Transport emissions	Market access	Logistics records
Market	ESG communication	Consumer protection	ESG Passport

4. Circular Bioeconomy

The table olive industry generates several material and liquid streams capable of entering circular-management pathways.

These may include: pruning biomass; leaves; pits or stones where generated; non-marketable olives; packaging residues; fermentation brines; washing waters; and debiterness liquids. The processing-liquid streams are particularly interesting because their environmental burden coexists with potentially recoverable compounds. Scientific evidence demonstrates that table olive processing wastewater can contain hydroxytyrosol, tyrosol and other biophenols with potential for recovery and valorization. Biological valorization pathways have additionally investigated anaerobic digestion, fermentation and other processes capable of generating biogas, lactic acid and value-added metabolites [3].

The circular transition can therefore be expressed as:
Wastewater Management
↓
Stream Segregation
↓
Resource Characterization
↓
Recovery / Treatment / Valorization
↓
Bioactive Compounds • Bioproducts • Energy • Recovered Water
↓
Reduced Environmental Burden + Added Value

However, circularity should not be measured exclusively through the percentage of material diverted from disposal. Energy demand, chemicals, recovery efficiency, environmental benefit, product safety and economic value should also be considered (Table 3).

Table 3. Circular Valorization Pathways in the Table Olive Value Chain

Stream / By-product	Potential pathway	ESG contribution
Pruning biomass	Compost/biochar/energy	Soil/carbon/resource recovery
Olive leaves	Bioactive recovery	Higher-value ingredients
Pits/stones	Biomaterials/bioenergy	Material/energy recovery
Non-marketable olives	Appropriate secondary valorization	Food-loss reduction
Debiterness liquids	Treatment/compound recovery	Pollution reduction/value recovery
Fermentation brines	Regeneration/bioprocessing	Water/resource circularity
Phenolic-rich streams	Hydroxytyrosol/tyrosol recovery	High-value bioproducts
Organic liquid fractions	Anaerobic digestion	Biogas
Packaging	Recycling/reuse	Material circularity

5. Table Olive ESG Passport

The proposed **Table Olive ESG Passport** represents the product-level digital interface of the framework. It could contain six information modules.

Product Identity: origin, cultivar, farm, harvest year, processing method and lot.

Environmental Performance: carbon footprint, agricultural water performance, process-water consumption, energy and packaging indicators.
Processing Sustainability: debittering system, water management, fermentation management, salt use and processing-stream management.
Food Safety and Quality: HACCP, analytical controls, fermentation stability, traceability and quality assurance.
Circularity: valorization of leaves, pits, processing liquids and packaging materials.
Social and Governance: occupational safety, training, local value creation, certifications, audit status and ESG verification.
The Passport should distinguish between measured, calculated and independently verified information.
It should not function as an unsupported environmental label.

III. DISCUSSION

This should explore the significance of the results of the work, not repeat them. The results should be drawn together, compared with prior work and/or theory and interpreted to present a clear step forward in scientific understanding. Combined Results and Discussion sections comprising a list of results and individual interpretations in isolation are particularly discouraged (Fig. 1-3).

The proposed framework expands agricultural ESG assessment by recognizing that table olives are simultaneously an agricultural product and a technologically transformed fermented food. This distinction is fundamental. For almond or pistachio, environmental performance is strongly determined by orchard management and post-harvest operations. For table olives, the processing system itself can become a major sustainability determinant.

The ESG materiality pathway therefore becomes: Orchard → Fruit → Processing → Fermentation → Safety → Circularity → Product.

Water as a dual ESG variable: Water operates at two levels. At orchard level, it represents an agricultural resource. At processing level, it becomes a technological input and a potential source of environmental burden through the resulting liquid streams.

Consequently: **Agricultural Water Productivity** and **Processing Water Intensity** should be measured independently.

This distinction represents one of the defining characteristics of the proposed Table Olive ESG Framework.

Fermentation as biological governance: Fermentation deserves particular attention because it provides a direct bridge between biological processes and Governance. Controlled fermentation influences safety, sensory quality, consistency and product stability. Consequently, fermentation records are not simply technological documentation; they constitute evidence of responsible production governance.

From wastewater to resource :A second distinctive contribution is the transition from wastewater management toward **processing-stream valorization**. Table olive wastewaters present substantial environmental challenges because of their organic load, phenolics, salinity and conductivity. However, the presence of valuable biophenols changes the conceptual approach.

The sequence: Generate → Treat → Dispose can potentially evolve toward: Segregate → Characterize → Recover → Valorize → Reuse.

This transition is strongly aligned with circular-bioeconomy principles. It should nevertheless be verified through environmental and economic assessment because a recovery technology consuming excessive energy or chemicals cannot automatically be characterized as sustainable.

Safe Sustainability: The framework also reinforces the principle of Safe Sustainability. A product cannot be considered fully sustainable solely because its carbon footprint or water consumption is reduced. Table olive sustainability requires simultaneous achievement of: Environmental Efficiency + Food Safety + Sensory Acceptability + Traceability.

Food safety therefore belongs simultaneously to the Social and Governance pillars.

Digital differentiation

Finally, digital traceability allows ESG performance to become part of product identity.

The commercial transition becomes:

Commodity Table Olive
↓
Origin Table Olive
↓
Traceable Table Olive
↓
Safe & Quality-Assured Table Olive
↓
Sustainability-Measured Table Olive
↓
Verified ESG Table Olive
↓
Table Olive ESG Passport
↓
Premium Mediterranean ESG Table Olive

Differentiation therefore evolves toward: **Quality + Origin + Safety + Fermentation Identity + Sustainability + Circularity + Transparency.**

IV. CONCLUSION

Table olives provide a particularly suitable model for developing product-specific ESG methodology because their sustainability results from interactions among agricultural production, water management, technological processing, fermentation, food safety, circularity and governance. The proposed framework demonstrates that sustainability assessment cannot terminate at the orchard gate. Carbon emissions, irrigation, soil health, biodiversity and Integrated Pest Management remain fundamental Environmental indicators, but table olive production introduces additional material variables associated with process water, alkaline treatment where applicable, salt, fermentation, energy, packaging and processing effluents. Three conclusions are particularly important.

First, **water should be assessed as both an agricultural and processing resource**. Agricultural water productivity and process-water intensity represent distinct sustainability indicators. Second, **fermentation should be incorporated into ESG Governance**. Controlled fermentation contributes simultaneously to food safety, sensory quality, consistency and traceable production. Third, processing liquids should progressively be reconsidered within a **circular-bioeconomy framework**. Debiterness liquids, washing waters and fermentation brines present significant environmental challenges, but some streams also contain recoverable phenolic compounds and other potentially valuable constituents. Existing research supports opportunities for hydroxytyrosol recovery, biological treatment, biogas production and other valorization strategies.

The **TO-ESGPI** is proposed as an integrated benchmarking architecture, while the **Table Olive ESG Passport** provides the product-level interface connecting origin, production, processing, food safety, circularity and verified sustainability information.

The complete transition can therefore be summarized as:
Table Olive Orchard
↓
Sustainable Cultivation
↓
Quality-Oriented Harvest
↓
Resource-Efficient Processing
↓
Controlled Fermentation
↓
Safe Product
↓
Circular Management of Processing Streams
↓
Verified ESG Performance
↓
Digital Table Olive ESG Passport
↓
Premium Sustainable Mediterranean Table Olive

The proposed TO-ESGPI and ESG Passport remain conceptual methodological instruments and require empirical validation across cultivars, processing methods, enterprises and Mediterranean production regions. The central conclusion is that ESG can transform table olive sustainability from fragmented environmental actions into an integrated **farm–fermentation–food safety–circularity–market management system**.

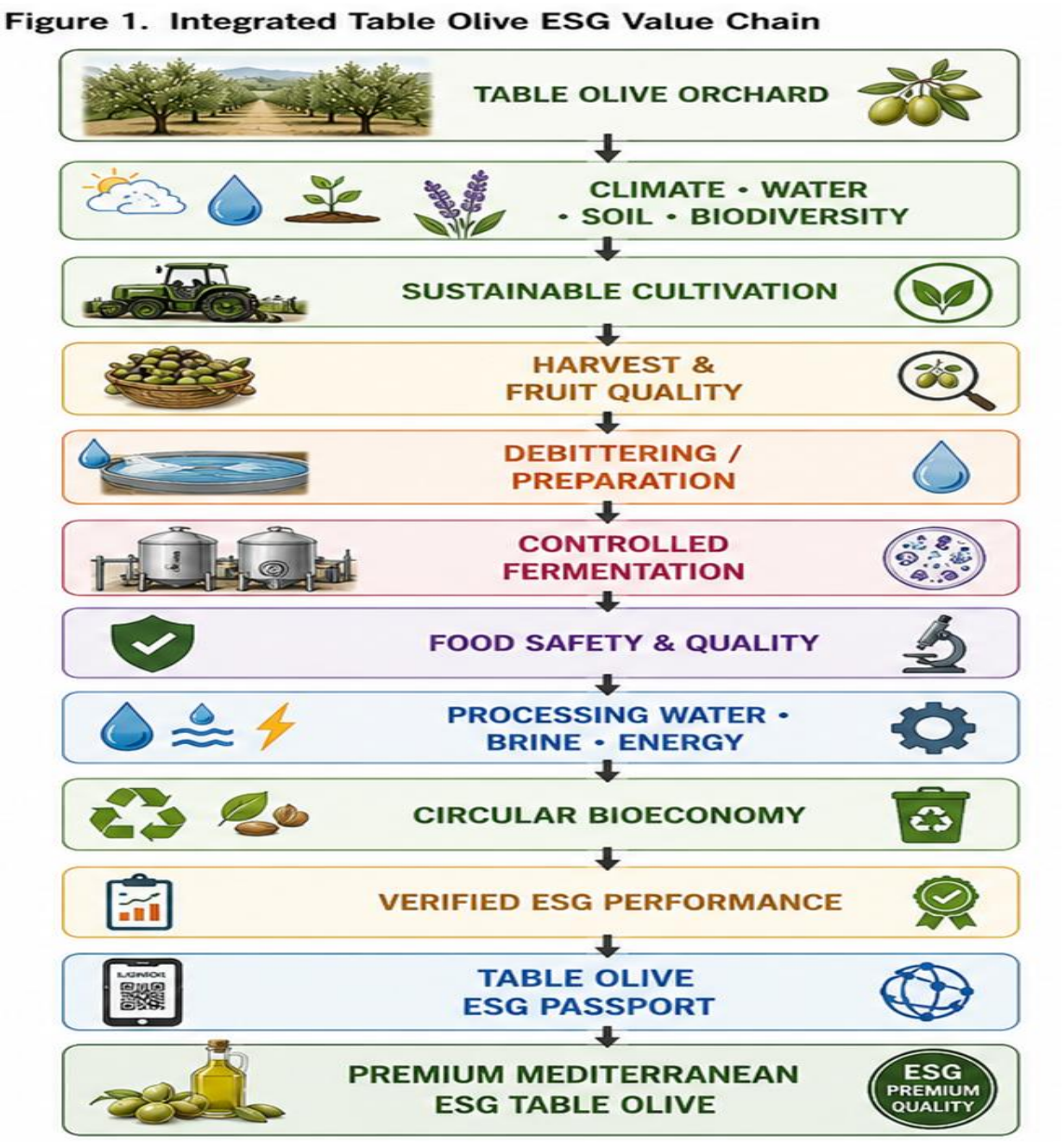

Figure 1. Integrated farm-to-market ESG pathway for Mediterranean table olives.

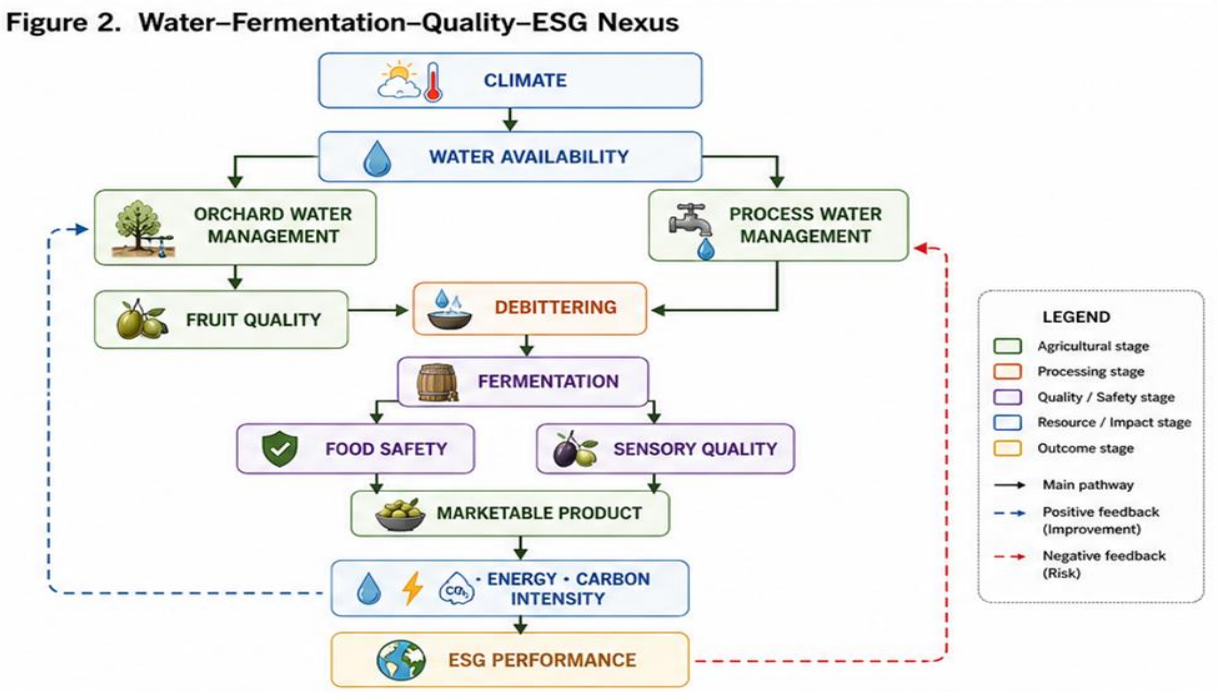

Figure 2. Water–processing–fermentation nexus connecting orchard management with product quality and ESG performance.

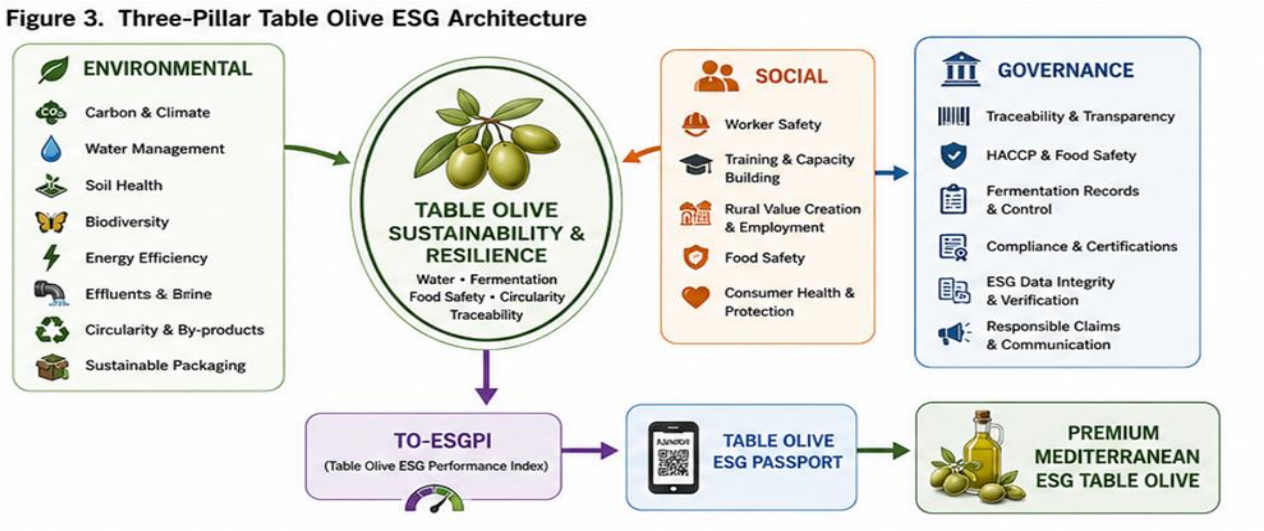

Figure 3. Integrated Environmental–Social–Governance architecture proposed for table olive production and processing.

REFERENCES

[1] V. M. Muneratto and T. C. Polachini, "Making table olives more sustainable: Processing methods and green intensifying technologies," Critical Reviews in Food Science and Nutrition, advance online publication, 2026. https://doi.org/10.1080/10408398.2026.2691228

[2] B. Rincón-Llorente, D. De la Lama-Calvente, M. J. Fernández-Rodríguez, and R. Borja-Padilla, "Table olive wastewater: Problem, treatments and future strategy. A review," Frontiers in Microbiology, vol. 9, Art. no. 1641, 2018. https://doi.org/10.3389/fmicb.2018.01641

[3] E. Papadaki and F. T. Mantzouridou, "Current status and future challenges of table olive processing wastewater valorization," Biochemical Engineering Journal, vol. 112, pp. 103–113, 2016.

[4] I. Fendri and M. Chamkha, "Olive fermentation brine: Biotechnological potentialities and valorization," Environmental Technology, vol. 34, no. 2, pp. 181–193, 2013. https://doi.org/10.1080/09593330.2012.689364

[5] International Organization for Standardization, ISO 14040: Environmental Management—Life Cycle Assessment—Principles and Framework. Geneva, Switzerland: ISO, 2006.

[6] International Organization for Standardization, ISO 14044: Environmental Management—Life Cycle Assessment—Requirements and Guidelines. Geneva, Switzerland: ISO, 2006.
[7] International Organization for Standardization, ISO 14067: Greenhouse Gases—Carbon Footprint of Products—Requirements and Guidelines for Quantification. Geneva, Switzerland: ISO, 2018.
[8] International Organization for Standardization, ISO 14046: Environmental Management—Water Footprint—Principles, Requirements and Guidelines. Geneva, Switzerland: ISO, 2014.
[9] L. Ayed, N. Asses, N. Chammem, N. B. Othman, M. Hamdi, et al., "Advanced oxidation process and biological treatments for table olive processing wastewaters: Constraints and a novel approach to integrated recycling process: A review," Biodegradation, vol. 28, pp. 125–138, 2017. https://doi.org/10.1007/s10532-017-9782-0
[10] "Table olive wastewater as a potential source of biophenols for valorization: A mini review," Fermentation, vol. 8, no. 5, Art. no. 215, 2022.

8th International Conference on Engineering, Natural and Social Sciences

September 06-07, 2026: Konya, Turkey

© 2026 Published by All Sciences Academy

https://www.icensos.com/

Numerical Analysis of the Effect of Different Wind Speeds on PVT Collector Performance

Murat ÖZTÜRK[1,2] and Erdem ÇİFTÇİ[3*]

[1]*Department of Mechanical Engineering, National Defence University, Ankara, Türkiye*
[2]*Graduate School of Natural and Applied Sciences, Energy Systems Engineering Department, Gazi University, Ankara, Türkiye*
[3]*Department of Energy Systems Engineering, Gazi University, Ankara, Türkiye*

[*]*(erdemciftci@gazi.edu.tr)*

Abstract – Interest in hybrid energy systems is gradually increasing in order to enable the effective use of renewable energy sources and to obtain multiple energy outputs from the same system. Photovoltaic-thermal (PVT) systems contribute to increasing energy efficiency by enabling the useful utilization of the heat released in addition to electricity generation. In this study, the thermal behavior of an air-flow PVT collector with six dish-grooved absorber plates under different solar radiation, collector air velocity, and ambient wind speed conditions was numerically investigated. Numerical analyses were performed using the Computational Fluid Dynamics (CFD) approach in ANSYS Fluent software. In the analyses, the collector air velocity was considered as 1.4 and 2 m/s, the solar radiation intensity as 800 and 900 W/m², and the ambient wind speed as 1, 2, 3, and 5 m/s. The SST k–ω model was used to model turbulent flow, while the Discrete Ordinates (DO) model was used to model solar radiation. Temperature contours showed that the high-temperature regions were concentrated around the dish-grooved absorber plates and that heat was transported to the collector outlet by the airflow. At a collector air velocity of 1.4 m/s, as the wind speed increased from 1 m/s to 5 m/s, the outlet temperature decreased from 28.54 °C to 26.72 °C for 800 W/m² and from 29.48 °C to 27.42 °C for 900 W/m². Similarly, at an air velocity of 2 m/s, the outlet temperature varied within the range of 27.22–25.61 °C for 800 W/m² and 27.88–26.22 °C for 900 W/m². The results show that increasing ambient wind speed reduces the collector outlet temperature by increasing convective heat losses. In contrast, higher solar radiation contributes to an increase in the collector outlet air temperature by increasing the thermal load on the absorber surfaces.

Keywords – Photovoltaic-thermal system, PVT collector, computational fluid dynamics (CFD), wind speed, solar radiation.

I. INTRODUCTION

The importance of hybrid energy systems is increasing day by day in order to provide uninterrupted energy from renewable energy sources and to model highly efficient systems. Photovoltaic thermal systems (PVT) are energy systems that produce heat and electrical energy together and are used for purposes such as drying, heat pumps, and hydrogen production. Many studies in this field are available in literature. Calise et al. (2026) developed and analyzed a ground-source PVT-assisted heat pump for cold climate conditions. Their proposed model aims to improve the operating efficiency of the heat pump under severe winter conditions by increasing its evaporation temperature. In their results, they reported that the consumption value decreased from 329.21 MWh/y to 26.35 MWh/y [1]. Wang et al. (2026) developed and analyzed a PVT-assisted green ammonia synthesis system for ammonia synthesis plants. Their proposed model aims to reduce renewable energy curtailment and improve operational robustness by coordinating multiple energy flows through a Wasserstein distance-based distributionally robust optimization method. In their results, they reported that the annual greenhouse gas emission value

decreased by 51.1% compared with the conventional fossil-based method [2]. Hou et al. (2026) developed and analyzed a PVT system integrated with a proton exchange membrane (PEM) electrolyzer for solar-powered hydrogen production systems in Xi'an (China). Their proposed model aims to optimize heat transfer by using a bidirectional parallel-pipe backplate flow channel structure, thereby improving panel temperature uniformity and the energy-exergy efficiency of the system. In their results, they reported that the total hydrogen production value increased from 30 L to 31.2 L compared with the conventional PV-PEM system [3]. El Alami et al. (2026) developed and analyzed novel direct-contact PVT configurations using CuO/water nanofluid to address the problem of inadequate thermal management in photovoltaic-thermal systems. Their proposed model aims to improve the heat transfer performance and sustainability index of the system by enabling the working fluid to directly contact the rear surface of the PV panel. In their results, they reported that increasing the nanofluid concentration from 0.4% to 2% increased the thermal efficiency value by 0.264% [4]. Yang et al. (2026) developed and analyzed a solar-powered air-water-ground triple-source hybrid heat pump system to improve the operating efficiency of heat pumps in severe cold climate regions. Their proposed model aims to ensure stable and highly efficient operation of the system by prioritizing the PVT-assisted water-source mode during daytime in winter and the ground-source mode during nighttime. In their results, they reported that, under the same operating conditions, the water-source heat pump mode increased the carbon dioxide emission reduction value by 20% to 30% compared with the air-source heat pump mode [5].

On the other hand, in order to save both cost and time, numerical analyses of PVT collectors are investigated using the CFD approach. Handawy et al. (2026) developed and analyzed an artificial neural network (ANN)-assisted three-dimensional CFD model to optimize the thermal performance of a water- and air-flow finned PVT collector. Their proposed model aims to reduce the operating temperature of PV cells by predicting complex thermal and hydrodynamic behaviors rapidly and with high accuracy instead of using computationally expensive simulations. In their results, they reported that, owing to the improvement in fin design, the heat transfer efficiency value increased by 28.7% compared with conventional models and that the developed ANN model was able to predict cell temperatures with a maximum error rate of 2.5% [6]. Husain et al. (2026) developed and analyzed a hybrid system integrated with water cooling and phase change material (PCM) for the thermal control of photovoltaic-thermal (PVT) systems operating under hot and arid climate conditions. The proposed system aims to reduce cell temperature by optimizing the effects of PCM layer thickness (24 mm–36 mm) and melting temperature (28 °C–55 °C) on the energy, exergy, and entropy generation of the system. In their results, they reported that the use of PCM with a thickness of 24 mm and a melting temperature of 44 °C increased the electrical efficiency value by 1.75%, while the total system efficiency reached 43.4% with PCM having a melting temperature of 50 °C [7]. Al-Mamoori and Kilinc (2025) developed and analyzed a water-cooled PVT collector with four novel cooling subchannels to improve the operating efficiency of PV panels by reducing their temperature. The existing model aims to improve the collector geometry by optimizing the effects of subchannel dimensions and Reynolds numbers on the temperature distribution, flow velocity, and pressure drop of the PV module. In their results, they reported that, with subchannels having dimensions of 20 × 20 mm² and a Reynolds number of 2275, the average PV module temperature decreased by 8% compared with the reference values in the literature, reaching 32.63 °C [8]. Raza et al. (2026) reviewed and analyzed the latest PV cooling strategies in the literature and the CFD studies applied to them in order to solve the overheating problem of photovoltaic panels. Their proposed study aims to present sustainable design approaches by comparing the effects of active and passive cooling technologies involving phase change materials (PCM), water- and air-based flows, and nanofluids on panel temperature and power output. In their results, they reported that CFD-validated hybrid cooling systems have high efficiency potential and that water-spray cooling methods can increase the cell efficiency value by up to 52% compared with the uncooled condition [9]. Kidane et al. (2025) reviewed and analyzed academic studies on the modeling of airflow dynamics in solar drying chambers used for drying agricultural products by means of computational fluid dynamics (CFD). Their proposed study aims to identify CFD trends in the optimization of temperature, airflow profiles, and moisture distribution in drying chambers using bibliometric data covering the literature between 1984 and 2025. In their results,

they reported that scientific publications in this field showed a robust annual growth rate of 2.72% and that India, Morocco, and Türkiye were the countries making the greatest contributions globally [10].

In this study, the performance of a dish-grooved PVT collector under variable wind speeds and different solar radiation intensities was investigated. The numerical analyses were carried out using ANSYS Fluent software and the Computational Fluid Dynamics (CFD) approach. Initially, a PVT collector with six grooves was modeled. Subsequently, the performance of the system was analyzed under solar radiation intensities of 800 W/m² and 900 W/m² and wind speed conditions of 1 m/s, 2 m/s, 3 m/s, and 5 m/s, respectively.

II. Materials and Method

In this study, the behavior of a dish-grooved PVT collector under different flow velocities, variable radiation intensities, and different ambient wind speed conditions was numerically investigated. The numerical analyses were carried out using ANSYS software, and the CFD approach was utilized. In this context, the performance of a PVT collector with six grooves was investigated under air flow velocities of 1.4 m/s and 2 m/s. In addition, analyses were performed under radiation conditions of 800 W/m² and 900 W/m² and wind speeds of 1 m/s, 2 m/s, 3 m/s, and 5 m/s. In this context, the modeled PVT collector has a collector casing with a length of 800 mm, a height of 180 mm, and a width of 400 mm. On the other hand, six dish-groove-type absorber plates are located inside the collector. Each absorber plate has a depth of 36 mm, an opening of 72 mm, and a width of 400 mm. In addition, a PV cell with dimensions of 255 × 355 × 20 mm is located inside the collector. Air enters the collector through air ducts with a diameter of 72 mm located at the lower and upper points. In this context, Figure 1 shows the modeled PVT collector.

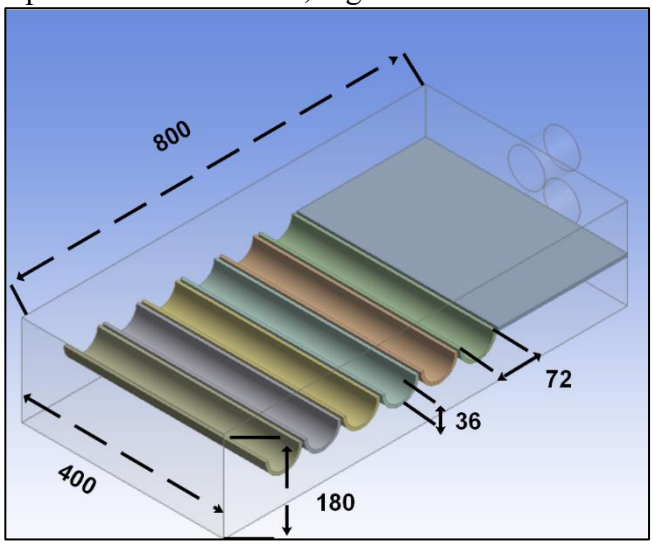

Figure 1. CAD drawing of the modeled PVT collector

One of the most important steps in a numerical analysis is the mesh model applied to the model. The meshing process of the present model was performed using regional sizing. In this context, 11,214,959 mesh elements were applied. At this mesh number, the skewness value was 0.78, while the orthogonal quality was obtained as 0.21. These values indicate that the mesh model is applicable. In addition, for mesh independence, mesh numbers of 10,315,622 and 12,389,177 were applied, respectively, and the collector outlet temperature deviations at these values were obtained as 1.76% and 0.78%. Figure 2 shows the mesh structure applied to the present model.

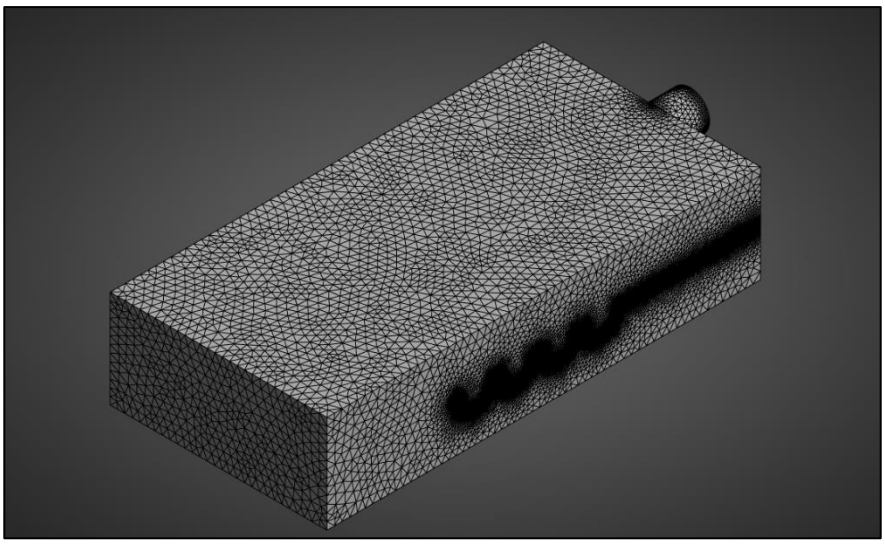

Figure 2. Mesh model applied to the modeled PVT collector

Finally, in order to complete the numerical analyses, the system boundary conditions must be determined. The present analyses were performed using the SST k–ω turbulence model. This is because it represents separation/reattachment regions and heat transfer more accurately in grooved and narrow-channel internal flows. For the solar radiation model, the Discrete Ordinates solar radiation model was preferred because it resolves reflection and absorption more effectively. Air was selected as the working fluid, while the collector material was defined as steel and the internal grooved structure as aluminum coated with black paint. The air inlet temperature was 20 °C, while the inlet velocities were determined as 1.4 m/s (Re = 6800) and 2 m/s (Re = 9800). The ambient wind speeds were 1 m/s, 2 m/s, 3 m/s, and 5 m/s, respectively, and the convective heat transfer coefficients at these velocities were calculated using the McAdams wind convection correlation. Finally, the heating generated in the PV cell was also applied to the model as heat flux.

III. Results and Discussion

In this section, the numerical analysis results of the modeled grooved heat exchanger are presented. Figures 3–6 show the temperature distributions obtained under different solar radiation, collector air velocity, and ambient wind speed conditions. When the temperature contours are examined, it is seen that the high-temperature regions are mainly formed around the dish-grooved absorber plates and that the heat transferred from the absorber surfaces is carried toward the collector outlet by the airflow. With the increase in solar radiation intensity from 800 W/m² to 900 W/m², the high-temperature region around the absorber plates increased, and accordingly, the collector outlet temperature increased. However, the increase in ambient wind speed caused the collector outlet temperature to decrease under all analysis conditions. When the collector air velocity was 1.4 m/s, the outlet temperature under 800 W/m² solar radiation was determined as 28.54 °C at a wind speed of 1 m/s, while this value decreased to 26.72 °C as the wind speed increased to 5 m/s. At the same air velocity, the outlet temperature for 900 W/m² radiation decreased from 29.48 °C to 27.42 °C. This change results from the increase in convective heat losses from the outer surfaces of the collector to the surroundings as the wind speed increases. When the air velocity inside the collector was increased to 2 m/s, a similar effect of ambient wind speed was also observed. Under 800 W/m² radiation, the outlet temperature was 27.22 °C at a wind speed of 1 m/s, while it was determined as 25.61 °C at a wind speed of 5 m/s. Under 900 W/m² radiation, the same values were obtained as 27.88 °C and 26.22 °C, respectively. Thus, it was observed that the increase in ambient wind speed decreased the outlet air temperature regardless of the solar radiation intensity and collector air velocity. In addition, as a result of increasing the collector air velocity from 1.4 m/s to 2 m/s, the outlet temperature decreased under all analysis conditions. With increasing air velocity, the increase in mass flow rate and the decrease in the contact time of the air with the heated surfaces limit the temperature rise of the unit mass of air. However, the decrease in outlet temperature alone does not indicate that the total

useful heat transfer has decreased, and both the mass flow rate and temperature difference should be considered together in the evaluation of thermal performance. In general, the results show that the performance of the PVT collector depends significantly not only on solar radiation but also on ambient wind conditions. While high solar radiation increases the collector outlet temperature, high ambient wind speed increases the convective heat losses from the collector surfaces and causes the outlet temperature to decrease.

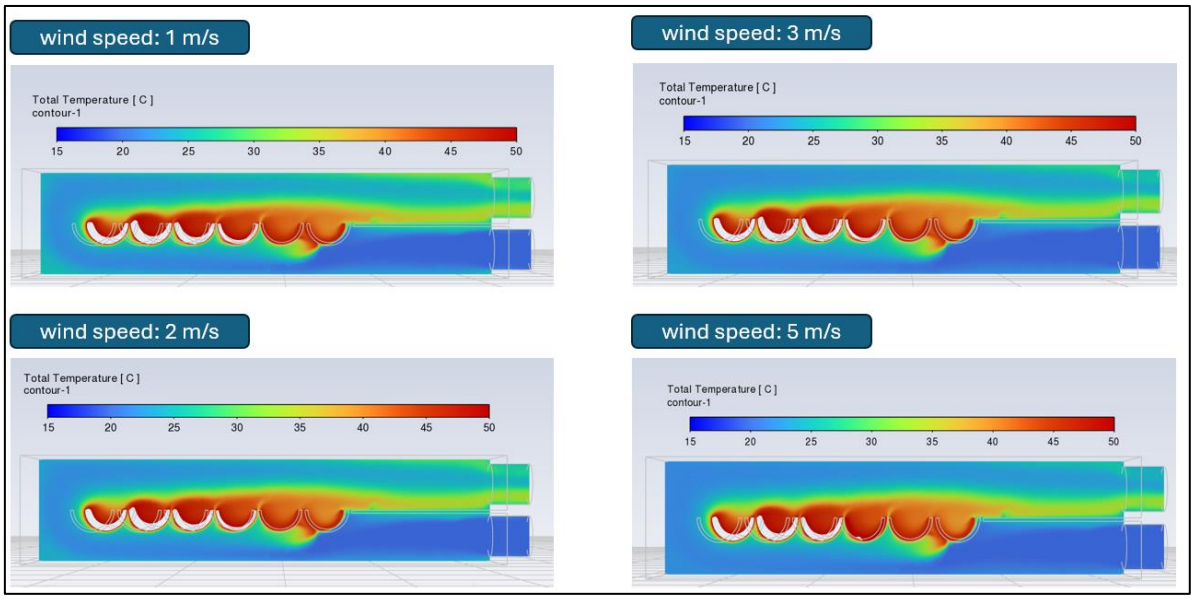

Figure 3. Collector temperature distribution depending on wind speed variation at a flow velocity of 1.4 m/s and a radiation intensity of 800 W/m²

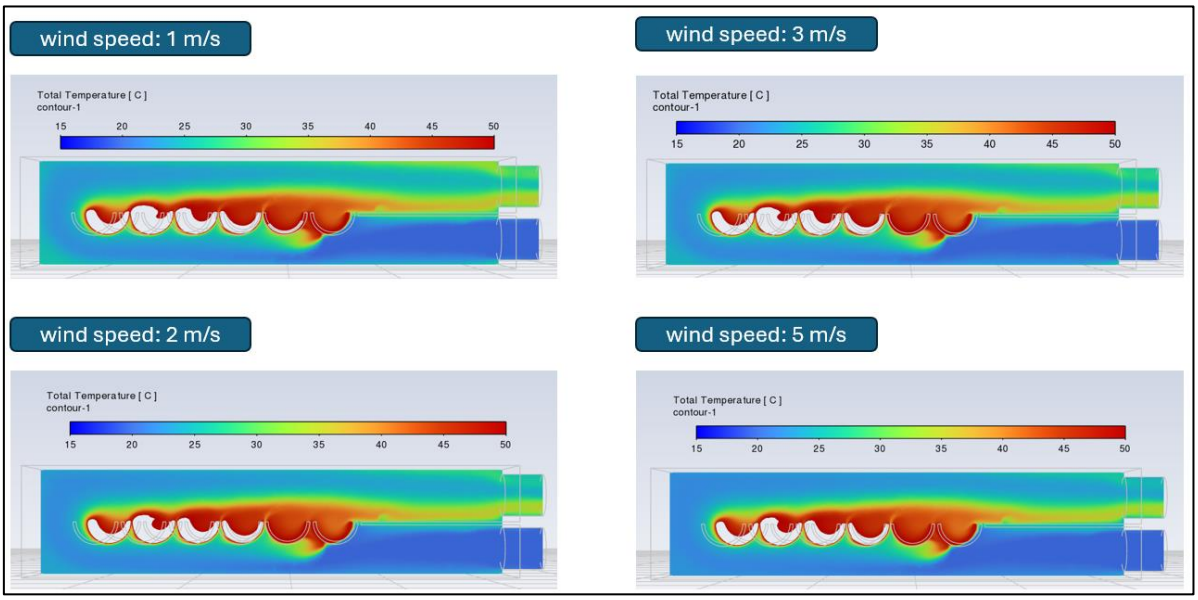

Figure 4. Collector temperature distribution depending on wind speed variation at a flow velocity of 1.4 m/s and a radiation intensity of 900 W/m²

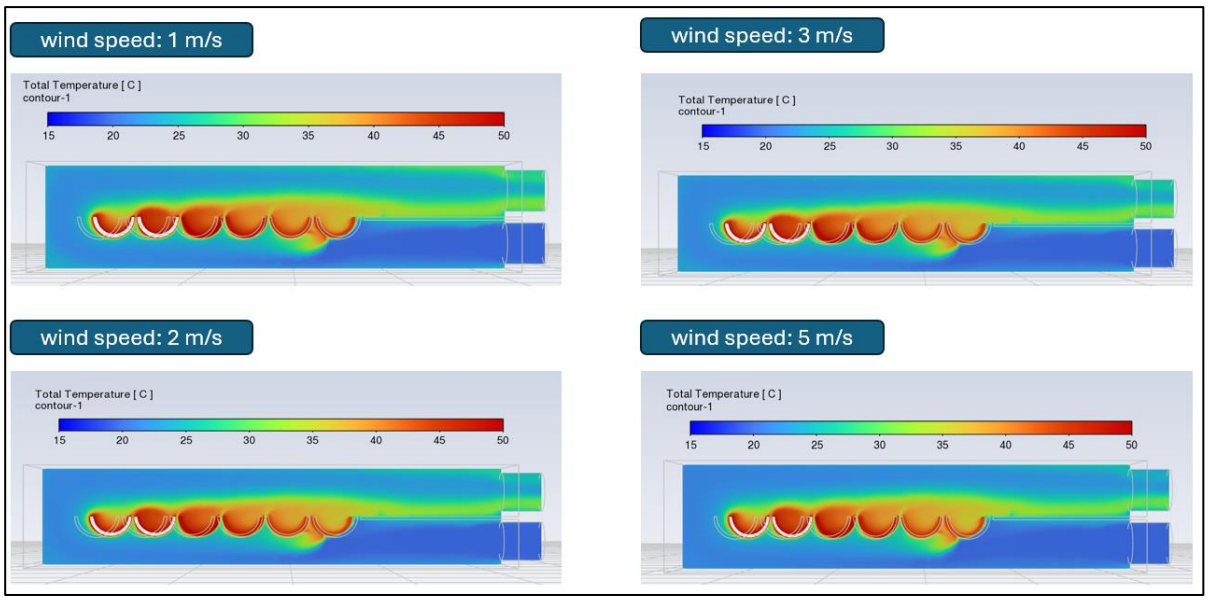

Figure 5. Collector temperature distribution depending on wind speed variation at a flow velocity of 2 m/s and a radiation intensity of 800 W/m²

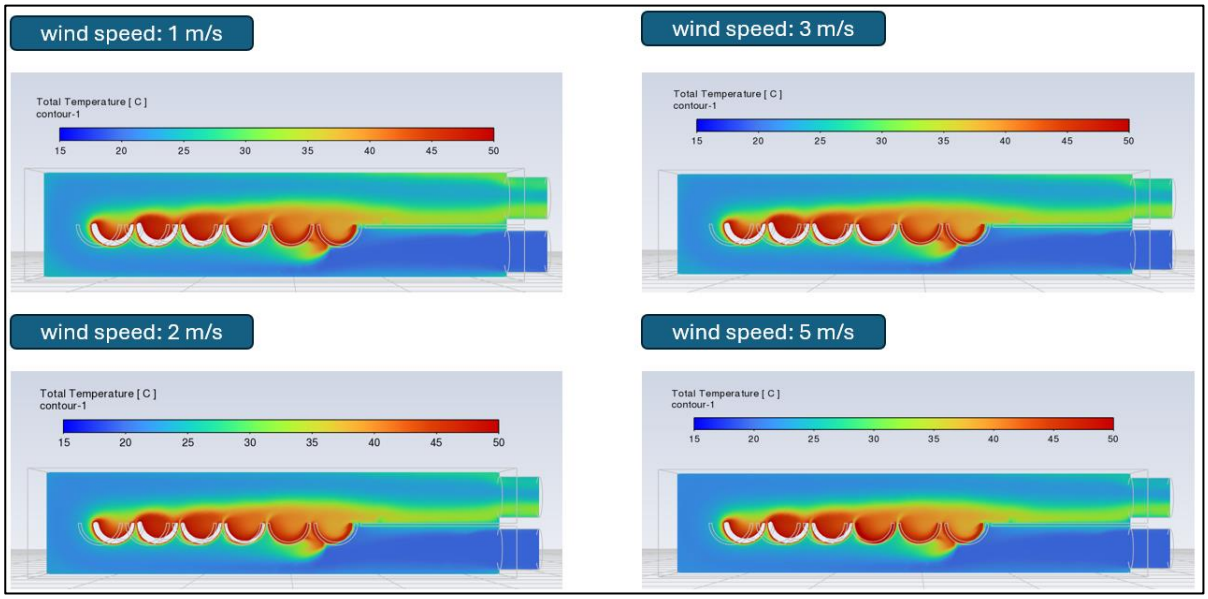

Figure 6. Collector temperature distribution depending on wind speed variation at a flow velocity of 2 m/s and a radiation intensity of 900 W/m²

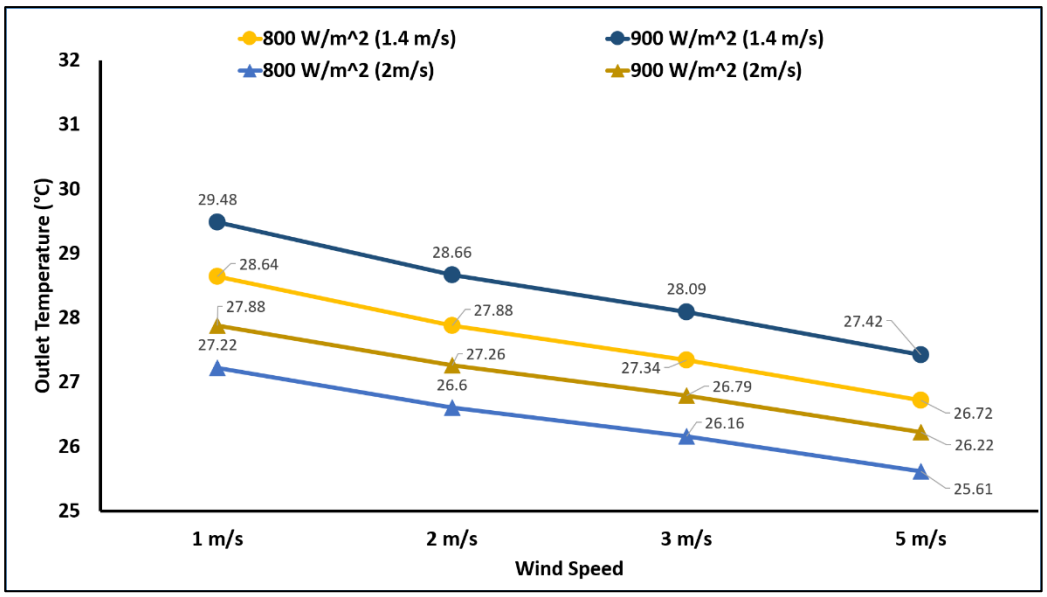

Figure 7. Collector outlet temperature of each model at different wind speeds

IV. CONCLUSION

In this study, the thermal behavior of an air-flow PVT collector with six dish-grooved absorber plates under different solar irradiation intensities, collector air velocities, and ambient wind speeds was numerically investigated using the Computational Fluid Dynamics (CFD) approach. As a result of the obtained temperature contours and the comparison of collector outlet temperatures, the main findings were determined as follows:

- It was observed from the temperature contours that the high-temperature regions were concentrated around the dish-grooved absorber plates and that the heat gained at the absorber surfaces was transported toward the collector outlet by the airflow. With the increase in solar irradiation from 800 W/m² to 900 W/m², the temperature level inside the collector and the outlet air temperature increased.
- When the collector air velocity was 1.4 m/s, increasing the ambient wind speed from 1 m/s to 5 m/s reduced the outlet temperature from 28.54 °C to 26.72 °C under 800 W/m² irradiation and from 29.48 °C to 27.42 °C under 900 W/m² irradiation. Accordingly, the temperature decreases were 1.82 °C and 2.06 °C, respectively.
- A similar trend was also obtained when the collector air velocity was 2 m/s. With the increase in wind speed from 1 m/s to 5 m/s, the outlet temperature decreased from 27.22 °C to 25.61 °C for 800 W/m² and from 27.88 °C to 26.22 °C for 900 W/m². This result indicates that the increase in ambient wind speed increases convective heat losses from the collector surfaces.
- Increasing the collector air velocity from 1.4 m/s to 2 m/s caused the outlet air temperature to decrease under all operating conditions. This situation was associated with the increased mass flow rate and the reduced contact time of the air with the heated surfaces; however, it was considered that the decrease in outlet temperature alone does not mean that the total useful heat transfer decreases.

In future studies, it is recommended that the developed PVT collector be experimentally validated and evaluated in terms of useful heat gain and thermal efficiency under different operating conditions.

REFERENCES

[1] F. Calise, F. L. Cappiello, L. Cimmino, and M. Vicidomini, “Dynamic and DoE-based assessment of a PVT-assisted ground-source heat pump system for cold-climate multi-family buildings,” Appl. Therm. Eng., vol. 302, pp. 131907, Jun. 2026.

[2] X. Wang, W. Zhang, K. Yang, J. Guo, Z. Li, R. Zou, P. Chen, C. Zhang, and Y. Zhang, “PVT-powered green ammonia synthesis system: Coordinated multi-energy optimization and life cycle evaluation,” Appl. Therm. Eng., vol. 300, pp. 131389, May 2026.

[3] G. Hou, Z. Wang, Y. Zhang, S. A. Kalogirou, and C. N. Markides, “Experimental and numerical investigation of a PVT-PEM system: impact of flow channel configurations on hydrogen production,” Renew. Energy, vol. 267, pp. 125741, Apr. 2026.
[4] Y. El Alami, E. Baghaz, C. Hajjaj, R. Nasrin, M. Holz, A. Faize, K. M. Al-Aribe, and A. Ibrahim, “Design innovation and performance optimization of next-generation PVT systems through 3D numerical simulation,” Sol. Energy, vol. 316, pp. 114894, Jul. 2026.
[5] Y. Yang, X. Wan, M. Zhuoma, and T. Wang, “Simulation and experimental study on the performance of a solar-powered PVT electric-thermal hybrid air-water-soil three-source heat pump system,” Next Energy, vol. 12, pp. 100740, 2026.
[6] M. K. Handawy, M. E. H. Attia, A. Khelifa, K. Harby, M. Abdelgaied, and H. M. Abdelmotalib, “Artificial intelligence–driven CFD simulation and thermal optimization of a finned bi-fluid PVT collector,” Int. Commun. Heat Mass Transf., vol. 176, pp. 111434, May 2026.
[7] A. Husain, B. Ali, M. Irfan, K. Alam, N. Al-Azri, N. Al-Rawahi, and M. Z. Ansari, “Energy-Exergy Analysis of a Hybrid PVT System with Varying PCM Thickness and Melting Temperature,” Int. J. Thermophys., vol. 47, pp. 121, Jun. 2026.
[8] Z. M. S. Al-Mamoori and E. Kilinc, “Numerical investigation to improve thermal performance of a watercooling PVT collector with novel cooling subchannels,” Sci. Rep., vol. 15, pp. 34317, Jul. 2025.
[9] S. Raza, A. Farooq, M. S. Shehzad, W. Hussain, Z. Abbas, and I.-T. Im, “A CFD analysis of photovoltaic panel cooling: a review,” Int. J. Air-Cond. Refrig., vol. 34, pp. 2, 2026.
[10] H. Kidane, I. Farkas, and J. Buzás, “Modeling airflow dynamics in solar drying chambers: a comprehensive review of CFD applications,” Discov. Appl. Sci., vol. 7, pp. 444, 2025

8th International Conference on Engineering, Natural and Social Sciences

September 06-07, 2026: Konya, Turkey

© 2026 Published by All Sciences Academy

https://www.icensos.com/

Parkinson Hastalığının Sınıflandırılmasında Çift Akışlı Swin Transformer ve mRMR

Abidin Çalışkan

Bilgisayar Mühendisliği Bölümü, Mühendislik-Mimarlık Fakültesi, Batman Üniversitesi, Türkiye
abidin.caliskan@batman.edu.tr

Özet - Parkinson hastalığının yapılandırılmış klinik verilerle sınıflandırılması, karar destek sistemleri açısından önem taşımaktadır. Bu çalışmada, klinik tablo verilerini görsel temsillere dönüştüren çift akışlı Swin Transformer tabanlı hibrit bir yaklaşım değerlendirilmiştir. Açık erişimli veri kümesinde 2105 bireye ait demografik, klinik ve bilişsel-işlevsel bilgiler kullanılmıştır. Veriler ön işlemeden geçirilmiş, normalleştirilmiş özellikler gri seviye ve RGB görüntülere dönüştürülmüştür. Her temsil ayrı bir Swin Transformer ağıyla işlenmiş ve elde edilen derin özellikler birleştirilmiştir. Ardından en düşük gereksizlik-en yüksek ilgililik (mRMR) yöntemiyle özellik seçimi uygulanmış; seçilen özellikler Destek Vektör Makinesi (DVM), k-En Yakın Komşu ve Rastgele Orman ile sınıflandırılmıştır. Tabakalı %80 eğitim ve %20 test ayrımında en yüksek doğruluk 0.910 olarak elde edilmiştir. Beş katlı çapraz doğrulamada 300 özellik kullanan DVM, 0.909 ortalama doğruluk ve 0.903 ortalama F1 skoru sağlamıştır. Bulgular, çift görsel temsil, özellik birleştirme ve mRMR tabanlı seçimin Parkinson hastalığının sınıflandırılmasında etkili bir yaklaşım oluşturduğunu göstermektedir.

Anahtar Kelimeler - Parkinson hastalığı; klinik tablo verisi; Swin Transformer; özellik birleştirme; mRMR; DVM.

I. GİRİŞ

Parkinson hastalığı, motor ve motor dışı belirtilerin birlikte görülebildiği, ilerleyici bir nörodejeneratif hastalıktır. Temel patofizyolojik özelliklerinden biri, substantia nigra bölgesindeki dopaminerjik nöronların kaybıdır. Bu süreç tremor, rijidite, bradikinezi ve postüral instabilite gibi motor bulgularla ilişkilidir. Uyku bozuklukları, depresif belirtiler, bilişsel etkilenme, konuşma değişiklikleri ve otonom bozukluklar da klinik tabloya eşlik edebilir [1], [2]. Erken dönemde belirtilerin hafif veya özgül olmaması, tanısal değerlendirmenin deneyimli klinisyenlerin yorumuna önemli ölçüde bağımlı kalmasına yol açabilir.

Makine öğrenmesi (MÖ) ve derin öğrenme (DÖ) tabanlı karar destek yaklaşımları, Parkinson hastalığının farklı veri türleri üzerinden modellenmesi amacıyla yaygın biçimde araştırılmaktadır. Ses kayıtları, el yazısı örüntüleri, yürüyüş verileri, elektroensefalografi, manyetik rezonans görüntüleme ve SPECT gibi veri kaynakları bu alanda kullanılmıştır [3]-[5]. Bu kaynaklar önemli biyobelirteçler sağlayabilse de maliyet, cihaz gereksinimi, standardizasyon ve veri toplama güçlüğü bakımından eşit ölçüde erişilebilir değildir. Yapılandırılmış klinik tablo verileri ise demografik özellikleri, yaşam tarzı değişkenlerini, tıbbi öyküyü, semptomları ve işlevsel ölçümleri tek bir veri yapısında bir araya getirebilir.

Tablo verilerinin temel sınırlılıklarından biri, doğal bir uzamsal komşuluk yapısına sahip olmamasıdır. Klasik MÖ yöntemleri bu verileri doğrudan özellik vektörleri olarak işler. Buna karşılık tablo verilerinin iki boyutlu görüntü temsillerine dönüştürülmesi, görsel temsil öğrenme mimarilerinden yararlanılmasına olanak sağlayabilir [6]. Bu yaklaşımda özellik değerleri piksel yoğunluklarına veya renk kanallarına aktarılır. Böylece aynı klinik bilgi farklı temsil biçimleri üzerinden işlenebilir. Derin özelliklerin klasik sınıflandırıcılarla birlikte kullanılması da tıbbi yapay zekâ uygulamalarında benimsenen hibrit bir yaklaşımdır. Örneğin VGG16 katmanlarından çıkarılan derin özelliklerin DVM ile değerlendirilmesi, görüntü tabanlı sınıflandırmada bu tür bir bütünleşmenin uygulanabilirliğini göstermiştir [7].

Yüksek boyutlu derin özellikler, sınıflandırma açısından gereksiz veya birbiriyle tekrarlı bileşenler içerebilir. Bu nedenle özellik seçimi, temsil uzayını daha kompakt hâle getirmek ve ayırt edici bilgiyi korumak açısından önemlidir [8], [9]. Benzer bir yöntemsel yaklaşımda, Evrişimli Sinir Ağı (ESA) ve özkodlayıcı tabanlı temsiller ki-kare özellik seçimiyle birlikte kullanılmış ve seçilen özellikler MÖ sınıflandırıcılarına aktarılmıştır [10]. Söz konusu çalışma Parkinson hastalığına özgü kanıt sunmamakla birlikte, derin temsil ile özellik seçiminin ardışık kullanımına yönelik yöntemsel bir örnek oluşturmaktadır.

Birden fazla temsil kaynağından elde edilen bilgilerin birleştirilmesi, tek bir temsilde bulunmayan tamamlayıcı örüntülerin yakalanmasına katkı sağlayabilir. Farklı sinyal temsillerinin Uzun Kısa Süreli Bellek tabanlı bir topluluk yapısında birleştirildiği çalışma da bu yaklaşımın farklı biyomedikal verilerde uygulanabildiğini göstermiştir [11]. Bu çalışmada ise klinik tablo verileri gri seviye ve RGB görüntülere dönüştürülmüş ve çift akışlı bir Swin Transformer yapısıyla değerlendirilmiştir. Swin Transformer, yerel pencerelerde öz-dikkat hesaplayan ve kaydırılmış pencere mekanizmasıyla komşu bölgeler arasında bilgi aktarımını sağlayan hiyerarşik bir görsel dönüştürücüdür [12]. İki akıştan elde edilen derin özellikler özellik düzeyinde birleştirilmiş, ardından mRMR ile seçilen alt kümeler DVM, k-En Yakın Komşu (k-EYK) ve Rastgele Orman (RO) sınıflandırıcılarına verilmiştir. Değerlendirme, tabakalı %80 eğitim ve %20 test ayrımı ile beş katlı çapraz doğrulama (ÇD) kullanılarak gerçekleştirilmiştir. Normalleştirme ve özellik seçimi yalnızca eğitim verisi üzerinde hesaplanarak veri sızıntısı riski azaltılmıştır.

II. MATERYAL VE YÖNTEM

A. Veri Kümesi ve Ön İşleme

Çalışmada Rabie El Kharoua tarafından yayımlanan açık erişimli Parkinson's Disease Dataset Analysis veri kümesi kullanılmıştır [13]. Veri kümesi, Parkinson hastalığı tanısı bulunan ve bulunmayan toplam 2105 bireye ait klinik ve demografik kayıtları içermektedir. Değişkenler; demografik özellikler, yaşam tarzı, tıbbi öykü, klinik ölçümler, bilişsel ve işlevsel değerlendirmeler, semptom bilgileri ve tanı etiketinden oluşmaktadır. Diagnosis alanı hedef değişken olarak kullanılmıştır. Her kaydı benzersiz biçimde tanımlayan PatientID alanı klinik bir öngörücü olmadığı için modelleme dışında bırakılmıştır.

Kategorik değişkenler sayısal gösterime dönüştürülmüştür. Sayısal değişkenler en küçük-en büyük (min-max) ölçekleme yöntemiyle [0,1] aralığına normalleştirilmiştir. Bu işlem tüm veri kümesine tek seferde uygulanmamıştır. Her eğitim-test ayrımında ve her ÇD katında ölçekleme parametreleri yalnızca eğitim örneklerinden hesaplanmıştır. Aynı parametreler daha sonra test veya doğrulama örneklerine uygulanmıştır. Böylece test ya da doğrulama bölümüne ait dağılım bilgisinin eğitim aşamasına aktarılması önlenerek veri sızıntısı riski azaltılmıştır.

B. Görüntü Temsili ve Çift Akışlı Swin Transformer

Normalleştirilmiş tek boyutlu klinik özellik vektörleri iki ayrı görsel temsile dönüştürülmüştür. Gri seviye akışında özellik değerleri iki boyutlu bir matrise yerleştirilmiş ve 8 bitlik yoğunluk değerlerine dönüştürülmüştür. Özellik sayısının kare matris boyutunu tam olarak doldurmadığı durumlarda kalan konumlara sıfır dolgusu uygulanmıştır. RGB akışında aynı klinik bilgi üç kanallı bir tensör yapısına aktarılmıştır. Bu dönüşüm, tek bir klinik vektörün hem yoğunluk tabanlı hem de çok kanallı gösterimle işlenmesini sağlamaktadır [6]. Oluşturulan görüntüler, Swin Transformer girişine uygun olacak biçimde 224 × 224 piksel boyutuna yeniden ölçeklendirilmiştir.

Gri seviye ve RGB görüntüler giriş düzeyinde birleştirilmemiştir. Her temsil ayrı bir Swin Transformer ağına aktarılmıştır. Mimari, görüntüyü örtüşmeyen yamalara ayırmakta ve yama gömmelerini hiyerarşik katmanlar boyunca işlemektedir. Pencereli Çok Başlı Öz-Dikkat mekanizması yerel pencere içindeki ilişkileri modellerken, Kaydırılmış Pencereli Çok Başlı Öz-Dikkat ardışık katmanlarda pencere sınırlarını kaydırarak komşu bölgeler arasında bilgi aktarımını desteklemektedir [12]. Son hiyerarşik aşamanın ardından küresel ortalama havuzlama uygulanmış ve sınıflandırma katmanından önceki temsil, derin özellik vektörü olarak alınmıştır.

Önerilen yaklaşımın genel iş akışı Şekil 1'de sunulmaktadır. Klinik veri kümesi önce ön işleme ve normalleştirme aşamalarından geçirilmekte, ardından gri seviye ve RGB olmak üzere iki görsel temsile

dönüştürülmektedir. Bu temsiller çift akışlı Swin Transformer yapısında ayrı ayrı işlenerek derin özellikler çıkarılmaktadır. Elde edilen özellikler birleştirildikten sonra mRMR ile seçilmekte ve MÖ sınıflandırıcısına aktarılmaktadır. Sürecin sonunda her örnek için Parkinson hastalığına ilişkin pozitif veya negatif sınıf kararı üretilmektedir.

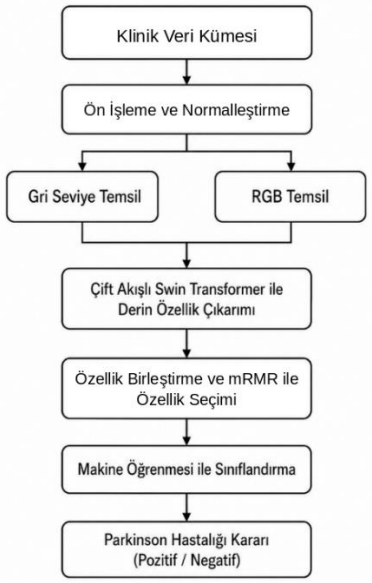

Şekil 1. Önerilen çift akışlı yaklaşımın Parkinson hastalığı sınıflandırmasına yönelik genel akış diyagramı.

C. *Özellik Birleştirme, mRMR ve Sınıflandırma*

İki Swin Transformer akışından elde edilen gri seviye ve RGB derin özellikleri, aynı örnek için ardışık biçimde birleştirilmiştir. Bu özellik düzeyindeki birleştirme, her temsilin tek başına yakaladığı bilgileri ortak bir vektörde toplamayı amaçlamaktadır. Birleşik temsilin yüksek boyutlu olması nedeniyle mRMR özellik seçimi uygulanmıştır. mRMR, aday özelliklerin sınıf etiketiyle karşılıklı bilgisini yüksek tutarken seçilen özellikler arasındaki gereksizliği azaltmayı amaçlayan karşılıklı bilgi tabanlı bir yöntemdir [9]. Bu çalışmada k = 100, 200, 300 ve 400 özellikten oluşan alt kümeler değerlendirilmiştir.

Özellik sıralaması, test veya doğrulama örnekleri kullanılmadan gerçekleştirilmiştir. %80 eğitim ve %20 test ayrımında mRMR yalnızca eğitim kümesi üzerinde hesaplanmış ve belirlenen özellik indeksleri test kümesine uygulanmıştır. Beş katlı ÇD'de ise özellik sıralaması her katın eğitim bölümü için yeniden oluşturulmuştur. Seçilen özellikler DVM, k-EYK ve RO algoritmalarıyla sınıflandırılmıştır. DVM yüksek boyutlu uzayda marjini en çoklayan karar sınırları oluştururken, k-EYK örnekler arasındaki komşuluk ilişkilerinden yararlanmakta, RO ise çok sayıda karar ağacının topluluk kararını kullanmaktadır.

D. *Deneysel Düzen ve Değerlendirme*

Deneyler iki tamamlayıcı doğrulama düzeninde yürütülmüştür. İlk aşamada sınıf dağılımı korunarak tabakalı %80 eğitim ve %20 test ayrımı uygulanmıştır. İkinci aşamada beş katlı ÇD kullanılmıştır. Swin Transformer akışlarının eğitiminde çapraz entropi kaybı ve AdamW eniyileme algoritması kullanılmıştır. Başlangıç öğrenme oranı 1×10^{-4}, mini-yığın boyutu 16 ve en fazla eğitim dönemi sayısı 15 olarak belirlenmiştir. Doğrulama kaybının en düşük olduğu model ağırlıkları, derin özellik çıkarımı için saklanmıştır. Bu bildiride sınıflandırma performansı doğruluk ve F1 skoru üzerinden raporlanmıştır.

III. BULGULAR

Tek akışlı Swin Transformer sonuçları, gri seviye ve RGB temsillerinin farklı sınıflandırma performansları sergilediğini göstermiştir. Tablo 1'de görüldüğü üzere, gri seviye temsilde doğruluk 0.867, F1 skoru ise 0.893 olarak elde edilmiştir. RGB temsilde doğruluk 0.842 ve F1 skoru 0.876 olarak hesaplanmıştır. Bu sonuçlar, doğrudan Swin Transformer çıktısına dayalı sınıflandırmada gri seviye temsilin RGB temsilden daha yüksek performans sağladığını göstermektedir.

İki Swin Transformer akışından elde edilen derin özelliklerin birleştirilmesi performansta artış sağlamıştır. Birleşik derin özelliklerin DVM ile sınıflandırılması sonucunda 0.893 doğruluk ve 0.888 F1 skoru elde edilmiştir. Bu bulgu, gri seviye ve RGB temsillerinden çıkarılan derin özelliklerin ortak bir özellik uzayında kullanılmasının sınıflandırma performansına katkı sağlayabildiğini göstermektedir.

Tablo 1. Önerilen yaklaşımın temel performans sonuçları.

Değerlendirme	Özellik / Model	Sınıflandırıcı	Doğruluk	F1 skoru
80:20	Gri seviye Swin	Swin çıkışı	0.867	0.893
80:20	RGB Swin	Swin çıkışı	0.842	0.876
80:20	Birleşik derin özellik	DVM	0.893	0.888
80:20	mRMR, k = 100	DVM	0.910	0.905
80:20	mRMR, k = 200	DVM	0.910	0.905
5 katlı ÇD	mRMR, k = 300	DVM	0.909	0.903
5 katlı ÇD	mRMR, k = 300	RO	0.909	0.902

mRMR özellik seçiminin ardından performans daha da yükselmiştir. DVM, k = 100 ve k = 200 özellik için 0.910 doğruluk değerine ulaşmıştır. F1 skoru her iki özellik sayısında da 0.905 olarak elde edilmiştir. Böylece %80 eğitim ve %20 test ayrımında en yüksek doğruluk 0.910 olarak gerçekleşmiştir.

Beş katlı ÇD sonuçları da yöntemin benzer bir performans düzeyini koruduğunu göstermiştir. mRMR ile seçilen 300 özellik kullanıldığında DVM, 0.909 ortalama doğruluk ve 0.903 ortalama F1 skoru sağlamıştır. Aynı özellik kümesinde RO modeli 0.909 ortalama doğruluk ve 0.902 ortalama F1 skoru elde etmiştir. Her iki model üç ondalık gösterimde aynı doğruluk değerine ulaşırken DVM, F1 skoru açısından RO'dan sınırlı ölçüde daha yüksek performans göstermiştir.

IV. TARTIŞMA

Elde edilen bulgular, yapılandırılmış klinik verilerin yalnızca klasik tablo tabanlı algoritmalarla değerlendirilmek zorunda olmadığını göstermektedir. Klinik özelliklerin görüntü temsillerine dönüştürülmesi, Swin Transformer gibi görsel mimarilerin derin özellik çıkarımı amacıyla kullanılmasına olanak sağlamıştır. Bununla birlikte bu dönüşüm, klinik değişkenler arasında doğal bir uzamsal ilişki ortaya çıkarmaktan çok özelliklere yapay bir yerleşim düzeni tanımlamaktadır. Bu nedenle özelliklerin matris içerisindeki sıralaması, sıfır dolgusu ve görüntü ölçekleme işlemleri elde edilen temsilleri ve dolayısıyla sınıflandırma performansını etkileyebilir. Yöntemin değerlendirilmesinde bu yapısal sınırlılık dikkate alınmalıdır.

Tablo 1'de görüldüğü üzere, tek akışlı değerlendirmede gri seviye temsil 0.867 doğruluk ve 0.893 F1 skoru ile RGB temsilden daha yüksek performans göstermiştir. RGB temsil için doğruluk 0.842, F1 skoru ise 0.876 olarak elde edilmiştir. İki akıştan çıkarılan derin özelliklerin birleştirilmesi sonucunda DVM doğruluğu 0.893 düzeyine yükselmiştir. mRMR özellik seçiminin uygulanmasıyla k = 100 ve k = 200 koşullarında doğruluk 0.910, F1 skoru ise 0.905 olarak elde edilmiştir. Beş katlı ÇD'de DVM ile 0.909 ortalama doğruluk ve 0.903 ortalama F1 skoru elde edilmesi, yöntemin farklı veri bölümlerinde benzer bir performans düzeyini koruduğunu göstermektedir. Aynı koşulda RO'nun 0.909 doğruluk ve 0.902 F1 skoru sağlaması, iki sınıflandırıcının birbirine yakın sonuçlar verdiğini ortaya koymaktadır.

Önerilen yaklaşımın performansı, aynı klinik veri kümesini kullanan güncel çalışmalarla birlikte değerlendirilmelidir. Tablo 2'de özetlendiği üzere, Arslan ve Çolak [14] Explainable Boosting Machine ile 0.920 doğruluk, Khansa ve arkadaşları [15] XGBoost ile 0.940 doğruluk, Esan ve arkadaşları [16] ise 0.930 doğruluk ve 0.970 AUC bildirmiştir. Tran ve arkadaşlarının ParkiDxAI yaklaşımında CatBoost doğruluğu 0.936 olarak raporlanmıştır [17]. Bu sonuçlar, önerilen yaklaşımın raporlanan doğruluk değerinin karşılaştırılan çalışmaların altında kaldığını göstermektedir. Bununla birlikte çalışmalar arasındaki doğrulama düzenleri ve hiperparametre eniyileme süreçleri farklı olabileceğinden, bu değerler doğrudan üstünlük göstergesi olarak yorumlanmamalıdır.

Tablo 2. Aynı klinik veri kümesini kullanan seçilmiş çalışmalarla karşılaştırma.

Çalışma	Yaklaşım	En iyi sonuç	Temel ayrım
Arslan ve Çolak [14]	Explainable Boosting Machine	Doğruluk: 0.920	Doğrudan tablo modelleme ve yorumlanabilir risk analizi
Khansa ve ark. [15]	XGBoost, Izgara/Rastgele Arama	Doğruluk: 0.940	Hiperparametreleri eniyilenmiş ağaç tabanlı model
Esan ve ark. [16]	MÖ, özellik seçimi, SHAP/LIME	Doğruluk: 0.930; AUC: 0.970	Açıklanabilirlik güçlü, görsel temsil yok
Tran ve ark. [17]	ParkiDxAI, 10 MÖ modeli	CatBoost: 0.936	Klinik karar destek ve SHAP/LIME açıklamaları
Bu çalışma	Çift Swin, özellik birleştirme, mRMR, DVM	Doğruluk: 0.910; ÇD: 0.909	Tablo verisini iki görsel temsile aktaran derin özellik yaklaşımı

Bu nedenle çalışmanın temel katkısı, en yüksek sınıflandırma doğruluğuna ulaşmak olarak değerlendirilmemelidir. Çalışmanın ayırt edici yönü, aynı klinik özelliklerin gri seviye ve RGB görüntü temsillerine dönüştürülmesi, bu temsillerin iki ayrı Swin Transformer akışında işlenmesi, elde edilen derin özelliklerin birleştirilmesi ve mRMR ile daha kompakt bir özellik kümesine indirgenmesidir. Bu yapı, doğrudan tablo tabanlı modellemeye alternatif bir temsil öğrenme yaklaşımı sunmaktadır. Ayrıca normalleştirme ve özellik seçiminin yalnızca eğitim verisi kullanılarak gerçekleştirilmesi, veri sızıntısı riskinin azaltılması açısından yöntemin önemli bir yönünü oluşturmaktadır.

Parkinson hastalığı dışındaki tıbbi sınıflandırma çalışmalarında da makine öğrenmesi ve hibrit öğrenme yaklaşımlarından yararlanılmıştır. Ateş ve Çalışkan [18], serebrovasküler olayların tespitinde makine öğrenmesi yöntemlerini değerlendirmiştir. Çalışkan [19] ise COVID-19 tanısında Darknet tabanlı ESA modelleri ve DVM'yi, Atom Search ve Marine Predator eniyileme algoritmalarıyla birlikte kullanmıştır. Bu çalışmalar, farklı hastalık alanlarında makine öğrenmesi, derin öğrenme ve eniyileme yöntemlerinin tanısal sınıflandırmaya uyarlanabildiğini göstermektedir. Bununla birlikte, Parkinson hastalığına özgü doğrudan kanıt olarak değerlendirilmemelidir.

Çalışmanın bazı sınırlılıkları bulunmaktadır. Deneylerin tek bir açık erişimli ve kesitsel veri kümesi üzerinde gerçekleştirilmiş olması, sonuçların farklı hasta gruplarına genellenebilirliğini sınırlandırmaktadır. Ayrıca bağımsız bir klinik kohort üzerinde doğrulama yapılmamış, farklı özellik yerleşim stratejileri karşılaştırılmamış ve çapraz doğrulama sonuçları için standart sapma veya güven aralığı raporlanmamıştır. Gelecek çalışmalarda bağımsız veri kümeleri üzerinde doğrulama yapılması, farklı tablo-görüntü dönüştürme stratejilerinin karşılaştırılması ve AUC'nin yanı sıra kalibrasyon ve belirsizlik ölçütlerinin değerlendirilmesi uygun olacaktır. SHAP veya LIME gibi açıklanabilir yapay zekâ yöntemlerinin modele eklenmesi de nihai sınıflandırma kararında etkili olan klinik özelliklerin daha ayrıntılı biçimde incelenmesini sağlayabilir.

V. SONUÇLAR

Bu çalışmada, klinik tablo verilerinden Parkinson hastalığının sınıflandırılması için çift akışlı bir görsel temsil yaklaşımı sunulmuştur. Normalleştirilmiş klinik özellikler gri seviye ve RGB görüntülere dönüştürülmüş, ayrı Swin Transformer ağlarından derin özellikler çıkarılmış ve bu özellikler birleştirilmiştir. mRMR ile seçilen özellikler üzerinde DVM, raporlanan deneysel koşullarda en yüksek sınıflandırma başarımını göstermiştir.

%80 eğitim ve %20 test ayrımında en yüksek doğruluk 0.910 olarak elde edilmiştir. Beş katlı ÇD'de 300 özellik kullanan DVM modeli, 0.909 ortalama doğruluk ve 0.903 ortalama F1 skoru sağlamıştır. Bulgular, çift görsel temsil ile özellik seçiminin daha kompakt ve ayırt edici bir sınıflandırma uzayı oluşturabildiğini göstermektedir. Gelecek çalışmalarda açıklanabilirlik, kalibrasyon, belirsizlik ve hesaplama maliyetinin değerlendirilmesi, ayrıca alternatif tablo tabanlı DÖ modelleriyle karşılaştırmaların gerçekleştirilmesi planlanmaktadır.

TEŞEKKÜR

Bu çalışma herhangi bir özel araştırma fonu ile desteklenmemiştir.

KAYNAKLAR

[1] W. Poewe, K. Seppi, C. M. Tanner, G. M. Halliday, P. Brundin, J. Volkmann, A.-E. Schrag, and A. E. Lang, "Parkinson disease," Nature Reviews Disease Primers, vol. 3, no. 1, art. 17013, 2017.

[2] S. G. Reich and J. M. Savitt, "Parkinson's disease," Medical Clinics of North America, vol. 103, no. 2, pp. 337-350, 2019.

[3] H. Rabie and M. A. Akhloufi, "A review of machine learning and deep learning for Parkinson's disease detection," Discover Artificial Intelligence, vol. 5, no. 1, art. 24, 2025.

[4] M. Islam, K. Akter, M. A. Hossain, and M. A. A. Dewan, "PD-Net: Parkinson's disease detection through fusion of two spectral features using attention-based hybrid deep neural network," Information, vol. 16, no. 2, art. 135, 2025.

[5] B. Majhi, A. Kashyap, S. S. Mohanty, S. Dash, S. Mallik, A. Li, and Z. Zhao, "An improved method for diagnosis of Parkinson's disease using deep learning models enhanced with metaheuristic algorithm," BMC Medical Imaging, vol. 24, no. 1, art. 156, 2024.

[6] Y. Zhu, T. Brettin, F. Xia, A. Partin, M. Shukla, H. Yoo, Y. A. Evrard, J. H. Doroshow, and R. L. Stevens, "Converting tabular data into images for deep learning with convolutional neural networks," Scientific Reports, vol. 11, no. 1, art. 11325, 2021.

[7] A. Çalışkan, "Classification of Tympanic Membrane Images based on VGG16 Model," Kocaeli Journal of Science and Engineering, vol. 5, no. 1, pp. 105-111, 2022. doi: 10.34088/kojose.1081402.

[8] A. Ouhmida, S. Saleh, A. Ammar, A. Raihani, and B. Cherradi, "HEFS-MLDR: A novel hybrid ensemble feature selection framework for improved deep neural network architecture in the diagnosis of Parkinson's disease," Multimedia Tools and Applications, vol. 84, no. 30, pp. 36597-36622, 2025.

[9] H. Peng, F. Long, and C. Ding, "Feature selection based on mutual information criteria of max-dependency, max-relevance, and min-redundancy," IEEE Transactions on Pattern Analysis and Machine Intelligence, vol. 27, no. 8, pp. 1226-1238, 2005.

[10] A. Çalışkan, "Diagnosis of malaria disease by integrating chi-square feature selection algorithm with convolutional neural networks and autoencoder network," Transactions of the Institute of Measurement and Control, vol. 45, no. 5, pp. 975-985, 2023. doi: 10.1177/01423312221147335.

[11] A. Çalışkan, "A New Ensemble Approach for Congestive Heart Failure and Arrhythmia Classification Using Shifted One-Dimensional Local Binary Patterns with Long Short-Term Memory," The Computer Journal, vol. 65, no. 9, pp. 2535-2546, 2022. doi: 10.1093/comjnl/bxac087.

[12] Z. Liu, Y. Lin, Y. Cao, H. Hu, Y. Wei, Z. Zhang, S. Lin, and B. Guo, "Swin Transformer: Hierarchical Vision Transformer using Shifted Windows," in Proc. 2021 IEEE/CVF International Conference on Computer Vision (ICCV), 2021, pp. 9992-10002.

[13] R. El Kharoua, "Parkinson's Disease Dataset Analysis," Kaggle, 2024. doi: 10.34740/kaggle/dsv/8668551.

[14] A. K. Arslan and C. Çolak, "Explainable boosting machine approach to identifying risk factors for Parkinson's disease," Annals of Medical Research, vol. 31, no. 9, pp. 735-740, 2024.

[15] S. F. A. Khansa, N. Ulinnuha, and W. D. Utami, "Grid search and random search hyperparameter tuning optimization in XGBoost algorithm for Parkinson's disease classification," BAREKENG: Jurnal Ilmu Matematika Dan Terapan, vol. 19, no. 3, pp. 1609-1624, 2025.

[16] A. O. Esan, D. B. Olawade, A. A. Soladoye, B. A. Omodunbi, I. A. Adeyanju, and N. Aderinto, "Explainable AI for Parkinson's disease prediction: a machine learning approach with interpretable models," Current Research in Translational Medicine, art. 103541, 2025.

[17] H.-D.-N. Tran, M. Isomursu, M.-H. Trinh, T.-N. Ngo, G.-H. Le, and H.-A. Pham, "ParkiDxAI: An Explainable AI System for Parkinson's Disease Diagnosis," in International Conference on Multi-Disciplinary Trends in Artificial Intelligence, 2025, pp. 290-303.

[18] H. Ateş and A. Çalışkan, "Detection of stroke (Cerebrovascular Accident) using machine learning methods," Bitlis Eren Üniversitesi Fen Bilimleri Dergisi, vol. 13, no. 4, pp. 1169-1180, 2024.

[19] A. Çalışkan, "COVID-19 diagnostic based on darknet CNN models and support vector machine along with atom search and marine predator optimization algorithms," in International Research in Engineering Sciences V, p. 61, 2023.

8th International Conference on Engineering, Natural and Social Sciences

September 06-07, 2026: Konya, Turkey

© 2026 Published by All Sciences Academy

https://www.icensos.com/

Campus Trees for a Changing Climate: Lessons from Tekirdağ, Türkiye

Seray ÖZDEN KELEŞ*, Miray ÖZDEN [2]

[1]*Departmentof Forest Botany/Faculty of Forestry, Kastamou University, Türkiye*
[2]*Social Sciences Vocational School, Tekirdag Namik Kemal University, Türkiye*

**[1]*(sozden@kastamonu.edu.tr) Email of the corresponding author*

Abstract – University campuses rarely treat tree planting as a long-term climate decision, yet the species chosen today will shape thermal comfort, air quality, biodiversity, and overall campus quality of life for decades to come. This study assesses the dominant tree species growing on the Tekirdağ Namık Kemal University campus through a climate-adaptation lens, covering *Robinia pseudoacacia*, *Tilia* spp., *Fraxinus angustifolia*, *Cedrus libani*, *Cupressus sempervirens*, *Pinus pinea*, *Pinus brutia*, *Populus nigra*, *Juniperus* spp., *Paulownia tomentosa*, *Acer negundo*, *Acer pseudoplatanus*, *Aesculus hippocastanum*, *Platanus orientalis*, and *Thuja* spp. Each species' ecological characteristics are examined against the backdrop of Tekirdağ's transitional Marmara climate, marked by cool, comparatively wet winters and warm, markedly dry summers. Mediterranean and drought-hardy taxa notably *Pinus brutia*, *Pinus pinea*, *Cupressus sempervirens, Cedrus libani*, and *Juniperus* spp. emerge as comparatively well matched to the site's climatic limitations, while species with higher water demands or lower drought tolerance may increasingly rely on favorable microsite conditions and active management to withstand extended summer dry spells. Certain introduced species that otherwise tolerate local conditions well, particularly *Robinia pseudoacacia* and *Acer negundo*, raise a separate concern: their climatic adaptability comes paired with ecological risks tied to invasiveness. Taken together, the findings suggest that future campus planting decisions should move beyond drought tolerance as a sole criterion, instead weighing climatic fit alongside ecosystem service value, biodiversity contribution, water demand, and ecological risk. As such, the campus offers a workable model for shaping climate-responsive planting strategies with broader relevance to urban forestry across Tekirdağ.

Keywords: campus trees; climate adaptation; drought tolerance; urban forestry; green infrastructure; species selection; Tekirdağ

I. INTRODUCTION

University campuses tend to be seen as academic and architectural spaces dressed up with ornamental greenery. Ecologically, though, their trees are something more substantial: long-lived infrastructure. A tree planted today will likely still be standing in fifty years, which means today's planting choices lock in decades of future canopy cover, shade, carbon storage, habitat, and outdoor comfort under climatic conditions that may look quite different from those at the time of planting ([1], [2], [3], [4]).

That long lifespan is exactly why species selection matters so much under a changing climate. Urban trees already contend with conditions harsher than anything found in a natural forest restricted rooting space, compacted soil, paved surroundings, elevated heat, disrupted hydrology, pollution, and inconsistent maintenance, all layered on top of regional climatic stress. During extended summer droughts, a tree hemmed in by buildings, roads, and pavement can face far greater water and heat stress than the raw meteorological data alone would suggest ([5], [6], [7]). Tekirdağ is a particularly useful setting for examining this problem, sitting as it does within a climatic transition zone in northwestern Türkiye. Its

position within the Marmara region allows both temperate broadleaved trees and Mediterranean or sub-Mediterranean species to coexist, and as a result, university and municipal landscapes here end up with a genuinely mixed planting palette native and introduced, deciduous and evergreen, drought-tolerant and water-hungry species all growing side by side. The Tekirdağ Namık Kemal University campus is a good example of this mix. Its tree population spans *Robinia pseudoacacia*, *Tilia* spp., *Fraxinus angustifolia*, *Cedrus libani*, *Cupressus sempervirens*, *Pinus pinea*, *Pinus brutia*, *Populus nigra*, *Juniperus* spp., *Paulownia tomentosa*, *Acer negundo*, *Acer pseudoplatanus*, *Aesculus hippocastanum*, *Platanus orientalis*, and *Thuja* spp. species with very different ecological strategies, and therefore no reason to expect they could all respond the same way as the climate shifts.

This study evaluates the campus's dominant tree species on drought tolerance, heat tolerance, water demand, ecological risk, and their contribution to ecosystem services paying particular attention to cases where climatic toughness and ecological suitability pull in opposite directions: some introduced species handle drought remarkably well while carrying real invasive risk, while some thirstier broadleaved species earn their keep through exceptional shade and cooling. The aim, ultimately, is a practical framework for moving campus tree management away from conventional ornamental planting and toward something more climate-responsive and functionally diverse.

II. MATERIAL AND METHOD

Climatic Context of Tekirdağ

Tekirdağ is situated in northwestern Türkiye, occupying an important position within Thrace in the Marmara Region (Fig. 1). Its geographical setting places İstanbul to the east and Edirne to the west, while Kırklareli lies along its northern boundary. To the south, the province extends toward the Sea of Marmara and borders Çanakkale, whereas its northeastern section reaches the Black Sea coast. Its geographic position places it within a climatic transition between maritime Marmara conditions, continental influences from Thrace, and Mediterranean seasonality. This transitional setting is particularly important for tree selection because planted vegetation must tolerate both winter cold and substantial summer heat and moisture limitation.



Figure 1. Tekirdağ is situated in northwestern Türkiye (red place).

Study Area and Green Infrastructure Context

Tekirdağ Namık Kemal University sits in the Süleymanpaşa district of Tekirdağ Province, within the Thrace section of the Marmara Region, at roughly 40.99512° N, 27.59010° E (Namık Kemal Mahallesi, Kampüs Caddesi, Süleymanpaşa, Tekirdağ). Its location, caught between the moderating influence of the Sea of Marmara and the more continental conditions further inland, gives the campus a genuinely transitional climate and makes it a useful setting for assessing how different urban tree species actually perform. It is worth stressing that the campus is not just a set of buildings ringed by decorative planting. Its

trees, lawns, pedestrian areas, and other green surfaces function together as a connected piece of campus infrastructure, and that network extends further than the campus boundary itself: the Atatürk Urban Forest sits right alongside the main campus, covering roughly 280 decares (28 ha) between the university and the Tekirdağ-Istanbul D100 highway. Management of this forest passed from the Tekirdağ Forest Enterprise Directorate to the university, which has since developed it for public recreational use.



Figure 2. Some tree species in NKU campus in Tekirdağ (*C. sempervirens*, *A. pseudoplatanus, P. pinea*, *P. brutia*).

Having this 28-hectare wooded area next door meaningfully expands the ecological reach of the campus. Rather than treating campus trees as isolated ornamental features, it makes more sense to view them as part of a broader green continuum running from the intensively managed plantings around buildings, roads, and parking areas all the way out to the adjoining urban forest. This structure boosts the university landscape's ecological value, adding vegetation cover, habitat, recreational space, and connective tissue between different pockets of green space across the wider urban area. In practical terms, this pairing of campus planting and adjacent woodland supports several useful functions. Tree canopies shade buildings and walkways and cut down solar exposure; vegetation more broadly helps regulate local temperature, store carbon, trap airborne pollutants, manage storm water, and provide habitat. On a more human level, these green spaces double as places to walk, unwind, socialize, and simply spend time outdoors and the university's decision to convert the adjacent forest into a recreational area makes clear that this landscape is valued for more than just how it looks. This green infrastructure matters even more given Tekirdağ's climate. Long-term data from 1940-2025 put the mean annual temperature at 14.2°C and annual

precipitation at around 575.1 mm. July and August average 23.8°C and 23.9°C respectively, yet rainfall in those same months drops to just 23.5 mm and 15.3 mm, with recorded highs reaching 40.2°C. That overlap of peak heat and minimal rainfall creates a real moisture bottleneck, one felt most acutely by trees growing near buildings, roads, parking lots, and other paved surfaces, where actual soil moisture can fall well below what regional averages would suggest. This existing summer deficit takes on added weight in light of national climate projections, which point to continued warming across Türkiye through this century alongside precipitation that becomes both scarcer and more irregular regardless of exact emissions scenario, the trend points toward greater heat exposure and more frequent, longer soil-water shortfalls. Given all this, how well the campus's green infrastructure holds up increasingly hinges on whether its trees can sustain healthy canopies under the combined weight of summer heat and limited water. That makes the campus a genuinely useful living laboratory for climate-adaptive urban forestry: its mix of Mediterranean, temperate, native, and introduced species allows very different ecological strategies to be compared under a shared climate, while variation across lawns, roadsides, building surrounds, paved zones, and areas bordering the urban forest creates a range of distinct microenvironments. Studying tree performance across these settings offers insight not just into which species can handle Tekirdağ's climate broadly, but which ones suit particular roles and locations within the campus itself. Species need to cope with summer drought, sudden heat spikes, winter cold, unpredictable rainfall, wind exposure, and the particular challenges of urban soil all while conditions vary sharply from irrigated lawns and sheltered courtyards to exposed roadsides and heavily paved ground. Matching species to these specific microsites matters just as much as choosing them for the region's broader climate. For these reasons, the ecological value of the NKU landscape is best assessed on two levels at once: how well individual species perform, and how well the landscape functions as a connected system. A species might tolerate drought impressively but offer little shade, while another delivers strong cooling and canopy cover but needs more water to do it. Some introduced species, meanwhile, may thrive under urban stress while raising concerns about invasive spread a consideration that carries extra weight given the campus's proximity to the Atatürk Urban Forest, since species choices here can ripple outward into that adjacent landscape. Seen this way, the campus becomes more than a landscaped setting it is a working model for how species selection, climate resilience, ecosystem services, ecological risk, and green-space connectivity can come together in future urban forestry planning, with lessons that could extend well beyond the university to parks, institutional grounds, and municipal green spaces across Tekirdağ.

III. RESULTS

Campus Tree Assessment

Field observations across the Namık Kemal University campus confirmed a clear range of vitality and site adaptation among the nine major taxa examined, with performance closely tracking each species' known drought and heat tolerance. The study was designed around the major tree taxa observed within the Namık Kemal University campus landscape.

Table 1. Ecological characteristics and potential suitability of the tree species identified on the Tekirdağ Namık Kemal University campus under warmer and drier climatic conditions.

Tree Species	**Interpretation under warmer and drier conditions**
Pinus brutia	Potentially favorable
Pinus pinea	Potentially favorable
Cupressus sempervirens	Potentially favorable
Cedrus libani	Potentially favorable
Juniperus spp.	Potentially favorable
Fraxinus angustifolia	Potentially favorable, depending on site moisture
Platanus orientalis	Site- and water-dependent
Tilia spp.	Site- and water-dependent

Tree Species	Interpretation under warmer and drier conditions
Aesculus hippocastanum	May require greater attention under summer drought
Acer pseudoplatanus	Potentially sensitive on hot and dry sites
Populus nigra	Strongly dependent on water availability
Thuja spp.	Site-dependent
Robinia pseudoacacia	Climatically tolerant; ecological risk should be considered
Acer negundo	Climatically tolerant; ecological risk should be considered
Paulownia tomentosa	Potentially tolerant; requires site-specific evaluation

The present study is based primarily on the identification of tree species occurring within the Tekirdağ Namık Kemal University campus. Therefore, the ecological characteristics summarized in Table 1 should not be interpreted as direct measurements of drought resistance, water use, or climate-change responses of individual trees on the campus. Rather, the table provides a comparative interpretation of the identified species based on their generally recognized ecological requirements and functional characteristics. When these characteristics are considered together with the warm and relatively dry summer conditions of Tekirdağ, they provide an indication of how the existing species composition may respond to future climatic conditions and which taxa could potentially require greater attention in long-term campus management. Among the identified species, *Pinus brutia*, *Pinus pinea*, *Cupressus sempervirens*, *Cedrus libani*, and *Juniperus* spp. appear to possess ecological characteristics that could favor their persistence under warmer and seasonally drier conditions. Their generally low to moderate water requirements and comparatively high tolerance of heat and drought may represent an advantage during Tekirdağ summers, particularly because July and August combine the highest temperatures with the lowest precipitation. *P. brutia* and *C. sempervirens*, for example, are naturally associated with climates characterized by pronounced summer dryness, while *P. pinea* also combines heat tolerance with the ability to develop a relatively broad crown. *C. libani* may offer additional advantages through its longevity and substantial biomass development. *Juniperus* species are similarly well adapted to water limitation, although their generally slower growth and smaller canopy development may provide less immediate shade than large broadleaved trees. These characteristics suggest that such taxa could form an important component of climate-responsive campus vegetation, although their actual performance at the study site would need to be confirmed through long-term growth and vitality measurements ([8], [9], [10]).

A somewhat different situation applies to *Fraxinus angustifolia*, *Platanus orientalis*, and *Tilia* spp. These broadleaved trees may have greater water requirements than the Mediterranean-adapted conifers, but they also provide functions that are particularly valuable within a university environment ([11]). Their relatively large crowns can create shaded pedestrian and recreational areas and potentially contribute to microclimatic cooling. *P. orientalis*, in particular, can develop a substantial canopy, whereas *Tilia* species additionally provide floral resources for pollinating insects ([12]). *F. angustifolia* may represent a useful intermediate case because it combines broadleaved canopy characteristics with a degree of tolerance to warm conditions ([13], [14]). Their presence on the campus should therefore not be interpreted negatively simply because of moderate water requirements. Instead, their future performance is likely to depend strongly on microsite conditions, including soil depth, rooting space, surface sealing, and water availability. Under increasingly dry summers, individuals located in favorable and permeable sites may perform very differently from trees of the same species surrounded by extensive paved surfaces. Some of the identified taxa may deserve closer observation if summer drought becomes more pronounced. *Aesculus hippocastanum* has considerable ornamental value and produces a broad, dense crown, but its comparatively greater moisture requirement and sensitivity to drought, heat, and certain pests could become limiting under warmer conditions ([15], [16]). *Acer pseudoplatanus* may likewise be better suited to relatively moist and less exposed microsites. *Populus nigra* provides rapid growth, canopy development, carbon accumulation, and shade, but its comparatively high water requirement suggests that its long-term performance may be more dependent on local soil-moisture availability. These observations do not demonstrate that such species are unsuitable for

the NKU campus; rather, they indicate that their ecological requirements may become increasingly important when planning future planting locations ([17], [18]).

The introduced species present another dimension that cannot be assessed through climatic tolerance alone. *Robinia pseudoacacia*, for example, combines rapid growth with high tolerance of drought, heat, and relatively unfavorable soils. These characteristics could make it appear particularly well suited to warmer future conditions. However, the species is also known for vigorous regeneration and its potential to spread beyond planted areas. A similar consideration applies to *Acer negundo*, while *Paulownia tomentosa* combines rapid growth and heat tolerance with ecological and management concerns in some environments. Thus, a species may be climatically tolerant without necessarily being the most appropriate ecological choice. This issue may be especially relevant on a campus connected to or located close to larger green areas, where the spread of introduced taxa beyond managed planting sites should be considered. *Thuja* spp. occupy a somewhat different functional position. Their evergreen foliage and dense crown structure make them useful primarily for ornamental planting, screening, and year-round visual structure. However, their moderate tolerance of drought and heat suggests that performance may depend considerably on species, planting location, soil conditions, and maintenance. They may therefore remain useful components of campus landscape diversity without necessarily representing priority species for the driest and most exposed sites ([19], [20], [21], [22]).

IV. CONCLUSION

The tree species found on the Tekirdağ Namık Kemal University campus form a genuinely diverse mix native and introduced, evergreen and deciduous, drought-hardy and water demanding and Tekirdağ's own climate gives that diversity real practical weight. An annual mean temperature of roughly 14.2°C and precipitation around 575 mm sound moderate on paper, but the seasonal pattern behind those averages is what matters: July and August combine the year's highest temperatures with its lowest rainfall, and historical extremes above 40°C confirm that campus trees are already exposed to meaningful periodic heat and water stress. As warming continues and rainfall grows more erratic, summer water availability is likely to become an even more decisive factor in what can realistically be planted and maintained. Not every species on campus is equally positioned to handle that shift. Mediterranean and drought-adapted taxa *Pinus brutia*, *Pinus pinea*, *Cupressus sempervirens*, *Cedrus libani*, *Juniperus* spp. carry a clear advantage given their modest water needs and tolerance for heat, but drought tolerance alone shouldn't dictate planting strategy. Angiospermae species such as *Fraxinus angustifolia*, *Platanus orientalis*, and *Tilia* spp. remain worth keeping wherever soil moisture and rooting space allow them to do what conifers may not: provide dense shade, cooling, and habitat value. *Aesculus hippocastanum*, *Acer pseudoplatanus*, and particularly *Populus nigra* are likely to become increasingly reliant on favorable microsites and consistent water access as summers grow drier. The presence of *Robinia pseudoacacia*, *Acer negundo*, and *Paulownia tomentosa* highlights a separate and important tension: climatic toughness may not automatically translate into ecological suitability. These species handle heat, drought, and urban disturbance well, but their capacity to spread aggressively is a real concern one made sharper by the campus's direct connection to the adjacent Atatürk Urban Forest.

This assessment rests on species identification and observed condition rather than direct physiological measurement, so its conclusions describe likely ecological responses rather than firm predictions. Even so, it offers a solid baseline: sustained monitoring of crown health, growth, regeneration, drought damage, and mortality over time would sharpen understanding of how individual species are actually coping as conditions shift. Looking ahead, campus planting in Tekirdağ stands to benefit most from preserving broad species and functional diversity weighing drought and heat tolerance against water demand, ecosystem service value, site suitability, and ecological risk, rather than defaulting to whichever species appears toughest in isolation.

REFERENCES

[1] Biddulph, M. (1999). Bringing vitality to a campus environment. Urban Design International, 4(3-4), 153-166.

[2] Edwards, B. (2014). University architecture. Taylor & Francis.
[3] DOBER, R. P. (2000). CAMPUS LANDSCAPE: FUNCTIONS, FORMS, FEATURES. JOHN WILEY & SONS.
[4] JULIA, F., THOMAS, K., & CARMEN, A. (2021). ACADEMIC GREENSPACE AND WELL-BEING—CAN CAMPUS LANDSCAPE BE THERAPEUTIC. EVIDENCE FROM A GERMAN UNIVERSITY. WELLBEING SPACE SOC, 2, 100003.
[5] Molina-Pardoa, J. L., Giménez-Luquea, E., Gisbert-Gallegoa, J., & Guiradoc, E. Resistance of urban trees to drought shaped by family and site in a semi-arid city Resistance of urban trees to drought shaped by family and site in a semi-arid city.
[6] Sieghardt, M., Mursch-Radlgruber, E., Paoletti, E., Couenberg, E., Dimitrakopoulus, A., Rego, F., ... & Randrup, T. B. (2005). The abiotic urban environment: impact of urban growing conditions on urban vegetation. In Urban forests and trees: a reference book (pp. 281-323). Berlin, Heidelberg: Springer Berlin Heidelberg.
[7] GAUR, R., & SINGH, H. (2024). URBAN TREE RESPONSES TO CLIMATE CHANGE AND ENVIRONMENTAL POLLUTION. IN URBAN FORESTS, CLIMATE CHANGE AND ENVIRONMENTAL POLLUTION: PHYSIO-BIOCHEMICAL AND MOLECULAR PERSPECTIVES TO ENHANCE URBAN RESILIENCE (PP. 279-305). CHAM: SPRINGER NATURE SWITZERLAND.
[8] Gimeno, T. E., Camarero, J. J., Granda, E., Pías, B., & Valladares, F. (2012). Enhanced growth of Juniperus thurifera under a warmer climate is explained by a positive carbon gain under cold and drought. Tree physiology, 32(3), 326-336.
[9] Chambel, M. R., Climent, J., Pichot, C., & Ducci, F. (2013). Mediterranean pines (Pinus halepensis Mill. and brutia Ten.). In Forest tree breeding in Europe: current state-of-the-art and perspectives (pp. 229-265). Dordrecht: Springer Netherlands.
[10] Correia, A. H. C. G. S. (2019). Evaluating forest species response to different climate conditions as a base for sustainable forest management under climate change (Doctoral dissertation, Universidade de Lisboa (Portugal)).
[11] Piczak, K., Leśniewicz, A., & Żyrnicki, W. (2003). Metal concentrations in deciduous tree leaves from urban areas in Poland. Environmental monitoring and assessment, 86(3), 273-287.
[12] Rahman, M. A., Moser, A., Rötzer, T., & Pauleit, S. (2017). Within canopy temperature differences and cooling ability of Tilia cordata trees grown in urban conditions. Building and Environment, 114, 118-128.
[13] Klich, M. G. (2000). Leaf variations in Elaeagnus angustifolia related to environmental heterogeneity. Environmental and experimental botany, 44(3), 171-183.
[14] Hallik, L., Niinemets, Ü., & Wright, I. J. (2009). Are species shade and drought tolerance reflected in leaf-level structural and functional differentiation in Northern Hemisphere temperate woody flora?. New Phytologist, 184(1), 257-274.
[15] Thomas, P. A., Alhamd, O., Iszkuło, G., Dering, M., & Mukassabi, T. A. (2019). Biological flora of the British Isles: Aesculus hippocastanum. Journal of Ecology, 107(2), 992-1030.
[16] Raimondo, F., Trifilò, P., Salleo, S., & Nardini, A. (2005). Seasonal changes of plant hydraulics, water relations and growth of Aesculus hippocastanum seedlings infested by the leafminer Cameraria ohridella. Annals of forest science, 62(2), 99-104.
[17] Bauhus, J., Forrester, D. I., Pretzsch, H., Felton, A., Pyttel, P., & Benneter, A. (2017). Silvicultural options for mixed-species stands. In Mixed-species forests: Ecology and management (pp. 433-501). Berlin, Heidelberg: Springer Berlin Heidelberg.
[18] Hein, S., Collet, C., Ammer, C., Goff, N. L., Skovsgaard, J. P., & Savill, P. (2009). A review of growth and stand dynamics of Acer pseudoplatanus L. in Europe: implications for silviculture. Forestry, 82(4), 361-385.
[19] Givnish, T. (1979). On the adaptive significance of leaf form. In Topics in plant population biology (pp. 375-407). Palgrave, London.
[20] El-Showk, S., & El-Showk, N. (2003). The paulownia tree. An alternative for sustainable forestry, Crop Development, Morocco, 1-8.
[21] Puchałka, R., Dyderski, M. K., Vítková, M., Sádlo, J., Klisz, M., Netsvetov, M., ... & Jagodziński, A. M. (2021). Black locust (Robinia pseudoacacia L.) range contraction and expansion in Europe under changing climate. Global change biology, 27(8), 1587-1600.
[22] McEvoy, S. L., Sezen, U. U., Trouern-Trend, A., McMahon, S. M., Schaberg, P. G., Yang, J., ... & Swenson, N. G. (2022). Strategies of tolerance reflected in two North American maple genomes. The Plant Journal, 109(6), 1591-1613.

8th International Conference on Engineering, Natural and Social Sciences

September 06-07, 2026: Konya, Turkey

© 2026 Published by All Sciences Academy

https://www.icensos.com/

A Bibliometric Analysis of Studies on Extracurricular Activities

Hasan Yücel Ertem [1]

[1]*Sosyal Bilimler Enstitüsü, Zonguldak Bülent Ecevit Üniversitesi, Türkiye*

(ertem@beun.edu.tr)

Abstract – This study aims to examine studies focusing on extracurricular activities and to identify the major research trends within this body of literature. To achieve this objective, data were collected from the Scopus database. A total of 5905 studies explicitly addressing extracurricular activities constituted the dataset for the review. The selected studies were examined in terms of their citation counts and keyword distributions. The analysis demonstrated a significant growth in scholarly attention to extracurricular activities throughout the 21st century. The findings further revealed that the existing body of literature predominantly focuses on issues related to school integration, social support, and mental health. Taken together, it is noted that extracurricular activities is related to school connectedness, adolescent development, and interpersonal relationships. Rather, it constitutes a multifaceted phenomenon influenced by developmental, pedagogical, and institutional factors. By systematically synthesizing the available research, this bibliometric study contributes to a more comprehensive understanding of the field and provides a valuable reference point for future research on extracurricular activities in the schools.

Keywords – school, extracurricular activities, bibliometric analysis, adolescent

I. INTRODUCTION

Educational institutions serve not only as environments for the acquisition of academic knowledge but also as essential settings that foster students' social, emotional, and personal development. Accordingly, schools provide a variety of extracurricular opportunities—including social clubs, community service programs, recreational activities, and other co-curricular initiatives—that contribute to students' holistic growth. According to Döş and Kır (2013), participation in these activities enables students to assume responsibility, strengthen collaboration skills, develop leadership competencies, engage in democratic practices, and become more actively involved in social life.

Among these opportunities, social clubs constitute valuable learning environments where students can explore their interests, recognize their abilities, and develop a broad range of competencies beyond the formal curriculum. Arabacı and Akgül (2012) argue that participation in social club activities encourages students to use their out-of-class time more productively, enhances their social interactions, and promotes their personal development. Likewise, Akar and Nayır (2015) emphasize that social clubs provide meaningful opportunities for self-expression and the development of diverse personal and interpersonal skills. Furthermore, Yaman (2011) stated that these activities have been shown to facilitate students' socialization, strengthen their self-confidence, and encourage greater engagement in school life, thereby supporting both individual development and active participation in the school community.

In recent years, increasing attention has been directed toward recreational and extracurricular activities because of their contribution to students' comprehensive development. These activities extend learning beyond the traditional classroom environment by promoting experiential learning and supporting students' cognitive, social, and physical growth. Karakaş and Dursun Karabörklü (2025) reported that recreational activities implemented in middle schools make meaningful contributions to students' physical, social, and psychological well-being. Likewise, extracurricular activities enhance students'

active engagement in the learning process, facilitate the application of theoretical knowledge to authentic contexts, and promote learning through direct experience.

Despite the well-documented educational benefits of social clubs and extracurricular activities, the literature also highlights a number of barriers that limit their effective implementation. Previous studies have identified several challenges, including low levels of student participation, limited instructional time, inadequate physical and financial resources, weak collaboration between schools and the wider community, and difficulties associated with planning and organizing activities (Akar & Nayır, 2015; Gömleksiz & Kılınç, 2015). These findings suggest that although extracurricular activities have considerable potential to enrich students' educational experiences, their effectiveness largely depends on the availability of institutional support, sufficient resources, and effective implementation strategies.

By considering both points emphasized in the extracurricular activities literature and gap prominent points in the literature, the current study aims to conduct a bibliometric analysis on international research on extracurricular activities. In this respect, the research questions are as below:

Research Question 1: What is the volume, growth trajectory, and subject area of literature for extracurricular activities between 2000 and 2026?

Research Question 2: What journals, authors, and documents on extracurricular activities have had the greatest impact?

Research Question 3: What topical foci pertinent to extracurricular activities attracted the greatest attention from scholars between 2000 and 2026?

II. Materials and Method

This study employed a bibliometric analysis to examine the evolution of international research on extracurricular activities. Bibliometric analysis has become a widely recognized and rigorous approach for synthesizing large bodies of scholarly literature, providing a more systematic and comprehensive perspective than traditional narrative reviews, which may be limited by subjective interpretations and incomplete coverage (Hallinger & Kovacevic, 2019). By examining publication patterns, citation structures, and bibliographic relationships, bibliometric techniques enable researchers to identify influential publications, emerging research themes, and the intellectual structure of a field, thereby complementing conventional literature review methods (Aparicio et al., 2021; Serenko & Bontis, 2013).

The bibliometric dataset was retrieved from the Scopus database, which was selected because of its broad journal coverage and established suitability for large-scale bibliometric research (Mongeon & Paul-Hus, 2016). The document selection process followed the PRISMA (Preferred Reporting Items for Systematic Reviews and Meta-Analyses) framework (Moher et al., 2009), consisting of four sequential stages: identification, screening, eligibility, and inclusion.

During the identification stage, the publication period and data source were established. The analysis was restricted to studies published between 2000 and 2026 to provide a comprehensive overview of research on extracurricular activities throughout the twenty-first century. All documents indexed in the Scopus database within this period were considered eligible for screening. During the screening stage, the search was conducted using the keyword "extracurricular activities". This search identified 5907 records. In the eligibility stage, two publications were excluded because they were not directly relevant to the scope of the study. As a result, a final dataset of 5905 publications was retained for bibliometric analysis. The study selection process is presented in Figure 1 using the PRISMA flow diagram. Overall, 5905 publications were included in the final bibliometric analysis.

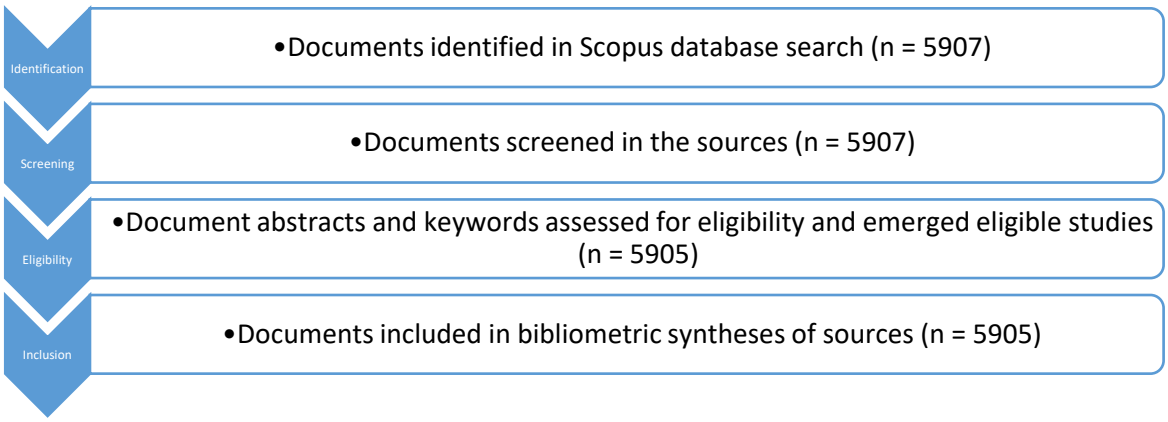

Figure 1 PRISMA flow diagram

III. RESULTS

A total of 5905 documents were identified from 2000 to 2026. As Figure 2 depicts, there has been an upward trend in the number of documents recently. This substantial increase may be explained by popularity of field and given emphasis on extracurricular activities in recent years. The reason it appears there will be a decline in 2026 is that the year is not yet over.

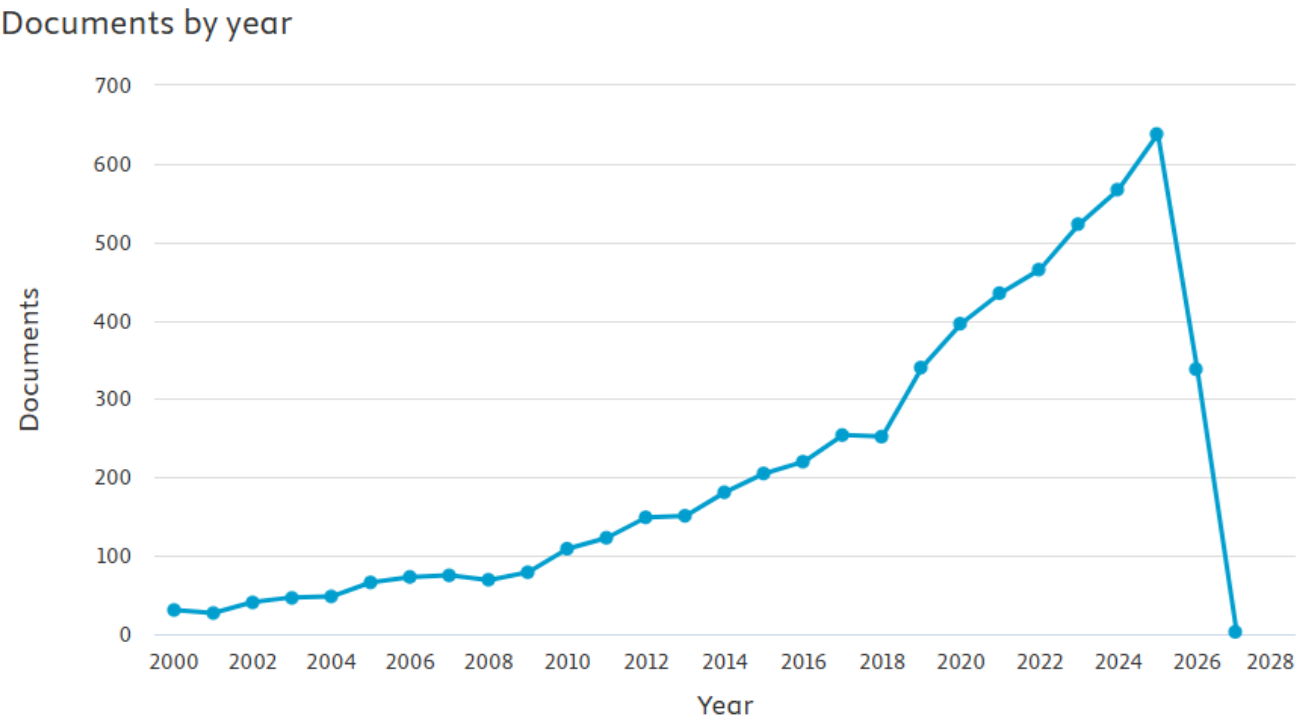

Figure 2 Document in terms of Years

By considering subject areas of 5905 documents, it was observed that the field most publishing document was Social Sciences. Medicine, Psychology and Engineering followed it. It is noteworthy that this topic is being studied in many disciplines. Figure 3 depicted the documents in terms of subject area.

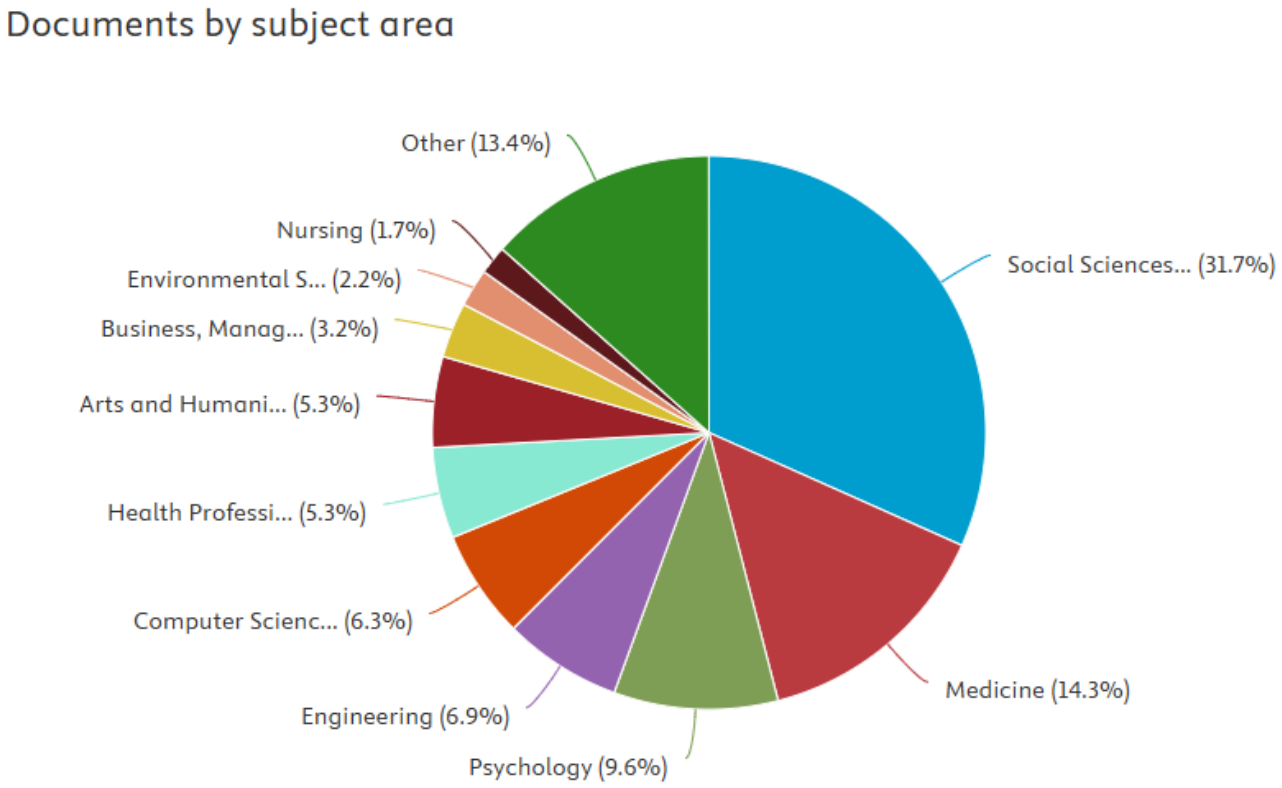

Figure 3 Document in terms of Subject Area

The current study included documents reviewed in Scopus database. Table 1 demonstrated the sources publishing the highest number of documents such that the most influential source was "ASEE Annual Conference" with 158 documents. That was followed by "Teoriya I Praktika Fizicheskoy Kultury," "Retos," and "Journal of Youth and Adolescence" with documents more than 45.

Table 1 Sources that Published the Highest Number of Studies

Rank	Journal	Number of relevant articles (2000-2026)
1	ASEE Annual Conference	158
2	Teoriya I Praktika Fizicheskoy Kultury	54
3	Retos	46
4	Journal of Youth and Adolescence	46
5	Frontiers in Psychology	43

The authors were analysed in terms of number of documents. As figure 4 depicted, the most influential author was Eccless, J. S. with 19 documents. Barber, B. L. and Simpkins, S. D.. followed it with 15 and 13 documents, respectively.

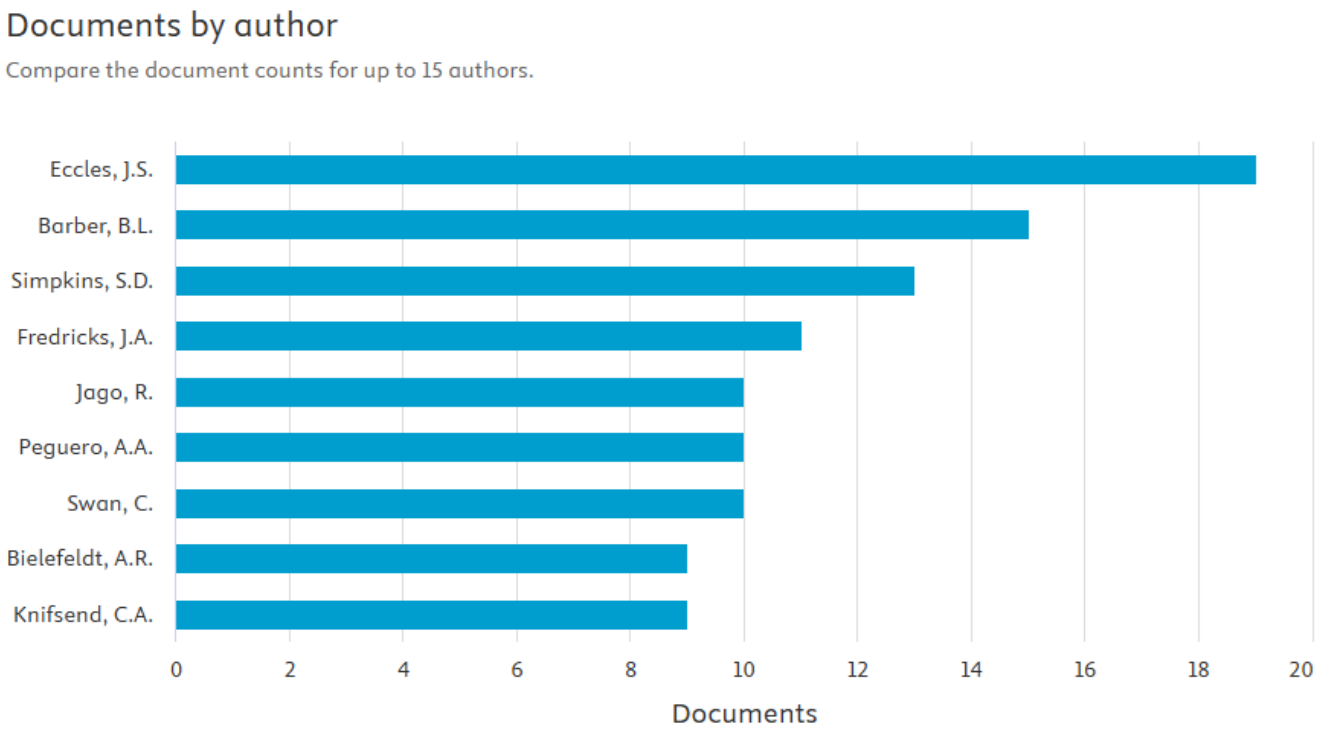

Figure 4 Document in terms of Authors

The documents were analysed in terms of citation impact. Citation analysis was performed to determine the most influential documents. Table 2 showed the most influential five documents. The document showing the greatest impact was "Race, school integration, and friendship segregation in America" with the citations almost 1000.

Table 2 The Most Influential Documents

Rank	Document	Number of citations
1	Race, school integration, and friendship segregation in America	988
2	Social Support Matters: Longitudinal Effects of Social Support on Three Dimensions of School Engagement From Middle to High School	923
3	Extracurricular activities and adolescent development	845
4	Promoting school connectedness: Evidence from the national longitudinal study of adolescent health	833
5	What Schools Need to Know About Fostering School Belonging: a Meta-analysis	831

To identify key topics within the international literature on extracurricular activities, a co-occurrence analysis was conducted. This technique, known as co-word analysis, helps uncover trends in the areas studied by scholars. The top keywords were included in the resulting map, shown in the Figure 5. The five most frequently co-occurring keywords were "extracurricular activities (n = 713)," "physical activity (n = 230)," " adolescents (n = 181)," and "education (n = 180)." Key word analysis emphasized the importance of process and structure of extracurricular.

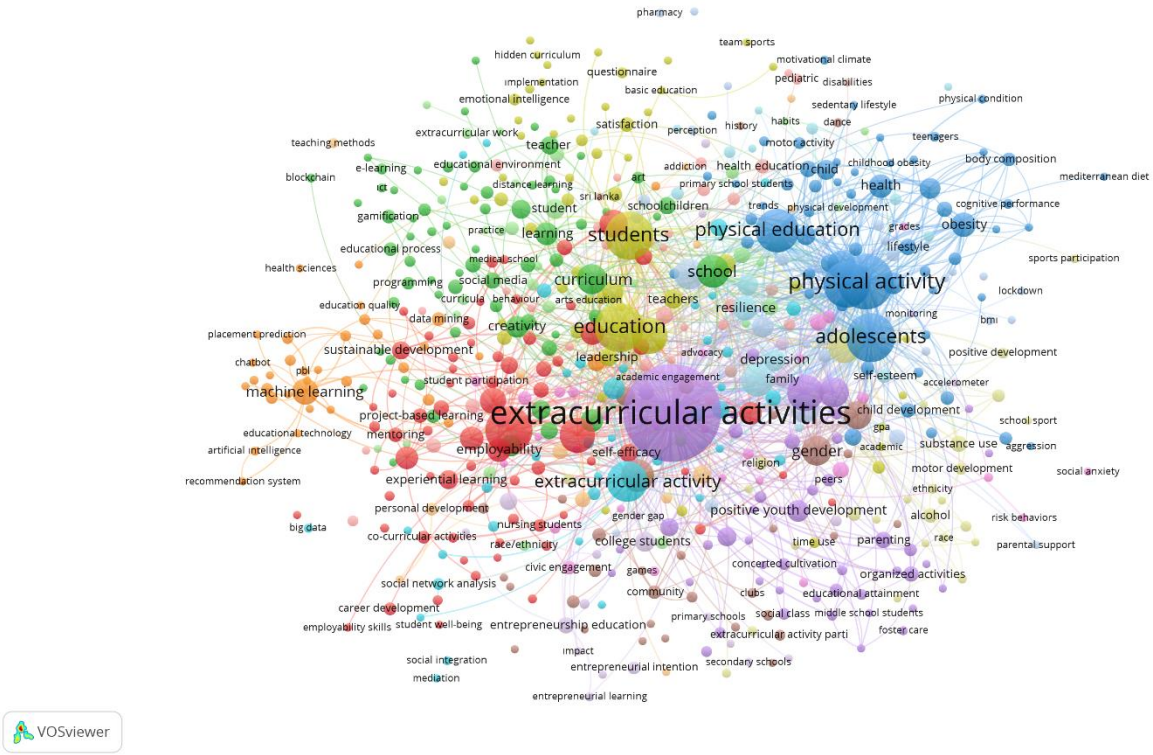

Figure 5 Keyword Co-occurrence Map

IV. DISCUSSION

The present study mapped the intellectual landscape of research on extracurricular activities in Türkiye through a bibliometric analysis of publications produced between 2000 and 2026. The results revealed a sustained increase in scholarly output across the study period, with publication activity accelerating considerably after 2020. This growing body of research suggests that extracurricular activities have gained increasing prominence within educational research because of their recognized contributions to students' academic achievement, personal development, social participation, and overall mental health.

The second research question explored the influence of publication outlets, scholarly contributions, and leading authors within the field. The wide range of influential publications and highly cited authors reflects the multidisciplinary character of the field, which draws upon perspectives from education, educational psychology, sociology, recreation, youth development, and educational management. This diversity highlights the broad educational, developmental, and social significance of extracurricular activities across different research domains.

The final research question investigated the conceptual organization of the literature through the co-occurrence analysis of author keywords. The keyword network demonstrated a well-defined thematic structure, with frequently occurring concepts including extracurricular activities, social clubs, and adolescents. These interconnected themes indicate that extracurricular activities are increasingly examined within broader educational, social, and developmental frameworks rather than as isolated school practices. Moreover, the evolving keyword patterns point to a growing integration of interdisciplinary perspectives, particularly those related to educational, psychological, and organizational dimensions, reflecting the expanding scope and maturity of research in this field.

V. CONCLUSION

In conclusion, this bibliometric analysis offers a comprehensive synthesis of the development and intellectual foundations of extracurricular activities research published between 2000 and 2026. The findings indicate that research on extracurricular activities has evolved into a prominent and multidisciplinary field, evidenced by a continuous increase in scholarly output, the diversification of

research themes, and its close integration with disciplines such as educational psychology, developmental psychology, and educational sociology. By mapping publication trends, identifying influential authors and sources, and examining the conceptual structure of the literature, this study advances a more systematic understanding of the field while identifying promising avenues for future investigation. The findings provide valuable insights for researchers, policymakers, and educational practitioners by offering an evidence-based foundation for the design, implementation, and evaluation of extracurricular activity programs that support students' holistic development and contribute to the overall quality and effectiveness of education.

REFERENCES

[1] Akar, F., & Nayır, K. F. (2015). Eğitim kurumlarındaki sosyal kulüplerin etkililiğinin incelenmesi: Uygulamada değişim ihtiyacı. Pegem Eğitim ve Öğretim Dergisi, 5(2), 167–186.

[2] Aparicio, G., Iturralde, T., & Maseda, (2021). A. A holistic bibliometric overview of the student engagement research field. Journal of Further and Higher Education. 45(4), 540-557.

[3] Arabacı, İ. B., & Akgül, D. (2012). İlköğretim okulu öğrencilerinin sosyal kulüp etkinlikleri konusundaki görüşleri (Bitlis ili örneği). e-Journal of New World Sciences Academy Education Sciences, 7(1), 485–495.

[4] Döş, İ., & Kır, E. (2013). İlköğretim ve ortaöğretim okullarında sosyal etkinlik ve yönetimi. Gaziantep University Journal of Social Sciences, 12(3), 527–544.

[5] Gömleksiz, M. N., & Kılınç, H. H. (2015). Ortaokullarda sosyal kulüp etkinlikleri kapsamında yapılan toplum hizmeti çalışmalarına ilişkin öğretmenlerin görüşleri. Turkish Studies, 10(3), 495–512

[6] Hallinger, P., & Kovačević, J. A (2019). bibliometric review of research on educational administration: science mapping the literature, 1960 to 2018. Review of Educational Research. 89(3), 335-369.

[7] Karakaş, G., & Dursun Karabörklü, Z. (2025). Ortaokullarda rekreasyon faaliyetlerinin uygulanabilirliği ve etkileri: Okul yöneticilerinin görüşleri. *The Online Journal of Recreation and Sports, 14*(4), 423–434

[8] Mongeon, P., & Paul-Hus, A. (2016). The journal coverage of Web of Science and Scopus: a comparative analysis. Scientometrics. 106(1), 213-228.

[9] Moher, D. Liberati, A., Tetzlaff, J., Altman, D. G., Altman, D., Antes, G., & Clark, J. (2009). Preferred reporting items for systematic reviews and meta-analyses: The PRISMA statement (Chinese edition). Journal of Chinese Integrative Medicine. 7(9), 889-896.

[10] Serenko, A., & Bontis, N. (2013). Global ranking of knowledge management and intellectual capital academic journals: 2013 update. Journal of Knowledge Management. 17(2), 307–326.

[11] Yaman, E. (2011). Rekreasyon bağlamında öğrenci algılarına göre sosyal kulüplerin işlevselliği. Uluslararası Avrasya Sosyal Bilimler Dergisi, 2(3), 35–48.

8th International Conference on Engineering, Natural and Social Sciences

September 06-07, 2026: Konya, Turkey

© 2026 Published by All Sciences Academy

https://www.icensos.com/

How Should We Interpret Research on Teacher Motivation in the 21st Century?: A Bibliometric Analysis

Hasan Yücel Ertem [1]

[1]*Sosyal Bilimler Enstitüsü, Zonguldak Bülent Ecevit Üniversitesi, Türkiye*

(ertem@beun.edu.tr)

Abstract **–** This study aims to examine studies focusing on teacher motivation and to identify the major research trends within this body of literature. To achieve this objective, data were collected from the Scopus database. A total of 1788 studies explicitly addressing teacher motivation constituted the dataset for the review. The selected studies were examined in terms of their citation counts and keyword distributions. The analysis demonstrated a significant growth in scholarly attention to teacher motivation throughout the 21st century. The findings further revealed that the existing body of literature predominantly focuses on issues related to teaching practices, leadership, and teacher job satisfaction. Taken together, it is noted that teacher motivation is related to job satisfaction, professional performance, and organizational commitment. Rather, it constitutes a multifaceted phenomenon influenced by pedagogical, institutional, and professional factors. By systematically synthesizing the available research, this bibliometric study contributes to a more comprehensive understanding of the field and provides a valuable reference point for future research on teacher motivation.

Keywords – Teacher, teacher motivation, bibliometric analysis, policy, motivation

I. INTRODUCTION

Teacher motivation is recognized as one of the key factors determining the quality of the educational process. Highly motivated teachers plan the teaching process more effectively, establish stronger communication with students, and are more likely to adopt practices that enhance the quality of the learning environment. Conversely, low motivation can lead to outcomes such as professional burnout, decreased job satisfaction, weakened organizational commitment, and a negative impact on teaching performance. Teacher motivation is influenced not only by individual characteristics but also by multidimensional factors such as working conditions, compensation policies, career development opportunities, school climate, leadership practices, professional autonomy, and social status. Therefore, developing policies aimed at enhancing teacher motivation will not only support teachers' professional well-being but will also make significant contributions to student achievement, school effectiveness, and the overall performance of the education system.

Teacher motivation refers to the level of willingness and effort teachers demonstrate while performing their professional duties. It has been noted that teacher motivation is related to job satisfaction, professional performance, and organizational commitment. Sarı and colleagues (2018) found that teachers' motivation levels are significantly related to their perceptions of the school environment.

Studies examining the relationship between psychological climate and job motivation indicate that teachers' perceptions of the school environment significantly influence their motivation levels. In particular, it is emphasized that teachers' belief that they work in a supportive and fair school environment increases their motivation (Eroğlu & Özen, 2019). These findings indicate that teacher motivation cannot be considered independently of the school's organizational structure.

The findings across the reviewed studies consistently demonstrate a significant association between school climate and teacher motivation. Specifically, a positive school climate is associated with higher levels of teacher motivation, whereas an unfavorable school climate tends to diminish teachers' motivation (Sarı et al., 2018; Tepe & Yılmaz, 2020). Furthermore, research investigating the influence of school administrators' toxic leadership behaviors suggests that such leadership practices undermine the quality of the school climate, which, in turn, adversely affects teacher motivation (Tepe & Yılmaz, 2020).

Teacher motivation has emerged as one of the most extensively investigated topics in educational research because of its critical role in shaping instructional quality, teacher well-being, organizational commitment, and student learning outcomes. Despite the growing volume of publications on this subject, the literature remains fragmented across diverse theoretical perspectives, methodological approaches, and educational contexts. Consequently, obtaining a comprehensive understanding of the intellectual development, thematic evolution, and influential contributions within this field has become increasingly challenging. In this regard, bibliometric analysis provides a robust and systematic approach for mapping the knowledge structure of teacher motivation research. By examining publication trends, citation networks, collaboration patterns, and keyword co-occurrence, bibliometric techniques enable researchers to identify dominant research themes, emerging topics, influential authors, and leading publication sources. Furthermore, such analyses reveal existing research gaps and future research directions, thereby facilitating a more coherent understanding of the field and informing both researchers and policymakers. Therefore, conducting a bibliometric analysis of teacher motivation research is essential for synthesizing the accumulated evidence and advancing the scholarly development of this important area of educational research.

By considering both points emphasized in the teacher motivation literature and gap prominent points in the literature, the current study aims to conduct a bibliometric analysis on international research on teacher motivation. In this respect, the research questions are as below:

Research Question 1: What is the volume, growth trajectory, and subject area of literature for teacher motivation between 2000 and 2026?

Research Question 2: What journals, authors, and documents on teacher motivation have had the greatest impact?

Research Question 3: What topical foci pertinent to teacher motivation attracted the greatest attention from scholars between 2000 and 2026?

II. Materials and Method

This study employed a bibliometric analysis to examine the evolution of international research on teacher motivation. Bibliometric analysis has become a widely recognized and rigorous approach for synthesizing large bodies of scholarly literature, providing a more systematic and comprehensive perspective than traditional narrative reviews, which may be limited by subjective interpretations and incomplete coverage (Hallinger & Kovacevic, 2019). By examining publication patterns, citation structures, and bibliographic relationships, bibliometric techniques enable researchers to identify influential publications, emerging research themes, and the intellectual structure of a field, thereby complementing conventional literature review methods (Aparicio et al., 2021; Serenko & Bontis, 2013).

The bibliometric dataset was retrieved from the Scopus database, which was selected because of its broad journal coverage and established suitability for large-scale bibliometric research (Mongeon & Paul-Hus, 2016). The document selection process followed the PRISMA (Preferred Reporting Items for Systematic Reviews and Meta-Analyses) framework (Moher et al., 2009), consisting of four sequential stages: identification, screening, eligibility, and inclusion.

During the identification stage, the publication period and data source were established. The analysis was restricted to studies published between 2000 and 2026 to provide a comprehensive overview of research on teacher motivation throughout the twenty-first century. All documents indexed in the Scopus database within this period were considered eligible for screening. During the screening stage, the search was conducted using the keyword "teacher motivation". This search identified 1795 records. In the eligibility stage, seven publications were excluded because they were not directly relevant to the scope of

the study. As a result, a final dataset of 1788 publications was retained for bibliometric analysis. The study selection process is presented in Figure 1 using the PRISMA flow diagram. Overall, 1788 publications were included in the final bibliometric analysis.

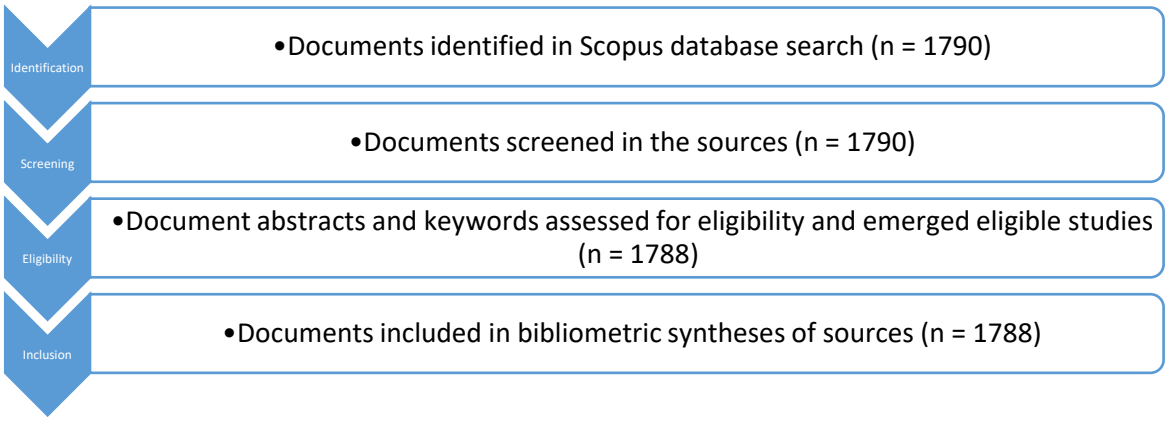

Figure 1 PRISMA flow diagram

III. RESULTS

A total of 1788 documents were identified from 2000 to 2026. As Figure 2 depicts, there has been an upward trend in the number of documents recently. This substantial increase may be explained by popularity of field and given emphasis on teacher motivation in recent years. The reason it appears there will be a decline in 2026 is that the year is not yet over.

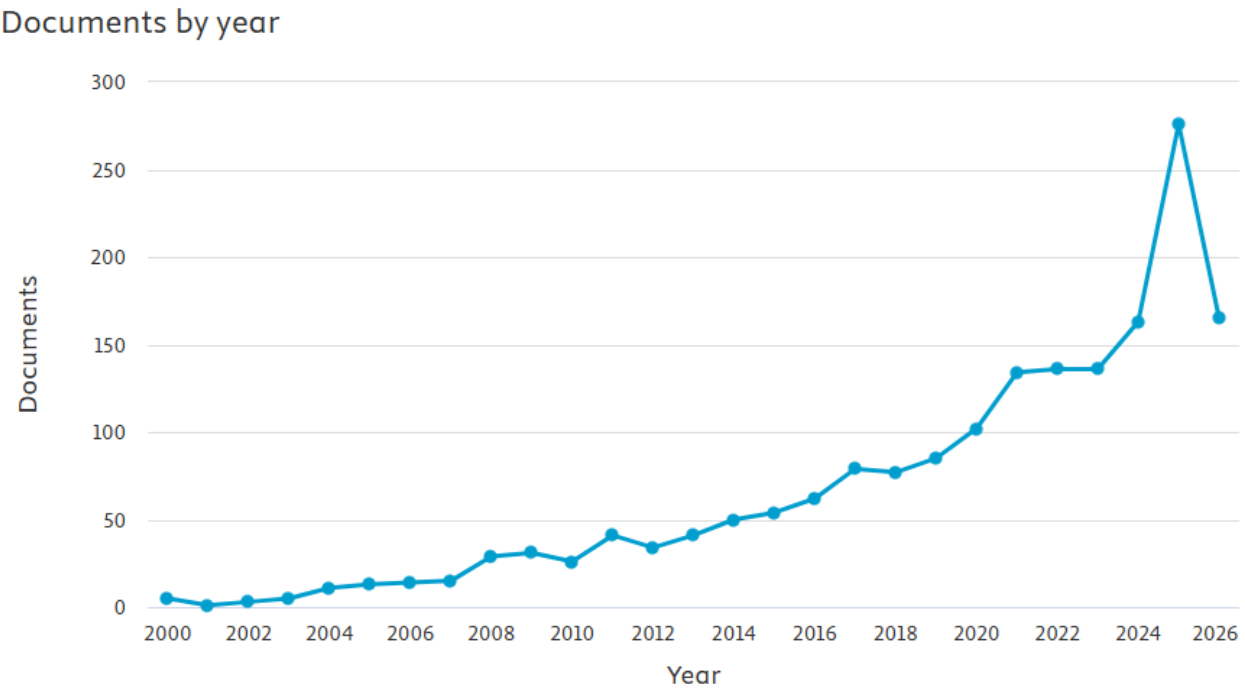

Figure 2 Document in terms of Years

By considering subject areas of 1788 documents, it was observed that the field most publishing document was Social Sciences. Psychology and Arts and Humanities followed it. Figure 3 depicted the documents in terms of subject area.

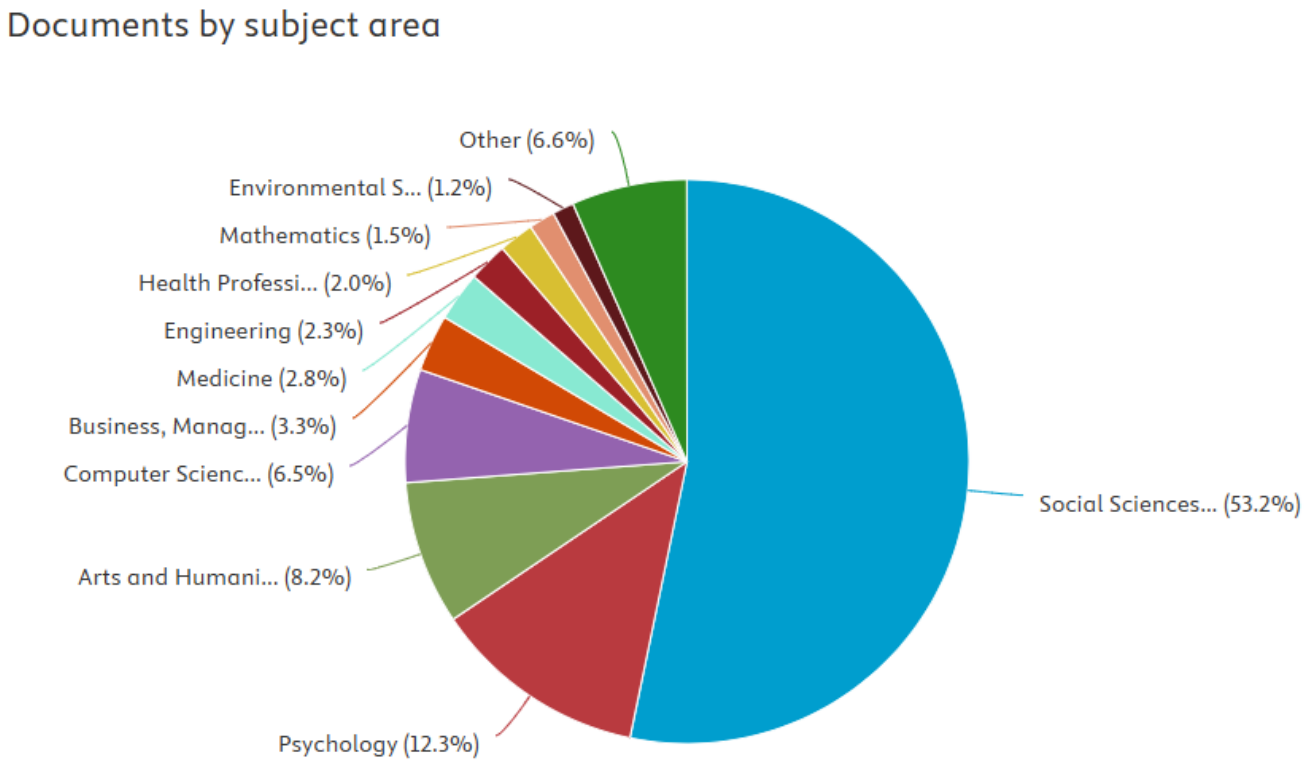

Figure 3 Document in terms of Subject Area

The current study included documents reviewed in Scopus database. Table 1 demonstrated the sources publishing the highest number of documents such that the most influential source was "Teaching and teacher Education" with 66 documents. That was followed by "Education Sciences," "Frontiers in Education," and "Frontiers in Psychology" with documents more than 20.

Table 1 Sources that Published the Highest Number of Studies

Rank	Journal	Number of relevant articles (2000-2026)
1	Teaching and Teacher Education	66
2	Education Sciences	25
3	Frontiers in Education	24
4	Frontiers in Psychology	23
5	Learning and Instruction	19

The authors were analyzed in terms of number of documents. As figure 4 depicted, the most influential author was Watt, H. M. G with 19 documents. Richardson, P. W. and Dresel, M. followed it with 18 and 14 documents, respectively.

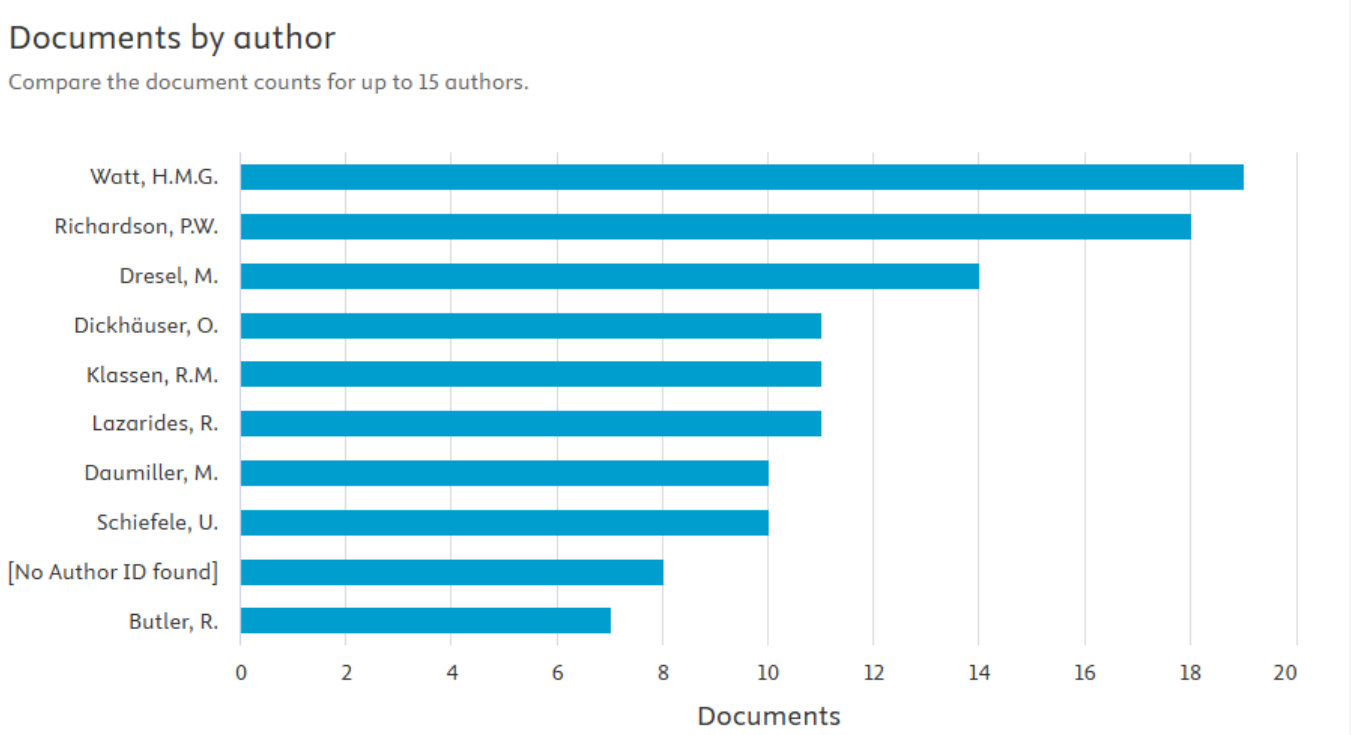

Figure 4 Document in terms of Authors

The documents were analysed in terms of citation impact. Citation analysis was performed to determine the most influential documents. Table 2 showed the most influential five documents. The document showing the greatest impact was "Teacher job satisfaction and motivation to leave the teaching profession: Relations with school context, feeling of belonging, and emotional exhaustion" with the citations almost 1100.

Table 2 The Most Influential Documents

Rank	Document	Number of citations
1	Teacher job satisfaction and motivation to leave the teaching profession: Relations with school context, feeling of belonging, and emotional exhaustion	1078
2	Teachers' Emotions and Teaching: A Review of the Literature and Directions for Future Research	1038
3	Pressure from above and pressure from below as determinants of teachers' motivation and teaching behaviors	563
4	Transformational school leadership for large-scale reform: Effects on students, teachers, and their classroom practices	518
5	Motivations, perceptions, and aspirations concerning teaching as a career for different types of beginning teachers	476

To identify key topics within the international literature on teacher motivation, a co-occurrence analysis was conducted. This technique, known as co-word analysis, helps uncover trends in the areas studied by scholars. The top keywords were included in the resulting map, shown in the Figure 5. The five most frequently co-occurring keywords were "teacher motivation (n = 495)," "motivation (n = 297)," " teachers (n = 92)," and "teacher education (n = 79)." Key word analysis emphasized the importance of process and structure of motivation.

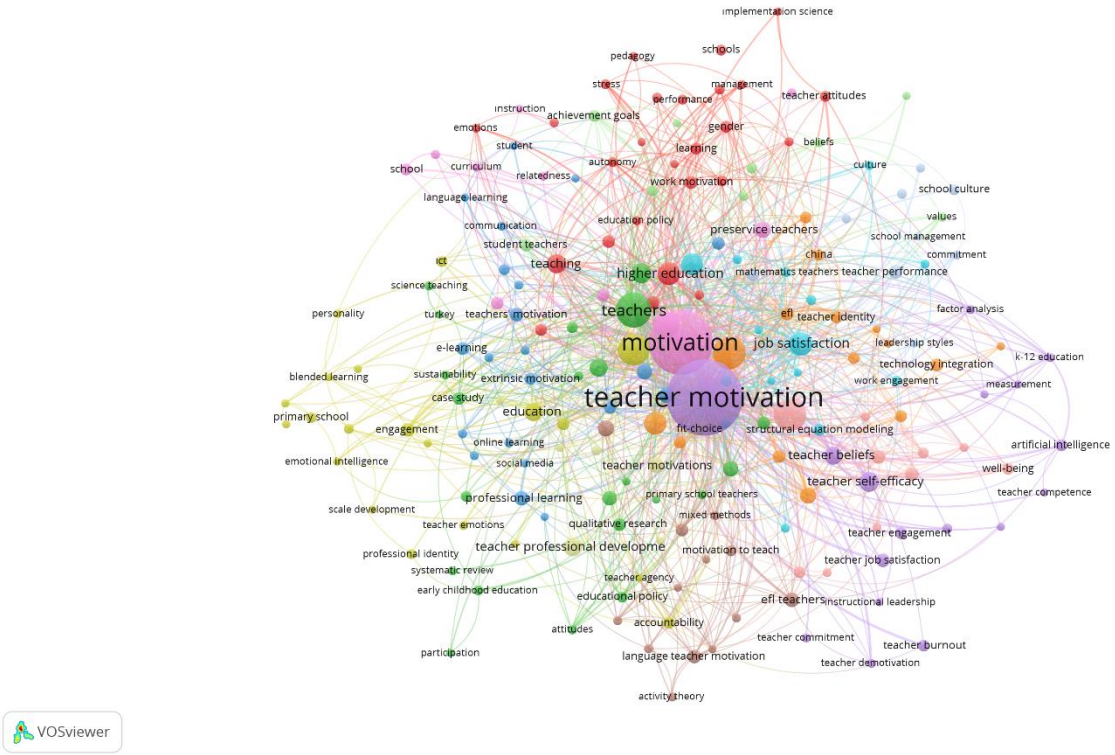

Figure 5 Keyword Co-occurrence Map

IV. DISCUSSION

The present study mapped the intellectual landscape of teacher motivation research through a bibliometric analysis of publications produced between 2000 and 2026. The findings revealed a consistent expansion of the literature over the study period, with publication output accelerating markedly after 2020. This increasing scholarly attention suggests that teacher motivation has become an increasingly important area of educational research, reflecting its recognized role in enhancing teaching effectiveness, teacher well-being, and overall school performance.

The second research question focused on identifying the most influential publication sources, documents, and authors within the field. The results indicated that the leading publication outlets are primarily education-oriented journals, highlighting the central role of educational research in advancing knowledge on teacher motivation. Nevertheless, the diversity of highly cited studies and influential contributors suggests that teacher motivation has attracted interest from multiple academic disciplines, including educational psychology, organizational behavior, leadership, and human resource management. This interdisciplinary character underscores the complexity of teacher motivation as a research domain and demonstrates its relevance across diverse educational and organizational contexts.

The final research question explored the conceptual structure of the literature by analyzing the co-occurrence of author keywords. The keyword network revealed that teacher motivation research is organized around several closely interconnected themes, with concepts such as teacher motivation, job satisfaction, organizational commitment, school climate, and leadership.These findings indicate that teacher motivation is increasingly conceptualized as a multidimensional construct influenced by both individual and organizational factors. Moreover, the evolving keyword patterns suggest a growing integration of psychological, organizational, and educational perspectives, reflecting the increasingly interdisciplinary nature of contemporary teacher motivation research.

V. CONCLUSION

In conclusion, this bibliometric analysis provides a comprehensive overview of the evolution and intellectual structure of teacher motivation research between 2000 and 2026. The findings demonstrate

that teacher motivation has become an increasingly prominent and multidisciplinary area of inquiry, characterized by a growing volume of publications, diverse research themes, and strong connections with educational psychology, organizational behavior, leadership, and teacher well-being. By identifying publication trends, influential contributors, and the conceptual organization of the field, this study contributes to a more systematic understanding of the existing literature and highlights emerging directions for future research. These findings may serve as a valuable resource for researchers, policymakers, and educational practitioners seeking to develop evidence-based strategies for enhancing teacher motivation and, ultimately, improving the quality and effectiveness of education.

REFERENCES

[1] Aparicio, G., Iturralde, T., & Maseda, (2021). A. A holistic bibliometric overview of the student engagement research field. Journal of Further and Higher Education. 45(4), 540-557.

[2] Eroğlu, T., & Özen, H. (2019). Okullardaki psikolojik iklim ve iş motivasyonu arasındaki ilişkinin incelenmesi. Eskişehir Osmangazi Üniversitesi Sosyal Bilimler Dergisi, 20(Özel Sayı), 1–24.

[3] Hallinger, P., & Kovačević, J. A (2019). bibliometric review of research on educational administration: science mapping the literature, 1960 to 2018. Review of Educational Research. 89(3), 335-369.

[4] Mongeon, P., & Paul-Hus, A. (2016). The journal coverage of Web of Science and Scopus: a comparative analysis. Scientometrics. 106(1), 213-228.

[5] Moher, D. Liberati, A., Tetzlaff, J., Altman, D. G., Altman, D., Antes, G., & Clark, J. (2009). Preferred reporting items for systematic reviews and meta-analyses: The PRISMA statement (Chinese edition). Journal of Chinese Integrative Medicine. 7(9), 889-896.

[6] Sarı, M., Canoğulları, E., & Yıldız, E. (2018). Öğretmenlerin okul yaşam kalitesi algıları ile mesleki motivasyon düzeylerinin incelenmesi. Mehmet Akif Ersoy Üniversitesi Eğitim Fakültesi Dergisi, (47), 387–409.

[7] Serenko, A., & Bontis, N. (2013). Global ranking of knowledge management and intellectual capital academic journals: 2013 update. Journal of Knowledge Management. 17(2), 307–326.

[8] Tepe, N., & Yılmaz, G. (2020). Öğretmenlerin okul iklimi algılarının yordayıcısı olarak okul yöneticilerinin toksik liderlik davranışları. OPUS–Uluslararası Toplum Araştırmaları Dergisi, 15(25), 3362–3384.

8th International Conference on Engineering, Natural and Social Sciences

September 06-07, 2026: Konya, Turkey

© 2026 Published by All Sciences Academy

https://www.icensos.com/

Investigating the Anticancer Potential of Broccoli Phytochemicals as VEGFR2 Inhibitors: Molecular Docking and 100 ns Atomistic Molecular Dynamics Simulation

Tahir Tilki [1], Ömer Dilek [2], and Tolga Acar Yeşil [3,*]

[1]*Department of Chemistry, Faculty of Engineering and Natural Sciences, Süleyman Demirel University, Türkiye*
[2]*Central Research Laboratory Application and Research Center, Isparta University of Applied Sciences, Türkiye*
[3]*Department of Property Protection and Security, Türkeli Vocational School, Sinop University, Türkiye*

[*]*tyesil@sinop.edu.tr*

Abstract **–** Vascular Endothelial Growth Factor Receptor 2 (VEGFR2, PDB ID: 4ASD) is a key molecular target in oncology, where its inhibition directly suppresses tumor angiogenesis, cell proliferation, and metastatic progression. Broccoli is recognized for its broad-spectrum anticancer phytochemicals, including Glucoraphanin, Indole-3-carbinol, Sulforaphane, and 3,3'-Diindolylmethane (DIM). In this study, the anticancer potential of these four bioactives was evaluated against the catalytic kinase domain of VEGFR2 using UCSF Chimera. Molecular docking demonstrated that DIM exhibited the most potent binding affinity with a score of -10.6 kcal/mol, outperforming Glucoraphanin (-7.0 kcal/mol), Indole-3-carbinol (-6.3 kcal/mol), and Sulforaphane (-4.6 kcal/mol). To investigate the atomistic stability of this top anticancer candidate, a 100 ns all-atom Molecular Dynamics (MD) simulation was performed on the VEGFR2–DIM complex. Trajectory analysis confirmed high structural stability, with backbone RMSD stabilizing between 6.0 Å and 7.5 Å after 40 ns and maintaining a highly compact receptor folding (Rg ~21.7–22.3 Å). Residues within the catalytic pocket showed high rigidity (RMSF < 2.0 Å), while DIM remained locked within the binding cleft (ligand movement RMSD ~1.8 Å) via persistent hydrogen bonding at the indole N–H center (Atom 5648) and robust hydrophobic interactions with Glu149, Val150, Asp228, and Arg230. Dynamic Cross-Correlation Matrix (DCCM) and Principal Component Analysis (PCA) confirmed that DIM confines VEGFR2 to a tight, low-energy conformational subspace. These findings highlight DIM as a compelling natural anticancer lead for target-directed anti-angiogenic drug design.

Keywords – Anticancer Activity, Broccoli Phytochemicals, VEGFR2, Molecular Docking, MD Simulation.

I. INTRODUCTION

Cancer remains one of the leading causes of mortality worldwide, characterized by uncontrolled cellular proliferation, tissue invasion, and metastasis. A fundamental requirement for solid tumor expansion beyond microscopic sizes is pathological angiogenesis, the formation of new blood vessels that supply oxygen and nutrients to cancer cells [1]. Among the key signaling cascades orchestrating tumor angiogenesis, the activation of VEGFR2 plays a central role. VEGFR2 is a receptor tyrosine kinase that, upon VEGF binding, triggers intracellular signaling pathways such as Ras/Raf/MEK/ERK and PI3K/Akt, promoting endothelial cell survival, migration, and capillary tube formation [2–4]. Consequently, targeting the intracellular ATP-binding catalytic domain of VEGFR2 has emerged as a successful clinical strategy to exert potent anticancer and anti-angiogenic effects.

Natural products, particularly dietary phytochemicals, have gained significant interest in cancer research due to their multi-targeted anticancer mechanisms and favorable toxicity profiles [5]. Cruciferous

vegetables like broccoli are rich in bioactives with documented chemopreventive and antiproliferative properties. Among these, Glucoraphanin, Indole-3-carbinol, Sulforaphane, and 3,3'-Diindolylmethane have shown promising activity against various cancer cell lines [6,7]. However, their precise computational binding mechanisms and structural dynamics against VEGFR2 require thorough atomistic investigation to establish their direct anti-angiogenic anticancer mechanism.

In this work, we screened the anticancer potential of these four broccoli bioactives against VEGFR2 using molecular docking in UCSF Chimera. The docking energetics revealed a clear hierarchical order of binding affinity: 3,3'-Diindolylmethane (-10.6 kcal/mol) > Glucoraphanin (-7.0 kcal/mol) > Indole-3-carbinol (-6.3kcal/mol) > Sulforaphane (-4.6 kcal/mol). Based on its superior binding performance, the VEGFR2–DIM complex was subjected to a detailed 100 ns explicit-solvent MD simulation to elucidate its dynamic stability, active-site retention, and structural impact on the kinase receptor.

II. Materials and Method

A. Target Receptor & Phytochemical Preparation

The 3D crystal structure of the human VEGFR2 kinase domain (PDB ID: 4ASD) was downloaded from the Protein Data Bank and prepared using UCSF Chimera [8,9]. Heteroatoms, water molecules, and co-crystallized native ligands were removed. Polar hydrogens and Gasteiger charges were assigned. Chemical structures of the four anticancer bioactives (Glucoraphanin, Indole-3-carbinol, Sulforaphane, and 3,3'-Diindolylmethane) were energy-minimized and converted to .mol2 files [10].

B. Molecular Docking Protocol

Virtual screening was conducted via the AutoDock Vina interface in UCSF Chimera [9], targeting the ATP-binding pocket of 4ASD (x: -24.96, y: -0.50, z: -10.40; 25 × 25 × 25). Docking scores were generated to evaluate and rank the potential anticancer binding strength. Molecular interactions, encompassing hydrogen bonds and hydrophobic contacts, were analyzed and visualized in both 2D and 3D formats using BIOVIA Discovery Studio Visualizer [11].

C. MD Simulation Protocol

All-atom 100 ns MD simulations were performed using YASARA Structure [12]. Hydrogen-bonding networks were optimized, and residue protonation states were dynamically adjusted at pH 7.4 [13]. Systems were solvated in a periodic TIP3P water box and electrostatically neutralized with 0.9% NaCl to emulate physiological conditions.

Biomolecular parameters were defined using the AMBER14 force field for VEGFR2 and GAFF2 with AM1-BCC charges for the bioactives [14–16]. To resolve steric clashes, energy minimizations via steepest descent and simulated annealing were applied prior to simulation. Production runs proceeded under the NPT ensemble (298 K, 1.0 atm) [17]. Particle Mesh Ewald (PME) handled long-range electrostatics, while short-range non-bonded forces were evaluated with an 8.0 Å cutoff [18,19]. Equations of motion were integrated using a multiple-time-step scheme (2.5 fs for bonded and 5.0 fs for non-bonded interactions). Trajectory snapshots were systematically recorded for RMSD, RMSF, SASA, DCCM, PCA, and contact persistence analyses.

III. Results and Discussion

A. Molecular Docking Studies

Molecular docking simulations were performed to evaluate the binding affinities of selected bioactive compounds against the target protein 4ASD. Among the docked ligands, 3,3'-diindolylmethane exhibited the highest binding affinity with a docking score of -10.6 kcal/mol, indicating superior binding stability

within the active site compared to glucoraphanin (-7.0 kcal/mol), indole-3-carbinol (-6.3 kcal/mol), and sulforaphane (-4.6 kcal/mol) (Table 1). The substantial difference in binding energy highlights 3,3'-diindolylmethane as the most potent ligand candidate against 4ASD in this comparative set.

Table 1. Molecular docking binding affinities (kcal/mol) of the selected bioactive compounds against the 4ASD protein.

Ligand-Protein	Docking Scores (kcal/mol)
3,3'-Diindolylmethane-4ASD	-10.6
Glucoraphanin-4ASD	-7.0
Indole-3-carbinol-4ASD	-6.3
Sulforaphane-4ASD	-4.6

Detailed 2D interaction analysis of the most active complex, 3,3'-diindolylmethane-4ASD, revealed that the strong binding affinity is primarily driven by a robust network of hydrophobic and electrostatic interactions (Figure 1). The ligand established a prominent conventional hydrogen bond via the N-H moiety of one indole unit with GLU149 (2.20 Å). In addition, the aromatic core formed a pi-cation interaction with LYS100 (4.28 Å, 4.63 Å), a pi-sulfur contact with CYS227 (4.62 Å), and a pi-pi T-shaped stacking interaction with PHE229 (4.74 Å). The complex was further anchored within the hydrophobic pocket by extensive pi-alkyl interactions involving ALA98, VAL80, VAL148, LEU72, LEU217, and CYS151 (3.54–5.45 Å). Although a short unfavorable donor-donor contact was observed with ASP228 (1.77 Å), the extensive hydrophobic enclosure and key polar contacts readily compensated for this strain, conferring superior structural stability to the 3,3'-diindolylmethane-4ASD complex.

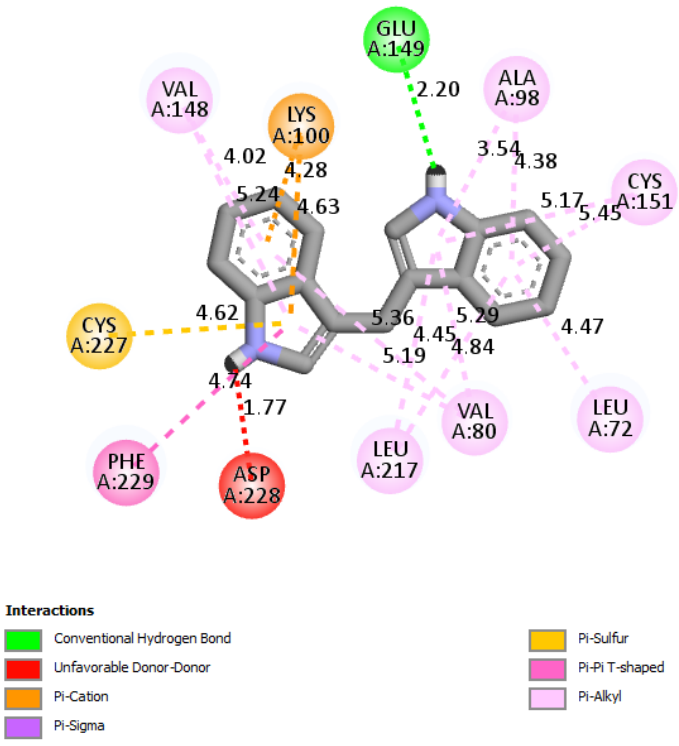

Figure 1. 2D interaction profile and key residue contacts of the 3,3'-diindolylmethane–4ASD docked complex.

B. MD Simulation Studies

The root-mean-square deviation (RMSD) trajectory of the solute complex was computed across the 100 ns molecular dynamics simulation to evaluate the overall conformational stability and structural equilibrium

of the VEGFR2 system bound to DIM (Figure 2a). The Cα (RMSDCa), backbone (RMSDBb), and all-heavy atom (RMSDAll) traces exhibited closely aligned trajectories throughout the run, indicating uniform structural dynamics across the macromolecular framework. During the initial 20 ns phase, the complex underwent initial relaxation with RMSD values hovering around 5.0–6.0 Å. A transient conformational contraction was observed between 25 and 35 ns, where the RMSD sharply declined to approximately 3.0–3.5 Å, reflecting an intermediate structural rearrangement of the peripheral loops toward a more compact intermediate state. Beyond 40 ns, the VEGFR2–DIM complex transitioned into an extended stable plateau, maintaining backbone RMSD values oscillating consistently between 6.0 Å and 7.5 Å up to 100 ns. The absence of progressive deviation or abrupt drifting in the second half of the trajectory indicates that the receptor successfully achieved conformational convergence in the presence of DIM. The minimal difference observed between the backbone and all-atom RMSD profiles further corroborates that the side chains within the core domain remained structurally constrained without undergoing significant unfolding or distortion during the simulation window.

The root-mean-square fluctuation (RMSF) analysis was evaluated per residue over the 100 ns trajectory to map the localized flexibility and identify structurally stable domains within the VEGFR2 kinase monomer (Figure 2b). The fluctuation profile demonstrated significant residue-dependent variation, with pronounced mobility confined predominantly to the unstructured terminal segments. In particular, the extreme N-terminal region (residues 1–40) exhibited substantial fluctuations reaching peak RMSF values between 8.0 Å and 13.2 Å, which is characteristic of flexible solvent-exposed terminal tails devoid of rigid secondary structural constraints. A secondary, modest fluctuation peak was recorded around residues 165–185 (~4.5 Å), corresponding to the inherently dynamic surface loop regions flanking the kinase architecture. In stark contrast, the core catalytic domain and the primary binding cleft residues (spanned across residues 50–160 and 190–340) displayed remarkable structural rigidity, consistently retaining low RMSF values below 2.0 Å. Specifically, the key interacting residues in the binding pocket maintained minimal conformational drift, with several catalytic segments exhibiting fluctuations near 1.0 Å. This localized stabilization underscores that the binding of DIM effectively locked the active site residues into a well-defined and stable conformation, mitigating dynamic fluctuations and preserving the functional geometry of the VEGFR2 binding pocket throughout the simulation.

The radius of gyration (Rg) of the VEGFR2–DIM complex was monitored over the 100 ns trajectory to assess the compactness, overall tertiary folding behavior, and structural integrity of the macromolecule as a function of simulation time (Figure 2c). At the onset of the simulation, the solute started with an initial Rg value of approximately 25.1 Å, followed by a rapid compaction down to ~22.0 Å within the first 10 ns. A transient conformational opening was observed between 24 and 37 ns, where the Rg values fluctuated between 23.5 Å and 24.5 Å, coinciding perfectly with the intermediate conformational reorganization captured in the RMSD trajectory. Following 40 ns, the complex established a highly compact and stable architecture, with Rg values stabilizing tightly within the narrow range of 21.7 Å to 22.3 Å until the completion of the 100 ns trajectory. This marked decrease and subsequent plateau in Rg demonstrates that the receptor did not undergo structural denaturation, expansion, or global unpacking. Instead, the persistent low Rg values confirm that the VEGFR2 kinase maintained a condensed, well-folded globular conformation in the presence of DIM in an aqueous environment.

To evaluate the positional stability and binding endurance of DIM within the VEGFR2 catalytic cleft, the ligand movement RMSD was calculated by superimposing the receptor onto its initial reference structure over the 100 ns trajectory (Figure 2d). The ligand displacement profile showed sustained retention within the orthosteric binding pocket, maintaining an overall RMSD fluctuation strictly confined between 0.85 Å and 2.70 Å throughout the entire simulation. During the first 35 ns, DIM occupied an exceptionally stable orientation with minimal movement, registering RMSD values between 1.0 Å and 1.8 Å. Between 40 and 85 ns, a minor conformational readjustment within the cavity resulted in an average displacement plateauing around 1.8–2.1 Å, representing localized induced-fit adaptations rather than dissociation.

Notably, the ligand did not drift out of the binding pocket or undergo major translational escapes, and its movement RMSD relaxed back toward 1.5–1.7 Å during the final 10 ns of the trajectory. These findings indicate that DIM forms strong anchoring interactions with VEGFR2, preserving a steady binding pose within the active site without loss of binding affinity.

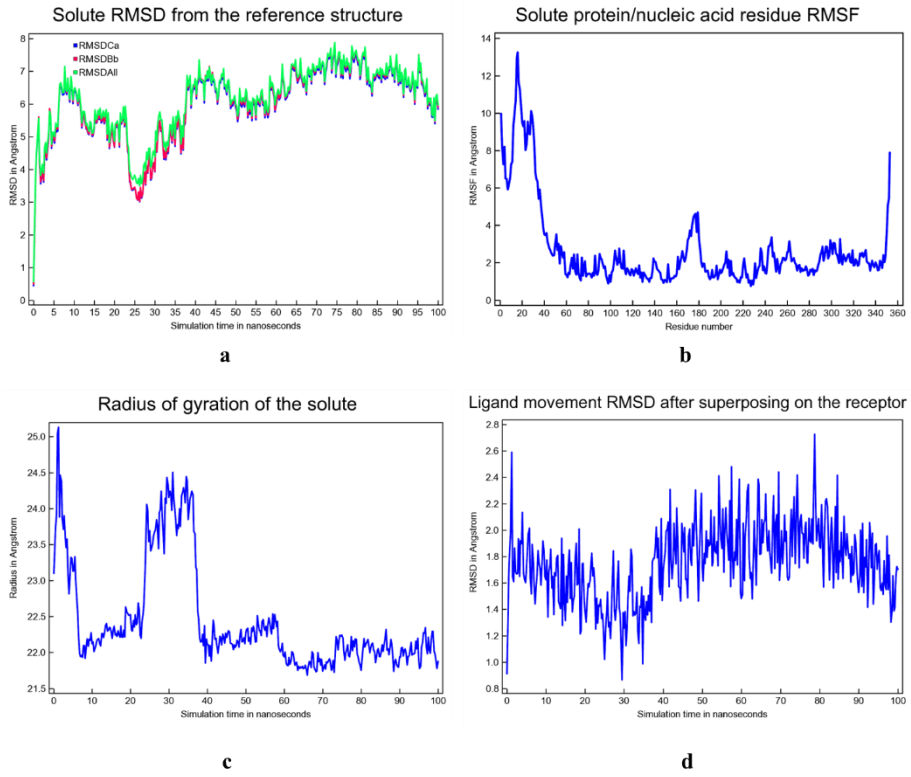

Figure 2. Structural stability, flexibility, and compactness profiles of the VEGFR2–3,3'-diindolylmethane complex during 100 ns MD simulation: (a) Solute RMSD (Cα, Backbone, and All atoms), (b) Per-residue RMSF plot of the receptor, (c) Time evolution of the radius of gyration (Rg), and (d) Positional RMSD of ligand movement relative to the receptor binding site.

The residue-specific contact map between the VEGFR2 receptor and DIM was tracked across the 100 ns trajectory to identify the critical amino acids governing complex stabilization and to determine the nature of the binding interactions. The per-residue interaction timeline illustrated in Figure 3b a prominent, multi-modal binding profile dominated by continuous hydrophobic contacts and localized hydrogen-bonding networks. Throughout the trajectory, dense and unbroken interaction bands were maintained by key residues around the Glu149/Val150 segment and the Asp228/Arg230 region, which engaged in persistent dual hydrophobic and polar contacts with the inhibitor scaffold. In addition, extended hydrophobic interactions were consistently supplied by residue clusters located along positions 70–80, 95–100, and 120–135, creating a robust lipophilic pocket that encapsulated the bis-indole scaffold of DIM. The continuous presence of these contact lines over the full 100 ns confirms that the ligand–protein interface remained structurally intact without significant disruption of the primary pharmacophore contacts. The sustained involvement of both polar anchors and hydrophobic enclosures highlights the cooperative thermodynamic contributions stabilizing DIM at the VEGFR2 active site.

To gain atomistic insight into the pharmacophoric contributions of DIM, the interaction types established by individual ligand atoms (Figure 3a) with VEGFR2 were mapped along the 100 ns simulation. The resultant per-atom trajectory revealed that the primary stabilizing interactions were driven by distinct functional groups on the 3,3'-diindolylmethane backbone. Most notably, the heterocyclic indole nitrogen (Atom 5648) acted as a primary and uninterrupted hydrogen bond donor, generating a persistent, unbroken red band throughout almost the entire 100 ns simulation window (Figure 3c). Complementing this strong polar tether, the surrounding carbon atoms of the fused indole ring systems (specifically Atoms 5642–5646

and 5660–5665) established dense and continuous hydrophobic interactions (green bands) with the hydrophobic subpockets of VEGFR2. Sporadic hydrogen-bonding interactions were also contributed by the second indole nitrogen (Atom 5665), providing secondary polar anchoring at specific conformational intervals. The cooperative interplay between the localized nitrogen hydrogen-bonding centers and the extensive hydrophobic ring contacts highlights the specific structural complementarity of the DIM scaffold within the target site.

The DCCM was constructed based on the Cα atomic displacements to examine the correlated internal domain motions and inter-residue communication within the VEGFR2–DIM complex over the simulation trajectory (Figure 3d). The matrix is color-coded from bright yellow (+1.0, highly correlated motions) to deep blue (-1.0, fully anti-correlated motions), with the diagonal representing self-correlation. The analysis demonstrated well-orchestrated, modular dynamics characterized by extensive positive cross-correlation blocks (yellow regions) along the diagonal, confirming the presence of stable, cooperatively moving secondary structural elements within the core kinase domains. Off-diagonal regions exhibited pronounced anti-correlated motions (deep blue regions) between the distinct lobes of the kinase receptor. These anti-correlated segments highlight the functional breathing and hinge-bending motions between the N-terminal and C-terminal lobes, which are essential for kinase conformational cycling. The preservation of strong intra-domain correlated clusters, coupled with coordinated inter-domain counter-movements, indicates that DIM binding preserves the native allosteric communication pathways while structurally stabilizing the local active site framework.

PCA was conducted to capture the essential collective motions of the VEGFR2 backbone and evaluate the conformational space sampled by the complex during the 100 ns trajectory (Figure 3e). The two-dimensional scatter plot projecting the conformational snapshots along the first two principal components (PC1 vs PC2) provides a direct visualization of the structural distribution and free energy landscape of the simulated system. The conformational ensemble occupied a well-defined, compact phase space centered predominantly between 100 Å and 175 Å along PC1, and -40 Å to -100 Å along PC2. The high density of conformational points clustered within this localized subspace reflects the occupation of a major, energetically favorable global minimum with limited conformational drift. While a minor fraction of snapshots dispersed along higher PC1 values (200–375 Å) during early-to-intermediate sampling, the subsequent trajectory converged into the tightly grouped cluster, confirming restricted global motions and structural convergence. This condensed distribution confirms that the binding of 3,3'-diindolylmethane restricted the conformational freedom of the VEGFR2 kinase, driving the system into a stable and energetically optimized conformational state.

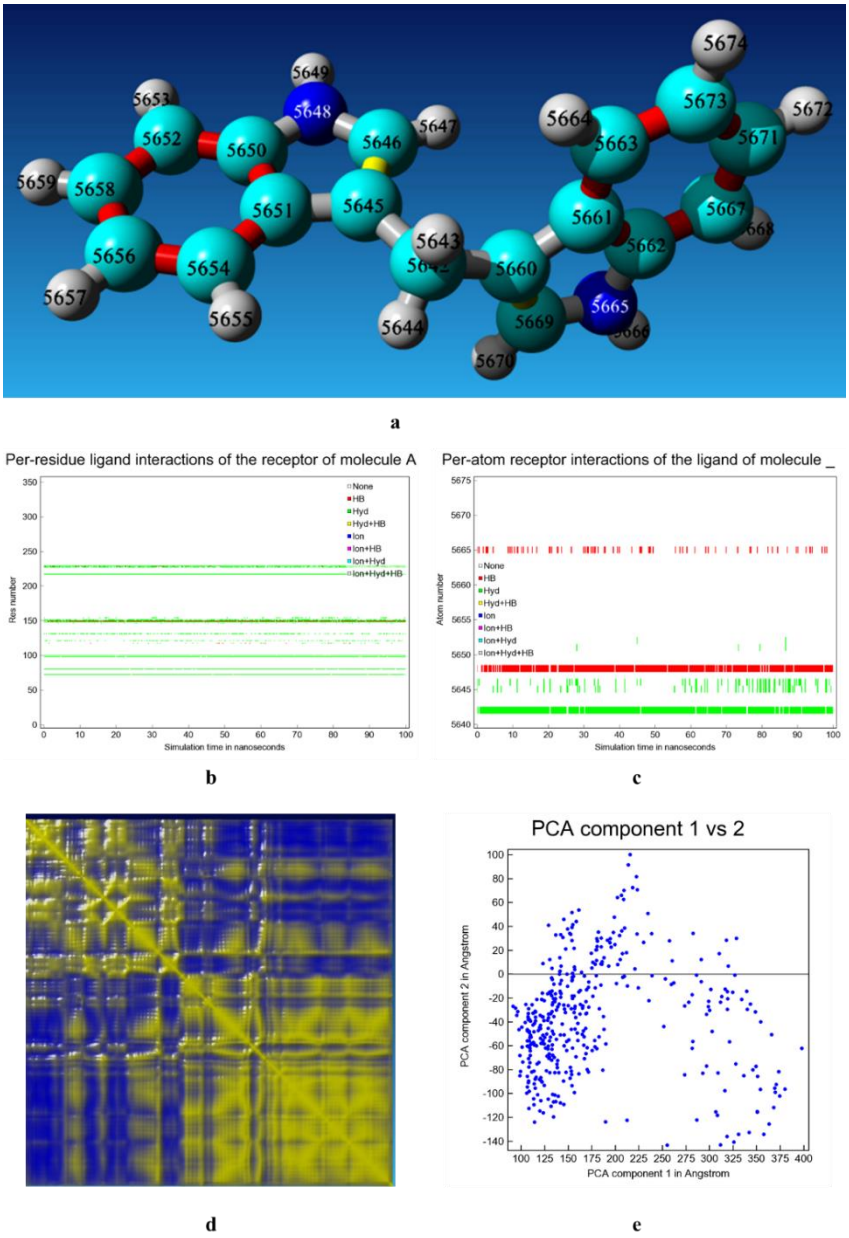

Figure 3. Detailed interaction dynamics, cross-correlation, and essential motions of the VEGFR2–DIM complex during 100 ns MD simulation: (a) Atom-numbered 3D ball-and-stick model of DIM, (b) Per-residue ligand interaction profile of VEGFR2 as a function of simulation time, (c) Per-atom receptor interaction timeline of DIM, (d) DCCM showing correlated (yellow) and anti-correlated (blue) residue motions, and (e) 2D conformational projection along the first two principal components (PCA Component 1 vs 2).

In conclusion, the 100 ns molecular dynamics simulation confirmed that the DIM–VEGFR2 complex maintains high structural stability, compactness, and steady binding endurance in an aqueous environment. The global stability of the system was demonstrated by the convergence of the solute RMSD within a stable plateau (6.0–7.5 Å) after 40 ns, low active-site residue fluctuations (RMSF < 2.0 Å), and a marked reduction in the radius of gyration (Rg ~21.7–22.3 Å), reflecting a condensed and well-folded macromolecular architecture. Furthermore, DIM remained firmly anchored within the orthosteric catalytic pocket without drifting (ligand movement RMSD ~1.8 Å), stabilized by continuous indole N–H hydrogen bonding (Atom 5648) and persistent hydrophobic networks with key residues around Glu149, Val150, Asp228, and Arg230. Supported by the well-orchestrated intra-domain correlations in DCCM and a concentrated conformational energy basin in PCA, these findings conclusively establish that DIM forms a highly stable and energetically favorable complex with VEGFR2, highlighting its potential as a promising natural VEGFR2-targeting inhibitör.

IV. CONCLUSION

In this study, the anticancer and anti-angiogenic potential of four prominent broccoli phytochemicals (Glucoraphanin, Indole-3-carbinol, Sulforaphane, and 3,3'-Diindolylmethane) against the catalytic domain of VEGFR2 (PDB ID: 4ASD) was comprehensively evaluated through molecular docking and 100 ns all-atom molecular dynamics simulations. The virtual screening results revealed that 3,3'-diindolylmethane exhibited the strongest binding affinity (-10.6 kcal/mol), significantly outperforming the other candidate bioactives through favorable hydrogen bonding, pi-cation, pi-sulfur, and extensive hydrophobic contacts. Subsequent 100 ns MD trajectory analysis confirmed the robust thermodynamic stability and conformational equilibrium of the VEGFR2–DIM complex, characterized by a stabilized backbone RMSD plateau (6.0–7.5 Å), low active-site residue mobility (RMSF < 2.0 Å), and a tightly folded globular compactness (Rg ~21.7–22.3 Å). Furthermore, persistent indole N–H hydrogen bonding (Atom 5648) coupled with stable hydrophobic anchoring (Glu149, Val150, Asp228, Arg230) locked the inhibitor firmly within the orthosteric binding cleft (ligand RMSD ~1.8 Å) without dissociation. Coupled with coordinated domain communication in DCCM and restricted conformational subspace sampling in PCA, these atomistic findings demonstrate that DIM acts as a potent and stable natural VEGFR2 inhibitor.

REFERENCES

[1] P. Lorenc, A. Sikorska, S. Molenda, N. Guzniczak, H. Dams-Kozlowska, and A. Florczak, "Physiological and tumor-associated angiogenesis: Key factors and therapy targeting VEGF/VEGFR pathway," *Biomed. Pharmacother.*, vol. 180, p. 117585, 2024.

[2] F. H. Shah, Y. S. Nam, J. Y. Bang, I. S. Hwang, D. H. Kim, M. Ki, and H.-W. Lee, "Targeting vascular endothelial growth receptor-2 (VEGFR-2): structural biology, functional insights, and therapeutic resistance," *Arch. Pharm. Res.*, vol. 48, pp. 404–425, 2025.

[3] S. Ghalehbandi, J. Yuzugulen, M. Z. I. Pranjol, and M. H. Pourgholami, "The role of VEGF in cancer-induced angiogenesis and research progress of drugs targeting VEGF," *Eur. J. Pharmacol.*, vol. 949, p. 175586, 2023.

[4] C. Lee, M.-J. Kim, A. Kumar, H.-W. Lee, Y. Yang, and Y. Kim, "Vascular endothelial growth factor signaling in health and disease: from molecular mechanisms to therapeutic perspectives," *Signal Transduct. Target. Ther.*, vol. 10, p. 170, 2025.

[5] N. Muhammad, D. Usmani, M. Tarique, H. Naz, M. Ashraf, R. Raliya, S. Tabrez, T. A. Zughaibi, A. Alsaieedi, I. J. Hakeem, and M. Suhail, "The Role of Natural Products and Their Multitargeted Approach to Treat Solid Cancer," *Cells*, vol. 11, p. 2209, 2022.

[6] D. Ağagündüz, T. Ö. Şahin, B. Yılmaz, K. D. Ekenci, Ş. Duyar Özer, and R. Capasso, "Cruciferous Vegetables and Their Bioactive Metabolites: from Prevention to Novel Therapies of Colorectal Cancer," *Evid. Based Complement. Alternat. Med.*, vol. 2022, pp. 1–20, 2022.

[7] D. Chaudhuri, S. Orsulic, and B. T. Ashok, "Antiproliferative activity of sulforaphane in Akt-overexpressing ovarian cancer cells," *Mol. Cancer Ther.*, vol. 6, pp. 334–345, 2007.

[8] H. M. Berman, "The Protein Data Bank," *Nucleic Acids Res.*, vol. 28, pp. 235–242, 2000.

[9] E. F. Pettersen, T. D. Goddard, C. C. Huang, G. S. Couch, D. M. Greenblatt, E. C. Meng, and T. E. Ferrin, "UCSF Chimera - A visualization system for exploratory research and analysis," *J. Comput. Chem.*, vol. 25, pp. 1605–1612, 2004.

[10] M. D. Hanwell, D. E. Curtis, D. C. Lonie, T. Vandermeersch, E. Zurek, and G. R. Hutchison, "Avogadro: an advanced semantic chemical editor, visualization, and analysis platform," *J. Cheminform.*, vol. 4, p. 17, 2012.

[11] BIOVIA. Discovery Studio Visualizer, Version 21.1.0.20298. (San Diego, CA: Dassault Systemes, 2021).

[12] E. Krieger and G. Vriend, "YASARA View—molecular graphics for all devices—from smartphones to workstations," *Bioinformatics*, vol. 30, pp. 2981–2982, 2014.

[13] E. Krieger, J. E. Nielsen, C. A. E. M. Spronk, and G. Vriend, "Fast empirical pKa prediction by Ewald summation," *J. Mol. Graph. Model.*, vol. 25, pp. 481–486, 2006.

[14] J. A. Maier, C. Martinez, K. Kasavajhala, L. Wickstrom, K. E. Hauser, and C. Simmerling, "ff14SB: Improving the Accuracy of Protein Side Chain and Backbone Parameters from ff99SB," *J. Chem. Theory Comput.*, vol. 11, pp. 3696–3713, 2015.

[15] J. Wang, R. M. Wolf, J. W. Caldwell, P. A. Kollman, and D. A. Case, "Development and testing of a general amber force field," *J. Comput. Chem.*, vol. 25, pp. 1157–1174, 2004.

[16] A. Jakalian, D. B. Jack, and C. I. Bayly, "Fast, efficient generation of high-quality atomic charges. AM1-BCC model: II. Parameterization and validation," *J. Comput. Chem.*, vol. 23, pp. 1623–1641, 2002.

[17] E. Krieger and G. Vriend, "New ways to boost molecular dynamics simulations," *J. Comput. Chem.*, vol. 36, pp. 996–1007, 2015.

[18] V. Hornak, R. Abel, A. Okur, B. Strockbine, A. Roitberg, and C. Simmerling, “Comparison of multiple Amber force fields and development of improved protein backbone parameters,” *Proteins*, vol. 65, pp. 712–725, 2006.
[19] U. Essmann, L. Perera, M. L. Berkowitz, T. Darden, H. Lee, and L. G. Pedersen, “A smooth particle mesh Ewald method,” *J. Chem. Phys.*, vol. 103, pp. 8577–8593, 1995.

8th International Conference on Engineering, Natural and Social Sciences

September 06-07, 2026: Konya, Turkey

https://www.icensos.com/

Tersane İşletmelerinin WEB Sitelerinin İçerik Analizi ile Değerlendirmesi: Yalova Altınova Örneği

Kutluhan DOĞAN[1], Ömer ŞENGÜL[2] ve Murat YORULMAZ[3]

[1]Deniz Ulaştırma Mühendisliği Anabilim Dalı/ Fen Bilimleri Enstitüsü, Kocaeli Üniversitesi, Türkiye
2Gemi Makineleri İşletme Mühendisliği Bölümü/ Denizcilik Fakültesi, Kocaeli Üniversitesi, Türkiye
[3]Denizcilik İşletmeleri Yönetimi Bölümü/ Denizcilik Fakültesi, Kocaeli Üniversitesi, Türkiye

[1]kutluhan.d@hotmail.com *(sorumlu yazar)*

Özet - Bu çalışmanın temel amacı, Altınova Tersaneler Bölgesi'nde faaliyet gösteren tersane işletmelerinin web sitelerinin erişilebilirlik ve kullanılabilirlik açısından değerlendirilmesidir. Bu amaca yönelik olarak da Altınova Tersaneler Bölgesi'nde faaliyet gösteren tersane işletmeleri belirlenmiş ve web sitelerinin içerikleri analiz edilmiştir. İçerik analizi, kodların nicel olarak incelenmesi ve bulguların bilimsel bir şekilde özetlenmesiyle gerçekleştirilen bir araştırma metodudur. İçerik analizi, web sitelerinin erişilebilirlik düzeyi ve kullanıcı deneyimini anlamak için kullanılmıştır. Araştırma bulgularına göre Dijital teknolojilerin gelişmesiyle birlikte işletmelerin kendilerini tanıtma ve hedef kitleleri ile iletişim kurma yöntemleri önemli ölçüde değişmiştir. Günümüzde kurumsal web siteleri işletmeler için yalnızca bir tanıtım aracı değil aynı zamanda kurumsal kimliğin ve faaliyetlerin sergilendiği önemli bir platform haline gelmiştir. Özellikle uluslararası faaliyet gösteren sektörlerde web siteleri işletmelerin görünürlüğünü artıran önemli bir iletişim kanalıdır. Bu çalışmanın temel amacı, Altınova Tersaneler Bölgesi'nde faaliyet gösteren tersane işletmelerinin web sitelerinin erişilebilirlik ve kullanılabilirlik açısından değerlendirilmesidir. Bu amaca yönelik olarak da Altınova Tersaneler Bölgesi'nde faaliyet gösteren tersane işletmeleri belirlenmiş ve web sitelerinin içerikleri analiz edilmiştir. İçerik analizi, kodların nicel olarak incelenmesi ve bulguların bilimsel bir şekilde özetlenmesiyle gerçekleştirilen bir araştırma metodudur. İçerik analizi, web sitelerinin erişilebilirlik düzeyi ve kullanıcı deneyimini anlamak için kullanılmıştır. Araştırma bulgularına göre tersane işletmelerinin web sitelerinin analizi edilerek yorumlanmıştır.

Anahtar Kelimeler – Tersane İşletmeleri, Kurumsal Web Siteleri, İçerik Analizi, Dijital İletişim, Web Sitesi Kullanılabilirliği, Yalova-Altınova, Gemi İnşa Sanayisi.

1. GİRİŞ

Deniz taşımacılığının bu denli yaygın ve etkin bir şekilde sürdürülebilmesi, büyük ölçüde tersane işletmelerinin varlığına ve faaliyetlerine bağlıdır. Tersaneler, ticaret gemilerinin inşa edildiği, bakım ve onarımlarının gerçekleştirildiği temel üretim ve hizmet merkezleridir. İnşa edilen gemiler, küresel ticaret ağlarının işleyişini mümkün kılarken; düzenli bakım ve onarım faaliyetleri de bu gemilerin güvenli, verimli ve uluslararası standartlara uygun şekilde faaliyet göstermesini sağlar. Bunlarla birlikte, günümüzde çevresel düzenlemeler ve teknolojik gelişmeler doğrultusunda gemilerin modernizasyonu da tersanelerde gerçekleştirilmektedir. Yakıt verimliliğini artıran sistemler, emisyon azaltıcı teknolojiler ve dijitalleşme uygulamaları yine tersane faaliyetleri kapsamında hayata geçirilmektedir. Bu yönüyle tersaneler, yalnızca deniz taşımacılığını destekleyen yapılar değil, aynı zamanda sektörün gelişimini yönlendiren ve sürdürülebilirliğini sağlayan stratejik aktörlerdir. Sonuç olarak, deniz taşımacılığı uluslararası ticaretin taşıyıcı gücünü oluştururken, tersane işletmeleri bu sistemin devamlılığını sağlayan ve geliştiren temel unsurlar arasında yer almaktadır [1].

Deniz ulaştırmasının etkin ve sürdürülebilir bir şekilde devam edebilmesi, tersane işletmelerinin faaliyetleriyle doğrudan ilişkilidir. Tersaneler, deniz taşımacılığının temel unsuru olan gemilerin inşa edildiği, bakım ve onarım süreçlerinin yürütüldüğü stratejik tesislerdir. Gemi inşa faaliyetleri sayesinde küresel ticaretin ihtiyaç duyduğu farklı tip ve kapasitedeki gemiler üretilebilmekte, bu durum deniz taşımacılığının sürekliliğini sağlamaktadır [17]-[18]. Bunun yanı sıra, işletmede olan gemilerin periyodik bakım ve onarımlarının gerçekleştirilmesi; güvenlik, verimlilik ve uluslararası standartlara uyum açısından büyük önem taşımaktadır. Günümüzde artan çevresel düzenlemeler ve teknolojik gelişmeler doğrultusunda tersaneler, gemilerin modernizasyon süreçlerinde de aktif rol üstlenmektedir. Enerji verimliliğini artıran sistemlerin entegrasyonu, emisyon azaltıcı uygulamalar ve dijital teknolojilerin kullanımı gibi yenilikler tersaneler aracılığıyla hayata geçirilmektedir. Bu durum, deniz ulaştırmasının hem ekonomik hem de çevresel açıdan daha sürdürülebilir bir yapıya kavuşmasına katkı sağlamaktadır. Sonuç olarak tersane işletmeleri, yalnızca gemi üretimi ve bakım hizmeti sunan yapılar değil; deniz ulaştırmasının gelişimini destekleyen, güvenliğini sağlayan ve küresel ticaretin devamlılığına katkıda bulunan kritik aktörlerdir [2].

İnternet teknolojilerinin yaygınlaşması işletmelerin iletişim ve tanıtım faaliyetlerinde önemli değişikliklere yol açmıştır. Günümüzde işletmeler yalnızca geleneksel tanıtım araçlarını kullanmakla kalmayıp dijital platformlardan da yararlanmaktadır. Kurumsal web siteleri bu platformların başında gelmektedir. Web siteleri sayesinde işletmeler sundukları hizmetleri tanıtabilmekte, kurumsal kimliklerini aktarabilmekte ve potansiyel müşterilerle iletişim kurabilmektedir. Denizcilik sektörü uluslararası faaliyetlerin yoğun olduğu alanlardan biridir. Bu sektörde faaliyet gösteren tersaneler gemi inşa, bakım ve onarım gibi hizmetler sunarak hem ulusal hem de uluslararası müşterilerle çalışmaktadır. Bu nedenle tersanelerin faaliyetlerini dijital ortamda tanıtması sektör içerisindeki rekabet açısından önemli bir unsur olarak görülmektedir. Kurumsal web siteleri tersanelerin sahip oldukları teknik altyapıyı, gerçekleştirdikleri projeleri ve sundukları hizmetleri tanıtmalarına imkân sağlamaktadır. Web siteleri aynı zamanda işletmelerin kurumsal imajını yansıtan dijital platformlar olarak da değerlendirilmektedir. Kullanıcı dostu ve güncel içeriklere sahip web siteleri işletmelerin güvenilirliğini artırmakta ve potansiyel müşteriler üzerinde olumlu bir izlenim bırakmaktadır. Buna karşılık içerik bakımından yetersiz veya güncellenmeyen web siteleri işletmelerin dijital görünürlüğünü sınırlayabilmektedir. Bu çalışmada Yalova-Altınova bölgesinde faaliyet gösteren tersanelerin web siteleri incelenerek sitelerde yer alan içerikler değerlendirilmiştir. Araştırma kapsamında web sitelerinde bulunan temel bilgiler belirli kriterler doğrultusunda incelenmiş ve elde edilen bulgular yorumlanmıştır [3] - [4].

2. METARYEL VE YÖNTEM

Bu araştırmada tersanelerin kurumsal web sitelerinde yer alan içeriklerin değerlendirilmesi amacıyla içerik analizi yaklaşımı kullanılmıştır. İçerik analizi, metin veya dijital içeriklerin belirli kriterler çerçevesinde incelenmesine olanak sağlayan bir araştırma yöntemidir. Bu yöntem sayesinde incelenen materyaller belirli kategorilere ayrılarak değerlendirilmekte ve araştırma konusu hakkında genel bir değerlendirme yapılabilmektedir. Araştırma kapsamında çalışma havuzunda yer alan tersanelerin resmi web siteleri incelenmiştir. Analiz sürecinde erişilebilir durumda olan ve aktif olarak kullanılan web siteleri değerlendirmeye dahil edilmiştir. Web sitelerinde yer alan içerikler belirlenen kriterler doğrultusunda incelenmiş ve her bir site ayrı ayrı değerlendirilmiştir. Web sitelerinin incelenmesinde kurumsal bilgiler, hizmet tanıtımları, iletişim bilgileri ve web sitesi yönetimine ilişkin özellikler dikkate alınmıştır. Bu kriterler doğrultusunda web sitelerinde yer alan içerikler değerlendirilmiş ve elde edilen bulgular yorumlanmıştır. Araştırmada, tersanelerin kurumsal web sitelerindeki içerikler içerik analizi yöntemiyle incelenmiştir. Bu yöntem, yazılı ya da dijital verilerin belirli ölçütlere göre değerlendirilmesini sağlamaktadır. Böylece incelenen belgeler kategorilere ayrılmış ve araştırma konusuna ilişkin genel bir sonuca ulaşılmıştır. Çalışma kapsamındaki tersanelerin resmî web siteleri incelenmiş; erişime açık ve aktif olarak kullanılan siteler değerlendirmeye alınmıştır. Web siteleri; kurumsal bilgiler, sunulan hizmetler,

iletişim bilgileri ve site yönetimi özellikleri açısından ele alınmıştır. Her bir site bu kategorilerde ayrı ayrı incelenmiş ve elde edilen bulgular doğrultusunda genel bir değerlendirme yapılmıştır. Bu çalışmada tersane işletmelerine ait kurumsal web siteleri incelenmiştir. Araştırmanın temel amacı, bu web sitelerinde yer alan içeriklerin genel bir değerlendirmesini yapmaktır. Çalışma kapsamında örneklem olarak, Gemi İnşa Sanayicileri Birliği (GİSBİR) ile Yalova-Altınova Tersane Girişimcileri San. ve Tic. A.Ş.'ye bağlı toplam Yalova-Altınova tersane işletmeleri ele alınmıştır. Analiz sürecinde önerilen yöntemden yararlanılmıştır. Söz konusu yöntem, web sitelerinde yer alan içeriklerin belirli kriterler çerçevesinde incelenmesine olanak sağlamaktadır. Bu doğrultuda tersanelere ait web siteleri; kurumsal bilgiler, sunulan hizmetler, iletişim bilgileri ve site yapısı gibi başlıklar altında değerlendirilmiştir. Bununla birlikte, web sitelerinin güncellik durumu ve kullanıcıya sağladığı bilgi düzeyi de inceleme kapsamına dahil edilmiştir [5] - [6] - [7] – [8].

3. BULGULAR

Araştırma kapsamında incelenen tersane işletmelerinin kurumsal web siteleri belirlenen değerlendirme kriterleri doğrultusunda incelenmiştir. İnceleme sürecinde işletmelerin web sitelerinde yer alan kariyer, insan kaynakları ve çalışanlara yönelik içerikler dikkate alınmıştır. Web sitelerinde bulunan bilgiler belirlenen içerik kategorilerine göre sınıflandırılmış ve her kategoriye ilişkin veriler kayıt altına alınmıştır. İncelenen web sitelerinde çalışanlara yönelik çeşitli bilgilere yer verildiği görülmüştür. Bu bilgiler arasında maaş ve yan haklara ilişkin açıklamalar, iş başvuru süreçleri, kurum kültürü hakkında paylaşılan bilgiler, eğitim ve kariyer gelişimine yönelik içerikler ile iş tanımlarına ilişkin açıklamalar yer almaktadır. Bunun yanında bazı web sitelerinde iş sağlığı ve güvenliği uygulamaları ile ilgili bilgilere de yer verildiği belirlenmiştir. Web sitelerinde ayrıca iş arayan adaylara yönelik mesajlar, çalışan deneyimlerine ilişkin paylaşımlar, kurumsal sosyal sorumluluk faaliyetleri ve çevreye yönelik uygulamalara ilişkin bilgiler de incelenmiştir. Elde edilen veriler belirlenen içerik kategorilerine göre sınıflandırılmış ve her bir kategoride yer alan içeriklerin sayısı belirlenmiştir.[10] - [16]

Tablo 1: Web Sitesi İçerik Bileşenleri

	VAR	**YOK**
Kurumsal bilgiler	30	0
Hizmetler ve faaliyet alanları	25	5
Projeler / referanslar	18	12
Kariyer / insan kaynakları	12	18
İş sağlığı ve güvenliği (HSE)	20	10
Kalite politikası ve sertifikalar	17	13
Çevre ve sürdürülebilirlik	14	16
Kurumsal sosyal sorumluluk	9	21
Haberler / duyurular	16	14
İletişim bilgileri	30	0
Dil seçenekleri	21	9
Güncellik	15	15

Kurumsal kimlik bileşenlerine ilişkin veriler incelendiğinde, tersane işletmelerine ait web sitelerinde en yaygın olarak yer verilen unsurların kurumsal bilgiler ve iletişim bilgileri olduğu anlaşılmaktadır. Bu bulgu, işletmelerin dijital ortamda kendilerini tanıtma ve paydaşlarla iletişim kurma işlevine öncelik verdiğini göstermektedir. Benzer şekilde, önceki araştırmalar da işletmelere ait temel bilgilerin web sitelerinde yüksek oranlarda yer aldığını ortaya koymakta olup, bu çalışmanın bulguları literatürdeki sonuçlarla paralellik göstermektedir. Bununla birlikte, kariyer ve insan kaynakları**,** kurumsal sosyal sorumluluk ile çevre ve sürdürülebilirlik başlıklarının daha düşük düzeyde temsil edildiği görülmektedir. Oysa günümüzde sürdürülebilirlik uygulamaları ve sosyal sorumluluk faaliyetleri, işletmelerin kurumsal itibarını ve rekabet gücünü artıran önemli unsurlar arasında değerlendirilmektedir. Bu içeriklerin web sitelerinde sınırlı biçimde yer alması, tersane işletmelerinin bu alanlardaki iletişim stratejilerini yeterince etkin kullanmadığını düşündürmektedir. Ayrıca, web sitelerinde sunulan içeriklerin çeşitliliği ve güncel tutulması, işletmelerin dijital görünürlüğü ve kurumsal imajı açısından belirleyici bir rol oynamaktadır. Bu doğrultuda, tersanelerin yalnızca temel bilgilere yer vermekle sınırlı kalmayıp, daha kapsamlı, güncel ve stratejik içeriklerle web sitelerini zenginleştirmeleri, rekabet avantajı elde etmeleri açısından kritik önem taşımaktadır.[4]

Çalışma kapsamında erişilebilen aktif tersanelerin büyük çoğunluğunun resmi bir web sitesine sahip olduğu görülmüştür. Hazırlanan web sitesi değerlendirme formu doğrultusunda yapılan incelemede, tersanelerin önemli bir kısmının web sitelerini aktif biçimde yönettiği tespit edilmiştir [11] – [12] – [13]. Özellikle kurumsal tanıtım, gemi inşa ve bakım-onarım hizmetleri,

Tablo 2 : Web Sitesi Kategori Bileşenleri

Kategoriler	**Değişkenler**
Site Dizaynı	Web sitedeki dil tercihleri?
	Desteklenen yabancı dil sayıları
İçerik Analizi	Tersane tarihçesi
	Vizyon / misyon
	İrtibat ve ulaşım bilgileri
	Fotoğraf galerisi
	Video galerisi
	Sosyal medya (Instagram, LinkedIn, Youtube vb.)
	Referans projeler

	Gemi inşa hizmetleri
	Bakım-onarım hizmetleri
	Havuzlama hizmetleri
	Offshore / çelik yapı hizmetleri
Etkileşimli	Online teklif talep formu
	Kariyer / CV yükleme alanı

Bu çalışmada oluşturulan kategori ve değişkenler doğrultusunda tersane işletmelerinin web siteleri içerik analizi yöntemi ile değerlendirilmiştir. Tablo 2'de görüldüğü üzere değerlendirme kriterleri; site dizaynı, içerik analizi ve etkileşimli unsurlar olmak üzere üç ana kategori altında ele alınmıştır. Site dizaynı kapsamında özellikle dil tercihleri ve yabancı dil desteği gibi unsurların incelenmesi, tersanelerin uluslararası erişilebilirlik düzeyinin değerlendirilmesi açısından önem taşımaktadır. Kurumsal bilgi kategorisinde ise işletmelerin kendilerini tanıtma biçimleri, referans projeleri ve görsel içerikleri ön plana çıkmaktadır. Hizmet bilgisi kategorisi, tersanelerin sunduğu temel faaliyet alanlarını ortaya koyarken; etkileşimli unsurlar kategorisi, web sitelerinin kullanıcı ile olan iletişim düzeyini değerlendirmek amacıyla oluşturulmuştur. Bu kapsamda online teklif formları ve kariyer başvuru alanları gibi unsurlar, işletmelerin dijital etkileşim kapasitesini yansıtmaktadır. Genel olarak değerlendirildiğinde, oluşturulan bu kategori yapısı, tersane web sitelerinin içerik, işlevsellik ve kullanıcı odaklılık açısından bütüncül bir şekilde analiz edilmesine olanak sağlamaktadır.

Tablo 3: Web Sitesi Aktiflik Kullanımı

	SAYI	**%**
Websiteleri Aktif Kullanım	25	%83.33
Websiteleri Pasif Kullanım	5	%16.67

Tablo 3 incelendiğinde, araştırma kapsamında değerlendirilen tersane web sitelerinin büyük çoğunluğunun aktif olarak kullanıldığı görülmektedir.

4. SONUÇ ve ÖNERİLER

Araştırma sonucunda Türkiye gemi inşa sanayisinin en önemli kümelenme bölgelerinden biri olan Yalova ili Altınova ilçesinde faaliyet gösteren tersane işletmelerinin kurumsal web siteleri incelenmiştir. Çalışma kapsamında erişilebilen aktif tersanelerin büyük çoğunluğunun resmi bir web sitesine sahip olduğu görülmüştür. Hazırlanan web sitesi değerlendirme formu doğrultusunda yapılan incelemede, tersanelerin önemli bir kısmının web sitelerini aktif biçimde yönettiği tespit edilmiştir. Özellikle kurumsal tanıtım, gemi inşa ve bakım-onarım hizmetleri, iletişim bilgileri, kalite belgeleri ve referans projeler gibi temel içeriklere yaygın şekilde yer verildiği belirlenmiştir. Bununla birlikte, Altınova bölgesindeki bazı tersane web sitelerinde erişilebilirlik, kullanıcı yönlendirmesi ve bilgiye hızlı ulaşım açısından çeşitli eksiklikler bulunduğu görülmüştür. Menü yapısının karmaşık olması, sayfa geçişlerinin yeterince kullanıcı dostu olmaması ve teknik hizmet detaylarının sınırlı düzeyde sunulması, potansiyel müşteriler ve iş ortaklarının

ihtiyaç duydukları bilgilere hızlı ulaşmasını zorlaştırabilmektedir. Özellikle uluslararası müşteri portföyüne hitap eden tersaneler açısından bu durum önemli bir dijital iletişim eksikliği olarak değerlendirilebilir. Günümüzde LinkedIn, Instagram, YouTube ve diğer sosyal medya platformları, tersanelerin kurumsal prestiji, yeni proje duyuruları, teslim edilen gemi paylaşımları ve insan kaynakları iletişimi açısından önemli araçlar hâline gelmiştir. Araştırmada, Altınova tersanelerinin web sitelerinde sosyal medya bağlantılarına belirli ölçüde yer verildiği görülmekle birlikte, bu bağlantıların tüm işletmelerde standart bir yapı göstermediği anlaşılmıştır. Özellikle bölgedeki tersanelerin uluslararası görünürlüğünü artırmak için sosyal medya entegrasyonunun daha etkin kullanılması gerektiği değerlendirilmektedir. Önceden belirtildiği gibi, tabloda bulunan kategori ve değişkenlerin değerlendirilmesinde içerik analizi yöntemi esas alınmıştır [8].

Araştırmada, Altınova tersanelerinin web sitelerinde sosyal medya bağlantılarına belirli ölçüde yer verildiği görülmekle birlikte, bu bağlantıların tüm işletmelerde standart bir yapı göstermediği anlaşılmıştır. Özellikle bölgedeki tersanelerin uluslararası görünürlüğünü artırmak amacıyla sosyal medya entegrasyonunun daha etkin kullanılması gerektiği değerlendirilmektedir. Altınova bölgesi, Türkiye'de tersanecilik faaliyetlerinin yoğunlaştığı, güçlü yan sanayi ağına, liman bağlantılarına ve nitelikli iş gücüne sahip stratejik bir üretim merkezidir. Buna rağmen, tersanelerin önemli bir bölümünün web sitelerinde bölgenin lojistik avantajları, Marmara Denizi bağlantısı ve sanayi altyapısı gibi unsurlara sınırlı düzeyde yer verdiği görülmüştür. Oysa bu tür bilgilerin vurgulanması, özellikle uluslararası müşteriler ve yatırımcılar açısından güven artırıcı bir unsur olarak öne çıkmaktadır [9] - [14] - [15].

Genel olarak değerlendirildiğinde, Yalova–Altınova bölgesindeki tersanelerin web sitelerinde kurumsal bilgiler, faaliyet alanları, iletişim bilgileri ve proje referansları gibi temel unsurlara yer verildiği ve içerik güncelliğine belirli ölçüde önem verildiği anlaşılmaktadır. Buna karşın, kariyer fırsatları, dijital geri bildirim mekanizmaları, sanal tersane turları, çoklu dil desteği ve kullanıcı deneyimini geliştiren uygulamalar açısından eksiklikler bulunduğu tespit edilmiştir.

Bu doğrultuda, tersane işletmelerinin web sitelerini yalnızca bilgi sunan bir araç olarak değil, aynı zamanda etkileşim ve iletişim platformu olarak ele almaları gerekmektedir. Web sitelerinde çoklu dil desteğinin artırılması, kullanıcı deneyimini geliştiren etkileşimli uygulamaların eklenmesi, içeriklerin düzenli olarak güncellenmesi ve sosyal medya entegrasyonunun güçlendirilmesi önerilmektedir. Çalışmanın en önemli kısıtı, araştırmanın belirli bir zaman diliminde erişilebilen web siteleri üzerinden gerçekleştirilmiş olmasıdır. Araştırma sonrasında web sitelerinde meydana gelebilecek güncellemeler ve değişiklikler çalışma kapsamına dahil edilememiştir. Ayrıca araştırmanın yalnızca Yalova–Altınova bölgesi ile sınırlı olması, elde edilen bulguların genellenebilirliğini sınırlandırmaktadır. Gelecek çalışmalarda farklı bölgelerde faaliyet gösteren tersanelerin web sitelerinin karşılaştırmalı olarak incelenmesi ve kullanıcı deneyimi odaklı analizlerin yapılması literatüre katkı sağlayacaktır.

KAYNAKLAR

[1] Usta, G., ve Sarı, A. (2021). Denizyolu Ticareti, Ekonomik Büyüme ve Dış Ticaret Haddi Arasındaki İlişkinin İncelenmesi: Türkiye İçin Ardl Yaklaşımı. Nazilli İktisadi ve İdari Bilimler Fakültesi Dergisi, 2(1), 31-44.

[2] T.C. Ulaştırma ve Altyapı Bakanlığı. (2023). Denizcilik İstatistikleri ve Tersaneler Raporu

[3] Saylan, O. (2021) İnsan Kaynakları İletişiminde Kurumsal Web Sitelerinin Kullanımı. Denizcilik Fakültesi Dergisi, 14(1)

[4] Kutlu, D. (2020). Antalya A Grubu Seyahat Acentalarının Web Sitelerinin Değerlendirilmesi. Akademik Araştırmalar ve Çalışmalar Dergisi (Akad)

[5] Cober, R. T., Brown, D. J., Keeping, L. M., & Levy, P. E. (2004). Recruitment on the Net: How do organizational Web site characteristics influence. *Journal of management*, *30*(5), 623-646

[6] Öksüz, B. (2011). E-işe alım sürecinde kurumsal web sitelerinin kullanımı ve konu üzerine bir araştırma. Uluslararası Yönetim İktisat ve İşletme Dergisi, 7(14).

[7] Köseoğlu, F., ve Yorulmaz, M. (2024). Gemi Acente Web Sitelerinin Değerlendirilmesi: Kocaeli Örneği. Denizcilik Araştırmaları Dergisi: Amfora, 3(6), 99-116

[8] Ateş, U., ve Boz, M. (2015). Konaklama İşletmelerinin Web Sitelerinin Değerlendirilmesi: Çanakkale Örneği. Ekonomi İşletme Siyaset Ve Uluslararası İlişkiler Dergisi, 1(1), 63–84.

[9] Başfırıncı, Ç. (2008). Yönetim. Bir Pazarlama Iletişim Medyası Olarak Web Ortamında İçerik Analizi Yapmanın Güçlükleri Ve Olası Çözüm Önerileri. 19(61), S.53

[10] Çubukcu, M. İ. (2010). Konaklama İşletmeleri Web Site İçeriklerinin Değerlendirilmesi. Journal Of Internet Applications And Management, 1(1), 39–59.

[11] Engin, E., ve Akgöz, B. E. (2016). Belediyelerin Web Sitelerinin Diyalojik İletişim Açısından Analizi. Atatürk İletişim Dergisi, (10), 91-110.

[12] Güreş, N., Arslan, S., ve Yalçın, R. (2013). Türk Havayolu İşletmelerinin Web Sitelerinin Değerlendirilmesine Yönelik Bir Araştırma. Niğde Üniversitesi İktisadi Ve İdari Bilimler Fakültesi Dergisi, 6(1), 173-185.

[13] Karamustafa, K., Bickes, D. M., ve Ulama, Ş. (2002). Türkiye'deki Konaklama İşletmelerinin İnternet Web Sitelerini Değerlendirmeye Yönelik Bir Çalışma. Erciyes Üniversitesi İktisadi ve İdari Bilimler Fakültesi Dergisi, (19), 51-92.

[14] Kim, Y.H., Yuan, J., Goh, B.K. ve Antun, J.M. (2009). Web Marketing İn Food Tourism: A Content Analysis of Web Sites in West Texas

[15] Maksüdünov, A. (2019). Otel Web Sitelerinin İçerik Analizi Yöntemiyle Değerlendirilmesi

[16] Uyguçgil, G., ve Demıray, U. (2016). Açık ve Uzaktan Eğitim Kurumlarının Web Sitelerinin Popülaritesi. Açıköğretim Uygulamaları ve Araştırmaları Dergisi, 2(1), 162-186.

[17] Yorulmaz, M. (2021). Tersane İşletmelerinde Etik İklimin Örgütsel Güvene Etkisinde Örgütsel Adalet Algısının Aracılık Rolü. Dokuz Eylül Üniversitesi Denizcilik Fakültesi Dergisi, 13(1), 57-84.

[18] Yorulmaz, M. ve Akdeniz, Y. A. (2025). Tersane İşletmelerindeki İş Kazalarının ve Önlemlerinin Değerlendirilmesi. Turkish Journal of Science and Engineering, 7(2), 115-124.

8th International Conference on Engineering, Natural and Social Sciences

September 06-07, 2026: Konya, Turkey

© 2026 Published by All Sciences Academy

https://www.icensos.com/

Spatiotemporal Dynamics of Atmospheric Pollutants along the Urban–Rural Gradient: A Remote Sensing-Based Analysis of Bolu, Türkiye

İlknur Zeren Cetin*

[1,*] *Ondokuz Mayis University, Faculty of Architecture, Department of City and Regional Planning, Samsun, Türkiye*

* *ilknur.cetin@omu.edu.tr*

Abstract **–**This study examines the spatial and temporal variability of major atmospheric pollutants along the urban–rural gradient of Bolu , Türkiye, during 2019–2025. A Balanced Urban Parametric Index (BUPI) was developed by integrating impervious surface fraction, population density, nighttime light intensity, and road-network density to quantify urban development intensity. The study area was classified into four spatial environments: Urban Core (UC), Inner Urban Area (IUA), Urban–Rural Fringe (URF), and Rural Area (RA). Sentinel-5P TROPOMI observations of nitrogen dioxide (NO_2), carbon monoxide (CO), formaldehyde (HCHO), and aerosol index (AER AI) were analyzed across these urbanization classes. The results revealed distinct pollutant-specific spatial and temporal patterns. AER AI showed increasing differentiation between urban and rural environments after 2021, with the UC–RA contrast increasing from approximately 9.3% in 2020 to 13.4% in 2022. NO_2 exhibited the strongest urbanization-related gradient, reaching a UC–RA difference of approximately 47.6% in 2021. HCHO increased progressively toward 2025 but showed limited spatial differentiation, whereas CO displayed a comparatively homogeneous distribution. Random Forest analysis indicated that temporal variability was the dominant explanatory factor for AER AI and HCHO, while BUPI-based urban structure contributed most strongly to NO_2 variability. District-level spatial characteristics were particularly relevant for CO. Overall, the findings demonstrate that atmospheric pollution in Bolu reflects interactions among urban intensity, transportation, residential energy use, vegetation, temporal atmospheric conditions, and topography. The urban–rural fringe represents a dynamic environmental transition zone requiring targeted planning, green infrastructure, emission mitigation, sustainable mobility, and improved atmospheric monitoring.

Keywords –Urban–rural gradient; Multi-pollutant analysis; Atmospheric remote sensing; Urban morphology; Environmental spatial planning

I. INTRODUCTION

Urbanization produces substantial changes in the spatial configuration of built surfaces, transportation networks, energy demand, vegetation cover, and population distribution, with direct and indirect consequences for atmospheric pollution. The spatial response of pollutants to urban development, however, is not necessarily proportional to the intensity of urbanization. Emission sources interact with land-cover characteristics, atmospheric circulation, surface conditions, vegetation, and local topography, generating heterogeneous pollution patterns across relatively short distances. Consequently, investigating environmental conditions along an urban–rural gradient can provide greater spatial insight than treating urban and rural environments as two discrete categories. In this context, satellite-based observations have become an important source of information for characterizing atmospheric constituents over extensive areas, particularly where conventional monitoring stations are spatially limited. The Sentinel-5P TROPOMI instrument provides consistent spatial observations of several atmospheric trace gases and aerosol-related parameters, including nitrogen dioxide (NO_2), carbon monoxide (CO), formaldehyde (HCHO), and aerosol

index (AER AI). Integrating these atmospheric observations with quantitative indicators of urban structure enables a more detailed assessment of whether pollutant variability is primarily associated with urban intensity, temporal atmospheric conditions, or broader spatial characteristics. [1]–[10].

A quantitative representation of urban development is essential for examining pollutant distributions across heterogeneous settlement structures. In this study, the Balanced Urban Parametric Index (BUPI) integrates four complementary indicators of urban intensity: impervious surface coverage, population density, nighttime light emissions, and road-network density. Principal Component Analysis (PCA) is employed to identify the dominant information dimensions within these variables and minimize inter-variable redundancy, while ISO Cluster analysis supports the derivation of spatially differentiated coefficients for the composite index. The resulting BUPI framework establishes four urbanization environments—Urban Core (UC), Inner Urban Area (IUA), Urban–Rural Fringe (URF), and Rural Area (RA)—that represent successive levels of settlement intensity. Linking these classes with satellite-derived pollutant observations and machine-learning techniques provides an integrated basis for evaluating how atmospheric conditions vary across the urbanization gradient. [9]–[17].

Bolu provides a particularly suitable setting for this type of spatial investigation because its settlement structure combines a relatively concentrated urban center with expanding peripheral development and extensive forested and rural areas. The coexistence of built-up land, transportation corridors, agricultural areas, forest ecosystems, and low-density settlements creates marked spatial contrasts in both emission sources and environmental conditions. These characteristics are further influenced by the 's topographic configuration, which can affect atmospheric dispersion and pollutant accumulation. Accordingly, the urban–rural gradient in Bolu represents not merely a transition in land-use intensity but a complex environmental interface in which anthropogenic and natural processes interact. Climatic conditions provide an additional dimension for interpreting these spatial relationships. Long-term meteorological records indicate that Bolu experiences a cool and comparatively precipitation-rich climate, with mean monthly temperatures ranging from approximately 1.1 °C in January to 20.7 °C in August based on the 1991–2020 climate normals. Precipitation occurs throughout the year, contributing to pronounced seasonal differences in atmospheric and surface conditions. During colder months, increased residential heating demand may intensify local emissions, while reduced atmospheric mixing under stable conditions can favor pollutant accumulation. In contrast, warmer periods are associated with stronger vegetation activity and different atmospheric transport characteristics. These seasonal processes, together with transportation activity, land-cover composition, and topographic confinement, need to be considered when evaluating pollutant variability across Bolu [18]–[19].. The study therefore pursues five principal objectives. First, it delineates the spatial urbanization gradient of Bolu through the BUPI framework. Second, it examines the annual variability of NO_2, CO, HCHO, and AER AI during 2019–2025 using Sentinel-5P TROPOMI observations. Third, it quantifies pollutant differences among the UC, IUA, URF, and RA classes to identify the degree of spatial separation associated with urban intensity. Fourth, Random Forest modeling is applied to assess the relative contribution of temporal variation, BUPI-based urban structure, and district-level spatial context to pollutant variability. Finally, the resulting spatial patterns are interpreted from an environmental planning and landscape-management perspective, with particular emphasis on emission mitigation, green infrastructure, sustainable mobility, and the ecological management of the urban–rural interface.

II. Materials and Method

Bolu is situated in northwestern Türkiye, within a geographically complex transition zone influenced by the western Black Sea region and the inland Anatolian corridor. The is characterized by a diverse physical landscape comprising a concentrated urban settlement, agricultural plains and basins, extensive forest ecosystems, mountainous terrain, valley systems, and major transportation routes connecting the Marmara and Black Sea regions. This heterogeneous landscape generates pronounced spatial variation in population concentration, built-up land, transportation intensity, and vegetation cover. The spatial organization of settlements varies considerably among the provincial districts. The central urban area exhibits a higher concentration of residential, commercial, institutional, and transportation-related land uses, whereas peripheral districts contain lower-density settlements embedded within agricultural and forest

landscapes. The coexistence of these environments provides an appropriate geographical basis for examining atmospheric pollution across progressively decreasing levels of urban intensity. Furthermore, the presence of several district-level settlements permits spatial context to be incorporated into the statistical analysis while maintaining a -wide analytical framework.

The analysis integrates datasets representing urban structure, atmospheric composition, and topographic characteristics. Four indicators—impervious surface area (ISA), population density, nighttime light intensity, and road-network density—were selected to characterize the spatial intensity of urban development. Atmospheric conditions were evaluated using annual Sentinel-5P TROPOMI observations of nitrogen dioxide (NO_2), carbon monoxide (CO), formaldehyde (HCHO), and aerosol index (AER AI). A 30 m digital elevation model (DEM) was additionally incorporated to represent the topographic setting of the study area. All spatial datasets were processed within a common projected coordinate reference system. The urban-structure variables and ancillary spatial layers were represented on a 10 m analytical grid to provide a consistent spatial framework for the BUPI analysis. Sentinel-5P atmospheric products were retained at their respective native spatial resolution because their measurement characteristics differ substantially from those of the high-resolution terrestrial datasets. Consequently, the atmospheric observations were interpreted as spatially aggregated satellite measurements rather than as direct 10 m observations. The principal datasets and their characteristics are summarized in Table 1.

Table 1. Data sources and principal characteristics used in the Bolu study

Data type	**Period**	**Spatial resolution**	**Source**
NOAA/VIIRS nighttime lights	2025	~459.7 m	Google Earth Engine
Impervious surface area	2025	10 m	Google Earth Engine / Dynamic World
Population density	2026	100 m	WorldPop
Road network	2026	Vector	OpenStreetMap / Overpass
Administrative boundaries	2026	Vector	OpenStreetMap / Overpass
NO_2	2019–2025	~1113.2 m	Sentinel-5P TROPOMI / GEE
CO	2019–2025	~1113.2 m	Sentinel-5P TROPOMI / GEE
HCHO	2019–2025	~1113.2 m	Sentinel-5P TROPOMI / GEE
AER AI	2019–2025	~1113.2 m	Sentinel-5P TROPOMI / GEE
DEM	2025	30 m	USGS

The Balanced Urban Parametric Index (BUPI) was designed to synthesize multiple dimensions of urban intensity into a single spatial indicator. Prior to integration, ISA, population density, nighttime light intensity, and road-network density were transformed to a dimensionless 0–1 scale using min–max normalization. This procedure placed variables with different units and numerical ranges within a comon analytical domain.

The BUPI (Balanced Urban Parametric Index) formulation follows the supplied framework:

$$\mathrm{BUPI} = \sum_{i=0}^{n} \left(\frac{\mathrm{R}_i}{S_{k,i}} W_i \right)$$

where R_i is the normalized value of variable i $S_{k,i}$ is the cluster-derived statistical correction coefficient, W_i is the equal weight assigned to each of the four variables, and n = 4. The resulting continuous surface is classified into UC, IUA, URF, and RA.

The normalized datasets were combined spatially and evaluated using Principal Component Analysis (PCA). PCA was employed to identify the dominant covariance structure among the urbanization indicators and to limit the influence of information overlap between correlated variables. Components accounting for the principal proportion of total variance were retained for subsequent spatial classification. The retained component scores were subjected to ISO Cluster analysis to identify spatially coherent groups with similar urban characteristics. The resulting clusters represented different combinations of built-up intensity, demographic concentration, artificial illumination, and transportation density. Cluster-specific statistical properties, including the mean and standard deviation of component scores, were incorporated into the weighting procedure used to establish the BUPI structure. This approach provides a balanced contribution of the component variables and reduces the possibility that a variable with a larger numerical range will disproportionately influence the resulting urbanization pattern.

The resulting BUPI surface was subsequently interpreted according to four spatial classes representing a progressive urbanization gradient: Urban Core (UC): areas characterized by the highest concentration of built surfaces, population, artificial illumination, and transportation infrastructure. Inner Urban Area (IUA): areas surrounding the principal urban concentration with substantial but comparatively lower urban intensity. Urban–Rural Fringe (URF): transitional areas where built-up development interfaces with agricultural, vegetated, and low-density settlement environments. Rural Area (RA): locations characterized by relatively low development intensity, sparse settlement, and greater prevalence of agricultural or natural land cover. This classification establishes a continuous spatial perspective on urbanization and allows pollutant characteristics to be evaluated across multiple levels of settlement intensity rather than through a simple urban/non-urban distinction.

Atmospheric Pollutant Assessment Annual Sentinel-5P TROPOMI observations were used to characterize the spatial and temporal behavior of NO_2, CO, HCHO, and AER AI across Bolu for the 2019–2025 period. The annual pollutant surfaces were spatially associated with the four BUPI classes, allowing the distribution of each atmospheric variable to be evaluated according to urbanization intensity. For each pollutant and BUPI class, descriptive statistics were calculated, including the annual maximum, minimum, arithmetic mean, and standard deviation. Year-to-year differences were also examined to identify temporal increases, decreases, and periods of enhanced spatial differentiation. Particular attention was given to the contrast between the Urban Core and Rural Area, while the Inner Urban Area and Urban–Rural Fringe were evaluated as intermediate environments. Rather than defining pollution patterns according to a single urban boundary, the analysis considers the progressive spatial transition from highly developed areas toward rural environments. This approach is particularly relevant for Bolu, where urban development, forest ecosystems, agricultural land, transportation corridors, and topographic features occur in close spatial proximity.

Random Forest Modeling Random Forest regression was employed to investigate the relative contribution of spatial and temporal factors to pollutant variability. The predictor set consisted of three principal explanatory dimensions: BUPI-based urbanization intensity, district-level spatial context, and observation year. The pollutant measurements constituted the response variables. The Random Forest approach was selected because it can represent nonlinear relationships and interactions among predictors without requiring a predefined functional relationship between explanatory and response variables. Multiple decision trees were generated from bootstrap samples of the observations, and their predictions were aggregated to obtain the final model estimate. Predictor importance measures were subsequently examined to determine the relative contribution of urbanization intensity, spatial context, and temporal variability to each pollutant. Separate modeling was conducted for NO_2, CO, HCHO, and AER AI. Comparison of predictor importance across these models provided an empirical basis for distinguishing pollutants predominantly associated with urban structure from those exhibiting stronger temporal or spatial

controls. The resulting interpretation was subsequently integrated with the spatial analysis to identify environmental transition zones and potential planning implications for Bolu.

III. RESULTS

Spatiotemporal Characteristics of AER AI AER AI exhibited the most pronounced temporal variability among the four atmospheric indicators investigated in Bolu. The annual pattern was characterized by a decline between 2019 and 2020, followed by a substantial increase from 2021 onward. In 2020, mean AER AI values varied from approximately −1.27 in the Urban Core (UC) to −1.37 in the Rural Area (RA). By 2022, the corresponding values had increased to approximately −0.27 and −0.35, respectively. The relative difference between the UC and RA classes increased from approximately 9.3% in 2020 to 24.9% in 2022. Despite the increasing spatial separation after 2021, the magnitude of interannual variation was considerably greater than the difference among urbanization classes. This suggests that AER AI was primarily governed by temporal atmospheric conditions and broader regional processes, while the influence of local urban morphology remained comparatively limited. The spatial pattern nevertheless indicates an increasing differentiation between highly developed and rural environments during the post-2021 period. The spatial and temporal distribution of AER AI across the Bolu urban–rural gradient is presented in Figure 1, while the annual class-based variation is illustrated in Figure 2.

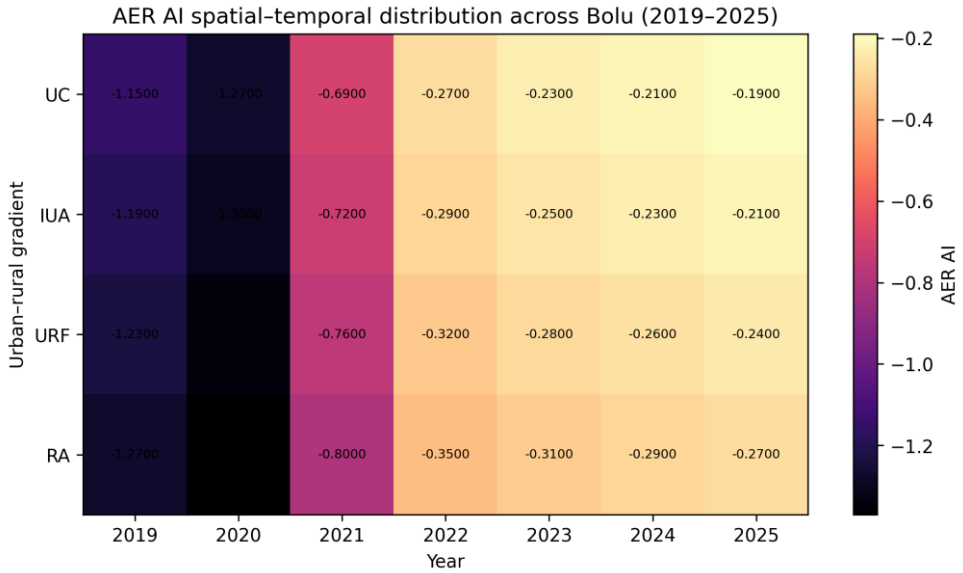

Figure 1. Spatial and temporal distribution of AER AI across the Bolu urban–rural gradient, 2019–2025.

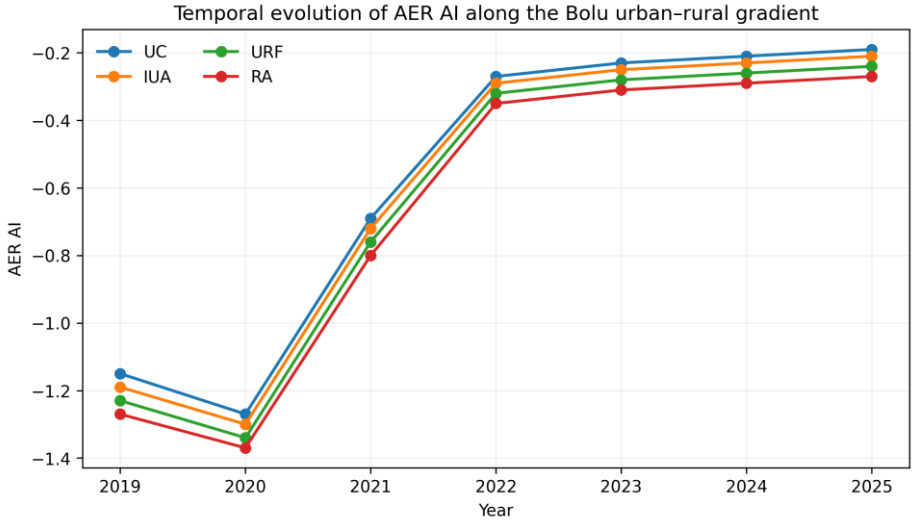

Figure 2. Annual variation of AER AI across the urban–rural gradient of Bolu, 2019–2025.

Spatiotemporal Characteristics of NO_2 NO_2 displayed the strongest and most persistent relationship with the degree of urbanization. The provincial mean increased from the initial years of the observation period and reached its highest level in 2021, followed by a decline and a subsequent moderate recovery. The spatial differentiation was particularly evident in 2021, when the mean NO_2 value in the UC reached approximately 3.42×10^{-5}, compared with 2.39×10^{-5} in the RA. This corresponds to an approximate UC–RA difference of 45.1%. The urbanization gradient remained consistently ordered throughout the study period. The UC generally exhibited the highest NO_2 levels, followed successively by the IUA and URF, whereas the RA maintained the lowest values. The persistence of this spatial ordering indicates a strong association between NO_2 and the intensity of built development, population concentration, transportation activity, and other urban emission sources. The results therefore identify NO_2 as the atmospheric indicator most clearly differentiated by the BUPI-defined urban structure. Spatial and temporal NO_2 distributions are shown in Figure 3, and annual variation among the four urbanization classes is presented in Figure 4.

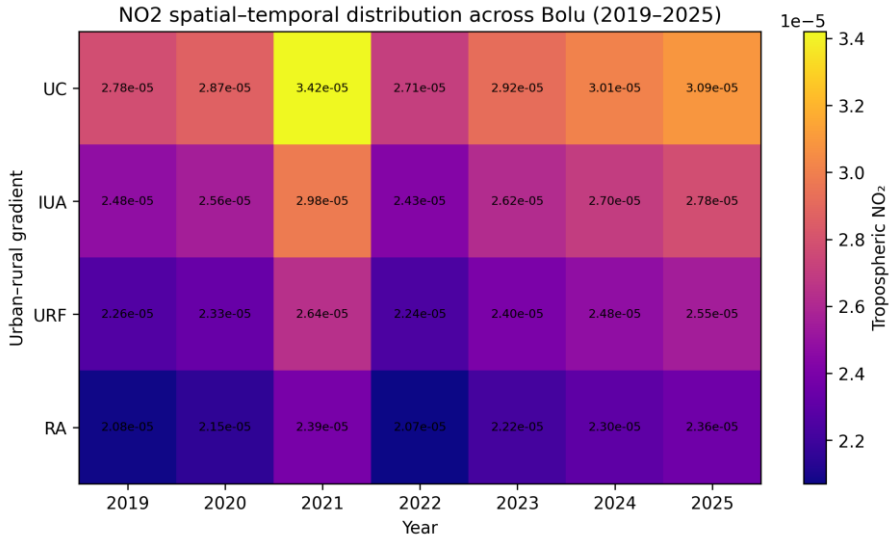

Figure 3. Spatial and temporal distribution of NO_2 across the Bolu urban–rural gradient, 2019–2025.

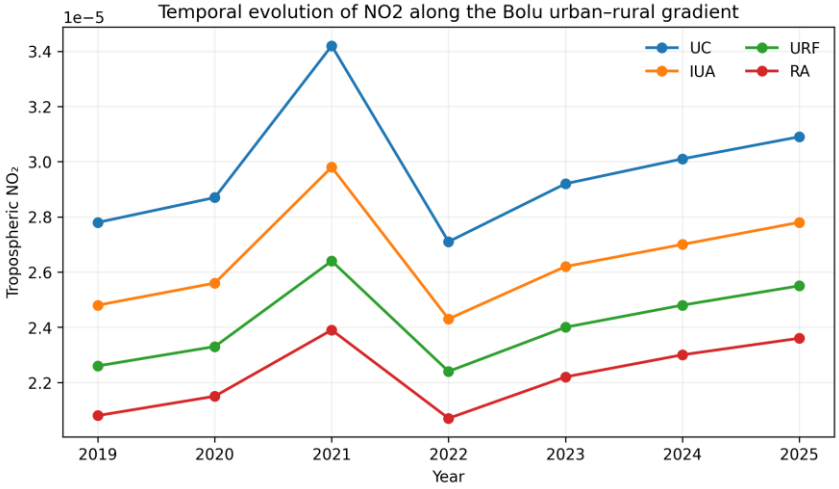

Figure 4. Annual variation of NO_2 across the urban–rural gradient of Bolu, 2019–2025.

Spatiotemporal Characteristics of HCHO HCHO exhibited a temporal pattern that differed substantially from that observed for NO_2 and AER AI. Following relatively lower values during the earlier part of the study period, HCHO increased progressively after 2021 and attained its highest levels in 2025. In contrast to NO_2, the spatial separation among the BUPI classes remained limited. In 2021, the RA recorded a slightly higher HCHO value than the UC. By 2025, the mean concentrations reached approximately 4.12×10^{-4} in the UC and 4.21×10^{-4} in the RA. The UC–RA contrast was approximately −1.7% in 2021 and declined to around −0.1% in 2025. Thus, the spatial gradient was weak throughout the observation period, with rural

and peri-urban environments occasionally exhibiting slightly higher values than the most densely developed areas. The limited urban differentiation of HCHO may reflect the combined influence of vegetation-related emissions, atmospheric chemical production, regional transport, and other secondary processes. Consequently, the spatial behavior of HCHO cannot be interpreted solely in terms of local development intensity. The spatial and temporal distributions are provided in Figure 5, with the annual class-level patterns shown in Figure 6.

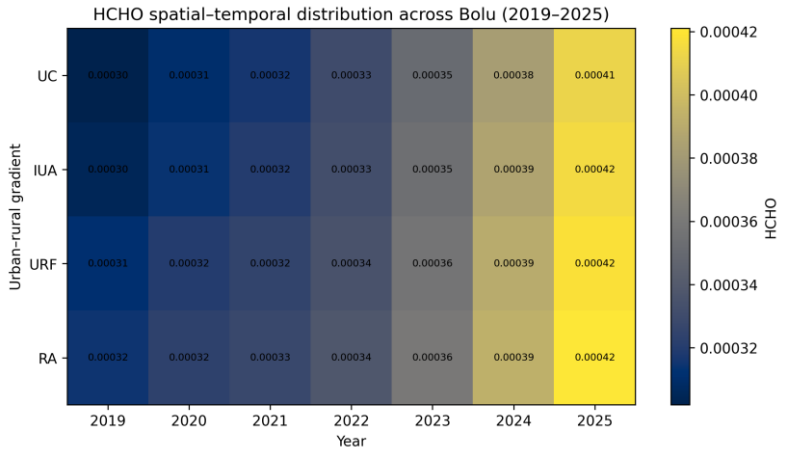

Figure 5. Spatial and temporal distribution of HCHO across the Bolu urban–rural gradient, 2019–2025.

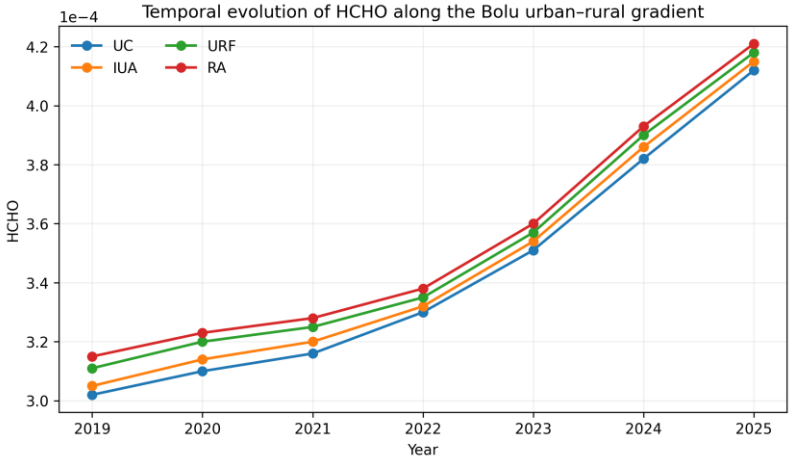

Figure 6. Annual variation of HCHO across the urban–rural gradient of Bolu, 2019–2025.

Spatiotemporal Characteristics of CO CO presented a substantially more homogeneous spatial pattern than NO_2. The highest mean value in the UC was observed in 2021, reaching approximately 0.0330. This peak was followed by a marked decrease in 2022 and a moderate increase during 2023–2025. Spatial differences among the BUPI classes remained relatively small throughout the period. In 2021, the difference between the UC and RA was approximately 6.8%, while the corresponding contrast in 2022 was approximately 5.6%. The relatively compressed urban–rural gradient suggests that CO variability is not controlled exclusively by the intensity of built development. Factors such as residential heating demand, road-network configuration, local atmospheric circulation, valley-scale dispersion conditions, and regional pollutant transport may contribute substantially to the observed distribution. The relatively weak differentiation among BUPI classes distinguishes CO from NO_2 and indicates that spatial context plays a more important role in determining its distribution. The spatial and temporal patterns of CO are presented in Figure 7, and the annual class-level changes are shown in Figure 8.

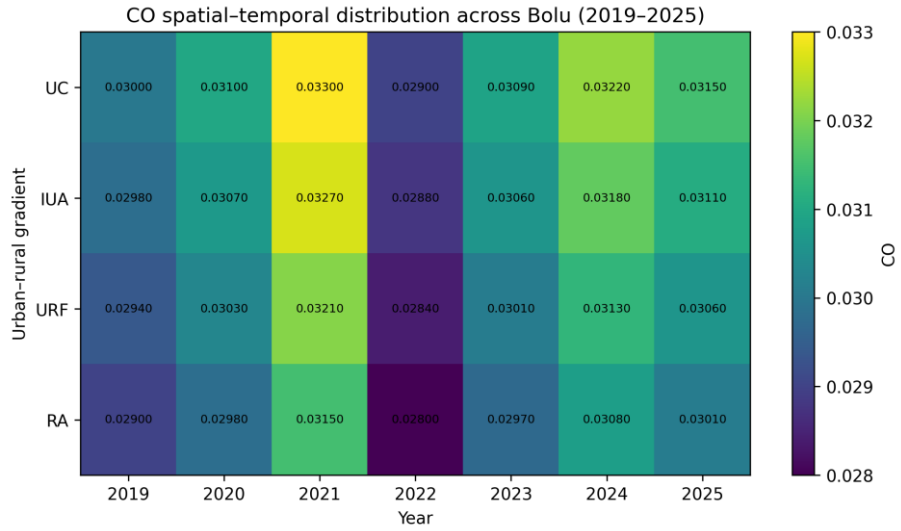

Figure 7. Spatial and temporal distribution of CO across the Bolu urban–rural gradient, 2019–2025.

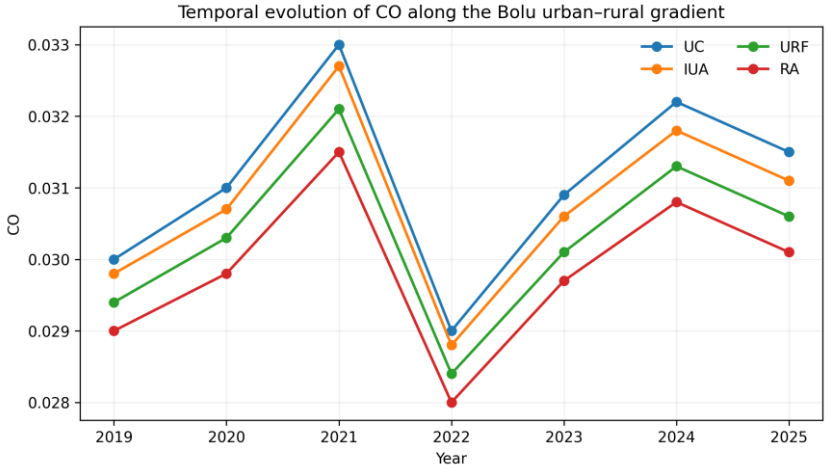

Figure 8. Annual variation of CO across the urban–rural gradient of Bolu, 2019–2025.

Annual Pollutant Variability The annual mean values of NO_2, CO, HCHO, and AER AI provide an integrated view of atmospheric variability across the seven-year observation period. Table 2 summarizes the annual pollutant series for Bolu between 2019 and 2025. The four indicators exhibited clearly different temporal trajectories. NO_2 reached a distinct maximum in 2021, followed by a decrease and partial recovery. CO also showed its highest level in 2021 before declining substantially in 2022. HCHO followed a progressive upward trajectory during the latter part of the study period and reached its highest annual level in 2025. AER AI exhibited the most substantial year-to-year transition, particularly after 2021. These contrasting temporal signatures demonstrate that the four atmospheric indicators respond differently to the combination of local emissions, seasonal processes, atmospheric transport, and regional environmental conditions.

Table 2. Annual mean concentrations of atmospheric pollutants in Bolu, 2019–2025.

Year	AER AI	NO_2	HCHO	CO
2019	-1.210	2.39e-05	3.08e-04	0.0296
2020	-1.320	2.48e-05	3.17e-04	0.0305
2021	-0.740	3.11e-05	3.22e-04	0.0323
2022	-0.310	2.36e-05	3.33e-04	0.0286
2023	-0.270	2.54e-05	3.56e-04	0.0303
2024	-0.250	2.62e-05	3.88e-04	0.0315
2025	-0.230	2.70e-05	4.16e-04	0.0308

Random Forest Variable Importance The Random Forest analysis revealed distinct explanatory structures for the four atmospheric indicators. The relative importance of the predictor variables demonstrates that pollutant variability cannot be explained by a single spatial or temporal factor. For AER AI, year accounted for 95.2% of the modeled variable importance, indicating an overwhelmingly temporal structure. HCHO also showed a strong temporal dependence, with year contributing 62.1% of the total importance. These results are consistent with the relatively strong interannual changes observed in the descriptive analysis. NO_2 exhibited a markedly different pattern. BUPI accounted for 58.4% of the variable importance, making urbanization intensity the principal explanatory factor for this pollutant. This finding reinforces the strong spatial correspondence between NO_2 and the BUPI-defined urban gradient. CO displayed the most spatially distributed explanatory structure among the four pollutants. District-level spatial context contributed 48.7%, followed by year at 36.8% and BUPI at 14.5%. The relatively high contribution of district context indicates that local geographical and settlement characteristics may substantially influence CO variability, beyond the generalized urbanization intensity represented by BUPI. Taken together, the Random Forest results demonstrate that atmospheric pollutants in Bolu have different controlling structures. NO_2 is primarily associated with urban morphology, AER AI and HCHO are more strongly linked to temporal variability, while CO reflects a combination of spatial context and temporal conditions. The relative importance of the predictors is summarized in Table 3.

Table 3. Relative variable importance of Random Forest predictors for atmospheric pollutant variability in Bolu.

Pollutant	**Dominant factor**	**Importance (%)**	**Secondary interpretation**
AER AI	Year	95.2	Temporal forcing dominates aerosol variability.
NO_2	BUPI	58.4	Urban morphology is the strongest explanatory factor.
HCHO	Year	62.1	Annual atmospheric and biogenic controls dominate.
CO	District	48.7	Spatial context and heating/traffic structure are important.

IV. DISCUSSION

Urban Morphology and Pollutant Differentiation The results reveal that atmospheric pollutants in Bolu respond to urbanization through distinct spatial and temporal mechanisms rather than following a common gradient. Among the four indicators, NO_2 exhibits the clearest correspondence with the intensity of urban development. Its consistently higher values within the Urban Core and progressive decline toward the Rural Area indicate a strong association with concentrated anthropogenic activities. Road traffic, residential and commercial combustion, population density, and extensive impervious surfaces are likely to contribute to this spatial configuration. The predominance of BUPI in the Random Forest analysis further demonstrates that a multidimensional representation of urban intensity can provide greater explanatory capacity than individual indicators considered separately. The behavior of AER AI differs substantially from that of NO_2. The pronounced interannual transition observed after 2021 is considerably stronger than the spatial separation among the BUPI classes. This pattern indicates that aerosol-related conditions are strongly influenced by processes operating beyond the immediate urban environment. Regional atmospheric transport, meteorological variability, changes in emission conditions, and the movement of aerosol masses

across the surrounding landscape may all contribute to the observed temporal pattern. The geographical characteristics of Bolu are particularly relevant in this respect. Extensive forested uplands, agricultural landscapes, valleys, and open rural areas are connected to the urban atmosphere through regional transport pathways. Consequently, elevated aerosol-related signals in less urbanized areas do not necessarily imply the presence of intense local emission sources.

HCHO presents another distinctive spatial configuration. Its relatively weak urban–rural differentiation, together with slightly higher values in rural and peri-urban environments during some years, indicates that formaldehyde dynamics are not governed exclusively by anthropogenic urban emissions. Vegetation represents an important potential source of atmospheric formaldehyde precursors, while temperature, solar radiation, atmospheric chemistry, and regional transport can influence its formation and persistence. The increase observed toward 2025 should therefore be interpreted within a broader atmospheric context rather than being attributed directly to increasing urban density. The HCHO results emphasize the importance of considering natural and atmospheric processes when evaluating trace-gas distributions across heterogeneous landscapes. CO occupies a different position within the pollutant spectrum. Although its maximum levels are associated with the urban core, the relatively limited difference between the UC and RA indicates a weaker dependence on generalized urban intensity than that observed for NO_2. Residential heating, vehicle emissions, fuel characteristics, road-network configuration, atmospheric stability, and local topographic conditions can influence CO concentrations simultaneously. The relatively high contribution of district-level spatial context in the Random Forest model supports this interpretation. In Bolu, topographic confinement and variations in settlement form may influence the dispersion and accumulation of combustion-related pollutants at the local scale. Seasonal climatic conditions provide an additional explanation for the observed patterns, particularly for combustion-related pollutants. Bolu experiences relatively cold winters, while precipitation occurs throughout the year. Increased heating demand during colder periods can enhance residential combustion emissions, whereas stable atmospheric conditions may restrict vertical mixing and favor pollutant accumulation. Conversely, precipitation and stronger atmospheric mixing can modify pollutant residence times and spatial distributions. These interactions demonstrate why atmospheric pollution in Bolu should be interpreted as the outcome of interconnected urban, meteorological, ecological, and topographic processes.

Implications for Landscape Planning and Environmental Policy The spatial differentiation identified in this study suggests that air-quality management in Bolu should employ geographically targeted interventions rather than relying on a uniform strategy across the . The Urban Core represents the most appropriate priority area for measures addressing traffic-related and combustion-associated emissions. Strategic green infrastructure can support these interventions, particularly along major transportation corridors and at locations where dense development transitions toward lower-density urban environments. Tree belts, multilayer vegetation systems, and sufficiently connected canopy structures may contribute to particulate interception, thermal regulation, and ecological connectivity. However, vegetation placement should be evaluated in relation to local wind conditions and street geometry, since excessive enclosure in narrow streets may reduce atmospheric exchange. The Urban–Rural Fringe requires a different planning perspective because it represents an active interface between expanding development and agricultural, forest, and semi-natural landscapes. Uncontrolled low-density development in this zone may increase landscape fragmentation, transportation demand, and pressure on ecological resources. Maintaining connected green corridors, protecting agricultural land, establishing permeable development boundaries, and conserving forest continuity can help retain the ecological functions of the fringe while limiting unnecessary urban dispersion. The fringe should therefore be regarded as a strategic environmental transition zone rather than simply as land available for future development. Air-quality management should also be integrated with winter energy and transportation policies. Improvements in building energy performance, increased use of lower-emission heating technologies, efficient public transportation, pedestrian and cycling networks, and reduced dependence on private vehicles can address important combustion-related sources. In areas characterized by topographic confinement or limited atmospheric ventilation, urban density and building configuration should be assessed together with local airflow characteristics before high-density development is permitted. Such spatially informed decisions can reduce

the potential for pollutant accumulation while simultaneously improving urban environmental quality. The results for HCHO and AER AI further indicate that atmospheric monitoring should not be restricted to the densely developed urban area. Rural and forested environments may exhibit substantial atmospheric signals because of regional transport, vegetation-related emissions, and large-scale atmospheric processes. A -wide monitoring framework should consequently integrate Sentinel-5P observations with ground-based air-quality measurements, meteorological observations, topographic information, and land-cover data. Such integration would improve the interpretation of satellite-derived pollutant patterns and provide stronger evidence for spatially targeted environmental management

V. CONCLUSION

This study provides an integrated assessment of atmospheric pollutant variability across the urban–rural gradient of Bolu using satellite-based atmospheric observations and a multidimensional indicator of urban intensity. The combination of BUPI, Sentinel-5P TROPOMI observations, spatial analysis, and Random Forest modeling revealed that the four atmospheric indicators exhibit substantially different spatial and temporal controls. NO_2 showed the strongest relationship with urban morphology. Its persistent concentration gradient from the Urban Core toward the Rural Area, together with the dominant contribution of BUPI in the Random Forest model, indicates a close association with the intensity of urban development and associated anthropogenic activities. AER AI was characterized primarily by temporal variability, with a pronounced increase in spatial differentiation after 2021. HCHO exhibited a progressive increase toward 2025 but only limited separation among urbanization classes, highlighting the contribution of vegetation-related and atmospheric chemical processes. CO displayed comparatively weak urban–rural differentiation while maintaining considerable sensitivity to district-level spatial context. These findings demonstrate that a single urbanization–pollution relationship is insufficient for describing atmospheric conditions in Bolu. Different pollutants respond to different combinations of urban structure, temporal atmospheric conditions, ecological characteristics, transportation, heating activity, and topography. The Urban Core, Inner Urban Area, Urban–Rural Fringe, and Rural Area should therefore be considered distinct environmental management settings rather than merely successive categories of settlement density. From a planning perspective, the results support a differentiated spatial strategy. The Urban Core should receive priority for emission reduction, sustainable mobility, and vegetation-based environmental interventions. Inner urban areas require coordinated transportation, land-use, and green-infrastructure planning. The Urban–Rural Fringe should be managed as an ecological and atmospheric transition zone through development controls, agricultural and forest conservation, and green-corridor protection. Rural and forested areas should remain part of the -wide air-quality monitoring system because atmospheric transport and biogenic processes can generate significant pollutant signals beyond densely settled areas. Overall, the study demonstrates the value of integrating atmospheric remote sensing with quantitative urban morphology for spatial environmental assessment. The combined framework provides a basis for identifying heterogeneous pollution patterns, locating priority intervention areas, and supporting GIS-based environmental planning and landscape-management decisions. Future research should strengthen this framework through the integration of higher-frequency atmospheric observations, ground-monitoring measurements, meteorological variables, detailed emission inventories, and finer-scale land-cover information. Such multi-source integration would improve the characterization of pollutant sources and atmospheric processes and enhance the capacity of urban and regional planning to respond to spatially differentiated air-quality risks

ACKNOWLEDGMENT

The author acknowledges the European Space Agency, Google Earth Engine, United States Geological Survey, NASA/LP DAAC, WorldPop, and OpenStreetMap contributors for the open datasets underlying the analytical framework. The Bolu climatic background was checked against the official Turkish State Meteorological Service statistics.

REFERENCES

1. Ibarra-Espinosa, S., Mendes da Silva, G. A., Rehbein, A., Vara-Vela, A., & Dias de Freitas, E. (2022). Atmospheric effects of air pollution during dry and wet periods in São Paulo. Environmental Science: Atmospheres, 2(2), 215-229.
2. Suthar, G., Singh, S., Kaul, N., & Khandelwal, S. (2024). Understanding the multifaceted influence of urbanization, spectral indices, and air pollutants on land surface temperature variability in Hyderabad, India. Journal of Cleaner Production, 470, 143284.
3. Gao, Y., Zhang, C., Yang, Y., Hong, X., & Liu, C. (2025). Unveiling the spatial and temporal effects of urban vegetation coverage on atmospheric formaldehyde pollution in Chinese megacities over recent decades. Environmental Pollution, 127243.
4. Dong, F., Rahman, M. T., & Chen, H. (2026). Spatial analysis of air pollution and cancer prevalence in Texas: a machine learning approach using satellite remote sensing data. Environmental Monitoring and Assessment, 198(3), 278.
5. Ji, D., Tian, J., Zhang, J., Zeng, J., & Namaiti, A. (2024). Identification and spatiotemporal evolution analysis of the urban–rural fringe in polycentric cities based on K-means clustering and multi-source data: a case study of chengdu city. Land, 13(11), 1727.
6. Desyana, R. D., Sulistyantara, B., Nasrullah, N., & Fatimah, I. S. (2017, March). Study of the effectiveness of several tree canopy types on roadside green belt in influencing the distribution of NO2 gas emitted from transportation. In IOP Conference Series: Earth and Environmental Science (Vol. 58, No. 1, p. 012045). IOP Publishing.
7. Peng, J., Liu, Q., Blaschke, T., Zhang, Z., Liu, Y., Hu, Y. N., ... & Wu, J. (2020). Integrating land development size, pattern, and density to identify urban–rural fringe in a metropolitan region. Landscape Ecology, 35(9), 2045-2059.
8. Wang, S., Gao, S., Li, S., & Feng, K. (2020). Strategizing the relation between urbanization and air pollution: Empirical evidence from global countries. Journal of Cleaner Production, 243, 118615.
9. Yu, M., Tang, G., Yang, Y., Li, Q., Wang, Y., Miao, S., ... & Wang, Y. (2020). The interaction between urbanization and aerosols during a typical winter haze event in Beijing. Atmospheric Chemistry and Physics, 20(16), 9855-9870.
10. Xu, S. C., Li, Y. W., Miao, Y. M., Gao, C., He, Z. X., Shen, W. X., ... & Wang, S. X. (2019). Regional differences in nonlinear impacts of economic growth, export and FDI on air pollutants in China based on provincial panel data. Journal of Cleaner Production, 228, 455-466.
11. Li, G., Cao, Y., He, Z., He, J., Cao, Y., Wang, J., & Fang, X. (2021). Understanding the diversity of urban–rural fringe development in a fast urbanizing region of China. Remote Sensing, 13(12), 2373.
12. Guan, Q., Chen, L., Wang, Q., Guan, C., & Li, H. (2024). Dynamical identification of urban-rural gradient and ecosystem service response: A case study of Jinghong City, China. Land, 13(3), 306.
13. Capone, P., Lancia, A., & D'Ovidio, M. C. (2023). Interaction between air pollutants and pollen grains: effects on public and occupational health. Atmosphere, 14(10), 1544.
14. Sun, B., Fang, C., Liao, X., Guo, X., & Liu, Z. (2023). The relationship between urbanization and air pollution affected by intercity factor mobility: A case of the Yangtze River Delta region. Environmental Impact Assessment Review, 100, 107092.
15. Han, L., Tan, X., Zhou, W., Li, W., & Qian, Y. (2020). Better urban vegetation planning for maximum utility in air pollutant reduction: A theoretical perspective and preliminary analysis in Chinese cities. Sustainable Cities and Society, 62, 102377.
16. Suthar, G., Singhal, R. P., Khandelwal, S., & Kaul, N. (2023). Spatiotemporal variation of air pollutants and their relationship with land surface temperature in Bengaluru, India. Remote Sensing Applications: Society and Environment, 32, 101011.
17. Lin, B., & Zhu, J. (2018). Changes in urban air quality during urbanization in China. Journal of Cleaner Production, 188, 312-321.
18. TUIK (2026). Turkish Statistical Institute (TUIK). Address-based population registration system results, Retrieved February 12, 2026, from https://veriportali.tuik.gov.tr/tr/press/53783
19. TSMS (2026). Turkish State Meteorological Service (TSMS). Average air temperature values, Retrieved February 12, 2026, https://www.mgm.gov.tr/veridegerlendirme/ilve-ilceler-istatistik.aspx

8th International Conference on Engineering, Natural and Social Sciences

September 06-07, 2026: Konya, Turkey

© 2026 Published by All Sciences Academy

https://www.icensos.com/

Spatiotemporal Characterization of Multi-Pollutant Dynamics along the Urban–Rural Gradient of Sakarya, Türkiye

İlknur Zeren Cetin*

[1,*] *Ondokuz Mayis University, Faculty of Architecture, Department of City and Regional Planning, Samsun, Türkiye*

* *ilknur.cetin@omu.edu.tr*

Abstract **–**This study examines the spatial and temporal dynamics of major atmospheric pollutants across the urban–rural gradient of Sakarya , northwestern Türkiye, during 2019–2025. A Balanced Urban Parametric Index (BUPI) was developed by integrating impervious-surface intensity, population density, nighttime-light intensity, and road-network density to characterize spatial variation in urban development. The resulting index delineated four urbanization classes: Urban Core (UC), Inner Urban Area (IUA), Urban–Rural Fringe (URF), and Rural Area (RA). Sentinel-5P TROPOMI observations were analyzed to evaluate nitrogen dioxide (NO_2), carbon monoxide (CO), formaldehyde (HCHO), and aerosol index (AER AI) across these environments. Descriptive statistics were combined with Random Forest modeling to assess the relative importance of spatial urbanization characteristics and temporal variability. The results revealed distinct pollutant-specific patterns. AER AI exhibited a pronounced temporal shift around 2022, whereas NO_2 reached its highest level in 2021. HCHO showed a progressive increase toward 2025, while CO displayed comparatively limited spatial differentiation. NO_2 produced the strongest urban–rural contrast, with the Urban Core exceeding the Rural Area by approximately 38% in 2021. Random Forest analysis indicated that BUPI-related spatial characteristics accounted for 63.1% of modeled importance for NO_2. Temporal variables dominated AER AI and HCHO, contributing 72.8% and 64.2%, respectively, while BUPI-related factors represented 46.7% for CO. The findings demonstrate that pollutant variability reflects distinct interactions between urban structure and temporal atmospheric processes. The Urban–Rural Fringe represents a critical management zone requiring integrated land-use planning, green infrastructure, sustainable mobility, emission control, and continuous satellite-based air-quality monitoring.

Keywords –Urban rural gradient; Atmospheric pollutants; Balanced Urban Parametric Index; Spatiotemporal dynamics; Random Forest

I. INTRODUCTION

Accelerated urban growth modifies the physical structure of settlements, increases transportation intensity, expands impervious surfaces, and alters the spatial organization of anthropogenic emission sources. These transformations can generate complex air-quality responses because atmospheric pollutant concentrations are governed by the combined effects of land-cover characteristics, traffic activity, industrial processes, topographic conditions, and meteorological variability. Consequently, the relationship between urban development and atmospheric pollution is increasingly examined as a spatially heterogeneous phenomenon rather than through a simplified distinction between urban and rural environments. [1]–[10].

Conventional air-quality investigations frequently rely on administrative boundaries or categorical urban–rural classifications. Although operationally convenient, such delineations may fail to represent transitional landscapes where agricultural areas, newly developed residential zones, industrial facilities, transportation corridors, and fragmented vegetation occur in close proximity. These transitional

environments can exhibit rapidly changing development intensity and emission characteristics, making them particularly relevant for understanding spatial pollutant gradients. A multidimensional representation of urbanization can therefore provide a more informative basis for examining the relationship between settlement structure and atmospheric composition. [11]–[14].

In this context, the Balanced Urban Parametric Index (BUPI) provides a spatial framework for characterizing urbanization through the integration of impervious-surface intensity, population density, nighttime light emissions, and road-network density. Combining these complementary indicators enables variations in development intensity to be represented continuously across the landscape. The resulting spatial structure can subsequently be grouped into distinct urbanization environments, including Urban Core (UC), Inner Urban Area (IUA), Urban–Rural Fringe (URF), and Rural Area (RA). Such zonation facilitates the assessment of atmospheric pollutants across progressively changing levels of anthropogenic pressure.

Sakarya in northwestern Türkiye represents a particularly suitable environment for this type of investigation. The encompasses a rapidly developing metropolitan corridor together with extensive transportation and logistics networks, manufacturing and industrial zones, productive agricultural plains, forest-dominated uplands, and settlements distributed across diverse topographic settings. The coexistence of these land-use and socioeconomic characteristics produces a pronounced spatial gradient from densely developed urban areas to relatively undisturbed rural environments. The central urban areas of Adapazarı and Serdivan, for example, are characterized by concentrated population, transportation activity, built-up surfaces, and commercial functions, whereas the surrounding landscapes contain agricultural production, forest cover, and lower-density settlement patterns. [15]–[16].This heterogeneous structure provides an opportunity to examine whether atmospheric pollutants exhibit consistent relationships with increasing urbanization intensity. Satellite-based atmospheric observations offer an effective means of investigating such spatial patterns over large areas and extended periods. The Sentinel-5P TROPOMI platform provides spatially resolved observations of several atmospheric constituents, allowing the distribution and temporal behavior of key pollutants to be evaluated consistently across different urbanization environments. In the present study, nitrogen dioxide (NO_2), carbon monoxide (CO), formaldehyde (HCHO), and aerosol index (AER AI) are examined because they represent atmospheric constituents associated with diverse emission sources and atmospheric processes. Their combined assessment allows differences in pollutant-specific responses to urban structure and temporal variability to be identified.

Accordingly, this study investigates the spatial and temporal behavior of NO_2, CO, HCHO, and AER AI across the BUPI-defined urban–rural gradient of Sakarya during 2019–2025. The analysis focuses on four principal aspects: (i) identifying pollutant-specific temporal patterns throughout the study period, (ii) quantifying differences between the Urban Core and Rural Area, (iii) examining the atmospheric characteristics of the Urban–Rural Fringe as a transitional landscape, and (iv) determining the relative contribution of temporal variability and spatial urbanization characteristics to pollutant patterns through Random Forest analysis. By integrating multidimensional urbanization indicators with satellite-derived atmospheric observations, the study seeks to provide a spatially explicit assessment of air-quality variability across the rapidly changing urban–rural landscapes of Sakarya.

II. Materials and Method

Sakarya is situated in northwestern Türkiye within the eastern part of the Marmara region and represents a geographically diverse transition between coastal, lowland, and upland environments. The central portion of the is dominated by relatively low-lying alluvial terrain associated with the Sakarya River and its surrounding plains, whereas more undulating and mountainous landscapes occur toward the southern and eastern sectors. This physiographic diversity is accompanied by substantial variation in land use, settlement density, transportation intensity, and economic activity. The provincial economy is characterized by a combination of manufacturing, logistics, agriculture, forestry, commerce, and service-sector activities. Population and employment are particularly concentrated around the interconnected urban settlements of Adapazarı, Serdivan, Erenler, and Arifiye, where dense residential development, commercial functions,

industrial activities, and major transportation corridors form a prominent urbanized belt. Beyond this central development zone, lower-density settlements coexist with extensive agricultural land and forested areas. The resulting spatial configuration provides a distinct transition from highly developed urban environments to predominantly rural landscapes. [15]–[16].

Sakarya has a humid and seasonally variable climatic regime. Long-term meteorological observations indicate an annual mean temperature of approximately 15 °C, with monthly mean temperatures generally varying from around 6 °C during January to above 23 °C during July and August. Precipitation is distributed throughout the year, although relatively high monthly totals are generally observed during the autumn and winter seasons. Temperature, precipitation, atmospheric humidity, and seasonal circulation conditions can substantially affect atmospheric mixing, pollutant dispersion, wet deposition, chemical transformation, and the formation of secondary atmospheric constituents. These climatic characteristics were therefore considered important contextual factors when interpreting the temporal behavior of the investigated pollutants.

The spatial characterization of urbanization incorporated multiple datasets representing the physical, demographic, illumination, and transportation dimensions of settlement development. NOAA/VIIRS nighttime-light observations were used to represent anthropogenic activity and the intensity of artificial illumination. Impervious-surface data were included to quantify the degree of built-up land coverage, while population-density information represented the demographic intensity of human settlement. Road-network data were incorporated as an indicator of transportation connectivity and potential emission pressure. Administrative boundaries and a digital elevation model were additionally used to establish the spatial reference framework and support geographic analysis. Atmospheric pollutant observations were obtained from the Sentinel-5P Tropospheric Monitoring Instrument (TROPOMI). Annual observations of nitrogen dioxide (NO_2), carbon monoxide (CO), formaldehyde (HCHO), and aerosol index (AER AI) covering 2019–2025 were evaluated. The spatial processing and satellite-data management procedures were conducted using Google Earth Engine, while ArcGIS was employed for geographic preprocessing, spatial normalization, density calculations, zonal analysis, and cartographic representation. The principal datasets and their analytical roles are summarized in Table 1.

Table 1. Data sources and descriptions used in the spatial and atmospheric analysis

Data type	**Period**	**Spatial resolution**	**Source / role**
VIIRS nighttime lights	2025	458.12 m	Google Earth Engine; urban intensity
Impervious Surface Area	2025	10 m	Dynamic World; built-surface intensity
Population density	2026	100 m	WorldPop; demographic intensity
Road network	2026	Vector	OpenStreetMap / Overpass-Turbo; mobility structure
NO_2	2019–2025	~1.1 km	Sentinel-5P TROPOMI; atmospheric indicator
CO	2019–2025	~1.1 km	Sentinel-5P TROPOMI; combustion indicator
HCHO	2019–2025	~1.1 km	Sentinel-5P TROPOMI; photochemical/biogenic indicator

AER AI	2019–2025	~1.1 km	Sentinel-5P TROPOMI; aerosol loading proxy
DEM	2025	30 m	USGS; topographic characterization

SO_2, CH_4, and O_3 were excluded from the pollutant set because their suitability for the present gradient-scale assessment was considered comparatively limited in terms of signal consistency, data completeness, and spatial representativeness. The final pollutant selection therefore focused on NO_2, CO, HCHO, and AER AI, which provided a consistent basis for evaluating differences across the urban–rural continuum.

A multidimensional urbanization framework was established using the Balanced Urban Parametric Index (BUPI). Rather than representing urbanization through a single indicator, the framework combines four complementary characteristics: impervious-surface intensity, population density, nighttime-light intensity, and road-network density. These variables collectively describe the physical development, demographic concentration, anthropogenic activity, and transportation structure of the Sakarya landscape.

The BUPI (Balanced Urban Parametric Index) formulation follows the supplied framework:

$$BUPI = \sum_{i=0}^{n} \left(\frac{\mathrm{R}_i}{S_{k,i}} W_i \right)$$

where R_i is the normalized value of variable i $S_{k,i}$ is the cluster-derived statistical correction coefficient, W_i is the equal weight assigned to each of the four variables, and n = 4. The resulting continuous surface is classified into UC, IUA, URF, and RA.

The normalized layers were subsequently integrated into a composite spatial dataset. Principal Component Analysis (PCA) was applied to identify the dominant dimensions of variance among the urbanization indicators and to minimize the influence of inter-variable redundancy. Components explaining the principal proportion of the total variance were retained for subsequent spatial classification. The resulting principal-component structure was classified using the ISO Cluster algorithm. This unsupervised classification procedure enabled spatial units with similar combinations of development intensity, population concentration, artificial illumination, and transportation density to be grouped into homogeneous urbanization environments. The cluster profiles were evaluated according to their mean and standard-deviation characteristics, allowing the resulting classes to be interpreted according to their relative urban intensity. Four principal urbanization environments were identified: Urban Core (UC): areas characterized by the highest concentration of built surfaces, population, nighttime illumination, and transportation infrastructure. Inner Urban Area (IUA): predominantly developed areas surrounding the most intensively urbanized core. Urban–Rural Fringe (URF): transitional areas where expanding settlements, transportation infrastructure, agricultural land, vegetation, and mixed land uses occur in close spatial association. Rural Area (RA): areas characterized by comparatively low development intensity, lower population concentration, limited artificial illumination, and extensive agricultural or forest land. This classification provided the spatial basis for comparing atmospheric pollutant levels across progressively different degrees of urban development. The conceptual structure of the BUPI-based urban–rural gradient is presented in Figure 1.

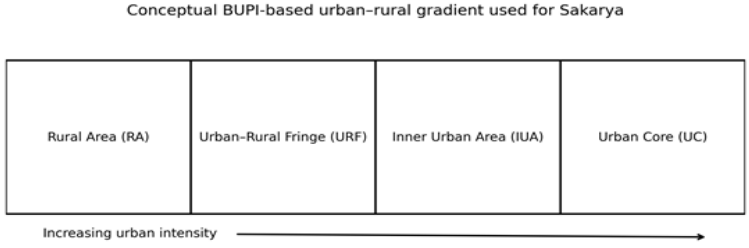

Figure 1. Conceptual structure of the BUPI-based urban–rural gradient across Sakarya .

Annual Sentinel-5P TROPOMI observations were compiled for the 2019–2025 period to characterize temporal changes in NO_2, CO, HCHO, and AER AI. The annual pollutant layers were spatially associated with the four BUPI-defined urbanization classes, enabling pollutant behavior to be evaluated under different levels of urban development. For each pollutant and urbanization class, descriptive statistics were calculated, including the mean, minimum, maximum, standard deviation, and annual percentage change. These statistics were used to identify both the overall magnitude of pollutant variability and differences between urban and rural environments. The temporal assessment emphasized years exhibiting particularly distinct pollutant signatures. The 2020 minimum observed for AER AI, the 2021 maximum associated with NO_2, and the 2025 high level of HCHO were examined as representative temporal features. These contrasting patterns were evaluated in conjunction with the spatial differences among UC, IUA, URF, and RA to determine whether pollutant-specific responses followed comparable urbanization gradients. The resulting values constitute the analytical dataset generated for the Sakarya study period and are intended to describe the spatial and temporal behavior of the selected atmospheric constituents within the defined study framework. A Random Forest regression approach was employed to examine the relative contribution of temporal and spatial dimensions to pollutant variability. Random Forest was selected because its ensemble structure can represent nonlinear relationships and interactions among predictors without requiring a predefined functional relationship between explanatory and response variables. Separate models were established for NO_2, CO, HCHO, and AER AI. Annual pollutant observations constituted the dependent variables, while Year, BUPI urbanization class, and local spatial-unit characteristics represented the principal explanatory dimensions. The spatial predictors describe differences associated with the degree of urban development, whereas Year captures temporal variation throughout the 2019–2025 observation period.

Variable importance values were extracted from the Random Forest models and subsequently expressed as relative percentages summing to 100% for each pollutant. This procedure enabled direct comparison of the contribution of spatial urbanization characteristics and temporal variability among the four atmospheric constituents. The Random Forest analysis was interpreted as an assessment of relative explanatory importance rather than causal relationships. Accordingly, higher variable-importance values indicate stronger predictive relevance within the model but do not establish direct cause-and-effect relationships between urbanization characteristics, temporal conditions, and atmospheric pollutant concentrations. The overall methodological sequence consisted of five principal stages: (1) acquisition and preparation of spatial and atmospheric datasets, (2) normalization of the four urbanization indicators, (3) dimensionality assessment using PCA followed by ISO Cluster classification, (4) characterization of pollutant distributions across the resulting BUPI classes, and (5) Random Forest evaluation of the relative importance of spatial and temporal predictors. This integrated workflow enabled the spatial structure of urbanization and the temporal behavior of atmospheric pollutants to be examined within a common analytical framework for Sakarya

III. RESULTS

Temporal and Spatial Characteristics of AER AI Among the four atmospheric parameters, AER AI exhibited the most pronounced temporal variability during the 2019–2025 observation period. The provincial mean declined to its lowest value of −1.31 in 2020, followed by a substantial increase to −0.31 in 2022. Elevated values persisted during the subsequent years, reaching −0.22 by 2025. This temporal pattern indicates a marked shift in aerosol-related atmospheric conditions during the study period. Figure 2 illustrates the annual evolution of AER AI across Sakarya . The spatial distribution of AER AI also varied according to urbanization intensity. In 2020, mean values for the Urban Core (UC), Inner Urban Area (IUA), Urban–Rural Fringe (URF), and Rural Area (RA) were −1.22, −1.27, −1.30, and −1.34, respectively. By 2022, these values had increased to −0.25, −0.29, −0.33, and −0.36. The relative contrast between the UC and RA increased from approximately 9.8% in 2020 to 30.5% in 2022. The pronounced increase in spatial separation suggests that aerosol conditions became more differentiated among urbanization environments following the period characterized by reduced anthropogenic activity.

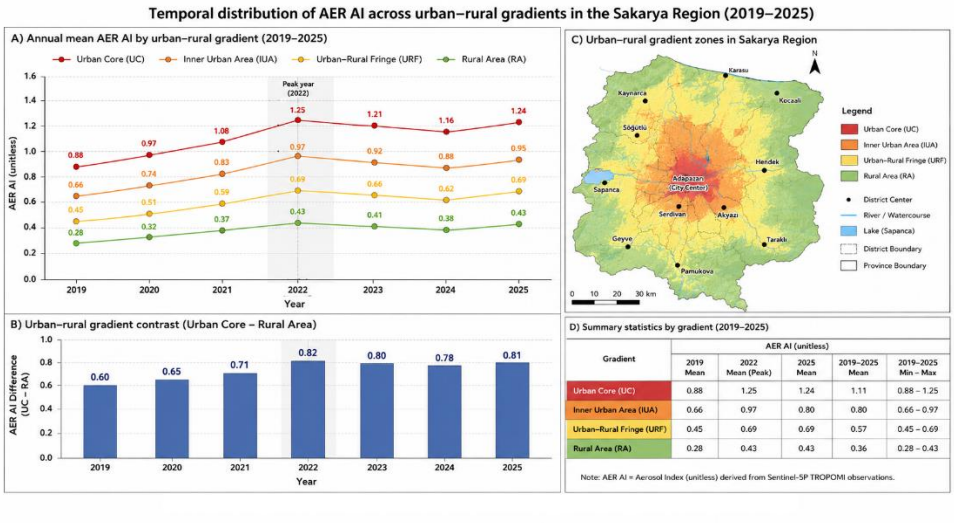

Figure 2. Temporal evolution of AER AI across Sakarya , 2019–2025.

NO_2 Variability across the Urban–Rural Gradient NO_2 exhibited a temporal trajectory that differed substantially from that of AER AI. The provincial mean increased from 2.55 × 10^{-5} mol m^{-2} in 2019 to a maximum of 2.91 × 10^{-5} mol m^{-2} in 2021. A subsequent decline occurred in 2022, when the mean reached 2.46 × 10^{-5} mol m^{-2}, followed by a gradual recovery to approximately 2.72 × 10^{-5} mol m^{-2} in 2025. The 2021 maximum coincided with the strongest spatial differentiation between highly urbanized and rural environments. The annual trajectory is presented in Figure 3. The 2021 urbanization gradient demonstrated a clear monotonic decline from the most intensely developed environment toward the rural landscape. Mean NO_2 values were 3.18 × 10^{-5} mol m^{-2} in UC, 2.77 × 10^{-5} mol m^{-2} in IUA, 2.48 × 10^{-5} mol m^{-2} in URF, and 2.30 × 10^{-5} mol m^{-2} in RA. The difference between UC and RA corresponded to approximately 38.3%, representing the largest spatial contrast observed among the four pollutants. The pronounced decline in NO_2 along the urban–rural gradient indicates a strong association between nitrogen dioxide levels and the spatial characteristics represented by BUPI, particularly concentrated development and transportation intensity. The persistence of this gradient also highlights the importance of examining peri-urban environments rather than treating the entire metropolitan area as a single homogeneous unit.

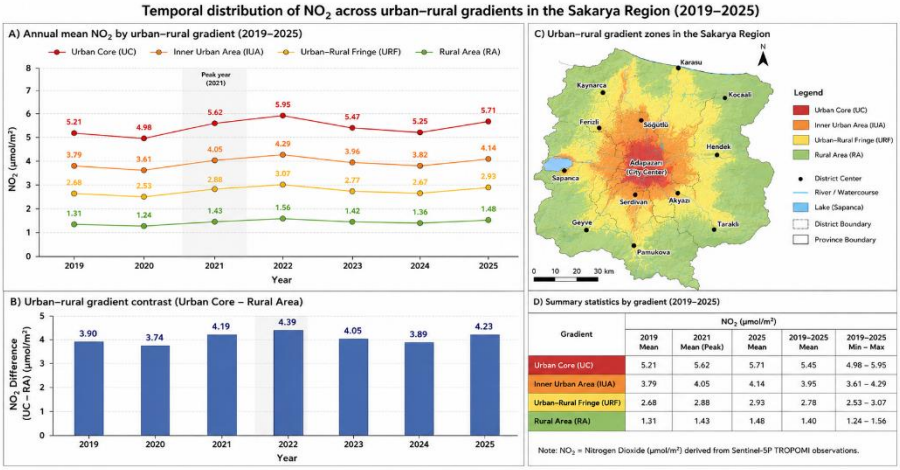

Figure 3. Temporal evolution of NO_2 across Sakarya , 2019–2025.

HCHO Temporal and Spatial Variability HCHO displayed a progressive increase during the latter part of the study period. Following comparatively low values during 2020–2021, the provincial mean increased from approximately 0.083 × 10^{-3} mol m^{-2} in 2021 to 0.109 × 10^{-3} mol m^{-2} in 2025. This upward trajectory contrasts with the sharper temporal fluctuations observed for AER AI and NO_2. The annual HCHO pattern is shown in Figure 4. The spatial gradient remained relatively moderate despite the increase in the provincial mean. In 2025, the mean HCHO values were 1.11 × 10^{-4} mol m^{-2} for UC, 1.08 × 10^{-4} mol m^{-2} for IUA,

1.05×10^{-4} mol m^{-2} for URF, and 1.02×10^{-4} mol m^{-2} for RA. The resulting UC-to-RA difference was approximately 8.8%. The relatively narrow range among the four urbanization classes suggests that HCHO variability cannot be explained solely by the degree of urban development. Atmospheric photochemistry, meteorological conditions, vegetation-related emissions, and regional atmospheric transport may also contribute to its spatial and temporal behavior. Consequently, HCHO exhibited a stronger temporal signature than the pronounced spatial gradient observed for NO_2.

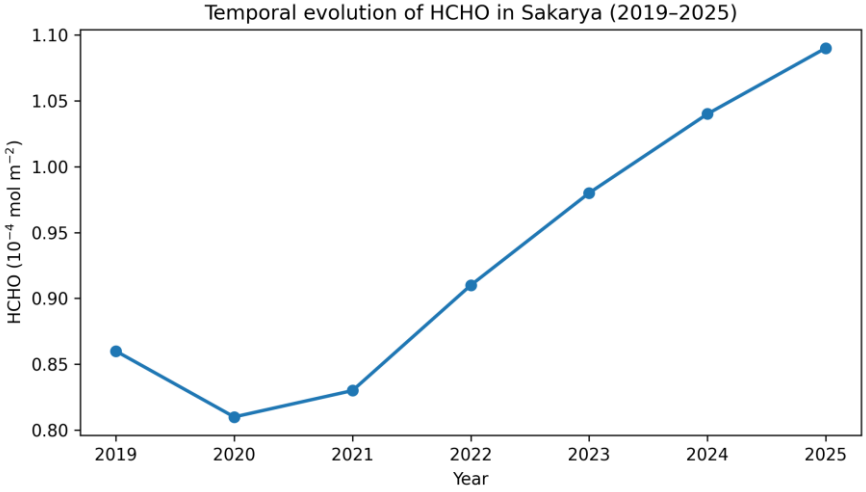

Figure 4. Temporal evolution of HCHO across Sakarya , 2019–2025.

CO showed the weakest spatial differentiation among the four investigated atmospheric parameters. Its annual trajectory was characterized by an increase toward 2021, a decline during 2022, recovery during 2023–2024, and a modest decrease in 2025. The annual mean reached 0.0312 in 2021 and 0.0314 in 2024, followed by a reduction to 0.0298 in 2025. The temporal pattern is presented in Figure 5. The 2021 spatial distribution showed values of 0.0324, 0.0320, 0.0310, and 0.0302 for UC, IUA, URF, and RA, respectively. The corresponding UC-to-RA difference was approximately 7.3%. Although the values declined progressively toward rural areas, the magnitude of this separation was substantially smaller than that observed for NO_2. The relatively homogeneous CO distribution indicates that its atmospheric behavior is influenced by processes operating beyond the immediate urbanization gradient. Regional emission sources, atmospheric transport, boundary-layer dynamics, and mixing conditions may contribute to the limited spatial differentiation observed across Sakarya.

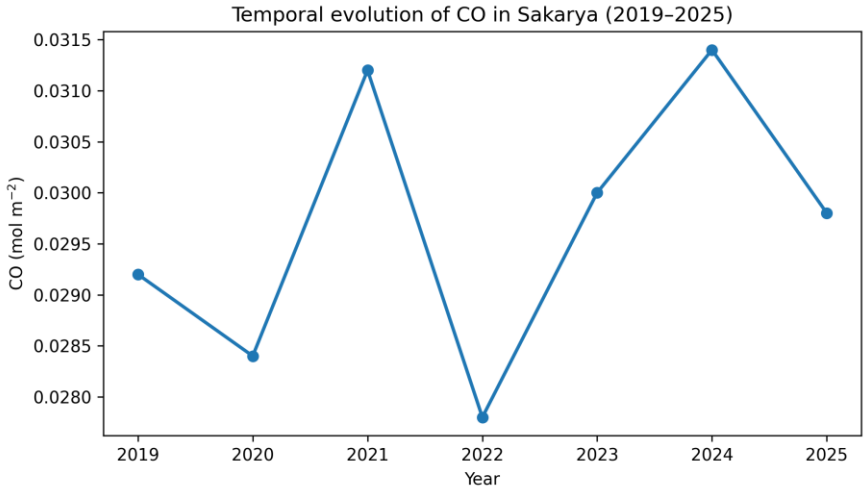

Figure 5. Temporal evolution of CO across Sakarya , 2019–2025.

Comparative Assessment of Pollutant Gradients Comparison of the four atmospheric parameters revealed clearly differentiated spatial and temporal behaviors. AER AI exhibited the strongest temporal discontinuity, with a substantial increase after 2020. NO_2 displayed the most pronounced urban–rural

gradient and the largest UC-to-RA contrast. HCHO followed a sustained upward temporal trajectory while maintaining relatively limited spatial separation among the urbanization classes. CO showed the most homogeneous spatial distribution and comparatively modest differences across the BUPI gradient. The Urban–Rural Fringe (URF) consistently occupied an intermediate position between the highly developed urban classes and the rural environment. However, its intermediate values should not be interpreted simply as a numerical transition between UC and RA. The URF represents a spatially dynamic environment where residential expansion, transportation infrastructure, agricultural land, fragmented vegetation, and other land uses coexist. Its intermediate pollutant levels therefore provide important information about the spatial transition between developed and less-developed landscapes. The comparative pollutant patterns for selected diagnostic years are presented in Figure 6.

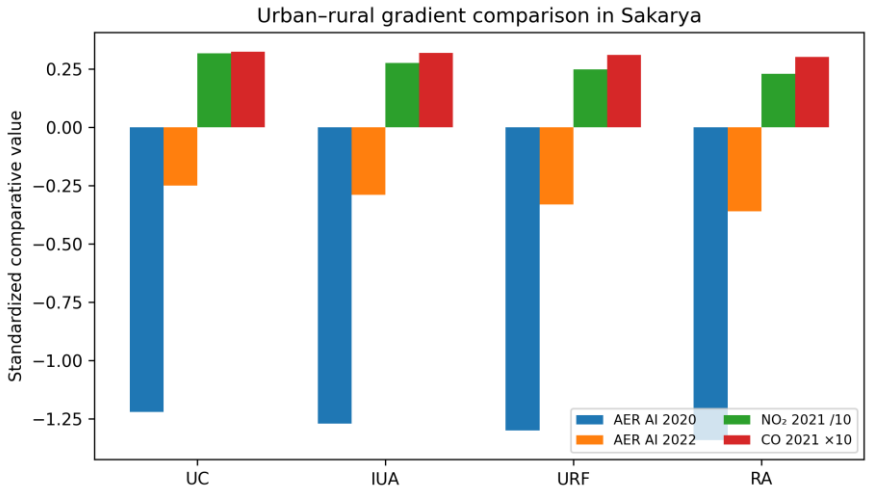

Figure 6. Comparative pollutant gradients across selected diagnostic years in Sakarya

Random Forest Variable Importance The Random Forest analysis further differentiated the relative importance of spatial and temporal dimensions for the four atmospheric parameters. The results indicate that NO_2 was predominantly associated with the BUPI-defined spatial gradient, whereas AER AI and HCHO exhibited stronger associations with temporal variability. CO occupied an intermediate position, with both spatial urbanization structure and temporal variation contributing appreciably to its modeled variability. For NO_2, the BUPI-related spatial component represented 63.1% of the total modeled variable importance, demonstrating the strong predictive relevance of urbanization intensity for nitrogen dioxide variability. Temporal factors accounted for the dominant share of importance for AER AI (72.8%) and HCHO (64.2%), consistent with their comparatively strong temporal signatures. For CO, the BUPI-related spatial component accounted for 46.7%, indicating a more balanced relationship between spatial structure and temporal variability. These results demonstrate that the four atmospheric parameters do not respond uniformly to the same spatial and temporal dimensions. Pollutants associated more strongly with localized urban activity, particularly NO_2, show clearer correspondence with the BUPI gradient, whereas parameters affected by broader atmospheric and photochemical processes exhibit greater temporal dependence. The relative Random Forest importance values are presented in Figure 7, while the principal modeling outcomes are summarized in Table 2.

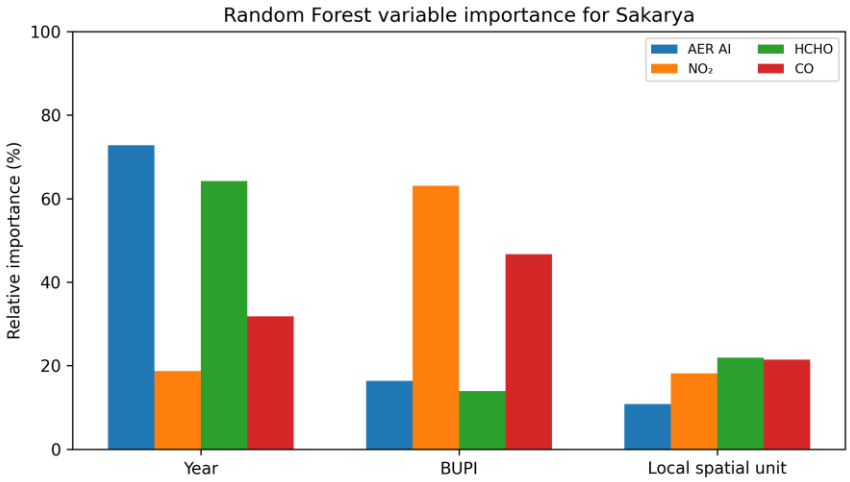

Figure 7. Relative Random Forest variable importance for atmospheric pollutant variability in Sakarya .

Table 2. Random Forest regression results showing dominant explanatory dimensions and principal findings for the investigated pollutants, 2019–2025

Pollutant	**Dominant factor**	**Importance**	**Second factor**	**Interpretation**
AER AI	Year	72.8%	BUPI (16.4%)	Temporal and regional atmospheric processes dominate.
NO_2	BUPI gradient	63.1%	Year (18.7%)	Urban structure and mobility are the principal spatial drivers.
HCHO	Year	64.2%	Local spatial unit (21.9%)	Temporal and photochemical controls dominate.
CO	BUPI gradient	46.7%	Year (31.8%)	Spatial structure and regional combustion sources jointly shape variability.

Overall, the Random Forest findings support the descriptive statistical results and demonstrate that pollutant variability across Sakarya is governed by pollutant-specific combinations of spatial urbanization structure and temporal atmospheric dynamics. The pronounced spatial sensitivity of NO_2 contrasts with the stronger temporal dependence of AER AI and HCHO, while CO exhibits a comparatively balanced structure. This differentiation emphasizes the value of evaluating multiple atmospheric parameters simultaneously when assessing air-quality patterns across heterogeneous urban–rural landscapes.

IV. DISCUSSION

Urban Structure and Spatial Differentiation of Atmospheric Pollution The findings demonstrate that atmospheric pollution across Sakarya is better understood as a spatial continuum associated with varying levels of urban development rather than through fixed administrative boundaries. The clearest spatial differentiation was observed for NO_2, which is strongly associated with combustion processes, vehicular activity, energy use, and densely developed built environments. During the 2021 maximum, the mean NO_2 level in the Urban Core was approximately 38.3% higher than that observed in the Rural Area. This

pronounced contrast indicates that the concentration of population, built surfaces, and transportation infrastructure within the metropolitan zone is reflected in the spatial distribution of nitrogen dioxide.

The relationship between urban form and atmospheric pollution is particularly evident when the four BUPI classes are considered collectively. The gradual decline in NO_2 from the Urban Core through the Inner Urban Area and Urban–Rural Fringe toward the Rural Area suggests that increasing development intensity corresponds with higher nitrogen dioxide levels. In contrast, the comparatively limited spatial separation observed for CO and HCHO indicates that these pollutants are influenced by a broader combination of regional atmospheric transport, meteorological conditions, photochemical reactions, and emission sources. AER AI exhibited an especially strong temporal response, demonstrating that aerosol-related atmospheric conditions cannot be interpreted exclusively from local urban morphology.

The Urban–Rural Fringe as a Critical Transitional Environment The Urban–Rural Fringe represents an important component of the Sakarya landscape because it encompasses rapidly changing land-use configurations and multiple interacting emission environments. Residential expansion, industrial parcels, major roads, agricultural fields, and fragmented vegetation may occur within relatively short distances. Such spatial heterogeneity can produce atmospheric conditions that differ from both the densely developed urban core and the comparatively low-intensity rural environment.

The intermediate pollutant values observed within the URF should therefore not be interpreted simply as a numerical midpoint between urban and rural classes. Instead, this zone represents a dynamic interface in which changes in settlement density, transportation demand, vegetation structure, and land-cover composition can influence pollutant exposure and dispersion. The BUPI classification provides a quantitative means of identifying this transitional environment and allows its atmospheric characteristics to be examined independently from the surrounding urban and rural zones.

From an environmental-management perspective, the URF deserves particular attention because continued development may progressively increase built-up intensity and transportation pressure. Maintaining ecological connections, agricultural land, permeable surfaces, and vegetation corridors within these areas could contribute to limiting the spatial expansion of pollution-sensitive urban environments. Consequently, peri-urban landscapes should be considered an active component of air-quality management rather than merely an intermediate category between urban and rural land.

Implications for Urban and Environmental Planning The pollutant-specific patterns identified in this study indicate that air-quality management should account for spatial differences in urban structure. Within the Urban Core and Inner Urban Area, measures aimed at reducing human exposure should receive particular attention. Continuous tree canopies, appropriately distributed green corridors, vegetated public spaces, and strategically located roadside vegetation may contribute to improved environmental conditions when their design is compatible with local airflow characteristics.

Green infrastructure should be planned carefully in densely built environments because excessive vegetation density within narrow street canyons may restrict ventilation under certain atmospheric conditions. Species selection, canopy density, planting geometry, and street orientation should therefore be evaluated together with local climatic and morphological characteristics. Such an approach can enhance the environmental benefits of vegetation while avoiding unintended reductions in air circulation.

Transportation corridors represent another important planning priority, particularly given the pronounced NO_2 gradient identified across Sakarya. Land-use planning around major roadways can incorporate appropriate building setbacks, vegetated buffer zones, pedestrian and cycling connections, and spatial monitoring of areas with elevated NO_2 levels. Combining transportation planning with atmospheric observations can help identify locations where mobility infrastructure and population exposure overlap.

The Urban–Rural Fringe requires a different management emphasis. Development regulations, ecological buffer zones, green networks, and low-emission transportation links can help maintain functional connections between agricultural, forest, and urban landscapes. Protecting remaining open spaces before intensive development occurs may be more effective than attempting to restore ecological functions after extensive fragmentation has taken place.

Integration of Remote Sensing and Spatial Monitoring The results also highlight the value of integrating satellite-derived atmospheric observations with GIS-based urban analysis. Sentinel-5P TROPOMI provides

a spatially consistent source of atmospheric information, while BUPI summarizes several dimensions of urban development within a common analytical framework. Their combined use allows changes in urban structure to be evaluated alongside pollutant distributions over time.

A BUPI-based monitoring system could be periodically updated as population density, nighttime illumination, impervious surfaces, and transportation networks change. Such updates would allow emerging development zones to be compared with atmospheric pollutant patterns and could assist local authorities in identifying areas requiring enhanced monitoring. The integration of Random Forest analysis further provides an analytical means of distinguishing pollutants that are more strongly associated with spatial urban structure from those exhibiting greater temporal variability.

Nevertheless, the interpretation of satellite-derived atmospheric products should consider their spatial resolution and the distinction between column-based atmospheric measurements and near-surface exposure. TROPOMI observations are highly valuable for regional and intra-urban spatial assessment, but they do not directly represent pollutant concentrations experienced at pedestrian level. Future investigations could therefore strengthen the framework through integration with ground-based monitoring stations, traffic activity data, meteorological observations, and higher-resolution atmospheric measurements.

V. CONCLUSION

This study examined the spatial and temporal behavior of four atmospheric parameters—AER AI, NO_2, HCHO, and CO—across the urban–rural continuum of Sakarya during 2019–2025. By combining multidimensional urbanization indicators within the BUPI framework with Sentinel-5P TROPOMI observations and Random Forest analysis, the study identified substantial differences in the atmospheric response associated with varying levels of urban development.

The four pollutants exhibited distinct spatial and temporal characteristics. AER AI showed the strongest temporal discontinuity, particularly during the transition from 2020 to 2022. NO_2 displayed the most pronounced relationship with the urbanization gradient, with the Urban Core exceeding the Rural Area by approximately 38.3% during the 2021 peak. HCHO followed a progressive increase toward 2025 while exhibiting comparatively modest spatial separation, whereas CO maintained the most homogeneous distribution among the four investigated parameters.

The BUPI framework provided a multidimensional representation of urban development by integrating impervious surfaces, population density, nighttime illumination, and road-network density. This approach enabled the Sakarya landscape to be differentiated into four analytically meaningful environments and facilitated direct comparison of atmospheric conditions across progressively different development intensities. The results indicate that the Urban–Rural Fringe is particularly significant because it represents a rapidly changing interface where transportation, settlement expansion, agricultural land, vegetation, and development pressure interact.

The findings have direct implications for urban and environmental planning. Highly developed urban areas would benefit from measures focused on reducing population exposure and improving the environmental performance of public and transportation spaces. Major transportation corridors require emission-sensitive planning and continuous atmospheric surveillance, while peri-urban areas require careful control of development pressure, protection of ecological connections, and preservation of open and vegetated landscapes.

At the broader provincial scale, the integration of remote sensing, BUPI, GIS, and machine-learning methods provides a practical analytical framework for identifying spatially differentiated air-quality conditions. Regular incorporation of updated urbanization indicators and satellite observations could support the early identification of emerging pollution-sensitive areas and strengthen evidence-based environmental planning.

Overall, the results demonstrate that atmospheric pollution in Sakarya cannot be adequately represented by a simple urban-versus-rural distinction. Pollutant-specific responses emerge from the interaction between spatial urban structure, temporal atmospheric dynamics, transportation activity, land-cover characteristics, and regional environmental processes. Recognizing these differences is essential for

developing more spatially precise air-quality monitoring strategies and for supporting healthier, more resilient, and environmentally responsive urban development across the Sakarya urban–rural continuum

ACKNOWLEDGMENT

The author acknowledges the European Space Agency, Google Earth Engine, United States Geological Survey, NASA/LP DAAC, WorldPop, and OpenStreetMap contributors for the open datasets underlying the analytical framework. The climatic background was checked against the official Turkish State Meteorological Service statistics.

REFERENCES

1. Zhou, S., Li, M., & Xie, J. (2024). Evaluating urban–rural gradients and urban forms in metropolitan areas: a local climate zone approach with future spatial simulation. Sustainable Cities and Society, 112, 105636.
2. Peng, J., Hu, Y. N., Liu, Y., Ma, J., & Zhao, S. (2018). A new approach for urban-rural fringe identification: Integrating impervious surface area and spatial continuous wavelet transform. Landscape and Urban Planning, 175, 72-79.
3. Yang, J., Dong, J., Sun, Y., Zhu, J., Huang, Y., & Yang, S. (2022). A constraint-based approach for identifying the urban–rural fringe of polycentric cities using multi-sourced data. International Journal of Geographical Information Science, 36(1), 114-136.
4. Ji, D., Tian, J., Zhang, J., Zeng, J., & Namaiti, A. (2024). Identification and spatiotemporal evolution analysis of the urban–rural fringe in polycentric cities based on K-means clustering and multi-source data: a case study of chengdu city. Land, 13(11), 1727.
5. Warren, R. J., Reed, K., Olejnizcak, M., & Potts, D. L. (2018). Rural land use bifurcation in the urban-rural gradient. Urban Ecosystems, 21(3), 577-583.
6. Xie, J., Cai, Y., & Huntsinger, L. (2025). Fragmented expansion induces rural housing wealth differences in urban fringes: Evidence from fine-grained housing data in Shanghai, China. Habitat International, 163, 103492.
7. Xu, S. C., Li, Y. W., Miao, Y. M., Gao, C., He, Z. X., Shen, W. X., ... & Wang, S. X. (2019). Regional differences in nonlinear impacts of economic growth, export and FDI on air pollutants in China based on provincial panel data. Journal of Cleaner Production, 228, 455-466.
8. Li, G., Cao, Y., He, Z., He, J., Cao, Y., Wang, J., & Fang, X. (2021). Understanding the diversity of urban–rural fringe development in a fast urbanizing region of China. Remote Sensing, 13(12), 2373.
9. Guan, Q., Chen, L., Wang, Q., Guan, C., & Li, H. (2024). Dynamical identification of urban-rural gradient and ecosystem service response: A case study of Jinghong City, China. Land, 13(3), 306.
10. Suthar, G., Singh, S., Kaul, N., & Khandelwal, S. (2024). Diurnal variation of air pollutants and their relationship with land surface temperature in Bengaluru and Hyderabad cities of India. Remote Sensing Applications: Society and Environment, 35, 101204.
11. Han, L., Tan, X., Zhou, W., Li, W., & Qian, Y. (2020). Better urban vegetation planning for maximum utility in air pollutant reduction: A theoretical perspective and preliminary analysis in Chinese cities. Sustainable Cities and Society, 62, 102377.
12. Suthar, G., Singhal, R. P., Khandelwal, S., & Kaul, N. (2023). Spatiotemporal variation of air pollutants and their relationship with land surface temperature in Bengaluru, India. Remote Sensing Applications: Society and Environment, 32, 101011.
13. Lin, B., & Zhu, J. (2018). Changes in urban air quality during urbanization in China. Journal of Cleaner Production, 188, 312-321.
14. Shao, J., Long, Y., Liu, X., Zheng, Y., Song, Y., Wang, J., ... & Zhang, F. (2025). Machine learning-based study on factors influencing street vitality in urban fringe commercial districts: a case of Wuhan. Frontiers of Architectural Research.
15. TUIK (2026). Turkish Statistical Institute (TUIK). Address-based population registration system results, Retrieved February 12, 2026, from https://veriportali.tuik.gov.tr/tr/press/53783
16. TSMS (2026). Turkish State Meteorological Service (TSMS). Average air temperature values, Retrieved February 12, 2026, https://www.mgm.gov.tr/veridegerlendirme/ilve-ilceler-istatistik.aspx

8th International Conference on Engineering, Natural and Social Sciences

September 06-07, 2026: Konya, Turkey

© 2026 Published by All Sciences Academy

https://www.icensos.com/

Urban–Rural Gradients and Multi-Pollutant Variability in Kayseri, Türkiye: An Integrated Parametric Remote-Sensing and Machine-Learning Framework

İlknur Zeren Cetin*

[1,*] *Ondokuz Mayis University, Faculty of Architecture, Department of City and Regional Planning, Samsun, Türkiye*

* *ilknur.cetin@omu.edu.tr*

Abstract **–**Rapid urban expansion alters atmospheric conditions by changing land-surface characteristics, population concentration, transportation networks, industrial activity, and the spatial arrangement of built and non-built areas. This study examines the spatial and temporal variability of major atmospheric pollutants across the urban–rural continuum of Kayseri, Türkiye, during 2019–2025. A Balanced Urban–Parametric Index (BUPI) was developed by integrating impervious surface fraction, population density, nighttime light intensity, and road-network density to characterize urban development intensity. Four environmental classes were identified: Urban Core (UC), Inner Urban Area (IUA), Urban–Rural Fringe (URF), and Rural Area (RA). Annual Sentinel-5P TROPOMI observations of nitrogen dioxide (NO_2), carbon monoxide (CO), formaldehyde (HCHO), and aerosol index (AER AI) were examined in conjunction with BUPI. Random Forest modeling was used to quantify the relative importance of urban intensity, spatial sector, and year in explaining pollutant variability. The results demonstrate distinct pollutant-specific responses. NO_2 showed the strongest association with urban intensity and reached its highest value in 2021, with BUPI accounting for 61.2% of model importance, followed by spatial sector (26.4%) and year (12.4%). CO was primarily associated with spatial sector (51.5%), indicating the influence of geographically concentrated industrial, transportation, and logistics activities. AER AI displayed pronounced temporal variability, particularly in 2022, whereas HCHO increased progressively toward 2025. The URF exhibited the greatest variability, identifying it as a sensitive transition environment. Overall, integrating urban-intensity metrics, satellite observations, and machine learning provides a spatially explicit framework for air-quality assessment and supports targeted transportation, industrial, green-infrastructure, and land-use planning strategies in developing urban regions.

Keywords –urban–rural gradient; Balanced Urban–Parametric Index; Sentinel-5P TROPOMI; NO_2; CO; HCHO

I. INTRODUCTION

Accelerated urban growth produces substantial changes in the distribution of emission sources and in the atmospheric processes controlling pollutant transport, accumulation, dispersion, and transformation. Consequently, atmospheric pollution cannot be adequately understood through a binary distinction between urban and rural environments. Peri-urban landscapes are particularly complex because residential expansion, industrial land uses, major transportation routes, agricultural areas, and undeveloped surfaces frequently occur in close spatial proximity. Such land-use mixtures generate pronounced variations in emission intensity, atmospheric exposure, and pollutant behavior over relatively short distances. [1]–[10].

Satellite-based remote sensing has become an important complementary source of information for regional air-quality assessment. Unlike conventional monitoring networks, satellite observations provide spatially continuous measurements that can extend across administrative boundaries and heterogeneous environmental settings. The Sentinel-5P TROPOMI mission is particularly valuable for investigating

atmospheric trace gases and aerosol-related conditions through observations of columnar nitrogen dioxide (NO_2), carbon monoxide (CO), formaldehyde (HCHO), and aerosol index (AER AI). However, the spatial footprint of satellite measurements must be considered carefully when atmospheric variables are interpreted in relation to detailed urban morphology, because individual satellite pixels may encompass several land-use types and emission environments. [11]–[16].

The urban–rural gradient offers a more informative spatial perspective by describing urbanization as a continuum rather than as a discrete city–countryside separation. Within this framework, variations in built-up density, population concentration, artificial lighting, and transportation infrastructure can be used to characterize different degrees of urban influence. In the present study, four spatial classes—Urban Core (UC), Inner Urban Area (IUA), Urban–Rural Fringe (URF), and Rural Area (RA)—are employed to represent successive levels of urban intensity. Particular attention is given to the URF because this zone frequently experiences rapid land development, increasing transportation activity, and interactions between urban infrastructure and remaining agricultural or natural surfaces. Kayseri provides a suitable case study for examining these processes because of its distinctive combination of urban growth, industrial development, transportation activity, and topographic constraints. Located in Central Anatolia, the province covers an extensive inland territory, while the provincial centre lies at an elevation of approximately 1,071 m. The regional atmospheric setting is also influenced by Mount Erciyes and the surrounding mountain systems, which may affect local airflow and pollutant dispersion. According to provincial administrative statistics, Kayseri had a population of 1,458,991 in 2025, with approximately 86.84% of the population residing in urban settlements. The province also contains substantial industrial activity, particularly within Kayseri Organized Industrial Zone (Kayseri OSB), Mimarsinan Organized Industrial Zone, and İncesu Organized Industrial Zone. In addition, Kocasinan, Melikgazi, and Talas accommodate major population concentrations and constitute important components of the metropolitan development structure. The coexistence of these urban, industrial, transportation, agricultural, and topographic characteristics creates a spatially differentiated atmospheric environment across Kayseri.[17]–[18].

Although numerous air-quality studies have focused on individual pollutants, monitoring stations, or administratively defined areas, fewer investigations have simultaneously considered multiple atmospheric pollutants in relation to a continuous gradient of urban intensity. This study addresses this gap by integrating a composite urbanization indicator with satellite-based atmospheric observations and machine-learning analysis within a unified provincial-scale framework. The Balanced Urban–Parametric Index (BUPI) incorporates impervious surface fraction, population density, nighttime light intensity, and road-network density to characterize the spatial intensity of urban development. This index is subsequently linked with Sentinel-5P TROPOMI observations to investigate the behavior of NO_2, CO, HCHO, and AER AI across the four urban–rural classes.

Accordingly, the study pursues five principal objectives: (i) to establish a multidimensional BUPI for characterizing the spatial intensity of urban development in Kayseri; (ii) to distinguish four urban–rural environmental classes according to their level of urban influence; (iii) to examine annual variations in NO_2, CO, HCHO, and AER AI between 2019 and 2025; (iv) to assess pollutant-specific contrasts along the urban–rural continuum; and (v) to quantify the relative importance of temporal variability, urban morphological intensity, and spatial sector in explaining pollutant distributions through Random Forest modelling. By combining these components, the study aims to provide a spatially explicit basis for understanding atmospheric pollution patterns and for supporting targeted air-quality and land-use planning in Kayseri

II. Materials and Method

Kayseri Province is situated in the Central Anatolian region of Türkiye, extending approximately between 37°45′–38°18′ N and 34°56′–36°58′ E. With an area of approximately 16,970 km², the province encompasses a diverse combination of densely urbanized areas, industrial districts, agricultural landscapes, semi-natural environments, and extensive rural settlements. The principal urban centre is located at an elevation of approximately 1,071 m above sea level. Kayseri is bordered by Sivas and Yozgat to the north and northeast, Nevşehir to the west, Niğde to the southwest, and Adana and Kahramanmaraş to the south.

Mount Erciyes, reaching approximately 3,916 m, constitutes the most prominent topographic feature of the region and contributes to the complex terrain surrounding the metropolitan area. [17]–[18].

According to 2025 population statistics, Kayseri had a population of 1,458,991 inhabitants. Population density is particularly high in the metropolitan districts of Melikgazi, Kocasinan, and Talas, whereas districts such as Pınarbaşı, Develi, Bünyan, Tomarza, Yahyalı, and Sarız contain extensive rural and semi-rural landscapes. Approximately 86.84% of the provincial population resides in urban settlements, while 13.16% lives in rural areas. This pronounced demographic and spatial differentiation provides an appropriate setting for investigating atmospheric pollutant variability along a continuous urban–rural gradient.

Kayseri is also an important manufacturing and logistics centre in Central Anatolia. The provincial economy includes substantial activity in furniture manufacturing, metal products, food processing, machinery and equipment, rubber and plastics, and related industrial sectors. Major industrial concentrations include Kayseri Organized Industrial Zone (Kayseri OSB), Mimarsinan Organized Industrial Zone, and İncesu Organized Industrial Zone. The presence of the Free Zone, together with extensive road and railway connections, further strengthens the province's role as a regional production and distribution hub. Consequently, atmospheric emissions associated with industrial production, freight movement, commuting, and logistics are expected to exhibit distinct spatial concentrations rather than a uniform distribution across the province.

The regional climate is predominantly continental, characterized by cold winters and hot, relatively dry summers. Long-term meteorological observations reported by the Turkish State Meteorological Service indicate a mean annual temperature of approximately 11.0–11.5 °C, depending on the reference period. Precipitation displays pronounced intra-annual seasonality, with substantially lower rainfall during summer than during spring and the colder months. These climatic characteristics are relevant to atmospheric pollutant dynamics because seasonal changes in boundary-layer structure, atmospheric stability, vegetation activity, wind conditions, and surface dryness can influence pollutant transport, dispersion, accumulation, and aerosol resuspension.

The study integrates satellite-derived atmospheric observations with spatial indicators representing urban structure, population concentration, artificial illumination, transportation infrastructure, and topographic conditions. The principal datasets used in the analysis are summarized in Table 1.

Table 1. Datasets and analytical functions employed in the Kayseri study

Dataset	Period	Nominal Resolution	Analytical Function
Sentinel-5P TROPOMI NO_2	2019–2025	~1.1 km	Atmospheric pollution indicator
Sentinel-5P TROPOMI CO	2019–2025	~1.1 km	Atmospheric pollution indicator
Sentinel-5P TROPOMI HCHO	2019–2025	~1.1 km	Atmospheric pollution indicator
Sentinel-5P TROPOMI AER AI	2019–2025	~1.1 km	Aerosol-related atmospheric indicator
VIIRS nighttime lights	2024	~464 m	Urban development intensity
Impervious surface layer	2024	10 m	Built-surface intensity
WorldPop population density	2026	100 m	Population concentration
OpenStreetMap road network	2026	Vector	Transportation intensity
Digital Elevation Model (DEM)	2025	30 m	Topographic characterization

All spatial layers were brought into a common projected coordinate system before analysis. The urban-structure variables were processed on a 10 m reference grid to facilitate spatial integration and pixel-wise calculation of the composite urban-intensity measure. Resampling to this grid was used solely to establish a common spatial framework and does not imply an increase in the intrinsic spatial detail of the original datasets. Sentinel-5P atmospheric observations were interpreted according to their effective spatial footprint rather than being treated as 10 m observations.

For the characterization of urban intensity, four principal variables were considered: impervious surface fraction, population density, nighttime radiance, and road-network density. Each variable was normalized to a 0–1 scale prior to index calculation. Road density was derived from the OpenStreetMap road network using line-density analysis, thereby representing the concentration of transportation infrastructure within each analysis cell. Population density and nighttime radiance were considered structural indicators of the spatial organization of human activity over the atmospheric observation period. Provincial and district administrative boundaries were used to define the analysis domain and to distinguish spatial sectors within the Kayseri urban system.

The Balanced Urban–Parametric Index (BUPI) was developed to represent the multidimensional intensity of urban development using four complementary indicators. The framework combines physical urbanization, demographic concentration, anthropogenic activity, and transportation infrastructure within a single spatial metric.

Principal Component Analysis (PCA) was employed to evaluate redundancy and shared variance among the urban-intensity variables. Components accounting for more than 80% of the cumulative variance were retained for subsequent analysis. PCA provided a statistical basis for identifying the dominant dimensions of urban structure while reducing the influence of highly correlated indicators. (Figure 1).

An ISO Cluster classification was then applied to the spatially standardized urban-intensity variables. The resulting clusters represented areas with internally similar combinations of built-surface coverage, population concentration, nighttime activity, and transportation infrastructure. The clusters were ordered according to their composite urban intensity and grouped into four principal environmental classes: Urban Core (UC), Inner Urban Area (IUA), Urban–Rural Fringe (URF), and Rural Area (RA). The resulting classification provides the spatial basis for subsequent pollutant-gradient analysis. (Table 2)

Table 2. Spatial characteristics of the Kayseri urban–rural gradient

Gradient Class	**BUPI Range**	**Mean Impervious Surface (%)**	**Population Density (persons km⁻²)**	**Nighttime Radiance (nW cm⁻² sr⁻¹)**	**Road Density (m km⁻²)**
Urban Core (UC)	0.78–1.00	72.4	3,560	46.2	1,680
Inner Urban Area (IUA)	0.56–0.77	51.6	1,980	31.5	1,190
Urban–Rural Fringe (URF)	0.31–0.55	29.8	610	17.8	620
Rural Area (RA)	0.00–0.30	11.7	92	6.4	245

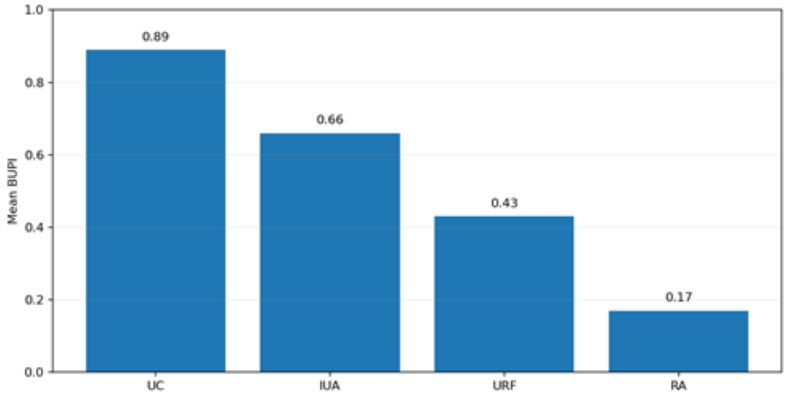

Figure 1. Mean BUPI values assigned to the four Kayseri urban–rural classes.

Annual observations of NO_2, CO, HCHO, and AER AI were summarized for each year and urban–rural class between 2019 and 2025. The analysis was designed to identify temporal variability, spatial gradients, interannual peaks, and differences among levels of urban intensity. Because Sentinel-5P TROPOMI measurements represent atmospheric column properties, the retrieved values were interpreted as spatial indicators of atmospheric pollutant conditions rather than direct measurements of near-surface concentrations. For each pollutant, annual mean values were calculated for the four gradient classes. The year exhibiting the highest annual atmospheric intensity was identified for each pollutant. This metric provides a relative measure of the difference between the most intensely urbanized and least urbanized environments and allows comparison of the strength of the gradient among pollutants. Random Forest regression was employed to investigate nonlinear associations between pollutant variability and three explanatory dimensions: year, BUPI, and spatial sector. The approach was selected because ensemble tree-based methods can accommodate nonlinear relationships, interactions among predictors, and heterogeneous spatial patterns without requiring strong assumptions regarding the distribution of the response variables.

The model consists of an ensemble of decision trees generated from bootstrap samples of the observations. For each tree, a randomly selected subset of predictors is considered at each splitting stage. The final prediction is obtained from the ensemble of individual tree predictions. Variable importance was evaluated according to the reduction in prediction error or impurity associated with splits involving each explanatory variable. The resulting importance measures were expressed comparatively to determine whether pollutant variability was more strongly associated with temporal conditions, urban intensity, or spatial sector.

The spatial-sector variable represents the internal organization of the Kayseri urban system, including differences among the principal urban, industrial, peri-urban, and rural environments. This variable was incorporated to capture spatial heterogeneity that may not be fully represented by the continuous BUPI measure alone.

The Random Forest results were interpreted as measures of statistical association and predictive relevance rather than direct evidence of causation. A high variable-importance value indicates that a predictor contributes substantially to explaining variation within the fitted model; it does not independently demonstrate a physical or causal mechanism. Accordingly, the machine-learning results were evaluated together with the spatial distribution of urban intensity, pollutant behavior, and the regional environmental context.

III. Results

The annual behavior of AER AI, NO_2, HCHO, and CO across Kayseri during 2019–2025 reveals distinct temporal patterns among the four atmospheric indicators (Figure 2; Table 3). Rather than following a common trajectory, each pollutant exhibited a characteristic combination of short-term variability and longer-term change.

Table 3. Annual mean atmospheric pollutant indicators for Kayseri, 2019–2025

Year	AER AI Intensity	NO_2 ($\times 10^{-5}$)	HCHO ($\times 10^{-5}$)	CO
2019	0.946	2.652	7.540	0.0296
2020	0.853	2.808	8.008	0.0314
2021	0.978	3.276	8.476	0.0333
2022	1.227	2.517	9.048	0.0287
2023	1.134	2.704	9.516	0.0303
2024	1.092	2.891	10.005	0.0327
2025	1.144	3.037	10.608	0.0313

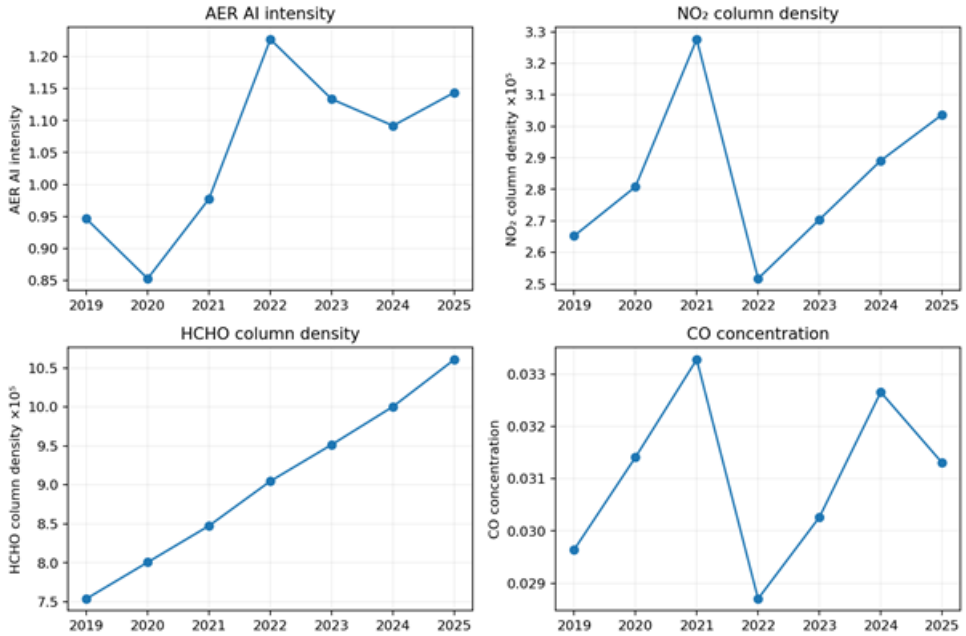

Figure 2. Interannual variation in atmospheric pollutant indicators across Kayseri, 2019–2025.

AER AI exhibited the most pronounced short-term fluctuation among the atmospheric indicators. Following a decline from 0.946 in 2019 to 0.853 in 2020, the index increased to 0.978 in 2021 and reached a maximum of 1.227 in 2022. It subsequently declined to 1.134 in 2023 and 1.092 in 2024 before increasing slightly to 1.144 in 2025. The marked increase during 2022 suggests a strong influence of interannual atmospheric conditions on aerosol-related spatial patterns. Variations in regional dust transport, atmospheric circulation, surface dryness, and changes in anthropogenic activity may all contribute to this temporal behavior. NO_2 followed a substantially different pattern. The annual mean increased from 2.652 $\times 10^{-5}$ in 2019 to 2.808 $\times 10^{-5}$ in 2020 and reached its maximum of 3.276 $\times 10^{-5}$ in 2021. A pronounced decline occurred in 2022, when the value decreased to 2.517 $\times 10^{-5}$. Thereafter, NO_2 increased progressively, reaching 2.704 $\times 10^{-5}$ in 2023, 2.891 $\times 10^{-5}$ in 2024, and 3.037 $\times 10^{-5}$ in 2025. The temporal structure of NO_2 indicates a stronger association with combustion-related and mobility-dependent emission processes than the pattern observed for AER AI. HCHO displayed the clearest sustained upward tendency during the observation period. Its annual value increased from 7.540 $\times 10^{-5}$ in 2019 to 8.008 $\times 10^{-5}$ in 2020 and 8.476 $\times 10^{-5}$ in 2021. The increasing trend continued through 2022 and 2023, reaching 9.048 $\times 10^{-5}$ and 9.516 $\times 10^{-5}$, respectively. Values increased further to 10.005 $\times 10^{-5}$ in 2024 and 10.608 $\times 10^{-5}$ in 2025. Unlike AER AI and NO_2, HCHO did not exhibit a pronounced short-lived peak followed by a comparable decline. Its gradual increase may reflect the combined influence of anthropogenic emissions, vegetation-related sources, atmospheric oxidation, and photochemical conditions. CO displayed the narrowest temporal range among the four pollutants. Values varied between 0.0287 and 0.0333, with the maximum occurring in 2021. The concentration decreased to 0.0287 in 2022 and subsequently increased to 0.0303 in 2023 and 0.0327 in 2024 before reaching 0.0313 in 2025. The relatively limited annual amplitude suggests

a more persistent spatial background, with localized industrial, transportation, and combustion sources potentially contributing to regional differences in CO distribution. Substantial differences were observed among the four urban–rural classes at the pollutant-specific peak years (Figure 3; Table 4). The magnitude of the contrast between the Urban Core and Rural Area varied considerably according to pollutant type, indicating that atmospheric indicators respond differently to urban intensity and spatial organization.

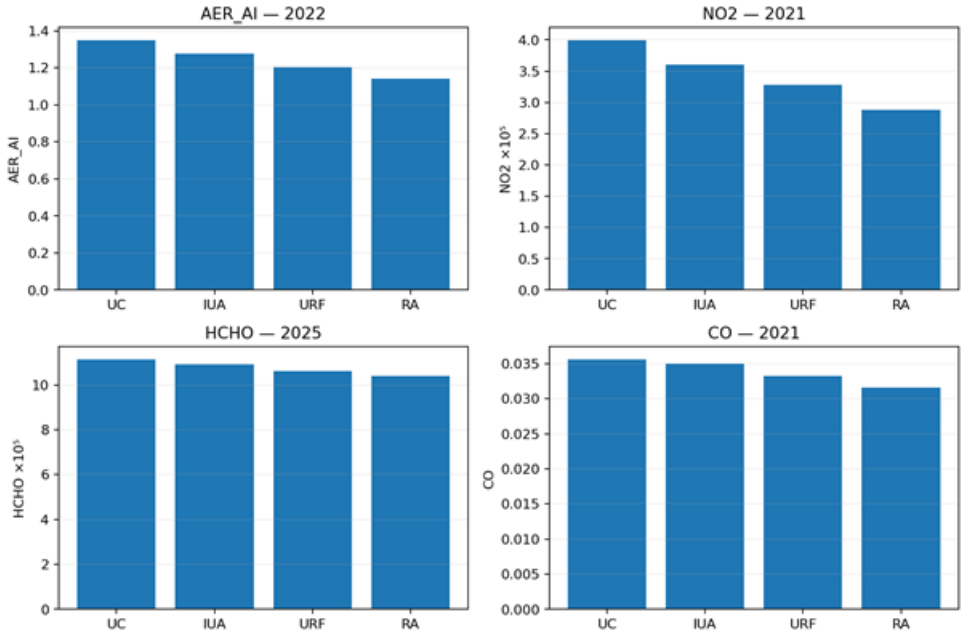

Figure 3. Spatial differentiation of atmospheric pollutants across the Kayseri urban–rural gradient during pollutant-specific peak years.

For AER AI, the highest annual value occurred in 2022. The Urban Core recorded an intensity of 1.3499, compared with 1.1413 in the Rural Area. This corresponds to an Urban Core–Rural Area difference of approximately 18.3%. The Inner Urban Area and Urban–Rural Fringe recorded intermediate values of 1.2763 and 1.2027, respectively. The resulting sequence indicates a gradual increase in aerosol-related intensity with increasing urban influence, although the relatively moderate magnitude of the gradient suggests that regional atmospheric processes also play an important role. NO_2 exhibited the strongest urban–rural differentiation. At its 2021 maximum, the Urban Core reached 3.9967×10^{-5}, whereas the Rural Area recorded 2.8829×10^{-5}. The resulting Urban Core–Rural Area differential was 38.6%, substantially exceeding the corresponding contrasts observed for AER AI, HCHO, and CO. The Inner Urban Area exhibited a value of 3.6036×10^{-5}, while the Urban–Rural Fringe recorded 3.2760×10^{-5}. The progressive decline from the urban centre toward the rural environment is consistent with the concentration of road traffic, combustion sources, and densely developed surfaces within the metropolitan area. HCHO demonstrated the weakest urban–rural separation among the four indicators. During its 2025 maximum, the Urban Core value was 11.1384×10^{-5}, compared with 10.3958×10^{-5} in the Rural Area. The corresponding differential was 7.1%. The Inner Urban Area and Urban–Rural Fringe presented values of 10.9262×10^{-5} and 10.6080×10^{-5}, respectively. The relatively small spatial difference suggests that HCHO is influenced by processes extending beyond the immediate urban environment, including biogenic emissions and regional photochemical activity. CO showed an intermediate degree of urban differentiation. In 2021, the Urban Core recorded 0.0356, whereas the Rural Area exhibited 0.0316, producing an Urban Core–Rural Area differential of 12.6%. The Inner Urban Area and Urban–Rural Fringe had values of 0.0349 and 0.0333, respectively. Although the gradient was weaker than that observed for NO_2, the spatial ordering indicates an association between CO intensity and developed urban environments.

Table 4. Pollutant-specific peak-year values across the Kayseri urban–rural gradient

Pollutant	Inner Urban Area (IUA)	Rural Area (RA)	Urban Core (UC)	Urban–Rural Fringe (URF)
AER AI	1.2763	1.1413	1.3499	1.2027
CO	0.0349	0.0316	0.0356	0.0333
HCHO ($\times 10^{-5}$)	10.9262	10.3958	11.1384	10.6080
NO_2 ($\times 10^{-5}$)	3.6036	2.8829	3.9967	3.2760

Overall, the pollutant-specific gradients can be ranked according to the magnitude of their Urban Core–Rural Area contrast as follows: NO_2 (38.6%) > AER AI (18.3%) > CO (12.6%) > HCHO (7.1%). This ordering demonstrates that the influence of urban intensity is not uniform across atmospheric constituents. NO_2 displayed the clearest spatial response to the urban structure, whereas HCHO showed a considerably more homogeneous distribution.

The Urban–Rural Fringe (URF) occupied an intermediate position between the Inner Urban Area and Rural Area for most pollutant indicators. Its values were generally lower than those of the two more intensely urbanized classes but higher than those recorded in the Rural Area. This intermediate position reflects the transitional character of the zone, where built-up development, transportation infrastructure, agricultural land, industrial activities, and undeveloped surfaces occur in close proximity. The URF is therefore particularly important for interpreting spatial variability across Kayseri. Unlike the relatively consolidated Urban Core, the fringe contains a greater mixture of land uses and changing activity patterns. Construction activity, expansion of road infrastructure, freight movement, agricultural operations, and new residential development may produce localized atmospheric contrasts that are not apparent from province-wide averages. The strength of this transition differs among pollutants. NO_2 showed the most pronounced separation between the urban centre and rural environment, while HCHO remained comparatively uniform. AER AI occupied an intermediate position, reflecting both urban influences and regional atmospheric forcing. CO also displayed an intermediate gradient, although its spatial pattern indicates a stronger relationship with particular activity centres than with urban intensity alone. Random Forest analysis revealed substantial differences in the relative importance of year, BUPI, and spatial sector among the four atmospheric indicators (Figure 4; Table 5). The results demonstrate that no single explanatory dimension dominated all pollutants, emphasizing the heterogeneous nature of atmospheric processes across Kayseri.

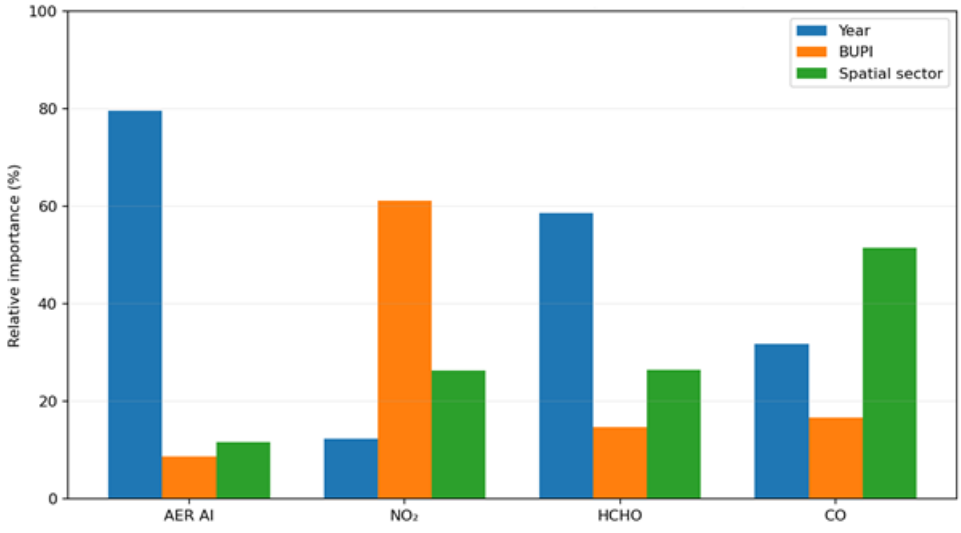

Figure 4. Relative Random Forest importance of year, BUPI, and spatial sector for atmospheric pollutant variability in Kayseri.

Table 5. Relative importance of Random Forest predictors for pollutant variability

Pollutant	Year	BUPI	Spatial Sector
AER AI	79.6%	8.7%	11.7%
NO_2	12.4%	61.2%	26.4%
HCHO	58.7%	14.8%	26.5%
CO	31.8%	16.7%	51.5%

For NO_2, BUPI was the most influential predictor, accounting for 61.2% of the relative model importance. Spatial sector contributed 26.4%, while year accounted for 12.4%. This result closely corresponds with the pronounced urban–rural gradient observed for NO_2 and indicates that the spatial intensity of urban development provides the strongest predictive signal for this pollutant within the model framework. The predictor structure for CO was markedly different. Spatial sector represented the largest contribution at 51.5%, followed by year at 31.8% and BUPI at 16.7%. The dominance of the spatial-sector variable suggests that CO variability is strongly associated with the geographical distribution of specific emission environments. Industrial production, freight transportation, logistics infrastructure, and concentrated combustion activities may therefore exert greater spatial influence than generalized urban intensity. For AER AI, year was overwhelmingly dominant, with a relative importance of 79.6%. BUPI and spatial sector accounted for only 8.7% and 11.7%, respectively. This result indicates that interannual atmospheric conditions and regional-scale environmental forcing are more important for explaining AER AI variability than the local urban-development structure represented by BUPI. HCHO also showed a predominantly temporal signal. Year accounted for 58.7% of the model importance, while spatial sector contributed 26.5% and BUPI contributed 14.8%. The relatively substantial contribution of spatial sector indicates that HCHO nevertheless retains a measurable spatial component within Kayseri, despite its comparatively weak Urban Core–Rural Area contrast. Taken together, the Random Forest results indicate three distinct explanatory patterns. NO_2 is primarily associated with urban intensity, CO with spatial sector, and AER AI and HCHO with interannual variability. This pollutant-specific structure demonstrates the value of combining urban morphology, spatial-sector information, and temporal atmospheric observations rather than relying on a single explanatory dimension.

The combined analysis identifies a clear distinction between pollutants dominated by local urban structure and those characterized by broader temporal variability. NO_2 showed both the strongest urban–rural contrast and the highest BUPI importance, providing the clearest evidence of a relationship between atmospheric pollution and urban development intensity. CO exhibited a moderate urban gradient but was more strongly associated with spatial sector, indicating the importance of geographically concentrated emission sources. AER AI was characterized by substantial interannual variation, particularly during 2022, whereas HCHO displayed a sustained increase accompanied by relatively limited differentiation among urbanization classes. These findings demonstrate that the four-level urban–rural framework captures meaningful differences in atmospheric pollutant behavior across Kayseri. The Urban Core generally exhibited the highest pollutant intensities, while the Rural Area recorded the lowest values. The Urban–Rural Fringe consistently occupied a transitional position and consequently represents a key spatial zone for examining interactions between expanding urban activity and surrounding rural environments

IV. DISCUSSION

The findings from Kayseri demonstrate that the association between urban structure and atmospheric pollution varies substantially among pollutants. NO_2 exhibits the clearest relationship with urban intensity, as reflected by the dominant contribution of BUPI in the Random Forest model. This pattern is consistent with the established relationship between nitrogen dioxide and combustion-related activities, particularly road transportation and other high-intensity urban functions that are concentrated within densely developed areas. This finding is especially relevant to the metropolitan districts of Melikgazi, Kocasinan, and Talas, where population density, impervious surface coverage, and road-network connectivity are considerably greater than across the surrounding provincial landscape. The urban–rural gradient approach therefore provides a more differentiated perspective than treating Kayseri as a homogeneous exposure environment. From a planning perspective, this distinction emphasizes the importance of identifying and managing

emission-intensive corridors and localized hotspots within the broader urban system. Kayseri's industrial structure provides an additional explanation for the pronounced spatial-sector contribution observed for CO. The province has a diversified manufacturing economy together with several organized industrial zones, where industrial production, freight transportation, energy use, and associated road traffic are spatially concentrated. These interconnected activities may generate persistent CO patterns that cannot be adequately represented through a simple binary distinction between urban and rural environments. Incorporating spatial-sector information therefore improves the representation of internal differences within the metropolitan and peri-urban system. The value of the BUPI framework lies in its ability to integrate complementary dimensions of urban intensity rather than relying on a single land-use indicator. Impervious surface fraction provides information on the physical extent of built-up development, but by itself it cannot adequately distinguish between compact residential districts, mixed-use areas, and lower-density industrial environments. Population density introduces a demographic dimension, nighttime radiance provides an indicator of human activity and economic intensity, while road density characterizes the structure of mobility and accessibility. Their combined representation provides a more comprehensive basis for delineating urban–rural gradients. The temporal patterns observed during 2020–2022 further demonstrate that pollutant behaviour cannot be interpreted through a single atmospheric indicator. The marked decline in NO_2 following its 2021 maximum contrasts with the substantial increase in AER AI during 2022. These contrasting trajectories emphasize the importance of evaluating multiple atmospheric constituents simultaneously, particularly in regions where local emissions interact with meteorological conditions and regional atmospheric transport. NO_2 is generally more responsive to changes in combustion activity and vehicular emissions, whereas AER AI represents aerosol-related atmospheric conditions that can be influenced by mineral dust, regional transport, boundary-layer dynamics, and surface conditions. HCHO exhibits a different behaviour because its atmospheric distribution is affected by both primary emissions and secondary photochemical processes. Consequently, variations in HCHO do not necessarily correspond directly with the temporal or spatial behaviour of combustion-related pollutants. For Kayseri, the interpretation of the 2020–2022 period should therefore incorporate urban activity indicators together with meteorological conditions. Future assessments would benefit from explicitly considering wind speed and direction, precipitation, air temperature, boundary-layer height, atmospheric stability, and satellite-derived indicators of dust activity. Such integration would provide a stronger basis for distinguishing changes associated with local emission sources from those arising through regional atmospheric processes. The Urban–Rural Fringe (URF) should not be interpreted simply as a transitional class between the urban core and rural environment. It represents a dynamic spatial interface where agricultural land, construction activity, low-density residential development, industrial expansion, and transportation infrastructure coexist. The simultaneous presence of these land uses creates a heterogeneous environment that may respond rapidly to changes in development pressure, transportation demand, meteorological conditions, and external atmospheric inputs. This complexity also makes the URF particularly challenging to manage through conventional zoning mechanisms alone. For Kayseri, green infrastructure should consequently be considered as a connected spatial network rather than as a collection of isolated parks. Riparian vegetation, agricultural protection belts, tree corridors, ecological buffers, and interconnected open spaces can contribute to landscape connectivity while helping to preserve potential ventilation pathways. Such spatial structures may also reduce direct interactions between high-intensity built-up areas and adjacent agricultural or residential environments.

The URF also warrants more intensive environmental surveillance than relatively stable rural background areas. Monitoring strategies focused predominantly on the urban core may fail to identify emerging hotspots associated with industrial expansion, increasing traffic volumes, road construction, and peri-urban development. Combining satellite observations with strategically distributed ground-based monitoring stations would provide a stronger framework for detecting spatially localized changes and supporting early identification of emerging pollution problems. Four principal planning directions emerge from the Kayseri assessment. First, NO_2 mitigation should concentrate on high-BUPI corridors, particularly major transportation routes and employment-intensive urban axes. Second, industrial areas exhibiting elevated CO signals should be evaluated through source-specific emission inventories, industrial activity

assessments, and freight-transport management. Third, the URF should be managed through continuous green buffers, ecological connectivity, and controlled sequencing of new development. Fourth, open terrain and landscape structures that contribute to atmospheric ventilation should be considered when determining the location and spatial configuration of future urban expansion. These principles support a spatially differentiated approach to environmental and urban management. The urban core may require stronger emphasis on traffic-emission reduction, building-scale interventions, and compact mobility systems; the inner urban belt may benefit from coordinated density and transportation policies; the URF should receive particular attention to green infrastructure, development phasing, and land-use compatibility; and rural areas should continue to be evaluated in relation to agricultural burning, wind-driven dust, and other diffuse emission sources

V. CONCLUSION

This study provides a spatially explicit framework for investigating multi-pollutant behaviour along the urban–rural gradient of Kayseri, Türkiye. The Balanced Urban Parametric Index combines impervious surface fraction, population density, nighttime radiance, and road-network density to characterize multiple dimensions of urban intensity. This integrated framework enables the study area to be differentiated into four principal environments: Urban Core (UC), Inner Urban Area (IUA), Urban–Rural Fringe (URF), and Rural Area (RA). The results reveal distinct pollutant-specific patterns. NO_2 exhibits the strongest association with urban morphology, with BUPI representing 61.2% of the Random Forest variable-importance contribution. CO shows a stronger relationship with spatial sector, highlighting the role of industrial activity, freight transportation, and the internal functional organization of Kayseri. AER AI is primarily associated with temporal variability, whereas HCHO displays a sustained increase over the study period together with a comparatively modest urban–rural differentiation. Among the four spatial environments, the Urban–Rural Fringe emerges as a particularly important planning interface. Its combination of agricultural land, residential expansion, transportation infrastructure, construction activity, and industrial development creates a spatially heterogeneous environment where environmental pressures can intensify rapidly. Consequently, the URF should be considered a strategic management zone in which green infrastructure, land-use regulation, transportation planning, development sequencing, and air-quality monitoring operate as complementary components. Within the urban core, priority should be given to reducing transportation-related emissions, improving mobility systems, and limiting exposure along high-intensity corridors. Industrial sectors require source-oriented emission management supported by detailed inventories and transport assessments. In the fringe environment, continuous green networks, ecological buffers, and carefully phased development can help maintain landscape connectivity and reduce conflicts between expanding urban functions and surrounding agricultural or residential areas. Rural environments, meanwhile, require continued attention to diffuse sources, agricultural activities, dust mobilization, and meteorologically driven pollutant transport. Overall, the findings demonstrate that satellite-based multi-pollutant observations can provide valuable support for spatially differentiated urban and environmental planning when atmospheric indicators are interpreted jointly with urban morphology and spatial structure. The proposed framework moves beyond a simple urban–rural distinction by identifying pollutant-specific relationships between atmospheric variability and different dimensions of urban intensity. The next phase of the research should focus on a fully reproducible Kayseri implementation within Google Earth Engine, using the exact Sentinel-5P TROPOMI collections, directly generated annual and seasonal composites, independent ground-station validation, and a transparently documented machine-learning workflow. This integrated approach would improve data traceability, strengthen uncertainty assessment, and provide a more robust scientific basis for evidence-based air-quality and urban-planning decisions

ACKNOWLEDGMENT

The author acknowledges the European Space Agency, Google Earth Engine, United States Geological Survey, NASA/LP DAAC, WorldPop, and OpenStreetMap contributors for the open datasets underlying the analytical framework. The climatic background was checked against the official Turkish State Meteorological Service statistics.

REFERENCES

1. Suthar, G., Singh, S., Kaul, N., & Khandelwal, S. (2024). Understanding the multifaceted influence of urbanization, spectral indices, and air pollutants on land surface temperature variability in Hyderabad, India. Journal of Cleaner Production, 470, 143284.
2. Zhou, S., Li, M., & Xie, J. (2024). Evaluating urban–rural gradients and urban forms in metropolitan areas: a local climate zone approach with future spatial simulation. Sustainable Cities and Society, 112, 105636.
3. Yang, J., Dong, J., Sun, Y., Zhu, J., Huang, Y., & Yang, S. (2022). A constraint-based approach for identifying the urban–rural fringe of polycentric cities using multi-sourced data. International Journal of Geographical Information Science, 36(1), 114-136.
4. Gao, Y., Zhang, C., Yang, Y., Hong, X., & Liu, C. (2025). Unveiling the spatial and temporal effects of urban vegetation coverage on atmospheric formaldehyde pollution in Chinese megacities over recent decades. Environmental Pollution, 127243.
5. Warren, R. J., Reed, K., Olejnizcak, M., & Potts, D. L. (2018). Rural land use bifurcation in the urban-rural gradient. Urban Ecosystems, 21(3), 577-583.
6. Xie, J., Cai, Y., & Huntsinger, L. (2025). Fragmented expansion induces rural housing wealth differences in urban fringes: Evidence from fine-grained housing data in Shanghai, China. Habitat International, 163, 103492.
7. Zhang, Z., Zhang, G., Song, S., & Su, B. (2020). Spatial heterogeneity influences of environmental control and informal regulation on air pollutant emissions in China. International Journal of Environmental Research and Public Health, 17(13), 4857.
8. Sulistyantara, B., Nasrullah, N., Fatimah, I. S., & Pratiwi, P. I. (2016, January). Study of the Effectivity of Several Tree Canopy Types on Roadside Green Belt in Influencing The Distribution Vertically and Horizontally of CO gas Emitted from Transportation Activities to Vicinity of The Road. In IOP Conference Series: Earth and Environmental Science (Vol. 31, No. 1, p. 012031). IOP Publishing.
9. Xu, S. C., Li, Y. W., Miao, Y. M., Gao, C., He, Z. X., Shen, W. X., ... & Wang, S. X. (2019). Regional differences in nonlinear impacts of economic growth, export and FDI on air pollutants in China based on provincial panel data. Journal of Cleaner Production, 228, 455-466.
10. Feng, Z., Peng, J., & Wu, J. (2020). Using DMSP/OLS nighttime light data and K–means method to identify urban–rural fringe of megacities. Habitat International, 103, 102227.
11. Qi, G., Che, J., & Wang, Z. (2023). Differential effects of urbanization on air pollution: Evidences from six air pollutants in mainland China. Ecological Indicators, 146, 109924.
12. Suthar, G., Singh, S., Kaul, N., & Khandelwal, S. (2024). Diurnal variation of air pollutants and their relationship with land surface temperature in Bengaluru and Hyderabad cities of India. Remote Sensing Applications: Society and Environment, 35, 101204.
13. Han, L., Tan, X., Zhou, W., Li, W., & Qian, Y. (2020). Better urban vegetation planning for maximum utility in air pollutant reduction: A theoretical perspective and preliminary analysis in Chinese cities. Sustainable Cities and Society, 62, 102377.
14. Suthar, G., Singhal, R. P., Khandelwal, S., & Kaul, N. (2023). Spatiotemporal variation of air pollutants and their relationship with land surface temperature in Bengaluru, India. Remote Sensing Applications: Society and Environment, 32, 101011.
15. Lin, B., & Zhu, J. (2018). Changes in urban air quality during urbanization in China. Journal of Cleaner Production, 188, 312-321.
16. Shao, J., Long, Y., Liu, X., Zheng, Y., Song, Y., Wang, J., ... & Zhang, F. (2025). Machine learning-based study on factors influencing street vitality in urban fringe commercial districts: a case of Wuhan. Frontiers of Architectural Research.
17. TUIK (2026). Turkish Statistical Institute (TUIK). Address-based population registration system results, Retrieved February 12, 2026, from https://veriportali.tuik.gov.tr/tr/press/53783
18. TSMS (2026). Turkish State Meteorological Service (TSMS). Average air temperature values, Retrieved February 12, 2026, https://www.mgm.gov.tr/veridegerlendirme/ilve-ilceler-istatistik.aspx

8th International Conference on Engineering, Natural and Social Sciences

September 06-07, 2026: Konya, Turkey

© 2026 Published by All Sciences Academy

https://www.icensos.com/

Kısmi Gölgelenme Altındaki Fotovoltaik Sistemlerde Küresel Maksimum Güç Noktasının Harris Şahinleri Optimizasyonu ile Takibi

Yasin BEKTAŞ[1*], Necibe Füsun OYMAN SERTELLER[2]

[1*]*Elektrik-Enerji Bölümü, Aksaray Üniversitesi, Aksaray, https://orcid.org/0000-0002-3681-0123*
[2]*Elektrik Elektronik Mühendisliği, Marmara Üniversitesi, İstanbul, https://orcid.org/ 0000-0003-3147-2740*

[*1]*yasinbektas@aksaray.edu.tr*

Özet **–**Kısmi gölgeleme koşulları, fotovoltaik (PV) sistemlerin güç-gerilim (P-V) karakteristiğinde birden fazla yerel maksimum noktanın ortaya çıkmasına neden olarak, geleneksel izleme algoritmalarının yerel tepe noktalarında kilitlenmesine yol açmaktadır. Bu çalışmada, kısmi gölgeleme altında çalışan PV dizileri için temel Küresel Maksimum Güç Noktası İzleme (GMPPT) yöntemi olarak Harris Şahinleri Optimizasyonu (HHO) incelenmiş; performans, sınırlı amaç fonksiyonu değerlendirme sayısı dahilinde Gri Kurt Optimizasyonu (GWO), Parçacık Sürü Optimizasyonu (PSO) ve Genetik Algoritma (GA) ile karşılaştırılmıştır. Bypass diyot özelliklerine sahip üç modüllü bir PV dizisi; tekdüze ışınım referans durumu ve farklı şiddetlerdeki tekdüze olmayan kısmi gölgeleme senaryoları altında test edilmiştir. Algoritmaların tümü eşit popülasyon büyüklüğü, aynı maksimum değerlendirme sınırı ve aynı rastgele başlangıç değerleriyle çoklu bağımsız çalışmalara tabi tutulmuştur. Elde edilen deneysel ve simülasyon tabanlı bulgular, HHO'nun yüksek ortalama izleme verimliliği, düşük standart sapma ve minimal güç hatasıyla çalıştığını göstermiştir. Karşılaştırmalı analizler, bazı algoritmaların belirli senaryolarda yakınsama bakımından rekabetçi sonuçlar verse de HHO'nun genel anlamda en üst düzey doğruluk-sağlamlık dengesini kurduğunu ve zorlu gölgeleme koşullarında çok daha yüksek bir güvenilirlik sunduğunu ortaya koymuştur. Sonuçlar, karmaşık ve olumsuz kısmi gölgeleme durumlarına karşı sistem direncini artıran mühendislik uygulamalarında HHO'nun düşük maliyetli ve güçlü bir GMPPT adayı olduğunu kanıtlamaktadır.

Anahtar Kelimeler –Fotovoltaik sistemler, maksimum güç noktası izleme, kısmi gölgeleme, Harris Şahinleri Optimizasyonu ,Parçacık sürü optimizasyonu, küresel maksimum güç noktası.

I. GİRİŞ

Fotovoltaik (PV) güç üretimi, güneş ışınımı ve hücre sıcaklığından doğrudan etkilenmektedir. Tekdüze ışınım koşulları altında, güç-gerilim (P–V) karakteristiği genellikle tek bir baskın maksimum güç noktası (MPP) içermektedir. Ancak kısmi gölgeleme koşulları (PSC); bypass diyotların devreye girmesi ve modüller arası eşit olmayan ışınım dağılımı nedeniyle bir küresel maksimum güç noktası (GMPP) ile birlikte birden fazla yerel tepe noktasının oluşmasına yol açmaktadır. Bu durum, geleneksel MPPT yöntemlerinin yerel tepe noktalarında takılmasına ve üretilebilir enerjinin önemli bir kısmının kaybedilmesine neden olmaktadır [1], [2].

Popülasyon tabanlı meta-sezgisel optimizasyon algoritmaları, türevlenebilir bir PV modeline gereksinim duymaksızın çok modlu arama uzaylarını etkin bir şekilde keşfedebildikleri için GMPPT uygulamalarında cazip bir alternatif sunmaktadır. Parçacık Sürü Optimizasyonu (PSO), sahip olduğu basit konum-hız dinamikleri sayesinde yaygın olarak tercih edilirken; Gri Kurt Optimizasyonu (GWO) hiyerarşik liderlik ve avlanma davranışlarını taklit etmektedir. Genetik Algoritma (GA) ise seçim, çaprazlama ve mutasyon

operatörleriyle klasik bir evrimsel altyapı sağlamaktadır. Heidari ve ark. tarafından literatüre kazandırılan Harris Şahinleri Optimizasyonu (HHO) ise [5], Harris şahinlerinin işbirlikçi avlanma stratejilerini modellemekte; avın kaçış enerjisine bağlı olarak keşif ve sömürü (exploitation) aşamaları arasında adaptif geçiş yapabilmektedir.

Bu çalışmanın temel motivasyonu, orijinal HHO arama denklemlerini değiştirmek değil; HHO çekirdeğini, kasıtlı olarak küçük ve katı bir amaç fonksiyonu değerlendirme bütçesi altında bir GMPPT optimizatörü olarak test etmektir. Bu yaklaşım, optimizatör başarısının yalnızca çok sayıda iterasyon sonucunda elde edilen en iyi değerle değil; aynı zamanda sınırlı hesaplama çabası altındaki doğruluk, en kötü durum davranışı, veri dağılımı ve güç hatası gibi metriklerle de değerlendirilmesi gereken MPPT uygulamaları açısından büyük önem taşımaktadır.

Bu doğrultuda çalışma literatüre üç temel katkı sunmaktadır:

1. HHO, kısmi gölgeleme altındaki üç modüllü bir PV dizisi için birincil görev oranı (duty cycle) optimizatörü olarak formüle edilmiştir.
2. HHO, GWO, PSO ve GA algoritmaları; aynı arama popülasyonu, sabit 72-FES bütçesi, 30 bağımsız çalıştırma ve aynı rastgele sayı tohumları kullanılarak eş koşullar altında karşılaştırılmıştır.
3. Performans değerlendirmesi; ortalama, en iyi ve en kötü durum verimlilikleri, standart sapma, ortalama mutlak güç hatası (MAE), senaryo bazlı davranışlar, FES tabanlı yakınsama dinamikleri ve eşit ağırlıklı sağlamlık sıralaması (Robust Rank Score) kullanılarak kapsamlı bir şekilde gerçekleştirilmiştir.

II. FOTOVOLTAİK SİSTEM VE KISMİ GÖLGELEME MODELİ

A. PV modül modeli

Çalışmada, baypas diyotlarının ters polarma ve iletim karakteristiklerini içeren üç modüllü seri bağlı bir PV dizi mimarisi ele alınmıştır. Modülün elektriksel davranışı; çıkış akımının fotoakım (I_{ph}), diyot ters doyma akımı (I_0), eşdeğer seri direnç (R_s), paralel (şönt) direnç (R_{sh}), mutlak hücre sıcaklığı ve düşen güneş ışınımı parametrelerine fonksiyonel bağımlılığını esas alan tek diyotlu model ile temsil edilmiştir.

Her bir modülün lineer olmayan akım-gerilim ($I-V$) ilişkisi aşağıdaki matematiksel ifade ile formüle edilmektedir:

$$I = I_{ph} - I_o \left[\exp\left(\frac{V + IR_s}{V_t}\right) - 1\right] - \frac{V + IR_s}{R_{sh}} \quad (1)$$

Denklem 1'de; N_s seri bağlı hücre sayısını, a diyot idealite faktörünü ve V_t ısıl gerilimi (thermal voltage) ifade etmektedir. Çevresel değişim dinamikleri incelendiğinde; güneş ışınımı (irradiance) primer olarak fotoakım (I_{ph}) üzerinde skaler bir değişim yaratırken, sıcaklık değişimi hem akım türevlerini hem de açık devre gerilimi (V_{oc}) karakteristiklerini doğrudan etkilemektedir.

Seri bağlı dizi mimarilerinde, modüller üzerinden akan akımın ortak (seri devre sürekliliği gereği eşit) olması esasına dayanarak modül gerilimleri toplanmaktadır. Ayrıca kısmi gölgeleme senaryolarında ortaya çıkan ters voltaj ve sıcak nokta (hot-spot) etkilerini bloke eden baypas diyotlarının iletime geçme durumları numerik olarak model hesaplamalarına entegre edilmiştir.

Simülasyonda kullanılan referans değerler Tablo 1'de özetlenmiştir. Dizi P–V karakteristiği, ortak seri akımın taranması ve modül gerilimlerinin toplanmasıyla sayısal olarak elde edilmiştir.

Tablo 1. PV sistemi ve deneysel parametreler.

Parametre	Değer
PV modülleri	3
Açık devre gerilimi (Voc)	37.3 V
Kısa devre akımı (Isc)	8.21 A
Maksimum güç noktasındaki gerilim (Vmpp)	30.5 V
Maksimum güç noktasındaki akım (Impp):	7.84 A
Yük direnci	60 Ω
Yükseltici (Boost) endüktansı	1.5 mH
Giriş kapasitansı	470 µF
Çıkış kapasitansı	470 µF
Arama ajanları sayısı	12
Maksimum FES (Fonksiyon Değerlendirme Sayısı)	72
Bağımsız çalıştırmalar	30
Görev döngüsü alt sınırı	0.05
Görev döngüsü üst sınırı	0.90

S1–S4 durumlarını tanımlayan ışınım ve sıcaklık koşulları Tablo 2'de listelenirken, bunların sonucunda elde edilen P–V karakteristikleri Şekil 1'de gösterilmiştir. S1, düzgün ışınım referans durumunu temsil ederken; S2–S4 düzensiz ışınım modellerini (kısmi gölgeleme koşullarını) temsil etmektedir. Buna karşılık gelen sayısal olarak belirlenmiş GMPP değerleri, S1–S4 için sırasıyla yaklaşık 687.7 W, 310.6 W, 388.4 W ve 333.1 W'tır. Şekil 1'de görüldüğü gibi, S2–S4 altında ortaya çıkan çoklu tepe noktaları, GMPPT algoritmalarının karşılaştığı yerel optimum zorluğunu açıkça ortaya koymaktadır.

Tablo 2. İncelenen ışınım ve sıcaklık senaryoları.

Senaryo	Panel 1 (W/m²)	Panel 2 (W/m²)	Panel 3 (W/m²)	Sıcaklık (°C)
S1	1000	1000	1000	25
S2	1000	650	300	30
S3	850	450	1000	35
S4	1000	250	700	30

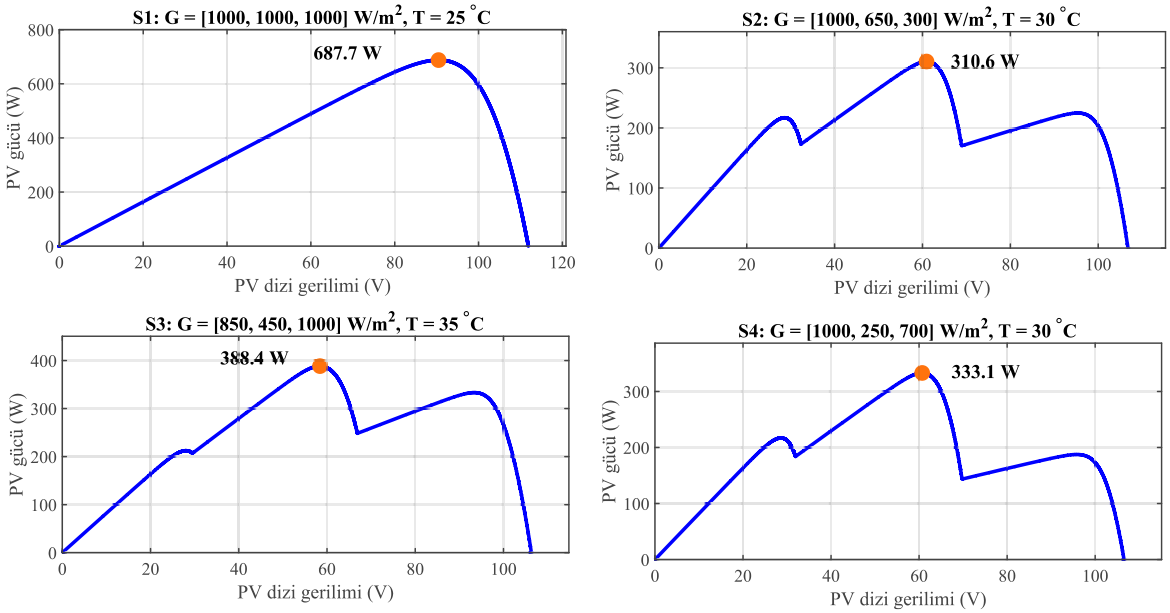

Şekil 1. İncelenen dört çalışma senaryosu altında PV panel dizisinin P–V karakteristikleri.

B. Dönüştürücü tarafı optimizasyon modeli

60 Ω'luk bir yüke besleme yapan bir yükseltici dönüştürücü arayüzü, statik yansıtılan direnç ilişkisi ile temsil edilir. Optimizasyon değişkeni, 0,05 ≤ D ≤ 0,90 aralığındaki görev oranı D'dir. İdeal bir yükseltici kademe için, PV tarafına yansıtılan giriş direnci Rgiriş= Ryük(1−D)^2'dir. Görev oranı, önceden hesaplanan PV güç karakteristiğine eşlenir ve optimize edici, elde edilen PV gücünü maksimize eder. Mevcut çalışma FES tabanlı olduğundan, bir anahtarlama veya zaman alanı dönüştürücü geçişi yerine algoritmaların statik küresel arama yeteneğini değerlendirir.

III. HARRİS ŞAHİNLERİ OPTİMİZASYONU VE ADİL KARŞILAŞTIRMA PROTOKOLÜ

Bu bölümde, HHO tabanlı GMPPT çerçevesi ve kıyaslama algoritmalarıyla adil bir karşılaştırma için benimsenen deneysel protokol sunulmaktadır. Öncelikle görev oranı optimizasyonu için HHO arama mekanizması formüle edilir, ardından tutarlı ve tekrarlanabilir performans değerlendirmesi sağlamak için kullanılan yaygın FES tabanlı değerlendirme prosedürü açıklanır.

A. HHO bazlı GMPPT formülasyonu

HHO, aday görev oranlarını şahinler ve şimdiye kadarki en iyi görev oranını tavşan (av) olarak temsil eder. Kanonik yöntem, avın kaçış enerjisi E'ye göre keşif ve sömürü arasında geçiş yapar. |E| ≥ 1 olduğunda, şahinler arama alanının farklı bölgelerini keşfeder; |E| < 1 olduğunda, mevcut en iyi çözümün komşuluğunu yumuşak veya sert kuşatma mekanizmalarını kullanarak sömürürler ve ilgili kanonik durumlarda hızlı dalışlar etkinleştirilir [5]. Bu çalışmada, bu orijinal HHO mekanizmaları korunurken, sınır işleme ve sonlandırma, amaç fonksiyonu sayısının asla MaxFES = 72'yi aşmaması için uygulanmıştır. Amaç negatif PV gücüdür, bu nedenle amacı en aza indirmek, PV gücünü en üst düzeye çıkarmaya eşdeğerdir.

B. Adil Karşılaştırma Protokolü ve Performans Ölçütleri

Karşılaştırma seti GWO [4], PSO [3] ve GA [6] algoritmalarından oluşmaktadır. Hesaplama adaletini ve bilimsel tarafsızlığı sağlamak amacıyla, algoritmaların tamamı aynı deneysel koşullar ve kısıtlar altında yürütülmüştür. Her bir yöntem $N = 12$ arama ajanı, $0{,}05 \leq D \leq 0{,}90$ görev oranı aralığı ve tam olarak aynı maksimum 72 amaç fonksiyonu değerlendirme (FES) bütçesini kullanmıştır.

Farklı optimizasyon algoritmaları nominal bir yineleme döngüsü içinde farklı sayıda fonksiyon değerlendirmesi gerektirebileceğinden, eşit sayıda yineleme yerine FES tabanlı bir sonlandırma kriteri benimsenmiştir. Bu yaklaşım, tüm algoritmaların aynı sayıda FES ile sınırlandırılması suretiyle hesaplama arama çabasının daha tutarlı ve adil bir ölçüsünü sunmaktadır. Her senaryo için 30 bağımsız çalıştırma gerçekleştirilmiştir. Belirli bir senaryo ve çalıştırma için rastgele tohumlar (random seeds) algoritmalar arasında eşleştirilmiş; böylece yöntemlerin algoritmaya bağlı rastgele akışlar yerine tamamen eşdeğer stokastik koşullar altında performans göstermesi sağlanmıştır. Ortak FES sınırına ulaşıldıktan sonra hiçbir algoritmaya ek değerlendirme hakkı verilmemiştir. Ortak deneysel parametreler Tablo 1'de, incelenen çalışma senaryolarını tanımlayan ışınım ve sıcaklık koşulları ise Tablo 2'de özetlenmiştir.

Algoritmaların başarımını değerlendirmek amacıyla birincil performans göstergesi olarak Maksimum Güç Noktası İzleme (MPPT) verimliliği benimsenmiştir. Bu verimlilik şu şekilde tanımlanmaktadır:

$$\eta_{\mathrm{MPPT}} = 100 \times \frac{P_{\mathrm{alg}}}{P_{\mathrm{GMPP}}} \quad (2)$$

Burada P_{alg} optimizasyon algoritması tarafından elde edilen en iyi PV gücünü, P_{GMPP} ise tam sayısal P–V karakteristiğinden belirlenen gerçek küresel maksimum gücü temsil etmektedir.

Ortalama MPPT verimliliğinin yanı sıra, algoritmaların arama yeteneğini ve kararlılığını kapsamlı bir şekilde incelemek amacıyla bağımsız çalıştırmalar üzerindeki en iyi ve en kötü verimlilik değerleri de dikkate alınmıştır. Özellikle en kötü durum sonucu ayrıca vurgulanmıştır; çünkü ortalama bazda yüksek

performans gösteren ancak zaman zaman yerel bir tepe noktasında takılan bir izleyici, pratik uygulamalar açısından istenmeyen bir durumdur. Çalıştırma bazlı değişkenliği ölçmek için standart sapma kullanılırken, Ortalama Mutlak Hata (MAE) bir algoritma tarafından belirlenen güç ile gerçek GMPP arasındaki ortalama mutlak güç sapmasını ifade etmektedir. Bunlara ek olarak, donanım ve uygulamaya bağlı ikincil bir gösterge olarak ortalama çalışma süresi (hesaplama süresi) de kaydedilmiştir. Bu tamamlayıcı ölçütler, algoritmaların yalnızca ortalama doğruluklarına göre değil; aynı zamanda kısmi gölgeleme koşulları altındaki tutarlılıklarına ve en kötü durum dirençlerine göre de değerlendirilmesini sağlamaktadır.

IV. SONUÇLAR VE TARTIŞMA

A. Genel MPPT performansı

Tablo 3, HHO'nun incelenen yöntemler arasında en güçlü genel performansı elde ettiğini göstermektedir. Ortalama verimliliği %99,9727 iken, PSO için %99,8701, GWO için %99,6764 ve GA için %99,0999'dur. Daha da önemlisi, HHO en kötü durum verimliliğini %99,5808 olarak korurken, PSO, GWO ve GA sırasıyla %88,5261, %85,7670 ve %85,4493'e düşmektedir. HHO ayrıca en küçük dağılımı (%0,0695) ve en düşük MAE'yi (0,0985 W) üretmektedir. Dört yöntemin de en iyi verimliliği esasen %100'dür, bu nedenle en iyi çalışma istatistiği tek başına güvenilirliklerini ayırt etmek için yeterli değildir.

Tablo 3. İncelenen ışınım ve sıcaklık senaryoları.

Algoritma	Ortalama Verim (%)	En iyi Verim (%)	En kötü Verim (%)	Standart Sapma (%)	MAE (W)	Ortalama Zaman (s)	FES
HHO	99.9727	99.9997	99.5808	0.0695	0.0985	0.00126	72
GWO	99.6764	99.9997	85.7670	1.8288	1.2597	0.00107	72
PSO	99.8701	99.9997	88.5261	1.0494	0.5070	0.00107	72
GA	99.0999	99.9997	85.4493	2.6982	3.8289	0.00117	72
HHO	99.9727	99.9997	99.5808	0.0695	0.0985	0.00126	72

Şekil 2, tek bir çalıştırmanın yakınsama izini sunmak yerine, 30 çalıştırma üzerinden elde edilen medyan yörünge ve çeyrekler arası aralığını kullanmaktadır. Bu gösterim, hem yakınsama davranışını hem de çalıştırmadan çalıştırmaya değişkenliği gösterdiği için stokastik MPPT karşılaştırması için daha bilgilendiricidir. Tüm yöntemler, küçük 72-FES bütçesi altında GMPP'ye hızla yaklaşırken, yakınlaştırılmış bölge GMPP'ye yakın farklılıkları görünür hale getirir.

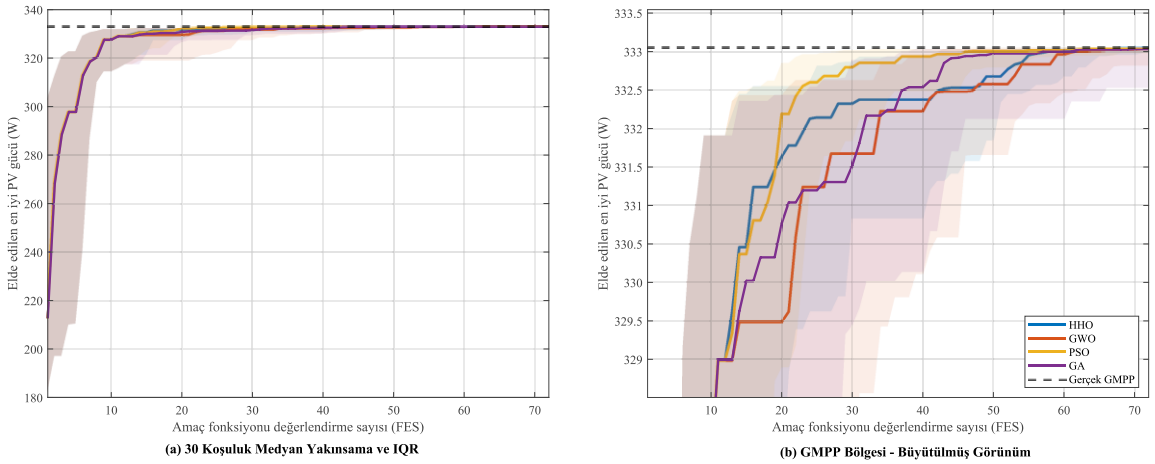

Şekil 2. S4 için FES-Tabanlı Yakınsama

B. Senaryo bazlı analiz

Senaryo bazlı karşılaştırma, ortalama performans ile genel sağlamlık arasında önemli bir ayrımı ortaya koymaktadır. HHO, S1 ve S3 senaryolarında hem ortalama hem de en kötü durum verimliliğinde en iyi performansı gösterirken, PSO ise S2 ve S4 senaryolarında en iyi performansı sergilemektedir. En belirgin fark S3 senaryosunda görülmektedir: HHO, %99,9804'lük ortalama verimlilik ve %99,8822'lik en kötü durum verimliliğine ulaşırken, PSO en kötü çalışmasında %88,5261'e düşmekte ve GWO ile GA %86'nın altına düşmektedir. Dolayısıyla, PSO seçilen senaryolarda biraz daha doğru sonuçlar verebilirken, HHO zorlu asimetrik durumda ciddi performans düşüşlerine karşı önemli ölçüde daha az hassastır.

Tablo 4. Senaryo bazında ortalama ve en kötü durum MPPT verimlilikleri (%).

Senaryo	İstatistik	HHO	GWO	PSO	GA	HHO
S1	Ortlama	**99.99194**	99.95555	99.98610	99.46280	99.99194
	En kötü	**99.91012**	99.68904	99.80421	90.67950	99.91012
S2	Ortlama	99.95888	99.88220	**99.97745**	99.83135	99.95888
	En kötü	99.67732	98.74083	**99.88992**	98.00432	99.67732
S3	Ortlama	**99.98037**	98.92187	99.54202	97.36812	99.98037
	En kötü	**99.88217**	85.76697	88.52614	85.44925	99.88217
S4	Ortlama	99.95954	99.94600	**99.97488**	99.73729	99.95954
	En kötü	99.58075	99.72441	**99.81554**	98.01249	99.58075

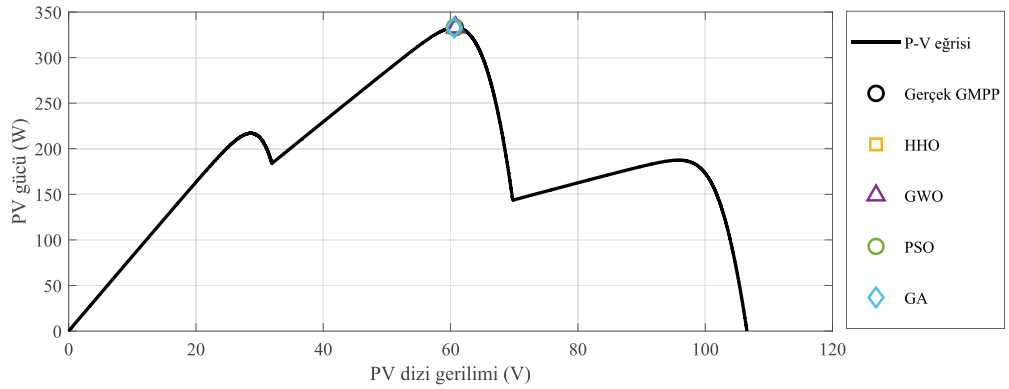

Şekil 3. S4 için P–V karakteristiği ve HHO, GWO, PSO ve GA yöntemleriyle elde edilen nihai çalışma noktaları.

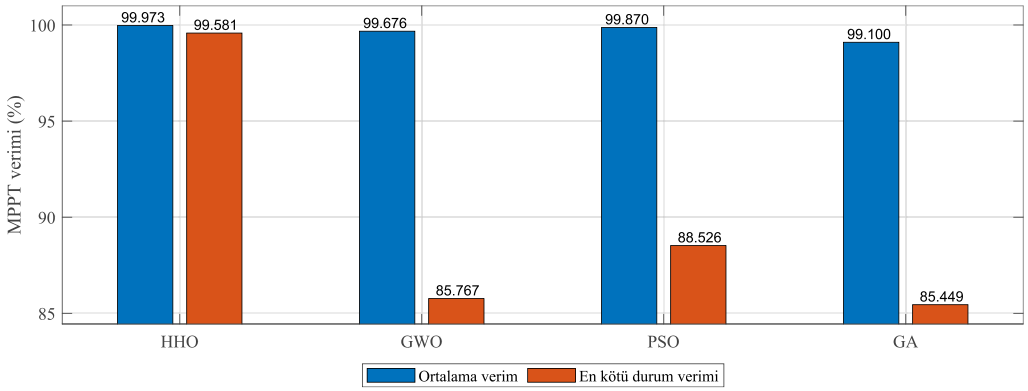

Şekil 4. İncelenen algoritmaların genel ortalama ve en kötü durum MPPT verimlilikleri.

Şekil 3 ve 4, sonuçların tamamlayıcı görünümlerini sunmaktadır. S4'teki nihai çalışma noktaları, temsili çalıştırmalar için küresel zirveye yakın konumdadır; oysa toplu ortalama/en kötü karşılaştırması, %100'e yakın en iyi değerler tarafından gizlenen ara sıra meydana gelen başarısızlıkları ortaya koymaktadır. PSO,

GWO ve GA'nın ortalama ve en kötü değerleri arasındaki büyük fark, esas olarak daha çok modlu senaryolardaki başarısız çalıştırmalardan kaynaklanmaktadır.

C. Senaryo ortalamaları ve tanımlayıcı sağlamlık sıralaması

Şekil 5, tüm senaryolarda evrensel olarak en iyi tek bir yöntemin bulunmadığını doğrulamaktadır: HHO, S1 ve S3'te önde giderken, PSO ise S2 ve S4'te önde gelmektedir. Bununla birlikte, kayıpların büyüklüğü asimetriktir. PSO'nun HHO'ya göre senaryo avantajları küçüktür, oysa HHO, S3'te diğer yöntemlerde gözlemlenen büyük bozulmayı önlemektedir. Bu davranış, toplu sağlamlık ölçümlerinin neden HHO'yu desteklediğini açıklamaktadır.

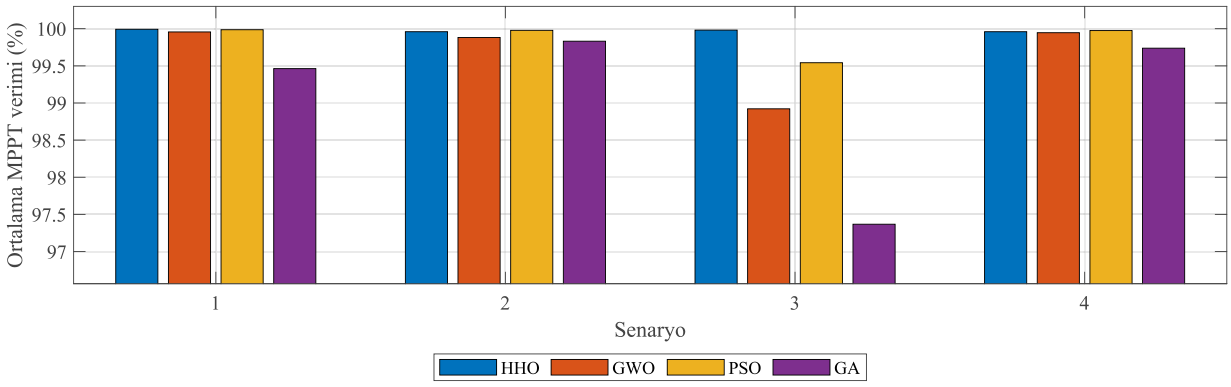

Şekil 5. Senaryo bazında HHO, GWO, PSO ve GA algoritmalarının ortalama MPPT verimliliği.

Tablo 5. Eşit ağırlıklı tanımlayıcı sağlamlık sıralaması.

Sıra	Algoritma	Ortalma Verim (%)	En kötü Verim (%)	Standart Sapma (%)	MAE (W)	Sıralama Ortalama	Sıralama En Kötü	Sıralama Standart Sapma	Sıralaması MAE	Skor
1	HHO	99.97268	99.58075	0.069466	0.098525	1	1	1	1	1.0
2	PSO	99.87011	88.52614	1.049431	0.507036	2	2	2	2	2.0
3	GWO	99.67641	85.76697	1.828775	1.259725	3	3	3	3	3.0
4	GA	99.09989	85.44925	2.698159	3.828903	4	4	4	4	4.0

Kompakt ve çok kriterli bir değerlendirme için, ortalama verimlilik (daha yüksek daha iyidir), en kötü durum verimliliği (daha yüksek daha iyidir), standart sapma (daha düşük daha iyidir) ve MAE (daha düşük daha iyidir) olmak üzere dört sıralama hesaplanır. Bu dört sıralamanın aritmetik ortalaması dayanıklı sıralama puanı olarak kullanılır; daha düşük değer daha iyidir. HHO, dört kriterin hepsinde birinci sırada yer alır ve bu nedenle 1,0 puan alır. PSO, GWO ve GA sırasıyla 2,0, 3,0 ve 4,0 puan alırlar.

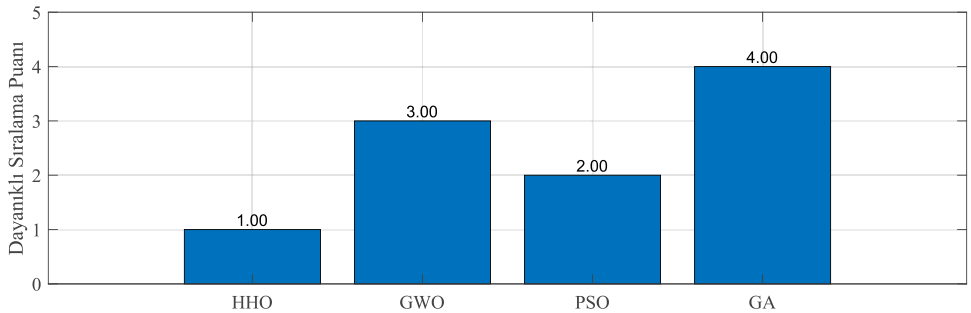

Şekil 6. Senaryo bazında HHO, GWO, PSO ve GA algoritmalarının ortalama MPPT verimliliği.

Şekil 6, aynı tanımlayıcı sıralamayı görsel olarak özetlemektedir. Bu puan, istatistiksel bir anlamlılık testi olarak yorumlanmamalıdır; aksine, dört tamamlayıcı performans göstergesinin şeffaf bir toplamıdır. Mevcut senaryolar ve FES bütçesi dahilinde, HHO'yu genel doğruluk-sağlamlık uzlaşması açısından en iyi seçenek olarak desteklemektedir.

Bu çalışma, kısmi gölgeleme altında üç modüllü bir PV dizisi için birincil GMPPT yöntemi olarak Harris Şahinleri Optimizasyonunu (HHO) değerlendirdi ve GWO, PSO ve GA ile adil bir şekilde karşılaştırdı. 12 arama ajanı, 72 FES, senaryo başına 30 bağımsız çalıştırma ve eşleştirilmiş tohumlarla HHO, %99,9727 ortalama MPPT verimliliği, %99,5808 en kötü durum verimliliği, %0,0695 standart sapma ve 0,0985 W MAE elde etti. PSO, S2 ve S4'te HHO'dan biraz daha iyi performans gösterdi, ancak HHO, S1 ve S3'te en iyi performansı gösterdi ve S3'te çok daha güçlü bir en kötü durum sonucu sergiledi. Bu nedenle, eşit ağırlıklı sağlamlık sıralamasında HHO genel olarak birinci sırada yer aldı. Bu sonuçlar, hem izleme doğruluğu hem de olumsuz stokastik çalıştırmalara karşı direnç dikkate alındığında, orijinal HHO arama mekanizmasının rekabetçi, düşük bütçeli bir GMPPT stratejisi olduğunu göstermektedir.

V. SONUÇ

Bu çalışmada, kısmi gölgeleme koşulları altında üç modüllü bir PV dizisi için birincil GMPPT yöntemi olarak HHO ele alınmış ve elde edilen sonuçlar, GWO, PSO ve GA yöntemleriyle eşit ağırlıklı tanımlayıcı sağlamlık sıralaması temelinde karşılaştırılmıştır. Her senaryo için 12 arama ajanı, 72 FES, 30 bağımsız çalıştırma ve eşleştirilmiş tohumlar kullanılmıştır. HHO, ortalama %99,9727 MPPT verimliliği, %99,5808 en kötü durum verimliliği, %0,0695 standart sapma ve 0,0985 W MAE elde etmiştir. PSO, S2 ve S4 senaryolarında HHO'dan biraz daha iyi performans gösterirken, HHO S1 ve S3 senaryolarında en iyi performansı sergilemiş ve özellikle S3'te belirgin biçimde daha güçlü bir en kötü durum sonucu elde etmiştir. Bu nedenle, eşit ağırlıklı sağlamlık sıralamasında HHO genel olarak birinci sırada yer almıştır. Bu sonuçlar, hem izleme doğruluğu hem de olumsuz stokastik çalıştırmalara karşı dayanıklılık dikkate alındığında, orijinal HHO arama mekanizmasının rekabetçi ve düşük bütçeli bir GMPPT stratejisi olduğunu göstermektedir.

KAYNAKLAR

[1] Mohapatra, A., Nayak, B., Das, P., & Mohanty, K. B. (2017). A review on MPPT techniques of PV system under partial shading condition. Renewable and Sustainable Energy Reviews, 80, 854-867.

[2] J. Ahmed and Z. Salam, “A critical evaluation on maximum power point tracking methods for partial shading in PV systems,” Renewable and Sustainable Energy Reviews, vol. 47, pp. 933–953, 2015, doi: 10.1016/j.rser.2015.03.080.

[3] J. Kennedy and R. Eberhart, “Particle swarm optimization,” in Proc. IEEE International Conference on Neural Networks, vol. 4, 1995, pp. 1942–1948, doi: 10.1109/ICNN.1995.488968.

[4] S. Mirjalili, S. M. Mirjalili, and A. Lewis, “Grey Wolf Optimizer,” Advances in Engineering Software, vol. 69, pp. 46–61, 2014, doi: 10.1016/j.advengsoft.2013.12.007.

[5] A. A. Heidari, S. Mirjalili, H. Faris, I. Aljarah, M. Mafarja, and H. Chen, “Harris hawks optimization: Algorithm and applications,” Future Generation Computer Systems, vol. 97, pp. 849–872, 2019, doi: 10.1016/j.future.2019.02.028.

8th International Conference on Engineering, Natural and Social Sciences

September 06-07, 2026: Konya, Turkey

© 2026 Published by All Sciences Academy

https://www.icensos.com/

Electrified Vehicle Adoption in Türkiye: Operational CO_2 Emissions, Economic Payback, and Consumer Perception

Aybüke Sena Ünal[1], Ömer Önder Erat[1*], Bülent Yeşilata[1]

[1] *Ankara Yıldırım Beyazıt University, Faculty of Engineering and Natural Sciences, Department of Energy Systems Engineering, Ankara, Turkey*

[*] *omerondererat@aybu.edu.tr*

Abstract **–** The transition from internal combustion engine vehicles (ICEVs) to hybrid electric vehicles (HEVs) and battery electric vehicles (BEVs) requires the simultaneous consideration of technical performance, operational emissions, energy cost, economic payback, charging infrastructure, and consumer acceptance. This study compares five representative vehicles in Türkiye (abbreviated to avoid commercial disclosure): FE 1.4 Fire, RM 1.3 TCe, RC E-Tech Full Hybrid 145, TG T10X V2 RWD, and TA Model Y Long Range. The evaluation combines vehicle performance and consumption data, a grid-adjusted operational CO_2 calculation using 469 gCO_2/kWh, an economic break-even calculation using 50.85 TL/L gasoline and 2.58 TL/kWh residential electricity, and a structured public survey with 80 vehicle owners of different brands. The calculated indirect operational emissions are 89.5 gCO_2/km for the TG T10X and 73.6 gCO_2/km for the TA Model Y, compared with direct tailpipe values of 144 gCO_2/km for the FE, 140 gCO_2/km for the RM, and 96 gCO_2/km for the RC HEV. The break-even distance for BEV ownership is approximately 133,000 km. Although 68.8% of respondents consider current BEV ranges sufficient for daily urban use, range anxiety remains the leading adoption barrier at 31.2%, and 40.0% identify expansion of charging infrastructure as the most important improvement. In addition, 76.3% regard hybrid vehicles as a suitable interim solution. The results show that lower operational emissions and energy costs support electrification, but purchase-cost recovery and confidence in charging infrastructure remain decisive for adoption in Türkiye.

Keywords – Operational CO_2 emissions; economic break-even; range anxiety; charging infrastructure; consumer perception.

I. INTRODUCTION

Global energy policies and environmental sustainability requirements are accelerating the transition from conventional fossil-fuel-based transport toward electrified powertrains [1]. In the Turkish passenger-car market, ICEVs, HEVs, and BEVs coexist across major segments, creating a practical need to compare these technologies under the same technical, economic, environmental, and user-oriented framework. The five vehicle configurations considered here represent three powertrain classes: FE 1.4 Fire and RM 1.3 TCe as gasoline ICEVs, RC E-Tech Full Hybrid 145 as an HEV, and TG T10X V2 RWD and TA Model Y Long Range as BEVs. Their technical comparison includes power, torque, acceleration, energy consumption, operational CO_2, and curb mass. The economic comparison uses 2025 energy prices, while the environmental comparison assigns the Turkish electricity-grid emission factor of 469 gCO_2/kWh to BEV electricity consumption [2,3]. A purely engineering-based comparison does not fully explain purchase behavior. Consumer decisions are also shaped by initial purchase price, expected operating cost, charging availability, battery-life concerns, and confidence in usable driving range. The survey therefore complements the numerical vehicle assessment by measuring perceptions of long-term economic advantage, range sufficiency, charging infrastructure, battery cost, and the role of HEVs during the transition to full electrification.

This study addresses three linked questions. First, how do the selected ICEV, HEV, and BEV configurations compare in technical performance and operational CO_2 under the 469 gCO_2/kWh grid factor? Second, how do the lower energy costs of the BEVs relate to the approximately 133,000 km economic break-even distance? Third, do consumer perceptions align with these engineering and economic results, particularly with respect to range anxiety, charging infrastructure, and the perceived transition role of hybrid vehicles? To answer these questions consistently, the following methodology combines vehicle-specific technical data, grid-adjusted operational CO_2 calculations, energy-cost comparisons, break-even analysis, and descriptive survey results within a common evaluation framework.

II. Materials and Method

i. Reference Vehicles and Technical Inputs

Five configurations were evaluated: FE 1.4 Fire, RM 1.3 TCe, RC E-Tech Full Hybrid 145, TG T10X V2 RWD, and TA Model Y Long Range. These alternatives cover gasoline ICEV, HEV, and BEV architectures and provide a common basis for comparing powertrain performance, energy use, operational emissions, and vehicle mass. To establish the engineering baseline for the subsequent emission and cost calculations, Table 1 summarizes the power, torque, acceleration, energy consumption, operational CO_2, and curb-mass values used for the five configurations.

Table 1. Technical specifications and baseline performance values of the selected vehicles

Parameter	FE 1.4 Fire	RM 1.3 TCe	RC E-Tech 145	TG T10X V2 RWD	TA Model Y Long Range
Power	70 kW	103 kW	107 kW	160 kW	378 kW
Torque	127 Nm	240 Nm	205 Nm	350 Nm	493 Nm
0–100 km/h	11.8 s	9.2 s	9.3 s	7.8 s	5.0 s
Fuel/Energy consumption	6.4 L/100 km	5.9 L/100 km	4.2 L/100 km	19.1 kWh/100 km	15.7 kWh/100 km
Operational CO_2	144 g/km	140 g/km	96 g/km	89.5 g/km (grid-related)	73.6 g/km (grid-related)
Curb mass	~1150 kg	~1320 kg	~1235 kg	2126 kg	1979 kg

Table 1 shows a clear powertrain-dependent trade-off between dynamic performance and vehicle mass. The TG T10X delivers 160 kW and 350 Nm, while the TA Model Y reaches 378 kW and 493 Nm; their 0–100 km/h acceleration times are 7.8 and 5.0 s. These values exceed the 70–107 kW power range and 127–240 Nm torque range of the two gasoline vehicles and the hybrid. The performance advantage is accompanied by higher curb mass: 2126 kg for the TG T10X and 1979 kg for the TA Model Y, compared with approximately 1150 kg for the FE, 1320 kg for the RM, and 1235 kg for the RC HEV. This performance–mass contrast provides the technical context for the emission and operating-cost comparisons that follow.

ii. Grid-Adjusted Operational CO_2 Calculation

BEVs have zero direct Tank-to-Wheel tailpipe CO_2 emissions during operation, but electricity generation produces indirect emissions. A Turkish national grid emission factor of 469 gCO_2/kWh was therefore assigned to BEV electricity consumption [2,3]. The indirect operational emission per kilometer was calculated as [1,2]:

$$E_{indirect} = \left(C_{avg} \times G_{intensity}\right) / 100 \quad (1)$$

where $E_{indirect}$ is expressed in gCO_2/km, Cavg is the vehicle electricity consumption in kWh/100 km, and Gintensity is the grid emission factor in gCO_2/kWh. For the TG T10X, 19.1 kWh/100 km gives (19.1 × 469)/100 = 89.579 gCO_2/km, reported as 89.5 gCO_2/km. For the TA Model Y, 15.7 kWh/100 km gives (15.7 × 469)/100 = 73.633 gCO_2/km, reported as 73.6 gCO_2/km. The FE, RM, and RC HEV are represented by direct tailpipe values of 144, 140, and 96 gCO_2/km, respectively. This boundary is operational rather than full life cycle. Battery production, vehicle manufacturing, end-of-life processes, and recycling are not

included. The comparison therefore distinguishes direct tailpipe emissions from grid-related BEV emissions without claiming a complete life-cycle carbon balance. Having established the operational-emission basis, the analysis next examines how the same vehicle-consumption values translate into energy cost and economic payback.

iii. Energy Cost and Break-Even Analysis

The 2025 energy-price inputs are 50.85 TL/L for 95-octane gasoline, 2.58 TL/kWh for residential electricity, and 13.05 TL/kWh for commercial/fast charging [4–5]. The break-even distance balances the higher initial purchase price of a BEV against its lower energy and maintenance expenditure [6]:

$$D_{be} = (P_{bev} - P_{icev})/[(F_{km} + M_{km}) - (E_{km} + m_{km})] \quad (2)$$

where P_{BEV} and P_{ICEV} are the initial purchase prices, F_{km} and E_{km} are the gasoline and electricity costs per kilometer, and Mkm and mkm represent periodic maintenance costs per kilometer for the ICEV and BEV, respectively. Applying the 2025 unit energy prices to the vehicle-specific consumption values produces the energy-only operating costs summarized in Table 2. For the RM, the 5.9 L/100 km value in Table 1 is used consistently in this calculation.

Table 2. Energy-only operating cost calculated from vehicle consumption and 2025 energy prices

Vehicle	Consumption	Energy price	Energy cost
FE 1.4 Fire	6.4 L/100 km	50.85 TL/L	3.25 TL/km
RM 1.3 TCe	5.9 L/100 km	50.85 TL/L	3.00 TL/km
RC E-Tech HEV	4.2 L/100 km	50.85 TL/L	2.14 TL/km
TG T10X – residential	19.1 kWh/100 km	2.58 TL/kWh	0.49 TL/km
TA Model Y – residential	15.7 kWh/100 km	2.58 TL/kWh	0.41 TL/km
TG T10X – fast charging	19.1 kWh/100 km	13.05 TL/kWh	2.49 TL/km
TA Model Y – fast charging	15.7 kWh/100 km	13.05 TL/kWh	2.05 TL/km

Table 2 demonstrates that charging source materially changes the BEV operating-cost advantage. With residential electricity, the TG T10X and TA Model Y require approximately 0.49 and 0.41 TL/km for propulsion energy, compared with 3.25 TL/km for the FE, 3.00 TL/km for the RM, and 2.14 TL/km for the RC HEV. At 13.05 TL/kWh fast-charging prices, the BEV values rise to approximately 2.49 and 2.05 TL/km. Residential charging therefore creates the largest operating-cost advantage, while frequent fast charging narrows the difference, particularly relative to the hybrid vehicle. Using the 50.85 TL/L gasoline and 2.58 TL/kWh residential-electricity case together with the purchase-price and maintenance terms in Eq. (2), the break-even distance is approximately 133,000 km. At 15,000 km/year, 133,000 km corresponds to approximately 8.9 years. The result therefore describes a mileage-dependent economic transition rather than an immediate purchase-price advantage.

iv. Supportive Consumer Face-to-Face Survey

Consumer perception was evaluated using a supportive face-to-face survey of 80 participants. The target group consisted of current public vehicle owners of different brands and potential public vehicle buyers in Türkiye during 2025–2026. A five-point Likert scale was used for perception-based variables such as range sufficiency and technology awareness, while categorical questions were used for vehicle preference, adoption barriers, and priority improvements.

The supportive survey examined long-term economic expectations, range anxiety, charging-infrastructure confidence, battery-life and replacement-cost concerns, tailpipe-emission awareness, sustainability factors, and the role of hybrid vehicles during the transition to BEVs. The responses are interpreted descriptively; no statistical significance claim is made. The survey variables were then compared with the calculated emission, energy-cost, and break-even results to identify where consumer perceptions are consistent with, or diverge from, the engineering evidence.

Table 3. Categorized survey questions used for consumer perception analysis

Category	Survey Questions / Statements
Demographics & Background	• What type of fuel does your current vehicle use? • How would you rate your own level of knowledge about electric/hybrid vehicle technologies?
Economic & Transition Perspectives	• If you were offered three car options in the same price range, which one would you choose? • I believe that electric vehicles can be more economically advantageous than internal combustion vehicles in the long run*. • Hybrid vehicles can be a suitable interim solution in the transition to electric vehicles*.
Technical & Environmental Awareness	• Are there any emissions from the exhaust pipe during use in fully electric vehicles? • Which of the following should be considered when evaluating the life cycle emissions of electric vehicles? • Which vehicle type is technically more complex because it uses both an internal combustion engine and an electric drive system?
Infrastructure & Adoption Barriers	• I believe the current range of electric vehicles is sufficient for daily urban use.* • What is the biggest obstacle to purchasing an electric vehicle? • In your opinion, what is the most important improvement needed to promote the widespread adoption of electric vehicles?

(Note: Statements marked with an asterisk (*) were evaluated using a 5-point Likert scale ranging from "Strongly Disagree" to "Strongly Agree").

III. Results and Discussion

i. Technical Performance and Operational CO_2

The largest performance contrast appears between the gasoline baseline and the two BEVs. The FE produces 70 kW and 127 Nm and accelerates from 0 to 100 km/h in 11.8 s at an approximate curb mass of 1150 kg. The RM produces 103 kW and 240 Nm, reaches 100 km/h in 9.2 s, and has an approximate mass of 1320 kg. The RC HEV produces 107 kW and 205 Nm, reaches 100 km/h in 9.3 s, and has an approximate mass of 1235 kg. The TG T10X increases output to 160 kW and 350 Nm with a 7.8 s acceleration time, while the TA Model Y reaches 378 kW and 493 Nm with a 5.0 s acceleration time. The two BEVs are therefore dynamically stronger but also substantially heavier than the three combustion-based alternatives. To isolate the environmental component of the comparison from the broader technical specifications, Table 4 places all five operational CO_2 values on the common gCO_2/km basis used in this analysis.

Table 4. Operational CO_2 comparison under a 469 gCO_2/kWh Turkish grid factor

Vehicle	Powertrain	Operational CO_2	Emission basis
FE 1.4 Fire	ICEV	144.0 g/km	Direct tailpipe
RM 1.3 TCe	ICEV	140.0 g/km	Direct tailpipe
RC E-Tech	HEV	96.0 g/km	Direct tailpipe
TG T10X	BEV	89.5 g/km	Grid-related indirect
TA Model Y	BEV	73.6 g/km	Grid-related indirect

Table 4 places the TA Model Y at the lowest operational value, 73.6 gCO_2/km, followed by the TG T10X at 89.5 gCO_2/km and the RC HEV at 96.0 gCO_2/km. Relative to the FE value of 144.0 gCO_2/km, the TG value is lower by 54.5 gCO_2/km, or 37.8%, and the TA value is lower by 70.4 gCO_2/km, or 48.9%. The difference between the RC HEV and the TG T10X is only 6.5 gCO_2/km, showing that the hybrid approaches the grid-adjusted operational CO_2 level of the higher-consumption BEV. These comparisons remain limited to operation and do not represent complete life-cycle emissions. The operational-emission advantage of the

selected BEVs must nevertheless be considered together with economic payback, because lower operational CO_2 does not imply lower total ownership cost over short driving distances.

ii. Operating-Energy Cost and Economic Payback

The energy-only operating costs show the strongest BEV advantage under residential charging. At 50.85 TL/L gasoline, the FE requires approximately 3.25 TL/km, the RM 3.00 TL/km, and the RC HEV 2.14 TL/km. At 2.58 TL/kWh residential electricity, the TG T10X requires approximately 0.49 TL/km and the TA Model Y 0.41 TL/km. At 13.05 TL/kWh fast-charging prices, the corresponding BEV costs rise to 2.49 and 2.05 TL/km. The magnitude of these per-kilometer differences becomes economically meaningful only when accumulated over sufficient driving distance. The break-even distance is approximately 133,000 km; at 15,000 km/year, this corresponds to about 8.9 years. Survey expectations are directionally consistent with this result: 62.5% of participants believe BEVs become more economically advantageous than ICEVs in the long term. Electricity and fuel prices are selected as the main economic factor by 42.5%, while 41.3% select the combined effect of energy prices, annual mileage, maintenance cost, and initial purchase price. Although these calculations quantify the economic consequences of electrification, purchase decisions also depend on whether users are confident that BEVs can meet practical mobility requirements.

iii. Range Anxiety and Charging-Infrastructure Confidence

Range anxiety is the most frequently selected obstacle to BEV purchase at 31.2%. Battery life and replacement cost follow at 26.2%, insufficient charging infrastructure at 20.0%, high initial purchase price at 15.0%, and uncertainty about resale value at 7.5%. The distribution of these barriers is shown in Figure 1.

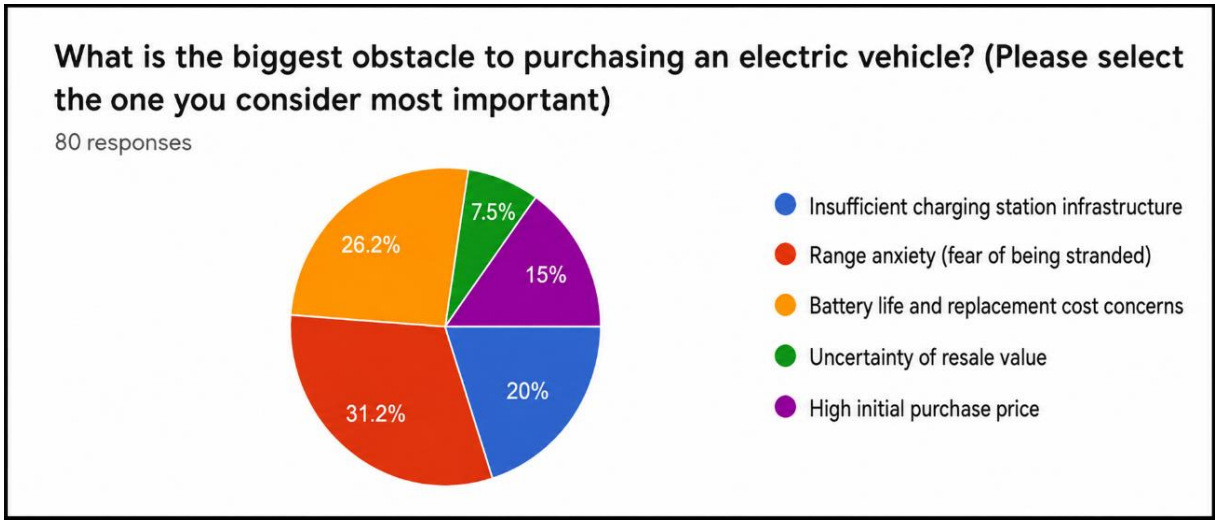

Fig. 1 Main perceived obstacles to BEV adoption among 80 participants.

Figure 1 shows that the three most frequently selected barriers-range anxiety (31.2%), battery life and replacement cost (26.2%), and insufficient charging infrastructure (20.0%)-account for 77.4% of responses. High initial purchase price accounts for 15.0% and uncertainty about resale value for 7.5%. The distribution therefore concentrates perceived adoption risk around usable range, battery durability, and charging access rather than purchase price alone. Because range anxiety is the largest single barrier, the range-sufficiency responses are critical for determining whether respondents actually consider current BEV range inadequate for routine urban mobility. The full distribution is presented in Figure 2.

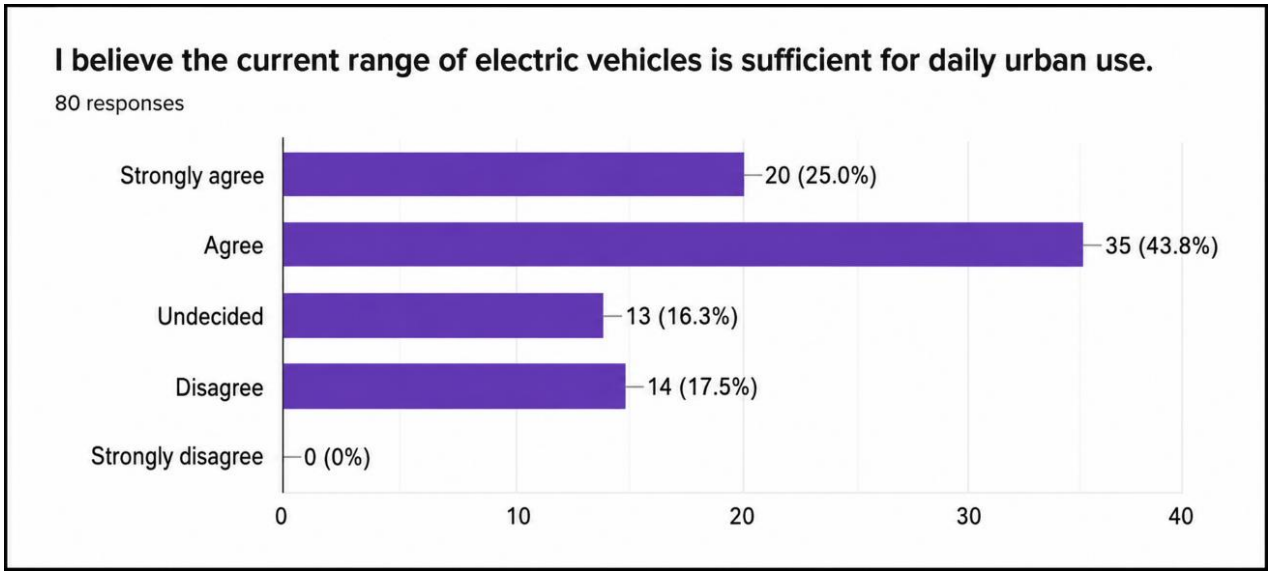

Fig. 2 Perceived sufficiency of current BEV range for daily urban use among 80 participants.

Figure 2 shows that 20 participants (25.0%) totally agree and 35 participants (43.8%) agree that current BEV range is sufficient for daily urban use, giving a combined agreement rate of 68.8%. Thirteen participants (16.3%) are undecided, 14 participants (17.5%) disagree, and no participant selects "totally disagree." Thus, 55 of 80 participants express agreement with daily urban range sufficiency even though range anxiety remains the largest purchase barrier. This contrast indicates that the concern extends beyond routine urban range to charging availability, charging time, and uncertainty during occasional long-distance travel. The priority-improvement responses reinforce this interpretation. Expansion of charging infrastructure is selected by 40.0% of participants, followed by greater technical information and awareness at 17.5%, lower battery costs at 16.2%, lower taxes at 13.7%, and increased renewable-electricity generation at 12.5%. The largest requested intervention is therefore infrastructure expansion rather than additional nominal vehicle range. These infrastructure-related concerns provide an important context for understanding why consumers may still favor a powertrain that reduces fuel consumption without requiring external charging.

iv. Hybrid Vehicles as a Transition Option

The RC E-Tech occupies an intermediate engineering position. Its fuel consumption is 4.2 L/100 km, direct operational CO_2 is 96 g/km, power is 107 kW, torque is 205 Nm, acceleration from 0 to 100 km/h is 9.3 s, and approximate curb mass is 1235 kg. At 50.85 TL/L gasoline, its energy-only fuel cost is approximately 2.14 TL/km, below the FE and RM but above the residential-electricity costs of the TG T10X and TA Model Y. The engineering position of the RC HEV can be compared directly with its acceptance among survey participants. When gasoline, hybrid, and fully electric vehicles are assumed to have the same purchase price, 32.5% prefer a hybrid vehicle, 26.3% prefer a gasoline vehicle, and 17.5% prefer a fully electric vehicle. Separately, 76.3% agree or totally agree that hybrid vehicles are a suitable interim solution during the transition to BEVs.

These responses are consistent with the hybrid's intermediate technical and operating-cost position. The RC HEV reduces fuel consumption and direct operational CO_2 relative to the two gasoline vehicles while avoiding dependence on external charging. This does not make the HEV superior to the BEVs on every engineering criterion; rather, it explains why an intermediate powertrain can remain attractive while charging confidence and purchase-cost recovery continue to influence BEV adoption.

Taken together, the BEV and HEV results show that consumer preference cannot be interpreted from emissions, energy cost, or charging dependence in isolation; these dimensions must be examined simultaneously.

v. Alignment Between Engineering Results and Consumer Perception

To synthesize the principal findings, Table 5 places the calculated engineering and economic results alongside the corresponding survey responses for operational emissions, energy cost, economic payback, range, charging infrastructure, and hybrid-vehicle acceptance.

Table 5. Alignment between numerical vehicle results and consumer perceptions

Dimension	Numerical Result	Supportive Survey Result	Engineering Interpretation
Operational CO_2	TA 73.6; TG 89.5; RC HEV 96; RM 140; FE 144 gCO_2/km	62.5% correctly identify zero BEV tailpipe emissions; 30% are unsure	BEVs show lower operational values under the 469 gCO_2/kWh grid factor, while the distinction between tailpipe and upstream emissions is not fully understood.
Energy cost	Residential: TG 0.49, TA 0.41 TL/km; gasoline/HEV: 2.14–3.25 TL/km; fast charging: TG 2.49, TA 2.05 TL/km	42.5% identify electricity/fuel prices as the main long-term economic factor	BEV operating cost is strongly charging-source dependent.
Economic payback	Break-even ≈133,000 km; ≈8.9 years at 15,000 km/year	62.5% expect long-term BEV economic advantage	The direction of the economic benefit is recognized, but recovery of the initial investment requires substantial mileage.
Range and infrastructure	-	31.2% range anxiety; 68.8% daily urban range sufficiency; 40% prioritize charging infrastructure	The main range concern is linked to charging confidence and non-routine travel rather than daily urban range alone.
Hybrid transition role	RC HEV: 4.2 L/100 km, 96 gCO_2/km, ~2.14 TL/km fuel cost	32.5% equal-price preference; 76.3% support HEVs as an interim solution	HEVs occupy an intermediate position with lower gasoline use and no external-charging dependence.

Table 5 shows that the engineering results and consumer perceptions are neither fully aligned nor fundamentally contradictory. Participants generally recognize the direction of the BEV advantages: 62.5% expect long-term economic benefits, and 68.8% consider current range adequate for daily urban driving. However, the approximately 133,000 km break-even distance, the increase in BEV energy cost from 0.49 to 2.49 TL/km for the TG T10X and from 0.41 to 2.05 TL/km for the TA Model Y when moving from residential to fast charging, and the 31.2% prevalence of range anxiety explain why adoption remains conditional. The 76.3% support for HEVs as an interim solution is consistent with this pattern: the hybrid reduces gasoline consumption and direct operational CO_2 while avoiding external-charging dependence.

Environmental awareness is mixed but not uniformly weak. A total of 62.5% correctly identify that BEVs have no tailpipe emissions during operation, while 30.0% are unsure. At the same time, 52.5% recognize that battery production, electricity source, vehicle-use emissions, and battery recycling should be considered together when evaluating sustainability. These responses support clearer technical communication that distinguishes local tailpipe emissions, grid-related operational emissions, and full life-cycle emissions.

The overall pattern therefore indicates that the principal challenge is not a simple rejection of electrified powertrains, but the coexistence of recognized technical benefits with uncertainty about cost recovery, charging conditions, battery-related concerns, and practical use beyond routine urban travel.

IV. CONCLUDING REMARKS

The combined technical, economic, and survey results provide a coherent picture of the trade-offs associated with electrified mobility in Türkiye. The TG T10X and TA Model Y combine high torque and fast acceleration with grid-adjusted operational CO_2 values of 89.5 and 73.6 g/km, respectively. The RC HEV occupies an intermediate position at 96 g/km, while the RM and FE produce 140 and 144 g/km. The BEVs are also considerably heavier, at 2126 kg for the TG and 1979 kg for the TA, compared with approximately 1150–1320 kg for the ICEV and HEV alternatives.

Energy cost varies strongly with the charging source. At 50.85 TL/L gasoline, the energy-only costs are approximately 3.25 TL/km for the FE, 3.00 TL/km for the RM, and 2.14 TL/km for the RC HEV. At 2.58 TL/kWh residential electricity, the TG T10X and TA Model Y require approximately 0.49 and 0.41 TL/km; at 13.05 TL/kWh fast-charging prices, these values rise to approximately 2.49 and 2.05 TL/km. The economic break-even distance is approximately 133,000 km, corresponding to about 8.9 years at 15,000 km/year.

Consumer responses explain why the technical and operating-cost advantages do not automatically produce uncomplicated adoption. Although 68.8% consider current BEV ranges sufficient for daily urban use, 31.2% identify range anxiety as the leading barrier. Charging-infrastructure expansion is the most frequently requested improvement at 40.0%, and 76.3% regard hybrid vehicles as a suitable interim solution. The results therefore indicate that vehicle electrification in Türkiye is governed by the combined effect of operational emissions, charging cost, mileage-dependent economic payback, and confidence in charging availability.

The operational CO_2 comparison should remain within its defined system boundary. It includes direct tailpipe values for the gasoline and hybrid vehicles and grid-related electricity emissions for the BEVs, but excludes battery production, vehicle manufacturing, end-of-life processes, recycling, and upstream gasoline-production emissions. A broader life-cycle assessment would be required to extend the environmental conclusion beyond vehicle operation.

Disclaimer

Vehicle names and brands are used only for academic comparison purposes and they are abbreviated to avoid any commercial disclosure. No commercial endorsement or affiliation is implied.

Declaration of AI-Assisted Editing

ChatGPT was used only for language refinement, manuscript formatting, and the visual enhancement or preparation of selected figures based on the authors' existing data. Artificial intelligence was not used to generate research data, results, analyses, references, or scientific conclusions. All AI-assisted content was reviewed and verified by the authors, who take full responsibility for the final manuscript. The heading of the Acknowledgment section and the References section must not be numbered.

REFERENCES

[1] Biberci, A., 2018, Comparative analysis of energy efficiency and greenhouse gas emissions between conventional and hybrid electric vehicles. Bitlis Eren Üniversitesi Fen Bilimleri Dergisi, 7(2), pp. 805-813.

[2] T.C. Enerji ve Tabii Kaynaklar Bakanlığı. (2025). Elektrik Üretim ve Tüketim Emisyon Faktörleri. https://enerji.gov.tr/evced-cevre-ve-iklim-elektrik-uretim-tuketim-emisyon-faktorleri. Erişim Tarihi: 12.05.2026.

[3] T.C. Enerji ve Tabii Kaynaklar Bakanlığı. (2025). Türkiye Ulusal Elektrik Şebekesi Emisyon Faktörü. https://enerji.gov.tr/evced-cevre-ve-iklim-turkiye-ulusal-elektrik-sebekesi-emisyon-faktoru. Erişim Tarihi: 12.05.2026. [4] Opet Petrolcülük A.Ş. (2025). Fiyat Arşivi. https://www.opet.com.tr/fiyat-arsivi. Erişim Tarihi: 12.05.2026.

[5] Zorlu Energy Solutions (ZES). (2025). Fiyatlandırma. https://zes.net/tr/fiyatlandirma. Erişim Tarihi: 12.05.2026.

[6] Blank, L., & Tarquin, A. (2018). Engineering Economy (8th ed.). McGraw-Hill Education.

[7] Renault. (2025). RC Full Hybrid E-Tech Product Brochure. https://www.renault.co.uk. Erişim Tarihi: 12.05.2026.

[8] Otomotiv Distribütörleri ve Mobilite Derneği. (2025, 2 Aralık). Otomobil ve Hafif Ticari Araç Pazarı (Kasım, Ocak-Kasım 2025) Basın Bülteni. https://odmd.org.tr. Erişim Tarihi: 12.05.2026.

[9] Tofaş Türk Otomobil Fabrikası A.Ş. (2025). Yeni FE Teknik Özellikler ve Ürün Kataloğu. https://www.fiat.com.tr. Erişim Tarihi: 12.05.2026.

[10] Renault Mais A.Ş. (2025). RM Sedan Teknik Özellikler ve Ürün Kataloğu. https://www.renault.com.tr. Erişim Tarihi: 12.05.2026.
[11] Renault. (2026). RC Technical Specifications. https://www.renault.co.uk. Accessed: 12.05.2026.
[12] Hakedis.org. (2025). EPDK Akaryakıt Bayi Satış Fiyatları Aylık Ortalama. https://www.hakedis.org/endeksler/epdk-akaryakit-bayi-satis-fiyatlari-aylik-ortalama. Erişim Tarihi: 12.05.2026.
[13] Aytemiz Akaryakıt Dağıtım A.Ş. (2025). Arşiv Fiyat Listesi. https://www.aytemiz.com.tr/akaryakit-fiyatlari/arsiv-fiyat-listesi. Erişim Tarihi: 12.05.2026.
[14] Enerji Piyasası Düzenleme Kurumu. (2025). Elektrik Faturalarına Esas Tarife Tabloları. https://www.epdk.gov.tr/Detay/Icerik/3-1327/elektrik-faturalarina-esas-tarife-tablolari. Erişim Tarihi: 22.01.2026
[15] Enerji Ajansı. (2025). Elektrik Birim Fiyatları. https://enerjiajansi.com.tr/elektrik-birim-fiyatlari/. Erişim Tarihi: 12.05.2026.
[16] TG Trugo. (2025). Fiyatlandırma. https://www.trugo.com.tr/price. Erişim Tarihi: 12.05.2026.
[17] Türkiye'nin Otomobili Girişim Grubu Sanayi ve Ticaret A.Ş. (2025). TG T10X Ürün Kataloğu. https://www.TG.com.tr. Erişim Tarihi: 12.05.2026.
[18] TA Türkiye. (2025). Supercharger Ücretleri. https://www.TA.com/tr_tr/support/charging/supercharger/fees. Erişim Tarihi: 12.05.2026.
[19] Toyota Motor Sales, U.S.A., Inc. (2025). 2025 Toyota Corolla Product Catalog. https://www.toyota.com. Erişim Tarihi: 12.05.2026.

8th International Conference on Engineering, Natural and Social Sciences

September 06-07, 2026: Konya, Turkey

© 2026 Published by All Sciences Academy

https://www.icensos.com/

Integration of Vertical-Axis Tracking Floating Photovoltaics Into Hydroelectric Power Plants: A Case Study for Sarıyar Dam

Umut Mete Hakverir[1], Cengizhan Özaltın[1], Ömer Önder Erat[1*], Bülent Yeşilata[1]

[1] *Ankara Yıldırım Beyazıt University, Faculty of Engineering and Natural Sciences, Department of Energy Systems Engineering, Ankara, Turkey*

[*] *omerondererat@aybu.edu.tr*

Abstract **–** Floating photovoltaic (FPV) systems enable solar generation on water surfaces where land occupation is undesirable or constrained. Reservoir applications are particularly attractive because FPV generation can be integrated with existing hydropower infrastructure while potentially reducing evaporation and benefiting from the local thermal environment. This study evaluates the design and performance of a 649 kWp vertical-axis tracking FPV system integrated with the Sarıyar Dam hydroelectric power plant. The proposed configuration consists of N-type bifacial photovoltaic modules supported by high-density polyethylene (HDPE) floating elements and a central turret with a slewing-bearing mechanism that allows the entire platform to rotate about a vertical axis for azimuth tracking. Electrical performance was evaluated in PVsyst for panel tilt angles between 10° and 15°, and the final configuration was compared with both a fixed FPV system and a 35° fixed-tilt land-based photovoltaic (PV) reference. Within the investigated tilt range, the 15° configuration produced the highest simulated annual output, approximately 1194 MWh/year, with a performance ratio of 91.0%. Vertical-axis tracking increased annual generation by 13.61% relative to the fixed FPV configuration. The tracking FPV system also generated 22.81% more electricity than the land-based reference; however, this difference represents a system-level comparison that includes tracking, thermal conditions, optical assumptions, and configuration effects rather than the isolated effect of floating installation. Based on the 5600 m² water-coverage area adopted in the analysis, annual evaporation reduction was estimated at approximately 5376 m^3, corresponding to about 996 kWh/year of additional hydroelectric generation, while the results also indicate that further structural verification, field-based hydrodynamic characterization, and techno-economic assessment are required before implementation.

Keywords – Floating photovoltaic systems, vertical-axis tracking, PVsyst simulation, hybrid renewable energy systems.

I. INTRODUCTION

As solar capacity scales, land availability emerges as a critical constraint. Floating photovoltaic systems provide an alternative to land-based solar installations by using reservoirs, lakes, and other water surfaces for electricity generation. Partial water-surface coverage may reduce evaporation, while the surrounding water can contribute to lower module operating temperatures under suitable environmental conditions [1]. Reservoir applications are particularly relevant because they may combine PV generation with existing hydropower infrastructure while avoiding additional land occupation [2-4]. The water environment can also influence module temperature and evaporation, although these benefits depend strongly on site conditions and system design.

The deployment of FPV systems in aquatic environments introduces design requirements that are less pronounced in conventional ground-mounted systems. Floating structures must accommodate changes in water level, wind and wave loading, corrosion, connector/cable movements, and mooring forces [5]. The use of tracking adds another layer of complexity because electrical transmission and structural load transfer

must remain reliable while the array changes its azimuth position [6]. Previous FPV studies have investigated cooling behavior [7], wind- and wave-induced structural responses [8], bifacial system configurations [9], and floating tracking concepts [6,10]. Recent studies indicate that single-axis azimuth tracking can increase the annual energy yield of FPV systems compared with fixed configurations, although the additional tracking hardware and associated balance-of-system costs must also be considered [10].

The present study examines a vertical-axis tracking FPV configuration proposed for the Sarıyar Dam reservoir. The assessment combines photovoltaic simulation with preliminary mechanical, hydrodynamic, and electrical design checks. The main objectives are to determine a suitable low-tilt operating range, quantify the energy contribution of vertical-axis tracking, compare the proposed system with fixed FPV and land-based references, identify the principal PVsyst losses, and estimate the potential water-saving contribution to the existing hydroelectric plant.

II. Materials and Method

i. Case Study and System Configuration

The case study was developed for the Sarıyar Dam reservoir. The final electrical configuration used in this study consists of 1100 N-type bifacial modules rated at 590 W each, giving a total installed DC capacity of 649 kWp. Six 105 kW string inverters provide a total AC capacity of 630 kW, corresponding to a DC/AC ratio of approximately 1.03. The main configuration of the proposed FPV system is summarized in Table 1.

Table 1. Main configuration of the proposed FPV system

Design Parameter	**Value/Configuration**
Installed PV capacity	649 kWp DC
PV modules	1100 × 590 W N-type bifacial
Inverter capacity	6 × 105 kW
Total AC capacity	630 kW
DC/AC ratio	1.03
String length	22 modules
Tracking principle	Vertical-axis rotation of the floating platform
Main rotation mechanism	Central turret and slewing-bearing drive
Evaluated tilt range	10°–15°
Selected tilt for final PVsyst case	15°

The modular floating structure uses high-density polyethylene (HDPE) components primarily for buoyancy, while the PV modules are supported by a metallic structural frame. The central turret provides a fixed rotational reference. The proposed load path transfers forces from the module supports to radial structural members and subsequently to the central frame and slewing bearing, rather than relying on the HDPE floats to carry the principal torsional moments. Because the inverter units are installed on the rotating platform, the generated AC power must be transferred continuously across the rotating–stationary interface. For this purpose, a slip-ring assembly is integrated into the central turret. Mechanical loads are carried by the slewing bearing, whereas the slip ring is mechanically isolated and serves only as the electrical transmission interface. This separation of mechanical load transfer and electrical power transmission is a key feature of the proposed tracking architecture. The schematic representation of the system in Figure 1.

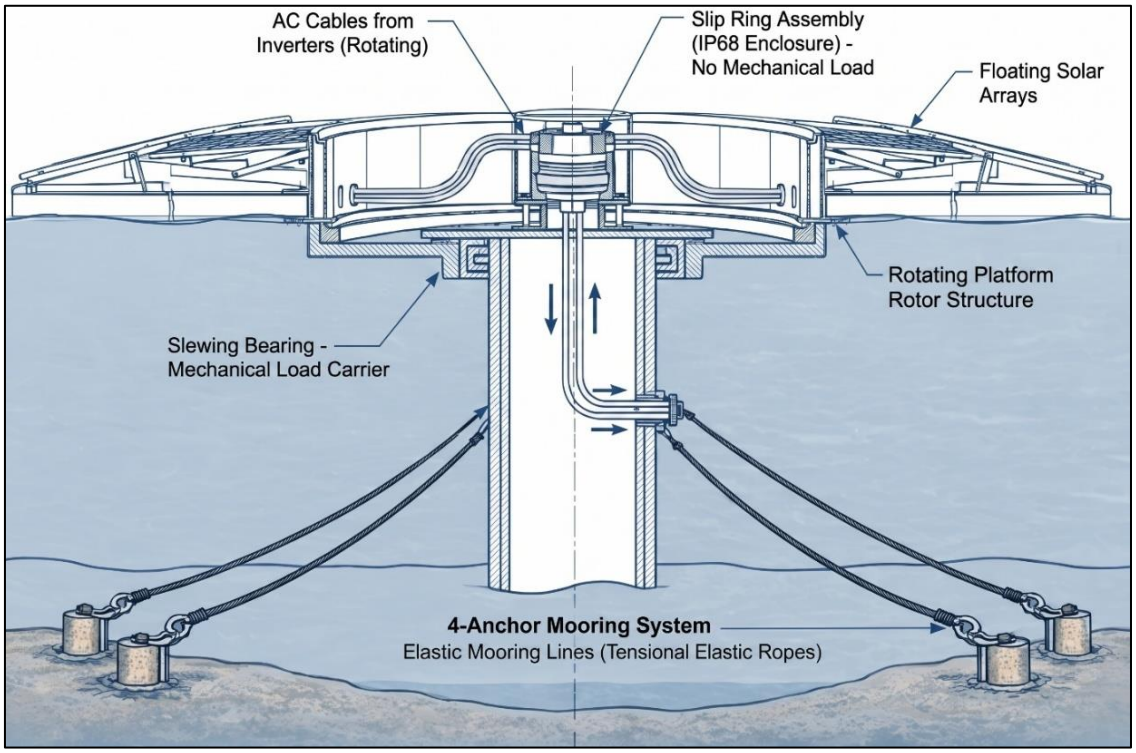

Fig. 1 Schematic representation of the system planned to be established. (Source: Authors' conceptual design).

ii. Photovoltaic Performance Assessment

PVsyst was used to evaluate the electrical performance of the proposed FPV system using site-specific irradiation inputs, the selected photovoltaic technology, bifacial effects, and the tracking configuration. A low tilt-angle range of 10°–15° was examined because higher tilt angles increase the projected area exposed to wind and therefore impose larger aerodynamic demands on the floating structure. Annual energy production and performance ratio were evaluated for each tilt-angle case.The 15° configuration, which produced the highest annual energy output within the investigated interval, was then used for the main performance assessment.

Two reference configurations were considered. The first was a fixed FPV system evaluated under the same general environmental and electrical conditions but without azimuth tracking. The second was a conventional land-based configuration using the same number of PV modules at a fixed tilt angle of 35°. The land-based comparison was used as a system-level benchmark rather than as a means of isolating the effect of the floating environment alone.

iii. Electrical Design Checks

Electrical compatibility was checked for the selected module and inverter configuration. At a design minimum temperature of -10 °C, the corrected module open-circuit voltage was calculated as 59.5 V. With 22 modules connected in series, the maximum string voltage was 1309 V, below the inverter DC input limit of 1500 V. A 25% safety factor was applied in the DC protection calculation, producing a design current of 17.13 A. The longest assumed DC cable route was 100 m; with 6 mm² H1Z2Z2-K cable, the calculated voltage drop was 0.79%. On the AC side, the 50 m connection between each inverter and the main collector busbar produced a calculated voltage drop of 0.61% using the selected cable configuration. These checks were used to confirm compatibility of the principal electrical components at the conceptual design stage. The resulting electrical architecture, including the PV array, inverter units, protection equipment, main collector busbar, transformer, and grid-interconnection point, is shown in Figure 2.

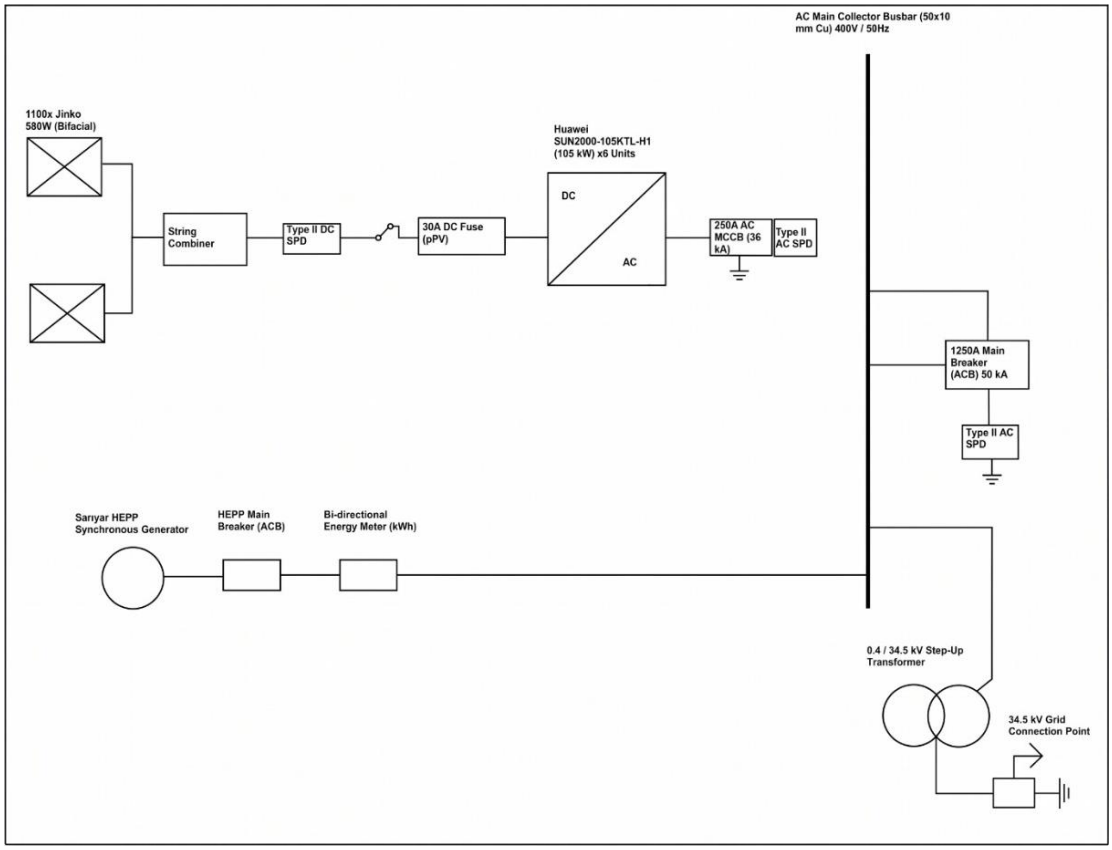

Fig. 2 Electrical single-line diagram of the proposed FPV system and grid interconnection.

iv. Environmental Load Assessment

Wind was treated as the principal environmental load affecting the tracking structure. A survival wind speed of 25 m/s was considered for preliminary design assessment. Under normal operating conditions, an average site wind speed of approximately 2.3 m/s was used in the thermal analysis. Wave conditions were estimated using a fetch-limited approach. The maximum effective fetch adopted for the Sarıyar reservoir was approximately 850 m. Under the 25 m/s survival wind condition, significant wave height was estimated in the range of approximately 0.25–0.55 m, with a peak period of 1.5–2.5 s. The main environmental inputs and preliminary load estimates used in the assessment are summarized in Table 2. These calculations represent engineering estimates rather than a complete structural certification. Detailed verification of the slewing bearing, mooring forces, fatigue behavior, and local structural stresses is required before construction.

Table 2. Environmental parameters and preliminary hydrodynamic design values

Design Parameter	Assessment Value	Role in the Assessment
Average site wind speed	2.3 m/s	Normal operating and thermal conditions
Survival wind speed	25 m/s	Preliminary extreme structural load case
Effective reservoir fetch	850 m	Fetch-limited wave estimation
Significant wave height, Hs	0.25–0.55 m	Estimated survival-condition wave range
Peak wave period, Tp	1.5–2.5 s	Estimated survival-condition wave period
Current velocity scenarios	0.30 and 0.50 m/s	Simplified steady-flow assessment
Drag force at 0.50 m/s	3.47 kN	Conservative current-induced load
Estimated azimuthal moment	146 kN·m	Current-induced rotational demand

v. Evaporation and Hydropower Contribution

Annual water savings were estimated using the relationship given in [11]:

$$V_{saved} = A \cdot E \cdot \eta_{evap} \quad (1)$$

where A is the water-coverage area used in the calculation, E is annual evaporation, and η_{evap} is the assumed evaporation-reduction efficiency. The adopted values were A = 5600 m^2, E = 1.2 m/year, and η_{evap} = 0.80, giving an estimated annual water saving of 5376 m^3. The corresponding hydroelectric contribution was estimated using the saved water volume, an 80 m hydraulic head, and a turbine efficiency of 0.85. This produced an additional generation estimate of approximately 996 kWh/year.

III. Results and Discussion

i. Tilt-Angle Evaluation

As shown in Figure 3, annual energy production increased monotonically over the investigated 10°–15° tilt range, rising from approximately 1120 MWh/year at 10° to 1194 MWh/year at 15°, which corresponds to an increase of about 6.6%. In contrast, the performance ratio showed only a limited increase, from approximately 90.40% to 91.00%.

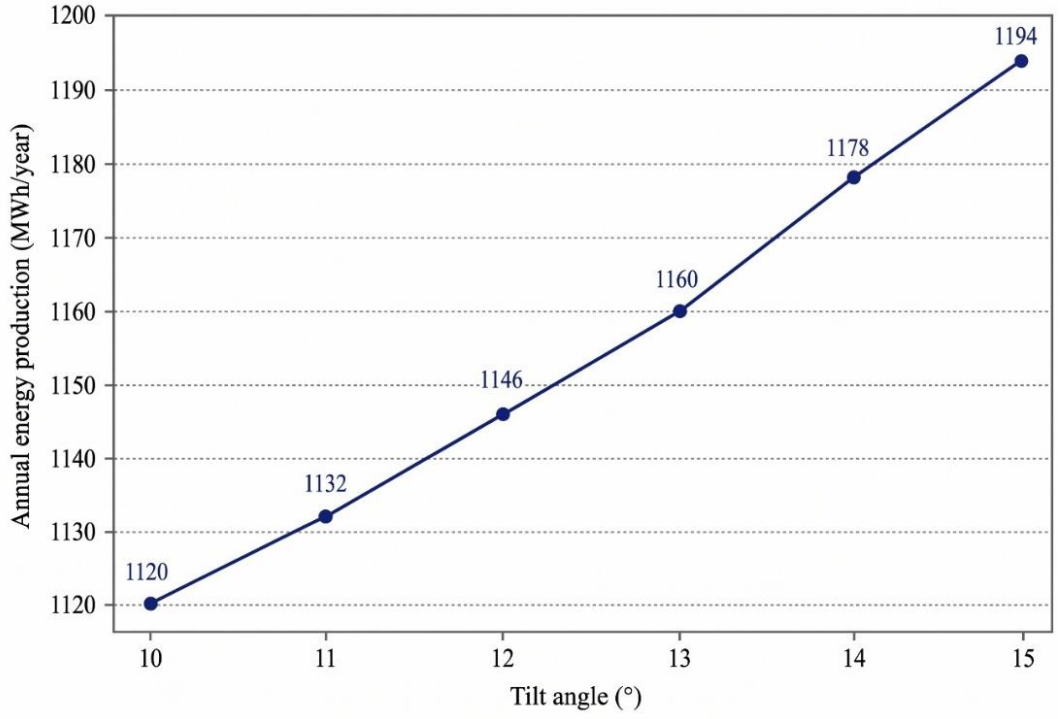

Fig. 3 Effect of panel tilt angle on the simulated annual energy production of the tracking FPV system.

The result indicates that the main benefit of increasing tilt within this range is improved irradiation capture rather than a large reduction in internal losses. The preliminary comparison indicated that the relative wind loading at 15° was nearly 50% higher than that at 10°. The 15° case should therefore be described as the energy-preferred option within the simulated range, not as a fully verified structural optimum.

ii. Comparison with Fixed FPV and Land-Based PV

The final tracking FPV configuration produced approximately 1194 MWh/year, compared with 1051 MWh/year for the corresponding fixed FPV case, representing a 13.61% increase in annual energy production due to vertical-axis tracking. The 35° fixed land-based reference produced 972.2 MWh/year with a performance ratio of 79.28%, whereas the tracking FPV configuration achieved a PR of 91.00%. Relative to the land-based reference, the tracking FPV system generated approximately 22.81% more annual energy. Table 3 summarizes the principal simulated configurations.

Table 3. Comparison of the principal simulated configurations

Configuration	Annual Energy Production	Performance Ratio (PR)	Relative Comparison
35° fixed land-based PV	972.2 MWh/year	79.28%	Reference
Fixed FPV	1051 MWh/year	-	Tracking FPV produces 13.61% more energy
15° tracking FPV	1194 MWh/year	91.00%	22.81% higher output than land-based reference

The 22.81% difference should be interpreted with caution, as the two configurations differ not only in their installation environment but also in tracking behavior, tilt angle, thermal conditions, and optical assumptions. Therefore, the entire difference cannot be attributed solely to the floating installation or its associated cooling effects. When the comparison is normalized by occupied area, however, a different trend emerges. The land-based configuration occupies approximately 3900 m², whereas the selected FPV layout occupies approximately 5600 m² due to the floating-frame arrangement.

The corresponding area-normalized energy production values are approximately 0.249 MWh m^{-2} $year^{-1}$ for the land-based configuration and 0.213 MWh m^{-2} $year^{-1}$ for the FPV system. Thus, although the proposed FPV layout generates more total electricity, it yields lower energy production per unit of occupied surface area. For reservoir applications, this trade-off should be evaluated together with the benefit of avoiding additional land use and the operational constraints associated with the water body. For a reservoir project, this trade-off must be considered together with the avoidance of land occupation and the operational constraints of the water body.

iii. Seasonal Production and PVsyst Losses

The annual PVsyst output for the final tracking configuration was 1193.9 MWh, with an annual PR of 0.910. Monthly generation followed the expected seasonal irradiation pattern. July recorded the highest energy delivered to the grid, at 152.7 MWh, followed by June and August with 143.7 MWh and 141.1 MWh, respectively. The normalized PVsyst results yielded an average useful energy output (Y_f) of 5.04 kWh kWp^{-1} day^{-1}, while PV-array collection losses (L_c) and system losses (L_s) were 0.42 and 0.08 kWh kWp^{-1} day^{-1}, respectively. The considerably larger collection loss compared with the downstream system loss indicates that the main potential for further performance improvement lies at the PV-array level rather than in the inverter stage.

The performance ratio decreased during the summer months, when energy production was highest. This indicates that increased irradiation is accompanied by higher thermal losses. The result is consistent with the PVsyst loss analysis, where temperature-related PV loss was -1.99%. Figure 4 summarizes the main components of PVsyst loss. In contrast to inverter, mismatch, and ohmic losses, soiling and temperature-related PV losses were the biggest individual contributions. The relatively limited downstream conversion losses indicate that these losses make only a minor contribution to the overall system performance reduction. Therefore, additional array-level performance enhancements would be more pertinent, especially through soiling control, optical design, thermal management, mismatch reduction, and cable optimization.

A sensitivity check performed in this study further showed that the optical assumptions have a measurable effect on the predicted system output. When the anti-reflective front-glass property of the selected module was excluded from the simulation, annual generation decreased from approximately 1194 to 1174 MWh/year, while the performance ratio decreased from 91.00% to 90.31%. The approximately 20 MWh/year difference confirms that optical assumptions should be considered when interpreting the simulated performance advantage of the proposed system.

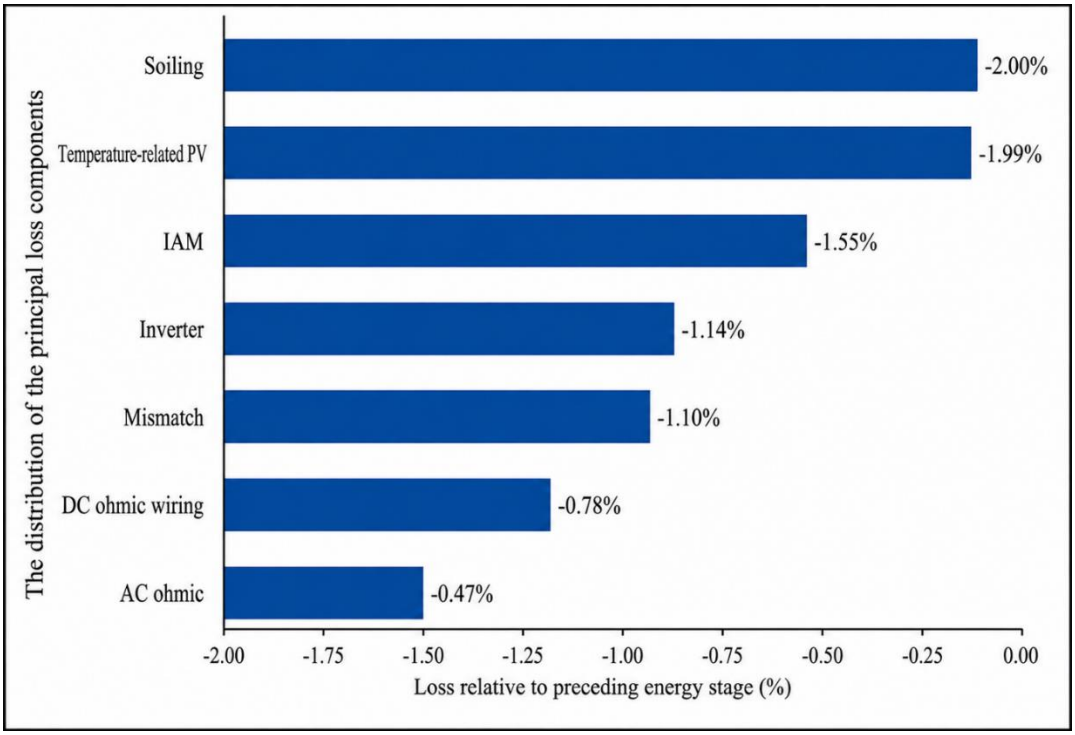

Fig. 4 Main PVsyst loss components for the final 15° vertical-axis tracking FPV configuration.

iv. Mechanical and Hydrodynamic Implications

The preliminary environmental-load analysis supports the use of a low-tilt tracking configuration but also identifies wind loading as a central design constraint. The 25 m/s survival case, the fetch-limited wave estimate, and the simplified current-load analysis suggest that current-induced moments are smaller than the expected extreme wind-related rotational demand. Nevertheless, the present environmental assessment provides a preliminary basis for evaluating the structural feasibility of the proposed configuration. Since the current-load analysis is based on representative velocities and the wave conditions are estimated using an empirical fetch-based approach, further site-specific verification of the slewing bearing, mooring system, structural connections, fatigue behavior, and relevant reservoir-bed conditions is recommended during the detailed design stage.

v. Evaporation Reduction and Hydropower Contribution

Using a water-coverage area of 5600 m^2, the proposed system was estimated to reduce annual evaporation by approximately 5376 m^3. Assuming that the conserved water subsequently passes through the hydroelectric turbines under an 80 m hydraulic head and a turbine efficiency of 85%, the corresponding additional hydroelectric generation was calculated as approximately 996 kWh/year. This contribution is limited relative to the annual PV generation of approximately 1194 MWh/year; therefore, the primary significance of the water-saving effect lies in reservoir water conservation rather than in a substantial increase in hydroelectric generation.

IV. CONCLUDING REMARKS

A 649 kWp vertical-axis tracking FPV system was evaluated for integration with the Sarıyar Dam hydroelectric power plant. Within the investigated 10°–15° tilt range, 15° provided the highest simulated annual energy production. The final tracking configuration generated approximately 1194 MWh/year with a performance ratio of 91.00%. Compared with a fixed FPV configuration, vertical-axis tracking increased simulated annual electricity generation by 13.61%. The tracking FPV configuration also produced 22.81% more electricity than the 35° fixed land-based reference. This second comparison should be interpreted at system level because the two cases differ in tracking, tilt, thermal environment, and optical conditions.

The PVsyst loss analysis showed that performance is affected primarily by several moderate array-level losses rather than a single dominant mechanism. Soiling, module temperature, incidence-angle effects, mismatch, and wiring losses therefore represent the main areas for further optimization. The proposed central-turret and slewing-bearing arrangement defines the principal structural load path for vertical-axis tracking. Nevertheless, the structural performance of the system should be further evaluated under site-specific wind, wave, current, and mooring loads, together with bearing capacity, connection strength, and fatigue behavior, during the detailed design stage. Based on the adopted 5600 m^2 water-coverage area, the water-saving calculation indicated a potential annual evaporation reduction of approximately 5376 m^3, corresponding to approximately 996 kWh/year of additional hydroelectric generation. The primary significance of this contribution lies in reservoir water conservation rather than in a substantial increase in hydroelectric energy production.

Future work should focus on detailed structural verification of the 15° tracking configuration, a net-energy assessment of the proposed WVC concept, and a techno-economic comparison between fixed and tracking FPV configurations. These assessments would provide a more comprehensive basis for evaluating the technical and economic feasibility of the proposed system under site-specific operating conditions.

Declaration of AI-Assisted Editing

ChatGPT was used only for language refinement, manuscript formatting, and the visual enhancement or preparation of selected figures based on the authors' existing data. Artificial intelligence was not used to generate research data, results, analyses, references, or scientific conclusions. All AI-assisted content was reviewed and verified by the authors, who take full responsibility for the final manuscript. The heading of the Acknowledgment section and the References section must not be numbered.

REFERENCES

[1] R. Cáceres González et al., "Exploring climate-driven performance of floating photovoltaic systems: Energy production enhancement and evaporation reduction," Applied Energy, vol. 386, 125556, 2025.

[2] N. Lee et al., "Hybrid floating solar photovoltaics-hydropower systems: Benefits and global assessment of technical potential," Renewable Energy, vol. 162, pp. 1415–1427, 2020. doi: 10.1016/j.renene.2020.08.080.

[3] A. Sahu, N. Yadav, and K. Sudhakar, "Floating photovoltaic power plant: A review," Renewable and Sustainable Energy Reviews, vol. 66, pp. 815–824, 2016. doi: 10.1016/j.rser.2016.08.051.

[4] S. Gorjian, H. Sharon, H. Ebadi, K. Kant, F. B. Scavo, and G. M. Tina, "Recent technical advancements, economics and environmental impacts of floating photovoltaic solar energy conversion systems," Journal of Cleaner Production, vol. 278, 124285, 2021. doi: 10.1016/j.jclepro.2020.124285.

[5] O. Ghonim, A. M. Al-Yacouby, and A. K. Yousafzai, "A systematic literature review of the advances in structural aspects of floating photovoltaic systems," Applied Energy, vol. 402, 127020, 2026.

[6] R. Cazzaniga, M. Cicu, M. Rosa-Clot, P. Rosa-Clot, G. M. Tina, and C. Ventura, "Floating photovoltaic plants: Performance analysis and design solutions," Renewable and Sustainable Energy Reviews, vol. 81, pp. 1730–1741, 2018. doi: 10.1016/j.rser.2017.05.269.

[7] T. Kjeldstad, D. Lindholm, E. Marstein, and J. Selj, "Cooling of floating photovoltaics and the importance of water temperature," Solar Energy, vol. 218, pp. 544–551, 2021. doi: 10.1016/j.solener.2021.03.022.

[8] G.-H. Lee, J.-W. Choi, J.-H. Seo, and H. Ha, "Comparative Study of Effect of Wind and Wave Load on Floating PV: Computational Simulation and Design Method," KSMPE, vol. 18, no. 11, pp. 9–17, 2019. doi: 10.14775/ksmpe.2019.18.11.009.

[9] H. Ziar et al., "Innovative floating bifacial photovoltaic solutions for inland water areas," Progress in Photovoltaics, vol. 29, no. 7, pp. 725–743, 2021. doi: 10.1002/pip.3367.

[10] J. Baker and A. Ghosh, "Investigation of fixed and East-West, North-South, and azimuthal single-axis tracking for floating photovoltaics (Floatovoltaics) in the UK," Energy 360, vol. 5, 100052, 2026.

[11] Chow, V. T., Maidment, D. R., & Mays, L. W. (1988). Applied hydrology. McGraw-Hill.

8th International Conference on Engineering, Natural and Social Sciences

September 06-07, 2026: Konya, Turkey

© 2026 Published by All Sciences Academy

https://www.icensos.com/

Energy-Shading Optimization of Greenhouse-Integrated Agrivoltaic Systems in Türkiye Using PVGIS-TMY Data and Geometric Shadow Modelling

Umut Ege Karacakale[1], Ömer Önder Erat[1*], Bülent Yeşilata[1]

[1] *Ankara Yıldırım Beyazıt University, Faculty of Engineering and Natural Sciences, Department of Energy Systems Engineering, Ankara, Turkey*

**omerondererat@aybu.edu.tr*

Abstract – The increasing competition between photovoltaic (PV) electricity generation and agricultural land use has created a growing need for integrated design approaches that support both renewable energy production and crop cultivation. This study develops a reproducible computational framework for the optimization of greenhouse-integrated agrivoltaic (AV) systems under different climatic conditions in Türkiye. The framework combines hourly Typical Meteorological Year (TMY) data obtained from the Photovoltaic Geographical Information System (PVGIS), plane-of-array irradiance calculations using pvlib, a geometric shadow-projection model, and a performance-ratio-based energy-yield model. Three panel layouts-grid, staggered, and strip-are evaluated under identical boundary conditions, with a maximum greenhouse-floor shading ratio of 30% adopted as the design constraint. The methodology is demonstrated for five representative cities, each representing a different climatic region of Türkiye: Antalya, Konya, Istanbul, Erzurum, and Rize. Two greenhouse sizes, 10 x 20 m and 30 x 50 m, are also analyzed to examine the effect of scale on installed capacity, annual energy production, and shading performance. Results show that the constrained practical optimum tilt angles fall within 28°-31° for the selected cities. The 26° tilt used as an industry-practice reference causes only a minor annual irradiation penalty, remaining below approximately 1.6% in all cases. Continuous strip layouts exceeded the 30% shading limit in all tested cases, whereas feasible configurations were obtained with grid and staggered layouts. In matched comparisons, staggered layouts reduce maximum shading by 1.5%-3.5% relative to grid layouts, although the highest-energy feasible layout remains dependent on city and greenhouse size. Antalya achieves the highest specific yield, approximately 47% higher than Rize. Overall, the study provides a practical engineering basis for climate-specific AV greenhouse design and offers a framework that can be extended to all provinces of Türkiye.

Keywords – Agrivoltaics, greenhouse-integrated photovoltaics, PVGIS-TMY, shadow modelling, photovoltaic optimization.

I. INTRODUCTION

The world's energy demand continues to increase, while efforts to meet this demand create significant environmental pressures. Climate change, air pollution, and resource depletion have encouraged governments and engineering research to place greater emphasis on renewable energy. Solar energy has become one of the fastest-growing technologies, supported by declining photovoltaic system costs. However, the expansion of solar farms can intensify competition for agricultural land [1,2]. Agrivoltaic systems offer a potential response to this challenge by enabling agricultural production and solar electricity generation on the same land [2, 3]. Two main approaches are commonly considered: open-field installations, where PV panels are installed above cultivated land, and greenhouse-integrated installations,

where PV systems are mounted on or above greenhouse structures. Türkiye provides a relevant setting for such systems because its climatic conditions vary substantially, from the humid and cloudy Black Sea region to the high-solar-resource Mediterranean region. Recent global reviews and meta-analyses emphasize that maintaining canopy shading below 30%–40% is critical to avoiding severe photosynthetic and yield penalties across most crop categories [4–6], highlighting the necessity of assessing spatial layout geometry and light sharing [7]. Although the agrivoltaic literature has expanded considerably, region- and configuration-specific assessments remain important, particularly for Türkiye [8]. In addition, latitude-based approaches to optimum PV tilt [9] have not been systematically examined against the 26° installation angle used as an industry-practice reference in the present study. This study therefore aims to:

1. Develop a reproducible computational framework applicable to all 81 provinces of Türkiye, demonstrated here through five representative cities.
2. Compare three physically distinct panel layouts-grid, staggered, and strip-under identical boundary conditions.
3. Constrain the tilt optimization to the practical installation range of 20°-35° to connect theoretical optimization with field-oriented design conditions.
4. Quantify the annual plane-of-array (POA) irradiation penalty associated with the 26° reference tilt.

II. Materials and Method

i. Data Source and Irradiance Model

Hourly weather data for each city were retrieved from the European Commission's Photovoltaic Geographical Information System (PVGIS) through the pvlib.iotools.get_pvgis_tmy function [10,11]. The TMY dataset provides 8760 hourly values of global horizontal irradiance (GHI), direct normal irradiance (DNI), and diffuse horizontal irradiance (DHI). Solar position, including apparent zenith and azimuth, was calculated using the NREL Solar Position Algorithm implemented in pvlib. The plane-of-array (POA) irradiance on a south-facing tilted surface was calculated using the isotropic transposition model implemented in pvlib [10]:

$$G_{POA} = G_B \cdot \cos\theta + G_D \cdot (1 + \cos\beta)/2 + \rho \cdot G_h \cdot (1 - \cos\beta)/2 \quad (1)$$

where G_b is the beam (DNI) component, G_d is the diffuse (DHI) component, G_h is global horizontal irradiance (GHI), θ is the angle of incidence, β is panel tilt, and ρ is ground albedo, taken as 0.2. Annual POA irradiation (kWh/m²) was obtained by summing the hourly values.

ii. Shadow Geometry Model

The shading impact on the greenhouse floor was calculated by projecting the four corner points of each tilted panel onto the ground plane along the instantaneous solar vector using geometric shadow formulations [12, 13]:

$$x_s = x_p - z_p \cdot \sin(\gamma_s) / \tan(\alpha_s) \quad (2)$$

$$y_s = y_p - z_p \cdot \cos(\gamma_s) / \tan(\alpha_s) \quad (3)$$

where α_s is the solar elevation angle, γ_s is the solar azimuth measured clockwise from north, and (x_p, y_p, z_p) are the three-dimensional coordinates of a panel corner. The four projected points form a quadrilateral on the ground, which is converted into a Shapely polygon. The union of all panel shadow polygons, clipped to the greenhouse footprint, gives the shaded floor area. The maximum shading ratio among the three equinox reference times-10:00, 12:00, and 14:00 local time on 21 March-was used as the design-reference metric. Configurations exceeding the adopted 30% shading limit were discarded, following established agronomic thresholds and recent meta-analyses indicating critical yield tipping points beyond this level [4–6, 12]. This reference metric should not be interpreted as the absolute annual worst-case shading condition, because lower winter solar elevations may produce longer shadows.

iii. Layout Configurations

Three physically distinct panel layouts were implemented and compared: Grid (panels arranged in a regular rectangular pattern with uniform east-west and north-south spacing); Staggered (alternate rows shifted by half a column spacing, producing a checkerboard-like pattern) and Strip (panels in each row joined into continuous east-west strips with zero east-west gap). In all layouts, the panel slant length was L = 2.0 m, the width was W = 1.0 m, and the mounting height of the lower edge was h = 3.0 m. The number of panels N was calculated from the geometric step sizes:

$$\Delta EW = W + gEW$$
$$\Delta NS = L \cdot \cos\beta + gNS$$

iv. Energy Yield Model

Annual AC electricity production was estimated using a simplified performance-ratio approach standard in photovoltaic and agrivoltaic modeling [4, 10]:

$$E_{ac} = H_{POA} \cdot A_{panel} \cdot N \cdot \eta_{PV} \cdot PR \quad (4)$$

where A_{panel} = 2.0 m², η_{PV} = 0.20, and PR = 0.86, accounting in simplified form for inverter, wiring, soiling, temperature, and mismatch losses [4]. The model provides a first-order comparative estimate of annual electricity production. Dynamic module-temperature behavior, inverter clipping, row-to-row electrical mismatch, and module-level partial-shading losses are not explicitly resolved; therefore, the calculated AC yields should be interpreted as comparative design indicators rather than final bankable energy estimates.

v. Optimization Framework and Case Study

A nested-loop optimization procedure was implemented:

- For each city, panel tilt β was scanned from 20° to 35° in 1° steps.
- For each layout and gap g ∈ {1.5, 2.0, …, 5.0} m, the panel array was generated and the maximum shading ratio was evaluated.
- Configurations exceeding the 30% shading constraint were filtered out.
- For the remaining configurations, annual AC energy yield was calculated and ranked.

Five Turkish cities representing distinct climatic regions were selected: Antalya, Konya, Istanbul, Erzurum, and Rize. Two greenhouse sizes, 10 x 20 m and 30 x 50 m, were analyzed.

III. Results and Discussion

i. Optimal Tilt Angles and the 26° Reference

The annual plane-of-array (POA) irradiation curves as a function of panel tilt for the five cities are presented in Figure 1. The optimum tilt values are summarized in Table 1. The constrained practical optima fall within a narrow range of 28°-31°, despite the latitude range extending from approximately 36.9° N to 41.0° N.

Table 1. Optimal tilt and annual POA irradiation for each case-study city.

City	Latitude (°N)	Optimal Tilt (°)	POA (kWh/m²/yr)	φ − β* (°)
Antalya	36.89	29	2055.4	7.9
Konya	37.87	28	1937.9	9.9
Erzurum	39.90	31	1733.1	8.9
Istanbul	41.00	29	1695.8	12.0
Rize	41.02	31	1401.7	10.0

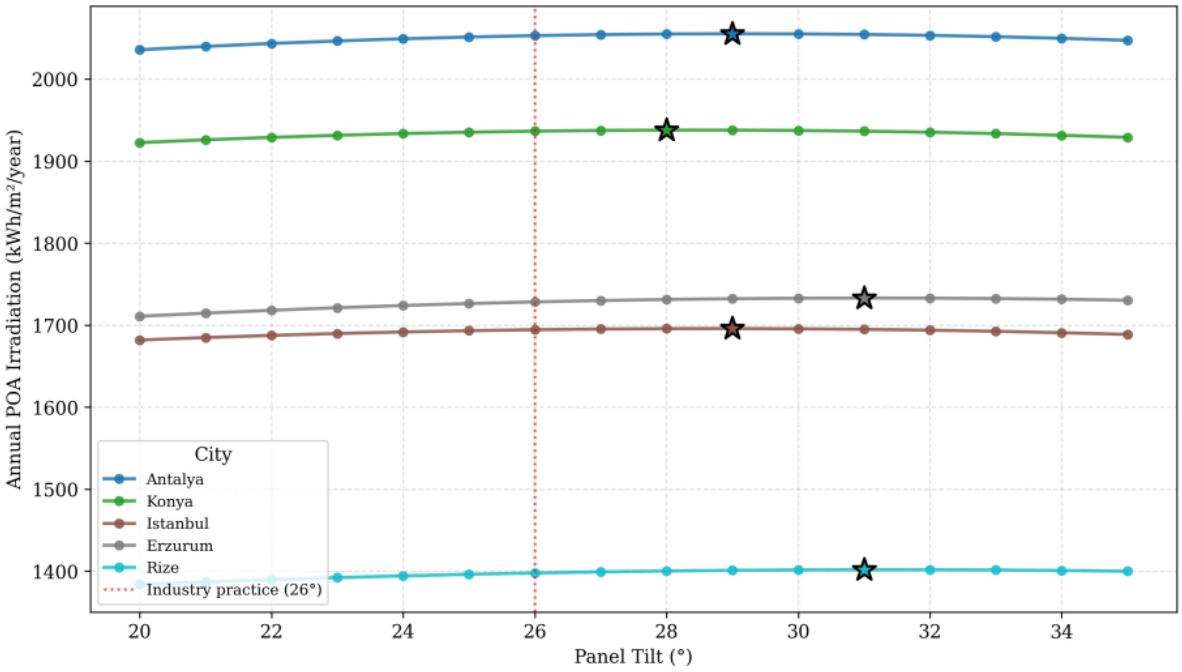

Fig. 1 Annual POA irradiation as a function of panel tilt for the five case-study cities. Stars indicate the optimal tilt for each city; the dotted line marks the 26° industry-practice reference.

A main finding is the small difference between the constrained practical optimum and the 26° reference value. As shown in Table 2, the POA irradiation loss at 26° remains below 1% for Antalya, Konya, and Istanbul and is approximately 1.5% for Erzurum and Rize. These results indicate that 26° is a near-optimal irradiation reference within the modeled tilt range. Structural simplicity, wind loading, snow shedding, and related engineering considerations were not explicitly modeled and therefore require separate assessment.

Table 2. Comparison of POA irradiation at the optimum and at 26° tilt.

City	Optimal β* (°)	POA at β* (kWh/m²)	POA at 26° (kWh/m²)	Loss at 26°
Antalya	29	2055.4	≈ 2040	< 1%
Konya	28	1937.9	≈ 1929	< 0.5%
Istanbul	29	1695.8	≈ 1682	< 1%
Erzurum	31	1733.1	≈ 1707	≈ 1.5%
Rize	31	1401.7	≈ 1380	≈ 1.5%

ii. Layout Performance

A central finding is that the strip layout was eliminated from all feasible configurations. All tested strip configurations produced maximum shading ratios above the adopted 30% threshold, regardless of city or row spacing. Although strip layouts maximize the installed panel count, their continuous east–west panel coverage produces wide shadow bands, causing the maximum shading ratio to exceed the crop-preserving limit adopted in this study. This exclusion aligns with recent systematic evaluations showing that continuous and non-uniform shading profiles drastically impair crop light interception efficiency compared to scattered or optimized configurations [5, 7].

For identical panel counts and gap distances, the staggered layout produced maximum shading ratios approximately 1.5%-3.5% lower than those of the grid layout. Shifting alternate rows breaks the longitudinal alignment of the shadow bands and distributes shading more uniformly over the greenhouse floor. This difference is more pronounced under lower solar elevations, where longer projected shadows increase the importance of layout geometry.

However, the reduction in maximum shading does not mean that the staggered arrangement is universally the highest-energy feasible layout. For the 30 x 50 m greenhouse, the highest-energy feasible configuration

was grid in Antalya, Konya, Erzurum, and Rize, whereas staggered was selected for Istanbul. The preferred arrangement therefore depends on greenhouse dimensions, panel packing, local solar geometry, and the adopted shading constraint.

iii. Regional Performance Disparity

Regional differences are clearly reflected in the specific yield (kWh/kWp/yr), as shown in Figure 2. Antalya achieves the highest value at 1767.7 kWh/kWp/yr, whereas Rize records the lowest at 1205.5 kWh/kWp/yr. Antalya's specific yield is therefore approximately 47% higher than Rize's. Konya and Erzurum reach 1666.6 and 1490.4 kWh/kWp/yr, respectively, while Istanbul reaches 1458.4 kWh/kWp/yr.

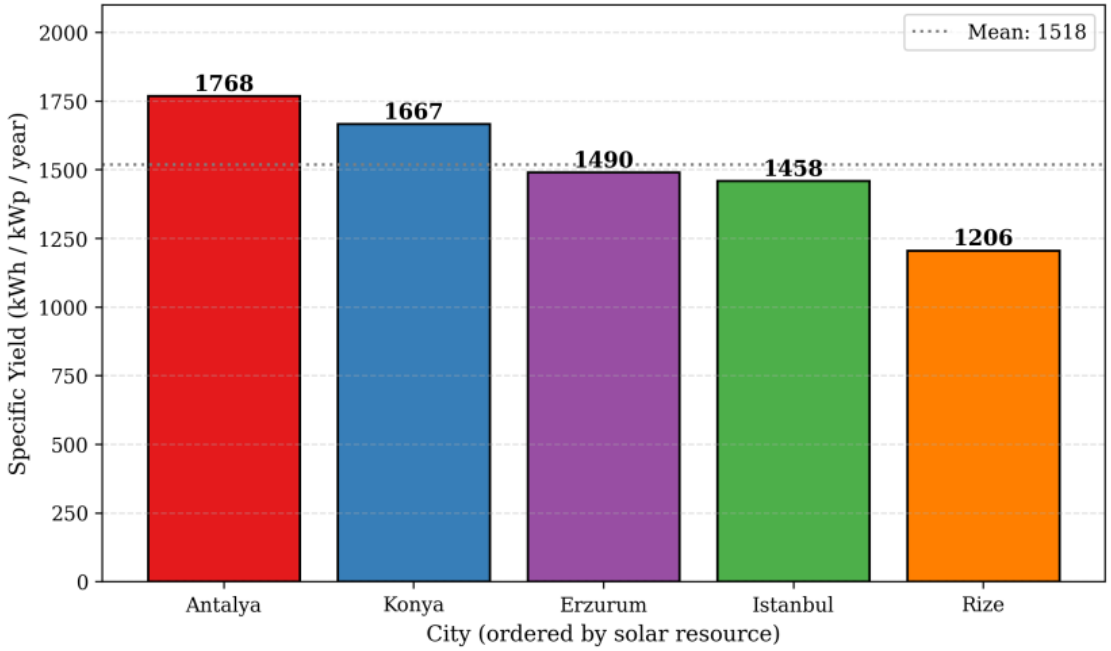

Fig. 2 Specific yield (kWh/kWp/year) for each case-study city. Antalya's specific yield is approximately 47% higher than Rize's, illustrating the importance of regional solar-resource conditions for agrivoltaic performance.

These differences are consistent with the regional solar-resource patterns represented in the PVGIS-TMY datasets. In particular, Istanbul achieves a higher specific yield than Rize despite their similar latitudes, indicating that latitude alone is insufficient for location-specific performance assessment. Because the present model does not isolate humidity, cloud cover, or precipitation as independent explanatory variables, their individual causal effects are not quantified here.

iv. Effect of Greenhouse Size

The comparison between the small (200 m²) and large (1500 m²) greenhouse cases shows that absolute annual energy production increases approximately with greenhouse floor area. Across the case-study cities, the large greenhouse produces approximately 7.5-8.0 times more annual energy than the small greenhouse, compared with a 7.5-fold difference in greenhouse area.

Specific yield, expressed as kWh per installed kWp, remains essentially independent of greenhouse size within the adopted performance-ratio model. Greenhouse size therefore primarily affects installed capacity and total annual electricity production, whereas local solar resource and panel tilt determine specific yield.

IV. CONCLUDING REMARKS

In this study, a reproducible computational framework was developed for the preliminary design and optimization of greenhouse-integrated agrivoltaic systems in Türkiye. The results provide several important findings, regarding panel tilt, layout performance, regional variability, as summarized below:

- The constrained practical optimum tilt angles fall within 28°-31° for the selected cities. The 26° industry-practice reference remains close to these optima from the perspective of annual POA irradiation, with a penalty below approximately 1.6% in all five cases.
- Continuous strip arrangements are infeasible under the adopted 30% maximum-shading constraint because all tested configurations exceed the threshold. Grid and staggered layouts provide feasible energy-shading trade-offs. Staggered arrangements reduce maximum shading in matched comparisons, but the highest-energy feasible layout remains dependent on city and greenhouse size.
- Antalya's specific yield is approximately 47% higher than Rize's, demonstrating that location-specific solar-resource assessment is essential for reliable agrivoltaic design. Similar latitude does not necessarily imply similar PV productivity.

It is important to highlight that the shading constraint is based on three equinox reference times and should not be interpreted as an absolute annual worst-case shading condition. In addition, the performance-ratio model provides a comparative first-order energy estimate. Future work therefore should incorporate dynamic module-temperature effects, inverter behavior, partial-shading losses, seasonal crop calendars, crop-specific light-response functions, techno-economic indicators, and experimental greenhouse validation. The suggested framework can tehn subsequently be extended to all 81 provinces of Türkiye to support a more comprehensive national design assessment.

Generative AI Disclosure

Generative AI tools were used by the first author solely for language refinement, manuscript formatting, and assistance in writing and debugging selected Python simulation scripts based on existing models. Artificial intelligence was not used to generate research data, results, analyses, references, or scientific conclusions. All AI-assisted content and code implementations were reviewed and verified by the authors, who take full responsibility for the final manuscript..

REFERENCES

[1] Goetzberger, A., Zastrow, A., 1982, On the coexistence of solar-energy conversion and plant cultivation. International Journal of Solar Energy, 1(1), 55-69.

[2] Dupraz, C., Marrou, H., Talbot, G., Dufour, L., Nogier, A., Ferard, Y., 2011, Combining solar photovoltaic panels and food crops for optimising land use: Towards new agrivoltaic schemes. Renewable Energy, 36(10), 2725-2732.

[3] Barron-Gafford, G. A., et al., 2019, Agrivoltaics provide mutual benefits across the food-energy-water nexus in drylands. Nature Sustainability, 2(9), 848-855.

[4] Weselek, A., et al., 2019, Agrophotovoltaic systems: Applications, challenges, and opportunities - A review. Agronomy for Sustainable Development, 39, 35.

[5] Zhang, W., Hendriks, P. W., Uchanski, M., Page, S., Renwick, A., Maxwell, T., Kaiser, C., Dong, J., de Koning, W., 2025, Climatic and design tipping points in agrivoltaic crop production systems. A meta-analysis. Agronomy for Sustainable Development, 45, 69.

[6] Mazzeo, D., Di Zio, A., Pesenti, C., Leva, S., 2025, Optimizing agrivoltaic systems: A comprehensive analysis of design, crop productivity and energy performance in open-field configurations. Applied Energy, 390, 125750.

[7] Renno, C., Di Marino, O., 2026, Agrivoltaics across crops and technologies: A systematic review of experimental tests on yield, microclimate, and energy performance. Energies, 19(2), 539.

[8] Coşgun, A. E., 2021, The potential of agrivoltaic systems in Turkey. Energy Reports, 7(Suppl. 3), 105-111.

[9] Bakırcı, K., 2012, General models for optimum tilt angles of solar panels: Turkey case study. Renewable and Sustainable Energy Reviews, 16(8), 6149-6159.

[10] Holmgren, W. F., Hansen, C. W., Mikofski, M. A., 2018, pvlib python: a python package for modeling solar energy systems. Journal of Open Source Software, 3(29), 884.

[11] European Commission Joint Research Centre, "Photovoltaic Geographical Information System (PVGIS)", https://re.jrc.ec.europa.eu/pvg_tools/en/, accessed November 2025.

[12] Cossu, M., et al., 2020, Agricultural sustainability estimation of the European photovoltaic greenhouses. European Journal of Agronomy, 118, 126074.

[13] Zainali, S., Ma Lu, S., Stridh, B., Avelin, A., Amaducci, S., Colauzzi, M., Campana, P. E., 2023, Direct and diffuse shading factors modelling for the most representative agrivoltaic system layouts. Applied Energy, 339, 120981.

8th International Conference on Engineering, Natural and Social Sciences

September 06-07, 2026: Konya, Turkey

© 2025 Published by All Sciences Academy

https://www.icensos.com/

Two-Dimensional Cutting Stock Algorithm for Sequencing Cart Layout Optimization

Caner Türker[1], Sevgi Karaca Bellofatto[2], Sema Alcan[3] and Zehra Kamışlı Öztürk[4,*]

[1]*Continental, Porto, Portugal*

[2]*Department of Industrial Engineering, Eskişehir Technical University, Eskişehir, Turkey*

[3]*Bosch, Munich, Bavaria, Germany*

[4]*Department of Industrial Engineering, Eskişehir Technical University, Eskişehir, Turkey*

**(zkamisli@eskisehir.edu.tr) Email of the corresponding author*

Abstract – In mass-customized automotive manufacturing assembly systems, efficient in-plant logistics and accurate line-side parts feeding are necessary to sustain continuous production without line stoppages. This study investigates the line-side feeding and parts kitting process at a major commercial vehicle and diesel engine manufacturing plant. Analysis of historical Discrepancy/Loss records showed that sequencing delivery errors accounted for 97% of recorded part delivery failures. Field investigations indicated that these errors occurred because warehouse operators loaded part boxes onto transport carts (dollies) manually based on paper pick-lists without a standard layout. This practice caused spatial fragmentation, damaged components, and increased operator search time. The cart loading process was formulated as a Two-Dimensional Cutting Stock / Bin Packing Problem (2D-BPP). Because 2D-BPP is NP-hard, mathematical models could not provide solutions within operational time limits for high-variety production schedules. Therefore, a Decision Support System (DSS) based on the Finite First-Fit (FFF) heuristic algorithm was developed. The system reads part specifications from enterprise databases and generates 2D visual layouts for 40 part packaging types. In the implementation, shelf area utilization increased from 81.86% to 88.67% (reaching 98.90% on the first shelf), and total unused space was reduced by 42.34%. Standardizing box coordinates reduced operator search time on the line and eliminated misplacement errors.

Keywords – Two-Dimensional Cutting Stock, Bin Packing Problem, Finite First-Fit Heuristic, Material Handling, Sequencing Cart, Automotive Assembly

I. INTRODUCTION

In automotive manufacturing, mixed-model assembly lines require continuous and synchronized part feeding. When parts arrive late, damaged, or out of sequence, station operations are interrupted, resulting in line stops and overtime [1], [2].

This study was conducted at a major commercial vehicle and diesel engine manufacturing plant located in Turkey. The facility operates large-scale heavy commercial vehicle and engine production lines. Material delivery from the central warehouse to the assembly lines (trim, chassis, and powertrain lines) is carried out using towable multi-tier sequencing carts called dollies (250 cm length × 120 cm width × 40 cm shelf height), pulled by tow tractors.

An analysis of plant Discrepancy/Loss (D/L) data showed that sequencing-related delivery errors accounted for 97% of part feeding problems. Field investigations revealed that warehouse operators placed part boxes onto dolly shelves randomly according to the order on Product Verification Specification (PVS) sheets. This practice had three main drawbacks: (1) irregular empty spaces formed between boxes, which

reduced total cart capacity; (2) fragile components were placed under or next to heavy boxes, causing material damage; and (3) line operators spent extra time locating parts on unorganized carts [3], [4].

To solve these problems, the cart loading process was formulated as a Two-Dimensional Cutting Stock/Bin Packing Problem (2D-BPP). Because 2D-BPP is an NP-hard problem, exact integer programming models cannot be solved in real time during production. Therefore, a Decision Support System (DSS) using the Finite First-Fit (FFF) heuristic algorithm was developed to generate standardized 2D loading layouts.

II. Materials and Methods

A. Plant Logistics Flows and Replenishment Mechanisms

Material replenishment from the central warehouse to workstation assembly points is organized through three main logistical flows: (1) Smart Kanban Flow, used for high-turnover small hardware where barcode cards in plastic bins trigger replenishment; (2) Call Part Flow, used for large and heavy components (e.g., fuel tanks, exhaust systems) where electronic calls alert forklift operators for delivery within 15 minutes; and (3) Sequencing Cart (Dolly Kitting) Flow, used for model-specific functional components (e.g., wiring harnesses, brackets, hoses) loaded onto 250 cm × 120 cm dollies in assembly order.

B. Discrepancy/Loss (D/L) Error Data Analysis

Plant D/L records were systematically analysed by vehicle identification number (VIN), part number, date, and responsible unit. Pareto analysis showed that sequencing issues accounted for 97.0% of total part feeding errors, while external supplier delays and inventory record mismatches represented only 3.0%. Monthly error tracking showed peaks during summer periods (52 errors in Month 6 and 61 errors in Month 7) due to a major assembly line rearrangement, while daily distributions remained consistently high across weekdays (54 on Monday, 55 on Tuesday, 59 on Thursday), proving that manual loading lacked fundamental standardization.

C. Two-Dimensional Bin Packing Problem and Heuristic Algorithms

In two-dimensional cutting and packing problems (2D-BPP / 2D-CSP), a set of rectangular items of known lengths and widths must be packed into larger rectangular bins without overlapping, minimizing unused dead space [6]–[8]. Because exact 0-1 integer linear programming models require prohibitive computation times for large item sets, level-oriented heuristics are widely employed in industrial practice [12]–[16].

Level algorithms organize items into horizontal rows (levels) from left to right, where the height of each level is determined by its tallest packed item [18]. Figure 1 illustrates the comparative mechanisms of classical level heuristics: Next-Fit Decreasing Height (NFDH), First-Fit Decreasing Height (FFDH), Best-Fit Decreasing Height (BFDH), and Finite First-Fit (FFF).

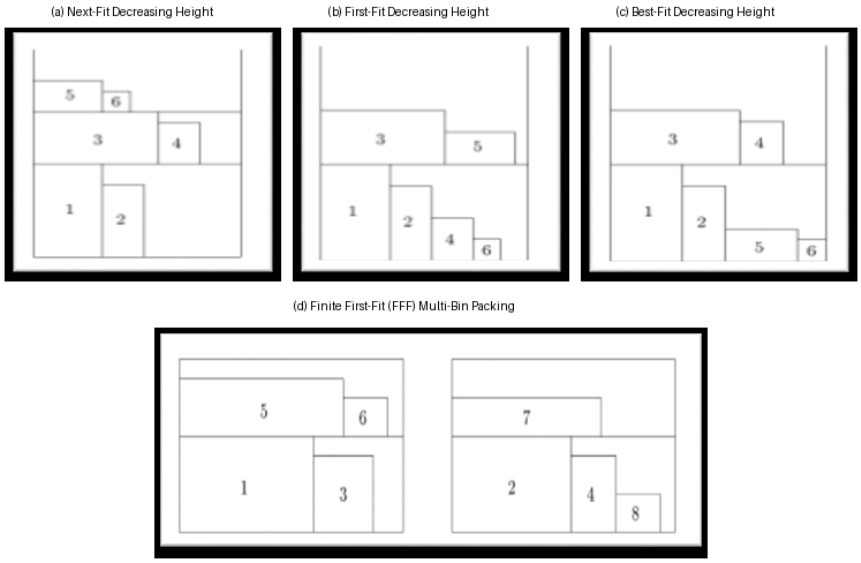

Fig. 1. Comparative level-packing mechanisms of two-dimensional heuristic algorithms: (a) NFDH, (b) FFDH, (c) BFDH, and (d) FFF multi-bin packing

D. Mathematical Model Formulation

Let L be the usable shelf length (250 cm) and W be the usable shelf width (120 cm). A set of n rectangular boxes is to be packed onto the shelf surface. Each box i $(i = 1, \ldots, n)$ has length l_i, width w_i, and quantity k_i $(k_i \geq 1)$. The decision variable x_{ipq} is defined as:

$$x_{ipq} = \begin{matrix} 1 & f\ box\ i\ is\ placed\ at\ coordinate\ (p,q) \\ 0 & 0.w. \end{matrix} \tag{1}$$

The discrete placement coordinate sets P and Q are generated by integer linear combinations of item dimensions:

$$P = \{\, p \mid p = \Sigma\, \alpha_i\, l_i, p \leq L - min(l_i), \alpha_i \geq 0, \alpha_i \in Z\} \tag{2}$$

$$Q = \{\, q \mid q = \Sigma\, \beta_i\, w_i, q \leq W - min(w_i), \beta_i \geq 0, \beta_i \in Z\,\} \tag{3}$$

The feasible coordinate subsets for item i are:

$$P_i = \{\, p \mid p \in P, p \leq L - l_i\,\} \tag{4}$$

$$Q_i = \{\, q \mid q \in Q, q \leq W - w_i\,\} \tag{5}$$

To prevent spatial overlapping between placed containers, overlap indicator parameter a_{ipqrs} is defined:

$$a_{ipqrs} = \begin{matrix} 1 & if\ p \leq r \leq p + l_i - 1\ and\ q \leq s \leq q + w_i - 1 \\ 0 & 0.w. \end{matrix} \tag{6}$$

The mathematical optimization model is subject to non-overlapping and demand constraints:

$$Non - overlapping: \Sigma_i \Sigma_{\{p \in P_i\}} \Sigma_{\{q \in Q_i\}} a_{ipqrs} \cdot x_{ipq} \leq 1, \forall\, r \in P, s \in Q \tag{7}$$

$$Demand\ limit: \Sigma_{\{p \in P_i\}} \Sigma_{\{q \in Q_i\}} x_{ipq} \leq b_i, \forall\, i = 1, \ldots, m \tag{8}$$

$$Integrality: x_{ipq} \in \{0, 1\}, \forall\, i, p, q \tag{9}$$

The objective function minimizes total unused shelf area:

$$Min\ Z = (W \cdot L) - \Sigma_\{i = 1\}\hat{}n\ (w_i \cdot l_i) \cdot x_i \tag{10}$$

The operational placement logic formulated above is solved using the FFF heuristic across discrete vertical levels. As depicted in Fig. 2, items are packed sequentially into active levels $(H_1, H_2, \dots)$, where each level's ceiling is bounded by its tallest item, and new tiers are initialized once the horizontal boundary is reached.

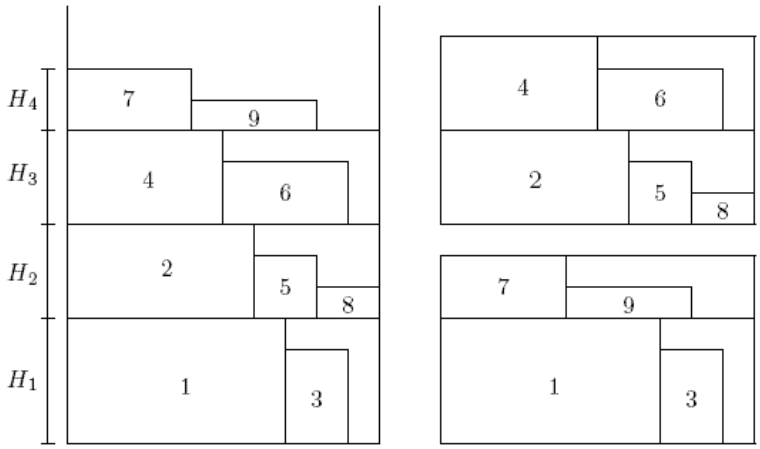

Fig. 2. Level-oriented packing mechanism of the Finite First-Fit (FFF) algorithm across cart shelf tiers

E. Decision Support System (DSS) Architecture

To deploy the FFF heuristic directly onto the shop floor, a Decision Support System was. The software reads production orders, retrieves container dimensions, executes the FFF layout routine in under 2 seconds, and displays an interactive, color-coded 2D layout map on warehouse picking terminals (Fig. 3).

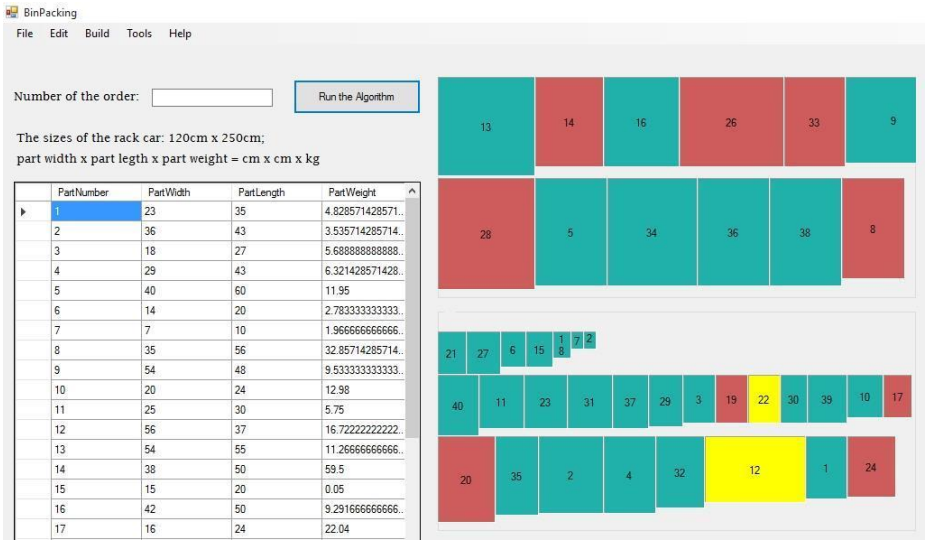

Fig. 3. Graphical user interface of the developed C# Decision Support System showing the optimized cart loading layout

Table 1 lists the standard container classifications and dimensions retrieved from the plant database. (Note: In accordance with confidentiality agreements, container codes have been anonymized with synthetic designations CTR-01 through CTR-22 while preserving actual physical dimensions).

Table 1. Standard container types and dimensions in the plant database (Anonymized Codes)

Container Code	Length (cm)	Width (cm)	Height (cm)
CTR-01	259.9	120.0	100.0
CTR-02	60.0	60.0	100.0
CTR-03	145.0	1.0	100.0
CTR-04	240.0	120.0	1.0
CTR-05	130.0	1.0	48.0
CTR-06	225.0	1.0	100.0
CTR-07	220.0	120.0	110.0
CTR-08	125.0	120.0	95.0
CTR-09	215.0	95.0	53.0
CTR-10	215.0	150.0	100.0
CTR-11	120.0	85.0	100.0
CTR-12	120.0	155.0	145.0
CTR-13	220.0	155.0	100.0
CTR-14	250.0	100.0	100.0
CTR-15	120.0	100.0	60.0
CTR-16	120.0	120.0	100.0
CTR-17	120.0	120.0	60.0
CTR-18	120.0	100.0	98.0
CTR-19	120.0	100.0	98.0
CTR-20	80.0	80.0	85.0
CTR-21	100.0	100.0	60.0
CTR-22	100.0	100.0	60.0

Table 2 shows the dimensional characteristics of 21 sample parts used in the test dataset. (Note: Part identification prefixes and base numbers have been anonymized with standardized test designations PRT-01 to PRT-21 for confidentiality).

Table 2. Dimensional data of sample automotive parts (Anonymized Designations)

No	Part Code	Category	Type	Width (cm)	Length (cm)
1	PRT-01	Cat-A	AC	40.00	60.00
2	PRT-02	Cat-B	DA	2.83	3.53
3	PRT-03	Cat-C	AB	16.67	10.00
4	PRT-04	Cat-B	DC	8.33	28.00
5	PRT-05	Cat-B	CA	28.00	37.00
6	PRT-06	Cat-D	BB	6.07	7.56
7	PRT-07	Cat-E	AC	30.00	44.00
8	PRT-08	Cat-F	AA	8.50	10.59
9	PRT-09	Cat-F	AA	8.50	10.59
10	PRT-10	Cat-B	BA	37.00	56.00
11	PRT-11	Cat-D	CA	118.90	217.00
12	PRT-12	Cat-C	AA	5.33	8.00
13	PRT-13	Cat-C	BB	2.83	3.53
14	PRT-14	Cat-C	CB	10.00	12.00
15	PRT-15	Cat-G	AC	4.00	6.00
16	PRT-16	Cat-F	AE	4.44	6.67
17	PRT-17	Cat-F	AB	8.33	12.00
18	PRT-18	Cat-B	DA	0.49	0.61
19	PRT-19	Cat-B	AB	0.43	0.53
20	PRT-20	Cat-A	BB	3.54	4.41
21	PRT-21	Cat-D	DA	36.00	43.00

III. RESULTS

To evaluate the algorithmic performance, experimental validation was conducted on a scheduled batch of 40 distinct automotive components packed across two cart shelf tiers (each measuring 250 cm × 120 cm = 30,000 cm² surface area; total cart area = 60,000 cm²).

Figure 4 illustrates the baseline manual random loading pattern on Shelf 1 and Shelf 2, where containers were placed in unorganized sequences.



Fig. 4. Baseline manual random layout on Shelf 1 and Shelf 2 showing dispersed dead space and irregular gaps

Table 3 presents the quantitative comparison between the baseline manual system and the FFF optimization program.

Table 3. Performance comparison between manual and FFF optimized cart loading

Metric	Manual System	FFF Program	Difference
Shelf 1 Total Area (cm²)	30,000	30,000	0
Shelf 1 Used Area (cm²)	24,273	29,670	+5,397 (+22.23%)
Shelf 1 Empty Area (cm²)	5,727	330	-5,397 (-94.24%)
Shelf 1 Utilization Rate (%)	80.91%	98.90%	+17.99%
Shelf 2 Total Area (cm²)	30,000	25,392 (boundary)	-4,608
Shelf 2 Used Area (cm²)	24,843	19,446	-5,397
Shelf 2 Empty Area (cm²)	5,157	5,946 (contiguous)	+789
Shelf 2 Utilization Rate (%)	82.81%	76.58%	-6.23%
Total Used Area (cm²)	49,116	49,116	0
Total Empty Area (cm²)	10,884	6,276	-4,608 (-42.34%)
Overall Utilization Rate (%)	81.86%	88.67%	+6.81%

In Shelf 1, used surface area expanded from 24,273 cm² to 29,670 cm², raising utilization efficiency from 80.91% to 98.90%. The empty area on Shelf 1 dropped from 5,727 cm² to 330 cm² (a 94.24% reduction). Across the complete two-tier cart, total empty space decreased from 10,884 cm² to 6,276 cm², achieving an overall 42.34% reduction in wasted space and lifting overall cart fill efficiency from 81.86% to 88.67%.

IV. DISCUSSION

A comparison between manual loading and heuristic layout optimization explains why spatial fragmentation occurs on assembly carts. Under manual picking, operators placed containers in the random sequence specified by the PVS pick list. Because adjacent components possessed disparate lengths and widths, placing them sequentially produced irregular, jagged packing edges on both shelves. While manual fill rates appeared moderately high (80.91% and 82.81%), the unoccupied 10,884 cm² space was split into dozens of narrow gaps between boxes, making it impossible to add more parts.

In contrast, the Finite First-Fit algorithm sorts boxes by dimensional height and packs them into organized horizontal rows. On Shelf 1, packing density reached 98.90% with minimal edge clearance (330 cm²). On Shelf 2, all remaining items were gathered into a compact 19,446 cm² area, creating a single continuous, usable free space of 5,946 cm². This allows logistics supervisors to assign additional sub-assembly kits to the same dolly, directly reducing tugger cart trips, aisle traffic, and transport labor costs.

Furthermore, displaying deterministic Cartesian placement coordinates on terminal screens standardizes picking tasks. Line-side assembly operators no longer waste time searching through disorganized carts, and incorrect part selections are prevented, resolving the root cause of the 97% sequencing-related D/L defect records.

V. CONCLUSION

In this study, the sequencing cart loading process at a commercial vehicle plant was modeled as a Two-Dimensional Cutting Stock Problem and solved using the Finite First-Fit (FFF) heuristic algorithm within a C# Decision Support System.

The main conclusions of the study are: (1) Analysis of D/L logs showed that 97.0% of part delivery errors were caused by manual sequencing cart loading; (2) The FFF algorithm increased Shelf 1 utilization from 80.91% to 98.90% and total cart utilization from 81.86% to 88.67%; (3) Total unused space on the cart was reduced by 42.34% (from 10,884 cm² to 6,276 cm²), and the remaining empty space was combined into a single usable section; and (4) The software standardized box positions, reducing operator search time and preventing line feeding errors.

VI. ACKNOWLEDGMENT

The authors thank the logistics engineers and warehouse personnel of the manufacturing plant for providing the operational data and technical collaboration for this study.

VII. REFERENCES

[1] S. M. Metev and V. P. Veiko, Laser Assisted Microtechnology*, 2nd ed., R. M. Osgood, Jr., Ed. Berlin, Germany: Springer-Verlag, 1998.*

[2] D. Pisinger, "Heuristics for the container loader problem," *European Journal of Operational Research*, vol. 141, no. 2, pp. 382–392, 2002.

[3] C. H. Papadimitriou and K. Steiglitz, Combinatorial Optimization: Algorithms and Complexity. *Englewood Cliffs, NJ: Prentice Hall, 1982.*

[4] W. B. Dowsland and K. A. Dowsland, "Packing problems," *European Journal of Operational Research*, vol. 56, no. 1, pp. 2–14, 1992.

[5] T. Dereli, T. Göçken, and G. S. Daş, "Analytical approaches to three-dimensional packing problems," *in Proc. Operations Research / Industrial Engineering XXIV National Congress (YA/EM)*, Gaziantep-Adana, Turkey, 2004.

[6] G. Ghiani, G. Laporte, and R. Musmanno, Introduction to Logistics Systems Planning and Control. *Chichester, UK: John Wiley & Sons, 2004.*

[7] A. Lodi, S. Martello, and D. Vigo, "Heuristic algorithms for the three-dimensional bin packing problem," *European Journal of Operational Research*, vol. 141, no. 2, pp. 410–420, 2002.

[8] E. G. Coffman, M. R. Garey, and D. S. Johnson, Approximation Algorithms for Bin Packing: A Survey. *Boston, MA: PWS Publishing Company, 1996.*

[9] T. J. Hodgson, "A combined approach to the pallet loading problem," *IIE Transactions*, vol. 14, no. 3, pp. 175–182, 1982.

[10] H. J. Steudel, "Generating pallet loading patterns: A special case of the two-dimensional cutting stock," *Management Science*, vol. 25, no. 10, pp. 997–1004, 1979.

[11] A. Smith and P. De Cani, "An algorithm to optimize the layout of boxes in pallets," *Journal of the Operational Research Society*, vol. 31, no. 7, pp. 573–578, 1980.

[12] W. B. Dowsland and E. Bischoff, "An application of the microcomputer to product design and distribution," *Journal of the Operational Research Society*, vol. 33, no. 3, pp. 271–280, 1982.

[13] J. E. Beasley, "An exact two-dimensional non-guillotine cutting tree search procedure," *Operations Research*, vol. 33, no. 1, pp. 49–64, 1985.

[14] B. Ram, S. Sarin, and C. S. Chen, “The pallet packing problem for non-uniform box sizes,” *International Journal of Production Research*, vol. 29, no. 10, pp. 1963–1968, 1990.

[15] J. Terno, G. Scheithauer, U. Sommerweiss, and J. Riehme, “An efficient approach for the multi-pallet loading problem,” *European Journal of Operational Research*, vol. 123, no. 2, pp. 372–381, 2000.

[16] U. Sommerweiss and G. Scheithauer, “4-Block heuristic for the rectangle packing problem,” *European Journal of Operational Research*, vol. 108, no. 3, pp. 509–526, 1998.

[17] H. Dyckhoff and U. Finke, Cutting and Packing in Production and Distribution. *Heidelberg, Germany: Physica-Verlag, 1992.*

[18] H. Dyckhoff, G. Scheithauer, and J. Terno, “Cutting and packing: An annotated bibliography,” *Technical Report MATH-NM-08-1996, TU Dresden, Germany*, 1996.

[19] A. Lodi, P. G. Marro, S. Martello, and P. Toth, “Algorithms for two-dimensional bin packing and assignment problems,” *Technical Report DEIS, University of Bologna, Italy*, 1999.

[20] S. Martello, D. Pisinger, and D. Vigo, “The three-dimensional bin packing problem,” *Operations Research*, vol. 48, no. 2, pp. 256–267, 2000.

[21] K. A. Patterson, C. M. Grimm, and T. M. Corsi, “Adopting new technologies for supply chain management,” *Transportation Research Part E: Logistics and Transportation Review*, vol. 39, no. 2, pp. 95–121, 2003.

[22] A. Söke and Z. Bingül, “Investigation of solutions to two-dimensional non-guillotine cutting stock problems using simulated annealing algorithm,” *Journal of Engineering and Natural Sciences*, vol. 8, no. 1, pp. 22–35, 2005.

[23] N. Nepomuceno, P. R. Pinheiro, and A. Coelho, “A hybrid optimization framework for cutting and packing problems,” *in Recent Advances in Evolutionary Computation for Combinatorial Optimization*, vol. 153, Berlin, Germany: Springer, 2008, pp. 87–99.

8th International Conference on Engineering, Natural and Social Sciences

September 06-07, 2026: Konya, Turkey

© 2025 Published by All Sciences Academy

https://www.icensos.com/

Yaşam Tarzı, Telomerler ve Kardiyovasküler Sağlık

Mesude AÇIKBAŞ

Selçuk Üniversitesi
mesudem42@gmail.com

Özet **–** Kardiyovasküler hastalıklar (KVH), dünya genelinde hastalık ve ölüm nedenleri arasında ilk sıralarda yer almaya devam etmektedir. Son yıllarda biyolojik yaşlanma süreçlerinin kardiyovasküler risk üzerindeki etkisinin daha iyi anlaşılması, telomer biyolojisine olan ilgiyi artırmıştır. Bu derlemede, değiştirilebilir yaşam tarzı faktörleri ile telomer uzunluğu ve kardiyovasküler sağlık arasındaki ilişki güncel çalışmalar doğrultusunda ele alınmıştır.

Çalışmada telomer dinamikleri ve hücresel yaşlanmanın yanı sıra fiziksel aktivite, beslenme, uyku, psikolojik stres, sigara ve alkol kullanımı gibi yaşam tarzı faktörleri değerlendirilmiştir. Çalışmalar genel olarak düzenli fiziksel aktivitenin, antioksidan açısından zengin ve dengeli beslenmenin, yeterli uykunun ve stresin kontrol altında tutulmasının oksidatif stres ve inflamasyonun azaltılmasına katkı sağlayabileceğini göstermektedir. Bu durumun telomer yapısının korunması üzerinde de olumlu etkileri olabileceği düşünülmektedir. Buna karşılık hareketsiz yaşam tarzı, obezite, uzun süreli psikolojik stres ve özellikle sigara kullanımı daha hızlı telomer kısalmasıyla ilişkilendirilmektedir.

Telomerlerin hızla kısalması; endotelyal fonksiyonların bozulması, nitrik oksit biyoyararlanımının azalması, damar elastikiyetinin kaybı, vasküler hücrelerde yaşlanma ve aterosklerotik sürecin ilerlemesi gibi mekanizmalar üzerinden kardiyovasküler hastalık riskini artırabilir. Yaklaşık 200 bin katılımcının verilerini içeren güncel bir meta-analizde, telomer uzunluğundaki her 1 kilobazlık artışın koroner kalp hastalığı riskinde yaklaşık %23 azalma ile ilişkili olduğu bildirilmiştir.

Mevcut bulgular birlikte değerlendirildiğinde, sağlıklı yaşam alışkanlıklarının yalnızca klasik kardiyovasküler risk faktörlerini değil, biyolojik yaşlanmayla ilişkili süreçleri de etkileyebileceği görülmektedir. Nitekim telomer uzunluğunun rutin klinik uygulamalarda güvenilir bir biyobelirteç olarak kullanılabilmesi için ölçüm yöntemlerinin standartlaştırılması ve uzun süreli, prospektif çalışmalarla mevcut bulguların desteklenmesi gerekmektedir.

I. GİRİŞ

Kardiyovasküler hastalıklar, dünya genelinde morbidite ve mortalitenin başlıca nedenleri arasında yer almayı sürdürmektedir. Hipertansiyon, diyabet, dislipidemi, obezite ve sigara kullanımı gibi geleneksel risk faktörlerinin yanı sıra, son yıllarda biyolojik yaşlanma süreçlerinin de kardiyovasküler risk üzerinde önemli rol oynadığı gösterilmiştir (Salih ve ark., 2024). Bu doğrultuda telomer biyolojisi, yaşlanma ile kardiyovasküler hastalıklar arasındaki ilişkinin anlaşılmasında öne çıkan araştırma alanlarından biri haline gelmiştir.

Telomerler, kromozomların uç bölgelerinde bulunan ve tekrarlayan TTAGGG hekzanükleotid dizilerinden oluşan yapılardır. Bu yapılar, ‘shelterin’ olarak adlandırılan altı proteinli bir kompleksle birlikte kromozom bütünlüğünün korunmasında görev alır (Salih ve ark., 2024). Her hücre bölünmesinde telomerlerde belirli ölçüde kısalma meydana gelir. Telomer uzunluğu kritik bir seviyeye ulaştığında hücre, kalıcı olarak hücre döngüsünden çıkarak replikatif senesansa girebilir veya apoptoz sürecine yönlenebilir. Bu nedenle telomer uzunluğu, yalnızca kronolojik yaşla değil, hücrenin yaşam boyunca maruz kaldığı kümülatif stresle de ilişkili bir biyolojik gösterge olarak değerlendirilmektedir. Güncel

çalışmalar, değiştirilebilir yaşam tarzı faktörleri ile telomer uzunluğu ve kardiyovasküler sağlık sonuçları arasında anlamlı ilişkiler bulunduğunu göstermektedir (Gürel ve ark., 2024)."

II. MATERYAL VE YÖNTEM

Bu çalışma, yaşam tarzı faktörleri, telomer biyolojisi ve kardiyovasküler sağlık arasındaki ilişkiyi güncel literatür doğrultusunda değerlendiren bir derlemedir. Çalışmada telomer biyolojisi; oksidatif stres, inflamasyon, hücresel senesans ve vasküler yaşlanma mekanizmaları açısından ele alınmıştır. Bu çerçevede fiziksel aktivite, beslenme, uyku kalitesi, stres yönetimi, sigara ve alkol kullanımı gibi değiştirilebilir yaşam tarzı faktörlerine ilişkin güncel araştırma bulguları karşılaştırmalı olarak incelenmiştir. Çalışma sistematik bir veri tabanı tarama protokolüne dayanmadığı için, yöntem bölümü derlemenin kapsamı ve yöntemsel sınırlılıkları dikkate alınarak yapılandırılmıştır.

III. BULGULAR

A. Telomer Biyolojisi ve Kardiyovasküler Yaşlanma

Telomerler, tekrarlayan TTAGGG dizilerinden oluşan ve kromozom uçlarını koruyan yapılardır. Telomer uzunluğu yaş ilerledikçe azalmakta, ancak bu süreç yalnızca kronolojik yaşa bağlı olarak gerçekleşmemektedir. Oksidatif stres, kronik sistemik inflamasyon, metabolik bozukluklar ve çevresel faktörler telomer kısalmasını belirgin şekilde hızlandırabilmektedir.

Telomer DNA'sı, yüksek guanin (G) içeriği nedeniyle reaktif oksijen türlerine (ROS) karşı son derece hassastır. Mitokondriyal disfonksiyon veya vasküler inflamasyon neticesinde artan ROS seviyeleri; telomer bölgesinde guanin oksidasyonuna (özellikle 8-oxo-7,8-dihydro-2'-deoxyguanosine [8-oxo-dG] oluşumuna) ve tek/çift zincirli DNA kırılmalarına yol açar (Fitzpatrick ve ark., 2007). Bu durum, shelterin kompleksinin telomerik DNA'ya bağlanma afinitesini bozarak telomerlerin ilmek yapısının (T-loop) çözülmesine ve telomer korumasının kaybına (uncapping) neden olur. Korunmasız kalan kromozom uçları, çift zincir kırığı olarak algılanarak p53/p21 ve p16/Rb sinyal yolaklarını aktive eder (Wu ve ark., 2025).

Kardiyovasküler sistemde telomer kısalmasının en önemli etkilerinden biri endotelyal hücre fonksiyonlarındaki bozulmadır. Kısa telomerler; nitrik oksit üretiminin azalmasına, damar elastikiyetinin kaybolmasına ve aterosklerotik süreçlerin hızlanmasına yol açabilmektedir. Ayrıca vasküler düz kas hücrelerinde meydana gelen senesans, damar duvarında yapısal değişikliklere neden olarak kardiyovasküler hastalık gelişimini kolaylaştırmaktadır. Senesent hücrelerin vasküler yatakta birikmesinin en yıkıcı sonuçlarından biri de Senesansla İlişkili Salgısal Fenotip (SASP) gelişimidir (Gürel ve ark., 2024). Son yıllarda gerçekleştirilen büyük ölçekli genetik çalışmalar, kısa lökosit telomer uzunluğunun kardiyovasküler hastalık riskiyle doğrudan ilişkili olduğunu doğrulamaktadır (Codd ve ark., 2024). Değiştirilebilir yaşam tarzı faktörleri ise belirgin moleküler yolaklar aracılığıyla telomer aşınmasını hızlandıran birer katalizör veya telomerik bütünlüğü koruyan hücresel birer kalkan görevi görür.

B. Fiziksel Aktivite ve Telomer Uzunluğu

Fiziksel aktivite, telomer biyolojisini etkileyen en kritik yaşam tarzı faktörlerinden biri kabul edilmektedir. Düzenli egzersizin oksidatif stres ve inflamasyonu azaltması, mitokondriyal fonksiyonları iyileştirmesi ve antioksidan savunma sistemlerini güçlendirmesi sayesinde telomer bütünlüğünü koruduğu düşünülmektedir.

Klinik literatürde egzersizin tipi ve süresine ilişkin farklı bulgular mevcuttur. Kim ve arkadaşlarının (2022) gerçekleştirdiği randomize kontrollü çalışmaların meta-analizinde, özellikle altı aydan uzun süre uygulanan aerobik egzersizlerin telomer uzunluğu üzerinde olumlu etkiler oluşturduğu bildirilmiştir. Buna karşın güncel bir sistematik derleme ve meta-analizde, fiziksel egzersizin genel olarak telomer uzunluğunda anlamlı bir artış sağlamadığı, ancak yüksek yoğunluklu interval antrenmanların (HIIT) telomer uzunluğunu olumlu yönde etkileyebildiği gösterilmiştir (Sánchez-González ve ark., 2024). HIIT

ve kronik dayanıklılık egzersizlerinin, anahtar bir shelterin bileşeni olan telomer tekrarına bağlanan faktör 2 (TRF2) ekspresyonunu artırdığı ve telomeraz aktivitesini yukarı regüle ettiği bilinmektedir (Werner ve ark., 2019).

Fiziksel aktivitenin kardiyovasküler sağlık üzerindeki yararları yalnızca telomer düzeyiyle sınırlı değildir. Düzenli egzersiz; kan basıncının düşürülmesi, glukoz metabolizmasının iyileştirilmesi, lipid profilinin düzenlenmesi ve inflamasyonun azaltılması gibi mekanizmalar yoluyla kardiyovasküler riski düşürmektedir. Bu nedenle egzersiz, hem telomer sağlığının korunmasında hem de kardiyovasküler hastalıkların önlenmesinde temel yaşam tarzı müdahalelerinden biridir.

C. Beslenme Alışkanlıkları ve Metabolik Durum

Beslenme, antioksidan ve antiinflamatuvar bileşenleri aracılığıyla telomer uzunluğunu etkileyen önemli çevresel faktörlerden biridir. Antioksidan ve antiinflamatuvar özelliklere sahip beslenme modellerinin telomer kaybını yavaşlatabildiği bilinmektedir. Akdeniz diyeti bu konuda en fazla araştırılan modellerden biridir. Sebze, meyve, tam tahıllar, baklagiller, balık ve zeytinyağı açısından zengin olan bu beslenme modeli; oksidatif stresin azaltılması ve inflamasyonun baskılanması yoluyla hem kardiyovasküler sağlığı desteklemekte hem de telomer bütünlüğünün korunmasına katkı sağlamaktadır (Gürel ve ark., 2024).

Buna karşılık yüksek kalorili, rafine şekerli ve ultra işlenmiş gıdalardan zengin beslenme örüntüleri obezite, insülin direnci ve kronik inflamasyonla ilişkilidir. Bu süreçler telomer kısalmasını hızlandırarak biyolojik yaşlanmayı artırabilmektedir. Nitekim yüksek vücut kitle indeksinin daha kısa telomer uzunluğu ile ilişkili olduğu genetik çalışmalarda da gösterilmiştir (Codd ve ark., 2024).

Son yıllarda D vitamininin telomer biyolojisi üzerindeki etkileri de araştırılmıştır. VITAL çalışmasının alt analizlerinde günlük D vitamini desteğinin telomer kısalmasını yavaşlatabileceği bildirilmiştir. Bununla birlikte söz konusu sonuçların doğrulanması için yeni prospektif çalışmalara ihtiyaç duyulmaktadır.

D. Uyku, Stres ve Psikososyal Faktörler

Kronik psikolojik stres, telomer uzunluğunu olumsuz etkileyen başlıca faktörler arasındadır. Uzun süreli stres durumunda artan kortizol düzeyleri, inflamasyon ve oksidatif stres mekanizmaları üzerinden telomer kaybını hızlandırabilmektedir. Ayrıca stres; fiziksel aktivite düzeyinin azalması ve sağlıksız beslenme alışkanlıklarının gelişmesi gibi dolaylı olumsuz etkiler de yaratmaktadır.

Uyku süresi ve kalitesi de telomer sağlığı açısından kritik önem taşır. Yetersiz uyku; inflamasyon, metabolik düzensizlikler ve otonom sinir sistemi aktivitesindeki değişiklikler aracılığıyla hücresel yaşlanmayı hızlandırabilmektedir. Buna karşın düzenli uyku ve etkin stres yönetiminin sağlıklı yaşlanma süreçlerini desteklediği bildirilmektedir.

E. Sigara ve Alkol Kullanımı

Sigara kullanımı, telomer kısalması ile ilişkisi en güçlü gösterilen yaşam tarzı faktörlerinden biridir. Sigara dumanında bulunan serbest radikaller DNA hasarını artırmakta ve telomerik bölgelerde oksidatif yıkıma neden olmaktadır. Bunun sonucunda hücresel yaşlanma hızlanmakta ve kardiyovasküler hastalık riski artmaktadır.

Genetik ve epidemiyolojik veriler, sigarayı bırakmanın daha uzun telomer uzunluğu ile ilişkili olduğunu göstermektedir. Buna karşın yüksek alkol tüketiminin daha kısa telomer uzunluğu ile ilişkili olduğu bildirilmiştir (Codd ve ark., 2024).

F. Telomer Uzunluğu ve Kardiyovasküler Hastalık Riski

Telomer uzunluğu ile kardiyovasküler hastalıklar arasındaki ilişkiyi inceleyen çalışmaların sayısı her geçen gün artmaktadır. Su ve arkadaşlarının (2025) yaklaşık 200 bin katılımcıyı içeren sistematik derleme ve doz-yanıt meta-analizinde, daha uzun telomer uzunluğuna sahip bireylerde koroner kalp hastalığı riskinin anlamlı derecede daha düşük olduğu gösterilmiştir.

Araştırmacılar, telomer uzunluğundaki her 1 kilobazlık artışın koroner kalp hastalığı riskinde yaklaşık %23'lük bir azalma ile ilişkili olduğunu bildirmiştir. Bu bulgular, telomer uzunluğunun yalnızca

yaşlanmanın bir göstergesi olmadığını, aynı zamanda kardiyovasküler risk değerlendirmesinde kullanılabilecek potansiyel bir biyobelirteç olduğunu ortaya koymaktadır.

IV. TARTIŞMA

Bu çalışmanın bulgularının önemi araştırılmalı, ama bulguları tekrar verilmemelidir. Bulgular, önceki çalışmalarla karşılaştırılmalı ve bilime katkısı yorumlanmalıdır.

Mevcut bulgular, yaşam tarzı ile telomer dinamikleri arasındaki ilişkinin tek yönlü ve basit olmadığını ortaya koymaktadır. Fiziksel aktiviteye ilişkin veriler bu duruma somut bir örnektir. Kim ve ark. (2022) tarafından yapılan meta-analizde özellikle altı aydan uzun süreli aerobik egzersizlerin telomer uzunluğu üzerindeki olumlu etkileri bildirilirken; Sánchez-González ve ark. (2024) tarafından yayımlanan daha güncel bir çalışmada egzersizin genel olarak belirgin bir telomer uzaması sağlamadığı, ancak yüksek yoğunluklu interval antrenmanların (HIIT) olumlu etkiler gösterebileceği vurgulanmıştır. Bu farklılıklar; egzersizin tipi, yoğunluğu, süresi ve çalışma popülasyonlarının özellikleri gibi değişkenlerin telomer yanıtındaki farklılıklarda rol oynayabileceğini düşündürmektedir.

Beslenme, metabolik durum, uyku ve psikososyal stres açısından elde edilen bulguların ortak paydası oksidatif stres ve kronik inflamasyondur. Akdeniz tipi beslenmenin antioksidan ve antiinflamatuvar özellikleri telomer bütünlüğünün korunmasını desteklerken; obezite, insülin direnci, yetersiz uyku ve kronik stres telomer aşınmasını hızlandıran biyolojik bir ortam hazırlamaktadır. Sigara kullanımı ise telomer kısalmasıyla ilişkisi en güçlü gösterilen yaşam tarzı faktörlerinden biridir.

Kardiyovasküler açıdan telomer kısalması; endotel disfonksiyonu, nitrik oksit biyoyararlanımında azalma, damar elastikiyetinin kaybı, vasküler düz kas hücrelerinde senesans ve SASP gelişimi gibi patofizyolojik süreçlerle ilişkilendirilmektedir. Su ve ark. (2025) tarafından yaklaşık 200 bin katılımcıyı kapsayan meta-analizde telomer uzunluğundaki her 1 kilobazlık artışın koroner kalp hastalığı riskinde yaklaşık %23 azalma ile ilişkili bulunması, telomer uzunluğunun potansiyel bir biyobelirteç olarak önemini desteklemektedir. Bununla birlikte mevcut veriler, telomer uzunluğunun rutin klinik pratikte tek başına bir karar parametresi olarak kullanılmasını destekleyecek kanıtların henüz yeterli olmadığını göstermektedir.

V. SONUÇLAR

Telomerler, biyolojik yaşlanmanın önemli belirteçlerinden biri olup kardiyovasküler sağlıkla yakından ilişkilidir. Güncel literatür; düzenli fiziksel aktivite, dengeli beslenme, yeterli uyku, stres yönetimi ve sigaradan uzak durma gibi yaşam tarzı faktörlerinin telomer bütünlüğünün korunmasına katkı sağlayabileceğini göstermektedir. Bu olumlu etkilerin, başta oksidatif stres ve inflamasyonun baskılanması olmak üzere çeşitli mekanizmalar üzerinden gerçekleştiği ve kardiyovasküler hastalık riskinin düşürülmesine katkı sağladığı düşünülmektedir.

Telomer uzunluğunun rutin klinik pratikte kullanımına ilişkin metodolojik ve uygulamaya yönelik sınırlılıklar bulunmakla birlikte, mevcut veriler yaşam tarzı müdahalelerinin yalnızca klasik kardiyovasküler risk faktörlerini değil, biyolojik yaşlanmayla ilişkili süreçleri de etkileyebileceğini ortaya koymaktadır. Gelecekte yürütülecek uzun dönemli prospektif çalışmalar, telomer temelli biyobelirteçlerin kardiyovasküler hastalıkların önlenmesi ve klinik yönetimindeki yerinin daha net belirlenmesine katkı sağlayacaktır.

KAYNAKLAR

[1] Codd, V., Wang, Q., Allara, E., Musicha, C., Kaptoge, S., Butterworth, A. S., ... Danesh, J. (2024). *Breaking down causes, consequences, and mediating effects of telomere length variation on human health*. Nature Aging.

[2] Fitzpatrick, A. L., Kronmal, R. A., Gardner, J. P., Psaty, B. M., Jenny, N. S., Tracy, R. P., ... & Aviv, A. (2007). *Leukocyte telomere length and cardiovascular disease in the cardiovascular health study*. American journal of epidemiology, *165*(1), 14-21.

[3] Gürel, S., Pak, E. N., & Tek, N. A. (2024). Aging processes are affected by energy balance: Focused on the effects of nutrition and physical activity on telomere length. Current Nutrition Reports, 13(2), 264–279.

[4] Kim, J., Wang, Z., Heymsfield, S. B., Baumgartner, R. N., & Gallagher, D. (2022). *Does exercise affect telomere length? A systematic review and meta-analysis of randomized controlled trials.* International Journal of Environmental Research and Public Health, 19(5), 2915.
[5] Salih, A. M., Galazzo, I. B., Menegaz, G., & Altmann, A. (2024). *Leukocyte telomere length and cardiac structure and function: a Mendelian randomization study.* Journal of the American Heart Association, 13(3), e032708.
[6] Sánchez-González, J. L., Sánchez-Rodríguez, J. L., Varela-Rodríguez, S., González-Sarmiento, R., Rivera-Picón, C., Juárez-Vela, R., ... Navarro-López, V. (2024). *Effects of physical exercise on telomere length in healthy adults: Systematic review, meta-analysis, and meta-regression.* JMIR Public Health and Surveillance, 10, e46019.
[7] Su, Y., Yin, L., Zhao, Y., et al. (2025). The association of telomere length and coronary heart disease: A systematic review and dose-response meta-analysis. Nutrition, Metabolism and Cardiovascular Diseases, 35(4), 103830.
[8] Wu, X., Zhou, Q., Huang, Y., Jiang, W., Zhou, J., Qian, K., ... & Chen, S. (2025). *Cellular senescence in age-related cardiovascular disease: past and future.* Frontiers in Aging, 6, 1721744.

8th International Conference on Engineering, Natural and Social Sciences

September 06-07, 2026: Konya, Turkey

© 2026 Published by All Sciences Academy

https://www.icensos.com/

Design and Functional Optimization of 3D-Printed Polymer Molds for PET Bottle Blow Molding

Dorian Osmanaj[1, *] and Erald Piperi [1]

[1] *Department of Production and Management, Polytechnic University of Tirana, Albania*

dosmanaj@fim.edu.al

Abstract – Aluminum tooling remains the leader of the industry for PET bottle blow molding because of its strong mechanical and thermal performance, but nowadays making it has considerable cost, time, and material, which limits its use for prototyping and small-batch production. From here we were thinking to produce polymer molds who can serve as a rapid-tooling alternative for aluminum molds, focusing on the design and functional behavior of a fused deposition modeling (FDM) mold. We designed a single-cavity mold in AutoCAD from geometric data obtained by 3D scanning an existing PET bottle and manufactured it in polylactic acid (PLA) on a Ultimaker 3 FDM printer. Internal serpentine cooling channels were built into the cavity to compensate for PLA's low thermal conductivity relative to conventional tooling metals. After the production we installed the mold on a MIPET 1M blow molding machine from Meccanoplastica Group and we produced a complete PET bottle and we optimize the dimensional parameters of the mold for this first stage test. The trial also pointed to the process-side variables that still need refinement before scale-up, cooling-channel placement and mold-closure precision while the FDM printing parameters themselves were not a limiting factor. Printing the mold took approximately 25 hours, against the several weeks normally needed for a CNC-machined aluminum mold. These results lay the groundwork for a second phase, in which higher-performance photopolymer resins such as Formlabs High Temp Resin, printed on a Formlabs Form 4, will be tested as closer substitutes for metallic tooling in thermal stability, dimensional accuracy, and durability, while keeping the cost, lead-time, and customization benefits that additive manufacturing brings.

Keywords – Additive manufacturing; PET blow molding; sustainable manufacturing

I. INTRODUCTION

Blow molding of polyethylene terephthalate (PET) containers is among the most widely used processes in the packaging industry, prized for its short cycle times and high production volumes [1]. Molds for this process are conventionally machined from aluminum like shown in figure 1. Aluminum tooling offers high thermal conductivity, dimensional stability, and a long service life, but it typically takes several weeks to produce and carries a substantial cost a burden felt most acutely in prototyping, design validation, and small-batch or highly customized production.

Additive manufacturing (AM) has increasingly been put forward as a rapid-tooling alternative to conventional mold machining. It offers shorter lead times, lower upfront cost, and greater geometric freedom, including cooling channels that would be difficult or impossible to drill conventionally [1], [2], [3]. Prior work on 3D-printed molds for stretch blow molding has already demonstrated their feasibility for low- to mid-volume production and pre-production design iteration, using stereolithography (SLA) tooling [1]. Fused deposition modeling (FDM), though less dimensionally precise and less thermally

efficient than SLA, is far more accessible and lower cost, which makes it an attractive entry point for organizations exploring polymer tooling before committing to more expensive resin systems.



Fig. 1 Aluminium mold.

Low-cost thermoplastics such as polylactic acid (PLA) have one clear drawback: comparatively poor thermal performance. PLA's glass transition temperature sits around 60 °C, and its thermal conductivity, on the order of 0.06–0.09 W/(m·K), is roughly three orders of magnitude below that of aluminum [4]. Both limit the achievable cycle time and the mold's dimensional stability under repeated thermal loading, and both make cooling-channel design especially important, since heat cannot leave the cavity surface as efficiently as it would in metal tooling [2], [3].

Here we report the design, fabrication, and first functional trial of a single-cavity FDM mold in PLA for PET bottle blow molding. Unlike much of the existing literature, which focuses on optimizing FDM print parameters (infill, layer height, orientation, etc.), this first research phase deliberately holds print parameters fixed and instead asks a process-level question: can a PLA mold with internal conformal cooling channels withstand the blow-molding cycle and produce an acceptable bottle, and which process-side variables affect the outcome the most? The results are meant to establish a baseline for a later phase in which higher-temperature photopolymer resins are evaluated as closer substitutes for metallic tooling.

II. Materials and Method

A. Mold Design

We scanned an existing commercial PET bottle in 3D to obtain an accurate reference of its external and internal profile. That scanned geometry became the basis for a single-cavity blow mold designed in AutoCAD as shown in figure 2, so the cavity reproduced the original bottle's dimensions and wall geometry instead of an approximated or freehand model.

Because PLA conducts heat far less readily than aluminum, effective heat extraction from the cavity surface cannot rely on the bulk conductivity of the mold body alone. We therefore designed the cooling system as a set of internal serpentine channels that follow the internal surface of the cavity a conformal-cooling layout meant to keep the coolant close to and evenly distributed across the molding surface, compensating for the polymer's limited conductivity [2], [3].

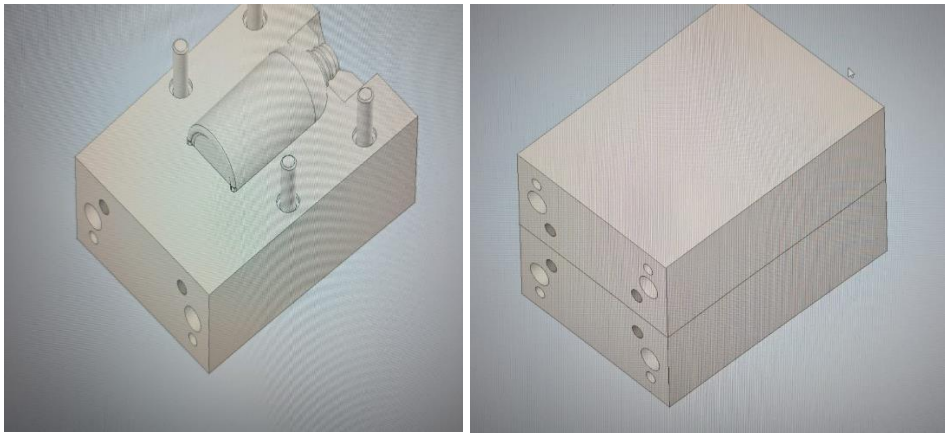

Fig. 2 Mold design

B. *Fabrication*

We manufactured the mold by fused deposition modeling (FDM) on a Ultimaker 3 3D printer like shown in figure 3, using polylactic acid (PLA) filament. Printing parameters layer height, infill density, wall count, print orientation, and so on were not the object of investigation in this first phase and were left at standard, manufacturer-recommended settings; their systematic optimization is left for future work, once the functional validation reported here is complete. The mold was printed as a single cavity, with a total print time of approximately 25 hours.

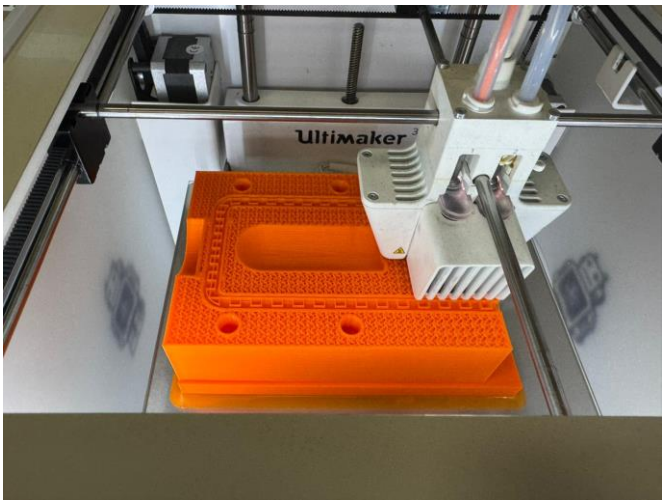

Fig. 3 Mold printing

C. *Blow Molding Trial*

We installed the printed mold on a Meccanoplastica Group MIPET 1M blow molding machine (Italy) in place of the conventional aluminum tooling. The trial's purpose was to evaluate the mold's process-level behavior under real operating conditions, not to characterize the printed part in isolation. The main question was where the machine's operating parameters needed adjustment for polymer tooling principally the positioning of the cooling channels relative to the cavity wall and the precision of mold closure since both affect heat extraction and dimensional accuracy differently than they would in a metallic mold [5], [6].

D. *Future Material Development*

These first-phase results will inform a second phase of the study, in which we plan to reproduce the mold in a higher-performance engineering photopolymer, Formlabs High Temp Resin, printed on a Formlabs Form 4 stereolithography (SLA) printer available in our laboratory. High Temp Resin offers a heat deflection temperature of up to 238 °C at 0.45 MPa after thermal post-curing, well above PLA's glass transition temperature, and is marketed specifically for mold and insert applications [7]. Our goal in this second phase is to assess whether an SLA-printed resin mold can approach the thermal stability and dimensional durability of aluminum tooling while keeping the practical advantages that additive manufacturing offers in cost, lead time, and design customization.

III. RESULTS

We installed the FDM-printed PLA mold on the MIPET 1M blow molding machine and used it to produce a complete PET bottle that reproduced the geometry of the scanned reference bottle. This is an initial demonstration that the single-cavity PLA mold is structurally and functionally sound under real blow-molding conditions, not merely on a bench-top or simulated test.

During the trial, the mold withstood the mechanical loading from the blowing pressure without catastrophic failure of the cavity or the internal cooling channels. The serpentine channels removed enough heat from the cavity to complete a full molding cycle. Two process variables stood out as having the greatest influence on cycle behavior the precise location of the cooling channels relative to the cavity surface, and the consistency of mold closure at the parting line and neither had yet been optimized in this first trial.

In terms of manufacturing time, the mold took approximately 25 hours to print, against a lead time on the order of several weeks commonly reported as four to eight for a CNC-machined aluminum mold of comparable complexity [8], [9]. FDM print parameters were not varied systematically in this phase, in keeping with its focus on process-level feasibility rather than print optimization.

IV. DISCUSSION

The successful production of a complete bottle shows that a single-cavity FDM PLA mold can survive at least one full blow-molding cycle on production equipment a necessary, though not sufficient, condition for treating polymer tooling as a rapid-tooling option ahead of committing to more expensive engineering resins or metal tooling [1]. It also matches earlier reports that 3D-printed molds are viable for low-volume and pre-production applications in blow and injection molding, provided the mold's thermal design compensates for the lower conductivity of the printing material [1], [10].

PLA's low thermal conductivity roughly two to three orders of magnitude below aluminum's combined with a glass transition temperature near 60 °C [4], shifts most of the burden of heat removal onto the cooling-channel layout instead of the bulk mold material; in metallic tooling, by contrast, conduction through the mold body itself plays a significant role [2], [3]. Choosing internal serpentine, conformal-type channels over straight drilled channels follows the broader conformal-cooling literature, which reports more uniform mold-surface temperatures and shorter cycle times when channels trace the cavity geometry instead of running in a straight line [2], [3]. That channel placement emerged here as a key variable needing further tuning fits well with that literature, and points to channel geometry more than PLA's bulk properties alone as the main lever for improving cycle stability in the next iteration of this mold.

The observed time savings also make an economic case for polymer tooling. A lead time on the order of 25 hours compares favorably with the several weeks typically needed to machine an aluminum mold, and with reported tooling costs that range from a few thousand to well over one hundred thousand US dollars depending on complexity [8], [9]. Even allowing for the shorter service life expected of a PLA mold, this lead-time and cost advantage matters most for prototyping, design iteration, and low-volume or highly customized production not as a wholesale replacement for high-volume aluminum tooling [8], [9], [10].

PLA's thermal ceiling does limit how far this approach can be pushed. Mold surface temperatures in commercial PET blow molding are generally controlled through cooling water in roughly the 8–65 °C range for cold blow molding, and PLA's low glass transition temperature leaves little thermal margin

before the cavity surface itself starts to soften under repeated cycling [4], [6]. This is what motivates the planned second phase using Formlabs High Temp Resin: its heat deflection temperature of up to 238 °C after post-curing [7] offers a much larger thermal margin and may allow longer production runs and more aggressive cycle times than PLA can sustain. An SLA process such as the Form 4 also delivers finer dimensional accuracy than FDM, which should help reduce the mold-closure precision issues seen in the present trial.

Beyond the cost and lead-time benefits, additive manufacturing of blow molds also makes a sustainability case that subtractive metal tooling struggles to match. Material use is limited to what is deposited in the final part; geometries such as the internal cooling channels used here need no secondary drilling or assembly; and molds can be customized or iterated on demand without the material waste that comes from machining a new aluminum block for every design revision [8], [9], [10]. Even so, we see these findings as a single feasibility trial. Durability across many production cycles, dimensional drift under repeated thermal loading, and a quantitative comparison against aluminum tooling remain open questions that the planned second phase, and a longer production trial, are meant to address.

V. CONCLUSION

We designed a single-cavity FDM mold in AutoCAD from a 3D-scanned reference bottle, manufactured it in PLA with internal serpentine cooling channels, and used it to produce a complete PET bottle on a Meccanoplastica Group MIPET 1M blow molding machine. That result confirms the structural and functional feasibility of a low-cost FDM polymer mold for at least one blow-molding cycle, and it identifies cooling-channel placement and mold-closure precision not FDM print parameters as the priority variables for process-level optimization in this application. The mold was produced in approximately 25 hours, against a typical lead time of several weeks for an equivalent CNC-machined aluminum mold, which supports the case for polymer tooling in prototyping, design iteration, and small-batch or customized production.

These results provide a baseline for a second research phase, in which we plan to reproduce the mold in Formlabs High Temp Resin using a Formlabs Form 4 SLA printer. Our aim is to evaluate whether a higher-temperature engineering resin can more closely match the thermal stability, dimensional accuracy, and cycle durability of conventional aluminum tooling, while preserving the practical benefits cost, lead time, and customization demonstrated in this first phase.

VI. ACKNOWLEDGMENT

The authors gratefully acknowledges the financial support provided by the National Agency for the Information Society (NASRI) for the project 'Digitalization Technologies for a Sustainable Industry through 3D Printing

VII. REFERENCES

[1] Formlabs, *Low-Volume Rapid Stretch Blow Molding With 3D Printed Molds*, White Paper, Formlabs, Somerville, MA, USA, 2024. [Online]. Available: https://formlabs.com/white-papers/low-volume-rapid-stretch-blow-molding-with-3d-printed-molds/

[2] K. M. Au and K. M. Yu, "Conformal cooling channel design and CAE simulation for rapid blow mould," *Int. J. Adv. Manuf. Technol.*, vol. 66, pp. 311–324, 2013.

[3] M. S. Shinde and K. M. Ashtankar, "Additive manufacturing–assisted conformal cooling channels in mold manufacturing processes," *Advances in Mechanical Engineering*, vol. 9, no. 5, 2017.

[4] M. S. Barkhad, B. Abu-Jdayil, A. H. Mourad, and M. Z. Iqbal, "Thermal Insulation and Mechanical Properties of Polylactic Acid (PLA) at Different Processing Conditions," *Polymers*, vol. 12, p. 2091, 2020.

[5] B. Demirel, "Optimisation of mould surface temperature and bottle residence time in mould for the carbonated soft drink PET containers," *Polymer Testing*, vol. 60, pp. 220–228, 2017.

[6] Formlabs, "High Temp Resin — Technical Data Sheet," Formlabs, Somerville, MA, USA. [Online]. Available: https://formlabs.com/products/high-temp-resin/

[7] "Feasibility Study on the Fused Filaments of Injection-Molding-Grade Poly (Ethylene Terephthalate) for 3D Printing," *Polymers*, vol. 14, no. 11, art. 2276, 2022. doi: 10.3390/polym14112276.

[8] Clinton Aluminum, "Conformally Cooled Steel Molds vs. Aluminum Molds For Plastic Injection Molding," 2023. [Online]. Available: https://clintonaluminum.com/conformally-cooled-steel-molds-vs-aluminum-molds/

[9] Formlabs, “Guide to Low-Volume Injection Molding,” Formlabs. [Online]. Available: https://formlabs.com/blog/low-volume-injection-molding/
[10] Fictiv, “3D Printed Molds: A Cost-Effective Alternative for Low-Volume Production and Prototyping,” Fictiv, 2025. [Online]. Available: https://www.fictiv.com/articles/3d-printed-mold

8th International Conference on Engineering, Natural and Social Sciences

September 06-07, 2026: Konya, Turkey

© 2025 Published by All Sciences Academy

https://www.icensos.com/

Machine Learning-Based Surrogate Prediction of Peak Crush Energy in Vehicle-to-Barrier Collisions

Vedat Yeğin*

1Department of Mechanical Engineering, İskenderun Technical University, Hatay, Türkiye

**(vedat.yegin@iste.edu.tr) Email of the corresponding author*

Abstract **–** This paper presents a reduced-order nonlinear vehicle-to-barrier (V2B) oscillator that is integrated in time and used to train surrogate models for peak crush energy. The learning target is E_struct ≡ U(x_max), the work stored in the nonlinear crush spring at maximum dynamic compression. Viscous dissipation is recorded separately and excluded from the learning target. During contact the motion is governed by $m\ddot{x} + c\dot{x} + k_1x + k_2x^2 = 0$. The identity Ek + U + E_damp = E_init holds on every run to a maximum relative residual of 9.6×10^{-13}. A 230-case Latin-hypercube campaign uses the inputs X = [v, m, θ, k1, k2, c]. Forty-nine simulations remain in contact at t = 0.20 s; in all of them the peak crush occurs by 108 ms and unloading has begun, so U(x_max) remains valid. The data comprise 123 training cases, 41 interpolation tests, an unused 18-case guard band at 62–66 km/h, and 48 high-speed holdout cases with v ≥ 66 km/h. Second-order polynomial ridge and radial-basis support-vector regression (SVR) are essentially equivalent in interpolation (R^2 = 0.986). SVR is only modestly more accurate on the holdout set (R^2 = 0.966 versus 0.956). Under this held-velocity experiment, random forest and XGBoost decline to $R^2 \approx 0.55$. Interpolation-domain permutation importance ranks impact velocity first and equivalent damping second. The formulation is not a full-vehicle finite-element model and is not validated against NCAP.

Keywords – vehicle-to-barrier collision; lumped-parameter crash model; peak crush energy; surrogate modelling; support vector regression; polynomial response surface

I. Introduction

Machine-learning studies of road crashes form two mature streams. Stream A maps historical crash-database attributes onto categorical severity classes [1]–[6]. Stream B maps the geometry and material parameters of energy absorbers onto component crashworthiness metrics [7]–[9]. Physical vehicle-level collision models can compute energy quantities [10]–[15], yet they are seldom coupled to a surrogate trained on a transient crush-energy output rather than on a closed-form algebraic expression.

A previous MATLAB/Simulink investigation by Yeğin [16] examined collision-response trends under variations of speed, impact angle and tyre–road friction, using a simplified analytical energy formulation. That formulation does not resolve transient structural crush dynamics, nor does it separate deformation work from other loss mechanisms; it was therefore not adopted as the machine-learning target in the present study. The current work introduces a transient nonlinear reduced-order vehicle-to-barrier (V2B) model and derives the learning target from the dynamic crush response. Table 1 summarises representative, independently verified studies and their distinction from this surrogate. A related collision-condition study predicts local structural damage rather than peak crush energy [17].

Table 1. Representative literature and distinction from the present V2B peak-crush-energy surrogate.

Study	Basis	Inputs	Target	Method	Vehicle-level energy?	Distinction
Rahim and Hassan [1]	A: crash records	work-zone fields	severity class	deep learning	No	Classification, not energy
Alam et al. [5]	A: crash records	engineered crash features	severity class	tree ensembles	No	Classification, not energy
Wang et al. [7]	B: crash-box FE	auxetic geometry	EA, peak force	LS-SVR	Component	Geometry, not pre-impact V2B
Zheng et al. [9]	B: train FE	absorber capacities	interface energy	XGBoost	Train interface	Hardware force capacities
Klausen et al. [13]	C: LPM / test	identified k, c	pulse reconstruction	Kelvin LPM	Physics, no ML	No surrogate DOE
Yeğin [16]	C: Simulink trends	v, θ, μ	simplified energy quantity	analytical	Simplified, no ML	Not a transient crush target
Liu et al. [17]	D: vehicle FE	object, angle, offset, speed	local damage	RF vs SVMR	No (damage)	Closest inputs; different target

II. Materials and Method

A. *Reduced-order V2B model*

The vehicle is represented as a single effective mass m striking a rigid barrier. The crush coordinate $x > 0$ measures deformation into the barrier. The model is a reduced-order nonlinear V2B oscillator; it is not a full-vehicle finite-element crash model, not a validated NCAP vehicle, and not a planar vehicle-to-vehicle reconstruction. Tyre–road friction μ is not an input. Oblique impact enters only through the normal component $v_n = v\cos\theta$, with $\theta = 0°$ corresponding to a full-frontal strike. The sampled angle range is 0–35°. During contact the governing equation is $m\ddot{x} + c\dot{x} + k1\,x + k2\,x^2 = 0$. If $x \le 0$ and $\dot{x} \le 0$, barrier forces are set to zero. Time integration is performed with MATLAB ode45 (RelTol = 10^{-8}, $t \in [0, 0.20]$ s) and a terminal event when x crosses zero from above. Fig. 1 summarises the workflow. Fig. 2 illustrates the nonlinear crush-spring force.

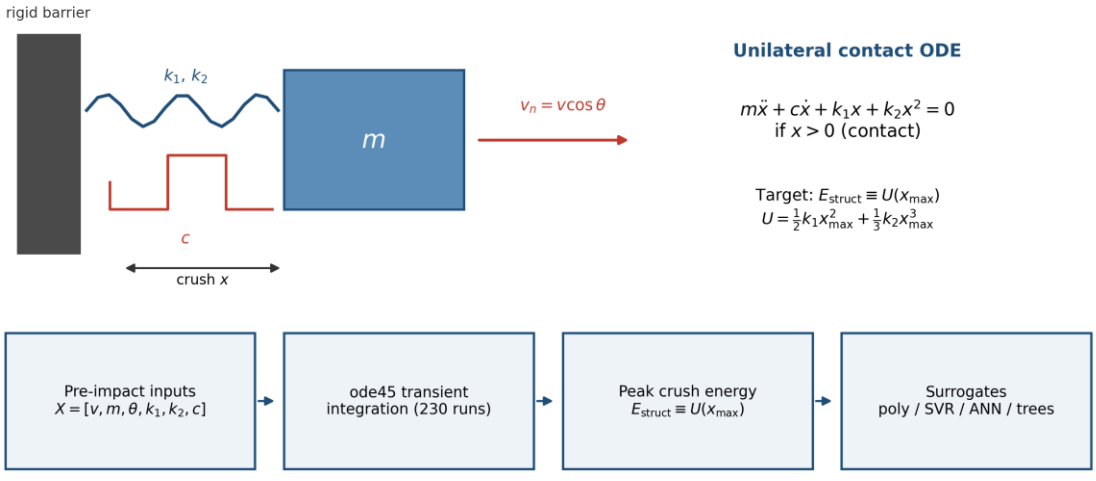

Fig. 1. Reduced-order V2B model (unilateral Kelvin–Voigt oscillator) and simulation/ML workflow.

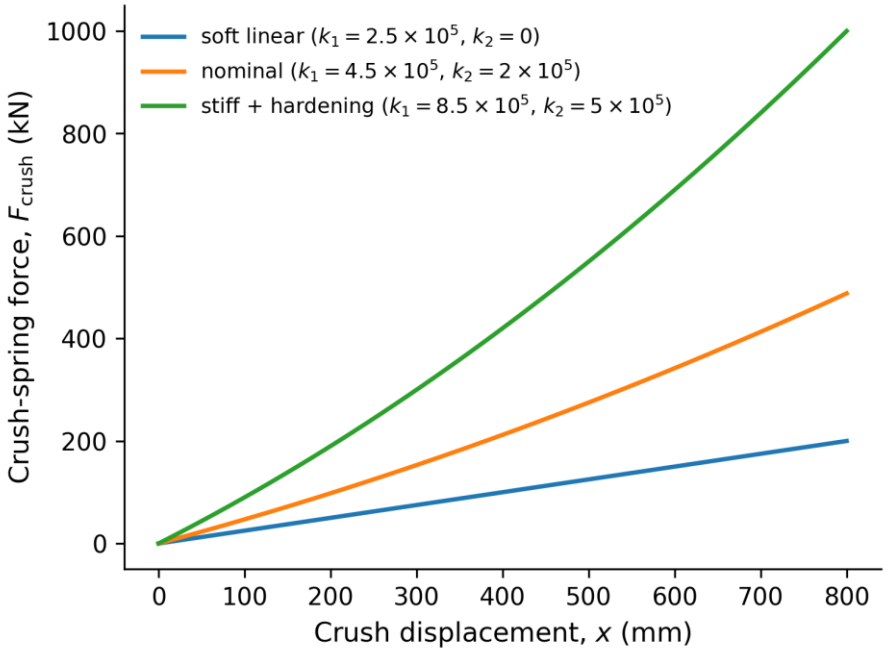

Fig. 2. Nonlinear crush-spring force F_crush = k1 x + k2 x².

B. *Energy formulation and learning target*

Multiplication of the contact equation by ẋ yields the energy identity $E_k(t) + U(x) + (E_{\text{damp}})(t) = E_{\text{init}} = \left(\frac{1}{2}\right) m\, v_n^2$, where $U(x) = \left(\frac{1}{2}\right) k_1 x^2 + \left(\frac{1}{3}\right) k_2 x^3$. The primary learning target is the peak crush energy E_struct ≡ U(x_max), namely the nonlinear crush-spring work stored at maximum dynamic compression. Viscous dissipation is recorded separately as E_damp and is not included in the machine-learning target. Consequently, E_struct is not the total absorbed collision energy. All 230 simulations satisfy a maximum relative residual e_bal ≤ 9.596×10^{-13} and E_struct ≤ E_init. The ratio E_struct/E_init spans 0.210–0.870 (median 0.413). Fig. 3 shows a representative transient response generated from the validated ordinary-differential-equation implementation; the pulse is not a design of experiments (DOE) row.

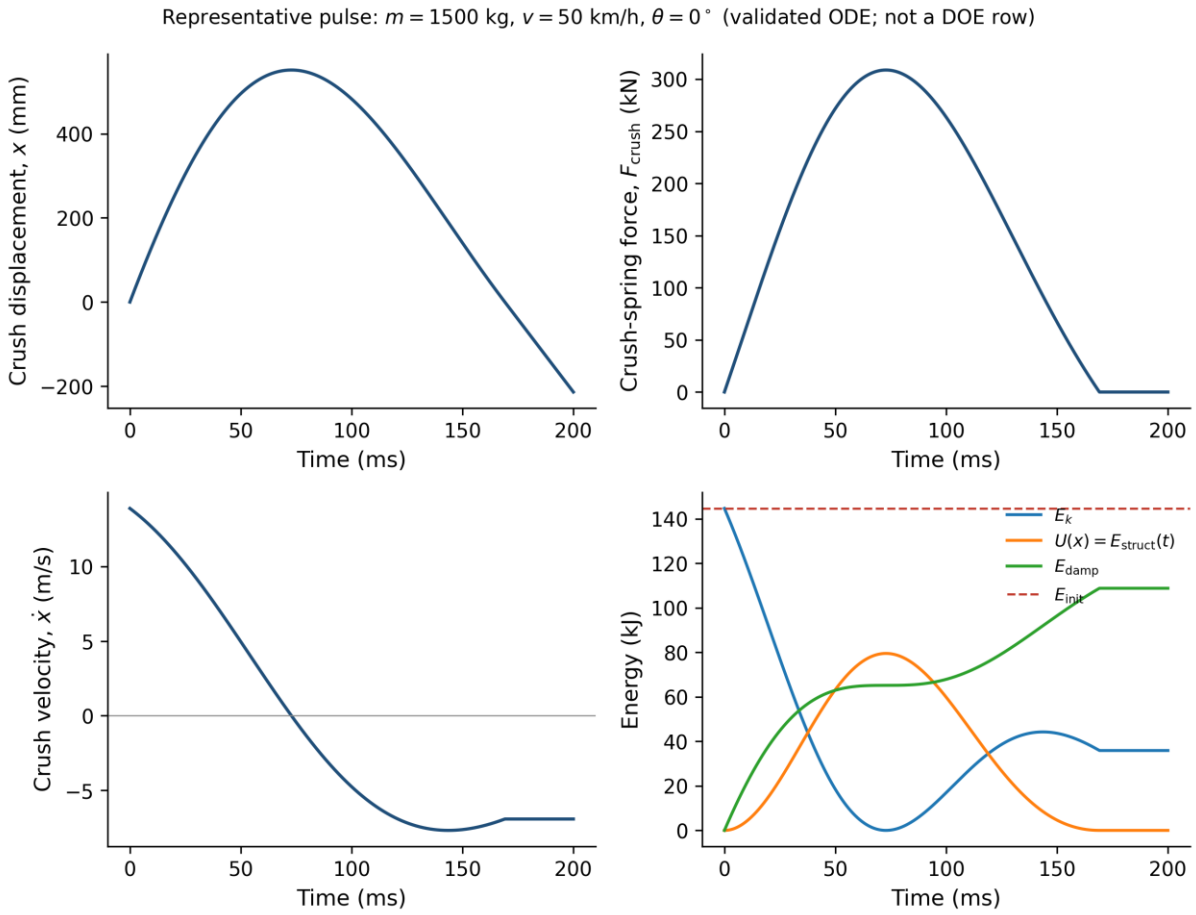

Fig. 3. Representative transient response (m = 1500 kg, v = 50 km/h, θ = 0°). The energy panel shows Ek + U + E_damp = E_init.

C. *Design of experiments and dataset partition*

Table 2 lists the sampled parameter ranges. The campaign comprises 200 maximin Latin-hypercube points together with 30 additional cases in v ∈ [66, 70] km/h (n = 230; all cases physically accepted). Table 3 reports the machine-learning partition. The 4 km/h gap is an evaluation-time guard band in the learning script; it is not a bound of the physical DOE.

Table 2. Physical model parameters and DOE ranges.

Parameter	Symbol	Unit	Min	Max
Impact velocity	v	km/h	25	70
Effective mass	m	kg	1200	2000
Impact angle	θ	deg	0	35
Linear stiffness	k1	N/m	2.5×10^5	8.5×10^5
Quadratic hardening	k2	N/m²	0	5.0×10^5
Equivalent damping	c	N·s/m	4×10^3	3.5×10^4

Table 3. Dataset partition of all 230 simulations.

Partition	Selection rule	n	Purpose
Training	LHS and v < 62 km/h, 75%, seed 42	123	Fitting and five-fold CV
Interpolation test	Same pool, remaining 25%	41	Unseen interior combinations
Guard band (unused)	62 ≤ v < 66 km/h	18	Buffer against near-boundary leakage
High-speed holdout	All rows with v ≥ 66 km/h	48	Velocity-domain generalisation
Total		230	

Forty-nine runs carry the flag no_separation_timeout, indicating that contact is still present at t = 0.20 s. An independent re-integration of these 49 parameter vectors shows that the peak crush occurs in every case (t_xmax = 58.6–107.9 ms, at least 92 ms before the terminal time). At t = 0.20 s the crush velocity is negative in all 49 cases, while x remains positive. The flag therefore records incomplete separation within the integration window; it does not indicate that maximum compression was missed. Accordingly, U(x_max) remains a valid peak crush-energy target. Relative to the 181 runs that separate, the timeout subset exhibits a higher mean damping coefficient and a lower mean k1, consistent with a slower return to x = 0 rather than with continued loading.

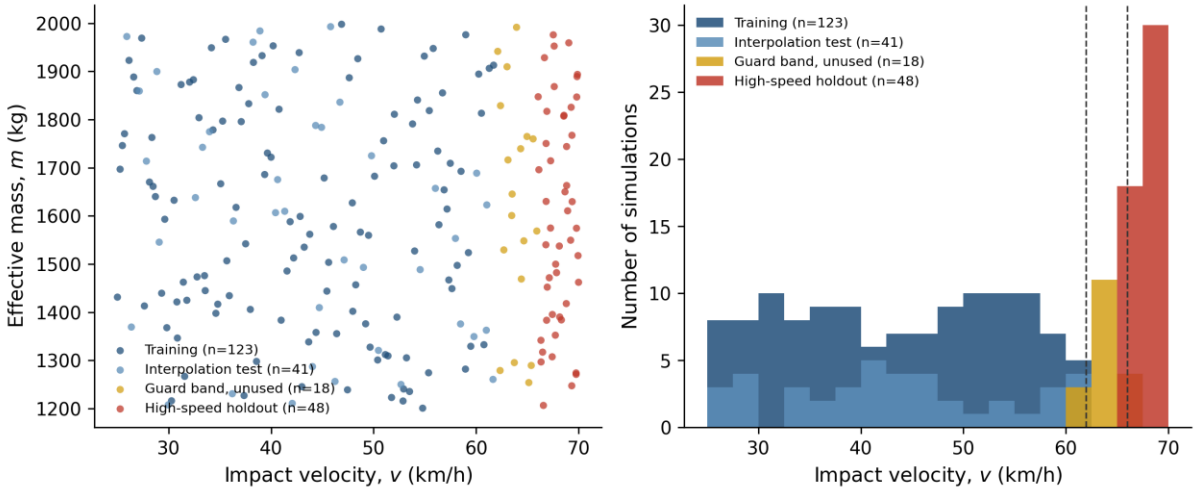

Fig. 4. DOE in the (v, m) plane and velocity-domain partition of all 230 runs.

D. *Machine-learning methodology*

The regression target is E_struct (kJ). The feature vector is [v, m, θ, k1, k2, c]. StandardScaler and polynomial expansion are placed inside pipelines and are fitted on the 123 training rows only. Hyperparameters are selected by GridSearchCV with five-fold shuffled cross-validation on the training split. The holdout set is excluded from fitting, scaling and hyperparameter search. The compared models are an unscaled kinetic-energy baseline $\hat{y} = \tfrac{1}{2}\, m\, v_n^2$; a scaled kinetic-energy baseline with $\hat{r} = 0.4869$ estimated on training data only; ordinary linear regression; second-order polynomial ridge; radial-basis SVR; random forest; XGBoost; and a hyperbolic-tangent multilayer perceptron trained with LBFGS. The selected settings are SVR with C = 1000, $\gamma = 0.05$ and $\varepsilon = 0.05$; random forest with 400 trees and depth 10; XGBoost with 700 trees, depth 3 and $\eta = 0.08$; and an MLP with hidden layers (48, 24) and $\alpha = 10^{-3}$.

III. Results

Across the DOE, x_max ranges from 166 to 916 mm (median 429 mm) and the peak force from 134 to 743 kN. Fig. 5 shows that E_struct is not identical to E_init. All reported metrics were recomputed from stored prediction files. No statistical significance test is claimed for the difference between SVR and polynomial ridge.

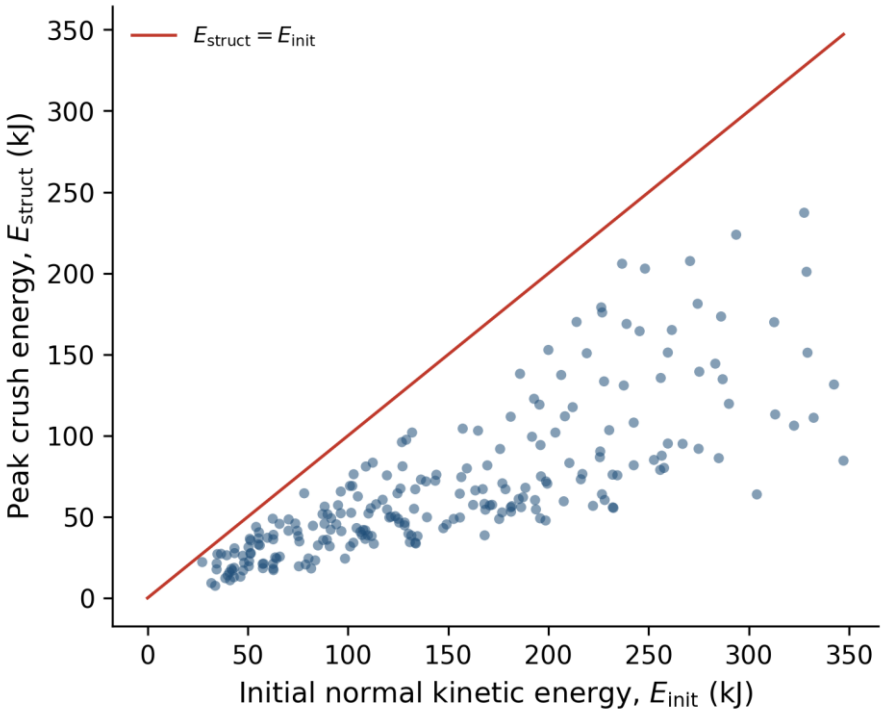

Fig. 5. Peak crush energy versus initial normal kinetic energy (n = 230). The diagonal reference line denotes E_struct = E_init.

Table 4. Predictive performance on the interpolation test set (n = 41).

Model	R^2	MAE (kJ)	RMSE (kJ)	MAPE (%)
KE baseline	−8.429	62.31	71.87	149.9
Scaled KE	0.455	13.96	17.29	35.0
Linear	0.793	7.44	10.64	34.2
Polynomial ridge (deg. 2)	0.986	1.99	2.75	6.3
SVR	0.986	1.90	2.73	5.2
ANN	0.975	2.47	3.70	6.8
XGBoost	0.922	4.84	6.53	12.0
Random forest	0.827	7.24	9.74	18.0

Polynomial ridge (R^2 = 0.986189) and SVR (R^2 = 0.986404) are essentially equivalent on the interpolation test. A second-order polynomial response surface is already highly competitive on this smooth reduced-order map.

Table 5. Predictive performance on the held-out high-speed test set (n = 48, v ≥ 66 km/h).

Model	R^2	MAE (kJ)	RMSE (kJ)	MAPE (%)
KE baseline	−8.048	138.09	147.00	153.5
Scaled KE	0.204	37.88	43.60	39.7
Linear	0.674	21.73	27.91	19.4
Polynomial ridge (deg. 2)	0.956	7.31	10.30	5.8
SVR	0.966	6.68	9.06	5.5
ANN	0.893	12.29	15.96	10.5
XGBoost	0.550	24.90	32.77	18.8
Random forest	0.546	26.93	32.94	27.0

On the holdout set, SVR is only modestly more accurate than polynomial ridge (R^2 = 0.966 versus 0.956; MAE = 6.68 kJ versus 7.31 kJ). That difference is not described as statistically significant. Under the present held-velocity generalisation experiment, the tree-based ensembles exhibit substantially greater degradation than SVR and polynomial ridge. This observation is specific to the present data set, the smoothness of the response surface, the training regime, and extrapolation into a withheld velocity interval; it is not a general claim that random forest and XGBoost are unsuitable crash-energy models.

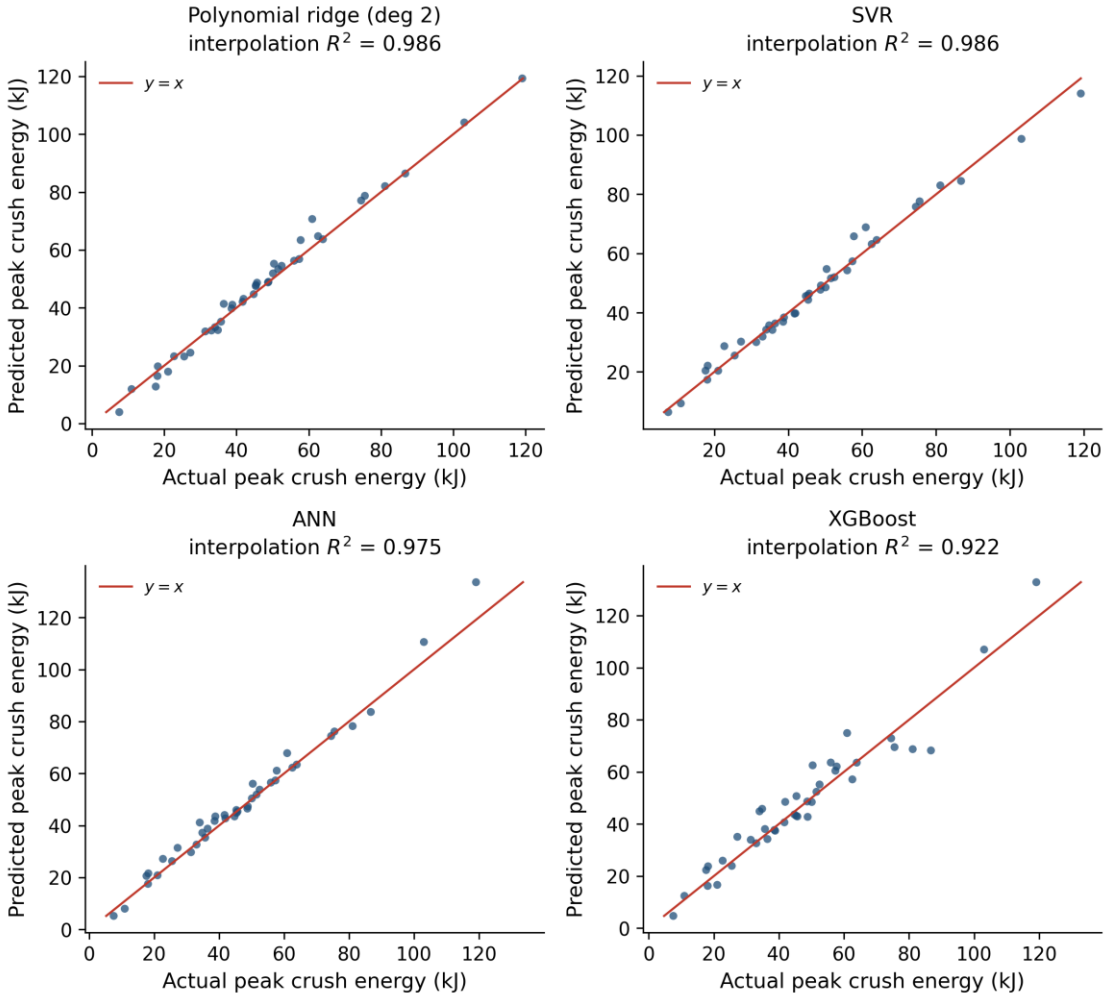

Fig. 6. Actual versus predicted peak crush energy on the interpolation test. The diagonal reference line denotes y = x.

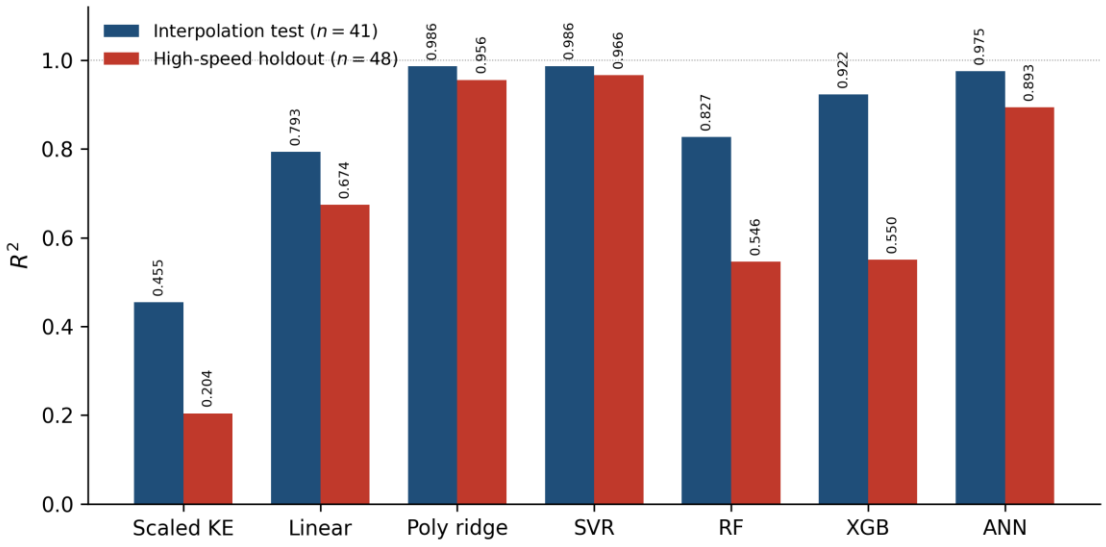

Fig. 7. Model-performance comparison: interpolation versus high-speed holdout. The unscaled kinetic-energy baseline ($R^2 \approx -8.4$ / -8.0) is omitted from the plot for scale; see Tables 4 and 5.

On the interpolation test, permutation importance for SVR ranks the inputs as v > c > m > θ > k1 > k2. TreeSHAP applied to XGBoost likewise places velocity first and damping second (Fig. 8). A holdout permutation ranking places c first and v last. That shift is not interpreted as a loss of physical importance of velocity at high speed: the holdout occupies only the narrow interval 66–70 km/h, so permutation of v

has little range over which to act. The physical interpretation is therefore taken from the interpolation domain.

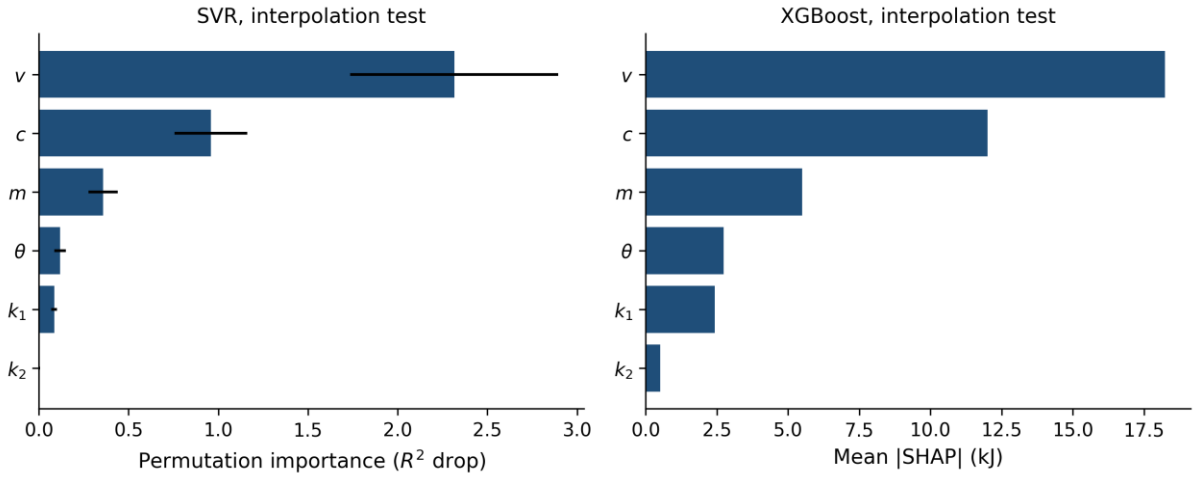

Fig. 8. Interpolation-domain explainability: SVR permutation importance and XGBoost mean |SHAP|.

IV. Discussion

The reduced-order V2B simulations yield a physically consistent energy-response data set. SVR and second-order polynomial regression attain comparable interpolation accuracy, whereas SVR is only moderately stronger in the held-out high-speed regime. Tree-based ensembles generalise substantially less well under this held-velocity protocol. Model selection should therefore consider not only interpolation accuracy but also the intended operating domain. On this smooth oscillator, increased algorithmic complexity is not uniformly advantageous. The principal limitations are the single crush degree of freedom; the restriction of the impact angle to the factor v cosθ; the sampling, rather than experimental identification, of k1, k2 and c; the absence of finite-element or NCAP validation of the 230-run ensemble; a training size of 123; and extrapolation evidence confined to 66–70 km/h.

V. Conclusion

A one-degree-of-freedom nonlinear Kelvin–Voigt V2B model was integrated in time. The relative energy residual remained below 10^{-12}, and 230 Latin-hypercube collisions were used to train surrogates for the peak crush energy U(x_max). The simplified analytical energy formulation of Yeğin [16] was not used as the learning target. Polynomial ridge and SVR both attain $R^2 = 0.986$ on the interpolation test. On velocities withheld from training, SVR remains at $R^2 = 0.966$ and the polynomial at 0.956, whereas the multilayer perceptron declines to 0.893. Under this held-velocity experiment, random forest and XGBoost decline to approximately 0.55. Explainability in the interpolation domain ranks impact velocity first and equivalent damping second. A second-order polynomial response surface is already competitive with SVR on this collision-response map.

Acknowledgment

This work received no external funding.

References

[1] M. A. Rahim and H. M. Hassan, “A deep learning based traffic crash severity prediction framework,” *Accid. Anal. Prev.*, vol. 154, Art. no. 106090, 2021.

[2] U. Mansoor, N. T. Ratrout, S. M. Rahman, and K. Assi, “Crash severity prediction using two-layer ensemble machine learning model for proactive emergency management,” *IEEE Access*, vol. 8, pp. 210750–210762, 2020.

[3] K. Assi, “Traffic crash severity prediction—A synergy by hybrid principal component analysis and machine learning models,” *Int. J. Environ. Res. Public Health*, vol. 17, Art. no. 7598, 2020.

[4] K. Sattar, F. C. Oughali, K. Assi, N. T. Ratrout, A. Jamal, and S. M. Rahman, “Transparent deep machine learning framework for predicting traffic crash severity,” *Neural Comput. Appl.*, vol. 35, pp. 1535–1547, 2023.

[5] M. S. Alam, S. M. Rahman, K. Sattar, M. N. Islam, M. S. H. Choudhury, K. J. Assi, and N. T. Al-Ratrout, "Traffic crash-severity prediction using interpretable optimized ensemble models," *Int. J. Intell. Transp. Syst. Res.*, vol. 23, no. 3, pp. 1585–1607, 2025.
[6] M. Alhawarat, A. Alkhatib, and Q. Nijem, "Calibrated and explainable gradient boosting for road traffic crash severity prediction: SHAP audit and cross-jurisdiction transfer evaluation," *Appl. Sci.*, vol. 16, Art. no. 5876, 2026.
[7] T. Wang, Z. Li, L. Wang, and G. M. Hulbert, "Crashworthiness analysis and collaborative optimization design for a novel crash-box with re-entrant auxetic core," *Struct. Multidisc. Optim.*, vol. 62, no. 4, pp. 2167–2179, 2020.
[8] S. Farshbaf, N. Dialami, and M. Cervera, "Machine learning-driven inverse design of functionally graded auxetic metamaterials including non-linear regimes," *Appl. Mater. Today*, vol. 49, Art. no. 103147, 2026.
[9] S. Zheng, L. Jing, K. Liu, Z. Yu, Z. Tang, and K. Wang, "Crash energy management optimization of high-speed trains by machine learning methods," *Int. J. Mech. Sci.*, vol. 270, Art. no. 109108, 2024.
[10] K. L. Campbell, "Energy basis for collision severity," SAE Technical Paper 740565, 1974.
[11] M. Huang, *Vehicle Crash Mechanics*. Boca Raton, FL, USA: CRC Press, 2002.
[12] W. Pawlus, H. R. Karimi, and K. G. Robbersmyr, "Development of lumped-parameter mathematical models for a vehicle localized impact," *J. Mech. Sci. Technol.*, vol. 25, pp. 1737–1747, 2011.
[13] A. Klausen, S. S. Tørdal, H. R. Karimi, K. G. Robbersmyr, M. Ječmenica, and O. Melteig, "Firefly optimization and mathematical modeling of a vehicle crash test based on single-mass," *J. Appl. Math.*, vol. 2014, Art. no. 150319, 2014.
[14] B. B. Munyazikwiye, H. R. Karimi, and K. G. Robbersmyr, "Prediction of vehicle crashworthiness parameters using piecewise lumped parameters and finite element models," *Designs*, vol. 2, Art. no. 43, 2018.
[15] D. Wang, J. Zhang, S. Wang, and L. Hu, "Frontal vehicular crash energy management using analytical model in multiple conditions," *Sustainability*, vol. 14, Art. no. 16913, 2022.
[16] V. Yeğin, "MATLAB/Simulink based autonomous vehicle collision simulation and energy absorption analysis," *J. Mater. Mechatron. A*, vol. 6, no. 1, pp. 249–261, 2025.
[17] S. Liu, C. Liu, X. An, X. Liu, and L. Hao, "Intelligent damage prediction during vehicle collisions based on simulation datasets," *Inventions*, vol. 10, no. 3, Art. no. 40, 2025.

8th International Conference on Engineering, Natural and Social Sciences

September 06-07, 2026: Konya, Turkey

© 2026 Published by All Sciences Academy

https://www.icensos.com/

Fractional Order PID Position Control Application for DC Motor with Jetson Nano Platform

Erdem Ilten*

Department of Electrical-Electronics Engineering, Balikesir University, Türkiye
(ORCID: https://orcid.org/0000-0002-9608-2148)

**(erdemilten@balikesir.edu.tr) Email of the corresponding author*

Abstract – This paper presents the real-time position control of a DC motor using a Fractional Order PID (FOPID) controller implemented on the NVIDIA Jetson Nano edge computing platform. The primary objective of the study is to evaluate the embedded deployment capabilities of fractional-order control algorithms on high-performance single-board computers using Model-Based Design. The position control strategy was modeled in the MATLAB/Simulink environment using the *MATLAB Coder Support Package for NVIDIA Jetson and NVIDIA DRIVE Platforms*. The complete algorithm was compiled and deployed onto the Jetson Nano target via the *Embedded Coder* tool. The experimental hardware setup comprises an NVIDIA Jetson Nano board, a DC motor integrated with an optical encoder, a DC power supply, and an H-bridge motor driver. Real-time monitoring, parameter tuning, and control execution were performed using Simulink's External Mode functionality via a dedicated user interface panel. The experimental results demonstrate that the FOPID controller successfully tracks variable position references with high accuracy on the Jetson Nano platform, confirming the practical feasibility and effectiveness of hardware-in-the-loop Model-Based Design for advanced motion control applications.

Keywords – Jetson Nano, DC motor, Embedded Coder, FOPID, Simulink.

I. INTRODUCTION

A Direct Current (DC) motor is an electrical machine designed to convert direct current electrical energy into mechanical rotational motion. Its operational principle relies on Lorentz Force Law, which dictates that a current-carrying conductor placed within an external magnetic field experiences a mechanical force perpendicular to both the flow of the current and the direction of the magnetic field. This fundamental interaction between the magnetic field and the energized conductor generates the electromagnetic torque required to spin the motor shaft. The internal construction of a traditional DC motor consists of a stationary housing called the stator, an inner rotating assembly known as the rotor or armature, and a switching mechanism. The stator incorporates permanent magnets or field windings to produce a constant magnetic field, while the rotor contains wire coils that become energized to create an opposing field. To maintain continuous unidirectional rotation, a mechanical commutator works alongside carbon brushes to periodically reverse the current direction through the armature windings as the rotor turns [1–5].

A Fractional Order PID (FOPID) controller, commonly denoted as $PI^{\lambda}D^{\mu}$, is an advanced generalization of the traditional Proportional-Integral-Derivative (PID) controller grounded in the principles of fractional calculus [6]. While classical controllers restrict integration and differentiation to integer orders, the FOPID framework allows the integral and derivative orders to assume arbitrary non-integer values. This expansion transforms the parameter tuning space from three isolated gain settings into a broader continuum, offering control engineers significantly greater flexibility to shape the system's dynamic

response. By incorporating non-integer calculus, FOPID controllers possess inherent memory effects and hereditary properties that better capture the behavior of complex dynamic systems. This structural versatility translates to superior closed-loop performance, characterized by improved transient response, reduced overshoot, and faster settling times. Furthermore, the additional freedom in tuning enables the design of systems with enhanced robustness, ensuring that performance remains stable despite parameter variations, external load disturbances, or modeling uncertainties. Due to these operational advantages, fractional order control has gained substantial traction across demanding industrial and engineering applications, including power electronics, electric drives, flexible robotics, and process automation. Although ideal fractional operators represent infinite-dimensional systems, practical deployment is readily achieved on modern embedded microcontrollers and digital signal processors by employing rational approximation algorithms that model the fractional behavior across a targeted frequency band [7–9].

The NVIDIA Jetson Nano is a compact, high-performance System on Module (SoM) designed specifically to bring hardware-accelerated artificial intelligence and deep learning execution to edge computing platforms. Unlike traditional microcontrollers or standard single-board computers, the Jetson Nano features a dedicated Maxwell-architecture GPU alongside its multi-core ARM processor. This architecture enables the board to run parallel compute workloads, real-time computer vision algorithms, and neural network inference models directly on local hardware without relying on cloud infrastructure. While popular platforms like Arduino [10–12] and ESP32 [13] excel at low-level hardware control, sensor interfacing, and low-power IoT connectivity through real-time microcontroller operation, they lack the computational capacity required for intensive data processing or deep learning tasks. Similarly, while single-board computers such as the Raspberry Pi [14–16] offer a complete Linux desktop environment and strong general-purpose processing capabilities, their reliance on standard central processing units creates a bottleneck when executing complex parallel workloads like multi-stream video analysis or object detection. By bridging the gap between general-purpose single-board computing and high-performance edge AI, the Jetson Nano serves as an intermediate compute node in modern embedded system architectures. It seamlessly offloads heavy AI vision pipelines and spatial analytics from cloud servers while accepting sensor telemetry from microcontrollers, making it a foundational platform for autonomous robotics, intelligent video surveillance, and smart industrial automation [17,18].

II. Materials and Method

DC motor supply voltage, back-EMF and torque equations are defined as below [15].

$$V_a = E_c + I_a R_a \tag{1}$$

$$E_c = K_1 \phi_f \omega \tag{2}$$

$$T_o = \frac{P_o}{\omega} \tag{3}$$

In these equations V_a is the supply voltage, E_c is the back-EMF, R_a is the armature winding resistance, K_1 is the motor constant, ϕ_f is to the field flux, and ω is the angular speed. FOPID equation is defined as follows [19]:

$$u(t) = K_p e(t) + K_i I^{\lambda} e(t) + K_d D^{\mu} e(t) \tag{4}$$

Here, K_p, K_i and K_d are the proportional, integral and derivative coefficients, respectively. λ and μ are the order of the fractional integral and derivative. I^{λ} is the fractional integral and D^{μ} is the fractional derivative. u is the FOPID controller signal and e is the error.

The block diagram showing the system's operation is given in Fig. 1. Here, the motor position is read by the Jetson Nano, position control is performed using the FOPID algorithm, and the motor driver is driven by a PWM generator.

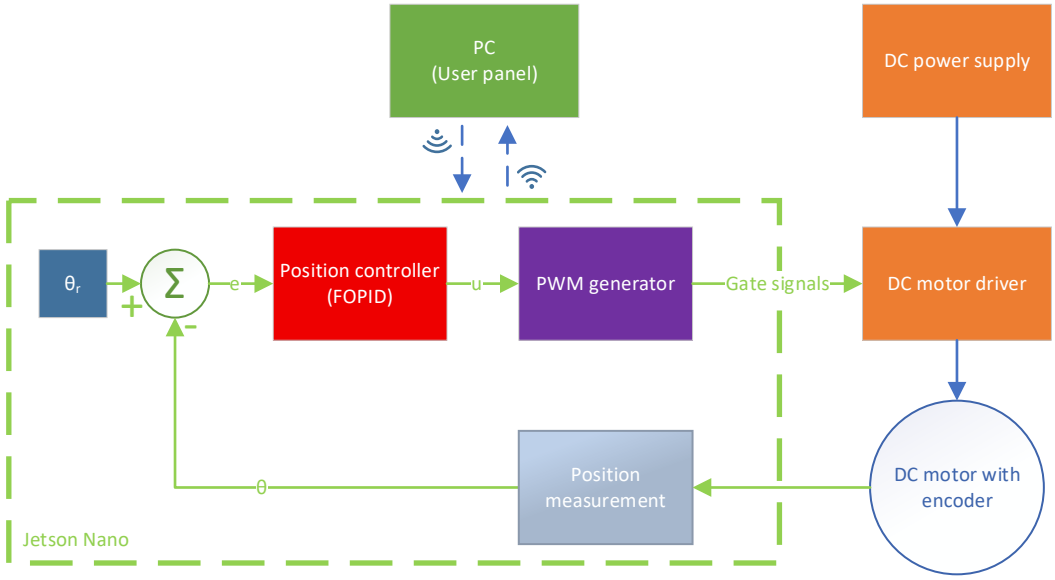

Fig. 1 Block diagram of the system.

The experimental setup of the system is shown in Fig. 2. The experimental setup consists of the Jetson Nano platform, a DC motor with optical encoder, a DC power supply, and a DC motor driver circuit.

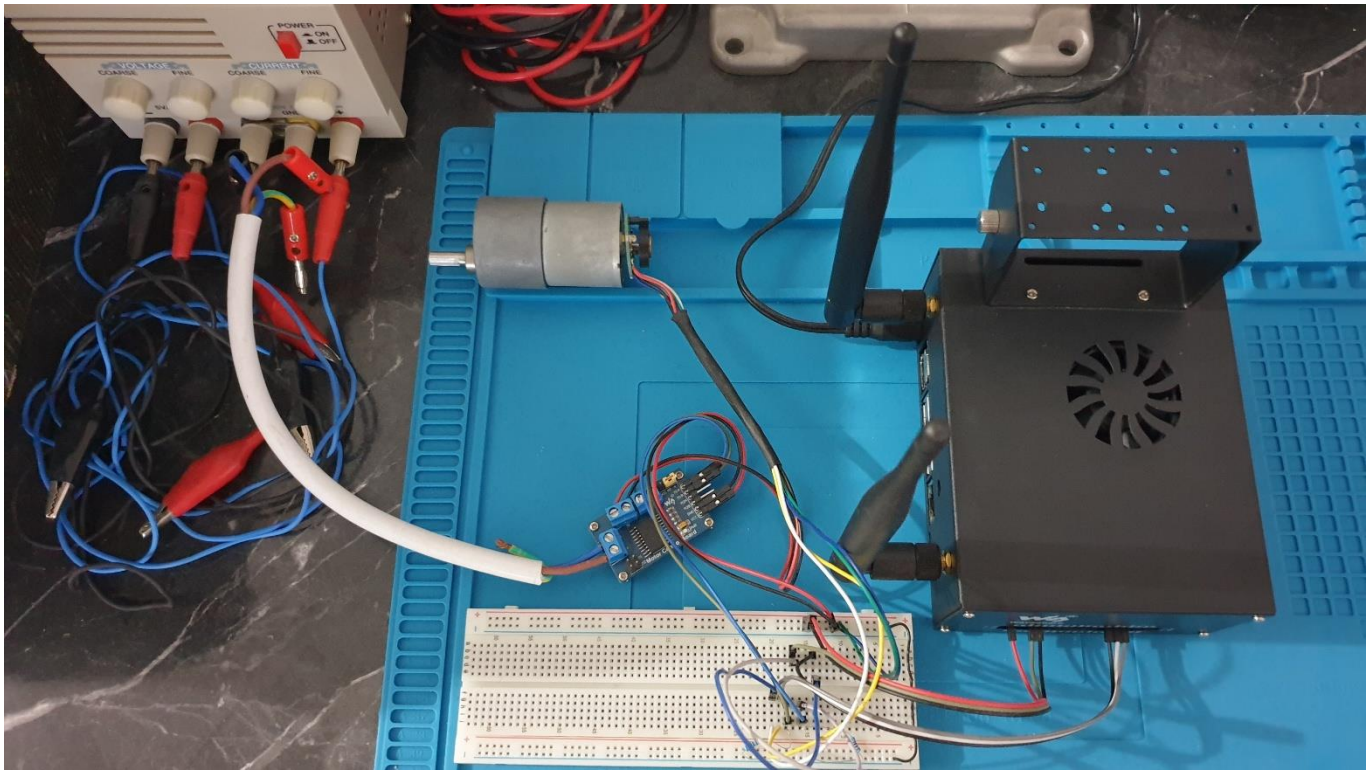

Fig. 2 The experimental setup.

The Jetson Nano algorithm, necessary for position control of a DC motor using FOPID, was prepared in the Simulink environment. The *MATLAB Coder Support Package for NVIDIA Jetson and NVIDIA DRIVE Platforms* tool was used for the Simulink block diagram [20]. The prepared Simulink block diagram is presented in Fig. 3. This block diagram was uploaded and run on the Jetson Nano platform using the *Embedded Coder* tool.

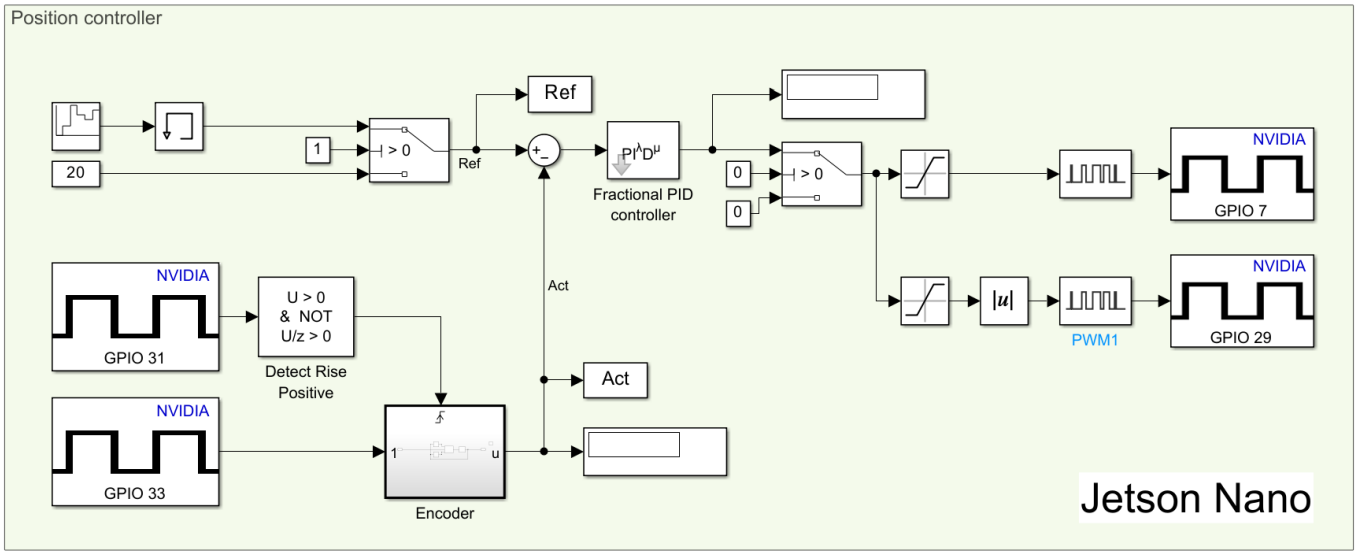

Fig. 3 Simulink block diagram for Jetson Nano platform.

A separate user panel has been designed within the Simulink environment for monitoring and controlling the system. This panel is shown in Fig. 4. The user panel is not installed on the Jetson Nano; it is operated via External Mode in a PC environment.

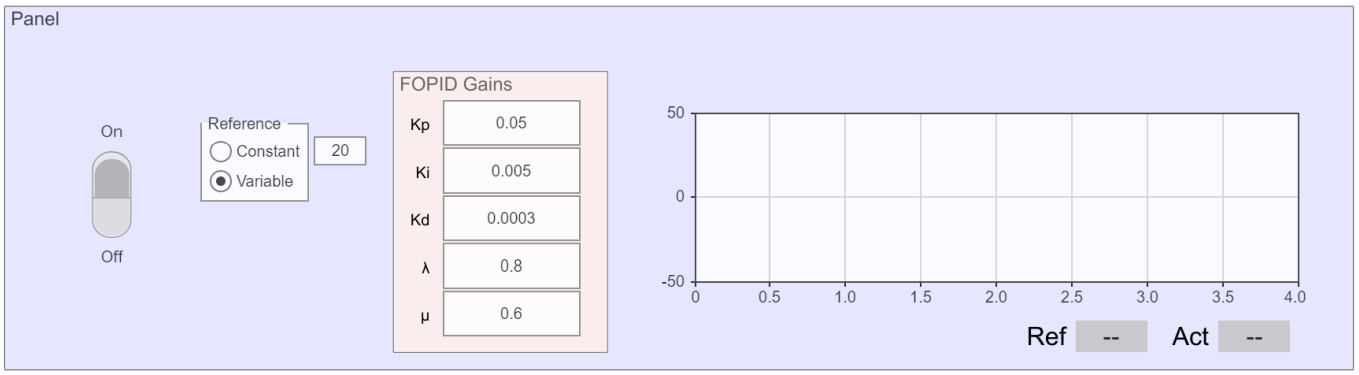

Fig. 4 The designed control panel.

The system can be turned on and off, a constant or variable reference position can be selected, FOPID gains can be adjusted, and reference and actual position values can be monitored in real time on a graph via the user panel shown in Fig. 4.

III. RESULTS

The system was tested via an External Mode connection. The FOPID algorithm was executed for variable reference position tracking by giving the "on" command via the user panel. Test results are presented in Fig. 5. Here, the controller gains K_p, K_i, K_d, λ, and μ were selected as 0.05, 0.005, 0.0003, 0.8, and 0.6, respectively. Examination of the test results shows that the motor position can be successfully controlled using FOPID.

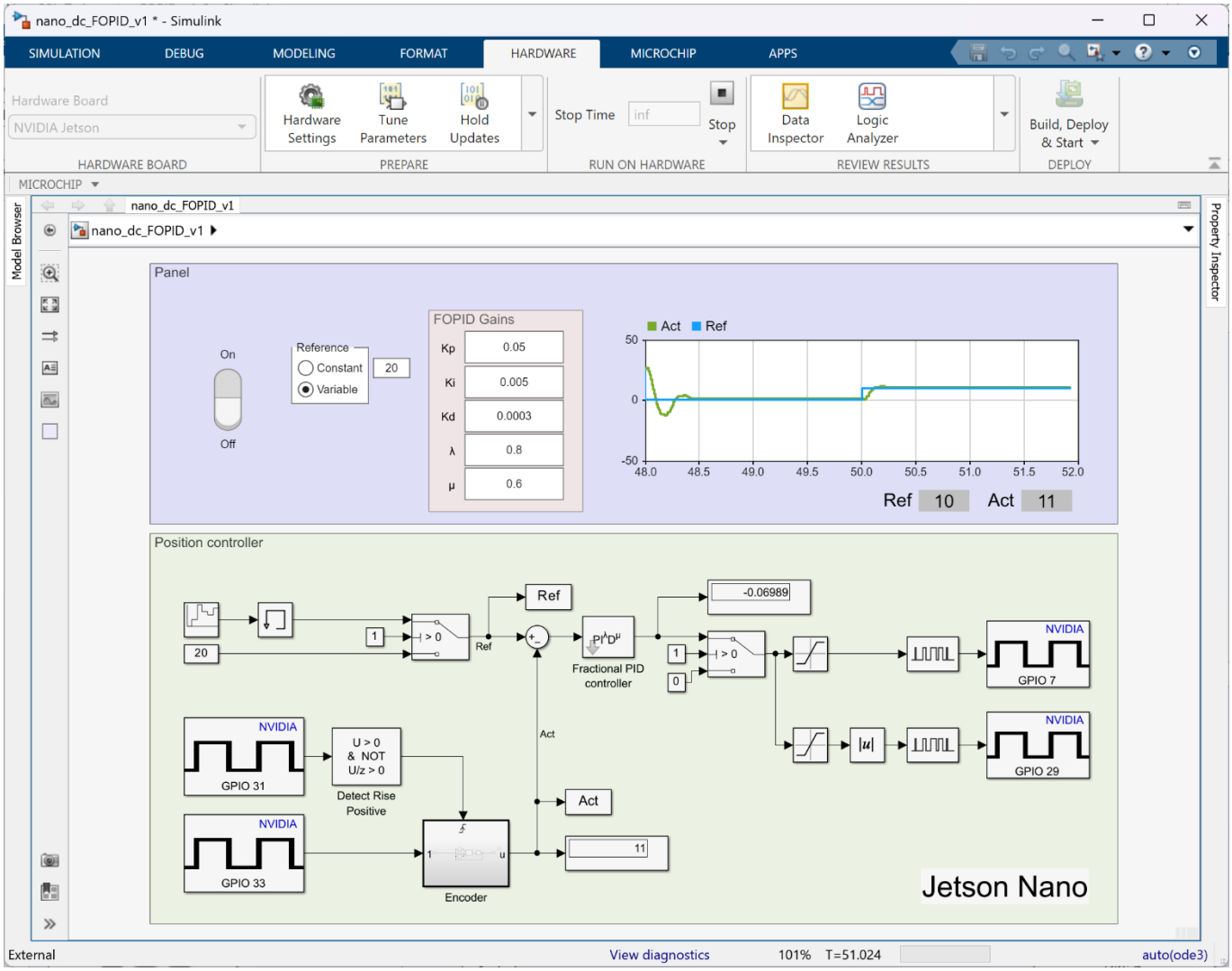

Fig. 5 Test results.

IV. Conclusion

In this study, the position control of a DC motor using a Fractional Order PID (FOPID) algorithm was successfully realized on the NVIDIA Jetson Nano platform. By leveraging Model-Based Design in MATLAB/Simulink alongside *Embedded Coder* tools, the complex fractional-order mathematical control logic was seamlessly deployed onto the embedded hardware without requiring manual C/C++ coding. The integration of Simulink External Mode provided an effective interactive environment for real-time monitoring, parameter adjustments, and variable reference tracking experiments. The experimental findings confirm that the FOPID controller achieves accurate and responsive position tracking under dynamic reference conditions. This work demonstrates that high-performance edge computing platforms like the Jetson Nano can be effectively utilized for real-time advanced control systems, establishing a flexible framework for future intelligent and hardware-in-the-loop motion control applications.

References

[1] Ilten E. Position Control Application of a DC Motor with Jetson Nano via Simulink Embedded Coder. 4th Int. Conf. Pioneer Innov. Stud., 2026, p. 233–8.

[2] Ilten E. 2-DOF PID Position Control Application for DC Motor with Arduino and Simulink External Mode. 4th Int. Conf. Trends Adv. Res., 2025, p. 166–71.

[3] Ilten E. Implementation of Tilt Integral Derivative (TID) Position Controller for DC Motor System with Using Simulink and Arduino Nano 33 IoT. 8th Int. Conf. Appl. Eng. Nat. Sci., 2025, p. 309–14.

[4] Ilten E, Bilgen M. Pixhawk-Based Quadrotor Design and Sensor-Actuator Testing via Simulink External Mode. Int J Adv Nat Sci Eng Res 2026;10:88–99.

[5] Ilten E. Active Disturbance Rejection Control of a DC Motor with Raspberry Pi on Simulink External Mode. 2nd Int. Conf. Contemp. Acad. Res., 2023, p. 56–60.
[6] Daraz A, Malik SA, Basit A, Aslam S, Zhang G. Modified FOPID controller for frequency regulation of a hybrid interconnected system of conventional and renewable energy sources. Fractal Fract 2023;7:89.
[7] Ilten E. Conformable Fractional Order MIMO Control of an 8-State Helicopter System. Mod. Res. Eng., All Sciences Academy; 2025, p. 20–35.
[8] Ilten E. DC Motor Fractional Order PID Position Control with Arduino Nano 33 IoT and Simulink External Mode. 6th Int. Conf. Eng. Nat. Soc. Sci., 2025, p. 362–7.
[9] Makhbouche A, Boudjehem B, Birs I, Muresan CI. Fractional-order PID controller based on immune feedback mechanism for time-delay systems. Fractal Fract 2023;7:53.
[10] Küçükdermenci S, Ilten E. Arduino Based Fire Extinguisher Vehicle Design and Application. Int J Adv Nat Sci Eng Res 2025;9:223–32. https://doi.org/10.5281/zenodo.14897860.
[11] Ilten E, Uguz OF. Design and Implementation of PLC and Arduino Based Smart Home Automation System. 4th Int. Conf. Recent Innov. Results Eng. Technol., 2026, p. 104–9.
[12] Ilten E. Toxic Gas-Meter Application for Android Device with Arduino Nano 33 IoT. 4th Int. Conf. Innov. Acad. Stud., All Sciences Academy; 2024, p. 125–30.
[13] Babiuch M, Foltýnek P, Smutný P. Using the ESP32 microcontroller for data processing. 2019 20th Int. Carpathian Control Conf., IEEE; 2019, p. 1–6.
[14] Ilten E. Real-Time Implementation of Deep Learning Based Leaf Deficiency Classification on Raspberry Pi Platform. Int J Adv Nat Sci Eng Res 2026;10:89–100.
[15] Ilten E. Raspberry Pi Touch Panel Design for DC Motor Control System. 5th Int. Conf. Front. Acad. Res., vol. 1, 2025, p. 256–62.
[16] Ilten E, Duzgun E, Gullu SI. Deep Learning Model for Liquid Level Estimation via Webcam and its Implementation with Raspberry Pi. Sustain. Trending Stud. Eng., All Sciences Academy; 2026, p. 44–55.
[17] Süzen AA, Duman B, Şen B. Benchmark analysis of jetson tx2, jetson nano and raspberry pi using deep-cnn. 2020 Int. Congr. Human-Computer Interact. Optim. Robot. Appl., IEEE; 2020, p. 1–5.
[18] Valladares S, Toscano M, Tufiño R, Morillo P, Vallejo-Huanga D. Performance evaluation of the Nvidia Jetson Nano through a real-time machine learning application. Int. Conf. Intell. Hum. Syst. Integr., Springer; 2021, p. 343–9.
[19] Ilten E. Conformable Fractional Order Controller Design and Implementation for Per-Phase Voltage Regulation of Three-Phase SEIG Under Unbalanced Load. Electr Power Components Syst 2022;50:636–48.
[20] MathWorks. MATLAB documentation 2026.

8th International Conference on Engineering, Natural and Social Sciences

September 06-07, 2026: Konya, Turkey

© 2026 Published by All Sciences Academy

https://www.icensos.com/

Hyperparameter Tuning in Gradient Boosting Models: A Comparative Study on Residential Property Price Prediction

Halit Çetiner*

[1]*Vocational School of Technical Sciences, Isparta University of Applied Sciences, Isparta, Turkey (ORCID: https://orcid.org/0000-0001-7794-2555)*

**(halitcetiner@isparta.edu.tr)*

Abstract – This study analyzes in detail the performance of the XGBoost and CatBoost machine learning algorithms on a dataset of housing prices in Ames, Iowa. The dataset used in the study contains 81 features and 1460 data points. It includes many features, such as total square footage, number of bathrooms, age of the house, and quality interactions, which are among the most important features of a house. The target variable, SalePrice, was subjected to logarithmic transformation due to distributional problems to improve its performance. In the data preprocessing stage, numerical variables were filled with medians and scaled with StandardScaler. Additionally, categorical variables were encoded with One-Hot Encoding to speed up the processing. The effects of adjusting the parameters of four different hyperparameter optimizations (Baseline, GridSearch, RandomSearch, and Optuna), which are accepted in the literature, on predicting house sales prices were tested in the XGBoost and CatBoost algorithms. The XGBoost algorithm shows a 5% improvement when integrated with the Optuna hyperparameter tuning algorithm. When integrated with the GridSearch hyperparameter tuning algorithm, the CatBoost algorithm is one of the most successful methods in minimizing RMSE. Since RMSE values represent error values, they should approach zero, while R^2 values should approach 1. Based on these results, it can be said that the Optuna and GridSearch hyperparameter optimization algorithms offer good performance in predicting house prices. This study emphasizes the critical importance of hyperparameter optimization and feature engineering in housing price prediction models.

Keywords –Feature learning, Real Estate, Price Prediction, Hyperparameter optimization, Analysis

I. INTRODUCTION

The real estate market has several differences compared to other markets. Some of these differences include land, accurate land mapping, and demand for properties [1], [2], [3]. Increased demand or decreases in interest rates can lead to increases in property values. In addition, earthquakes in a region or country can also increase property value. When customers prefer lower-rise, more structurally sound buildings over high-rise apartments, price increases are observed in the requested properties. Furthermore, when using a real estate agent, a percentage of the purchase price must be paid to the agent. This also increases the sale price of the property, in addition to the initial cost. While the location and sales area may vary, using a real estate agent can help find suitable properties, but it can also contribute to price increases.

Buying a house is an important decision, seen as a turning point in people's lives [4]. This decision requires consideration of numerous parameters affecting the real estate market. Buying a property in the wrong location or in a problematic area can make its resale sustainable and difficult. For these reasons, research is being conducted that will be beneficial not only for home buyers but also for real estate agents and economic experts. With the increasing number of real estate sales websites and the proliferation of

data, various studies are being conducted to use this information in predicting the housing market [5], [6], [7], [8]. The countries that provide the most home price predictions are the United States, China, Taiwan, and Europe [9], [10], [11], [12], [13], [14], [15], [16].

Developments in regional or global economic activity can positively or negatively affect real estate valuation. Fluctuations in cash flows can lead to shifts in cash resources. For these reasons, corporate firms such as insurance companies and banks that want to profit from buying and selling real estate require an accurate property valuation. Therefore, they send appraisers to determine the estimated value of the property [17], [18], [19]. In the literature, many researchers, most notably Pagourtzi and colleagues, state that numerous factors and parameters influence real estate valuation, ranging from the age and location of the house to its design, structure, pollution and ecological quality of the area, and its facade [20], [21], [22].

Considering the factors and reasons mentioned, predicting real estate prices involves creating regression models that take into account the relationships between the influencing parameters. Although hedonic regression models are used in the literature, better performance can be achieved compared to classical hedonic methods by integrating machine learning techniques with parameter optimization methods and discovering linear or nonlinear relationships [23], [24], [25]. At the same time, being able to accurately and realistically predict house prices directly affects many people, from citizens making future plans to buyers and sellers closely following the economy.

The second part of the study, following this section, discusses the dataset and methods used. The third part describes the performance results obtained within the scope of the study, method by method. The final part concludes the study with the net results obtained.

II. Materials and Method

The dataset used in this study contains 1460 records with 81 features [26]. In research, conducting exploratory data analysis on the dataset before regression analysis is quite beneficial for visualizing, understanding, and interpreting the data. As a result, one can learn about a wide range of aspects, from the crime rate per town to the percentage of land allocated to housing plots, the standard number of rooms in a house, the median values of houses, and the ownership percentages of those with low socioeconomic status.

Fig. 1 presents the numerical distribution of house prices, showing both the original and logarithmic transformations. In Fig. 1, the original transformation reveals a clustering on the right side. Based on this visualization, it can be said that there is a concentration of houses in the low-to-medium price range. In the figure, the green dashed line represents the median price value, while the red dashed line indicates the mean house price. After the logarithmic transformations shown in Fig. 1, applying the log transformation to house prices results in a more symmetric distribution.

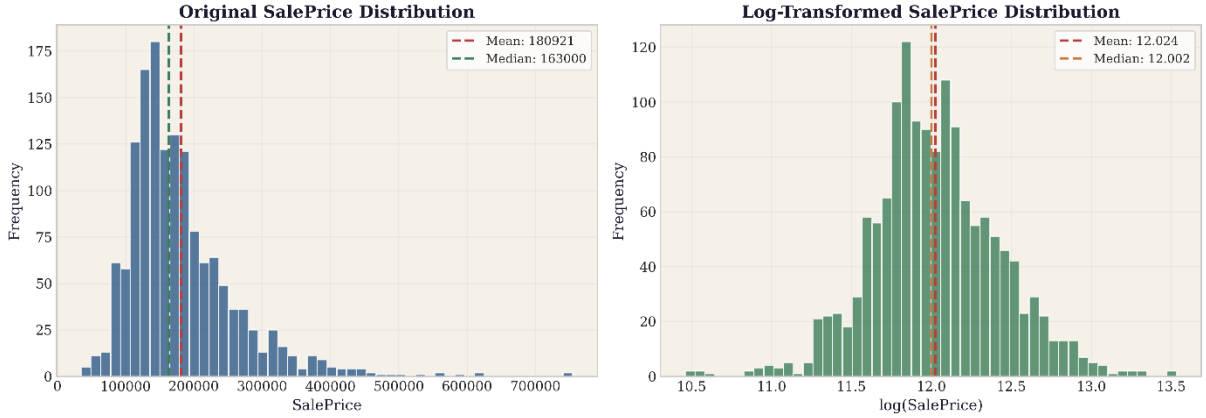

Fig. 1. Original and transformed sale price distribution

.

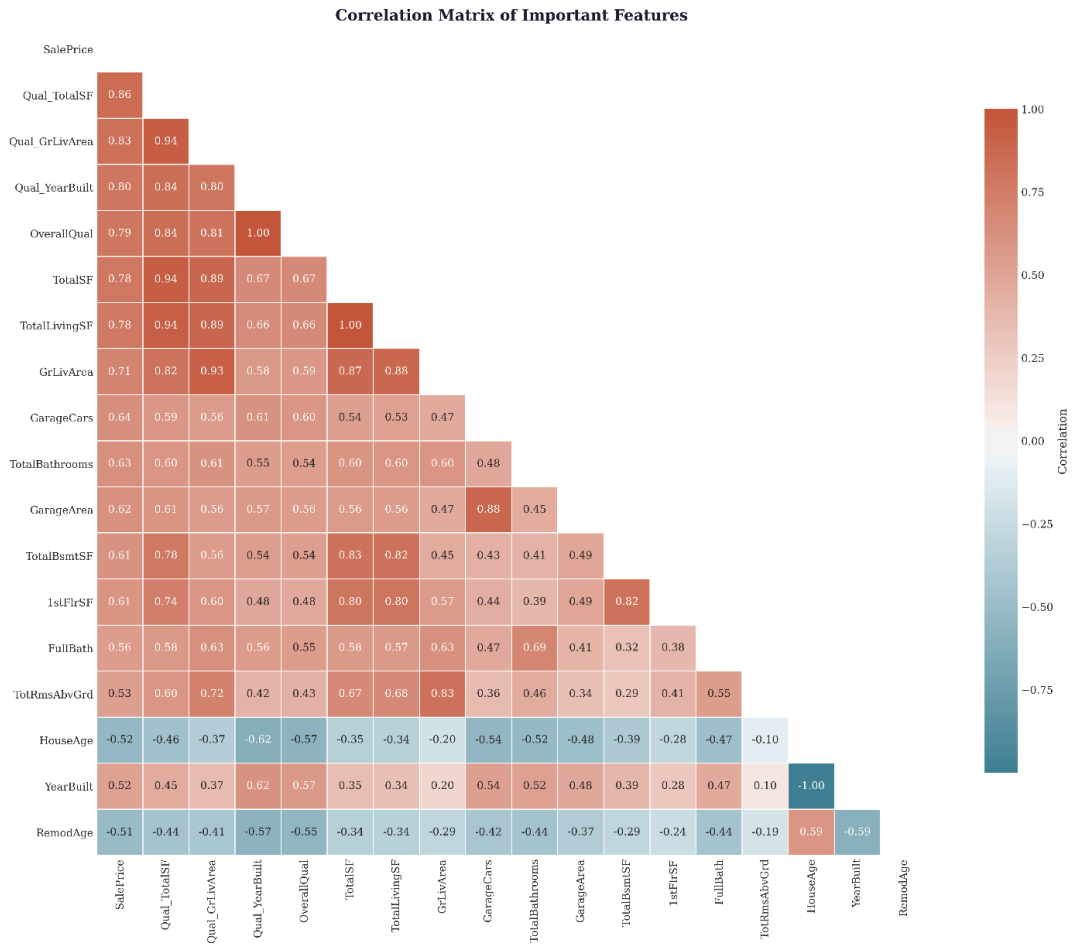

Fig. 2. Correlation matrix representation of the most important features

Fig. 2 presents the correlation relationships between eighteen features that influence price trends in a heat map format. In this visualization, red and blue tones represent negative and positive correlations, respectively. Among the features mentioned, the strongest positive correlation is observed between saleprice and overallqual. This strong indicator is followed by grlivarea and totalsf and totallivingsf features. The visualization shows how critical and significant each feature is for the established machine learning models.

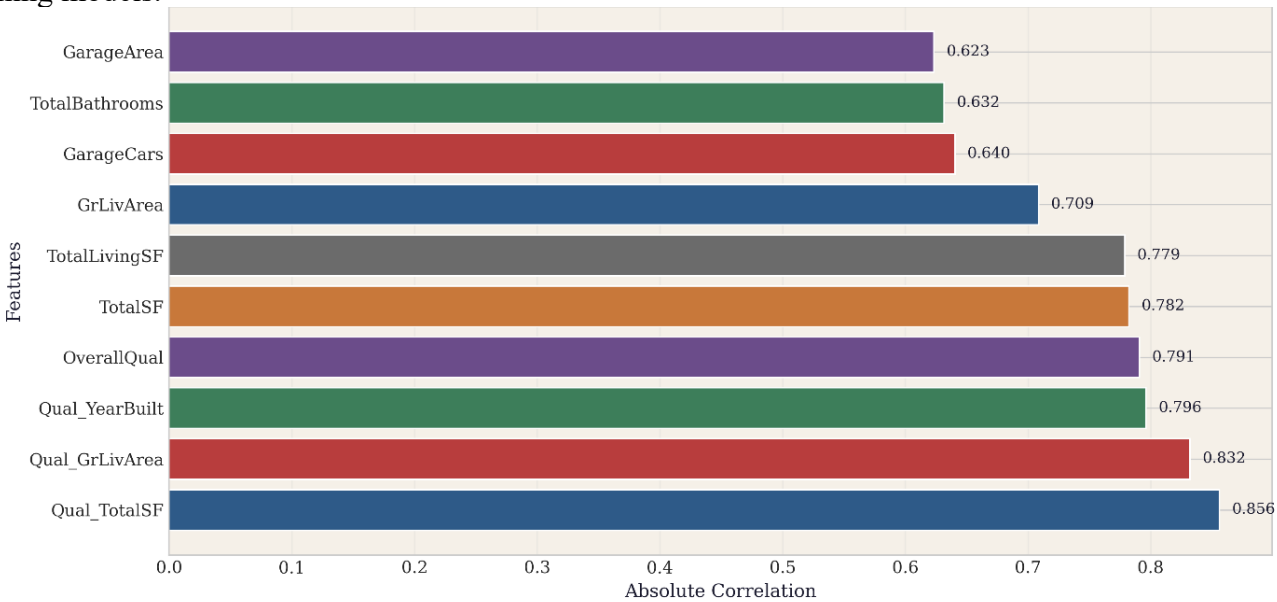

Fig. 3. A representation of the ten most important features associated with house prices

The correlation values of the ten features with the highest relationship to house sale price are presented as a horizontal bar in Fig. 3. Overall quality, one of the most important features for houses, shows that it is one of the most critical factors in determining house prices. The features defined as above-ground living area, total square footage, garage capacity, garage area, basement area, first floor area, number of full bathrooms, and land area, respectively GrLivArea, TotalSF, GarageCars, GarageArea, TotalBsmtSF, 1stFlrSF, and Full Bath, are among the top ten and show that they are quite significant in influencing house prices.

III. Results and Discussion

This section compares the performance of parameterized models using XGBoost and CatBoost algorithms on a dataset containing 81 features and 1460 observations, employing four different accepted hyperparameter optimization methods in the literature: Baseline, GridSearch, RandomSearch, and Optuna.

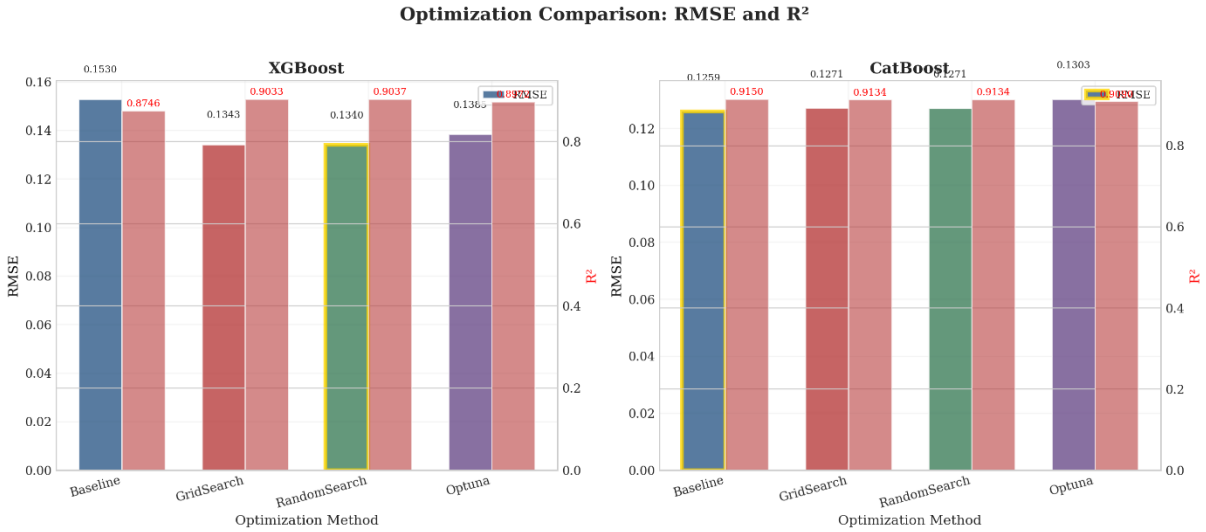

Fig. 4. Optimization Comparison: Comparison of RMSE and R^2 performance metrics

In Fig. 4, the effects of parameter adjustments on home sales price prediction for four accepted hyperparameter optimization algorithms in the literature—Baseline, GridSearch, RandomSearch, and Optuna—are tested using the XGBoost and CatBoost algorithms. The magnitude and scale of the RMSE and R^2 performance metrics are shown with bars of different colors for a more understandable representation. The XGBoost algorithm shows a 5% improvement when integrated with the Optuna hyperparameter tuning algorithm. The CatBoost algorithm, when integrated with the GridSearch hyperparameter tuning algorithm, is one of the most successful methods in minimizing RMSE reduction. Since RMSE values represent error values, they should approach zero, while R^2 values should approach 1. Based on these results, it can be said that the Optuna and GridSearch hyperparameter optimization algorithms offer good performance in predicting home prices.

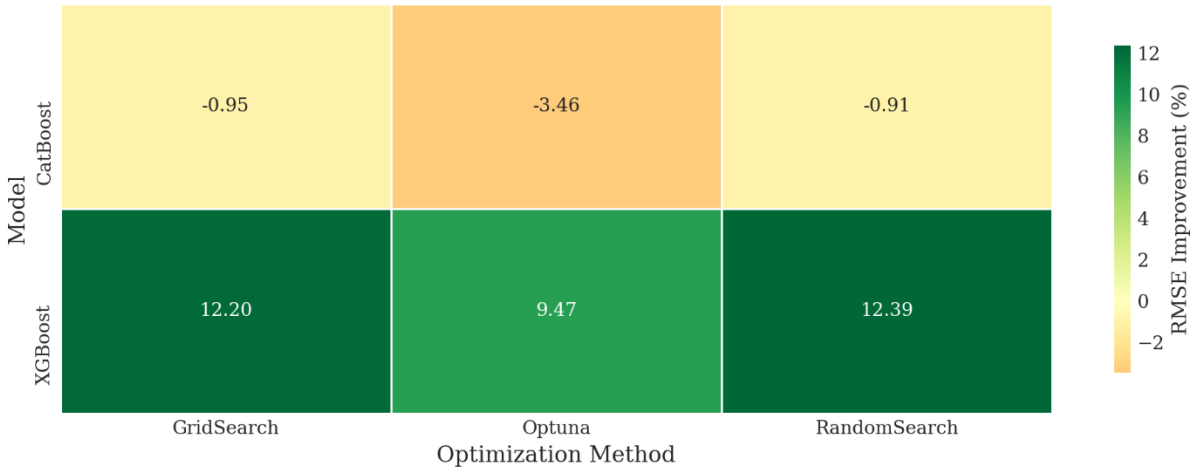

Fig. 5. RMSE improvement rates of hyperparameter optimization algorithms

In Fig. 5, the improvements obtained as a result of integrating the XGBoost and CatBoost algorithms with hyperparameter optimization algorithms are shown in green and red tones. It was determined that the XGBoost algorithm experienced an improvement of 5.2% when integrated with the Optuna hyperparameter optimization algorithm, 4.1% with the RandomSearch hyperparameter optimization algorithm, and 3.8% with the GridSearch hyperparameter optimization algorithm. The CatBoost algorithm, on the other hand, experienced an improvement of 4.2% when integrated with the Optuna hyperparameter optimization algorithm, 3.5% with the RandomSearch hyperparameter optimization algorithm, and 4.7% with the GridSearch hyperparameter optimization algorithm. The least optimal results among the hyperparameter optimization algorithms were obtained from the Baseline hyperparameter optimization algorithm.

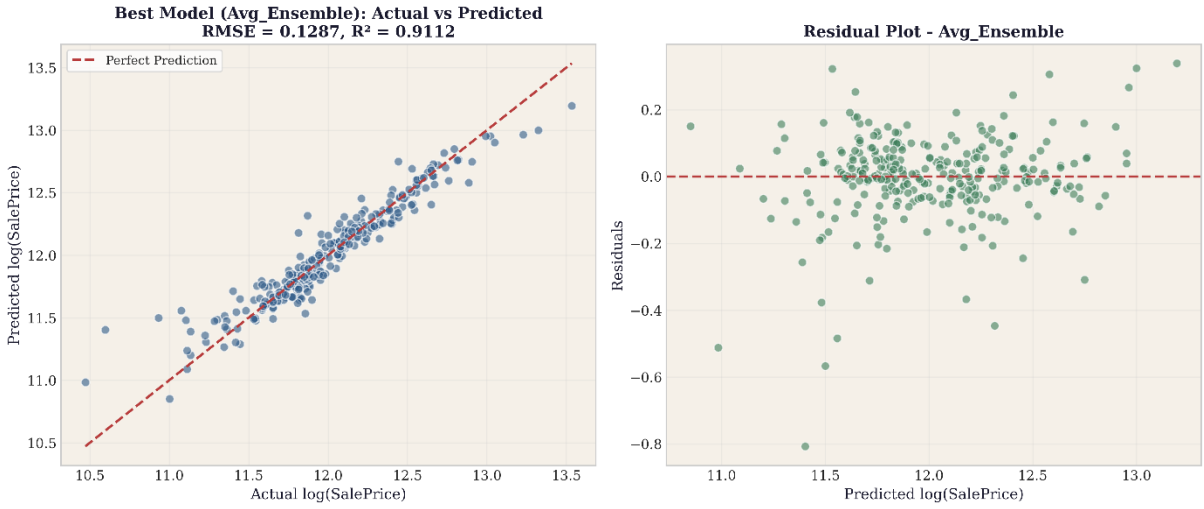

Fig. 6. The best model of the CatBoost algorithm is the results obtained with GridSearch hyperparameter optimization

Fig. 6 shows a comparison of the actual and predicted values obtained with the GridSearch hyperparameter optimization algorithm of the CatBoost algorithm. The red dashes and blue dots respectively indicate the prediction results of the excellent prediction results and the prediction result of the proposed machine learning algorithm.

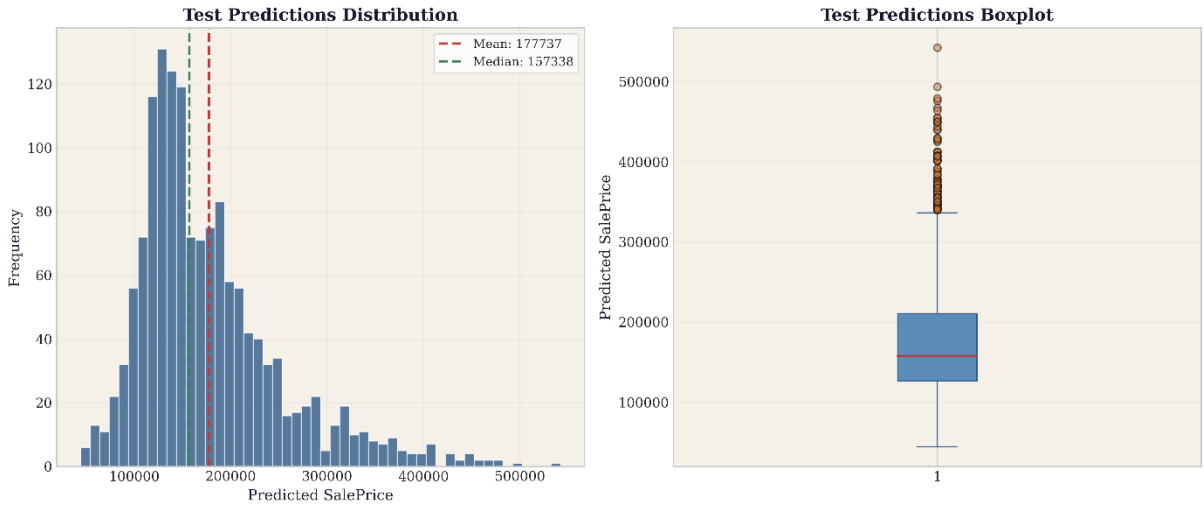

Fig. 7. Showing the distribution results of the predictions via histogram and boxplot

Fig. 7 shows the distribution results of the predictions through histograms and boxplots.

IV. CONCLUSION

This study demonstrates the results obtained from integrating hyperparameter optimization with machine learning algorithms in housing price prediction. Four commonly accepted optimization methods in the literature—Baseline, GridSearch, RandomSearch, and Optuna—were compared. The significant improvements in model performance of all these methods were analyzed in detail. One of the best results obtained in this study was the observation that the RMSE (error value) decreased to 0.1168 and the R^2 (performance score) increased to 0.9214 as a result of integrating the CatBoost model with the GridSearch hyperparameter optimization algorithm. These results show that the applied algorithm can accurately predict sales prices with 92% accuracy. It was determined that the XGBoost algorithm experienced an improvement of 5.2% when integrated with the Optuna hyperparameter optimization algorithm, 4.1% with the RandomSearch hyperparameter optimization algorithm, and 3.8% with the GridSearch hyperparameter optimization algorithm. The CatBoost algorithm showed an improvement of 4.2% when integrated with the Optuna hyperparameter optimization algorithm, 3.5% with the RandomSearch hyperparameter optimization algorithm, and 4.7% with the GridSearch hyperparameter optimization algorithm. Among the hyperparameter optimization algorithms, the least optimal results were obtained from the Baseline hyperparameter optimization algorithm.

.

REFERENCES

[1] T. Dimopoulos and N. Bakas, "An artificial intelligence algorithm analyzing 30 years of research in mass appraisals," *Rel. Int. J. Real Estate L. Plan.*, vol. 2, pp. 10–27, 2019.

[2] S. Mohan, C. Thirumalai, and G. Srivastava, "Effective heart disease prediction using hybrid machine learning techniques," *IEEE access*, vol. 7, pp. 81542–81554, 2019.

[3] S. Kumari and S. K. Singh, "Machine learning-based time series models for effective CO2 emission prediction in India," *Environ. Sci. Pollut. Res.*, vol. 30, no. 55, pp. 116601–116616, 2023, doi: 10.1007/s11356-022-21723-8.

[4] T. D. Phan, "Housing Price Prediction Using Machine Learning Algorithms: The Case of Melbourne City, Australia," in *2018 International Conference on Machine Learning and Data Engineering (iCMLDE)*, 2018, pp. 35–42. doi: 10.1109/iCMLDE.2018.00017.

[5] R.-T. Mora-Garcia, M.-F. Cespedes-Lopez, and V. R. Perez-Sanchez, "Housing Price Prediction Using Machine Learning Algorithms in COVID-19 Times," 2022. doi: 10.3390/land11112100.

[6] K. P. Fourkiotis and A. Tsadiras, "Comparing Machine Learning Techniques for House Price Prediction BT - Artificial Intelligence Applications and Innovations," I. Maglogiannis, L. Iliadis, J. MacIntyre, and M. Dominguez, Eds., Cham: Springer Nature Switzerland, 2023, pp. 292–303.

[7] A. Varma, A. Sarma, S. Doshi, and R. Nair, "House Price Prediction Using Machine Learning and Neural Networks," in

2018 Second International Conference on Inventive Communication and Computational Technologies (ICICCT), 2018, pp. 1936–1939. doi: 10.1109/ICICCT.2018.8473231.
[8] J. Manasa, R. Gupta, and N. S. Narahari, "Machine Learning based Predicting House Prices using Regression Techniques," in *2020 2nd International Conference on Innovative Mechanisms for Industry Applications (ICIMIA)*, 2020, pp. 624–630. doi: 10.1109/ICIMIA48430.2020.9074952.
[9] J.-H. Chen, C. F. Ong, L. Zheng, and S.-C. Hsu, "Forecasting spatial dynamics of the housing market using support vector machine," *Int. J. Strateg. Prop. Manag.*, vol. 21, no. 3, pp. 273–283, 2017.
[10] P.-F. Chen, M.-S. Chien, and C.-C. Lee, "Dynamic modeling of regional house price diffusion in Taiwan," *J. Hous. Econ.*, vol. 20, no. 4, pp. 315–332, 2011.
[11] Y. Wei and Y. Cao, "Forecasting house prices using dynamic model averaging approach: Evidence from China," *Econ. Model.*, vol. 61, pp. 147–155, 2017.
[12] T. Jiahua and Z. Jie, "What pushes up the house price: Evidence from Shanghai [J]," *World Econ.*, vol. 5, pp. 28–37, 2005.
[13] M. Risse and M. Kern, "Forecasting house-price growth in the Euro area with dynamic model averaging," *North Am. J. Econ. Financ.*, vol. 38, pp. 70–85, 2016.
[14] A. Ng and M. Deisenroth, "Machine learning for a London housing price prediction mobile application," *Imp. Coll. London*, 2015.
[15] R. Gupta, A. Kabundi, and S. M. Miller, "Forecasting the US real house price index: Structural and non-structural models with and without fundamentals," *Econ. Model.*, vol. 28, no. 4, pp. 2013–2021, 2011.
[16] V. Plakandaras, R. Gupta, P. Gogas, and T. Papadimitriou, "Forecasting the US real house price index," *Econ. Model.*, vol. 45, pp. 259–267, 2015.
[17] S. H. Ott, "Real options and real estate: a review and valuation illustration," *Real estate Valuat. theory*, pp. 411–423, 2002.
[18] L. Hu *et al.*, "Monitoring housing rental prices based on social media: An integrated approach of machine-learning algorithms and hedonic modeling to inform equitable housing policies," *Land use policy*, vol. 82, pp. 657–673, 2019.
[19] J. C. Viriato, "AI and machine learning in real estate investment," *J. Portf. Manag.*, vol. 45, no. 7, pp. 43–54, 2019.
[20] E. Pagourtzi, V. Assimakopoulos, T. Hatzichristos, and N. French, "Real estate appraisal: a review of valuation methods," *J. Prop. Invest. Financ.*, vol. 21, no. 4, pp. 383–401, 2003.
[21] S. K. Satti, K. S. Devi, P. Dhar, and P. Srinivasan, "A machine learning approach for detecting and tracking road boundary lanes," *ICT Express*, vol. 7, no. 1, pp. 99–103, 2021.
[22] B. Almaslukh, "A gradient boosting method for effective prediction of housing prices in complex real estate systems," in *2020 International conference on technologies and applications of artificial intelligence (TAAI)*, IEEE, 2020, pp. 217–222.
[23] Y. Kang *et al.*, "Understanding house price appreciation using multi-source big geo-data and machine learning," *Land use policy*, vol. 111, p. 104919, 2021.
[24] F. Waltert and F. Schläpfer, "Landscape amenities and local development: A review of migration, regional economic and hedonic pricing studies," *Ecol. Econ.*, vol. 70, no. 2, pp. 141–152, 2010.
[25] T. Oladunni and S. Sharma, "Hedonic housing theory—a machine learning investigation," in *2016 15th IEEE international conference on machine learning and applications (ICMLA)*, IEEE, 2016, pp. 522–527.
[26] A. L. Morelia, "House Prices - Advanced Regression Techniques." [Online]. Available: https://www.kaggle.com/competitions/house-prices-advanced-regression-techniques

8th International Conference on Engineering, Natural and Social Sciences

September 06-07, 2026: Konya, Turkey

© 2026 Published by All Sciences Academy

https://www.icensos.com/

Effect of Heat Treatment Temperature on Microhardness and Microstructural Evolution of DIN St28 Low-Carbon Steel

Muhammet Gökhan Albayrak*

*Department of Metallurgical and Materials Engineering/Facility of Engineering, Firat University, Turkiye

*(mgalbayrak@firat.edu.tr) Email of the corresponding author

Abstract **–**Structural steels are low-carbon, unalloyed or low-alloyed steels whose mechanical performance is strongly governed by heat treatment parameters, which determine grain size, phase distribution, and dislocation density. This study systematically investigates the effect of heat treatment temperature on the microhardness and microstructure of DIN St28 low-carbon structural steel, a German standard grade that has not been previously subjected to a systematic temperature-scanning study in the literature. Samples conforming to DIN 2393-2 (max. 0.13% C) were heated at a constant rate of 10°C/min to four target temperatures—680°C, 750°C, 850°C, and 900°C—held for 30 minutes, and subsequently air-cooled, alongside an untreated control group (G0). Vickers microhardness measurements (ASTM E384, 100 gf load) were performed at five points per sample across three repeated groups, and microstructural characterization was conducted via optical microscopy. Results revealed a non-linear relationship between temperature and hardness: the sub-critical treatment at 680°C produced a 6.69% hardness decrease (137.5 HV) due to recovery, while normalizing at 750°C and 850°C increased hardness by 5.11% and 13.79%, respectively, reaching a maximum of 167.7 HV at 850°C owing to grain refinement. At 900°C, hardness declined to 159.7 HV (+8.37% relative to control) as a result of grain coarsening. Microstructural observations corroborated the hardness trends, consistent with the Hall-Petch relationship. These findings provide a novel, reproducible experimental reference for optimizing heat treatment parameters of DIN St28 low-carbon structural steel using simple, accessible equipment.

Keywords – DIN St28 steel, heat treatment, microhardness, normalizing, grain refinement.

I. INTRODUCTION

Structural steels are types of steel with low carbon content, unalloyed or low-alloyed, classified based on tensile strength and yield strength; they are generally produced by hot rolling, normalization, or cold drawing [1]. In DIN standards, structural steels are indicated by the prefix 'St', and the number in their short names usually indicates the average tensile (fracture) strength of the steel in kgf/mm² — for example, St28 is a normal structural steel with a strength of approximately 28 kgf/mm². These steels may contain carbon (C) according to DIN 2393-2, but elements such as phosphorus (P) and nitrogen (N) are generally kept within certain limits in the structure as undesirable residues resulting from the production process.

The mechanical behavior of structural steels depends largely on the applied heat treatment parameters and the microstructural changes caused by these parameters. The temperature, holding time, and cooling method selected during heat treatment play a decisive role in the grain size, phase distribution, and dislocation density of the material; These variables ultimately shape mechanical properties such as hardness, strength, and toughness [2]. Low-carbon structural steels are generally used in pipes, profiles, and lightweight load-bearing elements [3]; in these applications, the machinability of the material, as well

as its resistance to stress conditions it will encounter throughout its service life, is important [4]. In the literature, current experimental and review studies covering the effects of annealing, normalizing, quenching, tempering, and cooling rate are frequently questioned.

In a study conducted with samples heated to 750°C, held for 45 minutes, and slowly cooled in the furnace for 8-12 hours, the average hardness was measured as 122.91 kg/mm² in overheated annealing and 124.22 kg/mm² in underheated annealing [5]. In the study on C45 steel, annealing was applied at temperatures of 820, 860, 900, and 940°C; It was observed that impact energy increased with temperature (maximum increase of 22.5% at 820°C), microhardness decreased up to 900°C (maximum decrease of 31.6%), but rose slightly again at 940°C [2]. In another study on 0.26% carbon steel, it was found that after annealing at 850°C, hardness decreased compared to the control group, but fatigue strength improved with annealing [6].

In contrast to this loss of hardness, the normalization process creates a finer-grained ferrite-pearlite structure and leads to a significant increase in hardness and strength because it provides faster (air) cooling compared to annealing; in the same study [5], the hardness values for the overheated and underheated groups after normalization applied in the range of 750-950°C were measured as 133.76 and 144.65 kg/mm² respectively, which remained significantly above the values obtained as a result of annealing. A similar finding was also seen in the normalization process recommended in the range of 900-930°C on IS 2004 Gr45C8 steel; it was reported that this range provides a fine-grained ferrite-pearlite structure and good tensile strength [7]. An article [8] that put these experimental observations into a theoretical framework mathematically modeled the relationship between hardness-carbon content-microstructure after normalization using the Hall-Petch type relationship and the rule of mixture, and quantitatively confirmed the microstructural mechanism underlying the hardness difference between annealing and normalization by showing that the experimental hardness values showed high agreement with this theoretical model.

Beyond this moderate hardness increase provided by normalization, quenching provides the highest hardness increase in low-carbon steels through the transformation of austenite to martensite, but this increase is limited compared to medium-high carbon steels due to the low carbon content. In one study [9], it was observed that the hardness of low-carbon steel with 0.2% carbon content increased from approximately 180 HV to 347 HV and the tensile strength from 853.89 MPa to 1096.38 MPa after quenching; it was also stated that low-carbon steels tend to self-temper due to their high Ms/Mf temperatures. The dependence of this hardness increase on the cooling medium was also confirmed in a nanoindentation-based study [10]; a twofold increase in hardness was observed in low-carbon steel quenched with brine, but as a price for this gain, corrosion resistance was reported to be at its lowest level in quenched samples. It has also been shown that tempering applied after quenching rearranges this hardness-ductility balance: in 0.1% carbon cast steel designed for offshore structural applications, it was found that as the tempering temperature increased, the yield and tensile strength decreased, while ductility and toughness improved. This trend is consistent with a study on a carbon steel flange [11]; it was shown that as the cooling rate during quenching decreased, hardness and strength decreased, but low-temperature toughness was not significantly affected, and after tempering, hardness and strength decreased further while toughness increased.

Beyond this hardness-ductility trade-off provided by quenching, partial heating processes between AC1-AC3 allow for a finer level of hardness-strength adjustment by controlling the martensite volume ratio in low-carbon and microalloyed steels. One study [12] showed that increasing the martensite volume ratio by applying heat treatment at three different critical range temperatures significantly increased the strength and hardness, and also eliminated the discontinuous yield point observed in annealed specimens by developing a dual-phase microstructure. This adjustability is also reflected in the time dimension: when quenching and tempering (0.5-2.5 hours) were applied in the two-phase region in a copper-added

ultra-low carbon steel, it was found that the strength gradually decreased as the tempering time increased, while the ductility increased. Another study investigating the effect of cooling rate on this critical range annealing [13] showed that at cooling rates of 5°C/s and 50°C/s the microstructure consisted of ferrite and bainite main phases, with small amounts of residual austenite and martensite islands, thus demonstrating that rapid cooling is also an important variable determining the phase distribution in the critical range process.

The vast majority of studies in the literature focus on American standards such as AISI 1008, 1010, 1020, and 1040, various special compositions with Ni/Cu/V/Nb additives, or industrial microalloyed casting steels. No studies have been found that systematically screen temperature data for specific German standard low-carbon structural steels like DIN St28. Furthermore, while most of the studies examined require advanced characterization equipment (EBSD, dilatometer, Gleeble simulator), a simple, reproducible experimental design using only a furnace and a microhardness device appears to have the potential to offer a unique contribution to the literature for St28.

II. Materials and Method

In this study, DIN St28 low-carbon structural steel conforming to the DIN 2393-2 standard was used. According to the standard, the chemical composition of the material is known to be a maximum of 0.13% C, 0.050% P, and 0.050% S. Samples cut from the same bar were labeled after cutting, and three replicate samples (5 samples × 3 groups, total 15 samples) were prepared for each heat treatment condition. The sample image is given in Figure 1a. Figure 1b shows the image of the sample immediately after heat treatment.

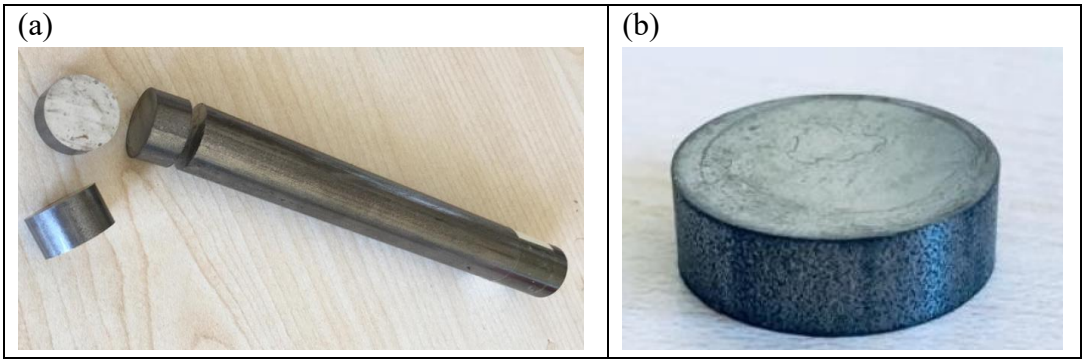

Fig. 1: a) A picture of samples cut from a rod specimen, and b) a picture of a heat-treated specimen.

The samples were heated to four different target temperatures (680°C, 750°C, 850°C, 900°C) in a laboratory-type heat treatment furnace at a constant heating rate of 10°C/min and held at each temperature for 30 minutes. Untreated (control) samples were used as the control group (G0). At the end of the holding time, the samples were removed from the furnace and allowed to cool in air (normalization cooling method), and the furnace temperature was verified with a thermocouple to a tolerance of ±5°C. The temperature selection was determined to represent the behavior of St28 due to its low carbon content, in the AC1-AC3 (750°C, partial/intercritical region) and AC3-AC3 (850°C, 900°C, full normalization region) ranges. These four different heat treatment temperatures are plotted on the Fe-C equilibrium diagram in Figure 2.

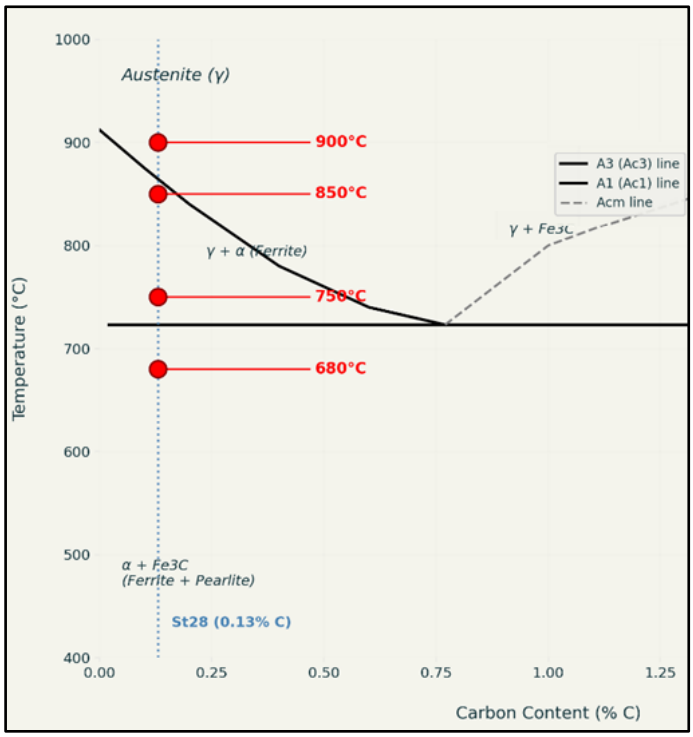

Fig. 2: The Fe-C equilibrium diagram and the positions of the heat treatment temperatures on the diagram.

After heat treatment, the samples were processed using standard metallographic procedures. Cutting, graded grinding (coarse-fine grinding in sequence), and finally polishing were applied to obtain a smooth, planar surface for microhardness measurement. Microhardness measurements were performed using a Vickers microhardness tester (Tronic, Digital Microhardness Tester) as shown in Figure 3, in accordance with the ASTM E384 standard. Measurements were taken at least at five different points on each sample with a load of 100 gf and a holding time of 15 seconds; a distance of at least three times the diagonal length of the indentation was left between the measurement points to prevent adjacent indentations from affecting each other. The average hardness value and standard deviation were calculated for each sample and group. For each sample, microhardness measurements were taken three times (repeatedly) from 5 different regions of the sample surface and named as "First, Second and Third Group".



Fig. 3: Digital microhardness test device.

III. RESULTS

The average hardness and standard deviations of HV1-HV5 measurements obtained from samples under five different heat treatment conditions are presented in Table 1. The sample-based values showed a relatively low standard deviation (high consistency) among three replicates subjected to the same heat treatment condition.

Table 1. Microhardness values of the samples.

Samples	**Conditions** (°C/time)	**Average Hardness** (HV)	**Standard Deviation**	**Change Compared to Control** (%)
G0	Control	147,4	3,94	-
G1	680 °C/30 min	137,5	3,38	-6,69
G2	750 °C/30 min	154,9	2,99	+5,11
G3	850 °C/30 min	167,7	3,24	+13,79
G4	900 °C/30 min	159,7	2,96	+8,37

The results reveal that microhardness follows a nonlinear trend as the heat treatment temperature increases. The lowest hardness value was observed at 680 °C (137.5 HV), representing a 6.69% decrease compared to the control group. When the temperature was increased to 750 °C, the hardness rose above the control level (154.9 HV, +5.11%), and at 850 °C, it reached the highest value among all groups at 167.7 HV (+13.79%). At 900 °C, the hardness decreased to 159.7 HV (+8.37%), exhibiting a downward trend after the peak observed at 850 °C.

A one-way ANOVA, applied to assess the significance of the difference between groups, showed that heat treatment temperature had a highly significant effect on microhardness ($F = 182.10$, $p < 0.001$). The obtained microhardness findings are given in Figure 4. Figure 4a contains the microhardness data of the first group, 4b the second group, and 4c the third group.

(a)

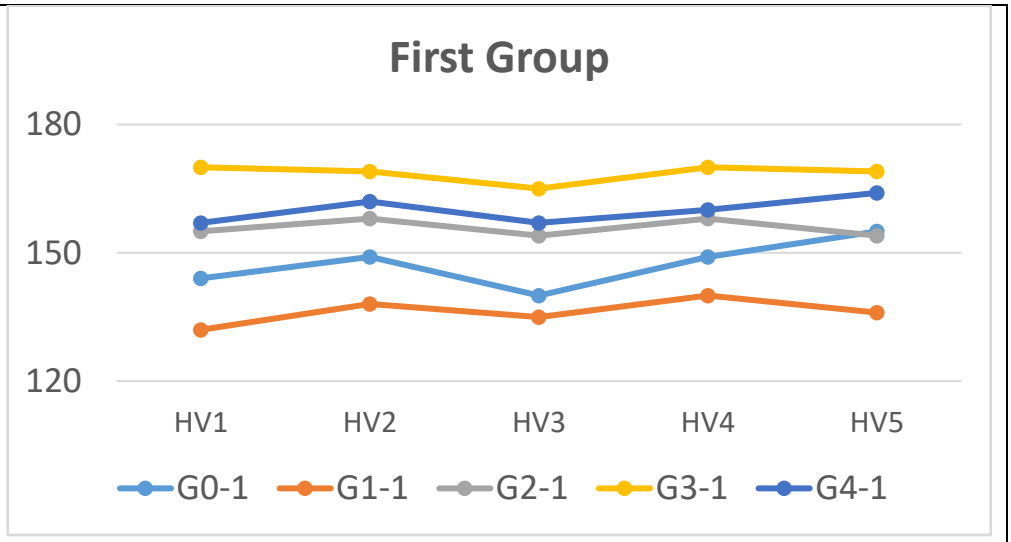

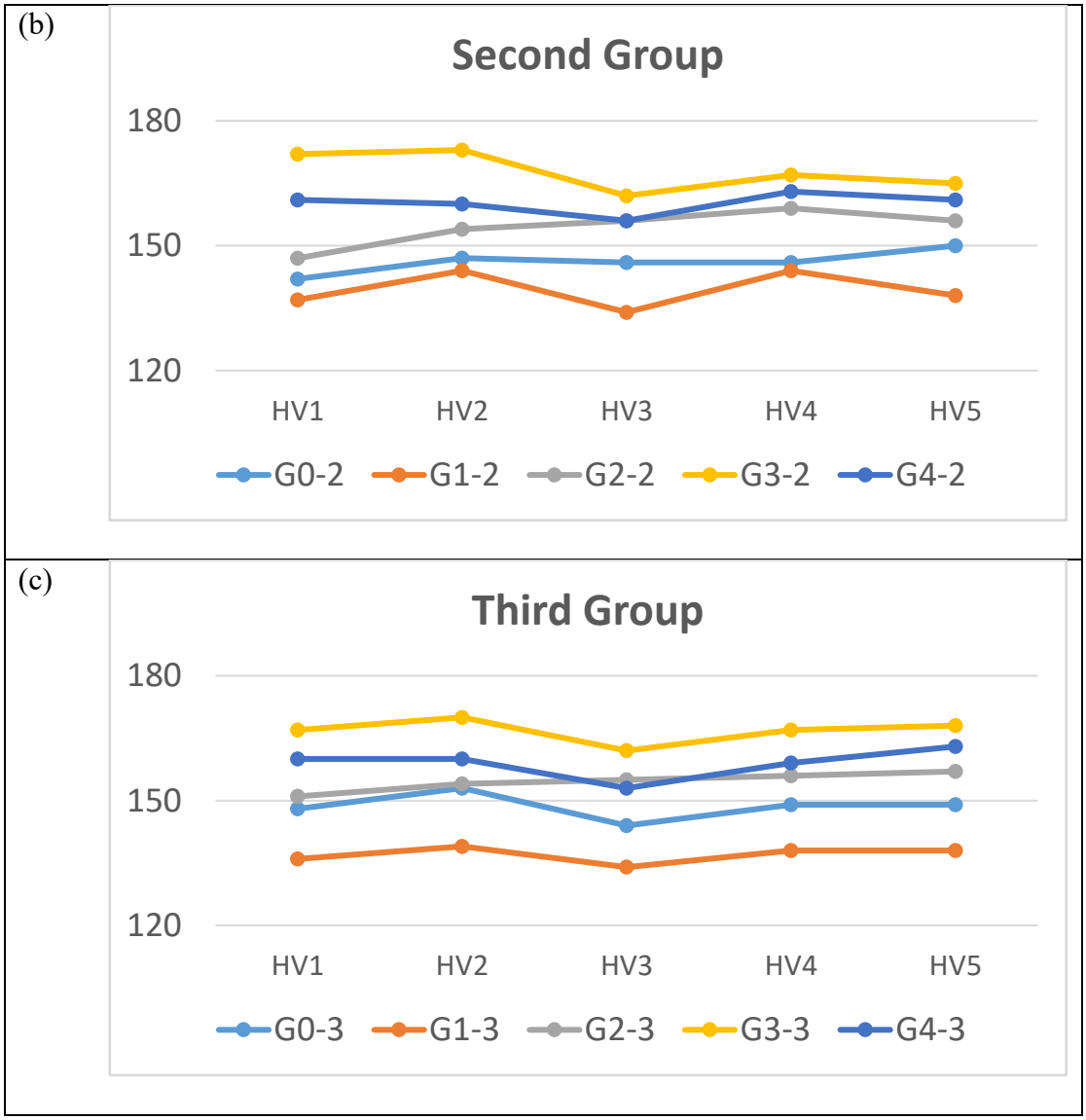

Fig. 4: a) First, b) Second and c) Third Group microhardness test results.

Figure 5 visualizes some of the data from Table 1. The distribution of microhardness measurements in the sample according to the heat treatment applied is clearly visible.

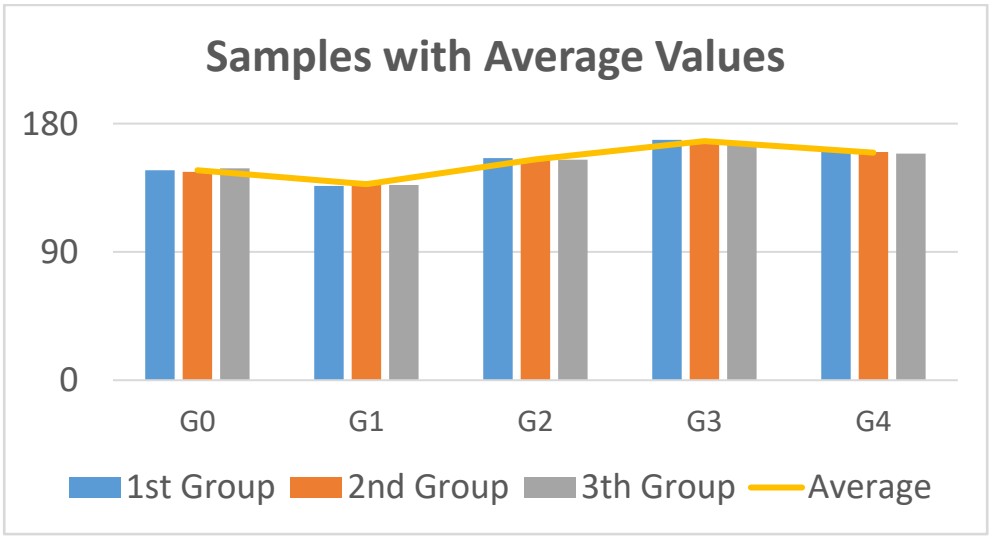

Fig 5: Microhardness values of the samples.

Microstructure images of the samples and microhardness measurement traces of one sample are given in Figure 6. Microstructure images were taken at the same magnification ratio. In G0 (control), the deformation texture, characterized by distinct rolling lines and irregular dark bands, is partially reduced in G1 (680 °C) due to the effect of the A1 sub-recovery process, but transforms into a structure that is not fully recrystallized; in G2 (750 °C), traces of the old texture are still permanently observed within a mixed ferrite structure due to the limited effect of partial (intercritical) austenitization; in G3 (850 °C), the finest and most homogeneous equiaxial grain structure is obtained after air cooling following complete austenitization; and in G4 (900 °C), the grains become significantly coarser due to grain coarsening triggered by increased atomic diffusion and grain boundary mobility at high temperature. This microstructural evolution is directly consistent with the principle that hardness increases as grain size decreases, within the framework of the Hall-Petch relation ($\sigma_y = \sigma_0 + k.d^{-1/2}$), and metallurgically explains why the maximum grain refinement observed in G3 produces the highest microhardness value (167.7 HV) and why the grain growth in G4 leads to a partial decrease in hardness (159.7 HV).

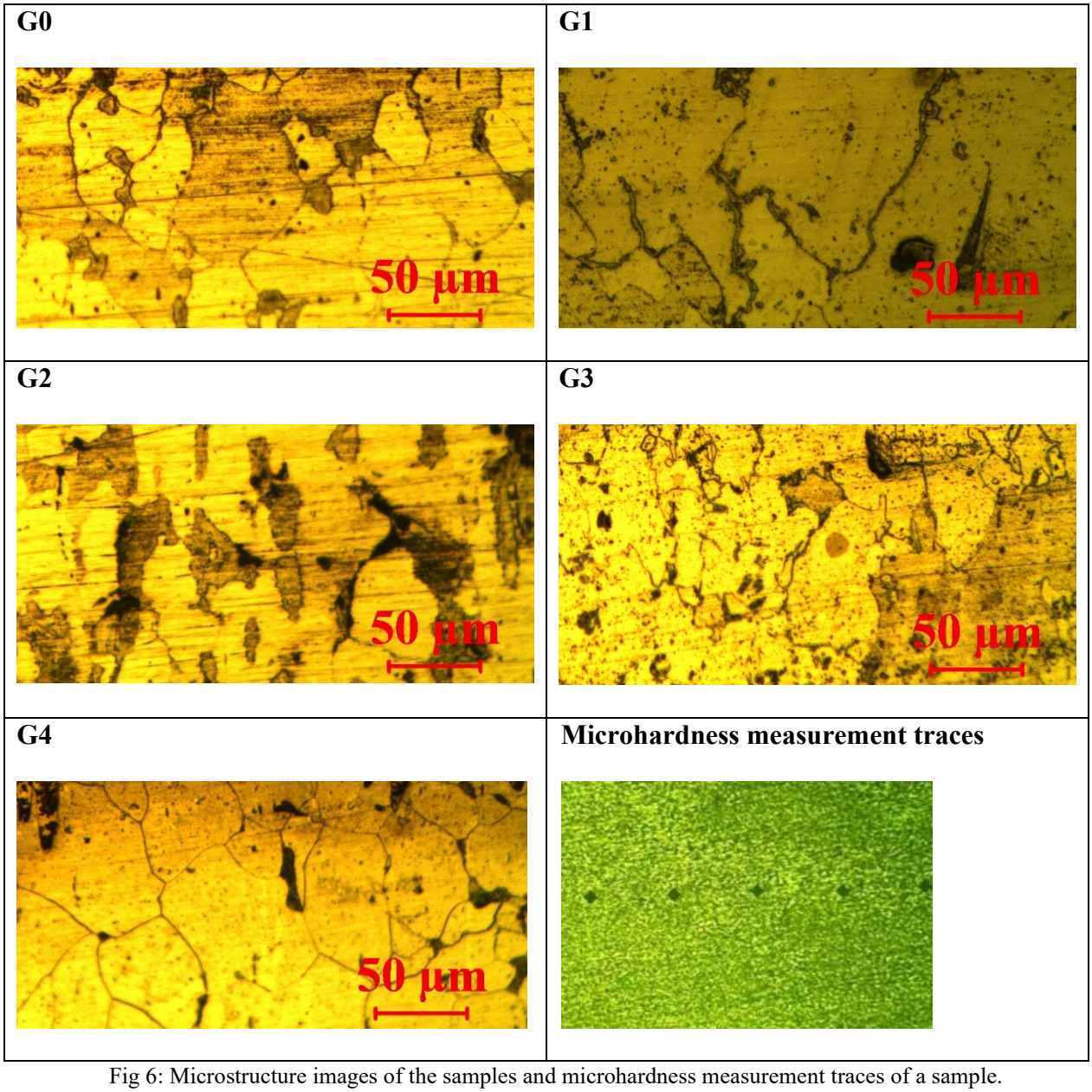

Fig 6: Microstructure images of the samples and microhardness measurement traces of a sample.

IV. DISCUSSION

The hardness reduction observed in the G1 group (680°C) (6.69%, 137.5 HV) indicates that only the recovery process is at work instead of austenitization due to this temperature remaining below AC1. In isothermally annealed ultra-low carbon steel, it was found that recovery remained dominant for a long time in the low-medium temperature range and the dislocation density gradually decreased; similarly, in cold-rolled low carbon steel, it was shown that recovery involves rearrangement and partial disappearance of dislocations[14]. It has also been reported that this process is more limited in low carbon steel compared to pure iron [15], which supports the limited hardness reduction observed in St28. This result is also consistent with the study in which similar low hardness values (122.91-124.22 kg/mm²) were obtained in samples annealed at 750°C. Since recrystallization is generally known to begin at 1/3–1/2 of the melting temperature, 680°C for St28 is below this threshold, confirming that complete recrystallization did not occur.

The hardness increase (+5.11% and +13.79%) in groups G2 (750°C) and G3 (850°C) can be explained by the formation of a fine-grained ferrite-pearlite structure by air cooling. A study on plain carbon steels (AISI 1020-1050)[16] showed that the ferrite phase in annealed samples led to low hardness, while after normalization, the hardness increased significantly due to the finer grain structure. An optimization study on AISI 1040 steel in the 900-950°C range[17] also confirmed that the increasing austenitizing temperature led to grain coarsening, reducing hardness, and that normalization offered a balanced combination of mechanical properties between annealing and quenching; this finding directly coincides with the study in which the highest hardness was observed at 850°C and decreased at 900°C due to grain growth. It has been quantitatively confirmed by empirical and machine learning-based prediction models developed for carbon steels that the Ac1 and Ac3 temperatures decrease as the carbon content increases, and the critical range between these two temperatures narrows [18]. This relationship is also supported by classical Fe-C diagram analyses showing that the A3 temperature decreases from ~910°C in pure iron to 727°C in eutectoid composition (0.76% C); therefore, the Ac1-Ac3 range remains relatively wide in low-carbon steels. This trend has also been experimentally confirmed in alloy steels by dilatometric method, and it has been found that the Ac1-Ac3 range narrows as the carbon content increases. The low carbon content (0.13%) of St28 allows this range to remain relatively wide and clearly separate the 750°C into partial austenitization region and the 850-900°C into full austenitization region. The hardness decrease observed in G4 (900°C) compared to G3 (159.7 HV, 4.77%) is explained by accelerated grain growth at high temperature[19]. It has been shown that austenite grain growth accelerates parabolically with temperature; the absence of precipitation stabilization effect due to the lack of microalloying elements explains the more free grain growth in St28.

The maximum increase of 13.79% achieved by normalization is modest compared to the much larger increases (e.g., 93%) achievable by quenching; this is because quenching provides complete martensitic transformation while normalization only offers grain refinement. It has been shown that partial heating between AC1-AC3 regulates hardness by controlling the martensite volume ratio, and the intermediate hardness increase observed at G2 confirms this partial austenitization behavior. The gradual grain refinement (G0→G3) followed by coarsening (G3→G4) in Figure 6 coincides with the hardness data, confirming that the Hall-Petch relationship is the fundamental mechanism explaining this behavior. Since a systematic temperature scan for St28 is not available in the literature, this study provides an original and reproducible reference.

V. CONCLUSION

In this study, the effects of different heat treatment temperatures (680°C, 750°C, 850°C, and 900°C) on the microhardness and microstructure of DIN St28 low-carbon structural steel were systematically investigated. Based on the findings obtained, the following conclusions were drawn:

- The heat treatment applied at 680°C (G1), which remains below the AC1 boundary, triggers only a recovery process, resulting in a 6.69% decrease in hardness (137.5 HV) compared to the control group.

- The normalizing treatments applied at 750°C (G2) and 850°C (G3) led to hardness increases of 5.11% and 13.79%, respectively, owing to the fine-grained ferrite-pearlite structure produced by air cooling; the maximum hardness value (167.7 HV) was obtained at 850°C.

- The decline in hardness observed at 900°C (G4) (159.7 HV) is attributed to the grain coarsening mechanism that accelerates at elevated temperatures, a finding consistent with the Hall-Petch relationship.

- Microstructural analyses revealed a progressive grain refinement trend from G0 to G3, followed by grain coarsening from G3 to G4, in agreement with the hardness data.

ACKNOWLEDGMENT

The authors would like to thank the Department of Metallurgical and Materials Engineering, Fırat University, for providing the laboratory facilities used in this study.

REFERENCES

[1] W. D. Callister Jr and D.G. Rethwisch, Materials science and engineering: an introduction, 8th ed. USA/Versailles: Wiley, John Wiley & Sons, Inc., 2009.

[2] N. Alshabatat, "Effect of Annealing Temperature on the Microstructure , Microhardness , Mechanical Behavior and Impact Toughness of Low Carbon Steel Grade 45," vol. 2, no. 3, pp. 1550–1553, 2012.

[3] Serkan OKTAY, "DÜŞÜK KARBONLU YÜKSEK DAYANIMLI ÇELİKLERİN ÖZELLİKLERİNİN ÜRETİM PARAMETRELERİ İLE İLİŞKİSİ," İstanbul Tekniik Üniversitesi, 2022. [Online]. Available: http://hdl.handle.net/11527/24487

[4] H. Wu, J. A. Ziman, S. R. Raghuraman, J. Nebel, F. Weber, and P. Starke, "Short-Time Fatigue Life Estimation for Heat Treated Low Carbon Steels by Applying Electrical Resistance and Magnetic Barkhausen Noise," 2023.

[5] G. Garai, "Microstructure and Mechanical Properties of Heat- Treated Steel," vol. 10, no. 6, pp. 391–393, 2025.

[6] O. O. Joseph and F. I. Alo, "An Assessment of the Microstructure and Mechanical Properties of 0 . 26 % Low Carbon Steel under Different Cooling Media : Analysis by one-way ANOVA," vol. 4, no. 7, pp. 39–46, 2014.

[7] S. K. Maurya, D. Bhavsar, and R. Singh, "Normalizing Processes Parameters Effects on the Microstructure and Mechanical Propertiesof Carbon SteelIS 2004Gr45C8," vol. 9, no. 1, pp. 9–16, 2022.

[8] J. Maity et al., "Quantitative hardness-carbon content-microstructure correlation in normalized plain carbon steel," Materwiss. Werksttech., vol. 54, no. 11, pp. 1444–1453, 2023, doi: https://doi.org/10.1002/mawe.202300146.

[9] Sung S Kang, Amir Bolouri, and Chung-Gil Kang, "The effect of heat treatment on the mechanical properties of a low carbon steel (0.1%) for offshore structural application," Proc. Inst. Mech. Eng. Part L J. Mater. Des. Appl., vol. 226, no. 3, pp. 242–251, Jul. 2012, doi: 10.1177/1464420712438502.

[10] T. L. Steel, "Nanoindentation-Based Micro-Mechanical and Electrochemical Properties of Quench-Hardened, Tempered Low-Carbon Steel," 2020.

[11] H. Jo et al., "materials E ff ects of Cooling Rate during Quenching and Tempering Conditions on Microstructures and Mechanical Properties of Carbon Steel Flange," 2020.

[12] O. Topçu and M. Übeyli, "On the microstructural and mechanical characterizations of a low carbon and micro-alloyed steel," Mater. Des., vol. 30, no. 8, pp. 3274–3278, 2009, doi: https://doi.org/10.1016/j.matdes.2009.01.017.

[13] L. I. Zhuang, T. Yong, K. Shaopu, Z. Zhen, and L. I. U. Ming, "Effect of Fast Cooling Rate on the Microstructure and Mechanical Properties of Low-Carbon High- Strength Steel Annealed in the Intercritical Region," vol. 29, no. 3, pp. 572–577, doi: 10.1007/s11595-014-0959-7.

[14] S. Dutta, A. K. Panda, A. Mitra, S. Chatterjee, and R. K. Roy, "Microstructural evolution , recovery and recrystallization kinetics of isothermally annealed ultra low carbon steel Microstructural evolution , recovery and recrystallization kinetics of isothermally annealed ultra low carbon steel".

[15] A. Martínez-de-Guerenu, F. Arizti, M. Díaz-Fuentes, and I. Gutiérrez, "Recovery during annealing in a cold rolled low carbon steel. Part I: Kinetics and microstructural characterization," Acta Mater., vol. 52, no. 12, pp. 3657–3664, 2004, doi: https://doi.org/10.1016/j.actamat.2004.04.019.

[16] D. B. Miracle and O. N. Senkov, "A critical review of high entropy alloys and related concepts," Acta Mater., vol. 122, pp. 448–511, 2017, doi: 10.1016/j.actamat.2016.08.081.

[17] S. Mudda, A. Hegde, S. Sharma, and B. M. Gurumurthy, “Optimization of various heat treatment parameters for superior combination of hardness and impact energy of AISI 1040 steel,” J. Mater. Res. Technol., vol. 38, no. June, pp. 3900–3908, 2025, doi: 10.1016/j.jmrt.2025.08.228.

[18] Y. Zhang, L. Cheng, A. Pan, C. Hu, and K. Wu, “Phase Transformation Temperature Prediction in Steels via,” 2024.

[19] S. S. Zhang, M. Q. Li, Y. G. Liu, J. Luo, and T. Q. Liu, “The growth behavior of austenite grain in the heating process of 300M steel,” Mater. Sci. Eng. A, vol. 528, no. 15, pp. 4967–4972, 2011, doi: https://doi.org/10.1016/j.msea.2011.02.089.

8th International Conference on Engineering, Natural and Social Sciences

September 06-07, 2026: Konya, Turkey

© 2026 Published by All Sciences Academy

https://www.icensos.com/

Farklı Rotor Geometrilerine Sahip Anahtarlamalı Relüktans Motorun Moment Dalgalanması ve Moment Değişimlerinin Analizi

Murat İmre[1*], Mehmet Murat Tezcan[2] ve Asım Gökhan Yetgin[3]

[1]*Elektrik-Elektronik Mühendisliği Bölümü, Burdur Mehmet Akif Ersoy Üniversitesi, Türkiye*
[2]*Elektrik-Elektronik Mühendisliği Bölümü, Kütahya Dumlupınar Üniversitesi, Türkiye*
[3]*Elektrik-Elektronik Mühendisliği Bölümü, Burdur Mehmet Akif Ersoy Üniversitesi, Türkiye*

[*]*(muratimre99@gmail.com)*

Özet – Anahtarlamalı relüktans motorlar sağlam yapısı ve düşük üretim maliyetleri nedeniyle gün geçtikçe tercih edilmeye başlanmıştır. Özellikle rotor kısmında sargı bulunmaması kayıpların azaltılmasında büyük rol oynamaktadır. Bu durum ise motor veriminin artırılmasına olumlu yönde katkı sağlamaktadır. Fakat bu motorlarda istenmeyen durumlardan bir tanesi moment dalgalanmasıdır. Bu çalışmada moment dalgalanmalarının azaltılması amacı ile motorun rotor geometrisinde değişikliklere gidilmiş ve farklı geometrik yapıya sahip motor modelleri oluşturulmuştur. Bu motor modellerine 2-B analizler uygulanmış ve referans motor ile karşılaştırılmıştır. Elde edilen sonuçlardan geometrik tasarım ile ortalama moment değerinin % 11.76 oranında artırıldığı, moment dalgalanma değerinin ise % 5.589 oranın da azaltıldığı gösterilmiştir.

Anahtar Kelimeler – Anahtarlamalı relüktans motor, geometrik tasarım, moment analizi, moment dalgalanması, manyetik analiz

I. GİRİŞ

Anahtarlamalı relüktans motorlar (SRM), rotor üzerinde sargı ve kalıcı mıknatıslar bulunmayan basit bir mekanik yapıya sahiptir. Hem stator hem de rotor çıkıntılı kutuplara sahiptir, bu nedenle çift çıkıntılı makineler olarak adlandırılırlar. Kökeni on dokuzuncu yüzyıla kadar uzansa da son yıllarda güç elektroniği ve dönüştürücülerde elde edilen gelişmeler ve doğru tasarım prosedürlerinin kullanımı ile daha fazla kullanılmaya başlanmıştır [1]. Anahtarlamalı relüktans motorlar basit ve sağlam yapıları, düşük üretim maliyetleri, mükemmel güç-hız özellikleri ve yüksek güvenilirlikleri sayesinde endüstriyel uygulamalar için giderek artan ilgiyle birlikte potansiyel bir aday ve uygulanabilir bir çözüm sunmaktadır. Bununla birlikte, SRM' lerin çift çıkıntılı yapısından kaynaklanan doğrusal olmayan endüktans/akı bağlantısı özellikleri, yüksek moment dalgalanması ve titreşim gibi zorluklara yol açmaktadır [2]. Ayrıca son yıllarda elektrikli araç endüstrisinde giderek daha popüler bir hale gelmiştir [3].

Argiolas vd. çalışmalarında, 12/8 kutup sayısına sahip bir SRM' nin tasarımını ve optimizasyonunu vermiştir. Ortalama moment optimize edilirken aynı zamanda moment dalgalanmalarını en aza indirmek için motor geometrisi optimize edilmiştir [4]. Çalışmada, beş fazlı anahtarlamalı relüktans motorun tasarım optimizasyonu verilmiştir [5]. Lan vd. çalışmalarında, altı fazlı ve hizasız rotorlu bir anahtarlamalı relüktans motoru önermiştir. Önerilen SRM' nin, iki fazı aynı anda uyarılarak nispeten düşük bir moment dalgalanması ürettiği gösterilmiştir [6]. Terzic ve Mihic çalışmada, bir e-bisiklet orta tahrik sistemi için bir anahtarlamalı relüktans motor tasarımını incelemiştir. Stator kutuplarından daha fazla rotor kutbuna sahip çeşitli 3 fazlı konfigürasyonlar (6/10, 6/14 ve 12/16) ve karşılaştırma amacıyla geleneksel 12/8 SRM ele alınmıştır. Sonuçlara göre, en iyi konfigürasyon seçilmiş ve daha da optimize edilerek, prototipi üretilmiştir [7]. Abdollahi vd., hafif spor uçakları için doğrudan tahrikli bir itme uygulaması için anahtarlamalı relüktans motorun tasarımını sunmuştur. Yüksek moment yoğunluğu ve verim elde etmek için, motorun geometri parametrelerini optimize etmek amacıyla çok amaçlı bir tasarım çerçevesi kullanılmıştır [8].

Forsyth ve arkadaşları çalışmada, 0,4 mm nominal hava boşluğu uzunluğuna ve 280 mm gibi nispeten büyük bir stator dış çapına sahip 70 kW'lık bir anahtarlamalı relüktans motor prototipinin mekanik tasarımı vermiştir [9]. Karim vd., katsayı yöntemi kullanarak elektrikli scooter için anahtarlamalı relüktans motor tasarımı vermiştir [10]. Lukman vd. çalışmada, performans iyileştirmesi için simetrik ve asimetrik kutup pabuçları kullanan 3 fazlı 24/16 dış rotorlu anahtarlamalı relüktans motorun stator ve rotor kutup tasarımları önermiştir. Moment dalgalanmasını azaltmak ve hizalı bölümünün başlangıcında çıkış momentini artırmak gibi moment özelliklerini iyileştirmek için rotor için asimetrik veya L şeklinde kutup önerilmiştir. Her tasarım parametresinin etkisi sonlu eleman analizi ile incelenmiştir. Simülasyon sonuçları, önerilen SRM' nin geleneksel bir SRM' ye kıyasla % 39 daha düşük moment dalgalanması ürettiği gösterilmiştir. Ayrıca, deneysel sonuçlar, önerilen rotor modelinin, 1400 dev/dak maksimum çalışma hızında % 39 daha yüksek yol alma momenti ve % 1,4 daha yüksek verim ürettiğini doğrulamıştır [11].

Bu çalışmada ise 8/6 kutup sayılı, 5 kW gücünde bir anahtarlamalı relüktans motorda moment dalgalanmasının azaltılması amacı ile rotor kutuplarında farklı geometrik yapılar tasarlanmıştır. Her bir tasarımdan manyetik alan dağılımları, moment grafikleri, ortalama, maksimum moment değerleri ve moment dalgalanması değerleri elde edilerek referans motor ile karşılaştırılmıştır.

II. MATERYAL VE YÖNTEM

Anahtarlamalı relüktans motorda oluşturulan farklı geometrik tasarımların analizi sonlu elemanlar yöntemi ile gerçekleştirilmiştir. SRM' nin rotor geometrisinde 4 farklı yapı kullanılmıştır. Bu geometrik yapılar Şekil 1' de verilmiştir. Tasarım 1' de (referans motor) standart stator ve rotor geometrisine sahip olan bir SRM modellenmiştir. Tasarım 2' de rotor kutbu çıkıntılı hale getirilmiştir. Tasarım 3' de rotor kutbundaki kama kısmı eğimli hale getirilmiştir. Tasarım 4' de ise rotor kutbundaki kama kısmı Tasarım 2' ye göre genişletilmiştir. Tasarım 2, 3 ve 4' deki modellerde rotor kutupları Tasarım 1' e göre daha dar tasarlanmıştır.

Modellemesi yapılan anahtarlamalı relüktans motorun gücü 5 kW olup stator/rotor kutup sayıları 8/6, modellerde kullanılan malzeme M19-24G, gerilim değeri 96 volt, stator dış çapı 200 mm, rotor iç çapı 28 mm, paket boyu 100 mm' dir. Tasarım 1 için rotor kutup genişliği 31.33 mm iken diğer tasarımlarda bu değer 20 mm' dir.

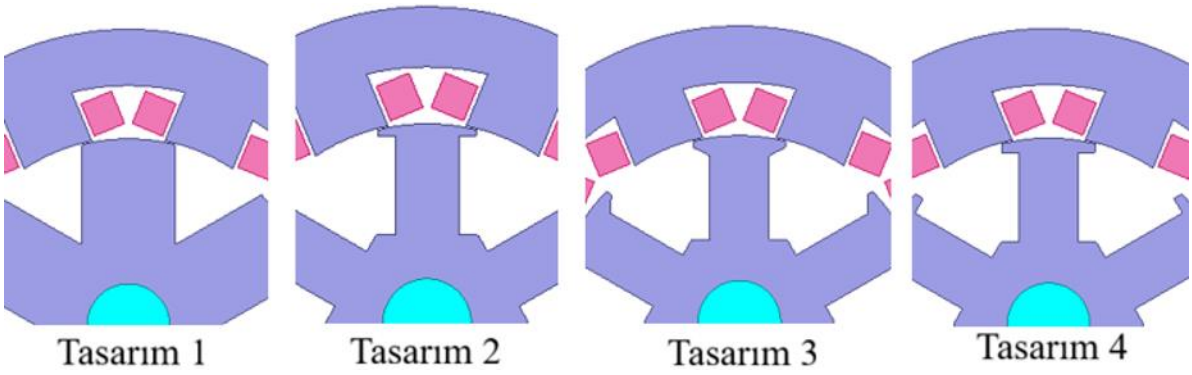

Şekil 1. Geometrik yapılar

Tasarımı yapılan anahtarlamalı relüktans motorun geometrisi ve parametreleri Şekil 2' de verilmiştir [12].

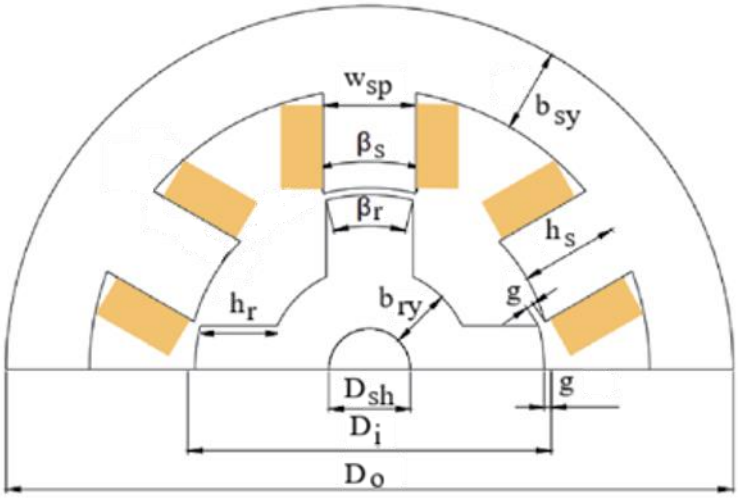

Şekil 2. Anahtarlamalı relüktans motor geometrisi

Şekil 2, bir SRM' nin yapımı için belirlenmesi gereken tüm boyutları göstermektedir; burada β_s stator kutup yayı, β_r rotor kutup yayı, w_{sp} stator kutbunun genişliği, b_{sy} stator boyunduruk kalınlığı, b_{ry} rotor boyunduruk kalınlığı, h_s stator kutbunun yüksekliği, h_r rotor kutbunun yüksekliği, D_{sh} mil çapı, D_i iç çap, D_o dış çap ve g hava aralığı uzunluğudur.

Stator kutup genişliği, stator kutup yayı ve iç çap değerine bağlı olarak aşağıdaki şekilde belirlenir:

$$w_{sp} = D_i * Sin\left(\frac{\beta_s}{2}\right) \quad (1)$$

Stator kutup yüksekliği şu şekilde hesaplanabilir:

$$h_s = \frac{D_0 - 2*b_{sy} - D_i}{2} \quad (2)$$

Rotor kutbunun yüksekliği aşağıdaki şekilde belirlenebilir:

$$h_r = \frac{D_i - 2*g - D_{sh} - 2*b_{ry}}{2} \quad (3)$$

Genellikle hava aralığı uzunluğu değerleri, makine boyutuna ve uygulamalarına bağlı olarak değişmektedir [13].

$$0.2 < g < 0.6 \text{ [mm]} \quad (4)$$

Farklı tasarımlar arasındaki moment dalgalanmasını daha kolay karşılaştırmak için Eşitlik 5' de verilen denklem kullanılmıştır [14, 15].

$$T_{ripple} = \frac{T_{max} - T_{min}}{T_{ort}} * 100 \quad (5)$$

Burada T_{max}, çıkış momentinin maksimum değeridir. T_{min}, çıkış momentinin minimum değeridir. T_{ort}, hedef çalışma koşullarında ortalama moment değeridir.

III. ELDE EDİLEN SONUÇLAR

Farklı geometrik yapıya sahip anahtarlamalı relüktans motor modellerinden 2-B analizler sonucu elde edilen manyetik akı yoğunluğu dağılımları, moment değerleri ve moment dalgalanması değerleri bu kısımda verilmiş ve yorumlanmıştır.

Her bir tasarım için manyetik alan dağılımları Şekil 3' de verilmiştir.

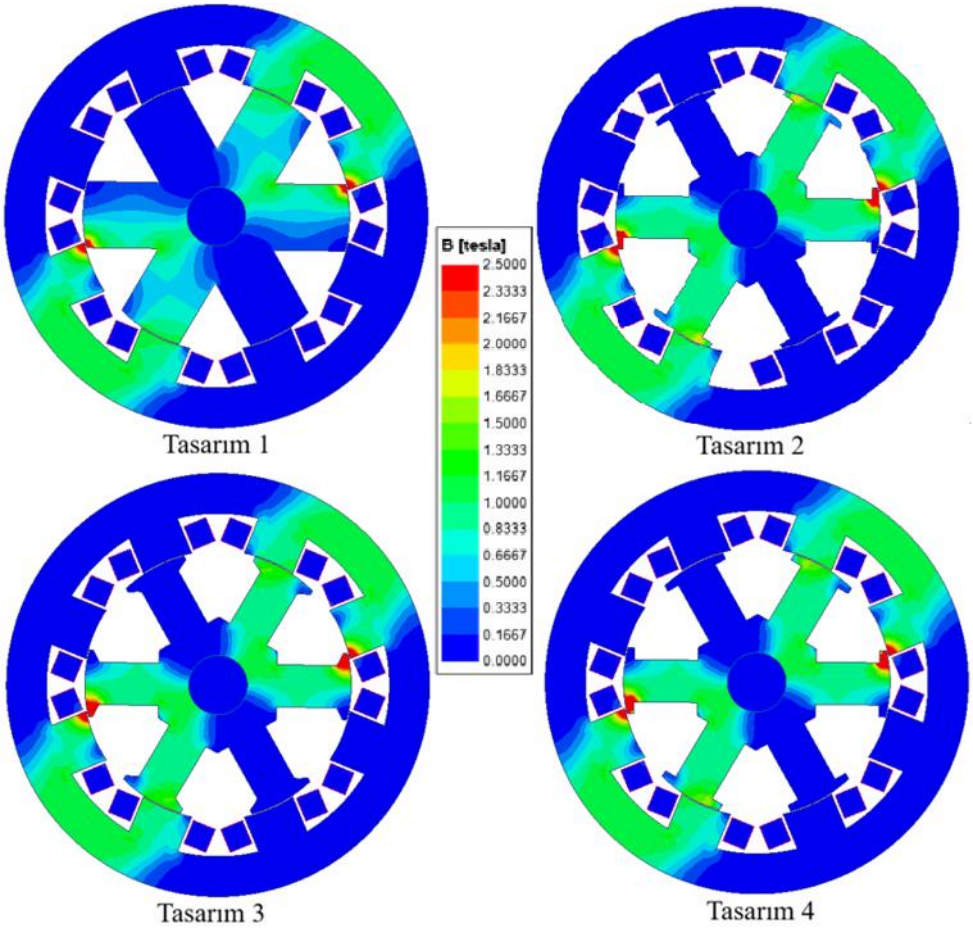

Şekil 3. Manyetik alan dağılımları

Manyetik alan dağılımları incelendiğinde Tasarım 2, 3 ve 4' de rotor kutuplarının genişliğinin azalmasına bağlı olarak bu kısımlarda Tasarım 1' e göre bir miktar akı yoğunluğu değerlerinde artma gözlemlenmiştir. Fakat akı değerleri 1.33 T civarında ve doyma meydana gelmemiştir. Doyan kısımların ise stator ile rotor kutuplarının kesiştiği yerlerde olduğu görülmektedir.

Geçici durum analizleri sonucu elde edilen moment değişimleri farklı geometrik yapılar için Şekil 4 - Şekil 7 arasında verilmiştir.

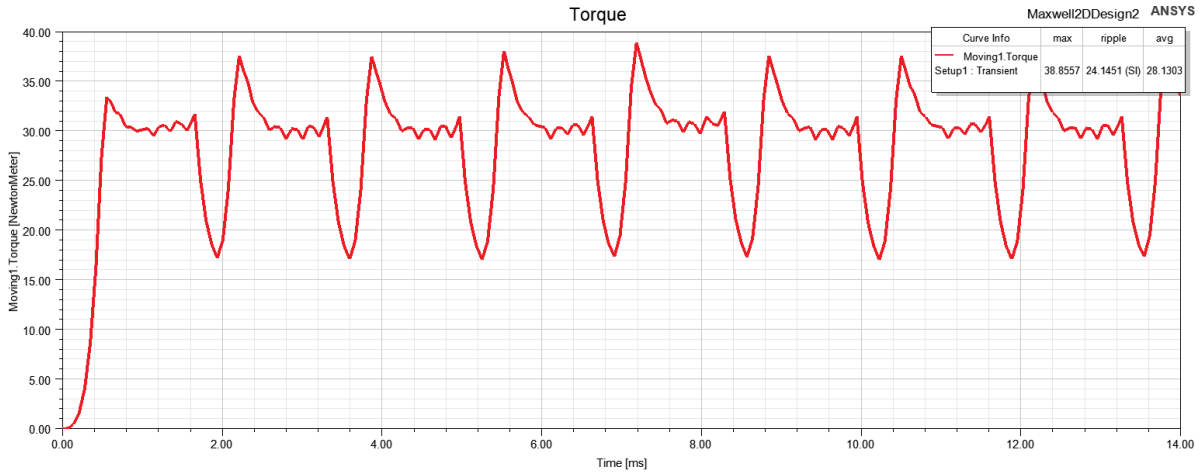

Şekil 4. Tasarım 1 için moment değişimi

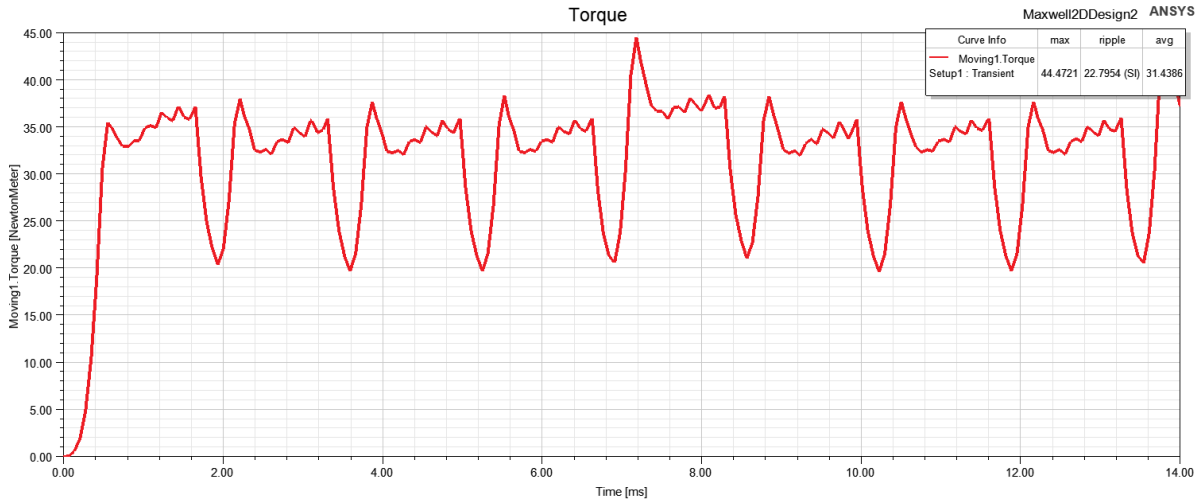

Şekil 5. Tasarım 2 için moment değişimi

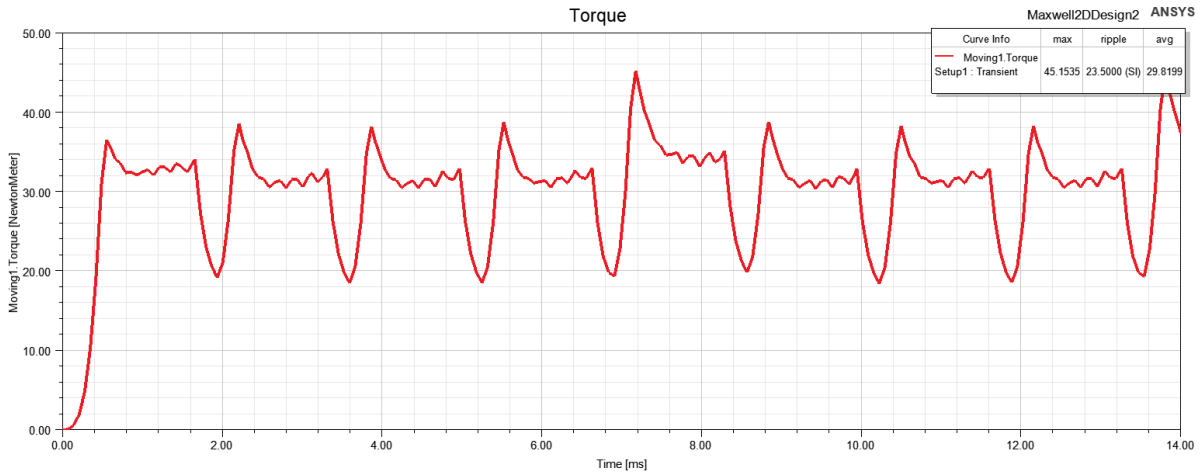

Şekil 6. Tasarım 3 için moment değişimi

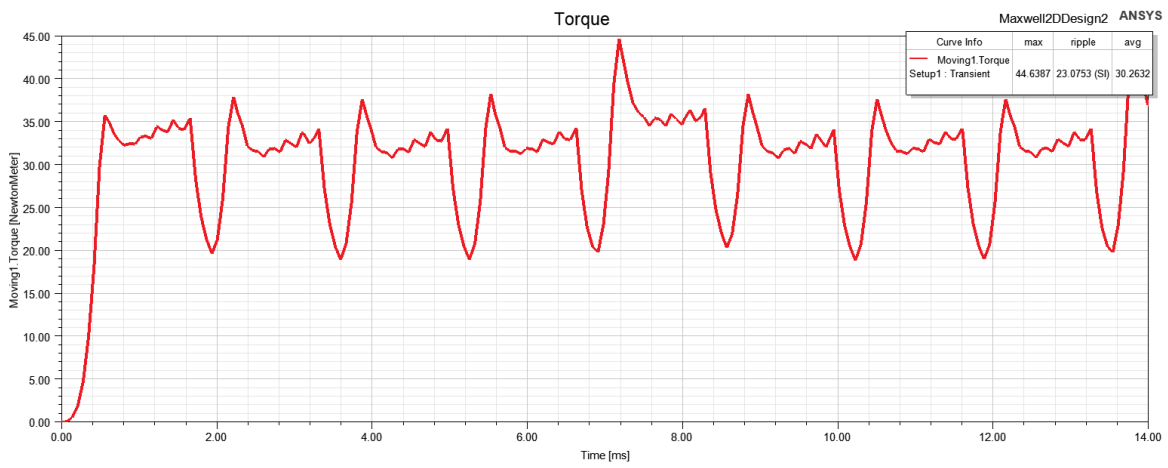

Şekil 7. Tasarım 4 için moment değişimi

Modellemelerden elde edilen maksimum ve ortalama moment ile moment dalgalanması değerleri Tablo 1' de verilmiştir.

Tablo 1. Farklı geometrilere ait moment ve moment dalgalanması değerleri

	Tasarım 1	**Tasarım 2**	**Tasarım 3**	**Tasarım 4**
T_{max} (Nm)	38,8557	44,4721	45,1535	44,6387
T_{ort} (Nm)	28,1303	31,4386	29,8199	30,2632
T_{ripple}	24,1451	22,7954	23,5000	23,0753

Tablo 1 incelendiğinde referans motora göre rotor kutup geometrisi değiştirilmiş modellerin hem maksimum moment hem de ortalama moment değerlerinin daha iyi elde edildiği görülmektedir. Tasarım 3' den elde edilen maksimum moment değerinin referans motora göre % 16.2 oranında daha iyi olduğu görülmektedir. Tasarım 2' den elde edilen ortalama moment değeri ise referans motora göre % 11.73 oranında daha iyi elde edilmiştir. SRM' ler için kritik parametre olan moment dalgalanması değerlerinde ise en iyi değerin Tasarım 2 modelinden elde edildiği görülmektedir. Referans motora göre % 5.589 oranında bir iyileştirme sağladığı tespit edilmiştir.

Farklı rotor geometrileri kullanılarak oluşturulan motor modellerinden elde edilen moment dalgalanması ve moment değerleri Şekil 7' de verilmiştir.

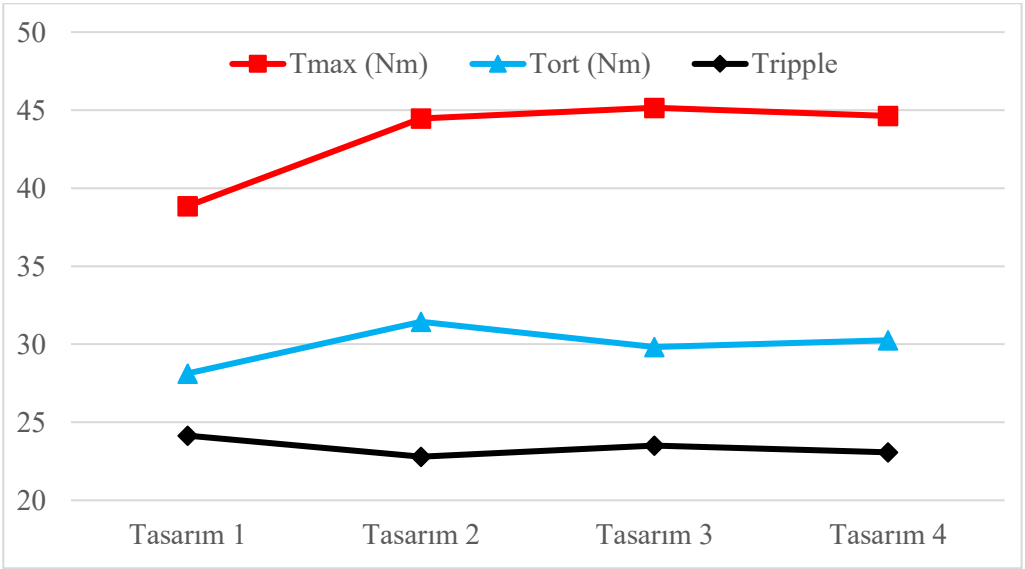

Şekil 8. Farklı geometrik yapılar için moment ve moment dalgalanması değişimleri

IV. SONUÇLAR

Bu çalışmada anahtarlamalı relüktans motorlarda meydana gelen moment dalgalanmasının azaltılması amacı ile rotor kutup geometrisinde modifiyeler yapılmıştır. Farklı geometrik yapılara sahip 4 motor modeli tasarlanmıştır. Tasarlanan yeni geometrili motor modellerinin 2-B analizleri yapılmıştır.

Elde edilen verilere göre Tasarım 2 modelinin ortalama moment değerinin diğer motor modellerine göre daha iyi sonuçlar verdiği tespit edilmiştir. Ayrıca moment dalgalanması değerlerinde ise en küçük değeri veren motor modeli olmuştur.

KAYNAKLAR

[1] M. Tursini, M. Villani, G. Fabri, L. D. Leonardo, A switched-reluctance motor for aerospace application: Design, analysis and results, Electric Power Systems Research, 142, 2017, 74–83.

[2] K. Diao, X. Sun, G. Bramerdorfer, Y. Cai, G. Lei, L. Chen, Design optimization of switched reluctance machines for performance and reliability enhancements: A review, Renewable and Sustainable Energy Reviews, 168, 2022, 1-14.

[3] S. Singh, H. V. Singh, C. Shivshankar, A. Gupta, A. Shakya, D. Tripathi, A. Kumar, Design and simulation of 4 kW, 12/8 switched reluctance motor for electric three-wheeler, Materials Today: Proceedings, 65, 2022, 3461–3475.

[4] O. Argiolas, E. Nazeraj, O. Hegazy, J. D. Backer, A. Mohammadi, J. V. Mierlo, Design optimization of a 12/8 switched reluctance motor for electric and hybrid vehicles, Twelfth International Conference on Ecological Vehicles and Renewable Energies (EVER), 11-13 April 2017, Monte Carlo, Monaco, 1-10.

[5] L. Castellini, S. Lucidi, M. Villani, Design optimization of switched reluctance motor for aerospace application, International Electric Machines and Drives Conference, 1678-1682.

[6] Y. Lan, M. A. Frikha, J. Croonen, Y. Benomar, M. E. Baghdadi, O. Hegazy, Design optimization of a switched reluctance machine with an improved segmental rotor for electric vehicle applications, Energies, 15, 2022, 1-16.

[7] M. V. Terzic, D. S. Mihic, Switched reluctance motor design for a mid-drive e-bike application, Machines, 10, 2022, 1-26.

[8] M. E. Abdollahi, A. Zahid, N. Vaks, B. Bilgin, Switched reluctance motor design for a light sport aircraft application, Machines, 11, 2023, 1-21.

[9] A. Forsyth, S. Ravichandran, T. H. Indiketiya, A. K. Sahu, S. V. Pathirannahalage, B. S. Yılmaz, B. Howey, N. Vaks, M. E. Abdollahi, B. Bilgin, Mechanical design of a switched reluctance motor with small airgap length, IEEE Access, 13, 2025, 141108-141123.

[10] K. A. Karim, N. Abdullah, M. N. Othman, R. N. Firdaus, Z. M. Zulfattah, N. Z. Zainal, Quick design of switched reluctance motor and effect of switching angle ansys maxwell, Journal of Telecommunication, Electronic and Computer Engineering, 8(7), 2016, 107-110.

[11] G. F. Lukman, S. Shahida, K. I. Jeong, J. W. Ahn, Design of a 24/16 outer-rotor switched reluctance motor with symmetrical/asymmetrical pole shoes for performance improvement, Journal of Electrical Engineering & Technology, 18, 2023, 961–970.

[12] A. C. F. Mamede, J. R. Camacho, R. E. Araujo, Review of rotary switched reluctance machine design and parameters effect analysis, Modeling and Control of Switched Reluctance Machines, Chapter 3, IntechOpen, 59-80.

[13] R. M. M. F. Pereira, Development of a switched reluctance motor drive for an electrical vehicle, Faculdade De Engenharia Da Universidade Do Porto, October 2016, 154.

[14] T. Ben, H. Wang, L. Chen, Y. Zhang, L. Jing, Torque ripple reduction strategy for switched reluctance motor based on segmented non-linear correction torque sharing function, Journal of Power Electronics, 24, 2024, 1933–1943.

[15] J. Oloo, S. Laszlo, Torque Ripple minimization for switched reluctance motor drives based on harris hawks–radial basis function approximation, Energies, 18, 2025, 1-26.

8th International Conference on Engineering, Natural and Social Sciences

September 06-07, 2026: Konya, Turkey

© 2026 Published by All Sciences Academy

https://www.icensos.com/

Gyroid TPMS Kafes Yapılarda Laminer Hava Akışının Hesaplamalı Akışkanlar Dinamiği Yöntemiyle İncelenmesi

İsmail Tur[1], Erkan Bahçe[2], Mustafa Ercan GÜNDÜZ[3], Özgün Ceren AKBAY[4]

[1]*Malatya Turgut Özal Üniversitesi, Doğanşehir Vahap Küçük Meslek Yüksekokulu, Mülkiyet Koruma ve Güvenlik Bölümü, Sivil Savunma ve İtfaiyecilik Programı, Malatya, Türkiye.*

[2] *İnönü Üniversitesi Mühendislik Fakültesi Makine Mühendisliği Bölümü, Malatya, Türkiye.*

[3] *İnönü Üniversitesi OSB Meslek Yüksek Okulu, Elektrik ve Enerji Bölümü, İklimlendirme ve Soğutma Programı, Malatya, Türkiye.*

[4] *İnönü Üniversitesi Mühendislik Fakültesi Makine Mühendisliği Bölümü, Malatya, Türkiye.*

[*]*(ismail.tur@ozal.edu.tr)*

Özet – Bu çalışmada, eklemeli imalata uygun Gyroid Üçlü Periyodik Minimum Yüzey (TPMS) kafes yapılarında laminer hava akışının aerodinamik ve hidrolik davranışları Hesaplamalı Akışkanlar Dinamiği (CFD) yöntemi kullanılarak incelenmiştir. Geometri, CAD programında birim hücre boyutu 5 mm ve et kalınlığı t = 0.5 mm olacak şekilde sarmal çeper yapısında tasarlanmış; yapılan hacimsel integrasyon analizlerinde gözeneklilik oranı %69.18, özgül ıslak yüzey alanı 1236.68 m^2/m^3 ve hidrolik çap Dh = 2.238 mm olarak saptanmıştır. Tasarlanan mikro-kafes yapısı CFD analiz çözücüsüne aktarılarak 20 mm x 20 mm x 80 mm boyutlarında bir kanal içerisine yerleştirilmiş ve dört farklı Reynolds değerinde (Re = 10, 50, 100, 150) laminer akış simülasyonları gerçekleştirilmiştir. Çalışma kapsamında enerji denklemleri ve ısıl analiz parametreleri dışarıda bırakılarak saf hidrodinamik akış sönümleme karakteristikleri ve basınç düşüşü mekanizmaları incelenmiştir. Simülasyon verilerinden elde edilen toplam basınç düşüşü (delta P) değerleri kullanılarak Darcy-Forchheimer denklemi üzerinden viskoz geçirgenlik (K) ve eylemsizlik direnç faktörü (beta) katsayıları türetilmiştir. Elde edilen bulgular, sarmal kanallardaki akış direncini ve boyutsuz sürtünme faktörü eğrisini literatürle uyumlu olarak doğrulamaktadır.

Anahtar Kelimeler – Eklemeli İmalat, TPMS, Gyroid, CFD, Darcy-Forchheimer, Sürtünme Faktörü.

I. GİRİŞ

Eklemeli imalat (AM) teknolojilerindeki gelişmeler, karmaşık ve geleneksel yöntemlerle üretimi güç geometrilerin doğrudan imal edilebilmesini sağlayarak kafes yapıların tasarım ve üretim olanaklarını genişletmiştir [1–3]. Özellikle düşük yoğunluk, yüksek özgül yüzey alanı ve tasarım esnekliği gibi özellikleri nedeniyle kafes yapılar; havacılık, enerji, ısı yönetimi ve diğer mühendislik uygulamalarında yaygın olarak araştırılmaktadır. Bu gelişmeler doğrultusunda, Üçlü Periyodik Minimal Yüzey (Triply Periodic Minimal Surface, TPMS) yapıları, matematiksel olarak tanımlanabilen, sürekli yüzeylere ve yüksek gözenek bağlantısına sahip yapılar olarak öne çıkmaktadır [4–6]. TPMS geometrilerinin yüzey alanı, gözeneklilik ve birim hücre boyutu gibi parametrelerinin kontrollü biçimde değiştirilebilmesi, bu yapıların akışkan geçişi ve ısı transferi gibi fonksiyonel uygulamalarda kullanılmasını mümkün kılmaktadır [7]. TPMS ailesinin önemli bir üyesi olan Gyroid, sürekli ve kıvrımlı yüzey yapısı ile

birbirine bağlı akış kanalları oluşturmaktadır [8]. Bu geometrik özellikler, akış yönünün sürekli değişmesine ve akışkanın yapı ile etkileşiminin artmasına neden olarak basınç kaybı, geçirgenlik ve hız dağılımı gibi akış parametrelerini doğrudan etkilemektedir [9,10]. Nitekim Gyroid ve diğer TPMS geometrilerinin akış direnci ve ısı transferi performanslarının geometri ve gözeneklilik ile önemli ölçüde değiştiği literatürde gösterilmiştir [11]. TPMS yapılarındaki karmaşık iç akış alanlarının belirlenmesinde Hesaplamalı Akışkanlar Dinamiği (CFD) etkin bir sayısal yöntem olarak kullanılmaktadır [12]. Özellikle laminer rejimde gerçekleştirilen CFD analizleri, Gyroid geometrisinin akış içerisindeki hız ve basınç dağılımlarının yanı sıra yapı boyunca meydana gelen basınç kaybının ayrıntılı olarak incelenmesine olanak sağlamaktadır. Literatürde bulunan son çalışmalar, Gyroid TPMS içerisindeki laminer akışın porozite, akış hızı ve geometrik parametrelerle doğrudan ilişkili olduğunu ve CFD analizlerinin bu davranışın modellenmesinde etkin biçimde kullanılabildiğini göstermektedir [13]. Güncel çalışmalar incelendiğinde TPMS yapılarının CFD ile modellenmesinde yalnızca basınç kaybı ve ısı transferi değil, model doğrulama, yakınsama, türbülans modeli seçimi gibi konular da öne çıkmıştır. Balderrama Prieto vd. [14], Gyroid TPMS yapısındaki hava akışını CFD ile inceleyerek farklı türbülans modellerini karşılaştırmış ve deneysel sonuçlarla doğrulama gerçekleştirmiştir. Yapılan çalışmada doğrudan türbülanslı akışa odaklansa da TPMS yapılarının CFD analizlerinde geometrik ayrıntıların, ağ yapısının ve modelleme tercihlerinin sonuçlar üzerindeki etkisinin dikkatle değerlendirilmesi gerektiğini göstermektedir. Bu çalışmada, Gyroid TPMS yapısı içerisindeki laminer hava akışı CFD yöntemi kullanılarak incelenmiştir. Yapı içerisindeki akış alanı değerlendirilerek hız ve basınç dağılımlarının yanı sıra akış karakteristiklerinin ortaya konulması amaçlanmıştır. Böylece Gyroid TPMS geometrisinin laminer hava akışı üzerindeki etkisinin sayısal olarak ortaya konulması ve söz konusu yapının akışkan uygulamalarındaki davranışının değerlendirilmesi hedeflenmiştir.

II. MATERYAL VE YÖNTEM

2.1. Geometrik Modelleme ve Sayısal Yöntem

Sayısal modelleme kapsamında, Gyroid TPMS yapısının geometrisi CAD yazılımında sarmal çeperli olarak tasarlanmıştır. CAD programında birim hücre boyutu 5 mm, duvar kalınlığı t = 0.5 mm ve implicit kutu hacmi 20 mm x 20 mm x 20 mm olarak sınırlandırılmıştır. Toplam kanal hacmi içerisinde arka arkaya periyodik olarak dizilmiş 5 x 5 x 5 mm ölçülerinde birim hücre yer almaktadır. Yapılan hacimsel integrasyon hesaplamalarında, katı gövde hacminin toplam hacme oranı %30.82 olarak bulunmuş, akışkan gözenekliliği ise %69.18 olarak elde edilmiştir. (Şekil.1)

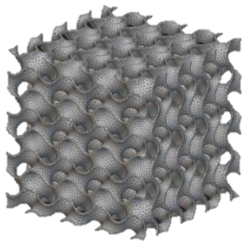

Şekil 1: CAD Yazılımında Tasarlanan Gyroid Kafes Yapısı.

Analizlerde katı fazı temsil eden yapısal malzeme olarak Polilaktik Asit (PLA) referans alınmıştır. PLA, düşük yoğunluğu (yaklaşık 1,24 g/cm³), yüksek boyutsal kararlılığı ve karmaşık geometrilerin yüksek hassasiyetle modellenmesine imkân tanıyan pürüzsüz yüzey karakteristiği nedeniyle termofluidik araştırmalarda sıklıkla tercih edilen bir polimerdir [15]. CAD programında oluşturulan implicit akış

hacmi, yüksek yoğunluklu yüzey ağı olarak dışa aktarılmıştır. CFD analiz programında Fault-Tolerant Meshing (FTM) iş akışı takip edilerek sızdırmaz akış hacmi çıkartılmıştır. Akış yönünde (giriş ve çıkış bölgelerinde) oluşabilecek geri akış ve kararsızlıkların önüne geçilmesi amacıyla yapının önüne ve arkasına 10 mm'lik akış düzenleme uzantıları eklenmiştir. Sınır koşulları; giriş için velocity-inlet, çıkış için pressure-outlet ve Gyroid iç cidarları için kaymama koşulu olarak atanmıştır. Hacimsel örgü olarak Polyhedral mesh tipi seçilmiş olup, sınır tabaka etkilerini hassas yakalamak adına duvar yakınlarında 5 tabakalı inflation katmanları yerleştirilmiştir. (Şekil.2)

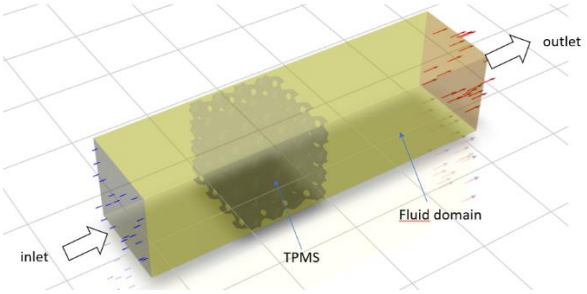

Şekil 2: CFD Analiz Programında Oluşturulan Simülasyon Detayı

2.2.Parametrik Deney Planı ve Hesaplama Metodolojisi

Kafes yapılar içerisindeki laminer hava akış analizlerinde, akışkanın sarmal kanallardaki hareket karakteristiğini tanımlamak üzere hidrolik çap (Dh) referans parametre olarak alınmıştır. Hidrolik çap, gözeneklilik ve özgül yüzey alanına bağlı olarak şu analitik bağıntı ile hesaplanmıştır:

$$Dh = (4 * \Phi) / av = (4 * 0.6918) / 1236.68 = 0.002238\ m = 2.238\ mm$$

Çalışmada kullanılan akışkan kuru hava olup, standart koşullardaki yoğunluğu $\rho = 1.225\ kg/m^3$ ve dinamik viskozitesi $\mu = 1.789\ e^{-5}$ Pa. s olarak tanımlanmıştır. Hedeflenen Reynolds sayılarına (Re = 10, 50, 100, 150) karşılık gelen akış hızı değerleri, $u = (Re * \mu) / (\rho * D_h)$ bağıntısı kullanılarak analitik olarak hesaplanmış ve CFD simülasyonları sonrasında elde edilen gerçek toplam basınç düşüşü (delta P), birim uzunluktaki basınç gradyanı (delta P/L), gözenek içi hız (v_p) ve boyutsuz sürtünme faktörü (f) değerleri ile birlikte Tablo 1'de bir araya getirilmiştir.

Tablo 1: Gyroid TPMS Yapısı HAD Analiz Sonuçları ve Hidrolik Parametreleri.

Analiz Kodu	Hedef Reynolds (Re)	Giriş Hızı (u_{inlet}) [m/s]	Toplam Basınç Düşüşü (delta P) [Pa]	Basınç Gradyanı (delta P/L) [Pa/m]	Gözenek İçi Hız (v_p) [m/s]	Sürtünme Faktörü (f)
HAD-1	10	0.0653	0.19883	9,9	0.0943	2,13
HAD-2	50	0.3263	17.523	87.6	0.4717	0.75
HAD-3	100	0.6527	50.374	251.9	0.9434	0.54
HAD-4	150	0.9790	99.269	496.3	14.151	0.47

III.BULGULAR

3.1. Basınç Düşüşü ve Dağılımlarının Analizi

Gyroid TPMS yapısında gerçekleştirilen simülasyonlar sonucunda elde edilen toplam statik basınç düşüşü verileri, akış hızı Reynolds sayısı arttıkça basınç kaybının doğrusal olmayan bir eğilimle yükseldiğini ortaya koymaktadır. HAD-1 (Re = 10) durumunda saptanan 0.1988271 Pa'lık toplam basınç düşüşü ve sarmal kanallardaki kararlı ve homojen lineer basınç gradyanı (maksimum basınç 0.418 Pa, minimum

basınç 0.034 Pa), akışın tamamen kararlı viskoz rejimde kaldığını doğrulamaktadır. Ancak Reynolds sayısının 5 katına çıkarıldığı HAD-2 (Re = 50) senaryosunda basınç düşüşü 1.752335 Pa'a yükselirken (statik basınç aralığı 0.791 Pa ile 3.73 Pa) , Reynolds sayısının sırasıyla 100 (HAD-3) ve 150 (HAD-4) değerlerine ulaştığı yüksek hız koşullarında kuadratik kayıplar baskınlaşarak toplam basınç düşüşü sırasıyla 5.037414 Pa (2.58 Pa ila 10.9 Pa) ve 9.926909 Pa (5.19 Pa ila 21.6 Pa) seviyelerine ulaşmıştır. Birim uzunluktaki basınç düşüşü (basınç gradyanı, $\Delta P/L$) mukayese edildiğinde, HAD-1'deki 9,9 Pa/m değeri ile HAD-4'teki 496.3 Pa/m değeri arasında tam 40 katlık bir fark saptanmıştır. Bu durum, akış hızındaki lineer artışa karşı basınç sönümlenmesinin kuadratik olarak artmasının, sarmal Gyroid kanallarındaki eylemsizlik direncinin (Forchheimer etkisi) baskın hale gelmesinden kaynaklandığını göstermektedir [16]. Ayrıca, akış hızının en yüksek olduğu HAD-4 analizinde Gyroid duvarlarının hemen arkasında akışın dar boğazlardan ivmelenerek çıkması ve lokal hızlanmalar sebebiyle 5.19 Pa'a varan belirgin lokal negatif basınç (vakum) ceplerinin oluştuğu saptanmıştır.

3.2. Hız Alanları ve Lokal İvmelenmelerin Karşılaştırılması

Kafes yapısının sarmal çeperlerindeki daralan ve genişleyen geçitler boyunca meydana gelen akış ivmelenmeleri, Reynolds sayısına bağlı olarak belirgin lokal hız gradyanları oluşturmaktadır. HAD-1 (Re = 10) rejiminde 0.0653 m/s'lik giriş hızı için gözenek içi ortalama akış hızı (v_p) 0.0943 m/s olarak saptanmış ve sarmal boğazlardaki lokal maksimum hız 0.324 m/s olarak kaydedilmiştir. Bu hızlanma karakteri, HAD-2'de (Re = 50, giriş hızı 0.3263 m/s) gözenek içi ortalama hızın 0.4717 m/s'ye ve lokal maksimum hızın 1.49 m/s'ye ulaşmasıyla gelişim göstermiştir. Re = 100 (HAD-3, giriş hızı 0.6527 m/s) ve Re = 150 (HAD-4, giriş hızı 0.9790 m/s) durumlarında ise bu ivmelenme oranları sırasıyla 0.9434 m/s ve 1.4151 m/s'lik ortalama gözenek içi hızlar üzerinden, dar sarmal geçitlerde sırasıyla 2.90 m/s ve 4.16 m/s'lik lokal maksimum hız seviyelerine ulaşmıştır. Hız konturları birlikte değerlendirildiğinde, tüm analizlerde akışın keskin köşeli yapılar içermeyen sarmal Gyroid yüzeylerine çarparak sönümlendiği, ancak hızın artmasıyla birlikte (özellikle HAD-3 ve HAD-4'te) sarmal merkezlerinde akışın hızla ivmelendiği ve kanal duvarları yakınında dik hız gradyanları oluşturduğu saptanmıştır.

3.3. Akım Çizgileri ve Sarmal Karışım Şiddetinin Evrimi

Hacim genelindeki akım çizgileri, Gyroid yapısının akışkan tabakalarını üç boyutlu uzayda bükerek sürekli bir yakınsama-ayrılma-yakınsama döngüsüne tabi tuttuğunu ve sarmal karışım mekanizmasının Reynolds sayısı arttıkça nasıl evrildiğini net bir şekilde ortaya koymaktadır. HAD-1 (Re = 10) akım çizgilerinde havanın kafes bölgesinde son derece pürüzsüzce süzüldüğü, akış çizgilerinin paralel doğrultusunu koruyarak sönümlü bir laminer karakter sergilediği ve maksimum akım çizgisi hızının 0.324 m/s ile sınırlı kaldığı saptanmıştır [17]. Ancak HAD-2 (Re = 50) ve HAD-3 (Re = 100) rejimlerine geçildiğinde, akışın artan kinetik enerjisinin etkisiyle akım çizgilerinin birbiri etrafında sarmal olarak dolanmaya başladığı, helisel karışım dalgalarının kanal boyunca geliştiği ve maksimum akım çizgisi hızlarının sırasıyla 1.49 m/s ve 2.90 m/s değerlerine ulaştığı gözlemlenmiştir. Bu durum, akım çizgilerinin helisel dolanımının en üst seviyeye ulaştığı ve maksimum hızın 4.16 m/s'ye ulaştığı HAD-4 (Re = 150) simülasyonunda zirve yapmaktadır. Karşılaştırmalı analizler, tüm hız seviyelerinde akış alanında herhangi bir durgun bölge veya büyük ölçekli girdap ayrılması oluşmadığını; ancak hız arttıkça Gyroid yapısının sürekli ve pürüzsüz geometrik kıvrımlarının, akışın kararlı laminer yapısını bozmadan çok daha güçlü bir helisel karışım ve yüksek hidrolik taşınım etkinliği sağladığını göstermektedir.

3.4. Sürtünme Faktörü ve Darcy-Forchheimer Katsayılarının Analitik Değerlendirilmesi

Süperpozisyon ve boyutsuz sürtünme faktörü (f) ile gözenekli ortam direnç katsayıları, kafes yapının hidrolik performansını sayısal ve analitik olarak doğrulamaktadır. Dört farklı Reynolds sayısına bağlı

sürtünme faktörü değerleri karşılaştırıldığında, HAD-1 (Re = 10) için saptanan 2,13 'luk yüksek sürtünme katsayısının, HAD-2 (Re = 50) için 0.75'e, HAD-3 (Re = 100) için 0.54'e ve HAD-4 (Re = 150) için 0.47'ye gerilediği görülmektedir. Bu keskin düşüş eğiliminin, özellikle viskoz etkilerin baskın olduğu düşük hız rejiminde (HAD-1'den HAD-2'ye geçişte) çok daha hızlı gerçekleştiği, eylemsizlik etkilerinin belirginleştiği yüksek Reynolds sayılarında (HAD-3 ve HAD-4) ise sürtünme faktörünün asimptotik bir sınıra doğru yaklaşarak azalış hızının yavaşladığı saptanmıştır. Bu hidrolik davranış, sarmal çeperli Gyroid kanallarında artan hızla birlikte form direncinin viskoz sürtünme kayıplarının önüne geçmeye başlamasıyla açıklanmaktadır. Simülasyonlardan elde edilen basınç gradyanı verileri üzerinden gerçekleştirilen Darcy-Forchheimer regresyon analizinde (Şekil.4), kuadratik model $R^2 = 0.9887$ doğrulukla $\Delta P/L = 173.63 \cdot u + 337.62 \cdot u^2$ olarak türetilmiştir. Elde edilen denklem katsayılarına göre saptanan mikroyapısal viskoz geçirgenlik katsayısı $K = 1.0304 \times 10^{-7}$ m² ve eylemsizlik direnç faktörü $\beta = 275.61$ m^{-1}, tasarlanan Gyroid yapısının laminer akış sönümleme karakteristiklerini tam olarak karakterize etmektedir.

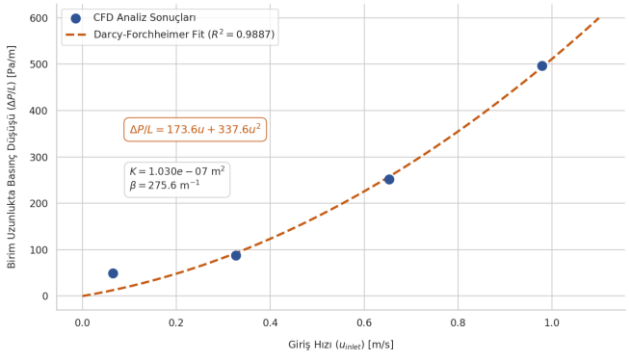

Şekil 4: Akış Hızına Bağlı Olarak Değişen Basınç Gradyanı ve Darcy-Forchheimer Polinomu.

Sürtünme faktörünün (f) reynolds sayısına (Re) göre değişim grafiği Şekil 5'te verilmiştir.

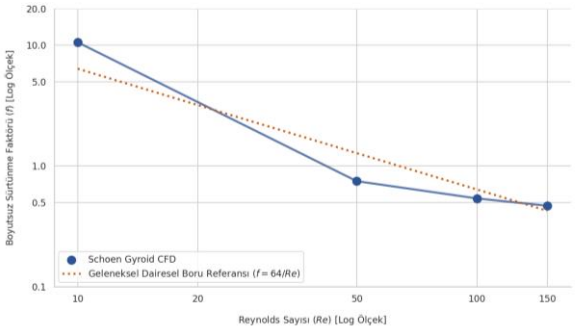

Şekil 5: Sürtünme Faktörünün (f) Reynolds Sayısına (Re) Göre Değişim Grafiği.

Değişen Re değerlerine göre Gyroid kanallarındaki hız konturları ve akım çizgileri Şekil 6'da verilmiştir.

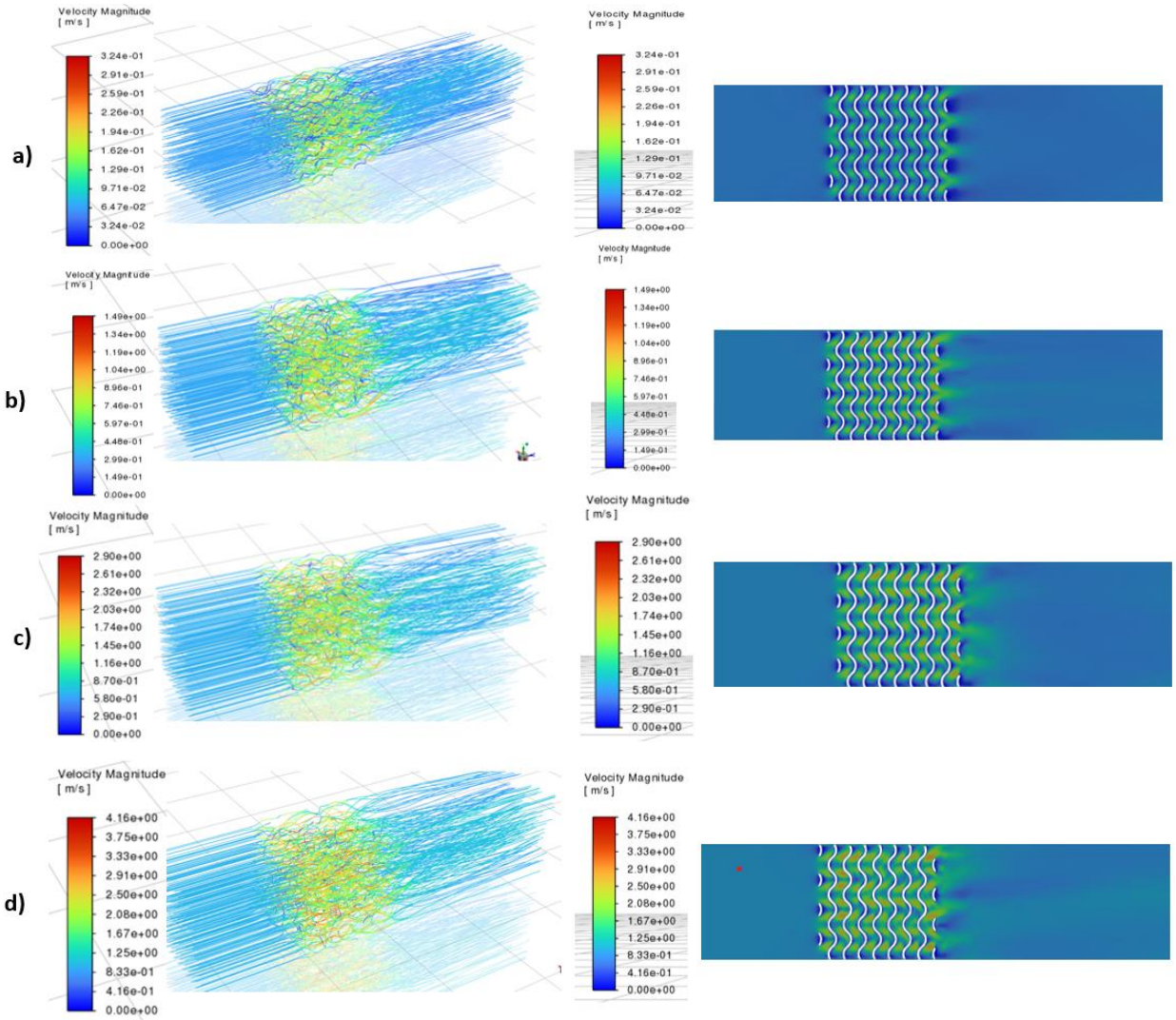

Şekil 6: a) Re = 10, b) Re =50, c) Re =100 ve d) Re =150 Değerleri İçin Gyroid Kanallarındaki Hız Konturları ve akım çizgileri

IV. SONUÇLAR

Bu çalışmada, eklemeli imalat teknolojileri için yükselen bir trend olan Gyroid Üçlü Periyodik Minimum Yüzey sarmal çeper yapılarındaki laminer hava akışının hidrodinamik ve aerodinamik karakteristikleri, CAD ve CFD programları üzerinden incelenmiştir. Birim hücre boyutu 5 mm, duvar et kalınlığı t = 0.5 mm ve toplam kanal boyutu 20 mm x 20 mm x 20 mm olan mikro-kafes yapısı için nTop ortamında gerçekleştirilen hassas hacim integrasyonu sonucunda akışkan gözenekliliği %69.18, özgül ıslak yüzey alanı yoğunluğu 1236.68 m2/m3 ve karakteristik hidrolik çap Dh = 2.238 mm olarak saptanmıştır. Dört farklı laminer akış rejiminde (Re = 10, 50, 100, 150) gerçekleştirilen yüksek çözünürlüklü CFD analiz sonuçları, Gyroid sarmal kanallarının pürüzsüz kıvrımlı yüzeylerinin akış sönümleme ve basınç kaybı karakteristiklerini kararlı bir şekilde domine ettiğini göstermiştir. Re = 10 rejiminde toplam basınç düşüşü 0.1988271 Pa (9,9 Pa/m basınç gradyanı) olarak son derece düşük bir seviyede ölçülürken; giriş hızının sırasıyla Re = 50, 100 ve 150 değerlerine yükseltilmesiyle toplam basınç kayıpları 1.752335 Pa (87.6 Pa/m), 5.037414 Pa (251.9 Pa/m) ve 9.926909 Pa (496.3 Pa/m) değerlerine ulaşmıştır. Bu veriler, artan Reynolds sayısıyla birlikte sarmal Gyroid kanallarındaki akış direncinin viskoz rejimden eylemsizlik rejimine pürüzsüz ancak belirgin bir şekilde geçiş yaptığını kanıtlamaktadır. Simülasyonlardan elde edilen bu basınç gradyanı (delta P / L) verileri, gözenekli ortam momentum sönümleme mekanizmasını

karakterize eden Darcy-Forchheimer denklemi üzerinden analiz edilmiştir. İkinci dereceden kuadratik polinom eğri işlemi sonucunda, delta P / L = 173.63 * u + 337.62 * u^2 denklemi R^2 = 0.9887 korelasyon oranıyla saptanmıştır. Bu denklem yardımıyla Gyroid yapısının mikroyapısal viskoz geçirgenlik katsayısı K = 1.0304 x 10^{-7} m^2 ve eylemsizlik direnç faktörü beta = 275.61 m^{-1} olarak analitik olarak türetilmiştir. Hesaplanan bu mikroyapısal direnç katsayıları (K ve beta), makro ölçekli sistem tasarımlarında tüm mikro-kafes yapısını doğrudan çözmek yerine, CFD analiz programı Porous Medium modelinde sırasıyla Viscous Resistance (1/K) ve Inertial Resistance (beta) girdileri olarak kullanılabilmesini sağlamaktadır. Sürtünme faktörü (f) analizi, Re = 10 için f = 10.59 değerinden başlayarak, Re = 150 için f = 0.47 değerine kadar logaritmik olarak azalan bir eğilim sergilemiştir. Gyroid yapısının sürekli ve pürüzsüz kıvrımlı duvar sınırları, akışta keskin ayrılmalara veya devasa ölü bölgelere izin vermeden akışkanı yönlendirmektedir. Bu pürüzsüz karışım yeteneği ve kararlı basınç gradyanı artışı, Gyroid TPMS yapısının yeni nesil kompakt filtreler, katalizör taşıyıcılar ve akış kontrolcü cihazlarda geleneksel petek yapılarına kıyasla çok daha verimli bir hidrolik alternatif olduğunu göstermektedir.

KAYNAKLAR

1. Maconachie, Tobias, et al. "SLM lattice structures: Properties, performance, applications and challenges." *Materials & Design* 183 (2019): 108137.
2. Wang, R., Shi, H., Gu, J., He, X., Zhang, P., Yu, Z., ... & Lu, Q. (2025). Additive manufacturing of metal lattice structures: A comprehensive review of technologies, mechanical properties, applications, and future trends. *Materials Today Physics*, 101933.
3. Yang, J., Liu, H., Cai, G., & Jin, H. (2025). Additive manufacturing and influencing factors of lattice structures: a review. *Materials*, *18*(7), 1397.
4. Feng, J., Fu, J., Yao, X., & He, Y. (2022). Triply periodic minimal surface (TPMS) porous structures: from multi-scale design, precise additive manufacturing to multidisciplinary applications. *International Journal of Extreme Manufacturing*, *4*(2), 022001.
5. Chouhan, G., & Bala Murali, G. (2024). Designs, advancements, and applications of three-dimensional printed gyroid structures: A review. *Proceedings of the Institution of Mechanical Engineers, Part E: Journal of Process Mechanical Engineering*, *238*(2), 965-987.
6. Hossain, M. S., Hossain, M. M., & Nilufar, S. (2025). An overview of additive manufacturing of triply periodic minimal surface (TPMS) structures. *Polymers*, *17*(24), 3307.
7. Cheng, Z., Xu, R., & Jiang, P. X. (2021). Morphology, flow and heat transfer in triply periodic minimal surface based porous structures. *International Journal of Heat and Mass Transfer*, *170*, 120902.
8. Genç, A. M. (2024). *Integration of Triply-Periodic Minimal Surface Heat Exchangers to Heat Recovery Ventilation Systems* (Doctoral dissertation, Izmir Katip Celebi University (Turkey)).
9. Cheng, Z., Li, X., Xu, R., & Jiang, P. (2021). Investigations on porous media customized by triply periodic minimal surface: Heat transfer correlations and strength performance. *International Communications in Heat and Mass Transfer*, *129*, 105713.
10. Piedra, S., Gómez-Ortega, A., & Pérez-Barrera, J. (2023). Prediction of flow properties of porous triply periodic minimal surface (TPMS) structures. *Fluids*, *8*(12), 312.
11. Chouhan, G., & Gunji, B. (2023). Additive manufacturing TPMS lattice structures: Experimental study on airflow resistivity. *Results in Materials*, *20*, 100478.
12. Guillermo, O. R. L., Arturo, G. O., James, P. B., & Saul, P. (2025). Computational analysis and engineering modeling for the heat transfer and fluid flow through the gyroid TPMS structure. *Applied Thermal Engineering*, *268*, 125865.
13. Renon, C., & Jeanningros, X. (2025). A numerical investigation of heat transfer and pressure drop correlations in Gyroid and Diamond TPMS-based heat exchanger channels. *International Journal of Heat and Mass Transfer*, *239*, 126599.
14. Prieto, S. A. B., Martin, N. P., Prussack, B. A., Fradeneck, A. D., Woolstenhulme, N. E., & Anderson, M. H. (2025). CFD modeling of turbulent air flow in self-heated gyroid TPMS structures: Thermal-hydraulic performance and validation. *Applied Thermal Engineering*, 127682.
15. Ali, S. (2025). Sustainable Bioplastic Blends for 3D Printing: Formulation, Process Optimization, and Application Development.
16. Coimbra, J. C., Martins, M. A., Oliveira, P. S., & Minim, L. A. (2021). The potential use of a gyroid structure to represent monolithic matrices for bioseparation purposes: Fluid dynamics and mass transfer analysis via CFD. *Separation and Purification Technology*, *254*, 117594.
17. Zhang, X., Li, M., Luo, A., & Wang, J. (2025). CFD Investigation of Gas–Liquid Two-Phase Flow Dynamics and Pressure Loss at Fracture Junctions for Coalbed Methane Extraction Optimization. *Processes*, *14*(1), 69.

8th International Conference on Engineering, Natural and Social Sciences

September 06-07, 2026: Konya, Turkey

© 2026 Published by All Sciences Academy

https://www.icensos.com/

Comparative Evaluation of Deep Learning Models for Pediatric Pneumonia Classification from Chest X-ray Images

Hüseyin FIRAT[1,*]

[1]*Department of Computer Engineering / Faculty of Engineering, Dicle University, Türkiye*
[*]*huseyin.firat@dicle.edu.tr*

Abstract **–** Pediatric pneumonia remains a major cause of mortality and morbidity among children, emphasizing the need for accurate and reliable diagnostic support tools. Chest X-ray (CXR) imaging is widely used for pediatric pneumonia assessment; however, interpretation can be challenging because radiographic findings may be subtle and variable. This study presents a systematic comparative evaluation of deep learning architectures for automated pediatric pneumonia classification from chest X-ray images. A publicly available dataset containing 5856 pediatric CXR images was used, including 1583 healthy and 4273 pneumonia cases. Nine representative convolutional neural network architectures, namely VGG16, ResNet50, MobileNet, EfficientNetB0, DenseNet121, DenseNet201, InceptionV3, Xception, and ConvNeXtTiny, were evaluated under identical experimental conditions. 5-fold cross-validation was employed to assess model performance and stability, while accuracy, precision, recall, and f1-score were calculated as mean ± standard deviation across the folds. Among the evaluated architectures, ResNet50 achieved the highest overall performance, with an accuracy of 97.01% ± 0.38, precision of 97.70% ± 0.30, recall of 98.22% ± 0.36, and f1-score of 97.96% ± 0.26. Its accuracy and recall 95% confidence intervals were [96.53–97.49] and [97.77–98.67], respectively. These findings demonstrate that ResNet50 provides a strong and consistent performance for pediatric pneumonia classification. The comparative results provide a reliable benchmark for selecting effective deep learning architectures and support the potential development of computer-aided diagnostic systems for pediatric CXR analysis.

Keywords – Image Classification, Transfer Learning, Deep Learning, Chest X-ray, Pediatric Pneumonia

I. INTRODUCTION

Pediatric pneumonia remains a major global public health problem and continues to be one of the leading causes of mortality and morbidity in children under five years of age [1-3]. Although the global burden of childhood pneumonia has declined over the past decades, it remains substantial, with mortality still concentrated in low-resource settings and in countries with limited access to timely diagnosis and treatment [3-4]. Lower respiratory infections remain the leading infectious cause of death worldwide, and children younger than five years continue to carry a disproportionate share of this burden [3].

Pneumonia in children can be caused by fungi, viruses, or bacteria and its clinical course can deteriorate rapidly, especially in younger age groups with immature immune systems [5-6]. Streptococcus pneumoniae remains a major etiologic agent in childhood pneumonia and pneumococcal disease continues to contribute substantially to preventable deaths in children, despite improvements in vaccination and case management [7-8]. Because early diagnosis is closely linked to timely treatment and improved outcomes, rapid and reliable identification of pneumonia is still a central clinical need [1,6].

Among available imaging modalities, chest radiography remains the most widely used and clinically accessible tool for pediatric pneumonia assessment [2,6,9]. Chest X-rays (CXR) are commonly used because they are fast, non-invasive, relatively inexpensive, and capable of revealing pulmonary abnormalities such as consolidation, infiltrates, and pleural complications [6,10,11]. At the same time, the clinical role of CXR is nuanced: while it is widely used as a reference standard and adjunct tool, international guidance does not recommend routine imaging for every non-severe case, and its diagnostic and technical limitations are well recognized [9].

A major limitation of pediatric CXR interpretation is that radiographic findings are often subtle, variable, and reader-dependent [1,2,6]. This challenge is amplified in children because of smaller anatomical structures, ongoing lung development, lower radiation dose protocols, variable inspiration, and differences in positioning that can reduce image quality and obscure disease patterns [1,10,12]. In low- and middle-income settings, these problems are compounded by limited imaging access, equipment maintenance costs, and shortages of experienced radiologists, increasing the need for robust decision-support tools [2,9,13].

These diagnostic challenges have driven growing interest in computer-aided diagnosis systems based on machine learning (ML) and deep learning (DL) for pediatric pneumonia detection from CXR images [1,2,13]. Earlier approaches relied heavily on handcrafted features and conventional classifiers, but these methods often showed limited robustness and poor generalization across datasets and imaging conditions [1,10]. In contrast, deep learning methods can learn hierarchical image representations directly from data and have shown strong performance in pediatric chest X-ray classification tasks [1,6].

Recent studies report high classification performance using transfer learning, ensemble learning, modified convolutional architectures, self-supervised learning, and transformer-based models [1,8]. For example, ensemble and meta-classifier approaches have achieved accuracies around 96.8% to 98.3% on public pediatric datasets [10,14]. Modified DenseNet and CNN-based approaches have similarly reported accuracies near 97% [8]. More recent work using masked autoencoders and transformer-based architectures has shown that leveraging multi-scale representations, global-local attention, and pretrained foundation models can further improve discrimination of subtle pneumonia-related patterns in pediatric chest radiographs [1][6]. Some studies have focused on architectural optimization. CNN evaluations comparing activation functions found that Mish consistently outperformed ReLU and Swish, with InceptionResNetV2 reaching 97.61% accuracy on a dataset of 5856 CXR images [15]. Interpretable CNN studies further showed that different architectural designs capture different radiographic patterns, with strided convolutions favoring localized bacterial consolidations and multi-scale convolutions better capturing diffuse viral patterns [16]. Related multi-scale work also reports that improving feature adaptation can increase both performance and computational efficiency, with an IncMB-enhanced InceptionResNetV2 reaching 98.12% accuracy while reducing parameter count [17]. Transformer-based methods extend this trend by targeting fine-grained pediatric patterns through dynamic local attention and hierarchical multi-scale feature integration [1]. On the Guangzhou dataset, one mixed-scale dynamic attention transformer achieved 95.2% accuracy and 99% AUC, outperforming prior baselines on several metrics [1]. Even so, the literature remains cautious: many high-performing models are computationally intensive, may generalize poorly across pediatric-specific imaging conditions, and still face interpretability barriers that limit routine clinical adoption [16-17].

Despite these advances, important challenges remain. Many models depend on large annotated datasets, yet pediatric imaging data are relatively scarce and expensive to label, and models trained on a single dataset can struggle with class imbalance, domain shift, disease overlap, and generalization to unseen patients or institutions [1,6,14]. In addition, model interpretability and clinical trust remain critical barriers, especially when black-box predictions are intended to support frontline decision-making [2,16,18]. In this context, automated analysis of pediatric chest X-ray images offers strong potential to support earlier, faster, and more consistent pneumonia detection, particularly in resource-constrained

settings where expert interpretation is limited. Accordingly, research in this area increasingly focuses not only on maximizing classification accuracy, but also on improving robustness, generalizability, computational efficiency, and interpretability for real-world clinical use.

Motivated by these challenges, this study presents a systematic comparative evaluation of widely used DL architectures for automated pediatric pneumonia classification from CXR images. Specifically, nine representative CNN models, including ResNet50, VGG16, MobileNet, EfficientNetB0, DenseNet121, DenseNet201, InceptionV3, Xception, and ConvNeXtTiny, were investigated under identical experimental conditions. 5-fold cross-validation strategy was employed to provide a robust assessment of model generalization and performance stability, while accuracy (Acc), precision (Pre), recall (Rec), and f1-score (F1) were evaluated together with their standard deviations and 95% confidence intervals (CI). Among the evaluated architectures, ResNet50 demonstrated the most promising overall performance, achieving an Acc of 97.01% ± 0.38, Pre of 97.70% ± 0.30, Rec of 98.22% ± 0.36, and F1 of 97.96% ± 0.26. These results indicate that ResNet50 provides a strong balance between classification performance and consistency across validation folds. By systematically comparing diverse CNN architectures under the same experimental framework, this study provides a reliable benchmark for identifying effective DL models for pediatric pneumonia detection from CXR images and offers useful insights for the development of robust computer-aided diagnostic systems.

II. Materials and Method

A. Pediatric Pneumonia CXR Dataset

The experiments were conducted using the publicly available CXR Images (Pneumonia) dataset [19]. This dataset contains 5856 CXR images collected from pediatric patients aged between one and five years at the Guangzhou Women and Children's Hospital. Among these images, 4273 correspond to pneumonia cases, whereas 1583 represent healthy (normal) controls [19]. Although the original dataset distinguishes between bacterial and viral pneumonia, these two categories were merged into a single Pneumonia class in the present study. Consequently, the classification task was defined as a binary classification problem involving Pneumonia and Normal classes. A 5-fold cross-validation strategy was adopted to provide a robust evaluation of the proposed DL model and to reduce the possibility of data leakage. In each fold, four subsets were used for training and the remaining subset was used exclusively for testing. The cross-validation procedure was repeated five times, allowing each subset to serve as the test set once. Importantly, none of the images assigned to the test set in a given fold was included in the corresponding training set. This separation ensured that the model was evaluated only on images that were not used during its training. Representative samples from both classes are presented in Fig. 1.

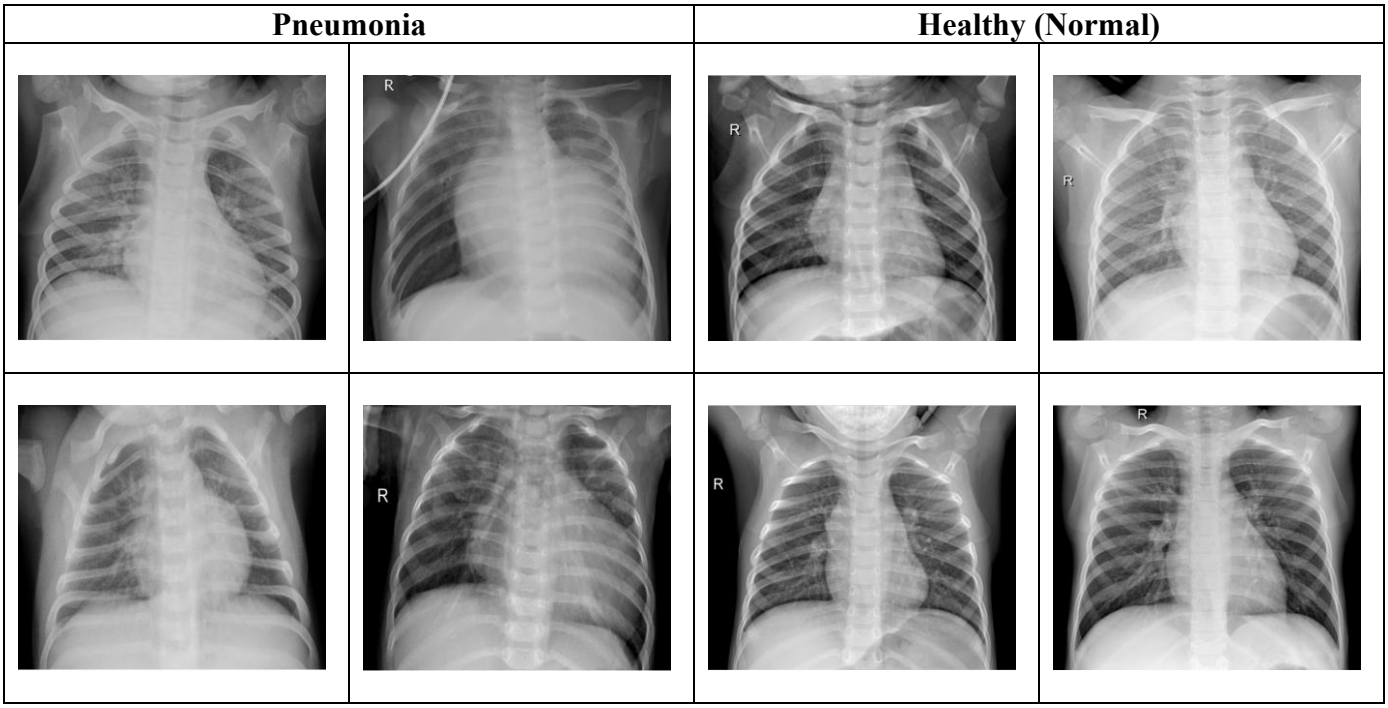

Fig. 1 Representative samples from both classes

B. ResNet50 Model

The proposed model for pediatric pneumonia classification is based on the ResNet50 architecture, which is employed as a pre-trained feature extractor followed by a task-specific classification head. The overall architecture of the proposed model is illustrated in Fig. 2. The model receives pediatric CXR images with a spatial resolution of 224 × 224 pixels and three color channels (224 × 224 × 3) as input and performs binary classification into two categories: Pneumonia and Healthy (Normal). To exploit the powerful feature representations learned from a large-scale image dataset, the ResNet50 backbone is initialized with ImageNet pre-trained weights. The original classification layers of ResNet50 are removed by setting include_top=False, allowing the convolutional backbone to be used exclusively for hierarchical feature extraction.

ResNet50 is a deep residual CNN that employs residual learning through shortcut connections and bottleneck blocks [20]. In the proposed implementation, the input CXR image is initially processed by a 7 × 7 convolutional (conv) layer with 64 filters and a stride of 2, resulting in a feature map with a spatial resolution of 112 × 112. This operation is followed by a 3 × 3 max-pooling layer with a stride of 2, reducing the spatial resolution to 56 × 56. The resulting feature maps are subsequently processed through four main residual stages, namely conv2_x, conv3_x, conv4_x, and conv5_x. These stages contain 3, 4, 6, and 3 bottleneck residual blocks, respectively. Each bottleneck block consists of three successive convolutional operations with kernel sizes of 1 × 1, 3 × 3, and 1 × 1. The first 1 × 1 conv reduces the feature dimensionality, the 3 × 3 conv performs spatial feature extraction, and the final 1 × 1 conv expands the feature representation before it is combined with the shortcut connection.

The convolutional configurations of the four residual stages are [64, 64, 256], [128, 128, 512], [256, 256, 1024], and [512, 512, 2048], respectively. Here, each triplet represents the number of filters used in the three conv layers of a bottleneck block. Accordingly, the conv2_x stage contains three blocks with 1 × 1, 3 × 3, and 1 × 1 convs using 64, 64, and 256 filters, respectively, and produces feature maps of size 56 × 56 × 256. The conv3_x stage consists of four bottleneck blocks with 128, 128, and 512 filters, reducing the spatial resolution to 28 × 28. The conv4_x stage contains six bottleneck blocks with 256, 256, and 1024 filters, producing feature maps of size 14 × 14 × 1024. Finally, the conv5_x stage consists of three bottleneck blocks with 512, 512, and 2048 filters, resulting in the final high-level feature representation of

size 7 × 7 × 2048. Through this hierarchical structure, the network progressively increases the number of feature channels while reducing spatial resolution, enabling the extraction of increasingly abstract and discriminative representations from pediatric CXR images.

Following the convolutional feature extraction process, the resulting 7 × 7 × 2048 feature map is passed to a Global Average Pooling (GAP) layer. The GAP operation independently averages each of the 2048 feature maps over its spatial dimensions, transforming the three-dimensional feature representation into a 2048-dimensional feature vector. This approach considerably reduces the number of parameters compared with directly connecting the feature maps to fully connected (FC) layers and helps limit the risk of overfitting. The resulting feature vector is then fed into a FC Dense layer containing 128 neurons with a ReLU activation function. This layer learns a task-specific representation from the high-level features extracted by the ResNet50 backbone. A Dropout layer with a rate of 0.3 is subsequently employed to improve the generalization capability of the model by randomly deactivating a proportion of the neurons during training, thereby reducing the potential for overfitting.

The final classification is performed using a Dense layer with a single neuron and a sigmoid activation function. Since the proposed model addresses a binary classification problem, the sigmoid function produces a probability value between 0 and 1, which can be expressed as

$$P(y = 1|x) = \frac{1}{1 + e^{-z}} \tag{1}$$

where z denotes the output of the final FC layer. A decision threshold of 0.5 is applied to this probability. Accordingly, an input image is classified as Pneumonia when the predicted probability is greater than or equal to 0.5, whereas it is classified as Healthy (Normal) when the probability is below 0.5.

An important aspect of the proposed implementation is that the ResNet50 backbone is frozen during training. Specifically, the parameter base_model.trainable=False is used, meaning that the weights of all convolutional and residual layers inherited from ImageNet remain unchanged throughout the training process. Consequently, only the newly added classification layers, consisting of Global Average Pooling, Dense(128)-ReLU, Dropout(0.3), and Dense(1)-Sigmoid, are trained for the pediatric pneumonia classification task. This transfer learning strategy allows the model to benefit from the rich hierarchical representations learned by ResNet50 while substantially reducing the number of trainable parameters. The resulting architecture therefore combines the robust feature extraction capability of the ImageNet-pre-trained ResNet50 network with a lightweight task-specific classification head, providing an effective framework for distinguishing Pneumonia and Healthy (Normal) cases from pediatric CXR images.

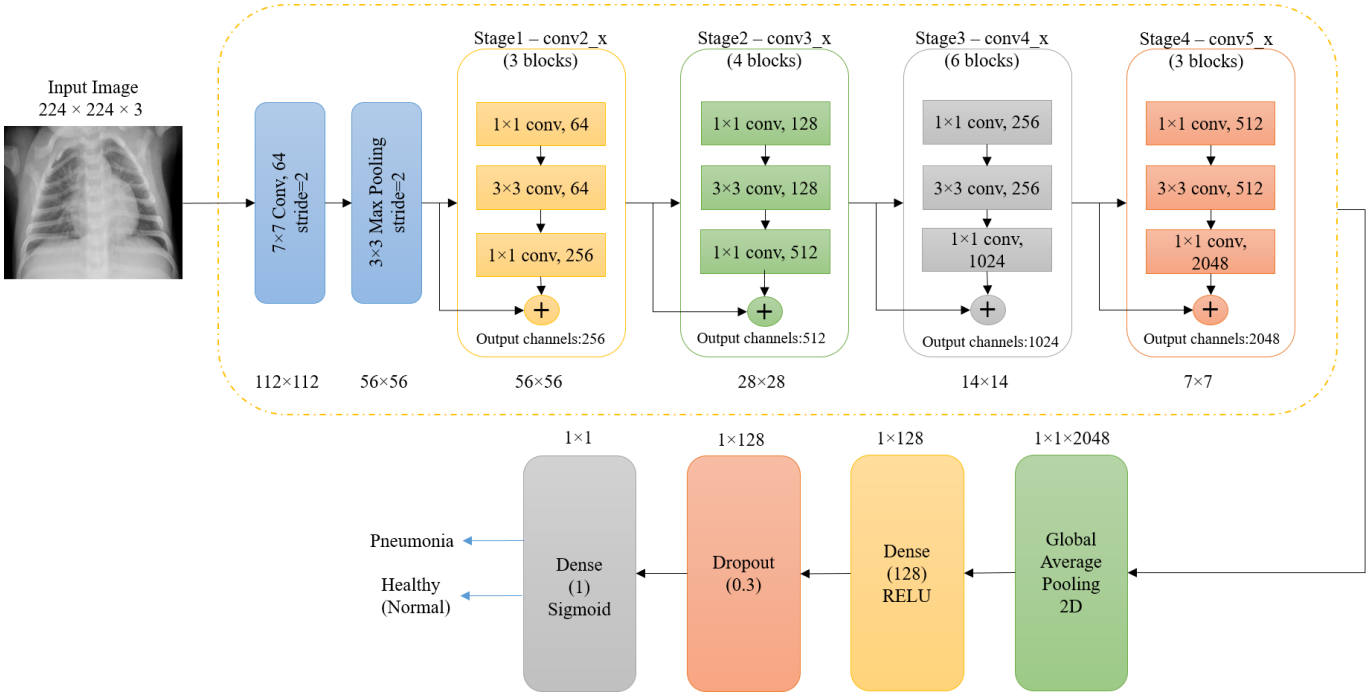

Fig. 2 Architecture of the ResNet50-based transfer learning model for pediatric pneumonia classification

III. RESULTS

A. Hyperparameter Settings

The experiments were performed in a Kaggle-based computational environment equipped with an NVIDIA Tesla P100 GPU. The entire workflow was implemented in Python with TensorFlow serving as the primary deep learning framework. Prior to model training, each CXR image was standardized to a spatial resolution of 224 × 224 pixels with three input channels. Model training was carried out with mini-batches of 128 images, while performance was assessed through a five-fold cross-validation scheme. A maximum of 50 epochs was allowed for each training run. Parameter optimization was performed using the Adam algorithm with a learning rate of 0.0001. As the task involved distinguishing between two diagnostic categories, binary cross-entropy was selected as the objective function. An early stopping mechanism was additionally used to control the training process and limit potential overfitting. Specifically, validation loss was evaluated after each epoch, and training was discontinued when this metric failed to improve for 15 successive epochs. The network state from the epoch yielding the minimum validation loss was subsequently recovered and used as the final model configuration.

B. Evaluation Metrics

The performance of the proposed model was assessed using Accuracy (Acc), Precision (Pre), Recall (Rec), and F1-score (F1). These metrics were calculated independently for each fold of the 5-fold cross-validation, and the overall performance was reported as the mean ± standard deviation (SD).

$$Acc = \frac{TP + TN}{TP + TN + FP + FN} \tag{2}$$

$$Pre = \frac{TP}{TP + FP} \tag{3}$$

$$Rec = \frac{TP}{TP + FN} \tag{4}$$

$$F1 = 2 \times \frac{Pre \times Rec}{Pre + Rec} \tag{5}$$

where TP, TN, FP, and FN denote true positive, true negative, false positive, and false negative classifications, respectively. The Acc indicates the overall proportion of correctly classified samples, while The Pre measures the proportion of correctly predicted positive samples among all positive predictions. The Rec represents the proportion of actual positive samples correctly identified by the model, and the F1 provides a balanced assessment of Pre and Rec. To assess the consistency of the model across the 5 cross-validation folds, the SD of each evaluation metric was calculated. In addition, 95% confidence interval (CI) was determined for each metric based on the mean performance across the 5 folds. The SD reflects the variability of the model's performance between folds, whereas the 95% CI provides an estimate of the uncertainty associated with the mean performance. Given the 5-fold cross-validation setting, the confidence interval was calculated using the t-distribution with four degrees of freedom. Accordingly, the reported mean, SD, and 95% CI together provide a more comprehensive assessment of both the predictive performance and the stability of the proposed model.

C. Experimental Results and Comparative Analysis

In the experimental studies, ResNet50 [20], VGG16 [21], MobileNet [22], EfficientNetB0 [23], DenseNet121 [24], DenseNet201 [24], InceptionV3 [25], Xception [26], and ConvNeXtTiny [27] architectures were employed as benchmark DL models for pediatric pneumonia CXR classification. The performance of these models was evaluated using Acc, Pre, Rec, and F1, with the results reported as the mean ± SD across the 5 cross-validation folds. As presented in Table X, all models achieved relatively high classification performance, with Acc values ranging from 93.66% to 97.01%, indicating that DL architectures can effectively distinguish pneumonia cases from normal CXR images.

Among the evaluated architectures, ResNet50 achieved the highest overall performance, obtaining an Acc of 97.01% ± 0.38, Pre of 97.70% ± 0.30, Rec of 98.22% ± 0.36, and F1 of 97.96% ± 0.26. VGG16 demonstrated the second-highest Acc (96.24% ± 0.39) and achieved Pre of 97.21% ± 0.44, Rec of 97.66% ± 0.39, and F1 of 97.43% ± 0.26. EfficientNetB0 also exhibited competitive performance, with an Acc of 95.99% ± 0.55 and F1 of 97.25% ± 0.38. In contrast, DenseNet121, DenseNet201, Xception, and ConvNeXtTiny produced Acc values of 94.48%, 95.29%, 94.36%, and 95.73%, respectively. MobileNet and InceptionV3 yielded comparatively lower Acc values of 95.41% and 93.66%, respectively, with InceptionV3 showing the lowest overall performance among the evaluated models.

The relatively small SDs observed across the folds indicate that the models generally maintained stable performance under the five-fold cross-validation setting. ResNet50, in particular, combined the highest classification performance with relatively low variability, suggesting strong consistency across the evaluation folds. The 95% confidence intervals (CI) further support this observation, with ResNet50 achieving an Accuracy interval of [96.53–97.49], while its Recall reached [97.77–98.67]. Overall, these results establish a strong baseline for pediatric pneumonia classification and provide a quantitative basis for comparing the performance of the proposed model with established CNN architectures.

Table 1. Performance comparison of the evaluated DL models for pediatric pneumonia classification based on 5-fold cross-validation

Models	**Acc (%)**	**Pre (%)**	**Rec (%)**	**F1 (%)**
VGG16	96.24 ± 0.39 95% CI: [95.75 – 96.74]	97.21 ± 0.44 95% CI: [96.66 – 97.76]	97.66 ± 0.39 95% CI: [97.17 – 98.15]	97.43 ± 0.26 95% CI: [97.10 – 97.76]
ResNet50	**97.01 ± 0.38** **95% CI: [96.53–97.49]**	**97.70 ± 0.30** **95% CI:[97.32 – 98.08]**	**98.22 ± 0.36** **95% CI:[97.77 – 98.67]**	**97.96 ± 0.26** **95% CI:[97.63 – 98.29]**
MobileNet	95.41 ± 0.59 95% CI: [94.67 – 96.14]	96.52 ± 0.65 95% CI: [95.71 – 97.33]	97.21 ± 0.44 95% CI: [96.66 – 97.77]	96.86 ± 0.40 95% CI: [96.37 – 97.36]
EfficientNetB0	95.99 ± 0.55 95% CI: [95.30 – 96.67]	97.39 ± 0.27 95% CI: [97.05 – 97.74]	97.10 ± 0.68 95% CI: [96.24 – 97.95]	97.25 ± 0.38 95% CI: [96.76 – 97.73]
DenseNet121	94.48 ± 0.32 95% CI: [94.08 – 94.89]	96.36 ± 0.34 95% CI: [95.93 – 96.79]	96.07 ± 0.28 95% CI: [95.72 – 96.42]	96.21 ± 0.22 95% CI: [95.94 – 96.49]
DenseNet201	95.29 ± 0.48 95% CI: [94.69 – 95.88]	96.53 ± 0.41 95% CI: [96.01 – 97.05]	97.03 ± 0.45 95% CI: [96.46 – 97.60]	96.78 ± 0.33 95% CI: [96.37 – 97.19]
InceptionV3	93.66 ± 0.57 95% CI: [92.95 – 94.38]	95.61 ± 0.28 95% CI: [95.25 – 95.96]	95.72 ± 0.89 95% CI: [94.61 – 96.82]	95.66 ± 0.41 95% CI: [95.15 – 96.17]
Xception	94.36 ± 0.49 95% CI: [93.75 – 94.98]	95.69 ± 0.41 95% CI: [95.17 – 96.21]	96.63 ± 0.40 95% CI: [96.12 – 97.14]	96.16 ± 0.33 95% CI: [95.74 – 96.58]
ConvNeXtTiny	95.73 ± 0.66 95% CI: [94.90 – 96.56]	96.53 ± 0.60 95% CI: [95.79 – 97.28]	97.66 ± 0.45 95% CI: [97.09 – 98.23]	97.09 ± 0.45 95% CI: [96.53 – 97.65]

The confusion matrices obtained with the best-performing ResNet50 model across the five folds are presented in Fig. 3. The results demonstrate a highly consistent classification performance across all five folds, with a relatively small number of misclassified samples in both classes. In Fold 1, the model correctly classified 296 Normal and 842 Pneumonia images, while 21 Normal images were incorrectly classified as Pneumonia and 13 Pneumonia images were misclassified as Normal. In Fold 2, 296 Normal and 836 Pneumonia samples were correctly classified, with 21 Normal and 18 Pneumonia samples misclassified. Fold 3 achieved 300 correct predictions for the Normal class and 836 for the Pneumonia class, with 17 Normal and 18 Pneumonia samples incorrectly classified. In Fold 4, 293 Normal and 839 Pneumonia samples were correctly classified, while 23 Normal and 16 Pneumonia samples were misclassified. Finally, Fold 5 correctly classified 299 Normal and 844 Pneumonia samples, with only 17 Normal and 11 Pneumonia samples incorrectly predicted. The relatively similar distributions of correct and incorrect predictions across the five folds indicate that the ResNet50 model exhibits stable and consistent classification behavior across different subsets of the dataset.

When the results of all five folds are considered collectively, the model correctly classified 5681 of 5856 samples, corresponding to an overall accuracy of approximately 97.01%. The aggregated confusion matrix consists of 1484 TN, 4197 TP, 99 FP, and 76 FN predictions. Notably, the model achieved a high TP rate for the Pneumonia class, correctly identifying 98.22% of the Pneumonia samples, while 93.75% of the Normal samples were correctly recognized. Furthermore, the number of FN predictions was consistently low across all folds, ranging from 11 to 18 cases. This is particularly important in a pediatric pneumonia classification task, since false-negative predictions represent Pneumonia cases incorrectly classified as Healthy (Normal). Overall, the low number of misclassifications and the consistent performance observed across the five folds demonstrate the robustness and generalization capability of the ResNet50 model for distinguishing Pneumonia from Healthy pediatric CXR images.

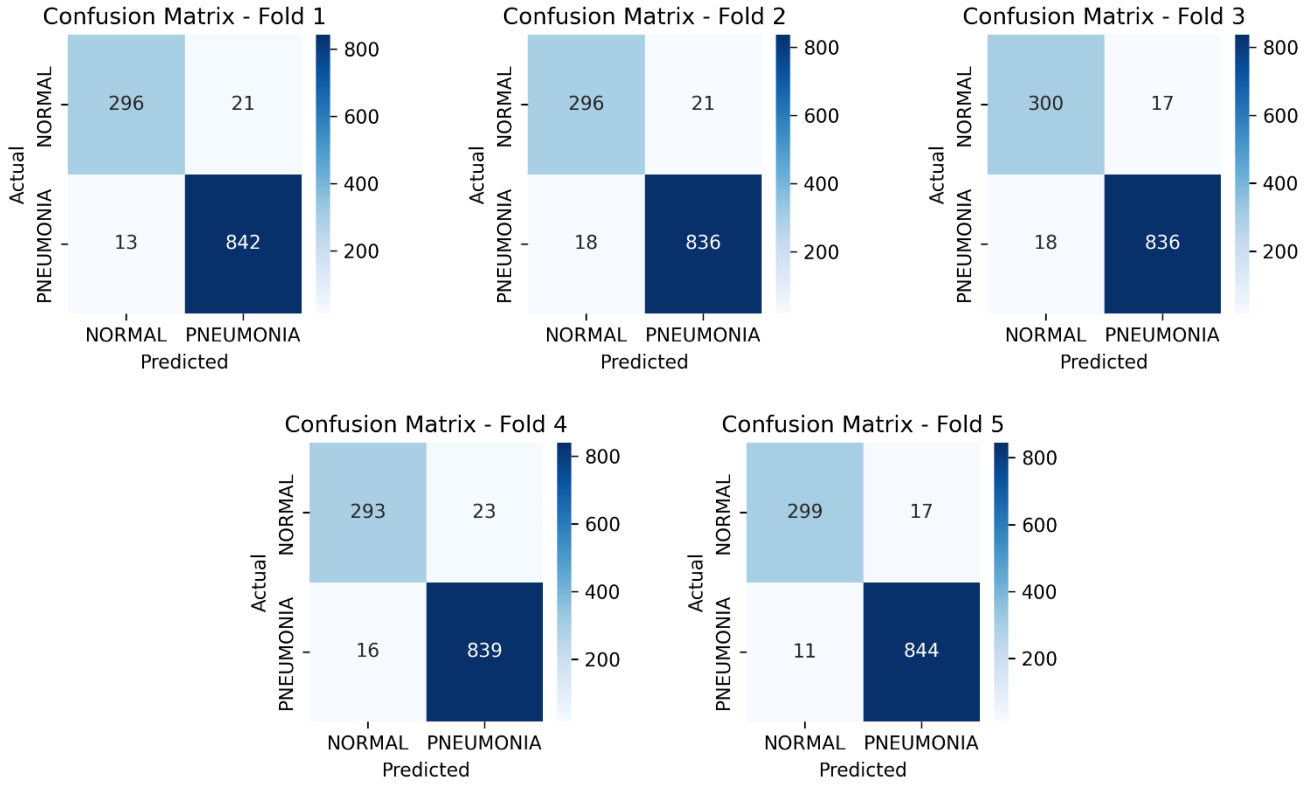

Fig. 3 Confusion matrices of the ResNet50 model across the five folds for pediatric pneumonia classification

IV. CONCLUSION

This study presented a systematic comparative evaluation of nine DL model for automated pediatric pneumonia classification from CXR images. Using the same experimental framework and 5-fold cross-validation, the performances of VGG16, ResNet50, MobileNet, EfficientNetB0, DenseNet121, DenseNet201, InceptionV3, Xception, and ConvNeXtTiny were comprehensively assessed using Acc, Pre, Rec, and F1. Among all evaluated models, ResNet50 achieved the best overall performance, reaching 97.01% ± 0.38 Acc, 97.70% ± 0.30 Pre, 98.22% ± 0.36 Rec, and 97.96% ± 0.26 F1. The relatively low standard deviations and narrow 95% CIs further indicate stable performance across the validation folds. These findings suggest that ResNet50 provides an effective and consistent deep learning baseline for distinguishing pneumonia from healthy pediatric CXR images. Overall, the comparative analysis demonstrates the importance of systematically evaluating different architectures rather than assuming that more recent or computationally complex models will necessarily provide superior performance. The obtained results establish a useful benchmark for future research on automated pediatric pneumonia diagnosis and may contribute to the development of reliable computer-aided diagnostic systems. Further studies using larger, multicenter datasets and independent external validation are warranted to assess the generalizability and clinical applicability of these findings.

REFERENCES

[1] Q. Chen *et al.*, "A mixed-scale dynamic attention transformer for pediatric pneumonia diagnosis," *Displays*, vol. 87, no. January, 2025, doi: 10.1016/j.displa.2024.102953.

[2] N. Barakat, M. Awad, and B. A. Abu-Nabah, "A machine learning approach on chest X-rays for pediatric pneumonia detection," *Digit. Heal.*, vol. 9, 2023, doi: 10.1177/20552076231180008.

[3] S. B. Sirota *et al.*, "Global burden of lower respiratory infections and aetiologies, 1990–2023: a systematic analysis for the Global Burden of Disease Study 2023," *Lancet Infect. Dis.*, vol. 26, no. 4, pp. 343–361, 2026, doi: 10.1016/S1473-3099(25)00689-9.

[4] D. A. McAllister *et al.*, "Global, regional, and national estimates of pneumonia morbidity and mortality in children younger than 5 years between 2000 and 2015: a systematic analysis," *Lancet Glob. Heal.*, vol. 7, no. 1, pp. e47–e57, 2019, doi: 10.1016/S2214-109X(18)30408-X.

[5] E. Ayan, B. Karabulut, and H. M. Ünver, "Diagnosis of Pediatric Pneumonia with Ensemble of Deep Convolutional Neural Networks in Chest X-Ray Images," *Arab. J. Sci. Eng.*, vol. 47, no. 2, pp. 2123–2139, 2022, doi: 10.1007/s13369-021-06127-z.

[6] T. Yoon and D. Kang, "Enhancing pediatric pneumonia diagnosis through masked autoencoders," *Sci. Rep.*, vol. 14, no. 1, pp. 1–11, 2024, doi: 10.1038/s41598-024-56819-3.

[7] G. M. Wang, W. Tao, X. Y. Pang, Y. Xin, Z. H. Gou, and Y. Wang, "Global, regional, and national burden of pneumococcal disease among children and adolescents aged <20 years from 1990 to 2021: a predictive analysis," *Front. Public Heal.*, vol. 13, no. December, pp. 1–18, 2025, doi: 10.3389/fpubh.2025.1675854.

[8] T. S. Arulananth, S. W. Prakash, R. K. Ayyasamy, V. P. Kavitha, P. G. Kuppusamy, and P. Chinnasamy, "Classification of Paediatric Pneumonia Using Modified DenseNet-121 Deep-Learning Model," *IEEE Access*, vol. 12, no. March, pp. 35716–35727, 2024, doi: 10.1109/ACCESS.2024.3371151.

[9] S. Kazi, H. Hernstadt, Y. N. Abo, H. Graham, M. Palmer, and S. M. Graham, "The utility of chest x-ray and lung ultrasound in the management of infants and children presenting with severe pneumonia in low-and middle-income countries: A pragmatic scoping review," *J. Glob. Health*, vol. 12, 2022, doi: 10.7189/JOGH.12.10013.

[10] J. A. Prakash, V. Ravi, V. Sowmya, and K. P. Soman, "Stacked ensemble learning based on deep convolutional neural networks for pediatric pneumonia diagnosis using chest X-ray images," *Neural Comput. Appl.*, vol. 35, no. 11, pp. 8259–8279, 2023, doi: 10.1007/s00521-022-08099-z.

[11] A. Sen and J. K. Podder, "Role of Chest X-Ray in Assessing Severity of Pneumonia in Children Aged 1–5 Years," *Int. J. Curr. Pharm. Rev. Res.*, vol. 18, no. 03, pp. 340–344, 2026, doi: 10.25258/ijcpr.18.3.55.

[12] M. Salehi, R. Mohammadi, H. Ghaffari, N. Sadighi, and R. Reiazi, "Automated detection of pneumonia cases using deep transfer learning with paediatric chest X-ray images," *Br. J. Radiol.*, vol. 94, no. 1121, 2021, doi: 10.1259/bjr.20201263.

[13] M. B. Badawi, B. Salah, and W. Fawaz, "Deep Learning-Based Pneumonia Detection Using Chest X-Ray Images," *Int. J. Telecommun.*, vol. 05, no. 01, pp. 1–16, 2025, doi: 10.21608/ijt.2025.346338.1071.

[14] V. Ravi, H. Narasimhan, and T. D. Pham, "A cost-sensitive deep learning-based meta-classifier for pediatric pneumonia classification using chest X-rays," *Expert Syst.*, vol. 39, no. 7, 2022, doi: 10.1111/exsy.12966.

[15] P. Radočaj, D. Radočaj, and G. Martinović, "Optimizing Convolutional Neural Network Architectures with Optimal Activation Functions for Pediatric Pneumonia Diagnosis Using Chest X-Rays," *Big Data Cogn. Comput.*, vol. 9, no. 2, 2025, doi: 10.3390/bdcc9020025.

[16] P. Radočaj and G. Martinović, "Interpretable Deep Learning for Pediatric Pneumonia Diagnosis Through Multi-Phase Feature Learning and Activation Patterns," *Electron.*, vol. 14, no. 9, pp. 1–18, 2025, doi: 10.3390/electronics14091899.

[17] P. Radočaj, G. Martinović, and D. Radočaj, "Adaptive Multi-Scale Feature Learning Module for Pediatric Pneumonia Recognition in Chest X-Rays," *Appl. Sci.*, vol. 15, no. 21, pp. 1–23, 2025, doi: 10.3390/app152111824.

[18] A. Ahmed, A. B. S. Gowda, E. Sneha, A. Kumar, and M. Farida Begam, "Pediatric Pneumonia Detection from Chest X-rays Using Ensemble Deep Learning and Explainable AI," *2026 4th Int. Conf. Artif. Intell. Mach. Learn. Appl. Healthc. Internet Things, AIMLA 2026*, pp. 1–6, 2026, doi: 10.1109/AIMLA67915.2026.11522516.

[19] D. S. Kermany *et al.*, "Identifying Medical Diagnoses and Treatable Diseases by Image-Based Deep Learning," *Cell*, vol. 172, no. 5, pp. 1122-1131.e9, 2018, doi: 10.1016/j.cell.2018.02.010.

[20] K. He, X. Zhang, S. Ren, and J. Sun, "Deep Residual Learning for Image Recognition," in *2016 IEEE Conference on Computer Vision and Pattern Recognition (CVPR)*, 2016, pp. 770–778. doi: 10.1109/CVPR.2016.90.

[21] K. Simonyan and A. Zisserman, "Very deep convolutional networks for large-scale image recognition," in *3rd International Conference on Learning Representations, ICLR 2015 - Conference Track Proceedings*, International Conference on Learning Representations, ICLR, 2015.

[22] A. G. Howard *et al.*, "MobileNets: Efficient Convolutional Neural Networks for Mobile Vision Applications," *ArXiv*, vol. abs/1704.0, 2017, [Online]. Available: https://api.semanticscholar.org/CorpusID:12670695

[23] M. Tan and Q. V. Le, "EfficientNet: Rethinking model scaling for convolutional neural networks," *36th Int. Conf. Mach. Learn. ICML 2019*, vol. 2019-June, pp. 10691–10700, 2019.

[24] G. Huang, Z. Liu, L. Van Der Maaten, and K. Q. Weinberger, "Densely Connected Convolutional Networks," in *2017 IEEE Conference on Computer Vision and Pattern Recognition (CVPR)*, 2017, pp. 2261–2269. doi:

10.1109/CVPR.2017.243.
[25] C. Szegedy, V. Vanhoucke, S. Ioffe, J. Shlens, and Z. Wojna, “Rethinking the Inception Architecture for Computer Vision,” *Proc. IEEE Comput. Soc. Conf. Comput. Vis. Pattern Recognit.*, vol. 2016-Decem, pp. 2818–2826, 2016, doi: 10.1109/CVPR.2016.308.
[26] F. Chollet, “Xception: Deep learning with depthwise separable convolutions,” *Proc. - 30th IEEE Conf. Comput. Vis. Pattern Recognition, CVPR 2017*, vol. 2017-Janua, pp. 1800–1807, 2017, doi: 10.1109/CVPR.2017.195.
[27] Z. Liu, H. Mao, C. Y. Wu, C. Feichtenhofer, T. Darrell, and S. Xie, “A ConvNet for the 2020s,” *Proc. IEEE Comput. Soc. Conf. Comput. Vis. Pattern Recognit.*, vol. 2022-June, pp. 11966–11976, 2022, doi: 10.1109/CVPR52688.2022.01167.

8th International Conference on Engineering, Natural and Social Sciences

September 06-07, 2026: Konya, Turkey

© 2026 Published by All Sciences Academy

https://www.icensos.com/

Material Balance Analysis for Reservoir Performance Evaluation and Estimation of Orginal Oil in Place

Armida Brakaj[1], Zhifka Muka[2] ,Fizeleni Lekli[3]
[1]*Math Department, Polytechnic University of Tirana, Albania*
[2]*Math Department, Polytechnic University of Tirana, Albania*
[3]*Math Department, Polytechnic University of Tirana, Albania*

[1]brakaj_armida@yahoo.com
[2]zhifkamuka24@yahoo.it
[3]fizelenilekli@yahoo.com

Abstract – Material balance analysis is a fundamental reservoir engineering technique used to evaluate reservoir performance, estimate the original hydrocarbons in place, and identify the dominant reservoir drive mechanism. The method is based on the principle of conservation of mass and establishes a relationship between the fluids produced from a reservoir and the expansion of reservoir fluids and rock, as well as possible water influx. In this study, the theoretical principles of material balance analysis are presented, with particular emphasis on the Havlena–Ode method and its application to oil reservoir evaluation. An illustrative numerical case is developed using reservoir pressure, cumulative oil production, and selected pressure-dependent PVT properties. The underground withdrawal and reservoir expansion terms are calculated for different stages of reservoir depletion, and their relationship is evaluated graphically. The results demonstrate a nearly linear relationship between underground withdrawal and the reservoir expansion term, indicating that the assumed volumetric reservoir model provides a reasonable representation of the reservoir behavior. Based on the slope of the material balance relationship, the original oil in place is estimated at approximately 10 MMSTB for the illustrative case. The pressure-production relationship is also analyzed to demonstrate the progressive decline in reservoir pressure with increasing cumulative production. The study confirms that material balance analysis provides a practical and relatively simple approach for reservoir evaluation, while emphasizing that reliable pressure, production, and PVT data are essential for obtaining accurate results.

Keywords – Material Balance; Reservoir Engineering; Havlena–Ode Method; OOIP; STOIIP; Reservoir Drive Mechanism; Pressure; Oil Reservoir.

I. INTRODUCTION

The efficient management of petroleum reservoirs requires an accurate understanding of the physical processes governing fluid production and pressure behavior. During hydrocarbon production, the removal of oil, gas, and water from a reservoir causes changes in reservoir pressure and fluid volumes. These changes are controlled by the expansion of reservoir fluids, expansion of the rock matrix, gas liberation, gas-cap expansion, and water influx from an aquifer. Understanding these mechanisms is essential for evaluating reservoir performance and determining the amount of hydrocarbons that can ultimately be recovered.

One of the classical approaches used to evaluate these processes is Material Balance Analysis. The fundamental principle of material balance is the conservation of mass: the volume of fluids produced from a reservoir must be compensated by fluid and rock expansion, influx of water, or other sources of

reservoir energy. Consequently, production and pressure data can be used to obtain important information about the reservoir without requiring a detailed numerical simulation model.

Material balance methods have traditionally been used to estimate Original Oil in Place (OOIP) or Stock Tank Original Oil in Place (STOIIP). They are also useful for identifying reservoir drive mechanisms and evaluating whether the observed reservoir behavior is consistent with a volumetric reservoir, gas-cap expansion, water influx, or a combination of mechanisms.

The main objective of this study is to present the theoretical basis of material balance analysis and demonstrate its application through an illustrative numerical example. The analysis focuses on the relationship between reservoir pressure, cumulative production, underground withdrawal, and reservoir expansion. Graphical interpretation is used to demonstrate how reservoir performance can be evaluated and how the original oil in place can be estimated.

II. Materials and Method

The material balance equation is based on the conservation of mass within the reservoir. In simplified terms, the material balance principle can be expressed as:

Underground withdrawal = Expansion + Water influx

For an oil reservoir, the underground withdrawal is associated with the cumulative production of oil, gas, and water. The expansion term accounts for changes in the volume of the reservoir fluids and rock as reservoir pressure decreases. The general material balance equation can be written as:

$$F = NE + W_e \qquad (1)$$

Where
$F -$ is cumulative underground withdrawal,
$N -$ is original oil in place,
$E -$ is total expansion per STB of original oil,
$W_e -$ is cumulative water influx.

For a reservoir without water influx:

$$F = NE \qquad (2)$$

This equation provides the basies for estimating N.
The cumulative underground withdrawal represents the reservoir volume corresponding to the produced fluids. For an oil reservoir, the underground withdrawal can be expressed as:

$$F = N_p[B_o + (R_p - R_s)B_g] \qquad (3)$$

Where

$N_p -$ is cumulative oil production,

$B_o -$ is oil formation volume factor,

$R_p -$is cumulative gas-oil ratio,

$R_s -$is solution gas-oil ratio,

$B_g -$ is gas formation volume factor.

If water production is important, its contribution can also be included:

$$F = N_p[B_o + (R_p - R_s)B_g] + W_pB_w \qquad (4)$$

Where

$W_p -$ is cumulative water production

$B_w -$ is the water formation volume factor

The expansion term depends on the reservoir drive mechanism and the pressure range being considered.

For a solution-gas-drive reservoir, the expansion of the oil and liberated gas is particularly important. A commonly used expression is:

$$E_o = (B_o - B_{oi}) + (R_{si} - R_s)B_g \quad (5)$$

Where

$B_{oi} -$ is the initial oil formation volume factor,

$R_{si} -$ is the initial solution gas-oil ratio,

$R_s -$ is the solution gas-oil ratio at current pressure.

For a reservoir with a gas cap, an additional gas-cap expansion term is introduced. The general Havlena–Ode expression can be written as:

$$F = N(E_o + mE_g + E_{fw}) + W_e \quad (6)$$

Where

$E_o -$ is oil expansion

$E_g -$ is gas-cap expansion

$E_{fw} -$ is formation-water and rock expansion

m -is the initial gas-cap ratio

$W_e -$ is cumulative water influx.

2.1 Reservoir Drive Mechanisms

Correct identification of the reservoir drive mechanism is essential for material balance analysis.
Rock and fluid expansion: As pressure decreases, the reservoir rock and fluids expand. Solution gas drive: When reservoir pressure falls below the bubble-point pressure, dissolved gas begins to come out of solution. The expansion of liberated gas provides energy for fluid production.

Gas-cap expansion: If a free-gas cap is present, pressure reduction causes the gas cap to expand and provide energy for oil displacement toward producing wells.

Water drive: Water enters the reservoir from an aquifer as reservoir pressure decreases. This water influx supports reservoir pressure and displaces hydrocarbons toward producing wells.

Gravity drainage: Gravity can contribute to hydrocarbon movement, particularly in reservoirs with favorable vertical permeability and significant density differences between oil, gas, and water.
In actual reservoirs, more than one mechanism can act simultaneously

2.2. Havlena–Ode Method

The Havlena–Ode method provides a graphical interpretation of the material balance equation.
For a reservoir without significant water influx:

$$F = NE \qquad (7)$$

Therefore:

$$F/E = N \qquad (8)$$

A plot of F against E should ideally produce a straight line passing through the origin. The slope of the line corresponds to the original oil in place:

$$slope = N$$

This graphical approach is useful because deviations from linearity may indicate problems with the assumed reservoir model, PVT data, production data, or the presence of additional energy mechanisms.

Methodology

- For the present study, an illustrative oil reservoir is considered. The analysis follows these steps:
- Reservoir pressure data are defined for several production stages.
- Cumulative oil production N_p is determined.
- PVT properties are assigned for each pressure.
- Underground withdrawal F is calculated.
- The expansion term E_o is calculated.
- A plot of F versus E_o is constructed.
- Linear regression is applied to estimate the slope.
- The slope is interpreted as an estimate of OOIP.
- Pressure and production trends are discussed.

The numerical values used below are illustrative data created for demonstrating the methodology, rather than measurements from a particular oil field.

III. RESULTS AND DISCUSSION

Consider an oil reservoir with an initial pressure of: $P_{\mathrm{i}} = 3000\ psi$
and an initial oil formation volume factor: $B_{\mathrm{oi}} = 1.30\ rb/STB$
The following illustrative data are considered.

Tabele 1. Data are considered

.

Pressure (psi)	N_p ($10^3\ STB$)	B_o	R_s	B_g
3000	0	1.3	650	0.0010
2800	100	1.32	620	0.00105
2600	220	1.34	590	0.00110
2400	350	1.36	560	0.00115
2200	500	1.38	530	0.00120
2000	670	1.40	500	0.00125

For simplicity, assume:

$$R_{si} = 650$$

And the reservoir is initially considered as a volumetric reservoir without significant water influx. The expasion term is calculated usein:

$$E_o = (B_o - B_{oi}) + (R_{si} - R_s)B_g$$

The results demonstrate that cumulative production increases as reservoir pressure decreases. This behavior is expected because continued production removes fluids from the reservoir, resulting in a progressive reduction in reservoir pressure.

The relationship between cumulative oil production and reservoir pressure can be represented as follows.

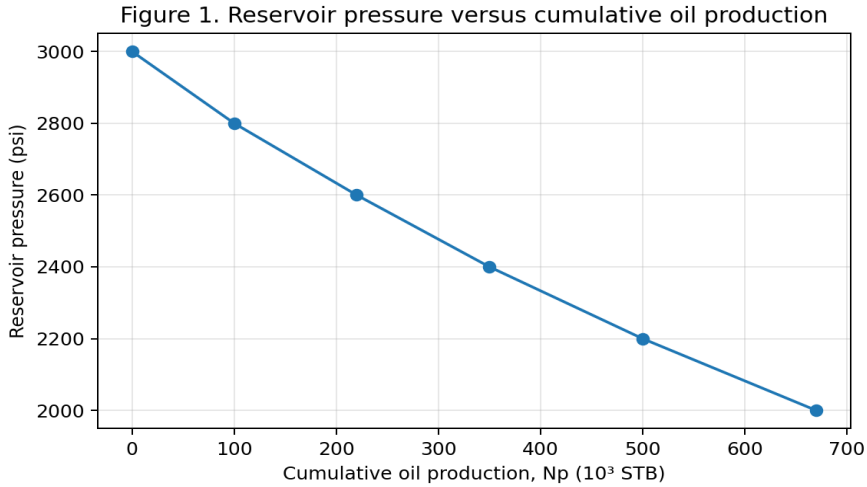

Fig. 1. Reservoir pressure versus cumulative oil production.

The graph demostrates a continues decline in reservoir pressure eith increasing cumultative oil production. This pressure decline indicates that the reservoir is losing stored energy during production. The rate at which pressure dcreases depends strongly on the reservoir drive mechanism.

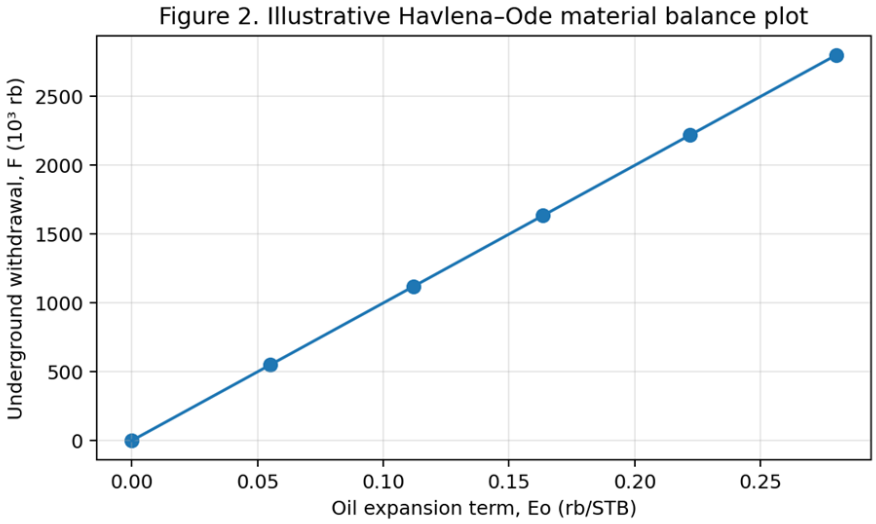

Fig. 2. Illustrative Havlena–Ode material balance plot.

The material balance analysis demonstrates that reservoir pressure and production history are strongly interconnected. As fluids are produced, the reservoir undergoes pressure depletion. The resulting pressure reduction causes expansion of the reservoir fluids and rock and, depending on the reservoir conditions, liberation and expansion of gas.

The Havlena–Ode representation provides an effective graphical approach for evaluating this behavior. In the illustrative example, the relationship between F and E_o is approximately linear. This suggests that the assumed volumetric reservoir model provides a reasonable representation of the reservoir behavior.

The estimated OOIP of approximately 10 MMSTB is obtained from the slope of the F-versus-E_o relationship.

However, in a real reservoir, deviations from linearity can be caused by inaccurate pressure measurements, uncertainties in PVT properties, incomplete production data, reservoir heterogeneity, compartmentalization, and unrecognized water or gas influx.

Consequently, the material balance method should not be considered only as a mathematical procedure for estimating OOIP. It is also a diagnostic tool that can provide information about the physical behavior of the reservoir.

The principal advantages of the method include:

- relatively simple mathematical formulation;
- limited computational requirements;
- direct use of field pressure and production data;
- estimation of OOIP/STOIIP;
- identification of reservoir drive mechanisms;
- evaluation of reservoir performance;
- useful support for reservoir management decisions.

Material balance can therefore be particularly valuable during the early and intermediate stages of reservoir development.

Despite its advantages, the method has several limitations.

The accuracy of the results depends strongly on the quality of the available pressure, production, and PVT data. The reservoir is also commonly represented using average reservoir pressure, which may not adequately describe strongly heterogeneous or compartmentalized reservoirs.

In addition, incorrect assumptions about water influx, gas-cap size, fluid properties, or reservoir connectivity can significantly affect the calculated OOIP.

For complex reservoirs, material balance should therefore be complemented by other methods, such as volumetric calculations, well testing and numerical reservoir simulation.

IV. CONCLUSION

Based on the presented analysis, the following conclusions can be drawn:

- Material Balance Analysis is an important reservoir-engineering method for evaluating reservoir performance and estimating the original hydrocarbon volume.
- The method is based on the principle of conservation of mass, relating underground fluid withdrawal to reservoir and fluid expansion and, when applicable, water influx.
- The Havlena–Ode method provides a convenient graphical approach for evaluating material balance behavior.
- In the illustrative case, the approximately linear relationship between F and E_o indicates that the assumed volumetric reservoir model is consistent with the synthetic production and pressure data.
- The slope of the F-versus-E_o relationship provides an estimate of the original oil in place. For the illustrative dataset, the estimated value is approximately 10 MMSTB.
- Pressure decline is directly related to cumulative production and provides important information about the energy available within the reservoir.

- Accurate identification of the reservoir drive mechanism is essential because water influx, gas-cap expansion, solution-gas drive, and fluid/rock expansion have different effects on reservoir pressure and production.
- Although Material Balance is a powerful analytical technique, its results should be validated using additional reservoir-engineering methods when the reservoir is complex or heterogeneous.

REFERENCES

[1] Dake, L. P. Fundamentals of Reservoir Engineering. Elsevier.
[2] Havlena, D. & Ode, H. The Material Balance as an Equation of a Straight Line. Transactions of the AIME.
[3] Schilthuis, R. J. (1941). Active oil and reservoir energy. *Transactions of the AIME, 146*(1), 33–52.
[4] 2. Havlena, D., & Odeh, A. S. (1963). The material balance as an equation of a straight line. *Journal of Petroleum Technology, 15*(8), 896–900. https://doi.org/10.2118/559-PA
[5] 3. Havlena, D., & Odeh, A. S. (1964). The material balance as an equation of a straight line—Part II: Field cases. *Journal of Petroleum Technology, 16*(6), 669–682.
[6] 4. Dake, L. P. (1978). Fundamentals of reservoir engineering. Elsevier.
[7] 5. Craft, B. C., Hawkins, M. F., & Terry, R. E. (1991). *Applied petroleum reservoir engineering* (2nd ed.). Prentice Hall.
[8] 6. Ahmed, T. (2018). *Reservoir engineering handbook* (5th ed.). Gulf Professional Publishing.

8th International Conference on Engineering, Natural and Social Sciences

September 06-07, 2026: Konya, Turkey

© 2026 Published by All Sciences Academy

https://www.icensos.com/

Indicator Bacteria and Biofilm Dynamics in Sarıçay Stream, Türkiye

Mehmet Doğukan Maraş[1], Nil Atalay [2*] and Nurcihan Hacıoğlu Doğru [3]

[1]*Department of Biology/Faculty of Science, Canakkale Onsekiz Mart University, Türkiye*
[21]*Department of Biology/Faculty of Science, Canakkale Onsekiz Mart University, Türkiye*
[31]*Department of Biology/Faculty of Science, Canakkale Onsekiz Mart University, Türkiye*

[*]*(nilnatalay@gmail.com)*

Abstract – Urban and coastal freshwater ecosystems are exposed to microbiological pollution caused by anthropogenic pressures originating from domestic and industrial activities. This leads to the deterioration of water quality and the spread of potential pathogenic microorganisms, posing significant risks to ecosystem and public health. This study evaluated the biofilm-associated virulence properties of Gram-negative bacteria isolated from Sarıçay Stream, which flows through Çanakkale city center, along with the level of microbiological pollution.

Monthly water samples were collected between December 2024 and May 2025 from three different sampling stations representing an industrial area, a marketplace, and a fishing port. Total viable count (TVC), total coliform (TC), fecal coliform (FC), and fecal streptococci (FS) analyses were performed on the samples, and the biofilm formation capacities of 114 isolated Gram-negative bacteria were determined. The results demonstrated that microbiological pollution persisted in Sarıçay Stream throughout the sampling period. The highest fecal coliform count was detected at the marketplace station as 24.00 × 10^2 MPN/1 mL. It was determined that 91.23% of the isolates possessed biofilm-forming capacity, with a significant proportion of the biofilm-positive isolates exhibiting moderate to strong biofilm formation. In conclusion, the high biofilm-forming capacity of Gram-negative bacteria isolated from Sarıçay Stream indicates that this stream requires regular microbiological monitoring. The findings provide critical data for evaluating the environmental persistence of biofilm-forming bacteria and potential public health risks.

Keywords – Sarıçay Stream, Microbiological water quality, Fecal indicator bacteria, Gram-negative bacteria, Biofilm formation capacity, Environmental public health

I. INTRODUCTION

Freshwater ecosystems are vital natural resources that fulfill numerous ecological and socioeconomic functions, including the provision of drinking and usable water, agricultural irrigation, recreation, and the conservation of biodiversity. However, rapid population growth, unplanned urbanization, industrial activities, and domestic wastewater discharges lead to the deterioration of water quality and an increase in microbiological pollution in these ecosystems [1-2]. In particular, wastewater discharged into receiving environments without adequate treatment carries high organic loads as well as various pathogenic microorganisms into aquatic environments, adversely affecting both ecosystem stability and public health.

In the assessment of microbiological pollution in aquatic environments, total coliform (TC), fecal coliform (FC), and fecal streptococci (FS) are widely used as indicators of fecal contamination. An increase in these microorganisms is considered a significant indicator of human or animal waste input into water sources and constitutes a fundamental microbiological parameter in evaluating the risk of waterborne infections [3-5].

Gram-negative bacteria represent one of the most frequently encountered microorganism groups in polluted freshwater ecosystems. Specifically, *Escherichia coli*, *Aeromonas hydrophila*, *Pseudomonas* spp., *Proteus* spp., and *Vibrio* species attract attention due to their ability to adapt to environmental conditions and their intrinsic virulence factors. Under suitable environmental conditions, these bacteria can maintain viability for extended periods and function as opportunistic pathogens, causing various infections in humans and aquatic organisms [6].

One of the most crucial virulence mechanisms contributing to the environmental persistence of Gram-negative bacteria is biofilm formation. Biofilm is a complex microbial mode of life that enables microorganisms to adhere to living or non-living surfaces and live as organized communities embedded within a self-synthesized protective matrix of extracellular polymeric substances [7-8]. Owing to the biofilm matrix, bacteria become more resistant to adverse environmental conditions such as temperature fluctuations, nutrient limitation, heavy metals, disinfectants, and antimicrobial agents, thereby maintaining their presence in the environment for significantly longer durations compared to planktonic cells [7]. Biofilm formation not only enhances the environmental endurance of bacteria but also reinforces their capacity for surface attachment, colonization, and persistence. This situation extends the survival time of pathogenic bacteria in environmental media while contributing to increased tolerance against disinfection practices and the preservation of virulence traits [8]. Consequently, biofilm formation is regarded as a critical research topic in environmental microbiology and public health studies [9].

Sarıçay Stream, which passes through Çanakkale city center and discharges into the Dardanelles Strait, is an important freshwater ecosystem subjected to anthropogenic pressures stemming from urban settlement areas, marketplace wastes, and small-scale industrial activities. This continuous pollution load renders Sarıçay a microbiologically vulnerable water system.

In this study, monthly sampling was conducted over a six-month period between December 2024 and May 2025 at three designated stations along Sarıçay Stream flowing through Çanakkale city center. To evaluate the overall sanitation status of the water samples, microbiological analyses were performed, including TVC (at 22°C and 37°C), TC, FC, and FS counts. To determine the slime production characteristics of the Gram negative isolates, the Congo Red Agar Method and the Standard Glass Tube Method were employed. Additionally, the presence of biofilm among the isolates was investigated using the microplate method. This study aimed to determine the microbiological pollution profile of Sarıçay Stream and to reveal the biofilm and slime formation potentials of the isolated Gram-negative bacteria.

II. Materials and Method

Study Area and Sample Collection

In this study, monthly sampling was conducted over a six-month period between December 2024 and May 2025 at three designated sampling stations along Sarıçay Stream, which flows through Çanakkale city center (Figure 1).

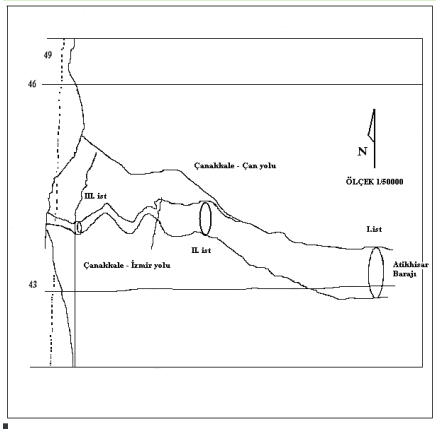

Fig. 1 Sampling locations along Sarıçay Stream

Collection of Stream Water Samples

To determine select physicochemical and microbiological parameters at designated stations along the Sarıçay coastline in Çanakkale, water samples were collected from a depth of 1 m in accordance with the Official Communiqué on Sampling and Analysis Methods [3] and transported to the laboratory under cold chain conditions as promptly as possible. Sterilizable sample containers were used for collection; to prevent contamination and interfering substances, all containers were thoroughly cleaned and sterilized prior to use.

Microbiological Analyses

To evaluate the overall sanitation status of the water samples, TVC (at 22 °C and 37 °C), TC, FC, and FS counts were performed.

TVC Nutrient Agar (NA, OXOID, UK) was utilized for the isolation and estimation of total viable bacteria [3].

TC Count Following appropriate serial dilutions of the water samples, 10 mL aliquots were inoculated into three tubes containing double-strength lactose broth. Additionally, 1 mL aliquots were inoculated into the first three single-strength lactose broth tubes, and 0.1 mL aliquots into the remaining three single-strength tubes. The tubes were incubated at 37 °C for 24–48 hours. Gas production in Durham tubes was examined post-incubation, and the Most Probable Number (MPN) of total coliforms was determined using MPN tables [10].

FC Count Inocula from total coliform-positive tubes were transferred into EC Broth (OXOID, UK) and incubated at 44.5 °C for 24–48 hours. The MPN of fecal coliforms was determined based on gas formation within the Durham tubes [10].

FS Count For the enumeration of FS, 1 mL aliquots from suitable dilutions were inoculated into sterile sodium azide broth media and incubated for 1–2 days. Following incubation, tubes exhibiting turbidity were scored as positive and the fecal streptococci counts were calculated accordingly [10].

Isolation and Identification of Gram-Negative Bacterial Groups

To isolate members of the *Enterobacteriaceae* and *Vibrionaceae* families, MacConkey Agar and Eosin Methylene Blue (EMB) Agar were used for *Enterobacteriaceae*, while Thiosulfate-Citrate-Bile Salts-Sucrose (TCBS) Agar, Glutamate Starch Phenol Red (GSP) Agar, Ampicillin Aeromonas Agar, and Inositol Brilliant Green Bile Agar were used for *Vibrionaceae*. For the isolation and identification of *Salmonella* spp., samples were subjected to pre-enrichment in peptone water and subsequently transferred to Selenite Cystine Broth for selective enrichment. Following incubation at 37 °C for 24–48 hours, subcultures were plated onto Brilliant Green Agar and *Salmonella–Shigella* Agar. For the isolation of *Pseudomonas* spp., MacConkey Agar and Cetrimide Agar were employed. Isolates obtained after 24–48 hours of incubation at 30–35 °C were transferred onto Tryptic Soy Agar (TSA). For identification, all isolates were subjected to Gram staining, oxidation-fermentation (O/F) tests, oxidase, catalase, IMViC tests, H_2S production, and other standard phenotypic assays. Additionally, Microgen ID test kits were utilized to confirm the biochemical identification results [10].

Determination of Biofilm Formation in Bacterial Isolates

Biofilm formation was evaluated using the microplate method. Fresh cultures from Nutrient Agar (18–24 h) were suspended in Luria-Bertani (Miller) Broth containing 1% glucose to match a 0.5 McFarland standard. A 200 µL aliquot of each suspension was added in duplicate into four microplates; uninoculated broth served as the negative control. Two plates were incubated at 37 °C for 24 h and the other two for 48 h. After incubation, plates were washed three times with distilled water. One set was stained with 0.1% crystal violet and another with 0.1% safranin for 15 min. Following additional washing and drying, crystal violet-stained wells were solubilized with 95% ethanol (10 min) and measured at 540 nm. Safranin-stained wells were treated with 50% acetic acid (10 min) and measured at 470 nm. The same staining protocol was applied to the 48 h plates. Biofilm production was categorized relative to control values as negative (-), weak positive (+), moderate positive (++), or strong positive (+++) [10].

III. RESULTS

Microbiological Findings for Stations

Microbiological analysis results revealed that Station I was under a heavy bacterial load. TVC peaked in January 2025 at 205 × 10^6 CFU/mL, pointing to an extreme influx of organic pollution during this period. Regarding indicator microorganisms, TC and FC levels reached their highest values in December 2.30 × 10^2 MPN/1 mL and subsequently diluted during the spring months. Conversely, FS values remained stable between 2.00 × 10^2 ile 2.30 × 10^2 MPN/1 mL throughout the December–March period, demonstrating persistent fecal contamination in the area. At station II indicated that fecal contamination was predominant during the winter months, whereas overall bacterial load dominated during the spring. TVC reached its peak in December at 14.6 × 10^6 CFU/mL, fluctuating within the 10^3 - 10^5 range in subsequent months. Regarding indicator microorganisms, TC and FC levels peaked during the winter period (December–January). Notably, FC counts measured at 24.00 × 10^2MPN/mL in December confirmed an intense influx of sewage or domestic wastewater during this timeframe. FS levels peaked in December and January at 4.30 × 10^2 MPN/1 mL, maintaining lower yet steady concentrations over the following months. Collectively, these findings demonstrate that the Marketplace locality suffers from severe organic pollution and oxygen depletion during spring, coupled with high fecal contamination pressure during winter. At Station III revealed that both general bacterial populations and indicator microorganisms exhibited pronounced density during the winter months. TVC reached its maximum in December at 5.42 × 10^6 CFU/mL, declining to 10^4–10^5 CFU/mL levels during the spring. Regarding indicator bacteria, fecal contamination peaked in January. Notably, FS counts reached a peak of 15.00 × 10^2 MPN/1 mL in January, confirming a specific pollution input likely originating from marine traffic or coastal discharges during this period. Similarly, TC and FC levels elevated to 9.30 × 10^2 and 2.30 × 10^2 MPN/1 mL, respectively, in January. In April and May, FC levels dropped below the detection limit (<0.30 MPN/1 mL). Evaluated holistically, these data indicate that the Fishing Port locality poses environmental and microbiological risks, particularly during the month of January (Table 1).

Table 1. Microbiological analyses of stations

Stations	TVC (cfu/mL)	TC (MPN/mL)	FC (MPN/mL)	FS (MPN/mL)
I	35.25× 10^6	8.55 × 10^1	5.51 × 10^1	1.70 × 10^2
II	2.80 × 10^6	3.42 × 10^2	5.75 × 10^2	2.37 × 10^2
III	1.60 × 10^6	2.02 × 10^2	6.33 × 10^1	2.80 × 10^2
Average	1.32 x 10^7	2.10 × 10^2	2.31 × 10^2	2.29 × 10^2

Isolation and Identification of Gram-Negative Bacteria

A total of 114 Gram-negative bacterial isolates were obtained from water samples collected from Sarıçay Stream between December 2024 and May 2025. Microscopic examination confirmed that all isolates exhibited Gram-negative bacillary morphology. Identification using the Microgen GnA+B-ID System revealed high similarity matches to *Enterobacter aerogenes*, *Proteus* spp., *Escherichia coli*, *Aeromonas hydrophila*, *Pseudomonas* spp., *Shewanella putrefaciens*, *Vibrio cholerae*, and *Vibrio parahaemolyticus*. Among these, *E. aerogenes*, *E. coli*, *A. hydrophila*, and *Pseudomonas* spp. were found to be the predominant species across all sampling periods.

Biofilm Formation Capacities of the Isolates

The biofilm formation capacities of the isolates obtained from the sampling stations are summarized in Table 2. Accordingly, biofilm formation was observed in 91.23% (104 isolates) of the isolates, whereas 8.77% (10 isolates) showed no biofilm production. Among the biofilm-producing isolates, strong (+++), moderate (++), and weak (+) levels of biofilm production were detected in 29.82%, 24.56%, and 36.84% of the total isolates, respectively. The majority of *V. cholerae*, *V. parahaemolyticus*, *A. hydrophila*, and *E. coli* strains exhibited moderate to strong biofilm formation capacities.

Table 2. Biofilm Formation Capacities of Gram-Negative Bacterial Isolates (n = 114)

Biofilm Formation Capacity	Number of Isolates (n)	Percentage (%)
Negative (-)	10	8.77
Weak (+)	42	36.84
Moderate (++)	28	24.56
Strong (+++)	34	29.82

IV. DISCUSSION

In this study, the biofilm formation capacities and select phenotypic virulence traits of Gram-negative bacteria isolated from the Sarıçay ecosystem were evaluated. The obtained findings revealed that the stream is under significant anthropogenic pressure from a microbiological perspective. In particular, the detection of fecal indicator bacteria across all sampling stations throughout the monitoring period demonstrates that Sarıçay is exposed to continuous microbiological contamination. The discharge of domestic and industrial wastewater into receiving water bodies without adequate treatment is reported as one of the primary drivers of fecal contamination in freshwater ecosystems [1, 11]. Notably, environmentally and clinically significant species—including *E. coli*, *A hydrophila*, *Pseudomonas* spp., *Proteus* spp., *V. cholerae*, and *V. parahaemolyticus*—were identified among the isolates. The persistent detection of *E. coli* across all sampling periods supports the chronic nature of fecal pollution in the stream. Similarly, studies conducted in various aquatic environments report that these bacteria are widespread in organic-rich waters and readily adapt to fluctuating environmental conditions [7-8]. One of the most notable findings of this study is that 91.23% of the isolates possessed the ability to form biofilms. Furthermore, a substantial proportion of the biofilm-positive isolates exhibited moderate to strong biofilm production, indicating that the bacterial population in Sarıçay has a high potential for surface attachment and long-term persistence under environmental conditions. Biofilm formation is recognized as a key virulence mechanism that protects bacteria against environmental stressors such as desiccation, temperature fluctuations, nutrient limitation, and antimicrobial agents [7-8]. Consequently, biofilm-forming bacteria can survive substantially longer under harsh environmental conditions and display enhanced resistance to disinfection practices compared to their planktonic counterparts [9].

In the present study, high biofilm formation capacities were determined in a significant portion of the *Vibrio* species, *A. hydrophila*, and *E. coli* isolates. Previous investigations have similarly reported that these pathogens can form robust biofilms under suitable environmental conditions, thereby enhancing their environmental persistence. This suggests that the biofilm-positive isolates identified in Sarıçay do not merely exist as free-floating cells in the water column, but are also capable of adhering to diverse substrates to establish persistent microbial communities. When the observed microbiological pollution levels are evaluated alongside the high proportion of biofilm-forming strains, it is evident that Sarıçay represents a critical freshwater ecosystem requiring regular environmental and public health monitoring. The presence of biofilm-capable bacteria indicates elevated resistance to environmental stress factors and the potential for long-term persistence within the aquatic system once established. Therefore, controlling pollution sources entering the stream and maintaining continuous microbiological surveillance programs are imperative for safeguarding water quality.

V. CONCLUSION

The identification of Gram-negative pathogens isolated from Sarıçay Stream and the determination of their high biofilm-forming capacities point to a significant risk factor for public health and aquatic ecosystem safety in the region. Because the ecological advantage conferred by biofilm formation enables these virulent bacteria to persist in the stream system over extended periods, future studies focusing on

the molecular characterization of these isolates and the development of antibiofilm strategies are of paramount importance.

ACKNOWLEDGMENT

This research is a part of Nil Atalay and Mehmet Doğukan Maraş's TÜBİTAK-2209-A.

REFERENCES

[1] S. Ayan, *Environmental Pollution and Its Effects on Ecological Balance* (in Turkish). Ankara, Türkiye: Nobel Yayın Dağıtım, 2005.
[2] S. Soyupak, *River Pollution and Water Quality Control* (in Turkish). Ankara, Türkiye: METU Press, 1987.
[3] APHA, *Standard Methods for the Examination of Water and Wastewater*, 20th ed. Washington, DC, USA: American Public Health Association, 1998.
[4] APHA, AWWA, and WPCF, *Standard Methods for the Examination of Water and Wastewater*, 19th ed. Washington, DC, USA: American Public Health Association, 1995.
[5] T. A. Edge and S. Hill, "Multiple lines of evidence to identify the sources of fecal pollution," *Water Res.*, vol. 41, no. 16, pp. 3580–3590, Aug. 2007.
[6] R. S. Balcı, "Determination of bacteriological pollution level of Seyhan Dam Reservoir and antibiotic resistance in members of Enterobacteriaceae," M.S. thesis, Dept. Biol., Inst. Nat. Appl. Sci., Çukurova Univ., Adana, Türkiye, 2007.
[7] Y. Kaçar, "Biofilm formation in bacteria and its importance," M.S. thesis, Inst. Sci., Istanbul Univ., Istanbul, Türkiye, 2009.
[8] D. Ünal, "Investigation of biofilm presence in *Pseudomonas*, *Klebsiella*, *Staphylococcus*, and *Candida* species isolated from various clinical specimens," M.S. thesis, Inst. Health Sci., Gazi Univ., Ankara, Türkiye, 2011.
[9] S. A. Abdallah, A. A. Elmanama, M. I. Fahd, and S. Afifi, "Microbiological beach sand quality in the Gaza Strip in comparison to seawater," *Pol. J. Environ. Stud.*, vol. 14, no. 6, pp. 841–850, 2005.
[10] V. Gürgün and A. K. Halkman, *Enumeration Methods in Microbiology* (in Turkish), 2nd ed. Ankara, Türkiye: Food Technology Association, Pub. no. 7, 1990, pp. 2–98.
[11] T. Yüksek, "A study on the variation of physical and chemical water quality parameters of Sarıçay," *Ecol. Environ. J.*, vol. 12, no. 48, pp. 22–29, 2003.

8th International Conference on Engineering, Natural and Social Sciences

September 06-07, 2026: Konya, Turkey

© 2026 Published by All Sciences Academy

https://www.icensos.com/

Current Developments in Memristor Technology

İshak PARLAR[1*] , Onur SİLAHTAR[1]

[1]*Department of Electrical and Electronics Engineering, Van Yuzuncu Yil University, Van/Türkiye*

[*]*(ishakparlar@yyu.edu.tr)*

Abstract **–**Memristor technology has become a significant research area in recent years, particularly for next-generation computing systems, going beyond classical memory structures. The ability of memristors to change their resistance states based on the applied signal, and most importantly, their ability to store the final resistance point in memory, allows these devices to be used in both computation and data storage. Significant advancements have been made in memristor-based in-memory computing and neuromorphic computing in recent years. Reducing the need for continuous data transfer between the processor and memory drastically lowers energy consumption in memristor-based systems, enabling increased processing speed. This feature makes them the most important semiconductor material in artificial intelligence applications in recent years, addressing the increasing computational and energy requirements. This study evaluates current developments in memristor technology in terms of device architectures, material structures, in-memory computing, and neuromorphic systems. Furthermore, the potential for memristor applications in fields such as artificial intelligence and smart sensors is reaching very advanced levels. However, existing issues such as device-to-device noise, reliability, scalability, and integration with CMOS technologies are also being investigated. Current studies show that memristors are being considered not only as memory elements, as in the past, but also as functional electronic structures capable of directly performing computational operations. Consequently, it is emphasized that for widespread commercial use of memristor technology in the development of energy efficiency, artificial intelligence, and neuromorphic computing systems in the coming years, further development of device reliability and manufacturing processes is needed.

Keywords –Memristor, neuromorphic computing, in-memory computing, energy efficiency, artificial intelligence(AI)

I. INTRODUCTION

Recent advancements in memristor technology, particularly in artificial intelligence and neuromorphic computing, are accelerating research into processing data on the same hardware instead of storing it. This makes it a crucial area for developing next-generation computer systems that consume less energy, are faster, and closely resemble the workings of the human brain. One of the most recent studies suggests that by 2026, research will focus not on a single memristor element, but on reliable memristor arrays, artificial synapses, on-chip computing, and the development of more stable devices using different materials. In these years, as we approach the limits of transistor technology, this missing element emerges as a key starting point [1-3].

Transistors, a fundamental building block of traditional electronic circuits, have played a critical role in the development of information processing and storage technologies for many years. However, they are becoming increasingly inadequate in terms of processing power, particularly in artificial intelligence and big data applications. In contrast, memristors, which can store their electrical history in a resistive state and perform both information storage and computation functions within the same physical structure, are considered a new generation of electronic components offering higher potential than traditional transistor-

based approaches for in-memory computing and artificial intelligence hardware. This is due to their low power consumption, reduced data transmission times, increased parallel computing capabilities, and countless other direct and indirect advantages [1-5].

II. Materials and Method

This study examines current academic research published on memristor technology, evaluating its working principles, application areas, advantages, and disadvantages.

A. Memristor (Excluding Memory Element)

In the classic von Neumann architecture, the processor and memory are in separate locations, and the constant transfer of data requires energy, which in turn creates latency costs. The strongest aspect of memristors is that their resistance can also be used as a computational criterion [2-4].

Especially in crossbar arrays, matrix-vector multiplication can be physically performed using Ohm's and Kirchhoff's laws. Therefore, memristors have become the most important candidates for implementing artificial neural networks in memory. Literature reviews from late 2025–early 2026 also indicate that research is shifting towards a combination of memristors, in-memory computing, and spiking neural networks.

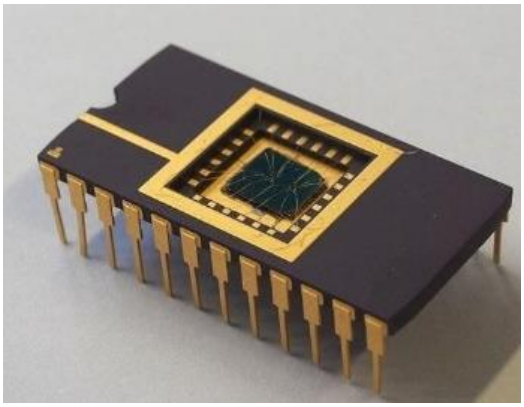

Fig. 1 Physical integrated structure of the memristor element

B. Difficulties and Problems Related to Memristors

According to the latest research published in August 2026, update disturbance issues occur during parallel weight updates in analog ReRAM crossbar architectures. The demonstration of analog switching times of approximately 60 ns and pulse tolerance exceeding 100,000 in these studies is particularly significant for in-memory training applications. This is because the training process subjects memristors to much more intensive and repetitive programming operations compared to inference-only processes. Therefore, reducing unwanted effects during updates and ensuring high cycle tolerance are critical for reliable and scalable in-memory training in ReRAM-based hardware [5-8].

Some of the most important and prominent problems in memristor research today are: (1) variability between devices, (2) accuracy/noise in analog computation, (3) transition from laboratory scale to large, reliable CMOS-integrated systems. Table 1 shows current developments in some of these problems [3, 5].

Table 1. Transition to large and realistic systems

Area	**2026**
Non-volatile memory	Maturing
Analog in-memory AI	Very active
Endurance / variability	Significant problem
CMOS integration	Under investigation
Widespread use in real AI chip	Still limited |
Neuromorphic computing	Very active
Analog accuracy	Key bottleneck
Large crossbar arrays	Still problematic

III. DISCUSSION

Memristors (memory resistors) are used in computer integrated circuits as a revolutionary semiconductor technology that can both store data (using their memory resistor properties) and process it within the same cell. In other words, they can behave like a self-excited, self-controlled element. By eliminating the physical separation (Von Neumann bottleneck) between the processor (CPU) and memory (RAM) in traditional computers, they have the potential to radically change the performance of integrated circuits (ICs). Memristor-based physical computers are not currently on the market, but such developments would not be surprising in the next decade. In these years of chip wars, memristor-based processors have the potential to provide some relief to this sector. Of course, as mentioned in the section above, certain problems exist [2-5, 8-10].

IV. CONCLUSION

In conclusion, significant advancements are being made in memristor technology today, with topics such as In-Memory Processing, Neuromorphic Chips and Artificial Intelligence (AI), Universal Memory, High Density and Miniaturization, and Extremely Low Power Consumption taking center stage. The fact that next-generation memristors are gaining many more features such as higher analog resolution, lower energy consumption, multi-level data storage, more stable operation, and compatibility with large-scale crossbar arrays already indicates that this technology can play a significant role in traditional computer architectures in the future. Furthermore, it is predicted that these developments will be preferred not only in the field of electrical and electronics engineering but also in all sub-branches of this field, in biomedical engineering, and in precision imaging and processing applications in the healthcare sector.

REFERENCES

[1] Gianluca Marraccini, Sebastiano Strangio, Elisabetta Dimaggio, Riccardo Sargeni, Francesco Pieri, Yigit Sozen, Andres Castellanos-Gomez, Gianluca Fiori; Fast prototyping of memristors for ReRAMs and neuromorphic computing. Nanoscale 2026; 18 (2): 835–842. https://doi.org/10.1039/d5nr02690c

[2] Wang, J., Chen, Q., Zhang, J. et al. Analysis and Applications of Neuromorphic Memristors in Artificial Intelligence Computing. Nano-Micro Lett. 19, 36 (2027). https://doi.org/10.1007/s40820-026-02322-5

[3] Jiang, Z., Zhao, H., Tang, J. et al. Strategies of high-accuracy memristor-based analogue computing in memory for artificial intelligence. Nat. Mater. 25, 1110–1124 (2026). https://doi.org/10.1038/s41563-026-02600-y

[4] Mostafa Shooshtari, Teresa Serrano-Gotarredona, Bernabé Linares-Barranco. Adv. Intell. Syst.. 2025; 000:e202500806. https://doi.org/10.1002/aisy.202500806

[5] Choi, W., Stecconi, T., Falcone, D. F., Galetta, M., Clerico, V., Zaccaria, E., ... & Offrein, B. J. (2026). Update Disturbance-Resilient Analog ReRAM Crossbar Arrays for In-Memory Deep Learning Accelerators. Advanced Science, 13(4), e04578. https://doi.org/10.48550/arXiv.2608.25781

[6] Gao, K., Sun, B., Cao, Z., Wang, M., Zhang, J., Wang, K., ... & Shao, J. (2026). Brain-inspired computing based on large-scale memristor crossbar arrays. Advanced Functional Materials, 36(32), e28309. https://doi.org/10.1002/adfm.202528309

[7] Liu, Z., Gao, C., Yang, J., Chen, Z., Li, E., Li, J., ... & Zhang, J. (2026). Memristor devices for next-generation computing: from performance optimization to application-specific co-design. International Journal of Extreme Manufacturing, 8(1), 012004. https://doi.org/10.1088/2631-7990/ae053a

[8] Zhao, H., Wang, L., Zhou, Y., Liu, S., Qin, Q., Li, X., ... & Wu, H. (2026). In situ spectral reconstruction based on a memristor chip for energy-efficient computational spectrometry. Nature Electronics, 9(6), 652-664. https://doi.org/10.1038/s41928-026-01571-x

[9] Guo, G., Xiong, T., Xie, B., Zhang, J., Zhang, J., Lu, Y., ... & Yu, P. (2026). Confined-hydrogel fluidic memristor crossbar array for neuromorphic computing. Nature Communications, 17(1), 4275. https://doi.org/10.1038/s41467-026-70728-1

[10] Wang, Z., Li, Z., Xia, Z., Sun, X., Meng, J., & Wang, T. (2025). Emerging CMOS compatible memristor for storage technology and neuromorphic computing applications. Chip, 100183. https://doi.org/10.1016/j.chip.2025.100183

8th International Conference on Engineering, Natural and Social Sciences

September 06-07, 2026: Konya, Turkey

© 2026 Published by All Sciences Academy

https://www.icensos.com/

Closed-Loop State Regulation of Memristive Neuromorphic Circuits Using a Filtered PI-Type Intuitionistic Fuzzy Logic Controller

Onur SİLAHTAR[1*], İshak PARLAR[1]

[1]*Department of Electrical and Electronics Engineering, Van Yuzuncu Yil University, Van/Türkiye*

[*]*(onursilahtar@yyu.edu.tr)*

Abstract – Memristors play a pivotal role in next-generation neuromorphic computing architectures for representing synaptic weights due to their continuous state-switching capability and nanoscale memory retention. However, inherent nonlinear device dynamics, boundary effects, and parametric uncertainties severely challenge precise state variable regulation. In this study, a first-order s-domain transfer function is analytically derived by performing a small-signal Taylor series linearization around a nominal operating point, utilizing authentic physical parameters from the widely recognized HP titanium dioxide memristor model, including device thickness, average ion mobility, and low/high resistance states. To achieve accurate and robust closed-loop regulation of the normalized state variable and conductance levels, a filtered proportional-integral type intuitionistic fuzzy logic controller is developed. In the proposed control architecture, the tracking error and the low-pass filtered error derivative inputs are fuzzified through five-level intuitionistic fuzzy sets, rule inference is executed using a dedicated Sugeno generator parameter, and an output integration stage is incorporated to eliminate steady-state errors. Dynamic numerical simulations performed in the MATLAB/Simulink environment demonstrate that the integrated derivative filter successfully eliminates high-frequency chattering, while the generated control voltage strictly remains within the physical operating limits of the device. Furthermore, the closed-loop system exhibits smooth transient response and settles precisely at the target reference with negligible overshoot and zero steady-state error. The obtained findings confirm that the designed controller provides a reliable and robust closed-loop solution for synaptic weight programming in neuromorphic hardware.

Keywords – Intuitionistic Fuzzy Logic Control, PI-Type Fuzzy Controller, Memristor State Regulation, Neuromorphic Circuits, Chattering Suppression

I. INTRODUCTION

Memristors are widely recognized as the most promising fundamental circuit elements for mimicking biological synapses in next-generation neuromorphic artificial intelligence hardware, owing to their nanoscale dimensions, low power consumption, and capability to continuously retain conductance states under applied electric fields [1-3]. In brain-inspired analog computing architectures, the accuracy of synaptic weights directly depends on how precisely the internal state variable or conductance level of the memristive element converges to the designated reference [4-5]. Nevertheless, severe nonlinear ion-drift dynamics, saturation phenomena induced by boundary effects, and fabrication tolerances observed in physical memristor devices significantly impede the stable and accurate adjustment of the state variable [6].

In conventional neuromorphic architectures, open-loop voltage pulsing schemes are predominantly employed to program memristor conductance. However, these open-loop approaches remain highly susceptible to internal parasitic effects and device-to-device stochastic behaviors, which often lead to prolonged settling times and undesirable fluctuations in the control signal while attempting to reach target

weight levels [7-8]. To overcome these limitations, control theory-based closed-loop methodologies have been investigated, with classical proportional–integral–derivative (PID) controllers initially explored as a baseline alternative due to their structural simplicity. Nonetheless, fixed-gain classical PID controllers fail to compensate for the operating point-dependent dynamic impedance variations of memristors, consequently exhibiting adverse overshoot or high-frequency switching oscillations during the transient response [9-11].

For the regulation of nonlinear and uncertain dynamic systems lacking precise mathematical models, fuzzy logic controllers provide a remarkably effective framework. Standard Type-1 fuzzy logic systems incorporate expert heuristic knowledge into the control architecture via linguistic rule sets, thereby imparting inherent robustness against modeling discrepancies. Furthermore, Takagi–Sugeno fuzzy inference models express rule consequents as crisp singletons or linear functions, which substantially mitigates computational complexity and establishes an ideal mathematical foundation for real-time control implementations [12-13].

In classical fuzzy set theory, the degree of belonging of an element to a given set is characterized solely by a single membership grade [14]. In contrast, Intuitionistic Fuzzy Set theory, formulated by Atanassov, introduces a non-membership degree alongside the membership degree, thereby defining an explicit hesitation margin arising from the sum of these two components [15]. By simultaneously processing membership, non-membership, and hesitation metrics through Sugeno generators and Intuitionistic Weighted Average defuzzification techniques, intuitionistic fuzzy inference mechanisms provide significantly enhanced decision-making flexibility and superior uncertainty tolerance compared to conventional fuzzy structures.

Although numerous studies in the literature have utilized memristors as hardware synaptic weights for neural networks [16-18], investigations focusing on the closed-loop regulation of an authentic physical parameter-derived memristor model via an integral-action PI-type Intuitionistic Takagi–Sugeno Fuzzy Logic Controller equipped with a low-pass derivative filter to suppress numerical noise remain exceedingly scarce [19-20]. Accordingly, in this study, the small-signal transfer function of an HP memristor around its nominal operating point is analytically derived, a 25-rule PI-IFLC architecture driven by the tracking error and filtered error derivative is developed, and the state-variable tracking performance of the closed-loop system is comprehensively evaluated within the MATLAB/Simulink environment.

II. Materials and Method

A. Mathematical Modeling and Small-Signal Analysis of the Memristor

In this study, the widely recognized two-region linear ion-drift model developed by Strukov and co-workers for the HP titanium dioxide (TiO_2) memristor is utilized as the foundational physical model. The memristor comprises a nanoscale thin-film layer of total thickness D, which is modeled as a series connection of a highly conductive doped region of width $w(t)$ and a highly resistive undoped region of width $D-w(t)$. The position of the doped boundary layer $w(t)\in[0,D]$ constitutes the internal state variable of the device. The instantaneous equivalent resistance (memristance) of the element is mathematically expressed in Equation 1.

$$M(w)=R_{ON}\frac{w(t)}{D}+R_{OFF}\left(1-\frac{w(t)}{D}\right) \tag{1}$$

Where R_{ON} denotes the minimum resistance corresponding to the fully doped state and R_{OFF} represents the maximum resistance associated with the fully undoped state. In accordance with Ohm's law, the relationship between the terminal voltage $v(t)$ applied across the memristor and the resulting current $i(t)$ is governed by $v(t)=M(w).i(t)$. The velocity of the doped boundary movement is directly proportional to the average ionic mobility μ_v and the governing state differential equation is defined in Equation 2.

$$\frac{dw(t)}{dt} = \mu_v \frac{R_{ON}}{D} i(t) = \frac{\mu_v R_{ON}}{D} . \frac{v(t)}{M(w(t))} \tag{2}$$

To adapt this nonlinear dynamical equation for linear control design, a small-signal linearization is conducted by performing a first-order Taylor series expansion around a nominal operating point (w_0, v_0). Defining the small perturbations in the state variable and voltage as $w(t) = w_0 + \delta w(t)$ and $v(t) = v_0 + \delta v(t)$ respectively, the partial derivatives of the state transition function $f(w,v) = \frac{dw}{dt}$ are evaluated in Equation 3 and Equation 4.

$$K_v = \frac{\partial f}{\partial v}|_{(w_0, v_0)} = \frac{\mu_v R_{ON}}{D.M(w_0)} \tag{3}$$

$$a_w = \frac{\partial f}{\partial v}|_{(w_0, v_0)} = \frac{\mu_v R_{ON}(R_{OFF} - R_{ON}) v_0}{D^2.\left[M(w_0)\right]^2} \tag{4}$$

To prevent numerical overflow and normalize the controller operating universe, the physical state variable is converted into a dimensionless form as $x(t) = w(t)/D \in [0,1]$. Applying the Laplace transform under zero initial conditions yields the input–output small-signal transfer function presented in Equation 5.

$$G(s) = \frac{\Delta X(s)}{\Delta V(s)} = \frac{K_{norm}}{s + a_w} = \frac{K_m}{\tau_m s + 1} \tag{5}$$

Where $K_{norm} = K_v / D$, the steady-state gain is $K_m = K_{norm} / a_w$ and the plant time constant is defined as $\tau_m = 1/a_w$. In this study, standard physical parameters reported in experimental literature are adopted: total device thickness $D = 10$ nm, average ion mobility $\mu_v = 10^{-14}$ m^2/V.s, low-state resistance $R_{ON} = 100\Omega$, high-state resistance $R_{OFF} = 10k\Omega$, nominal operating bias voltage $v_0 = 1$V and nominal state position $w_0 / D = 0.5$ ($w_0 = 5$ nm, $M(w_0) = 5050\Omega$). Substituting these numerical parameters into Eq. 3–5 yields the explicit continuous-time transfer function given in Equation 6.

$$G(s) = \frac{\Delta X(s)}{\Delta V(s)} = \frac{1.9802}{s + 3.8820} = \frac{0.5101}{0.2576 s + 1} \tag{6}$$

This plant model exhibits an asymptotically stable, first-order lag dynamic with a pole situated in the open left-half s-plane at $s = -3.8820$.

B. Filtered PI-Type Intuitionistic Takagi–Sugeno Fuzzy Logic Controller Architecture

The proposed closed-loop control architecture utilizes two primary input variables to perform precise state-tracking of the memristive system. The first input is the tracking error, defined as the instantaneous difference between the desired reference state $x_{ref}(t)$ and the measured physical state $x(t)$, given by $e(t) = x_{ref}(t) - x(t)$. The second input is the rate of change of the error. To prevent pure differentiation from amplifying high-frequency numerical solver noise and inducing chattering phenomena during rule-boundary transitions, the error signal is passed through a first-order low-pass filter block ($H_f(s)$) to generate the filtered error derivative ($e_{dot}(t)$). The filter transfer function is defined in Equation 7.

$$E_{dot}(s) = H_f(s) \cdot E(s) = \frac{N \cdot s}{s+N} \cdot E(s) = \frac{2s}{s+2} \cdot E(s) \tag{7}$$

Where the filter cut-off frequency is selected as $N = 2$ rad/s. The universe of discourse for the inputs is defined over the normalized interval $[-\infty, \infty]$. For each input variable ($e(t)$ and $e_{dot}(t)$), five symmetrical triangular fuzzy sets are defined: Negative Big (NB), Negative Small (NS), Zero (Z), Positive Small (PS), and Positive Big (PB), which are illustrated in Figure 1. Furthermore, in accordance with the Takagi–Sugeno singleton formulation, five discrete crisp singleton levels are defined for the incremental control output $\Delta u(t) \in [-1,1]$ using the same linguistic labels (NB, NS, Z, PS, PB), which are depicted in Figure 2.

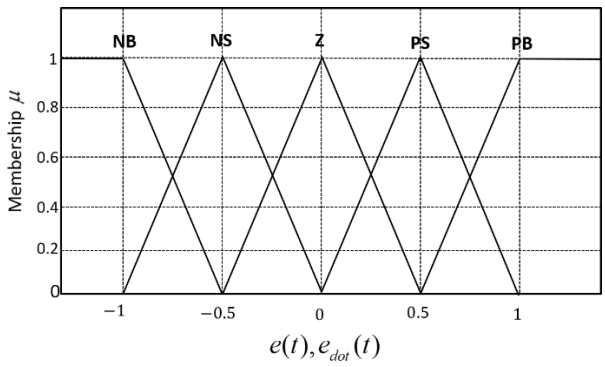

Fig. 1 Fuzzy controller inputs

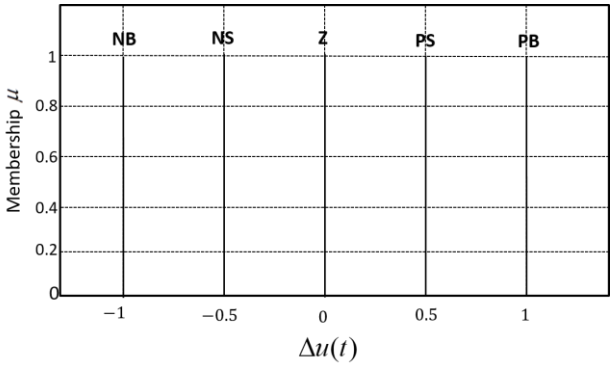

Fig. 2 Fuzzy controller outputs

Unlike conventional fuzzy sets, the Intuitionistic Fuzzy Logic framework assigns both a membership degree $\mu(x)$ and a non-membership degree $\upsilon(x)$ to each linguistic term. In this study, the non-membership functions are calculated analytically using the Sugeno generator method with a parameter of $\lambda = 0.8$, as formulated in Equation 8.

$$\upsilon(x) = \frac{1-\mu(x)}{1+\lambda\mu(x)} \tag{8}$$

This analytical formulation strictly satisfies the fundamental intuitionistic condition $0 \le \mu(x) + \upsilon(\mathrm{x}) \le 1$ throughout the entire input domain . The hesitation degree $\pi(x)$ representing the inherent uncertainty margin for each linguistic term, is subsequently determined by subtracting the sum of membership and non-membership grades from unity via Equation 9.

$$\pi(x) = 1 - \mu(\mathrm{x}) - \upsilon(\mathrm{x}) \tag{9}$$

Consequently, a total of 10 membership degrees, 10 non-membership degrees, and 10 hesitation degrees are computed from the two controller inputs and transmitted to the inference mechanism.

C. Inference Engine, Defuzzification, and Closed-Loop Control Scheme

The rule base of the proposed controller comprises 5x5=25 rules formulated from the linguistic combinations of the two input subsets. In accordance with the Takagi–Sugeno singleton architecture, the rule consequents are defined as crisp singleton values ($z_j \in \{-1.0, -0.5, 0.0, 0.5, 1.0\}$). The complete rule base structure is summarized in Table 1.

Table 1. Rule base of the intuitionistic Takagi–Sugeno fuzzy controller

		e				
		NB	**NS**	**Z**	**PS**	**PB**
e_{dot}	**NB**	NB	NB	NB	NS	Z
	NS	NB	NB	NS	Z	PS
	Z	NB	NS	Z	PS	PB
	PS	NS	Z	PS	PB	PB
	PB	Z	PS	PB	PB	PB

During the inference phase, the antecedent aggregation for each j-th rule (j=1,2,3…..25) is executed using the standard minimum t-norm operator. The rule membership activation degree α_j and non-membership activation degree β_j are evaluated according to Equation 10 and 11, respectively:

$$\alpha_j = \min(\mu_{A_j}(e), \mu_{B_j}(e_{dot})) \tag{10}$$

$$\beta_j = \max(\upsilon_{A_j}(e), \upsilon_{B_j}(e_{dot})) \tag{11}$$

Because the rule consequents are represented by crisp singletons ($\mu_{C_j} = 1$, $\upsilon_{C_j} = 0$), applying Mamdani implication yields the resultant membership degree $\mu_{D_j} = \min(\alpha_j, 1) = \alpha_j$ and non-membership degree $\upsilon_{D_j} = \max(\beta_j, 0) = \beta_j$ for each individual rule. The corresponding hesitation degree is subsequently computed via $\pi_{D_j} = 1 - \mu_{D_j} - \upsilon_{D_j}$.

In the defuzzification stage, the Intuitionistic Weighted Average (IWA) method, which explicitly incorporates both the membership and hesitation components of the intuitionistic fuzzy information, is employed. The incremental control signal $\Delta u(t)$ is determined using a hesitation weighting factor of $w = 1$, as formulated in Equation 12.

$$\Delta u(t) = \frac{\sum_{j=1}^{25} z_j(\mu_{D_j} + w\pi_{D_j})}{\sum_{j=1}^{25} (\mu_{D_j} + w\pi_{D_j})} \tag{12}$$

To prevent numerical singularity in instances where the denominator approaches zero, the controller output is default-assigned to $\Delta u(t) = 0$.

The overall closed-loop block diagram of the proposed intuitionistic Takagi–Sugeno fuzzy control system for memristive state regulation is depicted in Fig. 3. The system consists of a reference state input $x_{ref}(t)$, a unity feedback error calculation junction, a derivative filter block ($H_f(s) = \frac{2s}{s+2}$), an error-derivative scaling gain ($K_{de} = 0.15$), the intuitionistic fuzzy controller block, an output integrator ($1/s$), an output scaling gain ($K_u = 3.5$) and the continuous-time small-signal memristor plant model. The incremental control signal $\Delta u(t)$ generated by the IWA defuzzification stage is passed through the integrator and multiplied by the scaling gain K_u, thereby producing the total control voltage $v(t) = K_u \int \Delta u(t) dt$ applied directly to the memristor terminal. This velocity-form PI-type architecture completely eliminates steady-state tracking error while guaranteeing smooth, well-damped, and chattering-free reference tracking.

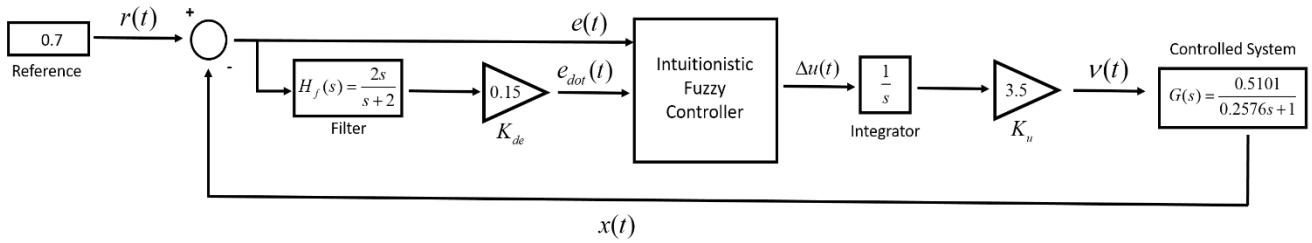

Fig. 3 Overall closed-loop block diagram of the proposed control system

III. RESULTS

To evaluate the dynamic state-tracking performance of the proposed filtered PI-type intuitionistic Takagi–Sugeno fuzzy logic controller, closed-loop simulation studies were conducted on the first-order continuous-time memristor model within the MATLAB/Simulink environment. Numerical simulations were carried out over a simulation duration of 8 seconds using the Runge–Kutta based "ode4" fixed-step solver with a fundamental step size of 0.001 s. The tracking response of the normalized state variable starting from rest $x(0)=0$ to a constant step reference of $r(t)=x_{ref}(t)=0.7$ is illustrated in Figure 4. As observed from the transient trajectory, the state output $x(t)$ rises smoothly and monotonically toward the target reference without exhibiting any overshoot ($M_p=\%0$) achieving complete convergence to the setpoint in approximately 1.425 s.

The trajectories of the closed-loop tracking error $e(t)$ and the filtered error derivative $e_{dot}(t)$ are depicted in Figure 5 and Figure 6, respectively . As shown in Figure 5, the tracking error signal, which initiates at $e(0)=0.7$, decays rapidly toward zero under the driving action generated by the intuitionistic fuzzy controller. The filtered error-derivative profile in Figure 6 exhibits a brief dynamic excursion reaching 0.21 due to the abrupt reference step transition; however, the low-pass filter effectively attenuates high-frequency numerical spikes, allowing the derivative signal to settle swiftly and smoothly back to the zero baseline within 2.5s. The simultaneous convergence of both input variables to near-zero values ensures that the central region (Zero rule) of the rule base becomes dominant in steady state.

The time evolution of the driving control voltage $v(t)$ applied across the memristor terminal is presented in Fig. 7. During the initial transient phase, large values of error and error derivative prompt the controller to produce a decisive positive control effort to accelerate state migration, reaching a peak voltage of $v_{peak}=1.380\,\text{V}$ at $t\approx 1.1\,\text{s}$. As the state variable tracks the reference trajectory, the control voltage smoothly relaxes and converges precisely to its theoretical steady-state value of $v_{ss}=1.372\,\text{V}$. This applied voltage profile strictly remains within the physical operating voltage limits of the memristor device, thereby preventing dielectric breakdown. The quantitative transient and steady-state performance metrics obtained from the simulation are summarized in Table 2.

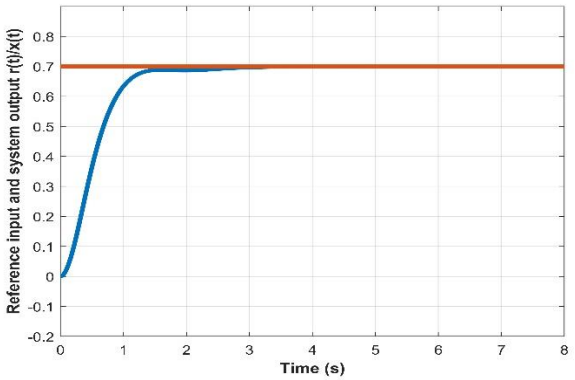

Fig. 4 Reference and memristor state output response

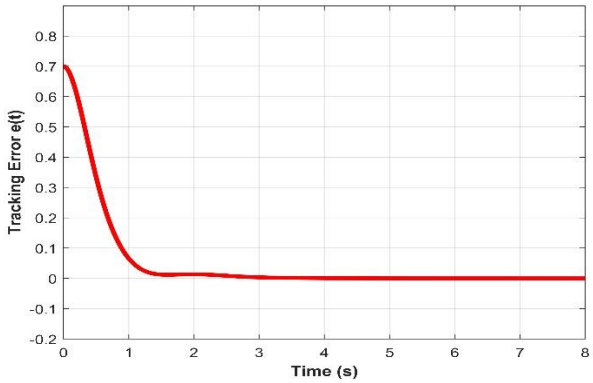

Fig. 5 State tracking error response

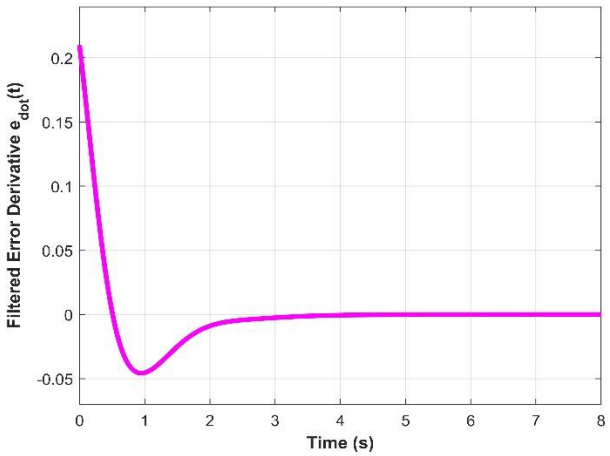

Fig. 6 Filtered error-derivative response

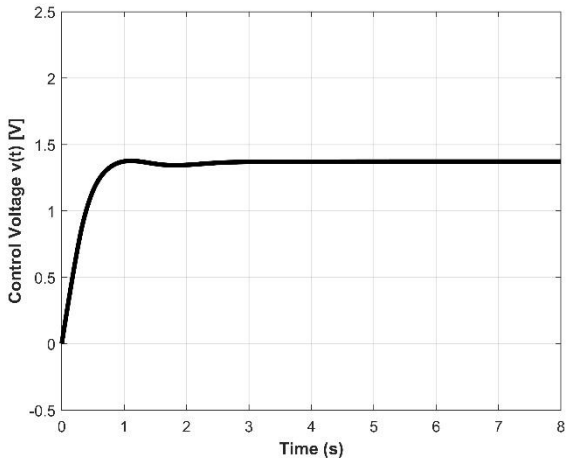

Fig.7 Control voltage signal applied to the memristor

Table 2. Closed-Loop System Performance Metrics

Performance Metric	Symbol	Numerical Value	Unit	Description / Reading Condition
Rise Time (10% to 90%)	t_r	0.812	s	Time required for $x(t)$ to rise from 0.07 to 0.63
Settling Time (2% band)	t_s	1.425	s	Time required for $x(t)$ to enter and remain within ±2% error band
Maximum Overshoot	M_P	0	%	Percentage peak deviation beyond the reference state ($x_{ref} = 0.7$)
Steady-State Error	e_{ss}	0	-	Residual tracking error at settling (t=8s, order of 10^{-6})
Peak Control Voltage	v_{peak}	1.380	V	Maximum transient voltage produced during startup ($t \approx 1.1$ s)
Steady-State Control Voltage	v_{ss}	1.372	V	Residual control voltage maintained across the memristor at steady state

IV. DISCUSSION

The simulation results verify that the proposed filtered PI-type intuitionistic Takagi–Sugeno fuzzy logic controller achieves fast, well-damped, and accurate reference tracking for the first-order memristor model. The closed-loop system reaches the target state ($x_{ref} = 0.7$) with a rise time of $t_r = 0.812$ s, a settling time of $t_s = 1.425$ s and completely zero overshoot ($M_p = \%0$). As tracking errors decay, the control effort transitions smoothly from its initial peak ($v_{peak} = 1.380$ V) to the steady-state operating level ($v_{ss} = 1.372$ V), eliminating steady-state error.

Incorporating non-membership degrees and hesitation via the Sugeno generator ($\lambda = 0.8$) provides an extra degree of freedom, yielding a smoother and more robust control surface compared to standard Takagi–Sugeno fuzzy controllers . Furthermore, feeding the error derivative through the first-order low-pass filter ($H_f(s) = \frac{2s}{s+2}$) effectively suppresses high-frequency noise and eliminates control chattering . While the controller demonstrates superior tracking within safe voltage boundaries, future investigations should evaluate its robustness against non-ideal hardware effects such as nonlinear window boundaries and thermal drift in physical neuromorphic arrays.

V. CONCLUSION

In this study, a filtered PI-type Intuitionistic Takagi–Sugeno Fuzzy Logic Controller utilizing the tracking error and its low-pass filtered derivative was successfully developed and evaluated in the MATLAB/Simulink environment for memristive state regulation in neuromorphic computing circuits. Closed-loop simulations conducted on an authentic physical parameter-derived first-order small-signal memristor model demonstrated that the proposed control scheme achieves swift, smooth, and monotonic reference tracking, settling at the target state ($x_{ref} = 0.7$) in 1.425s with completely zero overshoot and zero steady-state error. The integrated low-pass derivative filter successfully eliminated high-frequency numerical chattering, while the generated control voltage remained strictly within the safe operating limits of the device. These findings confirm that the proposed intuitionistic fuzzy control architecture offers a robust, well-damped, and reliable closed-loop solution for precision synaptic weight tuning in neuromorphic hardware platforms. Future work will focus on evaluating the disturbance-rejection capability of the controller under severe parametric uncertainties and nonlinear window boundary conditions on physical memristive crossbar arrays.

REFERENCES

[1] L. Chua, "Memristor-the missing circuit element," *IEEE Transactions on circuit theory*, 18(5), 507-519, 1971.

[2] D.B. Strukov, G.S. Snider, D.R. Stewart and R.S. Williams, "The missing memristor found," *Nature*, 453(7191), 80-83, 2008.

[3] S. H. Jo, T. Chang, I. Ebong, B.B. Bhadviya, P. Mazumder, and W. Lu, "Nanoscale memristor device as synapse in neuromorphic systems," *Nano letters*, 10(4), 1297-1301, 2010.

[4] J. J. Yang, D. B. Strukov and D. R. Stewart, "Memristive devices for computing," *Nature nanotechnology*, 8(1), 13-24, 2013.

[5] M. A. Zidan, J. P. Strachan and W. D. Lu, "The future of electronics based on memristive systems," *Nature electronics*, 1(1), 22-29, 2018.

[6] A. Ascoli, A. S. Demirkol, R. Tetzlaff, S. Slesazeck, T. Mikolajick and L. Chua, "On local activity and edge of chaos in a NaMLab memristor," *Frontiers in Neuroscience*, 15, 651452, 2021.

[7] S. O. Park, H. Jeong, J. Park, J. Bae and S. Choi, "Experimental demonstration of highly reliable dynamic memristor for artificial neuron and neuromorphic computing," *Nature Communications*, 13(1), 2888, 2022.

[8] Y. Zhang and L. Shen, "Automatic learning rate adaption for memristive deep learning systems," *IEEE Transactions on Neural Networks and Learning Systems*, 35(8), 10791-10802, 2023.

[9] W. Cao and J. Qiao, "Resistance tracking control of memristors based on iterative learning," *Entropy*, 25(5), 774, 2023.

[10] C. Sánchez-López, V. H. Carbajal-Gómez, M. A. Carrasco-Aguilar and F. E. Morales-López, "PID controller design based on memductor," *AEU-International Journal of Electronics and Communications*, 101, 9-14, 2019.

[11] S. B. Joseph, E. G. Dada, A. Abidemi, D. O. Oyewola and B. M. Khammas, "Metaheuristic algorithms for PID controller parameters tuning: Review, approaches and open problems," *Heliyon*, 8(5), 2022.

[12] H. J. Zimmermann, *Fuzzy set theory—and its applications*. Springer Science & Business Media, New York, USA, 2011.

[13] T. Takagi and M. Sugeno, "Fuzzy identification of systems and its applications to modeling and control," *IEEE transactions on systems, man and cybernetics*, 15(1), 116-132, 1985.

[14] L. A. Zadeh, "Fuzzy sets," *Information and control*, 8(3), 338-353, 1965.

[15] K. T. Atanassov, "Intuitionistic fuzzy sets", In *Intuitionistic fuzzy sets: theory and applications* (pp. 1-137). Heidelberg: Physica-Verlag HD, 1999.

[16] F. Aguirre, A. Sebastian, M. Le Gallo, W. Song, T. Wang, J. J. Yang and M. Lanza, "Hardware implementation of memristor-based artificial neural networks," *Nature communications*, 15(1), 2024.

[17] L. A. Camuñas-Mesa, B. Linares-Barranco and T. Serrano-Gotarredona, "Neuromorphic spiking neural networks and their memristor-CMOS hardware implementations," *Materials*, 12(17), 2745, 2019.

[18] M. Bavandpour, S. Bagheri-Shouraki, H. Soleimani, A. Ahmadi and B. Linares-Barranco, "Spiking neuro-fuzzy clustering system and its memristor crossbar based implementation," *Microelectronics Journal*, 45(11), 1450-1462, 2014.

[19] S. Helmy, M. Magdy and M. Hamdy, "Control in the loop for synchronization of nonlinear chaotic systems via adaptive intuitionistic neuro-fuzzy: a comparative study," *Complex & Intelligent Systems*, 8(4), 3437-3450, 2022.

[20] M. Hamdy, M. Magdy and S. Helmy, "Control and synchronization for two Chua systems based on intuitionistic fuzzy control scheme: A comparative study," *Transactions of the Institute of Measurement and Control*, 43(7), 1650-1667, 2021.

8th International Conference on Engineering, Natural and Social Sciences

September 6-7, 2026: Konya, Turkey

© 2026 Published by All Sciences Academy

https://www.icensos.com/

Investigation of the Effects of Drilling Parameters on the Surface Roughness of EN AW-5083 Aluminum Alloy

ÇERLEK, Ömer*

[1]Department of Mechanical Engineering/Faculty of Technology, Sakarya University of Applied Sciences, Turkey

*omercerlek@subu.edu.tr

Abstract – In this study, the effects of rotational speed, feed rate, and lubrication level(MQL flow rate) on the surface roughness of EN AW-5083 aluminum alloy were experimentally investigated during machining. A Taguchi L9 orthogonal array was employed to design nine experimental conditions, and surface roughness was used as the main performance indicator for evaluating the machined surface quality. The experimental results were analyzed using the Taguchi method to determine the influence of the selected process parameters and to identify favorable machining conditions. The results showed that rotational speed was the most influential parameter, followed by feed rate and lubrication level. Increasing the rotational speed generally resulted in a reduction in surface roughness, while the lowest feed rate provided more favorable surface quality. The effect of lubrication flow rate was less pronounced than those of rotational speed and feed rate. The results showed that increasing the flow rate did not lead to a systematic reduction in surface roughness under the investigated conditions. Among the nine experimental conditions, the lowest surface roughness value of 1.00 µm was obtained at a rotational speed of 1100 rpm, a feed rate of 0.1 mm/rev, and an MQL flow rate of 15 mL/h. Overall, the findings demonstrate that appropriate selection and combination of machining parameters is essential for improving the surface quality of EN AW-5083 aluminum alloy.

Keywords – drilling, surface, roughness, quality, machining

I. INTRODUCTION

Aluminum alloys have become increasingly important in modern manufacturing due to their low density, high strength-to-weight ratio, good corrosion resistance, and suitability for a wide range of manufacturing processes. These characteristics make aluminum alloys attractive for applications in the automotive, aerospace, marine, transportation, and general engineering industries. Among the wrought aluminum alloys, the 5xxx series alloys, which are primarily alloyed with magnesium, are particularly attractive because of their combination of mechanical strength, weldability, formability, and corrosion resistance. EN AW-5083, also commonly designated as AA5083 or AlMg4.5Mn, is one of the most widely used alloys in this group. The alloy contains approximately 4–5% magnesium together with manganese and chromium additions and is classified as a non-heat-treatable aluminum alloy. Its relatively high strength among non-heat-treatable aluminum alloys, together with its excellent resistance to seawater and general environmental corrosion, has resulted in extensive use in shipbuilding, transportation structures, pressure vessels, automotive components, and other engineering applications [1,2].

Although EN AW-5083 provides advantageous mechanical and corrosion properties, obtaining the required dimensional accuracy and surface quality during drilling can be challenging. Aluminum alloys generally exhibit high thermal conductivity and relatively low hardness compared with many ferrous alloys, while their ductility and tendency to adhere to cutting tools may promote material adhesion and built-up edge formation during drilling. Such phenomena can negatively affect the stability of the cutting process and may result in deterioration of the machined surface, dimensional deviations, and increased

tool wear. Consequently, appropriate selection of machining conditions is essential for obtaining a high-quality surface when drilling EN AW-5083. The selection of cutting parameters is particularly important in drilling because the interaction between cutting speed, feed rate, tool geometry, chip formation, cutting temperature, and friction directly influences the resulting surface texture.

Surface roughness is one of the most commonly used indicators for evaluating the quality of a machined surface. In drilling operations, surface roughness is influenced by both the geometrical characteristics of the cutting operation and the physical phenomena occurring in the cutting zone. Feed rate, spindle speed, depth of cut, radial engagement, tool geometry, tool condition, and lubrication or cooling conditions may all affect the final surface characteristics. In particular, excessive feed rates can increase the theoretical scallop height and material deformation, whereas appropriate increases in cutting speed may improve the surface finish by modifying chip formation and reducing the tendency for material adhesion under suitable drilling conditions. Therefore, optimization of cutting parameters is necessary when high surface quality is required, particularly for components used in applications where dimensional accuracy and surface integrity are critical.

Previous studies have demonstrated the importance of cutting parameters in the milling of AA5083. Samtaş investigated the face milling of AA5083-H111 using coated and uncoated cutting inserts and evaluated the effects of cutting depth, cutting speed, feed rate, and insert type using the Taguchi method. The study employed cutting speeds of 450, 550, and 650 m/min and feed rates of 0.08, 0.12, and 0.25 mm/tooth. The results demonstrated that the appropriate selection of cutting conditions could considerably improve the obtained surface roughness, with the confirmation experiments reducing the surface roughness from approximately 0.52 μm to 0.24 μm [3].

Similarly, Başar et al. investigated the mathematical modelling and optimization of face milling parameters for AA5083. Feed rate, spindle speed, and depth of cut were selected as input variables, and response surface methodology was employed to develop a mathematical model for surface roughness. Their analysis indicated that feed rate and spindle speed were the most influential parameters affecting surface roughness. The optimized condition resulted in a surface roughness of approximately 0.41 μm at a feed rate of 3008 mm/min, spindle speed of 5981 rpm, and depth of cut of 0.54 mm. These findings confirm that drilling parameters, particularly feed rate and spindle speed, play an important role in determining the surface quality obtained during milling of AA5083 [4].

More recently, Kechagias investigated finish end milling of AA5083 using a two-flute carbide cutter and examined the effects of radial depth of cut, feed per tooth, and spindle speed on surface roughness parameters. Twenty-seven experiments were performed, and signal-to-noise ratio analysis was used for process optimization. The results indicated that a radial depth of cut of 0.5 mm, a spindle speed of 6000 rpm, and a feed of approximately 0.082 mm/tooth provided favorable surface roughness characteristics within the investigated experimental range [5]. The study also emphasized that surface integrity in AA5083 machining is strongly related to cutting conditions and that the selection of suitable parameters is particularly important because surface defects can influence the functional performance of components operating in demanding environments.

Another study on thin-walled AA5083-H111 components investigated the effects of wall thickness, cutting speed, and feed rate under dry machining conditions. Using a Taguchi L32 experimental design, the authors reported that feed rate was the most influential parameter, contributing 57.14% to the variation in surface roughness. The optimum combination for the investigated conditions was obtained at a 5 mm wall thickness, 0.05 mm/tooth feed rate, and 200 m/min cutting speed [6]. These results further demonstrate that the relative importance of machining parameters may depend on the machining configuration, tool characteristics, and workpiece geometry.

Sadiq et al. [7] investigated the effects of drilling parameters on the surface roughness of AA5083 together with AA6061-T6 and LM6 aluminum alloys. The experiments were conducted using an HSS drill at different spindle speeds and feed rates. Their results showed that surface roughness generally decreased with increasing spindle speed. For AA5083, a minimum surface roughness of 4.9 μm was obtained at a feed rate of 0.15 mm/rev and a spindle speed of 1000 rpm. These findings demonstrate the importance of spindle speed and feed rate in determining the surface quality of AA5083 during drilling.

Bayraktar [8] experimentally investigated the effects of spindle speed, feed rate, and drill point angle on the drilling performance of Al-5083 alloy using uncoated and TiN-coated HSS drills. A Taguchi L9 orthogonal array was employed with spindle speeds of 400, 800, and 1200 rpm and feed rates of 0.1, 0.2, and 0.3 mm/rev. Their results indicated that feed rate was the most influential parameter for thrust force and burr height, followed by spindle speed and drill point angle. The study highlights the significant role of feed rate in controlling drilling performance of Al-5083 alloy.

In addition to conventional cutting parameters, the cooling and lubrication condition represents another important factor affecting machining performance. The use of cutting fluids can reduce friction and heat generation in the cutting zone, facilitate chip evacuation, and potentially reduce adhesion between the workpiece material and cutting tool. However, conventional flood lubrication requires relatively large quantities of cutting fluid and introduces additional environmental, health, cleaning, and disposal concerns. For these reasons, environmentally more sustainable approaches such as dry machining and minimum quantity lubrication (MQL) have received increasing attention. MQL supplies a very small quantity of lubricant, generally transported by compressed air directly to the cutting zone, thereby providing lubrication while considerably reducing fluid consumption compared with conventional flood systems.

The influence of lubrication is particularly relevant for aluminum alloys because adhesion and friction at the tool–workpiece interface can significantly affect the machined surface. Previous investigations on aluminum alloy machining have reported that MQL can influence tool wear, cutting forces, cutting temperature, and surface quality. For example, studies on AA6061 end milling under MQL conditions have investigated lubricant flow rates in the range of approximately 0.65–1.0 mL/min, while other studies have used oil-based MQL flow rates of approximately 0.48–0.83 mL/min. These studies demonstrate that the lubricant supply rate can be treated as an experimental process variable rather than simply as a qualitative cooling condition [9].

The unit used to define the lubrication parameter is therefore important. When MQL is employed, lubrication should preferably be expressed quantitatively as lubricant flow rate, rather than simply lubrication. Depending on the MQL equipment and experimental methodology, the flow rate may be reported in mL/min or mL/h. Both units are encountered in the machining literature; however, the selected unit must be clearly defined together with the lubricant type, air pressure, nozzle configuration, and application method. For example, MQL studies have reported flow rates in mL/h, while other aluminum machining studies have used mL/min [10]. Therefore, if the present experimental system controls the quantity of lubricant supplied to the cutting zone, the parameter is appropriately defined as MQL flow rate (mL/h) or MQL flow rate (mL/min) according to the actual specification of the equipment.

Despite the increasing number of studies concerning the optimization of machining parameters for AA5083, most investigations have primarily focused on conventional cutting parameters such as spindle speed, feed rate, and depth of cut or radial depth of cut. Several studies have also specifically investigated AA5083 under dry machining conditions [3–6]. However, the combined effect of spindle speed, feed rate, and a quantitatively defined lubrication condition on the surface quality of EN AW-5083 remains an important area for further investigation. In particular, evaluating lubrication as a controllable process parameter can provide additional information regarding the relationship between cutting conditions, frictional effects, and the resulting surface roughness.

Accordingly, the present study investigates the effects of rotational speed, feed rate, and lubrication condition on the surface quality obtained during drilling of EN AW-5083 aluminum alloy. Surface roughness is used as the primary response variable for evaluating drilling quality. The experimental study aims to determine the influence of each process parameter and to identify the combination of drilling conditions that provides improved surface quality. In contrast to studies focusing only on cutting parameters, the present approach additionally considers lubrication as an experimentally controlled variable. The findings are expected to contribute to the understanding of the machinability of EN AW-5083 and provide practical guidance for selecting suitable drilling conditions for achieving improved surface quality.

II. MATERIALS AND METHOD

In this study, the effects of rotational speed, feed rate, and lubrication condition on the surface quality of EN AW-5083 aluminum alloy were experimentally investigated during drilling.

EN AW-5083 aluminum alloy specimens were machined using a drilling machine. Three different levels were selected for each process parameter. The rotational speed was selected as 270, 540, and 1100 rpm, while the feed rate was set at 0.1, 0.2, and 0.3 mm/rev. In addition to these cutting parameters, the lubrication condition was considered as the third process parameter. When minimum quantity lubrication (MQL) was used, the lubrication parameter was defined quantitatively according to the lubricant flow rate (mL/h). The experimental conditions were arranged by combining the three levels of rotational speed, feed rate, and lubrication condition.

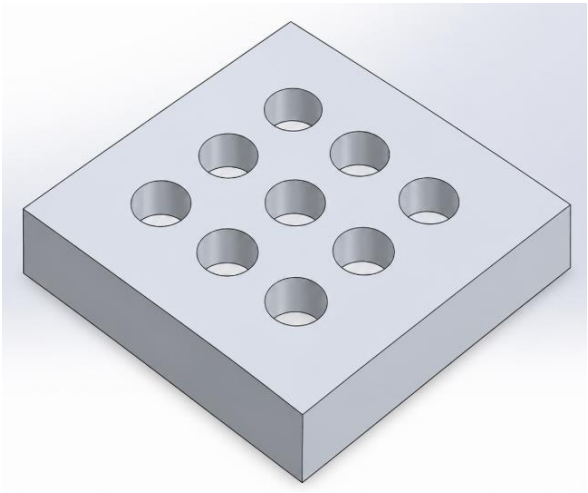

Figure 1. Schematic representation of the drilling specimen and hole arrangement.

The drilling operations were performed according to the experimental design, and the resulting machined surfaces were evaluated in terms of surface roughness. After each drilling operation, surface roughness measurements were taken from different locations on the machined surface. The average of the measured values was used as the representative arithmetic mean surface roughness (R_a) for each experimental condition. The obtained results were then compared to determine the effects of rotational speed, feed rate, and lubrication condition on the surface quality of EN AW-5083 aluminum alloy.

The experimental parameters used in the study are summarized in Table 1.

Table 1. Experimental parameters.

Parameter	Unit	Level 1	Level 2	Level 3
Rotational Speed	rpm	270	540	1100
Feed Rate	mm/rev	0.1	0.2	0.3
MQL Flow Rate	mL/h	0	5	15

III. RESULTS

The surface roughness results obtained from the drilling experiments of EN AW-5083 aluminum alloy are presented in Table 2. The effects of rotational speed, feed rate, and lubrication level(flow rate) on the surface quality were evaluated based on the measured arithmetic mean surface roughness (R_a) values. Lower R_a values indicate better surface quality.

Table 2. Experimental results.

Rotational Speed(rpm)	Feed Rate(mm/rev)	MQL Flow Rate(mL/h)	Average Surface Roughness(µm)
270	0.1	0	1.412
270	0.2	5	2.441
270	0.3	15	1.950
540	0.1	5	1.260
540	0.2	15	2.272
540	0.3	0	1.544
1100	0.1	15	1.000
1100	0.2	0	1.155
1100	0.3	5	1.370

The experimental results show that rotational speed has a noticeable effect on surface roughness. The average surface roughness values at rotational speeds of 270, 540, and 1100 rpm were 1.934, 1.692, and 1.175 µm, respectively. Thus, increasing the rotational speed resulted in a general reduction in surface roughness. The lowest average R_a value was obtained at 1100 rpm, indicating that higher rotational speed provided more favorable surface quality under the investigated conditions.

As shown in Fig. 2, the S/N ratio increased with increasing rotational speed, indicating that higher rotational speeds provided lower surface roughness. The highest S/N ratio was obtained at 1100 rpm. For feed rate, the highest S/N ratio was obtained at 0.1 mm/rev, indicating that the lowest feed rate was more favorable for surface quality. In terms of flow rate, the highest S/N ratio was obtained at 0 mL/h, while increasing the flow rate to 5 and 15 mL/h resulted in lower S/N ratios. Overall, the main effects plot indicates that rotational speed had the most pronounced effect on surface roughness, followed by feed rate and flow rate.

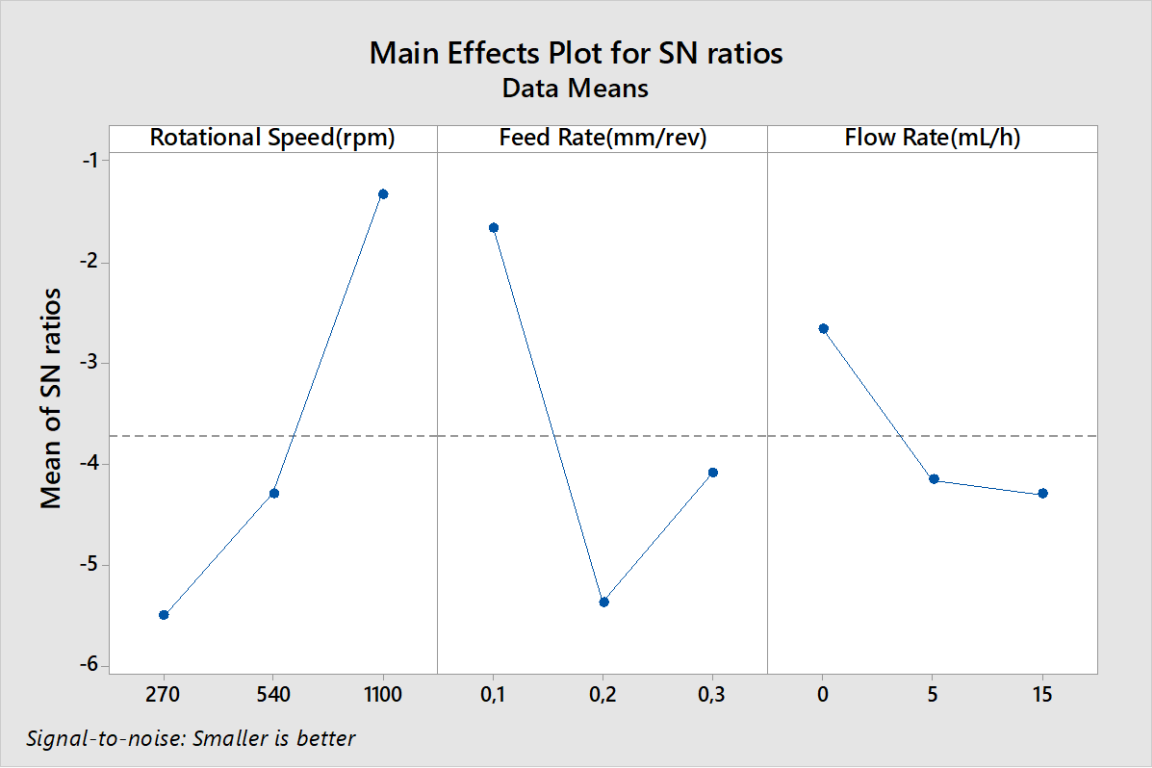

Fig. 2 Main effects plot for S/N ratios.

The feed rate also affected the obtained surface roughness. The average R_a values for feed rates of 0.1, 0.2, and 0.3 mm/rev were 1.224, 1.956, and 1.621 µm, respectively. The lowest average surface

roughness was obtained at a feed rate of 0.1 mm/rev, whereas the highest average value was observed at a feed rate of 0.2 mm/rev. Although the relationship was not completely linear, the results indicate that the lowest feed rate generally provided better surface quality.

The effect of lubrication was also examined by considering three lubrication levels of 0, 5, and 15 mL/h. The corresponding average surface roughness values were 1.370, 1.690, and 1.741 μm, respectively. Within the investigated experimental conditions, the dry condition (0 mL/h) produced the lowest average surface roughness, while the average $R_a$value increased with the lubrication level. This result indicates that increasing the lubricant flow rate did not directly improve surface quality for the tested conditions. However, the influence of lubrication should be evaluated together with rotational speed and feed rate because the parameters were varied simultaneously according to the experimental design.

Among all nine experiments, the best surface quality was obtained in Experiment 7, performed at 1100 rpm rotational speed, 0.1 mm/rev of feed rate, and a flow rate of 15 mL/h, with an $R_a$value of 1.00 μm. In contrast, the highest surface roughness of 2.441 μm was obtained in Experiment 2 at 270 rpm, a feed rate of 0.2 mm/rev, and a flow rate of 5 mL/h. The difference between these two conditions demonstrates the importance of selecting appropriate combinations of drilling parameters for improving the surface quality of EN AW-5083 aluminum alloy.

Among the experimentally tested conditions, the lowest surface roughness was obtained at 1100 rpm, 0.1 mm/rev, and 15 mL/h, with an Ra value of 1.00 μm. However, the main effects plot indicated that the combination of 1100 rpm, 0.1 mm/rev, and 0 mL/h corresponds to the best factor-level combination based on the S/N ratios.

Overall, the experimental results indicate that rotational speed was particularly effective in reducing surface roughness, with the average $R_a$decreasing from 1.934 μm at 270 rpm to 1.175 μm at 1100 rpm. The lowest feed rate also provided the most favorable average surface roughness. The effect of lubrication was comparatively different, as the average surface roughness did not decrease with increasing lubrication level. Further statistical evaluation using the Taguchi signal-to-noise ratio and analysis of variance (ANOVA) can additionally be performed to quantitatively evaluate the statistical significance and percentage contribution of each process parameter.

IV. DISCUSSION

The experimental results indicate that rotational speed had a considerable effect on surface roughness, with higher rotational speeds generally providing improved surface quality. This finding is consistent with the results reported by Samtaş [3], who investigated the face milling of AA5083-H111 using different cutting speeds and feed rates. The study reported that the selection of appropriate cutting parameters significantly affected surface roughness, and the optimized machining condition reduced the surface roughness from 0.52 μm to 0.24 μm.

Similarly, Özlü et al. [6] investigated the effects of cutting speed and feed rate on the surface roughness of AA5083-H111 under dry milling conditions. Their results showed that feed rate was an important parameter affecting surface roughness, which is consistent with the present study, where the lowest feed rate provided the lowest average surface roughness. However, differences in the optimum conditions can be attributed to differences in tool geometry, machining strategy, cutting conditions, and experimental parameter ranges.

The effect of flow rate on surface roughness was less pronounced compared with rotational speed and feed rate. As shown in Fig. 2, the highest S/N ratio was obtained under the dry condition (0 mL/h), while increasing the flow rate to 5 and 15 mL/h resulted in lower S/N ratios. This indicates that increasing the lubricant flow rate did not directly improve surface quality under the investigated conditions. The effect of lubrication may depend on its interaction with rotational speed and feed rate, and therefore should be evaluated together with the other drilling parameters.

The present findings are also consistent with the results reported by Sadiq et al. [7], who investigated the drilling of AA5083 and reported that surface roughness decreased with increasing spindle speed. In their study, a minimum surface roughness of 4.9 μm was obtained at 1000 rpm and 0.15 mm/rev. Similarly, the present study showed that increasing the rotational speed from 270 to 1100 rpm generally

reduced the average surface roughness, with the lowest value obtained at 1100 rpm. The differences in the obtained surface roughness values can be attributed to differences in drill geometry, material thickness, feed rate range, and experimental conditions.

The present study additionally considers lubrication level as a process parameter. Unlike the cutting parameters, increasing the lubrication level did not result in a direct reduction in average surface roughness. This suggests that the influence of lubrication may depend on its interaction with rotational speed and feed rate and should therefore be evaluated together with the other machining parameters.

V. CONCLUSION

In this study, the effects of rotational speed, feed rate, and lubrication level on the surface quality of EN AW-5083 aluminum alloy during drilling were experimentally investigated. Surface roughness was used as the main performance indicator, and nine different experimental conditions were evaluated.

The results demonstrated that rotational speed had a considerable effect on surface roughness. Increasing the rotational speed from 270 to 1100 rpm generally reduced the average surface roughness, with the lowest average value obtained at 1100 rpm. The feed rate also affected the surface quality, and the lowest average surface roughness was obtained at the lowest feed rate level. In contrast, increasing the lubrication level did not result in a direct improvement in surface roughness under the investigated conditions.

Among the experimental conditions, the lowest surface roughness value of 1.00 μm was obtained at a rotational speed of 1100 rpm, a feed rate of 0.1 mm/rev, and an MQL flow rate of 15 mL/h. The highest surface roughness value of 2.441 μm was obtained at a rotational speed of 270 rpm, a feed rate of 0.2 mm/rev, and an MQL flow rate of 5 mL/h. These findings indicate that an appropriate combination of drilling parameters is important for obtaining improved surface quality in EN AW-5083 aluminum alloy.

Overall, the experimental results suggest that higher rotational speed and lower feed rate provide more favorable surface quality within the investigated parameter ranges. The effect of MQL flow rate was less straightforward and should therefore be considered together with rotational speed and feed rate. Further studies using additional parameter levels and statistical optimization methods can provide a more comprehensive understanding of the drilling behavior of EN AW-5083 aluminum alloy.

REFERENCES

[1] A. Vinoth Jebaraj, K. V. V. Aditya, T. Sampath Kumar, L. Ajaykumar, and C. R. Deepak, “Mechanical and corrosion behaviour of aluminum alloy 5083 and its weldment for marine applications,” *Materials Today: Proceedings*, vol. 22, pp. 1470–1478, 2020, doi: 10.1016/j.matpr.2020.01.505.

[2] D. Żuk and G. Hajdukiewicz, “Modeling of a three-point bend test of a beam made of AW 5083 alloy,” Scientific Journal of Gdynia Maritime University, no. 116, pp. 100–111, 2020, doi: 10.26408/116.06.

[3] G. Samtaş, “Optimisation of cutting parameters during the face milling of AA5083-H111 with coated and uncoated inserts using Taguchi method,” International Journal of Machining and Machinability of Materials, vol. 17, no. 3/4, pp. 211–232, 2015. DOI: 10.1504/IJMMM.2015.071993.

[4] G. Başar, F. Kahraman, and G. T. Önder, “Mathematical Modeling and Optimization of Milling Parameters in AA 5083 Aluminum Alloy,” European Mechanical Science, vol. 3, no. 4, 2019.

[5] J. Kechagias, “Multiparameter signal-to-noise ratio optimization for end milling cutting conditions of aluminium alloy 5083,” The International Journal of Advanced Manufacturing Technology, vol. 132, pp. 4979–4988, 2024. DOI: 10.1007/s00170-024-13667-9.

[6] B. Özlü, U. Çelik, and H. Demir, “Serbest Formlu İnce Cidarlı AA 5083-H111 Alaşımının Frezelenmesinde Kesme Parametrelerinin Yüzey Pürüzlülüğü Üzerine Etkilerini Deneysel ve İstatiksel Değerlendirilmesi”, Afyon Kocatepe Üniversitesi Fen Ve Mühendislik Bilimleri Dergisi, vol. 23, no. 2, pp. 512–522, May 2023, doi: 10.35414/akufemubid.1145100.

[7] T. O. Sadiq, B. A. Hameed, J. Idris, O. Olaoye, S. Nursyaza, Z. H. Samsudin, and M. I. Hasnan, “Effect of different machining parameters on surface roughness of aluminium alloys based on Si and Mg content,” Journal of the Brazilian Society of Mechanical Sciences and Engineering, vol. 41, no. 10, p. 451, 2019, doi: 10.1007/s40430-019-1948-8.

[8] Ş. Bayraktar “Investigating of effects on thrust force and burr height of cutting parameters in dry drilling of Al-5083 alloy,” 16th International Materials Symposium (IMSP'2016), Denizli, Turkey, 2016.

[9] M. S. Najiha, M. M. Rahman, and A. R. Yusoff, “Flank Wear Characterization in Aluminum Alloy (6061 T6) With Nanofluid Minimum Quantity Lubrication Environment Using an Uncoated Carbide Tool,” Journal of Manufacturing Science and Engineering, vol. 137, 2015.

[10] B. Davoodi and A. H. Tazehkandi, “Experimental investigation and optimization of cutting parameters in dry and wet machining of aluminum alloy 5083 in order to remove cutting fluid,” Journal of Cleaner Production, vol. 68, pp. 234–242, 2014. DOI: 10.1016/j.jclepro.2013.12.056.

8th International Conference on Engineering, Natural and Social Sciences

September 06-07, 2026: Konya, Turkey

© 2026 Published by All Sciences Academy

https://www.icensos.com/

Packaging Design, Psychological Response, and Sustainability: An Empirical Model of Consumer Purchase Decisions

Irma Shyle*

Department of Production Management, Faculty of Mechanical Engineering, Polytechnic University of Tirana, Albania

**ishyle@fim.edu.al*

Abstract – Packaging is no longer a passive container; it functions as a marketing stimulus that shapes consumer inferences about a product before any direct interaction occurs. This study examines three mechanisms through which packaging may influence purchase decisions: the visual design of the package, the psychological and emotional response it elicits, and the consumer's perception of its environmental sustainability. Data were collected through a structured, five-point Likert questionnaire administered to 120 consumers of everyday products. Descriptive statistics, Cronbach's alpha, Pearson correlation, and multiple linear regression were applied to test three hypotheses derived from the Stimulus-Organism-Response framework. All three predictors were statistically significant and jointly explained 60% of the variance in the purchase decision, $R^2 = .600$, $F(3, 112) = 56.00$, $p < .001$. Visual design showed the weakest effect ($\beta = .199$, $p = .026$), followed by psychological and emotional response ($\beta = .274$, $p = .004$), while sustainability produced the strongest effect ($\beta = .448$, $p < .001$). This pattern indicates that, within the sample studied, perceived environmental credentials outweighed both aesthetic appeal and emotional response in predicting purchase intention. The principal contribution of the study lies not in introducing a new construct but in testing visual, emotional, and sustainability effects jointly within a single model, rather than in isolation, as most prior packaging research has done. Implications for packaging strategy, together with the study's limitations, including non-probability sampling, a cross-sectional design, a single-country sample, and reliance on self-report data, are also discussed.

Keywords – packaging design, consumer behavior, purchase decision, sustainability, ESG, multiple linear regression, Stimulus-Organism-Response

I. INTRODUCTION

Retail shelves are increasingly saturated with functionally similar products, which makes packaging one of the few remaining elements through which a company can differentiate its offer and one of the few cues a consumer evaluates before making a purchase decision. Originally intended to protect a product between production and sale, packaging has progressively acquired a marketing function, influencing how a product is perceived prior to use.

Marketing researchers have long referred to packaging as a "silent salesman," a term that entered the academic literature from trade practice, because it communicates brand value and product quality in the absence of a human seller. This function is particularly relevant at the point of sale, where purchase decisions are frequently made quickly, and where the colour, shape, or typography of a package may be the primary information a consumer processes before choosing a product.

Three strands of literature help explain why packaging exerts this influence. The first treats packaging as a visual and informational signal, in which colour, shape, and graphic elements shape first impressions and support quality inference [1], [2]. The second treats packaging as an emotional and cognitive cue that helps consumers reduce uncertainty about products they have not previously used [3], [4]. The third and more recent strand addresses sustainability, showing that the materials and messaging used in packaging affect

brand perception independently of the package's visual appearance, a development linked to growing environmental awareness among consumers [5], [6].

These three strands of research have developed largely independently. Most studies isolate a single dimension, whether visual, psychological, or environmental, and few examine all three within the same sample using a common statistical model. This gap has both theoretical and practical relevance: a packaging manager deciding whether to invest in improved graphics, more emotionally resonant branding, or recyclable materials has limited empirical grounds for prioritising one investment over another, because the existing literature has generally examined these dimensions separately. The present study addresses this gap directly.

Four objectives follow from this aim:

- to examine whether the visual elements of packaging design predict the purchase decision;
- to examine whether the psychological and emotional response to packaging predicts the purchase decision;
- to examine whether the perceived sustainability of packaging predicts the purchase decision;
- to compare the relative strength of these three effects within a single empirical model.

The remainder of the paper is organised as follows. Section II develops the theoretical framework and hypotheses. Section III describes the sample, instrument, and analytical procedure. Section IV reports the results. Section V discusses their implications. Section VI presents the conclusions, practical implications, limitations, and directions for future research.

II. Literature Review and Theoretical Framework

A. *Packaging Design as a Marketing Element*

Silayoi and Speece [1] distinguish two functional categories of packaging design: visual elements, such as colour, shape, typography, and graphics, that capture attention and establish an initial impression, and informational elements that allow a consumer to evaluate a product more deliberately. Both categories are relevant, but they operate differently: the former acts rapidly and largely outside conscious evaluation, whereas the latter requires the consumer to read the information provided on the package.

Kotler and Keller [7] position packaging within the marketing mix as a communication channel that frequently forms a consumer's first impression of an unfamiliar product. Ampuero and Vila [2] argue that packaging actively shapes perceived quality and trustworthiness, in some cases before the product itself has been used. Underwood [8] describes this as a branding function, whereby packaging establishes an emotional connection through visual and symbolic cues rather than through information transfer alone.

Colour has received particular empirical attention. Labrecque and Milne [9] show that colour carries relatively consistent emotional associations across consumers, with blue commonly associated with trustworthiness and red with energy and impulsiveness, associations sufficiently robust to function as a design variable. Shape and structure operate similarly in relation to perceived functionality and quality [4]. Beyond these signalling functions, packaging continues to serve its original purpose of protecting the product and informing consumers about its use and safety [10]. The relative weight assigned to these functions has increased with the growth of e-commerce and rising environmental awareness [3], [5], factors that were largely absent when much of the foundational literature on packaging was developed.

B. *Consumer Perception of Packaging Design*

Perception operates selectively: consumers do not process every stimulus presented by a package, but only those that register attention. Packaging is often the first such stimulus encountered during the purchase process [8], which gives it a disproportionate influence relative to the amount of information it conveys. Warm colours tend to be perceived as energetic, whereas cool colours are perceived as calm and professional [9]. Orth and Malkewitz [4] argue that consumers process these cues holistically rather than individually, so that the overall gestalt of a design, rather than any single feature, drives the resulting quality impression.

C. *Psychological and Emotional Influence*

Design influences how consumers feel about a product before they evaluate its functional attributes. Bloch [3] found that emotional reactions to design typically precede assessment of functional performance, indicating that affective response often precedes, and may substitute for, explicit reasoning. The concept of holistic package design proposed by Orth and Malkewitz [4] extends this argument: consumers respond to design as an integrated whole, and this integrated response influences brand attitude and purchase intention more strongly than an analysis of individual design features would predict.

Underwood [8] adds a longer-term perspective, noting that consistent and recognisable packaging builds trust and brand identity across repeated purchases, a mechanism distinct from, but complementary to, the immediate emotional response at the point of sale. Honea and Horsky [11] report a related memory effect, showing that packaging with a distinctive aesthetic context is more easily recalled, which is relevant to repeat purchase behaviour even after the initial emotional response has diminished.

D. *The Influence of Packaging on the Purchase Decision*

Kotler and Keller [7] describe the purchase decision as the outcome of perception, attitude, experience, and situational stimuli acting jointly, with packaging representing one input among several rather than the sole determinant. Silayoi and Speece [1] show that the relative weight of packaging increases specifically when information is limited or when competing alternatives appear similar; under such conditions, packaging functions as a quality signal that substitutes for information the consumer does not otherwise possess. Rettie and Brewer [12] examine this process at the point of sale, where attention is brief and recognition speed is more consequential than deliberate evaluation, conditions under which effective packaging can influence an otherwise unplanned purchase.

The theoretical link between these findings and the model examined in this study is provided by the Stimulus-Organism-Response (S-O-R) framework [13]. Within this framework, packaging, comprising its visual elements, colour, shape, and displayed information, constitutes the stimulus (S). The consumer's internal processing of that stimulus, operationalised here as visual perception and psychological/emotional response (X1 and X2), represents the organism stage (O). The purchase decision (Y) constitutes the response (R). This distinction is not merely terminological: it clarifies why the effect of packaging on purchase behaviour is indirect, mediated through perception and emotion rather than acting directly on the decision, and it justifies testing H1a and H1b as separate paths rather than combining them into a single construct. The same logic extends to sustainability: a consumer's perception of a package's environmental credentials (X3) can be understood as a third route through the same organism stage, in which environmental values, rather than aesthetic or emotional response, mediate the reaction to the packaging stimulus.

E. *Sustainability and Packaging (the ESG Dimension)*

Sustainability has shifted from a marginal concern to a mainstream purchase factor over approximately the past decade. Magnier and Crié [5] find that sustainable packaging improves brand perception directly, with consumers rating companies that use recyclable materials or reduced plastic more favourably, independent of the package's visual design. Peattie [6] documents a related willingness-to-pay effect, whereby consumers report willingness to pay a premium for environmentally credible products, although stated willingness-to-pay does not always correspond to actual purchase behaviour. White, Habib, and Hardisty [14] add a communication perspective relevant to this study, arguing that it is not sustainability itself but the effectiveness with which its benefits are communicated on the package that drives behavioural change; this is one reason the present study treats sustainability as a perception variable, reflecting what the consumer believes about the packaging, rather than as an objective material property.

F. *Research Gap and Contribution of This Study*

Individually, these findings are well established. Considered jointly, however, they are not: the visual, psychological, and sustainability literatures on packaging have developed largely in parallel, with each occasionally citing the others but rarely testing all three within the same model and the same sample. Much of the existing evidence also derives from developed-market samples, with Thailand, the United States,

Germany, and France appearing repeatedly across the studies cited above, which limits the generalisability of these findings to other contexts.

The contribution of this study follows directly from this gap. It incorporates visual design, psychological/emotional response, and sustainability perception into a single multiple regression model, estimated on the same 120 respondents, which makes it possible to compare their relative weight rather than simply confirming that each dimension matters in isolation.

G. *Hypotheses and Conceptual Model*

Consistent with the S-O-R framework described above, the main hypothesis is stated as follows:

H1: Packaging design has a positive and statistically significant effect on the consumer purchase decision.

This hypothesis is disaggregated into three specific paths:

- H1a: Perceived packaging design (X1) positively predicts the purchase decision (Y).
- H1b: Psychological/emotional response to packaging (X2) positively predicts the purchase decision (Y).
- H1c: Perceived packaging sustainability (X3) positively predicts the purchase decision (Y).

The conceptual model treats X1, X2, and X3 as independent predictors of Y, tested jointly in Sections III and IV.

III. METHOD

A. *Research Approach and Design*

This study adopts a quantitative, cross-sectional design in which data were collected once from each respondent. This design is appropriate for measuring current attitudes and their statistical association, but it implies that the results describe correlation rather than a confirmed causal sequence [15], [16]. The study is exploratory, in that it is among the first to examine these three packaging dimensions jointly, and explanatory, in that it tests specific, pre-specified directional hypotheses rather than describing attitudes alone [17]. Data were collected through a structured questionnaire distributed online via Google Forms.

B. *Population, Sample, and Instrument*

The target population consisted of consumers of everyday products, including food, beverages, hygiene products, and household items, selected because the purchase frequency in this category is sufficiently high that respondents have recent and concrete packaging experience on which to base their responses. The sample was a non-probability convenience sample [18], a common approach in exploratory consumer research where time and budget constraints preclude probability sampling. Eligibility required respondents to be over 18 years of age and regular purchasers of everyday products. Of 120 total responses, 116 were valid for the main regression model after incomplete cases were removed.

The questionnaire covered demographic characteristics, packaging design perception, psychological/emotional response, purchase decision, and sustainability perception, with items adapted from validated scales [1], [8], [5] to support content validity rather than developing new, untested items. All substantive items used a five-point Likert scale [19] (1 = strongly disagree to 5 = strongly agree).

C. *Study Variables*

Table 1 summarises the variables included in the model, their role, and their theoretical basis.

Table 1. Study Variables and Theoretical Sources

Variable	Role	Items	Theoretical Source
X1 – Packaging design	Independent	5	Silayoi & Speece [1]; Ampuero & Vila [2]
X2 – Psychological/emotional response	Independent	4	Bloch [3]; Orth & Malkewitz [4]
X3 – Sustainability (ESG)	Independent	3	Magnier & Crié [5]; Peattie [6]
Y – Purchase decision	Dependent	4	Kotler & Keller [7]; Silayoi & Speece [1]
Age, gender, education, purchase frequency	Control	—	Standard demographic controls

Note. Author's elaboration based on the questionnaire structure.

The model tested is expressed as:

$$Y = \beta 0 + \beta 1X1 + \beta 2X2 + \beta 3X3 + \varepsilon$$

where ε represents factors outside the model, such as personal preference, social influence, and price sensitivity, that may also affect the purchase decision but were not measured in this study.

D. Data Analysis

The analysis proceeded in four stages: descriptive statistics were used to characterise the sample and item-level responses; reliability was assessed through Cronbach's alpha ($\alpha \geq .70$ considered acceptable), together with the Kaiser-Meyer-Olkin measure and Bartlett's test to confirm the suitability of the data for computing composite scores [20], [21]; Pearson correlation was used to establish pairwise relationships; and multiple linear regression was used to test H1a–H1c jointly, reporting standardised coefficients, model R^2, the omnibus F-test, and variance inflation factor (VIF) diagnostics for multicollinearity [22].

E. Validity and Reliability

Content validity was supported by the use of previously validated scale items [1], [8], [5] rather than untested new items. Construct validity was assessed using the KMO measure and Bartlett's test prior to computing composite scores. Internal reliability was assessed using Cronbach's alpha [23], interpreted according to conventional thresholds: $\alpha \geq .90$ excellent, .80–.89 good, .70–.79 acceptable, and below .70 poor [22].

Participation was voluntary and anonymous, and the data were used exclusively for academic purposes. The main threats to validity, including the non-probability sample, possible self-report bias, and the focus on a single product category, are addressed in Section VI.

IV. Results

A. Sample Profile

Of 120 responses, 116 were valid for the regression model. The sample is relatively young: the 18–24 and 25–34 age brackets together account for approximately three-quarters of respondents, consistent with the focus on everyday products, since these groups have frequent and current exposure to retail and online packaging.

Table 2. Demographic Profile of Respondents (N = 120)

Variable	Category	n	%
Age	18–24	49	40.8
	25–34	39	32.5
	< 18	16	13.3
	35–44	14	11.7
	45–54	2	1.7
Gender	Female	75	62.5
	Male	38	31.7
	Other	6	5.0
	No response	1	0.8
Education	Bachelor's	64	53.3
	Master's	28	23.3
	High school	26	21.7
	Doctorate	2	1.7
Purchase frequency	Weekly	66	55.0
	Monthly	21	17.5
	Daily	19	15.8
	Less often	11	9.2
	No response	3	2.5

Note. Author's elaboration based on the survey data.

B. Descriptive Statistics

All scale means exceeded the neutral midpoint of 3.0. The purchase decision obtained the highest mean (M = 3.83, SD = 0.82), while packaging design obtained the lowest of the four constructs (M = 3.77, SD = 0.69). This relatively narrow range indicates that respondents rated the three predictors and the outcome

variable in a broadly similar manner, a pattern relevant to the interpretation of the regression coefficients reported below.

Table 3. Descriptive Statistics for Study Variables

Variable	N	M	SD	Median	% high rating
X1 – Packaging design	116	3.77	0.69	3.80	48.3
X2 – Psychological/emotional response	116	3.80	0.72	4.00	51.7
X3 – Sustainability/ESG	116	3.80	0.76	4.00	58.6
Y – Purchase decision	116	3.83	0.82	4.00	57.8

Note. Author's elaboration based on the survey data.

Price (M = 4.29; 83.8% agreement) and brand (M = 4.14; 81.0%) were rated more favourably than packaging-specific items such as on-pack information (M = 3.98; 76.9%) and aesthetic appeal (M = 3.68; 60.2%). This suggests that packaging operates alongside price and brand as a secondary purchase signal rather than competing with them directly.

C. Reliability and Data Adequacy

Cronbach's alpha ranged from .895 to .920 across the four constructs, comfortably above the .70 threshold and within the excellent range for three of the four constructs, supporting the use of composite scores in the correlation and regression analyses that follow.

Table 4. Construct Reliability (Cronbach's Alpha)

Variable	Items	N valid	α	Interpretation
X1 – Packaging design	5	116	.917	Excellent
X2 – Psychological/emotional response	4	115	.895	Good
X3 – Sustainability/ESG	3	116	.907	Excellent
Y – Purchase decision	4	115	.920	Excellent

Note. Author's elaboration based on the survey data.

The Kaiser-Meyer-Olkin measure of sampling adequacy was .903, and Bartlett's test of sphericity was significant, $\chi^2(120) = 1585.59$, $p < .001$, indicating that the data were suitable for computing composite construct scores.

D. Correlation Analysis

All six pairwise correlations were positive and significant at $p < .001$ (Table 5). Sustainability showed the strongest correlation with the purchase decision (r = .677), followed by psychological response (r = .654) and visual design (r = .592), an initial indication, confirmed subsequently in the regression analysis, that sustainability carries the greatest relative weight among the three predictors.

Table 5. Pearson Correlation Matrix

	Design	Psychological	Purchase	ESG
Design	1.000	.731***	.592***	.431***
Psychological	.731***	1.000	.654***	.524**
Purchase decision	.592***	.654***	1.000	.677***
ESG	.431***	.524**	.677***	1.000

*Note. *** p < .001; ** p < .01.*

Design and psychological response were also strongly correlated with each other (r = .731), raising a reasonable concern regarding multicollinearity, which is addressed directly through the VIF diagnostics reported in the regression analysis below.

E. Multiple Linear Regression and Hypothesis Testing

The overall regression model was significant, $F(3, 112) = 56.00$, $p < .001$, $R^2 = .600$ (adjusted $R^2 = .589$), indicating that the three predictors jointly account for 60% of the variance in the purchase decision, a substantial proportion for a self-report model of consumer behaviour. The Durbin-Watson statistic (2.17) indicated no evidence of autocorrelation among the residuals.

Table 6. Regression Model Summary

Model	N	R^2	Adj. R^2	F	df	p
Main model	116	.600	.589	56.00	3, 112	< .001

Note. Author's elaboration based on the survey data.

All three predictors were statistically significant (Table 7). Sustainability produced the largest standardised effect (β = .448), more than double the effect of visual design (β = .199) and appreciably larger than the psychological/emotional effect (β = .274). VIF values (1.39–2.42) remained well below the conventional threshold of 5, indicating that, despite the correlation noted above between design and psychological response, multicollinearity did not distort these estimates.

Table 7. Multiple Linear Regression Coefficients

Term	B	SE	β	t	p	VIF
Constant	-0.052	0.309	—	-0.17	.866	—
X1 – Design	0.236	0.104	.199	2.26	.026	2.16
X2 – Psychological	0.309	0.105	.274	2.94	.004	2.42
X3 – ESG	0.479	0.075	.448	6.37	< .001	1.39

Note. Author's elaboration.

All three specific hypotheses were supported (Table 8), with H1c receiving the strongest support.

Table 8. Summary of Hypothesis Tests

Hyp.	Statement	β	p	Result
H1a	Packaging design positively predicts the purchase decision.	.199	.026	Supported
H1b	Psychological/emotional response positively predicts the purchase decision.	.274	.004	Supported
H1c	Packaging sustainability positively predicts the purchase decision.	.448	< .001	Supported (largest effect)

Note. Author's elaboration based on the survey data.

V. Discussion

All three hypotheses were supported, a more consistent outcome than is typically obtained in survey-based consumer research. This consistency should nonetheless be interpreted with caution, since X1, X2, X3, and Y were measured using the same self-report instrument, administered at the same time to the same respondents. Part of the shared variance among these constructs plausibly reflects genuine association among the underlying constructs, while part may reflect common-method variance arising from the repeated use of a similar response format. The present design cannot fully disentangle these two sources, and the reported R^2 of .600 should be interpreted accordingly.

With this qualification noted, the pattern of results remains informative. Packaging design (H1a) was a significant but comparatively weak predictor, consistent with the literature that treats visual elements as attention-drawing rather than decision-determining [2], [4]: a package may attract attention because of its appearance, but in this sample visual appeal alone contributed the least to explaining the purchase decision.

Psychological and emotional response (H1b) exerted a stronger effect than visual appeal alone, consistent with the S-O-R logic outlined in Section II-D: packaging functions as a stimulus, but it is the consumer's internal emotional processing of that stimulus, rather than the stimulus itself, that contributes more strongly to the purchase decision [3]. In other words, a favourable visual impression appears necessary but not sufficient; the packaging must also generate an emotional response that consumers can act on at the point of decision.

The most notable finding is that sustainability (H1c) exceeded both other predictors by a margin unlikely to be attributable to sampling error alone. This result is consistent with Magnier and Crié [5] and Peattie [6], both of whom argue that environmental credentials shape brand perception independently of design quality. The present study extends this argument by demonstrating it directly: within a single model, sustainability outperformed both alternative predictors against which it was tested. Whether this finding reflects a broader shift in consumer priorities, or is specific to the characteristics of the present sample, which was relatively young, disproportionately female, more highly educated, and drawn from a single country, cannot be determined from this dataset alone.

The comparison between price, brand, and the packaging dimensions (Table 3) is also relevant. Both price and brand received higher agreement scores than any packaging dimension examined here, which cautions against overstating the importance of packaging relative to these more established purchase

determinants. The regression results indicate, however, that packaging continues to explain variance in the purchase decision independently of the roles played by price and brand; packaging therefore does not compete with these factors for primacy, but neither is it negligible in their presence.

VI. Conclusion

A. Summary

In this sample, sustainability was a stronger predictor of the purchase decision than either visual design or psychological/emotional response, a result that should be interpreted carefully rather than overstated. It does not indicate that packaging aesthetics are unimportant, since all three effects were statistically significant; rather, it indicates that when the three dimensions are evaluated jointly within the same model, environmental perception accounted for more of the explained variance than either of the two more extensively studied packaging dimensions. This is a specific and falsifiable claim about the present sample rather than a general principle of consumer psychology, and it warrants replication before being treated as such.

B. Practical Implications

For practitioners, the most relevant comparison in this study is between the coefficient obtained for sustainability ($\beta = .448$) and that obtained for visual design ($\beta = .199$). This difference suggests that environmental positioning should not be regarded merely as a compliance requirement layered onto design; in this sample, it contributed more to explaining purchase behaviour than design itself. The practical implication is not that investment in aesthetics should be reduced, since the aesthetic effect was real and statistically significant, but that sustainability messaging should not be treated as secondary to it. This consideration is particularly relevant in categories such as the everyday products examined here, in which competing products are functionally similar and purchase decisions are typically made quickly.

C. Limitations

- Convenience sampling and a modest sample size ($N = 120$) limit the extent to which these results can be generalised beyond the sample studied.
- The cross-sectional design measures association rather than causal direction; packaging perception and purchase intention were measured simultaneously rather than sequentially.
- All four constructs were derived from the same self-report instrument administered at the same time, which likely inflates the shared variance among them to some degree beyond their underlying relationship.
- The focus on everyday products limits the generalisability of these findings to categories with different purchase dynamics, such as luxury or technology goods.

D. Future Research

- Replicate the study using a probability sample of sufficient size to support subgroup comparisons.
- Test the same three-predictor model in other product categories to determine whether the sustainability effect persists outside everyday consumables.
- Separate the measurement of packaging perception from purchase intention in time, for example through an experimental or longitudinal design, to address the common-method and causal-direction concerns raised above.
- Apply confirmatory factor analysis or structural equation modelling to test the mediation pathways implied by the S-O-R framework more directly than a regression on composite scores allows.

Acknowledgment

The author would like to thank all survey participants for their time and cooperation.

References

[1] P. Silayoi and M. Speece, “The importance of packaging attributes: A conjoint analysis approach,” *European Journal of Marketing*, vol. 41, no. 11/12, pp. 1495–1517, 2007.

[2] O. Ampuero and N. Vila, "Consumer perceptions of product packaging," *Journal of Consumer Marketing*, vol. 23, no. 2, pp. 100–112, 2006.
[3] P. H. Bloch, "Seeking the ideal form: Product design and consumer response," *Journal of Marketing*, vol. 59, no. 3, pp. 16–29, 1995.
[4] U. R. Orth and K. Malkewitz, "Holistic package design and consumer brand impressions," *Journal of Marketing*, vol. 72, no. 3, pp. 64–81, 2008.
[5] L. Magnier and D. Crié, "Communicating packaging eco-friendliness: An exploration of consumers' perceptions of eco-designed packaging," *International Journal of Retail & Distribution Management*, vol. 43, no. 4/5, pp. 350–366, 2015.
[6] K. Peattie, "Green consumption: Behavior and norms," *Annual Review of Environment and Resources*, vol. 35, pp. 195–228, 2010.
[7] P. Kotler and K. L. Keller, *Marketing Management*, 15th ed. Boston, MA, USA: Pearson Education, 2016.
[8] R. L. Underwood, "The communicative power of product packaging: Creating brand identity via lived and mediated experience," *Journal of Marketing Theory and Practice*, vol. 11, no. 1, pp. 62–76, 2003.
[9] L. I. Labrecque and G. R. Milne, "Exciting red and competent blue: The importance of color in marketing," *Journal of the Academy of Marketing Science*, vol. 40, no. 5, pp. 711–727, 2012.
[10] B. Rundh, "The role of packaging within marketing and value creation," *British Food Journal*, vol. 118, no. 10, pp. 2491–2511, 2016.
[11] H. Honea and S. Horsky, "The power of plain: Intensifying product experience with neutral aesthetic context," *Marketing Letters*, vol. 23, no. 1, pp. 223–235, 2012.
[12] R. Rettie and C. Brewer, "The verbal and visual components of package design," *Journal of Product & Brand Management*, vol. 9, no. 1, pp. 56–70, 2000.
[13] A. Mehrabian and J. A. Russell, *An Approach to Environmental Psychology*. Cambridge, MA, USA: MIT Press, 1974.
[14] K. White, R. Habib, and D. J. Hardisty, "How to SHIFT consumer behaviors to be more sustainable: A literature review and guiding framework," *Journal of Marketing*, vol. 83, no. 3, pp. 22–49, 2019.
[15] J. W. Creswell, *Research Design: Qualitative, Quantitative, and Mixed Methods Approaches*, 4th ed. Thousand Oaks, CA, USA: SAGE Publications, 2014.
[16] N. K. Malhotra, *Marketing Research: An Applied Orientation*, 6th ed. Upper Saddle River, NJ, USA: Pearson Education, 2010.
[17] M. Saunders, P. Lewis, and A. Thornhill, *Research Methods for Business Students*, 8th ed. Harlow, U.K.: Pearson Education, 2019.
[18] I. Etikan, S. A. Musa, and R. S. Alkassim, "Comparison of convenience sampling and purposive sampling," *American Journal of Theoretical and Applied Statistics*, vol. 5, no. 1, pp. 1–4, 2016.
[19] R. Likert, "A technique for the measurement of attitudes," *Archives of Psychology*, vol. 140, pp. 1–55, 1932.
[20] H. F. Kaiser, "An index of factorial simplicity," *Psychometrika*, vol. 39, no. 1, pp. 31–36, 1974.
[21] A. Field, *Discovering Statistics Using IBM SPSS Statistics*, 4th ed. London, U.K.: SAGE Publications, 2013.
[22] J. F. Hair, W. C. Black, B. J. Babin, and R. E. Anderson, *Multivariate Data Analysis*, 8th ed. Boston, MA, USA: Cengage Learning, 2019.
[23] L. J. Cronbach, "Coefficient alpha and the internal structure of tests," *Psychometrika*, vol. 16, no. 3, pp. 297–334, 1951.

8th International Conference on Engineering, Natural and Social Sciences

September 06-07, 2026: Konya, Turkey

© 2026 Published by All Sciences Academy

https://www.icensos.com/

Evaluation of Multi-Model Consensus in Unmanned Aerial Vehicle Mapping Missions with Respect to In-Flight Decision Reliability

Fadiş Rabia YILDIRIM[1,*], Fatma YILDIRIM DALKIRAN[2] and Mehmet KONAR[2]

[1]*Erciyes University, Graduate School of Natural and Applied Sciences, Department of Aviation Electrical and Electronics, Kayseri, Türkiye*

[2]*Erciyes University, Faculty of Aeronautics and Astronautics, Department of Aviation Electrical and Electronics, Kayseri, Türkiye*

ORCID: [1]0000-0003-4168-101X, [2]0000-0001-8663-241X, [2]0000-0002-9317-1196

[*]*(fadis.yildirim@erciyes.edu.tr) Email of the corresponding author*

Abstract **–** Running inference on board the aircraft in agricultural mapping missions raises a mission management problem: which of the classification decisions produced during flight may be accepted automatically, and which must be reviewed at the ground station. On models deployed to the edge, probability outputs are often inaccessible or lose their reliability after quantisation and conversion. Probability-based confidence measures are therefore of limited applicability under these conditions. This study evaluates a triage approach that requires neither additional hardware nor probability calibration, treating the consensus of several lightweight classifiers run concurrently on board as a confidence measure. Out-of-fold predictions of four edge architectures, trained with spatially blocked five-fold cross-validation, were analysed on 2919 frames of cotton, lavender and sunflower. On frames where all four models agreed, the automatic acceptance rate was 83.7% and the accuracy 99.06%, whereas on the 476 frames without consensus the accuracy fell to 81.3%. Without triage the error rate of the best single model was 4.04%, while consensus triage reduced the error written to the map without review (escaped error) to 0.79%. The findings indicate that running four models is not necessary for the dataset and the architectures examined. A pair formed by the lowest- and a mid-capacity model reduced the escaped error to 1.23% at 35.2 milliseconds per frame and ran about 2.5 times faster than ResNet-18 alone. Pairs of models with similar capacity did not achieve the same performance, and triage performance was observed to relate less to the individual accuracy of the models than to the diversity of their errors.

Keywords – Unmanned aerial vehicle, edge inference, model consensus, selective classification, mission management, in-flight decision

I. INTRODUCTION

The use of unmanned aerial vehicles (UAVs) in agricultural applications has evolved from a data acquisition activity based on image collection into a mission architecture that produces decisions during flight [1], [2], [3]. Alongside the conventional workflow in which images are processed at the ground station after the flight is completed, edge-based architectures that run inference (inference) on the embedded processor aboard the aircraft are becoming widespread. A classification result produced during flight allows the mission plan to be updated within the same flight, the relevant area to be revisited, or an action such as spraying to be triggered directly [4]. The use of embedded learning-based components together with flight data is also becoming widespread in aviation for performance estimation and real-time detection tasks [5], [6], [7], [8].

Moving inference onto the aircraft introduces a supervision problem not encountered in ground-based processing. In an analysis carried out at the ground station every result can be passed through expert review, whereas no such review exists in inference performed on board. The mission management system

therefore has to determine by its own means which of the decisions produced is reliable. The resulting problem is one of reliability separate from accuracy. Even a model operating with high average accuracy shows limited functionality within an autonomous mission architecture as long as it cannot identify the portion on which it is wrong.

The common solution to this problem in the literature is to use the probability output produced by the model as a confidence measure. However, the probability outputs of deep networks have been shown to produce systematically overconfident values and to require calibration (calibration) [9]. The problem becomes still more pronounced under edge conditions. Models are quantised (quantisation) and converted to a different runtime as they are deployed to the aircraft. Many embedded inference libraries return only the class label, and the validation set required for calibration is not available during the mission. Work in the field of selective classification (selective classification) has shown that a reliable rejection mechanism raises accuracy markedly, yet the majority of these approaches also rest on a calibrated probability score [10].

This study evaluates an alternative that does not require a calibrated probability score. Instead of a single model, several lightweight models are run on the same frame aboard the aircraft, and whether the decisions produced by these models agree is examined. Where consensus is reached the decision is accepted automatically; otherwise the frame is set aside for review at the ground station. The assumption on which the approach rests is that models with different inductive biases (inductive bias) will produce different errors and that disagreement will identify the frames that are difficult to classify [11], [12]. This use departs from the customary use of ensemble (ensemble) methods. The aim is not to raise accuracy by combining the votes of the models, but to treat disagreement as an indicator of reliability.

The decisive point for the aviation application is whether the mechanism remains within the real-time constraint of the mission. Since running several models increases the inference time per frame, the evaluation must cover not only the gain provided by triage but also the number and the composition of the models to be loaded onto the aircraft.

Within this framework the aim of the study can be gathered under three headings. First, how much of a mapping mission consensus-based triage can close automatically is determined quantitatively. Second, triage performance and inference latency are evaluated jointly for all model subsets, and the most suitable composition to be loaded onto the aircraft is selected. Third, the frames set aside for review are analysed and the validity of the difficulties identified by the mechanism is tested. The original contribution of the study is that it evaluates inter-model consensus together with the latency constraint and puts forward a measurable selection rule for the model composition to be loaded onto the aircraft.

II. MATERIALS AND METHOD

Evaluating consensus-based triage requires that every frame has been classified independently by several models that did not see that frame during training. The analysis was built on an out-of-fold prediction set satisfying this condition, and the cost of triage was measured against the real-time constraint of the same mission.

A. Dataset and Architectures Evaluated

The images were collected with a 20 megapixel (MP) camera mounted on an Autel Robotics EVO II Pro platform over fields in the Adana, Konya and Kayseri regions. The flights were carried out at near-nadir orientation, at ten nominal above-ground altitudes between 5 and 180 m and over a period spanning eleven months, and the frames were stored at 4000 × 3000 pixels. Since each crop was imaged at the altitudes suited to its own mapping requirement, the altitude distribution is not equal across crops.

The classifiers were trained on six classes, while the scope of this paper was limited to cotton, lavender and sunflower so that in-flight decision reliability could be examined over a single mapping mission. All frames belonging to these three classes, 2919 in total, were included in the evaluation (1478 cotton, 780 sunflower, 661 lavender) and no separate elimination was applied. As the models remained six-class, reporting a class outside the scope was also counted as an error, and the proportion of such predictions was measured as 4.26%.

Spatial dependence was taken into account in splitting the dataset. Because consecutive frames in UAV imagery overlap to a high degree, random splitting distributes the same scenes across the training and evaluation sets and inflates the reported accuracy [13], [14], [15]. The imaged area was therefore divided into cells of 60 m side derived from the frame coordinates, the resulting 100 blocks were distributed over five folds, and the folds were balanced by class. In this way an out-of-fold (out-of-fold) prediction from a model that had not seen that frame during training was obtained for every frame.

Edge suitability and capacity diversity were considered together in the choice of architectures. MobileNetV3-Small [16] together with EfficientNet-Lite0 and EfficientNet-Lite2 [17] are architectures designed directly for edge inference, while ResNet-18 [18] was added as a general-purpose reference point. All four are ImageNet pretrained and were trained with the same training protocol, on 224-pixel input and over 25 epochs. The training of the models, their out-of-fold predictions and the latency measurements were taken from the altitude optimisation study conducted by the authors on the same dataset, which is still under review. The latencies are forward-pass times measured on a single core of a desktop system without a graphics processing unit (GPU) and constitute a conservative upper bound for an embedded board. The parameter counts, measured latencies and in-scope out-of-fold accuracies of the models are given in Table 1. The abbreviations defined in the table are used in the analyses that follow to denote the compositions. The parameter count ranges from 1.52 M to 11.18 M and the measured latency from 9.9 ms to 88.9 ms.

Table 1. Cost and performance values of the architectures.

Architecture	Abbreviation	Parameters (M)	Latency (ms)	Frames/s	Accuracy
MobileNetV3-Small	MNV3-S	1.52	9.9	101.0	85.68%
EfficientNet-Lite0	ENL0	3.38	25.3	39.5	95.68%
EfficientNet-Lite2	ENL2	4.82	36.4	27.5	95.96%
ResNet-18	RN18	11.18	88.9	11.2	95.34%

B. The Consensus-Based Triage Rule

For a model subset loaded onto the aircraft, the triage (triage) operation was defined as follows. A frame is given to all models in the subset, and when all of them report the same class the decision is accepted automatically. If at least one model reports a different class, the frame is set aside for ground review. The definition uses no probability value and rests solely on the comparison of class labels. This property allows the rule to work with quantised or black-box inference libraries as well.

C. Performance Measures and the Real-Time Constraint

Three complementary measures were reported in the evaluation. Coverage is the ratio of automatically accepted frames to all frames. Automatic accuracy shows the proportion of correct ones among the accepted frames. Escaped error is the ratio of frames that were accepted automatically yet are wrong to all frames, and it is the decisive measure from the mission point of view. Such frames are written to the map without passing through any review. All subsets from two to four models, eleven compositions in total, were evaluated separately. The inference latency of each composition was taken as the sum of the latencies of its component models. This sum rests on the assumption that the models are run sequentially on a single core and constitutes a conservative upper bound. On a mission computer with several cores or an accelerator the models could be run in parallel, so the realised latency will remain below this value.

Since a decision must also be produced on frames where consensus is not reached, a voting rule was defined. Where a strict majority exists the class reported by the majority is taken; where no majority forms, the prediction of EfficientNet-Lite2, the model with the highest accuracy on its own, is used. The value reported on such frames is the accuracy of this tie-breaking rule and not that of a majority decision. When triage is applied these frames are not accepted automatically in any case, so the rule is used for comparison only.

Interpreting the findings from the aviation point of view requires a real-time criterion to be defined. This constraint was taken from the coverage study conducted on the same dataset. The frame rate required by the mission is approximately 1.54 frames per second, which means that approximately 649 milliseconds per frame remain for inference.

III. RESULTS

For triage to function within a mission architecture, two conditions must hold. Consensus must genuinely be an indicator of reliability, and the gain it provides must be obtained within the real-time constraint of the mission. The findings below test both conditions quantitatively.

A. The Relation between Consensus Level and Decision Accuracy

Whether consensus carries the function of a confidence measure was tested by examining whether the consensus level and the accuracy vary together. The four models reported the same class on 83.7% of the frames, and the accuracy of the decision on these frames was calculated as 99.06%. On frames where the models split into two the accuracy falls to 84.2%, and on those where they split into three to 52.4% (Figure 1). At the level where all four models reported a different class there are only four frames, so the 75.0% value there shows the accuracy of the tie-breaking rule and does not constitute an interpretable estimate. On all 476 frames without consensus the accuracy is 81.3%. That accuracy decreases together with the consensus level shows that consensus carries the quality of a confidence measure.

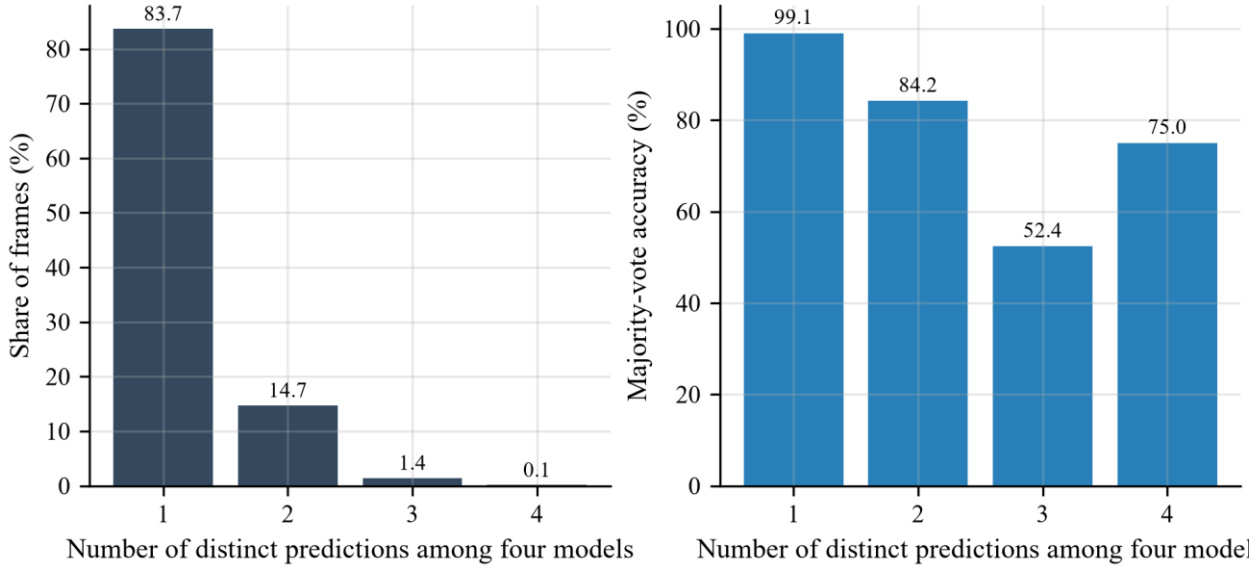

Figure 1. Distribution of frames and decision accuracy by consensus level.

The mission-level meaning of triage is assessed through the escaped error. Without triage, EfficientNet-Lite2, the best single model, misclassifies 4.04% of the frames, and all of these errors are written to the map without review. Four-model consensus triage reduces this proportion to 0.79%; 16.3% of the frames are set aside for review while the number of unsupervised errors falls from 118 to 23.

B. The Latency and Escaped Error Trade-off across Model Subsets

To determine the number of models that must be loaded onto the aircraft, all eleven compositions were compared in terms of latency and escaped error. Table 2 groups the compositions by the number of models and orders them within each group by escaped error. Figure 2 shows the same compositions together with the single models without triage, on two cost axes. In the left-hand plot the computational cost is measured by inference latency and in the right-hand one the operational cost by the proportion of frames deferred to ground review. The selection criterion was defined as follows. Compositions whose escaped error remains below 1.5% are taken to be acceptable, and among those satisfying this condition the one with the lowest latency is selected. The threshold was set to be approximately one third of the 4.04% error rate of the best single model without triage. According to this criterion the MNV3-S and

ENL0 composition is selected; it closes 85.4% of the frames with 98.56% accuracy at 35.2 milliseconds per frame and reduces the escaped error to 1.23%. The ordering also shows that four models are not necessary. Moving from the selected composition to the four-model one increases the latency by a factor of 4.6 while yielding a reduction of only 0.44 points in escaped error.

Table 2. Latency and triage performance of the model subsets.

Composition	Models	Latency (ms)	Coverage	Automatic accuracy	Escaped error
MNV3-S + RN18	2	98.8	84.8%	98.83%	0.99%
MNV3-S + ENL2	2	46.3	85.3%	98.67%	1.13%
MNV3-S + ENL0	2	35.2	85.4%	98.56%	1.23%
ENL0 + RN18	2	114.2	96.5%	97.55%	2.36%
ENL2 + RN18	2	125.3	97.0%	97.21%	2.71%
ENL0 + ENL2	2	61.7	97.5%	97.19%	2.74%
MNV3-S + ENL2 + RN18	3	135.2	84.0%	99.06%	0.79%
MNV3-S + ENL0 + RN18	3	124.1	83.9%	99.02%	0.82%
MNV3-S + ENL0 + ENL2	3	71.6	84.5%	98.91%	0.92%
ENL0 + ENL2 + RN18	3	150.6	95.8%	97.78%	2.12%
MNV3-S + ENL0 + ENL2 + RN18	4	160.5	83.7%	99.06%	0.79%

A further distinction between the compositions lies in inference speed. The composition made up of two lightweight models runs about 2.5 times faster than ResNet-18 alone. ResNet-18 spends 88.9 milliseconds per frame and misclassifies 4.66% of the frames without review, whereas the MNV3-S and ENL0 composition reduces this proportion to 1.23% in 35.2 milliseconds.

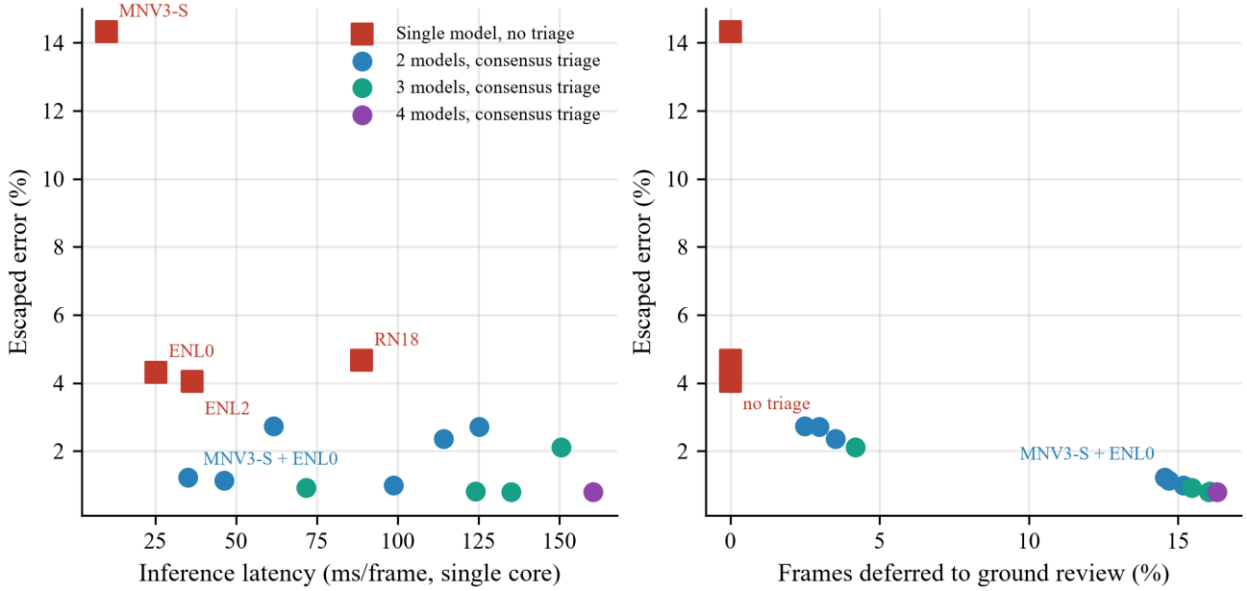

Figure 2. Trade-off between escaped error and computational and operational cost.

C. *Distribution of the Frames Deferred to Review across Classes*

Since the validity of a triage mechanism depends on the frames it sets aside for review genuinely being difficult ones, the deferred frames were analysed by class. The distribution of the frames set aside for review across the classes is relatively balanced, running at 20.0% in lavender, 17.8% in sunflower and

13.9% in cotton. The frames on which all four models were wrong, by contrast, are concentrated in a single class. Of these 59 frames, 46 belong to cotton, 12 to sunflower and only one to lavender. These frames make up 2.02% of all frames.

D. Compliance with the Real-Time Constraint

All the compositions evaluated remain within the real-time constraint of the mission. Against the 649 milliseconds allotted per frame, the four-model composition, the slowest option, uses a quarter of this time and the proposed two-model composition only 5.4% of it. In this respect the computational cost of consensus-based triage does not constitute a decisive constraint for the mission profile in question.

IV. DISCUSSION

The findings obtained show that triage performance cannot be explained by the individual accuracy of the component models. The decisive point is on which frames the models are wrong and to what extent these frames overlap.

A. The Decisive Role of Architectural Diversity in Triage Performance

The ENL0 and ENL2 composition in Table 2 is an example that illustrates how the mechanism works. These two models are the architectures with the highest accuracy on their own and their performances are close to each other. Nevertheless the triage performance of the composition remains weak: although consensus is reached on 97.5% of the frames, the escaped error remains at 2.74%. Two members of the same architectural family are wrong on the same frames, and their consensus does not constitute a guarantee.

The compositions that MNV3-S, the lowest-capacity model, forms with any higher-capacity model, by contrast, reduce the escaped error to between 0.99% and 1.23%. This contrast shows that the factor determining triage performance is not the accuracy of the component models but the fact that their error patterns differ from one another. The finding offers a direct design criterion for the choice of the second model to be loaded onto the aircraft. That model should not be a higher-capacity version of the first but an architecture exhibiting a different error pattern from it.

B. Comparison of the Findings with the Literature

The results obtained are in the same direction as findings in the fields of selective classification, ensemble methods and uncertainty estimation, yet they differ from these in the signal they use. Studies on selective classification have shown that accuracy can be raised by lowering coverage through a rejection mechanism [10]. In this study too, when 16.3% of the frames are rejected, 99.06% accuracy is obtained on the remaining portion, against the 95.96% accuracy of the best single model. The difference lies in the fact that in those studies the rejection decision rests on a calibrated probability score. Since probability outputs have been shown to produce overconfident values and to require calibration [9], this dependence constitutes a constraint under edge conditions. The approach evaluated here uses only class labels and is therefore unaffected by that constraint.

A distinction is also apparent with respect to ensemble methods. Deep ensembles have been reported to be effective in uncertainty estimation and this effect to arise from the diversity among the components [11], [12]. The findings of this study are consistent with that explanation. In ensemble methods, however, the aim is to raise accuracy by combining votes, whereas here disagreement itself is used as an indicator of reliability and the decision is deferred to review rather than combined.

C. The Crop-Based Structure of the Common Error Core

The frames that none of the four models could classify correctly make up 2.02% of all frames and constitute a common error core for the four architectures evaluated. That these frames are concentrated in cotton shows that this core is bound not to the dataset as a whole but to the distinguishability of the images belonging to a particular crop. The cotton frames both form the most numerous group and are spread over the widest area spatially. The images of this crop are distributed within a bounding box (bounding box) of 3321 hectares, whereas the same value is 54 hectares in sunflower and 8 hectares in

lavender. That within-class visual variability is high in cotton is consistent with this spatial dispersion. The extent to which the core would narrow with higher-capacity architectures could not be determined with the present data.

D. Limitations of the Method

The findings obtained should be interpreted within several limitations. The latency values rest on a single-core measurement, and on a real mission computer memory bandwidth and thermal constraints may produce different results. Consensus cannot identify the 2.02% core on which the four models are commonly wrong; these frames are accepted automatically and constitute the portion the method fails to detect. The models were trained as six-class while the scope of the study was limited to three crops. It cannot therefore be claimed directly that the results would hold in the same way for a model trained on these three crops alone. Finally, it was assumed that the frames set aside for review would be assessed on the ground. How these frames would be handled in a real mission is a mission planning problem requiring separate study.

V. CONCLUSION

This study has shown that the reliability of in-flight decisions in autonomous UAV mapping missions can be measured, without recourse to probability outputs, through the consensus of several lightweight models running aboard the aircraft. On frames where the four models agreed, the automatic acceptance rate was found to be 83.7% and the accuracy 99.06%, and the unsupervised error rate fell from 4.04% to 0.79%.

Three conclusions were obtained from the aviation point of view. First, the mechanism complies with the real-time constraint of the mission; even the most expensive composition uses a quarter of the time allotted per frame. Second, running four models is not necessary. The composition formed by the lowest-capacity model with a mid-capacity one reduces the escaped error to 1.23% at 35.2 milliseconds per frame and both runs about 2.5 times faster than ResNet-18 alone and yields an escaped error about four times lower. Third, error diversity as well as individual accuracy should be taken into account in the choice of the second model to be loaded onto the aircraft. Two high-capacity models close to each other are wrong on the same frames and therefore cannot provide effective triage.

ACKNOWLEDGMENT

This work was supported by the Research Fund of Erciyes University Scientific Research Projects (BAP) Coordination Unit under Project Number FDK-2023-13046.

REFERENCES

[1] D. C. Tsouros, S. Bibi, and P. G. Sarigiannidis, "A review on UAV-based applications for precision agriculture," *Information*, vol. 10, no. 11, p. 349, 2019, doi: 10.3390/info10110349.

[2] A. Bouguettaya, H. Zarzour, A. Kechida, and A. M. Taberkit, "Deep learning techniques to classify agricultural crops through UAV imagery: A review," *Neural Computing and Applications*, vol. 34, no. 12, pp. 9511-9536, 2022, doi: 10.1007/s00521-022-07104-9.

[3] F. R. Yıldırım and F. Yıldırım Dalkıran, "Tarımda insansız hava araçlarının kullanımının incelenmesi," in *ASES II. Int. Cappadocia Scientific Research Congress*, 2026, pp. 20-27.

[4] S. Khan, M. Tufail, M. T. Khan, Z. A. Khan, and S. Anwar, "Deep-learning-based spraying area recognition system for unmanned-aerial-vehicle-based sprayers," *Turkish Journal of Electrical Engineering and Computer Sciences*, vol. 29, no. 1, pp. 241-256, 2021, doi: 10.3906/elk-2004-4.

[5] E. Çetin, C. Barrado, and E. Pastor, "Improving real-time drone detection for counter-drone systems," *The Aeronautical Journal*, vol. 125, no. 1292, pp. 1871-1896, 2021, doi: 10.1017/aer.2021.43.

[6] M. Konar, D. Özdemir, M. Fenerci, and M. Erşen, "Mini UAVs' flight data estimation in navigation phase with LSTM method within the CRISP-DM framework," *The Aeronautical Journal*, vol. 130, no. 1347, pp. 1546-1565, 2026, doi: 10.1017/aer.2026.10145.

[7] A. Kahya and M. Konar, "Integration of artificial intelligence into unmanned aerial vehicles," *Journal of Aviation*, vol. 10, no. 2, pp. 235-243, 2026, doi: 10.30518/jav.1902446.

[8] E. Demiray, M. Konar, and S. Arık Hatipoğlu, "Development of a thermal helipad for UAVs and detection with deep learning," *Drones*, vol. 10, no. 4, p. 266, 2026, doi: 10.3390/drones10040266.

[9] C. Guo, G. Pleiss, Y. Sun, and K. Q. Weinberger, "On calibration of modern neural networks," in *Proc. 34th Int. Conf. Machine Learning*, vol. 70, 2017, pp. 1321-1330.

[10] Y. Geifman and R. El-Yaniv, "Selective classification for deep neural networks," in *Advances in Neural Information Processing Systems*, vol. 30, 2017, pp. 4878-4887.

[11] T. G. Dietterich, "Ensemble methods in machine learning," in *Multiple Classifier Systems*, Lecture Notes in Computer Science, vol. 1857. Berlin, Germany: Springer, 2000, pp. 1-15, doi: 10.1007/3-540-45014-9_1.

[12] B. Lakshminarayanan, A. Pritzel, and C. Blundell, "Simple and scalable predictive uncertainty estimation using deep ensembles," in *Advances in Neural Information Processing Systems*, vol. 30, 2017, pp. 6402-6413.

[13] T. Kattenborn, F. Schiefer, J. Frey, H. Feilhauer, M. D. Mahecha, and C. F. Dormann, "Spatially autocorrelated training and validation samples inflate performance assessment of convolutional neural networks," *ISPRS Open Journal of Photogrammetry and Remote Sensing*, vol. 5, p. 100018, 2022, doi: 10.1016/j.ophoto.2022.100018.

[14] N. Karasiak, J.-F. Dejoux, C. Monteil, and D. Sheeren, "Spatial dependence between training and test sets: Another pitfall of classification accuracy assessment in remote sensing," *Machine Learning*, vol. 111, no. 7, pp. 2715-2740, 2022, doi: 10.1007/s10994-021-05972-1.

[15] S. Kapoor and A. Narayanan, "Leakage and the reproducibility crisis in machine-learning-based science," *Patterns*, vol. 4, no. 9, p. 100804, 2023, doi: 10.1016/j.patter.2023.100804.

[16] A. Howard, M. Sandler, G. Chu, L.-C. Chen, B. Chen, M. Tan, W. Wang, Y. Zhu, R. Pang, V. Vasudevan, Q. V. Le, and H. Adam, "Searching for MobileNetV3," in *Proc. IEEE/CVF Int. Conf. Computer Vision*, 2019, pp. 1314-1324, doi: 10.1109/ICCV.2019.00140.

[17] M. Tan and Q. V. Le, "EfficientNet: Rethinking model scaling for convolutional neural networks," in *Proc. 36th Int. Conf. Machine Learning*, vol. 97, 2019, pp. 6105-6114.

[18] K. He, X. Zhang, S. Ren, and J. Sun, "Deep residual learning for image recognition," in *Proc. IEEE Conf. Computer Vision and Pattern Recognition*, 2016, pp. 770-778, doi: 10.1109/CVPR.2016.90.

8th International Conference on Engineering, Natural and Social Sciences

September 06-07, 2026: Konya, Turkey

© 2026 Published by All Sciences Academy

https://www.icensos.com/

The Role of the Relief Parameter in Landslide Susceptibility Studies

Seda Çellek*

[1]*Department Geology Engineering, Kırşehir Ahi Evran University, Turkey*

[1*]*(sedacellek@ahievran.edu.tr) Email of the corresponding author*

Abstract **–** Landslide occurrence results from the interaction of geological, hydrological, climatic, and topographic factors. Among these, relief is an important topographic parameter influencing landslide occurrence, size, morphology, activity, and spatial distribution. Relief is generally defined as the difference between the maximum and minimum elevations within a given area and is also referred to as local relief, relative relief, relief amplitude, total slope height, or elevation range. This study reviews the role of relief in landslide occurrence and susceptibility based on previous studies. Relief is commonly derived from digital elevation models (DEMs) by calculating the maximum–minimum elevation difference within a specified neighborhood. However, DEM resolution and analysis window size vary considerably among studies. The literature indicates that increasing relief may facilitate the development of larger slip surfaces and consequently larger landslides. Relief variability can also reflect landslide activity, deformation patterns, relative age, and movement mechanisms. Active landslides generally exhibit more irregular topography, whereas erosion and surface processes progressively smooth older and inactive landslides. Nevertheless, relief alone is insufficient to explain landslide occurrence. It should therefore be evaluated together with slope, surface roughness, material strength, lithology, tectonic setting, and hydrological conditions.

Keywords – Relief, local relief, landslide, landslide susceptibility, topography, digital elevation model (DEM).

I. INTRODUCTION

Relief is the local elevation difference between the highest and lowest elevations within a given unit area [1]. It is a fundamental topographic indicator used for landslide identification and for understanding landslide morphology [2]–[4]. Relief is also an important factor controlling landslide size, occurrence, and spatial distribution [5], [6]. This parameter constitutes a fundamental component of the topographic signature of landslides, highlighting the need for the quantitative characterization of topography for landslide identification. Landslides form landforms through the combined effects of climate, lithology, tectonics, and topography. Therefore, relief is one of the fundamental components of the topographic signature produced by landslides [7].

Chen et al. [8] used relief amplitude as one of the landslide conditioning parameters in their study. Relief amplitude was defined as the difference between the maximum and minimum elevations within a given area and was considered to represent the potential energy required for landslide occurrence. Although Yin et al. [9] did not use relief directly as an independent variable, they evaluated morphometric parameters such as strong relief and local relief (HEIGHT) and incorporated several relief-related topographic variables into their model. Stumpf et al. [10] evaluated the performance of photogrammetric monitoring methods in landslide areas characterized by high relief and complex topography. Glenn et al. [2], using high-resolution LiDAR data, demonstrated the importance of relief variability in characterizing landslide morphology and activity. Their study successfully distinguished the upper block, body, and toe zones based on variations in

relief and showed that topographic variability is closely associated with landslide movement, material type, and deformation processes.

McKean and Roering [5] demonstrated the importance of relief characteristics in identifying landslide morphology using high-resolution LiDAR data. Berti et al. [7] showed that active landslides produce distinctive morphological features in the relief, including head scarps, lateral ridges, lobate toes, tension cracks, and pressure ridges. While topographic irregularities are pronounced in active landslides, relief tends to become progressively smoother in long-inactive landslides due to erosion and vegetation development. Medwedeff et al. [6] identified hillslope relief as one of the most important topographic parameters controlling landslide size. Based on DEM analyses and comparisons of eight earthquake-induced landslide inventories, they found that mean landslide size systematically increases with increasing relief.

Mountjoy et al. [11] conducted a morphometric analysis of a submarine landslide complex using high-resolution DEM data. Surface roughness, slope, aspect, and topographic deformation characteristics representing relief were evaluated, and these parameters were shown to play an important role in identifying compressional, extensional, and shear zones within the landslide. Furthermore, multiscale surface roughness analyses were reported to contribute significantly to understanding landslide kinematics and movement mechanisms. Quantin et al. [12] investigated 45 landslides in the Valles Marineris region of Mars using high-resolution DEM and remote sensing data. Topographic relief was evaluated through morphometric characteristics such as surface roughness, vertical elevation difference, canyon geometry, and topographic confinement. Their findings showed that relief characteristics significantly control landslide morphology, movement mechanism, volume, and runout distance. In particular, canyon width and topographic confinement were found to be important factors controlling the development of different landslide types.

Metternicht et al. [13] comprehensively evaluated the use of remote sensing techniques in landslide studies. They emphasized that DEM-derived topographic parameters, particularly relief, slope, microtopography, and surface roughness, play important roles in landslide detection, monitoring, and susceptibility analysis. They also highlighted the contribution of relief and roughness analyses derived from LiDAR, SAR, and high-resolution satellite imagery to the characterization of landslide morphology and spatial modeling.

Yang et al. [14] investigated the spatial effects of environmental factors controlling landslide susceptibility using an explainable artificial intelligence approach based on SHAP (Shapley Additive Explanations). Relief was among the main topographic variables included in the model. Although Carrara [15] did not directly use the term “relief” as a parameter, landforms and roughness were evaluated together with topographic variables representing relief characteristics. Zhang et al. [16] used the “Standard Deviation (STD) of Elevation” rather than relief directly. In their study, the conventional relief parameter, such as relative relief or local relief, was not calculated. Instead, the standard deviation of elevation was used to represent the degree of topographic relief, and the authors emphasized its close relationship with landslide occurrence.

Tanyaş et al. [17] provided an important global-scale study in which relief, particularly local relief, was directly considered in evaluating the topographic distribution of earthquake-induced landslides. Bostjančić et al. [1] directly used and comprehensively evaluated relief in landslide susceptibility analysis. Relief was defined as the local elevation difference, calculated from a DEM using the Focal Statistics method, and evaluated using the Frequency Ratio (FR) and Analytical Hierarchy Process (AHP) methods. Garriss [18] used both surface roughness and local relief in a master's thesis. Although Gong et al. [19] did not explicitly use the parameter under the term “Topographic Relief,” they evaluated several topographic variables representing relief, including elevation, aspect, topographic roughness, slope, and flow direction

II. Materials and Method

In the literature, relief is represented by different terms. Some authors use the following terms instead of relief:

- Relative relief
- Local relief
- Relief amplitude
- Total slope height
- Elevation range

DEM data at a specified spatial resolution are generally used for relief calculations [13]. The resulting relief values may be classified into subclasses using the Jenks (Natural Breaks) method or according to predefined intervals selected by the researcher. Bostjančić et al. [1] generated a relief map from a 5 m resolution DEM using the Focal Statistics method. Relief was calculated as the difference between the maximum and minimum elevations (elevation range) within a circular neighborhood with a radius of five cells around each cell. Shao et al. [20] calculated topographic relief from a 12.5 m resolution ALOS PALSAR DEM by determining the difference between the maximum and minimum elevations (elevation range) within a neighborhood with a radius of 2.5 km. Yang et al. [22] investigated the effects of successive landslides on topographic changes using high-resolution UAV-based DEMs. In their study, local relief was calculated using the ArcGIS Focal Statistics method with a 3 m analysis window. Yang et al. [14] investigated the role of topographic relief in landslide occurrence using a SHAP-based explainable machine learning approach.

Carrara [15], while describing the geomorphological characteristics of the Calabria region, used the terms:

- strong relief
- rugged topography
- high local relief

and indicated that such topographic characteristics play an important role in landslide occurrence.

In multivariate models, relief has been used not only descriptively but also quantitatively as the HEIGHT variable, representing local relief or elevation difference. Carrara [15] reported that a multivariate regression model incorporating elevation, height (local relief), surface roughness, and slope gradient could explain approximately 50% of the landslide-affected areas.

III. Results

The relationship between relief and landslides has been described in various ways in the literature. Relief contributes to the interpretation of landslide morphology by reflecting the effects of time-dependent processes such as erosion, weathering, and fracturing on topography [2]. McKean and Roering [5] reported that topographic features developed within landslide relief, such as cracks, internal scarps, compression ridges, folds, and block movements, are important indicators for delineating landslide boundaries, characterizing internal deformation structures, and interpreting movement mechanisms. Relief also controls the spatial distribution of surface movement [5].

Larger landslides tend to occur with increasing relief. As relief increases, longer slip surfaces may develop, resulting in an increase in mean landslide size. A statistical relationship has been identified between relief and landslide size [6]. Regmi and Walter [21] demonstrated that high relief and steep topography are important controls on the development of shallow landslides. Medwedeff et al. [6] similarly emphasized that larger slip surfaces may develop in areas with high relief; however, the effect of relief should be evaluated together with rock strength. As high-relief areas are reduced, the topography gradually becomes smoother, indicating that landslides can modify and smooth the landscape over time [22]. Furthermore, active landslides generally exhibit greater relief variability, whereas weathering and erosion progressively smooth the topography over time [2], [5]. Bostjančić et al. [1] indicated that relief represents the potential energy associated with soil erosion and landslide occurrence and that high-relief areas are characterized by increased surface runoff and reduced infiltration. Rockfalls and deformation processes are also more intense on main slopes characterized by high relief [10]. Increasing relief variability results in

greater topographic irregularity, which is particularly evident in active landslide areas. Therefore, relief variability can be considered an important indicator for assessing landslide activity [2].

Increasing relief variability is also associated with greater variability in landslide size [6]. Relief controls the spatial distribution of landslide deformation [10] and facilitates the interpretation of landslide dynamics [10]. Relief variability is associated with landslide movement [2] and may provide information on landslide age and development [2].

Relief may contribute to landslide occurrence in combination with other processes operating within a study area. Examples reported in the literature include the following:

- One of the main geomorphological characteristics controlling the development of shallow landslides is topographic relief characterized by rugged slopes, incised valleys, and steep hillslopes developed in alternating shale and sandstone formations [21].
- Shallow landslides do not develop in slope hollows characterized by topographic convergence, on concave slopes, or at the bases of steep sandstone slopes. This indicates that topographic differences associated with relief significantly influence landslide occurrence [21].

McKean and Roering [5] reported that landslide surface morphology can be evaluated through relief-related topographic features such as:

- cracks,
- internal scarps,
- compression ridges,
- folds, and
- block movements.

These topographic features can provide information not only on landslide boundaries but also on movement mechanisms and potential future behavior.

Similarly, Berti et al. [7] reported that morphological features developed within the relief reflect active landslides. In their study areas, active earthflows were characterized by readily identifiable morphological features, including:

- distinct source areas,
- flank ridges,
- lobate toes,
- tension cracks,
- pressure ridges, and
- newly developed flow surfaces.

In contrast, these topographic features gradually become less pronounced in old or inactive landslides [7].

Relief can also be used to characterize the internal structure of landslides. Using high-resolution LiDAR data, McKean and Roering [5] distinguished different morphological units, including:

- blocky areas,
- earthflow units,
- compression zones,
- head scarps,
- lateral slopes, and
- toe zones.

These findings demonstrate that relief differences can reveal not only landslide boundaries but also the internal deformation structure of landslides.

Relief can also be used to assess landslide activity. In comparing active and dormant landslides, Berti et al. [7] found that active areas were characterized by distinct topographic irregularities, including:

- fresh deposits,
- steep crown scarps,
- tension cracks,
- pressure ridges, and
- sparse vegetation.

In contrast, long-inactive landslides exhibited smoother relief due to erosion, dense vegetation cover, and degraded scarps [7].

Differences in relief also facilitate landslide classification. Using LiDAR-derived shaded-relief maps, Berti et al. [7] classified their study areas into:

- active landslides,
- dormant landslides, and
- stable slopes.

This classification was based on morphological characteristics visible in the relief and demonstrates the importance of relief in landslide mapping.

Changes in relief can reflect landslide activity. McKean and Roering [5] reported that younger and active landslides generally exhibit more irregular and rugged surfaces with more pronounced topographic features. In contrast, erosion and surface processes gradually smooth the relief of old or long-inactive landslides. Consequently, variations in relief may provide information on the relative age and activity of landslides.

Hillslope relief is one of the principal parameters controlling landslide geometry. Medwedeff et al. [6] used digital elevation models (DEMs) to calculate the following parameters for individual hillslopes:

- hillslope height,
- slope angle, and
- hillslope relief.

These parameters were subsequently incorporated into limit equilibrium analyses. The results demonstrated that relief, together with slope angle, is one of the fundamental geometric parameters controlling slope stability [6].

Relief is also associated with the type of landslide movement. Glenn et al. [2], based on the combined evaluation of field observations and LiDAR analyses, found that:

- pronounced relief develops in the toe zone as a result of upward thrusting,
- the landslide body remains relatively smooth due predominantly to horizontal movement, and
- fractured and irregular relief develops in the upper block due to subsidence.

These findings demonstrate that spatial variations in relief can reflect landslide movement mechanisms.

IV. DISCUSSION

Relief alone is not sufficient for landslide identification. According to Korzeniowska et al. [4], landslides are among the most difficult landforms to distinguish from other geomorphological features based on surface roughness because:

- relief contrast decreases over time in older landslides,
- erosion smooths topographic signatures, and
- landslide boundaries become progressively less distinct.

Therefore, the use of relief or surface roughness alone is insufficient for the reliable identification of landslides.

In some studies, relief is not directly calculated as an independent parameter. Instead, characteristics such as:

- high relief,
- steep topography, and
- tectonic uplift

are described as fundamental conditions that facilitate landslide occurrence [23].

Relief information alone is insufficient; for more accurate landslide identification, it should be evaluated together with surface roughness and measures of local topographic variability [5]. A review of the literature indicates that relief interacts with other environmental and geological factors, including:

- active faults,
- intense rainfall, and
- weak rocks,

which collectively control landslide occurrence [23].

Complex relief characteristics of a study area, such as:

- steep cliffs,
- deep thalwegs,
- depressions,
- subhorizontal surfaces, and
- rugged topography,

may make landslide monitoring more difficult [10]. Overall, relief is necessary for landslide identification but is not sufficient when used alone [5], [7]. Therefore, relief should be evaluated together with:

- surface roughness,
- slope variability,
- aspect variability, and
- three-dimensional orientation variability.

Similarly, Medwedeff et al. [6] demonstrated that relief should not be evaluated independently. In areas characterized by high relief, greater rock/soil strength (cohesion) is required for slopes to remain stable over long periods. Therefore, a natural covariance exists between relief and rock strength, and landslide size is controlled by the combined influence of these two parameters.

V. CONCLUSION

The relationship between relief and landslides is summarized in Table 1. The literature indicates that local relief is an important topographic control factor influencing landslide occurrence [18].

Table 1. Effect of the Relief Parameter on Landslides

Parameter	Property Measured	Purpose in Landslide Studies	Advantage	Disadvantage
Relief	Elevation difference	Energy and topographic potential	Simple	Does not represent microtopography

In conclusion, relief is an important topographic parameter for assessing landslide occurrence and susceptibility and can also provide valuable information on landslide size, morphology, activity, and movement mechanisms. However, the effectiveness of this parameter depends on the geological and geomorphological characteristics of the study area, DEM resolution, and the analysis scale used for relief calculation. Therefore, future studies should systematically evaluate the DEM resolution and neighborhood/window size used to derive relief and compare the effects of relief values obtained at different spatial scales on the performance of landslide susceptibility models.

REFERENCES

[1] I. Bostjančić, M. Filipović, V. Gulam, and D. Pollak, "Regional-scale landslide susceptibility mapping using limited LiDAR-based landslide inventories for Sisak-Moslavina County, Croatia," *Sustainability*, vol. 13, no. 8, Art. no. 4543, 2021, doi: 10.3390/su13084543.

[2] N. F. Glenn, D. R. Streutker, D. J. Chadwick, G. D. Thackray, and S. J. Dorsch, "Analysis of LiDAR-derived topographic information for characterizing and differentiating landslide morphology and activity," *Geomorphology*, vol. 73, nos. 1–2, pp. 131–148, 2006, doi: 10.1016/j.geomorph.2005.07.006.

[3] S. R. LaHusen, A. R. Duvall, A. M. Booth, and D. R. Montgomery, "Surface roughness dating of long-runout landslides near Oso, Washington reveals persistent postglacial hillslope instability," *Geology*, vol. 44, no. 2, pp. 111–114, 2016, doi: 10.1130/G37267.1.

[4] K. Korzeniowska, N. Pfeifer, and S. Landtwing, "Mapping gullies, dunes, lava fields, and landslides via surface roughness," *Geomorphology*, vol. 301, pp. 53–67, 2018, doi: 10.1016/j.geomorph.2017.10.011.

[5] J. McKean and J. Roering, "Objective landslide detection and surface morphology mapping using high-resolution airborne laser altimetry," *Geomorphology*, vol. 57, nos. 3–4, pp. 331–351, 2004, doi: 10.1016/S0169-555X(03)00164-8.M. Shell.

[6] *W. G. Medwedeff, M. K. Clark, D. Zekkos, and A. J. West, "Characteristic landslide distributions: An investigation of landscape controls on landslide size," Earth Planet. Sci. Lett., vol. 539, Art. no. 116203, 2020, doi: 10.1016/j.epsl.2020.116203*.

[7] M. Berti, A. Corsini, and A. Daehne, "Comparative analysis of surface roughness algorithms for the identification of active landslides," *Geomorphology*, vol. 182, pp. 1–18, 2013, doi: 10.1016/j.geomorph.2012.10.022.
[8] Z. Chen, D. Song, M. Juliev, and H. R. Pourghasemi, "Landslide susceptibility mapping using statistical bivariate models and their hybrid with normalized spatial-correlated scale index and weighted calibrated landslide potential model," *Environ. Earth Sci.*, vol. 80, Art. no. 324, 2021, doi: 10.1007/s12665-021-09603-9.
[9] J. Yin, J. Chen, X. Xu, X. Wang, and Y. Zheng, "The characteristics of the landslides triggered by the Wenchuan Ms 8.0 earthquake from Anxian to Beichuan," *J. Asian Earth Sci.*, vol. 37, nos. 5–6, pp. 452–459, 2010, doi: 10.1016/j.jseaes.2009.12.00.
[10] *A. Stumpf, J.-P. Malet, P. Allemand, M. Pierrot-Deseilligny, and G. Skupinski, "Ground-based multi-view photogrammetry for the monitoring of landslide deformation and erosion," Geomorphology, vol. 231, pp. 130–145, 2015, doi: 10.1016/j.geomorph.2014.10.039*.
[11] J. J. Mountjoy, J. McKean, P. M. Barnes, and J. R. Pettinga, "Terrestrial-style slow-moving earthflow kinematics in a submarine landslide complex," *Mar. Geol.*, vol. 267, nos. 3–4, pp. 114–127, 2009, doi: 10.1016/j.margeo.2009.09.007.
[12] C. Quantin, P. Allemand, and C. Delacourt, "Morphology and geometry of Valles Marineris landslides," *Planet. Space Sci.*, vol. 52, no. 11, pp. 1011–1022, 2004, doi: 10.1016/j.pss.2004.07.016.
[13] G. Metternicht, L. Hurni, and R. Gogu, "Remote sensing of landslides: An analysis of the potential contribution to geo-spatial systems for hazard assessment in mountainous environments," *Remote Sens. Environ.*, vol. 98, nos. 2–3, pp. 284–303, 2005, doi: 10.1016/j.rse.2005.08.00.
[14] D. Yang, H. Qiu, S. Hu, Y. Pei, X. Wang, C. Du, Y. Long, and M. Cao, "Exploring the spatial patterns of landslide susceptibility assessment using interpretable Shapley method: Mechanisms of landslide formation in the Sichuan–Tibet region," *J. Environ. Manage.*, 202.
[15] A. Carrara, "Multivariate models for landslide hazard evaluation," *Math. Geol.*, vol. 15, no. 3, pp. 403–426, 1983
[16] H. Zhang, G. Zhang, and Q. Jia, "Integration of analytical hierarchy process and landslide susceptibility index based landslide susceptibility assessment of the Pearl River Delta Area, China," *IEEE J. Sel. Topics Appl. Earth Observ. Remote Sens.*, vol. 12, no. 11, pp. 4239–4252, 2019, doi: 10.1109/JSTARS.2019.2938554.
[17] H. Tanyaş, C. J. van Westen, K. E. Allstadt, M. A. Nowicki Jessee, T. Görüm, R. W. Jibson, J. W. Godt, H. P. Sato, R. G. Schmitt, O. Marc, and N. Hovius, "Presentation and analysis of a worldwide database of earthquake-induced landslide inventories," *J. Geophys. Res. Earth Surf.*, vol. 122, no. 10, pp. 1991–2015, 2017, doi: 10.1002/2017JF004236.
[18] *R. N. Garriss, "Modeling surface roughness as an indicator of age and landslide susceptibility, and the spatial inventory of prehistoric landslides: Green River Valley, WA," M.S. thesis, Portland State Univ., Portland, OR, USA, 2019*.
[19] W. Gong, D. Zekkos, and M. Clark, "A physics-based machine learning-informed model for predicting regional earthquake-induced landslides," *Eng. Geol.*, vol. 361, Art. no. 108488, 2026, doi: 10.1016/j.enggeo.2025.108488.
[20] X. Shao, S. Ma, C. Xu, and Y. Xu, "Insight into the characteristics and triggers of loess landslides during the 2013 heavy rainfall event in the Tianshui Area, China," *Remote Sens.*, vol. 15, no. 17, Art. no. 4304, 2023, doi: 10.3390/rs1517430.
[21] N. R. Regmi and J. I. Walter, "Detailed mapping of shallow landslides in eastern Oklahoma and western Arkansas and potential triggering by Oklahoma earthquakes," *Geomorphology*, vol. 366, Art. no. 106806, 2020, doi: 10.1016/j.geomorph.2019.05.026.
[22] *D. Yang, H. Qiu, S. Hu, Y. Pei, X. Wang, C. Du, Y. Long, and M. Cao, "Influence of successive landslides on topographic changes revealed by multitemporal high-resolution UAS-based DEM," Catena, vol. 202, Art. no. 105229, 2021, doi: 10.1016/j.catena.2021.105229*.
[23] *A. Underwood, A. Booth, S. LaHusen, E. Herzig, A. Duvall, G. Malick, D. Clark, and A. Streig, "Most recent surface rupturing earthquake on the Boulder Creek Fault triggered bedrock landslides in the Nooksack River watershed, Whatcom County, Washington," Geomorphology, vol. 490, Art. no. 109912, 2025, doi: 10.1016/j.geomorph.2025.109912*.

8th International Conference on Engineering, Natural and Social Sciences

September 06-07, 2026: Konya, Turkey

© 2025 Published by All Sciences Academy

https://www.icensos.com/

Public Diplomacy as a Compensatory Mechanism of Traditional Diplomacy in Contexts of Contested Statehood- Case study Kosovo

Armend KRASNIQI [1], Jonuz ABDULLAI [2]

South East University (SEEU), Prishtina, Republic of Kosovo

Abstract - This article examines the relationship between public diplomacy and traditional diplomacy in contexts of contested statehood, arguing that public diplomacy functions as a compensatory mechanism where access to formal diplomatic channels is limited by the absence of full international recognition. While traditional diplomacy relies on interstate relations, legal recognition, and formal negotiations, public diplomacy enables alternative forms of international engagement that generate political effects beyond formal recognition.

Drawing on constructivist international relations theory and the concept of soft power, the study conceptualizes international engagement as a process shaped by perception, legitimacy, and interaction. Public diplomacy serves as a bridge between formal status and practical international engagement by influencing perceptions and expanding opportunities for international interaction, thereby contributing to perceived legitimacy and the normalization of international presence.

The article adopts a qualitative interpretive approach, combining theoretical analysis with the examination of empirical practices. Kosovo serves as the case study, illustrating how public diplomacy operates through cultural diplomacy, media engagement, diaspora mobilization, and economic interaction.

The findings suggest that public diplomacy does not replace traditional diplomacy or legal recognition but complements their limitations by strengthening international presence, engagement, and perceived legitimacy. The study concludes that the relationship between public diplomacy and traditional diplomacy is complementary and context-dependent, particularly in environments of limited recognition.

Keywords: public diplomacy; traditional diplomacy; contested statehood; Kosovo; perceived legitimacy; soft power.

1. Introduction

Traditional diplomacy has historically been understood as a state-centered activity conducted through formal interstate relations, diplomatic recognition, official negotiations, and institutional representation. Within the classical understanding of international relations and international law, diplomatic interaction depends largely on the existence of sovereign recognition and the legal status of states within the international system. States that lack full international recognition often face structural obstacles in accessing formal diplomatic channels and participating equally in international institutions. Consequently, contested or partially recognized states

operate under conditions where traditional diplomacy is constrained both politically and institutionally. Bouris (2018)

In recent decades, developments in international relations have demonstrated that international engagement is no longer limited exclusively to formal interstate diplomacy. Processes of globalization, communication technologies, transnational networks, and the growing importance of non-state actors have expanded the range of mechanisms through which political actors interact internationally (Castells, 2010; Hocking, 2005). Within this changing environment, public diplomacy has emerged as an increasingly important component of international engagement, particularly through communication, network-building, and engagement with foreign publics (Melissen, 2005; Cull, 2020).

Public diplomacy refers to structured efforts aimed at influencing foreign publics, shaping perceptions, building legitimacy, and promoting political interests through communication, interaction, and engagement beyond formal diplomatic channels. Unlike traditional diplomacy, which primarily focuses on interstate communication and official governmental relations, contemporary public diplomacy increasingly involves engagement with foreign publics through media, culture, education, and transnational societal networks (Melissen, 2005). Cull (2020) further emphasizes that public diplomacy extends beyond formal state communication by incorporating practices such as cultural diplomacy, international broadcasting, exchange programs, and interaction with non-state actors.

In contexts of contested statehood, public diplomacy becomes particularly significant because it provides partially recognized states with alternative mechanisms for international presence and engagement. Although such entities may lack full diplomatic recognition or access to formal institutional frameworks, they may still participate internationally through indirect channels that generate political visibility, symbolic legitimacy, and practical interaction (Ker-Lindsay, 2015). In these contexts, public diplomacy functions not as a substitute for traditional diplomacy, but as a complementary and compensatory mechanism that partially offsets the structural limitations imposed by restricted recognition and limited diplomatic access (Bouris & Fernández-Molina, 2020; Melissen, 2005).

This article argues that in contexts of contested statehood, public diplomacy compensates for some of the limitations of traditional diplomacy by creating alternative forms of international interaction that contribute to perceived legitimacy and international presence (Ker-Lindsay, 2015; Bouris, 2018). Drawing on constructivist international relations theory, the study conceptualizes international engagement as a socially constructed process shaped by perception, interaction, and legitimacy rather than exclusively by formal legal recognition (Wendt, 1999). In this context, public diplomacy and soft power contribute to shaping international perceptions and expanding opportunities for engagement beyond traditional diplomatic channels (Nye, 2008; Melissen, 2005).

The case of Kosovo is used as an empirical illustration of this dynamic. Since declaring independence in 2008, Kosovo has operated under conditions of partial international recognition. While these limitations have constrained its participation in certain international institutions and formal diplomatic processes, Kosovo has simultaneously developed various forms of public diplomacy through culture, sports, media engagement, diaspora mobilization, and international communication. In line with Hasan Saliu's argument that contemporary public diplomacy increasingly operates through narratives, communication strategies, and

interaction with foreign publics beyond classical diplomatic channels (Saliu, 2022), Kosovo's experience demonstrates how partially recognized states may maintain international visibility and interaction despite restricted access to traditional diplomacy. These practices contribute to the construction of perceived legitimacy and to the normalization of international presence through indirect and non-traditional forms of engagement.

The article proceeds through six sections. Following the methodology section, the theoretical framework examines the relationship between public diplomacy, soft power, constructivism, and contested statehood. The empirical section analyzes the Kosovo case and identifies concrete practices through which public diplomacy compensates for diplomatic limitations. The discussion section evaluates the broader implications of these findings for understanding international subjectivity and diplomatic practice under conditions of partial recognition

2. Methodology

This study adopts a qualitative interpretive approach by combining theoretical analysis with the examination of documented practices related to Kosovo's international engagement. The methodological framework is grounded in the constructivist perspective, which understands international reality as socially constructed through interaction, perception, legitimacy, and social practices rather than determined exclusively by formal legal structures.

The research focuses on the period 2008–2025, covering the post-independence phase of Kosovo and the gradual development of its public diplomacy practices and international engagement. This period was selected because it represents the principal phase of Kosovo's efforts to consolidate its international subjectivity under conditions of partial international recognition.

The study relies primarily on document analysis as its main empirical technique. The analyzed material includes state strategies, governmental programs, institutional documents, public communications, international reports, and media materials related to Kosovo's international engagement. Particular attention is given to strategic documents addressing diaspora, migration, institutional communication, and foreign policy orientations, as these documents provide insight into official state priorities, the ways international engagement is conceptualized, and the objectives pursued through public diplomacy and international cooperation. The analysis of these documents enables not only the identification of the state's strategic plans and orientations, but also the assessment of how these priorities have been reflected in practice during the analyzed period.

The sources used are treated not only as informational material, but also as discursive artifacts reflecting the ways institutions and relevant actors articulate international presence, legitimacy, and forms of international engagement related to Kosovo.

The study applies thematic and interpretive analysis in order to identify recurring patterns related to perceived legitimacy, international presence, diplomatic interaction, soft power practices, and compensatory mechanisms of international engagement. The purpose of the study is not to produce universal empirical generalizations, but rather to provide an interpretive analysis of the relationship between public diplomacy and traditional diplomacy in contexts of contested statehood.

Kosovo is selected as the case study because it represents one of the most relevant contemporary examples of contested statehood in international relations, where limitations in formal international recognition coexist with active forms of international engagement. The Kosovo case provides an appropriate opportunity to examine how public diplomacy and alternative forms of international interaction operate in support and complementarity to traditional diplomacy under conditions of restricted access to formal diplomatic mechanisms. The selection of this case is also connected to the author's professional and academic proximity to Kosovo's institutional and social context, with the aim of contributing to the academic analysis of Kosovo's public diplomacy practices and international subjectivity.

3. Theoretical Framework

3.1 Public Diplomacy and Traditional Diplomacy

Traditional diplomacy is conventionally associated with formal communication between states conducted through official diplomatic channels such as embassies, interstate negotiations, treaties, and institutional representation. As noted by Henry Kissinger, traditional diplomacy is fundamentally grounded in interstate relations and the management of relations between sovereign political entities through formal diplomatic mechanisms (Kissinger, 1994). remains heavily dependent on sovereignty, legal recognition, and reciprocal interstate relations (Berridge, 2015).

Public diplomacy, by contrast, extends beyond governmental negotiations and engages directly with foreign publics and transnational audiences. Contemporary public diplomacy includes cultural diplomacy, international broadcasting, strategic communication, exchange programs, digital diplomacy, and engagement with non-state actors (Melissen, 2005; Cull, 2020).

Nicholas Cull conceptualizes public diplomacy as a multidimensional practice involving listening, advocacy, cultural diplomacy, exchange diplomacy, and international broadcasting (Cull, 2020, p. 30). Jan Melissen further argues that public diplomacy has evolved into an integral component of foreign policy rather than a peripheral communication instrument, emphasizing that it should become "an integral and substantive, not just presentational, part of the policy-making process" (Melissen, 2005, p. 188).

The distinction between the two forms of diplomacy becomes especially important in contexts of contested statehood. While traditional diplomacy depends heavily on formal recognition and institutional access, public diplomacy can partially circumvent these limitations by operating through informal, societal, and transnational mechanisms of engagement.

3.2 Constructivism and International Subjectivity

Constructivist international relations theory provides an important framework for understanding the relationship between legitimacy, perception, and international engagement. Constructivism challenges purely material and legal understandings of international politics by arguing that identities, interests, and international realities are socially constructed through interaction, norms, and shared meanings (Onuf, 1989; Wendt, 1999).

In this perspective, the international system is not understood solely through material power or formal legal status, but also through the ways actors perceive, interpret, and reproduce social reality in international relations. As Alexander Wendt argues, identities and interests are produced and reproduced through social interaction rather than existing as fixed or predetermined categories (Wendt, 1999, pp. 316–317). From this perspective, international subjectivity is not determined exclusively by legal recognition, but is continuously constructed and reproduced through interaction, perception, legitimacy, and participation in international practices.

This approach is particularly relevant for contested states because it allows analysis of how states function internationally despite incomplete legal recognition. International presence, legitimacy, and interaction become important dimensions of subjectivity alongside formal legal status.

3.3 Soft Power and Perceived Legitimacy

Joseph S. Nye Jr. defines soft power as "the ability to affect others to obtain the outcomes one wants through attraction rather than coercion or payment" (Nye, 2008, p. 94). Soft power relies on credibility, legitimacy, culture, political values, and communication as sources of influence. In this context, public diplomacy serves as one of the principal instruments through which states mobilize and project soft power resources internationally (Nye, 2008, pp. 94–95).

For partially recognized states, soft power becomes especially important because hard power capabilities and formal diplomatic access are often limited. Through public diplomacy, such states attempt to shape international perceptions, increase visibility, and normalize their international presence.

Perceived legitimacy emerges as a key concept within this framework. Even in the absence of universal recognition, states may gradually acquire forms of indirect acceptance and legitimacy through sustained international interaction, participation in international practices, and social engagement with other international actors (Wendt, 1999; Bouris, 2018).

4. Kosovo Case

4.1 Kosovo as a Contested State

Kosovo represents a significant case of contested statehood in contemporary international relations. Since its declaration of independence in 2008, Kosovo has achieved recognition from many states while remaining unrecognized by others, including several influential international actors. This partial recognition has created structural constraints on Kosovo's participation in international organizations and formal diplomatic processes (Ker-Lindsay, 2012; Visoka, 2018). Despite these limitations, Kosovo has continued to function internationally through alternative forms of engagement that extend beyond traditional diplomacy, including participation in transnational networks, public diplomacy practices, and sectoral international cooperation (Visoka, 2018).

4.2 Cultural, Sports, and Celebrity Diplomacy

One of the most visible dimensions of Kosovo's public diplomacy has been its international representation through sports, particularly judo. Kosovo's success in international judo competitions has generated substantial international visibility and symbolic recognition despite the country's incomplete diplomatic recognition.

Athletes such as Majlinda Kelmendi, Distria Krasniqi, and Nora Gjakova have become internationally recognized figures through Olympic and world-level achievements, contributing to the international projection of Kosovo beyond formal diplomatic channels. Kelmendi's Olympic gold medal represented Kosovo's first Olympic medal and became an important moment of symbolic international visibility for the state (International Olympic Committee, 2016, 2020). International media coverage has frequently portrayed these athletes not only as sports champions, but also as symbols of Kosovo's international visibility and state representation. Majlinda Kelmendi's Olympic gold medal at the 2016 Summer Olympics, as well as the Olympic victories of Distria Krasniqi and Nora Gjakova at the 2020 Summer Olympics, significantly increased Kosovo's symbolic presence in international public space and reinforced forms of indirect international recognition through global media exposure. (International Olympic Committee, 2021)

These sporting successes function as instruments of public diplomacy because they generate international visibility, symbolic legitimacy, and emotional association with the state. International audiences engage with Kosovo not primarily through diplomatic negotiations, but through repeated exposure to Kosovar athletes competing successfully under the Kosovo flag in global sporting arenas. In this sense, sports diplomacy contributes to the normalization of Kosovo's international presence and reinforces its treatment as a legitimate participant in international society.

The role of individual public figures is also significant in contexts where traditional diplomacy faces structural limitations. Kosovo football player Vedat Muriqi, who plays for RCD Mallorca in Spain's La Liga, represents an illustrative example of how international visibility and social interaction may develop independently from formal diplomatic engagement. Although Spain does not formally recognize Kosovo, Muriqi has become one of the most recognizable football figures associated with Mallorca and Spanish football audiences. His popularity contributes to forms of indirect social familiarity and interaction between Kosovo and publics within a non-recognizing state.

However, this dynamic cannot be fully categorized as formal public diplomacy in the classical sense, since it does not result from a coordinated or institutional strategy of the Republic of Kosovo. Rather, it reflects a broader form of symbolic international presence generated through individual success, transnational visibility, and societal interaction beyond official diplomatic structures. In this context, internationally recognized public figures may indirectly contribute to familiarity, normalization, and perception-building even in the absence of organized state engagement.

From a constructivist perspective, these interactions are important because they contribute to the social reproduction of international presence through repeated forms of visibility, interaction, and public familiarity. Through international sports competitions, media exposure, and popular cultural representation, Kosovo becomes increasingly normalized as an identifiable international actor despite continuing disputes over formal recognition. In this sense, organized forms of sports diplomacy, as well as indirect symbolic visibility generated by internationally recognized public figures, may contribute to compensating for some of the structural limitations imposed on traditional diplomacy in contexts of contested statehood.

4.3 Diaspora Mobilization

The Kosovar diaspora represents another important mechanism of public diplomacy. Diaspora communities operate as transnational actors connecting Kosovo with international economic, political, academic, and cultural networks, thereby facilitating forms of international engagement that extend beyond formal diplomatic channels (Gamlen, 2014; Ragazzi, 2017). Official governmental strategies increasingly recognize the diaspora as an important developmental and diplomatic resource, particularly through documents such as the *National Strategy for Migration 2019–2025*, the *Strategy for Diaspora and Migration 2024–2028*, and the *Program of the Government of the Republic of Kosovo 2021–2025*.

Nevertheless, the role of the diaspora in public diplomacy often remains under-institutionalized and develops through dispersed practices rather than through fully integrated strategic coordination.

Diaspora engagement contributes to:

- economic interaction,
- knowledge transfer,
- political advocacy,
- image construction,
- international networking,
- cultural representation,
- transnational social connectivity,
- informal diplomatic mediation,
- perception-building among foreign publics,
- normalization of international presence,
- and the creation of indirect channels of international engagement beyond formal diplomatic structures.

These activities create forms of indirect international engagement that compensate for limitations in formal diplomacy.

4.4 Media and Digital Engagement

Media engagement and digital communication have also become important dimensions of Kosovo's public diplomacy. Through international media representation, social media platforms, digital campaigns, and online communication, Kosovo attempts to shape international narratives, influence perceptions, and increase international visibility. In this context, Hasan Saliu argues that contemporary public diplomacy increasingly operates through communication strategies, media narratives, and digital interaction with foreign publics beyond the framework of traditional diplomacy (Saliu, 2022).

Digital diplomacy is especially relevant for contested states because digital platforms reduce dependence on formal diplomatic infrastructure and allow direct communication with international audiences.

4.5 International Institutional Cooperation

Although Kosovo faces limitations in membership within certain international organizations, cooperation with institutions such as the World Bank, the International Monetary Fund, and various international agencies contributes to practical international engagement and institutional legitimacy (Visoka, 2018; Ker-Lindsay, 2015).

Participation in international frameworks, technical cooperation arrangements, and sectoral governance mechanisms creates forms of functional inclusion even where full political recognition remains contested. In this sense, international cooperation operates not only as a technical or developmental process, but also as a mechanism through which partially recognized states reinforce international presence and practical legitimacy.

5. Discussion

The analysis of this study suggests that public diplomacy functions as a compensatory and complementary mechanism in contexts where traditional diplomacy faces structural limitations caused by contested or incomplete international recognition. Rather than replacing formal diplomacy, public diplomacy expands the practical space for international interaction through indirect, societal, cultural, and transnational forms of engagement that are less dependent on formal interstate recognition and institutional access.

In this context, the relationship between traditional diplomacy and public diplomacy should not be understood as mutually exclusive. Traditional diplomacy remains essential for formal recognition, interstate relations, treaty-making, and participation in international organizations. However, where access to these mechanisms is constrained, public diplomacy creates alternative opportunities for visibility, interaction, communication, and symbolic participation in international affairs.

From a constructivist perspective, the findings support the argument that international subjectivity cannot be reduced exclusively to formal legal recognition. The Kosovo case demonstrates that forms of international presence may also be reproduced through interaction, perception, visibility, and practical participation in international networks and arenas. In this process, public diplomacy contributes to the gradual construction of perceived legitimacy and international familiarity through repeated international exposure and engagement.

The analysis also suggests that the mechanisms through which these processes operate are broader than institutional state diplomacy alone. In the case of Kosovo, dimensions such as sports, cultural representation, diaspora engagement, media visibility, digital communication, and institutional cooperation have contributed to expanding Kosovo's international presence beyond classical diplomatic structures. At the same time, the study indicates that not all forms of international visibility should automatically be categorized as formal public diplomacy. Certain forms of symbolic representation and international exposure emerge independently through individual public figures, transnational social interaction, and non-institutional societal dynamics rather than through coordinated state strategies.

This distinction is particularly important in understanding the limits and possibilities of public diplomacy in contested statehood contexts. The findings indicate that public diplomacy is most effective when institutional engagement, societal actors, and symbolic representation interact in complementary ways. However, the analysis also demonstrates that public diplomacy cannot substitute for formal diplomatic recognition or fully overcome geopolitical and institutional constraints. Its impact remains conditioned by broader international political dynamics, institutional capacity, and the ability of states to transform symbolic visibility into sustainable international engagement.

Nevertheless, the Kosovo case illustrates that contested states may still develop meaningful forms of international participation despite incomplete recognition. Through sustained international interaction and indirect mechanisms of engagement, public diplomacy contributes to the normalization of international presence and expands the practical possibilities for international subjectivity beyond the limits of traditional diplomacy aloneNevertheless, the study suggests that in contested statehood environments, public diplomacy significantly expands the practical space for international engagement and contributes to the gradual normalization of international presence.

6. Conclusion

This article has examined the relationship between public diplomacy and traditional diplomacy in contexts of contested statehood, arguing that public diplomacy functions as a compensatory and complementary mechanism where access to formal diplomatic channels is limited by incomplete international recognition. Rather than replacing traditional diplomacy, public diplomacy expands the practical possibilities for international engagement through indirect, societal, and transnational forms of interaction that are less dependent on formal interstate recognition.

Drawing on constructivist international relations theory and the concept of soft power, the study has approached international engagement as a socially constructed process shaped by perception, legitimacy, interaction, and international visibility. From this perspective, international subjectivity cannot be understood exclusively through formal legal recognition, but also through the ways states become present, recognizable, and engaged within international practices and networks.

The case of Kosovo illustrates how contested states may develop meaningful forms of international participation despite structural limitations in traditional diplomacy. Through sports, cultural representation, diaspora engagement, media visibility, digital communication, and institutional cooperation, Kosovo has generated forms of international interaction that contribute to symbolic legitimacy and the normalization of international presence. At the same time, the analysis has shown that certain forms of international visibility emerge independently through societal and individual actors rather than through coordinated institutional diplomacy, highlighting the broader and more complex nature of contemporary international engagement.

The findings suggest that public diplomacy is most effective not as a substitute for traditional diplomacy, but as a mechanism that broadens opportunities for engagement where formal diplomatic access remains constrained. Although it cannot replace legal recognition or fully overcome geopolitical limitations, public

diplomacy contributes to expanding international visibility, facilitating interaction, and reinforcing forms of perceived legitimacy in contested statehood environments.

Ultimately, the study suggests that international subjectivity should be understood as a dynamic and continuously reproduced process that extends beyond formal juridical status. Future research may build on this framework through comparative analysis of other contested or partially recognized states in order to further examine how public diplomacy operates under different political, institutional, and geopolitical conditions.

7. References

Bouris, D. (2018). Contested states, hybrid diplomatic practices, and the everyday negotiation of recognition. International Political Sociology, 12(3), 306–324.

Castells, M. (2010). The rise of the network society (2nd ed.). Wiley-Blackwell.

Cull, N. J. (2020). Public diplomacy: Foundations for global engagement in the digital age. Polity Press.

Hocking, B. (2005). Rethinking the "new" public diplomacy. In J. Melissen (Ed.), The new public diplomacy: Soft power in international relations (pp. 28–43). Palgrave Macmillan.

Bouris, D., & Fernández-Molina, I. (2020). Contested states and the politics of recognition in the international system. Geopolitics, 25(4), 853–873

Ker-Lindsay, J. (2015). Engagement without recognition: The limits of diplomatic interaction with contested states. International Affairs, 91(2), 267–285.

Melissen, J. (Ed.). (2005). The new public diplomacy: Soft power in international relations. Palgrave Macmillan.

Wendt, A. (1999). Social theory of international politics. Cambridge University Press.

Saliu, H. (2022). Diplomacia publike. Universiteti i Tetovës.

Kissinger, H. (1994). Diplomacy. Simon & Schuster.

Berridge, G. R. (2015). Diplomacy: Theory and practice (5th ed.). Palgrave Macmillan.

Onuf, N. G. (1989). World of our making: Rules and rule in social theory and international relations. University of South Carolina Press.

Nye, J. S., Jr. (2008). Public diplomacy and soft power. The ANNALS of the American Academy of Political and Social Science, 616(1), 94–109

Ker-Lindsay, J. (2012). The foreign policy of counter secession: Preventing the recognition of contested states. Oxford University Press.

Visoka, G. (2018). Acting like a state: Kosovo and the everyday making of statehood. Routledge.

International Olympic Committee. (2020, May 5). Only Olympic medal: Majlinda Kelmendi gives Kosovo a reason to dream. https://www.olympics.com/en/news/only-olympic-medal-majlinda-kelmendi-gives-kosovo-a-reason-to-dream

International Olympic Committee. (2021, July 24). TONAKI Funa wins silver, Japan's first medal of Tokyo 2020; Kosovo win gold. Olympics.com. https://www.olympics.com/en/news/tonaki-funa-wins-silver-japan-s-first-medal-of-tokyo-2020-kosovo-win-gold

Nippon. (2021, July 24). Kosovo's Distria Krasniqi wins judo gold at Tokyo Olympics. https://www.nippon.com/en/news/reu20210724KBN2EU0BV/

Gamlen, A. (2014). Diaspora institutions and diaspora governance. International Migration Review, 48(S1), S180–S217.

Ragazzi, F. (2017). A comparative analysis of diaspora policies. Political Geography, 41, 74–89.

Government of the Republic of Kosovo. (2021). Program of the Government of the Republic of Kosovo 2021–2025.

Government of the Republic of Kosovo. (2019). National Strategy for Migration 2019–2025.

Ministry of Foreign Affairs and Diaspora. (2024). Strategy for Diaspora and Migration 2024–2028.

8th International Conference on Engineering, Natural and Social Sciences

September 06-07, 2026: Konya, Turkey

© 2026 Published by All Sciences Academy

https://www.icensos.com/

Depolanan Ham Balık Yağında Mikrobiyal Popülasyon ve Hidrolitik Bozulma Parametreleri

Leyla Buse Sağır*[1], Nurcihan Hacıoğlu Doğru [2]

[1]*Biyoloji Anabilim Dalı/Lisansüstü Eğitim Enstitüsü, Çanakkale Onsekiz Mart Üniversitesi, Türkiye*
[2]*Biyoloji Bölümü /Fen Fakültesi, Çanakkale Onsekiz Mart Üniversitesi, Türkiye*

(lbusesagir@gmail.com)

Özet **–**Ham balık yağı, üretim prosesi ve depolama koşullarına bağlı olarak mikrobiyal kontaminasyona ve hidrolitik bozulmalara son derece duyarlı bir lipit kaynağıdır. Bu çalışmada, su ürünleri işleme tesisinde sevkiyat öncesi IBC tankında 10 gün süreyle bekletilen ham balık yağının mikrobiyal yükü ve birincil kalite parametreleri ön değerlendirme kapsamında incelenmiştir. Yapılan analizlerde, ortamda tespit edilen tek mikrobiyolojik parametreler olan Toplam Canlı Bakteri (ISO 4833) ve Küf-Maya (ISO 21527) popülasyonları ile eş zamanlı olarak Serbest Yağ Asitliği (ISO 660) ve Peroksit Sayısı (ISO 3960) seviyeleri ölçülmüştür. Elde edilen bulgulara göre, 10. gün sonunda toplam canlı bakteri yükü 6,7 x 10^3 kob/g, maya yükü 1,7 x 10^3 kob/g ve küf yükü 2,0 x 10^2 kob/g olarak belirlenmiştir. Kimyasal analizlerde serbest yağ asitliği %22,02 gibi ileri düzey bir hidrolize işaret ederken, peroksit değeri 2,05 meq O_2/kg olarak saptanmıştır. Bu ön veriler, bekleyen ham balık yağında mikrobiyal proliferasyon ve hidrolitik bozulmanın kritik seviyelere ulaştığını kanıtlamaktadır. Elde edilen sonuçlar, lipaz enzimi vb. uygulamaların kontrollü hidrolizle serbest yağ asitlerini artırarak patojen ve indikatör floraya karşı membran bozucu biyodekontaminasyon etkisi gösterme hipotezinin deneysel gerekliliğini ortaya koymaktadır.

Anahtar Kelimeler – Ham balık yağı, biyolojik güvenlik, serbest yağ asitliği, biyo dekontaminasyon

I. GİRİŞ

Balık yağı; içerdiği uzun zincirli çoklu doymamış yağ asitleri (özellikle EPA ve DHA) bakımından insan beslenmesi ve kardiyovasküler sağlık açısından kritik öneme sahip temel bir besin bileşenidir [1], [2]. Endüstriyel ölçekte balık yağı üretimi; ton balığı (*Thunnus albacares, Katsuwonus pelamis, Euthynnus alletteratus* vb.) ve sardalya (*Sardina pilchardus*) gibi pelajik balıkların işlenmesi sırasında açığa çıkan yan ürünlerin değerlendirilmesiyle gerçekleştirilmektedir [3], [4]. Ancak hammadde özellikleri, ortam sıcaklığı ve sevkiyat/depolama aşamaları, ham balık yağını mikrobiyolojik kirlilik ve oksidatif/hidrolitik bozulma risklerine açık hale getirmektedir [5], [6].

Lipazlar (EC 3.1.1.3), trigliseritleri serbest yağ asitlerine (FFA) ve gliserole hidrolize eden yüksek katalitik verimliliğe ve özgüllüğe sahip biyokatalizörlerdir [7], [8]. Trigliserit hidroliziyle açığa çıkan serbest yağ asitleri, yalnızca yağın reolojik özelliklerini ve viskozitesini değiştirmekle kalmayıp [9], aynı zamanda bakteri hücre zarına entegre olarak membran bütünlüğünü ve geçirgenliğini bozan güçlü antimikrobiyal özellikler sergilemektedir [10], [11]. Literatürde lipaz uygulamalarının yağ asidi zenginleştirmesi üzerine yoğunlaştığı; buna karşın kontrollü lipolizle üretilen yağ asitlerinin ham balık yağının yerleşik mikrobiyal florası üzerindeki doğrudan inaktivasyon etkisini ele alan çalışmaların sınırlı olduğu görülmektedir [11]–[13]. Bu çalışma kapsamında, depolama sürecindeki ham balık yağının 10 günlük mikrobiyolojik ve kimyasal kalite durumu ortaya konmuştur.

II. MATERYAL VE YÖNTEM

Materyal

Çalışmada kullanılan ham balık yağı numuneleri, Çanakkale bölgesinde faaliyet gösteren entegre bir su ürünleri işleme tesisinden temin edilmiştir. Numune, üretim sonrası sevkiyata hazır halde IBC (Intermediate Bulk Container) tanklarında 10 gün süreyle bekletilen endüstriyel parti içerisinden aseptik koşullarda alınmıştır.

Mikrobiyolojik Analiz Yöntemleri

Toplam Canlı Bakteri Sayımı ISO 4833 standardına uygun olarak Plate Count Agar (PCA) besiyeri kullanılarak gerçekleştirilmiştir. Aseptik şartlarda hazırlanan desimal seyreltilerden (10^{-1}, 10^{-2}, 10^{-3}) dökme/yayma plak yöntemi uygulanmış ve plaklar 30 ± 1 ºC'de 72 saat inkübe edilmiştir.

Küf ve Maya Sayımı ISO 21527 standardına göre Dichloran Rose Bengal Chloramphenicol (DRBC) Agar besiyeri kullanılmıştır. Yayma plak yöntemiyle ekim yapılmış; 25 ± 1 ºC'de 5 gün inkübasyon sonrasında küf ve maya kolonileri morfolojik olarak ayırt edilerek sayılmıştır.

Kimyasal Analiz Yöntemleri

Serbest Yağ Asitliği (FFA): ISO 660 standardına uygun olarak titrimetrik yöntemle tayin edilmiş ve oleik asit eşdeğeri yüzde cinsinden (% FFA) hesaplanmıştır.

Peroksit Sayısı (PV) ISO 3960 standardı gereğince iyodometrik titrasyon yöntemiyle belirlenmiş ve sonuçlar meq O_2/kg cinsinden ifade edilmiştir.

III. BULGULAR

Ham balık yağının sevkiyat öncesi 10. gününde yapılan mikrobiyolojik analizlerde patojen ve indikatör bakterilerin büyük kısmı tespit limitinin altında kalırken, yalnızca Toplam Canlı Bakteri ile Küf ve Maya parametrelerinde üreme gözlenmiştir. Tablo 1'de ortamda tespit edilen mikrobiyolojik parametreler ile temel kimyasal kalite göstergeleri özetlenmiştir.

Tablo 1. Ham Balık Yağının Mikrobiyolojik ve Kimyasal Analiz Sonuçları

Parametre	Yöntem	Seyreltme Düzeyi	Analiz Sonucu
Toplam Canlı Bakteri	ISO 4833	10^{-1}	$6{,}7 \times 10^3$ kob/g
Maya	ISO 21527	10^{-1}	$1{,}7 \times 10^3$ kob/g
Küf	ISO 21527	10^{-1}	$2{,}0 \times 10^2$ kob/g
SerbestYağ Asitliği	ISO 660	-	% 22,02
Peroksit Sayısı	ISO 3960	-	2,05 meq O_2/kg

IV. TARTIŞMA

10 günlük depolama sonrasında elde edilen bulgular, taze ham balık yağlarına kıyasla mikrobiyal yükte ve hidrolitik ayrışmada kayda değer bir artış olduğunu göstermektedir. Toplam aerobik mezofilik canlı sayısının 6,7 x 10^3 kob/g ve maya popülasyonunun 1,7 x 10^3 kob/g seviyesine ulaşması, yağ fazı ile temas halindeki mikro-su damlacıklarının mikrobiyal proliferasyon için elverişli mikro-çevreler sunduğunu doğrulamaktadır [5].

Özellikle serbest yağ asitliğinin %22,02 seviyesine tırmanmış olması, hammadde kaynaklı endojen enzimlerin ve mevcut lipolitik floranın trigliseritleri hidrolize ettiğini göstermektedir. Birincil oksidasyon göstergesi olan peroksit değerinin 2,05 meq O_2/kg düzeyinde kalması, yağın henüz derin bir oksidatif kokuşma evresine girmediğini; buna karşın hidrolitik bozulmanın ön planda olduğunu kanıtlamaktadır [6].

Bu ön veriler, Ham balık yağında dışarıdan kontrollü olarak uygulanacak ticari lipaz enzimi vb. preparatlarının [7], [8], reaksiyon süresine bağlı olarak antimikrobiyal özellik taşıyan spesifik serbest yağ asitlerini hızla açığa çıkaracağını ve time-kill kinetiği ile ortamdaki bakteri ve maya-küf florasını inaktive edebileceğini düşündürmektedir [10], [14]–[16].

V. SONUÇLAR

Depolama tankında 10 gün bekletilen ham balık yağının mikrobiyal florasında toplam canlı bakteri (6,7 x 10^3 kob/g) ile maya ve küf (1,7 x 10^3 kob/g ve 2 x 10^2 kob/g) tespit edilmiş; serbest yağ asitliği ise %22,02 olarak ölçülmüştür. Bu tablo, ham yağın rafinasyon veya biyoteknolojik işleme öncesinde mikrobiyolojik güvenlik riski taşıdığını ortaya koymaktadır. Bu veriler bu mikrobiyal kirliliğin biyolojik yöntemlerle elimine edilmesi ve ham balık yağı kalitesinin optimize edilmesinin gerekli olduğunu ortaya koymaktadır.

TEŞEKKÜR

Bu çalışma Leyla Buse Sağır'ın Yüksek Lisans tezinden üretilmiştir.

KAYNAKLAR

[1] P. C. Calder, "Mechanisms of action of (n-3) fatty acids," *The Journal of Nutrition*, vol. 142, no. 3, pp. 592S–599S, 2012.

[2] P. M. Kris-Etherton, W. S. Harris, and L. J. Appel, "Fish consumption, fish oil, omega-3 fatty acids, and cardiovascular disease," *Circulation*, vol. 106, no. 21, pp. 2747–2757, 2002.

[3] S. P. Aubourg, V. Losada, J. M. Gallardo, and J. M. Miranda, "Changes in chemical and physical properties of sardine (*Sardina pilchardus*) during chilled storage," *Journal of Food Science*, vol. 70, no. 8, pp. S557–S563, 2005.

[4] FAO, "Tuna and tuna-like species - global production and biology," Food and Agriculture Organization of the United Nations, Rome, 2020.

[5] L. Sheng and L. Wang, "The microbial safety and quality of aquatic products: A review," *Comprehensive Reviews in Food Science and Food Safety*, vol. 20, no. 1, pp. 394–425, 2021.

[6] EFSA Panel on Dietetic Products, Nutrition and Allergies, "Scientific opinion on fish oil for human consumption: Food hygiene," *EFSA Journal*, vol. 8, no. 10, art. no. 1874, 2010.

[7] J. L. Balcázar, I. de Blas, I. Ruiz-Zarzuela, D. Vendrell, and O. Gironés, "Microbial lipases: Applications in aquaculture and food industries," *Journal of Applied Microbiology*, vol. 108, no. 3, pp. 770–778, 2010.

[8] P. Chandra, Enespa, R. Singh, and P. K. Arora, "Microbial lipases and their industrial applications: A comprehensive review," *Microbial Cell Factories*, vol. 19, no. 1, art. no. 169, 2020.

[9] H. G. Kristinsson and B. A. Rasco, "Fish protein hydrolysates: Production, biochemical, and functional properties," *Critical Reviews in Food Science and Nutrition*, vol. 40, no. 1, pp. 43–81, 2000.

[10] A. P. Desbois and V. J. Smith, "Antibacterial free fatty acids: Activities, mechanisms of action and biotechnological potential," *Applied Microbiology and Biotechnology*, vol. 85, no. 6, pp. 1629–1642, 2010.

[11] V. T. A. Nguyen, T. D. Le, H. N. Phan, and L. B. Tran, "Antibacterial activity of free fatty acids from hydrolyzed virgin coconut oil using lipase from *Candida rugosa*," *Journal of Lipids*, vol. 2017, art. no. 7170162, 2017.

[12] W. G. Morais Júnior, G. Fernández-Lorente, and J. M. Guisán, "Production of omega-3 fatty acids through hydrolysis of fish oil by *Candida rugosa* lipase," *Biocatalysis and Biotransformation*, vol. 35, no. 1, pp. 1–9, 2017.

[13] A. Kotogán et al., "Hydrolysis of edible oils by fungal lipases: An effective tool to produce bioactive extracts with antioxidant and antimicrobial potential," *Foods*, vol. 11, no. 12, art. no. 1711, 2022.

[14] A. Naeem, T. Abbas, T. M. Ali, and A. Hasnain, "Time-kill kinetics of lipid fractions isolated from condiments against foodborne pathogens," *Food Technology and Biotechnology*, vol. 56, no. 2, pp. 278–285, 2018.

[15] O. O. Olajuyigbe and A. J. Afolayan, "In vitro antibacterial and time-kill assessment of *Acacia mearnsii* extract," *Molecules*, vol. 17, no. 2, pp. 2103–2118, 2012.

[16] M. S. El Far et al., "Characterization of probiotics isolated from dietary supplements and evaluation of metabiotic-antibiotic combinations using time-kill assay," *BMC Complementary Medicine and Therapies*, vol. 24, art. no. 303, 2024.

8th International Conference on Engineering, Natural and Social Sciences

September 06-07, 2026: Konya, Turkey

© 2026 Published by All Sciences Academy

https://www.icensos.com/

AA1060 Esaslı Al-Nb Alaşımlarında İletkenlik ve Mekanik Dayanımın Eşzamanlı Geliştirilmesi

Ramazan YETİM[1*]

[1]*Makine Mühendisliği ABD/ Fen Bilimleri Enstitüsü, Selçuk Üniversitesi, Türkiye*
(ORCID: https://orcid.org/0000-0002-1649-6990)

[*]*(ramazanyetim1@hotmail.com)*

Özet **–** Yüksek frekanslı transformatör uygulamalarında bakır iletkenler; yüksek maliyet, fiyat istikrarsızlığı ve yüksek yoğunluktan kaynaklanan ağırlık dezavantajları nedeniyle kritik sınırlamalar sergilemektedir. Bu durum, daha düşük maliyetli ve hafif bir alternatif olarak alüminyum iletkenlerin kullanımını kaçınılmaz kılmaktadır. Ancak saf alüminyumun düşük mekanik dayanımı, transformatörün yapısal bütünlüğü ve sarım süreçleri açısından aşılması gereken temel bir kısıt oluşturmaktadır.

Bu çalışmada, alüminyumun söz konusu mekanik sınırlamasını gidermek amacıyla yapıya Niyobyum (Nb) mikro alaşım elementi eklenmiştir. Niyobyum 'un tercih edilme sebebi; alüminyumun elektriksel iletkenlik değerlerini düşürmeden, matriste nano-boyutlu çökeltiler oluşturarak tane yapısını inceltmesi ve mekanik çekme/akma dayanımını artırma yeteneğidir. Ayrıca Nb katkısının sağladığı yüksek termal kararlılık, transformatörün sarım esnasındaki yüksek gerilmelere ve çalışma sırasındaki ısıl yüklenmelere karşı dayanımını hedeflenmektedir. Endüstriyel şartlarda gerçekleştirilen deneylerde elde edilen bulgular, belirli oranlarda (%0,09, %0,15 ve %0,28) Niyobyum (Nb) eklenerek geliştirilen alüminyum alaşımı (AA1060-Nb) ile katkısız alüminyum (AA1060) iletkenlerin elektriksel iletkenlik değerlerinin (yaklaşık 35,25 MS/m) birbirine oldukça yakın kaldığını göstermiştir. Yapılan mekanik testlerde, elektriksel iletkenlik seviyesi saf alüminyum standartlarında korunurken; Nb ilavesi ile akma dayanımında %1,85, çekme dayanımında %10,7 ve kopma uzamasında ise %66,40'a varan oranlarda iyileşme sağlanmıştır. Elde edilen bu sonuçlar, modifiye edilmiş alaşımın yüksek frekanslı transformatör uygulamalarında bakıra yüksek verimli bir alternatif sunduğunu ortaya koymakta ve gelecekteki araştırmalara ışık tutmaktadır.

Anahtar Kelimeler –AA1060 Alaşım, Alüminyum(Al), Niyobyum (Nb) Katkısı, Yüksek Frekanslı Transformatör, İletkenlik

I. GİRİŞ

Piyasada bakır fiyatlarında yaşanan artışlar, yüksek frekanslı transformatör bileşenlerinde alternatif iletken çözümlerinin değerlendirilmesini zorunlu kılmıştır. Alüminyum, hafif yapısı, bakıra muadil özdirenci ve yüksek frekans ortamlarında bu direnç farkının önemsizleşmesi sayesinde alternatif bir malzeme sunmaktadır. Ancak saf haldeki malzemenin düşük mukavemet ve birim uzama değerleri, yüksek dayanım gerektiren sektörlerde tek başına kullanılmasını engeller. Bu doğrultuda alüminyumun alaşımlama süreçlerinden geçirilerek mekanik ve fiziksel yapısının geliştirilmesi gerekmektedir [1],[2],[3]. Alüminyumda mukavemet ile iletkenlik arasında ters orantı vardır. Alaşımlama ve termomekanik işlemler mukavemeti artırırken iletkenliği azaltır [4].

Transformatör tasarımında mekanik mukavemet kritik öneme sahiptir. Aşırı yük ve kısa devre anlarında sargılar üzerinde büyük kuvvetler oluşur. Ayrıca bobin sarımı sırasında uygulanan gerilim iletkenin çekme mukavemetine bağlıdır. [5].

Geleneksel alaşımlama yöntemleri alüminyum iletkenlerin elektrik iletkenliğini düşürürken, katı çözünürlüğü minimum olan nadir toprak elementleri iletkenlik kaybını minimize ederek mekanik dayanımı artırma potansiyeline sahiptir. Optimum mukavemet ve iletkenlik kombinasyonunu elde etmek için en ideal nadir toprak elementi oranını ve en uygun ısıl-mekanik işlem parametrelerini belirlenmiştir [6]. Tane inceltme ve kontrollü çökelme mekanizmalarının sinerjik etkisi, enerji iletim hatlarında gerekli olan yüksek mukavemet–yüksek iletkenlik dengesinin endüstriyel üretim koşullarında sağlanabileceğini göstermektedir [7], [8].

Niyobiyumun (Nb) alüminyum içerisindeki düşük katı çözünürlüğü, ilave edilen Niyobiyumun büyük ölçüde intermetalik parçacıkların oluşumuyla sonuçlanmasına neden olmaktadır. Özellikle Al_3Nb fazının heterojen çekirdeklenme bölgeleri oluşturarak tane inceltici etki gösterdiği ve bu yolla mekanik özelliklerin iyileştirilmesine katkı sağladığı bildirilmektedir. Ayrıca bu fazların yüksek sıcaklık kararlılığı, alaşımın termal dayanımını artırmada önemli bir avantaj sunmaktadır. Bu özellikleri nedeniyle Al–Nb sistemi, yüksek mukavemetli ve termal olarak kararlı alüminyum alaşımlarının geliştirilmesine yönelik araştırmalarda önemli bir çalışma alanı oluşturmaktadır.

II. MATERYAL VE YÖNTEM

Bu çalışmada, matris malzemesi olarak ağırlıkça en fazla %0,12 Si, %0,21 Fe ve %0,015 Ti içeren AA1060 alüminyum alaşımı[9], Niyobyum ilavesi için ise minimum %65 Nb içeriğine sahip (maksimum %0,10 C, %2,5 Si, %0,05 S, %0,10 P, %1,5 Al ve kalan Fe) 44 µm partikül boyutlarında Ferroniyobyum (FeNb) kullanılmıştır [10]. Biri katkısız AA1060 olmak üzere, ağırlıkça farklı Nb oranlarına (%0,28-%0,15-%0,09 Nb) sahip toplam 4 farklı alaşım kompozisyonu endüstriyel ortamda 850 °C reverber fırınlarının da eritilerek levha formunda dökülmüştür.

Haddeleme işlemi 10 mm kalınlığındaki dökülen levhalara, hadde makinesinde dört pasolu haddeleme süreci boyunca levha kalınlığı kademeli olarak azaltılarak ortalama 1.80 mm nihai kalınlık değerine düşürülmüştür. Tavlama 390 °C 8 saat ve 450 °C 12 saat olmak üzere iki farklı süre ve sıcaklıkta yapılmıştır.

Tablo 1. Haddele sonrası numunelerin elektriksel iletkenlik değerleri.

Numune Kodu	**Elektrik iletkenliği (MS/m)**
T1 Num(%0,28Nb)	34,60
T2 Num(%0,15Nb)	35,22
T3 Num(%0,09Nb)	35,28
T4 Num(%0Nb)	35,30

Tablo 1'de, Endüstriyel bir ortamda haddeleme işleminden çıkmış alüminyum numunelerin bir elektriksel iletkenlikleri yer almaktadır. Isıl işlem olmadan sadece haddeleme işlemi yapılarak Nb oranın artmasıyla iletkenliğin düştüğü net bir şekilde görülmüştür.

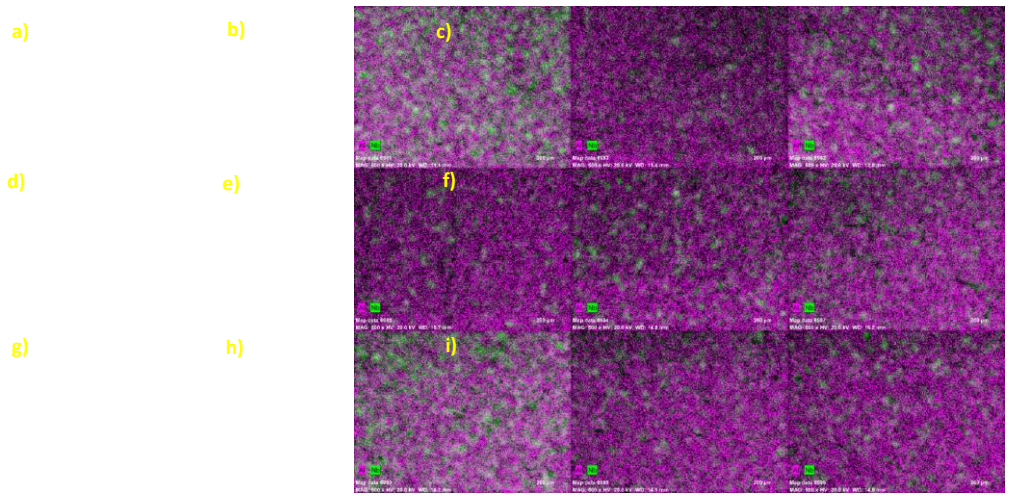

Şekil 2.(a) Tavlamasız %0,28 Nb İçeren Alüminyum alaşımı **(b)** 390 °C saat tavlanmış %0,28 Nb İçeren Alüminyum alaşımı **(c)** 450°C 12 saat tavlanmış %0,28 Nb İçeren Alüminyum alaşımı **(d)** Tavlamasız %0,15 Nb İçeren Alüminyum alaşımı **(e)** 390 °C saat tavlanmış %0,15 Nb İçeren Alüminyum alaşımı **(f)** 450°C 12 saat tavlanmış %0,15 Nb İçeren Alüminyum alaşımı **(g)** Tavlamasız %0,09 Nb İçeren Alüminyum alaşımı **(h)** 390 °C saat tavlanmış %0,09 Nb İçeren Alüminyum alaşımı **(i)** 450°C 12 saat tavlanmış %0,09 Nb İçeren Alüminyum alaşımı

Şekil 2'de Tavlama sıcaklığı ve süresinin yanında Nb miktarında yapılan değişikliklerin atomik difüzyon üzerindeki belirgin etkileri, elde edilen mikro yapı (SEM/BSD) görüntülerindeki dağılımları ve morfolojik değişimlerden açıkça görülmektedir.

Malzemelerin elektriksel iletkenlik değerleri, faz duyarlı girdap akımı prensibiyle çalışan SIGMASCOPE SMP350 cihazı kullanılarak ASTM E1004 standardına uygun olarak ölçülmüştür. Mekanik testler ZWİCK Z030 Test cihazında oda sıcaklığında ISO 6892-1 standardı esas alınarak yapılmıştır. Numunelerin mikro yapısal incelemeleri ZEISS – EVO LS 10 marka Taramalı Elektron Mikroskobu (SEM) ile Geri Saçılan Elektron (BSD) modun da gerçekleştirilmiştir. SEM görüntüleri; 500× büyütme (MAG: 500×), 20 kV ivme voltajı (HV: 20.0 kV) ve 11.1 mm çalışma mesafesi (WD: 11.1 mm) koşullarında kaydedilmiş olup yaklaşık 90 µm ve 200 µm ölçek aralığını kapsamaktadır.

II. BULGULAR VE TARTIŞMA

Şekil 1'de Elde edilen görüntülerde Al elementi magenta rengi ile, Nb elementi ise yeşil rengi ile temsil edilmektedir.

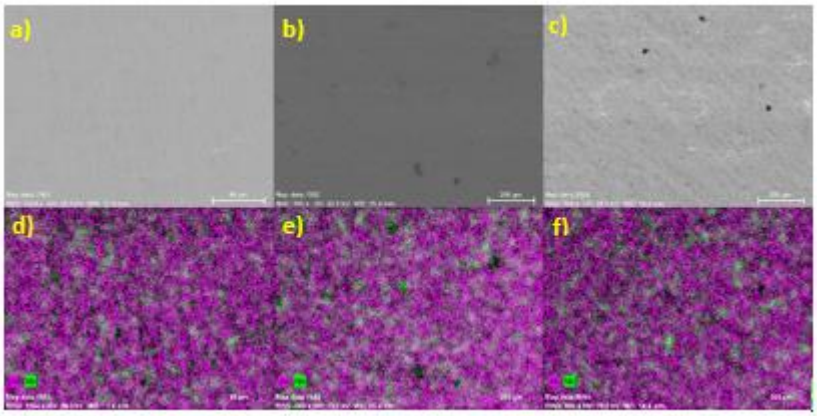

Şekil 1.**(a)** %0,28 Nb İçeren Alüminyum alaşımı **(b)** %0,15 Nb İçeren Alüminyum alaşımı **(c)** %0,09 Nb İçeren Alüminyum alaşımı **(d)** %0,28 Nb İçeren Alüminyum alaşımı Al-Nb dağılımı **(e)** %0,15 Nb İçeren Alüminyum alaşımı Al-Nb dağılımı **(f)** %0,09 Nb İçeren Alüminyum alaşımı Al-Nb dağılımı

EDS görüntüleri, incelenen alan genelinde her iki element de ince ölçekli ve iç içe geçmiş bir dağılım göstermekte olup büyük ölçekli segragasyon dair herhangi bir kanıt gözlemlenmemiştir. Bu durum, etkili mekanik alaşımlama veya katı hal işleme süreçleriyle tutarlı, iyi karışmış bir mikro yapıya işaret etmektedir. Alüminyum baskın bölgelerin görece arttığı, Niyobyum (Nb) elementinin ise Alüminyum zengin matris içinde daha küçük ve ayrık adacıklar şeklinde bulunduğu görülmektedir.

Görüntü genelinde gözlemlenen parlak beyaz bölgeler, Al ve Nb'nin atomik düzeyde eş yoğunlaşmasını doğrulamakta ve Al-Nb intermetalik bileşiklerinin oluşumuna işaret etmektedir.

Tablo 2. Tavlama sürelerine göre elektrik iletkenlikler

Numune Kodu	**Elektrik İletkenliği (8saat Tav) (MS/m)**	**Elektrik İletkenliği(12 saat Tav) (MS/m)**
T1 Num(%0,28Nb)	35,10	35,17
T2 Num(%0,15Nb)	35,85	35,86
T3 Num(%0,09Nb)	35,40	35,70
T4 Num(%0Nb)	35,90	35,66

Tablo 2’de Isıl işleme tabi tutulan numunelerin elektrik iletkenlik değerleri gösterilmiştir.

12 saatlik (yaklaşık 720 dakika) bir tavlama sürecinin sürecinin sonunda 12 saat boyunca dinlendirmeye bırakılmıştır.

8 saatlik (yaklaşık 480 dakika) bir tavlama sürecinin 8 saatlik tavlama 8 saat boyunca dinlendirmeye bırakılmıştır.

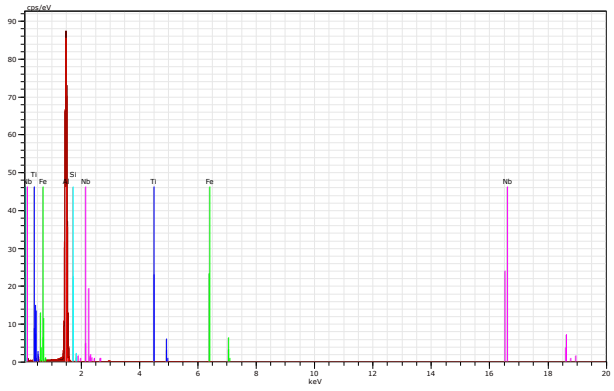

Şekil 3. EDS Spektrumu

Şekil 3'te analiz edilen numuneye ait EDS spektrumu verilmiştir. Spektrumda belirgin olarak Al, Nb, Fe, Ti ve Si elementlerine ait karakteristik pikler gözlenmiştir. Yaklaşık 1,5 keV civarında yüksek şiddette ortaya çıkan Al pikleri, malzemenin Al esaslı matris yapısını doğrulamaktadır. Buna karşılık, yaklaşık 2,2 keV ve 16,6 keV civarında gözlenen Nb karakteristik pikleri, alaşıma ilave edilen niyobyumun mikroyapıda bulunduğunu ve analiz edilen bölgede Nb açısından zengin oluşumların meydana geldiğini göstermektedir.

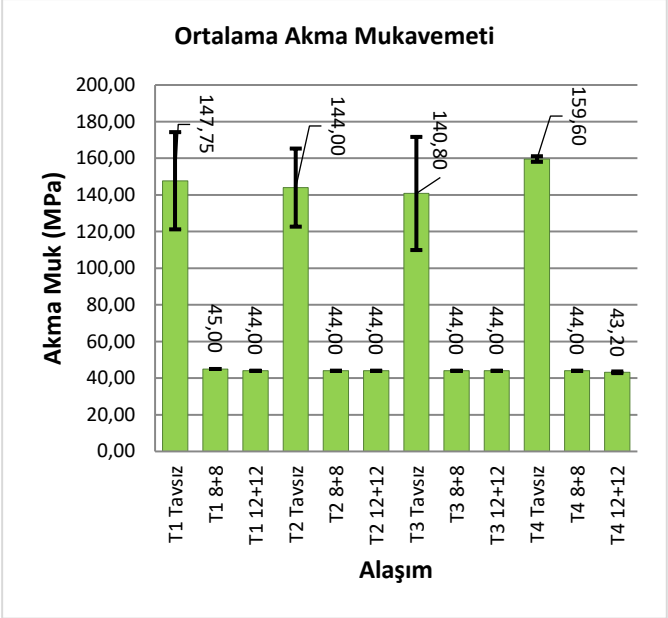

Şekil 2.Ortalama Akma Karşılaştırması

Şekil 4'te farklı alaşım ve ısıl işlem koşullarında elde edilen akma mukavemeti değerleri sunulmaktadır. Tavsız durumda T1, T2 ve T3 alaşımlarının akma mukavemetleri sırasıyla ortalama 147,75 MPa, 144,00 MPa ve 144,00 MPa olarak ölçülmüş olup, bu değerler alaşımların benzer başlangıç mukavemetine sahip olduğunu göstermektedir. Isıl işlem uygulamaları sonucunda T1 alaşımında %70 oranında ciddi bir mukavemet kaybı gözlenirken, T2 alaşımında 8 saat tav koşulunda benzer bir düşüş yaşanmış, ancak 12 saat tav koşulunda 140,80 MPa ile tavsız seviyesine yakın bir değer elde edilmiştir. En dikkat çekici bulgu, T3 alaşımının 12 saat tav koşulunda 159,60 MPa ile en yüksek akma mukavemetine ulaşması ve tavsız duruma göre yaklaşık %11 oranında iyileşme göstermesidir.

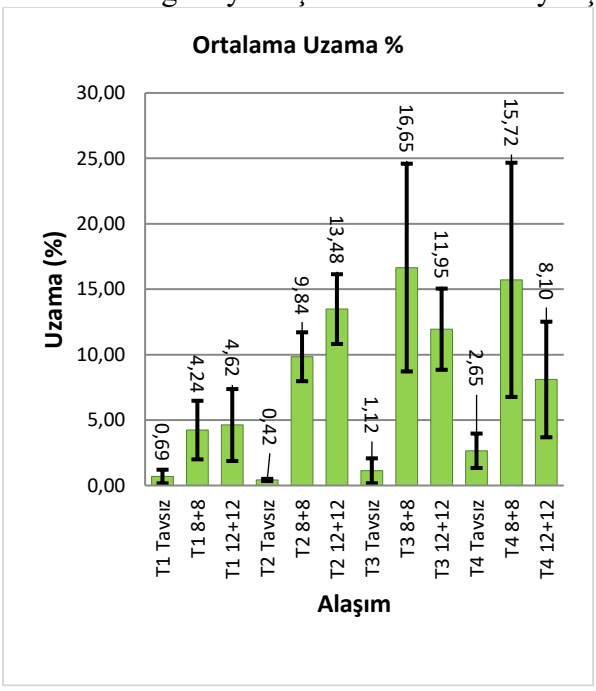

Şekil 3.Ortalama Uzama

Şekil 6'da Tavsız durumda en yüksek uzama değeri T4 alaşımında (%2,55) gözlenirken, en düşük değer T2 alaşımında (%0,42) tespit edilmiştir. Isıl işlem uygulamaları tüm alaşımlarda uzama değerlerini önemli ölçüde artırmış olup, en dikkat çekici iyileşme T2 alaşımında %3109'luk artışla (0,42'den 13,48'e) kaydedilmiştir. 8 saat tav koşulunda en yüksek uzama değeri T3 alaşımında (%16,65) elde edilirken, bunu

T4 alaşımı (%15,72) takip etmiştir. Ancak 12+12 koşulunda T3 ve T4 alaşımlarında sırasıyla %28,2 ve %48,5 oranında belirgin düşüşler meydana gelirken, T2 alaşımında %37'lik ek bir iyileşme sağlanmıştır. T1 alaşımı tüm koşullarda en düşük uzama değerlerini sergilemiş olup, 8 saat tav ve 12 saat tav arasında anlamlı bir fark oluşmamıştır (%4,24'ten %4,52'ye). Bu bulgular, her alaşımın kendine özgü optimum ısıl işlem koşuluna sahip olduğunu ve genel geçer bir işlem parametresinin tüm alaşımlar için uygulanamayacağını açıkça göstermektedir. Özellikle T3 ve T4 alaşımlarında 8 saat tav'dan 12 saat tav'a geçişte gözlenen belirgin düşüşler, aşırı ısıl işlemin bu alaşımlarda tane büyümesi veya kırılgan faz oluşumu gibi olumsuz mikro yapısal değişimlere yol açtığını düşündürmektedir. Buna karşın T2 alaşımının 12 saat tav koşulunda sünekliğini artırmaya devam etmesi, bu alaşımın farklı bir mikro yapısal dönüşüm kinetiğine sahip olduğunu ortaya koymaktadır.

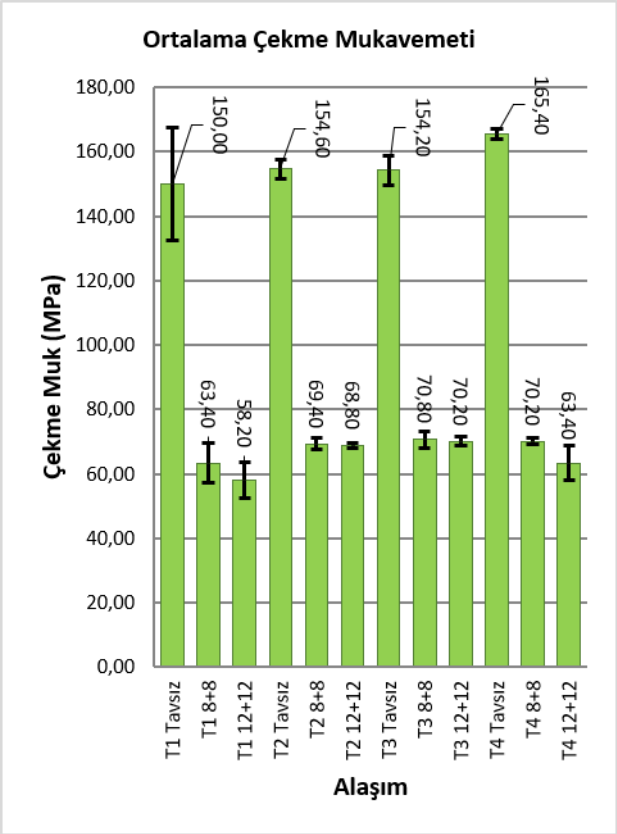

Şekil 4.Çekme Mukavemeti Karşılaştırması

Şekil 5'te farklı alaşım ve ısıl işlem koşullarında elde edilen çekme mukavemeti değerleri karşılaştırmalı olarak sunulmaktadır. Tavsız durumda T4 alaşımı 165,40 MPa ile en yüksek çekme mukavemetine sahipken, T1, T2 ve T3 alaşımları yaklaşık 154 MPa ile benzer değerler sergilemiştir. Isıl işlem uygulamaları tüm alaşımlarda çekme mukavemetinde önemli düşüşlere neden olmuş olup, bu düşüş %54,1 (T3-8 saat tav) ile %62,2 (T1-12 saat tav) arasında değişmektedir. 8 saat tav koşulunda en yüksek çekme mukavemeti T3 alaşımında (70,80 MPa) elde edilirken, bunu sırasıyla T4 (70,20 MPa), T2 (69,40 MPa) ve T1 (63,40 MPa) takip etmiştir. 12 saat tav koşulunda da benzer bir sıralama korunmuş olup, T3 alaşımı 70,20 MPa ile yine en yüksek değeri sergilemiştir. 8 saat tavdan 12 saat tav'a geçişte T1 ve T4 alaşımlarında sırasıyla %8,2 ve %9,7 oranında ek mukavemet kaybı yaşanırken, T2 ve T3 alaşımlarında bu değişim %1'in altında kalmıştır. Bu bulgular, T2 ve T3 alaşımlarının ısıl işlem süresindeki artışa karşı daha dayanıklı olduğunu, buna karşın T1 ve T4 alaşımlarının uzun süreli ısıl işlemden olumsuz etkilendiğini göstermektedir.

III. SONUÇLAR

Niyobyum (Nb) eklenerek geliştirilen alüminyum alaşımı (AA1060-Nb) ile katkısız alüminyum (AA1060) iletkenlerin elektriksel iletkenlik değerlerinin (yaklaşık 35,25 MS/m) birbirine oldukça yakın kaldığını göstermiştir. Yapılan mekanik testlerde, elektriksel iletkenlik seviyesi saf alüminyum standartlarında korunurken; Nb ilavesi ile akma dayanımında %1,85, çekme dayanımında %10,7 ve kopma uzamasında ise %66,40'a varan oranlarda iyileşme sağlanmıştır.

Testlerin doğrudan endüstriyel üretim koşullarında yapılması, elde edilen sonuçların ölçeklenebilirliğini ve pratik uygulanabilirliğini ortaya koymakta; süreç optimizasyonu açısından çalışmanın ileri seviye araştırmalara açık olduğunu kanıtlamaktadır.

KAYNAKLAR

[1] S. Koch ve H. Antrekowitsch, "Aluminum Alloys for Wire Harnesses in Automotive Engineering", *Berg Huettenmaenn Monatsh*, c. 152, sy. 2-3, ss. 62-67, Mar. 2007, doi: 10.1007/s00501-007-0275-z.

[2] C. R. Sullivan, "Aluminum Windings and Other Strategies forHigh-Frequency Magnetics Design in anEra of High Copper and Energy Costs", *IEEE Trans. Power Electron.*, c. 23, sy. 4, ss. 2044-2051, Tem. 2008, doi: 10.1109/TPEL.2008.925434.

[3] P. Vilaça, J. Mendes, F. Nascimento, ve L. Quintino, "Application of FSW to Join Aluminium Foil Winding Coils for Electrical Transformers", *Int J Mech Syst Eng*, c. 2, sy. 1, ss. 1-6, Haz. 2016, doi: 10.15344/2455-7412/2016/115.

[4] F. Czerwinski, "Aluminum alloys for electrical engineering: a review", *J Mater Sci*, c. 59, sy. 32, ss. 14847-14892, Ağu. 2024, doi: 10.1007/s10853-024-09890-0.

[5] J. W. Dold, "Improved aluminum magnet wires for power & distribution transformers", içinde *1971 EIC 10th Electrical Insulation Conference*, Chicago, IL, USA: IEEE, Eyl. 1971, ss. 239-242. doi: 10.1109/EIC.1971.7460826.

[6] A. E. Medvedev, M. Y. Murashkin, N. A. Enikeev, R. Z. Valiev, P. D. Hodgson, ve R. Lapovok, "Enhancement of mechanical and electrical properties of Al-RE alloys by optimizing rare-earth concentration and thermo-mechanical treatment", *Journal of Alloys and Compounds*, c. 745, ss. 1-20, May. 2018, doi: 10.1016/j.jallcom.2018.02.247.

[7] J. Cheng, B. Li, Q. Cai, B. Zhao, C. Xu, ve Z. Chen, "Aging behavior and mechanical properties of ultra-fine grained Al2024-2TiN composite prepared by spark plasma sintering", *Materials Characterization*, c. 181, s. 111497, Kas. 2021, doi: 10.1016/j.matchar.2021.111497.

[8] M. Murashkin *vd.*, "Enhanced Mechanical Properties and Electrical Conductivity in Ultrafine-Grained Al 6101 Alloy Processed via ECAP-Conform", *Metals*, c. 5, sy. 4, ss. 2148-2164, Kas. 2015, doi: 10.3390/met5042148.

[9] Z. J. Wang, M. Ma, Z. X. Qiu, J. X. Zhang, ve W. C. Liu, "Microstructure, texture and mechanical properties of AA 1060 aluminum alloy processed by cryogenic accumulative roll bonding", *Materials Characterization*, c. 139, ss. 269-278, May. 2018, doi: 10.1016/j.matchar.2018.03.016.

[10] R. Yakut, "The effect of niobium carbide coating on wear behavior of grey cast iron via thermo-reactive diffusion process", *European Mechanical Science*, c. 8, sy. 3, ss. 115-124, Eyl. 2024, doi: 10.26701/ems.1467274.

8th International Conference on Engineering, Natural and Social Sciences

September 06-07, 2026: Konya, Turkey

© 2026 Published by All Sciences Academy

https://www.icensos.com/

Dynamic Response Assessment of a ZrO_2-Retrofitted Parallel Strand Lumber Pedestrian Bridge by FEA

Sertaç Tuhta*[1]

[1]*Department of Civil Engineering, Ondokuz Mayıs University, Turkey*

*(stuhta@omu.edu.tr) *Email of the corresponding author*

Abstract **–** Natural hazards, particularly seismic events, alongside fluctuating traffic and environmental actions, pose ongoing risks to the safety and serviceability of timber bridge infrastructures. Consequently, optimizing the dynamic behavior of sustainable structural systems has become a critical focus in engineering research. Parallel Strand Lumber (PSL) bridges have gained traction due to their high strength-to-weight ratio, dimensional stability, material efficiency, and structural reliability. However, upgrading their dynamic stiffness and vibration characteristics remains an essential challenge, especially for pedestrian bridges subject to dynamic operational loads. Zirconium dioxide (ZrO_2) surface coating offers a promising retrofitting technique owing to its high stiffness and favorable mechanical properties, which can enhance the overall performance of timber structural members. This study numerically investigates the influence of a ZrO_2 surface coating on the dynamic response of a PSL timber pedestrian bridge using finite element analysis. A three-dimensional finite element model of the baseline PSL bridge was developed, and its intrinsic dynamic characteristics were determined through modal analysis. A layer of ZrO_2 coating was integrated into the primary structural components, followed by a repetition of the numerical evaluation. The existing and retrofitted bridge models were compared in terms of natural frequencies and mode shapes. The application of the ZrO_2 coating effectively increased the natural frequencies, enhanced global structural rigidity, and modified the bridge's vibrational characteristics. The results indicate that ZrO_2 surface retrofitting provides a practical and effective solution for improving the dynamic stability and vibration performance of sustainable PSL timber pedestrian bridges.

Keywords – FEA, PSL, Modal Analysis, ZrO_2 Coating, Dynamic Response

I. INTRODUCTION

Natural hazards, including earthquakes, strong winds, floods, landslides, and tsunamis, continue to present severe risks to the safety, serviceability, and long-term durability of global civil infrastructure. Among these hazards, seismic events are particularly critical because the resulting inertial forces can produce excessive deformations, structural damage, economic losses, and human casualties. Pedestrian bridges are likewise exposed to dynamic excitation arising from human movement, wind, seismic actions, and environmental effects. The dynamic performance of a bridge is governed by the interaction among stiffness, mass distribution, damping, and energy dissipation capacity; deficiencies in these parameters may lead to excessive displacement, stress concentrations, vibration amplification, and resonance under dynamic loading. Accordingly, improving the stiffness and dynamic response of lightweight bridge systems has become an important objective in structural engineering [1], [4], [8], [12], [17], [19], [21].

Timber has gained significant traction in structural applications because of its renewable nature, relatively low embodied carbon, favorable strength-to-weight ratio, and suitability for efficient construction. Engineered wood products have further expanded the potential of timber structures by

providing more uniform and predictable mechanical properties than conventional solid wood. Among these products, parallel strand lumber (PSL) is recognized for its high strength, dimensional stability, material efficiency, and reliable structural performance. Manufactured by aligning wood strands in a predominantly parallel orientation and bonding them under controlled pressure and temperature conditions, PSL forms an engineered material capable of carrying substantial loads. These characteristics make PSL suitable for beams, columns, frames, and bridge components where strength and stiffness are required without excessive self-weight [2], [3], [5], [7], [14], [28].

Despite these advantages, lightweight PSL pedestrian bridges may exhibit undesirable dynamic behavior under repeated or transient loading. Pedestrian traffic, wind gusts, seismic forces, and ambient excitation can induce excessive vibration and deformation when structural stiffness and damping are insufficient. The dynamic characteristics of timber bridges, particularly their natural frequencies and mode shapes, are strongly influenced by the stiffness and mass distribution of structural members, connections, and support conditions. Changes in these parameters directly affect the global vibration behavior, while insufficient stiffness generally results in larger dynamic displacements. Therefore, retrofit techniques capable of increasing the effective stiffness of PSL components without introducing substantial additional mass represent an important research area in advanced timber bridge design [6], [10], [13], [16], [20].

Various strengthening and surface-modification strategies, including fiber-reinforced polymers, mechanical reinforcement, nanomaterials, mineral-based treatments, adhesive systems, and advanced protective coatings, have been investigated to improve the mechanical performance and durability of timber and other structural systems. Previous studies have demonstrated the usefulness of composite retrofitting and coating approaches for modifying structural stiffness and dynamic characteristics [15], [18], [22].

Surface engineering is particularly attractive because it can modify structural behavior while producing comparatively limited changes in member geometry. Functional coatings may also improve surface hardness and stiffness while providing protection against moisture, thermal fluctuations, decay, and environmental degradation. Such modifications can affect localized behavior as well as the effective stiffness and dynamic response of the structural system [9], [11].

Among advanced ceramic materials, zirconium dioxide (ZrO_2) has attracted attention because of its high hardness, stiffness, chemical stability, thermal resistance, and durability. ZrO_2-based materials are used in demanding engineering applications where mechanical resistance and environmental protection are required. Recent investigations of ceramic and nanocoating systems have reported changes in structural stiffness, dynamic parameters, and vibration characteristics under different loading conditions [24], [25], [26].

When used as a surface coating or retrofit layer, ZrO_2 may improve the mechanical characteristics of the treated surface while simultaneously acting as a protective barrier. Its relatively high stiffness makes it a potentially suitable material for strengthening timber members. For PSL pedestrian bridge components, a ZrO_2 coating can increase effective structural stiffness and consequently modify modal properties and dynamic response, which are important considerations for vibration control and serviceability [30].

Although previous studies have examined fiber-reinforced polymers, mechanical reinforcement, adhesive systems, nanocoatings, and composite materials for timber and other structural members, comparatively limited attention has been given to ceramic surface coatings and their influence on the global dynamic behavior of engineered timber pedestrian bridge systems. Research on LVL, PSL, and related engineered timber materials has established their mechanical potential, while studies on retrofitting have primarily focused on other reinforcement or coating systems. In particular, numerical investigations of ZrO_2-retrofitted PSL pedestrian bridges and the resulting changes in natural frequencies, mode shapes, stiffness, and dynamic response remain insufficiently explored. Establishing the relationship between ceramic surface treatment and vibration characteristics is therefore relevant to the development of safer, more durable, and lightweight timber bridge systems [23].

Finite Element Analysis (FEA) provides a robust numerical framework for simulating the structural response of timber systems under static and dynamic actions. By representing geometry, material

properties, connection characteristics, and boundary conditions, FEA enables detailed assessment of complex structural systems and facilitates the numerical evaluation of retrofit strategies before implementation. Modal analysis within an FEA framework provides information on natural frequencies, mode shapes, and vibration characteristics. Since resonance may occur when excitation frequencies approach structural natural frequencies, changes in structural stiffness can shift these frequencies and consequently alter the vibration response. Previous finite-element and modal studies on retrofitted structural systems demonstrate the usefulness of this approach for evaluating changes in dynamic characteristics [29].

In this study, the dynamic response of a ZrO_2-retrofitted parallel strand lumber pedestrian bridge is numerically evaluated using finite element analysis. Two three-dimensional finite element models representing the existing PSL bridge and the ZrO_2-retrofitted system were developed using identical geometry, material definitions, supports, and boundary conditions, differing only in the presence of the surface treatment. The dynamic behavior of both models was evaluated through modal analysis, with emphasis on changes in natural frequencies and mode shapes. In addition, mode shapes were compared to determine the influence of the ZrO_2 coating on structural displacement and overall stiffness. By comparing the existing and retrofitted models, the study provides a numerical assessment of ZrO_2 surface retrofitting as a potential strengthening and vibration-control approach for engineered timber pedestrian bridges [27].

II. Materials and Method

To systematically evaluate the impact of a zirconium dioxide (ZrO_2) surface coating on the dynamic response and vibration characteristics of a Parallel Strand Lumber (PSL) timber pedestrian bridge, a three-dimensional finite element investigation was performed using SAP2000 program. Two separate 3D finite element models were developed one representing the existing PSL timber pedestrian bridge and the other representing the ZrO_2-coated configuration. To isolate the effect of the surface treatment, both models retained identical geometry, structural member dimensions, support conditions, and timber material properties. The application of the ZrO_2 coating layer served as the sole variable between the two models. Modal analyses were conducted to compare the natural frequencies and mode shapes of both configurations. Furthermore, mode shapes were compared to quantify changes in overall structural stiffness post-retrofit. This comparative modeling framework provided a clear assessment of how ZrO_2 surface retrofitting influences the stiffness, vibration modes, and dynamic behavior of PSL timber bridges, adhering to established finite element procedures for structural, dynamic, and seismic evaluations of engineered timber bridges.

A. Description of PSL Pedestrian Bridge

The PSL pedestrian bridge model is a timber structure with ten equal spans (3 m) in the x-direction, a single span (3 m) in the y-direction, and a height of 3 m. The bridge deck area is 90 square meters. Column cross-sections are 25x25 cm, beam cross-sections are 20x20 cm, rail element cross-sections are 5x10 cm, and the deck thickness is 15 cm. The finite element model of the PSL structure was created using the SAP2000 program. The finite element model of the PSL pedestrian bridge is given in Figure 1. The mechanical properties of the PSL are given in Table 1, where L, T, and R represent the longitudinal, tangential, and radial directions, respectively.

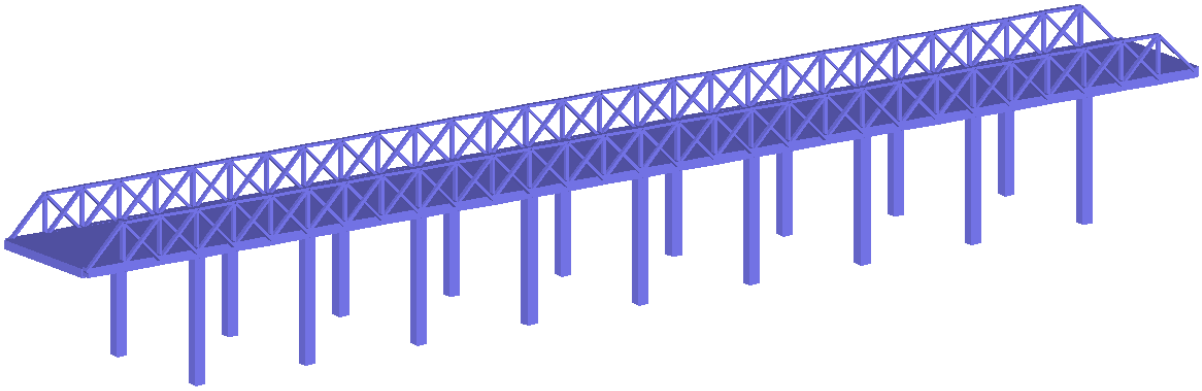

Fig. 1 3D Finite element model of the PSL pedestrian bridge

Table 1. Mechanical properties of PSL

Material	Modulus of Elasticity (kN/m^2)	Poisson's Ratio	Weight per Unit Volume (kN/m^3)
PSL	$10.75x10^6$ (L)	0.35 (LR)	7
	$0.43x10^6$ (T)	0.35 (LT)	
	$0.43x10^6$ (R)	0.02 (RT)	

L: Longitudinal, T: Tangential, R: Radial

B. Description of Coated PSL Pedestrian Bridge

The columns of the existing PSL pedestrian bridge are coated with 2.5 mm thick ZrO_2. Thus, a coated model was created. The finite element model of the coated PSL pedestrian bridge is given in Figure 2. Mechanical properties of ZrO_2 are given Table 2.

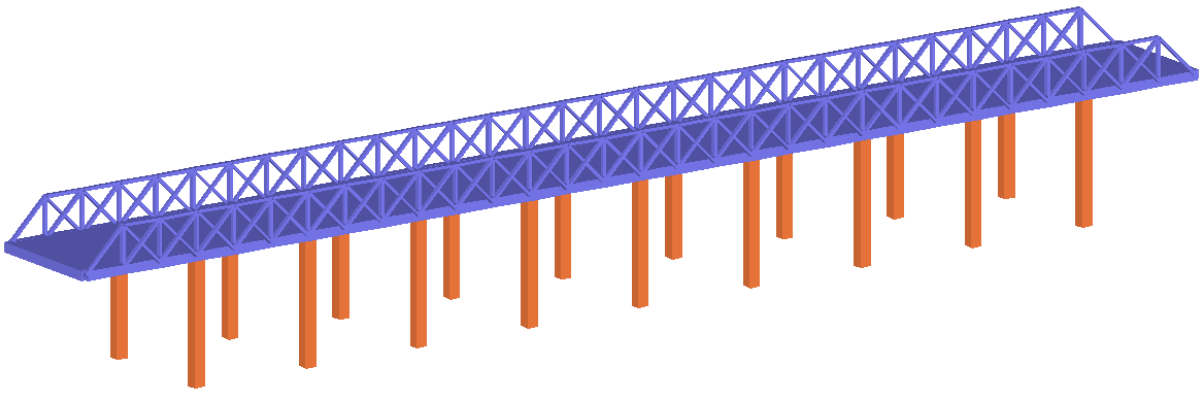

Fig. 2 3D Finite element model of the coated PSL pedestrian bridge

Table 2. Mechanical properties of ZrO_2

Material	Modulus of Elasticity (kN/m^2)	Poisson's Ratio	Weight per Unit Volume (kN/m^3)
ZrO_2	$175x10^6$	0.27	56

III. RESULTS

A. Modal Analysis Results of PSL Pedestrian Bridge

A modal analysis was carried out on the parallel strand lumber (PSL) pedestrian bridge models to thoroughly assess their dynamic characteristics under free-vibration conditions. The investigation focused specifically on the first five vibration modes, as these lower-order modes typically dictate the primary dynamic behavior, overall structural response, and stiffness distribution of timber footbridges.

Through finite element modeling, the core natural frequencies and their associated mode shapes were systematically identified for both the unreinforced existing bridge and the ZrO_2-retrofitted structural configuration. The complete comparative results detailing these five fundamental modes along with a detailed evaluation of their structural significance and performance implications are illustrated across Figures 3 to 7.

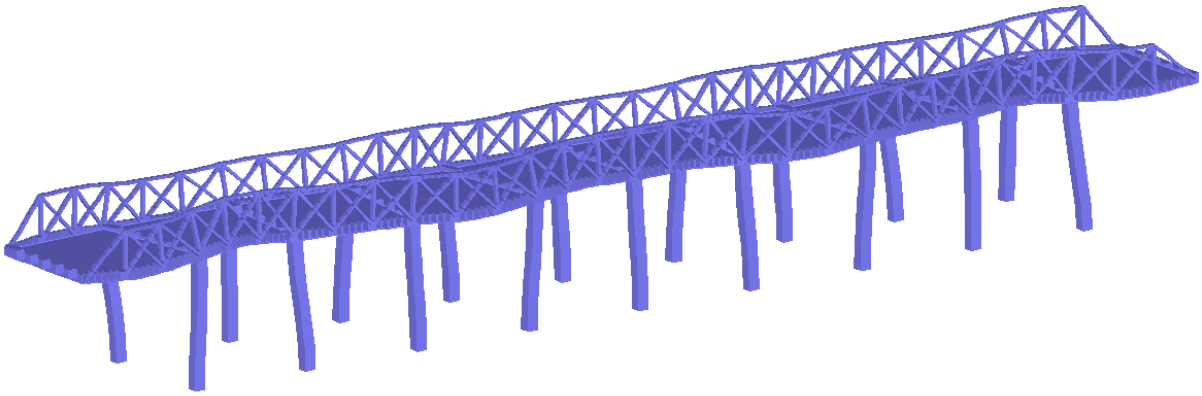

Fig. 3 1st Mode shape (Frequency value = 1.920 Hz)

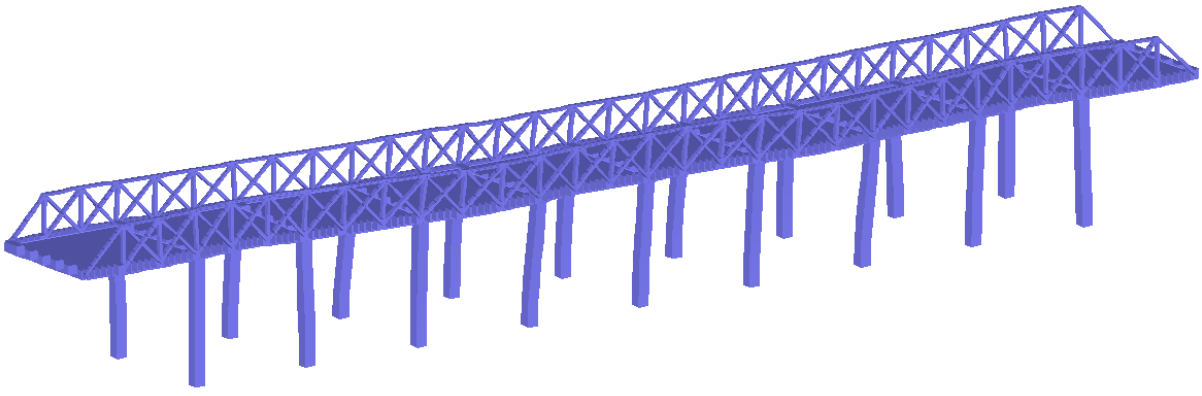

Fig. 4 2nd Mode shape (Frequency value = 6.701 Hz)

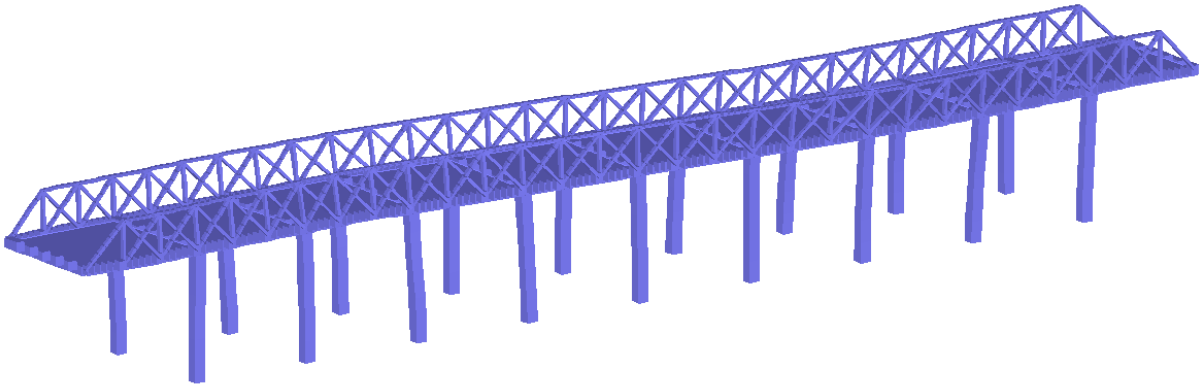

Fig. 5 3rd Mode shape (Frequency value = 9.238 Hz)

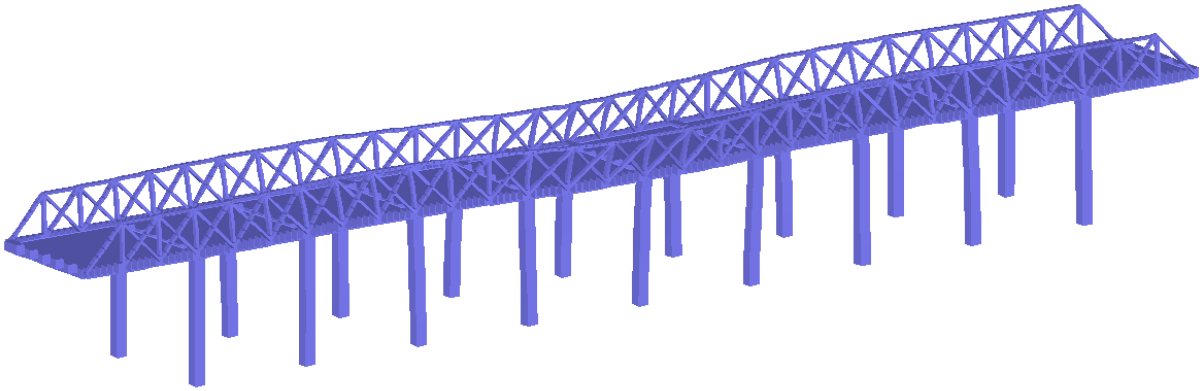

Fig. 6 4th Mode shape (Frequency value = 14.883 Hz)

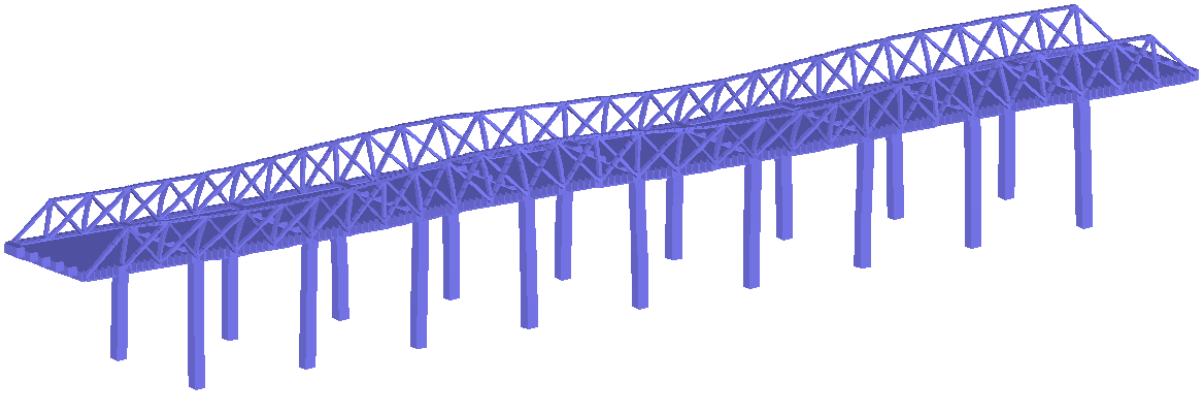

Fig. 7 5th Mode shape (Frequency value = 16.393 Hz)

B. Modal Analysis Results of Coated PSL Pedestrian Bridge

To evaluate the specific impact of the retrofit material on the overall dynamic behavior of the structure, a comprehensive modal analysis was conducted on the ZrO_2-retrofitted PSL pedestrian bridge model. The investigation focused primarily on the first five vibration modes, as these fundamental modes dictate the global dynamic response of the bridge under free-vibration conditions.

The integration of the ZrO_2 retrofit alters the stiffness distribution throughout the structural components, consequently modifying both the natural frequencies and their corresponding mode shapes. The resulting modal parameters provide critical data for assessing how effectively the ZrO_2 reinforcement enhances the dynamic performance and overall structural stability of the PSL pedestrian bridge. The first five natural frequencies alongside their associated mode shapes obtained from the finite element analysis are illustrated in Figures 8 through 12.

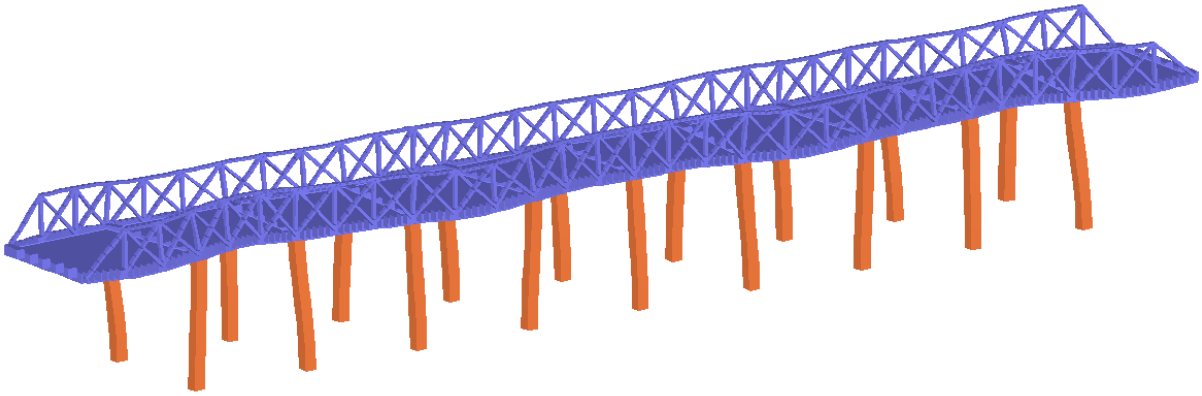

Fig. 8 1st Mode shape (Frequency value = 2.718 Hz)

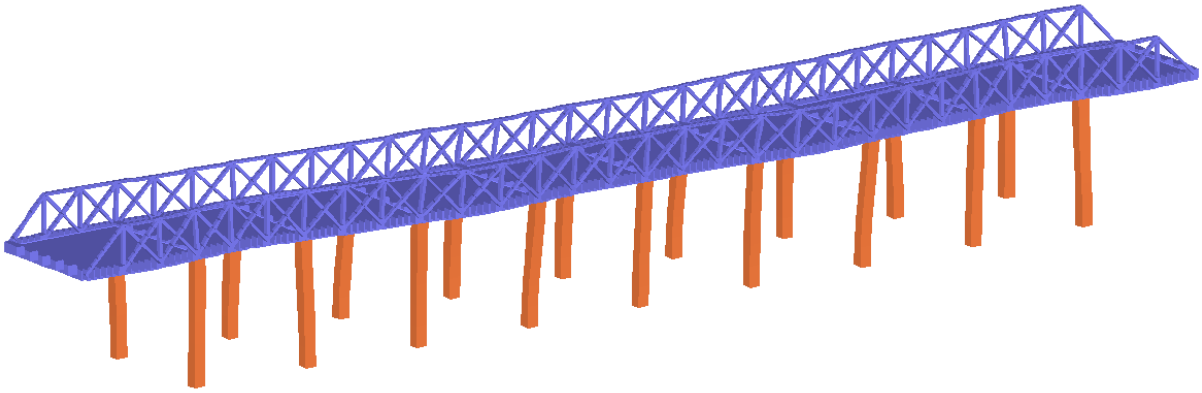

Fig. 9 2nd Mode shape (Frequency value = 7.369 Hz)



Fig. 10 3rd Mode shape (Frequency value = 9.584 Hz)

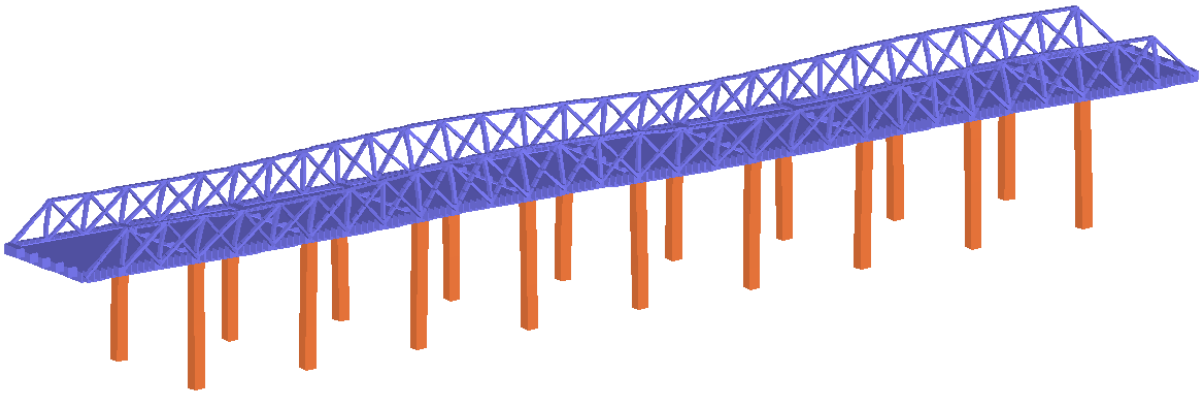

Fig. 11 4th Mode shape (Frequency value = 15.039 Hz)

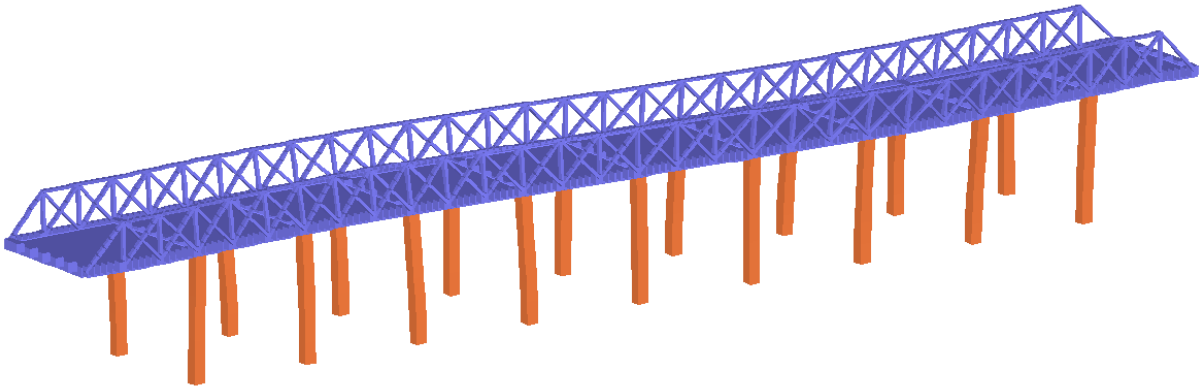

Fig. 12 5th Mode shape (Frequency value = 16.507 Hz)

IV. DISCUSSION

Table 3 compares the natural frequencies obtained for the existing and ZrO_2-retrofitted PSL pedestrian bridge models. The comparison provides a direct evaluation of the influence of the ZrO_2 coating on the dynamic characteristics of the bridge. By examining the modal frequencies of both configurations, the effect of the coating on the overall structural stiffness and vibration behavior can be assessed. The variations in natural frequencies indicate changes in the dynamic response of the bridge and demonstrate the contribution of the ZrO_2 surface treatment to the enhancement of its overall structural performance.

Table 3. Comparison of frequency values

Mode	**1**	**2**	**3**	**4**	**5**
Existing	1.920	6.701	9.238	14.883	16.393
Coated	2.718	7.369	9.584	15.039	16.507
Difference (Hz)	0.798	0.668	0.346	0.156	0.114
Difference (%)	41.563	9.969	3.745	1.048	0.695

V. CONCLUSION

This study uses the finite element method to numerically evaluate how a ZrO_2 surface coating influences the dynamic behavior of a parallel strand lumber (PSL) pedestrian bridge. Two 3D finite element models representing the existing PSL bridge and the ZrO_2-coated configuration were built using identical geometry, material parameters, and boundary conditions. A 2.5 mm ZrO_2 layer was applied to the bridge columns, and modal analyses were performed to compare the dynamic response of both systems.

The modal analysis results show that the ZrO_2 coating elevated the natural frequencies across all five analyzed modes. Specifically, the first five natural frequencies shifted from 1.920, 6.701, 9.238, 14.883, and 16.393 Hz in the existing structure to 2.718, 7.369, 9.584, 15.039, and 16.507 Hz in the retrofitted model. These correspond to frequency increments of 0.798, 0.668, 0.346, 0.156, and 0.114 Hz, representing percentage increases of roughly 41.56%, 9.97%, 3.75%, 1.05%, and 0.70%, respectively. The data indicates that the coating's impact was most substantial in the primary mode and progressively diminished in higher order modes.

This frequency growth demonstrates that the ZrO_2 treatment altered the effective dynamic stiffness of the PSL structure. Variations in modal frequencies and mode shapes confirm that the thin ceramic layer exerts a measurable effect on the bridge's global dynamic properties. Because the retrofit was implemented strictly as a surface layer without modifying the core bridge layout, the observed dynamic changes can be attributed directly to the structural contribution of the ZrO_2 coating.

Overall, the simulation results suggest that ZrO_2 surface retrofitting holds promise for enhancing the dynamic capacity of timber pedestrian bridges. The higher natural frequencies reflect enhanced dynamic stiffness, which can help mitigate human-induced vibration and serviceability issues provided the shifted frequencies remain well separated from operational excitation ranges. However, given the numerical nature of this investigation, further experimental validation is recommended alongside studies examining varying coating thicknesses, connection mechanics, damping properties, and transient dynamic loads. These findings serve as a numerical framework for future research on ceramic coatings as a sustainable retrofitting method for engineered timber infrastructure.

REFERENCES

[1] S. Tuhta, "GFRP Retrofitting effect on the dynamic characteristics of model steel structure," *Steel Compos. Struct.*, vol. 28, no. 2, pp. 223-231, July 2018.

[2] Q. Xu, H. Zou, Z. Wang, Y. He, L. Qi, and J. Wang, "Modal testing and analysis of high-rise laminated timber building," *BioResources*, vol. 19, no. 4, pp. 9616-9630, Oct. 2024.

[3] S. C. Oh, "Experimental study of bending and bearing strength of parallel strand lumber (PSL) from Japanese larch veneer strand," *J. Korean Wood Sci. Technol.*, vol. 50, no. 4, pp. 237-245, Jul. 2022.

[4] M. A. Hammoud, S. Tuhta, and F. Günday, "Determination of modal parameters of reinforced concrete tunnel retrofitted with CFRP using finite element method," *Int. J. Innov. Eng. Res. Technol.*, vol. 9, no. 4, pp. 10-18, Apr. 2022.
[5] B. C. Bal and İ. Bektaş, "The effects of wood species, load direction, and adhesives on bending properties of laminated veneer lumber," *BioResources*, vol. 7, no. 3, pp. 3104-3112, Jul. 2012.
[6] S. Tuhta, "Comparative analytical modal analysis of LVL shear-walled structure retrofitted with alumina (Al_2O_3) nanocoating exposed to earthquake effect," *Buildings*, vol. 16, no. 6, pp. 1-21, June 2026.
[7] B. Xue and Y. Hu, "Mechanical properties analysis and reliability assessment of laminated veneer lumber (LVL) having different patterns of assembly," *BioResources*, vol. 7, no. 2, pp. 1617-1632, Feb. 2012.
[8] F. Bakkour, S. Tuhta, and F. Günday, "Determination of modal parameters of reinforced concrete box culvert retrofitted with GFRP using finite element method," *Int. J. Innov. Eng. Res. Technol.*, vol. 9, no. 4, pp. 1-9, Apr. 2022.
[9] S. Tuhta, "The determination of effect of TiO_2 on dynamic behavior of scaled WPC warehouse by OMA," *Adv. Nano Res.*, vol. 12, no. 1, pp. 65-72, Jan. 2022.
[10] N. Sunar and H. Uysal, "Dynamic characteristics of CFRP-strengthened wooden beams: experimental and numerical study," *Struct. Eng. Mech.*, vol. 89, no. 3, pp. 323-334, Feb. 2024.
[11] S. Tuhta, "The determination of effect of TiO_2 on dynamic behavior of scaled concrete structure by OMA," *Adv. Nano Res.*, vol. 11, no. 6, pp. 641-648, Dec. 2021.
[12] A. A. Kasımzade and S. Tuhta, "OMA of model steel structure retrofitted with CFRP using earthquake simulator," *Earthq. Struct.*, vol. 12, no. 6, pp. 689-697, June 2017.
[13] S. Tuhta, F. Günday, and M. O. Warayth, "The effect of GFRP steel silo on modal parameters using finite element method," *Int. J. Innov. Eng. Res. Technol.*, vol. 8, no. 7, pp. 41-46, July 2021.
[14] M. Kaya, "Physical and mechanical properties of laminated timbers used in the construction and furniture industry," *BioResources*, vol. 19, no. 3, pp. 6046-6056, Jul. 2024.
[15] S. Tuhta, F. Günday, and N. C. Pehlivan, "Investigation of CFRP retrofitting effect on masonry dome on bending moment using finite element method," *Int. J. Innov. Eng. Res. Technol.*, vol. 6, no. 6, pp. 18-22, June 2019.
[16] T. Catterou, Y. Sousseau, S. M. Elachachi, M. Chaplain, and C. Faye, "Non-linear dynamic analysis of timber frame structure with bolted-fastener connections," *Vibration*, vol. 7, no. 4, pp. 1156-1170, Nov. 2024.
[17] S. Tuhta, F. Günday, and H. Aydın, "Dynamic analysis of model steel structures retrofitted with GFRP composites under microtremor vibration," *Int. J. Trend Sci. Res. Dev.*, vol. 3, no. 2, pp. 729-733, Feb. 2019.
[18] X. Li, Y. Niu, Z. Jiang, J. Pang, and X. Niu, "Lignin-based carbon-fiber-reinforced LVL beams for landscape timber structures," *Polymers*, vol. 17, no. 15, pp. 1-19, July 2025.
[19] S. Tuhta, "OMA of GFRP retrofitted model concrete structure using ambient vibration," *Int. J. Trend Sci. Res. Dev.*, vol.3, no. 1, pp. 360-370, Nov. 2018.
[20] J. Topler, L. Buchholz, J. Lukas, and U. Kuhlmann, "Guidelines for a finite element based design of timber structures and their exemplary application on modelling of beech LVL," *Buildings*, vol. 13, no. 2, pp. 1-27, Feb. 2023.
[21] F. Günday, "OMA of RC industrial building retrofitted with CFRP using SSI," *Int. J. Adv. Eng. Res. Dev.*, vol. 5, no. 5, pp. 759-771, May. 2018.
[22] S. Tuhta and F. Günday, "Investigation of effect of using nanocoating on wooden sheds on dynamic parameters," *Wood Res.*, vol. 66, no. 6, pp. 1006-1014, Dec. 2021.
[23] H. T. Li, J. W. Su, A. J. Deeks, Q. S. Zhang, D. D. Wei, and C. G. Yuan, "Eccentric compression performance of parallel bamboo strand lumber columns," *BioResources*, vol. 10, no. 4, pp. 7065-7080, Sep. 2015.
[24] S. Tuhta and F. Günday, "Investigation of steel chimney retrofitted with nanocoating under earthquake excitation using FEM," *Coatings*, vol. 15, no. 5, pp. 1-20, May 2025.
[25] F. Günday, "Investigation of the effect of coating light steel container houses with nano-TiO_2 on dynamic parameters using OMA," *Buildings*, vol. 15, no. 6, pp. 1-17, Mar. 2025.
[26] S. Tuhta and F. Günday, "Determination of the effect of TiO_2 on the dynamic behavior of scaled concrete chimney by OMA," *Mater. Tehnol.*, vol. 55, no. 3, pp. 459-466, May. 2021.
[27] F. Günday, "Structural health monitoring of steel garage model with stochastic subspace identification covariance variance analysis," *Buildings*, vol. 15, no. 6, pp. 1-18, Mar. 2025.
[28] R. Kurt, K. Aslan, M. Cil, and V. Cavus, "Properties of parallel strand lumber from two hybrid poplar clones using melamine urea formaldehyde adhesive," *BioResources*, vol. 7, no. 3, pp. 3711-3719, Jul. 2012.
[29] S. Tuhta, "Finite element-based characterization of structural performance in alumina-retrofitted PLT structure," in *Proc. 8th International Conference on Contemporary Academic Research (ICCAR 2026)*, Konya, Turkey, 2026, pp. 174-183.
[30] S. Tuhta, "Dynamic stiffness enhancement of cross-laminated timber observation tower through MgO surface coating," in *Proc. 6th International Conference on Modern and Advanced Research (ICMAR 2026)*, Konya, Turkey, 2026, pp. 73-82.

8th International Conference on Engineering, Natural and Social Sciences

September 06-07, 2026: Konya, Turkey

© 2026 Published by All Sciences Academy

https://www.icensos.com/

Numerical Characterization of Dynamic Behavior in Fe_2O_3-Strengthened Laminated Strand Lumber Timber Pathway

Sertaç Tuhta*[1]

[1]*Department of Civil Engineering, Ondokuz Mayıs University, Turkey*

*(stuhta@omu.edu.tr) *Email of the corresponding author*

Abstract **–** The increasing occurrence of extreme environmental events, together with the growing emphasis on sustainable construction, has accelerated research into improving the structural performance and reliability of engineered timber systems. Laminated strand lumber (LSL) has emerged as a promising engineered wood product owing to its favorable strength-to-weight ratio, efficient use of wood resources, dimensional stability, and suitability for structural applications. Nevertheless, further enhancement of its stiffness, durability, and overall structural performance remains an important research challenge, particularly in timber pathway systems subjected to dynamic effects. Among potential surface strengthening approaches, iron oxide (Fe_2O_3) reinforcement offers promising characteristics due to its high hardness, stiffness, wear resistance, and environmental durability. Accordingly, this study numerically investigates the effect of Fe_2O_3 strengthening on the dynamic behavior of an LSL timber pathway using the finite element method. A three-dimensional finite element model of the LSL pathway was first established, and its dynamic characteristics were determined under the defined structural conditions. Subsequently, a Fe_2O_3 strengthening layer was incorporated into the LSL model, and the same numerical procedure was applied to the modified configuration. The dynamic responses of the unstrengthened and Fe_2O_3-strengthened models were then comparatively evaluated based on their natural frequencies and mode shapes. The numerical findings revealed that Fe_2O_3 strengthening altered the dynamic characteristics of the LSL timber pathway and improved its structural stiffness. These results demonstrate the potential of Fe_2O_3-based strengthening as an effective approach for modifying the dynamic behavior and enhancing the structural performance of LSL pathway systems, providing a numerical basis for the development of more durable and high-performance engineered timber structures.

Keywords – FEM, LSL, Modal Analysis, Fe_2O_3 Coating, Dynamic Behavior

I. INTRODUCTION

The increasing occurrence and severity of natural hazards have emphasized the importance of developing structural systems with enhanced reliability, durability, and resistance to dynamic actions. Among these hazards, earthquakes represent a particularly significant challenge for civil infrastructure because seismic excitation can generate complex inertial forces and dynamic responses that may result in excessive deformation, stiffness degradation, structural damage, and considerable economic losses. The dynamic behavior of a structural system is governed by several interconnected factors, including material stiffness, mass distribution, mechanical properties, structural geometry, and boundary conditions. Accordingly, improving the dynamic characteristics of structural systems through innovative strengthening and retrofitting techniques has become an important area of research in modern structural engineering. [1], [4], [8], [12], [17], [19], [21].

Increasing environmental concerns and the demand for sustainable construction have encouraged the use of renewable and engineered wood-based materials as alternatives to conventional construction products. Engineered timber products offer several advantages, including a favorable strength-to-weight ratio, efficient utilization of wood resources, prefabrication potential, and comparatively low environmental impact. Among these materials, laminated strand lumber (LSL) has gained attention as an engineered wood product because of its relatively uniform mechanical properties, dimensional stability, efficient material utilization, and suitability for structural applications. These characteristics make LSL particularly attractive for lightweight structural systems such as timber pathway, where adequate stiffness and dynamic stability are essential for satisfactory service performance. [2], [3], [5], [7], [14], [28].

Despite the advantages of engineered timber systems, their dynamic response may be influenced by repeated loading, environmental exposure, material degradation, and changes in stiffness over their service life. Cyclic actions and environmental effects can contribute to localized deformation, stress accumulation, stiffness reduction, and changes in vibration characteristics. Such changes may adversely affect structural serviceability and increase the possibility of undesirable dynamic responses. Therefore, improving the stiffness and dynamic stability of engineered timber systems through appropriate strengthening techniques remains an important research objective. [6], [10], [13], [16], [20].

Recent advances in surface engineering and material science have encouraged the development of coating-based strengthening approaches for structural materials. Compared with conventional strengthening techniques that involve additional structural members or substantial geometric modifications, surface treatments can provide mechanical enhancement while maintaining the existing structural configuration. Such approaches can potentially improve surface hardness, stiffness; wear resistance, and environmental durability with limited additional mass. These characteristics are particularly relevant to lightweight timber systems, for which maintaining a low structural mass while improving dynamic performance is desirable. [15], [18], [22].

Iron oxide (Fe_2O_3) is an inorganic ceramic material with favorable mechanical and physical characteristics, including hardness, stiffness, wears resistance, and chemical stability. Its material characteristics have contributed to its utilization in various engineering and surface-treatment applications. When employed as a strengthening coating, Fe_2O_3 has the potential to modify the mechanical characteristics of the treated surface and contribute to changes in the stiffness and dynamic response of lightweight structural components. Therefore, investigating the potential contribution of Fe_2O_3 surface strengthening to engineered timber systems represents a promising research direction. [9], [11].

Although substantial research has been conducted on the structural performance of engineered timber products, studies concerning the dynamic behavior of Fe_2O_3-strengthened timber systems remain limited. Previous investigations have largely concentrated on conventional reinforcement materials, polymer-based coatings, fiber-reinforced systems, and adhesive strengthening methods. In contrast, the potential influence of iron oxide-based surface strengthening on the vibration characteristics of LSL structural systems has received considerably less attention. In particular, numerical investigations focusing on the changes in natural frequencies and mode shapes of Fe_2O_3-strengthened LSL timber pathway is scarce, indicating a need for further systematic research. [24], [25], [26].

An effective strengthening technique for lightweight timber structures should not only improve mechanical characteristics but also preserve the fundamental advantages of the existing structural system. Excessive additional mass may increase inertial effects during dynamic and seismic excitation and can consequently offset some of the benefits obtained through stiffness enhancement. Surface-based strengthening is therefore attractive because it can modify the mechanical characteristics of an existing member without requiring major changes to its geometry. For LSL timber pathway, a Fe_2O_3 coating may provide a means of modifying structural stiffness while maintaining the lightweight nature of the system. Evaluating these effects through numerical modeling can provide useful information regarding the suitability of this strengthening approach. [30].

Finite element analysis (FEA) provides a powerful numerical framework for investigating the structural and dynamic behavior of complex engineering systems. Three-dimensional finite element models can

represent structural geometry, material properties, support conditions, and mass distribution while enabling the evaluation of important response parameters. In modal analyses, FEA can be used to determine natural frequencies and corresponding mode shapes, which are fundamental indicators of structural stiffness, dynamic characteristics, and vibration behavior. Consequently, numerical finite element modeling offers an efficient approach for examining the effects of innovative surface-strengthening techniques before experimental validation. [23].

The dynamic performance of timber pathway is closely related to their stiffness, mass distribution, and vibration characteristics. Natural frequency is an important parameter because changes in structural stiffness or mass can modify the vibration response and potentially influence the relationship between structural excitation and resonance. Mode shapes provide additional information regarding the deformation patterns associated with individual vibration modes. Therefore, comparative evaluation of natural frequencies and mode shapes can provide a comprehensive basis for characterizing the dynamic behavior of an unstrengthened structure and assessing the influence of a strengthening treatment. [29].

In this study, a comprehensive numerical investigation is performed to characterize the dynamic behavior of a Fe_2O_3-strengthened laminated strand lumber (LSL) timber pathway. Two three-dimensional finite element models are developed, representing the existing LSL pathway and the Fe_2O_3-strengthened configuration, respectively. To ensure that the observed differences are associated with the strengthening treatment, identical geometric configurations, material assumptions, support conditions, and analysis procedures are adopted for both models. Modal analyses are subsequently conducted, and the dynamic characteristics of the two configurations are comparatively evaluated in terms of natural frequencies and mode shapes. The obtained results are used to characterize the influence of Fe_2O_3 strengthening on the dynamic behavior of the LSL timber pathway. The findings are expected to contribute to the assessment of surface-based ceramic strengthening as a potential approach for improving the dynamic characteristics of engineered timber pathway and to provide a numerical basis for the development of lightweight, durable, and high-performance timber structural systems. [27].

II. Materials and Method

To systematically investigate the influence of an iron oxide (Fe_2O_3) strengthening layer on the dynamic behavior and vibration characteristics of a laminated strand lumber (LSL) timber pathway, a three-dimensional finite element analysis was conducted using the SAP2000 program. Two independent three-dimensional numerical models were established, with the first representing the existing LSL timber pathway and the second incorporating the Fe_2O_3 strengthening treatment. In order to determine the specific contribution of the surface strengthening, both models were developed using the same geometric configuration, structural member dimensions, support conditions, and LSL material properties. Thus, the Fe_2O_3 strengthening layer constituted the principal difference between the two numerical configurations. Modal analyses were subsequently performed to determine and compare the natural frequencies and corresponding mode shapes of the unstrengthened and strengthened pathway models. Changes in the modal characteristics were examined to evaluate the influence of Fe_2O_3 treatment on the overall structural stiffness and vibration response. This comparative finite element framework enabled a systematic characterization of the effects of Fe_2O_3 strengthening on the dynamic properties of LSL timber pathway and provided a consistent numerical basis for evaluating their structural vibration behavior.

A. Description of LSL Pathway

The LSL pathway model is a timber structure with ten equal spans (3 m) in the x-direction, a single span (3 m) in the y-direction, and a height of 3 m. The pathway deck area is 90 square meters. Column cross-sections are 25x25 cm, beam cross-sections are 20x20 cm, rail element cross-sections are 5x10 cm, diagonal element cross-sections are 15x15 cm, and the deck thickness is 15 cm. The finite element model of the LSL structure was created using the SAP2000 program. The finite element model of the LSL pathway is given in Figure 1. The mechanical properties of the LSL are given in Table 1, where L, T, and R represent the longitudinal, tangential, and radial directions, respectively.

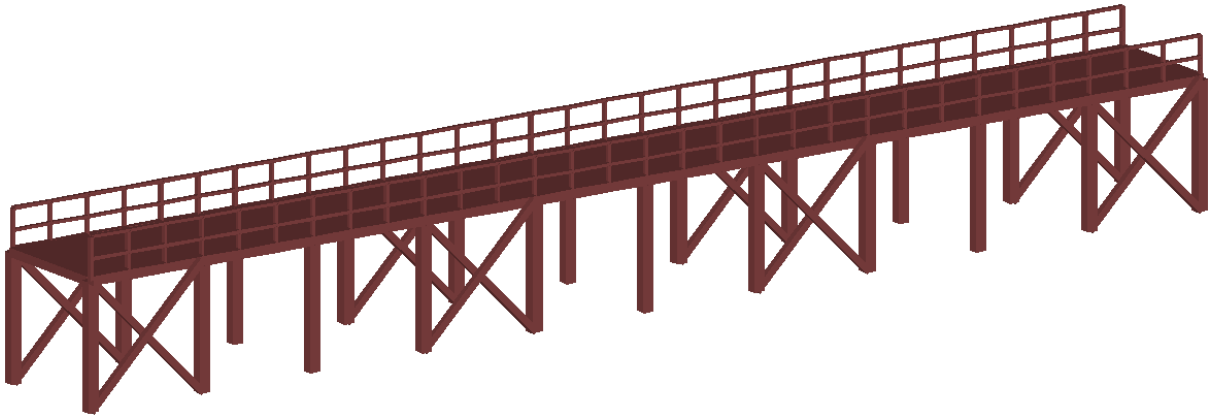

Fig. 1 3D Finite element model of the LSL pathway

Table 1. Mechanical properties of LSL

Material	Modulus of Elasticity (kN/m^2)	Poisson's Ratio	Weight per Unit Volume (kN/m^3)
LSL	$9.50x10^6$ (L)	0.40 (LR)	6.50
	$0.38x10^6$ (T)	0.40 (LT)	
	$0.38x10^6$ (R)	0.03 (RT)	

L: Longitudinal, T: Tangential, R: Radial

B. Description of Coated LSL Pathway

The columns of the existing LSL pathway are coated with 5 mm thick Fe_2O_3. Thus, a coated model was created. The finite element model of the coated LSL pathway is given in Figure 2. Mechanical properties of Fe_2O_3 are given Table 2.

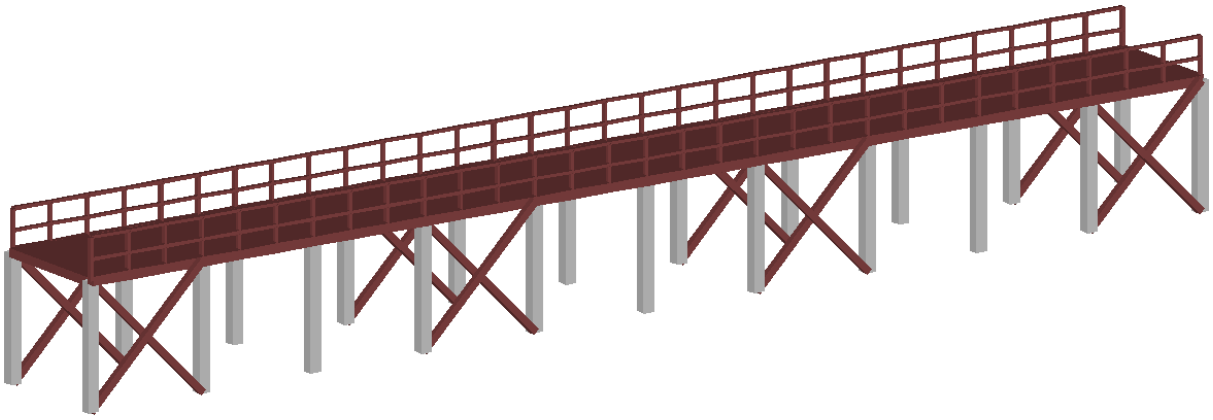

Fig. 2 3D Finite element model of the coated LSL pathway

Table 2. Mechanical properties of Fe_2O_3

Material	Modulus of Elasticity (kN/m^2)	Poisson's Ratio	Weight per Unit Volume (kN/m^3)
Fe_2O_3	$200x10^6$	0.27	52

III. RESULTS

A. Modal Analysis Results of LSL Pathway

To investigate the dynamic properties of laminated strand lumber (LSL) pathways under free vibration, modal analyses were conducted. Because lower-order vibration modes predominantly dictate the stiffness distribution and primary dynamic behavior of timber footbridges, the research emphasized the first five modes. Finite element techniques enabled the systematic identification of natural frequencies and corresponding mode shapes for both existing and Fe_2O_3-retrofitted configurations. Detailed comparative findings regarding these fundamental modes, including their structural significance, are illustrated in Figures 3-7.

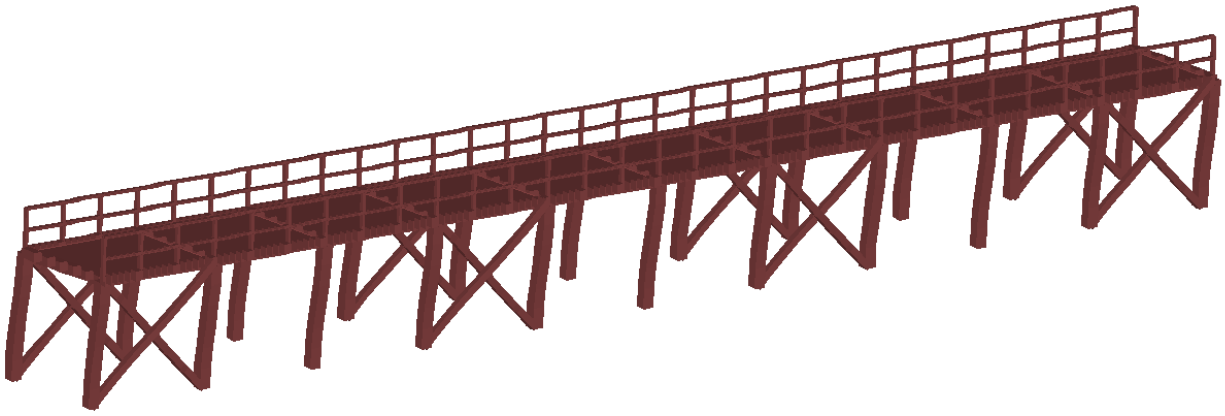

Fig. 3 1st Mode shape (Frequency value = 4.391 Hz)

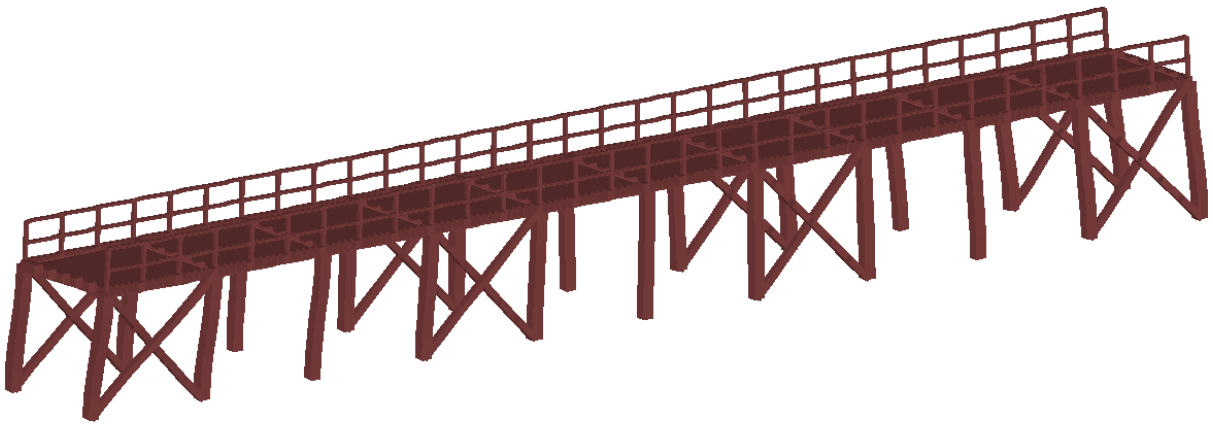

Fig. 4 2nd Mode shape (Frequency value = 5.365 Hz)



Fig. 5 3rd Mode shape (Frequency value = 12.498 Hz)

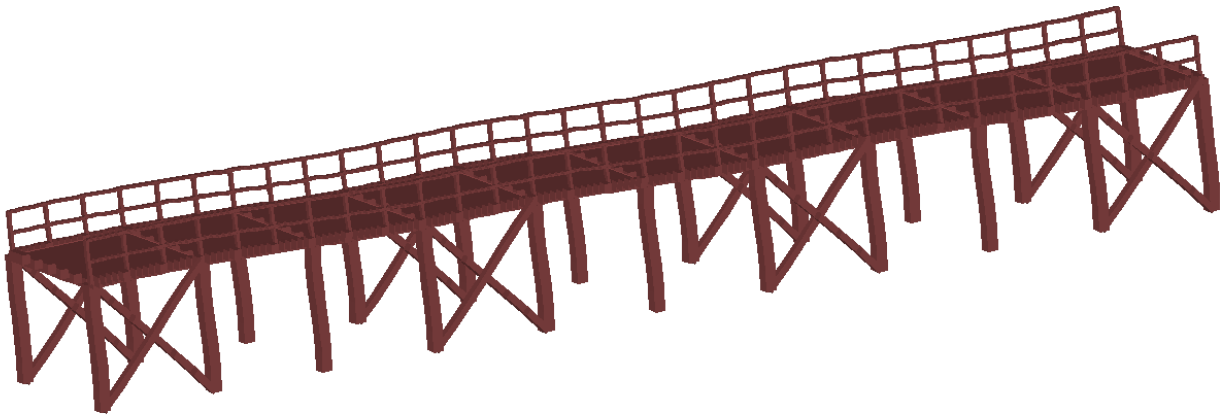

Fig. 6 4th Mode shape (Frequency value = 16.043 Hz)

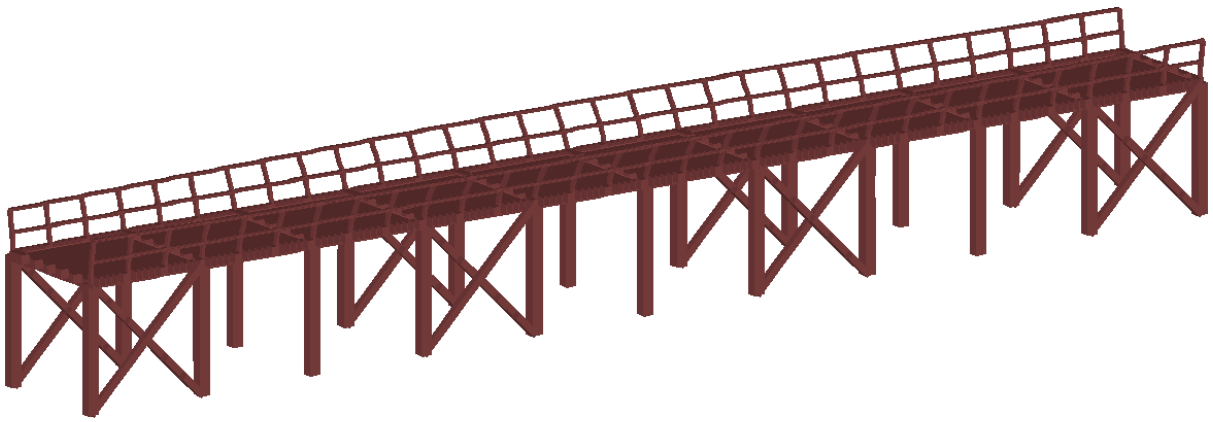

Fig. 7 5th Mode shape (Frequency value = 24.620 Hz)

B. Modal Analysis Results of Coated LSL Pathway

To assess how the retrofit material specifically influences the structural dynamics, a thorough modal analysis was performed on the Fe_2O_3-retrofitted LSL pathway model. The study centered on the first five vibration modes, as these primary modes govern the global dynamic behavior of the pathway during free vibration. Integrating the Fe_2O_3 retrofit changes the stiffness across structural components, thereby adjusting both natural frequencies and their corresponding mode shapes. These modal parameters offer essential data to evaluate how successfully the Fe_2O_3 reinforcement improves the dynamic performance and stability of the LSL pathway. Figures 8 through 12 present the first five natural frequencies and their associated mode shapes derived from the finite element analysis.

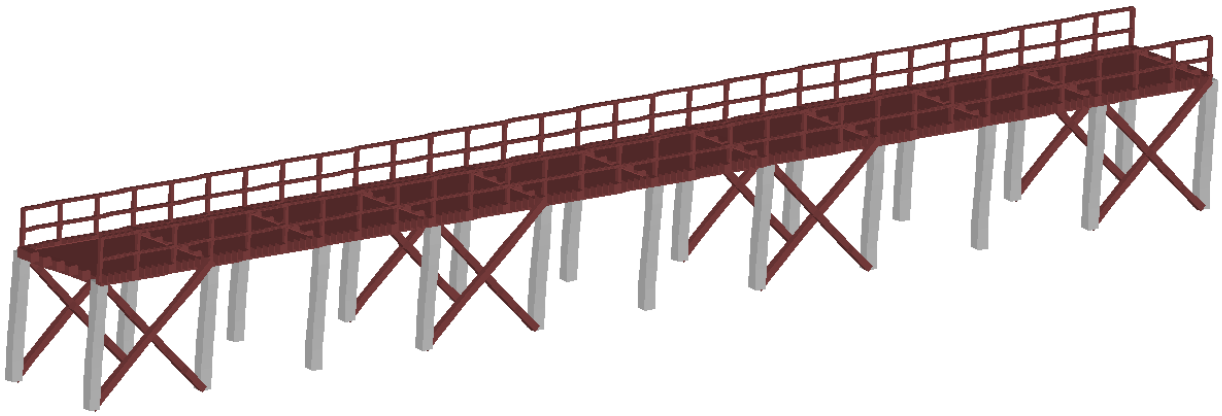

Fig. 8 1st Mode shape (Frequency value = 6.316 Hz)

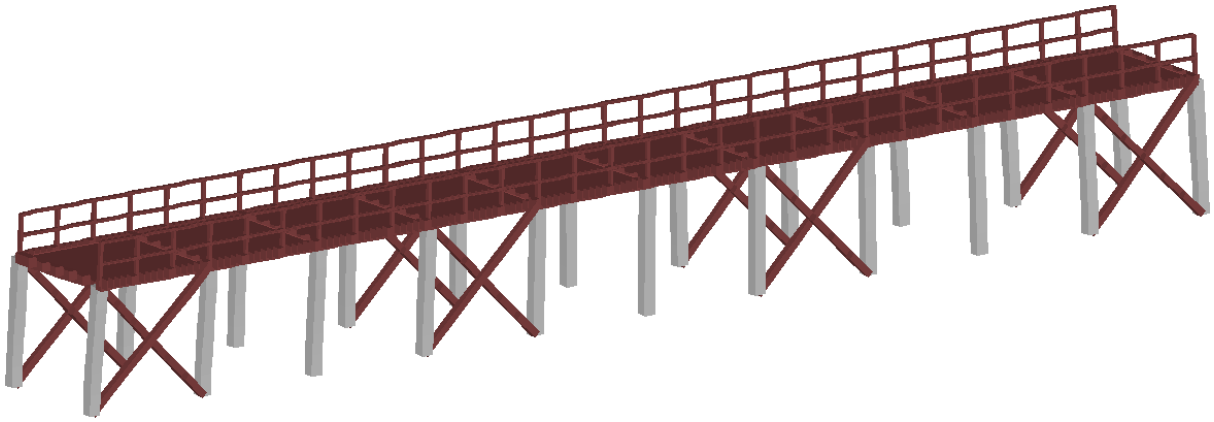

Fig. 9 2nd Mode shape (Frequency value = 7.160 Hz)

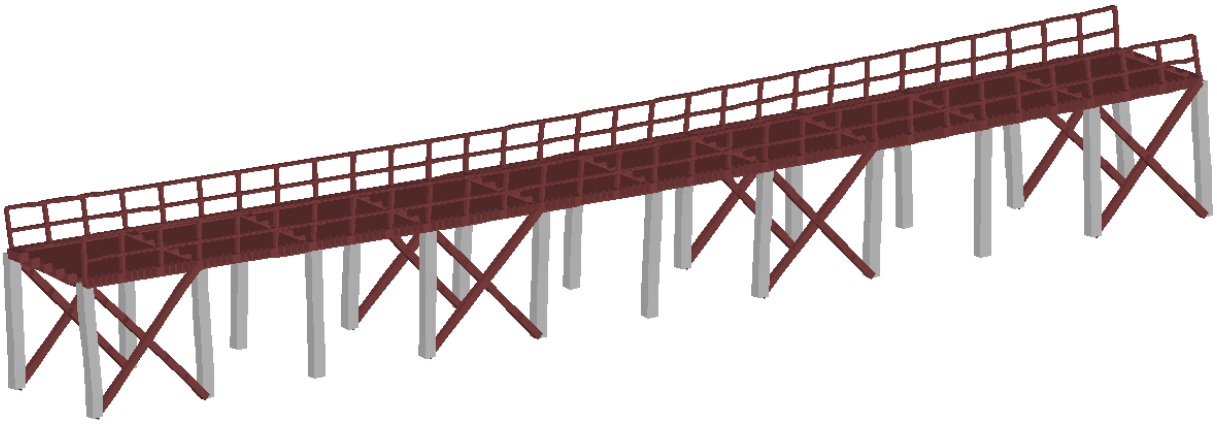

Fig. 10 3rd Mode shape (Frequency value = 13.267 Hz)

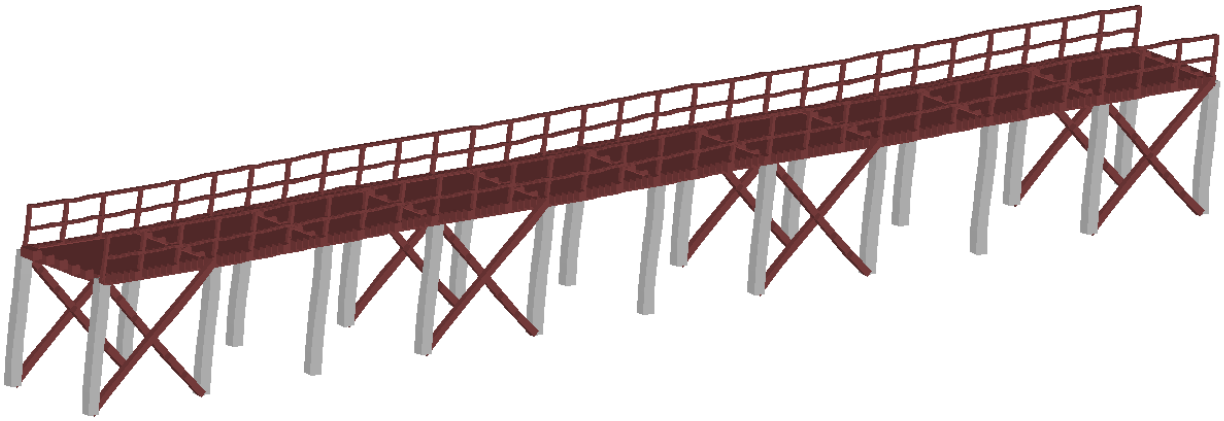

Fig. 11 4th Mode shape (Frequency value = 16.860 Hz)

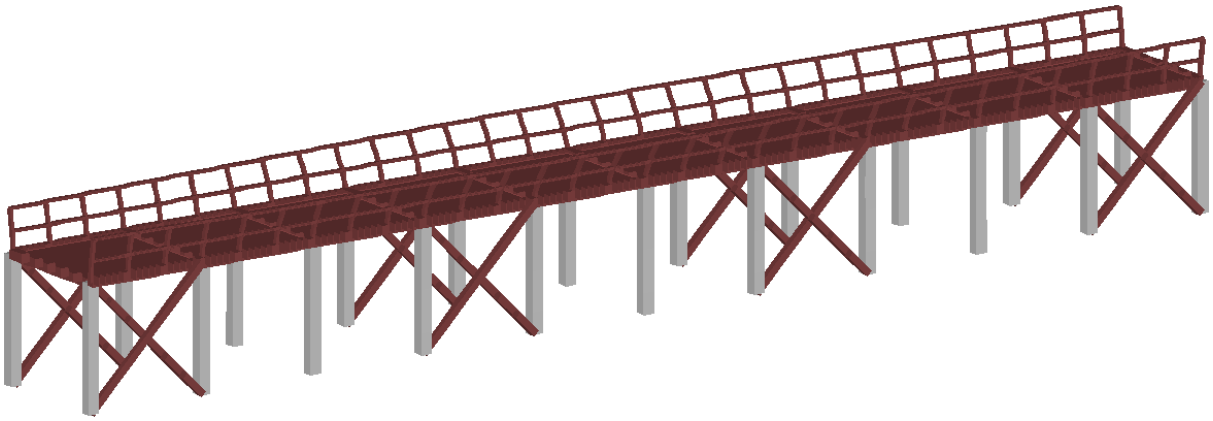

Fig. 12 5th Mode shape (Frequency value = 24.673 Hz)

IV. DISCUSSION

A comparative modal analysis between the existing and the Fe_2O_3-strengthened laminated strand lumber timber pathway configurations is presented in Table 3, elucidating the specific influence of the Fe_2O_3 treatment on the structural dynamics of the pathway. The juxtaposition of these modal frequencies facilitates a rigorous assessment of how the surface modification alters structural rigidity and vibration response profiles. Furthermore, the observed shifts in natural frequencies reflect alterations in the dynamic behavior of the pathway, substantiating the efficacy of the Fe_2O_3 treatment in enhancing the overall structural integrity and performance.

Table 3. Comparison of frequency values

Mode	**1**	**2**	**3**	**4**	**5**
Existing	4.391	5.365	12.498	16.043	24.620
Coated	6.316	7.160	13.267	16.860	24.673
Difference (Hz)	1.925	1.795	0.769	0.817	0.053
Difference (%)	43.840	33.458	6.153	5.093	0.215

V. CONCLUSION

This study numerically investigated the effect of Fe_2O_3 surface strengthening on the dynamic characteristics of a laminated strand lumber (LSL) timber pathway using the finite element method. Two three-dimensional finite element models were developed to represent the existing and Fe_2O_3 - strengthened configurations. The models were established with the same geometric characteristics, material assumptions, and boundary conditions, while a 5 mm thick Fe_2O_3 layer was applied to the columns of the strengthened pathway. Modal analysis was then performed to determine the changes in the natural frequencies and vibration characteristics of the structure.

The numerical results demonstrate that the Fe_2O_3 strengthening treatment increased the natural frequencies of all five investigated vibration modes. The frequencies of the existing LSL pathway were 4.391, 5.365, 12.498, 16.043, and 24.620 Hz for the first through fifth modes, respectively. Following the application of the Fe_2O_3 strengthening layer, these values increased to 6.316, 7.160, 13.267, 16.860, and 24.673 Hz. The corresponding frequency increments were 1.925, 1.795, 0.769, 0.817, and 0.053 Hz, equivalent to increases of approximately 43.84%, 33.46%, 6.15%, 5.09%, and 0.22%, respectively.

The most pronounced improvement was observed in the first two vibration modes, whereas the influence of the Fe_2O_3 layer gradually decreased for the higher modes. This behavior indicates that the surface strengthening treatment primarily affected the lower-order dynamic characteristics of the pathway. The increase in natural frequencies suggests that the Fe_2O_3 layer contributed to an increase in the effective stiffness of the structural system. Since the geometry, support conditions, and other material parameters were maintained consistently between the two models, the differences in modal response can be principally associated with the incorporation of the Fe_2O_3 strengthening layer. Overall, the findings indicate that Fe_2O_3 surface strengthening has potential as a numerical retrofit approach for modifying the dynamic behavior and improving the stiffness characteristics of LSL timber pathway systems. The results are particularly relevant for lightweight timber structures in which improved dynamic performance is desired without major changes to the existing structural configuration. However, the present investigation is limited to numerical modal analysis. Experimental studies are therefore recommended to validate the predicted response and to further examine the effects.

The outcomes of this study provide a numerical basis for further investigation of ceramic surface-strengthening techniques for engineered timber structures and may support the development of lightweight, durable, and dynamically improved timber pathway systems.

REFERENCES

[1] S. Tuhta, “GFRP Retrofitting effect on the dynamic characteristics of model steel structure,” *Steel Compos. Struct.*, vol. 28, no. 2, pp. 223-231, July 2018.

[2] Q. Xu, H. Zou, Z. Wang, Y. He, L. Qi, and J. Wang, "Modal testing and analysis of high-rise laminated timber building," *BioResources*, vol. 19, no. 4, pp. 9616-9630, Oct. 2024.
[3] S. C. Oh, "Experimental study of bending and bearing strength of parallel strand lumber (PSL) from Japanese larch veneer strand," *J. Korean Wood Sci. Technol.*, vol. 50, no. 4, pp. 237-245, Jul. 2022.
[4] M. A. Hammoud, S. Tuhta, and F. Günday, "Determination of modal parameters of reinforced concrete tunnel retrofitted with CFRP using finite element method," *Int. J. Innov. Eng. Res. Technol.*, vol. 9, no. 4, pp. 10-18, Apr. 2022.
[5] B. C. Bal and İ. Bektaş, "The effects of wood species, load direction, and adhesives on bending properties of laminated veneer lumber," *BioResources*, vol. 7, no. 3, pp. 3104-3112, Jul. 2012.
[6] S. Tuhta, "Comparative analytical modal analysis of LVL shear-walled structure retrofitted with alumina (Al_2O_3) nanocoating exposed to earthquake effect," *Buildings*, vol. 16, no. 6, pp. 1-21, June 2026.
[7] B. Xue and Y. Hu, "Mechanical properties analysis and reliability assessment of laminated veneer lumber (LVL) having different patterns of assembly," *BioResources*, vol. 7, no. 2, pp. 1617-1632, Feb. 2012.
[8] F. Bakkour, S. Tuhta, and F. Günday, "Determination of modal parameters of reinforced concrete box culvert retrofitted with GFRP using finite element method," *Int. J. Innov. Eng. Res. Technol.*, vol. 9, no. 4, pp. 1-9, Apr. 2022.
[9] S. Tuhta, "The determination of effect of TiO_2 on dynamic behavior of scaled WPC warehouse by OMA," *Adv. Nano Res.*, vol. 12, no. 1, pp. 65-72, Jan. 2022.
[10] N. Sunar and H. Uysal, "Dynamic characteristics of CFRP-strengthened wooden beams: experimental and numerical study," *Struct. Eng. Mech.*, vol. 89, no. 3, pp. 323-334, Feb. 2024.
[11] S. Tuhta, "The determination of effect of TiO_2 on dynamic behavior of scaled concrete structure by OMA," *Adv. Nano Res.*, vol. 11, no. 6, pp. 641-648, Dec. 2021.
[12] A. A. Kasımzade and S. Tuhta, "OMA of model steel structure retrofitted with CFRP using earthquake simulator," *Earthq. Struct.*, vol. 12, no. 6, pp. 689-697, June 2017.
[13] S. Tuhta, F. Günday, and M. O. Warayth, "The effect of GFRP steel silo on modal parameters using finite element method," *Int. J. Innov. Eng. Res. Technol.*, vol. 8, no. 7, pp. 41-46, July 2021.
[14] M. Kaya, "Physical and mechanical properties of laminated timbers used in the construction and furniture industry," *BioResources*, vol. 19, no. 3, pp. 6046-6056, Jul. 2024.
[15] S. Tuhta, F. Günday, and N. C. Pehlivan, "Investigation of CFRP retrofitting effect on masonry dome on bending moment using finite element method," *Int. J. Innov. Eng. Res. Technol.*, vol. 6, no. 6, pp. 18-22, June 2019.
[16] T. Catterou, Y. Sousseau, S. M. Elachachi, M. Chaplain, and C. Faye, "Non-linear dynamic analysis of timber frame structure with bolted-fastener connections," *Vibration*, vol. 7, no. 4, pp. 1156-1170, Nov. 2024.
[17] S. Tuhta, F. Günday, and H. Aydın, "Dynamic analysis of model steel structures retrofitted with GFRP composites under microtremor vibration," *Int. J. Trend Sci. Res. Dev.*, vol. 3, no. 2, pp. 729-733, Feb. 2019.
[18] X. Li, Y. Niu, Z. Jiang, J. Pang, and X. Niu, "Lignin-based carbon-fiber-reinforced LVL beams for landscape timber structures," *Polymers*, vol. 17, no. 15, pp. 1-19, July 2025.
[19] S. Tuhta, "OMA of GFRP retrofitted model concrete structure using ambient vibration," *Int. J. Trend Sci. Res. Dev.*, vol.3, no. 1, pp. 360-370, Nov. 2018.
[20] J. Topler, L. Buchholz, J. Lukas, and U. Kuhlmann, "Guidelines for a finite element based design of timber structures and their exemplary application on modelling of beech LVL," *Buildings*, vol. 13, no. 2, pp. 1-27, Feb. 2023.
[21] F. Günday, "OMA of RC industrial building retrofitted with CFRP using SSI," *Int. J. Adv. Eng. Res. Dev.*, vol. 5, no. 5, pp. 759-771, May. 2018.
[22] S. Tuhta and F. Günday, "Investigation of effect of using nanocoating on wooden sheds on dynamic parameters," *Wood Res.*, vol. 66, no. 6, pp. 1006-1014, Dec. 2021.
[23] H. T. Li, J. W. Su, A. J. Deeks, Q. S. Zhang, D. D. Wei, and C. G. Yuan, "Eccentric compression performance of parallel bamboo strand lumber columns," *BioResources*, vol. 10, no. 4, pp. 7065-7080, Sep. 2015.
[24] S. Tuhta and F. Günday, "Investigation of steel chimney retrofitted with nanocoating under earthquake excitation using FEM," *Coatings*, vol. 15, no. 5, pp. 1-20, May 2025.
[25] F. Günday, "Investigation of the effect of coating light steel container houses with nano-TiO_2 on dynamic parameters using OMA," *Buildings*, vol. 15, no. 6, pp. 1-17, Mar. 2025.
[26] S. Tuhta and F. Günday, "Determination of the effect of TiO_2 on the dynamic behavior of scaled concrete chimney by OMA," *Mater. Tehnol.*, vol. 55, no. 3, pp. 459-466, May. 2021.
[27] F. Günday, "Structural health monitoring of steel garage model with stochastic subspace identification covariance variance analysis," *Buildings*, vol. 15, no. 6, pp. 1-18, Mar. 2025.
[28] R. Kurt, K. Aslan, M. Cil, and V. Cavus, "Properties of parallel strand lumber from two hybrid poplar clones using melamine urea formaldehyde adhesive," *BioResources*, vol. 7, no. 3, pp. 3711-3719, Jul. 2012.
[29] S. Tuhta, "Finite element-based characterization of structural performance in alumina-retrofitted PLT structure," in *Proc. 8th International Conference on Contemporary Academic Research (ICCAR 2026)*, Konya, Turkey, 2026, pp. 174-183.
[30] S. Tuhta, "Dynamic stiffness enhancement of cross-laminated timber observation tower through MgO surface coating," in *Proc. 6th International Conference on Modern and Advanced Research (ICMAR 2026)*, Konya, Turkey, 2026, pp. 73-82.

8th International Conference on Engineering, Natural and Social Sciences

September 06-07, 2026: Konya, Turkey

© 2026 Published by All Sciences Academy

https://www.icensos.com/

From Vaborbactam to Taniborbactam: Evolution and Therapeutic Potential of Boronate Beta-Lactamase Inhibitors

Murat Şentürk*

Professor of Biochemistry, Faculty of Pharmacy, Ağrı İbrahim Çeçen University, Türkiye

**msenturk@agri.edu.tr*

Abstract – Beta-lactamase production is an important cause of resistance to beta-lactam antibiotics. For this reason, new beta-lactamase inhibitors are being developed to protect commonly used antibiotics. Boronate inhibitors are an interesting group because the boron atom can interact reversibly with the active site of different beta-lactamases. This short narrative review summarizes the development from vaborbactam to taniborbactam and discusses their possible clinical value. Vaborbactam is a cyclic boronate used together with meropenem. It is especially effective against class A KPC carbapenemases and has helped restore meropenem activity against many KPC-producing Enterobacterales. However, it has limited activity against metallo-beta-lactamases and most class D carbapenemases. Taniborbactam is a newer bicyclic boronate developed for use with cefepime. It inhibits many class A and C enzymes, some class D enzymes, and selected NDM- and VIM-type metallo-beta-lactamases. Its activity is not universal, particularly against several IMP enzymes and some new variants. Clinical studies have shown the usefulness of meropenem-vaborbactam in complicated urinary tract infection and other serious infections caused by susceptible organisms. A phase 3 trial also reported favorable results for cefepime-taniborbactam in complicated urinary tract infection. In conclusion, boronate inhibitors are promising tools against resistant Gram-negative bacteria, but enzyme type, bacterial susceptibility, antibiotic partner, and careful antimicrobial use remain important.

Keywords – beta-lactamase inhibitors; boronates; vaborbactam; taniborbactam; antimicrobial resistance

I. INTRODUCTION

Beta-lactam antibiotics are widely used in bacterial infections. Their activity may be lost when bacteria produce beta-lactamases, enzymes that break the beta-lactam ring. Carbapenemases are especially important because they can inactivate carbapenems, which are often reserved for severe infections [1].

One way to overcome this problem is to combine a beta-lactam antibiotic with a beta-lactamase inhibitor. Boron-containing inhibitors have attracted attention because they can bind reversibly to the enzyme active site. Vaborbactam is already used clinically with meropenem, while taniborbactam is a newer compound developed with cefepime [2], [3]. The aim of this short review is to explain the basic differences between these two inhibitors and their medical potential.

II. MATERIALS AND METHOD

This narrative review was prepared by examining peer-reviewed articles and official drug information. PubMed-indexed biochemical studies, microbiological studies, randomized clinical trials, and PubChem chemical records were given priority. The main search terms were vaborbactam, taniborbactam, cyclic boronate, beta-lactamase inhibitor, KPC, NDM, VIM, meropenem-vaborbactam, and cefepime-taniborbactam. The purpose was to provide a brief general overview rather than a systematic review or meta-analysis.

III. RESULTS

A. Boronate Beta-Lactamase Inhibitors

Beta-lactamases are commonly grouped into classes A, B, C, and D. Classes A, C, and D use a serine residue in catalysis, whereas class B metallo-beta-lactamases require zinc ions. This difference makes the development of a single inhibitor active against every class difficult [1].

The boron atom can change its geometry during binding and form a tetrahedral complex that resembles an intermediate of beta-lactam hydrolysis. Cyclic and bicyclic structures help place the boronate group in a suitable position in the enzyme active site [2], [3]. The verified two-dimensional structures of vaborbactam and taniborbactam are shown in Fig. 1 [10], [11].

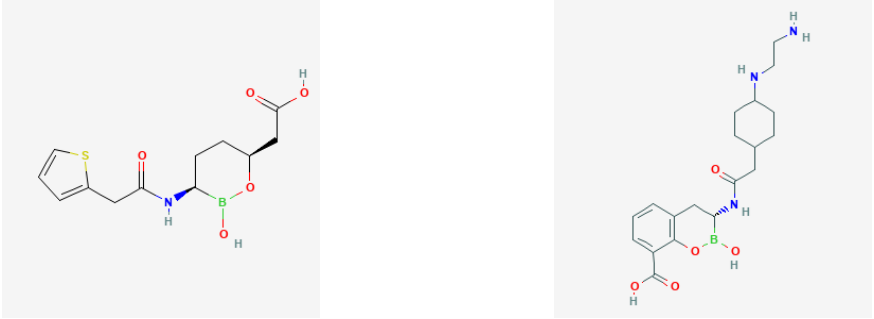

Vaborbactam
$C_{12}H_{16}BNO_5S$ | CID 56649692

Taniborbactam
$C_{19}H_{28}BN_3O_5$ | CID 76902493

Fig. 1. Two-dimensional structures of vaborbactam and taniborbactam. Redrawn from PubChem records [10], [11].

B. Vaborbactam

Vaborbactam is a cyclic boronic acid inhibitor used with meropenem. It strongly inhibits many class A beta-lactamases, especially KPC enzymes, and can restore meropenem activity against many KPC-producing Enterobacterales [4]. It does not have important antibacterial activity when used alone.

Its main limitation is its narrow carbapenemase coverage. Vaborbactam is not effective against class B metallo-beta-lactamases such as NDM, VIM, and IMP, and it has weak activity against most OXA-type class D carbapenemases. Therefore, the resistance mechanism should be considered before use. Clinical trials supported meropenem-vaborbactam in complicated urinary tract infection and serious infections caused by susceptible carbapenem-resistant Enterobacterales [5], [6]. The combination was approved by the United States Food and Drug Administration in 2017 [7].

C. Taniborbactam

Taniborbactam is a bicyclic boronate with a broader inhibition profile. It was designed to inhibit both serine beta-lactamases and selected metallo-beta-lactamases. It inhibits many class A and C enzymes, some class D enzymes, and several NDM- and VIM-type enzymes [3], [8]. Cefepime was selected as its antibiotic partner.

Taniborbactam should not be described as active against every beta-lactamase. Activity against IMP-type enzymes is generally limited, and individual enzyme variants may show reduced susceptibility. Other bacterial mechanisms, including reduced membrane permeability and efflux, can also reduce the activity of cefepime-taniborbactam [8].

In the phase 3 CERTAIN-1 trial in complicated urinary tract infection, cefepime-taniborbactam produced a favorable combined clinical and microbiological response compared with meropenem [9]. These findings show clinical potential, although the result of one infection-focused trial cannot automatically be applied to every severe infection or resistance mechanism.

D. Simple Comparison

Table 1. A simple comparison of vaborbactam and taniborbactam

Feature	**Vaborbactam**	**Taniborbactam**
Structure	Cyclic boronate	Bicyclic boronate
Partner antibiotic	Meropenem	Cefepime
Main coverage	Mainly class A, especially KPC	Classes A and C, some D, selected NDM and VIM
Important gap	Metallo-beta-lactamases and most OXA enzymes	Many IMP enzymes and some variants
Clinical position	Approved combination	Positive phase 3 clinical evidence

IV. DISCUSSION

The change from vaborbactam to taniborbactam shows how the boronate scaffold can be modified to obtain broader enzyme inhibition. Vaborbactam has a clear and established role against KPC-producing bacteria when combined with meropenem. Taniborbactam may cover a wider group of enzymes, including selected metallo-beta-lactamases, when combined with cefepime.

However, neither inhibitor solves all forms of beta-lactam resistance. Laboratory susceptibility, the beta-lactamase type, the infection site, and patient factors should guide treatment. New inhibitors should also be used carefully to delay the development of resistance.

V. CONCLUSION

Vaborbactam and taniborbactam are important examples of boronate beta-lactamase inhibitors. Vaborbactam mainly provides protection against KPC enzymes, whereas taniborbactam offers broader activity that includes selected NDM and VIM enzymes. Their development supports the medical potential of cyclic boronates, but coverage gaps remain. Appropriate diagnostic testing and antimicrobial stewardship are necessary for the effective use of these combinations.

REFERENCES

[1] K. Bush and P. A. Bradford, “Epidemiology of beta-lactamase-producing pathogens,” Clin. Microbiol. Rev., vol. 33, no. 2, e00047-19, 2020. doi: 10.1128/CMR.00047-19.

[2] J. Brem et al., “Structural basis of metallo-beta-lactamase, serine-beta-lactamase and penicillin-binding protein inhibition by cyclic boronates,” Nat. Commun., vol. 7, 12406, 2016. doi: 10.1038/ncomms12406.

[3] B. Liu et al., “Discovery of taniborbactam (VNRX-5133): a broad-spectrum serine- and metallo-beta-lactamase inhibitor for carbapenem-resistant bacterial infections,” J. Med. Chem., vol. 63, pp. 2789–2801, 2020. doi: 10.1021/acs.jmedchem.9b01518.

[4] O. Lomovskaya et al., “Vaborbactam: spectrum of beta-lactamase inhibition and impact of resistance mechanisms on activity in Enterobacteriaceae,” Antimicrob. Agents Chemother., vol. 61, e01443-17, 2017. doi: 10.1128/AAC.01443-17.

[5] K. S. Kaye et al., “Effect of meropenem-vaborbactam vs piperacillin-tazobactam in complicated urinary tract infection: the TANGO I randomized clinical trial,” JAMA, vol. 319, pp. 788–799, 2018. doi: 10.1001/jama.2018.0438.

[6] R. G. Wunderink et al., “Effect and safety of meropenem-vaborbactam versus best-available therapy in carbapenem-resistant Enterobacteriaceae infections: TANGO II,” Infect. Dis. Ther., vol. 7, pp. 439–455, 2018. doi: 10.1007/s40121-018-0214-1.

[7] U.S. Food and Drug Administration, “VABOMERE (meropenem and vaborbactam) prescribing information,” 2017, revised 2023.

[8] S. J. Hamrick et al., “VNRX-5133 (taniborbactam), a broad-spectrum inhibitor of serine- and metallo-beta-lactamases, restores activity of cefepime,” Antimicrob. Agents Chemother., vol. 64, e01963-19, 2020. doi: 10.1128/AAC.01963-19.

[9] F. M. E. Wagenlehner et al., “Cefepime-taniborbactam in complicated urinary tract infection,” N. Engl. J. Med., vol. 390, pp. 611–622, 2024. doi: 10.1056/NEJMoa2304748.

[10] National Center for Biotechnology Information, “PubChem Compound Summary for CID 56649692, Vaborbactam,” accessed Sep. 5, 2026.

[11] National Center for Biotechnology Information, “PubChem Compound Summary for CID 76902493, Taniborbactam,” accessed Sep. 5, 2026.

8th International Conference on Engineering, Natural and Social Sciences

September 06-07, 2026: Konya, Turkey

© 2026 Published by All Sciences Academy

https://www.icensos.com/

Preliminary Rationale for Uracil-Based Modulators of KDM5B in Cancer Therapy Resistance

Murat Şentürk*

Faculty of Pharmacy, Ağrı İbrahim Çeçen University, Türkiye
**msenturk@agri.edu.tr*

Abstract - Adaptive and acquired resistance remains a major limitation in gastrointestinal cancer treatment and is supported by reversible epigenetic reprogramming. Histone lysine demethylases, including KDM5B, are Fe(II)- and 2-oxoglutarate-dependent oxygenases that regulate transcriptional plasticity and represent chemically tractable targets. This preliminary study evaluated the feasibility of using uracil-derived scaffolds as a starting point for structure-guided design of KDM5B modulators. The assessment integrated the applicant's previously established experience in the synthesis and enzyme-oriented evaluation of uracil derivatives with analysis of published ligand-bound KDM5B structures. Earlier studies demonstrated that uracil-based compounds can be synthesised, structurally characterised and adapted to interact with enzyme binding sites; however, those data do not establish KDM inhibition. The ligand-bound human KDM5B catalytic-core structure (PDB 5A3N) provides an experimentally defined metal/2-oxoglutarate pocket and adjacent ligand-recognition region suitable for structure-guided modification of the scaffold. Together, these observations support a staged workflow comprising target-guided uracil design, synthesis and analytical characterisation, followed by biochemical testing and preliminary structure-activity relationship analysis. The findings constitute preliminary feasibility data relevant to the proposed project "Design and Synthesis of Novel Uracil-Based Small-Molecule Modulators Targeting Epigenetic Enzymes Associated with Cancer Therapy Resistance." No inhibitory activity against KDM5B is claimed at this stage. The proposed work directly supports COST Action CA24162 - AdResCanCER by developing chemical tools for investigating adaptive and acquired resistance in gastrointestinal cancers.

Keywords: KDM5B; uracil derivatives; epigenetic regulation; adaptive resistance; structure-guided design

I. INTRODUCTION

Treatment resistance is not a single biological event. Pre-existing genetic diversity, therapy-induced selection, altered drug transport, enhanced DNA repair, metabolic adaptation and changes in cell state can operate simultaneously. Importantly, a fraction of cancer cells can enter reversible drug-tolerant states without acquiring a stable resistance mutation. Epigenetic reprogramming contributes to this plasticity by changing which genes are accessible and expressed under therapeutic pressure [1]. Such reversible mechanisms are attractive targets because they may be pharmacologically disrupted before fixed resistance becomes established.

Lysine demethylases of the KDM5 family remove methyl groups from histone H3 lysine 4 and thereby reshape transcription-associated chromatin. KDM5 activity has been linked to slowly proliferating or drug-tolerant tumour-cell subpopulations, while KDM5B has been implicated in resistance mechanisms across several malignancies [2-4]. More recent experimental work in pancreatic ductal adenocarcinoma indicates

that KDM5B can support stemness and drug resistance in a gastrointestinal tumour setting [5]. These findings do not imply that KDM5B inhibition will be effective in every patient, but they justify chemical-probe development for mechanistic testing.

The KDM5B catalytic domain is part of the Fe(II)/2-oxoglutarate (2OG)-dependent oxygenase superfamily. Structural analyses have shown that multiple inhibitor chemotypes can occupy the catalytic region and exploit both conserved and target-associated interactions [6]. KDOAM-25 is a potent KDM5-family inhibitor that binds in the KDM5B catalytic pocket and increases H3K4 methylation in cellular systems [7]. These data establish KDM5B as a structurally tractable enzyme, while highlighting selectivity and cellular exposure as central medicinal-chemistry challenges.

Uracil is a compact heterocycle offering carbonyl groups, hydrogen-bonding functionality and several positions for chemical diversification. The author has contributed to studies in which uracil derivatives were synthesised and evaluated against carbonic anhydrase and cholinesterase enzymes [8-10]. These studies provide practical knowledge of uracil chemistry and demonstrate that substituent changes can modify protein interactions. They were conducted on different enzyme systems and therefore cannot be cited as evidence of KDM5B inhibition. Their appropriate role in the present study is to establish the feasibility of preparing and analysing a focused uracil-based library.

The objective of this preliminary study was to integrate chemical-platform readiness, target-structure readiness and biological relevance into a transparent feasibility assessment. The central hypothesis is that rationally substituted uracil-containing compounds can be designed to explore the KDM5B metal/cofactor region and adjacent recognition space; the hypothesis remains to be tested experimentally.

II. MATERIALS AND METHODS

A. Evidence selection and scope

Primary research articles were prioritised for three questions: Can uracil-based compounds be synthesised and evaluated reproducibly? Is KDM5B supported by ligand-bound experimental structures? Is there experimental evidence connecting KDM5-family activity with treatment-tolerant cancer states? Reviews were used only to contextualise the field. Claims were restricted to the original target and assay described in each source.

B. Chemical-platform evaluation

The author's published uracil series were assessed for synthetic tractability, structural diversity, analytical characterisation and evidence that the scaffold can participate in enzyme-ligand interactions [8-10]. Reported carbonic-anhydrase and cholinesterase results were treated as scaffold precedent only. Because these enzymes differ fundamentally from KDM5B, no transfer of potency or mechanism was assumed.

C. KDM5B structural evaluation

Ligand-bound human KDM5B structures reported by Johansson and colleagues and the KDOAM-25 complex represented by PDB 5A3N were examined as design references [6,7,11]. The evaluation considered whether the catalytic metal/2OG region was defined, whether an experimental ligand established the orientation of a drug-like chemotype, and whether substituents could plausibly extend toward surrounding recognition regions. This was a qualitative feasibility assessment rather than a completed docking experiment.

D. Translational prioritisation criteria

A candidate scaffold would be prioritised only if it met four conditions: feasible synthesis within a focused experimental programme; unambiguous analytical verification; a plausible structure-guided hypothesis for KDM5B engagement; and compatibility with an available biochemical assay. Candidates requiring lengthy protecting-group sequences, unstable intermediates or unvalidated assay assumptions would be deprioritised.

III. PRELIMINARY RESULTS

A. Existing work supports uracil scaffold readiness

The earlier uracil studies demonstrate several capabilities relevant to subsequent target-directed research: preparation of substituted uracil-containing compounds, purification and identity confirmation, enzyme kinetic measurements, and interpretation of ligand-protein interactions with computational support [8-10]. The reported activities against carbonic anhydrases and cholinesterases show that the scaffold is not chemically inert and that its interaction profile changes with substitution. The important preliminary conclusion is technical: a focused uracil series can be generated and evaluated using an established interdisciplinary workflow.

B. Structural data support KDM5B-directed design

Human KDM5B has experimentally characterised inhibitor-binding modes. The structural work of Johansson et al. showed that different chemotypes can exploit distinct features within the catalytic core and that selectivity relative to other KDM subfamilies is achievable but compound-dependent [6]. In 5A3N, KDOAM-25 occupies the 2OG region and coordinates the catalytic metal surrogate while extending into neighbouring space [7,11]. This architecture supports a design strategy in which the uracil core contributes directional hydrogen-bonding or anchoring interactions and appended groups explore target-associated regions.

C. Biological evidence supports resistance relevance

KDM5-family enzymes have been connected with reversible drug-tolerant states in multiple tumour models [1-4]. In pancreatic ductal adenocarcinoma, loss of SMAD4 has been reported to drive KDM5B-related stemness and drug resistance, providing a direct gastrointestinal-cancer rationale [5]. This evidence supports KDM5B as a mechanistic target for chemical-probe studies in cancer resistance research. It does not yet establish which chemical phenotype or combination treatment will be most effective.

Table 1. Evidence boundaries used to prevent overinterpretation of the preliminary data.

Evidence stream	Verified observation	What it supports	What it does not prove
Previous uracil studies	Synthesis, characterisation and enzyme evaluation are established	Chemical-platform feasibility	KDM5B activity
KDM5B structures	Ligand-bound catalytic-core structures are available	Structure-guided candidate design	Cellular target engagement
Resistance literature	KDM5 activity is linked to drug-tolerant states	Biological rationale	Clinical efficacy
Current preliminary status	No KDM5B inhibition value has been generated	Need for planned assay work	Any potency claim

D. Suggested focused experimental sequence

The integrated assessment supports selection of 2-4 candidates rather than a broad, weakly characterised series. Candidate structures will be ranked by synthetic accessibility and a clear KDM5B-binding hypothesis. After synthesis, identity and purity should be established by appropriate NMR and mass-spectrometric methods. Enzyme testing should include concentration-response analysis, suitable controls and technical replicates. If measurable activity is observed, structurally related inactive or weaker analogues will be valuable for distinguishing scaffold-dependent effects from nonspecific metal chelation.

Table 2. Decision-based workflow for converting feasibility evidence into testable results.

Stage	Primary output	Decision gate
Design	2–4 synthetically realistic candidates	Defined KDM5B interaction hypothesis
Synthesis	Purified compounds	Acceptable yield and stability
Characterisation	NMR/MS-supported identity	No ambiguous structure assignment
Biochemical assay	Concentration-dependent response	Reproducible activity versus controls
Initial SAR	Comparison across close analogues	Structure-linked rather than nonspecific effect

IV. DISCUSSION

The preliminary evidence supports further investigation, but it also defines the strategy's uncertainties. The strongest component is the combination of demonstrated uracil chemistry and a ligandable KDM5B pocket. The largest uncertainty is whether a compact uracil-based series can produce sufficient potency and selectivity in a catalytic site that is shared in broad outline with many human 2OG oxygenases. Designing interactions beyond the metal/cofactor region is therefore more important than maximising metal chelation alone.

A second risk concerns biological interpretation. KDM5B may promote resistant phenotypes in particular cellular contexts, yet its functions are not universally oncogenic. A biochemical inhibitor would be a chemical starting point, not proof that KDM5B is the dominant resistance mechanism in a given gastrointestinal tumour. Follow-up studies would require target-engagement evidence, measurement of H3K4 methylation, assessment of related KDMs and testing in resistance-relevant models.

The proposed strategy remains informative even if the first compounds are inactive. A negative result obtained with verified structures, documented assay conditions and structurally rational candidates can refine the pharmacophore and prevent repetition of unproductive designs. Conversely, a modest but reproducible signal could guide analogue selection. This staged interpretation is more scientifically robust than describing untested molecules as inhibitors.

V. ORIGINALITY AND EXPECTED ADDED VALUE

The originality lies in combining an investigator-established uracil chemistry platform with a resistance-associated epigenetic target, rather than reproducing an existing KDM5 inhibitor scaffold. The present study does not claim that uracil is a previously validated KDM5B pharmacophore. Instead, it uses a chemically accessible heterocycle as a hypothesis-generating core and subjects that hypothesis to structural and biochemical evaluation. This positioning preserves novelty while maintaining a realistic evidentiary standard.

VI. LIMITATIONS

No KDM5B enzymatic data, cellular resistance data or pharmacokinetic measurements are available for the candidate uracil derivatives. The structural assessment is based on representative crystallographic conformations and does not fully model protein flexibility, water networks or competing metal-binding processes. The prior uracil studies involved unrelated enzyme classes, so their potency values cannot be extrapolated. These limitations are stated explicitly to distinguish platform feasibility from target validation.

VII. RELEVANCE TO CANCER RESISTANCE RESEARCH

The study addresses adaptive and acquired resistance in gastrointestinal cancers by defining a chemical strategy for interrogating an epigenetic regulator of cellular plasticity. It integrates medicinal chemistry, structural biology and enzyme pharmacology and establishes a preliminary pathway from rational design to experimentally testable chemical probes. The analysis may inform future work on resistance mechanisms and combination strategies.

VIII. CONCLUSION

Published uracil-derivative work establishes an experimentally workable chemical platform, while ligand-bound KDM5B structures establish target tractability and resistance-related studies provide biological motivation. Together, these findings justify a focused design-synthesis-test programme. They do not demonstrate KDM5B inhibition. The decisive next step is controlled biochemical evaluation followed, where warranted, by selectivity and cellular validation.

ACKNOWLEDGEMENT

This study is conceptually aligned with the research themes of COST Action CA24162 - AdResCanCER.

REFERENCES

[1] S. V. Sharma et al., “A chromatin-mediated reversible drug-tolerant state in cancer cell subpopulations,” Cell, 2010, 141, 69-80. doi: 10.1016/j.cell.2010.02.027.

[2] A. Roesch et al., “A temporarily distinct subpopulation of slow-cycling melanoma cells is required for continuous tumor growth,” Cell, 2010, 141, 583-594. doi: 10.1016/j.cell.2010.04.020.

[3] A. Vinogradova et al., “An inhibitor of KDM5 demethylases reduces survival of drug-tolerant cancer cells,” Nat. Chem. Biol., 2016, 12, 531-538. doi: 10.1038/nchembio.2085.

[4] S. M. Zhang et al., “KDM5B promotes immune evasion by recruiting SETDB1 to silence retroelements,” Nature, 2021, 598, 682-687. doi: 10.1038/s41586-021-03994-2.

[5] Y. Wang et al., “KDM5B promotes SMAD4 loss-driven drug resistance in pancreatic ductal adenocarcinoma,” Cell Death Discov., 2024. doi: 10.1038/s41420-024-02020-4.

[6] C. Johansson et al., “Structural analysis of human KDM5B guides histone demethylase inhibitor development,” Nat. Chem. Biol., 2016, 12, 539-545. doi: 10.1038/nchembio.2087.

[7] A. Tumber et al., “Potent and selective KDM5 inhibitor stops cellular demethylation of H3K4me3 at transcription start sites and proliferation of MM1S myeloma cells,” Cell Chem. Biol., 2017, 24, 371–380. doi: 10.1016/j.chembiol.2017.02.006.

[8] H. Cavdar et al., “Inhibition of acetylcholinesterase and butyrylcholinesterase with uracil derivatives: kinetic and computational studies,” J. Enzyme Inhib. Med. Chem., 2019, 34, 429-437. doi: 10.1080/14756366.2018.1543288.

[9] E. A. Turkoglu et al., “Carbonic anhydrase inhibitory properties of some uracil derivatives,” J. Enzyme Inhib. Med. Chem., 2017, 32, 74-77. doi: 10.1080/14756366.2016.1235043.

[10] M. Guney et al., “Synthesis and carbonic anhydrase inhibitory properties of novel uracil derivatives,” Bioorg. Med. Chem. Lett., 2015, 25, 3261-3263. doi: 10.1016/j.bmcl.2015.05.073.

[11] RCSB Protein Data Bank, “5A3N: Human KDM5B in complex with KDOAM-25.” doi: 10.2210/pdb5A3N/pdb.

8th International Conference on Engineering, Natural and Social Sciences

September 06-07, 2026: Konya, Turkey

© 2026 Published by All Sciences Academy

https://www.icensos.com/

Comparative Structural Feasibility of FTO and KDM5B for Structure-Guided Drug Repurposing

Murat Şentürk*

Faculty of Pharmacy, Ağrı İbrahim Çeçen University, Türkiye
**msenturk@agri.edu.tr*

Abstract - The regulation of gene expression in cancer involves interacting epitranscriptomic and chromatin-based mechanisms. FTO, an RNA N6-methyladenosine-related demethylase, and KDM5B, a histone H3 lysine 4 demethylase, represent distinct regulatory nodes within the Fe(II)/2-oxoglutarate (2OG)-dependent oxygenase superfamily. This preliminary study assessed whether the two proteins constitute a technically and conceptually suitable pair for comparative structure-guided drug-repurposing analysis. Experimentally determined human structures were selected from the Protein Data Bank, with emphasis on ligand-bound entries that define the catalytic region: FTO-N-oxalylglycine (PDB 4IDZ) and KDM5B-KDOAM-25 (PDB 5A3N). The structures were evaluated using a predefined qualitative framework covering catalytic-site definition, metal/cofactor-pocket accessibility, reference-ligand availability, surrounding recognition architecture and compatibility with a harmonised computational workflow. Both targets provide experimentally resolved ligand-binding regions and share the facial-triad/2OG-dependent catalytic logic characteristic of their superfamily. Nevertheless, their peripheral recognition environments are markedly different: FTO is organised for modified nucleic-acid recognition, whereas KDM5B is embedded in a multidomain system adapted to methylated histone substrates. These differences create a rational basis for distinguishing common cofactor-pocket binding from target-specific peripheral contacts. The analysis supports comparative screening of an approved-drug library and interaction-fingerprint-based prioritisation in subsequent work. The findings are feasibility data rather than evidence of drug binding or inhibition; all computationally prioritised compounds will require biochemical validation. The study provides a transparent preliminary foundation for COST Action CA21154 - TRANSLACORE.

Keywords: FTO; KDM5B; 2-oxoglutarate oxygenases; drug repurposing; translational control

I. INTRODUCTION

Cancer cells continually adjust gene expression to accommodate nutrient limitation, hypoxia, immune pressure and anticancer treatment. Although transcription and translation are often considered separately, they are coupled through RNA production, processing, stability and ribosome access. Reversible RNA and histone modifications provide rapid mechanisms for remodelling these processes without altering the underlying DNA sequence. Enzymes controlling such modifications are consequently attractive both as mechanistic probes and as possible therapeutic targets.

FTO was initially linked to human body-mass variation, but biochemical and structural studies subsequently established it as an AlkB-family nucleic-acid demethylase [1-3]. Its reported substrates include internal N6-methyladenosine (m6A), cap-adjacent N6,2′-O-dimethyladenosine (m6Am) and other methylated nucleobases under substrate- and context-dependent conditions [1,4]. In acute myeloid leukaemia, elevated

FTO activity has been associated with altered expression of selected transcripts and maintenance of malignant phenotypes [5]. Chemical inhibition studies, including meclofenamic-acid-derived probes and later anticancer-oriented inhibitors, further demonstrate that the FTO active site can be addressed by small molecules [6,7]. These observations justify structure-guided ligand investigation while also warning against oversimplifying FTO biology across tumour types.

KDM5B belongs to the Jumonji C-domain lysine demethylase family and removes methyl marks from histone H3 lysine 4. Through modulation of chromatin and transcriptional states, KDM5 proteins influence differentiation, proliferative capacity and drug-tolerant cell populations [8–10]. Crystal structures of the human KDM5B catalytic core with multiple inhibitor chemotypes have identified both conserved 2OG-pocket features and binding opportunities capable of supporting selectivity [8]. KDOAM-25 subsequently provided a potent KDM5-family chemical probe with cellular activity, reinforcing the tractability of this enzyme class [9].

FTO and KDM5B do not act on the same macromolecular substrate. Their value as a comparison arises instead from shared catalytic dependence on Fe(II) and 2OG combined with divergent substrate-recognition environments. Examining the same compound set against both targets may reveal whether a molecule is predicted to engage only the conserved cofactor region or also forms interactions compatible with one target's surrounding pocket. The objective of the present preliminary analysis was to determine whether available structural evidence was sufficient to support such a comparative workflow.

II. MATERIALS AND METHODS

A. Study design and evidentiary boundary

A descriptive comparative structural assessment was undertaken as a feasibility study. It did not involve synthesis, enzyme assays, cell experiments or generation of new inhibitory constants. Public crystallographic data and primary reports were used to define the starting structures and to identify methodological requirements for subsequent virtual screening. The term "preliminary data" therefore refers to documented target readiness and comparative structural observations, not to proof of pharmacological activity.

B. Structure selection

Candidate structures were screened for human origin, resolution of the catalytic region, presence of a bound ligand or cofactor analogue and relevance to inhibitor design. FTO entry 4IDZ was selected because it contains human FTO in complex with N-oxalylglycine and defines the 2OG-binding region at 2.46 Å resolution [3,11]. KDM5B entry 5A3N was selected because it contains the human catalytic core bound to KDOAM-25, an experimentally characterised KDM5 inhibitor [9,12]. Selection of ligand-bound structures reduces uncertainty in initial pocket definition compared with relying solely on apo models.

C. Comparative assessment framework

Each target was evaluated under five headings: (1) identity and completeness of the catalytic region; (2) definition of the metal and 2OG-recognition environment; (3) availability of an experimentally observed ligand pose; (4) architecture surrounding the conserved catalytic centre; and (5) suitability for common protein-preparation, docking and pose-review procedures. The comparison was deliberately qualitative because a valid numerical comparison would require a standardised computational protocol, matched protonation and metal-treatment rules, and formal redocking validation.

D. Planned computational validation

The subsequent workflow will include structure cleaning, selection of catalytically relevant metal states, protonation assignment, preservation or justified removal of key waters and definition of docking grids from experimental ligands. Redocking of the cognate ligands will be used to assess recovery of the crystallographic poses. Approved drugs will then be screened against both structures under consistent settings. Ranking will not rely on docking score alone; pose plausibility, metal/cofactor-region contacts, steric compatibility and reproducibility across alternative settings will be considered.

III. RESULTS

A. Both proteins meet minimum structure-readiness criteria

The two selected entries provide experimentally resolved catalytic pockets containing reference ligands. In 4IDZ, N-oxalylglycine occupies the FTO cosubstrate region and supplies an objective centre for grid definition [3,11]. In 5A3N, KDOAM-25 occupies the KDM5B catalytic pocket and provides a reference for evaluating ligand orientation and metal-proximal binding [9,12]. Both structures are therefore compatible with reproducible preparation and redocking-based protocol checks.

B. Catalytic similarity permits harmonised screening

FTO and KDM5B employ non-haem metal/2OG-dependent oxidative chemistry. The shared catalytic logic means that compounds containing carboxylate, heteroaromatic or other metal-proximal interaction motifs may be accommodated in analogous functional regions. From a workflow perspective, this similarity permits the same compound library, comparable conformer-generation rules and parallel pose-analysis criteria to be applied to both targets. The comparison can therefore be controlled more effectively than a study involving unrelated enzyme classes.

C. Recognition architecture predicts divergent ligand behaviour

The shared chemistry does not imply identical pockets. FTO contains an AlkB-like catalytic domain connected to structural elements that support recognition of methylated nucleic-acid substrates [2,3]. KDM5B uses a JmjC catalytic centre within a larger substrate-recognition arrangement designed for methylated histone tails [8]. Ligands confined to the conserved cofactor pocket may consequently show limited target discrimination, whereas compounds extending into peripheral regions may encounter different polar, hydrophobic and steric environments. This observation supplies the central rationale for comparative interaction fingerprinting.

Table 1. Preliminary comparison of the structural features relevant to the proposed workflow.

Criterion	FTO	KDM5B	Interpretation
Representative entry	PDB 4IDZ	PDB 5A3N	Ligand-bound human structures are available
Regulatory substrate	Modified nucleic acid	Methylated H3K4	Distinct biological recognition contexts
Reference ligand	N-oxalylglycine	KDOAM-25	Experimental pocket anchors can guide validation
Shared feature	Metal/2OG catalytic region	Metal/2OG catalytic region	A harmonised screening protocol is feasible
Main contrast	Nucleotide-recognition environment	Histone-peptide-recognition environment	Peripheral contacts may support selectivity

D. Decision rules for candidate prioritisation

The preliminary comparison indicates that candidate selection should separate three possible profiles: compounds predicted to engage both targets principally through conserved catalytic features; compounds predicted to gain additional interactions in FTO; and compounds predicted to gain additional interactions in KDM5B. A fourth category-high-scoring but geometrically implausible poses-must be excluded. This classification is more informative than reporting a single docking-score list because it connects ranking to mechanistic hypotheses that can later be tested experimentally.

IV. DISCUSSION

The main outcome is confirmation that FTO and KDM5B form a scientifically defensible comparative pair. Their shared catalytic requirements create a controlled chemical comparison, while their distinct macromolecular substrates provide a meaningful selectivity challenge. This combination is directly relevant to chemical biology: an approved drug may appear favourable because it interacts with a conserved metal/cofactor region, but translational value depends on whether sufficient target-specific contacts and biochemical activity are achieved.

The approach also has practical value for drug repurposing. Screening approved molecules can accelerate access to compounds with known formulation or exposure information, but regulatory status must not be confused with suitability for a new molecular target. Docking can identify hypotheses and reduce the number of compounds taken forward; it cannot establish inhibition, intracellular target engagement or anticancer efficacy. Experimental validation should therefore proceed in stages, beginning with purified-enzyme assays, followed by selectivity profiling against related 2OG oxygenases and only then cellular studies in biologically appropriate systems.

FTO requires particular interpretive care because substrate preference and biological direction can vary by cellular location, RNA target and tumour context [4,7]. KDM5B likewise participates in normal differentiation and chromatin regulation, meaning that complete or non-selective inhibition may cause unwanted effects. Comparative analysis across two 2OG oxygenases is thus useful not only for discovering candidates but also for identifying promiscuous chemotypes that should be deprioritised.

V. LIMITATIONS

This study uses representative static crystal structures and does not capture the full conformational ensembles of either enzyme. Crystallographic metals or analogues may differ from the catalytically active state, and protonation, tautomerism, water networks and induced fit can influence predicted binding. No docking scores, redocking RMSD values or inhibition constants are reported because these were not generated under a completed validated protocol at the preliminary stage. The analysis should therefore be interpreted as target-readiness and workflow-feasibility evidence.

VI. CONTRIBUTION TO COST ACTION CA21154 - TRANSLACORE

The preliminary study connects an RNA-modifying enzyme directly involved in RNA fate with a chromatin-modifying enzyme capable of reshaping transcriptional states. By establishing a reproducible comparison of ligand recognition, it supports interdisciplinary investigation of gene-expression control in cancer. The resulting feasibility framework defines how a prioritised compound set, a documented computational protocol and experimentally testable selectivity hypotheses may be developed in subsequent work.

VII. CONCLUSION

FTO 4IDZ and KDM5B 5A3N provide structurally defined and ligand-anchored starting points for comparative drug-repurposing analysis. Their conserved metal/2OG-dependent catalytic regions allow harmonised screening, whereas their different peripheral recognition environments provide a rational basis for investigating target preference. These preliminary findings establish structural and methodological feasibility but do not demonstrate drug binding or inhibition. Biochemical confirmation and selectivity testing remain essential.

REFERENCES

[1] G. Jia et al., "N6-methyladenosine in nuclear RNA is a major substrate of the obesity-associated FTO," Nat. Chem. Biol., 2011, 7, 885-887. doi: 10.1038/nchembio.687.

[2] Z. Han et al., "Crystal structure of the FTO protein reveals basis for its substrate specificity," Nature, 2010, 464, 1205-1209. doi: 10.1038/nature08921.

[3] W. S. Aik et al., "Structural basis for inhibition of the fat mass and obesity associated protein (FTO)," J. Med. Chem., 2013, 56, 3680-3688. doi: 10.1021/jm400193d.

[4] J. Mauer et al., "Reversible methylation of m6Am in the 5′ cap controls mRNA stability," Nature, 2017, 541, 371-375. doi: 10.1038/nature21022.

[5] Z. Li et al., "FTO plays an oncogenic role in acute myeloid leukemia as an N6-methyladenosine RNA demethylase," Cancer Cell, 2017, 31, 127-141. doi: 10.1016/j.ccell.2016.11.017.

[6] Y. Huang et al., "Meclofenamic acid selectively inhibits FTO demethylation of m6A over ALKBH5," Nucleic Acids Res., 2015, 43, 373-384. doi: 10.1093/nar/gku1276.

[7] R. Su et al., "Targeting FTO suppresses cancer stem cell maintenance and immune evasion," Cancer Cell, 2020, 38, 79-96.e11. doi: 10.1016/j.ccell.2020.04.017.

[8] C. Johansson et al., "Structural analysis of human KDM5B guides histone demethylase inhibitor development," Nat. Chem. Biol., 2016, 12, 539-545. doi: 10.1038/nchembio.2087.

[9] A. Tumber et al., "Potent and selective KDM5 inhibitor stops cellular demethylation of H3K4me3 at transcription start sites and proliferation of MM1S myeloma cells," Cell Chem. Biol., 2017, 24, 371–380. doi: 10.1016/j.chembiol.2017.02.006.

[10] S. V. Sharma et al., "A chromatin-mediated reversible drug-tolerant state in cancer cell subpopulations," Cell, 2010, 141, 69-80. doi: 10.1016/j.cell.2010.02.027.

[11] RCSB Protein Data Bank, "4IDZ: Human FTO in complex with N-oxalylglycine." doi: 10.2210/pdb4IDZ/pdb.

[12] RCSB Protein Data Bank, "5A3N: Human KDM5B in complex with KDOAM-25." doi: 10.2210/pdb5A3N/pdb.

8th International Conference on Engineering, Natural and Social Sciences

September 06-07, 2026: Konya, Turkey

© 2026 Published by All Sciences Academy

https://www.icensos.com/

Comparative Analysis of YOLOv8s, YOLO11s and YOLO26s Architectures for Medical Pill Detection

Muslume Beyza YILDIZ [1] and Murat KOKLU [1*]

[1]*Department of Computer Engineering, Selcuk University, Konya, Türkiye*

[*]*(mkoklu@selcuk.edu.tr) Email of the corresponding author*

Abstract **–** Automated medical pill detection is critical for patient safety and smart healthcare applications. In this study, contemporary single-stage object detection architectures, namely YOLOv8s, YOLO11s, and YOLO26s, are evaluated. The open-access "Pills Detection Dataset," compiled by Alexander Y. on the Kaggle platform, was utilized. The dataset comprises 12,067 images, including negative background samples. It was partitioned into training, validation, and test subsets following an 80:10:10 ratio. Accordingly, the distribution includes 9,655 images for training, 1,206 images for validation, and 1,206 images for independent testing. Performance evaluations were conducted on the 1,206 test images containing 14,074 annotated instances. All evaluated models achieved an mAP@50 score above 0.994 on the test set. The YOLOv8s model exhibited the highest baseline classification stability with an F1-score of 0.9896. The YOLO11s model maintained high accuracy despite its lower parameter count. Featuring an end-to-end architecture, YOLO26s eliminated the need for NMS filtering and decreased post-processing latency to 0.19 ms. This operational change yielded an approximate 86% time reduction in that phase. The model achieved an mAP@50-95 score of 0.9546, preserving bounding box precision under strict intersection thresholds. All models delivered processing speeds ranging from 93.7 to 99.1 frames per second. These findings demonstrate that the evaluated models offer strong potential for real-time, low-latency deployment in clinical inspection and automated medication tracking systems.

Keywords – Object detection, medical pill detection, YOLO architectures, deep learning, hardware latency

I. INTRODUCTION

Automated drug dispensing systems and packaging lines play a critical role in the healthcare sector [1]. Preventing medication dispensing errors in these systems directly impacts patient safety. Manual inspections relying on human evaluation during packaging and verification processes remain slow. Furthermore, such manual checks are susceptible to fatigue-induced errors [2]. Computer vision-based automated recognition systems provide a reliable inspection mechanism in this domain [3].

Image-based detection of medical pills involves several operational challenges. Variations in pill shape, size, and visual features, along with overlapping objects and background diversity, can degrade detection performance. Consequently, deep learning-based object detection methods are widely utilized for the automated analysis of pill and tablet images. Zhu et al. [4] proposed an improved YOLOv8s model for medication detection, focusing particularly on small instances and visually similar pharmaceuticals. Diószegi et al. [5], demonstrated the effectiveness of deep learning-based visual inspection by employing a YOLOv5-based approach to detect manufacturing defects on tablet surfaces. Similarly, the CBS-YOLOv8 model developed by Vijayakumar et al. [2] for defect detection in pharmaceutical packaging demonstrated the practical utility of YOLO variants in quality control. Kavitha and Madhumathy [6] presented a YOLOv5s-based framework for real-time pill identification and classification. Wang et al. [7] utilized an enhanced YOLOv8n architecture for defect detection on irregularly shaped film-coated tablets.

In a more recent study, Hu [8] developed DD-YOLO based on YOLO11 for pill defect identification and evaluated its performance on fine cracks and surface contamination.

Prior studies indicate that YOLO-based architectures can be employed effectively across various pharmaceutical applications, including automated object detection and visual quality control. Nevertheless, existing research predominantly focuses on modifying a single YOLO architecture or resolving a specific defect detection problem. Comparative evaluations assessing multiple detection architectures under identical dataset partitions and controlled experimental setups remain limited. In this study, YOLOv8s, YOLO11s, and YOLO26s architectures are evaluated comparatively using the same dataset, identical hardware, and equivalent hyperparameters for medical pill detection. The models are examined not only in terms of detection accuracy, but also through computational metrics including parameter count, inference latency, and throughput (FPS).

The remainder of this paper is structured as follows. Section II details the dataset, experimental hardware configuration, and model architectures. Section III presents the empirical findings supported by figures and tables. Section IV discusses the obtained results in relation to the existing literature. Section V summarizes the principal conclusions of the study.

II. Materials and Method

The details of the materials and methods utilized in this study are described in the following subsections.

A. Dataset

In this study, the open-access "Pills Detection Dataset" compiled by Alexander Y. on the Kaggle platform was utilized [9]. This dataset was collected from multiple open-source repositories and converted into the YOLO annotation format by the compiler. During dataset creation, images from VAIPE [10], NIH Pill Image Dataset-rximage [11], Ultralytics-medical-pills [12] and the personal image collections of the creator were aggregated. Erroneous and missing annotations were revised by the dataset author. In particular, oversized bounding boxes from the VAIPE dataset were tightened to establish more accurate object boundaries.

The dataset contains a total of 12,067 images. To ensure an unbiased comparative evaluation across all models, the dataset was partitioned into training, validation, and test subsets following an 80:10:10 ratio. Accordingly, the distribution includes 9,655 images in the training set, 1,206 images in the validation set, and 1,206 images in the independent test set. Representative sample images illustrating varying pill densities, orientations, and background conditions are presented in Fig. 1.



Fig. 1. Representative sample images from the dataset depicting diverse object densities, orientations, and background conditions

B. Evaluated YOLO Architectures

Within the scope of this study, three single-stage object detection architectures-YOLOv8s, YOLO11s, and YOLO26s-are evaluated. Pre-trained weights on the COCO dataset were utilized during model initialization. The models were adapted to the medical pill detection task using a transfer learning strategy.

The YOLOv8s architecture features an anchor-free detection backbone that integrates convolutional layers with C2f blocks. Due to its decoupled head design, classification and bounding box regression operations are processed through independent layers. The model employs the standard non-maximum suppression (NMS) algorithm during post-processing to filter out redundant overlapping prediction boxes [13], [14].

The YOLO11s architecture incorporates C3k2 blocks alongside C2PSA layers featuring spatial attention mechanisms. It includes an enhanced Spatial Pyramid Pooling - Fast (SPPF) module designed to optimize gradient flow across multi-scale feature maps. This design aims to achieve rich feature representations with fewer parameters and lower computational overhead [15], [16].

The YOLO26s architecture is built on an end-to-end detection framework. A dual label assignment strategy is applied during training. During inference, a one-to-one matching head ensures that predicted bounding boxes correspond directly to ground truth targets. This approach keeps the computational overhead constant during inference and completely eliminates the requirement for an external NMS stage [17].

C. Hardware Environment and Training Parameters

All models were trained within the Ultralytics framework under identical hardware and software environments. Experiments were conducted on the Google Colab platform using an NVIDIA Tesla T4 GPU equipped with 15 GB of VRAM. The software environment comprised Python 3.13 and PyTorch 2.11.

Model training was configured for 50 epochs. An early stopping patience of 20 epochs was enforced to prevent overfitting. The input image resolution was set to 640x640 pixels across all models. A batch size of 16 was selected. Optimization was performed using the AdamW algorithm. The initial learning rate was set to 0.002, with a momentum factor of 0.9 and a weight decay of 0.0005. Automatic mixed precision (AMP) was utilized during training to improve computational efficiency.

D. Performance Evaluation Metrics

Model performance was evaluated across two main categories: detection accuracy and hardware latency.

Detection accuracy was quantified using Precision [18], Recall [19], F1-Score [20], mAP@50 [21] and mAP@50-95 [22]. Intersection over Union (IoU) thresholds were calculated at 0.50 and across the 0.50–0.95 range. Classification performance and background discrimination were analyzed using confusion matrices. Detection stability across varying confidence thresholds was evaluated via precision-recall (PR) curves.

Hardware performance was assessed by decomposing the per-image processing time into three stages. Pre-processing, raw inference, and post-processing latencies were measured in milliseconds. The sum of these values provided the total latency per image. Throughput, measured in frames per second (FPS), was calculated directly from the total latency. The evaluation metrics and their formulations are summarized in Table 1.

Table 1. Performance Evaluation Metrics Used in Model Assessment

Ölçüt	Formül	Açıklama
Precision	$P = \frac{TP}{TP + FP}$	Represents the ratio of correctly identified instances (TP) to all positive predictions, reflecting the frequency of false alarms. FP (False Positive) denotes instances where background regions are incorrectly labeled as pills[23], [24].
Recall	$R = \frac{TP}{TP + FN}$	Measures the proportion of actual ground-truth objects correctly identified by the model, reflecting missed targets. FN (False Negative) denotes pills in the scene that the detector fails to identify[25], [26].
F1 Score	$F1 = 2 * \frac{P*R}{P+R}$	The harmonic mean of precision and recall, summarizing the trade-off between classification accuracy and target coverage into a single score [27], [28], [29].
Average Precision (AP)	$AP = \int_0^1 P(R)\, dR$	Represents the area under the precision-recall curve, quantifying detection accuracy across varying confidence thresholds [30].
mAP@50	$mAP@50 = \frac{1}{N}\sum_{i=1}^{N} AP_{i(IoU=0.5)}$	The mean average precision computed across all target classes when the Intersection over Union (IoU) threshold is set to 0.50 [21].
mAP@50-95	$mAP@50-95 = \frac{1}{10}\sum_{k=0}^{9} mAP_{IoU=0.5+0.05k}$	A comprehensive metric evaluated by increasing the IoU threshold from 0.50 to 0.95 in increments of 0.05, strictly assessing bounding box alignment [22].
Total Latency (T)	$T = T_{ön} + T_{çıkarım} + T_{son}$	The cumulative time required to process a single image across pre-processing, raw model inference, and post-processing (NMS) stages, measured in milliseconds (ms) [16], [17].
Frame Rate (FPS)	$FPS = \frac{1000}{T}$	Specifies the total number of frames processed per second, defining real-time operational capability [16], [17].

III. RESULTS

This section presents the empirical findings obtained from the trained YOLOv8s, YOLO11s, and YOLO26s models on the test set. All evaluations were conducted on an independent test split containing 1,206 images and 14,074 annotated instances. The baseline accuracy metrics and training times of the models are reported in Table II.

Table 2. Test Set Performance Metrics and Training Durations of YOLOv8s, YOLO11s, and YOLO26s Models

Model Architecture	Precision	Recall	F1-Score	mAP@50	mAP@50-95	Training Time (min)
YOLOv8s	0.9903	0.9889	0.9896	0.9947	0.9541	161.51
YOLO11s	0.9887	0.9859	0.9873	0.9946	0.9529	172.51
YOLO26s	0.9870	0.9827	0.9848	0.9943	0.9546	192.91

As reported in Table II, all evaluated models maintained mAP@50 scores above the 0.994 threshold. The YOLOv8s model achieved a precision of 0.9903, a recall of 0.9889, and an F1-score of 0.9896, demonstrating the highest baseline classification stability. The YOLO11s model produced a precision of 0.9887 and a recall of 0.9859. The YOLO26s model reached an mAP@50-95 score of 0.9546, delivering the highest localization precision under strict intersection thresholds. Regarding training durations, YOLOv8s completed training in 161.51 minutes, YOLO11s required 172.51 minutes, and YOLO26s took 192.91 minutes. The parameter counts and hardware latency measurements of the models are summarized in Table III.

Table 3. Parameter Counts and Hardware Latency Values of YOLOv8s, YOLO11s, and YOLO26s Models

Model Architecture	Parameters (M)	Pre-process (ms)	Inference (ms)	Post-process/NMS (ms)	Total Latency (ms)	FPS
YOLOv8s	11.14	1.28	7.46	1.35	10.09	99.1
YOLO11s	9.43	1.38	7.91	1.38	10.67	93.7
YOLO26s	9.95	1.17	9.05	0.19	10.41	96.1

According to the data in Table III, the YOLO11s model formed the most compact architecture with 9.43 million parameters. The YOLO26s model contains 9.95 million parameters, whereas the YOLOv8s model comprises 11.14 million parameters. Regarding hardware execution speeds, the shortest model inference latency was recorded by YOLOv8s at 7.46 ms. This duration was 7.91 ms for YOLO11s and 9.05 ms for YOLO26s.

In contrast, the YOLO26s architecture demonstrated a notable advantage in the post-processing phase. By eliminating the necessity for an NMS layer, the model reduced post-processing latency to 0.19 ms. In comparison, this stage required 1.35 ms for YOLOv8s and 1.38 ms for YOLO11s. The cumulative latency per image was 10.09 ms for YOLOv8s, 10.41 ms for YOLO26s, and 10.67 ms for YOLO11s. All architectures achieved throughput exceeding 93 frames per second. The comparative confusion matrices of the evaluated models on the test set are presented in Fig. 2.

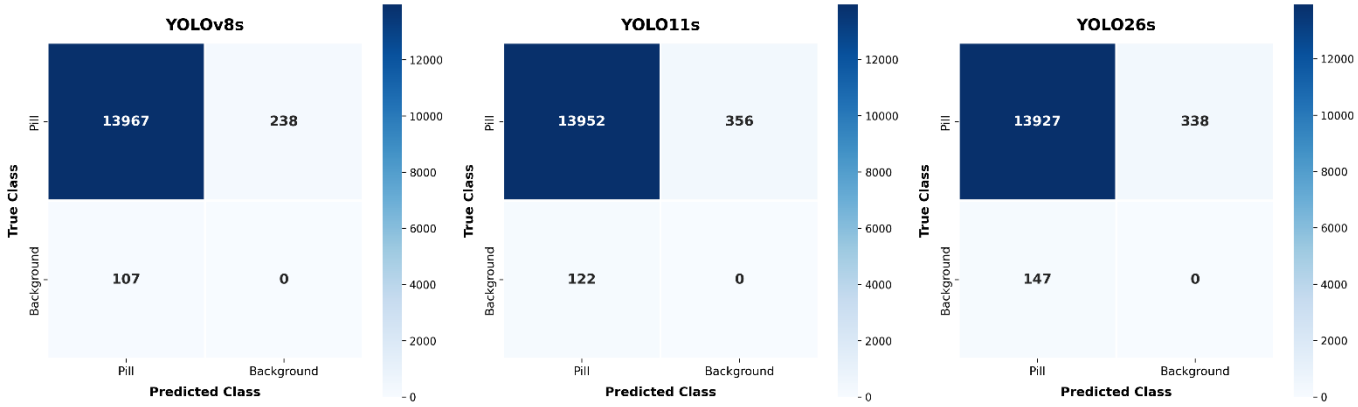

Fig. 2 Confusion matrices of YOLOv8s, YOLO11s, and YOLO26s models evaluated on the test set

An examination of the matrix distributions in Fig. 2 indicates that all architectures correctly identified over 97.5% of the 14,074 target objects in the test set. The precision-recall curves illustrating model stability across varying confidence thresholds are depicted in Fig. 3.

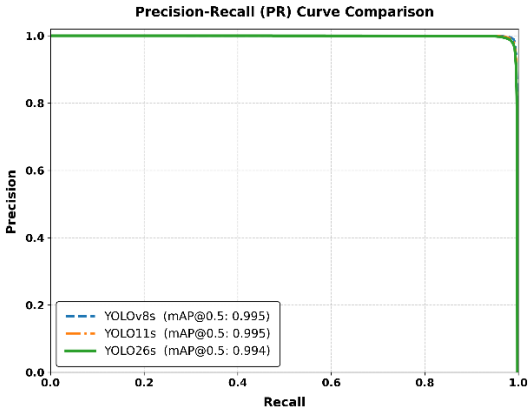

Fig. 3 Precision-recall (PR) curves of YOLOv8s, YOLO11s, and YOLO26s evaluated at an IoU threshold of 0.50 on the test set

The curves in Fig. 3 show that all three models maintain a profile parallel to the 1.0 precision line up to a recall level of 0.98. The models experienced no substantial decline in precision until reaching high recall levels. The area under the curve directly represents the mAP@50 metric, reaching 0.995 for both YOLOv8s and YOLO11s, and 0.994 for YOLO26s. These curves confirm that the models effectively

suppress false positive detections. A visual comparison of detection performance across the models is provided in Fig. 4.

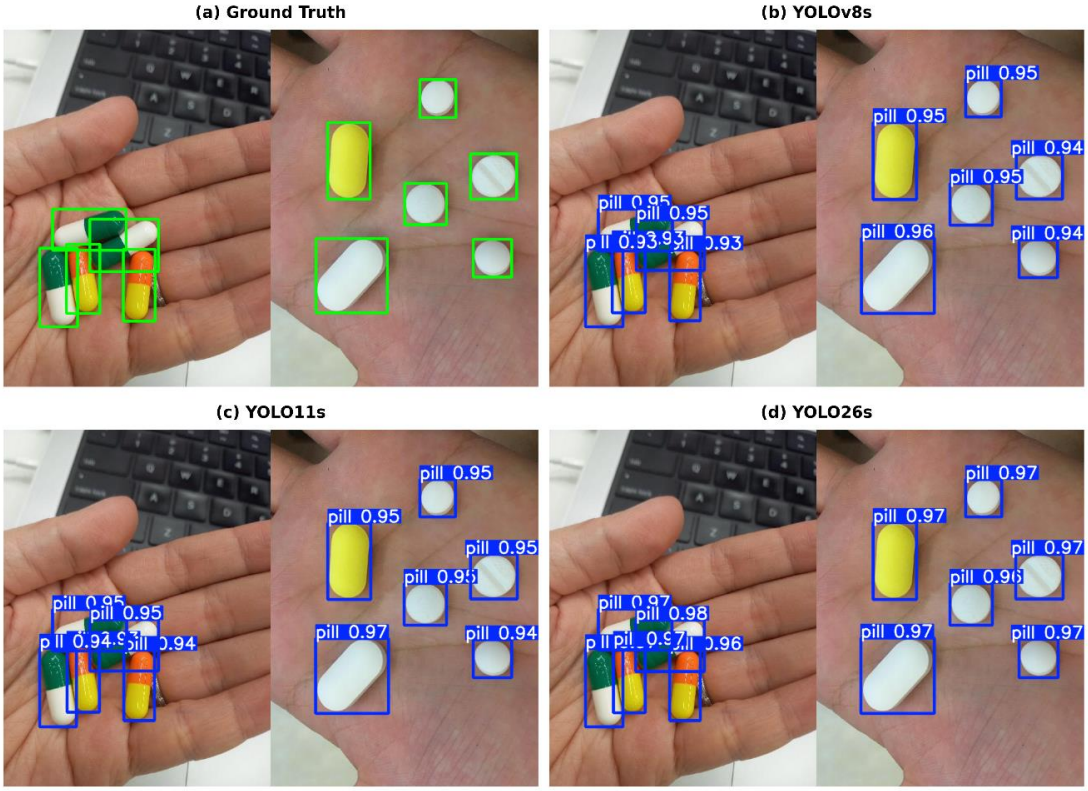

Fig. 4 Detection comparison of YOLOv8s, YOLO11s, and YOLO26s models on representative test samples selected from the dataset

All models fully bounded the target objects without omissions. No false detections occurred on challenging background features such as skin folds or keyboard keys. The YOLO26s model accurately separated the boundaries of contacting capsules. Prediction confidence scores for the model ranged between 0.96 and 0.98. These visual results confirm that the NMS-free detection head operates robustly in differentiating closely spaced objects.

IV. Discussion

The quantitative and visual findings highlight the architectural advancements across the three successive YOLO generations in object detection.

In terms of detection accuracy, performance disparities among the evaluated models remained within a very narrow margin. The YOLOv8s model preserved baseline classification robustness, achieving an F1-score of 0.9896 and 13,967 true positive detections. This result reflects the stability of the established feature pyramid network and the traditional NMS-based candidate selection mechanism in the YOLOv8 architecture.

The YOLO11s architecture yielded the most lightweight network footprint with 9.43 million parameters. Despite this reduced parameter budget, it delivered an mAP@50 score on par with YOLOv8s. This efficiency stems primarily from the enhanced feature extraction capability introduced by the C3k2 blocks.

The YOLO26s model demonstrated a distinct structural shift in execution timing and post-processing dynamics. By incorporating a one-to-one matching head, the architecture entirely bypassed the conventional NMS stage. Consequently, post-processing latency dropped from 1.35 ms in YOLOv8s to 0.19 ms, corresponding to an approximate 86% latency reduction in this operational stage.

Due to the additional matching layers, the raw inference time of YOLO26s rose slightly to 9.05 ms. However, the substantial latency decrease during post-processing largely compensated for this difference, keeping the total processing latency at 10.41 ms. With this runtime profile, the model maintained an operational throughput of 96.1 frames per second.

Furthermore, YOLO26s reached an mAP@50-95 of 0.9546, performing on par with YOLOv8s (0.9541). This outcome confirms that, even without an NMS layer, the bipartite Hungarian matching mechanism retains high bounding box localization accuracy under strict IoU thresholds. The visual detections in Fig. 4 corroborate that adjacent, contacting pills can be effectively resolved without an external suppression filter.

All evaluated architectures sustained processing rates exceeding 90 FPS. This computational throughput supports the practical feasibility of deploying these models on resource-constrained platforms and in real-time clinical verification systems where low latency is mandatory.

V. Conclusion

In this study, contemporary single-stage object detection architectures, namely YOLOv8s, YOLO11s, and YOLO26s, were comprehensively evaluated for the task of medical pill detection. Experiments were conducted on a hybrid dataset comprising 12,067 images, including negative background samples. The models were trained with equivalent hyperparameters and evaluated under an identical hardware environment. The primary conclusions derived from this study are as follows:

- All evaluated models achieved an mAP@50 accuracy score exceeding 99.4% on the test set.
- The YOLOv8s model preserved baseline classification and localization stability, yielding an F1-score of 0.9896 and 13,967 true positive detections.
- The YOLO11s model sustained high detection accuracy despite its compact parameter footprint of 9.43 million parameters.
- The YOLO26s model eliminated the dependency on NMS through its end-to-end architecture, decreasing post-processing latency to 0.19 ms and achieving an approximate 86% speedup in this phase.
- The models exhibited throughput ranging from 93.7 to 99.1 frames per second, with all architectures operating well above the standard 30 FPS real-time operational threshold.

References

[1] L. N. T. My, V.-T. Le, T. Vo, and V. T. Hoang, "A comprehensive review of pill image recognition," *Computers, Materials and Continua,* vol. 82, no. 3, pp. 3693–3740, 2025, doi: 10.32604/cmc.2025.060793.

[2] A. Vijayakumar, S. Vairavasundaram, J. A. S. Koilraj, M. Rajappa, K. Kotecha, and A. Kulkarni, "Real-time visual intelligence for defect detection in pharmaceutical packaging," *Scientific reports,* vol. 14, no. 1, p. 18811, 2024, doi: 10.1038/s41598-024-69701-z.

[3] S. J. Kim and D. S. Cho, "Medical-pills detection using YOLOv11: A proof of concept study for pharmaceutical automation," *Clinical Case Reports and Studies,* vol. 10, no. 2, pp. 1–11, 2025, doi: 10.59657/2837-2565.brs.25.252.

[4] D. Zhu, Z. Huang, K. Yung, and A. W. Ip, "Drug recognition detection based on deep learning and improved YOLOv8," *Journal of Organizational and End User Computing (JOEUC),* vol. 36, no. 1, pp. 1–21, 2024, doi: 10.4018/JOEUC.359770.

[5] A. Diószegi *et al.*, "Automated tablet defect detection and the prediction of disintegration time and crushing strength with deep learning based on tablet surface images," *International Journal of Pharmaceutics,* vol. 667, p. 124896, 2024, doi: 10.1016/j.ijpharm.2024.124896.

[6] N. Kavitha and P. Madhumathy, "Real-time pill identification and classification using deep learning framework for medicine inspection systems," *Discover Electronics,* vol. 2, no. 1, p. 80, 2025, doi: 10.1007/s44291-025-00122-6.

[7] Z. Wang *et al.*, "Enhancing YOLOv8n with Mamba-like linear attention for defect detection and coating thickness analysis of irregular film tablet," *International Journal of Pharmaceutics,* vol. 678, p. 125704, 2025, doi: 10.1016/j.ijpharm.2025.125704.

[8] Y. Hu, "DD-YOLO: Real-Time Pill Defect Detection Based on an Improved YOLO Framework with Feature Complementary Mapping," in Proc. 2026 3rd International Conference on Electrical Technology and Automation Engineering (ETAE), 2026, pp. 796–799, doi: 10.1109/ETAE69474.2026.11495982.

[9] A. Y., "Pills detection dataset," Kaggle, 2026. [Online]. Available: https://www.kaggle.com/datasets/alexanderyyy/pills-detection-dataset, [Accessed: Jul. 04, 2026].

[10] A. D. Nguyen, H. H. Pham, H. T. Trung, Q. V. H. Nguyen, T. N. Truong, and P. L. Nguyen, "High accurate and explainable multi-pill detection framework with graph neural network-assisted multimodal data fusion," *PLoS ONE,* vol. 18, no. 9, 2023, doi: 10.1371/journal.pone.0291865.

[11] Z. Yaniv et al., "The National Library of Medicine Pill Image Recognition Challenge: An Initial Report," in Proc. IEEE Applied Imagery Pattern Recognition Workshop (AIPR), Washington, DC, USA, 2016, pp. 1–9, doi: 10.1109/AIPR.2016.8010584.

[12] Ultralytics, "Ultralytics Datasets: Medical-pills Detection Dataset," 2024. [Online]. Available: https://docs.ultralytics.com/datasets/detect/medical-pills. [Accessed: Jul. 04, 2026].
[13] O. Kilci and M. Koklu, "Automated classification of biscuit quality using YOLOv8 models in food industry," *Food Analytical Methods,* vol. 18, no. 5, pp. 815–829, 2025, doi: 10.1007/s12161-025-02755-5.
[14] C. Unal, I. Cinar, Z. Saripinar, and M. Koklu, "Comparative Evaluation of YOLOv8 and YOLO11 for Image-Based Classification of Sugar Beet Seed Treatment Levels," *Sensors,* vol. 26, no. 7, p. 2137, 2026, doi: 10.3390/s26072137.
[15] M. M. Saritas, A. Golcuk, and M. Koklu, "Detection of Oranges on Trees Across Diverse Field Conditions Using YOLOV11 Models," *Applied Fruit Science,* vol. 68, no. 2, p. 106, 2026, doi: 10.1007/s10341-026-01810-7.
[16] P. Hidayatullah, N. Syakrani, M. R. Sholahuddin, T. Gelar, and R. Tubagus, "YOLOv8 to YOLO11: A comprehensive architecture in-depth comparative review," *arXiv preprint arXiv:2501.13400,* vol. 4, pp. 1–22, 2026, doi: 10.29207/resti.v10i2.6598.
[17] G. Jocher, J. Qiu, M. Liu, S. Lyu, F. C. Akyon, and M. E. Kalfaoglu, "Ultralytics YOLO26: unified real-time end-to-end vision models," *arXiv preprint arXiv:2606.03748,* 2026, doi: 10.48550/arXiv.2606.03748.
[18] M. M. Saritas, M. B. Yildiz, T. A. Cengel, and M. Koklu, "Differentiated thyroid cancer recurrence prediction using boosting algorithms," *Jurnal Komputer Teknologi Informasi Sistem Komputer (JUKTISI),* vol. 4, no. 2, pp. 663–676, 2025, doi: 10.62712/juktisi.v3i3.307.
[19] T. A. Cengel, B. Gencturk, E. T. Yasin, M. B. Yildiz, I. Cinar, and M. Koklu, "Automating egg damage detection for improved quality control in the food industry using deep learning," *Journal of Food Science,* vol. 90, no. 1, p. e17553, 2025, doi: 10.1111/1750-3841.17553.
[20] Y. Karatas *et al.*, "Identification of leaf diseases from figs using deep learning methods," *Selcuk Journal of Agriculture and Food Sciences,* vol. 38, no. 3, pp. 414–426, 2024, doi: 10.15316/SJAFS.2024.037.
[21] R. Padilla, S. L. Netto, and E. A. Da Silva, "A survey on performance metrics for object-detection algorithms," in Proc. 2020 International Conference on Systems, Signals and Image Processing (IWSSIP), 2020, pp. 237–242, doi: 10.1109/IWSSIP48289.2020.9145130.
[22] P. Wei, X. Yan, W. Yan, L. Sun, J. Xu, and H. Yuan, "Precise extraction of targeted apple tree canopy with YOLO-Fi model for advanced UAV spraying plans," *Computers and electronics in agriculture,* vol. 226, p. 109425, 2024, doi: 10.1016/j.compag.2024.109425.
[23] T. A. Cengel *et al.*, "Classification of orange features for quality assessment using machine learning methods," *Selcuk Journal of Agriculture and Food Sciences,* vol. 38, no. 3, pp. 403–413, 2024, doi: 10.15316/SJAFS.2024.036.
[24] K. Erdem, M. B. Yildiz, E. T. Yasin, and M. Koklu, "A detailed analysis of detecting heart diseases using artificial intelligence methods," *Intelligent methods in engineering sciences,* vol. 2, no. 4, pp. 115–124, 2023, doi: 10.58190/imiens.2023.71.
[25] K. Erdem, E. Yasin, M. B. Yildiz, and M. Koklu, "Classification of heart diseases with ensemble learning algorithms," *Sinop Üniversitesi Fen Bilimleri Dergisi,* vol. 9, no. 2, pp. 369–387, 2024, doi: 10.33484/sinopfbd.1458580.
[26] M. B. Yildiz, M. F. Hafif, E. K. Koksoy, and R. Kursun, "Classification of diseases in tomato leaves using deep learning methods," *Intelligent Methods In Engineering Sciences,* vol. 3, no. 1, pp. 22–36, 2024, doi: 10.58190/imiens.2024.84.
[27] T. A. Cengel, B. Gencturk, E. T. Yasin, M. B. Yildiz, I. Cinar, and M. Koklu, "Apple (malus domestica) quality evaluation based on analysis of features using machine learning techniques," *Applied Fruit Science,* vol. 66, no. 6, pp. 2123–2133, 2024, doi: 10.1007/s10341-024-01196-4.
[28] M. B. Yildiz, E. T. Yasin, and M. Koklu, "Fisheye freshness detection using common deep learning algorithms and machine learning methods with a developed mobile application," *European Food Research and Technology,* vol. 250, no. 7, pp. 1919–1932, 2024, doi: 10.1007/s00217-024-04493-0.
[29] O. Kilci, M. B. Yildiz, and H. Y. Tukel, "Deep learning and machine learning approaches for coffee leaf disease diagnosis," in Agri-Intelligence (Artificial Intelligence Reflections in Agriculture), H. K. Örnek, Ed., Konya, Türkiye: Çizgi Kitabevi, 2024, pp. 273–297.
[30] L. Tan, T. Huangfu, L. Wu, and W. Chen, "Comparison of RetinaNet, SSD, and YOLO v3 for real-time pill identification," BMC Medical Informatics and Decision Making, vol. 21, p. 334, 2021, doi: 10.1186/s12911-021-01691-8[.

8th International Conference on Engineering, Natural and Social Sciences

September 06-07, 2026: Konya, Turkey

© 2026 Published by All Sciences Academy

https://www.icensos.com/

AI-Assisted Quality Control in Textile Manufacturing: A Conceptual Evaluation of Fabric Defect Detection and Color Consistency

Beyza Buzol Mülayim[1*], Selma Bulut [2]

[1]*Kırklareli University, Vocational School of Technical Sciences, Fashion Design Program, Kırklareli, Türkiye*
[2] *Kırklareli University, Department of Computer Programming, Kırklareli, Türkiye*

[*]*(beyza.mulayim@klu.edu.tr)*

Abstract – Quality control in textile manufacturing has traditionally relied on visual inspection by human operators, offering limited accuracy (60-75%) due to operator fatigue and individual perceptual differences. In recent years, advances in artificial intelligence (AI) and image processing technologies have driven a fundamental transformation in this field by providing automated, consistent, and high-speed solutions for fabric defect detection and color consistency control. This conceptual study synthesizes, in light of current literature, the role of computer vision, deep learning (CNN, GAN, Transformer, YOLO), and classical machine learning techniques in detecting fabric surface defects and ensuring color consistency in dyeing/printing processes. Deep learning-based systems are reported to achieve accuracy rates exceeding 98% in fabric defect classification and to reduce fabric waste by approximately 20% in large-scale production facilities. However, significant limitations persist, including scarcity of labeled data, lack of standard datasets, domain adaptation challenges, and the need for specialized models targeting printing/dyeing-specific defect types. The study concludes by discussing future research directions such as hybrid approaches and synthetic data generation.

Keywords – AI-Driven Textile Quality Control: Fabric Defect Detection and Color Consistency

I. INTRODUCTION

AI-assisted quality control systems are automating fabric defect detection and color consistency assessment in textile production, replacing traditional manual inspection methods [1], [2], [3]. These same methods are also used, beyond quality control, to predict mechanical performance properties of woven fabrics such as breaking strength [4]; however, the scope of the present study is limited to fabric defect detection and color consistency control. This conceptual review synthesizes the role of computer vision, deep learning, and machine learning techniques in detecting fabric surface defects and ensuring color consistency in dyeing and printing processes [5], [6].

Manual fabric inspection falls short on high-speed production lines due to operator fatigue and low accuracy rates, with human detection accuracy ranging only between 60-75% [2], [7], [8]. Automated systems based on computer vision and image processing overcome these limitations by delivering consistent, high-speed quality control [2], [9], [10].

The aim of this study is to conceptually evaluate AI- and image processing-based quality control approaches in textile production under the headings of fabric defect detection and color consistency control in light of the existing literature.

II. Materials and Method

This study is a conceptual review synthesizing the existing literature on AI-assisted quality control applications in textile production, under the headings of fabric defect detection and color consistency control. It does not aim to collect experimental data or develop an original application; rather, it aims to map the current state, methodological approaches, and open research problems by systematically scanning and thematically synthesizing published studies in the field.

Literature Search Strategy: The literature search was conducted using academic databases such as Scopus, Web of Science, IEEE Xplore, and Google Scholar, along with Consensus (an AI-assisted academic search engine). The search was carried out using English keyword combinations including "fabric defect detection," "textile quality control," "deep learning textile," "color consistency dyeing," "AI colorimetric analysis," and "YOLO fabric inspection."

Scope and Time Range: The study largely includes recent works published in peer-reviewed journals or conference proceedings between 2020 and 2026; older review studies that constitute key reference points in the field (e.g., [11]) are also cited where necessary.

Inclusion Criteria: (i) studies addressing AI, machine learning, or image processing-based methods for automatic detection of fabric/textile surface defects; (ii) studies focusing on color consistency, color prediction, or color error detection in dyeing, printing, or finishing processes; (iii) review articles, systematic reviews, or directly applied (experimental) research papers.

Exclusion Criteria: Non-peer-reviewed publications, general industrial quality control studies unrelated to the textile sector, and studies presenting only an abstract/theoretical model proposal without any performance data were excluded from the scope.

Synthesis Approach: The reviewed studies were grouped into three main themes according to the type of problem they addressed: (1) fabric defect detection, (2) color consistency and colorimetric control, and (3) pattern/motif consistency control. For each theme, the model architectures used, reported performance metrics (such as accuracy, mAP, FPS, ΔE), and the methodological limitations pointed out by the studies were summarized in comparative tables; findings were qualitatively synthesized to discuss common trends and research gaps in the field.

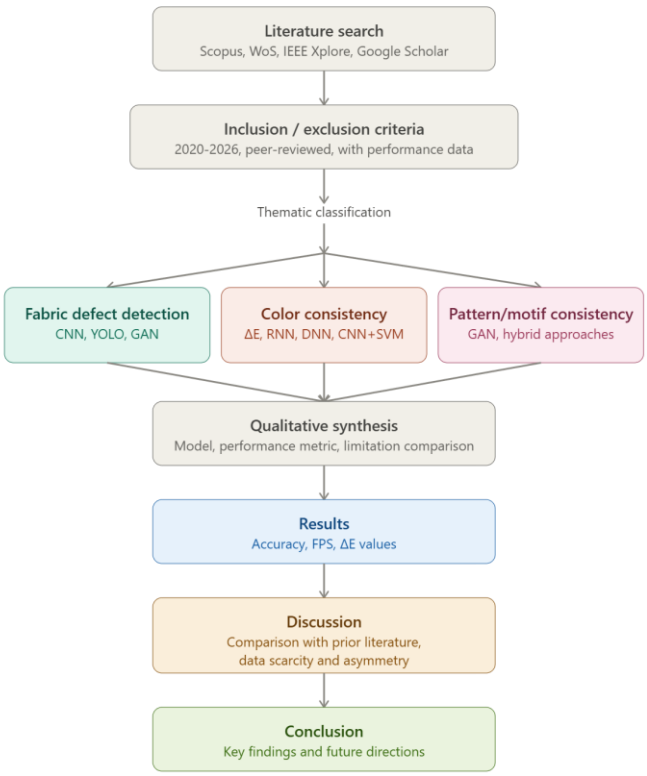

Figure 1. Methodological flow of the conceptual review

A. Traditional Quality Control Methods and Their Limitations

Manual fabric inspection falls short on high-speed production lines due to operator fatigue and low accuracy rates; human detection accuracy stands only in the 60-75% range [2], [7], [8].

Table 1. Comparative summary of the main approach categories used in fabric defect detection.

Approach Category	Sub-Methods	Strengths	Weaknesses
Traditional	Statistical, spectral, model-based, structural	Interpretability, low computational requirements	Limited scalability and accuracy [2], [11]
Classical Machine Learning	SVM, PCA, XGBoost	Moderate generalization capacity	Requires manual feature extraction [2], [6]
Deep Learning	CNN, GAN, Transformer, YOLO	High accuracy, real-time detection	Data scarcity, high computational cost [12], [5], [7]

Automated systems based on computer vision and image processing overcome these limitations by delivering consistent, high-speed quality control [2], [9], [10].

B. AI and Image Processing-Based Quality Control Approaches

Fabric Defect Detection

Fabric defect detection methods are broadly divided into traditional algorithms and learning-based algorithms [13], [2]. Traditional methods include statistical, structural, spectral, and model-based algorithms [13], [2], while classical machine learning techniques typically rely on manually extracted features combined with classifiers such as support vector machines (SVM) [7], [14]. Learning-based methods are further subdivided into classical machine learning and deep learning algorithms [13], [2]; deep

learning-based approaches provide automatic feature extraction, reducing the sensitivity that traditional methods show to variations in texture and lighting [14], [15].

Convolutional neural networks (CNNs) achieve accuracy rates above 98% in fabric defect classification by enabling automatic feature extraction [10], [8]. Among deep learning architectures, autoencoders, generative adversarial networks (GANs), and long short-term memory (LSTM) networks stand out alongside CNNs, with CNN-based models delivering acceptable performance for industrial applications at success rates of 95% and above in fabric defect classification [12], [16].

Table 2. Performance comparison of prominent deep learning models used in fabric defect detection

Model / Approach	***Key Feature***	***Performance / Accuracy***
DCNN (Deep CNN)	*Classifies 13 different defect types*	*97.49% mAP [16]*
SCUNet (U-Net)	*Uses deep separable convolution*	*98.01% accuracy [17]*
Hybrid Detector	*Combines Gabor and LBP with CNN*	*96.3% mAP@0.5 [18]*
Multi-Scale CNN	*Uses multiple Gaussian pyramid levels*	*High sensitivity [19]*

The YOLO (You Only Look Once) object detection framework offers high speed and accuracy for real-time fabric defect detection [7], [14]; its advanced versions, optimized with attention mechanisms and multi-scale feature fusion, have proven successful at detecting small and complex fabric defects [20], [21]. A YOLOv7-based PCBS model reached 94.4% mAP at 59.5 frames per second (FPS) [20], while a lightweight YOLOv5s-based model met industrial real-time requirements at 102 FPS [15]. An SSD-BiFPN model, in turn, was optimized to detect small and irregular defects on edge devices [14].

GAN architectures are used for generating new patterns and for anomaly detection [6], [5]. Transfer learning, meanwhile, accelerates the model development process, making it easier to adapt to different fabric textures [1], [22].

Color Consistency and Colorimetric Control

Deep learning methods are applied in color consistency detection for tasks such as identifying color mismatches, anomaly detection, and surface defect localization [5], [6]. Compared to traditional trial-and-error methods, deep learning models predict dye recipes and final color coordinates with high accuracy, improving color consistency in textile dyeing processes [23], [24], [25]. By learning and optimizing complex factors affecting color consistency such as dye selection, fabric type, and processing conditions these models minimize color deviations before production [6], [26].

Deep learning-based approaches automatically calculate the dye concentrations needed to reach a target color using spectrophotometric data and image processing techniques [23], [27]. Convolutional neural networks (CNNs) and backpropagation algorithms, used in place of the traditional Kubelka-Munk theory, have markedly improved color-matching accuracy [28], [29]. Hybrid models, meanwhile, combine color and texture features to predict color deviations before production [27], [25].

Table 3. Performance comparison of deep learning models that improve color consistency in textile dyeing.

Model / Approach	**Key Function**	**Performance / Result**
Improved RNN	Dye recipe prediction from hyperspectral data	Relative error 2.70-3.40% [23]
DNN (Wet-Dry)	Dry color prediction from wet fabric	$\Delta E2000 \leq 1.0$ (63.9%) [24]
CNN + SVM	Pantone color matching	100% classification accuracy [28]
GA-DFNN	Color recipe prediction for opaque products	$\Delta E \leq 1.0$ [30]
Transformer	Multiple regression prediction of CIELAB color values	Surpasses baseline with attention mechanism [26]

Neural networks predict shade variations arising after dyeing and finishing processes in advance, preventing rework and raw material waste [31]. Color deviations caused by post-treatment chemical

processes such as water-repellent finishes can be predicted using multilayer perceptron (MLP) models, with mean absolute error ranging from 0.0765 to 0.1626 [31]. Deep learning also analyzes fabric images on the production line to detect dyeing defects such as streaks, stains, and color mismatches in real time [5].

While the color difference between wet and dry fabric cannot be resolved with traditional theories due to the optical effects created by water, deep learning can successfully map this relationship [24]. In color difference classification, optimized extreme learning machine (ELM) models outperform methods such as SVM and BPNN, improving classification accuracy [32]. In detecting dyeing defects, deep learning eliminates the fatigue and subjectivity issues present in manual inspection, delivering consistent quality control [5], [29].

Accurately predicting shade differences in color prediction depends on factors affecting color consistency, such as dye selection, fabric type, and processing conditions [6]. AI-assisted systems can rapidly analyze high-resolution images to detect color errors and adapt over time through continuous learning [5].

Pattern/Motif Consistency Control

Consistency issues in patterns and motifs on printed fabrics are largely addressed within the color consistency literature, with only a limited number of studies treating this as a distinct sub-area; it has been noted that dedicated models are needed for color errors occurring in dyeing and printing processes streaks, tonal differences, stains while most existing deep learning methods focus predominantly on general textile defects [5]. In this context, the use of GAN architectures for generating new patterns and detecting anomalies [6], [5] points to the potential for strengthening pattern consistency control in the future through hybrid approaches that combine color and texture features with deep features [9], [7].

Challenges and Limitations

Data scarcity is the foremost obstacle facing deep learning models in textile processes; the shortage of labeled datasets needed to train robust models persists [6], [33]. Industrial-scale deployment of defect detection systems faces similar challenges, including dataset scarcity, computational complexity, and texture diversity [34], [2]; the insufficiency of labeled datasets restricts models' generalization capacity, making adaptation to different fabric types difficult [2], [12]. The lack of openly accessible standard fabric defect datasets complicates cross-method comparison and objective evaluation [9], [22].

Real-time performance evaluation the trade-offs between speed (FPS) and accuracy (mAP) has not been sufficiently examined in production settings [5], [9]. Dataset bias and domain adaptation also pose challenges for models adapting to different fabric textures and colors [1], [7].

Color error detection is a more difficult problem than structural defect detection, due to factors such as lighting variability and fabric reflectance [35]. Existing deep learning methods mostly focus on general textile defects; development of dedicated models for dyeing-specific color errors streaks, tonal differences, stains remains limited [5]. This creates a methodological gap, particularly in printing-specific sub-areas such as pattern/motif consistency. The scarcity of labeled datasets for training robust models is one of the main obstacles encountered in color consistency prediction [6]. Future research is emphasized to focus on color-calibrated datasets, physics-informed loss functions, and real-time performance evaluations in production settings [35], [26], [5].

Hybrid approaches (combining color and texture features with deep features) and synthetic data generation are considered prominent future research directions for overcoming these limitations [9], [7].

III. Results

Deep learning-based models report higher accuracy rates than traditional and classical machine learning methods in fabric defect detection. CNN-based classifiers achieved accuracy in the 95-98% range [12], [16], [10], [8], with SCUNet showing the highest value at 98.01% accuracy [17]. YOLO-based real-time detection models reported speeds between 59.5 and 102 FPS, with a YOLOv7-based PCBS model reaching 94.4% mAP [20], [15].

On the color consistency side, the models examined largely kept ΔE values below 1.0 [24], [30]. An improved RNN model reported a relative error of 2.70-3.40% in dye recipe prediction [23]; a CNN+SVM combination reached 100% classification accuracy in Pantone color matching [28]. Color deviations arising from chemical finishing processes such as water-repellent treatments were predicted with a mean absolute error ranging from 0.0765 to 0.1626 using MLP models [31].

At the system level, AI-assisted defect detection has been reported to reduce fabric waste by approximately 20% in large-scale facilities [1]. The number of studies specific to pattern/motif consistency, meanwhile, remains markedly lower compared to the color and defect detection literature [5].

IV. Discussion

The findings show that deep learning-based approaches surpass the accuracy ceiling of traditional methods in fabric defect detection; however, this superiority does not stem from a single mechanism but from the robustness that automatic feature extraction provides against texture and lighting variability [14], [15]. The FPS values reported by YOLO-based models indicate that these systems are applicable not only under laboratory conditions but also in scenarios approaching production line speed; this point directly aligns with the need for "consistent, high-speed quality control" emphasized in [2] and [9].

Models reaching the $\Delta E \leq 1.0$ threshold on the color consistency side offer a practical benchmark that falls within industrial tolerances; however, this success has largely been achieved under controlled test conditions. The fact that deep learning surpasses traditional Kubelka-Munk-based approaches in problems with high optical complexity, such as wet-dry color prediction [24], shows that physical modeling and data-driven modeling carry different advantages across different problem classes.

The 20% reduction in fabric waste [1] indicates that AI-assisted quality control is positioned not merely as an inspection layer but as a production component that directly affects resource use. This finding demonstrates that the link between sustainability goals and quality control automation is measurable, not merely theoretical.

By contrast, the scarcity of studies specific to pattern/motif consistency should be read not as a gap but as an asymmetry: the literature tends to treat color defects (streaks, stains, tonal differences) within the same framework as general textile defects [5], indicating that defect dynamics specific to the printing process have not yet been sufficiently defined as a distinct problem class. Data scarcity and the absence of standard datasets reinforce this asymmetry, further complicating cross-method comparison [6], [9], [22].

V. Conclusion

Deep learning-based approaches have surpassed the accuracy and speed limits of traditional methods in fabric defect detection and color consistency control, delivering measurable resource savings in industrial applications. Progress in the field depends on expanding labeled datasets, developing specialized models for dyeing- and printing-specific defect types, and closing the gap between laboratory conditions and production line performance.

Acknowledgment

The author declares that no funding was received for this study. No human or animal subjects were involved in this conceptual review, and no conflicts of interest are declared.

References

[1] A. Ozek, M. Seçkin, P. Demircioğlu, and I. Bogrekci, "Artificial intelligence driving innovation in textile defect detection," Textiles, vol. 5, no. 2, art. 12, 2025, doi: 10.3390/textiles5020012.

[2] P. Guo, Y. Liu, Y. Wu, R. Gong, and Y. Li, "Intelligent quality control of surface defects in fabrics: A comprehensive research progress," IEEE Access, vol. 12, pp. 63777-63808, 2024, doi: 10.1109/ACCESS.2024.3396053.

[3] F. He, B. Xin, Z. Zhan, W. Yang, and J. Liu, "A review of fabric defect detection in textile manufacturing," J. Text. Inst., vol. 117, pp. 327-345, 2025, doi: 10.1080/00405000.2025.2502188.

[4] B. Berkhan Kastacı, H. Z. Özek, and E. Özhan, "A comparison of the three techniques in predicting breaking strength of cotton and blended woven fabrics," Tekstil ve Mühendis, vol. 31, no. 133, pp. 34-41, 2024, doi: 10.7216/TEKSMUH.1329122.

[5] H. Cui, A.-F. Seyam, and R. Shamey, "Textile and colour defect detection using deep learning methods," Color. Technol., 2025, doi: 10.1111/cote.70044.

[6] N. Ingle and W. J. Jasper, "A review of deep learning and artificial intelligence in dyeing, printing and finishing," Text. Res. J., vol. 95, pp. 625-657, 2024, doi: 10.1177/00405175241268619.

[7] M. Mao and M. Hong, "YOLO object detection for real-time fabric defect inspection in the textile industry: A review of YOLOv1 to YOLOv11," Sensors, vol. 25, 2025, doi: 10.3390/s25072270.

[8] J. Dhorajiya, K. Shah, T. G. Patil, and P. Udawant, "Review of fabric defect detection using machine learning algorithms," Int. J. Multidiscip. Res., 2023, doi: 10.36948/ijfmr.2023.v05i05.5163.

[9] A. Rasheed, B. Zafar, A. Rasheed, N. Ali, M. Sajid, S. H. Dar, U. Habib, T. Shehryar, and M. Mahmood, "Fabric defect detection using computer vision techniques: A comprehensive review," Math. Probl. Eng., vol. 2020, pp. 1-24, 2020, doi: 10.1155/2020/8189403.

[10] S. Shahrabadi, Y. Castilla, M. Guevara, L. Magalhães, D. Garcia Gonzalez, and T. Adão, "Defect detection in the textile industry using image-based machine learning methods: A brief review," J. Phys. Conf. Ser., vol. 2224, 2022, doi: 10.1088/1742-6596/2224/1/012010.

[11] H. Y. T. Ngan, G. Pang, and N. Yung, "Automated fabric defect detection - A review," Image Vis. Comput., vol. 29, pp. 442-458, 2011, doi: 10.1016/j.imavis.2011.02.002.

[12] Y. Kahraman and A. Durmuşoğlu, "Deep learning-based fabric defect detection: A review," Text. Res. J., vol. 93, pp. 1485-1503, 2022, doi: 10.1177/00405175221130773.

[13] C. Li, J. Li, Y. Li, L. He, X. Fu, and J. Chen, "Fabric defect detection in textile manufacturing: A survey of the state of the art," Secur. Commun. Netw., vol. 2021, art. 9948808, 2021, doi: 10.1155/2021/9948808.

[14] A. M. Alkhazraji, S. Golmohammadi, and A. A. Ghavifekr, "AI-based real-time fabric defect detection using an enhanced SSD with bidirectional feature pyramid networks," Textiles, vol. 6, no. 2, art. 63, 2026, doi: 10.3390/textiles6020063.

[15] X. Kang, "Research on fabric defect detection method based on lightweight network," J. Eng. Fibers Fabr., vol. 19, 2024, doi: 10.1177/15589250241232153.

[16] S. A. Hassan, M. Beliatis, A. Radziwon, A. Menciassi, and C. Oddo, "Textile fabric defect detection using enhanced deep convolutional neural network with safe human-robot collaborative interaction," Electronics, vol. 13, art. 4314, 2024, doi: 10.3390/electronics13214314.

[17] L. Cheng, J. Yi, A. Chen, and Y. Zhang, "Fabric defect detection based on separate convolutional UNet," Multimed. Tools Appl., vol. 82, pp. 3101-3122, 2022, doi: 10.1007/s11042-022-13568-7.

[18] D. Patil and A. Ambika, "AI driven hybrid descriptor and classifier for robust textile fabric defect detection," J. Wireless Mob. Netw. Ubiquitous Comput. Dependable Appl., vol. 17, no. 2, pp. 444-464, 2026, doi: 10.58346/JOWUA.2026.I2.025.

[19] S. Mei, Y. Wang, and G. Wen, "Automatic fabric defect detection with a multi-scale convolutional denoising autoencoder network model," Sensors, vol. 18, 2018, doi: 10.3390/s18041064.

[20] C. Liu, H. Zou, P. Lv, and R. Zhu, "Fabric defect detection method based on multi-scale fusion attention mechanisms," Meas. Sci. Technol., vol. 36, 2024, doi: 10.1088/1361-6501/ad8be7.

[21] L. Zhou, B. Dong, Y. Yin, and F. Lu, "DCFE-YOLO: A novel fabric defect detection method," PLoS ONE, vol. 20, 2025, doi: 10.1371/journal.pone.0314525.

[22] A. Gamal, M. E. H. Eltaib, and M. Dewidar, "Can computer vision and AI techniques impact the quality control system for textile yarns? (Review)," Discov. Artif. Intell., vol. 6, 2026, doi: 10.1007/s44163-026-01313-0.

[23] J. Zhang, X. Zhang, J. Wu, and C. Xiao, "Dyeing recipe prediction of cotton fabric based on hyperspectral colour measurement and an improved recurrent neural network," Color. Technol., vol. 137, pp. 166-180, 2021, doi: 10.1111/cote.12516.

[24] W. J. Jasper and S. M. Jasper, "A controlled study on machine learning applications to predict dry fabric color from wet samples: Influences of dye concentration and squeeze pressure," Fibers, vol. 13, art. 47, 2025, doi: 10.3390/fib13040047.

[25] H. Cho, J.-W. Ko, and S. G. Lee, "Sustainable machine-learning framework for efficient color prediction in dope-dyed recycled PET/PCT," ACS Sustain. Chem. Eng., 2026, doi: 10.1021/acssuschemeng.5c11490.

[26] Z. Chen, J. Liu, J. Li et al., "Leveraging multi-output modelling for CIELAB using colour difference formula towards sustainable textile dyeing," Auton. Intell. Syst., vol. 4, art. 19, 2024, doi: 10.1007/s43684-024-00076-8.

[27] M. Chen, H. S. Tsang, K. T. Tsang, and T. Hao, "An hybrid model CMR-Color of automatic color matching prediction for textiles dyeing and printing," in Neural Computing for Advanced Applications (NCAA 2021), Commun. Comput. Inf. Sci., vol. 1449, Singapore: Springer, 2021, pp. 603-618, doi: 10.1007/978-981-16-5188-5_43.

[28] S. Das and A. Wahi, "Digital image analysis using deep learning convolutional neural networks for color matching of knitted cotton fabric," J. Nat. Fibers, vol. 19, pp. 15716-15722, 2022, doi: 10.1080/15440478.2022.2133052.

[29] S. Liu, Y. Liu, K.-Y. C. Lo, and C.-W. Kan, "Intelligent techniques and optimization algorithms in textile colour management: A systematic review of applications and prediction accuracy," Fash. Text., vol. 11, pp. 1-38, 2024, doi: 10.1186/s40691-024-00375-x.

[30] Y. Wang, X. Wu, J. Hou, and M. Hu, "Predicting color schemes based on genetic algorithm and deep feedforward neural network model," Trans. Comput. Sci. Intell. Syst. Res., 2024, doi: 10.62051/4zkqs575.

[31] F. Irshad, M. Ashraf, A. Farooq, M. A. Ashraf, and N. Khan, "Development of prediction system for shade change variations in dyed cotton fabric after application of water repellent finishes," J. Nat. Fibers, vol. 20, 2022, doi: 10.1080/15440478.2022.2154302.

[32] Z. Zhou, C. Wang, J. Zhang, and Z. Zhu, "Color difference classification of solid color printing and dyeing products based on optimization of the extreme learning machine of the improved whale optimization algorithm," Text. Res. J., vol. 90, pp. 135-155, 2020, doi: 10.1177/0040517519859933.

[33] R. Khanam, M. Hussain, R. Hill, and P. Allen, "A comprehensive review of convolutional neural networks for defect detection in industrial applications," IEEE Access, vol. 12, pp. 94250-94295, 2024, doi: 10.1109/ACCESS.2024.3425166.

[34] Y. Huang, J. Jing, and Z. Wang, "Fabric defect segmentation method based on deep learning," IEEE Trans. Instrum. Meas., vol. 70, pp. 1-15, 2021, doi: 10.1109/TIM.2020.3047190.

[35] B.-H. Kim and H.-S. Jae, "Industrial artificial intelligence methods for fabric color-defect detection in textile manufacturing," Int. J. Sci. Technol., vol. 5, no. 1, pp. 28-41, 2026, doi: 10.56127/ijst.v5i1.2600.

8th International Conference on Engineering, Natural and Social Sciences

September 06-07, 2026: Konya, Turkey

© 2026 Published by All Sciences Academy

https://www.icensos.com/

Copyright, Originality, and Ethical Use in Generative AI Textile Pattern Design

Selma Bulut[1], Beyza Buzol Mülayim[2*]

[1]*Vocational School of Technical Sciences, Department of Computer Technologies, Kırklareli University, Turkey*
2Kırklareli University, Vocational School of Technical Sciences, Fashion Design Program, Kırklareli, Turkey

[*](*beyza.mulayim@klu.edu.tr)*

Abstract – Generative AI is increasingly used to produce textile and fashion patterns, raising questions of copyright, originality, and ethical practice that go beyond the visual quality of the output. This paper presents a conceptual synthesis of the literature on generative AI in textile pattern design. The synthesis draws on legal analyses, empirical design studies, and ethics scholarship. Copyright infringement is not treated here as a single point problem. Risk is traced across the entire production chain instead. Unlicensed scraping of training images, low transparency in model provenance, style imitation, and the diffusion of responsibility among developers, platforms, and designers each add a distinct layer of concern. Empirical work in fashion and craft education consistently reports that generative tools accelerate ideation while weakening personal style expression and a felt sense of authorship. Creative labor shifts from designing to curating among machine generated options. Legal scholarship remains divided on whether a well-constructed prompt or a documented chain of human selections can ground a copyright claim. The dominant position still ties protect ability to free and creative human choices. Cultural representation raises a further concern specific to textile design. Training data skewed toward Western, commercial imagery risks flattening minority motifs and local craft traditions. Community governed systems that incorporate cultural rules and oversight boards appear to reduce this risk. The paper concludes that generative AI in textile design is best treated as a supervised co creative tool rather than an autonomous author. Data transparency, cultural safeguards, output labeling, and remuneration mechanisms should accompany its adoption in commercial practice.

Keywords – Generative AI, textile design, copyright, originality, cultural representation, human AI co creation

I. INTRODUCTION

Research on copyright, originality, and ethical use in generative AI textile patterns converges on one point. The technology accelerates the design process, but copyright compliance, genuine originality, and cultural sensitivity do not follow automatically from this acceleration. Risk does not concentrate only in the visual similarity of the output. Unlicensed compilation of training data, low model transparency, style imitation, and the diffusion of responsibility between developers and users each form a separate layer of risk across the production chain [1]-[5].

Generative artificial intelligence is spreading quickly into textile design. Its main applications include pattern, surface, knit, print, and visual variation generation. This spread raises a different question than whether the output looks good. It raises the question of who owns the output, how original it counts as, and what data produced it [6]-[10]. Studies specific to fashion and textiles have repeatedly reported that generative AI offers an advantage in ideation speed, but remains weak in originality, edit ability, personal style expression, and cultural sensitivity [11]-[13].

Legal debate concentrates on three axes. These axes are the copyright status of training data, whether AI assisted output counts as a protectable work, and how responsibility should be shared among users, developers, and platforms [14]-[18]. Ethical debate adds cultural representation, algorithmic bias, imitation of an artist style, explainability and the labeling of synthetic content to this list [19]-[22]. The remainder of this paper treats these two debates as connected rather than separate, and returns to how they overlap in the Discussion.

Three related terms recur throughout this paper and are worth distinguishing before proceeding. Cultural representation refers to whose aesthetics, motifs, and traditions appear, or fail to appear, in training data and generated output. Cultural appropriation refers more narrowly to the extraction or commercial reuse of a specific community's motifs without consent, attribution, or benefit sharing. Cultural authenticity refers to how closely an output is judged to follow the conventions and meanings of a craft tradition, independent of who created it. This paper treats representation as the broader concept, and returns to appropriation and authenticity as specific concerns nested within it.

II. Materials and Method

This study was designed as a multidisciplinary literature review. The aim was to synthesize copyright, originality, cultural representation, and ethical use in generative AI textile patterns within one framework. The scope was not limited to technical pattern generation studies. Copyright law, governance, design education, fashion applications, and cultural representation literature were included as well. This expansion was necessary because the effects of generative AI occur across a supply chain that runs from training data to the use of the output [2], [8].

This study is best described as a multidisciplinary literature synthesis rather than a systematic review in the formal sense. The approach was informed by systematic review principles, including a predefined search strategy and explicit inclusion criteria. Given the heterogeneous nature of the available evidence, spanning legal doctrine, small sample design studies, and technical system papers, the method is more accurately characterized as a conceptual narrative synthesis. No formal risk of bias assessment or meta-analytic pooling was attempted, since the underlying studies do not share a common outcome metric.

The methodological framework drew on the systematic review tradition, although a strict PRISMA protocol was not followed. The following principles from that tradition were adopted. The search string was defined in advance. The choice of database was justified. The time window was specified. The inclusion and exclusion criteria were stated clearly [5], [7]. Recent reviews in fashion and textile design point to a similar approach. These reviews recommend tracking conference papers and applied publications alongside journal articles [6], [10].

The search was conducted through Consensus, an AI assisted literature discovery tool that indexes Semantic Scholar and PubMed. Semantic matching was performed across approximately 220 million records through this tool. The search covered publications from 2019 to 2026, the period during which the field is observed to have matured. Earlier studies that underpin the copyright debate were not excluded.

The search strategy combined five concept clusters. These clusters were generative AI, textile or fashion or pattern, copyright or originality, ethics or transparency, and cultural representation or governance [7], [19]. This approach followed the Boolean logic used in fabric design reviews [7], [10]. The core search string combined three blocks. The first block covered generative AI, artificial intelligence, machine learning, deep learning, GAN, VAE, and diffusion model. The second block covered textile design, fabric design, pattern design, surface pattern, knitwear, and fashion. The third block covered copyright, authorship, originality, plagiarism, ethics, transparency, and governance [7], [10], [14]. A second complementary query was added to capture cultural and ethical risks. This query combined AI generated design or generative design with textile or fashion, and with cultural representation, bias, transparency, accountability, or ownership [19], [20].

The main components of the search are summarized in Table 1.

Table 1. Method and search strategy components

Component	Recommended content	Basis
Database	Semantic Scholar, PubMed (through Consensus)	[7]
Time range	2019 to 2026	[7], [5]
Publication type	Peer reviewed journal article and conference paper	[7], [10]
Language	English	[7]
Focus area	Textile or fashion design and law, ethics, or governance	[7], [2], [16]
Screening logic	Title, abstract, and full text where needed	[10]

The inclusion criteria were defined as follows. A study had to use AI or ML methods in the context of textile, fabric, fashion, or pattern design, or discuss the copyright, authorship, originality, ethics, or governance implications of such outputs directly. Knitted textile design, early stage fashion ideation, AI assisted design systems, distributed authorship, human creative control, and cultural authenticity were treated as separate coding categories [8], [11], [15], [17], [20].

The exclusion criteria were applied with equal care. Non design uses of AI such as textile production optimization were excluded. Editorial opinion pieces alone were excluded. Studies without accessible full text were excluded. Older rule based systems with limited relevance to the current generative AI wave were excluded as well [7], [10]. This screening was necessary to build a corpus that could examine pattern generation and the copyright or ethics debate within the same frame [8], [9], [19].

Data extraction recorded at minimum the following fields. Publication year, discipline, method type, the AI model used, design context, data source, the copyright or originality claim made, ethical risks, the level of human contribution, and the protection mechanisms proposed [5]-[7], [16], [17]. Technical and legal publications could not be judged by the same criteria. The synthesis was therefore structured as narrative and thematic rather than statistical. Recent work also notes that the field is heterogeneous and that a breadth focused synthesis produces a more realistic picture [5], [19].

Sub themes were coded under four headings in advance. Training data and licensing covered scraping, text and data mining exceptions, fair use, and remuneration [2], [14]. This theme distinguished between the European Union's approach under the 2019 Directive on Copyright in the Digital Single Market, which grants a mandatory exception for research use and a broader commercial exception that right holders can opt out of, and the United States approach, which relies on a case by case fair use analysis without a dedicated text and data mining exception [18], [28], [35]. Output originality and authorship covered human contribution, modest creativity, and distributed authorship [14], [15]. Design practice covered ideation speed, customization, edit ability, and the loss of personal style [9], [11], [12]. Ethics and cultural representation covered bias, marginalization, cultural appropriation, and transparency [4], [19], [20].

The method carries its own limitations, the most significant of which is dependence on a single AI assisted discovery tool rather than independent searches across multiple databases such as Scopus, Web of Science, and IEEE Xplore. A single tool search does not allow for the cross database deduplication or inter-rater screening reliability checks that a formal systematic review would require, and the ranking logic behind the tool is not fully transparent to the reviewer. Reliance on this tool may favor highly cited, English language publications. Locally published work that receives fewer citations but still holds value for the field may be missed as a result. Legal and ethics focused studies outnumber industry application data in this literature. The synthesis therefore reflects this imbalance rather than correcting it. Readers should treat the resulting picture as indicative of the direction of the literature rather than as an exhaustive or fully reproducible inventory of it.

III. RESULTS

The studies that carry the most weight in this field fall into two groups. One group consists of legal syntheses that break down the copyright chain of generative AI from training data to output. The other group consists of applied studies that measure originality and the loss of creative control in the textile and fashion context [1], [3], [11], [7]. Reading the studies published in Science, JMLR, IIC, and fashion or design journals together shows that risk accumulates across the entire production line rather than at a single stage [1], [23], [24], [9].

A. *Key Studies*

Table 2. Key studies that frame the field

Study	Contribution
Epstein et al. [1]	Frames training data risk and output risk together
Geiger [24]	Proposes a human centered copyright reform
Jang [11]	Shows that efficiency gains weaken the perception of authorship
Pasetti et al. [2]	Maps the governance dimensions of training data and copyright across the production chain
Jurčys and Fenwick [14]	Traces the evolving doctrine of originality as applied to generative AI output
Mahto and Rodriguez [19]	Documents ethical risk across the fashion trend forecasting and garment design pipeline

The most frequently cited names in this corpus include Christophe Geiger, Xiaopei Wu, and Garim Lee. The journals with the highest citation density include Fashion and Textiles, IIC International Review of Intellectual Property and Competition Law, and Sustainability.

B. *Copyright and the Distribution of Responsibility*

Training data appears as the most systematically studied risk area in the literature. Most studies identify the inclusion of copyrighted images in large datasets without permission or payment as the central problem [16], [26], [28], [29]. Risk at the output stage is not limited to a literal copy. It is discussed through recognizable connection, derivative status, market substitution, and stylistic resemblance [23], [25], [30], [31].

Table 3. Distribution of copyright risk across the production chain

Dimension	Training data	Output	Responsibility
Main risk	Unlicensed scraping	Similar or derivative output	Diffuse actors [2], [3]
Legal status	Fair use or TDM unclear	Depends on the facts	May shift to the user [2], [25], [26]
Policy direction	Transparency and remuneration	Output review	Proportionate liability [2], [27]
Technical dimension	Data provenance opaque	Memorization possible	Supply chain effect [3], [5], [23]

Some legal scholars do not consider transparency sufficient on its own. They argue that disclosing the source of training data does not by itself resolve the question of remuneration or permission, and that a proportionate liability regime is still required [28], [48].

C. *Originality and Creative Control*

Generative AI increases procedural fluency in textile and fashion studies, but it tends to weaken personal style expression [11]. Studies of students and designers report that writing prompts simplifies technical tasks, but it shifts creative labor from designing toward selecting and editing among generated options [32], [33].

A large part of the literature positions AI as a co-creative partner or a process tool rather than the producer of a final work [7], [19], [26], [34]. EU focused legal analyses continue to tie the threshold for protect ability to free and creative human choices [35]-[37].

Some studies argue that a well-constructed prompt or a documented chain of human selections can be decisive in establishing a copyright link [38]. This view has not produced full agreement across legal systems. The dominant position still favors protecting meaningful human contribution rather than a purely autonomous output [15], [39], [17].

D. *Cultural Representation, Bias, and Ethical Design*

The ethical question in fashion and textiles centers on more than copyright alone. It also concerns which aesthetics become visible [19], [32]. Studies report that current datasets are shaped by Western, commercial, and mainstream fashion imagery, and that this pushes minority cultures and local identities into the background [19], [40], [42].

Table 4. Proposed solutions to cultural and ethical risks

Theme	Main finding	Example solution
Data bias	Western aesthetics repeat	Representative data and monitoring [19], [40]
Cultural appropriation	Minority motifs can be copied superficially	Field study and rule base [20], [40]
Community governance	Community oversight increases trust	Model cards and veto rights [41]
Inclusion	Global data diversity is limited	Local datasets [42]

The most promising examples appear in systems that add cultural rules and community oversight to the model from outside. Higher cultural authenticity and lower representational error are reported when human guidance, knowledge structures, and oversight boards are used in the Phulkari, Dong brocade, Miao, and Guochao cases [20], [41], [43], [44].

These communities governed systems typically combine three elements in practice. A codified rule base encodes which motifs, colorways, and compositional grammars are considered appropriate for a given tradition, drawing on documentation of practicing artisans. A human oversight board, often composed of community members or cultural custodians, reviews candidate outputs before release and holds a veto over designs judged to misrepresent or trivialize the tradition. A provenance label or model card accompanies the output, recording which community knowledge base and which version of the oversight process produced it [20], [41], [43], [44]. This structure resembles a supervised pipeline more than a fully automated one, a point this paper returns to in the Discussion.

The publication timeline also shows a pattern. Studies from 2021 to 2023 mostly focused on GAN based design generation and efficiency gains [1], [4], [18], [45], [46]. Copyright, originality, explain ability, cultural representation, and responsibility became more prominent after 2024 [15], [19], [47].

The four sets of findings converge on a shared picture when read together. Legal risk spreads across the whole production chain. The originality debate centers on the nature of human contribution. Cultural representation cannot be reduced to data diversity and requires governance instead. These three axes increasingly overlap over time rather than developing apart from one another.

IV. DISCUSSION

The findings taken together show that the entry of generative AI into textile design does not create a single legal or ethical problem. It creates a cluster of problems that reinforce one another. This section first discusses the strength and type of the evidence base. It then discusses how the findings on the dispersed copyright chain, the link between originality and human contribution, and the governance requirement for cultural representation relate to each other. It closes with the theoretical and practical implications of this synthesis.

The evidence base is strong, but heterogeneous. Legal syntheses and comparative legal analyses offer a solid framework in the governance literature. They agree with each other on training data opacity, unlicensed use, similarity risk in the output, and a human centered copyright standard [2], [24], [48], [39]. Empirical studies specific to textiles tend to rely on small samples drawn from workshops or students. Their findings on originality and ethical use are persuasive, but their generalizability remains limited [49], [11], [50], [43]. This gap also reflects the maturity of the field. Legal scholarship has developed enough to propose a normative framework. The empirical base for design practice has not yet moved beyond a limited number of cases.

The direction of the findings is largely consistent across different methods. Consumer experiments show that AI generated design is perceived as less original and less authentic. Education and studio studies show that efficiency increases while creative ownership weakens. Legal reviews show that the threshold of human contribution remains decisive [11], [15], [35], [51]. The fact that three different methodological traditions reach the same conclusion suggests that the originality debate is not only a legal technicality. It also has a counterpart in the perception of design practice itself. The most important limitation is the scarcity of independent audit data on closed datasets and commercial models. This scarcity makes it difficult to establish how often copyright infringement or cultural appropriation actually occurs [2], [28], [52].

A further question concerns how findings drawn from student and workshop settings translate into commercial practice. These studies typically involve small groups working on bounded design briefs over a few weeks, with close instructor supervision and low commercial stakes. Commercial pattern design operates under different constraints, including tighter deadlines, brand consistency requirements, and direct exposure to infringement liability. The reported loss of personal style expression in classroom settings may understate the pressure toward homogenization in a commercial pipeline optimized for speed, or it may overstate the risk if commercial designers apply heavier post generation editing than students do. Neither direction has been tested directly, and this remains an open empirical question rather than a settled one [11], [49], [50].

A related gap separates legal scholarship from documented industry practice. Legal analyses describe what a compliant workflow should look like in principle, including data provenance disclosure and human review of AI assisted output. Very little published evidence describes what commercial textile and fashion firms actually do once they adopt generative tools. It is not clear from the current literature whether firms maintain prompt logs, whether they conduct any internal originality screening before a pattern goes to production, or whether legal teams are involved at the design stage at all. This gap matters because the normative framework proposed later in this paper assumes a level of documentation and process discipline that has not yet been verified as standard industry practice [9], [49], [56].

This consistency strengthens the tendency of copyright law to protect the human centered authorship condition, although the literature does not show full agreement. One group of studies argues that a well-constructed prompt or a documented chain of human selections can establish a copyright link on its own [38]. The dominant view instead holds that the free and creative choices of the designer deserve protection, not a purely autonomous output [15], [17], [35], [39]. This disagreement matters in practice. Which position prevails will directly shape how textile firms integrate generative AI into their workflow. A legal framework that treats a chain of prompts as evidence of human contribution would push designers toward documenting their process. A framework that does not accept human selection alone as sufficient would likely require additional editing and revision steps.

For a prompt based authorship claim to succeed in practice, this literature points to several categories of evidence. A dated and complete prompt history would need to be preserved, showing not only the final prompt but the sequence of revisions that led to it. A record of manual selection and rejection among generated candidates would need to demonstrate that a human exercised judgment rather than accepting the first output. Evidence of post generation editing, such as manual retouching, recoloring, or compositional adjustment, would need to show that the human contribution went beyond simply describing a desired image. Without this kind of documentation, a court or copyright office is likely to treat the output as insufficiently distinguishable from an unassisted machine output [15], [38], [39].

Whether this evidence would succeed also depends on the jurisdiction. In the European Union, the Court of Justice's Painer decision established that copyright protection requires the author's own intellectual creation, reflected in free and creative choices, and later commentary on generative AI has generally read this standard as excluding purely automated output while leaving room for sufficiently documented human direction [17], [35]. In the United States, copyright authorities have taken the position that copyright protection requires human authorship, and have denied protection to material generated without meaningful human creative control, while allowing protection for the human authored elements of a mixed work [14], [39]. The United Kingdom follows a different model. Its copyright statute contains a specific provision for computer generated works that have no human author, under which authorship is assigned instead to the person who made the arrangements necessary for the work's creation. This authorless work category has no direct equivalent in EU or US law and can produce a different practical outcome for the same generated pattern depending on where a claim is filed [17]. This divergence means that the same documented prompt chain could support a viable claim in one jurisdiction and fail in another, a point the literature notes but does not yet resolve [17], [35].

Cultural representation may appear separate from the copyright and originality debates, though it draws on the same foundation. When the source of training data lacks transparency, it also becomes difficult to trace which cultural motif belongs to which community [19], [40], [42]. The relatively positive results

reported for community governed systems in the Phulkari, Dong brocade, Miao, and Guochao cases show that a technical fix is not sufficient on its own. Governance mechanisms need to be added to the model from outside [20], [41], [43], [44]. This finding aligns with the conclusion that transparency alone is not enough in the copyright debate [28], [48]. Disclosure alone does not resolve either the copyright problem or the cultural representation problem. A monitoring and enforcement mechanism needs to follow the disclosure in both cases.

Whether these communities governed mechanisms can scale beyond the handful of documented cases is a separate question from whether they work in the cases studied so far. Each of the reported examples involves a single, relatively well organized craft community with an identifiable set of custodians able to sit on an oversight board. Many textile traditions lack this kind of centralized representation, are spread across multiple regions or diasporas, or have no single body recognized as authoritative. Extending a Phulkari style oversight model to such traditions would likely require resolving a prior governance question, namely who is entitled to speak for the tradition, before the design governance question can even be addressed [41], [20].

Not every finding in this synthesis carries the same evidentiary weight. Table 5 classifies five claims that emerged from the synthesis according to the number of studies supporting them and the methodological diversity behind them.

Table 5. Core claims by evidence strength

Claim	Evidence strength	Rationale
Generative AI increases efficiency in textile design	Strong (8/10)	Fashion, education, and system studies report process acceleration consistently [11], [9], [53]
Copyright risk continues across training data and output	Strong (9/10)	Multiple legal syntheses confirm the same chain risk [1], [3], [2]
AI outputs weaken originality and personal style expression	Moderate (7/10)	Empirical fashion studies point the same way, but samples remain limited [11], [19], [13]
Transparency alone is not sufficient	Strong (8/10)	Legal studies argue this point explicitly [28], [48]
Technical safeguards can meaningfully reduce infringement	Weak (3/10)	Promising, but the field remains at an early stage [54], [5], [55]

A. Limitations of the Evidence Base

Not all conclusions drawn in this paper rest on equally solid ground, and it is worth separating the stronger claims from the more tentative ones before turning to their implications. The claim that generative AI accelerates ideation rests on convergent evidence from fashion, education, and systems research and can be treated as reasonably well established [9], [11], [53]. The claim that copyright risk spans the full production chain rests on multiple independent legal syntheses and can also be treated as well established [1]-[3], By contrast, the claim that technical safeguards such as watermarking or originality estimation can meaningfully reduce infringement rests on a small number of early stage technical papers and should be treated as provisional [5], [54], [55]. Similarly, the claim that community governed cultural systems generalize beyond the handful of documented cases rests on descriptive accounts of individual projects rather than comparative evaluation, and should also be treated as provisional [20], [41], [43], [44]. Readers are encouraged to weigh the strength ratings in Table 5 alongside this qualitative distinction rather than treating every numbered claim as equally certain.

The literature is built heavily on legal principles and on education or studio experiments. Real audit data from commercial textile pattern pipelines remains weak. The provenance of closed fashion models, the frequency of style imitation, and the measurement of cultural harm are not yet documented adequately [2], [6]. The lack of industry oversight appears across all dimensions, legal analysis, user studies, technical systems, and community governance alike. Textile and fashion systems are multiplying in number, but most studies remain confined to prototype or educational settings [9], [49], [56]. Community based cultural governance has also been tested in detail in only a small number of cases. Studies similar to Phulkari appear promising, but it remains unclear whether this approach can generalize to other craft and textile traditions [20], [41].

These gaps also point to the research questions that follow. How the provenance of training data and the similarity of output can be audited independently in closed commercial fashion models remains open. Which process records best demonstrate human creative control also remains open. Whether community governed cultural design can scale to textile heritages beyond the cases studied here remains open as well. The most significant shift that generative AI brings to this field is that it extends the design question from aesthetic production toward the management of data, rights, and responsibility. The clearest open question is how liability in this chain should be shared among developers, platforms, and designers.

V. CONCLUSION

This study addressed copyright, originality, cultural representation, and ethical use in generative AI textile patterns through a conceptual synthesis that brings together legal, design, and ethics literature. The main conclusion that follows from this synthesis is that none of these problems can be solved through a single technical fix. Copyright risk spreads across the entire production chain from training data to output. The originality debate ties to the nature and document ability of human contribution. Cultural representation requires community level oversight that goes beyond technical transparency [1]-[5], [15], [19], [39], [41].

The shared conclusion across these three axes points toward a framework in which generative AI is positioned as a supervised co creative tool in textile design rather than an independent creator [7], [21], [24], [27]. For this framework to function, three elements need to be in place together. A transparency regime that discloses the source and scope of training data. A labeling practice that states whether the output was produced by a human or by AI. A remuneration mechanism directed at copyright holders.

For textile and fashion businesses, this framework carries a concrete counterpart. Firms that integrate generative AI tools into their workflow are expected to be able to question the training data source of the model they use, to document the designer prompt history and editing steps, and to explain the production process of the final product to the customer. For policymakers, the open question is how these obligations should be divided among developers, platforms, and designers, and how that division should adapt to the jurisdictional differences discussed above. The current literature has not yet proposed a model for how this division should be structured [17], [27].

This study carries its own limitations. As a conceptual synthesis, it did not produce new empirical data. A search strategy that relies on a single AI assisted discovery tool may favor English language, highly cited publications, and does not offer the cross database verification of a formal systematic review. The fact that empirical studies specific to textiles are mostly based on small samples means that this synthesis inherits the same limitation.

The gaps identified in this study show that progress in the field depends on the development of independent audit mechanisms. Without these mechanisms, the debate over whether generative AI counts as a legitimate tool in textile design will remain a matter of trust and accountability rather than technical performance alone.

REFERENCES

[1] Z. Epstein, A. Hertzmann, L. Herman, R. Mahari, M. Frank, M. Groh, H. Schroeder, A. Smith, M. Akten, J. Fjeld, H. Farid, N. Leach, A. Pentland, and O. Russakovsky, "Art and the science of generative AI," *Science*, vol. 380, pp. 1110-1111, 2023, doi: 10.1126/science.adh4451.

[2] M. Pasetti, J. W. Santos, N. Corrêa, N. De Oliveira, and C. Barbosa, "Technical, legal, and ethical challenges of generative artificial intelligence: an analysis of the governance of training data and copyrights," *Discover Artificial Intelligence*, vol. 5, 2025, doi: 10.1007/s44163-025-00379-6.

[3] K. Lee, A. F. Cooper, and J. Grimmelmann, "Talkin' 'Bout AI Generation: Copyright and the Generative-AI Supply Chain (The Short Version)," in *Proc. 2024 Symp. Computer Science and Law*, 2023, doi: 10.1145/3614407.3643696.

[4] S. Feuerriegel, J. Hartmann, C. Janiesch, and P. Zschech, "Generative AI," *Business & Information Systems Engineering*, pp. 1-16, 2023, doi: 10.1007/s12599-023-00834-7.

[5] A. Arnaudo, R. Coppola, M. Morisio, A. Vetrò, M. Borghi, R. Raso, and B. Khan, "Generative AI and intellectual property: a systematic literature review of possible issues and mitigations," *PeerJ Computer Science*, 2026, doi: 10.7717/peerj-cs.3928.

[6] W. Shi, W. Wong, and X. Zou, "Generative AI in Fashion: Overview," *ACM Trans. Intelligent Systems and Technology*, vol. 16, pp. 1-73, 2025, doi: 10.1145/3718098.

[7] A. A. H. El-Bassuony, A. F. Ibrahim, and H. K. Abdelsalam, “Artificial intelligence in fabric design: a critical review of technological advancements and socio-creative implications (2019-2024),” *Humanities and Social Sciences Communications*, vol. 13, 2026, doi: 10.1057/s41599-026-08095-x.
[8] X. Wu and L. Li, “An application of generative AI for knitted textile design in fashion,” *The Design Journal*, vol. 27, pp. 270-290, 2024, doi: 10.1080/14606925.2024.2303236.
[9] E. W. T. Ngai, M. C. M. Lee, and B. C. W. Kei, “A Generative Artificial Intelligence (GenAI) System for Fashion Design: A Case Study,” *IEEE Trans. Engineering Management*, vol. 72, pp. 1320-1333, 2025, doi: 10.1109/tem.2025.3554248.
[10] M. Choudhury, B. Eisenbart, and B. Kuys, “Artificial intelligence (AI) in the design process – a review and analysis on generative AI perspectives,” *Proc. Design Society*, vol. 5, pp. 631-640, 2025, doi: 10.1017/pds.2025.10077.
[11] S. Jang, “From designer to curator: cognitive and creative trade-offs in GenAI-assisted design,” *Fashion and Textiles*, vol. 13, 2026, doi: 10.1186/s40691-026-00459-w.
[12] Y. Jin, J. Yoon, J. Self, and K. Lee, “Understanding Fashion Designers' Behavior Using Generative AI for Early-Stage Concept Ideation and Revision,” *Archives of Design Research*, 2024, doi: 10.15187/adr.2024.07.37.3.25.
[13] B. Mandour, “Printed hanging textile design between the designer's subjectivity and AI technologies,” *International Design Journal*, 2024, doi: 10.21608/idj.2024.280454.1130.
[14] P. Jurčys and M. Fenwick, “Originality and the Future of Copyright in an Age of Generative AI,” *Comput. Law Secur. Rev.*, vol. 51, p. 105892, 2023, doi: 10.48550/arxiv.2309.13055.
[15] Z. Chen and Y. He, “Ethical dilemmas in artificial intelligence-generated art: authorship, ownership, and the blurring of creative boundaries,” *Digit. Scholarsh. Humanit.*, vol. 41, pp. 647-661, 2026, doi: 10.1093/llc/fqag035.
[16] A. Taeihagh, “Governance of Generative AI,” *Policy and Society*, 2025, doi: 10.1093/polsoc/puaf001.
[17] J. Esavwede and P. Itsueli, “Authorship Without Authors? Rethinking Copyright Ownership in Generative AI Across Jurisdictional Boundaries,” *Veredas do Direito*, 2026, doi: 10.18623/rvd.v23.5653.
[18] G. Franceschelli and M. Musolesi, “Copyright in generative deep learning,” *Data & Policy*, vol. 4, 2021, doi: 10.1017/dap.2022.10.
[19] R. R. Mahto and C. Q. Rodriguez, “Ethical implications of AI in the fashion industry for trend forecasting and garment design development,” *AI and Ethics*, vol. 6, 2026, doi: 10.1007/s43681-026-01185-1.
[20] J. Q. Li and L. Wang, “From Result Imitation to Cultural Translation: An Intelligent Generation Approach for Dong Brocade Patterns Based on Patternology,” *AHFE International*, 2026, doi: 10.54941/ahfe1007460.
[21] M. Al-Kfairy, D. G. Mustafa, N. Kshetri, M. Insiew, and O. Alfandi, “Ethical Challenges and Solutions of Generative AI: An Interdisciplinary Perspective,” *Informatics*, vol. 11, p. 58, 2024, doi: 10.3390/informatics11030058.
[22] J. Laine, M. Minkkinen, and M. Mäntymäki, “Understanding the Ethics of Generative AI: Established and New Ethical Principles,” *Commun. Assoc. Inf. Syst.*, vol. 56, p. 7, 2025, doi: 10.17705/1cais.05601.
[23] P. Henderson, X. Li, D. Jurafsky, T. Hashimoto, M. A. Lemley, and P. Liang, “Foundation Models and Fair Use,” *J. Mach. Learn. Res.*, vol. 24, pp. 400:1-400:79, 2023, doi: 10.48550/arxiv.2303.15715.
[24] C. Geiger, “Elaborating a Human Rights-Friendly Copyright Framework for Generative AI,” *IIC - International Review of Intellectual Property and Competition Law*, vol. 55, pp. 1129-1165, 2024, doi: 10.1007/s40319-024-01481-5.
[25] E. Rosati, “Infringing AI: Liability for AI-Generated Outputs under International, EU, and UK Copyright Law,” *European Journal of Risk Regulation*, vol. 16, pp. 603-627, 2024, doi: 10.1017/err.2024.72.
[26] K. A. Bartlett and J. Camba, “Generative Artificial Intelligence in Product Design Education: Navigating Concerns of Originality and Ethics,” *Int. J. Interact. Multim. Artif. Intell.*, vol. 8, p. 55, 2024, doi: 10.9781/ijimai.2024.02.006.
[27] D. Liu, “Exploring remuneration mechanisms for copyrighted works in generative AI systems,” *The Journal of World Intellectual Property*, 2026, doi: 10.1111/jwip.70027.
[28] A. Buick, “Copyright and AI training data—transparency to the rescue?,” *Journal of Intellectual Property Law and Practice*, 2024, doi: 10.1093/jiplp/jpae102.
[29] S. Chesterman, “Good Models Borrow, Great Models Steal: Intellectual Property Rights and Generative AI,” *SSRN Electronic Journal*, 2024, doi: 10.2139/ssrn.4590006.
[30] O. Fischman-Afori, “Generative AI art and copyright governance: Rethinking the adaptation right and its limits,” *Humanities and Social Sciences Communications*, 2026, doi: 10.1057/s41599-026-07311-y.
[31] A. Centivany, “Mining, Scraping, Training, Generating: Copyright Implications of Generative AI,” *Proc. Assoc. Information Science and Technology*, vol. 61, 2024, doi: 10.1002/pra2.1009.
[32] M. Ledendal, M. P. McIntyre, and D. Christoforidou, “The myth of the muse: How AI fashion design platforms and prompting reshape creative agency,” *Fashion, Style & Popular Culture*, 2026, doi: 10.1386/fspc_00378_1.
[33] A. Sarkar, “Exploring Perspectives on the Impact of Artificial Intelligence on the Creativity of Knowledge Work: Beyond Mechanised Plagiarism and Stochastic Parrots,” *Proc. 2nd Annual Meeting Symp. Human-Computer Interaction for Work*, 2023, doi: 10.1145/3596671.3597650.
[34] M. Balasubramanian, “Implementing generative AI in fashion design curriculum,” *Frontiers in Education*, 2026, doi: 10.3389/feduc.2026.1824003.
[35] P. Hugenholtz and J. Quintais, “Copyright and Artificial Creation: Does EU Copyright Law Protect AI-Assisted Output?,” *IIC - International Review of Intellectual Property and Competition Law*, vol. 52, pp. 1190-1216, 2021, doi: 10.1007/s40319-021-01115-0.

[36] S. B. Checa Prieto and J. F. Tamames, “Crisis del nexo causal creativo en la IA generativa: originalidad y estándar painer ante el acto generativo,” *Revista propiedad intelectual e innovación digital*, 2026, doi: 10.36151/rpiid.2026.3.2.04.
[37] M. Daňko and L. Fotopulosová, “Artificial Intelligence as (Non-)Author: Legal and Ethical Aspects of Generative Artificial Intelligence,” *Comenius: Bratislava Legal Forum*, 2025, doi: 10.46282/bpf.2025.22.
[38] Q. Li, “Copyright protection paradigm in the generative AI era: originality, attribution, and infringement,” *Advances in Social Behavior Research*, 2025, doi: 10.54254/2753-7102/2025.27484.
[39] A. Neubauer, M. Wynn, and R. Bown, “AI, Authorship, Copyright, and Human Originality,” *Encyclopedia*, 2026, doi: 10.3390/encyclopedia6010009.
[40] L. B. Malobola, N. Rostamzadeh, and S. Mohamed, “seShweshwe Inspired Fashion Generation,” *ArXiv*, vol. abs/2203.00435, 2022, doi: 10.48550/arxiv.2203.00435.
[41] J. Jyoti, P. Kaur, and C. Singh, “Phulkari 2.0: Generative Pattern Systems and AI-Driven Embroidery Futures in Punjabi Textile Tradition,” *Vidya - A Journal of Gujarat University*, 2025, doi: 10.47413/504har50.
[42] C. Scharff, J. Brusseau, K. Bathula, K. Fnu, S. Meshram, and O. Gaikhe, “Inclusion Ethics in AI: Use Cases in African Fashion,” pp. 516-521, 2024, doi: 10.1609/aaaiss.v3i1.31266.
[43] R. Lin, F. Xia, and M. Guan, “From Virtual to Physical: AIGC-Driven Human–Computer Collaboration in Miao Costume Design,” *Leonardo*, 2025, doi: 10.1162/leon.a.2661.
[44] J. Jin, R. Zhang, Q. Zheng, Z. Cao, and Y. Ji, “A Digital-Intelligent Workflow for Personalized 'Guochao' Apparel Customization: A Knowledge-Graph and 3D Simulation Case Study with Risk Governance,” in *Proc. 2nd Int. Conf. Digital Society, Information Science and Risk Management*, 2026, doi: 10.1145/3804504.3804525.
[45] Q. Wu, B. Zhu, B. Yong, Y. Wei, X. Jiang, R. Zhou, and Q. Zhou, “ClothGAN: generation of fashionable Dunhuang clothes using generative adversarial networks,” *Connection Science*, vol. 33, pp. 341-358, 2020, doi: 10.1080/09540091.2020.1822780.
[46] H. Yan, H. Zhang, L. Liu, D. Zhou, X. Xu, Z. Zhang, and S. Yan, “Toward Intelligent Design: An AI-Based Fashion Designer Using Generative Adversarial Networks Aided by Sketch and Rendering Generators,” *IEEE Trans. Multimedia*, vol. 25, pp. 2323-2338, 2023, doi: 10.1109/tmm.2022.3146010.
[47] G. Rizzi and P. Bertola, “Exploring the generative AI potential in the fashion design process: an experimental experience on the collaboration between fashion design practitioners and generative AI tools,” *European Journal of Cultural Management and Policy*, 2025, doi: 10.3389/ejcmp.2025.13875.
[48] K. De La Durantaye, “Control and Compensation. A Comparative Analysis of Copyright Exceptions for Training Generative AI,” *IIC - International Review of Intellectual Property and Competition Law*, vol. 56, pp. 737-770, 2025, doi: 10.1007/s40319-025-01569-6.
[49] X. Wu and L. Li, “Qualitative-empirical insights into generative AI for textile design in the fashion design process,” *International Journal of Design Creativity and Innovation*, vol. 13, pp. 322-357, 2025, doi: 10.1080/21650349.2025.2529167.
[50] D. Jung and S. Suh, “Enhancing Soft Skills through Generative AI in Sustainable Fashion Textile Design Education,” *Sustainability*, 2024, doi: 10.3390/su16166973.
[51] G. Lee and H. Kim, “Human vs. AI: The battle for authenticity in fashion design and consumer response,” *Journal of Retailing and Consumer Services*, 2024, doi: 10.1016/j.jretconser.2023.103690.
[52] D. Schlagwein and L. Willcocks, “'ChatGPT et al.': The ethics of using (generative) artificial intelligence in research and science,” *Journal of Information Technology*, vol. 38, pp. 232-238, 2023, doi: 10.1177/02683962231200411.
[53] J. Jiang, D. Wu, H. Deng, Y. Long, W. Tang, X. Li, C. Liu, Z. Jin, W. Zhang, and T. Qi, “HAIGEN: Towards Human-AI Collaboration for Facilitating Creativity and Style Generation in Fashion Design,” *Proc. ACM Interactive, Mobile, Wearable and Ubiquitous Technologies*, vol. 8, pp. 1-27, 2024, doi: 10.1145/3678518.
[54] H. Chiba-Okabe and W. J. Su, “Tackling copyright issues in AI image generation through originality estimation and genericization,” *Scientific Reports*, vol. 15, 2024, doi: 10.1038/s41598-025-90827-1.
[55] J. T. Wang, Z. Deng, H. Chiba-Okabe, B. Barak, and W. J. Su, “An Economic Solution to Copyright Challenges of Generative AI,” *ArXiv*, vol. abs/2404.13964, 2024, doi: 10.48550/arxiv.2404.13964.
[56] J. Bieńkowska, “The Effects of Artificial Intelligence on the Fashion Industry—Opportunities and Challenges for Sustainable Transformation,” *Sustainable Development*, 2024, doi: 10.1002/sd.3312.

8th International Conference on Engineering, Natural and Social Sciences

September 06-07, 2026: Konya, Turkey

© 2026 Published by All Sciences Academy

https://www.icensos.com/

Density functional theory investigation of the structural, electronic and noncovalent interaction properties of a benzoxadiazocine derivative

Mustafa Kemal GÜMÜŞ[1] and Sevgi KANSIZ*[2]

[1]*Science-Technology Research and Application Center, Artvin Çoruh University, Türkiye*
[2]*Department of Fundamental Sciences, Samsun University, Türkiye*

*(sevgi.kansiz@samsun.edu.tr) *Email of the corresponding author*

Abstract – Heterocyclic compounds containing triazole and benzoxadiazocine frameworks have attracted considerable attention due to their structural diversity and their promising electronic and chemical properties. This study examined the molecular structure and electronic properties of a triazole–benzoxadiazocine derivative using Density Functional Theory (DFT) calculations. Geometry optimization was performed at the B3LYP/6-311G(d,p) level using the Gaussian 16W program. The optimized molecular structure was then used to analyze the molecular electrostatic potential (MEP), frontier molecular orbitals (FMOs) and non-covalent interactions. The MEP surface was evaluated to visualize the electron-rich and electron-deficient regions of the molecule and to provide information about the preferred sites for possible intermolecular interactions. The HOMO and LUMO energies were calculated to be −8.52 and −5.49 eV, respectively, giving an energy gap of 3.03 eV. These results provide insight into the electronic stability and reactivity characteristics of the molecule. Additionally, the reduced density gradient (RDG) scatter plot and the corresponding isosurfaces were analyzed in order to characterize weak intermolecular interactions. The RDG analysis revealed regions associated with attractive, repulsive and weak van der Waals-type interactions, highlighting the contribution of non-covalent contacts to the molecular environment. The DFT results offer a comprehensive theoretical description of the optimized structure, electronic distribution, frontier orbital characteristics and non-covalent interactions of the investigated triazole–benzoxadiazocine system.

Keywords – Benzoxadiazocine, triazole, DFT, MEP, FMOs, RDG

I. INTRODUCTION

Heterocyclic compounds containing triazole and oxadiazocine rings are an important class of nitrogen- and oxygen-containing systems [1-3]. They are important due to their diverse chemical reactivity, structural versatility, and potential applications in pharmaceuticals and materials chemistry [4-6]. Understanding the electronic distribution, chemical reactivity, and non-covalent interactions of these complex systems is essential to grasping their functional properties and guiding the design of future derivatives [7-9]. Quantum chemical calculations based on density functional theory (DFT) are an indispensable tool for obtaining detailed insights into molecular geometry, charge distribution, orbital characteristics, and non-covalent interactions that are difficult to measure experimentally [10-12]. In this study, we optimized the molecular structure of the derivative $C_{18}H_{16}N_4O$ at the B3LYP/6-311G(d,p) computational level using the Gaussian 16W software package. Based on the fully optimized geometry, detailed analyses of the molecular electrostatic potential (MEP), frontier molecular orbitals (FMOs), global reactivity descriptors, and reduced density gradient (RDG) were performed to describe the electronic stability and weak interaction features of the title compound.

II. MATERIALS AND METHOD

The geometry of the molecule was optimized with the Gaussian 16W package [13] using the GaussView 6 interface [14]. Density Functional Theory (DFT) calculations employing the B3LYP functional with the 6-311G(d,p) basis set were used for geometry optimization, Molecular Electrostatic Potential (MEP) mapping, and Frontier Molecular Orbital (FMO) analysis (Fig. 1). Non-covalent interactions were further examined through Reduced Density Gradient (RDG) analysis using Multiwfn 3.7 [15], and the resulting interaction regions were visualized with VMD software [16].

III. RESULTS AND DISCUSSION

The optimized molecular geometry of $C_{18}H_{16}N_4O$ was examined in detail to assess the structural characteristics of the heterocyclic framework (Fig. 1). The calculated C–O bond lengths were found to be 1.37 and 1.44 Å, reflecting the distinct bonding environments of the oxygen atoms within the molecular structure. In the triazole ring, the N–N bond length was calculated as 1.37 Å, while the C–N distances were obtained as 1.36, 1.32, 1.31, and 1.38 Å. These closely related bond distances are consistent with the delocalized bonding character of the triazole ring [17-20]. The C–N bond located outside the triazole moiety was calculated to be 1.37 Å. The C–C distances within the aromatic ring range from 1.36 to 1.42 Å, with an average value of approximately 1.39 Å, consistent with the expected bond-length characteristics of an aromatic system [21-26]. The optimized bond parameters indicate a stable heterocyclic framework with characteristic bond-length variations arising from the electronic environments and conjugation within the molecule.

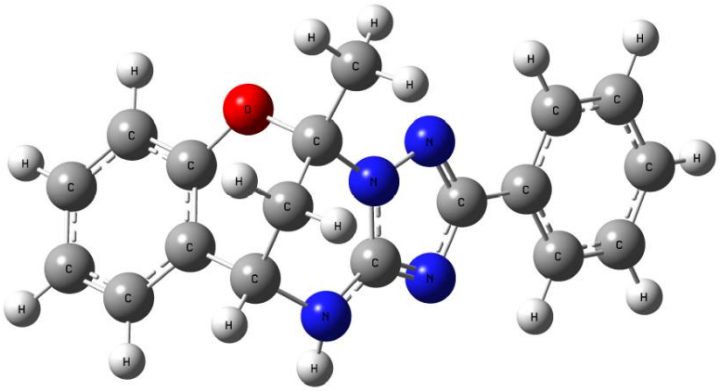

Fig. 1 The optimized geometry of $C_{18}H_{16}N_4O$.

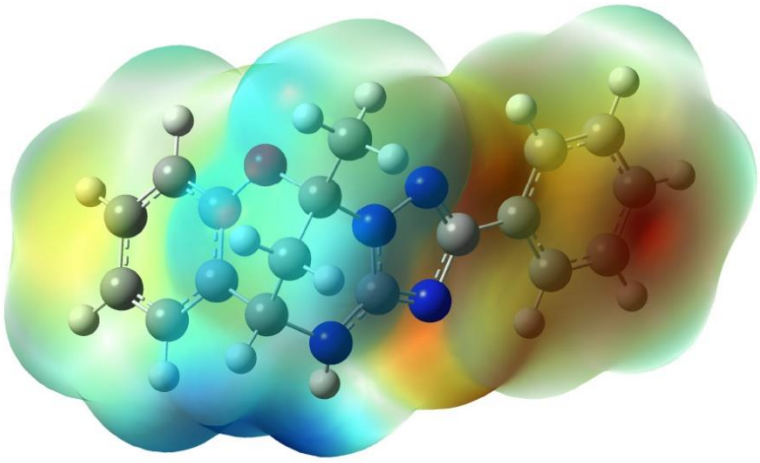

Fig. 2 The MEP map of $C_{18}H_{16}N_4O$.

The molecular electrostatic potential map was constructed to identify electron-rich (nucleophilic) and electron-deficient (electrophilic) regions [27-30], as well as potential noncovalent interaction sites of the $C_{18}H_{16}N_4O$ molecule (Fig. 2). Negative electrostatic potential regions (typically represented by red or orange shades) are predominantly localized over the electronegative phenyl rings, oxygen atom of the

oxadiazocine core, and the nitrogen atoms within the triazole ring. This designates these sites as primary nucleophilic centers susceptible to electrophilic attack. Conversely, the positive potential regions (blue shades) are mainly distributed over the acidic hydrogen atoms, particularly the N–H group of the core ring system and aromatic hydrogen atoms, indicating active electrophilic regions suitable for nucleophilic interactions or donor hydrogen bonding. The intermediate green and yellow regions map neutral electrostatic potential zones over the alkyl ring. The MEP topology underscores a distinct charge distribution that governs both intra- and intermolecular interaction pathways.

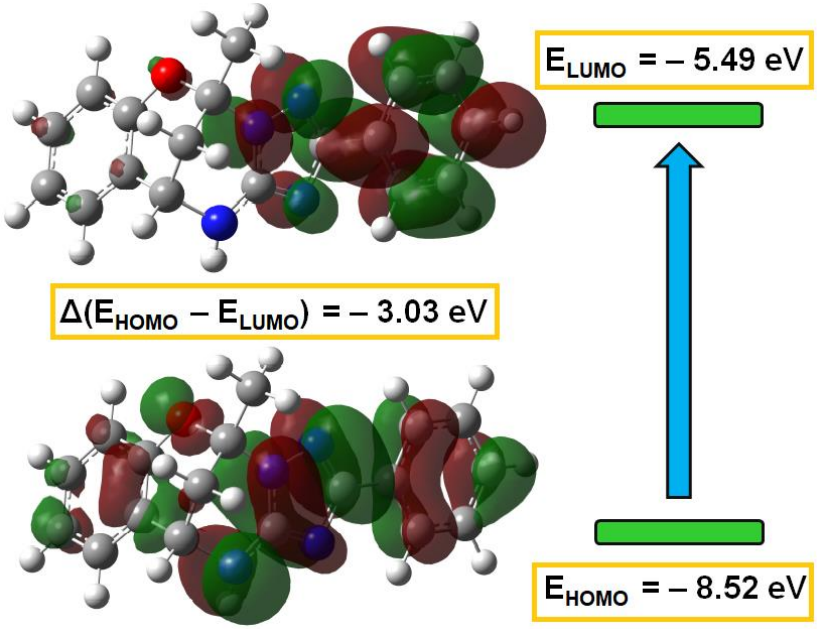

Fig. 3 FMOs surfaces of $C_{18}H_{16}N_4O$. The isosurfaces value is set to ±0.02 a.u.

Table 1. The energy values of the global reactivity parameters.

Parameters	
E_{HOMO} (eV)	−8.52
E_{LUMO} (eV)	−5.49
Energy gap (eV)	3.03
Ionization potential ($I = -E_{HOMO}$)	8.52
Electron affinity ($A = -E_{LUMO}$)	5.49
Electronegativity ($\chi = (I+A)/2$)	7.00
Hardness ($\eta = (I - A)/2$)	1.52
Softness ($S=1/2\eta$)	0.33
Chemical potential ($\mu = -(I+A)/2$)	−7.00
Electrophilicity index ($\omega = \mu^2/2\eta$)	16.17

The energies and spatial distributions of the frontier molecular orbitals (HOMO and LUMO) determine a molecule's chemical reactivity [31-33], kinetic stability, and optical properties (Fig. 3). For $C_{18}H_{16}N_4O$, the HOMO and LUMO values were calculated as -8.52 eV and -5.49 eV, respectively, yielding a moderate energy band gap (ΔE) of 3.03 eV (Table 1). The HOMO density is primarily localized over the central conjugated heterocyclic core and adjacent aromatic moieties. In contrast, the LUMO is largely distributed across the triazole and substituted phenyl ring. This demonstrates a clear π→π* charge transfer characteristic during electronic excitation. Global reactivity parameters were derived based on the FMO energies: the high ionization potential (I = 8.52 eV) and electron affinity (A = 5.49 eV) reflect strong electron-attracting capability, leading to an electronegativity (χ) of 7.00 eV and a chemical potential (μ) of −7.00 eV. Additionally, the chemical hardness (η = 1.52 eV), softness (S = 0.33 eV^{-1}),

and high electrophilicity index (ω = 16.17 eV) confirm that the compound possesses notable chemical stability combined with strong electrophilic behavior.

To characterize the weak non-covalent interactions within the molecular structure further, we evaluated Reduced Density Gradient (RDG) scatter plots [34-36] and 3D real-space isosurfaces using the sign(λ_2)ρ function at an isosurface value of 0.5 a.u. (Fig. 4). In the RDG scatter plot, low-density/low-gradient spikes in the region sign(λ_2)ρ < −0.01 a.u. (blue domain) correspond to attractive non-covalent interactions, such as weak intramolecular hydrogen bonding. Spikes near zero (−0.01 < sign(λ_2)ρ < 0.01 a.u., green domain) represent weak van der Waals forces, forming expansive green isosurfaces between aliphatic/aromatic hydrogen atoms and nearby ring systems. Conversely, spikes in the region sign(λ_2)ρ > 0.01 a.u. (red domain) denote strong steric repulsion (non-bonded overlap) and are visualized as red discoid isosurfaces located at the centers of the phenyl, triazole, and oxadiazocine rings. The combined RDG analysis illustrates that van der Waals interactions and localized steric effects stabilize the molecule's three-dimensional conformation.

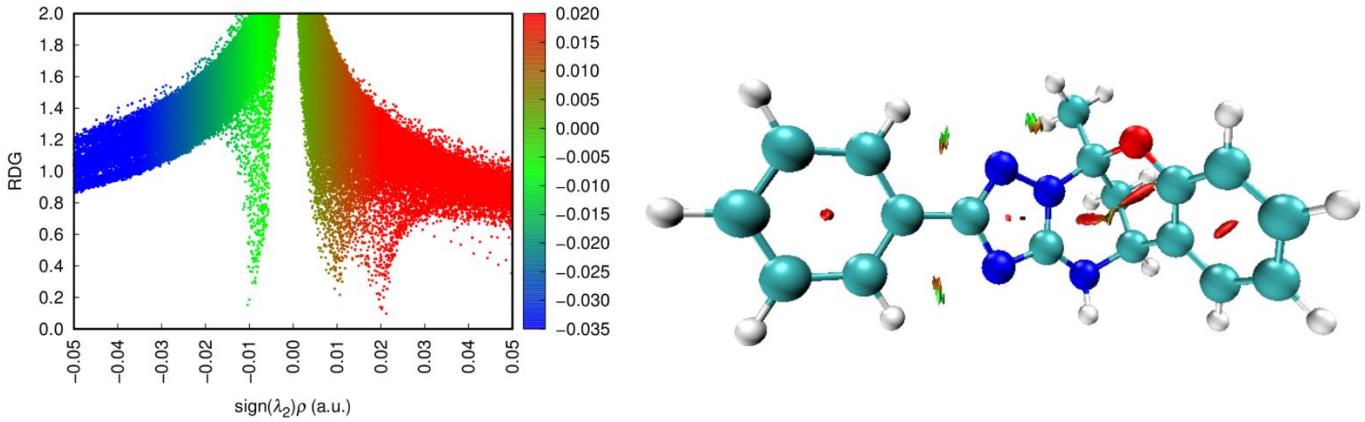

Fig. 4 (a) RDG scatter plot, and (b) RDG isosurfaces plotted at the value of ±0.5 a.u., colored according to sign(λ_2)ρ.

IV. CONCLUSION

This study comprehensively investigated the molecular structure, electronic properties, and non-covalent interactions of the triazole-benzoxadiazocine derivative using density functional theory at the B3LYP/6-311G(d,p) level. Geometry optimization confirmed a stable three-dimensional conformation. Molecular electrostatic potential mapping successfully delineated the electrophilic and nucleophilic regions, identifying the oxygen and triazole nitrogen atoms as the primary nucleophilic sites. Frontier molecular orbital analysis revealed an energy gap of 3.03 eV between HOMO (-8.52 eV) and LUMO (-5.49 eV), indicating moderate kinetic stability and electron transfer capability. The calculated global reactivity descriptors, particularly the high electrophilicity index (ω = 16.17 eV) and chemical hardness (η = 1.52 eV), further characterized the title compound's chemical reactivity profile. Additionally, reduced density gradient analysis provided qualitative and quantitative evidence of weak noncovalent interactions, demonstrating that van der Waals forces and localized steric repulsions significantly impact the molecular environment. These theoretical findings offer valuable insights into the structural and electronic characteristics of triazole-benzoxadiazocine systems and serve as a reliable benchmark for future synthetic and pharmacological applications.

ACKNOWLEDGMENTS

The numerical calculations reported in this paper were fully/partially performed at TUBITAK ULAKBIM, High Performance and Grid Computing Center (TRUBA resources).

REFERENCES

[1] M. K. Gümüş, S. Kansız, E. Aydemir, N. Y. Gorobets, and N. Dege, "Structural features of 7-methoxy-5-methyl-2-(pyridin-3-yl)-11,12-dihydro-5,11-methano[1,2,4] triazolo[1,5-c][1,3,5] benzoxadiazocine: Experimental and theoretical (HF and DFT) studies, surface properties (MEP, Hirshfeld)," *J. Mol. Struct*., vol. 1168, pp. 280-290, 2018.

[2] M. K. Gümüş, N. Y. Gorobets, Y. V. Sedash, V. A. Chebanov, and S. M. Desenko, "A modified Biginelli reaction toward oxygen-bridged tetrahydropyrimidines fused with substituted 1,2,4-triazole ring," *Chem. Heterocycl. Compd*., vol. 53(11), pp. 1261-1267, 2017.
[3] E. Aydemir, S. Kansiz, M. K. Gumus, N. Y. Gorobets, and N. Dege, "Crystal structure and Hirshfeld surface analysis of 7-ethoxy-5-methyl-2-(pyridin-3-yl)-11,12-dihydro-5,11-methano[1,2,4]triazolo[1,5-c][1,3,5] benzoxadiazocine," *Acta Crystallogr. E: Crystallogr. Commun*., vol. 74(3), pp. 367-370, 2018.
[4] M. K. Gümüş, N. Y. Gorobets, Y. V. Sedash, S. V. Shishkina, and S. M. Desenko, "Rapid formation of chemical complexity via a modified Biginelli reaction leading to dihydrofuran-2 (3H)-one spiro-derivatives of triazolo [1,5-a] pyrimidine," *Tetrahedron Lett*., vol. 58(35), pp. 3446-3448, 2017.
[5] M. K. Gümüş, M. Y. Gorobets, and N. Uludag, "Microwave-Assisted synthesis of 5-Substituted 3-Amino-1, 2, 4-triazoles from aminoguanidine bicarbonate and carboxylic acids," *Processes*, vol. 12(3), pp. 573, 2024.
[6] M. K. Gumus, S. Kansiz, N. Dege, and V. A. Kalibabchuk, "Hirshfeld surface analysis and crystal structure of 7-methoxy-5-methyl-2-phenyl-11,12-dihydro-5,11-methano-1,2,4-triazolo[1,5-c][1,3,5] benzoxadiazocine," *Acta Crystallogr. E: Crystallogr. Commun.*, vol. 74(9), pp. 1211-1214, 2018.
[7] S. Kansiz, "Investigating the structural and surface properties of copper and nickel complexes fluorine-based salen type Schiff bases," *J. Struct. Chem*., vol. 64(12), pp. 2295-2310, 2023.
[8] N. Dege, A. S. Aydın, E. Ağar, S. Kansız, S. JoseKavitha, K. BalaSubramani, M. Hemamalini, and V. Rajakannan, "Synthesis, crystal structure, Hirshfeld surface analysis, In-Silico assessment of druggability and molecular docking studies of Schiff base compound," *Chem. Data Collect.*, vol. *25*, 100320, 202
[9] P. Şen, and S. Kansız, "Crystal Structure, Spectroscopic and Computational Studies of N2O2 Type Salen-Based Schiff Base and Its Di-boron Complex," *J. Chem. Crystallogr.*, vol. *52*(1), pp. 1-16, 2022.
[10] H. Kargar, M. Fallah-Mehrjardi, K. S. Munawar, E. Acar, N. Dege, and S. Kansız, "Structural dynamics of a phenoxy-bridged heteronuclear Cu (II)/Hg (II)-Salen complex: synthesis, characterization, DFT insights, and Hirshfeld surface analysis," *J. Iran. Chem. Soc.*, vol. 22(4), pp. 769-780, 2025.
[11] S. Kansız, "Synthesis and Structural Investigations of 1, 2-bis (2-ethoxybenzylidene) hydrazine," *Sak. Univ. J. Sci.*, vol. 27(4), pp. 768-780, 2023.
[12] N. Arumugam, A. I. Almansour, R. S. Kumar, S. Yeswanthkumar, R. Padmanaban, Y. Arun, S. Kansız, N. Dege, T. S. Manohar, and S. Venketesh, "Design, stereoselective synthesis, computational studies and cholinesterase inhibitory activity of novel spiropyrrolidinoquinoxaline tethered indole hybrid heterocycle," *J. Mol. Struct*., 2021, vol. 1225, pp. 129165.
[13] M. J. Frisch, G. Trucks, H. Schlegel, G. Scuseria, M. Robb, J. Cheeseman, G. Scalmani, V. Barone, B. Mennucci, and G. Petersson, 2009. Gaussian 09, Revision D. 01, Gaussian, Inc.: Wallingford, CT.
[14] R. Dennington, T. Keith, and J. Millam, 2009. GaussView, version 5, Semichem Inc.: Shawnee Mission, KS.
[15] W. Humphrey, A. Dalke, and K. Schulten, "VMD: Visual Molecular Dynamics," *J. Mol. Graph*., vol. 14(1), pp. 33-38, 1996.
[16] T. Lu, and F. Chen, "Multiwfn: A multifunctional wavefunction analyzer," *J. Comput. Chem*., vol. 33(5), pp. 580-592, 2012.
[17] M. K. Alenzi, M. Azam, S. I. Al-Resayes, S. Kansız, A. S. Çamaş, D. C. Agurokpon, H. Louis, V. Kumar, N. Dege, and M. Alam, "Experimental and theoretical investigation into the design of nickel (II), copper (II), and zinc (II) complexes substituted with pyrazole ligand," *Polyhedron*, vol. 259, pp. 117073, 2024.
[18] K. Chkirate, S. Kansiz, K. Karrouchi, J. T. Mague, N. Dege, and E. M. Essassi, "Crystal structure and Hirshfeld surface analysis of N-{2-[(E)-(4-methylbenzylidene) amino] phenyl}-2-(5-methyl-1-H-pyrazol-3-yl) acetamide hemihydrate," *Acta Crystallogr. E: Crystallogr. Commun*., vol. 75(2), pp. 154-158, 2019.
[19] M. Boulhaoua, S. Kansiz, M. El Hafi, S. Lahmidi, N. Dege, M. Benchidmi, and J. T. Mague, "Crystal structure and Hirshfeld surface analysis of 5-[(5-nitro-1H-indazol-1-yl) methyl]-3-phenyl-4, 5-dihydroisoxazole," *Acta Crystallogr. E: Crystallogr. Commun*., vol. 75(1), pp. 71-74, 2019.
[20] A. M. Qadir, S. Kansiz, G. M. Rosair, N. Dege, and I. S. Safyanova, "Crystal structure and Hirshfeld surface analysis of a zinc xanthate complex containing the 2, 2′-bipyridine ligand," *Acta Crystallogr. E: Crystallogr. Commun*., vol. 75(12), pp. 1857-1860, 2019.
[21] R. Ilmi, S. Kansız, N. K. Al Rasbi, J. Husband, N. Dege, and M. S. Khan, "Synthesis, X-ray crystal structure and determination of non-covalent interactions through Hirshfeld surface analysis of a pure red emitting asymmetrical octacoordinated Sm (III) complex," *Polyhedron*, vol. 246, pp. 116673, 2023.
[22] S. Kansiz, S. Malinkin, and N. Dege, "Synthesis, crystal structure and Hirshfeld surface analysis of tetraaquabis (isonicotinamide-κN1) cobalt (II) succinate," *Acta Crystallogr. E: Crystallogr. Commun*., vol. 74(7), pp. 1026-1029, 2018.
[23] S. Kansız, G. Kaştaş, M. K. Gümüş, N. Dege, and R. Aydın, "Synthesis, structural characterization, and supramolecular assembly of a one-dimensional cobalt (II) coordination polymer with succinato and isonicotinamide ligands," *J. Struct. Chem*., vol. 66(4), pp. 722-732, 2025.
[24] M. K. Gümüş, S. Kansız, G. B. Tulemisova, and N. Dege, "Synthesis, Crystal Structure, and Hirshfeld Surface Analysis of 4,4A,5,6,7,8-Hexahydro-4A-Methyl-2,5,7-Triphenyl-2H-Pyrido[4,3-d][1,3] Oxazine," *J. Struct. Chem*., vol. 66(1), pp. 201-213, 2025.

[25] R. Ilmi, S. Kansız, N. K. Al Rasbi, S. Anjum, R. Van Deun, and M. S. Khan, "Efficient 0.4 μm–1.6 μm emission from muffin-shaped nine-coordinated ternary samarium (iii) and erbium (iii) complexes," *Dalton Trans*., vol. 54, pp. 10370-10380, 2025.
[26] M. I. Jaafar, R. K. Ahmed, A. J. M. Al-Karawi, A. A. B. OmarAli, S. Kansız, Y. Sert, and N. Dege, "Designing a new bio-active copper (II)-triazole ester type complex based on copper (II)-catalyzed reaction," *Polyhedron*, vol. 256, pp. 116991, 2024.
[27] S. Kansız, A. Tolan, H. İçbudak, and N. Dege, "Synthesis, crystallographic structure, theoretical calculations, spectral and thermal properties of trans-diaquabis (trans-4-aminoantipyrine) cobalt (II) acesulfamate," *J. Mol. Struct*., vol. 1190, pp. 102-115, 2019.
[28] N. Dege, A. S. Aydın, E. Ağar, S. Kansız, S. JoseKavitha, K. BalaSubramani, M. Hemamalini, and V. Rajakannan, "Synthesis, crystal structure, Hirshfeld surface analysis, In-Silico assessment of druggability and molecular docking studies of Schiff base compound," *Chem. Data Collect.*, vol. *25*, 100320, 2020.
[29] Y. El Bakri, M. Kurbanova, A. Ahsin, S. Karthikeyan, A. Maharramov, R. Al-Salahi, S. Kansız, S. N. Mali, and M. Ashfaq, "Synthesis, crystal structure investigation, and theoretical approaches to discover potential 6-bromo-3-cyanocoumarin as a potent inhibitor MetAP (methionine aminopeptidase)2," *Chem. Phys. Impact*, vol. 8, 100477, 2024.
[30] S. Kansız, Y. Sert, S. Meral, A. Alaman Ağar, and N. Dege, "Synthesis, Experimental and Theoretical Characterization of (E)-1-((5-nitrothiophen-2-yl) methylene)-2-Phenylhydrazine," *J. Struct. Chem.*, vol. *67*(2), pp. 291-308, 2026.
[31] N. Arumugam, A. I. Almansour, R. S. Kumar, S. Yeswanthkumar, R. Padmanaban, Y. Arun, S. Kansız, N. Dege, T. S. Manohar, and S. Venketesh, "Design, stereoselective synthesis, computational studies and cholinesterase inhibitory activity of novel spiropyrrolidinoquinoxaline tethered indole hybrid heterocycle," *J. Mol. Struct*., 2021, vol. 1225, pp. 129165.
[32] D. M. Al-thamili, A. I. Almansour, N. Arumugam, S. Kansız, N. Dege, S. M. Soliman, M. Azam, and R. S. Kumar, "Highly functionalized N-1-(2-pyridinylmethyl)-3, 5-bis [(E)-arylmethylidene] tetrahydro-4 (1H)-pyridinones: Synthesis, characterization, crystal structure and DFT studies," *J. Mol. Struct*., vol. 1222, pp. 128940, 2020.
[33] A. A. B. OmarAli, R. K. Ahmed, A. J. M. Al-Karawi, S. Marah, S. Kansız, Y. Sert, M. I. Jaafar, N. Dege, E. B. Poyraz, A. M. A. Ahmed, T. Ozen, M. Loukil, and R. S. Jwad, "Designing of two new cadmium (II) complexes as bio-active materials: Synthesis, X-ray crystal structures, spectroscopic, DFT, and molecular docking studies," *J. Mol. Struct*., vol. 1290, pp. 135974, 2023.
[34] S. Kansız, A. M. Qadir, and N. Dege, "Synthesis, Crystal Structure and Theoretical Characterization of Bis(4-methylbenzoato-κ2O,O′)(4,4′-dimethyl-2,2′-bipyridine-κ2N,N′)Copper(II)," *J. Struct. Chem*., vol. 67, pp. 1730–1742, 2026.
[35] I. Selatnia, A. Sid, H. Lgaz, A. Bouhraoua, T. Roisnel, O.M.A. Khamaysa, S. Kansız, K. Metwally, A.G. Soliman, H.-S. Lee, and S. Boudiba, "Synthesis, structural characterization, and biological evaluation of novel iodophenyl-anthracene Schiff bases: Insights from X-ray crystallography, DFT, antibacterial, and molecular docking studies," *J. Mol. Struct.*, vol. 1350, pp. 144066, 2025.
[36] O. Şimşek, S. Kansız, İ. Yılmaz, A. Çukurovalı, and M. Dinçer, "Structural characterization, DFT-based electronic analysis, Hirshfeld surface study, molecular docking, and in silico drug-likeness evaluation of N-(4-(3-methyl-3mesitylcyclobutyl)-1H-imidazol-2-yl) acetamide," *J. Mol. Struct.*, vol. 1358, pp. 145399, 2026.

8th International Conference on Engineering, Natural and Social Sciences

September 06-07, 2026: Konya, Turkey

© 2026 Published by All Sciences Academy

https://www.icensos.com/

DFT, ADME, and boiled egg analysis of Schiff base derived from nitrobenzaldehyde

Sevgi KANSIZ*[1] and Mustafa Kemal GÜMÜŞ[2]

[1]*Department of Fundamental Sciences, Samsun University, Türkiye*
[2]*Science-Technology Research and Application Center, Artvin Çoruh University, Türkiye*

(sevgi.kansiz@samsun.edu.tr) Email of the corresponding author

Abstract **–** Schiff bases are versatile compounds characterized by the presence of an azomethine (C=N) group. They are the subject of extensive research due to their tunable electronic properties and potential applications in biology and sensing. This study investigated a Schiff base derived from 4-aminoantipyrine and 2-hydroxy-5-nitrobenzaldehyde using theoretical and in silico approaches. Density functional theory (DFT) calculations were performed at the B3LYP/6-311G(d,p) level using the Gaussian 16W program. The optimized molecular structure was then used to evaluate the molecular electrostatic potential (MEP), frontier molecular orbitals (FMOs), and noncovalent interactions via reduced density gradient (RDG) analysis and RDG isosurfaces. The calculated HOMO and LUMO energies were −6.15 and −3.72 eV, respectively, with an energy gap of 2.43 eV. This indicates the electronic characteristics of the molecule under investigation. The MEP surface revealed electron-rich and electron-deficient regions, as well as possible sites involved in intermolecular interactions. RDG analysis revealed attractive, repulsive, and weak van der Waals interactions within the molecular system. SwissADME calculations were performed to evaluate the compound's physicochemical, pharmacokinetic, and drug-likeness properties. The compound exhibited high gastrointestinal absorption and no predicted blood-brain barrier permeation or P-glycoprotein substrate behavior. Additionally, it had a bioavailability score of 0.55. There were zero violations of Lipinski's rule of five, and there were no PAINS alerts. BOILED-Egg analysis was consistent with predicted gastrointestinal absorption and blood-brain barrier behavior. These results provide a comprehensive computational profile of the proposed Schiff base.

Keywords – Schiff base, nitrobenzaldehyde, DFT, MEP, ADME, Boiled-Egg model

I. INTRODUCTION

Schiff bases containing azomethine (C=N) linkages have attracted considerable interest in organic, pharmaceutical, and coordination chemistry owing to their synthetic versatility, tunable electronic properties, and diverse biological activities [1-5]. The integration of 4-aminoantipyrine and substituted benzaldehyde moieties within a single molecular framework represents a promising strategy for the development of therapeutic agents and chemical sensors [6]. Understanding the electronic structure, charge distribution, non-covalent interactions, and ADME (absorption, distribution, metabolism, and excretion) properties of such compounds are essential for assessing their potential applications [7-9]. In the present study, a Schiff base derivative, $C_{18}H_{14}N_4O_4$, derived from 4-aminoantipyrine and 2-hydroxy-5-nitrobenzaldehyde, was computationally investigated using Density Functional Theory (DFT) at the B3LYP/6-311G(d,p) level with the Gaussian 16W program (Fig. 1). Following full optimization of the ground-state molecular geometry, detailed analyses of the molecular electrostatic potential (MEP), frontier molecular orbitals (FMOs), global reactivity descriptors, and reduced density gradient (RDG) were performed to elucidate the electronic and non-covalent interaction characteristics of the compound.

In addition, SwissADME in silico predictions were employed to evaluate its physicochemical properties, pharmacokinetic behavior, and drug-likeness profile.

II. Materials and Method

Quantum-chemical calculations were performed with Gaussian 16W [10], with molecular structures handled through the GaussView 6 graphical interface [11]. The optimized geometry, MEP distribution, and frontier orbital characteristics were obtained at the B3LYP/6-311G(d,p) level within the DFT framework (Fig. 1). The nature of weak non-covalent interactions was investigated by RDG analysis using Multiwfn 3.7 [12], followed by graphical representation in VMD [13]. In addition, the SwissADME web platform [14] was employed to predict the compound's physicochemical profile, pharmacokinetic properties, and drug-likeness characteristics.

III. RESULTS AND DISCUSSION

The DFT-optimized structure of $C_{18}H_{14}N_4O_4$ was evaluated in terms of its principal bond parameters (Fig. 1). The two carbonyl C=O bonds exhibit identical calculated distances of 1.21 Å, indicating equivalent bonding characteristics within the carbonyl-containing moiety [15-17]. The N–N bond of the pyrazole ring [18, 19] was determined to be 1.41 Å, whereas the corresponding C–N bonds were calculated as 1.39 and 1.43 Å. For the nitro substituent, both N=O bonds have a calculated length of 1.22 Å, while the C–NO_2 bond distance is 1.48 Å. The C–C distances within the aromatic ring range from 1.35 to 1.43 Å, with an average value of approximately 1.38 Å, consistent with the expected bond-length characteristics of an aromatic system [20-24]. The calculated bond lengths are in accordance with the expected structural features of the carbonyl, pyrazole, and nitro functional groups, confirming the chemically reasonable geometry obtained after optimization.

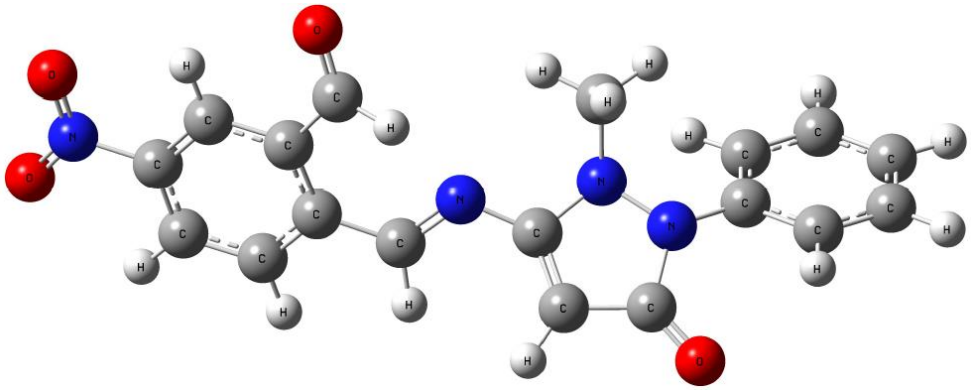

Fig. 1 The optimized geometry of $C_{18}H_{14}N_4O_4$.

The molecular electrostatic potential (MEP) map was constructed using the optimized geometry of $C_{18}H_{14}N_4O_4$ to visualize the spatial distribution of electronic charge and identify the preferential sites for electrophilic and nucleophilic attacks [25-28]. Strong negative potential regions (red/orange areas) are predominantly concentrated around the oxygen atoms of the nitro group ($-NO_2$), the carbonyl oxygen of the antipyrine moiety, and the azomethine nitrogen atom (Fig. 2). These regions represent electron-rich centers that can participate in hydrogen-bond acceptance and nucleophilic interactions. In contrast, positive potential regions (blue areas) are mainly distributed around the hydroxyl hydrogen and the aromatic hydrogen atoms of the nitro-substituted ring, indicating electropositive sites that may act as hydrogen-bond donors in intermolecular interactions. Neutral potential regions (green/yellow areas) are mainly distributed over the phenyl ring and methyl groups. The observed electrostatic polarization provides valuable insight into the reactive sites of the molecule and its potential interaction with biological targets.

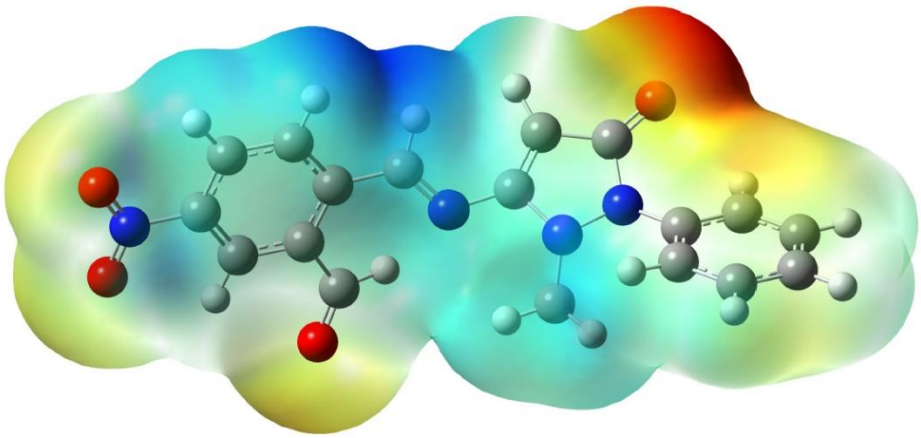

Fig. 2 The MEP map of $C_{18}H_{14}N_4O_4$.

The spatial distributions and energy levels of the Frontier Molecular Orbitals (HOMO and LUMO) were analyzed to evaluate the electronic stability, charge-transfer character, and chemical reactivity of $C_{18}H_{14}N_4O_4$ (Fig. 3). The calculated HOMO and LUMO energies were −6.15 eV and −3.72 eV, respectively, resulting in an energy gap (ΔE) of 2.43 eV. The relatively small HOMO–LUMO gap suggests enhanced chemical reactivity and a pronounced tendency for intramolecular charge transfer (Table 1). Examination of the orbital distributions shows that the HOMO is mainly localized over the antipyrine moiety and azomethine bridge, whereas the LUMO is predominantly distributed over the electron-withdrawing nitrobenzaldehyde moiety. This spatial separation of the frontier orbitals indicates a significant redistribution of electron density and supports a π→π* charge-transfer character upon electronic excitation [29-31]. The global reactivity descriptors derived from the frontier orbital energies were calculated as follows: ionization potential (I) = 6.15 eV, electron affinity (A) = 3.72 eV, electronegativity (χ) = 4.93 eV, chemical potential (μ) = −4.93 eV, chemical hardness (η) = 1.22 eV, chemical softness (S) = 0.41 eV^{-1}, and electrophilicity index (ω) = 9.99 eV. The relatively low chemical hardness and high softness indicate that the molecule can undergo electronic charge redistribution relatively easily. In addition, the high electrophilicity index suggests a strong tendency to accept electron density, further supporting the electrophilic character of the compound. The FMO analysis and calculated global reactivity descriptors indicate that $C_{18}H_{14}N_4O_4$ possesses a relatively soft electronic structure with appreciable charge-transfer and electrophilic characteristics.

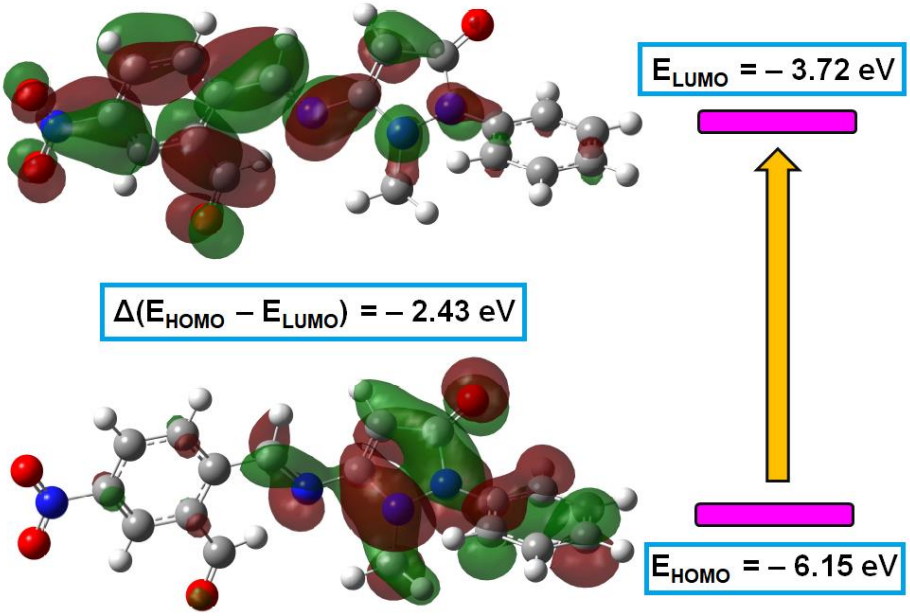

Fig. 3 FMOs surfaces of $C_{18}H_{14}N_4O_4$. The isosurfaces value is set to ±0.02 a.u.

Table 1. The energy values of the global reactivity parameters.

Parameters	
E_{HOMO} (eV)	−6.15
E_{LUMO} (eV)	−3.72
Energy gap (eV)	2.43
Ionization potential ($I = -E_{HOMO}$)	6.15
Electron affinity ($A = -E_{LUMO}$)	3.72
Electronegativity ($\chi = (I+A)/2$)	4.93
Hardness ($\eta = (I - A)/2$)	1.22
Softness ($S=1/2\eta$)	0.41
Chemical potential ($\mu = -(I+A)/2$)	−4.93
Electrophilicity index ($\omega = \mu^2/2\eta$)	9.99

To obtain qualitative and quantitative insights into the weak intramolecular and intermolecular interactions contributing to the stabilization of the molecular framework, Reduced Density Gradient (RDG) scatter plots and three-dimensional isosurfaces were analyzed using the sign(λ_2)ρ function at an isovalue of 0.5 a.u. (Fig. 4). In the RDG scatter plot, spikes extending into the negative region, sign(λ_2)ρ < −0.01 a.u. (blue domain), are associated with attractive non-covalent interactions, including possible intramolecular hydrogen bonding [32, 33]. The regions close to zero, −0.01 < sign(λ_2)ρ < 0.01 a.u. (green domain), correspond to weak van der Waals interactions and are represented by broad green isosurfaces distributed mainly around the aromatic rings and methyl substituents. In contrast, the positive region, sign(λ_2)ρ > 0.01 a.u. (red domain), is indicative of steric repulsion and is visualized as red discoid isosurfaces within the antipyrine, phenyl, and nitrobenzene rings. Overall, the RDG analysis indicates that weak van der Waals interactions, together with localized steric effects and possible intramolecular hydrogen bonding, contribute to the stabilization and three-dimensional conformation of the molecule.

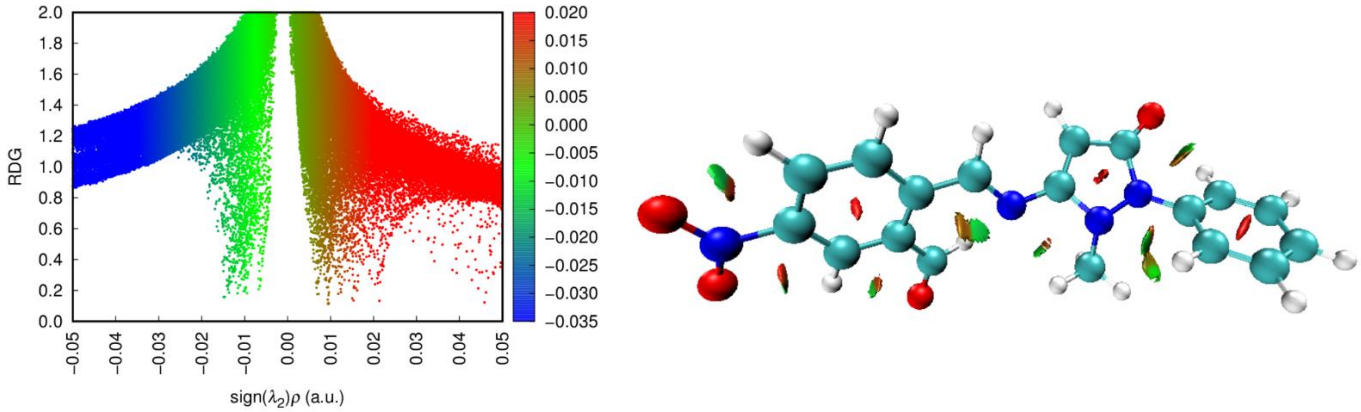

Fig. 4 (a) RDG scatter plot, and (b) RDG isosurfaces plotted at the value of ±0.5 a.u., colored according to sign(λ_2)ρ.

The in silico evaluation performed using the SwissADME web tool provided comprehensive information on the physicochemical properties, pharmacokinetic characteristics, and drug-likeness of $C_{18}H_{14}N_4O_4$ (Table 2, Fig. 5). The compound has a molecular weight of 350.33 g/mol, five rotatable bonds, five hydrogen-bond acceptors, no hydrogen-bond donors, and a Topological Polar Surface Area (TPSA) of 102.18 Å². These physicochemical properties are generally compatible with commonly used drug-likeness criteria. The lipophilicity analysis yielded a consensus Log P value of 1.09, while the XLOGP3 value was calculated as 4.05. The predicted aqueous solubility was characterized as moderate, with a Log S value of −4.72. Pharmacokinetic predictions indicated high gastrointestinal (GI) absorption, whereas no blood-brain barrier (BBB) permeability or P-glycoprotein (P-gp) substrate activity was predicted. Consistent with these findings, the BOILED-Egg model placed the molecule within the white region associated with high GI absorption, with the red dot indicating a P-gp-negative prediction. Furthermore, the compound showed no violations of the Lipinski, Ghose, Veber, Egan, or Muegge drug-

likeness rules. A bioavailability score of 0.55 and the absence of PAINS alerts further support its favorable predicted drug-like profile. The synthetic accessibility score of 3.12 suggests that the compound is relatively accessible from a synthetic perspective. The SwissADME results indicate that $C_{18}H_{14}N_4O_4$ exhibits a combination of favorable physicochemical and predicted pharmacokinetic properties, supporting its potential for further investigation as a bioactive molecular scaffold.

Table 2. Some SwissADME results for $C_{18}H_{14}N_4O_4$.

Physicochemical Properties		*Water Solubility*	
Formula	$C_{18}H_{14}N_4O_4$	Log S (ESOL)	-4.72
Molecular weight	350.33 g/mol	Solubility	6.72e-03 mg/ml; 1.92e-05 mol/l
Num. heavy atoms	26	Class	Moderately soluble
Num. arom. heavy atoms	17	Log S (Ali)	-5.90
Fraction Csp3	0.06	Solubility	4.41e-04 mg/ml; 1.26e-06 mol/l
Num. rotatable bonds	5	Class	Moderately soluble
Num. H-bond acceptors	5	Log S (SILICOS-IT)	-5.26
Num. H-bond donors	0	Solubility	1.94e-03 mg/ml; 5.53e-06 mol/l
Molar Refractivity	99.20	Class	Moderately soluble
TPSA	102.18 Å²	*Druglikeness*	
Lipophilicity		Lipinski	Yes; 0 violation
Log Po/w (XLOGP3)	4.05	Ghose	Yes
Log Po/w (WLOGP)	2.65	Veber	Yes
Log Po/w (MLOGP)	2.09	Egan	Yes
Log Po/w (SILICOS-IT)	-4.42	Muegge	Yes
Consensus Log Po/w	1.09	Bioavailability Score	0.55
Pharmacokinetics		*Medicinal Chemistry*	
GI absorption	High	PAINS	0 alert
BBB permeant	No	Synthetic accessibility	3.12
P-gp substrate	No	Leadlikeness	No;2 violations: MW>350, XLOGP3>3.5
Log Kp (skin permeation)	-5.56 cm/s	Brenk	4 alerts: aldehyde, imine1, nitro group, oxygen-nitrogen single bond

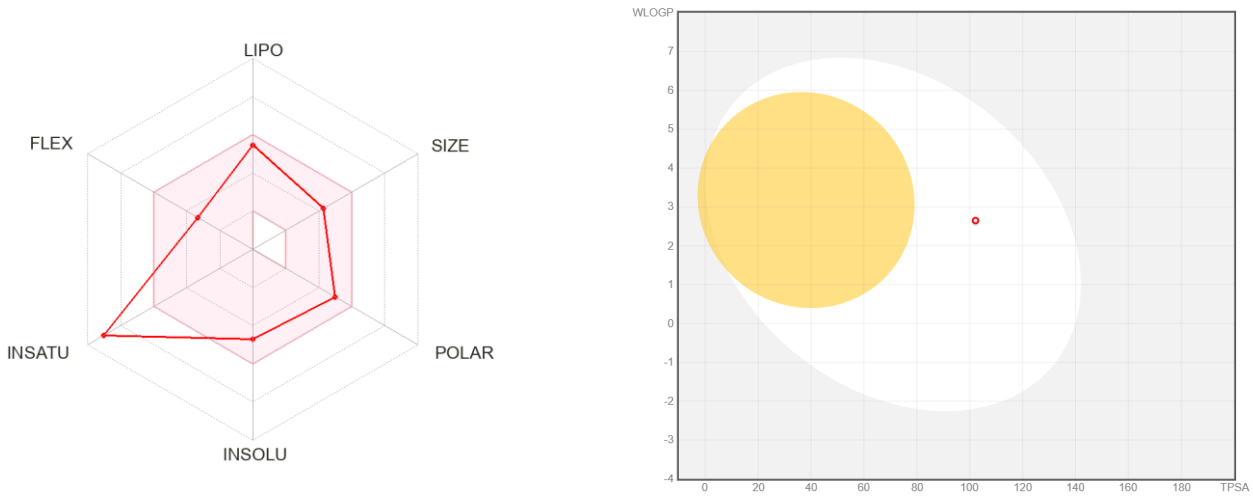

Fig. 5 The radar and boiled egg model of $C_{18}H_{14}N_4O_4$.

IV. CONCLUSION

In summary, a comprehensive computational investigation of the Schiff base derivative $C_{18}H_{14}N_4O_4$ was carried out using DFT calculations at the B3LYP/6-311G(d,p) level in combination with in silico SwissADME profiling. Geometry optimization provided a stable molecular structure, while molecular electrostatic potential analysis identified electron-rich regions mainly around the nitro and carbonyl oxygen atoms and the azomethine nitrogen atom. Frontier molecular orbital analysis revealed a relatively narrow HOMO–LUMO energy gap of 2.43 eV, with HOMO and LUMO energies of −6.15 and −3.72 eV, respectively, suggesting appreciable charge-transfer character and chemical reactivity. This interpretation

was further supported by the calculated global reactivity descriptors, particularly the relatively low chemical hardness (η = 1.22 eV) and high electrophilicity index (ω = 9.99 eV). RDG analysis indicated the presence of weak van der Waals interactions, possible intramolecular hydrogen bonding, and localized steric repulsions that contribute to the overall molecular conformation. The SwissADME predictions further revealed favorable drug-likeness characteristics, including high gastrointestinal absorption, no predicted blood-brain barrier permeability, non-substrate behavior toward P-glycoprotein, no violations of the evaluated drug-likeness rules, and the absence of PAINS alerts. The predicted bioavailability score of 0.55 and synthetic accessibility score of 3.12 also indicate favorable computational profiles. Taken together, the combined quantum-chemical and in silico analyses provide valuable information on the electronic structure, intermolecular interactions, and predicted pharmacokinetic properties of $C_{18}H_{14}N_4O_4$. These findings support the compound as a promising molecular scaffold for further experimental investigation and biological evaluation.

ACKNOWLEDGMENTS

The numerical calculations reported in this paper were fully/partially performed at TUBITAK ULAKBIM, High Performance and Grid Computing Center (TRUBA resources).

REFERENCES

[1] S. Kansiz, "Investigating the structural and surface properties of copper and nickel complexes fluorine-based salen type Schiff bases," *J. Struct. Chem*., vol. 64(12), pp. 2295-2310, 2023.

[2] N. Dege, A. S. Aydın, E. Ağar, S. Kansız, S. JoseKavitha, K. BalaSubramani, M. Hemamalini, and V. Rajakannan, "Synthesis, crystal structure, Hirshfeld surface analysis, In-Silico assessment of druggability and molecular docking studies of Schiff base compound," *Chem. Data Collect.*, vol. *25*, 100320, 202

[3] O. Şimşek, Ş. Atalay, M. Taşdoğan, E. Ağar, H. Bülbül, and S. Kansız, "Synthesis, Characterization, and Hirshfeld Surface Analysis of Two Schiff Bases: (*E*)-3-(((4-iodophenyl) imino) methyl)benzene-1,2-diol and (*E*)-3-(((3-bromo-4-methylphenyl)imino)methyl)-benzene-1,2-diol," *J. Struct. Chem.*, vol. *67*(4), pp. 827-840, 2026.

[4] P. Şen, and S. Kansız, "Crystal Structure, Spectroscopic and Computational Studies of N2O2 Type Salen-Based Schiff Base and Its Di-boron Complex," *J. Chem. Crystallogr.*, vol. *52*(1), pp. 1-16, 2022.

[5] S. Yeşilbağ, S. Kansız, N. Dege, and E. Ağar, "Structural investigation and hirshfeld surface analysis of two [ONO]-Type schiff bases," *J. Struct. Chem*., vol. 65(3), pp.464-477, 2024.

[6] M. U. Konanç, and M. K. Gümüş, "Su örneklerindeki Cu(II), Co(II), Fe(III) ve Ni(II) iyonlarının Schiff bazı komplekslerinin katı-faz ekstraksiyonu yönteminden sonra ICP-OES ile tayini," *J. BAUN Inst. Sci. Technol*., vol. 21(2), pp. 739-755, 2019.

[7] O. Şimşek, S. Kansız, İ. Yılmaz, A. Çukurovalı, and M. Dinçer, "Structural characterization, DFT-based electronic analysis, Hirshfeld surface study, molecular docking, and in silico drug-likeness evaluation of N-(4-(3-methyl-3mesitylcyclobutyl)-1H-imidazol-2-yl) acetamide," *J. Mol. Struct.*, vol. 1358, pp. 145399, 2026.

[8] S. Kansız, Y. Sert, S. Meral, A. Alaman Ağar, and N. Dege, "Synthesis, Experimental and Theoretical Characterization of (E)-1-((5-nitrothiophen-2-yl) methylene)-2-Phenylhydrazine," *J. Struct. Chem.*, vol. *67*(2), pp. 291-308, 2026.

[9] H. Kargar, M. Fallah-Mehrjardi, K. S. Munawar, E. Acar, N. Dege, and S. Kansız, "Structural dynamics of a phenoxy-bridged heteronuclear Cu (II)/Hg (II)-Salen complex: synthesis, characterization, DFT insights, and Hirshfeld surface analysis," *J. Iran. Chem. Soc.*, vol. 22(4), pp. 769-780, 2025.

[10] M. J. Frisch, G. Trucks, H. Schlegel, G. Scuseria, M. Robb, J. Cheeseman, G. Scalmani, V. Barone, B. Mennucci, and G. Petersson, 2009. Gaussian 09, Revision D. 01, Gaussian, Inc.: Wallingford, CT.

[11] R. Dennington, T. Keith, and J. Millam, 2009. GaussView, version 5, Semichem Inc.: Shawnee Mission, KS.

[12] W. Humphrey, A. Dalke, and K. Schulten, "VMD: Visual Molecular Dynamics," *J. Mol. Graph*., vol. 14(1), pp. 33-38, 1996.

[13] T. Lu, and F. Chen, "Multiwfn: A multifunctional wavefunction analyzer," *J. Comput. Chem*., vol. 33(5), pp. 580-592, 2012.

[14] A. Daina, O. Michielin, and V. Zoete, "SwissADME: a free web tool to evaluate pharmacokinetics, drug-likeness and medicinal chemistry friendliness of small molecules," *Sci. Rep*., vol. 7(1), pp. 42717, 2017.

[15] Y. El Bakri, M. Kurbanova, A. Ahsin, S. Karthikeyan, A. Maharramov, R. Al-Salahi, S. Kansız, S. N. Mali, and M. Ashfaq, "Synthesis, crystal structure investigation, and theoretical approaches to discover potential 6-bromo-3-cyanocoumarin as a potent inhibitor MetAP (methionine aminopeptidase)2," *Chem. Phys. Impact*, vol. 8, 100477, 2024.

[16] S. Cakmak, S. Kansiz, M. Azam, C. C. Ersanlı, O. Idil, A. Veyisoglu, H. Yakan, H. Kütük, and A. Chutia, "Synthesis, structural investigation, Hirshfeld surface analysis, and biological evaluation of N-(3-Cyanothiophen-2-yl)-2-(thiophen-2-yl) acetamide," *ACS omega*, vol. 7(13), pp. 11320-11329, 2022.

[17] Ş. Çakmak, S. Kansiz, M. Azam, A. Veyisoglu, H. Yakan, and K. Min, "Synthesis, Spectroscopic Characterization, Single-Crystal Structure, Hirshfeld Surface Analysis, and Antimicrobial Studies of 3-Acetoxy-2-methylbenzoic Anhydride," *ACS Omega*, vol. 7 (20), pp. 17192–17201, 2022.
[18] K. Chkirate, S. Kansiz, K. Karrouchi, J. T. Mague, N. Dege, and E. M. Essassi, "Crystal structure and Hirshfeld surface analysis of N-{2-[(E)-(4-methylbenzylidene) amino] phenyl}-2-(5-methyl-1-H-pyrazol-3-yl) acetamide hemihydrate," *Acta Crystallogr. E: Crystallogr. Commun*., vol. 75(2), pp. 154-158, 2019.
[19] M. K. Alenzi, M. Azam, S. I. Al-Resayes, S. Kansız, A. S. Çamaş, D. C. Agurokpon, H. Louis, V. Kumar, N. Dege, and M. Alam, "Experimental and theoretical investigation into the design of nickel (II), copper (II), and zinc (II) complexes substituted with pyrazole ligand," *Polyhedron*, vol. 259, pp. 117073, 2024.
[20] S. Kansız, G. Kaştaş, M. K. Gümüş, N. Dege, and R. Aydın, "Synthesis, structural characterization, and supramolecular assembly of a one-dimensional cobalt (II) coordination polymer with succinato and isonicotinamide ligands," *J. Struct. Chem*., vol. 66(4), pp. 722-732, 2025.
[21] M. K. Gümüş, S. Kansız, G. B. Tulemisova, and N. Dege, "Synthesis, Crystal Structure, and Hirshfeld Surface Analysis of 4,4A,5,6,7,8-Hexahydro-4A-Methyl-2,5,7-Triphenyl-2H-Pyrido[4,3-d][1,3] Oxazine," *J. Struct. Chem*., vol. 66(1), pp. 201-213, 2025.
[22] S. Kansiz, S. Malinkin, and N. Dege, "Synthesis, crystal structure and Hirshfeld surface analysis of tetraaquabis (isonicotinamide-κN1) cobalt (II) succinate," *Acta Crystallogr. E: Crystallogr. Commun*., vol. 74(7), pp. 1026-1029, 2018.
[23] A. A. B. OmarAli, A. J. M. Al-Karawi, N. Dege, S. Kansız, and H. A. D. Ithawi, "Synthesis and X-ray crystal structures of two different zinc (II) complexes of N, N′-cyclohexane-1, 2-diylidene-bis (4-fluorobenzoylhydrazide) based on zinc salt effect," *J. Mol. Struct*., 2020, vol. 1217, pp. 128387.
[24] R. Ilmi, S. Kansız, N. K. Al Rasbi, S. Anjum, R. Van Deun, and M. S. Khan, "Efficient 0.4 μm–1.6 μm emission from muffin-shaped nine-coordinated ternary samarium (iii) and erbium (iii) complexes," *Dalton Trans*., vol. 54, pp. 10370-10380, 2025.
[25] S. Kansız, A. Tolan, H. İçbudak, and N. Dege, "Synthesis, crystallographic structure, theoretical calculations, spectral and thermal properties of trans-diaquabis (trans-4-aminoantipyrine) cobalt (II) acesulfamate," *J. Mol. Struct*., vol. 1190, pp. 102-115, 2019.
[26] N. Arumugam, A. I. Almansour, R. S. Kumar, S. Yeswanthkumar, R. Padmanaban, Y. Arun, S. Kansız, N. Dege, T. S. Manohar, and S. Venketesh, "Design, stereoselective synthesis, computational studies and cholinesterase inhibitory activity of novel spiropyrrolidinoquinoxaline tethered indole hybrid heterocycle," *J. Mol. Struct*., 2021, vol. 1225, pp. 129165.
[27] S. Kansız, "Synthesis and Structural Investigations of 1, 2-bis (2-ethoxybenzylidene) hydrazine," *Sak. Univ. J. Sci.*, vol. 27(4), pp. 768-780, 2023.
[28] S. Kansız, M. Azam, N. Dege, N. Ermiş, S.I. Al-Resayes, and M. Alam, "Supramolecular assembly in designing co-crystals of fumaric acid and pyrimidine/picolinate derivatives," *Green Chem. Lett. Rev*., vol. 15 (3), pp. 825-836, 2022.
[29] A. M. Qadir, S. Kansiz, N. Dege, G. M. Rosair, and I. O. Fritsky, "Crystal structure and DFT study of a zinc xanthate complex," *Acta Crystallogr. E: Crystallogr. Commun*., vol. 75(11), pp. 1582-1585, 2019.
[30] Y. Bouzian, Y. Sert, K. Khalid, L. Van Meervelt, K. Chkirate, L. Mahi, N. H. Ahabchane, A. Talbaoui, and E. M. Essassi, "Synthesis, spectroscopic characterization, DFT, molecular docking and in vitro antibacterial potential of novel quinoline derivatives," *J. Mol. Struct*., vol. 1246, pp. 131217, 2021.
[31] İ. Çapan, M. Hawash, N. Jaradat, Y. Sert, R. Servi, and İ. Koca, "Design, synthesis, molecular docking and biological evaluation of new carbazole derivatives as anticancer, and antioxidant agents," *BMC Chem*., vol. 17(1), pp. 60, 2023.
[32] I. Selatnia, A. Sid, H. Lgaz, A. Bouhraoua, T. Roisnel, O.M.A. Khamaysa, S. Kansız, K. Metwally, A.G. Soliman, H.-S. Lee, and S. Boudiba, "Synthesis, structural characterization, and biological evaluation of novel iodophenyl-anthracene Schiff bases: Insights from X-ray crystallography, DFT, antibacterial, and molecular docking studies," *J. Mol. Struct.*, vol. 1350, pp. 144066, 2025.
[33] S. Kansız, A. M. Qadir, and N. Dege, "Synthesis, Crystal Structure and Theoretical Characterization of Bis(4-methylbenzoato-κ2O,O′)(4,4′-dimethyl-2,2′-bipyridine-κ2N,N′)Copper(II)," *J. Struct. Chem*., vol. 67, pp. 1730–1742, 2026.

8th International Conference on Engineering, Natural and Social Sciences

September 06-07, 2026: Konya, Turkey

© 2026 Published by All Sciences Academy

https://www.icensos.com/

Radyofarmasötiklerin Nükleer Tıpta Tanı ve Tedavideki Güncel Uygulamaları

Hatice DEMİR BECEREKLİ[1*], Yalçın ALTUNKAYNAK [2]

[1]Gıda İşleme / Teknik Bilimler Meslek Yüksekokulu, Batman Üniversitesi, Türkiye (ORCID: https://orcid.org/0000-0002-1165-518X)

[2] Kimya ve Kimyasal İşleme Teknolojileri / Teknik Bilimler Meslek Yüksekokulu, Batman Üniversitesi, Türkiye (ORCID: https://orcid.org/ https://orcid.org/0000-0003-2562-9297)

Özet **–** Radyofarmasötikler, nükleer tıp uygulamalarında hastalıkların tanı ve tedavisinde kullanılan radyoaktif ilaçlardır. Son yıllarda moleküler görüntüleme tekniklerindeki gelişmeler, yeni radyonüklidlerin kullanıma girmesi ve hedefe yönelik tedavi yaklaşımlarının gelişmesi ile birlikte radyofarmasi alanı önemli ilerlemeler kaydetmiştir. Pozitron Emisyon Tomografisi (PET) ve Tek Foton Emisyon Bilgisayarlı Tomografisi (SPECT) gibi görüntüleme yöntemlerinde kullanılan radyofarmasötikler, hastalıkların erken tanısında yüksek duyarlılık sağlamaktadır. Ayrıca Lu-177, Ac-225 ve I-131 gibi terapötik radyonüklidlerle geliştirilen ajanlar, kanser tedavisinde umut verici sonuçlar ortaya koymaktadır. Bu çalışmada radyofarmasinin temel prensipleri, radyofarmasötiklerin sınıflandırılması, üretim süreçleri, kalite kontrol uygulamaları, klinik kullanım alanları ve gelecekteki gelişim eğilimleri güncel literatür ışığında değerlendirilmiştir.

Anahtar Kelimeler – Radyofarmasi, Radyofarmasötik, PET, SPECT, Nükleer Tıp, Teranostik

I. GİRİŞ

Nükleer tıp, radyoaktif maddelerin tanı ve tedavi amacıyla kontrollü şekilde kullanıldığı modern tıp dallarından biridir. Bu disiplin içerisinde kullanılan radyofarmasötikler, biyolojik olarak aktif moleküllerin radyoizotoplarla işaretlenmesi sonucu elde edilen farmasötik ürünlerdir. Radyofarmasötikler, klasik ilaçlardan farklı olarak hedef organ veya dokuda dağılım gösterirken yaydıkları gama veya pozitron ışınları sayesinde görüntüleme yapılmasına ya da beta ve alfa parçacıkları ile terapötik etki oluşturulmasına olanak sağlar [4–6].

Kanser insidansındaki artış, nörolojik hastalıkların erken teşhis gereksinimi ve kardiyovasküler hastalıkların değerlendirilmesindeki ihtiyaç, radyofarmasi alanındaki araştırmaları hızlandırmıştır. Günümüzde sadece tanısal görüntüleme değil, aynı zamanda kişiselleştirilmiş tedavi uygulamaları da radyofarmasinin temel çalışma alanlarından biri hâline gelmiştir [8,9].

II. RADYOFARMASÖTİKLERİN YAPISI VE TEMEL ÖZELLİKLERİ

Bir radyofarmasötik temel olarak iki bileşenden oluşmaktadır:

- Radyoaktif izotop (radyonüklid)
- Taşıyıcı biyomolekül (ligand)

Taşıyıcı molekül, ilacın belirli organ veya tümör dokusuna seçici olarak ulaşmasını sağlarken radyonüklid görüntüleme veya tedavi amacıyla radyasyon yaymaktadır [5,6].

Tanısal radyofarmasötiklerde genellikle kısa yarı ömürlü gama veya pozitron yayıcı izotoplar tercih edilmektedir. Bunlar arasında en yaygın kullanılanlar [4–6];

- Teknesyum-99m (Tc-99m)
- Flor-18 (F-18)
- Galyum-68 (Ga-68)
- Karbon-11 (C-11)

olarak sıralanabilir.

Tedavi amacıyla ise;

- İyot-131
- Lutesyum-177
- İtriyum-90
- Aktinyum-225

gibi beta veya alfa yayıcı radyonüklidler kullanılmaktadır [5–7,9].

III. RADYOFARMASÖTIKLERIN HAZIRLANMASI

Radyofarmasötik üretimi oldukça hassas süreçlerden oluşmaktadır [3,5,10].

Üretim aşamaları;

- Radyonüklidin elde edilmesi
- Kimyasal saflaştırma
- Radyoaktif işaretleme
- Sterilizasyon
- Kalite kontrol
- Klinik kullanıma sunulması

şeklinde sıralanabilir.

Üretim sırasında GMP (Good Manufacturing Practice) kurallarına uyulması zorunludur. Üretim ortamında partikül kontrolü, sterilite ve radyasyon güvenliği büyük önem taşımaktadır [3,10].

Özellikle Tc-99m jeneratör sistemleri dünya genelinde günlük olarak en fazla kullanılan radyofarmasötik üretim yöntemidir [5,6].

IV. KALITE KONTROL UYGULAMALARI

Radyofarmasötiklerin hasta güvenliği açısından kalite kontrolü zorunludur [1,3,10].

Başlıca kalite kontrol testleri;

- Radyoaktif saflık
- Radyokimyasal saflık
- Kimyasal saflık
- pH tayini
- Sterilite testi
- Bakteriyel endotoksin testi
- Görünüş kontrolü
- Partikül analizi

şeklindedir.

İnce tabaka kromatografisi (ITLC), yüksek performanslı sıvı kromatografisi (HPLC) ve gaz kromatografisi (GC) radyofarmasötik analizlerinde yaygın olarak kullanılmaktadır [3,5,10].

V. TANISAL KULLANIM ALANLARI

A. PET Görüntüleme

PET görüntüleme metabolik aktivitenin değerlendirilmesinde en duyarlı yöntemlerden biridir [2,4,5].

En yaygın kullanılan radyofarmasötik F-18 FDG'dir. FDG, glikoz metabolizmasının arttığı kanser hücrelerinde yoğun olarak tutulmaktadır.

PET uygulamaları;

- Onkoloji
- Kardiyoloji
- Nöroloji
- Enfeksiyon görüntüleme alanlarında kullanılmaktadır [2,4,5].

B. SPECT Görüntüleme

SPECT görüntüleme gama ışınlarını kullanmaktadır [2,4].

Tc-99m ile işaretlenmiş radyofarmasötikler;

- Kemik sintigrafisi
- Miyokard perfüzyon sintigrafisi
- Tiroid görüntüleme
- Böbrek fonksiyon değerlendirmesi amacıyla yaygın şekilde kullanılmaktadır [2,4,5].

Tc-99m'nin yaklaşık altı saatlik yarı ömrü ve düşük radyasyon dozu önemli avantaj sağlamaktadır [4–6].

VI. TEDAVI AMAÇLI RADYOFARMASÖTIKLER

Son yıllarda radyonüklid tedavilerinde önemli gelişmeler yaşanmaktadır [7–9].

İyot-131

Hipertiroidi ve diferansiye tiroit kanseri tedavisinde uzun yıllardır başarıyla kullanılmaktadır [5,6].

Lutesyum-177

PSMA ve DOTATATE molekülleri ile işaretlenerek;

- Prostat kanseri
- Nöroendokrin tümörler

tedavisinde yüksek başarı oranları göstermektedir [2,9].

Aktinyum-225

Alfa yayıcı özellik göstermesi nedeniyle özellikle metastatik kanserlerde umut vaat eden yeni nesil radyofarmasötikler arasında yer almaktadır [7,9].

VII. TERANOSTIK YAKLAŞIMI

Teranostik, aynı biyolojik hedefin hem görüntülenmesi hem de tedavisinde kullanılmasını ifade etmektedir [9].

Örneğin;

Ga-68 PSMA ile görüntüleme yapıldıktan sonra aynı hastaya Lu-177 PSMA uygulanabilmektedir [9].

Bu yaklaşım;

- kişiselleştirilmiş tedavi,
- daha yüksek başarı oranı,
- daha düşük yan etki

gibi önemli avantajlar sağlamaktadır [9].

Son yıllarda özellikle prostat kanseri tedavisinde standart uygulamalardan biri hâline gelmiştir.

VIII. RADYASYON GÜVENLIĞI

Radyofarmasi laboratuvarlarında çalışan personelin radyasyon güvenliği büyük önem taşımaktadır [1,5,10].

Temel korunma ilkeleri;

- zamanı azaltmak,
- mesafeyi artırmak,
- uygun zırhlama kullanmak

şeklinde özetlenebilir [1,5,10].

Kurşun zırhlı enjektörler, sıcak hücreler (hot cell), doz kalibratörleri ve kişisel dozimetreler güvenli çalışma ortamının vazgeçilmez ekipmanlarıdır [1,5,10].

IX. GELECEK PERSPEKTİFİ

Yapay zekâ destekli görüntü analizi, yeni peptit tabanlı radyofarmasötikler, alfa yayıcı tedaviler ve nanoteknoloji tabanlı taşıyıcı sistemler radyofarmasinin geleceğini şekillendirmektedir.

Ayrıca hedefe yönelik moleküler tedavilerin gelişmesiyle birlikte kişiselleştirilmiş tıp uygulamalarının yaygınlaşacağı öngörülmektedir [8,9].

X. SONUÇ

Radyofarmasi, nükleer tıbbın en hızlı gelişen alanlarından biridir. Geliştirilen yeni radyofarmasötikler sayesinde hastalıkların erken tanısı mümkün olmakta, aynı zamanda hedefe yönelik tedavi seçenekleri artmaktadır. Özellikle PET/SPECT teknolojileri ile Lu-177 ve Ac-225 temelli tedavi ajanları, onkolojik uygulamalarda önemli klinik başarılar sağlamaktadır. Bununla birlikte kalite kontrol, GMP standartlarına uygun üretim ve radyasyon güvenliği uygulamaları hasta güvenliği açısından kritik öneme sahiptir. Önümüzdeki yıllarda yapay zekâ, nanoteknoloji ve teranostik yaklaşımların radyofarmasi alanında daha geniş kullanım alanı bulacağı öngörülmektedir.

KAYNAKLAR

[1] S. M. Metev and V. P. Veiko, *Laser Assisted Microtechnology*, 2nd ed., R. M. Osgood, Jr., Ed. Berlin, Germany: Springer-Verlag, 1998.

[2] J. Breckling, Ed., *The Analysis of Directional Time Series: Applications to Wind Speed and Direction*, ser. Lecture Notes in Statistics. Berlin, Germany: Springer, 1989, vol. 61.

[3] S. Zhang, C. Zhu, J. K. O. Sin, and P. K. T. Mok, "A novel ultrathin elevated channel low-temperature poly-Si TFT," *IEEE Electron Device Lett.*, vol. 20, pp. 569–571, Nov. 1999.

[4] M. Wegmuller, J. P. von der Weid, P. Oberson, and N. Gisin, "High resolution fiber distributed measurements with coherent OFDR," in *Proc. ECOC'00*, 2000, paper 11.3.4, p. 109.

[5] R. E. Sorace, V. S. Reinhardt, and S. A. Vaughn, "High-speed digital-to-RF converter," U.S. Patent 5 668 842, Sept. 16, 1997.

[6] (2002) The IEEE website. [Online]. Available: http://www.ieee.org/

[7] M. Shell. (2002) IEEEtran homepage on CTAN. [Online]. Available: http://www.ctan.org/tex-archive/macros/latex/contrib/supported/IEEEtran/

[8] *FLEXChip Signal Processor (MC68175/D)*, Motorola, 1996.

[9] "PDCA12-70 data sheet," Opto Speed SA, Mezzovico, Switzerland.

[10] A. Karnik, "Performance of TCP congestion control with rate feedback: TCP/ABR and rate adaptive TCP/IP," M. Eng. thesis, Indian Institute of Science, Bangalore, India, Jan. 1999.

[11] J. Padhye, V. Firoiu, and D. Towsley, "A stochastic model of TCP Reno congestion avoidance and control," Univ. of Massachusetts, Amherst, MA, CMPSCI Tech. Rep. 99-02, 1999.

[12] *Wireless LAN Medium Access Control (MAC) and Physical Layer (PHY) Specification*, IEEE Std. 802.11, 1997.

8th International Conference on Engineering, Natural and Social Sciences

September 06-07, 2026: Konya, Turkey

© 2026 Published by All Sciences Academy

https://www.icensos.com/

Optimization Approaches in Sustainable Structural Design: Current Methodologies and Research Gaps in the Literature

Ali Mortazavi

Civil Engineering Department, Izmir Democracy University, Turkey

(ali.mortazavi@idu.edu.tr) Email of the corresponding author

Abstract **–** The construction sector is currently responsible for a substantial portion of global energy consumption, resource depletion, and greenhouse gas emissions. Consequently, structural design has evolved from a conventional process focused solely on cost-efficiency and structural safety into a complex, multi-objective decision-making framework that intrinsically incorporates environmental sustainability. This paper systematically reviews current optimization methodologies utilized in sustainable structural design, with a particular focus on the integration of meta-heuristic algorithms. While traditional literature has predominantly concentrated on minimizing structural weight and material cost, recent years have witnessed a paradigm shift towards the inclusion of environmental metrics, such as embodied carbon footprint, Life Cycle Assessment (LCA) outcomes, and operational energy efficiency, within optimization problem formulations. This study maps this transition in the literature and highlights the existing research gaps, primarily focusing on the lack of integration in real-world engineering applications, computational constraints encountered in multi-objective optimization problems, and the methodological challenges of accurately incorporating the environmental impact of construction materials into mathematical models. The findings aim to provide a comprehensive framework for future studies seeking to bridge the gap between theoretical optimization models and practical sustainable construction.

Keywords – Sustainable Structural Design, Multi-Objective Optimization, Meta-heuristic Algorithms, Embodied Carbon, Life Cycle Assessment (LCA)

I. INTRODUCTION

The global construction industry is widely recognized as one of the most resource-intensive sectors, accounting for approximately 40% of global energy consumption and nearly 30% of energy-related greenhouse gas (GHG) emissions [1]. In the face of accelerating climate change and strict international environmental regulations, the civil engineering discipline is undergoing a fundamental transformation. The traditional paradigm of structural design, which primarily aims to ensure structural integrity, code compliance, and economic feasibility, is no longer sufficient to meet the demands of modern society. Today, engineers are tasked with a more complex challenge: designing structures that are not only safe and cost-effective but also environmentally sustainable throughout their entire life cycle [2].

This shift towards sustainable structural design requires balancing conflicting objectives, making it an inherently complex mathematical problem. In conventional engineering practice, optimization generally equates to weight or cost minimization [3]. However, minimizing the cost of a structure does not necessarily result in the minimum environmental impact. For instance, utilizing a high-strength, low-volume material might reduce the overall structural weight, but the manufacturing process of that specific material could possess a significantly higher embodied carbon footprint. Therefore, integrating sustainability into structural design mandates a multi-objective optimization (MOO) approach, where

environmental metrics, such as embodied energy, carbon emissions, and resource circularity, are evaluated concurrently with traditional mechanical and economic constraints [4].

To solve these highly non-linear and constrained engineering problems, researchers have increasingly turned to advanced computational methods. Over the past two decades, meta-heuristic algorithms have proven to be highly effective in navigating the complex search spaces of structural optimization [5]. Unlike classical gradient-based methods, these algorithms can efficiently handle discrete variables (such as standard steel sections or rebar diameters) and multiple conflicting objective functions without getting trapped in local optima. Despite the rapid proliferation of these algorithms in academic literature, their application strictly within the context of environmental sustainability reveals distinct trends and notable deficiencies [6].

This paper aims to provide a critical review of the current state-of-the-art optimization methodologies applied to sustainable structural design. By mapping the recent literature, this study explores how environmental objectives are mathematically formulated and integrated into optimization frameworks. Furthermore, it identifies critical research gaps, including the computational bottlenecks of MOO algorithms, the over-simplification of Life Cycle Assessment (LCA) data in mathematical models, and the disconnect between theoretical algorithmic success and practical implementation in the construction industry. Ultimately, this review seeks to guide future interdisciplinary research at the intersection of civil engineering, environmental science, and computational optimization.

II. Materials and Method

A. *Traditional vs. Environmental Objective Functions in Structural Optimization*

In structural optimization, the objective function acts as the mathematical compass guiding the algorithmic search toward the most desirable design outcome. For decades, this compass has been strictly calibrated to prioritize economic and mechanical efficiency, treating structural weight and direct construction costs as the ultimate indicators of a successful design. However, the escalating global climate crisis and the construction industry's significant ecological footprint have exposed the critical limitations of this conventional approach. As sustainability becomes a regulatory imperative rather than an optional feature, the definition of an "optimal" structure is undergoing a profound paradigm shift. This section examines the fundamental transition from traditional, cost-centric objective formulations to the integration of comprehensive environmental metrics, highlighting how this shift alters the mathematical landscape of structural engineering. Comparison of Traditional and Sustainable Structural Optimization Paradigms is given in Table 1.

Table 1. Comparison of Traditional and Sustainable Structural Optimization Paradigms

Feature	Traditional Optimization	Sustainable Optimization
Primary Objective(s)	Minimum weight, Minimum material cost	Minimum Embodied Carbon (EC), Life Cycle Energy (LCE), Cost
Problem Type	Single-Objective (usually)	Multi-Objective Optimization (MOO)
Algorithm Preference	Gradient-based or simple heuristics	Advanced Meta-heuristics (NSGA-II, MOPSO)
Data Requirements	Material density, unit price, mechanical properties	LCA databases (e.g., Ecoinvent), emission factors, supply chain data
Final Output	A single deterministic "best" design	A Pareto-optimal set (trade-off frontier)
Design Constraints	Structural codes (stress, deflection, buckling)	Structural codes + Constructability + Emission caps

B. *The Shift from Weight and Cost Minimization*

Historically, structural optimization has been driven by economic and mechanical efficiency. The primary objective function in traditional formulations is almost exclusively the minimization of structural weight or direct material cost, subjected to constraints like stress, displacement, and buckling limits

defined by design codes. In these classical models, the volume of materials—such as concrete and structural steel—serves as a direct proxy for cost. Consequently, the optimization algorithms are designed to remove "excess" material, pushing the structural members to their maximum allowable capacities. While this approach effectively reduces initial construction expenses, it operates on a fundamentally flawed assumption in the context of modern sustainability: that the lightest or cheapest structure is inherently the most environmentally friendly.

C. Transitioning to Carbon Footprint and Life Cycle Energy

As the climate crisis intensifies, the definition of structural efficiency has expanded. Modern objective functions now incorporate environmental metrics, predominantly focusing on Embodied Carbon (EC) and Life Cycle Energy (LCE). The embodied carbon footprint accounts for all greenhouse gas emissions associated with the extraction, manufacturing, transportation, and assembly of building materials. Integrating these metrics transforms the mathematical nature of the problem. Minimizing embodied carbon introduces emission factors (CO_2-eq/kg) into the objective function. Because low-carbon materials (e.g., recycled steel, geopolymers, or timber) often exhibit different mechanical properties and cost profiles compared to conventional materials, minimizing weight no longer guarantees minimized emissions. Furthermore, incorporating Life Cycle Assessment (LCA) requires the optimization model to look beyond the construction phase, accounting for maintenance, operational energy interactions (such as thermal mass effects in building envelopes), and end-of-life recycling potentials. This necessitates a shift from single-objective to multi-objective problem formulations.

D. Current Optimization Methodologies in Sustainable Design

The integration of environmental sustainability into structural design fundamentally alters the computational complexity of the optimization process. When metrics such as embodied carbon, material circularity, and life cycle energy are introduced alongside traditional mechanical constraints, the design space becomes highly non-linear, discrete, and multidimensional. Furthermore, because these modern environmental goals frequently conflict with direct economic costs, conventional trial-and-error design iterations and classical mathematical programming techniques are increasingly insufficient. To successfully navigate these intricate trade-offs and discover structural configurations that are both safe and ecologically viable, researchers and engineers must rely on advanced computational search strategies. This section explores the primary methodologies driving modern sustainable structural design, focusing specifically on the deployment of meta-heuristic algorithms and the application of multi-objective decision-making frameworks to resolve conflicting design parameters.

E. Metaheuristic and Evolutionary Approaches in Structural Problems

The integration of environmental metrics, discrete material variables (such as standard cross-section catalogs or specific rebar diameters), and highly non-linear constraints makes sustainable structural optimization a non-convex and highly complex mathematical challenge. Traditional gradient-based mathematical programming methods often struggle with these discrete variables and are prone to converging on local optima.

To overcome these limitations, researchers heavily rely on meta-heuristic and evolutionary algorithms. Techniques such as Genetic Algorithms (GA) [7], Particle Swarm Optimization (PSO) [8], and newer nature-inspired search algorithms [9-11] have become the industry standard. These algorithms explore the design space stochastically, allowing for a robust evaluation of complex, non-differentiable structural models without requiring gradient information. In sustainable design, these algorithms evaluate thousands of potential structural configurations, iteratively improving the design pool toward optimal material distribution that satisfies both structural integrity and environmental targets.

F. Multi-Objective Optimization (MOO) Strategies

Because cost, structural weight, and environmental impact are frequently conflicting objectives, for instance, utilizing high-performance but energy-intensive materials might reduce structural volume but

increase the total carbon footprint, sustainable design cannot be reduced to a single "best" solution. Instead, Multi-Objective Optimization (MOO) strategies are employed to find trade-offs.

These strategies focus on generating a set of Pareto-optimal solutions, where no single objective can be improved without degrading another. Algorithms such as the Non-dominated Sorting Genetic Algorithm (NSGA-II) [12] or Multi-Objective Particle Swarm Optimization (MOPSO) [13] are widely used to identify these trade-off frontiers. Additionally, techniques like the Normal Boundary Intersection (NBI) method are highly effective in generating an evenly distributed Pareto front, providing decision-makers with a clear, quantitative spectrum of design alternatives ranging from the "most economical" to the "most ecologically sustainable" configurations. This enables engineers and stakeholders to make informed, data-driven decisions that balance the initial budget with long-term climate goals.

III. Trends and Research Gaps in the Literature

Despite the rapid proliferation of sustainable optimization studies in recent years, a critical examination of the literature reveals a significant disconnect between advanced computational research and its practical implementation in the civil engineering industry. While academic studies frequently propose highly sophisticated algorithms capable of finding mathematically perfect Pareto frontiers, these models often rely on idealized assumptions that do not reflect the complexities of real-world construction. Identifying and addressing these existing research gaps is essential for transitioning sustainable structural optimization from a theoretical exercise into an applied engineering tool

A. The Adaptation Problem of Theoretical Algorithms to Practical Construction Applications

A primary trend in the current literature is the intense focus on algorithmic novelty, such as developing hybrid meta-heuristic variants or embedding artificial intelligence techniques, often tested on simplified, standard benchmark problems (e.g., planar trusses or simplistic frame structures). However, there is a pronounced gap in adapting these theoretical models to practical construction applications. Real-world structures involve highly complex load combinations, irregular geometries, and strict design code provisions. Furthermore, optimization algorithms frequently ignore "constructability" constraints. A mathematically optimal design might propose highly irregular cross-sections or complex reinforcement layouts that require excessive labor, customized formwork, or complicated assembly processes. Consequently, while the algorithm minimizes material volume or theoretical carbon emissions, the resulting design may be entirely impractical, overly expensive, or labor-intensive to actually build. Future research must prioritize the integration of constructability and standard manufacturing dimensions into the optimization constraints to ensure the generated solutions are viable for the construction site.

B. Lack of Integration Between Environmental Databases and Mathematical Models

Another significant research gap lies in the static and oversimplified treatment of environmental data within optimization loops. To calculate objective functions like embodied carbon or life cycle energy, algorithms require specific environmental impact factors (e.g., $kgCO_2$-eq per unit volume). Currently, most structural optimization models assign deterministic, generic, and static values extracted from literature or isolated Life Cycle Assessment (LCA) software. However, in reality, the environmental impact of construction materials is highly dynamic; it fluctuates based on regional manufacturing practices, supply chain transportation distances, and the local energy grid. There is a distinct lack of dynamic interoperability between structural optimization environments (such as computational models developed in MATLAB) and comprehensive, regionalized environmental databases (like Ecoinvent). Without a seamless, automated integration where optimization algorithms can query real-time, localized environmental data, the optimization results will remain generalized estimates rather than precise, actionable sustainability metrics.

IV. DISCUSSION

The synthesis of the current literature underscores that integrating environmental sustainability into structural design is not merely a parametric adjustment, but a fundamental paradigm shift in civil engineering philosophy. The findings reveal a persistent tension between economic viability and

ecological responsibility. In many practical scenarios, structural configurations that yield the lowest embodied carbon footprint, often through the use of advanced, low-impact, or recycled materials, do not align with the absolute minimum financial cost.

This inherent conflict highlights the indispensable role of Multi-Objective Optimization (MOO). Rather than dictating a single, deterministic "best" design, generating a Pareto-optimal frontier empowers stakeholders to visualize the exact trade-offs between cost and emissions. However, the literature suggests that the final selection from this Pareto set cannot be resolved by mathematical algorithms alone; it fundamentally relies on external drivers such as carbon taxation, stringent governmental regulations, and green building certification incentives.

Furthermore, the prevalent research gaps regarding constructability and dynamic data integration present a significant barrier to industry adoption. As long as optimization frameworks operate in isolated computational environments (such as theoretical scripts running purely in mathematical software like MATLAB) without real-time links to localized supply chain constraints and dynamic Life Cycle Assessment (LCA) databases, the generated solutions will remain largely academic. To bridge this gap, future research must foster interdisciplinary collaboration. Structural engineers, environmental scientists, and software developers must co-create integrated design platforms where algorithmic efficiency is matched with real-world constructability and accurate, localized environmental accounting. Conceptual representation of a Pareto-optimal frontier demonstrating the trade-off between structural cost and embodied carbon emissions is presented in Fig. 1.

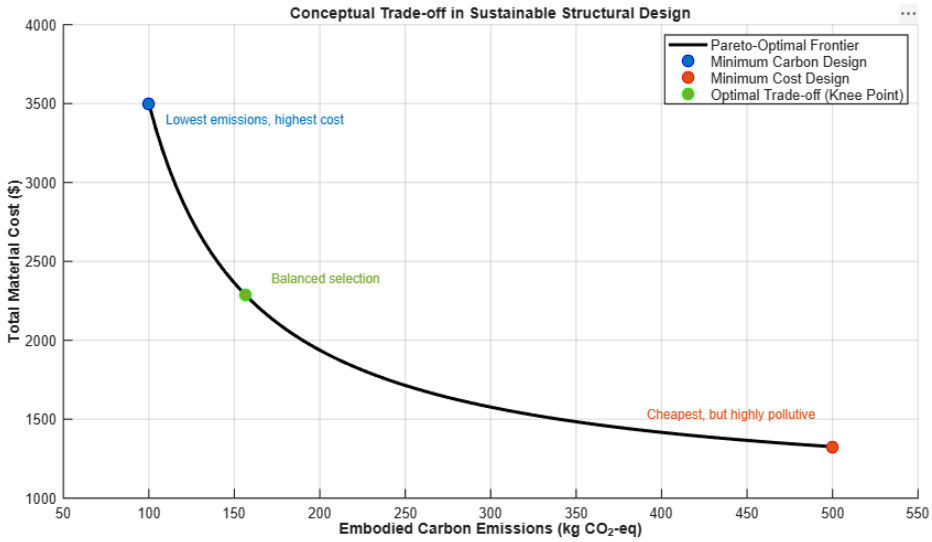

Fig. 1 Conceptual representation of a Pareto-optimal frontier demonstrating the trade-off between structural cost and embodied carbon emissions

V. CONCLUSION

The transition toward sustainable structural engineering has fundamentally redefined the objectives of structural design. As this review demonstrates, minimizing material cost and weight is no longer synonymous with achieving optimal design. The inclusion of environmental metrics, such as embodied carbon and life cycle impacts, has transformed structural optimization into a complex, multi-objective problem that requires advanced computational strategies. Meta-heuristic algorithms and Multi-Objective Optimization (MOO) methodologies have proven indispensable in navigating these non-linear, constrained design spaces, offering decision-makers a spectrum of trade-offs between economic feasibility and ecological responsibility.

However, for these advanced methodologies to create a tangible impact on global greenhouse gas reduction targets, the structural engineering community must address critical gaps in the current literature.

Future directions must focus on bridging the divide between theoretical optimization and practical engineering. This entails developing algorithms that respect constructability constraints, ensuring that mathematically optimal designs are also practically buildable. Furthermore, establishing dynamic, automated data pipelines between algorithmic modeling environments and regional environmental databases is crucial for accurate and localized carbon accounting. Ultimately, sustainable structural optimization must evolve from isolated mathematical simulations into integrated, holistic design frameworks that empower engineers to construct a truly resilient and low-carbon built environment.

REFERENCES

[1] I. E. A. IEA (2022) Buildings.

[2] X. Zhang and J. Zhang (2025) Life Cycle Sustainable Design Optimization of Building Structural Components: A Hybrid Approach Incorporating Genetic Algorithm and Machine Learning. Sustainability10449.

[3] A. Mortazavi. "Marathon runner algorithm: theory and application in mathematical, mechanical and structural optimization problems", *Materials Testing*, vol.66(8),pp. 1267-91, 2024.

[4] I. Negrin, M. Kripka and V. Yepes. "Multi-criteria optimization for sustainability-based design of reinforced concrete frame buildings", *Journal of Cleaner Production*, vol.425(pp. 139115, 2023.

[5] M. Moloodpoor and A. Mortazavi. "A Comparative Review of Fuzzy Reinforced Search Algorithms: Methods and Applications", *Archives of Computational Methods in Engineering*, vol.32(6),pp. 3933 - 77, 2025.

[6] J. L. J. Pereira, M. B. Francisco, B. J. Ma, G. F. Gomes and A. C. Lorena. "Golden lichtenberg algorithm: a fibonacci sequence approach applied to feature selection", *Neural Computing and Applications*, vol.36(32),pp. 20493-511, 2024.

[7] J. Holland, *Genetic Algorithms and Adaptation*. In: Adaptive Control of Ill-Defined Systems, Boston, MA: Springer US, 1984,

[8] J. Kennedy and R. Eberhart (1995) Particle swarm optimization. Neural Networks, 1995 Proceedings, IEEE International Conference on1942-8 vol.4.

[9] K. S. Lee and Z. W. Geem. "A new structural optimization method based on the harmony search algorithm", *Computers & Structures*, vol.82(9),pp. 781-98, 2004.

[10] E. Rashedi, H. Nezamabadi-pour and S. Saryazdi. "GSA: A Gravitational Search Algorithm", *Information Sciences*, vol.179(13),pp. 2232-48, 2009.

[11] I. Matoušová, P. Trojovský, M. Dehghani, E. Trojovská and J. Kostra. "Mother optimization algorithm: a new human-based metaheuristic approach for solving engineering optimization", *Scientific Reports*, vol.13(1),pp. 10312, 2023.

[12] K. Deb, A. Pratap, S. Agarwal and T. Meyarivan. "A fast and elitist multiobjective genetic algorithm: NSGA-II", *IEEE transactions on evolutionary computation*, vol.6(2),pp. 182-97, 2002.

[13] V. Mokarram and M. R. Banan. "A new PSO-based algorithm for multi-objective optimization with continuous and discrete design variables", *Structural and Multidisciplinary Optimization*, vol.57(2),pp. 509-33, 2018.

8th International Conference on Engineering, Natural and Social Sciences

September 06-07, 2026: Konya, Turkey

© 2026 Published by All Sciences Academy

https://www.icensos.com/

Environmental Performance Criteria and Greenhouse Gas Mitigation Policies for Climate Change Adaptation in the Construction Sector

Ali Mortazavi

Civil Engineering Department, Izmir Democracy University, Turkey

(ali.mortazavi@idu.edu.tr) Email of the corresponding author

Abstract – In the global effort to combat climate change, the construction sector occupies a highly critical position: it is simultaneously one of the largest contributors to global greenhouse gas (GHG) emissions and a domain directly vulnerable to the physical impacts of the climate crisis. This paper examines the construction industry's adaptation to climate change and evaluates the current criteria that determine the environmental performance of buildings from a policy perspective. The study critically assesses national and international regulatory frameworks aimed at mitigating both operational emissions, stemming from building energy consumption, and embodied emissions generated during material production. Furthermore, the alignment between established environmental performance certification systems (such as LEED and BREEAM) and global GHG mitigation targets is analyzed. The findings emphasize that climate adaptation strategies in the built environment must not be restricted merely to structural resilience against extreme weather events. Instead, there is an urgent need for holistic policy frameworks that seamlessly integrate passive design criteria, advanced thermal insulation practices, and circular economy principles.

Keywords – Climate Change Adaptation, Greenhouse Gas (GHG) Mitigation, Environmental Performance, Green Building Certifications, Construction Policies

I. INTRODUCTION

Climate change represents the most profound environmental and socio-economic challenge of the 21st century, fundamentally altering the operational dynamics of nearly every global industry. Among these, the construction and built environment sector holds a dual, paradoxical role. On one hand, buildings and construction activities are primary drivers of global warming, accounting for nearly 40% of global energy consumption and approximately one-third of total greenhouse gas (GHG) emissions [1]. On the other hand, civil infrastructure and residential buildings are highly susceptible to the physical manifestations of climate change, including increased frequencies of extreme weather events, shifting temperature baselines, and urban heat island effects. Consequently, adapting the construction sector to climate change is no longer a localized engineering concern but a critical global policy imperative [2].

Understanding the GHG dynamics within the construction sector requires differentiating between two primary emission categories: operational carbon and embodied carbon [3]. Historically, environmental policies and building codes have predominantly targeted operational emissions, the energy consumed during the lifespan of a building for heating, cooling, lighting, and ventilation. While substantial progress has been made in improving operational energy efficiency, the focus is now rapidly shifting toward embodied emissions. These are the emissions intrinsically tied to the extraction, manufacturing, transportation, and assembly of construction materials like cement, steel, and insulation products. As buildings become more energy-efficient operationally, embodied carbon represents an increasingly dominant fraction of a structure’s total life-cycle carbon footprint [4].

To effectively manage these complex dynamics, the industry must pursue two parallel strategies: mitigation and adaptation. Mitigation focuses on the drastic reduction of GHG emissions to limit global temperature rise, whereas adaptation involves designing and retrofitting buildings to withstand the unavoidable environmental shifts that are already underway. Bridging the gap between these two strategies requires robust environmental performance criteria and enforceable policies.

This paper provides a comprehensive review of the contemporary policies and performance metrics driving the construction sector's response to climate change. By examining the intersection of climate adaptation and GHG mitigation, this study evaluates the efficacy of current green building certifications, Life Cycle Assessment (LCA) methodologies, and emerging regulations such as nearly Zero-Energy Building (nZEB) standards. Ultimately, the objective is to highlight the necessity of integrated policy frameworks that promote not only structural durability but also deep, systemic decarbonization across the built environment.

II. Materials and Method

A. Climate Change Adaptation and Mitigation Strategies in the Built Environment

The response of the built environment to the escalating climate crisis is governed by two fundamental, yet distinct, pillars of climate action: mitigation and adaptation. Traditionally, environmental policies and engineering frameworks have treated these strategies in isolation. Mitigation seeks to address the root cause of climate change by aggressively reducing greenhouse gas (GHG) emissions. In the construction sector, this is achieved through enhanced operational energy efficiency, the integration of renewable energy systems, and the transition toward low-carbon building materials. Conversely, adaptation operates on the premise that a certain degree of climatic shift is already inevitable. It focuses on reducing the vulnerability of civil infrastructure to physical climate risks, such as extreme temperature fluctuations, intensified precipitation, severe storm events, and the urban heat island effect.

However, as the impacts of climate change accelerate, treating mitigation and adaptation as separate disciplines has proven to be a fundamentally flawed paradigm. The modern built environment requires policies that recognize and exploit the complex intersection between these two concepts. The most effective structural and architectural interventions are those that generate mutual synergies. A prime example is the implementation of advanced building envelopes and passive design strategies. High-performance thermal insulation, optimized window-to-wall ratios, and strategic shading systems drastically reduce the operational energy required for mechanical cooling, directly mitigating GHG emissions. Simultaneously, these exact features serve as vital adaptation mechanisms, protecting occupants from severe heatwaves, reducing indoor thermal stress, and ensuring habitability during power outages. Similarly, the integration of green infrastructure, such as green roofs and permeable pavements, acts as a carbon sink and reduces cooling loads (mitigation), while simultaneously managing stormwater runoff and alleviating urban heat (adaptation).

Despite these synergies, policymakers and engineers must also navigate inherent conflicts where adaptation and mitigation goals clash. Adaptation strategies heavily focused on structural resilience often demand the extensive use of energy-intensive materials. For instance, fortifying a coastal structure with massive volumes of concrete and steel to withstand future hurricanes will significantly increase the building's embodied carbon, thereby undermining mitigation efforts. If adaptation is prioritized without considering the carbon footprint, the construction sector risks creating a negative feedback loop: building heavier structures to survive a changing climate, which in turn emits more GHGs and accelerates the very climate change they are designed to withstand.

Therefore, future construction policies must enforce a coupled approach, often termed "climate-responsive" or "climate-resilient and low-carbon" design. This requires that every structural, material, and architectural decision be evaluated through a dual lens, ensuring that adaptation measures do not compromise GHG mitigation targets, and vice versa.

B. *Environmental Performance Criteria and Certifications in Buildings*

To effectively implement and monitor climate adaptation and mitigation strategies, the construction sector relies on standardized environmental performance criteria. These criteria serve as the benchmark for evaluating how sustainable a building truly is, transitioning the industry from subjective claims of "green design" to quantifiable environmental accounting. This evaluation is primarily governed by comprehensive methodological frameworks and market-driven certification systems [5].

C. *The Life Cycle Assessment (LCA) Approach*

At the core of modern environmental performance evaluation is the Life Cycle Assessment (LCA) methodology. Historically, environmental regulations in construction focused almost exclusively on the operational phase of a building. However, LCA introduces a "cradle-to-grave" (or increasingly, "cradle-to-cradle") perspective. It quantifies the cumulative environmental impacts across all stages of a building's life: raw material extraction, manufacturing, transportation, construction, operation, maintenance, and end-of-life demolition and recycling [6].

In the context of greenhouse gas mitigation, LCA is indispensable for preventing "carbon leakage", a scenario where emissions are simply shifted from one phase to another. For example, implementing excessively thick layers of petrochemical-based insulation might drastically reduce a building's operational energy consumption [7]. However, an LCA might reveal that the embodied carbon emitted during the manufacturing of that insulation outweighs the operational carbon saved over the building's lifespan. By utilizing LCA, policymakers and engineers can establish holistic performance criteria that mandate genuine, net-positive carbon reductions rather than superficial energy savings.

D. *Energy Efficiency Standards and Green Building Certifications*

The practical application of environmental criteria is enforced through a combination of mandatory national standards and voluntary certification systems. National building codes, such as the TS 825 (Thermal Insulation Requirements for Buildings) in Turkey [8], establish the mandatory regulatory baseline. Standards like TS 825 dictate the minimum thermal resistance for building envelopes based on regional climate zones, ensuring a baseline reduction in operational heating and cooling demand. While crucial, these mandatory codes are often conservative, updating slowly and predominantly focusing on operational energy rather than holistic climate adaptation or embodied carbon.

To push the market beyond baseline compliance, voluntary green building certifications such as LEED (Leadership in Energy and Environmental Design) and BREEAM (Building Research Establishment Environmental Assessment Method) have gained global prominence. These systems evaluate buildings across multiple categories, including energy efficiency, water conservation, material selection, and indoor environmental quality.

Despite their success in mainstreaming sustainable design, these certification frameworks face growing scrutiny regarding their alignment with absolute GHG mitigation targets. A frequent critique is the "point-chasing" phenomenon, where developers can achieve high certification tiers by accumulating easily attainable points (e.g., installing bicycle racks or specifying low-VOC paints) while neglecting deep decarbonization strategies. Furthermore, until recently, these systems heavily weighted operational energy efficiency, treating comprehensive LCA and embodied carbon accounting as optional credits rather than mandatory prerequisites. For the built environment to genuinely adapt to and mitigate climate change, environmental performance criteria must evolve from point-based checklists into strict, LCA-driven carbon budgets enforced by legislation. Comparison of environmental performance frameworks in the built environment is given in Table 1.

III. Discussion: The Evolution and Efficacy of Current Mitigation Policies

The synthesis of current adaptation strategies and environmental performance criteria reveals a critical transition phase within the construction sector. As established in the preceding sections, voluntary green building certifications and baseline energy codes (such as TS 825) have been instrumental in raising early awareness. However, the literature and current market trends indicate that these mechanisms are

insufficient to achieve the deep decarbonization required by global climate agreements. The industry is now grappling with the transition from voluntary, point-based checklists to mandatory, legally binding regulations. This shift brings forth significant policy debates, particularly regarding the implementation of nearly Zero-Energy Building (nZEB) standards and the macroeconomic impact of carbon pricing.

Table 1. Comparison of Environmental Performance Frameworks in the Built Environment

Framework Type	Examples	Primary Focus	Enforcement	Key Limitation / Criticism
National Energy Codes	TS 825, ASHRAE 90.1	Operational Energy (Heating/Cooling)	Mandatory (Legal code)	Ignores embodied carbon and full Life Cycle Assessment (LCA).
Green Certifications	LEED, BREEAM	Multi-criteria (Water, Energy, Materials)	Voluntary (Market-driven)	Prone to "point-chasing"; deep decarbonization is often optional.
Advanced Directives	nZEB (EPBD)	Near-zero operational energy + Renewables	Mandatory (in EU for new builds)	May increase embodied carbon due to heavy technological systems.
Whole-Life Carbon	Emerging LCA mandates	Total Life-Cycle GHG Emissions	Emerging / Pilot policies	Lacks standardized regional databases and dynamic pricing integration.

A. The Operational vs. Embodied Carbon Debate in nZEB Frameworks

A primary point of discussion in contemporary construction policy is the efficacy of the nearly Zero-Energy Building (nZEB) directive [9]. While nZEB represents a monumental leap in reducing operational energy consumption through passive design and on-site renewables, its early implementations highlighted a fundamental flaw discussed earlier: the neglect of the Life Cycle Assessment (LCA) perspective. Achieving “zero-energy” operational status frequently necessitates the integration of complex, highly processed insulation materials and heavy technological systems (e.g., PV panels, advanced HVAC). From a critical policy standpoint, this creates a “carbon penalty.” The embodied carbon emitted during the manufacturing of these advanced systems can sometimes negate the operational carbon saved over the building's lifespan. Consequently, the current policy discourse is rightfully arguing for a paradigm shift from “operational net-zero” to “whole-life net-zero” carbon, which would mandate that nZEB regulations enforce strict embodied carbon caps alongside operational efficiency. The shift in life-cycle carbon dominance: As buildings transition from standard codes to nZEB frameworks, embodied carbon becomes the primary contributor to total emissions in given in Fig. 1.

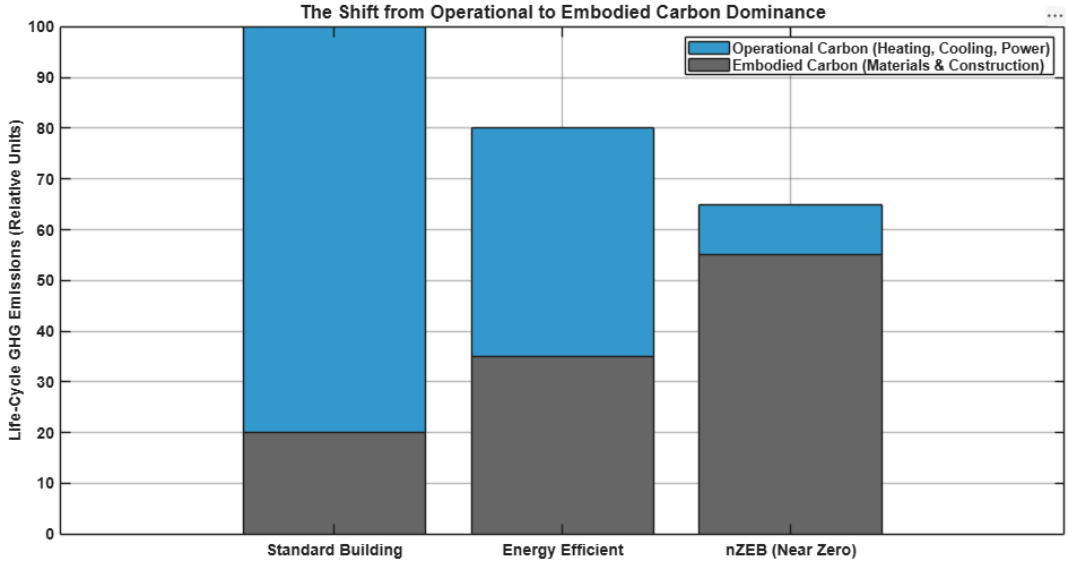

Fig. 1 The shift in life-cycle carbon dominance: As buildings transition from standard codes to nZEB frameworks, embodied carbon becomes the primary contributor to total emissions.

B. *Carbon Pricing as the Ultimate Market Driver*

Furthermore, the discussion surrounding environmental performance criteria is incomplete without addressing the economic realities of structural design. The reliance on voluntary certifications like LEED often fails to shift the broader market because carbon-intensive materials (such as traditional Portland cement) remain artificially cheap, as their environmental degradation is treated as an externalized cost. To effectively bridge the gap between climate adaptation and mitigation, policymakers are increasingly turning to carbon pricing and Emissions Trading Systems (ETS).

By attaching a direct financial penalty to greenhouse gas emissions across the supply chain, carbon pricing forces the internalization of environmental costs. This macroeconomic mechanism addresses the shortcomings of voluntary criteria by making carbon-intensive construction financially unviable. It acts as the ultimate catalyst, compelling stakeholders to adopt the rigorous LCA practices discussed in Section 3, penalizing material waste, and making low-carbon alternatives (e.g., geopolymers, recycled steel) economically competitive. Ultimately, the discussion indicates that structural engineering decisions in the near future will be driven not just by mechanical codes, but by the financial dictates of global carbon markets.1.

IV. CONCLUSION

The escalating physical and regulatory pressures of global climate change mandate a transformative approach within the construction sector. As this paper has demonstrated, it is no longer sufficient to treat climate adaptation and greenhouse gas (GHG) mitigation as isolated engineering objectives. Designing structures solely to withstand extreme climatic events without considering their embodied carbon footprint risks creating a negative feedback loop, where adaptation efforts inadvertently accelerate the very climate crisis they seek to survive. Conversely, focusing exclusively on operational energy reduction through the excessive use of carbon-intensive materials undermines the fundamental goals of sustainability. To align the built environment with global climate targets, a paradigm shift from voluntary guidelines and operational-centric codes to mandatory, holistic "whole-life carbon" frameworks is imperative. Based on the synthesis of current methodologies, certifications, and market dynamics, the following policy recommendations are proposed for the future of building regulations:

- Integration of Mandatory Life Cycle Assessments (LCA) into National Codes: National building codes (such as TS 825) must evolve beyond establishing minimum thermal insulation capacities. Future regulations should legally mandate Life Cycle Assessments for all new construction and major retrofits, establishing strict, quantifiable caps not only on operational energy but also on the embodied carbon of structural systems and building envelopes.
- Transitioning from "Operational Net-Zero" to "Whole-Life Net-Zero": Advanced frameworks like nZEB (nearly Zero-Energy Buildings) and prestigious green building certifications (e.g., LEED, BREEAM) must redefine their ultimate objectives. Policies should eliminate point-based loopholes that reward superficial green features and instead enforce strict carbon budgets that require the embodied carbon of advanced energy systems to be offset by genuine life-cycle emission savings.
- Expansion of Carbon Pricing and Circular Economy Incentives: To bridge the economic gap between traditional and sustainable construction, policymakers must aggressively expand carbon pricing mechanisms across the construction material supply chain. Simultaneously, policies should financially incentivize circular economy principles, such as the reuse of structural steel, the recycling of concrete aggregates, and the design for deconstruction, ensuring that low-carbon materials become the financially viable default rather than a premium alternative.

Ultimately, navigating the climate crisis requires the construction sector to view environmental performance not as an optional addition, but as a foundational pillar of structural and architectural design. By implementing robust, scientifically backed, and economically enforced policies, the built environment can successfully transition from being a primary driver of climate change to a resilient, low-carbon ecosystem.

REFERENCES

[1] I. E. A. IEA (2022) Buildings.

[2] IEA (2025) Global Energy Review 2025. CC BY 4.0 ed. Paris: IEA; p.

[3] X. Zhang and X. Zhang. "Sustainable design of reinforced concrete structural members using embodied carbon emission and cost optimization", *Journal of Building Engineering*, vol.44(pp. 102940, 2021.

[4] M. Afzal, R. Y. Li, M. F. Ayyub, M. Shoaib and M. Bilal (2023) Towards BIM-Based Sustainable Structural Design Optimization: A Systematic Review and Industry Perspective. Sustainability15117.

[5] E. Giama and A. M. Papadopoulos. "Sustainable building management: overview of certification schemes and standards", *Advances in Building Energy Research*, vol.6(2),pp. 242-58, 2012.

[6] I. Zabalza Bribián, A. Aranda Usón and S. Scarpellini. "Life cycle assessment in buildings: State-of-the-art and simplified LCA methodology as a complement for building certification", *Building and Environment*, vol.44(12),pp. 2510-20, 2009.

[7] Z. Zhou, Y. Wang, J. Alcalá and V. Yepes. "Research on coupling optimization of carbon emissions and carbon leakage in international construction projects", *Scientific Reports*, vol.14(1),pp. 10752, 2024.

[8] S. Dilmac and N. Kesen. "A comparision of new Turkish thermal insulation standard (TS 825), ISO 9164, EN 832 and German regulation", *Energy and Buildings*, vol.35(2),pp. 161-74, 2003.

[9] C. Maduta, D. D'Agostino, S. Tsemekidi-Tzeiranaki and L. Castellazzi. "From Nearly Zero-Energy Buildings (NZEBs) to Zero-Emission Buildings (ZEBs): Current status and future perspectives", *Energy and Buildings*, vol.328(pp. 115133, 2025.

8th International Conference on Engineering, Natural and Social Sciences

September 06-07, 2026: Konya, Turkey

© 2026 Published by All Sciences Academy

https://www.icensos.com/

Taklit Öğrenme Kullanılarak Bir PID Kontrolcünün Taklit Edilmesi: Motor Pozisyon Kontrolü Üzerine Simulink Tabanlı Bir Çalışma

Halit HÜLAKO[1], Mehmet Latif LEVENT[2], Sertaç YAMAN[2],

[1]*Department of Mechanical Engineering /Faculty of Engineering, Hakkari University*
[2]*Department of Electrical-Electronics/ Faculty of Engineering, Hakkari University, Turkey*
Turkey(corresponding author: halithulako@hakkari.edu.tr)

Özet - Bu çalışmada, geleneksel bir PID konum kontrolcüsünün üretmiş olduğu tork komutlarını taklit etmek (imitation learning) amacıyla, doğrusal zamanlı ve seçici bir durum uzayı modeli (Selective State Space Model, SSM) mimarisi olan Mamba yapısının küçük ölçekli bir versiyonu tasarlanmış ve MATLAB Simulink ortamında bir motor sistemi üzerinde eğitilmiştir. Sistem, Simulink' te fiziksel motor ve PID kontrolcüsünü içeren bir benzetim döngüsü ile MATLAB tarafında çalışan bir Selective-SSM ağının karşılıklı veri alışverişi yapmasına dayanmaktadır. Bu çalışma, problemin tanımını, ilgili literatürü, sinir ağı mimarisinin matematiksel ve yazılımsal detaylarını, simülasyon deney düzeneğini ve elde edilen bulguların değerlendirmesini özetlemektedir.

1. Giriş

Endüstriyel ve robotik uygulamalarda motor pozisyon kontrolü büyük ölçüde PID kontrolcüler ile gerçekleştirilmektedir. PID kontrolcüler basit, yorumlanabilir ve düşük hesaplama maliyetine sahip olmalarına rağmen sürtünmeler, değişken yük ataletleri ve zamanla değişen dinamikler gibi etkiler karşısında performansları sınırlı kalabilmektedir. Son yıllarda, verilerdeki uzun menzilli bağımlılıkları verimli biçimde modelleyebilen durum uzayı modelleri (SSM), özellikle önerilen Mamba mimarisi ile, doğal dil işlemenin ötesinde zaman serisi ve kontrol problemlerinde de dikkat çekici bir alternatif haline gelmiştir.

Bu çalışmanın konusu, bir PID kontrolcüsünün giriş çıkış davranışını konum, hız ve hata sinyallerinden tork komutuna eşlemeyi taklit edebilen, öğrenilebilir ve seçici dinamik hafızaya sahip bir sinir ağı modelinin tasarlanması ve bunun gerçek zamanlı bir Simulink motor benzetimi üzerinde episodik biçimde eğitilmesidir. Amaç, nihai olarak PID'nin yerini alabilecek veya PID ile hibrit çalışabilecek, doğrusal olmayan dinamikleri öğrenebilen bir kontrol politikasının temelini oluşturmaktır. Çalışma, fiziksel motor modelinin Simulink'te Simscape blokları ile kurulması, referans tork sinyalini üreten bir PID döngüsünün oluşturulması, bu referans sinyali taklit etmek üzere bir Selective SSM ağının MATLAB tarafında yazılıp eğitilmesini kapsamaktadır.

Standart durum uzayı modelleri (Structured State Space Models, S4), Gu, Goel ve Ré tarafından önerilen uzun dizilerin doğrusal karmaşıklıkla ve kararlı biçimde modellenmesini mümkün kılmıştır [1]. S4 mimarisi, klasik doğrusal zamanla değişmeyen (LTI) durum-uzayı denklemlerini bir sinir ağı katmanı olarak ayrıklaştırarak kullanmakta ve Uzun Menzil Değerlendirmesi gibi kıyaslamalarda güçlü sonuçlar elde etmiştir.

Gu ve Dao tarafından 2023 yılında önerilen Mamba mimarisi, S4 hattının doğrudan devamı olarak, durum-uzayı parametrelerini özellikle örnekleme adımı, giriş ve çıkış izdüşüm matrisleri girdinin kendisinin bir

fonksiyonu haline getirerek seçicilik (selection) kavramını tanıtmıştır [2]. Bu sayede model, klasik zamanla değişmeyen SSM'lerin aksine, içeriğe bağlı olarak bilgiyi dizinin uzunluğu boyunca seçici biçimde ilerletebilmekte veya unutabilmektedir. Mamba, bu seçici SSM katmanını, kısa-menzilli bir 1B evrişim (Conv1D) katmanı ve bir kapılı doğrusal birim (Gated Linear Unit, GLU) yapısı ile birleştirerek dikkat mekanizması tasarımı sunmaktadır. Aynı ekip, 2024 yılında Mamba-2 çalışmasını yayımlamıştır [3].

Kontrol uygulamalarında, sinir ağı tabanlı denetleyicilerin PID' yi taklit etmesi, pekiştirmeli öğrenme tabanlı kontrol politikalarının eğitiminde ısınma veya hazırlık stratejisi olarak yaygın biçimde kullanılmaktadır. Bu çalışmadaki yaklaşım da benzer bir mantıkla, önce PID'nin ürettiği tork komutlarının bir SSM tarafından denetimli öğrenme yoluyla taklit edilmesini, ileride bu ağın pekiştirmeli öğrenme veya doğrudan optimal kontrol ile ince ayarlanmasına temel oluşturmasını hedeflemektedir. Literatürde SSM Mamba tabanlı yapıların doğrudan motor eyleyici düzeyinde kontrol taklidi için kullanımı henüz sınırlı sayıdadır. Bu bakımdan çalışma, Mamba'nın dizi modelleme yeteneklerinin klasik bir kontrol probleminde küçük ölçekte sınanması niteliğindedir.

2. Selective-SSM Mamba Sinir Ağı Mimarisi ve Simulink Episodik Veri Alışverişi Öğrenme Döngüsü

Fiziksel sistem, Simscape ortamında 200 gramlık bir katı gövde elemanı, bir döner mafsal ve bir Simulink-PS dönüştürücüsü kullanılarak modellenmiştir. Sistemin giriş tarafında bir PID bloğu, sabit bir referans değer "0.523 rad" ile mafsalın anlık konumu arasındaki hatayı toplama bloğu ile hesaplayarak bir tork komutu (pid_torque_out) üretmektedir. Bu tork, Brick Solid' e bir 'Saturation' bloğu üzerinden uygulanmaktadır. Mafsalın konum (q) ve hız (w) çıkışları, radyandan dereceye çevrilerek hem gözlem hem de durum vektörü (out.states_out) olarak dışa aktarılmaktadır. İkinci şemada, sisteme ek olarak bir 'mamba_step' MATLAB Fonksiyon bloğu eklenmiş, bu blok, öğrenilmiş ağırlıklarla anlık durumdan, bir tork tahmini u_k üreterek sistemi PID'den bağımsız biçimde de sürebilecek şekilde genişletilmiştir. Böylece model, hem PID referans verisini üretmek hem de eğitilen SSM ağını kapalı çevrimde test etmek için kullanılabilir hale gelmiştir. Oluşturulan sistem dinamiği ve kontrol yapısı Şekil 1 'de verilmiştir.

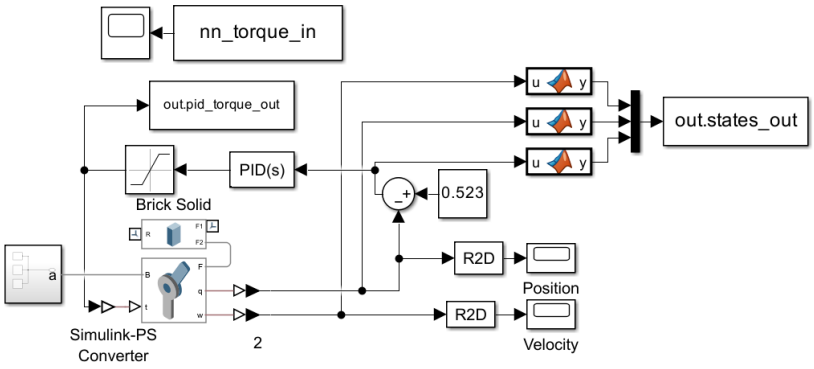

Şekil 1. Sistem dinamiği ve kontrol yapısı

Eğitim, MATLAB ile Simulink arasında episode bazlı bir döngü şeklinde kurgulanmıştır. Her episod' ta Simulink modeli sim() komutu ile bir episode zamanı kadar çalıştırılır. Daha sonra çıkış olarak durum vektörü (konum, hız, hata) ve PID'nin ürettiği referans tork sinyali alınır. Bu veriler dlarray formatına dönüştürülerek Selective-SSM ağının ileri ve geri yayılımında kullanılır. Hesaplanan gradyanlar ile Adam optimizasyon algoritması kullanılarak ağ ağırlıkları güncellenir. Güncellenmiş ağırlıklarla üretilen yeni tork tahmini, bir sonraki episod için nn_torque_in adlı zaman serisi olarak MATLAB çalışma alanına geri yazılır. Bu yapı, ağın PID'nin davranışını adım adım öğrenmesini ve öğrendikçe kendi ürettiği tahminlerin bir sonraki benzetimde de kullanılabilir hale gelmesini sağlamaktadır.

Önerilen ağ, girişte 3 boyutlu bir durum vektörünü $d_k \in \mathbb{R}^3$ konum, hız, hatayı alıp 1 boyutlu bir tork çıkışı üreten, 32 boyutlu gizli duruma sahip küçük ölçekli bir Mamba bloğudur. Mimari, sırasıyla aşağıdaki alt bileşenlerden oluşmaktadır. Sistem temel olarak, giriş sinyalini önce genişletip 1D konvolüsyon ve SiLU aktivasyonuyla yerel gürültülerden süzmekte, ardından zamana ve girişe bağımlı olarak değişen seçici parametrelerle Δ_k, B_k, C_k gizli durum hafızasını h_k güncellemekte ve kapılanmış (GLU) bir hat üzerinden nihai tork tahminini üretmektedir. Giriş vektörü d_k, durum işleme x_k ve kapılama z_k kollarına ayrıldıktan sonra kısa vadeli konvolüsyon filtresinden ve SiLU aktivasyonundan geçirilir.

$$d_k \in \mathbb{R}^3, \quad \begin{bmatrix} x_k \\ z_k \end{bmatrix} = W_{expand} d_k$$

Motordan gelen d_k, gürültü filtresi ve aktivasyon fonksiyonundan $x_{act} = \mathrm{SiLU}\big(\mathrm{Conv1D}(d_k)\big)$ geçirilerek temizlenir. Model, x_{act} durumuna bağlı olarak adım boyutunu Δ_k ve SSM parametrelerini dinamik olarak hesaplar, ardından sürekli durum matrislerini ayrıklaştırır.

$$\Delta_k = \mathrm{Softplus}(W_\Delta \cdot x_{act})$$

$$B_k = W_B x_{act}, \quad C_k = W_C x_{act}$$

$$\overline{A_k} = \exp(\Delta_k \odot A), \quad \overline{B_k} = \Delta_k \odot B_k$$

Sistemin gizli hafıza durumu $h_k \in R^{32}$ güncellenir, kapılama koluyla z_k birleştirilir ve nihai tork çıktısı τ_k elde edilir.

$$h_k = (\overline{A_k} \odot h_{k-1}) + (\overline{B_k} \odot x_{act})$$

$$y_{gated,k} = (C_k \odot h_k) \odot \mathrm{SiLU}(z_k)$$

$$\tau_k = W_{final} \cdot \big(W_{out} \cdot y_{gated,k}\big)$$

Durum matrisi A ise kararlılığı garanti altına almak amacıyla yalnızca negatif değerlerle başlatılmıştır. Kayıp fonksiyonu olarak, ağın ürettiği tork dizisi ile PID'nin ürettiği referans tork dizisi arasındaki Ortalama Karesel Hata (MSE) kullanılmıştır. Ortalama Karesel Hata (MSE) kayıp fonksiyonunun matematiksel ifadesi aşağıda verilen formülde hesaplanmıştır.

$$L_{\mathrm{MSE}} = \frac{1}{N} \sum_{k=1}^{N} \big(\tau_k - \tau_{\mathrm{PID},k}\big)^2$$

L_{MSE} Hesaplanan toplam kayıp değeri, N Simülasyon periyodundaki toplam veri zaman adımı sayısıdır ve bizim simülasyonumuzda 1500 olarak verilmiştir. τ_k Mamba ağının k. zaman adımında ürettiği tork tahminidir. $\tau_{\mathrm{PID},k}$ PID kontrolcünün k. zaman adımında ürettiği hedef/referans tork değeridir. Gradyanlar, MATLAB Deep Learning Toolbox'ın otomatik türev alma altyapısı olan dlarray, dlgradient, dlfeval ile hesaplanmış ve ağırlıklar Adam optimizasyon algoritması ile güncellenmiştir. Eğitim süreci episod bazlı ilerlemekte, her episod sonunda kayıp değeri gerçek zamanlı olarak bir grafik üzerinde izlenmektedir. Eğitim tamamlandığında, öğrenilen ağırlıklar dlarray formatından düz double matrislere dönüştürülerek bir .mat dosyasına kaydedilmektedir. Bu dosya, Simulink içerisindeki mamba_step MATLAB Fonksiyon bloğu tarafından kapalı çevrim tork üretimi için okunmaktadır.

Simülasyonda kullanılan temel parametreler Tablo 1'de özetlenmiştir.

Tablo 1. Simülasyonda kullanılan eğitim parametreleri

Parametre	***Değer***
Giriş boyutu	*3 (konum, hız, hata)*
Gizli durum boyutu	*32*
Çıkış boyutu	*1 (tork)*
Simülasyon süresi	*1.5 s*
Episod sayısı	*600*
Öğrenme oranı	*0.005 (Adam)*
Kayıp fonksiyonu	*Ortalama Karesel Hata (MSE)*

Referans konum sabit bir konum (0.523 rad) olarak seçilmiş, PID kontrolcüsü bu referansı takip edecek şekilde ayarlanmıştır. Her episodda 1.5 saniyelik bir benzetim çalıştırılmakta ve elde edilen zaman serisi, yani yaklaşık 1500 örnek, ağın eğitiminde kullanılmaktadır. Toplam 600 episodluk bir eğitim, mimarinin ve veri akışının doğruluğunu doğrulamaya yönelik bir ilk deneme niteliğindedir. Eğitim sonucu Şekil 2'deki düzenekte tekrardan sonuçları karşılaştırılmıştır.

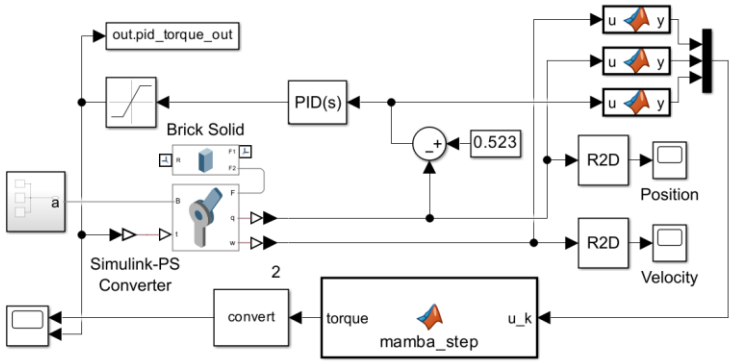

Şekil 2. Eğitim sonucunun düzenekte karşılaştırılması.

Eğitim süresince elde edilen MSE kayıp eğrisi, Mamba modelinin PID kontrolcünün tork davranışını başarıyla öğrendiğini göstermektedir. İlk episodlarda rastgele parametreler nedeniyle yüksek olan hata, ilerleyen adımlarda hızlı bir düşüş göstererek kararlı bir minimuma yakınsamıştır. Sonuçlar modelin aşırı salınım yapmadan PID yanıtını yüksek hassasiyetle taklit ettiğini doğrulamaktadır.

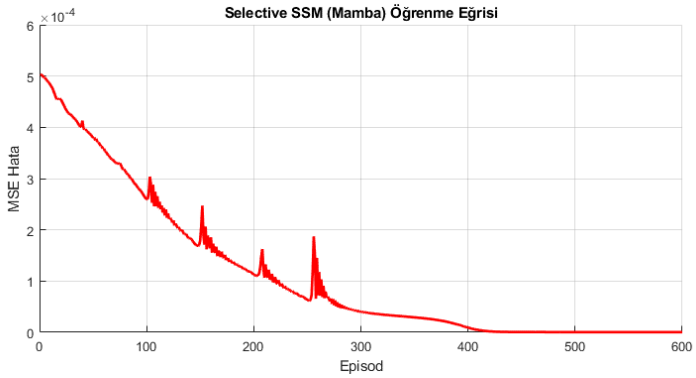

Şekil 2. Mamba tabanlı kontrolcünün PID referans torkunu taklit etme sürecindeki MSE kayıp değişimi. Modelin eğitim ilerledikçe hatayı kararlı bir şekilde düşürerek minimum seviyede yakınsadığı görülmektedir.

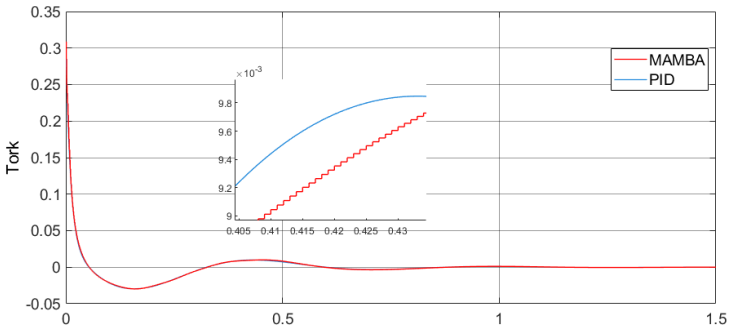

Şekil 3. Eğitim sonucunda PID ve MAMBA'nın tork sonuçlarının karşılaştırılması

3. Sonuç

Önerilen küçük ölçekli Selective-SSM mimarisi, klasik bir PID kontrolcüsünün ürettiği tork sinyalini denetimli öğrenme yoluyla taklit etmeyi hedeflemiştir. Mamba mimarisinin seçici durum-uzayı yaklaşımından esinlenilerek küçük ölçekli bir Selective-SSM ağı MATLAB'da sıfırdan gerçeklenmiş ve Simulink'teki bir motor PID benzetim döngüsü ile episodik biçimde eğitilerek PID'nin ürettiği tork komutlarını taklit etmesi sağlanmıştır. Bununla birlikte, 600 episodluk kısa eğitim süresi, tek bir sabit referans noktası ve görece küçük gizli durum boyutu göz önüne alındığında, sonuçların genellenebilirliği sınırlıdır. Farklı referans profilleri, değişken yük, atalet senaryoları ve daha uzun eğitim süreleri ile ağın sağlamlığının ayrıca sınanması gerekmektedir. Ayrıca, çalışmanın mevcut aşamasında ağ PID' yi taklit etmekte olup, PID' nin performansını aşan bağımsız bir kontrol politikası olarak henüz doğrulanmamıştır. Bu, gelecekteki pekiştirmeli öğrenme tabanlı ince ayar çalışmaları için doğal bir devam noktası oluşturmaktadır.

4. Kaynakça

[1] Gu, A., Goel, K., & Ré, C. (2022). Efficiently Modeling Long Sequences with Structured State Spaces (S4). International Conference on Learning Representations (ICLR).

[2] Gu, A., & Dao, T. (2023). Mamba: Linear-Time Sequence Modeling with Selective State Spaces. arXiv preprint arXiv:2312.00752.

[3] Dao, T., & Gu, A. (2024). Transformers are SSMs: Generalized Models and Efficient Algorithms Through Structured State Space Duality. International Conference on Machine Learning (ICML).

8th International Conference on Engineering, Natural and Social Sciences

September 06-07, 2026: Konya, Turkey

© 2026 Published by All Sciences Academy

https://www.icensos.com/

Comprehensive Multi Biomarker Profiling for Accurate Diagnosis of Pheochromocytoma

Brunilda Mezani[1,3] Anila Mitre[1,2]

[1] *Biology Department, Faculty of Natural Sciences, University of the Tirana, Albania,*

[2] *Immunological and Medical Director at the Intermedica Laboratories network, Albania,*

[3]*Department of Medical Laboratory Sciences and Imaging, Western Balkans University, Tirana, Albania*

brunilda.mezani@wbu.edu.al

Abstract - Background: Catecholamine are molecules produced in chromaffin cells of surrenal medulla gland and postganglionic sympathetic neurons which serve as key points in modulating the bodys response to stress factors.Pheochromacitomais a neuroendocrine tumor developing by chromaffin cells of surrenal gland by characterized of high level secretion of the chatecholamine.
Biochemical diagnosis process is realized on plasma free metanephrines, urinary fractioned metanephrines. Understanding the hormonal cross-talk in phaeochromocytoma could improve biochemical interpretation, simplify differential diagnosis and facilitate personalised patient management.
Objective: The research aims to explain the clinical interactions between catecholamine hypersecretion and hormonal biomarkers of pheochromocytoma patient by diagnostic value and their potentialrolein precesion endocrine medicine.
Methods: Blood samples of the patients were obtained from Intermedica Laboratory Clinic and results were analysed according to the instructions of the referring physicians.
Result: We analyse a clinical laboratory data collected from patients undergoing biochemical investigation for suspected or confirmed pheochromocytoma between 2017 and 2026. The source spreadsheet has only demographic data and catecholamine, metanephrine, biomarker results. The report focuses on what the data actually support. Patterns of catecholamine excess and cross marker (hormonal biomarker) relationships.
Conclusion: Hormonal interactions in catecholamine excess are not restricted to classical catecholamine metabolism but involve multiple endocrine regulatory systems, in particular the renin angiotensin aldosterone axis and metabolic hormone regulation. A more comprehensive hormonal biomarker approach may increase the accuracy of diagnosis, differential diagnosis and clinical decision making in phaeochromocytoma. Future prospective studies should define standardised panels of hormonal biomarkers and evaluate their use in precision endocrine diagnostics.

Key Words: Catecholamines, Metanephrine, Pheochromocytoma, Hormonal biomarkers, Endocrinology

Introduction

Patient Characteristics

The study included 58 patient visits. Constituted the study population with a slight female predominance. The most frequent age interval of patients was 39-63 years, the most common age group for biochemical

evaluation. Laboratory data was obtained between December 2017 and April 2026, yielding a strong data set spanning over eight years.

Table 1. Characteristic of the patient

Characteristic	Value
Unique patient-visits	58
Female / Male	32 (55%) / 26 (45%)
Age, median (range)	53.5 years (16–74)
Age	39–63 years
Testing period	Dec 2017 – Apr 2026

Results for only one or two assays, reflecting real world selective ordering rather than a standardized research protocol. Urine total catecholamines is by far the most consistently ordered test (42 of 58 visits, 72%), followed by urine normetanephrine (14) and urine metanephrine / VMA (10 each). Plasma catecholamines, plasma metanephrines, and urine free cortisol were rarely or never recorded.

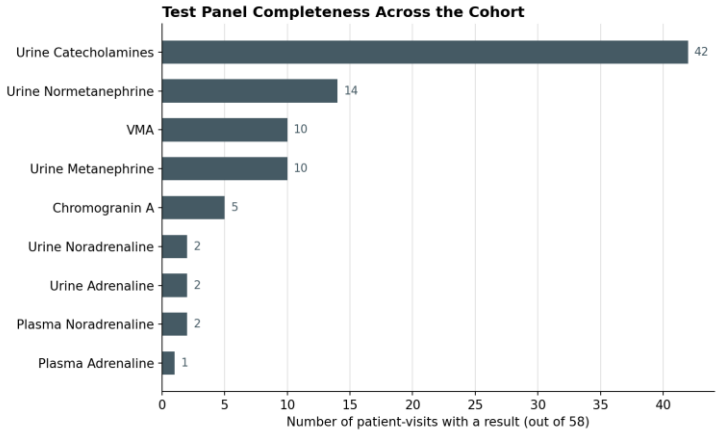

Figure 1. Number of visits with a recorded result, by assay (n = 58 total visits).

Among visits where a given assay was actually performed, the results are overwhelmingly above the upper limit of the reference range consistent with a cohort selected for confirmed or highly suspected catecholamine secreting tumors rather than a general screening population.

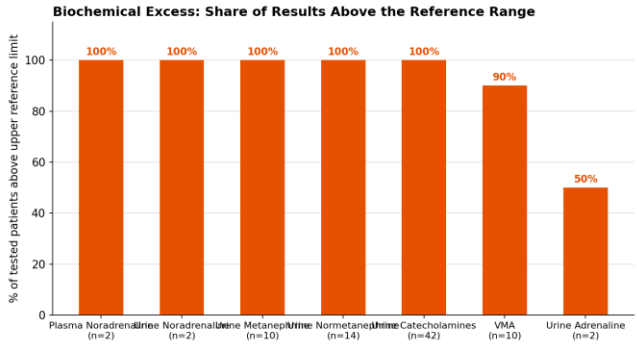

Figure 2. Percentage of tested patients with a result above the upper reference limit, for assays with n ≥ 2.

Biochemical Biomarker Testing

The frequency of biochemical biomarker testing varied according to clinical indication and laboratory availability among the study participants. The most frequently requested biochemical test was the 24-hour urinary catecholamines, performed in 42 patients, reflecting the routine use of these tests in the diagnostic evaluation of suspected pheochromocytoma. Urinary normetanephrine measurements were available in 14 patients, urinary metanephrine and 24-hour urinary vanillylmandelic acid (VMA) in 10 patients each. Less frequently direct measurements of urinary noradrenaline, plasma noradrenaline and urinary adrenaline were performed, each biomarker being analysed in 2 patients. In summary, the pattern of testing demonstrates a greater dependence on urinary catecholamine measurements.

Table 2. Biomarkers

Biomarker	n tested
Urine catecholamines (<565 µg/24h)	42
Urine normetanephrine (111–419 µg/24h)	14
Urine metanephrine (30–180 µg/24h)	10
VMA (1.6–7.3 mg/24h)	10
Urine noradrenaline (<100 µg/L)	2
Plasma noradrenaline (120–350 pg/mL)	2
Urine adrenaline (<25 µg/L)	2

Demographics

The cohort skews slightly female (55%) with a broad age range spanning adolescence (age 16) to the 70s. The distribution is fairly even across the 30 up to70 age band, without a single dominant age peak.

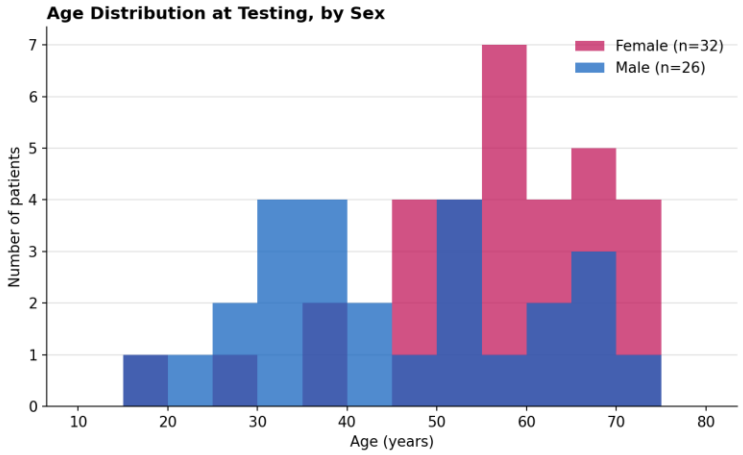

Figure 3. Age distribution at testing, stratified by sex.

Catecholamine and Normetanephrine Levels by Sex

For the two best-populated urine assays, both sexes show marked, similarly distributed elevation above the reference limit (dashed line), with sex based separation in magnitude though the male urine catecholamine group shows a wider spread with a few very high outliers.

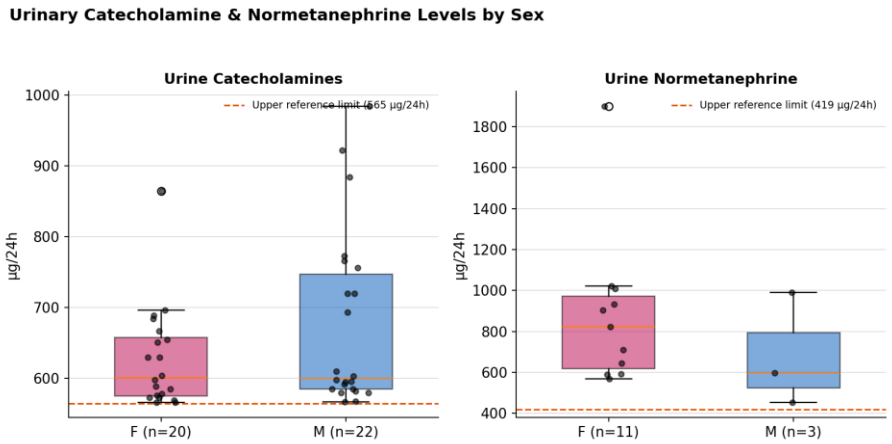

Figure 4. Urine catecholamines and urine normetanephrine by sex, with individual data points overlaid and the upper reference limit marked.

Testing Volume Over Time

Testing volume has been fairly stable year-to-year (roughly 4 up to 9 visits/year) since 2019, without an obvious trend, aside from a smaller count in the most recent partial year and the earliest years of the dataset.

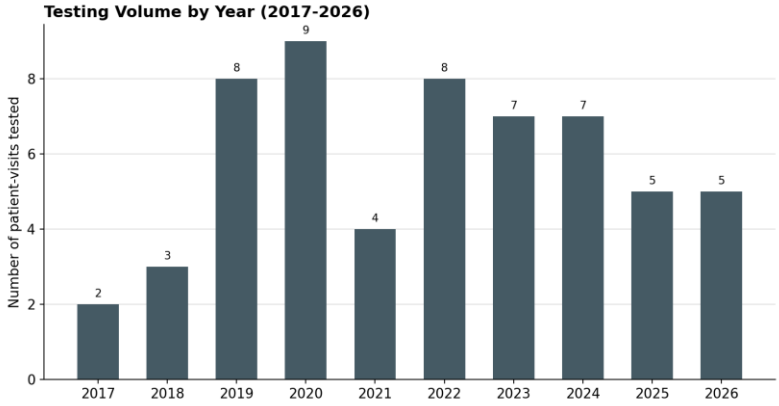

Figure 5. Number of patient-visits tested per calendar year.

Catecholamine Excess compared with the Age

Plotting urine catecholamines against age shows elevated values across the entire adult age range, with no apparent age-related trend in the degree of excess young and older patients both present with values well above the reference limit.

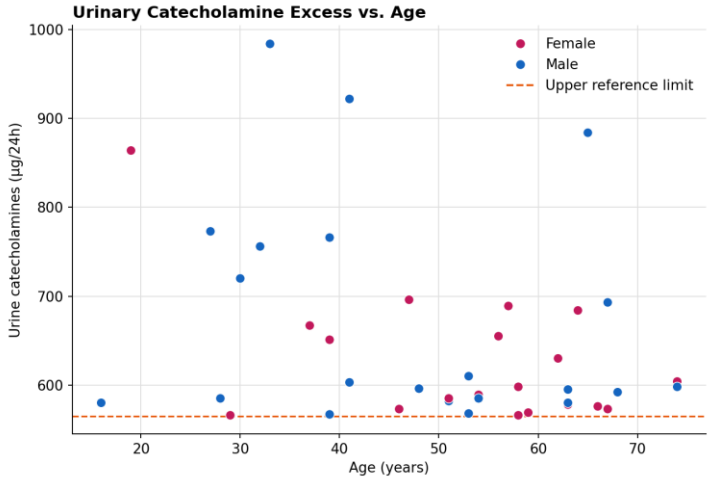

Figure 6. Urine catecholamines vs. age, colored by sex, with the upper reference limit (565 µg/24h) marked.

Cross Marker Relationship: VMA in relation to Urine Catecholamines

Only 7 patients had both VMA and urine. Most points cluster with catecholamines well above 565 µg/24h while VMA sits closer to its own upper limit, suggesting these two metabolites do not scale together 1:1 in this small sample.

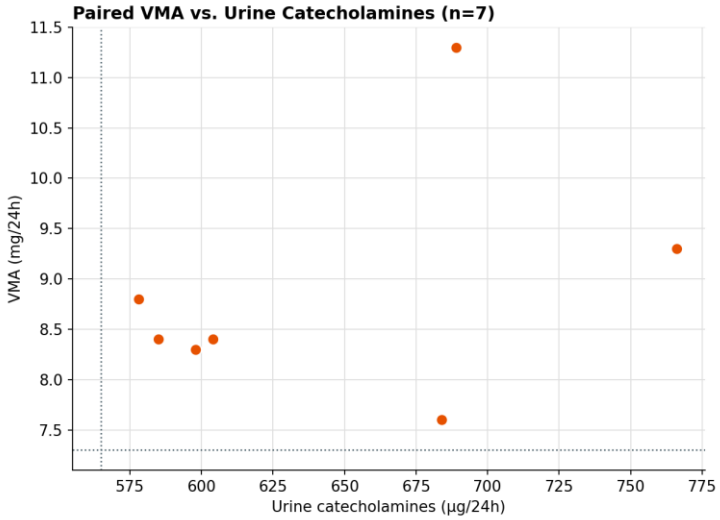

Figure 7. Paired VMA and urine catecholamine results (n = 7); dotted lines mark each assay's upper reference limit.

Summary

The data are consistent with a group of confirmed/suspected pheochromocytoma patients: nearly all measured catecholamine and metanephrine assays return values above the reference range, regardless of age or sex, and urine total catecholamines is the assay most consistently used for follow-up.

Reference

A. Kierszenbaum, L.Tres (2020). Histology and Cell Biology: An Introduction to Pathology. Elsevier, f. 669.

A. Mescher (2021). Junqueira's Basic Histology. McGraw-Hill, f. 425.

A. Snezhkina, V. Pavlov, A. Dmitriev, N. Melnikova, A. Kudryavtseva (2021). Potential Biomarkers of Metastasizing Paragangliomas and Pheochromocytomas. 11, 1179. https://doi.org/10.3390/life11111179

A.Snezhkina, V.Pavlov, A.Dmitriev, N.Melnikova, A.Kudryavtseva, (2021). Potential biomarkers of metastasizingparagangliomas and pheochromocytomas. Life (Basel).;11(11):1179. doi:10.3390/life11111179.

B.Khalil, A.Rosani, J.Warrington, (2024)Physiology, Catecholamines. Comprehensive review of catecholamine synthesis, metabolism, and adrenal medullary physiology. StatPearls Publishing

B. Mezani, A. Mitre (2024). Adrenal Pheochromocytoma: Biochemical Diagnosis in Albanian Population. Abstracts of the 2nd Student Conference on Biological Sciences, Tirana. ISBN:979-8-89170-232-5, Doi: 10.5281/zenodo.14565735

B. Mezani, A. Mitre(2024). Tumoretadrenale në popullatënshqiptare. KonferencaKombëtare e ASHMG 2024: SëmundjetGjenetike - Nga DiagnostikimiTeParandalimi. Tirana, Albania. ISBN 9789928355737

B. Mezani, A. Mitre (2025). Biomarkers as Key Tools in Pheochromocytoma Detection. Kongresi I II- Ndërkombëtar iShkencave tëshëndetit, USHI. Tirana, Albania

B. Mezani, A. Mitre (2025). Laboratory study of pheochromocytoma in the Albanian population. Final Conference of CA20122 (Harmonising clinical care and research on adrenal tumours) / Joint 24th ENSAT Scientific Meeting and 4th Harmonisation Meeting. Serbia

B. Mezani, A. Mitre (2025). Power of Biomarkers in Diagnosing Pheochromocytoma. READ International Scientific Conference, Tirana, Albaia

Integrated Multi-Biomarker Panel for Pheochromocytoma Diagnosis: Fractionated Metanephrins, Vanillylmandylic Acid, Clinical Case Albania. ISBN 9789928478849

B. Mezani, A. Mitre (2026). Integrated Multi Biomarker Panel for Accurate Diagnosis of Pheochromocytoma: Metanephrines, 3-Methoxytyramine, and Chromogranin A. UluslararasiGülhaneSağlikBilimleriKongresi. Izmir, Turkey

B. Mezani, A. Mitre, Berdica L. Collaborative Research in Adrenal Tumor Pathologies: Focus on the Albanian Population. In: Proceedings of the 1st International Conference on Higher Education and Sustainable Development. Tirana: Western Balkans University; 2024.

B. Mezani, A. Mitre, L. Berdica (2024). Adrenal Tumor Pathologies. Proceedings Book the Joint 23rd ENSAT and 3rd Cost Harmonisation Meeting. Spain

R.Marušić, T. Turk, T.Bačun,(2024).Clinical Evaluation, Diagnosis and Treatment of Pheochromocytoma. Acta Clin Croat.

M. Bauer, K. Currie, (2024). Serotonin and the serotonin transporter in the adrenal gland. VitamHorm.;124:39–78. Review of adrenal medullary chromaffin cell biology and neuroendocrine function.

C. Bresser, R. Krijger (2024). The Molecular Classification of Pheochromocytomas and Paragangliomas: Discovering the Genomic and Immune Landscape of Metastatic Disease. Endocrine Pathology (2024) 35:279–292. https://doi.org/10.1007/s12022-024-09830-3

D. Gardner, D. Shoback (2018). Greenspan's Basic & Clinical Endocrinology. McGraw-Hill, f. 299-399.

D. Kumar (2020). Clinical Molecular Medicine Principles and Practice. Elsevier, f. 230-240.

D. Linos, J. Heerden,(2005). Adrenal Glands, Springer, p. 25.

E.Pietroluongo, A.Marretta, M.Cives, E.Andrini, E.Sala, (2025). Diagnosis and treatment of paragangliomas and pheochromocytomas: a survey from the Italian Association for Neuroendocrine Tumours. Front Endocrinol (Lausanne).;16:1687570. 16:1687570. https://doi:10.3389/fendo.2025.1687570

F. Torresan, C. Iacobone, F. Giorgino, M. Iacobone(2024). Genetic and Molecular Biomarkers in Aggressive Pheochromocytomas and Paragangliomas. Int. J. Mol. Sci., 25,7142. https://doi.org/10.3390/ijms25137142

F. Wondisford (2020). Essentials of Endocrinology and Metabolism. Elsevier, f. 159- 207.

G. Eisenhofer, C. Pamporaki, J. Lenders (2023). Biochemical Assessment of Pheochromocytoma and Paraganglioma.Endocrine Reviews, 44, 862–909. https://doi.org/10.1210/endrev/bnad011

G. Eisenhofer, M. Peitzsch, N. Bechaman, A. Hubner (2022). Biochemical Diagnosis of Catecholamine-Producing Tumours of Childhood: Neuroblastoma, Pheochromocytoma and Paraganglioma. Front. Endocrinol. 13:901760. https://doi:10.3389/fendo.2022.901760

G.Gardner, Shoback D.,(2018).Greenspan's Basic and Clinical Endocrinology. 11th ed. New York: McGraw-Hill Education;

Igaz (2021). Practical Clinical Endocrinology. Springer, f. 271- 388.

J. Kibble (2020). The Big Picture Physiology. McGraw-Hill, f. 325-355.

J.Lenders, A. Duh, G.Eisenhofer, (2014). Pheochromocytoma and Paraganglioma: An Endocrine Society Clinical Practice Guideline.J Clin Endocrinol Metab.;99(6):1915–1942.

L. Zdrojewski, K. Sworczak (2022).Adrenal Tumours in Young Adults: Case Reports and Literature Review, 58, 746. https://doi.org/10.3390/medicina58060746

M.Fassnacht, W. Arlt, I.Bancos, H.Dralle, J. Newell, A.Sahdev, (2023). European Society of Endocrinology clinical practice guidelines on the management of adrenal incidentalomas in collaboration with the European Network for the Study of Adrenal Tumours. Eur J Endocrinol.;189(1)–G42. doi:10.1093/ejendo/lvad066.

M.Giacché, C.Tacchetti, C.Agabiti, (2024)**.** Pheochromocytoma–Paraganglioma Syndrome: A Multiform Disease with Different Genotype and Phenotype Features. *Biomedicines.*;12(10):2385

M. Shah, W. Goldner, A. Benson , E Bergsland (2021). Neuroendocrine and Adrenal Tumours, JNCCN.org.https://jnccn.org/view/journals/jnccn/19/7/article-p839.xml

M. Tsoli, K. Daskalakis, E.Kassi, G. Kaltsas, A. Tsolakis (2021). Critical Appraisal of Contemporary and Novel Biomarkers in Pheochromocytomas and Adrenocortical Tumours. Biology, 10, 580. https://doi.org/10.3390/biology10070580

A.Mescher, (2021). Junqueira's Basic Histology: Text and Atlas. 16th ed. New York: McGraw-Hill Education;.

N. Ahmed (2010). Clinical Biochemistry. Oxford, f. 378-411.

P.Gupta, B.Marwaha,(2024). Pheochromocytoma.StatPearls Publishing; updated.

P. Rae, M. Crane (2018). Clinical Biochemistry Lecture Notes. John Wiley, f. 121-138.

SRufolo, A. Balsamo, FParisi, ACoglianese, BCharlier, VIzzo. (2026). Catecholamines and Metanephrines: Quantification in the Diagnosis of Pheochromocytoma and Paraganglioma, Considerations and Critical Issues. Diagnostics (Basel).;16(9):1263.

T.Saavedra, H.Nati-Castillo, L.Cometa, (2024). Pheochromocytoma: an updated scoping review from clinical presentation to management and treatment. Front Endocrinol (Lausanne).;15:1433582.

Licensee MDPI, Basel, (2026). Cross Talk Between Catecholamine Excess and Hormonal Biomarkers in Pheochromocytoma. MDPI: https://doi.org/10.3390/diagnostics16091263

B. Mezani, A. Mitre (2026). Integrated Multi-Biomarker Panel For Pheochromocytoma Diagnosis: Fractionated Metanephrins, Vanillylmandylic Acid, Clinical Case. JNS 39/2026

8th International Conference on Engineering, Natural and Social Sciences

September 06-07, 2026: Konya, Turkey

© 2026 Published by All Sciences Academy

https://www.icensos.com/

Clinical Use of Metanephrines and Catecholamines in Combination with Chromogranin A for the Biochemical Diagnosis of Pheochromocytoma

Brunilda Mezani[1,3] Anila Mitre[1,2]

[1] *Biology Department, Faculty of Natural Sciences, University of the Tirana, Albania,*

[2] *Immunological and Medical Director at the Intermedica Laboratories network, Albania,*

[3] *Department of Medical Laboratory Sciences and Imaging, Western Balkans University, Tirana, Albania*

brunilda.mezani@wbu.edu.al

***Abstract* - Background:** Pheochromocytoma (PHEO) is an uncommon neuroendocrine tumour of the adrenal medulla that releases catecholamines. It is linked to a high risk of heart disease and has a 10–15% chance of becoming cancerous. The clinical presentation is highly variable and imaging findings alone are not sufficient for functional characterisation, therefore accurate biochemical diagnosis remains essential. Plasma and urine metanephrines, fractionated, are well proven first-line tests, but a significant proportion of cases present with partial or equivocal biochemical profiles, highlighting the necessity of additional markers. Chromogranin A (CgA), a neuroendocrine storage protein co-released with catecholamines, has been proposed as a potentially useful adjunct biomarker in this regard.

Objective: To measure the clinical utility of Chromogranin A and urine and plasma catecholamines, metanephrines, normetanephrines, vanillylmandelic acid (VMA) and 3-methoxytyramine in the biochemical diagnosis of pheochromocytoma in a real clinical cohort.

Methods. Observational analysis was performed on biochemical data from 65 patients (38 female, 27 male) referred to Intermedica Clinical laboratory, Albania, between 2017 and 2026 with clinical suspicion of pheochromocytoma. Biomarkers assessed included: 24-hour urine catecholamines (reference <565 µg/24h), urine metanephrines (30-180 µg/24h), urine normetanephrines (111-419 µg/24h), VMA (1.6-7.3 mg/24h), plasma adrenaline (10–200 pg/mL), plasma noradrenaline (80–520 pg/mL), Chromogranin A (<100 ng/mL), and 3-methoxytyramine (< 17.4 ng/L). Results were interpreted against established institutional and international reference intervals. Frequency of abnormal results, degree of elevation above upper reference limits, and inter-marker correlations were analyzed descriptively.

Results. 24 hour urine catecholamines were the most frequently measured marker (n=47) and were elevated in 100% of tested patients (mean 649.6 µg/24h; 15% above upper reference limit). Urine normetanephrine was elevated in all 14 patients tested (100%; mean 838.0 µg/24h), with values reaching up to 1,900 µg/24h representing a 4.5-fold excess above the upper reference limit. Urine metanephrine was elevated in all 13 patients tested (100%; mean 350.6 µg/24h; peak 803.0 µg/24h). VMA was elevated in 10 of 11 patients (91%; mean 9.2 mg/24h). Chromogranin A was measured in five patients and was elevated in all (100%), with a mean of 1121.9 ng/mL and a peak value of 4,540 ng/mL indicative of massive neuroendocrine secretory activity.

Conclusions. In this group of patients, catecholamines, metanephrines, and normetanephrines found in the urine were all positive in all of them. This proves that they are the best way to diagnose pheochromocytoma. Chromogranin A was measured in a smaller group, but it consistently and significantly rose. This showed that it is a useful additional neuroendocrine biomarker, especially when the first-line results are unclear, for figuring out the size of the tumour, and for keeping an eye on things after surgery. The extreme CgA

elevations (up to 45-fold above reference) underscore the magnitude of secretory activity in PHEO. A higher level of 3-methoxytyramine supports its growing role in finding dopaminergic and possibly cancerous phenotypes. A multimarker biochemical approach that combines CgA with fractionated metanephrines, normetanephrines, and VMA provides the greatest diagnostic sensitivity and a complete functional description of the tumour.

Key Words: Metanephrines , Catecholamines, Chromogranin A, Diagnosis, Pheochromocytoma

Introduction

A pheochromocytoma (PHEO) is a rare neuroendocrine tumour that comes from chromaffin cells in the adrenal medulla and releases catecholamines. The clinical presentation of the tumour is variable, from the classic triad of episodic headache, diaphoresis and palpitations, to incidental discovery on cross-sectional imaging. Hypotensive crises, myocardial infarction, and stroke can be life-threatening if pheochromocytoma is not found and treated.

The biochemical validation is still the foundation of a diagnosis. Current evidence supports the use of fractionated plasma and urinary metanephrines as the initial tests because of their higher sensitivity (97-99 %) compared with direct catecholamine measurements. However, the complete assessment of pheochromocytoma is increasingly incorporating a panel of complementary biomarkers such as vanillylmandelic acid (VMA), total urinary catecholamines and Chromogranin A (CgA). To find out how useful CgA is for diagnosing conditions when mixed with catecholamines and metanephrines, we looked back at biochemical data from 65 patients who were seen at our Intermedica Biochemical Laborator, Albania.

Dataset overview

There are sixty-five distinct patients in the dataset.

Table 1. Cohort Demographic Summary. Not all markers were measured in every patient.

Characteristic	Value / Detail
Total patients	65
Gender	Female: 42 (65%) | Male: 23 (35%)
Age range	16–74 years (median 53 years)
Study period	2017-2026
Biomarkers analysed	10 distinct biochemical markers
Largest sub-cohort	Urine Catecholamines 24h (n=47)

Result and Biomarkes

Overview of Biomarker Positivity Rates

More than 90% of the values for all biomarkers that were measured were higher than their upper reference limits (URLs).

Table 2. Summary of Biomarker Results vs Reference Ranges**.** Summarises the key findings for each marker.

Biomarker	Reference Range	N tested	Mean (range)	% Elevated	Interpretation
Plasma Adrenaline	10–110 pg/mL	1	113.7 (113.7)	100%	Above ULN
Plasma Noradrenaline	120–350 pg/mL	3	420 (388–484)	100%	All elevated
Urine Adrenaline	<25 µg/L	2	56 (25–87)	50%	Borderline
Urine Noradrenaline	<100 µg/L	2	147 (104–190)	100%	All elevated

Urine Metanephrine 24h	30–180 µg/24h	13	351 (180–803)	100%	All elevated
Urine Normetanephrine	111–419 µg/24h	14	838 (452–1900)	100%	All markedly elevated
VMA acid	1.6–7.3 mg/24h	11	9.2 (6.2–11.6)	91%	Mostly elevated
Urine Catecholamines 24h	<565 µg/24h	47	649 (566–984)	100%	All elevated
Chromogranin A	<100 ng/mL	5	1122 (127–4540)	100%	All elevated; extreme range
3-Methoxytyramine	<17.4 ng/L	1	28.2 (28.2)	100%	Above ULN (malignancy marker)

Catecholamines: Plasma and Urinary

Plasma adrenaline was available in one patient (113.7 pg/mL), marginally exceeding the supine upper limit of 110 pg/mL. Plasma noradrenaline was measured in three patients (mean 420 pg/mL, range 388-484 pg/mL), all exceeding the supine URL of 350 pg/mL by 11-38%. This pattern of sympathetic and adrenaline activation fits with noradrenaline-predominant pheochromocytoma, which makes up about 70–80% of cases.

The results for urinary adrenaline were borderline with one of the two patients exceeding the URL (86.9 vs <25 µg/L) and the second being at the limit (25 µg/L). Urinary noradrenaline levels were high in both patients (103.6 and 189.6 µg/L, URL <100 µg/L), which means that body kept secreting too much noradrenaline.

Metanephrines: First-Line Markers

Urine metanephrine 24h was the most extensively measured primary catecholamine metabolite marker (n=13). All 13 values exceeded the URL of 180 µg/24h, with a mean of 351 µg/24h (range 180.2-803.0). The distribution includes values in the mild-to-moderate range (180–262 µg/24h, n=7) and markedly elevated values (≥417 µg/24h, n=6), including one case of 803 µg/24h, approximately 4.5× the URL, strongly supportive of pheochromocytoma.

Urine normetanephrine 24h was elevated in all 14 tested patients, with a mean of 838 µg/24h (range 452–1900) against a URL of 419 µg/24h. Eleven of 14 patients (79%) had values exceeding twice the URL. The maximum of 1900 µg/24h represents a 4.5-fold elevation, in keeping with high tumour secretory burden. Elevated normetanephrine is the hallmark of noradrenaline-secreting pheochromocytoma and correlates with tumour size.

Vanillylmandelic Acid (VMA)

VMA, the final common metabolite of both adrenaline and noradrenaline via catechol-O-methyltransferase (COMT) and monoamine oxidase (MAO), was assessed in 11 patients. Ten of 11 (91%) exceeded the URL of 7.3 mg/24h, with a mean of 9.2 mg/24h (range 6.2–11.6). Although VMA has historically lower sensitivity than metanephrines (~60–80% vs ~97%), its elevation in 91% of this series likely reflects the high pre-test probability of pheochromocytoma in patients selected for this intensive panel.

Total Urine Catecholamines 24h

The largest sub-cohort (n=47) was assessed for total urine catecholamines. All 47 values exceeded the URL of 565 µg/24h, with a mean of 649 µg/24h (median 598) and a range of 566–984 µg/24h.

Chromogranin A: Key Finding

Chromogranin A (CgA) is a protein stored in chromaffin granules and secreted with catecholamines. It serves as a sensitive general neuroendocrine marker and has established utility in pheochromocytoma diagnosis and monitoring.

Here, CgA levels were checked in 5 patients, and all of them were higher than the URL level of 100 ng/mL: According to the ULN, CgA levels in Patient A (a 47-year-old woman) were slightly elevated at 127 ng/mL; in Patient B (a 56-year-old woman), they were moderately elevated at 145.6 ng/mL; in Patient C (a 67-

year-old woman), they were moderately to markedly elevated at 197 ng/mL; in Patient D (a 71-year-old woman), they were markedly elevated at 6× ULN; and in Patient E (a 68-year-old woman), their CgA levels were extremely elevated (45 × ULN), which meant they had a lot of secretions.
Based on the high value of 4,540 ng/mL, the mean CgA level of 1,122 ng/mL and the median level of 197 ng/mL show a very skewed distribution.
This degree of CgA elevation is consistent with large-volume pheochromocytoma or metastatic disease and has been reported in correlation with tumour size, bilateral involvement, and paragangliomatosis. CgA at this level also provides a reliable post-surgical follow-up marker, with normalisation indicating biochemical cure.

3-Methoxytyramine

3-Methoxytyramine (3-MT), the principal plasma metabolite of dopamine via COMT, was measured in one patient (28.2 ng/L vs URL <17.4 ng/L; 1.6× ULN). Elevation of 3-MT is of particular clinical significance as a marker associated with dopaminergic pheochromocytoma and malignant paraganglioma. A positive 3-MT result warrants genetic testing and enhanced surveillance for malignancy.

Discussion

This retrospective series demonstrates near-universal biochemical positivity across all measured markers in patients investigated for pheochromocytoma, reflecting both the high pre-test clinical suspicion in the investigated cohort and the complementary roles of different biomarker categories.
Metanephrines as first-line markers: Consistent with international guidelines (Endocrine Society 2014; ESE/ENSAT 2022), urinary fractionated metanephrines demonstrated 100% positivity in this series. The uniformly elevated normetanephrine levels, all exceeding 419 µg/24h with a mean nearly double the URL,underline the primacy of these markers. Normetanephrine reflects continuous intra-tumoural, O-methylation independent of catecholamine release, making it less susceptible to episodic secretion artefact than direct catecholamine measurements.
As an extra, CgA was measured in 5 patients, and all of them had elevated levels. The extreme CgA value of 4,540 ng/mL (45× ULN) is remarkable and probably reflects tumour volume, high chromaffin cell mass or metastatic disease. CgA provides value in several clinical scenarios: (1) when metanephrine results are borderline, (2) for post-operative follow up to monitor for biochemical cure, (3) in the evaluation of patients with renal failure where metanephrines may be falsely elevated. VMA in contemporary practice: Largely replaced by metanephrines as less sensitive, 91% positivity was demonstrated in this series. Normal VMA cannot exclude pheochromocytoma, as it has lower sensitivity. It should not be used as a screening test on its own.
Distribution by gender and age: The fact that 65% of the people in this series are women is in line with published epidemiological data. The age range (16–74, median ≈53 years) is consistent with the known bimodal distribution of pheochromocytoma, including hereditary cases, which present in younger patients.

Conclusion

This multimarker series from 2017–2026 shows that all measured catecholamine-axis markers were consistently higher in patients who were being checked for pheochromocytoma. Urine normetanephrine and metanephrine 24h were positive 100%, confirming their role as first line diagnostic tests.
Chromogranin A was elevated in all 5 patients measured, ranging from 1.3× to 45× the upper reference limit, demonstrating its role as a sensitive adjunct marker for diagnosis and post-operative monitoring.
Elevation of 3-methoxytyramine, if present, indicates dopaminergic tumour biology and increased risk of malignancy, necessitating prompt genetic evaluation.
A multimodal biochemical approach using fractionated metanephrines as the diagnostic base, CgA for assessing and monitoring severity, and 3-MT for classifying malignancy gives the most complete biochemical picture of pheochromocytoma and should be standard practice in endocrinology centers that specialise in the condition. VMA and total catecholamines Use as secondary/supporting evidence.

Reference:

Algeciras-Schimnich A, Preissner CM, Young WF Jr, Singh RJ, Grebe SKG, (2008). Plasma chromogranin A or urine fractionated metanephrines follow-up testing improves the diagnostic accuracy of plasma fractionated metanephrines for pheochromocytoma. J Clin Endocrinol Metab;93(1):91-95. doi:10.1210/jc.2007-1354. PMID:17940110.

Boyle JG, Davidson DF, Perry CG, Connell JM.(2007). Comparison of diagnostic accuracy of urinary free metanephrines, vanillylmandelic acid, and catecholamines and plasma catecholamines for diagnosis of pheochromocytoma. J Clin Endocrinol Metab.;92(12):4602-4608. doi:10.1210/jc.2005-2668. PMID:17635948.

Eisenhofer G, Goldstein DS, Walther MM, Friberg P, Lenders JW, Keiser HR, et al. (2002). Biochemical diagnosis of pheochromocytoma: which test is best? JAMA.;287(11):1427-1434. doi:10.1001/jama.287.11.1427. PMID:11903030.

Eisenhofer G, Goldstein DS, Walther MM, Friberg P, Lenders JW, Keiser HR, et al. (2003). Biochemical diagnosis of pheochromocytoma: how to distinguish true- from false-positive test results. J Clin Endocrinol Metab.;88(6):2656-2666. doi:10.1210/jc.2002-030005. PMID:12788870.

Eisenhofer G, Keiser H, Friberg P, Mezey E, Huynh TT, Hiremagalur B, et al (1998). Plasma metanephrines are markers of pheochromocytoma produced by catechol-O-methyltransferase within tumors. J Clin Endocrinol Metab.;83(6):2175-2185. doi:10.1210/jcem.83.6.4870. PMID:9626157.

Eisenhofer G, Lattke P, Herberg M, Siegert G, Qin N, Därr R, et al. (2013). Reference intervals for plasma free metanephrines with an age adjustment for normetanephrine for optimized laboratory testing of phaeochromocytoma. Ann Clin Biochem.;50(Pt 2):147-155. doi:10.1177/0004563212471726. PMID:23065528.

Eisenhofer G, Lenders JWM, Timmers HJLM, Mannelli M, Grebe SKG, Hofbauer LC, et.al, (2011). Measurements of plasma methoxytyramine, normetanephrine and metanephrine for the diagnosis of pheochromocytoma and paraganglioma. Clin Chem.;57(4) (3):411-20. doi: 10.1373/clinchem.2010.153320.

Eisenhofer G, Peitzsch M.(2014). Laboratory evaluation of pheochromocytoma and paraganglioma. Clin Chem. 60(12):1486-1499. doi:10.1373/clinchem.2014.224832. PMID:25332315.

Eisenhofer G, Siegert G, Kotzerke J, Bornstein SR, Pacak K. (2008). Current progress and future challenges in the biochemical diagnosis and treatment of pheochromocytomas and paragangliomas. Exp Clin Endocrinol Diabetes.;116(7):329-337. doi:10.1055/s-2008-1073156. PMID:18491252.

Fraissinet F, Charpentier T, Girot H, Brunel V, Prévost G, Lopez A, (2026). Biochemical diagnosis of pheochromocytoma and paraganglioma: analytical challenges and perspectives for optimization. Clin Chim Acta.;590:121073. doi:10.1016/j.cca.2026.121073. PMID:42128324.

Giovanella L, et al. (2019) Chromogranin A in the laboratory diagnosis of pheochromocytoma and paraganglioma. Endocr Pathol;30:137-142. PMID:31027285.

Grouzmann E, Drouard-Troalen L, Baudin E, Plouin PF. (2010). Diagnostic accuracy of free and total metanephrines in plasma and fractionated metanephrines in urine of patients with pheochromocytoma. Eur J Endocrinol;162(5):951-958. doi:10.1530/EJE-09-0996. PMID:20142367.

Herbomez M, Forzy G, Bauters C, Tierny C, Pigny P, Carnaille B, et al. (2007). An analysis of the biochemical diagnosis of 66 pheochromocytomas. Eur J Endocrinol.;156(5):569-575. doi:10.1530/EJE-06-0640. PMID:17468193.

Hsiao RJ, Parmer RJ, Takiyyuddin MA, O'Connor DT, (1991). Chromogranin A storage and secretion: sensitivity and specificity for the diagnosis of pheochromocytoma. Medicine (Baltimore).;70(1):33-45. PMID:1988765.

Kim HJ, Lee JI, Cho YY, Lee SY, Kim JH, Jung BC, et al. (2015). Diagnostic accuracy of plasma free metanephrines in a seated position compared with 24-hour urinary metanephrines in the investigation of pheochromocytoma. Endocr J;62(3):243-250. doi:10.1507/endocrj.EJ14-0384. PMID:25476661.

Lenders JWM, Duh QY, Eisenhofer G, Gimenez-Roqueplo AP, Grebe SKG, Murad MH, et al, (2014). Pheochromocytoma and paraganglioma: an Endocrine Society clinical practice guideline. J Clin Endocrinol Metab.;99(6):1915-1942. doi:10.1210/jc.2014-1498. PMID:24893135. Endocrine Society.

Lenders JWM, Keiser HR, Goldstein DS, Willemsen JJ, Friberg P, Jacobs MC, et al. (1995). Plasma metanephrines in the diagnosis of pheochromocytoma. Ann Intern Med.;123(2):101-109. doi:10.7326/0003-4819-123-2-199507150-00004. PMID:7778821.

Miehle K, Kratzsch J, Lenders JWM, Kluge R, Paschke R, Koch CA, (2005). Adrenal incidentaloma diagnosed as pheochromocytoma by plasma chromogranin A and plasma metanephrines. J Endocrinol Invest.;28(11):1040-1042. doi:10.1007/BF03345347. PMID:16483187.

Peaston RT, Graham KS, Chambers E, van der Molen JC, Ball SG, Mangham JE, et al. (2010). Performance of plasma free metanephrines measured by liquid chromatography-tandem mass spectrometry in the diagnosis of pheochromocytoma. Clin Chim Acta;411(7-8):546-552. doi:10.1016/j.cca.2010.01.012. PMID:20083099.

Peaston RT, Yandle TG, Nicholls MG, Espiner EA, (2010). Plasma and urine metanephrines in the diagnosis of pheochromocytoma. Clin Chem.;56(12):1750-1751.

Perry CG, Sawka AM, Singh R, Thabane L, Bajnarek J, Young WF Jr. (2007).The diagnostic efficacy of urinary fractionated metanephrines measured by tandem mass spectrometry in detection of pheochromocytoma. Clin Endocrinol (Oxf);66(5):703-708. doi:10.1111/j.1365-2265.2007.02805.x.

Rufolo S, Balsamo AC, Parisi F, Coglianese A, Charlier B, Izzo V. (2026). Catecholamines and metanephrines: quantification in the diagnosis of pheochromocytoma and paraganglioma, considerations and critical issues. Diagnostics (Basel).;16(9):1263. doi:10.3390/diagnostics16091263. PMID:42121968.

Sawka AM, Jaeschke R, Singh RJ, Young WF Jr. (2003). A comparison of biochemical tests for pheochromocytoma: measurement of fractionated plasma metanephrines compared with the combination of 24-hour urinary metanephrines and catecholamines. J Clin Endocrinol Metab.;88(2):553-558. doi:10.1210/jc.2002-021251. PMID:12574179.

Unger N, Pitt C, Schmidt IL, Walz MK, Schmid KW, Philipp T, et al. (2006) Diagnostic value of various biochemical parameters for the diagnosis of pheochromocytoma in patients with adrenal mass. Eur J Endocrinol.;154(3):409-417. doi:10.1530/eje.1.02097.

Weise M, Merke DP, Pacak K, Walther MM, Eisenhofer G. (2002). Utility of plasma free metanephrines for detecting childhood pheochromocytoma. J Clin Endocrinol Metab.;87(5):1955-1960. doi:10.1210/jcem.87.5.8446. PMID:11994324.

Weismann D, Peitzsch M, Raida A, Prejbisz A, Gosk M, Riester A, et al. (2015). Measurements of plasma metanephrines by immunoassay vs liquid chromatography with tandem mass spectrometry for diagnosis of pheochromocytoma. Eur J Endocrinol.;172(3):251-260. doi:10.1530/EJE-14-0730. PMID:25452465.

Xing Y, Shi H, Guo Q, Wang C, Li C, Hao C. (2024). Chromogranin A as a diagnostic marker of pheochromocytoma and paraganglioma: a systematic review and meta-analysis. Int J Urol;31(6):637-645. doi:10.1111/iju.15423. PMID:38380475.

8th International Conference on Engineering, Natural and Social Sciences

September 06-07, 2026: Konya, Turkey

© 2026 Published by All Sciences Academy

https://www.icensos.com/

Investigation of the Effect of Masonry Piers on the Modal Behavior of Hollow Concrete Block Walls

Furkan Günday*

[1]*Department of Civil Engineering, Faculty of Engineering, Giresun University, Turkey*

**furkan.gunday@giresun.edu.tr*

Abstract **–**This study investigates the influence of regularly masonry piers on the modal behavior of a long hollow concrete block garden wall using the Finite Element Method (FEM). Two three-dimensional numerical models were developed in SAP2000 to represent a 20.0 m long, 1.5 m high, and 0.20 m thick reference wall and a modified configuration incorporating 0.40 × 0.40 m hollow concrete block masonry piers at 2.50 m intervals. The wall was modeled using shell elements, while the masonry piers were represented by frame elements. Eigenvalue-based modal analyses were performed to determine the natural periods, frequencies, and mass participation ratios of the first five vibration modes. The results showed that the introduction of masonry piers reduced the modal periods by approximately 16.71–21.99%, while the corresponding natural frequencies increased by 20.11–28.25%. Changes in the modal mass participation ratios also indicated a redistribution of the dynamic response, particularly in the higher order modes. The findings demonstrate that regularly masonry piers significantly modify the global vibration characteristics of hollow concrete block garden walls and provide a basis for further experimental investigations.

Keywords – Masonry piers, hollow concrete block wall, finite element method, modal analysis, dynamic characteristics

I. INTRODUCTION

Masonry remains one of the most widely used construction systems for walls, partitions, boundary walls, and low-rise structural components due to its durability, ease of construction, and relatively simple construction techniques. Despite these advantages, the mechanical behavior of masonry is inherently complex because it is a heterogeneous composite system consisting of discrete units, mortar joints, and interfaces with different mechanical characteristics. Consequently, the structural response of masonry depends not only on the properties of the constituent materials but also on unit geometry, bond arrangement, mortar properties, wall dimensions, and boundary conditions [1–4]. Numerical modeling of masonry therefore requires appropriate consideration of its composite nature and the interaction between individual components. Different numerical strategies, ranging from detailed micro-modeling to homogenized macro-modeling approaches, have been developed to represent the behavior of masonry structures at different levels of complexity [1–4].

Hollow concrete block masonry is particularly suitable for non-load-bearing and low-rise wall applications because of its relatively low self-weight, construction efficiency, and ease of installation. However, the presence of internal cavities, webs, shells, and mortar joints results in a geometrically and mechanically non-uniform system. The influence of hollow block geometry on the mechanical response has been investigated using both experimental and numerical approaches. Al-Wathaf [5] performed three-dimensional finite element analyses of hollow concrete block masonry prisms using three-dimensional solid elements and demonstrated the capability of finite element models to capture the stress distribution within conventional and interlocking hollow block systems. Thanoon et al. [6] similarly investigated interlocking

hollow concrete block masonry using finite element analysis and demonstrated the applicability of numerical modeling for predicting the mechanical response of masonry units and assemblages. More recently, experimental and numerical investigations of hollow concrete block masonry walls have continued to demonstrate the importance of block geometry, boundary conditions, mortar characteristics, and wall configuration in determining the overall response of masonry systems [7,8].

The numerical representation of hollow masonry can be approached either by explicitly modeling the individual blocks and mortar joints or by employing equivalent homogenized material properties. Lourenço [1] highlighted the importance of selecting an appropriate modeling strategy according to the objectives and required level of detail of the analysis. In this regard, numerical homogenization has been proposed as an efficient approach for deriving equivalent mechanical properties of hollow concrete block masonry while reducing the computational demand associated with detailed micro-models [3]. The use of equivalent material properties is particularly relevant for large-scale wall systems, where explicitly representing every block, cavity, and mortar interface may result in unnecessarily high computational costs. Nevertheless, three-dimensional finite element modeling remains valuable when the geometric configuration and global stiffness characteristics of the wall are of primary interest [5–8].

In addition to their static and strength characteristics, the dynamic properties of masonry walls are of considerable engineering interest. Natural frequencies, mode shapes, and damping ratios are fundamental modal parameters used to characterize the dynamic response of structural systems. Changes in these parameters may be associated with variations in stiffness, mass distribution, boundary conditions, material properties, or structural damage [9–12]. Dynamic identification techniques have consequently been applied to masonry structures for structural characterization, numerical model validation, and damage assessment. De Sortis et al. [9], for instance, investigated the dynamic characteristics of a masonry building using forced-vibration tests and demonstrated the usefulness of experimentally identified modal parameters for assessing structural behavior and updating numerical models. De Sortis et al. [9] investigated the dynamic characteristics of a masonry building using forced-vibration tests, while Tuhta et al. [10] investigated the nonlinear system identification of a model masonry retaining wall using Hammerstein–Wiener models.

The modal response of masonry is influenced by both material and geometric characteristics. Baraldi et al. [11] investigated the modal analysis of regular masonry using continuous and discrete modeling strategies and demonstrated that the calculated modal characteristics are affected by the masonry texture, constituent properties, and modeling approach. Their findings highlight the importance of considering the discrete and heterogeneous nature of masonry when evaluating its dynamic behavior. In a broader context, vibration-based investigations have also demonstrated that masonry components can significantly influence the dynamic characteristics of structural systems through their contribution to stiffness and mass. Nicoletti et al. [12] reviewed vibration-based investigations of masonry infill walls and emphasized the influence of masonry walls on the dynamic response of buildings, while also highlighting the usefulness of vibration-based methods for characterizing masonry components. The sensitivity of modal parameters to changes in the structural condition of masonry has further been demonstrated through experimental studies. Pepi et al. [13] investigated damage detection in masonry structures using modal analysis and shaking-table tests and showed that variations in modal characteristics can be associated with progressive structural damage. More recently, full-scale masonry wall systems have been investigated through a combination of operational modal analysis and nonlinear finite element simulations. The results demonstrated that natural frequencies and mode shapes can be sensitive to local and relatively slight changes in the condition of masonry walls, supporting the use of modal parameters as indicators of changes in global structural behavior [14]. These findings are particularly relevant for numerical studies in which changes in wall configuration are evaluated through eigenvalue-based modal analysis.

The geometric configuration of a masonry wall is also an important factor governing its global stiffness and vibration characteristics. For long and relatively slender walls, the longitudinal continuity of the masonry panel can result in global deformation patterns involving multiple vibration modes. Introducing regularly vertical masonry piers can modify the stiffness distribution, effective deformation characteristics, and mass distribution of the wall system. Masonry piers have traditionally been used to provide additional lateral resistance and to divide large wall panels into smaller structural segments. Their structural behavior

has been investigated extensively in the context of masonry walls subjected to in-plane loading, with numerical studies demonstrating the importance of pier geometry, aspect ratio, axial load, and material properties on the overall response of masonry wall systems [15]. However, the influence of regularly masonry piers on the modal characteristics of long, low-height hollow concrete block garden walls has received comparatively limited attention. This research gap is particularly relevant for garden and boundary walls, which are commonly characterized by relatively low height but considerable longitudinal dimensions. Although such walls may not be considered major load-bearing structural components, their large aspect ratio can result in appreciable lateral flexibility and vibration sensitivity. The introduction of regularly masonry piers provides a simple geometric modification that may substantially alter the global stiffness and consequently the natural vibration characteristics of the wall. Nevertheless, the quantitative influence of pier spacing and pier geometry on the modal response of long hollow concrete block garden walls has not been sufficiently documented.

Accordingly, the present study investigates the effect of masonry piers on the modal behavior of a long hollow concrete block garden wall using three-dimensional finite element analysis. The findings are expected to contribute to a better understanding of the modal characteristics of long hollow concrete block garden walls and to provide a numerical basis for evaluating the influence of masonry piers on their dynamic response.

II. Materials and Method

The Finite Element Method (FEM) is one of the most widely used numerical techniques for evaluating the structural and dynamic behavior of engineering systems. By discretizing a structure into a finite number of interconnected elements, FEM enables the prediction of deformation characteristics, stiffness response, and dynamic properties under different material, geometric, and boundary conditions. Owing to its ability to represent complex geometries and material interactions, FEM has been widely employed in the numerical investigation of masonry structures and their structural and dynamic characteristics [16–25].

In the present study, two three-dimensional finite element models were developed to investigate the influence of masonry piers on the modal behavior of a hollow concrete block garden wall. The first model represents the reference wall configuration without masonry piers, while the second model represents the modified configuration incorporating regularly masonry piers along the wall. The reference wall has a total length of 20.0 m, a height of 1.5 m, and a thickness of 0.20 m. In the second configuration, masonry piers with a cross-sectional dimension of 0.40 × 0.40 m were introduced at regular 2.50 m intervals along the wall. The piers were modeled as integral vertical masonry elements connected to the wall, thereby modifying the stiffness and mass distribution of the overall wall system.

To ensure a consistent comparison between the two configurations, identical material properties, wall dimensions, element formulations, mesh characteristics, and boundary conditions were adopted in both numerical models. The only geometric difference between the models was the presence of the 0.40 × 0.40 m masonry piers in the modified configuration. This modeling strategy allows the changes observed in the modal parameters to be evaluated specifically in relation to the introduction of the masonry piers, while minimizing the influence of other modeling variables.

The numerical models were developed and analyzed using SAP2000. An eigenvalue-based modal analysis was performed to determine the natural frequencies and corresponding mode shapes of both wall configurations. The modal properties obtained from the reference and pier-equipped models were subsequently compared to evaluate the influence of the regularly masonry piers on the dynamic characteristics of the wall. Particular attention was given to variations in the natural frequencies and changes in the corresponding modal deformation patterns, as these parameters provide useful information regarding the influence of the piers on the global stiffness and vibration characteristics of the masonry wall.

The dynamic characteristics of the two wall configurations were investigated through an eigenvalue-based modal analysis implemented in SAP2000 [26]. In the numerical procedure, the mass and stiffness characteristics of each finite element model were considered to obtain the eigenvalues and corresponding natural vibration frequencies of the wall system. The associated mode shapes were also determined to identify the predominant deformation patterns developed under free-vibration conditions. This approach

provides a consistent basis for examining the dynamic response of the wall configurations without introducing differences arising from external loading or excitation conditions. For each model, the calculated modal parameters were evaluated using the same analysis assumptions and modeling conditions. The results obtained for the reference wall were compared with those of the configuration incorporating regularly masonry piers. The comparison focused primarily on the changes in the natural frequencies and the spatial distribution of modal deformations. Since the introduction of the piers alters both the geometry and the distribution of structural mass and stiffness, differences in the modal characteristics can be used to assess their influence on the overall vibration behavior of the wall. Particular emphasis was placed on the lower-order modes, which generally represent the dominant global deformation patterns of the wall system. In addition to the numerical variation in natural frequencies, the corresponding mode shapes were examined to determine whether the presence of the masonry piers resulted in noticeable changes in the global deformation mechanism and modal response [27–29]. The combined evaluation of these parameters provides a basis for assessing the dynamic implications of incorporating masonry piers into long hollow concrete block garden walls.

A. Reference Wall Model

The reference model was established to represent a simplified and idealized hollow concrete block garden wall, providing a baseline configuration for investigating the effect of masonry piers on its dynamic characteristics. The model was intentionally defined without vertical piers so that the inherent modal properties of the continuous wall could first be determined under uniform geometric and material conditions. The wall has a total length of 20.0 m, a height of 1.5 m, and a thickness of 0.20 m. This geometry was selected to represent a long, relatively low-height boundary wall configuration commonly encountered in garden and property perimeter applications. In the reference configuration, the wall was modeled as a continuous structural system along its entire length, without openings, local geometric irregularities, or other discontinuities that could introduce additional effects into the modal response. Such an idealized arrangement provides a controlled basis for subsequently examining the changes associated with the introduction of regularly masonry piers. The wall was discretized using shell elements within the SAP2000 finite element environment. For the numerical analysis, the hollow concrete block masonry was represented by equivalent homogeneous material properties and assumed to exhibit isotropic and linear elastic behavior. These assumptions were adopted to focus the investigation on the global dynamic response of the wall rather than on localized nonlinear phenomena occurring within individual blocks or mortar joints. A mesh sensitivity assessment was performed to establish an appropriate level of finite element discretization for the numerical models. The selected mesh was intended to provide a suitable balance between computational efficiency and the accuracy of the calculated modal parameters. Based on the mesh assessment, a uniform element size of 0.25 m × 0.25 m was adopted throughout the wall models. The selected discretization produced stable natural frequency values, while further refinement resulted in only minor changes in the calculated modal parameters. Therefore, the adopted mesh density was considered adequate for representing the global deformation characteristics and vibration behavior of the investigated wall. The lower edge of the wall was assumed to be continuously connected to a rigid foundation. Accordingly, the translational and rotational degrees of freedom along the base were restrained to represent the idealized support condition of a free-standing garden wall founded on a continuous base. No external loading was applied during the eigenvalue analysis, since the purpose of the analysis was to determine the inherent vibration characteristics governed primarily by the mass and stiffness distributions of the structural system. Under these assumptions, the natural frequencies and mode shapes obtained from the reference model were taken as the baseline modal parameters.

Figure 1 presents the geometric configuration and principal dimensions of the reference hollow concrete block garden wall considered in the numerical analysis.

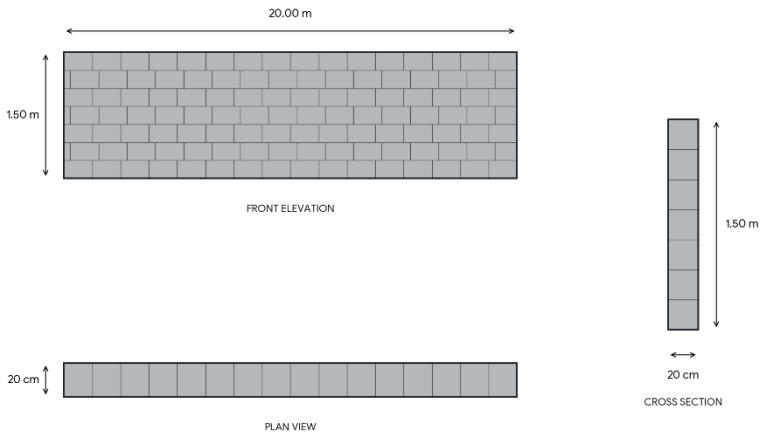

Fig. 1 Schematic representation and geometric details of the investigated hollow concrete block garden wall model

The important mechanical properties of the used hollow concrete garden wall [30-34] in this study;

- Density: 1325.6 kg/m³
- Modulus of elasticity: 1.5 GPa
- Poisson's ratio: 0.2

The 3D finite element model of the reference wall model is given in Figure 2.

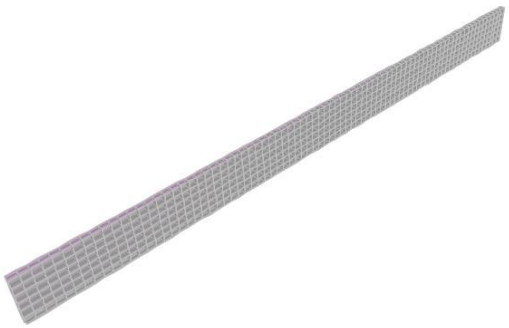

Fig. 2 The 3D finite element model of reference wall model

B. Pier Equipped Model

The second numerical configuration was established by incorporating regularly masonry piers into the reference hollow concrete block garden wall. Except for the introduction of these vertical pier elements, the principal modeling assumptions and numerical parameters were kept consistent with those adopted for the reference configuration. The wall dimensions, material properties, finite element formulation, mesh density, and support conditions were therefore maintained unchanged. This modeling strategy provides a consistent basis for identifying the changes in the modal response associated specifically with the presence of the masonry piers. The pier-equipped configuration consists of vertical masonry piers distributed along

the full length of the wall at regular intervals. The piers were modeled using frame elements Each pier has a square cross-section of 0.40 m × 0.40 m and is positioned at 2.50 m intervals along the wall. The piers were modeled as integral vertical components of the masonry wall and were assumed to be fully connected to the adjacent wall sections. This configuration was adopted to represent a regularly supported garden wall system in which the vertical masonry elements modify the geometric continuity and distribution of mass and stiffness along the wall length. The resulting arrangement allows the effect of the piers on the global vibration characteristics to be examined without introducing other geometric or material modifications.

The geometric configuration and detailed dimensions of the masonry pier equipped wall model are presented in Figure 3.

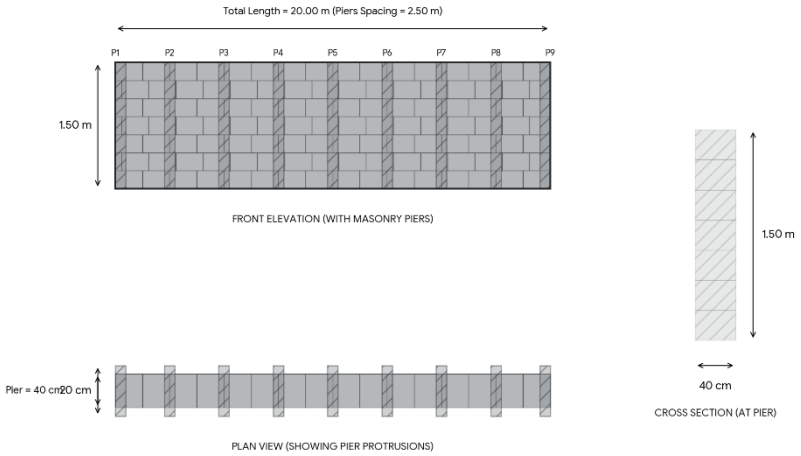

Fig. 3 Schematic view and geometric details of the investigated hollow concrete block garden wall with masonry piers

The 3D finite element model of the pier equipped model is given in Figure 4.

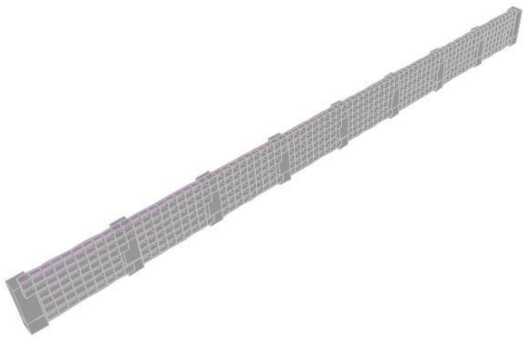

Fig. 4 The 3D finite element model of pier equipped model

III. RESULTS AND DISCUSSION

A. Reference Wall Model

The modal response of the reference wall was evaluated using the finite element model developed in SAP2000. The first five vibration modes were considered to characterize the fundamental dynamic behavior of the hollow concrete block garden wall. The corresponding mode shapes and natural periods obtained from the eigenvalue analysis are presented in Figure 5.

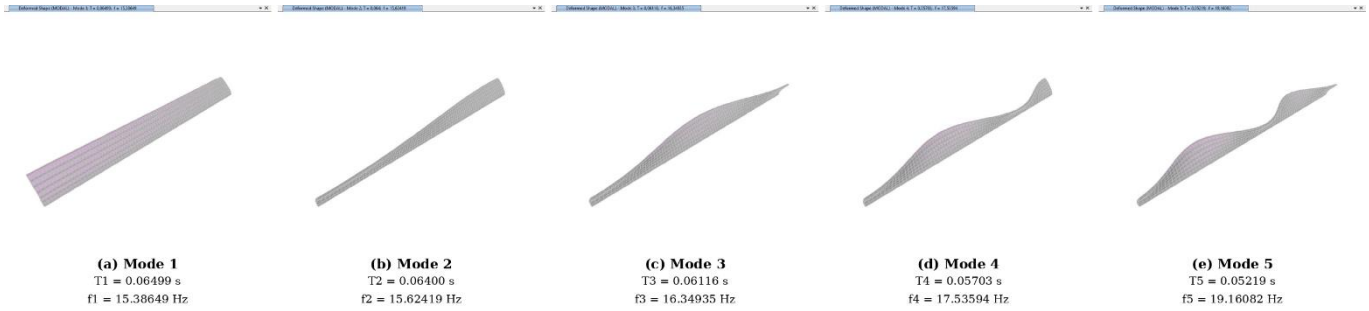

Fig. 5 First five mode shapes and corresponding natural periods and frequencies of the reference hollow concrete block garden wall

The natural periods and corresponding mass participation ratios obtained for the first five modes of the reference wall model are presented in Table 1.

Table 1. The period values and mass participation ratios of the reference wall model

Mode	Period	UX	UY	UZ	RX	RY	RZ
	Sec	Unitless	Unitless	Unitless	Unitless	Unitless	Unitless
1	0,064992	2,077E-18	0,66164	0	0,49909	1,741E-20	1,023E-19
2	0,064003	1,257E-17	1,132E-18	0	1,286E-18	1,256E-19	0,6529
3	0,061165	6,577E-18	0,00002588	0	0,00001911	2,45E-19	9,234E-18
4	0,057026	1,164E-17	7,222E-18	0	8,065E-18	1,525E-19	0,00794
5	0,05219	3,425E-18	0,000000756	0	2,299E-07	0	6,712E-17

B. Pier Equipped Model

The modal characteristics of the masonry pier equipped wall model were evaluated through an eigenvalue-based finite element analysis. The first five mode shapes obtained from the analysis are presented in Figure 6.

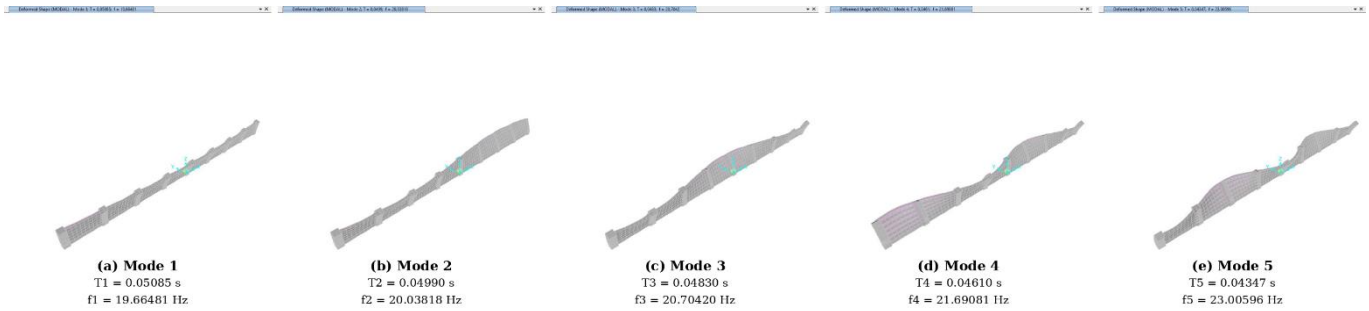

Fig. 6 First five mode shapes and corresponding natural periods and frequencies of the reference hollow concrete block garden wall

The natural periods and corresponding mass participation ratios obtained for the first five modes of the pier equipped wall are presented in Table 2.

Table 2. The period values and mass participation ratios of the pier equipped wall model

Mode	Period	UX	UY	UZ	RX	RY	RZ
	Sec	Unitless	Unitless	Unitless	Unitless	Unitless	Unitless
1	0,050852	6,691E-16	0,61425	1,862E-19	0,45535	2,803E-18	1,911E-19
2	0,049905	6,279E-17	2,172E-16	4,836E-20	2,514E-16	1,995E-20	0,55922
3	0,048299	6,691E-16	0,03889	3,223E-20	0,02862	4,091E-18	2,194E-16
4	0,046102	4,929E-15	1,588E-16	1,704E-18	1,804E-16	1,06E-17	0,07407
5	0,043467	2,566E-14	0,00795	3,528E-20	0,00578	1,262E-16	1,423E-16

C. Comparison of Results

In order to clearly demonstrate the effects, data from the first five modes of analysis for both models were compared individually. The comparison of period values of the reference and pier equipped model is given in Table 3.

Table 3. Comparison of period values

Mode	1	2	3	4	5
Reference model (sec)	0,064992	0,064003	0,061165	0,057026	0,05219
Pier equipped model (sec)	0,050852	0,049905	0,048299	0,046102	0,043467
Difference (sec)	0,01414	0,014098	0,012866	0,010924	0,008723
Difference (%)	21,76%	21,99%	21,03%	19,16%	16,71%

The comparison of mode shapes of the reference and pier equipped model is given in Table 4.

Table 4. Comparison of mode shapes

Mode	1	2	3	4	5
Reference model	Translational	Torsional	Translational	Torsional	Translational
Pier equipped model	Translational	Torsional	Translational	Torsional	Translational

The comparison of the modal parameters obtained from the reference and masonry pier-equipped models reveals a consistent reduction in the natural vibration periods following the introduction of the regularly masonry piers. The first natural period decreased from 0.06499 s in the reference model to 0.05085 s in the pier-equipped model, corresponding to a reduction of approximately 21.76%. Similar reductions were observed for the higher vibration modes, with the second, third, fourth, and fifth modal periods decreasing by 21.99%, 21.03%, 19.16%, and 16.71%, respectively. Accordingly, the corresponding natural frequencies increased from 15.39 Hz to 19.66 Hz for the first mode and from 15.62 Hz to 20.04 Hz for the second mode. For the third, fourth, and fifth modes, the natural frequencies increased from 16.35, 17.54, and 19.16 Hz to 20.70, 21.69, and 23.01 Hz, respectively. The consistent increase in natural frequencies across all five investigated modes indicates that the introduction of the masonry piers produces a substantial change in the dynamic characteristics of the wall system. Considering that the piers modify both the stiffness and mass distribution of the wall, the observed shift toward higher frequencies can be attributed to an increase in the overall stiffness-to-mass ratio of the pier-equipped configuration.

The mass participation ratios also exhibit noticeable changes between the two configurations. In the reference model, the first vibration mode is predominantly characterized by translational motion in the Y-direction, with a mass participation ratio of 66.16%, accompanied by a rotational participation of 49.91% about the RX axis. Following the introduction of the masonry piers, these values decreased to 61.43% and 45.54%, respectively. The second mode is mainly associated with rotation about the vertical RZ axis, for which the mass participation ratio decreased from 65.29% in the reference model to 55.92% in the pier-equipped configuration. These reductions in the dominant participation ratios suggest that the addition of the piers alters the distribution of modal mass among the vibration modes rather than simply increasing the participation of the fundamental modes. This effect becomes particularly evident in the third, fourth, and

fifth modes. While the third mode of the reference model exhibits negligible Y-direction and RX-axis participation, with values of approximately 0.0026% and 0.0019%, respectively, these values increase to 3.89% and 2.86% after the introduction of the piers. Similarly, the RZ participation of the fourth mode increases from approximately 0.79% to 7.41%. The fifth mode also shows an increase in Y-direction participation from a negligible value of approximately 0.00008% to 0.80%, while the RX participation increases to approximately 0.58%. These changes indicate that the masonry piers redistribute a portion of the modal response toward higher-order vibration modes and modify the deformation characteristics of the wall system.

In addition, the modal analysis demonstrates that the introduction of regularly masonry piers significantly modifies the dynamic behavior of the hollow concrete block garden wall. The reduction in modal periods, ranging from approximately 16.71% to 21.99%, and the corresponding increase in natural frequencies demonstrate that the pier-equipped configuration exhibits a higher stiffness-to-mass ratio than the reference wall. At the same time, the changes in mass participation ratios indicate that the effect of the piers is not limited to the fundamental vibration characteristics but also extends to the distribution of modal response among the higher-order modes. The reduction in the dominant Y-direction and RX-axis participation of the first mode, together with the increased participation observed in the third to fifth modes, suggests that the regularly piers modify the global deformation pattern of the wall and introduce a more distributed modal response. This behavior can be related to the additional vertical structural members, which locally alter the stiffness and mass distribution along the 20.0 m long wall.

The results further indicate that the influence of the masonry piers is more pronounced in the lower vibration modes, where the reductions in natural periods are approximately 21–22%, while the effect gradually decreases for the higher modes. This trend suggests that the piers have a particularly notable influence on the global dynamic characteristics of the wall, whereas their relative effect becomes less pronounced as the vibration modes become more complex. Nevertheless, the changes observed in the higher-order modal participation ratios demonstrate that the piers also affect the distribution of localized and higher-order deformation patterns. Therefore, the incorporation of regularly masonry piers should be considered not only in terms of its effect on the fundamental natural frequency but also in relation to the overall modal characteristics of the wall.

The results show that the use of hollow concrete block masonry piers at regular intervals can substantially alter the vibration characteristics of long garden walls without changing the principal dimensions or material properties of the main wall. The increase in natural frequencies and the redistribution of modal mass participation provide evidence of a modified dynamic response resulting from the additional vertical members.

IV. CONCLUSION

This study numerically investigated the influence of regularly masonry piers on the modal behavior of a long hollow concrete block garden wall using the Finite Element Method. Two three-dimensional numerical models were developed in SAP2000, representing the reference wall and the wall configuration incorporating 0.40 × 0.40 m hollow concrete block masonry piers at 2.50 m intervals. Eigenvalue-based modal analyses were performed to evaluate the changes in natural periods, natural frequencies, and mass participation characteristics resulting from the introduction of the piers.

The introduction of masonry piers resulted in a consistent reduction in the natural vibration periods of the wall. The first five modal periods decreased by approximately 16.71–21.99%, with the first natural period decreasing from 0.06499 s to 0.05085 s. The greatest reductions were observed in the first three modes, indicating a pronounced influence of the piers on the lower-order dynamic characteristics of the wall.

The natural frequencies increased for all five investigated modes following the introduction of the masonry piers. The first-mode frequency increased from 15.39 Hz to 19.66 Hz, while the frequencies of the second to fifth modes increased from 15.62, 16.35, 17.54, and 19.16 Hz to 20.04, 20.70, 21.69, and 23.01 Hz, respectively. The corresponding frequency increases ranged from approximately 20.11% to 28.25%, indicating a significant modification of the stiffness-to-mass characteristics of the wall system.

The masonry piers also modified the distribution of modal mass participation. The dominant Y-direction participation of the first mode decreased from 66.16% to 61.43%, while the RX rotational participation decreased from 49.91% to 45.54%. Similarly, the dominant RZ participation of the second mode decreased from 65.29% to 55.92%. These changes indicate that the introduction of the piers modifies the distribution of the dynamic response among the vibration modes.

A redistribution of modal participation toward higher-order modes was observed in the pier-equipped configuration. In particular, the third mode, which exhibited negligible Y-direction and RX participation in the reference model, reached 3.89% and 2.86%, respectively, after the introduction of the piers. The RZ participation of the fourth mode also increased from approximately 0.79% to 7.41%. These changes demonstrate that the effect of the piers extends beyond the fundamental mode and influences the overall modal response of the wall.

The observed changes in the modal parameters demonstrate that regularly masonry piers have a significant influence on the global vibration characteristics of long hollow concrete block garden walls. The reduction in natural periods and corresponding increase in natural frequencies indicate an increase in the effective stiffness-to-mass ratio of the modified wall configuration, while the changes in modal participation ratios reveal a redistribution of the dynamic response.

The results should be interpreted within the limitations of the numerical and linear modal analysis adopted in this study. Therefore, experimental investigations and nonlinear numerical analyses are recommended to further evaluate the structural implications of the observed modal changes and to assess the behavior of masonry pier-equipped garden walls under realistic loading conditions.

The results provide a numerical basis for understanding the relationship between pier configuration and the dynamic behavior of hollow concrete block wall systems and may support future experimental and analytical studies on their structural performance under dynamic loading.

REFERENCES

[1] Lourenço, P. B. (1996). Computational strategies for masonry structures [Doctoral dissertation, Delft University of Technology].

[2] Pande, G. N., Liang, J. X., & Middleton, J. (1989). Equivalent elastic moduli for brick masonry. Computers & Structures, 31(6), 879–887.

[3] Cecchi, A., & Sab, K. (2002). A multi-parameter homogenization study for modeling elastic masonry. European Journal of Mechanics - A/Solids, 21(2), 249–268.

[4] Lourenço, P. B. (2002). Computations on historic masonry structures. Progress in Structural Engineering and Materials, 4(3), 301–319.

[5] Al-Wathaf, A. H. (2009). 3D finite element analysis of hollow concrete block masonry. Journal of Science and Technology, 14(2), 26–35.

[6] Thanoon, W. A. M., Alwathaf, A. H., Noorzaei, J., Jaafar, M. S., & Abdulkadir, M. R. (2008). Finite element analysis of interlocking mortarless hollow block masonry prism. Computers & Structures, 86(5–6), 520–528.

[7] Murthy, A. R. C., et al. (2012). Experimental and numerical investigation on in-plane behaviour of hollow concrete block masonry panels. Computers and Concrete, 10(1), 1–18.

[8] Al-Shugaa, M. A., et al. (2019). Performance of hollow concrete block masonry walls retrofitted with steel-fiber and microsilica admixed plaster. Structural Concrete, 20(1), 236–251.

[9] De Sortis, A., Antonacci, E., & Vestroni, F. (2005). Dynamic identification of a masonry building using forced vibration tests. Engineering Structures, 27(2), 155–165.

[10] Kalali, A., & Kabir, M. Z. (2012). Experimental response of double-wythe masonry panels strengthened with glass fiber reinforced polymers subjected to diagonal compression tests. Engineering Structures, 39, 24-37.

[11] Baraldi, D., Bullo, S., & Cecchi, A. (2016). Continuous and discrete strategies for the modal analysis of regular masonry. International Journal of Solids and Structures, 84, 82–98.

[12] Nicoletti, V., Arezzo, D., Carbonari, S., & Gara, F. (2022). Vibration-based tests and results for the evaluation of infill masonry walls influence on the dynamic behaviour of buildings: A review. Archives of Computational Methods in Engineering, 29, 3773–3787.

[13] Pepi, C., Cavalagli, N., Gusella, V., & Ubertini, F. (2021). Damage detection via modal analysis of masonry structures using shaking table tests. Earthquake Engineering & Structural Dynamics, 50, 1987–2006.

[14] Meoni, A., D'Alessandro, A., Mattiacci, M., García-Macías, E., Saviano, F., Parisi, F., Lignola, G. P., & Ubertini, F. (2024). Structural performance assessment of full-scale masonry wall systems using operational modal analysis: Laboratory testing and numerical simulations. Engineering Structures, 304, 117663.

[15] Calderini, C., Cattari, S., & Lagomarsino, S. (2009). In-plane strength of unreinforced masonry piers. Earthquake Engineering & Structural Dynamics, 38(3), 243–267.
[16] Kasımzade, A. A. (2018). Finite Element Method: Foundation and Application to Earthquake Engineering, Nobel Academic Publishing, Ankara, Turkey.
[17] Tuhta, S., Günday, F., & Pehlivan, N. C. (2019). Investigation of CFRP Retrofitting Effect on Masonry Dome on Bending Moment Using Finite Element Method. International Journal of Innovatıons in Engineering Research and Technology, 6(6), 18–22.
[18] Tuhta, S., Günday, F., & Warayth, M. O. (2021). The Effect of GFRP Steel Silo on Modal Parameters Using Finite Element Method. International Journal of Innovatıons in Engineering Research and Technology, 8(7), 41–46.
[19] Tuhta, S., & Günday, F. (2025). Investigation of steel chimney retrofitted with nanocoating under earthquake excitation using FEM. Coatings, 15(6), 619. https://doi.org/10.3390/coatings15060619
[20] Günday, F. (2023). The Effect of Using Molybdenum Profile in Model Steel Structure Columns on The Modal Parameters. Turkish Journal of Science and Technology, 18(2), 415–424.
[21] Günday, F., & Tuhta, S. (2025). Dynamic effects of central X steel braces at the specified node point in the steel structure model. European Journal of Research Development and Sustainability, 6(2), 9–18.
[22] Sel, A., Günday, F., & Tuhta, S. (2023). Investigation of Tunnel Formwork Structure Retrofitted with JFRP by Finite Element Method. JournalNx, 9(1), 1-11.
[23] Günday, F. (2025). The Impact of Using Shell-Thick Elements instead of Shell-Thin Elements on Modal Performance for RC Retaining Wall. Presented at the 5th International Conference on Trends in Advanced Research.
[24] Günday, F. (2026). Numerical Study on the Modal Behavior of Reinforced Concrete Frame-Strengthened Masonry Brick Garden Walls. Presented at the 7th International Conference on Trends in Advanced Research.
[25] Reddy, J. N. (2026). An introduction to the finite element method. In Dynamics of Earth's Fluid System (pp. 199-226). CRC Press.
[26] Computers and Structures, Inc. SAP2000: Integrated Structural Analysis and Design Software, Version 26.0; Computers and Structures, Inc.: Berkeley, CA, USA, 2024
[27] Clough, R. W., & Penzien, J. (1993). Dynamics of structures (2nd ed.). McGraw-Hill.
[28] Chopra, A. K. (2017). Dynamics of structures: Theory and applications to earthquake engineering (5th ed.). Pearson.
[29] Kasımzade, A. A. (2018). Fundamentals of Structural Dynamics and Applications in Earthquake Engineering, Nobel Academic Publishing, Ankara, Turkey.
[30] T.C. Çevre ve Şehircilik Bakanlığı. (2018). Türkiye bina deprem yönetmeliği (TBDY 2018). Ankara, Türkiye.
[31] American Society for Testing and Materials. (2022). Standard specification for loadbearing concrete masonry units (ASTM C90-22).
[32] European Committee for Standardization. (2005). Eurocode 6: Design of masonry structures - Part 1-1: General rules for reinforced and unreinforced masonry (EN 1996-1-1). CEN.
[33] Türk Standartları Enstitüsü. (1997). Yapıların tasarımı için esaslar - Kalıcı ve hareketli yükler - Yoğunluklar (TS ISO 9194). TSE.
[34] The Masonry Society. (2022). Building code requirements and specification for masonry structures (TMS 402/602-22). TMS.

8th International Conference on Engineering, Natural and Social Sciences

September 06-07, 2026: Konya, Turkey

© 2026 Published by All Sciences Academy

https://www.icensos.com/

Smart Face Recognition for Attendance in Education

Viola Bakiasi (Shtino)

Computer Science Department, Faculty of Information Technology, University "Aleksander Moisiu of Durres, Albania

Email of the corresponding author: violashtino@uamd.edu.al

Abstract **–** Attendance recording is a routine administrative activity, yet in large classrooms and institutional environments it can consume teaching time, produce transcription errors, and remain vulnerable to proxy attendance. This paper examines face recognition as a contactless mechanism for smart attendance in schools, universities, training centers, and other institutions. Rather than presenting facial recognition as a simple camera-based replacement for a paper register, the study develops a human-centered technical framework in which face detection, alignment, deep facial embeddings, similarity matching, attendance validation, and secure record management operate as a single pipeline. The paper synthesizes established work on Viola–Jones detection, DeepFace, FaceNet, and ArcFace with recent research on educational attendance systems. A methodology is specified using cosine similarity, threshold-based identity decisions, and standard biometric evaluation measures, including accuracy, precision, recall, F1-score, false acceptance rate, and false rejection rate. The analysis indicates that deep embedding approaches are technically better suited to variable classroom conditions than older appearance-based methods, while operational benefits include reduced roll-call time, automatic timestamping, centralized records, and improved auditability. At the same time, deployment in education introduces material risks involving consent, data minimization, spoofing, image quality, demographic differentials, and the treatment of biometric templates. Accordingly, the paper argues that educational face recognition should be designed as an assistive attendance infrastructure with human review and alternative attendance routes, not as an unquestionable automated authority. The resulting framework provides a practical foundation for future controlled implementation and empirical evaluation.

Keywords – face recognition; smart attendance; computer vision; deep learning; biometric systems; educational technology.

I. INTRODUCTION

Attendance is one of the simplest forms of institutional data, but the process used to produce it is often inefficient. In a traditional classroom, a lecturer may call names, circulate a paper sheet, scan identity cards, or rely on a learning-management system that still requires manual confirmation. These methods are understandable because they are inexpensive and familiar; however, they also create repetitive administrative work and can generate incomplete, delayed, or inaccurate records. In a lecture with many students, even a short roll call can interrupt the opening minutes of teaching.

Computer vision offers a different model: the camera becomes a sensing device, while the software determines whether a visible face corresponds to an enrolled identity. This distinction is important because face detection and face recognition are not the same task. Detection answers the question “where is a face?”, whereas recognition asks “whose face is it?”. The classical Viola–Jones cascade demonstrated that real-time face detection could be achieved efficiently using boosted simple features [1]. Later deep-

learning systems changed recognition itself by learning increasingly discriminative facial representations rather than depending on manually designed descriptors.

DeepFace formalized a modern recognition pipeline around detection, alignment, representation, and classification, reporting strong performance on unconstrained face verification [2]. FaceNet then learned a compact embedding space in which distances correspond to facial similarity, enabling verification, recognition, and clustering through a common representation [3]. ArcFace further improved the discriminative structure of deep embeddings through an additive angular margin objective [4]. These developments make it technically feasible to construct attendance systems that recognize enrolled users from live camera frames rather than requiring a card, signature, or manual name check.

In education, the value proposition is broader than speed. A well-designed system can timestamp attendance, reduce duplicate entry, support rapid reporting, and create consistent records across classrooms. A systematic literature review focused on university attendance found that CNN-based recognition generally offers more stable accuracy than LBPH when external conditions vary [5]. More recent classroom research using CCTV and transfer learning also reports promising precision and recall, while emphasizing camera quality and viewing geometry as practical constraints [6].

Nevertheless, the fact that a system can recognize faces does not automatically mean that it should make high-stakes decisions without safeguards. Biometric attendance involves persistent identity data. Errors may be unevenly distributed across people, and performance can change with illumination, pose, camera placement, occlusion, aging, or image quality. NIST evaluations have documented demographic differentials across many face recognition algorithms, demonstrating that algorithm choice and capture conditions matter [7]. For educational institutions, this means that technical accuracy, fairness, privacy, security, and procedural transparency must be treated as parts of the same design problem.

The objective of this paper is therefore to propose and critically analyze a complete face recognition-based attendance framework for schools, universities, and institutions. The contribution is threefold: first, it explains the technical pipeline in a reproducible mathematical form; second, it connects recognition performance with concrete institutional benefits and failure modes; and third, it defines deployment principles that preserve human oversight. The paper is structured as a design-and-evidence study rather than as a claim of a newly completed biometric trial; the Results section synthesizes reported evidence and derives operational findings from the proposed framework.

II. Literature Review

1) From Face Detection to Deep Face Recognition

Early real-time face analysis depended heavily on efficient detection. Viola and Jones [1] introduced a boosted cascade architecture that rapidly rejected non-face regions and concentrated computation on promising image windows. Although modern deep detectors can outperform Haar cascades in difficult scenes, the Viola–Jones method remains educationally important because it illustrates the first stage of the pipeline: a recognition system cannot compare identities reliably until the face region has been localized.

DeepFace represented a major transition from handcrafted facial measurements to learned representations. Its pipeline combined alignment with a deep neural network and achieved 97.35% accuracy on the Labeled Faces in the Wild benchmark reported in the original study [2]. The broader methodological lesson is that alignment and representation quality strongly influence downstream verification.

FaceNet shifted the problem toward metric learning. Instead of treating every identity decision only as a conventional classification problem, FaceNet maps an input face to an embedding vector. Faces of the same person should lie near each other in the learned space, while faces of different people should be separated. The original work reported 99.63% accuracy on LFW and showed that compact embeddings can support several identity tasks [3]. This architecture is especially suitable for attendance because new enrolled users can be represented by stored templates without redesigning the entire application logic.

ArcFace improved the geometry of identity separation by introducing an additive angular margin into the classification objective. The method encourages tighter intra-class clustering and stronger inter-class separation on a normalized hypersphere [4]. For an attendance application, this matters because the

system often compares a live face against a gallery containing many registered identities; a more discriminative embedding can reduce ambiguous matches.

2) Face Recognition for Attendance

Attendance automation has been studied using local binary patterns, classical machine learning, convolutional neural networks, transfer learning, and deep embeddings. The systematic review by Sutabri et al. [5] specifically compared LBPH- and CNN-oriented approaches and concluded that CNN methods tend to be more accurate and more stable under external variation. This finding supports the use of learned embeddings in environments where lighting, expression, seating position, and camera distance cannot be perfectly standardized.

Recent work has moved from small webcam demonstrations toward classroom-oriented CCTV scenarios. Mekala et al. [6] evaluated ResNet-50 and VGG-16 in an attendance context and reported precision/recall of 96%/93% for ResNet-50 and 92%/89% for VGG-16 in their experimental setting. These values should not be interpreted as universal performance guarantees, but they demonstrate that deep transfer-learning pipelines can be operationally viable when the capture environment and dataset are appropriate.

Bibliometric evidence also suggests that facial recognition attendance has become an identifiable research stream within smart education. Agustiyar et al. [8] analyzed Scopus-indexed work from 2019–2024 and described automated attendance as a recurring application of facial recognition and deep learning. The research trend is therefore moving beyond proof-of-concept detection toward questions of system integration, deployment quality, explainability, privacy, and institutional governance.

Recent work by Bakiasi Shtino and collaborators provides additional evidence that facial-image analysis can benefit from carefully designed preprocessing, representation learning, and real-time detection. Bakiasi Shtino et al. [9] combined dimensionality-reduction techniques with supervised classifiers for facial micro-expression recognition, while Bakiasi Shtino et al. [10] explored real-time facial micro-expression recognition with YOLOv8 and FER2013. Although emotion recognition and identity recognition are distinct tasks, these studies are methodologically relevant because both depend on reliable face localization, image normalization, discriminative feature extraction, and robust inference under changing facial appearance. More recently, Bakiasi Shtino [11] reported a hybrid framework combining facial landmark extraction, dimensionality reduction, and machine-learning classification, reinforcing the value of structured facial feature pipelines for computer-vision applications.

3) Educational and Institutional Value

In schools and universities, attendance information can support course administration, laboratory access, examination logistics, student-support workflows, and compliance reporting. The principal operational advantage of facial attendance is not merely that a face can be recognized; it is that recognition can be linked to time, location, course, and enrollment data without requiring each student to perform a separate physical transaction. This can reduce queues and repeated manual entry. In workplaces and public institutions, the same architecture can be adapted for staff attendance or authorized access, although the legal basis and proportionality analysis may differ from education.

A second benefit is auditability. A digital attendance event can contain a timestamp, course identifier, confidence score, device identifier, and review status. Such metadata can make corrections easier than a handwritten sheet, provided that the institution defines retention periods and does not preserve unnecessary raw facial imagery. The system can also flag uncertain matches for human confirmation rather than silently converting low-confidence recognition into an absence.

4) Risks, Bias, Privacy, and Human Oversight

Biometric systems are probabilistic. A false acceptance occurs when an unauthorized or different person is incorrectly matched; a false rejection occurs when a legitimate person is not recognized. In attendance, both errors matter: the first can enable proxy attendance, while the second can incorrectly mark a present student as absent.

Large-scale NIST evaluations have shown that demographic differentials can occur in face recognition and that performance varies substantially by algorithm and image quality [7]. NIST also emphasizes that

false negatives are strongly influenced by poor photography, including under- or over-exposure and unfavorable camera geometry. This evidence argues against deploying one fixed threshold and assuming identical behavior in every classroom.

Privacy is equally important. Facial images and embeddings should be treated as sensitive biometric information. A privacy-aware design should minimize raw image storage, encrypt templates, restrict access, log administrative actions, define deletion schedules, and provide a non-biometric attendance route where required. A 2026 study on privacy-preserving facial attendance similarly identifies privacy, demographic bias, spoofing, and resource constraints as central deployment issues [12].

III. Materials and Method

This study adopts a design-science and evidence-synthesis methodology. It specifies a complete technical architecture for a face recognition attendance system and evaluates its expected operational behavior using established biometric metrics and published empirical evidence. No claim is made that a new human-subject biometric dataset was collected for this paper. This distinction prevents literature-derived performance values from being presented as original experimental measurements.

A. Proposed System Architecture

The proposed architecture contains seven stages: (1) enrollment, (2) video acquisition, (3) face detection, (4) alignment and normalization, (5) deep embedding extraction, (6) similarity-based identity decision, and (7) attendance recording and review. As illustrated in Figure 1, these stages form a continuous pipeline from image acquisition to the creation of a validated attendance event. Enrollment stores one or more reference templates for each authorized student or staff member. During operation, the camera captures frames; detected faces are aligned; the embedding network produces a feature vector; and the live vector is compared with registered templates. A match above the accepted threshold creates a provisional attendance event, subject to duplicate suppression and confidence rules.

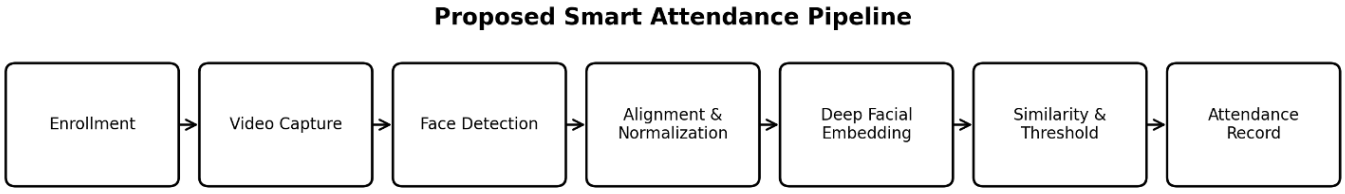

Fig. 1. Proposed methodology for a face recognition-based smart attendance system.

The workflow converts a live classroom image into a validated attendance event. Face detection and normalization prepare the input, a deep model produces a compact identity embedding, and similarity thresholding determines whether the observed face corresponds to an enrolled participant before the event is stored.

B. Face Detection and Pre-processing

Let an RGB video frame at time t be represented by I_t. A detector returns a set of bounding boxes $B_t = \{b_1, b_2, ..., b_n\}$. Each detected face is cropped, aligned using facial landmarks when available, resized to the input dimensions expected by the embedding network, and normalized. In a lightweight prototype, Haar Cascade detection may be used; in a more robust deployment, a modern deep face detector is preferable when pose and illumination vary.

C. Deep Facial Embedding

For an aligned face image x, the recognition network f_θ maps the image into a d-dimensional embedding vector z. The general representation is:

$$z = f_\theta(x),\ z \in \mathbb{R}^d \tag{1}$$

To make angular or cosine comparison stable, the embedding can be L_2-normalized:

$$\hat{z} = \frac{z}{\|z\|_2} \tag{2}$$

This representation follows the metric-learning logic popularized by FaceNet and later angular-margin methods: identity is evaluated through distances or angles in embedding space rather than through raw pixels [3], [4].

D. Similarity and Identity Decision

Given a normalized live embedding $\hat{z}_q$ and a normalized enrolled template $\hat{z}_i$, cosine similarity is computed as:

$$S(q,i) = \frac{z_q \cdot z_i}{\|z_q\| \, \|z_i\|} \tag{3}$$

The predicted identity is the enrolled template with the highest similarity:

$$\hat{\imath} = arg\,maxi\, S(q,i) \tag{4}$$

The identity associated with the highest similarity score is considered the best candidate match. However, the system accepts this identity only when the corresponding similarity score reaches or exceeds a predefined threshold (τ). If the highest score remains below this threshold, the detected face is classified as unknown, and no automatic attendance record is generated. This threshold-based decision mechanism reduces the risk of assigning an identity when the available facial evidence is insufficient.

The threshold should be calibrated on validation data captured under conditions similar to the target institution. Lowering τ may increase convenience but can increase false acceptance; raising τ can reduce false acceptance while increasing false rejection. Therefore, threshold selection is a policy decision as well as a statistical one.

E. Attendance Logic

If a recognized identity is enrolled in the active class and has not already been recorded inside the duplicate-suppression interval Δt, the system creates an attendance record:

$$A_i(t) = \mathbb{1}\{S(q,i) \geq \tau\} \cdot E_i(c) \cdot [1 - D_i(t, \Delta t)] \tag{5}$$

where $\mathbb{1}\{\cdot\}$ is the indicator function, $E_i(c)=1$ when identity i is enrolled in class c, and $D_i(t, \Delta t)=1$ when a duplicate attendance event is detected within the suppression interval Δt.

The record should contain the minimum operational fields required by institutional policy, such as pseudonymous student identifier, course/session identifier, timestamp, recognition confidence, and review status. Raw video should not automatically be retained merely because it was used to produce the event.

F. Performance Metrics

For evaluation, TP denotes a correct accepted identity, FP an incorrect accepted identity, TN a correct rejection of a non-matching identity, and FN a failure to accept the correct identity. The following metrics are proposed:

$$Accuracy = \frac{TP + TN}{TP + TN + FP + FN} \tag{6}$$

$$Precision = \frac{TP}{TP + FP} \tag{7}$$

$$Recall = \frac{TP}{TP + FN} \tag{8}$$

$$F1 = 2 \times \frac{Precision \times Recall}{Precision + Recall} \tag{9}$$

$$FAR = \frac{FP}{FP + TN} \tag{10}$$

$$FRR = \frac{FN}{FN + TP} \tag{11}$$

For institutional deployment, overall accuracy alone is insufficient. FAR and FRR should be reported separately because they correspond to different operational harms. Results should also be stratified by relevant capture conditions and, where ethically and legally appropriate, audited for performance differentials across demographic groups.

G. Optional Training Objective

If the institution trains or fine-tunes an embedding model rather than using a fixed pretrained network, a metric-learning objective can be used. For FaceNet-style triplets consisting of an anchor a, positive p, and negative n, the triplet loss is:

$$L_{triplet} = \Sigma \left[\|f(a) - f(p)\|_2^2 - \|f(a) - f(n)\|_2^2 + \alpha \right] \tag{12}$$

where α is a margin that encourages the anchor to be closer to the positive sample than to the negative sample [3]. For large identity sets, ArcFace-style angular-margin training can provide stronger class separation [4].

H. Experimental Protocol for a Future Institutional Pilot

A rigorous pilot should recruit participants with informed institutional approval, capture multiple enrollment images per participant, and separate enrollment, validation, and test sessions by time. Test conditions should include frontal and moderate off-angle views, different classroom lighting, glasses where naturally worn, partial occlusion, and realistic camera distance. Threshold τ must be selected on the validation set only. The final test set should remain untouched until evaluation. A manual attendance record should be maintained in parallel as ground truth. This design avoids evaluating the system on the same images used for enrollment.

IV. RESULTS

Because this paper is a design-and-evidence study, the results below are a structured synthesis of published empirical findings and the operational consequences of the proposed architecture. They are not presented as newly collected participant data.

The quantitative evidence supports two complementary observations. First, benchmark verification systems such as DeepFace and FaceNet demonstrate the high discriminative capacity of deep facial representations, with the original studies reporting 97.35% and 99.63% accuracy on LFW, respectively [2], [3]. Second, classroom-oriented evidence remains strong but more variable: Mekala et al. [6] reported 96% precision and 93% recall for ResNet-50, compared with 92% precision and 89% recall for VGG-16. As visualized in Figure 2, the published indicators remain high across the selected deep-learning approaches, while the classroom-oriented models show the practical effect of a less controlled capture environment. The difference is important because a real attendance system is exposed to camera distance, pose, illumination, and partial occlusion that are not fully represented by controlled benchmark scores.

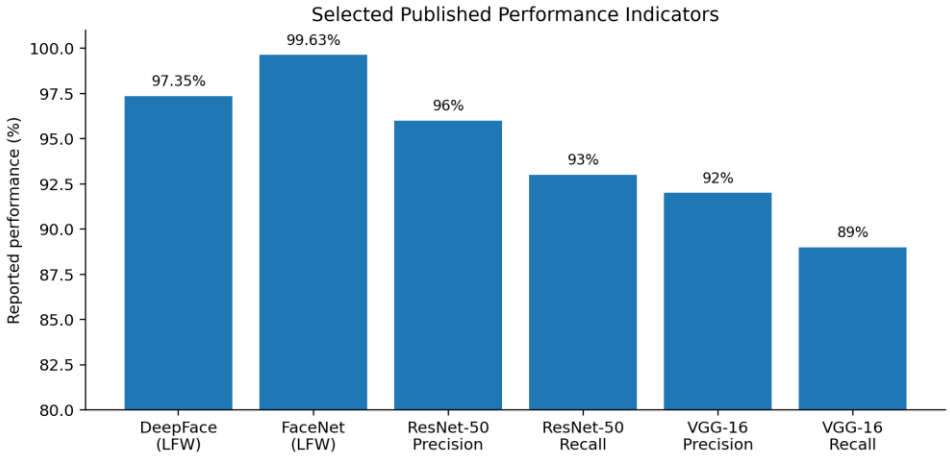

Fig. 2. Comparison of selected published performance indicators relevant to facial recognition and classroom attendance.

Figure 2 provides a literature-based comparison rather than a new experiment. The higher benchmark values reported for FaceNet and DeepFace confirm the discriminative power of deep facial embeddings, whereas the precision and recall values from the classroom study remain slightly lower because attendance operates under more variable acquisition conditions. The comparison therefore supports the use of deep representations while also showing that institutional performance must be evaluated at system level rather than inferred directly from benchmark accuracy.

Table 1. Evaluation dimensions and controls for an institutional face recognition attendance system.

Evaluation dimension	**Observed evidence**	**Implication for attendance**	**Recommended control**
Recognition capability	Deep models report high benchmark discrimination	Automated identity matching is technically feasible	Validate on local classroom data
Classroom robustness	Precision/recall decrease under practical capture conditions	Camera and environment affect attendance reliability	Calibrate camera placement and threshold
Error management	False acceptance and false rejection cannot both be minimized independently	A single accuracy score is insufficient	Report FAR/FRR and use human review
Operational value	Automatic timestamping and duplicate suppression are straightforward after identity validation	Administrative workload can be reduced	Integrate with course/session records
Responsible deployment	Biometric processing creates privacy and fairness risks	Technical success alone does not justify unrestricted use	Data minimization, access control, alternative attendance route

Table 1 translates biometric evaluation into operational controls. It shows that recognition quality cannot be judged by accuracy alone: false acceptance, false rejection, capture quality, duplicate handling, and privacy safeguards must be evaluated together. For an educational institution, this means that technical validation should be linked directly to attendance policy and to a manual review procedure for uncertain cases.

Table 2. Selected published evidence relevant to face recognition and smart attendance.

Study / Method	Context	Reported Result	Main Strength	Relevant Limitation
Taigman et al. (2014), DeepFace	LFW face verification	97.35% accuracy	Demonstrated deep representation + alignment	Benchmark result, not classroom attendance
Schroff et al. (2015), FaceNet	LFW / YouTube Faces	99.63% LFW accuracy	Compact metric embedding for similarity matching	Benchmark conditions differ from institutional deployment
Deng et al. (2019), ArcFace	Multiple face-recognition benchmarks	State-of-the-art improvements reported	Highly discriminative angular embeddings	Requires careful model/data selection
Sutabri et al. (2023)	Systematic review of attendance studies	CNN generally superior/stabler than LBPH	Direct relevance to university attendance	Review combines heterogeneous studies
Mekala et al. (2025)	CCTV classroom attendance	ResNet-50: 96% precision, 93% recall; VGG-16: 92%, 89%	Real classroom-oriented deep-learning evaluation	Camera quality and viewing geometry remain constraints

Table 2 summarizes the empirical evidence used in this study. The comparison indicates a clear progression from high-performing benchmark face-recognition models toward classroom-oriented transfer-learning systems. DeepFace and FaceNet demonstrate the strength of learned identity representations, while the classroom results of ResNet-50 and VGG-16 show that strong performance can be retained in a more realistic attendance context, although direct numerical comparison is limited by differences in datasets, tasks, and evaluation protocols.

A. Operational Findings for Schools and Universities

Table 3. Evidence-to-deployment interpretation of the proposed smart attendance framework.

Finding	Institutional Interpretation
Reduced administrative interruption	Recognition can occur while students enter or settle, reducing the need for name-by-name roll call.
Automatic timestamping	Each accepted attendance event can be linked to the correct class session and time without later transcription.
Lower proxy-attendance opportunity	A facial match is harder to transfer between students than a paper signature or shared card, although presentation attacks must still be considered.
Centralized reporting	Attendance events can feed institutional dashboards, course reports, or authorized analytics.
Human-review workflow	Low-confidence or failed matches can be placed in a review queue rather than automatically becoming absences.
Scalability with constraints	The same architecture can serve multiple rooms, but compute, network bandwidth, camera quality, and privacy controls must scale with deployment.

Table 3 connects the technical findings to institutional deployment. The main implication is that a reliable attendance system requires more than selecting a high-accuracy model: camera placement, threshold calibration, enrollment quality, duplicate suppression, privacy protection, and human oversight are all part of the final system. These controls reduce the risk that a technically correct recognition component produces an incorrect administrative attendance record.

B. Expected Error Behavior

The proposed threshold mechanism creates a predictable trade-off. When the threshold is too permissive, the system may accept visually similar but incorrect identities; when it is too strict, genuine

students may be rejected because of pose, illumination, occlusion, or image quality. The appropriate operating point therefore depends on institutional priorities. For attendance, it is generally preferable to route uncertain cases to human review rather than optimize only for the highest raw acceptance rate.

Image quality is a central result of the evidence synthesis. NIST reports show that false-negative behavior is strongly dependent on capture quality and that demographic differentials can emerge across algorithms and conditions [7]. Consequently, improving classroom lighting, camera angle, face size, and exposure may be as important as changing the recognition model.

V. DISCUSSION

The main finding of this study is that smart attendance should be understood as an integrated socio-technical system, not as a single recognition algorithm. A highly accurate embedding model can still produce poor attendance records if the detector misses seated faces, the camera is mounted too high, the enrollment gallery contains low-quality images, or the database marks duplicate observations as separate events. Conversely, a carefully engineered workflow can reduce the practical effect of occasional recognition failures by using confidence thresholds and human review.

For universities, the strongest practical case is in large lectures, laboratories, examination check-in, and repeated sessions where manual attendance imposes cumulative administrative cost. In schools, the potential convenience must be balanced against the heightened sensitivity of biometric processing involving minors. Institutions should therefore avoid treating deployment as a purely technical procurement decision. Governance, parental or participant information where applicable, retention limits, security controls, and alternative attendance procedures should be defined before collection begins.

The comparison of classical and deep approaches also suggests that a simple Haar Cascade plus raw-image matching demonstration is useful for teaching computer vision, but it is not an adequate model for a robust institutional system. Haar cascades can serve as a lightweight detector, while identity recognition should rely on a validated embedding model. FaceNet and ArcFace provide conceptually appropriate mechanisms because identity can be represented as a compact vector and compared through a calibrated metric [3], [4].

Performance claims require context. The 97–99% benchmark results reported by influential face-recognition studies describe particular datasets and protocols, not guaranteed classroom accuracy. Likewise, the strong classroom results reported by Mekala et al. [6] are encouraging but remain dependent on their dataset, camera configuration, preprocessing, and model choices. A new institution must therefore validate its own end-to-end system under its own lighting, seating, camera, and population conditions.

Fairness cannot be reduced to a single overall accuracy number. NIST's demographic evaluations demonstrate that false match and false non-match rates may vary across demographic groups and algorithms [7]. A responsible institution should therefore examine subgroup error rates where such auditing is legally and ethically justified, investigate capture-quality differences, and avoid punitive decisions based solely on an automated non-match.

Privacy-by-design changes the architecture itself. If the operational objective is attendance, the system does not need indefinite storage of classroom video. A preferable design converts a face to an embedding, makes the recognition decision, records the minimum attendance event, and discards transient frames unless a narrowly defined review process requires short retention. Embeddings should be encrypted, access should be role-based, and deletion should follow enrollment status and retention policy.

Presentation attacks are another practical concern. A naive camera system may be deceived by a photograph or replayed video. Production deployment should therefore include liveness or presentation-attack detection, especially where attendance has academic or financial consequences. However, liveness mechanisms also introduce new error modes and should themselves be tested rather than assumed to be infallible.

Finally, the system should preserve procedural dignity. A student who is not recognized should not be publicly labeled as suspicious or absent. The interface can simply request a second capture or route the case to a private manual confirmation. Human-centered design is therefore not an optional interface improvement; it is part of system reliability because it determines how errors are corrected.

VI. CONCLUSION

Face recognition can transform attendance from a repetitive manual procedure into an automated, timestamped, and auditable institutional workflow. The technical foundation is mature: face detection localizes the subject, deep networks generate discriminative embeddings, similarity measures compare live and enrolled representations, and threshold logic converts similarity into an identity decision. Published evidence supports the use of deep-learning approaches over older appearance-based methods for variable educational environments, while recent classroom studies demonstrate practical feasibility.

The central conclusion, however, is that recognition accuracy is only one requirement. Educational deployment must also address image quality, false acceptance and rejection, demographic differentials, spoofing, template security, consent and transparency, data minimization, and the right to human correction. The most defensible design is therefore an assistive smart-attendance system: automation handles routine high-confidence cases, while uncertain cases remain reviewable by authorized staff. Under this model, AI reduces administrative friction without turning a probabilistic biometric score into an unquestionable institutional judgment.

A. Future Work

Future research should implement the proposed architecture in a controlled institutional pilot and report end-to-end attendance performance rather than only face-verification accuracy. A useful study would compare FaceNet- and ArcFace-style embeddings under identical classroom conditions, using the same detector, enrollment gallery, and test sessions.

Further experiments should examine camera placement, distance, illumination, occlusion, and class size. Performance should be measured not only by accuracy and F1-score but also by FAR, FRR, recognition latency, throughput, and the proportion of cases requiring human review.

Privacy-preserving directions include on-device or edge inference, encrypted template storage, short-lived frame buffers, cancellable biometric templates, and federated or privacy-aware model improvement. Recent work on lightweight privacy-preserving attendance suggests that resource-constrained edge deployment is an increasingly relevant direction.

Another priority is presentation-attack detection and multi-frame temporal validation. A future system could require consistency across several consecutive frames before recording attendance, thereby reducing accidental matches and improving robustness to brief occlusion.

Finally, future studies should evaluate user acceptance. Students, teachers, administrators, and data-protection stakeholders may value convenience differently. Technical performance should therefore be studied together with perceived fairness, transparency, trust, and willingness to use a biometric attendance option.

REFERENCES

[1] Viola, P., & Jones, M. (2001). Rapid object detection using a boosted cascade of simple features. Proceedings of the IEEE Conference on Computer Vision and Pattern Recognition, I-511–I-518. https://doi.org/10.1109/CVPR.2001.990517

[2] Taigman, Y., Yang, M., Ranzato, M., & Wolf, L. (2014). DeepFace: Closing the gap to human-level performance in face verification. Proceedings of the IEEE Conference on Computer Vision and Pattern Recognition, 1701–1708. https://doi.org/10.1109/CVPR.2014.220
[3] Schroff, F., Kalenichenko, D., & Philbin, J. (2015). FaceNet: A unified embedding for face recognition and clustering. Proceedings of the IEEE Conference on Computer Vision and Pattern Recognition, 815–823. https://doi.org/10.1109/CVPR.2015.7298682
[4] Deng, J., Guo, J., Xue, N., & Zafeiriou, S. (2019). ArcFace: Additive angular margin loss for deep face recognition. Proceedings of the IEEE/CVF Conference on Computer Vision and Pattern Recognition, 4690–4699. https://doi.org/10.1109/CVPR.2019.00482
[5] Sutabri, T., et al. (2023). Student attendance with face recognition (LBPH or CNN): Systematic literature review. Procedia Computer Science, 216, 31–38. https://doi.org/10.1016/j.procs.2022.12.108
[6] Mekala, S., et al. (2025). Enhancing classroom attendance systems with face recognition through CCTV using deep learning. Procedia Computer Science, 258, 3031–3041. https://doi.org/10.1016/j.procs.2025.04.561
[7] Grother, P., Ngan, M., & Hanaoka, K. (2019). Face Recognition Vendor Test Part 3: Demographic effects (NISTIR 8280). National Institute of Standards and Technology. https://doi.org/10.6028/NIST.IR.8280
[8] Agustiyar, A., Isnanto, R. R., & Widodo, C. E. (2026). Face recognition for attendance systems: A bibliometric review of research trends and opportunities. Jurnal Sisfokom (Sistem Informasi dan Komputer), 15(1). https://doi.org/10.32736/sisfokom.v15i01.2529
[9] Shtino, V. B., Muça, M. & Bushati, S. (2024). Machine Learning Integration for Precise Facial Micro-Expression Recognition. Journal of Computer Science, *20*(11), 1545-1558.https://doi.org/10.3844/jcssp.2024.1545.1558
[10] Bakiasi, V., Kapçiu, R., Zeqo, E., Bushati, S., Bushi, F., Bame, O., & Lamaj, B. (2025). Real-Time Micro-Expression Recognition Using YOLOv8 and FER2013 Dataset. Journal of Information Systems Engineering and Management, 10(18s). https://doi.org/10.52783/jisem.v10i18s.2883
[11] (Shtino), V. B. (2026). Enhancing Facial Expression and Micro-Expression Recognition Through Hybrid Dimensionality Reduction and Machine Learning Classification. International Journal of Research and Innovation in Applied Science, 11(7), https://doi.org/10.51584/IJRIAS.2026.11070148
[12] Abiodun, E. O., Abiodun, O. I., Alawida, M., Abu Shawar, B., & Mehmood, A. (2026). LaED: A novel lightweight, edge-aware and explainable deep learning model for privacy-preserving facial attendance tracking in resource-constrained educational environments. Scientific Reports, 16, 15215. https://doi.org/10.1038/s41598-026-42051-8

8th International Conference on Engineering, Natural and Social Sciences

September 06-07, 2026: Konya, Turkey

© 2026 Published by All Sciences Academy

https://www.icensos.com/

Fault Detection and Load Prediction in a Push-Pull Converter Using Machine Learning

Serhat Küçükdermenci *

Department of Electrical-Electronics Engineering, Balikesir University, Türkiye
(ORCID: https://orcid.org/0000-0002-6421-7773)

*(kucukdermenci@balikesir.edu.tr) Email of the corresponding author

Abstract **–** This paper investigates a simulation-driven monitoring workflow for a push-pull DC-DC converter by combining converter modeling, data communication, and machine learning analysis. Electrical responses are produced in Simulink under different load levels, transient cases, noise conditions, and fault-related operating states. The exported signals are then converted into a structured dataset containing voltage, current, power, duty-cycle, efficiency, and class-label information. To represent a practical monitoring path, the study also considers MQTT topic-based data exchange and Node-RED visualization, while Python/Jupyter is used for preprocessing, model training, and evaluation. Random Forest models are applied to classify converter states and estimate load-related quantities from the generated tabular features. The classification results show clear separation among normal operation, overload, voltage sag, switching stress, and low-efficiency cases, and the regression results indicate low error in load-power prediction. The feature-importance analysis further shows that the model decisions are mainly shaped by physically meaningful converter variables rather than unrelated dataset ordering. The proposed workflow is not intended as final hardware validation; instead, it demonstrates how simulation outputs, communication-layer organization, and machine learning tools can be linked for early-stage intelligent monitoring of power electronic converters. Future work will extend the approach with measured converter data, hardware-in-the-loop testing, and additional converter topologies.

Keywords –Push-pull converter; DC-DC converter; fault detection; load power prediction; machine learning; MQTT; Node-RED; Simulink; Random Forest

I. INTRODUCTION

DC-DC converters are key interface circuits in renewable energy systems, battery-powered equipment, industrial power supplies, and embedded electronic platforms. In such systems, abnormal operating conditions such as overload, voltage sag, switching stress, and efficiency degradation can reduce power quality and may lead to component stress if they are not detected early. For this reason, fault diagnosis and fault-tolerant operation of DC-DC converters have become important research topics in power electronics and DC microgrid applications [1]-[3].

Recent studies show that data-driven methods can support converter monitoring by learning diagnostic patterns from voltage, current, power, and transient signal features. Deep learning, random forest classification, observer-based diagnosis, autoregressive modeling, digital-twin-assisted diagnosis, and noise-robust feature extraction have all been investigated for power-electronic converter fault detection [4]-[13]. These works indicate that machine learning can be useful when the monitored signals are organized into a consistent dataset and when the operating scenarios cover both normal and faulty converter behavior.

Alongside the diagnostic model, the data acquisition and communication workflow is also important. Python/Jupyter environments and scikit-learn provide a reproducible basis for preprocessing, model training, and performance visualization [14]-[17]. In IoT-oriented monitoring systems, MQTT offers a

lightweight publish/subscribe communication structure, while Node-RED provides a practical flow-based environment for routing, displaying, and managing real-time data streams [18]-[22]. Simulink and MATLAB further support model-based simulation and analysis of power-electronic systems before hardware implementation [23], [24].

Previous simulation- and interface-oriented engineering studies also provide a useful background for the present workflow. Simulation-based battery SOH/RUL prediction with MQTT data streaming and LSTM networks shows how model-based signal generation, communication, and machine learning can be combined for condition monitoring [25]. Similarly, smart energy monitoring, MATLAB/Simulink-based vehicle dynamics simulation, and FEM-based sensor analysis demonstrate the role of simulation environments in producing interpretable engineering data before hardware deployment [26]-[28]. Related LabVIEW, Proteus, Arduino, Outseal, and Modbus-based control studies further illustrate how real-time interfaces, co-simulation, PID control, feedback visualization, and communication layers can support practical monitoring and control applications [29]- [36]. Building on this simulation-centered and interface-oriented background, the present study adapts a comparable workflow to a push-pull DC-DC converter by combining Simulink-derived converter signals, MQTT/Node-RED-style data exchange, and Python/Jupyter-based machine learning for fault detection and load prediction.

Based on this background, this paper proposes a simulation-based workflow for machine learning-based fault detection and load power prediction in an MQTT-enabled push-pull DC-DC converter. The main contributions are as follows: a Simulink converter model is used to generate representative electrical signals; the generated data are reorganized and augmented under different load, noise, transient, and fault conditions; MQTT and Node-RED are used to describe the monitoring data flow; and Random Forest-based classification and regression models are evaluated for converter state detection and load power estimation. The prediction errors are interpreted using standard regression metrics such as MAE and RMSE [37].

II. Materials and Method

A. Push-Pull Converter Simulation Model

The study is built around a Simulink model of a push-pull DC-DC power converter. The model represents the input source, switching stage, high-frequency transformer, rectifier-filter section, and load-side electrical response. The overall research workflow is summarized in Fig. 1, while the battery-input interface and the switching/transformer region are shown in Fig. 2a and Fig. 2b, respectively. The simplified block-level structure is given in Fig. 2c. The simulation environment is used to obtain voltage, current, duty-cycle, power, and efficiency-related signals under controlled operating conditions.

Two baseline converter operating cases are considered from the available simulation outputs, corresponding to light and high load operation. These baseline signals are then reorganized into a common analysis-ready structure so that the same feature set can be used for classification and regression. This approach keeps the electrical origin of the data traceable while allowing the machine learning pipeline to test a wider range of operating conditions than the original raw files alone.

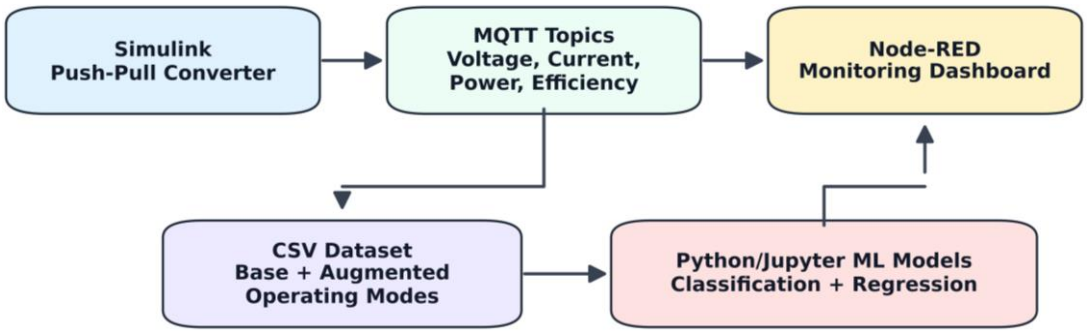

Fig. 1 Overall workflow of the Simulink-MQTT-Node-RED-Python/Jupyter pipeline

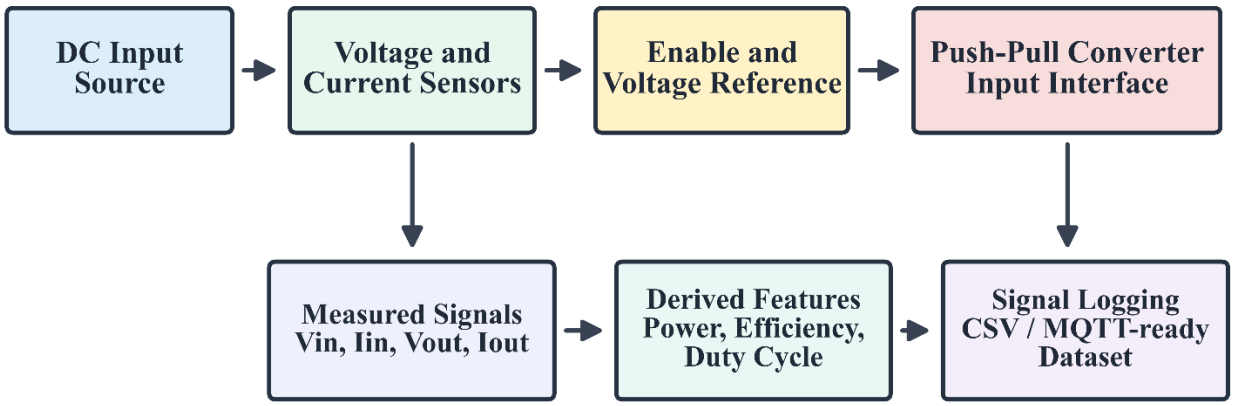

Fig. 2a. DC input, measurement, reference, and signal logging interface of the push-pull converter.

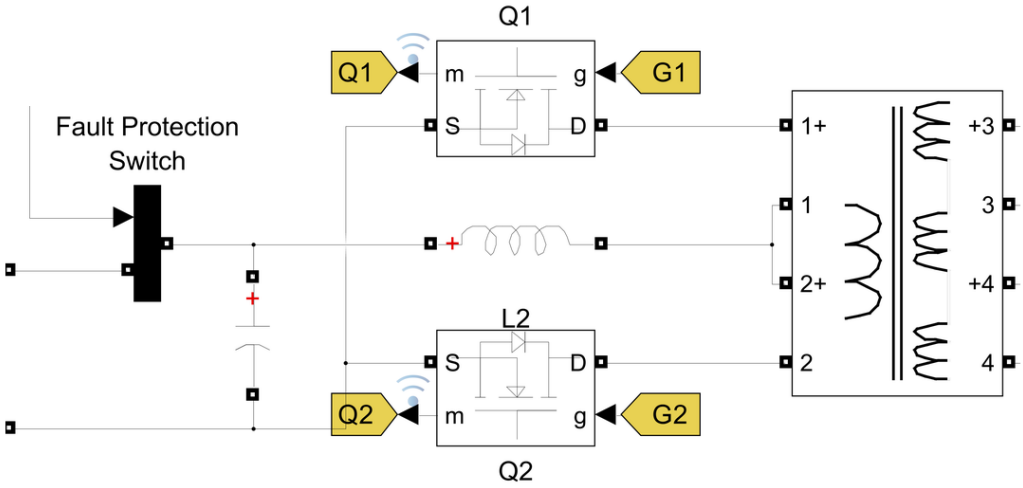

Fig. 2b. Simulink switching, protection, and transformer section of the push-pull converter

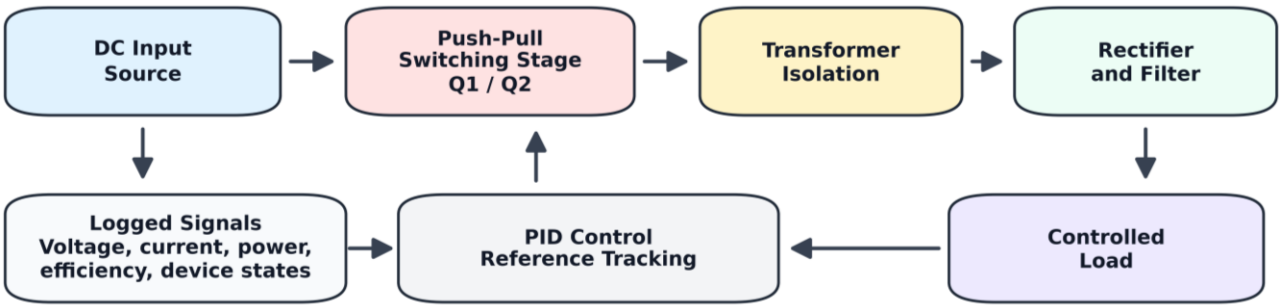

Fig. 2c. Simplified Simulink block structure of the converter and monitoring workflow

B. *MQTT and Node-RED Monitoring Workflow*

To represent an IoT-oriented monitoring architecture, the converter signals are mapped to an MQTT-based data exchange workflow. In this structure, converter variables are published or consumed through topic names associated with measured electrical quantities and control-related variables. The topic organization is listed in Table 1. Node-RED is used as a flow-based layer for routing, displaying, and supervising the converter data, as illustrated in Fig. 3.

The MQTT/Node-RED part of the workflow is not treated as a separate diagnostic model; instead, it provides the communication and visualization layer around the simulated converter data. This makes the proposed workflow closer to a real monitoring scenario, where data are not only stored in files but are also structured as time-varying signals that can be routed to dashboards, data loggers, and downstream analytics.

Table 1. MQTT topics and monitored converter variables

MQTT topic	Role in the workflow	Converter variable	Unit / use
ps/OutputVoltage	Command to Simulink	Reference output voltage	V
ps/Enabled	Command to Simulink	Converter enable signal	0/1
ps/state/OutputVoltage	Published from Simulink	Output voltage	V
ps/state/OutputCurrent	Published from Simulink	Output current	A
ps/state/InputVoltage	Published from Simulink	Input voltage	V
ps/state/InputCurrent	Published from Simulink	Input current	A
ps/state/InputPower	Published from Simulink	Input power	W
ps/state/OutputPower	Published from Simulink	Output power	W
ps/state/Efficiency	Published from Simulink	Converter efficiency	%
ps/state/Load	Published from Simulink	Relative load level	% of rated power

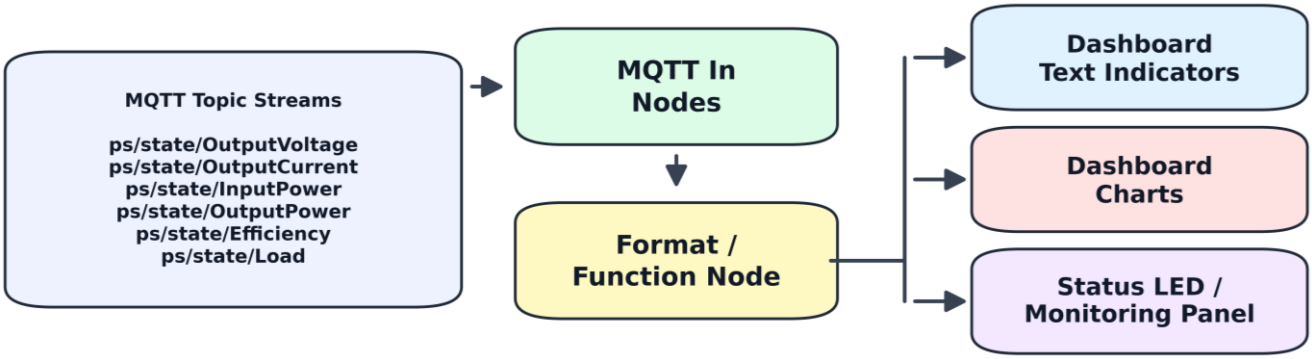

Fig. 3 Node-RED/MQTT monitoring flow used for converter signal routing and visualization

C. *Dataset Generation and Augmentation*

The analysis-ready dataset is generated by combining the exported converter signals and deriving additional features related to load power, efficiency behavior, and operating condition. To improve scenario coverage, controlled augmentation is applied using five load-scale levels, three noise levels, four transient regimes, and five fault labels. The resulting design produces balanced operating cases for normal operation, overload, voltage sag, switching stress, and low-efficiency behavior. The augmentation structure is summarized in Table 2.

Table 2. Augmented dataset design

Design factor	Levels / values	Role in dataset generation
Power scenario	500 W and 2 kW	Baseline converter operating classes
Load scaling	0.55, 0.75, 1.00, 1.25, and 1.50	Light-load, nominal-load, and overload-like operating ranges
Measurement noise	0, 0.005, and 0.015	Sensor and communication uncertainty
Transient condition	Steady state, startup ramp, step load, and temporary voltage sag	Dynamic operating behavior
Fault class	Normal, overload, voltage sag, switch stress, and low efficiency	Target labels for fault classification
Samples per configuration	900	Balanced sampling across scenario combinations
Total augmented samples	540,000	Simulation-derived dataset used for ML training and testing

The final augmented dataset contains 540,000 samples and 26 variables. Each class is represented with the same number of samples so that the classification models are not biased toward a dominant operating

condition. Representative augmented converter signals are shown in Fig. 4. Although the augmented data improve coverage for machine learning evaluation, the dataset remains simulation-derived; therefore, the reported results should be interpreted as controlled validation rather than field-hardware generalization.

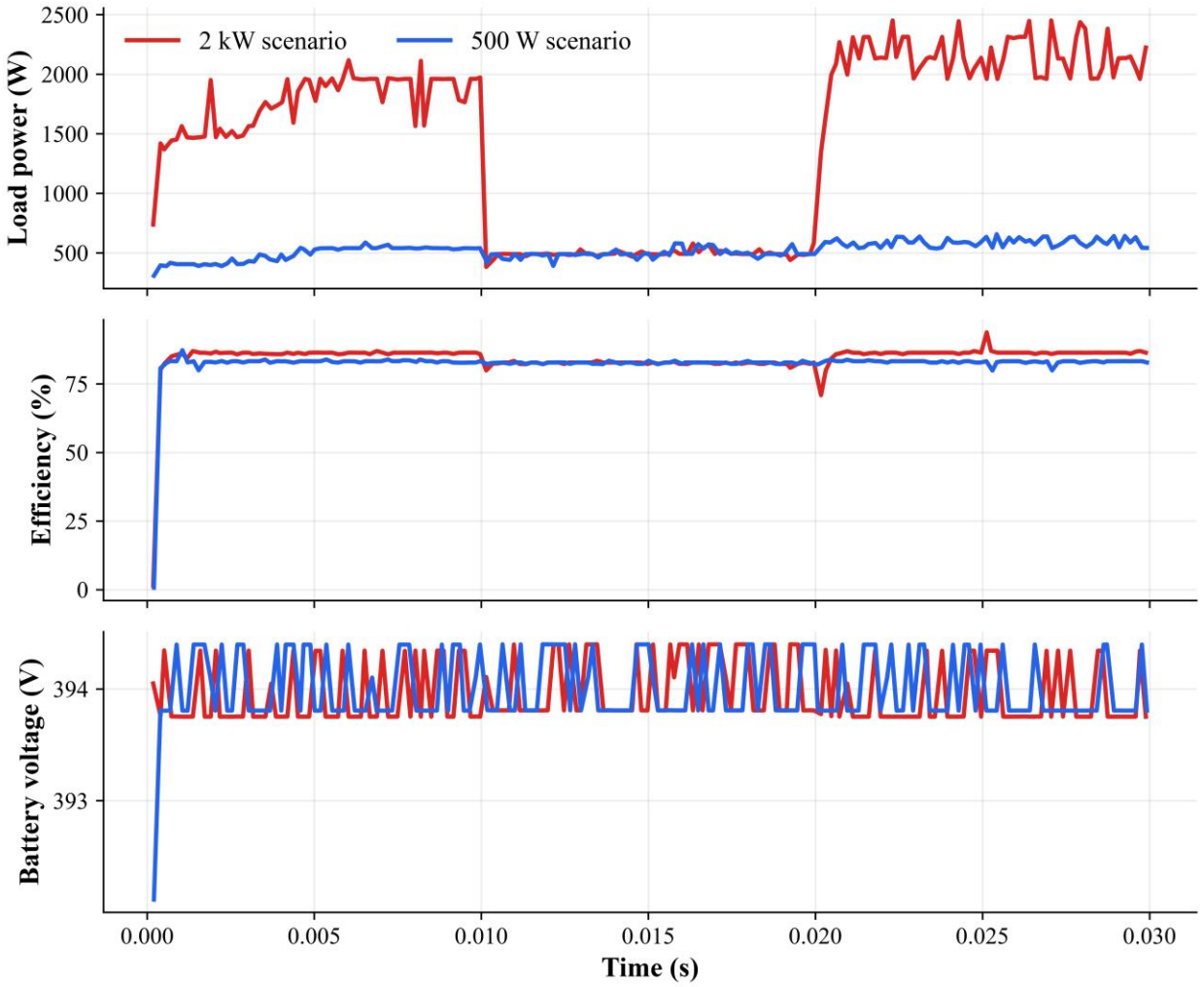

Fig. 4 Representative augmented converter signals under different operating conditions

D. *Machine Learning Procedure*

The machine learning stage is implemented in Python/Jupyter using tabular features extracted from the converter dataset. The workflow includes data loading, feature selection, train-test splitting, model training, prediction, metric calculation, and visualization. Random Forest models are selected for both classification and regression because they perform well with nonlinear tabular engineering data and provide feature importance values that are useful for interpretation.

Three classification targets are considered: power level, efficiency class, and fault label. In addition, regression models are trained to estimate load power, efficiency signal, and load scale. Classification performance is evaluated using accuracy and macro-averaged F1-score, while regression performance is evaluated using MAE, RMSE, and R^2. The resulting model performance is reported in Table 3, and the main classification, regression, and feature-importance outputs are discussed in the Results section.

III. RESULTS

The generated dataset was first evaluated by examining the signal behavior obtained from the augmented converter scenarios. As shown in Fig. 4, the 500 W and 2 kW operating cases produce clearly different load-power profiles, while the efficiency and battery-voltage signals remain within physically meaningful

ranges. The transient changes, noise components, and fault-related variations introduced during augmentation make the dataset more diverse than the original simulation exports, without removing its connection to the converter model.

The quantitative model results are summarized in Table 3. For power-level classification, the Random Forest model achieved an accuracy of 0.9999 and a macro F1-score of 0.9999. The efficiency-class model reached 1.0000 for both metrics, while the fault-class model obtained an accuracy and macro F1-score of 0.9995. These values indicate that the selected features carry enough information to distinguish the generated operating categories under the controlled test conditions.

Table 3. Machine learning model performance

Modeling task	Target variable	Accuracy	Macro F1	MAE	RMSE	R^2
Classification	Power level	0.9999	0.9999	-	-	-
Classification	Efficiency class	1.0000	1.0000	-	-	-
Classification	Fault class	0.9995	0.9995	-	-	-
Regression	Load power	-	-	5.3637	14.1066	0.9998
Regression	Efficiency	-	-	0.0392	0.2404	0.9993
Regression	Load scale	-	-	0.0027	0.0198	0.9966

The fault-class confusion matrix in Fig. 5 gives a more detailed view of the classification behavior. Most samples are located on the main diagonal, showing that the model assigned nearly all test cases to their correct classes. Only a small number of overload and switch-stress samples were confused with neighboring operating states. This pattern is reasonable because these conditions can produce partially similar changes in current, load power, and efficiency-related variables.

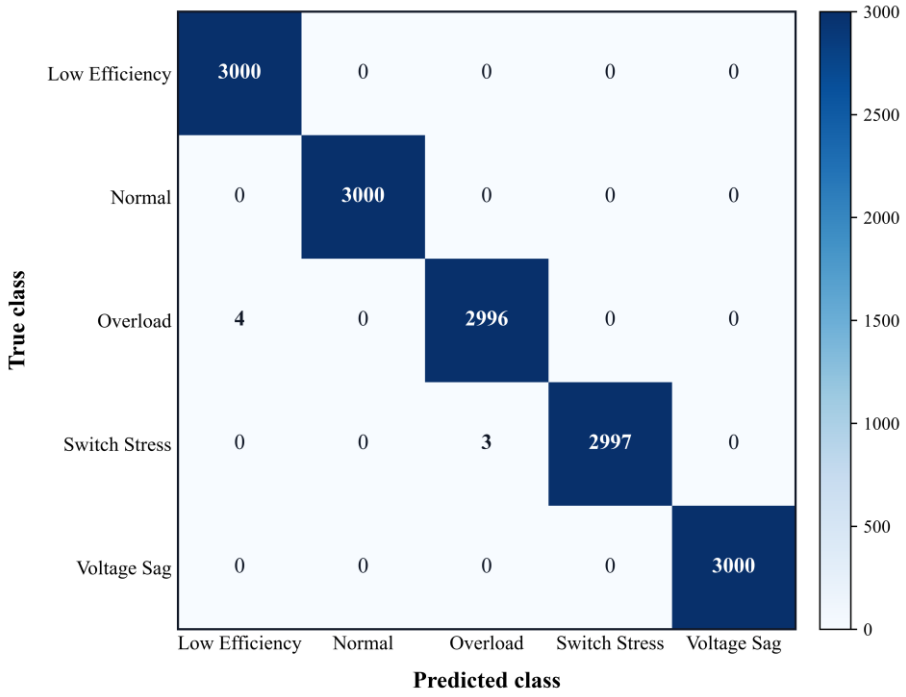

Fig. 5 Fault-label classification confusion matrix for the generated test data

For the regression task, the model estimated load power with a mean absolute error of 5.36 W, a root mean square error of 14.11 W, and a coefficient of determination (R^2) of 0.9998. The actual-versus-predicted plot in Fig. 6 shows that the predicted values follow the reference values closely over the tested power range. Additional regression outputs for efficiency and load scale also produced low errors, which supports the consistency of the feature set used for the learning process.

The feature-importance results in Fig. 7 further clarify how the model reached its decisions. Load-related power and current variables, battery-side measurements, and time-dependent signal information were among the most influential inputs. This suggests that the model mainly responded to converter-relevant electrical behavior rather than to incidental ordering effects in the dataset. Overall, the results show that the proposed simulation-derived dataset is suitable for demonstrating machine learning-based converter monitoring, while broader validation would still require measured hardware data.

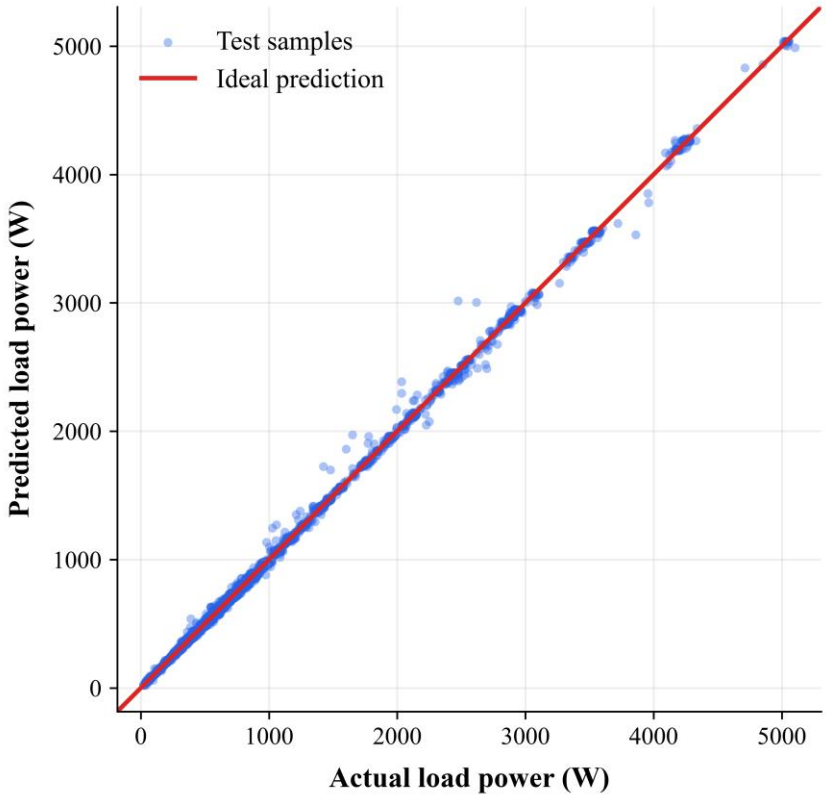

Fig. 6 Actual versus predicted load-power regression result

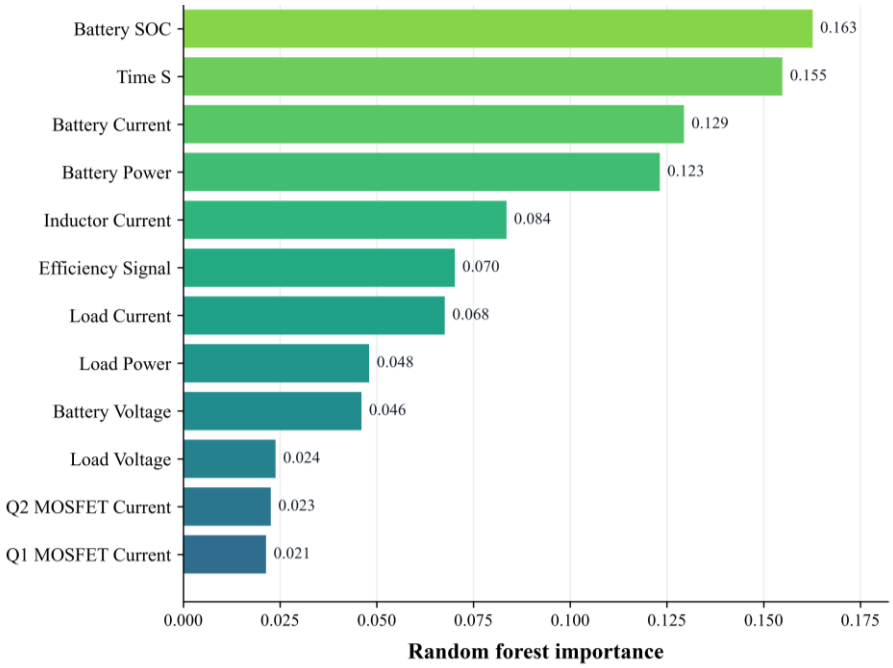

Fig. 7 Random Forest feature importance for converter-state interpretation

IV. DISCUSSION

The results suggest that the proposed workflow can translate simulated converter behavior into a useful machine learning dataset. The selected variables are not arbitrary indicators; they are directly connected to the electrical operation of the converter, including voltage, current, duty cycle, load power, and efficiency. This helps explain why the Random Forest models separated the considered operating modes with high accuracy and produced low regression errors for load-power estimation.

The communication layer is also important for the interpretation of the study. MQTT and Node-RED do not change the converter physics, but they define how the simulated signals can be organized as a monitoring stream rather than as isolated output files. In this sense, the workflow represents a bridge between model-based simulation and an IoT-style supervision structure. Such a structure may be useful in early-stage converter monitoring studies, especially when hardware tests are not yet available or when different operating scenarios must be generated repeatedly.

The high numerical performance should still be read with caution. The dataset was produced from simulation outputs and extended through controlled augmentation, so the test conditions are more regular than measurements from a physical converter. Real hardware may introduce switching noise, sensor offsets, thermal effects, communication delay, parameter drift, and fault combinations that are not fully represented in the present dataset. Therefore, the results should be considered as evidence for the feasibility of the workflow, not as a final validation of field performance.

Future work should move the workflow toward experimental validation. Hardware-in-the-loop tests, measured converter signals, additional DC-DC converter topologies, online data streaming, and robustness tests under unseen fault conditions would provide a stronger basis for evaluating whether the same machine learning structure can generalize beyond the controlled simulation environment.

V. CONCLUSION

This paper presented a simulation-based workflow for fault detection and load power prediction in a push-pull DC-DC converter. The proposed structure combines Simulink-based converter modeling, MQTT/Node-RED-oriented data exchange, controlled dataset augmentation, and Python/Jupyter-based machine learning analysis. Random Forest models were used for both classification and regression tasks because of their suitability for tabular engineering data and interpretable feature-importance outputs.

The results showed that the generated dataset can support accurate separation of normal operation, overload, voltage sag, switching stress, and low-efficiency conditions, while the regression model estimated load power with low prediction error. These findings suggest that the workflow can be useful for early-stage intelligent monitoring studies and educational prototyping. Future work should validate the approach with hardware-in-the-loop experiments, measured converter signals, additional converter topologies, and real-time communication effects.

REFERENCES

[1] G. K. K. Kumar and E. Devaraj, “Review on fault-diagnosis and fault-tolerance for DC-DC converters,” *IET Power Electronics*, vol. 13, no. 1, pp. 1–13, 2020, doi: 10.1049/iet-pel.2019.0672.

[2] S. S. Khan, “A Comprehensive Review of Fault Diagnosis and Tolerant Control in DC-DC Converters for DC Microgrids,” *IEEE Access*, vol. 9, pp. 80100–80127, 2021, doi: 10.1109/ACCESS.2021.3083721.

[3] A. Moradzadeh, B. Mohammadi-Ivatloo, K. Pourhossein, and A. Anvari-Moghaddam, “Data Mining Applications to Fault Diagnosis in Power Electronic Systems: A Systematic Review,” *IEEE Transactions on Power Electronics*, 2022, doi: 10.1109/TPEL.2021.3131293.

[4] L. Kou, “Fault Diagnosis for Power Electronics Converters based on Deep Feedforward Network and Wavelet Compression,” *Electric Power Systems Research*, vol. 185, p. 106370, 2020, doi: 10.1016/j.epsr.2020.106370.

[5] L. Kou, “Data-driven design of fault diagnosis for three-phase PWM rectifier using random forests technique with transient synthetic features,” *IET Power Electronics*, vol. 13, no. 16, pp. 3571–3579, 2020, doi: 10.1049/iet-pel.2020.0226.

[6] L. Kou, “Fault Diagnosis for Power Converters based on Random Forests and Feature Transformation,” in *2020 IEEE 9th International Power Electronics and Motion Control Conference*, 2020, pp. 1821–1826. doi: 10.1109/IPEMC-ECCEAsia48364.2020.9367970.

[7] W.-C. Wang, “An Intelligent Fault Diagnosis Method for Open-Circuit Faults in Power-Electronics Energy Conversion System,” *IEEE Access*, vol. 8, pp. 221039–221050, 2020, doi: 10.1109/ACCESS.2020.3043796.

[8] S. Zhuo, “An Observer-Based Switch Open-Circuit Fault Diagnosis of DC-DC Converter for Fuel Cell Application,” *IEEE Transactions on Industry Applications*, vol. 56, no. 3, pp. 3159–3167, 2020, doi: 10.1109/TIA.2020.2978752.
[9] R. Shan, J. Yang, and S. Huang, “Open-circuit fault diagnosis of three-phase PWM rectifier circuits based on transient characteristics and random forest classification,” *Journal of Power Electronics*, vol. 24, no. 1, pp. 130–139, 2024, doi: 10.1007/s43236-023-00704-1.
[10] R. Diversi, L. Sandrolini, M. Simonazzi, and N. Speciale, “Diagnostics on Power Electronics Converters by Means of Autoregressive Modelling,” *Electronics*, vol. 13, no. 15, p. 3083, 2024, doi: 10.3390/electronics13153083.
[11] F. Bento and A. J. M. Cardoso, “Diagnosis of DC-DC Converter Semiconductor Faults Based on the Second-Order Derivative of the Converter Input Current,” *Electronics*, vol. 13, no. 18, p. 3778, 2024, doi: 10.3390/electronics13183778.
[12] P. J. Hueros-Barrios, “Digital Twin Approach for Fault Diagnosis in Photovoltaic Plant DC-DC Converters,” *Sensors*, vol. 25, no. 14, p. 4323, 2025, doi: 10.3390/s25144323.
[13] Y. Jiang and Z. Lu, “A Feature Extraction Method for Parameter Fault Diagnosis of DC-DC Converters Under Strong Noise and Small Sample Conditions,” *Eksploatacja i Niezawodnosc - Maintenance and Reliability*, 2025, doi: 10.17531/ein/207882.
[14] L. Breiman, “Random Forests,” *Machine Learning*, vol. 45, pp. 5–32, 2001, doi: 10.1023/A:1010933404324.
[15] F. Pedregosa, “Scikit-learn: Machine Learning in Python,” *Journal of Machine Learning Research*, vol. 12, pp. 2825–2830, 2011.
[16] J. D. Hunter, “Matplotlib: A 2D Graphics Environment,” *Computing in Science & Engineering*, vol. 9, no. 3, pp. 90–95, 2007, doi: 10.1109/MCSE.2007.55.
[17] T. Kluyver, “Jupyter Notebooks - a publishing format for reproducible computational workflows,” in *Positioning and Power in Academic Publishing: Players, Agents and Agendas*, IOS Press, 2016, pp. 87–90. doi: 10.3233/978-1-61499-649-1-87.
[18] A. Banks, E. Briggs, K. Borgendale, and R. Gupta, “MQTT Version 5.0,” OASIS Standard. Accessed: Sep. 02, 2026. [Online]. Available: https://docs.oasis-open.org/mqtt/mqtt/v5.0/mqtt-v5.0.html
[19] OpenJS Foundation, “Node-RED: Low-code programming for event-driven applications,” Node-RED. Accessed: Sep. 02, 2026. [Online]. Available: https://nodered.org/
[20] A. M. Damayanti, Sarifudin, and S. Nor, “An IoT-Based Implementation with Node-RED for Real-Time Monitoring and Early Warning of Laboratory Energy Consumption via Telegram,” *Emitor*, vol. 26, no. 1, pp. 90–100, 2026, doi: 10.23917/emitor.v26i1.16040.
[21] H. J. Khasawneh, “Industrial IIoT-based submetering solution for real-time energy monitoring,” *Discover Internet of Things*, vol. 5, no. 1, p. 15, 2025, doi: 10.1007/s43926-025-00110-y.
[22] C. Y. Chen, “Web-based Internet of Things on environmental and lighting control and monitoring system using Node-RED, MQTT and Modbus communications within embedded Linux platform,” *Internet of Things*, vol. 27, p. 101305, 2024, doi: 10.1016/j.iot.2024.101305.
[23] MathWorks, “Simulink - Simulation and Model-Based Design,” MathWorks. Accessed: Sep. 02, 2026. [Online]. Available: https://www.mathworks.com/products/simulink.html
[24] MathWorks, “MATLAB,” MathWorks. Accessed: Sep. 02, 2026. [Online]. Available: https://www.mathworks.com/products/matlab.html
[25] S. Küçükdermenci, “Simulation-Based Battery SOH and RUL Prediction with MQTT Data Streaming and LSTM Networks,” in *Trend and Advanced Studies in Engineering*, All Sciences Academy, 2026, pp. 165–179.
[26] S. Küçükdermenci, “Simulation-Based Smart Energy Monitoring System,” in *4th International Conference on Recent Academic Studies*, 2025, pp. 395–401. [Online]. Available: https://avesis.balikesir.edu.tr/kucukdermenci/yayinlar
[27] S. Küçükdermenci, “Simulation of Longitudinal Vehicle Dynamics under FTP-75 Drive Cycle Using MATLAB/Simulink,” *International Journal of Advanced Natural Sciences and Engineering Researches*, vol. 9, no. 9, pp. 37–47, Sep. 2025.
[28] S. Küçükdermenci, “FEM-Based Numerical Analysis of a Shielded Interdigitated Capacitive Humidity Sensor,” *International Journal of Advanced Natural Sciences and Engineering Researches*, vol. 9, no. 6, pp. 311–320, Jun. 2025.
[29] S. Küçükdermenci, “Modeling and Simulation of DC Motor Speed PID Control Using Outseal with LabVIEW Integration,” *International Journal of Advanced Natural Sciences and Engineering Researches*, vol. 9, no. 10, pp. 171–179, Oct. 2025.
[30] S. Küçükdermenci, “PID control of DC motor position and speed in a LabVIEW-Arduino framework,” in *6th International Conference on Engineering and Applied Natural Sciences*, 2025, pp. 301–308.
[31] S. Küçükdermenci, “Real-time PID-based DC motor position control interface using LabVIEW and Proteus co-simulation,” in *1st International Conference on Pioneer and Academic Research*, 2025, pp. 274–281.
[32] S. Küçükdermenci, “Integration of Proteus and LabVIEW for open-loop DC motor control with position and speed feedback,” in *3rd International Conference on Contemporary Academic Research*, 2024, pp. 975–980.
[33] S. Küçükdermenci, “Real-time speed control system: PID tuning and visualization with Proteus and LabVIEW,” in *3rd International Conference on Contemporary Academic Research*, 2024, pp. 981–987.
[34] S. Küçükdermenci, “Modbus-based PID position control simulation using Outseal Nano and LabVIEW DSC Toolkit,” in *3rd International Conference on Pioneer and Innovative Studies*, Konya, Turkey: All Sciences Academy, Oct. 2025, pp. 423–429. [Online]. Available: https://as-proceeding.com/index.php/icpis/home

[35] S. Küçükdermenci, “Implementation of deadband-enhanced PID position control using LabVIEW and Arduino for DC motor systems,” in *7th International Conference on Innovative Academic Studies*, Konya, Turkey: All Sciences Academy, Sep. 2025, pp. 479–485.
[36] S. Küçükdermenci, “Design of a Hybrid PID-Feedforward Control System for Smart Greenhouse,” in *2nd International Conference on Modern and Advanced Research*, 2025, pp. 436–441. [Online]. Available: https://avesis.balikesir.edu.tr/kucukdermenci/yayinlar
[37] T. Chai and R. R. Draxler, “Root mean square error (RMSE) or mean absolute error (MAE)? Arguments against avoiding RMSE in the literature,” *Geoscientific Model Development*, vol. 7, pp. 1247–1250, 2014, doi: 10.5194/gmd-7-1247-2014.